Abdelhamid Elgazzar

The Pathophysiologic Basis of Nuclear Medicine

Second Edition

Springer

Abdelhamid H. Elgazzar (Ed.) The Pathophysiologic Basis of Nuclear Medicine
Second Edition

Abdelhamid H. Elgazzar (Ed.)

The Pathophysiologic Basis of Nuclear Medicine

Second Edition

With 325 Figures in 676 Parts and 87 Tables

Springer

Abdelhamid H. Elgazzar, MD, FCAP
Diplomate, American Board of Pathology
Diplomate, American Board of Nuclear Medicine
Professor and Chairman
Department of Nuclear Medicine
Faculty of Medicine Kuwait University Health Sciences Center
PO Box 24923, 13110 Safat, Kuwait

ISBN 3-540-23992-8 Springer-Verlag Berlin Heidelberg New York

Library of Congress Control Number: 2006931132

Springer is a part of Springer Science+Business Media
http://www.springer.com

Printed in Germany

Editor: Dr. Ute Heilmann
Desk Editor: Wilma McHugh
Copy-editing: WS Editorial Ltd, Shrewsbury, UK
Production Editor: Joachim W. Schmidt

Cover design: eStudio Calamar, Spain

Typesetting: FotoSatz Pfeifer GmbH, D-82166 Gräfelfing
Printed on acid-free paper – 24/3150 – 5 4 3 2 1 0

To Heba, Moda and Kareem

Preface to the First Edition

There is a great difference between the superficial reading of a film and the proper interpretation of a clinical scintigraphic image by an imaging specialist. Fully utilizing the clinical image, the imaging specialist evaluates both the anatomical and the physiological structure of the human body. First the specialist must appreciate the patient's clinical problem. Working from this clinical context, he then applies his understanding of the pathophysiological basis of disease and his knowledge of how such pathology may translate into various imaging patterns. This awareness of the impact of pathophysiology on imaging studies is critical to the proper practice of nuclear medicine.

Nuclear medicine is a unique and growing medical specialty that contributes most significantly to our understanding of the functional changes which accompany disease. In this way, nuclear medicine helps to advance scientific understanding. Both the diagnostic and the therapeutic aspects of nuclear medicine rely for their efficacy on the physiological changes produced by disease. Clearly, a detailed understanding of both normal and morbid pathophysiology is prerequisite to a successful career in this growing field of medicine.

Today nuclear medicine is one of the medical specialties with great opportunities for innovation and creative thinking. We are fortunate to be practicing nuclear medicine at a time of rapid scientific progress and significant growth in our contributions to patient care and well-being. The resources devoted to nuclear medicine, however, will be most profitably used when both researchers and practicing physicians have taken the time to understand the pathophysiological basis of scintigraphy and radionuclide therapy.

As a practicing nuclear medicine physician and teacher, I know that beginning students and physicians in both radiology and nuclear medicine have in the past lacked a concise textbook which focuses on the pathophysiological basis of nuclear medicine. I feel that the contributing authors to this book have collectively fulfilled this need. In addition, I hope that this book will serve as a practical reference for practicing radiologists and nuclear medicine physicians. Given the rapid pace of research in the field of nuclear medicine, keeping up to date after the completion of formal training is a challenge for all of us.

Along with the contributing authors, I hope that this book will help to spread medical knowledge and enhance patient care within the field of nuclear medicine.

Abdelhamid H. Elgazzar, MD, FCAP

Forward to the First Edition

Diagnostic imaging studies may be interpreted in one of two ways. The initial approach is that of the „imager", dealing solely with pattern recognition. In this respect, the experienced observer will surely outperform the younger physician who possesses a more limited fund of such knowledge in his or her memory bank. The other means of interpreting images draws basic pathophysiology and clinical knowledge of a disease entity into the interpretive process. Functional nuclear medicine imaging studies are exquisitely sensitive but notoriously non-specific. For this reason, nuclear medicine is most often used as a screening tool or as a monitor of changes in function when therapeutic interventions are performed.

The non-specificity of radionuclide imaging studies makes it particularly important that nuclear medicine physicians have a broad, in-depth understanding of the basic pathophysiology of the disease processes which they are being asked to study. It is in this area that Dr. Abdelhamid H. Elgazzar and his many colleagues have excelled. In the following 22 chapters, they provide us with a lucid, systemic presentation of the pathophysiology associated with various disease processes and how this knowledge impacts on scintigraphic interpretations. In addition to the clinical presentations, chapters dealing with cell structure and function, radiopharmaceutical localization, biologic effects of ionizing radiation and radionuclide therapy provide very useful information. The format employed by this gifted international panel of authors provides us with an extraordinary text which differs from some of the other fine publications in our field. It remains true to the very essence of functional imaging which characterizes the field of nuclear medicine and distinguishes it from the more morphologically based radiologic imaging procedures.

Both residents and active practitioners of nuclear medicine will profit from the enormous amount of clinically relevant information provided herein. This volume will surely enhance our role as well-rounded nuclear medicine physicians, as opposed to being more limited „imagers". It is only in this manner that we can fulfill our obligation as true consultants and play a pivotal role in assisting patient management decisions.

We are most indebted to Dr. Elgazzar and his co-authors for enhancing our diagnostic skills with this extraordinary textbook.

Leonard M. Freeman, MD

Preface to the Second Edition

The field of nuclear medicine is continuing to grow rapidly, incorporating advances in molecular biology, pathophysiology and molecular imaging. In an effort to accommodate these changes and be in line with the future direction of nuclear medicine, we have updated the first edition of *The Pathophysiologic Basis of Nuclear Medicine*, building on its strengths and making modifications to remedy any weak areas.

To reflect new developments in the area of molecular imaging, a separate chapter on the basis of positron emission tomography has been included, more information about therapy using radionuclides has been added, and the chapters on the cell, radiopharmaceutical uptake, inflammation, bone, respiratory system and neurology have been expanded. Furthermore, the clinical aspects of the role of molecular imaging in nuclear imaging are emphasized, since an imaging specialist must appreciate the patient's clinical problem for a full utilization of nuclear images. For instance, the difference between a superficial film reading and the proper interpretation of a clinical scintigraphic image by a holistic approach has been highlighted. Working from this clinical context, the specialist can then apply his or her understanding of the pathophysiologic basis of disease and the knowledge of how such pathology may translate into various imaging patterns. Awareness of the impact of pathophysiology on imaging studies is critical to the proper practice of nuclear medicine. The additional information about clinical and imaging correlation will make this text an important companion to those who are being trained in nuclear medicine technology and clinical nuclear medicine.

Appreciation is extended to reviewers of the first edition in several journals as well as members of the nuclear medicine community from around the world for their helpful and motivating feedback, both published and private. It is my sincere hope that this book will help medical professionals to further understand what nuclear medicine technology can offer in the diagnosis and treatment of disease. A deeper understanding of the scientific and clinical basis of new directions in medical imaging will certainly lead to further modifications and new innovations. I also hope that this revised text will help to advance knowledge in the field of nuclear medicine and improve currently available diagnostic and therapeutic tools in the treatment of patients with various diseases.

Abdelhamid H. Elgazzar, MD, FCAP

Acknowledgements

It is with my deepest appreciation that I thank all whose sincere support made this edition a reality. To Dr. A.I. Behbehani, Fatma Al-Rasheedi, Jehan Al-Shammari, Dr. Jarah Ali Al-Tabeekh, Ahmed M. Mohammed, Magdi Khalil, Heba Essam, Dr. K. Narayana, Dr. Abdelmonem Omar, Dr. Hussein Abdel-Dayem, James D'Almeida, Veronica Cody, Ayman Taha and to a great pathologist and artist, my very good friend Dr. Saif Abdel-Aziz, who passed away before this edition appears, to all I am very grateful.

Contents

List of Contributors

Hussein M. Abdel-Dayem, MD, PhD
Professor of Radiology
Director, Nuclear Medicine
St.Vincent's Hospital and Medical Center
153 West 11th Street
New York, NY 10011
USA
E-mail: HusseinAD@aol.com

Abbas Alavi, MD
Professor of Radiology and Medicine
Director of Research Education,
Hospital of University of Pennsylvania
Donner Bldg, 3400 Spruce Street
Philadelphia, PA 19104-4283
USA
E-mail: Abass.Alavi@uphs.upenn.edu

Abdullatif A. Al-bader, PhD
Professor of Pathology
Faculty of Medicine
Kuwait University Health Science Center
P.O. Box 24923, 13110 Safat
KUWAIT
E-mail: albadera@hsc.edu.kw

Eman Al-Enizi, MD
Senior Registrar in Nuclear Medicine
Department of Nuclear Medicine
Mubarak Al Kabeer Hospital
P.O. Box 24923, 13110 Safat
KUWAIT
E-mail: emanfmf@hotmail.com

Jaudah Ahmed Al-Maghrabi, MD, MSc, FRCPC, FCAP
Consultant Oncologic Pathologist & Associate Professor
Department of Pathology
King Faisal Specialist Hospital & Research Centre &
Department of Pathology,
King Abdulaziz University,
Faculty of Medicine.
Jeddah
SAUDI ARABIA

Kshitish Chandra DAS, MD, PhD, FAMS,FRCPath, FACP
Professor of Hematology
Department of Pathology
Faculty of Medicine
Kuwait University Health Science Center
P.O. Box 24923, 13110 Safat
KUWAIT
E-mail: daskshitish@yahoo.ca

Abdelhamid H. Elgazzar, MD, FCAP
Professor and Chairman,
Department of Nuclear Medicine
Faculty of Medicine
Kuwait University Health Science Center
P.O. Box 24923, 13110 Safat
KUWAIT
E-mail: aelgazzar49@hotmail.com
aelgazzar@hsc.edu.kw

Magda Elmonayeri, MD
Professor of Pathology
Faculty of Medicine
Ain Shams University
Abassia, Cairo
EGYPT
E-mail: mmonayeri@yahoo.com

Fuad A.M. Hassan, MD
Professor, Department of Medicine
Associate Dean,
Faculty of Medicine
Kuwait University Health Science Center
P.O. Box 24923, 13110 Safat
KUWAIT
E-mail: fuad@hsc.edu.kw

Sherif Heiba, MD
Associate Professor of Radiology
Director of Nuclear Medicine Residency Program
Mount Sinai Medical Center
Box 1141
One Gustave L. Levy Place
New York, NY 10029-6574
USA
E-mail: heibas@pol.net

Ezzuldin Ibrahim, MD, FRCP, FACP
Professor of Medicine and Oncology
Chairman, Department of Oncology
Executive Director, Research Center
King Faisal Specialist Hospital & Research Center
PO Box 40047, Jeddah 21499
SAUDI ARABIA
E-mail: ezzibrahim@kfshrc.edu
ezzibrahim@hotmail.com

Suman S. Jana, MD
Assistant Professor
Nuclear Medicine and Medicine (Endocrinology)
Albert Einstein College of Medicine (AECOM)
Director, AECOM microPET imaging facility
Attending Physician, Montefiore Medical Center
1695 Eastchester Road
Bronx, New York 10461
USA
E-mail: janasuman@pol.net

Nafisah Kazem, MD
Senior Registrar,
Department of Nuclear Medicine,
Mubarak Al-Kabeer Hospital
P.O. Box 24923, 13110 Safat
KUWAIT

Moussa Khadada, MD
Associate Professor,
Department of Medicine
Faculty of Medicine
Kuwait University Health Science Center
P.O. Box 24923, 13110 Safat
KUWAIT

Chun K. Kim, MD
Professor of Radiology
University of Maryland School of Medicine
Baltimore, Maryland
USA
E-mail: chunkikim@gmail.com

Arthur Z. Kraskow
E-mail: krasnow@mcw.edu

Borys R. Krynyckyi, MD
Assistant Proessor of Radiology
Division of Nuclear Medicine
Mount Sinai Medical Center
Box 1141
One Gustave L. Levy Place
New York, NY 10029-6574
USA

Josef Machac, MD, FACC, FACNM
Professor of Radiology
Chief, Division of Nuclear Medicine
Mount Sinai Medical Center
Box 1141
One Gustave L. Levy Place
New York, NY 10029-6574
USA
E-mail: Josef.Machac@msnyuhealth.org

James M. Mountz, MD, PhD
Professor of Radiology
Chief of Nuclear Medicine
Director NeuroNuclear Medicine
UPMC Health System
University of Pittsburgh
PET Facility – B-932
200 Lothrop Street
Pittsburgh, PA 15213
USA
E-mail: mountzjm@upmc.edu

Seham Mustafa, PhD
Assistant Professor
Department of Pharmaceutical Sciences
College of Health Sciences
Authority of Applied Education and Training
Kuwait
E-mail: seham@hsc.edu.kw

Sleiman Y. Naddaf, MD
Assistant Professor
Department of Nuclear Medicine
Faculty of Medicine
Kuwait University Health Science Center
P.O. Box 24923, 13110 Safat
KUWAIT
E-mail: snaddaf@hsc.edu.kw

Azu Owunwanne, PhD
Professor of Radiochemistry,
Department of Nuclear Medicine
Faculty of Medicine
Kuwait University Health Science Center
P.O. Box 24923, 13110 Safat
KUWAIT
E-mail: azu522@hotmail.com

Elmer C. San Pedro, MD
Staff Radiologist and Medical Director of PET Imaging
Halifax Regional Hospital
South Boston, VA,
USA 24592
E-mail: esanpedro@adelphia.net

Salil D. Sarkar, MD, FACP
Chief of Service, Nuclear Medicine
Jacobi Medical Center, North Bronx Health Network
Associate Professor, Albert Einstein College of Medicine of Yeshiva University
Bronx, New York, USA
E-mail: Salil.sarkar@nbhn.net

Dia Shehab, MD, FRCPC
Associate Professor,
Department of Medicine
Faculty of Medicine
Kuwait University Health Science Center
P.O. Box 24923, 13110 Safat
KUWAIT
E-mail: diaa@hsc.edu.kw

Pravin Singhal, MD
Division of Nephrology
Department of Internal Medicine
Long Island Jewish Medical Center
New Hyde Park, New York,
USA

Shankar Vallabhajosula, PhD
Professor of Radiopharmacy/Radiology
Division of Nuclear Medicine,
Department of Radiology
New York Hospital – Cornell Medical Center
New York, NY 10021
USA
E-mail: svallabh@med.cornell.edu

Mohamad Zubaid, MD
Associate Professor,
Department of Medicine
Faculty of Medicine
Kuwait University Health Science Center
P.O. Box 24923, 13110 Safat
KUWAIT
E-mail: zubaid@hsc.edu.kw

Lionel S. Zuckier, MD
Professor of Radiology
New Jersey Medical School, UMDNJ
Director of Nuclear Medicine and PET
University Hospital, Newark, New Jersey
USA
E-mail: zuckier@umdnj.edu

The Cell: Structure, Function, and Molecular Biology

1

Shankar Vallabhajosula, Seham Mustafa

1.1 Introduction

The cell is the basic unit of life in all forms of living organisms, from the smallest bacterium to the most complex animal. On the basis of microscopic and biochemical differences, living cells are divided into two major classes: prokaryotes, which include bacteria, blue-green algae, and rickettsiae, and eukaryotes, which include yeasts and plant and animal cells. Eukaryotic cells are far more complex internally than their bacterial ancestors, and the cells are organized into compartments or organelles, each delineated by a membrane (Fig. 1.1a,b). The DNA of the cell is packaged with protein into compact units called chromosomes that are located within a separate organelle, the nucleus. In addition, all eukaryotic cells have an internal skeleton, the cytoskeleton of protein filaments that gives the cell its shape, its capacity to move, and its ability to arrange its organelles and that provides the machinery for movement.

The entire human body contains about 100 trillion cells that are generated by repeated division from a single precursor cell. Therefore, they constitute clones. As proliferation continues, some of the cells become differentiated from others, adopting a different structure, a different chemistry, and a different function. In the

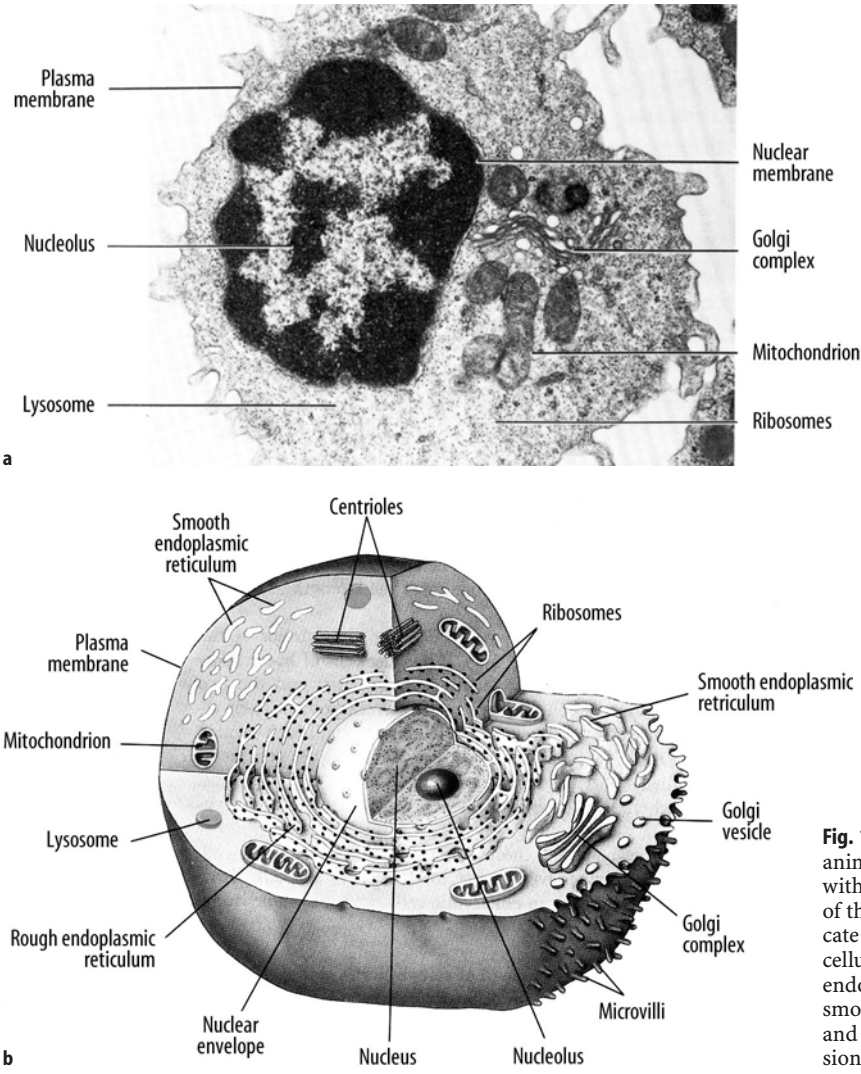

Fig. 1.1. a Electron micrograph of an animal cell showing major organelles within the cell. b Schematic drawing of the cell clearly depicting the intricate network of interconnecting intracellular membrane structures such as endoplasmic reticulum (rough and smooth), mitochondria, lysosomes, and nucleus. (Reprinted with permission from [3])

human body, more than 200 distinct cell types are assembled into a variety of types of tissues such as epithelia, connective tissue, muscle, and nervous tissue. Each organ in the body is an aggregate of many different cells held together by intercellular supporting structures. Although the many cells of the body often differ markedly from each other, all of them have certain basic characteristics that are alike. Each cell is a complex structure whose purpose is to maintain an intracellular environment favorable for complex metabolic reactions, to reproduce itself when necessary, and to protect itself from the hazards of its surrounding environment.

1.2 Cell Structure and Function

The different substances that make up the cell are collectively called protoplasm, which is composed mainly of water, electrolytes, proteins, lipids, and carbohydrates. The two major parts of the cell are the nucleus and cytoplasm. The nucleus is separated from the cytoplasm by a nuclear membrane, while the cytoplasm is separated from the extracellular fluid by a cell membrane. The major organelles in the cell are of three general kinds: organelles derived from membranes, organelles involved in gene expression, and organelles involved in energy production. The important subcellular structures of the cell and their functions are summarized in Table 1.1.

Table 1.1. Cell structures (compartments) and their function

Cell structure	Major functions
Plasma membrane	Cell morphology and movement, transport of ions and molecules, cell-to-cell recognition, cell surface receptors
Endoplasmic reticulum	Formation of compartments and vesicles, membrane synthesis, synthesis of proteins and lipids, detoxification reactions
Lysosomes	Digestion of worn-out mitochondria and cell debris, hydrolysis of proteins, carbohydrates, lipids, nucleic acids
Peroxisomes	Oxidative reactions involving molecular oxygen, utilization of hydrogen peroxide (H_2O_2)
Golgi complex	Modification and sorting of proteins for incorporation into organelles and for export; formation of secretory vesicles
Microbodies	Isolation of particular chemical activities from rest of the cell body
Mitochondria	Cellular respiration; oxidation of carbohydrates, proteins and lipids; urea and heme synthesis
Nucleus	DNA synthesis and repair; RNA synthesis and control; center of the cell; directs protein synthesis and reproduction
Chromosomes	Contain hereditary information in the form of genes
Nucleolus	RNA processing, assembles ribosomes
Ribosomes	Sites of protein synthesis in cytoplasm
Cytoplasm	Metabolism of carbohydrates, lipids, amino acids, nucleotides
Cytoskeleton	Structural support, cell movement, cell morphology

1.2.1 The Plasma Membrane

1.2.1.1 Plasma Membrane Structure

The plasma membrane encloses the cell, defines its boundaries, and maintains the essential difference between the cytosol and the extracellular environment. The cell membrane is an organized sea of lipid in a fluid state, a nonaqueous dynamic compartment of cells.

The cell membranes are assembled from four major components: a lipid bilayer, membrane proteins, sugar residues, and a network of supporting fibers.

The basic structure of a cell membrane is a lipid bilayer of phospholipid molecules. The fatty acid portions of the molecules are hydrophobic and occupy the center of the membrane, while the hydrophilic phosphate portions form the two surfaces in contact with intra- and extracellular fluid. This lipid bilayer of 7 – 10 nm thickness is a major barrier, impermeable to water-soluble molecules such as ions, glucose, and urea. The three major classes of membrane lipid molecules are phospholipids (phosphatidylcholine, phosphatidylserine, phosphatidylethanolamine, sphingomyelin), cholesterol, and glycolipids. The lipid composition of different biological membranes varies depending upon the specific function of the cell or cell membrane, as summarized in Table 1.2.

The proteins of the membrane are responsible for most membrane functions such as transport, cell identity, and cell adhesion and constitute transport channels, transporters, specific receptors, and enzymes. The membrane proteins can be associated with the lipid bilayer in various ways depending on the function of the protein. The polypeptide chain may extend across the

Table 1.2. Specific functions of the cell membrane components

Component	Composition	Function	How it works	Example
Lipid	Phospholipid bilayer	Permeability barrier	Polar molecules excluded	Glucose
Transmembrane protein	Channels	Passive transport	Creates a tunnel	Na^+, K^+ ions
	Carrier or transporters	Facilitates diffusion	Carrier "flip-flops"	Glucose transport
	Receptors	Transmits information into cell	Following receptor binding, inducing activity in the cell	Peptide hormones, neurotransmitters
Cell surface markers	Glycoprotein (GP)	"Self"-recognition	Shape of GP is characteristic of a cell or tissue	Major histocompatibility complex recognized by immune system
	Glycolipid	Tissue recognition	Shape of carbohydrate chain is characteristic of tissue	A, B, O blood group markers
Interior protein network	Clathrins	Anchor certain proteins to specific sites	Form network above membrane to which proteins are anchored	Localization of LDL receptor within coated pits
	Spectrin	Determines cell shape	Forms supporting scaffold by binding to both membrane and cytoskeleton	Red blood cell

lipid bilayer (transmembrane proteins) or may simply be attached to one or the other side of the membrane.

The cell surface often has a loose carbohydrate coat called glycocalyx. The sugar residues generally occur in combination with proteins (glycoproteins, proteoglycans) or lipids (glycolipids). The oligosaccharide side chains are generally negatively charged and provide the cell with an overall negative surface charge. While some carbohydrates act as receptors for binding hormones such as insulin, others may be involved in immune reactions and cell-cell adhesion events.

1.2.1.2 Plasma Membrane Function

The water-soluble molecules such as ions, glucose, and urea only cross the membrane through transmembrane channels, carriers, and pumps, which regulate the supply of the cell with nutrients, control internal ion concentrations, and establish a transmembrane electrical potential. Transmembrane receptors bind extracellular signaling molecules such as hormones and growth factors, and transduce their presence into chemical or electrical signals that influence the activities of the cell. Genetic defects in signaling proteins can lead to signals for growth in the absence of appropriate extracellular stimuli, causing some human cancers.

Adhesive glycoproteins of the plasma membrane allow cells to bind specifically to each other or to the extracellular matrix. These selective interactions allow cells to form multicellular structures, like epithelia. Similar interactions allow white blood cells to bind bacteria, so that they can be ingested and digested in lysosomes.

Although lipid bilayers provide a barrier to diffusion of ions and polar molecules larger than about 150 D, protein pores provide selective passages for these larger molecules across membranes. These proteins allow cells to control solute traffic across membranes, an essential feature of many physiological processes. Integral proteins that control membrane permeability fall into three broad classes: pumps, carriers, and channels each with distinct properties.

- Pumps are enzymes using energy from adenosine triphosphate (ATP), light, or other sources of energy to move ions mainly cations and other solutes across membranes at relatively modest rates, up concentration gradients as great as 100,000-fold.
- Carriers are enzyme-like proteins that provide passive pathways for solutes to move across membranes from a region of higher concentration to one of lower concentration. Carriers use ion gradients as a source of energy. Some carriers use translocation of an ion down its concentration gradient to drive another ion or solute up a concentration gradient. Carrier can also provide a pathway for substrates to move up concentration gradients, provided that their passage through the carrier is coupled to the transport of another substrate down its electrochemical gradient. Glucose provides good examples of both downhill and uphill movement through different carriers. The reactions mediated by carriers are reversible, so that substrates can move in either direction across the membrane, depending on the polarity of the driving forces. Carriers and pumps are found in all cell membranes for exchanging molecules for metabolism, storage, or extruding wastes.
- Channels are ion specific pores that open and close transiently in a regulated manner. When a channel is open, ions pass quickly across the membrane through the channel, driven by electrical and concentration gradients. The movement of ions through open channels controls the potential across membranes, and produces rapid electrical signals in excitable membranes of nerves, muscle, and other cells. Channels can perform three essential functions. First, certain channels cooperate with pumps and carriers to transport water and ions across cell membranes, to regulate cellular volume and also for secretion and absorption of fluid, as in salivary glands and kidney. Second, ion channels regulate the electrical potential across membranes. The sign and magnitude of the membrane potential depend on ion gradients created by pumps and carriers and the relative permeabilities of various channels. Open channels allow unpaired ions to diffuse down concentration gradients across a membrane producing a membrane potential. Coordinated opening and closing of channels change the membrane potential and produce an electrical signal that spreads rapidly over the surface of a cell. Nerve and muscle cells use these action potentials for high-speed communication. Third, other channels permit calcium ion from outside the cell or from the endoplasmic reticulum to enter the cytoplasm, where it triggers a variety of processes, such as muscle contraction and secretion.

1.2.2 Cytoplasm and Its Organelles

Cytoplasm is an aqueous solution (cytosol) that fills the cytoplasmic matrix, the space between the nuclear envelope and the cell membrane. The cytosol contains many dissolved proteins, electrolytes, glucose, certain lipid compounds, and thousands of enzymes. In addition, glycogen granules, neutral fat globules, ribosomes, and secretory granules are dispersed throughout the cytosol. Many chemical reactions of metabolism occur in the cytosol, where substrates and cofac-

tors interact with various enzymes. The various organelles suspended in the cytosol are either surrounded by membranes (nucleus, mitochondria, and lysosomes) or derived from membranous structures (endoplasmic reticulum, Golgi apparatus). Within the cell, these membranes interact as an endomembrane system by being in contact with one another, giving rise to one another, or passing tiny membrane-bound sacs called vesicles to one another. All biological membranes are phospholipid bilayers with embedded proteins. The chemical composition of lipids and proteins in membranes varies depending upon a specific function of an organelle or a specific cell in a tissue or an organ.

1.2.2.1 The Endoplasmic Reticulum

The cytoplasm contains an interconnecting network of tubular and flat membranous vesicular structures called the endoplasmic reticulum (ER). Like the cell membrane, the walls of the ER are composed of a lipid bilayer containing many proteins and enzymes. The regions of ER rich in ribosomes are termed rough or granular ER, while the regions of ER with relatively few ribosomes are called smooth or agranular ER. Ribosomes are large molecular aggregates of protein and ribonucleic acid (RNA) that are involved in the manufacture of various proteins by translating the messenger RNA (mRNA) copies of genes. Subsequently, the newly synthesized proteins (hormones and enzymes) are incorporated into other organelles (Golgi complex, lysosomes) or transported or exported to other target areas outside the cell. Enzymes anchored within the smooth ER catalyze the synthesis of a variety of lipids and carbohydrates. Many of these enzyme systems are involved in the biosynthesis of steroid hormones and in detoxification of a variety of substances.

1.2.2.2 The Golgi Complex

The Golgi complex or apparatus is a network of flattened smooth membranes and vesicles. It is the delivery system of the cell. It collects, packages, modifies, and distributes molecules within the cell or secretes the molecules to the external environment. Within the Golgi bodies, the proteins and lipids synthesized by the ER are converted to glycoproteins and glycolipids and collected in membranous folds or vesicles called cisternae, which subsequently move to various locations within the cell. In a highly secretory cell, the vesicles diffuse to the cell membrane and then fuse with it and empty their contents to the exterior by a mechanism called exocytosis. The Golgi apparatus is also involved in the formation of intracellular organelles such as lysosomes and peroxisomes.

1.2.2.3 Lysosomes

Lysosomes are small vesicles (0.2 – 0.5 μm) formed by the Golgi complex and have a single limiting membrane. Lysosomes maintain an acidic matrix (pH 5 and below) and contain a group of glycoprotein digestive enzymes (hydrolases) that catalyze the rapid breakdown of proteins, nucleic acids, lipids, and carbohydrates into small basic building molecules. The enzyme content within lysosomes varies and depends on the specific needs of an individual tissue. Through a process of endocytosis, a number of cells remove either extracellular particles (phagocytosis) such as micro-organisms or engulf extracellular fluid with the unwanted substances (pinocytosis). Subsequently, the lysosomes fuse with the endocytotic vesicles and form secondary lysosomes or digestive vacuoles. Products of lysosomal digestion are either reutilized by the cell or removed from the cell by exocytosis. Throughout the life of a cell, lysosomes break down the organelles and recycle their component proteins and other molecules at a fairly constant rate. However, in metabolically inactive cells, the hydrolases digest the lysosomal membrane and release the enzymes, resulting in the digestion of the entire cell. By contrast, metabolically inactive bacteria do not die, since they do not possess lysosomes. Programmed cell death (apoptosis) or selective cell death is one of the principal mechanisms involved in the removal of unwanted cells and tissues in the body. In this process, however, lysosomes release the hydrolytic enzymes into the cytoplasm to digest the entire cell.

1.2.2.4 Peroxisomes

Peroxisomes are small membrane-bound vesicles or microbodies (0.2 – 0.5 μm), derived from the ER or Golgi apparatus. Many of the enzymes within the peroxisomes are oxidative enzymes that generate or utilize hydrogen peroxide (H_2O_2). Some enzymes produce hydrogen peroxide by oxidizing D-amino acids, uric acid, and various 2-hydroxy acids using molecular oxygen, while certain enzymes such as catalase convert hydrogen peroxide to water and oxygen. Peroxisomes are also involved in the oxidative metabolism of long-chain fatty acids, and different tissues contain different complements of enzymes depending on cellular conditions.

1.2.2.5 Mitochondria

Mitochondria are tubular or sausage-shaped organelles (1 – 3 μm). They are composed mainly of two lipid bilayer-protein membranes. The outer membrane is

smooth and derived from the ER. The inner membrane contains many infoldings or shelves called cristae which partition the mitochondrion into an inner matrix called mitosol and an outer compartment. The outer membrane is relatively permeable but the inner membrane is highly selective and contains different transporters. The inner membrane contains various proteins and enzymes necessary for oxidative metabolism, while the matrix contains dissolved enzymes necessary to extract energy from nutrients. Mitochondria contain a specific DNA. However, the genes that encode the enzymes for oxidative phosphorylation and mitochondrial division have been transferred to the chromosomes in the nucleus. The cell does not produce brand new mitochondria each time the cell divides; instead, mitochondria are self-replicative: the mitochondrion divides into two and these are partitioned between the new cells. The mitochondrial reproduction, however, is not autonomous but is controlled by the cellular genome. The total number of mitochondria per cell depends on the specific energy requirements of the cell and may vary from less than a hundred to up to several thousand. Mitochondria are called the "powerhouses" of the cell. The cell derives energy from glucose, amino acids, and fatty acids. In a process called glycolysis, glucose is converted to pyruvic acid, which subsequently enters mitochondria where it begins a sequence of chemical reactions called the citric acid or Krebs cycle. Various enzymes present in the inner membrane oxidize the pyruvic acid to carbon dioxide and water. The oxidative metabolism of the glucose molecule generates 36 molecules of ATP. The amino acids and fatty acids are converted to acetyl-coenzyme A (in the cytoplasm) which also enters the citric acid cycle and gets oxidized with the generation of ATP molecules.

1.2.2.6 Ribosomes

Ribosomes are large complexes of RNA and protein molecules and are normally attached to the outer surfaces of the ER. The major function of ribosomes is to synthesize proteins. Each ribosome is composed of one large and one small subunit with a mass of several million daltons.

1.2.3 Cytoskeleton

The cytoplasm contains a network of protein fibers, called the cytoskeleton, that provides a shape to the cell and anchors various organelles suspended in the cytosol. The fibers of the cytoskeleton are made up of different proteins of different sizes and shapes such as actin (actin filaments), tubulin (microtubules), and vimentin and keratin (intermediate filaments). The exact composition of the cytoskeleton varies depending upon the cell type and function. Centrioles are small organelles that occur in pairs within the cytoplasm, usually located near the nuclear envelope, and are involved in the organization of microtubules. Each centriole is composed of nine triplets of microtubules (long hollow cylinders about 25 nm long) and plays a major role in cell division.

1.2.4 Nucleus

The nucleus is the largest membrane-bound organelle in the cell, occupying about 10% of the total cell volume. The nucleus is composed of a double membrane, called the nuclear envelope, that encloses the fluid-filled interior, called nucleoplasm. The outer membrane is contiguous with the ER. The nuclear envelope has numerous nuclear pores about 90 $\pm$A in diameter and 50 – 80 nm apart, permitting certain molecules to pass into and out of the nucleus.

The primary functions of the nucleus are cell division and the control of phenotypic expression of genetic information that directs all of the activities of a living cell. The cellular deoxyribonucleic acid (DNA) is located in the nucleus as a DNA-histone protein complex known as chromatin that is organized into chromosomes. The total genetic information stored in the chromosomes of an organism is said to constitute its genome. The human genome consists of 24 chromosomes (22 different chromosomes and two different sex chromosomes) and contains about $3'10^9$ nucleotide pairs. The smallest unit of DNA that encodes a protein product is called a gene and consists of an ordered sequence of nucleotides located in a particular position on a particular chromosome. There are approximately 100,000 genes per human genome, and only a small fraction (15%) of the genome is actively expressed in any specific cell type. The genetic information is transcribed into ribonucleic acid (RNA), which subsequently is translated into a specific protein on the ribosome. The nucleus contains a subcompartment called the nucleolus that contains large amounts of RNA and protein. The main function of the nucleolus is to form granular subunits of ribosomes, which are transported into the cytoplasm where they play an essential role in the formation of cellular proteins.

1.3 DNA and Gene Expression

1.3.1 DNA: The Genetic Material

The ability of cells to maintain a high degree of order depends on the hereditary or genetic information that is stored in the genetic material, the DNA. Within the

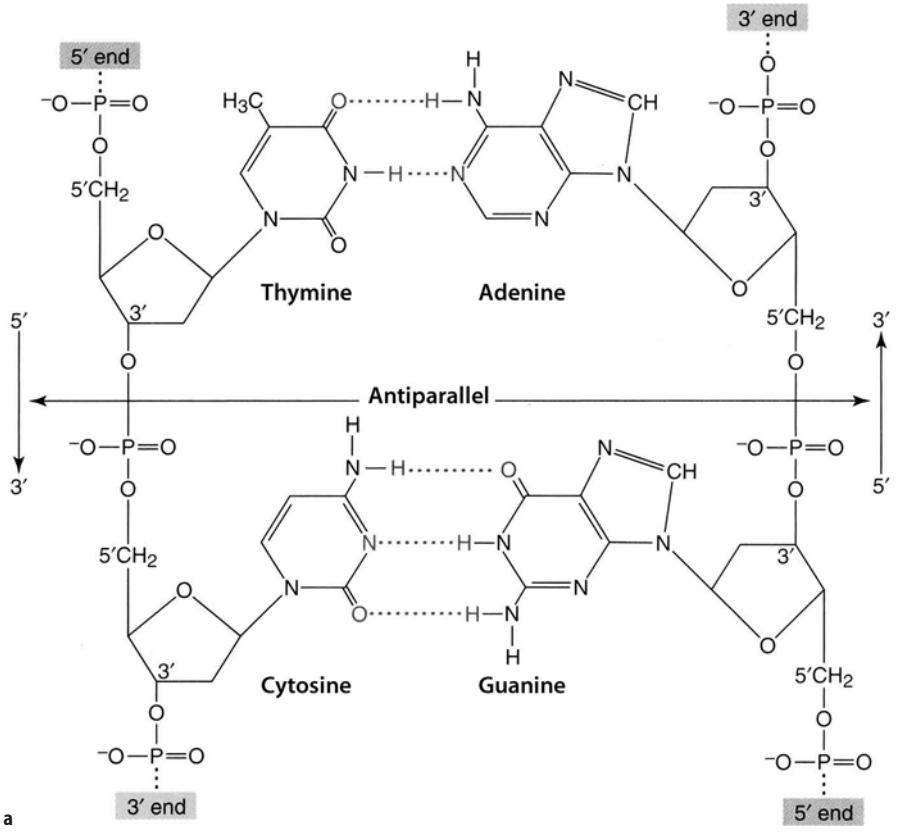

Fig. 1.2. a The double-stranded DNA molecule consists of four bases (thymine, cytosine, adenine, and guanine), deoxyribose sugar, and phosphate. The antiparallel nature of DNA strands shows the opposite direction of the two strands of a double helix. Note the hydrogen bonds between the two strands of DNA molecules. (Reprinted with permission from [2])

nucleus of all mammalian cells a full complement of genetic information is stored, and the entire DNA is packaged into 23 pairs of chromosomes. A chromosome is formed from a single, enormously long DNA molecule that consists of many small subsets called genes; these represent a specific combination of DNA sequence designed for a specific cellular function. The three most important events in the existence of a DNA molecule are replication, repair, and expression.

The chromosomes can undergo self-replication, permitting the DNA to make copies of itself as the cell divides and transfers the DNA (23 pairs of chromosomes) to daughter cells, which can thus inherit every property and characteristic of the original cell. There are approximately 100,000 genes per human genome, and genes control every aspect of cellular function, primarily through protein synthesis. The sequence of amino acids in a particular protein or enzyme is encoded in a specific gene. Most chromosomal DNA, however, does not code for proteins or RNAs. The central dogma of molecular biology is that the overall process of information transfer in the cell involves transcription of DNA into RNA molecules, which subsequently generate specific proteins on ribosomes by a process known as translation.

A major characteristic of DNA is its ability to encode an enormous quantity of biological information. Only a few picograms (10^{-12} g) of DNA are sufficient to direct the synthesis of as many as 100,000 distinct proteins within a cell. Such a supreme coding effectiveness of DNA is due to its unique chemical structure.

1.3.1.1 DNA Structure

DNA was first discovered in 1869 by a chemist, Friedrich Miescher, who extracted a white substance from the cell nuclei of human pus and called it "nuclein". Since nuclein was slightly acidic, it was known as nucleic acid. In the 1920s, a biochemist, P.A. Levine, identified two sorts of nucleic acid: DNA and RNA. Levine also concluded that the DNA molecule is a polynucleotide (Fig. 1.2a), formed by the polymerization of nucleotides. Each nucleotide subunit of DNA molecule is composed of three basic elements: a phosphate group, a five-carbon sugar (deoxyribose), and one of the four types of nitrogen-containing organic bases. Two of the bases, thymine and cytosine, are called pyrimidines while the other two, adenine and guanine, are called purines. Their first letters commonly represent the four bases: T, C, and A, G.

The presence of 5'-phosphate and the 3'-hydroxyl groups in the deoxyribose molecule allows DNA to form a long chain of polynucleotides via the joining of

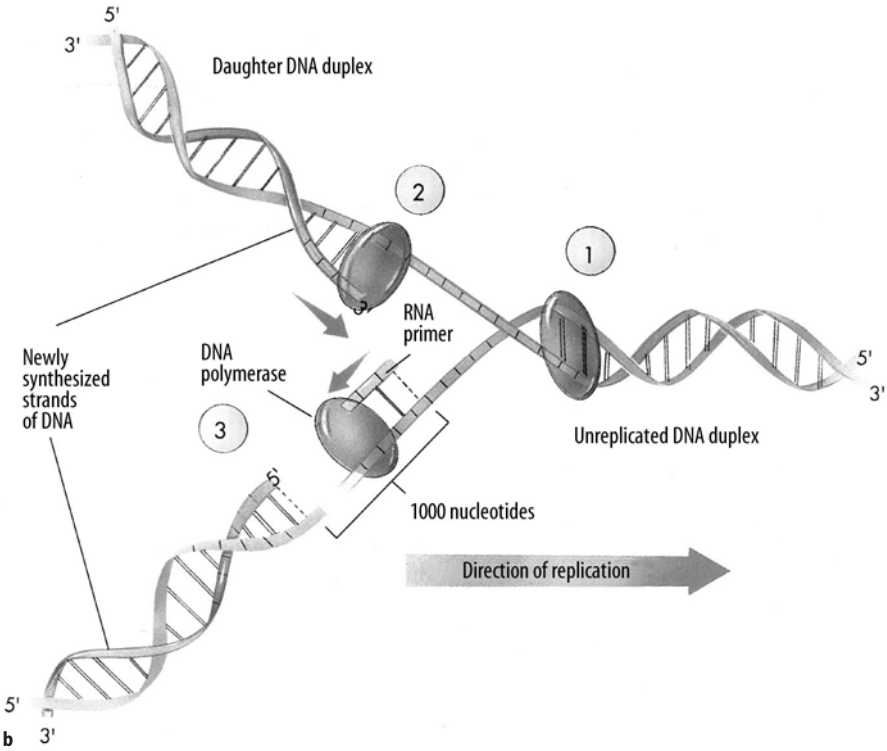

Fig. 1.2 b DNA replication fork. Replication occurs in three stages: special proteins separate and stabilize the strands of the double helix, creating a fork (*1*). During continuous synthesis of a new DNA strand, DNA polymerase adds nucleotides to the 3' end of a leading strand (*2*). In discontinuous synthesis, a short RNA primer is added 1,000 nucleotides ahead of the end of lagging strand. DNA polymerase then adds nucleotides to the primer until the gap is filled (*3*). (Reprinted with permission from [3])

nucleotides by phosphodiester bonds. Any linear strand of DNA will always have a free 5'-phosphate group at one end and a free 3'-hydroxyl group at the other. Therefore, the DNA molecule has an intrinsic directionality (5' to 3' direction). Although some forms of cellular DNA exist as single-stranded structures, the most widespread DNA structure, discovered by Watson and Crick in 1953, represents DNA as a double helix containing two polynucleotide strands that are complementary mirror images of each other. The "backbone" of the DNA molecule is composed of the deoxyribose sugars joined by phosphodiester bonds to a phosphate group, while the bases are linked in the middle of the molecule by hydrogen bonds. The relationship between the bases in a double helix is described as complementarity, since adenine always bonds with thymine and guanine always bonds with cytosine. As a consequence, the double-stranded DNA contains equal amounts of purines and pyrimidines. An important structural characteristic of double-stranded DNA is that its strands are antiparallel, meaning that they are aligned in opposite directions.

1.3.1.2 DNA Replication

In order to serve as the basic genetic material, all the chromosomes in the nucleus duplicate their DNA prior to every cell division. When a DNA molecule replicates, the double-stranded DNA separates or unzips at one end, forming a replication fork (Fig. 1.2b). The principle of complementary base pairing dictates that the process of replication proceeds by a mechanism in which a new DNA strand is synthesized that matches each of the original strands serving as a template. If the sequence of the template is ATTGCAT, the sequence of a new strand in the duplex must be TAACGTA. Replication is semiconservative, in the sense that at the end of each round of replication one of the parental strands is maintained intact, and it combines with one newly synthesized complementary strand.

DNA replication requires the cooperation of many proteins and enzymes. While DNA helicases and single-strand binding proteins help unzip the double helix and hold the strands apart, a self-correcting DNA polymerase moves along in a 5'®3' direction on a single strand (leading strand) and catalyzes nucleotide polymerization or base pairing. Since the two strands are antiparallel, this 5'®3' DNA synthesis can take place continuously on the leading strand only, while the base pairing on the lagging strand is discontinuous, and involves synthesis of a series of short DNA molecules that are subsequently sealed together by the enzyme DNA ligase. In mammals, DNA replication occurs at a polymerization rate of about 50 nucleotides per second. At the end of replication, a repair process known as DNA proofreading is catalyzed by DNA ligase and DNA polymerase enzymes, which cut out the inappropriate or mismatched nucleotides from the new strand and replace these with the appropriate complementary nucle-

otides. The replication process almost never makes a mistake and the DNA sequences are maintained with very high fidelity. For example, a mammalian germline cell with a genome of $3'10^9$ base pairs is subjected on average to only about 10 – 20 base pair changes per year. Genetic change, however, has great implications for evolution and human health; it is the product of mutation and recombination.

1.3.1.3 Gene Mutation

A mutation is any inherited change in the genetic material involving irreversible alterations in the sequence of DNA nucleotides. These mutations may be phenotypically silent (hidden) or expressed (visible). Mutations may be classified into two categories: base substitutions and frameshift mutations. Point mutations are base substitutions involving one or a few nucleotides in the coding sequence and may include replacement of a purine-pyrimidine base pair by another base pair (transitions) or a pyrimidine-purine base pair (transversions). Point mutations cause changes in the hereditary message of an organism and may result from physical or chemical damage to the DNA or from spontaneous errors during replication. Frameshift mutation involves spontaneous mispairing and may result from insertion or deletion of a base pair. Mutational damage to DNA is generally caused by one of three events: (a) ionizing radiation causes double-strand breaks in DNA due to the action of free radicals on phosphodiester bonds; (b) ultraviolet radiation creates DNA cross-links due to the absorption of UV energy by pyrimidines; (c) chemical mutagens modify DNA bases and alter base-pairing behavior. Mutations in germline tissue are of enormous biological significance, while somatic mutations may cause cancer.

1.3.1.4 DNA Recombination

DNA can undergo important and elegant exchange events through recombination, which refers to a number of distinct processes of genetic material rearrangement. Recombination is defined as the creation of new gene combinations and may include exchange of an entire chromosome or rearranging the position of a gene or a segment of a gene on a chromosome. Homologous or general recombination produces an exchange between a pair of distinct DNA molecules, usually located on two copies of the same chromosome. Sections of DNA may be moved back and forth between chromosomes, but the arrangement of genes on a chromosome is not altered. An important example is the exchange of sections of homologous chromosomes in the course of meiosis that is characteristic of gametes. As a result, homologous recombination generates new combinations of genes that can lead to genetic diversity. Site-specific recombination does not require DNA homology and involves alteration of the relative positions of short and specific nucleotide sequences in either one or both of the two participating DNA molecules. Transpositional recombination involves insertion of viruses, plasmids, and transposable elements, or transposons, into chromosomal DNA. Gene transfer in general represents the unidirectional transfer of genes from one chromosome to another. The acquisition of an AIDS-bearing virus by a human chromosome is an example of gene transfer.

1.3.2 Gene Expression and Protein Synthesis

1.3.2.1 DNA Transcription

Proteins are the tools of heredity. The essence of heredity is the ability of the cell to use the information in its DNA to control and direct the synthesis of all proteins in the body. The production of RNA is called transcription and is the first stage of gene expression. The result is the formation of messenger RNA (mRNA) from the base sequence specified by the DNA template. All types of RNA molecules are transcribed from the DNA. An enzyme called RNA polymerase first binds to a promoter site (beginning of a gene), then unwinds the two strands of DNA double helix, moves along the DNA strand, and synthesizes the RNA molecule by binding complementary RNA nucleotides with the DNA strand. Upon reaching the termination sequence, the enzyme breaks away from the DNA strand, and at the same time the RNA molecule is released into the nucleoplasm. It is important to recognize that only one strand (the *sense* strand) of the DNA helix contains the appropriate sequence of bases to be copied into an RNA *sense* strand. This is accomplished by maintaining the 5'-3' direction in producing the RNA molecule. As a result, the RNA chain is complementary to the DNA strand and is called the primary RNA transcript of the gene. This primary RNA transcript consists of long stretches of noncoding nucleotide sequences called introns that intervene between the protein-coding nucleotide sequences called exons. In order to generate mRNA molecules, all the introns are cut out and the exons are spliced together. Further modifications to stabilize the transcript include 5-methylguanine capping at the 5' end and polyadenylation at the 3' end. The spliced, stabilized mRNA molecules are finally transported to the ER in the cytoplasm, where proteins are synthesized.

1.3.2.2 RNA Structure

Both transcription and translation are mediated by the RNA molecule, an unbranched linear polymer of ribonucleoside 5'-monophophates. RNA is chemically similar to DNA, the main difference being that the RNA molecule contains ribose sugar and another pyrimidine, uracil, in place of thymine. RNAs are classified according to the different roles they play in the course of protein synthesis. The length of the molecules varies from approximately 65 to 200,000 nucleotides, depending upon the role they play. There are many types of RNA molecules within a cell, and some RNAs contain modified nucleotides which provide greater metabolic stability. mRNA molecules carry the genetic code to the ribosomes, where they serve as templates for the synthesis of proteins. The transfer RNA (tRNA) molecule, also generated in the nucleus, transfers specific amino acids from the soluble amino acid pool to the ribosomes and ensures the alignment of these amino acids in a proper sequence. Ribosomal RNA (rRNA) forms the structural framework of ribosomes, where most proteins are synthesized. All RNA molecules are synthesized in the nucleus. While the enzyme RNA polymerize II is mainly responsible for the synthesis of mRNA, RNA polymerases I and III mediate the synthesis of rRNA and tRNA, respectively.

1.3.3 Genetic Code

The genetic code in a DNA sense strand consists of a specific nucleotide sequence coded in successive "triplets" that will eventually control the sequence of amino acids in a protein molecule. During transcription, a complementary code of triplets in the mRNA molecule, called codons, are synthesized. For example, the successive triplets in a DNA sense strand are represented by bases, GGC, AGA, CTT. The corresponding complementary mRNA codons are CCG, UCU, GAA representing the three amino acids proline, serine, and glutamic acid, respectively. Each amino acid is represented by a specific mRNA codon. The various mRNA codons for the 20 amino acids and the codons for starting and stopping protein synthesis are summarized in Table 1.3. The genetic code is regarded as *degenerate*, since most of the amino acids are represented by more than one codon. An important feature of the genetic code is that it is universal; all living organisms use precisely the same DNA codes to specify proteins.

1.3.4 DNA Translation: Protein Synthesis

More than half of the total dry mass of a cell is made up of proteins. The second stage of gene expression is the synthesis of proteins, which requires complex catalytic machinery. The process of mRNA-directed protein synthesis by ribosomes is called translation and is dependent on two other RNA molecules, rRNA and tRNA. Ribosomes are the physical structures in which proteins are actually synthesized and they are composed of two subunits: a small subunit with one rRNA molecule and 33 proteins and a large subunit with four rRNAs and 40 proteins. Proteins that are transported out of the cell are synthesized on ribosomes that are attached to the ER, while most of the intracellular proteins are

Amino acid	Letter code	RNA codons					
Alanine	A	GCU	GCC	GCA	GCG		
Arginine	R	CGU	CGC	CGA	CGG	AGA	AGG
Asparagine	D	AAU	AAC				
Aspartic acid	N	GAU	GAC				
Cysteine	C	UGU	UGC				
Glutamic acid	E	GAA	GAG				
Glutamine	Q	CAA	CAG				
Glycine	G	GGU	GGC	GGA	GGG		
Histidine	H	CAU	CAC				
Isoleucine	I	AUU	AUC	AUA			
Leucine	L	CUU	CUC	CUA	CUG	UUA	UUG
Lysine	K	AAA	AAG				
Methionine	M	AUG					
Phenylalanine	F	UUU	UUC				
Proline	P	CCU	CCC	CCA	CCG		
Serine	S	UCU	UCC	UCA	UCG	AGC	AGU
Threonine	T	ACU	ACC	ACA	ACG		
Tryptophan	W	UGG					
Tyrosine	Y	UAU	UAC				
Valine	V	GAU	GUC	GUA	GUG		
Start		AUG					
Stop		UAA	UAG	UGA			

Table 1.3. The genetic code: RNA codons for the different amino acids and for the start and stop of protein synthesis

Note: Some amino acids such as arginine, leucine, and serine are coded by six different codons each, while methionine and tryptophan can be coded by only one specific codon, respectively.

made on free ribosomes in the cytoplasm. The tRNA molecule contains about 80 nucleotides and has a site for attachment of an amino acid. Since tRNA needs to bind to mRNA to deliver a specific amino acid, tRNA molecules consist of a complementary triplet of nucleotide bases called the anticodon. Each tRNA acts as a carrier to transport a specific amino acid to the ribosomes, and for each of the 20 amino acids there is a different tRNA molecule.

Protein biosynthesis is a complex process and involves bringing together mRNA, ribosomal subunits, and the tRNAs. Such an ordered process requires a complex group of proteins known as initiation factors that help to initiate the synthesis of the protein. The first step in translation is the recognition of mRNA by the ribosome and binding to the mRNA molecule at the 5' end. Immediately, the appropriate tRNA that carries a particular amino acid (methionine) to the 3' end of mRNA is attached to the ribosome and binds mRNA at the start codon (AUG). The process of translation then begins by bringing in tRNAs that are specified by the codon-anticodon interaction. The ribosome exposes the codon on mRNA immediately adjacent to the AUG to allow a specific anticodon to bind to a codon, and at the same time the amino acids (methionine and in the incoming amino acid) are linked together by a peptide bond and the tRNA carrying methionine is released. Next, the ribosome moves along the mRNA molecule to the next codon when the next tRNA binds to the complementary codon, placing the amino acid adjacent to the growing polypeptide chain. The process continues until the ribosome reaches a chain-terminating nonsense stop codon (UAA, UAG, UGA) at which point a release factor binds to the nonsense codon, stops the synthesis of protein, and releases the protein from the ribosome. Some proteins emerging from the ribosome are ready to function, while others undergo a variety of post-translational modifications in order to convert the protein to a functional form, or to facilitate transport to an intracellular or an extracellular target.

1.4 Cell Reproduction

The human body consists of some 200 trillion cells ($2'10^{14}$), all of them derived from a single cell, the fertilized egg, which undergoes millions of cell divisions in order to become a new individual human being. Cells reproduce by duplicating their contents and then dividing in two. The reproduction of a somatic cell involves two sequential phases: *mitosis* (the process of nuclear division) and *cytokinesis* (cell division). In gametes, the nuclear division occurs through a process called *meiosis*. The life cycle of the cell is the period of time from cell division to the next cell division. The duration of the cell cycle, however, varies greatly from one cell type to another and is controlled by the DNA-genetic system.

1.4.1 The Cell Cycle

In all somatic cells, the cell cycle (Fig. 1.3) is broadly divided into M-phase (or mitosis) and interphase (growth phase). In most cells, M-phase takes only a small fraction of the total cycle when the cell actually divides. The rest of the time the cell is in interphase, subcategorized into three phases: G_1, S, and G_2. During the G_1-phase most cells continue to grow until they are committed to divide. If they are not ready to go into S-phase, they may remain for a long time in a resting state known as G_0 before they are ready to resume proliferation. During G_2-phase, cells synthesize RNA and proteins and continue to grow, until they enter into M-phase.

The reproduction of the cell really begins in the nucleus itself, where the synthesis and replication of the total cellular genome occurs during the S-phase. Every somatic cell is in a diploid phase, where the nucleus

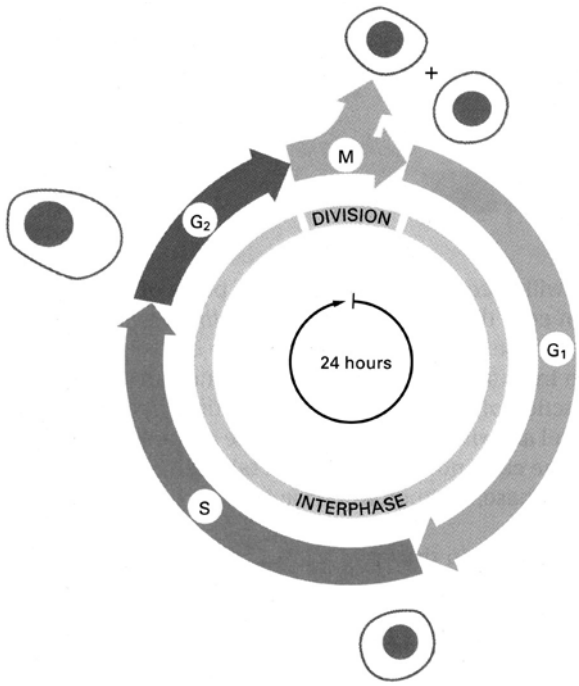

Fig. 1.3. The cell division cycle is generally represented by four successive phases. During the interphase the cell grows continuously, and only during M-phase does it undergo division. DNA replication occurs during S-phase, while G_1 and G_2 are the gaps during which cells normally show additional growth such as protein and enzyme synthesis. Cells in G_1, if they are not committed to DNA replication (that is, entering S-phase), may enter into a resting state, often called G_0, where they can remain for days, or even years, before resuming proliferation. (Reprinted with permission from [1])

contains 23 pairs of chromosomes. Following replication, the nucleus has a total of 46 pairs of chromosomes. The chromosome pairs are attached at a point called the centromere and are called chromatids.

1.4.2 Mitosis and Cytokinesis

One of the first events of mitosis takes place in the cytoplasm. A pair of centrioles is duplicated just prior to DNA replication. Towards the end of interphase the two pairs of centrioles move to the opposite poles of the cell. The complex of microtubules (spindle) pushes the centrioles farther apart, creating the so-called mitotic apparatus. It is very important to note that mitochondria in the cytoplasm are also replicated before mitosis starts, since they have their own DNA. Based on specific events during nuclear division, mitosis is subcategorized into four phases. During prophase, the nuclear envelope breaks down, chromosome condensation continues, and the centromere of the chromatids is attached to opposite poles of the spindle. During early metaphase, the spindle fibers pull the centromeres to the center, forming an equatorial plate. At the end of metaphase, the centromeres divide the chromatids into equal halves. During anaphase, the sister chromatids are pulled apart and physically separated, and drawn to opposite poles, thus completing the accurate division of the replicated genome. By the end of anaphase, 23 identical pairs of chromosomes are on the opposite sides of the cell. During telophase, the mitotic apparatus is disassembled, the nuclear envelope is reestablished around each group of 23 chromosomes, the nucleolus reappears, and finally chromosomes begin to uncoil into a more extended form to permit expression of rRNA genes.

Cytokinesis is the physical division of the cytoplasm and the cell into two daughter cells, which inherit the genome as well as the mitochondria.

1.4.3 Rates of Cell Division

For many mammalian cells the standard cell cycle is generally quite long and may be 12 – 24 h for fast-growing tissues. Many adult cells such as nerve cells, cells of the lens of the eye, and muscle cells lose their ability to reproduce. Certain epithelial cells of the intestine, lungs, and skin divide continuously and rapidly in less than 10 h. The early embryonic cells do not grow but divide very rapidly with a cell cycle time of less than 1 h. In general mitosis requires less than an hour, while most of the cell cycle time is spent during G_1- or G_0-phase. It is possible to estimate the duration of S-phase by using tracers such as ^{3}H-thymidine or bromodeoxyuridine (BrdU).

The essential processes of cell reproduction such as DNA replication and the sequence of cell cycle events are governed by a cell-cycle control system that is based on two key families of proteins: cyclin-dependent protein kinases (Cdk) and activating proteins called cyclins. These two protein complexes regulate the normal cell cycle at the end of G_1- and G_2-phases. The key component of the control system is a protein kinase known as M-phase-promoting factor (MPF), whose activation by phosphorylation drives the cell into mitosis. The mechanisms that control division of mammalian cells in various tissues and organs depend on social control genes and protein growth factors, since survival of the entire organism is the key and not the proliferation of individual cells. Growth factors such as platelet-derived growth factor (PDGF), fibroblast growth factor (FGF), and interlukin-2 regulate cell proliferation through a complex network of intracellular signaling cascades, which ultimately regulate gene transcription and the activation of the cell-cycle control system.

1.4.4 Chromosomes and Diseases

Many of the processes involved in maintaining the organization and equal division of chromosomes between daughter cells such as DNA replication and repair, or mitosis and meiosis, are very complicated and can go wrong from time to time. A chromosomal disease is found in situations in which defects in some aspect of chromosome organization or behavior lead to a disease state. The most important diseases are:

- Numerical chromosome defects (errors in cell division): in which there is an extra chromosome of a particular type such as Down's syndrome.
- Diseases produced by chromosome deletions and duplications: the absence of one chromosome of a pair as in retinoblastoma. Charcot-Marie-Tooth disease type 1A is the result of a duplication in 17p12.
- Chromosome breakage syndromes (failures in DNA repair): There is a high incidence of chromosome breakage as a result of defects in DNA repair as in Werner's syndrome, which can cause cancer.
- Fragile sites: Fragile sites are locations on chromosomes that have a tendency to break when cells are grown under appropriate conditions. Fragile sites are classified as common type (found in all people), which do not appear to be associated with any disease condition, or rare type, which is associated with disease. Most rare fragile sites are induced by a reduction in folate levels. A few rare fragile sites are induced by bromodeoxyuridine or by distamycin.

- Diseases of imprinting: resulting from the loss of one or more maternally expressed genes in the human chromosome specific region. An example is Angelman syndrome, which is a chromosomal disease that causes neurological deficits and problems including flat heads, jerky movements, protruding tongues, and bouts of laughter.
- Diseases due to DNA methylation: in which DNA methylation levels often differ from those in normal cells as in Down's syndrome.
- Cancer: A wide variety of chromosomal changes are found in cancers. Chromosomal alterations in cancers include changes in number, translocations and other rearrangements, amplifications and deletions, many of which are associated with genes that are directly responsible for causing cancers. The genome of cancer cells often shows a lower overall level of methylation than that of normal cells. Imprinting and chromosome instability are also associated with cancers (see Chapter 11). Additionally, most of the above mentioned chromosomal diseases are also associated with an increased risk of cancer.

1.5 Cell Transformation and Differentiation

The zygote and blastomeres resulting from the first few cleavage divisions are totipotent, capable of forming any cell in the body. As the development progresses, certain decisions are made that narrow the developmental options of cells. At the point where cells become committed, a restriction event has occurred. The commitment of cells during cleavage to become either inner cell mass or trophoblast and the segregation of embryonic cells into the three germ layers are the early restriction events in the mammalian embryo. When a cell has passed its last decision point, its fate is fixed and it is said to be determined. A cell is determined if it has undergone a self-perpetuating change of internal character that distinguishes it and its progeny from other cells in the embryo and commits them to a specialized course of development. The determined cell may pass through many developmental stages but cannot move onto another developmental track. For example, a muscle cell cannot become a nerve cell. Restriction and determination signify the progressive limitation of the development capacities in the embryo. Differentiation refers to the actual morphological or functional expression of the portion of genome that remains available to a determined cell or group of cells, and characterizes the phenotypic specialization of cells. Thus differentiation is the process of acquiring specific new characteristics resulting in observable changes in cellular function. By contrast, cells within a developing embryo display the least amount of differentiation. In the adult, undifferentiated cells are known as pluripotent cells, precursor cells, or stem cells that are not totally committed to a specific function.

The three germ layers, ectoderm, mesoderm, and endoderm, have different fates. The endoderm forms a tube, the primordium of the digestive tract. It gives rise to the pharynx, esophagus, stomach, intestines, and several other associated organs such as liver, pancreas, and lungs. While the endoderm forms the epithelial components of these structures, the supporting muscular and fibrous elements arise from the mesoderm. In general, the mesoderm gives rise to the muscles and connective tissues of the body, first in the form of mesenchyme and ultimately cartilage, bone and fibrous tissue, and the dermis (the inner layer of the skin). In addition, the tubules of the urogenital system, vascular system, and the cells of the blood also develop from the mesoderm. The ectoderm forms the epidermis and the entire nervous system. In a process known as neurulation, the central portion of the ectoderm creates a neural tube that pinches off from the rest of ectoderm and will form the brain and spinal cord. Some of the ectodermal cells develop into the neural crest and form all of the peripheral nervous system as well as the pigment cells of the skin.

Cells differentiate through several mechanisms. A cell and its progeny may contain sufficient intrinsic information to determine their phenotypic character. Cell differentiation generally depends on changes in gene expression rather than on gene loss, since the genome of a differentiated cell has the entire DNA content of the undifferentiated parent cell. In the regulation of gene expression, the most important point of control is the initiation of RNA transcription. These gene-regulatory proteins can switch the transcription of individual genes on or off by recognizing short stretches of DNA double helix of defined sequence and thereby determining which of the thousands of genes in a cell will be transcribed. Each cell may have a specific combination or different combinations of gene-regulatory proteins. According to environmental models, cells respond to external signals and differentiate accordingly. For example, following exposure to 5-azacytidine, fibroblasts from a standard tissue culture line differentiate into skeletal muscle, cartilage, or adipose tissue (Fig. 1.4).

1.6 Degradation of Cellular Components

The cell's constituent proteins, lipids and RNA turn over continuously, although an individual cell can live for weeks, months, years or the entire lifetime of the organism. There are three functions for this molecular degradation and replacement, constitutive, induced and macroautophagy turnovers. Constitutive turnover is a housekeeping function that maintains regular re-

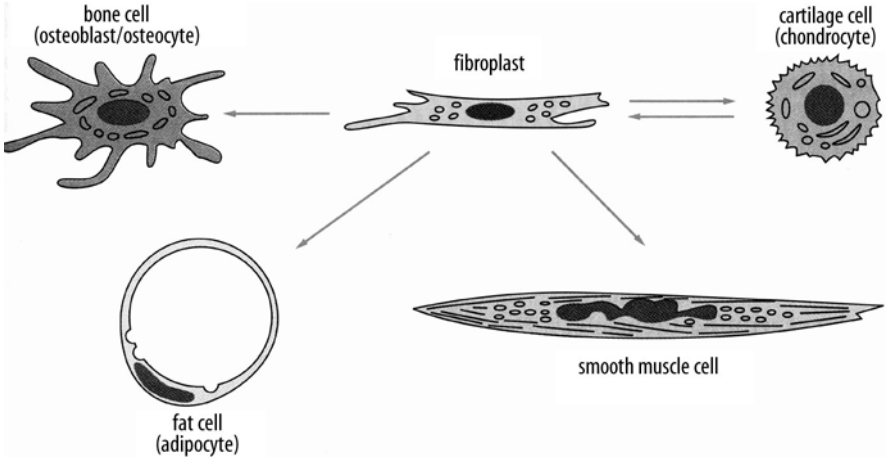

Fig. 1.4. The family of connective-tissue cells includes fibroblasts, cartilage cells, and bone cells, as well as fat cells and smooth muscle cells, which appear to have a common origin. *Arrows* show the possible interconversions. Many types of fibroblasts may exist, with differences in their differentiation potential. (Reprinted with permission from [1])

placement of older molecules with newly synthesized ones, or that removes damaged misfolded, mislocalized molecules so they do not affect the function of native molecules. Induced turnover results in rapid degradation of specific molecules and functions in signal transduction, regulation of the cell cycle, and remodeling of cells and tissues during development. Macroautophagy, a global mechanism for degradation of cellular proteins or lipids, can be triggered under conditions of starvation, when the cell has a shortage of amino acids or any other specific raw materials.

1.6.1 Protein Turnover

The rate of synthesis and degradation are balanced to reach the steady-state turnover of body constituents. A protein may have specific sequences or structural configurations that are recognized by the proteolytic machinery. There are two compartments for proteolytic activity. Lysosomes are membrane-bound protease compartments that sequester proteases and provide a low pH, which leads to the optimum enzyme effect. Proteasomes are a second type of compartment for proteolysis. These proteolytic machines are composed of multiple protein subunits that form a small cylindrical compartment with proeolytically active sites sequestered on the inside.

1.6.2 Lipid Turnover

There are three classes of cellular lipids: phosphoglycerides, glycolipids, and cholesterol. Glycolipids, which are found in the extracellular layer of a lipid bilayer, are degraded in lysosomes. Turnover of phosphoglycerides varies in mechanism and location. Some phosphoglycerides are degraded in lysosomes to their constituents, fatty acids, head group, and glycerol. Phosphoglyceride degradation is only partial and the degradative products are reutilized. Old phospholipids are remodeled, forming new ones with altered properties. These phospholipid remolding reactions are catalyzed by a variety of phospholipases that cleave distinct products.

1.6.2.1 Cholesterol Homeostasis

The free cholesterol is mainly found in the plasma membrane. An individual cell cannot degrade cholesterol. Cellular levels of cholesterol are regulated by a balance of endogenous synthesis, efflux of intracellular cholesterol to vascular fluids and uptake of extracellular cholesterol. When present in excess, cholesterol accumulates as insoluble plaques in the walls of blood vessels, leading to atherosclerosis. Many genetic diseases are known as a result of faulty regulation of cholesterol metabolism. Since cholesterol is the precursor of steroid hormones and bile acids, these vital materials are affected by cholesterol homeostasis. Cholesterol metabolism is accordingly critical to human health.

1.7 Normal and Malignant Growth

1.7.1 Normal Growth

1.7.1.1 Cell Types

The human body is an ordered clone of cells, all containing the same genome but specialized in different ways. There are approximately 200 different cell types that represent, for the most part, discrete and distinctly different categories based on histological and morphological characteristics and cellular function. Recent, more subtle, techniques involving immunohistology and mRNA expression are even revealing new subdivi-

sions of cell types within the traditional classification. The different cell types such as neuron and lymphocyte have the same genome, but the structural and functional differences are so extreme that it is difficult to imagine that they came from the same cell.

Different cell types synthesize different sets of proteins. Many processes are common to all cells and have many proteins in common, but some proteins are unique in the specialized cells in which they function and cannot be detected anywhere else. The genome of a cell contains in its DNA sequence the information to make many thousands of different proteins and RNA molecules. A cell typically expresses only a fraction of these genes, and the different types of cells in a human body arise because different sets of genes are expressed. Moreover, cells can change the pattern of genes they express in response to signals from other cells or the environment. Different cells perform different functions. The most important cellular functions are movement, conductivity, metabolic absorption, secretion, excretion, respiration, and reproduction.

1.7.1.2 Tissue Types

In the human body, specialized cells of one or more types are organized into cooperative assemblies called tissues that perform one or more unique functions. Different types of tissue compose organs, and organs in turn are integrated to perform complex functions.

The four major types of tissues are epithelial, muscle, connective, and nervous. There are also tissues that do not exist as isolated units but rather in association with one another and in variable proportions, forming different organs and systems of the body such as blood, and lymphoid tissues. Such tissue cells are in contact with a network of extracellular macromolecules known as extracellular matrix, which holds cells and tissues together but provides an organized latticework within which cells can migrate and interact with one another. All tissues are further divided into many subtypes (Table 1.4).

1.7.1.3 Tissue Cells

1.7.1.3.1 Muscle Tissue

There are three types of specialized contractile cells that contain actin and myosin: smooth muscle, skeletal muscle, and cardiac muscle cells. Muscular tissue is composed of elongated cells that have the specialized function of contraction. These muscles are similar in many aspects but differ in their activation mechanisms, energy supplies and arrangement of contractile filaments. The nervous system controls the timing, speed, and force of skeletal muscle contraction. Cardiac muscle generates its own rhythmic, fatigue-free contractions that spread through the heart in a reproducible way. Neurotransmitters acting like hormones regulate the force and frequency of heart beats. Smooth muscle contracts slowly and its activity is controlled by hormones, nerves and intrinsic signals.

Skeletal Muscle. Skeletal muscle is composed of bundles of very long, cylindrical, multinucleated cells

Table 1.4. Tissue types

Tissue	Tissue type	Location	Function
Epithelial	Simple squamous	Lines major organs	Absorption, filtration, secretion
	Simple cuboidal	Lines tubules and ducts of glands	Absorption and secretion
	Simple columnar	Lines GI tract	Secretion and absorption
	Stratified squamous	Lines interior of mouth, tongue, vagina	Protection
	Transitional	Lines urinary bladder	Permits stretching
Connective	Loose connective	Deep layers of skin, blood vessels, organs	Support, elasticity
	Dense connective	Tendons, ligaments	Attaches structures together, provides strength
	Elastic connective	Lungs, arteries, trachea, vocal cards	Provides elasticity
	Reticular connective	Spleen, liver, lymph nodes	Provides internal scaffold for soft organs
	Cartilage	Ends of long bones, trachea, tip of nose	Provides flexibility and support
	Bone	Bones	Protection, support, muscle attachment
	Vascular connective tissue	Within blood vessels	Transport of gases, blood clotting
	Adipose tissue	Deep layers of skin, surrounds heart, kidney	Support, protection, heat conservation
Muscle	Smooth muscle	GI tract, uterus, blood vessels, and bladder	Propulsion of materials
	Cardiac muscle	Heart	Contraction
	Skeletal muscle	Attached to bones	Movement
Neural	Different types of neurons	Brain and spinal cord	Conduction of electrical impulse, neurotransmission

that show cross-striations. Skeletal muscle cells are designed for rapid, forceful contractions. They have a massive concentration of highly ordered contractile units composed of actin, myosin and associated proteins. Actin and myosin filaments are organized into sarcomeres, semicrystalline arrays that give the cells a striped appearance; therefore they are called striated muscles. Contraction is generated by the energy supplied by adenosine triphosphate (ATP). Nerve impulses stimulate a transient rise in cytoplasmic calcium that activates the contractile proteins. An action potential in a T tubule triggers the release of calcium from endoplasmic reticulum into the cytoplasm. Calcium binding to troponin allows myosin to interact with the thin filament, initiating contraction. The signal transduction process is called excitation-contraction, coupling calcium release in skeletal muscle.

Cardiac Muscle. Cardiac muscle is specialized for repetitive, fatigue-free contractions to maintain the circulation of blood. The muscle contracts at regular intervals by action potentials from specialized pacemaking cells. Gap junctions allow these action potentials to spread from one muscle cell to the next. Cardiac muscles have sarcomeres like skeletal muscle. Cardiac muscle cells are short, and branched with a nucleus in the center and squared-off ends where neighboring cells attach to each other. Extracellular calcium is required for cardiac and smooth muscles but not for skeletal muscle. Action potentials open voltage-sensitive calcium channels in T tubules, releasing calcium locally. This small burst of calcium opens ryanodine receptors in the endoplasmic reticulum, releasing a flood of calcium to trigger contraction. Motor nerves do not stimulate cardiac muscle directly, but the heart is rich in autonomic nerves from the sympathetic and parasympathetic nervous systems. These nerves secrete acetylcholine and norepinephrine, which act as hormones to regulate the rate and force of heart contraction.

Smooth Muscle. This type of muscle consists of collections of fusiform cells, specialized for slow, powerful contractions controlled by a variety of involuntary mechanisms. Smooth muscle cells are generally confined to internal organs, such as blood vessels to regulate blood pressure, the gastrointestinal tract to control food movement, and the respiratory system. Calcium enters the cytoplasm through either voltage-dependent or receptor operated calcium channels in the plasma membrane or ryanodine as well as inositol 1,4,5-triphosphate (IP_3)-induced calcium release from endoplasmic reticulum. Following stimulation, intracellular calcium increases rapidly, leading to muscle contraction. Calcium pumps in both smooth endoplasmic reticulum and plasma membrane clear the cytoplasm of calcium so that calcium levels decrease to resting levels and the muscle relaxes when the activating stimulus is removed.

1.7.1.3.2 Nerve Tissue

Nerve tissues develop from embryonic ectoderm induced to differentiate by the underlying notochord. Nerve cells, or neurons, are independent anatomic and functional units with complex morphologic characteristics. They are responsible for the reception, transmission, and processing of stimuli, and the release of neurotransmitters and other formational molecules. Most neurons consist of three parts: the dendrites, which are multiple elongated processes specialized in receiving stimuli from the environment, sensory epithelial cells, or other neurons; the cell body or perikaryon, which represents the trophic center for the whole nerve cell and is also receptive to stimuli; and the axon, which is a single process specialized in generating or conducting nerve impulses to other cells. Axons may also receive information from other neurons; this information modifies the transmission of action potentials to other neurons.

The blood-brain barrier is a functional barrier that prevents the passage of some substances, from the blood to the nerve tissue. Lipid soluble substance can penetrate while polar substance generally fails to enter nerve tissue. The blood-brain barrier results from the reduced permeability that is a property of the blood capillaries of nerve tissue and act as a protective mechanism.

1.7.1.3.3 Epithelial Tissue

Epithelial tissues are composed of closely aggregated polyhedral cells with very little intracellular substance. Adhesion between these cells is strong, forming cellular sheets that cover the surface of the body and line its cavities. The principal functions of epithelial tissues are covering and lining surfaces, absorption, secretion, and contractility. Both benign and malignant tumors can arise from most types of epithelial cells. Acarcinoma is a malignant tumor of epithelial cell origin. Malignant tumors derived from glandular epithelial tissue are usually called adenocarcinomas.

1.7.1.4 Matrix Cells

These connective tissues are responsible for providing and maintaining form in the body. They provide a matrix that serves to connect and bind the cells and organs and give support to the body. Unlike the other previous tissue types that are formed mainly by cells, the major

constituent of connective tissue is its extracellular matrix, composed of protein fibers, an amorphous ground substance, and tissue fluid in addition to cells.

1.7.1.4.1 Indigenous Connective Tissue Cells

These cells arise in connective tissue and remain there. They include fibroblasts, fat cells, mast cells, chondrocytes, and osteoblasts and arise from primitive mesenchymal cells.

Fibroblasts. These are spindle shaped, with oval flattened nuclei. They synthesize and secrete most of the macromolecules of the extracellular matrix. In response to tissue damage, fibroblasts proliferate and migrate into the wound, where they synthesize new matrix to restore the integrity of the tissue.

Mast Cells. These are secretory cells that mediate immediate hypersensitivity reactions. Mast cells are distributed along the blood vessels within the connective tissue. A variety of stimuli such as mechanical trauma, heat, X-rays, toxins and other stimuli can induce secretion of the contents of their granules, mainly histamine.

Fat Cells. Fat cells (adipocytes) are round cells of different sizes. These cells take up fatty acids and glycerol from the blood after a meal and synthesize triglycerides for storage in the lipid droplet. During fasting, these triglycerides are hydrolyzed and the fatty acids are released back into the blood to provide energy for organs. Fat cells also secrete leptin, a hormone that binds to receptors in the brain and modulate appetite to avoid obesity. There are two types of fat cells which have different locations, structure and color. White fat cell, which is common, contains one large central droplet of white or yellow fat in the cytoplasm. Brown fat is less abundant than white fat. It contains numerous lipid droplets, vascular blood vessels and abundant brown mitochondria, giving it its color and are used to generate heat in response to cold. Unlike white fat tissue, which is present throughout the body, brown adipose tissue has a more limited distribution. In animals ending their hibernation period, or in newborn mammals (including humans) who are exposed to a cold environment, nerve impulses liberate norepinephrine into the tissue. This neurotransmitter activates the hormone lipase, promoting hydrolysis of triglycerides to fatty acids and glycerol. Liberated fatty acids are metabolized, producing heat, elevating the temperature of the tissue and warming the blood passing through it. Heat production is increased, because the mitochondria in the cell have a transmembrane protein called thermogenin in their inner membrane. White fat cells can generate very common benign tumors called lipomas. Malignant adipocyte-derived tumors (liposarcomas) are among the more common tumors of connective tissue. Tumors of the brown adipose cells (hibernomas) are relatively rare.

Bone Cells. Bone is a specialized connective tissue composed of intracellular calcified material, the bone matrix and three cell types: osteocytes, which are found in cavities within the matrix; osteoblasts, which synthesize the organic components of the matrix; and osteoclasts, which are multinucleated cells involved in the resorption and remodeling of bone tissue. Since metabolites are unable to diffuse through the calcified matrix of bone, the exchanges between osteocytes and blood capillaries depend on communication through the canaliculi, which are thin cylindrical spaces that perforate the matrix.

Cartilage Cells. Cartilage is characterized by an extracellular matrix enriched with glycosaminoglycans and proteoglycans. These macromolecules interact with collagen and elastic fibers. Cartilage supports soft tissues. Since it is smooth surfaced and resilient, cartilage is a shock-absorbing and sliding area for joints. Cartilage is also essential for the development and growth of long bones. Cartilage consists of cells, chondrocytes, and an extensive extracellular matrix composed of fibers and ground substance. Chondrocytes synthesize and secrete the extracellular matrix, and cells themselves are located in matrix cavities called lacunae. Collagen, hyaluronic acid, proteoglycans, and small amounts of several glycoproteins are the principal macromolecules present in all types of cartilage matrix.

1.7.1.4.2 Immigrant Cells

These cells travel transiently through blood or lymph and enter connective tissue as needed. The blood contains many cells with a specialized function. All blood cells derive from pleuripotential stem cells. These stem cells are also responsible for restoring blood cell production. Destruction of stem cells for example by chloramphenicol leads to aplastic anemia. These cells include erythrocytes (red blood cells), granulocytes , monocytes, lymphocytes, plasma cells and platelets (see Chapter 5).

1.7.2 Malignant Growth

Social control genes regulate cell division, proliferation, and differentiation under normal conditions. The uncontrolled growth of an abnormal cell will give raise to a tumor or neoplasm that can be either benign or

malignant. A tumor is regarded as cancer only if it is malignant. Transformation is the process by which a normal cell becomes a cancer cell. Cancer cells are characterized by anaplasia, or loss of differentiation, and become more like embryonic undifferentiated cells. Tumors are graded according to their degree of differentiation.

Cancer cells differ according to the cell type from which they derive. The common characteristics of cancerous tissue include local increase in cell population, loss of normal arrangement of cells, variation of cell shape and size, increase in nuclear size and density of staining, increase in mitotic activity, and abnormal mitoses and chromosomes. Progressive infiltration, invasion, and destruction of the surrounding tissue accompany the growth of cancer. Metastases are tumor implants discontinuous with the primary tumor. A number of cell surface changes occur in cancer cells, resulting in decreased communication or signaling between cells and altered membrane transport or permeability. Cells become anchorage independent and are allowed to metastasize. Cancer cells produce a number of substances known as tumor cell markers, such as hormones, enzymes, gene products, and antigens, that are found on tumor cell plasma membrane or in the blood, spinal fluid, or urine.

An interesting observation regarding the tissue origin of cancer is worth noting. In children up to age 10 years, most tumors develop from hematopoietic organs, nerve tissues, connective tissues, and epithelial tissues (in decreasing order). This proportion gradually changes with age, so that after 45 years of age, more than 90% of all tumors are of epithelial origin.

1.7.2.1 Molecular Basis of Cancer (see also Chapter 11)

Carcinogenesis is a multistep process at both the phenotypic and the genetic level. The genetic hypothesis of cancer implies that cancer results from the clonal expansion of a single progenitor cell. In the first step (initiation), the cell has incurred genetic damage in its DNA caused by a point mutation, gene deletion, or gene rearrangement. In the second step (promotion), the initiated cell becomes cancerous. In the third step (progression), the cancerous cell becomes biologically defective or undifferentiated. The principle targets of genetic damage are three classes of normal regulatory genes: oncogenes, anti-oncogenes, and genes that regulate apoptosis. Damage to DNA repair genes may also be involved in carcinogenesis.

Oncogenes, or cancer-causing genes, derived from proto-oncogenes, are present in the human genome and are a necessary part of normal cell growth. Many oncogene products and oncoproteins are part of a cell's signal transduction pathway (Table 1.5). Some oncogenes code for proteins that are either growth factors or growth factor receptors. Some oncoproteins are transmembrane signal molecules, such as tyrosine kinases. The activation of a mutated oncogene can greatly affect a cell's growth potential by increasing the production of growth factors, by increasing the growth factor receptor expression on the cell surface, or by encoding a protein that binds to DNA and stimulates cell division.

In a normal cell, the physiologic function of anti-oncogenes or cancer-suppressor genes is to regulate cell

Table 1.5. Oncogenes and anti-oncogenes

Gene	Gene product	Biologic function	Cancer
Oncogenes: cancer-causing genes			
sis	PDGF-β chain	Heparin binding GF	Astrocytoma, osteosarcoma
int-2	Fibroblast GF	Platelet-derived GF	Breast cancer, melanoma
erb-B2	EGF receptor	GF receptor	Breast, ovarian, and lung cancer
fms	CSF-1 receptor	GF receptor	Leukemia
abl	Tyrosine kinase	Intracellular signaling	Chronic myeloid leukemia
ras	GTP binding protein	Intracellular signaling	Many cancers
c-*myc*	Transcription factor	Binds DNA	Burkitt's lymphoma
L-*myc*	Transcription factor	Binds DNA	Small cell carcinoma of lung
Anti-oncogenes: tumor-suppressor genes			
Rb	Transcription factor	Regulation of cell cycle	Retinoblastoma, osteosarcoma
p53	Transcription factor	Regulation of cell cycle and apoptosis	Most human cancers
NF-1	GTPase activating protein	Inhibition of *ras* signal transduction	Schwannoma, neurofibroma
WT-1	Nuclear transcription factor	Binds DNA	Wilms' tumor

growth and not to prevent tumor formation. The loss of these genes, however, is a key event in many human tumors. Tumor-suppressor genes encode for proteins that act as negative transducers of growth factor stimulation. The p53 gene is an excellent example of a tumor-suppressor gene that encodes a 53-kd protein that binds in the nucleus and, at high levels, causes the cell to undergo apoptosis. A mutated p53 gene in a cancer cell may encode a mutant form of p53 protein without the ability to induce apoptosis. Mutations of the p53 gene are the most common DNA abnormality in more than 50% of cancers. Some cancers in which loss of function of tumor-suppressor genes may be involved are summarized in Table 1.5.

1.7.2.2 Tumor Angiogenesis

Blood supply is the most important factor that can modify the rate of tumor growth. Perfusion supplies nutrients and oxygen, as well as growth factors. Beyond 1 – 2 mm in diameter, the tumor fails to proliferate because hypoxia induces apoptosis. Angiogenesis is a necessary biological correlate of malignancy. Tumor-associated angiogenic factors such as vascular endothelial growth factor (VEGF) and basic fibroblast growth factor (bFGF) may be produced by tumor cells or derived from inflammatory cells. A number of anti-angiogenesis molecules may be produced by tumor cells themselves (such as thrombospondin-1) or may induce the production of these factors (angiostatin, endostatin, and vasculostatin) by other cells. The balance between the angiogenic and anti-angiogenic factors controls tumor growth.

1.7.2.3 Tumor Antigens

Most tumor cells synthesize many proteins or glycoproteins that are antigenic in nature. These antigens may be intracellular, or expressed on the cell surface, or shed or secreted from the cell into extracellular fluid or the circulation. These tumor-associated antigens (TAA) such as CEA, TAG-72, PSA, and PSMA may also be expressed in small amounts in normal cells, but tumor cells typically produce them in large amounts. Based on the source and origin of the antigen, TAAs can be categorized into five different groups.

1. Oncofetal antigens: These are derived from epitopes that were expressed in fetal life and appear on tumor cells as a result of an undifferentiated growth process associated with the malignant process. These antigens are not expressed in completely differentiated cells. Some of these antigens, such as carcinoembryonic antigen (CEA) and alpha-fetoprotein (AFP), are expressed on the cell surface and are also present in the circulation.
2. Epithelial surface antigens: These are derived from cell surface structural components that are exposed due to an architectural disruption of the malignant tissue. Antigens such as epithelial membrane antigen (EMA) and human milk fat globule (HMFG) are excluded from the blood by biological barriers and are present in the tumor tissue only.
3. Tumor-derived antigens: These epitopes are expressed mainly by tumor tissue, and in certain tumors there is even increased expression. The antigen tumor-associated glycoprotein-72 (TAG-72) is expressed on the tumor cell surface in a variety of adenocarcinomas such as those of the colon, breast, and ovary. Prostate-specific antigen (PSA) and prostatic acid phosphatase (PAP) are secreted by prostate carcinoma cells and are present in tumor tissue and in the circulation. Prostate-specific membrane antigen (PSMA) is an integral transmembrane glycoprotein with intra- and extracellular epitopes.
4. Receptor antigens: Tumor cells express regulator receptors that promote interaction with a number of growth factors. The increased expression of receptor proteins on tumor tissues may be regarded as receptor antigens. The human epidermal growth factor receptor (EGF-r) is a transmembrane glycoprotein that contains extracellular and cytoplasmic epitopes for EGF binding. EGF-r overexpression has been found in a variety of malignant epithelial tumors arising in the breast, colon, lung, and bladder.
5. Viral antigens: These epitopes are present in certain tumor cell membranes where the induction of malignancy is associated with the presence of transforming genes carried by DNA viruses. Epstein-Barr virus (EBV)-positive malignancies (such as Burkitt's lymphoma) developed from congenital or acquired immunodeficiency are examples of receptor antigens.

1.8 Cell-to-Cell Communication

Cells in the human body are programmed to communicate with each other and to respond to a specific set of signals in order to regulate their growth, replication, development, and organization into tissues, and to coordinate their overall biochemical behavior. Cells communicate with each other in three ways: (a) through physical contact with each other by forming cell junctions, (b) by secreting chemical signaling molecules that help communication at a distance, and (c) by cellular receptors which bind to specific to signaling mole-

cules and respond by generating intracellular messengers.

1.8.1 Cell-Cell Interaction

Cells in tissues are in physical contact with neighboring cells and extracellular matrix at specialized contact sites called cell junctions (communicating, occluding, and anchoring), which allow transport of molecules between cells or provide a barrier to passage of molecules between cells. Gap or communicating junctions are composed of clusters of channel proteins that create an intercellular gap (1.5 nm wide) to allow small molecules to pass directly from cell to cell. Cells connected by gap junctions are electrically and chemically coupled, since the cells share ions and small molecules. Occluding or tight junctions exist primarily in epithelial sheets. The tight junctions form a continuous, impermeable or semipermeable barrier to diffusion and play an important part in maintaining the concentration differences of small hydrophilic molecules across epithelial sheets and restricting the diffusion of membrane transport proteins. Anchoring junctions such as maculae adherens, desmosomes, and hemidesmosomes are most abundant in tissues that are subjected to severe mechanical stress; they connect the cytoskeletal elements (actin or intermediate filaments) of a cell to those of another cell or to the extracellular matrix. To form an anchoring junction, cells must first adhere. Such a selective cell adhesion or tissue-specific recognition process is mediated by two distinct classes of cell-cell adhesion molecules (CAMs). Cadherins, the transmembrane glycoproteins, mediate Ca^{2+}-dependent cell-cell adhesion, while the neural cell adhesion molecule, N-CAM, mediates the Ca^{2+}-independent cell-cell adhesion systems.

A substantial part of the tissue volume is extracellular space that is filled by extracellular matrix, composed of proteins and polysaccharides secreted locally by the cells in the matrix. The extracellular matrix not only binds the cells together but also influences their development, polarity, and behavior. The two main classes of macromolecules that make up the matrix are glycosaminoglycans (GAGs) and fibrous proteins.

1.8.2 Cell Signaling and Cellular Receptors

Cells communicate by means of hundreds of kinds of intercellular signaling molecules that include amino acids, peptides, proteins, steroids, nucleotides, fatty acid derivatives, and dissolved gases. The four primary modes of chemical signaling are endocrine, paracrine, autocrine, and synaptic. Endocrine signaling involves specialized endocrine cells that secrete the signaling molecules (hormones) into the blood stream; these are transported to distant target cells distributed throughout the body in order to produce a response in different cells and tissues. In paracrine signaling, signal molecules that a cell secretes may act as local mediators, affecting only the neighboring cells. In autocrine signaling, the signal molecules secreted by a cell act on the same cell that generates them. In synaptic signaling, the signal molecules secreted by a cell (neuron) bind to the receptors on a target cell at specialized cell junctions called synapses.

The cellular receptors are very specific protein molecules on the plasma membrane, in the cytoplasm, or in the nucleus that are capable of recognizing and binding the extracellular signaling molecules, also called ligands. As a consequence of ligand-receptor interaction, the cell may generate a cascade of intracellular signals that alter the pattern of gene expression and the behavior of the cell. One of the final steps in the signal transduction pathway is the phosphorylation of an effector protein by a protein kinase. Through cascades of highly regulated protein phosphorylation, elaborate sets of interacting proteins relay most signals from the cell surface to the nucleus, thereby altering the cell's pattern of gene expression and, as a consequence, its behavior. Small hydrophobic signal molecules including the thyroid and steroid hormones diffuse into the cell and activate receptor proteins that regulate gene expression. Some dissolved gases, such as nitric oxide and carbon monoxide activate an intracellular enzyme (guanyl cyclase) which produces cyclic GMP in the target cell. Most of the extracellular signal molecules are hydrophilic and activate transmembrane receptor proteins on the surface of cell membrane. The ligands that bind with membrane receptors include hormones, neurotransmitters, lipoproteins, antigens, infectious agents, drugs and metabolites.

Generally, receptors are classified on the basis of their location and function. Three main families of cell-surface receptors (Table 1.6) have been identified. Following binding of a specific signal, ion-channel-linked receptors open or close briefly to allow transport of molecules into the cell. G-protein-linked receptors activate or inactivate plasma membrane-bound enzymes or ion channels via trimeric GTP-binding proteins (G-proteins). Some G-protein-linked receptors activate or inactivate adenyl cyclase and alter the intracellular concentration of cyclic AMP, while others generate inositol triphosphate (IP_3), which increases intracellular Ca^{2+} levels. A rise in cyclic AMP or Ca^{2+} levels stimulates a number of kinases and phosphorylates target proteins on serine or threonine residues. Enzyme-linked receptors such as protein kinases phosphorylate specific proteins in the target cell. There are five known classes of enzyme-linked receptors (Table 1.6). Among these, receptor tyrosine kinases and tyrosine-kinase-associated

Table 1.6. Cell surface receptors

Receptor family	Enzyme	Second messenger	Signaling molecule
Ion-channel-linked			
G-protein-linked	Activate adenyl cyclase	Increase cyclic AMP	TSH, ACTH, LH, adrenaline, glucagon, vasopressin, glucagon
	Inhibit adenyl cyclase	Decrease cyclic AMP	Cholera toxin, pertussis toxin
	Activate phosphoinositide-specific phospholipase C	Inositol triphosphate (IP3) (increases Ca^{2+})	Vasopressin, acetylcholine, thrombin
	Activate or inactivate ion channels		Acetylcholine (nicotinic ACh receptors)
Enzyme-linked			
Receptor guanylyl cyclases	Activate guanylyl cyclase	Increase cyclic GMP	Atrial natriuretic peptides (ANPs)
Receptor tyrosine kinases	Activate tyrosine kinase	Phosphorylate specific tyrosine residues	Growth factors (PDGF, FGF, VEGF, M-CSF), insulin
Tyrosine-kinase-associated receptors	Receptor dimerization	Same as above	Cytokines, interleukin-2, growth hormone, prolactin
Receptor tyrosine phosphatases	Activate tyrosine phosphatase	Remove phosphate groups from tyrosine residues and extracellular antibodies	
Receptor serine/threonine kinases		Phosphorylate serine and threonine residues	

receptors are by far the most common. Most of the mutant genes (*Ras, Src, Raf, Fos, and Jun*) that encode the proteins in the intracellular signaling cascades activated by tyrosine kinases were identified as oncogenes in cancer cells, since their inappropriate activation causes a cell to proliferate excessively. By contrast, the normal genes are therefore sometimes referred to as proto-oncogenes.

1.9 Cellular Metabolism

1.9.1 Role of ATP

The chemical reactions involved in maintaining essential cellular functions are referred to together as cellular metabolism. The life processes are driven by energy; anabolism requires energy while catabolism releases energy. Atoms can store potential energy by means of electrons at higher energy levels. Energy is stored in chemical bonds when atoms combine to form molecules. Cells extract the chemical energy from nutrients and transfer the energy to a molecule known as adenosine triphosphate (ATP). Each molecule of ATP has two high-energy phosphate bonds, and each of the phosphate bonds contains about 12,000 calories of energy per mole of ATP under physiological conditions. Oxidative cellular metabolism and oxidative phosphorylation reactions result in the formation of ATP that is used throughout the cell to energize all the intracellular metabolic reactions. The function of ATP is not only to store energy but also to transfer it from one molecule to another. The phosphate bond in the ATP molecule is very labile and is broken down to form adenosine diphosphate (ADP) and a phosphoric acid radical with the release of energy. ATP is used to promote three major categories of cellular function: membrane transport of ions such as Na^+, K^+, Ca^{2+}, Mg^{2+}, Cl^-; synthesis of biochemicals such as proteins, enzymes, and nucleotides, and mechanical work such as muscle contraction.

1.9.2 Production of ATP

The catabolism of nutrients can be divided into three different phases. Phase 1 represents the process of digestion that happens outside the cells where proteins, polysaccharides, and fats are broken down into their corresponding smaller subunits: amino acids, glucose, and fatty acid. In phase 2, the small molecules are transported into the cell, where the major catabolic processes take place with the formation of acetyl coenzyme A (acetyl-CoA) and a limited amount of ATP and NADH. Finally, in phase 3, the acetyl-CoA molecules are degraded in mitochondria to CO_2 and H_2O with the generation of ATP.

Cellular oxidation-reduction reactions play a key role in energy flow within a cell and electrons transfer the energy from one atom to another either by oxidation (loss of electrons) or by reduction (gain of electrons). In a biological system, oxidation refers to removal of a hydrogen atom (proton plus electron) from a molecule while reduction involves gain of a hydrogen

atom by another molecule. In many of these enzyme-catalyzed oxidation-reduction reactions involving the formation of ATP, cells employ coenzymes (cofactors) that shuttle energy, as hydrogen atoms, from one reaction to another. One of the most important coenzymes is nicotinamide adenine dinucleotide (NAD^+), which can accept an electron and a hydrogen atom and gets reduced to NADH.

1.9.2.1 Glycolysis

The most important process in phase 2 of catabolism is the degradation of glucose in a sequence of ten biochemical reactions known as glycolysis, or oxidative cellular metabolism. Glycolysis can produce ATP in the absence of oxygen. Each glucose molecule is converted into two pyruvate molecules with a net generation of six ATP molecules. If oxygen is absent, or significantly reduced within the cell, the pyruvate is converted to lactic acid, which then diffuses into extracellular fluid. In many of the normal cells, glycolysis accounts for less than 5% of the overall ATP generation with in the cell.

1.9.2.2 Oxidative Phosphorylation

Phase 3 begins in mitochondria with a series of reactions called the citric acid cycle (also known as the tricarboxylic acid cycle or the Krebs cycle) and ends with oxidative phosphorylation. Following glycolysis, in the presence of oxygen, pyruvate molecules enter mitochondria and are converted to acetyl groups of acetyl-CoA. The amino acid and fatty acid molecules are also converted to acetyl-CoA.

The citric acid cycle begins with the interaction of acetyl-CoA and oxaloacetate to form the tricarboxylic acid molecule called citric acid, which subsequently is oxidized to generate two molecules of CO_2 and oxaloacetate. The energy liberated from the oxidation reactions is utilized to produce three molecules of NADH and one molecule of reduced flavin adenine nucleotide ($FADH_2$). Oxidative phosphorylation is the last step in catabolism, in which NADH and $FADH_2$ transfer the electrons to a series of carrier molecules such as cytochromes (the electron-transport chain) on the inner surfaces of the mitochondria with the release of hydrogen ions. Subsequently, molecular oxygen picks up electrons from the electron-transport chain to form water, releasing a great deal of chemical energy that is used to make the major portion of cellular ATP. The energy released in the electron-transfer steps causes the protons to be pumped outward. The resulting electrochemical proton gradient across the inner mitochondrial membrane induces the formation of ATP from ADP and phosphoric acid radical. The aerobic oxidation of glucose results in a maximal net production of 36 ATP molecules, all but four of them produced by oxidative phosphorylation.

1.10 Transport Through the Cell Membrane

About 56% of the adult human body is fluid. One third of the fluid is outside the cells and is called extracellular fluid while the remainder is intracellular fluid. The extracellular fluid (the internal environment) is in constant motion throughout the body and contains the ions (sodium, chloride, and bicarbonate) and nutrients (oxygen, glucose, fatty acids, and amino acids) needed by cells to maintain life. Cells secrete various intracellular signal molecules and expel metabolites and waste products into the extracellular fluid. The cellular intake or output of different molecules occurs by different transport mechanisms of the plasma membrane, depending on chemical and biochemical characteristics of the solute molecule.

The cell membrane consists of a lipid bilayer that is not miscible with either the extracellular fluid or the intracellular fluid and provides a barrier for the transport of water molecules and water-soluble substances across the cell membrane. Water and small molecules diffuse through the membrane via gaps or transitory spaces in the hydrophobic environment created by the random movement of fatty acyl chains of lipids.

The transport proteins with in the lipid bilayer, however, provide different mechanisms for the transport of molecules across the membrane. Membranes of most cells contain pores or specific channels that permit the rapid movement of solute molecules across the plasma membrane. Examples are plasma membrane gap junctions and nuclear membrane pores. Channels are selective for specific inorganic ions, whereas pores are not selective. Voltage-gated channels such as the sodium channel control the opening or closing of some channels by changes in the transmembrane potential. Chemically regulated channels such as the nicotinic-acetylcholine channel open or close based on the binding of a chemical to the channel.

Plasma membranes contain transport systems (transporters) that involve intrinsic membrane proteins and actually translocate the molecule or ion across the membrane by binding and physically moving the substance. Transporters have an important role in the uptake of nutrients, maintenance of ion concentrations, and control of metabolism. Some carrier proteins transport a single solute or molecule across a membrane and these are called uniporters. With some other carrier proteins (coupled transporters) transfer of one solute depends on the simultaneous or sequential transfer of a second solute, either in the same direc-

Table 1.7. Transport mechanisms across plasma cell membrane

Mechanism	Transport process	Examples
Nonspecific processes		
Simple diffusion	Direct through the membrane and dependent on concentration gradient	Oxygen movement into cells
Osmosis	Direct and via diffusion of water molecules across a semipermeable membrane	Movement of water into cells when placed in hypotonic solution
Endocytosis		
Phagocytosis	Particles are engulfed by membrane through vesicle formation	Ingestion of bacteria or particles by leukocytes
Pinocytosis	Fluid is engulfed by membrane through vesicle formation	Transport of nutrients by human egg cells
Exocytosis	Extrusion of material from a cell involves membrane vesicles	Secretion of proteins by cells via small membrane vesicles
Specific processes		
Facilitated diffusion (passive diffusion)	Transport of molecules into the cells involves protein channels or transporters and is dependent on concentration gradient	Movement of glucose into most cells
Primary active transport	Transport of molecules against concentration gradient involves carrier protein and requires energy derived from hydrolysis of ATP	Na^+, K^+, Ca^{2+}, H^+ and Cl^- ions
Secondary active transport	As a consequence of primary active transport, diffusion energy sodium ions can pull other solutes into the cell (co-transport)	Glucose and amino acids
Receptor-mediated endocytosis	Endocytosis is triggered by the binding of a molecule to a specific receptor on the cell surface, followed by internalization of vesicles	Cholesterol (LDL) and transferrin uptake by cells

tion (symport) or in the opposite direction (antiport). Transporters are classified on the basis of their mechanism of translocation of substance and the energetics of the system. Transporters have specificity for the substance to be transported, have defined reaction kinetics, and can be inhibited by both competitive and noncompetitive inhibitors. Membranes of all cells contain highly specific transporters for the movement of inorganic anions and cations (Na^+, K^+, Ca^{2+}, Cl^-, HCO_3^-) and uncharged and charged organic compounds (amino acids, sugars).

Transport through the lipid bilayer or through the transport proteins involves simple diffusion, passive transport (facilitated diffusion), or active transport mechanisms. Certain macromolecules may also be transported by vesicle formation involving either endocytosis or exocytosis mechanisms. The major transport systems in mammalian cells are summarized in Table 1.7.

1.10.1 Transport of Water and Solutes

1.10.1.1 Diffusion

Body fluids are composed of two types of solutes: electrolytes, which ionize in solution and exhibit polarity (cations and anions), and nonelectrolytes such as glucose, creatinine, and urea that do not ionize in solution. The continual movement of solute molecules among each other in liquids or in gases is called diffusion. The solute molecules in the extracellular fluid or in the cytoplasm can spontaneously diffuse across the plasma membrane. However, the direction of movement of solutes by diffusion is always from a higher to a lower concentration, and Fick's first law of diffusion describes the rate. The overall effect of diffusion is the passive movement of molecules down a concentration until the concentration in each side is at chemical equilibrium. Diffusion through the cell membrane is divided into two separate subtypes known as simple diffusion and facilitated diffusion (Fig. 1.5a).

Simple diffusion can occur through the cell membrane, either through the intermolecular interstices of the lipid bilayer or through transport proteins (watery channels). The diffusion rate of a solute depends on its size (diffusion coefficient) and its lipid solubility. In addition, the diffusion rate is influenced by the differences in electrical potential across the membrane. Diffusion of small uncharged molecules (water, urea, glycerol) and hydrophobic molecules such as gases (O_2, N_2, CO_2, NO) occurs rapidly and depends entirely on the concentration gradient. Uncharged lipophilic molecules (fatty acids, steroids) diffuse relatively rapidly, but hydrophilic substances (glucose, inorganic ions) diffuse very slowly. Osmosis is a special case of diffusion in which free passage of water molecules across a cell membrane is permitted, but not that of solute molecules.

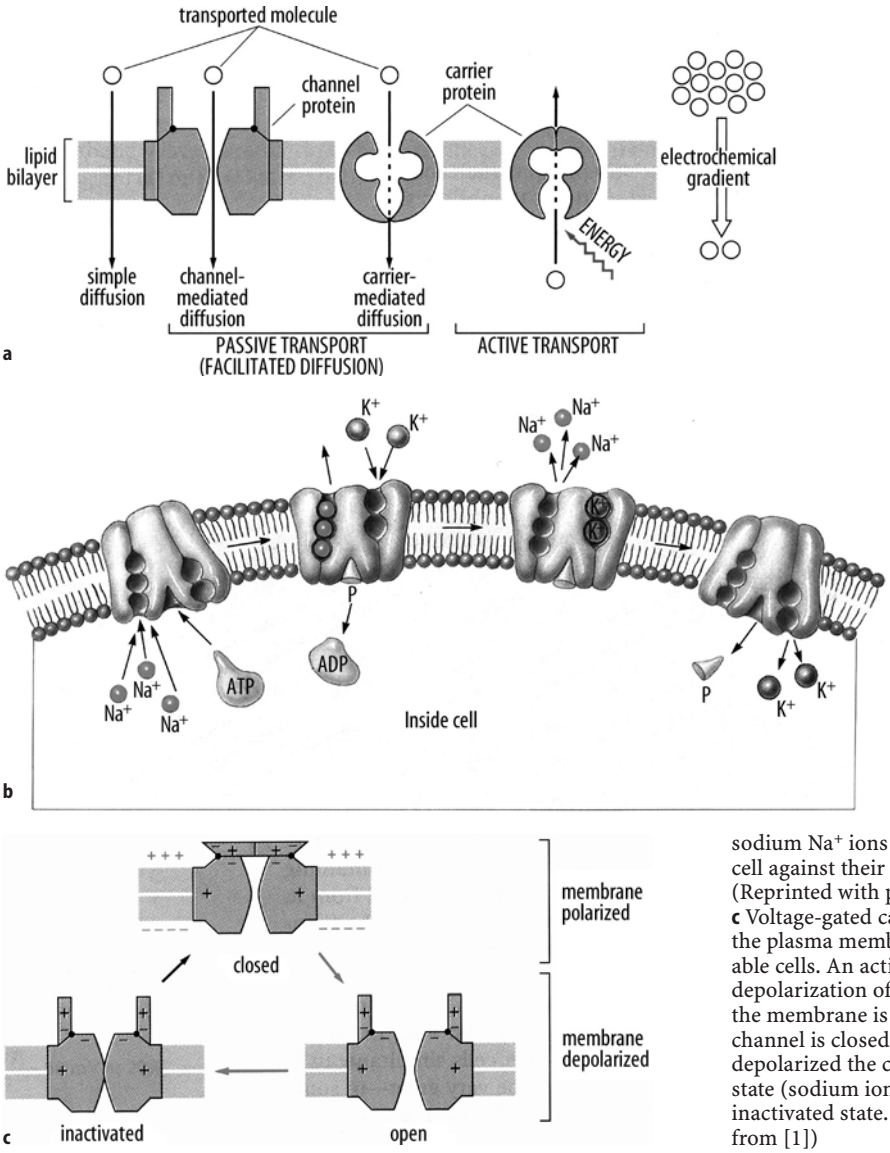

Fig. 1.5. a Membrane transport mechanisms of small molecules. Simple diffusion is dependent purely on concentration gradient. Facilitated diffusion involves either channel proteins or carrier proteins within the plasma membrane. While diffusion of molecules occur spontaneously, active transport also requires an input of metabolic energy. (Reprinted with permission from [1]). **b** The sodium-potassium pump. For every molecule of ATP hydrolyzed, the Na^+/K^+ ATPase carrier protein in the plasma membrane actively pumps three sodium Na^+ ions out of and two K^+ ions into the cell against their electrochemical gradients. (Reprinted with permission from [3]). **c** Voltage-gated cation channels are present on the plasma membrane of all electrically excitable cells. An action potential is triggered by a depolarization of the plasma membrane. When the membrane is at rest (highly polarized) the channel is closed, but when the membrane is depolarized the channel may exist in an open state (sodium ions move into the cell) or in an inactivated state. (Reprinted with permission from [1])

1.10.1.2 Facilitated Diffusion (Carrier-Mediated Diffusion)

Passive transport or facilitated diffusion involves translocating a solute through a cell membrane down its concentration gradient as in simple diffusion, without expenditure of metabolic energy. However, facilitated diffusion requires the interaction of a carrier protein (transporter) with the solute molecules. Upon entering the protein channel, the solute chemically binds to the transporter and induces a conformational change in the carrier protein, so that the channel is open in the intracellular side and releases the molecule (Fig. 1.5a). The rate of diffusion is dependent on the concentration gradient and approaches a maximum, called V_{max}, as the concentration of solute increases. It is important to recognize that in facilitated diffusion, the transporters are very specific for a solute and exhibit saturation kinetics. Transport of d-glucose is facilitated and a family of transporters (glucose permeases or GLUT 1 – 6) have been identified. Similarly, an anion transporter (Cl^--HCO_3^- exchanger) in erythrocytes involves antiport (two molecules in opposite directions) movement of Cl^- and HCO_3^- ions.

1.10.1.3 Active Mediated Transport

Active transport systems, or pumps, move the solute molecules through a cell membrane against its concentration gradient, and this requires the expenditure of some form of energy (Fig. 1.5a). As a result, the concentration of solute molecules on either side of the plasma

membrane is not equal. For example, the concentration of Na^+ ions in the extracellular fluid is ten times more than the concentration of Na^+ ions in the cytoplasm, while the converse is true with K^+ ions. In active transport, the transporters are very specific for a solute and exhibit saturation kinetics. In addition, the carrier protein imparts energy to the solute to move against electrochemical or concentration gradient. If the energy source is removed or inhibited, active transport mechanism is abolished. Most of the ions, amino acids, and certain sugars are actively transported across the plasma membrane.

In primary active transport, the energy is derived directly from the hydrolysis of ATP to ADP. The best-known active transport system is the Na^+/K^+-dependent ATPase pump (Fig. 5b), found in virtually all mammalian cells. The transporter protein is an enzyme ATPase. When three sodium ions bind on the inside and two potassium ions bind on the outside, the ATPase function of the transporter is activated. Following hydrolysis of one molecule of ATP, the liberated energy causes a conformational change in the carrier protein, releasing the sodium ions to the outside and potassium ions to the inside. The process leads to an electrical potential, with the inside of the cell more negative than the outside. The excitable tissues (muscle and nerve), kidneys, and salivary glands have a high concentration of the Na^+/K^+-dependent ATPase pump. The other important primary active transport pumps are for the transport of Ca^{2+} and H^+ ions.

Secondary active transport represents a phenomenon called co-transport, in which molecules are transported through the plasma membrane from the energy obtained not directly from the hydrolysis of ATP, but from the electrochemical gradient across the membrane. When sodium ions are transported out of the cells, an electrical potential develops which provides energy for the sodium ions to diffuse into the interior. This diffusion energy of sodium ions can pull other molecules into the cell. Glucose and many amino acids are transported into most cells via the sodium co-transport system. Following binding of sodium and glucose molecules to specific sites on the sodium-glucose transport protein, a conformational change is induced, and both the molecules are transported into the cell.

1.10.2 Transport by Vesicle Formation

Transport of macromolecules such as large proteins, polysaccharides, nucleotides, and even other cells across the plasma membrane is accomplished by a unique process called endocytosis, which involves special membrane-bound vesicles. The material to be ingested is progressively enclosed by a small portion of the plasma membrane, which first invaginates and then pinches off to form an intracellular vesicle. Many of the endocytosed vesicles end up in lysosomes, where they are degraded. Endocytosis is subcategorized into two types; pinocytosis involves ingestion of fluid and solutes via small vesicles, while phagocytosis involves ingestion of large particles such as micro-organisms via large vesicles called phagosomes.

Specialized cells that are professional phagocytes, such as macrophages and neutrophils, mainly carry out phagocytosis. For example, more than 10^{11} senescent red blood cells are phagocytosed by macrophages every day in a human body. In order to be phagocytosed, particles must bind to specialized receptors on the plasma membrane. Phagocytosis is a triggered process that requires the activated receptors to transmit signals to the interior of the cell to initiate the response. The Fc receptors on macrophages recognize and bind the Fc portion of antibodies that recognize and bind micro-organisms.

Most cells continually ingest bits of their plasma membrane in the form of small pinocytic (endocytic) vesicles that are subsequently returned to the cell surface. The plasma membrane has highly specialized regions called clathrin-coated pits that provide an efficient pathway for taking up macromolecules via a process called receptor-mediated endocytosis. Following binding of macromolecules to specific cell surface receptors in these clathrin-coated pits, the macromolecule-receptor complex is internalized. Most receptors are recycled via transport vesicles back to the cell surface for reuse. More than 25 different receptors are known to participate in receptor-mediated endocytosis of different types of molecules. Low-density lipoprotein (LDL) and transferrin are the most common macromolecules that are transported into the cell via receptor-mediated endocytosis.

The reverse of endocytosis is exocytosis, which involves transport of macromolecules within vesicles from the interior of the cell to a cell surface or into the extracellular fluid. Proteins and certain neurotransmitters can be secreted from the cells by exocytosis in either a constitutive or a regulated process. For example, insulin molecules stored in intracellular vesicles are secreted into the extracellular fluid following fusion of these vesicles with plasma membrane. By contrast, neurotransmitter molecules stored in synaptic vesicles of a presynaptic neuron are released into synapse only in response to an extracellular signal.

1.10.3 Transmission of Electrical Impulses

Nerve and muscle cells are "excitable"; this implies that they are capable of self-generation of electrochemical impulses at their cell membranes. These impulses can

be employed to transmit signals such as nerve signals from the central nervous system to many tissues and organs throughout the body. There is a difference in the ionic composition of extracellular fluid (ECF) and intracellular fluid (ICF). Whenever ion channels open or close there is a change in the movement of ions across a cell membrane. Movement of electrical charges is called a current. The flow of current reflects the charge separation across the membrane, i.e., its voltage or membrane potential, and is a measure of electrical driving force that causes ions to move. When cells are excited there is a change in current or voltage, and information passes along the nerves as electrical currents and associated voltage changes (impulses).

All body cells are electrically polarized, with the inside of the cell more negatively charged than the outside. The difference in electrical charge, or voltage, is known as the resting membrane potential and is about –70 to –85 mV. The resting membrane potential is the result of the concentration gradient of ions and differences in the relative permeability of membrane for different ions. The concentration of K^+ is higher inside the cell than outside, whereas the concentration of Na^+ is low inside cells and high outside. This difference in concentration is maintained by the Na^+/K^+-ATPase pump. In addition, the cell membrane is more permeable to K^+ than to other ions such as Na^+ and Cl^-, and K^+ can diffuse easily from ICF to ECF. Within the cell, there is an excess of anions due to negatively charged proteins that are impermeable.

When a cell such as a neuron is stimulated through voltage-regulated channels in sensory receptors or at synapses, ion channels for sodium open and, as a result, there is a net movement of Na^+ into the cell and the membrane potential decreases, making the cell more positively charged (Fig. 5c). The decrease in resting membrane potential is known as depolarization. At the point where the rapid change in the resting membrane potential reverses the polarity of the cell it is referred to as an action potential or simply a nerve impulse. Immediately following an action potential, the membrane potential returns to the resting membrane potential. The increase in membrane potential is known as repolarization, which results in the negative polarity of the cell as the voltage-gated sodium channels close and potassium channels open. The Na^+/K^+-ATPase pump moves K^+ back into the cell and Na^+ out of it. The absolute refractory period is the period of time during which it is impossible to generate another action potential, while the relative refractory period is the period of time in which a second action potential can be initiated by a stronger-than-normal stimulus.

Depolarization, i.e., the opening of sodium ion channels, generates a nerve impulse and is propagated along the nerve, because the opening of sodium ion channels facilitates the opening of other adjacent channels, causing a wave of depolarization to travel down the membrane of a nerve cell. When a nerve impulse reaches the far end of a nerve cell, the axon tip, the wave of depolarization causes the release of a neurotransmitter. At a neuromuscular junction, the release of acetylcholine depolarizes the muscle membrane and opens the calcium ion channels, permitting the entry of calcium ions into the cell, which triggers muscle contraction. In an excitatory neural synapse, the neurotrasmitter (acetylcholine) binds to the receptor in post-synaptic nerve fiber and opens sodium ion channels that result in the depolarization and propagation of impulse. By contrast, in an inhibitory synapse the neurotransmitter (gamma aminobutyric acid or GABA, glycine) binds to the receptor in post-synaptic nerve fiber and opens the potassium ion channels or chloride ion channels, resulting in the repolarization and inhibition of the impulse.

1.11 Cell Death

Cell death is extremely important in the maintenance of tissue homeostasis, embryonic development, immune self-tolerance, killing by immune effector cells, and regulation of cell viability by hormones and growth factors.

1.11.1 Programmed Cell Death

Apoptosis, or programmed cell death, is an important counterpart to mitosis for the regulation of cell numbers during development, in homeostatic cell turnover in the adult and in many other organs. Programmed cell death is an active cellular process that occurs in response to developmental or environmental changes, or as a response to physiological damage detected by the cell's internal surveillance networks.

Apoptosis is characterized by a series of biochemical and morphological alterations to the cell such as cell shrinkage, DNA fragmentation, and chromatin condensation. Two major apoptotic pathways have been defined in mammalian cells: the death-receptor pathway and the mitochondrial pathway (see Chapter 11 for details).

Cells undergo programmed death in response to both internal surveillance mechanisms and signals sent by other cells (Fig 1.6a). Thus, some cells effectively volunteer to die, whereas other cells are nominated for death by others. Cells that volunteer to die do so for a number of reasons, such as DNA damage and inappropriate signals to proliferate.

Cells can be nominated for death by other cells in many ways. Cells recognized as foreign pathogens un-

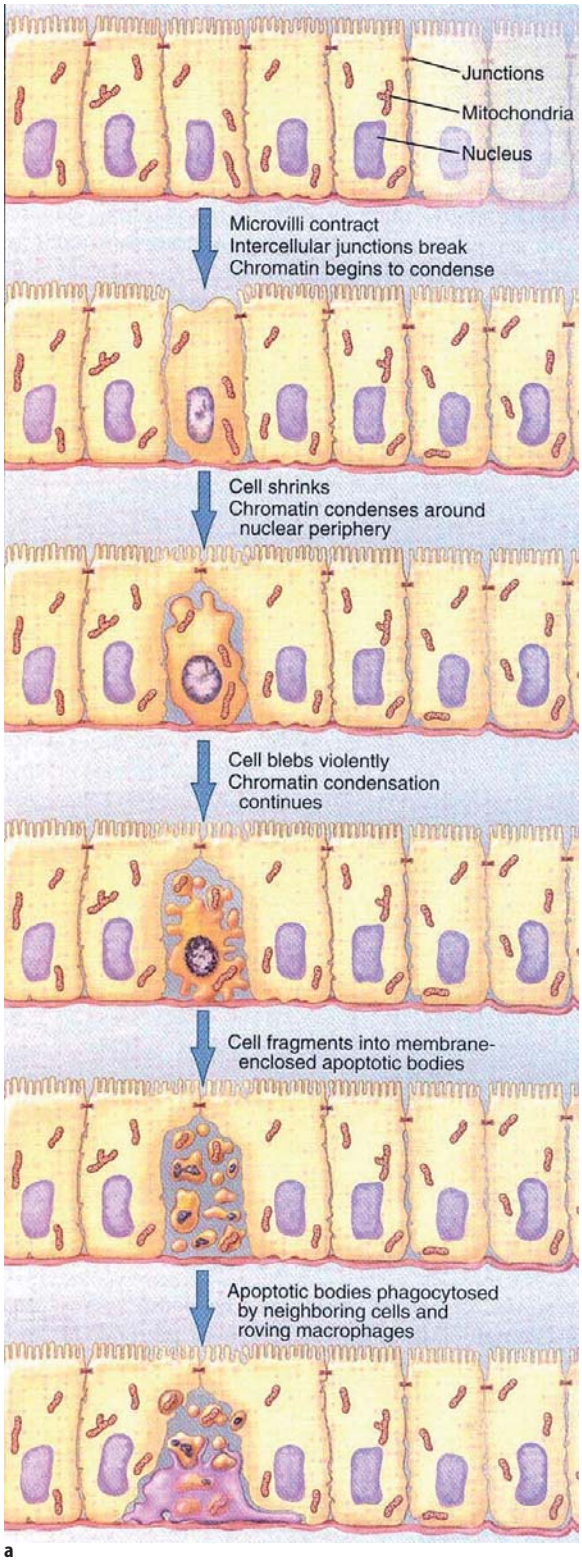

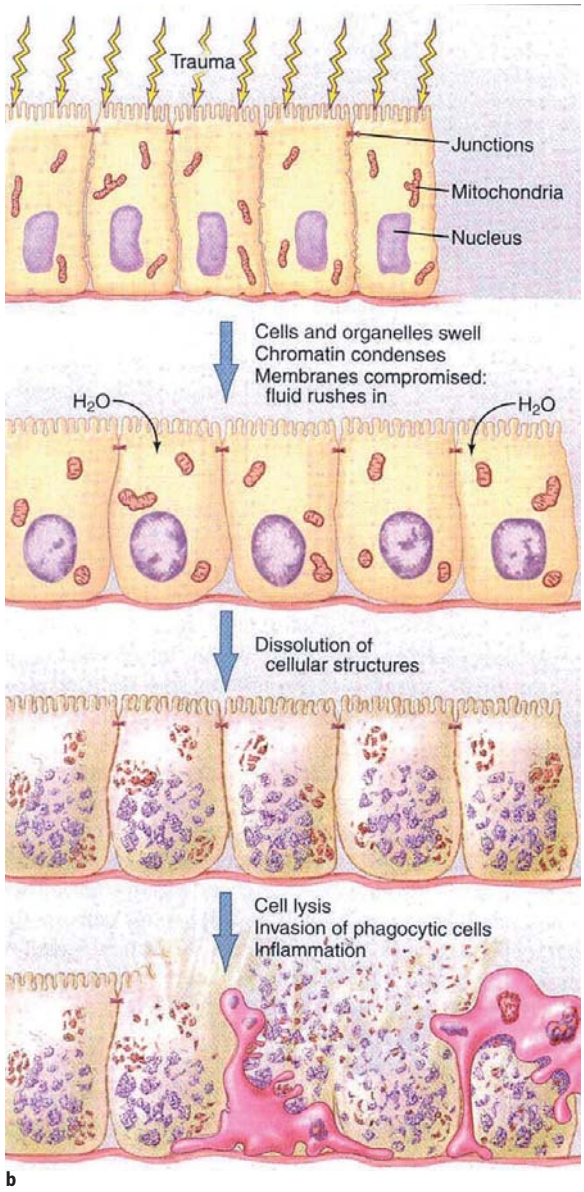

Fig. 1.6 a, b. Diagram illustrating cell death. Accidental cell death (**a**) where necrosis occurs as a result of injury to cells. Typically, groups of cells are affected. In most cases, necrotic cell death leads to an inflammatory response (red "angry" macrophages). **b** illustrates apoptosis or active cell suicide which typically affects single cells. Neighboring cells remain healthy. Apoptotic cell death does not lead to an inflammatory response. [From Pollard TD, Earnshaw WC (2002) Cell Biology, Saunders, Philadelphia, with permission]

dergo programmed cell death when attacked by cytotoxic T lymphocytes. Or cells may undergo programmed cell death if nurturing signals sent by other cells. Some cells respond to certain growth factors such as glucocorticoid hormones by undergoing programmed cell death.

A variety of cells undergo programmed cell death. These can be classified into many classes:

- Excess cells
  Embryonic ganglia have many more neurons than required to innervate their target muscles. Excess neurons that do not make appropriate connections have no function and so are eliminated by programmed cell death. Up to 80% of neurons in certain developing ganglia die in this way.
- Unnecessary cells
  These include the müllerian ducts, which develop into the female oviduct. In male embryos, progenitors of the müllerian duct develop, but they have no use. Programmed cell death eliminates the constituent cells of these embryonic ducts.
- Harmful cells
  These include cells with damaged DNA which tend to accumulate mutations, and they are potentially harmful to the organism. DNA damage induces programmed cell death in many cell types. Cells that harbor infectious agents, such as viruses, are also harmful to the organism. Infected cells are eliminated through the action of cytotoxic T lymphocytes, which kill these cells by inducing them to undergo programmed cell death. The cancer cells die during the treatment with chemotherapy agents because the drugs cause intracellular damage that acts as a signal for the induction of apoptotic cell death.
- Developmentally defective cells:
  For example, defects in T-cell receptor assembly are extremely common, and up to 95% of immature T cells die by apoptosis without leaving the thymus.
- Obsolete cells:
  Populations of cells that are fully functional may become obsolete as a result of physiological changes in the status of an organism. Tissues may disappear in a very brief time as their constituent cells undergo massive programmed death. Certain cells die when hormonal levels rise whereas others die as hormone levels decline, for example, in female mammals; difference in the size and composition of cells in the lactating and nonlactating states have been recognized. Therefore sex hormones can be used in the management of breast cancer.

Apoptosis is inhibited by a family of proteins [inhibitor of apoptosis (IAP)] which suppress apoptosis by interacting with and inhibiting the enzymatic activity of mature caspases. At least eight distinct mammalian IAPs have been identified and they all have antiapoptotic activity in the cell.

1.11.2 Accidental Cell Death

Necrosis or accidental cell death is cell death that results from irreversible injury to the cell. Cell membranes swell and become permeable. Lytic enzymes destroy the cellular contents, which then leak out into the intercellular space, leading to the mounting of an inflammatory response (Fig. 6b).

Accidental cell death occurs when cells receive a structural or chemical insult from which they cannot recover. Examples of such insults include ischemia (lack of oxygen), extremes of temperature, and physical trauma. The hallmark of necrosis is that cells die because they are damaged. In contrast, cells that die by programmed cell death commit suicide actively as a result of activation of a dedicated intracellular program. They appear completely healthy prior to committing suicide.

References

1. Alberts B, Bray D, Lewis J, et al (1994) Molecular biology of the cell, 3rd edn. Garland Publishing, New York
2. Kumar V, Abbas A, Faust N (2004) Robbins and Cotran pathologic basis of disease, 7th edn. W.B. Saunders, Philadelphia
3. Devin TM (1997) Textbook of biochemistry with clinical correlates, 4th edn. Wiley-Liss, New York
4. Guyton AC, Hall JE (1997) Human physiology and mechanisms of disease, 6th edn. W.B. Saunders, Philadelphia
5. Junqueira LC, Carneiro J, Kelley R (1995) Basic histology, 8th edn. Prentice-Hall, NJ, USA
6. McCance KL, Huether SE (1998) Pathophysiology. The biologic basis for disease in adults and children, 3rd edn. Mosby Year Book, St. Louis
7. Pollard TD, Earnshaw WC (2002) Cell biology, 1st edn. Saunders, Philadelphia
8. Raven PH, Johnson GB (1992) Biology, 3rd edn. Mosby Year Book, St. Louis
9. Sumner AT (2003) Chromosomes organization and function, 1st edn. Blackwell, Oxford
10. Yin XM, Dong Z (2003) Essentials of apoptosis: A guide for basic and clinical research, 1st edn. Humana Press, New Jersey, USA

Pathophysiology and Mechanisms of Radiopharmaceutical Localization

2

Shankar Vallabhajosula, Azu Owunwanne

2.1 Definition of Disease

At the present time, the precise definition of disease is as complex as an exact definition of life. It may be relatively more easy to define disease at a cellular and molecular level than at the level of an individual. Throughout the history of medicine, two main concepts of disease have predominated [1]. The ontological concept views a disease as an entity that is independent, self-sufficient, and runs a regular course with a natural history of its own. The physiological concept defines disease as a deviation from normal physiology or biochemistry; the disease is a statistically defined deviation of one or more functions from those of healthy people under circumstances as close as possible to those of a person of the same sex and age of the patient.

The term homeostasis is used by physiologists to mean maintenance of static, or constant, conditions in the internal environment by means of positive and negative feedback of information. About 56% of the adult human body is fluid. Most of the fluid is intracellular, and about one third is extracellular fluid that is in constant motion throughout the body and contains the ions (sodium, chloride, and bicarbonate) and nutrients (oxygen, glucose, fatty acids, and amino acids) needed by the cells to maintain life. Claude Bernard (1813 – 1878) described extracellular fluid as the internal environment of the body and hypothesized that the same biological processes that make life possible are also involved in disease [1]. The laws of disease are the same as the laws of life [1]. As long as all the organs and tissues of the body perform functions that help to maintain homeostasis, the cells of the body continue to live and function properly.

At birth, molecular blueprints collectively make up a person's genome or genotype that will be translated into cellular structure and function. A single gene defect can lead to biochemical abnormalities that produce many different clinical manifestations of disease, or phenotypes, a process called pleotropism. Many different gene abnormalities can result in the same clinical manifestations of disease – a process called genetic heterogeneity. Thus, diseases can be defined as abnormal processes as well as abnormalities in molecular concentrations of different biological markers, signaling molecules, and receptors.

2.2 Pathophysiology

In the year 1839, Theodor Schwann discovered that all living organisms are made up of discrete cells [2]. In 1858, Rudolph Virchow observed that a disease could not be understood unless it were realized that the ultimate abnormality must lie in the cell. He correlated disease with cellular abnormalities as revealed by chemical stains, thereby founding the field of cellular pathology. He defined pathology as physiology with obstacles [2].

Most diseases begin with cell injury, which occurs if the cell is unable to maintain homeostasis. Since the time of Virchow, gross pathology and histopathology have been a foundation of the diagnostic process and the classification of disease. Traditionally, the four aspects of a disease process that form the core of pathology are etiology, pathogenesis, morphological changes, and clinical significance [3]. The altered cellular and tissue biology and all forms of loss of function of tissues and organs are ultimately the result of cell injury and cell death. Therefore, knowledge of the structural and functional reactions of cells and tissues to injurious agents, including genetic defects, is the key to understanding the disease process. Currently, diseases are defined and interpreted in molecular terms and not just as general descriptions of altered structure. Pathology is evolving into a bridging discipline that involves both basic science and clinical practice and is devoted to the study of the structural and functional changes in cells, tissues, and organs that underlie disease [3]. The use of molecular, genetic, microbiological, immunological, and morphological techniques is helping us to understand both ontological and physiological causes of disease.

2.3 Altered Cellular and Tissue Biology

The normal cell is able to handle normal physiological and functional demands, so-called normal homeostasis. However, physiological and morphological cellular adaptations normally occur in response to excessive physiological conditions or to some adverse or pathological stimuli [3]. The cells adapt in order to escape and protect themselves from injury. An adapted cell is neither normal nor injured but has an altered steady state, and its viability is preserved. If a cell cannot adapt to severe stress or pathological stimuli, the consequence may be cellular injury that disrupts cell structures or deprives the cell of oxygen and nutrients. Cell injury is reversible up to a certain point, but irreversible (lethal) cell injury ultimately leads to cell death, generally known as necrosis. By contrast, an internally controlled suicide program, resulting in cell death, is called apoptosis.

2.3.1 Cellular Adaptations

Some of the most significant physiological and pathological adaptations of cells involve changes in cellular size, growth, or differentiation [3, 4]. These include (a) atrophy, a decrease in size and function of the cell; (b) hypertrophy, an increase in cell size; (c) hyperplasia, an increase in cell number; and (d) metaplasia, an alteration of cell differentiation. The adaptive response may also include the intracellular accumulation of normal endogenous substances (lipids, protein, glycogen, bilirubin, and pigments) or abnormal exogenous products. Cellular adaptations are a common and central part of many disease states. The molecular mechanisms leading to cellular adaptation may involve a wide variety of stimuli and various steps in cellular metabolism. Increased production of cell signaling molecules, alterations in the expression of cell surface receptors, and overexpression of intracellular proteins are typical examples.

2.3.2 Cellular Injury

Cellular injury occurs if the cell is unable to maintain homeostasis. The causes of cellular injury may be hypoxia (oxygen deprivation), infection, or exposure to toxic chemicals. In addition, immunological reactions, genetic derangements, and nutritional imbalances may also cause cellular injury. In hypoxia, glycolytic energy production may continue, but ischemia (loss of blood supply) compromises the availability of metabolic substrates and may injure tissues faster than hypoxia. Various types of cellular injury and their responses are summarized in Table 2.1.

Biochemical Mechanisms. Regardless of the nature of injurious agents, there are a number of common biochemical themes or mechanisms responsible for cell injury [4].

1. ATP depletion: Depletion of ATP is one of the most common consequences of ischemic and toxic inju-

Table 2.1. Progressive types of cell injury and responses (from [3])

Type	Responses
Adaptation	Atrophy, hypertrophy, hyperplasia, metaplasia
Active cell injury	Immediate response of "entire cell"
Reversible	Loss of ATP, cellular swelling, detachment of ribosomes, autophagy of lysosomes
Irreversible	"Point of no return" structurally when vacuolization of the mitochondria occurs and calcium moves into the cell
Necrosis	Common type of cell death with severe cell swelling and breakdown of organelles
Apoptosis	Cellular self-destruction to eliminate unwanted cell population
Chronic cell injury (subcellular alterations)	Persistent stimuli response may involve only specific organelles or cytoskeleton, e.g., phagocytosis of bacteria
Accumulations or infiltrations	Water, pigments, lipids, glycogen, proteins
Pathological calcification	Dystrophic and metastatic calcification

ry. ATP depletion induces cell swelling, decreases protein synthesis, decreases membrane transport, and increases membrane permeability.
2. Oxygen and oxygen-derived free radicals: Ischemia causes cell injury by reducing blood supply and cellular oxygen. Radiation, chemicals, and inflammation generate oxygen free radicals that cause destruction of the cell membrane and cell structure.
3. Intracellular Ca^{2+} and loss of calcium homeostasis: Most intracellular calcium is in mitochondria and endoplasmic reticulum. Ischemia and certain toxins increase the concentration of Ca^{2+} in cytoplasm, which activates a number of enzymes and causes intracellular damage and increases membrane permeability.
4. Mitochondrial dysfunction: A variety of stimuli (free Ca^{2+} levels in cytosol, oxidative stress) cause mitochondrial permeability transition (MPT) in the inner mitochondrial membrane, resulting in the leakage of cytochrome *c* into the cytoplasm.
5. Defects in membrane permeability: All forms of cell injury and many bacterial toxins and viral proteins damage the plasma membrane. The result is an early loss of selective membrane permeability.

Intracellular Accumulations. Normal cells generally accumulate certain substances such as electrolytes, lipids, glycogen, proteins, calcium, uric acid, and bilirubin that are involved in normal metabolic processes. As a manifestation of injury and metabolic derangements in cells, abnormal amounts of various substances, either normal cellular constituents or exogenous substances, may accumulate within the cytoplasm or in the nucleus, either transiently or permanently. One of the major consequences of failure of transport mechanisms is cell swelling due to excess intracellular fluid. Abnormal accumulations of organic substances such as triglycerides, cholesterol and cholesterol esters, glycogen, proteins, pigments, and melanin may be caused by disorders in which the cellular capacity exceeds the synthesis or catabolism of these substances. Dystrophic calcification occurs mainly in injured or dead cells, while metastatic calcification may occur in normal tissues due to hypercalcemia that may be a consequence of increased parathyroid hormone, destruction of bone tissue, renal failure, and vitamin-D-related disorders. All these accumulations harm cells by "crowding" the organelles and by causing excessive and harmful metabolites that may be retained within the cell or expelled into extracellular fluid and circulation.

2.3.3 Necrosis

Necrosis is cellular death resulting from the progressive degradative action of enzymes on the lethally injured cells, ultimately leading to the processes of cellular swelling, dissolution, and rupture. The morphological appearance of necrosis is the result of denaturation of proteins and enzymatic digestion (autolysis or heterolysis) of the cell. Different types of necrosis occur in different organs or tissues. The most common type is coagulative necrosis, resulting from hypoxia and ischemia. It is characterized by denaturation of cytoplasmic proteins, breakdown of organelles, and cell swelling, and it occurs primarily in the kidneys, heart, and adrenal glands. Liquefactive necrosis may result from ischemia or bacterial infections. The cells are digested by hydrolases and the tissue becomes soft and liquefies. As a result of ischemia, the brain tissue liquefies and forms cysts. In infected tissue, hydrolases are released from the lysosomes of neutrophils; they kill bacterial cells and the surrounding tissue cells, resulting in the accumulation of pus. Caseous necrosis, present in the foci of tuberculous infection, is a combination of coagulative and liquefactive necrosis. In fat necrosis, the lipase enzymes break down triglycerides and form opaque, chalky necrotic tissue as a result of saponification of free fatty acids with alkali metal ions. The necrotic tissue and the debris usually disappear by a combined process of enzymatic digestion and fragmentation or they become calcified.

2.3.4 Apoptosis

Apoptosis, a type of cell death implicated in both normal and pathological tissue, is designed to eliminate unwanted host cells in an active process of cellular self-destruction effected by a dedicated set of gene products. Apoptosis occurs during normal embryonic development and is a homeostatic mechanism to maintain cell populations in tissues. It also occurs as a defense mechanism in immune reactions and during cell damage by disease or noxious agents. Various kinds of stimuli may activate apoptosis. These include injurious agents (radiation, toxins, free radicals), specific death signals (TNF and Fas ligands), and withdrawal of growth factors and hormones. Within the cytoplasm a number of protein regulators (Bcl-2 family of proteins) either promote or inhibit cell death. In the final phase, the execution caspases activate the proteolytic cascade that eventually leads to intracellular degradation, fragmentation of nuclear chromatin, and breakdown of cytoskeleton. The most important morphological characteristics are cell shrinkage, chromatin condensation, and the formation of cytoplasmic blebs and apoptotic bodies that are subsequently phagocytosed by adjacent healthy cells and macrophages. Unlike necrosis, apoptosis is nuclear and cytoplasmic shrinkage and affects scattered single cells.

2.4 Radiopharmaceuticals

Chemistry is the language of health and disease, because the body is a vast network of interacting molecules. If the definition of the disease is molecular, diagnosis becomes molecular [5]. Because the treatment of many diseases is chemical, it becomes more and more appropriate that chemistry be the basis of diagnosis and of the planning and monitoring of treatment [1]. Nuclear medicine, in the simplest terms, is the medical specialty based on examining the regional chemistry of the living human body. In the 1920s, Georg DeHevesy coined the term "radioindicator" (radiotracer) and introduced the "tracer principle" to the biomedical sciences [1]. One of the most important characteristics of a true tracer is the ability to study the components of a homeostatic system without disturbing their function. Since the physiological approach defines a disease in terms of the failure of a normal physiological or biochemical process, the nuclear medicine diagnostic procedures involve four types of measurement: (a) regional blood flow, transport, and cellular localization of various molecules; (b) metabolism and bioenergetics of tissues; (c) physiological function of organs; and (d) intracellular and intercellular communication.

A number of radiopharmaceuticals (Table 2.2) have been designed and developed over the past four decades to image the structure and function of many organs and tissues. Radiopharmaceutical agents exhibit a huge range of physical and chemical properties and may be classified into eight different categories. The most important factors that influence the transport, uptake, and retention of radiopharmaceuticals in different organs and tissues include the chemical and biochemical nature of the carrier molecule transporting the radionuclide of choice to the targeted area. The use of radiopharmaceuticals to deliver therapeutic doses of ionizing radiation has been extensively investigated. Targeted radionuclide therapy by systemic administration of a radiopharmaceutical provides a potential to treat widely disseminated cancer tissue. A number of radiopharmaceuticals (Table 2.3) are now available for the treatment of different malignancies or palliation of pain due to bony metastases. Tumor-specific radiopharmaceuticals that are clinically useful for noninvasive imaging of tumors are being modified for radionuclide therapy of tumors.

Table 2.2. Radiopharmaceuticals for diagnostic imaging studies

Radiopharmaceutical	Application	Indication for imaging
Radiolabeled particles		
^{99m}Tc-MAA, 10 – 50 μm	Capillary blockade	Lung perfusion
^{99m}Tc-DTPA, aerosol, 1 – 4 μm	Sedimentation in bronchioles	Lung ventilation
^{99m}Tc-Sulfur colloid, 0.1 – 1.0 μm	Reticuloendothelial function	Liver, spleen, and bone marrow
^{99m}Tc-SC, filtered 0.1 – 0.3 μm	Lymphatic drainage	Breast cancer and melanoma
^{99m}Tc-HSA (nanocolloid), 0.02 μm	Lymphatic drainage	Breast cancer and melanoma
^{99m}Tc-Antimony sulfide colloid, 0.1 μm	Lymphatic drainage	Breast cancer and melanoma
Radiolabeled gases		
^{133}Xe, ^{127}Xe, ^{81m}Kr	Alveolar transit-capillary diffusion	Lung ventilation
^{99m}Tc-Technegas, 0.004 – 0.25 μ	Alveolar transit-capillary diffusion	Lung ventilation
Radiolabeled chelates		
^{99m}Tc-MDP, HDP	Bone formation	Metastatic bone disease, neuroblastoma, osteosarcoma
^{99m}Tc-DTPA	Blood brain barrier disruption Renal function glomerular filtration	Brain tumors Renal blood flow and renogram
^{99m}Tc-MAG3	Renal function, tubular secretion	Renogram
^{99m}TcIII-DMSA	Binding to renal parenchyma	Renal scan
^{99m}TcV-DMSA	Tumor cell uptake	Medullary carcinoma of thyroid
^{99m}Tc-Disofenin and mebrofenin	Hepatobiliary function	Hepatobiliary imaging
^{99m}Tc-Ceretec and Neurolite	Blood flow	Brain imaging
^{99m}Tc-sestamibi and tetrafosmin	Blood flow	Myocardial perfusion
^{99m}Tc-sestamibi, and tetrafosmin	Tumor viability and multidrug resistance, MDR (Pgp expression)	Breast cancer, parathyroid adenoma, brain tumor
^{111}In-DTPA	CSF flow	Cisternogram
^{111}In-oxine	Radiolabeling white cells	Labeled leukocyte thrombus imaging
^{67}Ga-citrate	Tumor viability, capillary leakage	Tumor and infection imaging
Radiotracers as ions		
^{99m}Tc-pertechnetate (TcO_4^-)	Thyroid function (trapping)	Thyroid imaging
^{123}I,^{131}I-sodium iodide (I^-)	Thyroid function (trapping)	Thyroid uptake, imaging therapy
^{82}Rb-chloride, Rb^+	Blood flow	Myocardial perfusion
^{201}Tl-thallous chloride, $Tl(OH)_2^+$	Blood flow Tumor viability	Myocardial perfusion Tumor imaging (brain, parathyroid, thyroid)

Table 2.2. *(cont.)*

Radiopharmaceutical	Application	Indication for imaging
Radiolabeled cells		
^{111}In-leukocytes	Cell migration and phagocytosis	Infection imaging
^{111}In-platelets	Cell incorporation in thrombus	Thrombus imaging
^{51}Cr-RBCs	Dilution in blood compartment	RBC mass and blood volume
^{99m}Tc-RBCs	Cardiac function	Cardiac ejection fraction, wall motion
	Blood pool	Hemangioma, GI bleeding
^{99m}Tc-RBC (heat denatured)	Spleen	Accessory splenic tissue
Receptor binding radiotracers		
^{111}In-pentetreotide, Octreoscan	Somatostatin receptors	Neuroendocrine tumors
^{99m}Tc-P829, Neotec	Somatostatin receptors	Lung cancer, NE tumors
^{99m}Tc-P280, Acutect	GP IIb/IIIa receptors	Thrombus imaging, DVT
^{99m}Tc-TRODAT-1	Dopamine transporter	Brain imaging-dopamine D2 receptors
^{123}I-VIP	VIP receptors	Gastrointestinal tumors
^{131}I-NP-59	LDL receptor, cholesterol metabolism	Adrenal carcinoma, adenoma, Cushing's syndrome
^{123}I- or ^{131}I-MIBG	Presynaptic adrenergic receptors	Myocardial failure
	Adrenergic tissue uptake	Tumor imaging (pheochromocytoma, neuroendocrine, neuroblastomas)
[^{11}C]Raclopride	Dopamine D2 receptors	Brain imaging-dopamine D2 receptors
^{123}I-IBZM	Dopamine D2 receptors	Brain imaging-dopamine D2 receptors, tumor imaging, malignant melanoma
[^{18}F]fluoro-estradiol (FES)	Estrogen receptors	Breast tumor imaging
Radiolabeled monoclonal antibodies		
^{111}In-Oncoscint, B72.3 IgG	TAG-72 antigen	Colorectal and ovarian cancer
^{111}In-Prostascint, 7E11-C5.3 IgG	PSMA (intracellular epitope)	Prostate cancer
^{99m}Tc-CEA-Scan, IMMU-4 Fab'	CEA	Colorectal cancer
^{99m}Tc-Verluma, NR-LU-10 Fab'	Cell surface GP as antigen	Small cell lung cancer
^{99m}Tc-fanolesomab (CD15)	Granulocyte antigen CD15	Appendicitis
^{111}In-antimyosin	Antimyosin	Acute myocardial infarction, heart transplant rejection
Radiolabeled metabolic substrates		
^{18}F-Fluorodeoxyglucose, FDG	Tumor viability and metabolism	Tumor imaging
	Glucose metabolism	Brain and cardiac imaging
^{18}F-Fluorothymidine	Cell proliferation	Tumor imaging and monitoring treatment
^{11}C-choline	Cell proliferation	Brain tumors
[^{11}C] or ^{123}I-methyl tyrosine	Protein synthesis, protein upregulation	Brain tumors
^{11}C-methionine	Amino acid transport	Brain and pancreatic tumors
[^{11}C]-thymidine	DNA synthesis, cell proliferation	Brain tumors
[^{18}F] and ^{123}I-fatty acids	Myocardial metabolism	Cardiac imaging
[^{57}Co]-vitamin B_{12}	Vitamin B_{12} absorption	Pernicious anemia
^{18}F-fluoromisonidazole	Hypoxia and oxidative metabolism	Tumors selected for radiotherapy
^{18}F-fluoroethyltyrosine(FET)	Amino acid transporter	Brain tumors

Table 2.3. Radiopharmaceuticals for therapy

Radiopharmaceutical	Application	Specific tumors
^{131}I-sodium iodide	Thyroid function	Differentiated thyroid carcinoma
^{131}I-MIBG	Adrenergic tissue	Colorectal cancer metastatic to liver and bladder cancer
^{131}I-anti B1 antibody	Anti CD22 antigen	Lymphoma
^{90}Y-MXDTPA-anti B1 antibody	Anti CD22 antigen	Lymphoma
^{32}P-chromic phosphate (colloid)	Cell proliferation and protein synthesis	Peritoneal metastases, recurrent malignant ascites
^{32}P-orthophosphate	Cell proliferation and protein synthesis	Polycythemia vera
^{89}Sr chloride	Exchanges with Ca in bone	Palliation of pain due to bony metastases
^{153}Sm-EDTMP	Binds to hydroxyapatite	Palliation of pain due to bony metastases
^{117m}Sn-DTPA	Binds to hydroxyapatite	Palliation of pain due to bony metastases
^{186}Re-HEDP	Binds to hydroxyapatite	Palliation of pain due to bony metastases
^{90}Y-DOTA-Tyr^3-octreotide	Somatostatin receptors	Neuroendocrine tumors
^{90}Y-DOTA-lanreotide	Somatostatin receptors	Neuroendocrine tumors
^{90}Yb-ibritumomab	Lymphocyte antigen CD20	Lymphoma

2.5 Mechanism(s) of Radiopharmaceutical Localization

The uptake and retention of radiopharmaceuticals by different tissues and organs involve many different mechanisms, as summarized in Table 2.4. The pharmacokinetics, biodistribution, and metabolism of the radiopharmaceutical are very important to understanding the mechanisms of radiopharmaceutical localization in the organ or tissue of interest. As discussed above under Pathophysiology, the injury to a cell or tissue significantly alters the morphology and molecular biology compared with that of normal tissue or organs. This is especially true of malignant tissue. Compared with normal cells, the tumor cells have very distinct characteristics. These include (a) an increased rate of cell proliferation, (b) altered membrane transport features associated with blood vessels and tumor cells, (c) altered perfusion within the tumor, (d) altered metabolism, (e) altered expression of specific receptors for hormones, and (f) expression of specific tumor-associated antigens.

The mechanisms of radiopharmaceutical localization may be substrate-nonspecific (not participating in any specific biochemical reaction) or substrate specific (participating in a specific biochemical reaction), depending upon the chemistry of the molecule. Many radiopharmaceuticals were designed to take advantage of the pathophysiology in order to increase the specificity of the nuclear medicine imaging techniques. Since some radiopharmaceuticals are not specific for a particular disease, the cellular uptake might include a combination of different mechanisms, as in the case of ^{67}Ga citrate. However, the unique chemistry of each radiopharmaceutical may determine the manner in which it is transported and retained within a specific tissue or organ. It is very important to recognize that since the radiopharmaceutical may have significant metabolism and degradation in vivo, the observed bio-

Table 2.4. Mechanisms of radiopharmaceutical localization

	Mechanism	Radiopharmaceutical
1.	Isotope dilution	^{125}I-HSA, ^{51}Cr-RBC, and ^{99m}Tc-RBC
2.	Capillary blockade	^{99m}Tc-MAA
3.	Physicochemical adsorption	^{99m}Tc-MDP, HDP
4.	Cellular migration	^{111}In- and ^{99m}Tc-leukocytes, ^{111}In-platelets
5.	Cell sequestration	Heat denatured ^{99m}Tc-RBC
6.	Simple diffusion	^{133}Xe, ^{81m}Kr, ^{99m}Tc-pertechnegas
	Diffusion and mitochondrial binding	^{99m}Tc-sestamibi and tetrafosmin
	Diffusion and intracellular binding	^{99m}Tc-Ceretec and Neurolite
	Diffusion and increased capillary permeability	^{67}Ga-citrate
7.	Facilitated diffusion and transport, protein upregulation	[^{18}F]-FDG, radiolabeled amino acids
8.	Active transport	Radioiodide, $^{99m}TcO_4^-$, ^{201}Tl thallous cation
		[^{18}F]-FDG, radiolabeled amino acids
	Na^+/K^+ ATPase pump	^{201}Tl thallous cation
9.	Phagocytosis	^{99m}Tc-colloids in RES and lymph nodes
10.	Increased vascular permeability and capillary leakage	^{67}Ga-citrate, radiolabeled proteins
11.	Cell proliferation	[^{11}C]-thymidine, [^{124}I]-iododeoxyuridine (IudR), ^{18}F-fluorothymidine (FLT)
12.	Metabolic trapping	[^{18}F]-FDG, ^{99m}Tc-pertechnetate
13.	Metabolic substrates	^{123}I and ^{131}I as sodium iodide, ^{123}I-fatty acids
14.	Tissue hypoxia and acidic pH	[^{18}F]fluoromisonidazole, ^{67}Ga-citrate
15.	Specific receptor binding	
	Somatostatin receptors	OctreoScan, NeoTect
	VIP receptors	^{123}I-VIP
	Transferrin receptors	^{67}Ga-citrate
	Estrogen receptors	16α-[^{18}F]fluoro-17β-estradiol (FES)
	Dopamine D2 receptors	[^{123}I]-IBZM, ^{99m}Tc-TRODAT
	LDL receptors	^{131}I-6β-iodomethyl-19-norcholesterol (NP-59)
	Presynaptic adrenergic reuptake	[^{131}I or ^{123}I]-MIBG
16.	Specific binding to tumor antigens	
17.	PSMA	ProstaScint
	CEA	CEA-Scan
	TAG-72	OncoScint
	Cell surface 40-kd glycoprotein	Verluma
	CD22	Bexaar
	CD15	^{99m}Tc-fanolesomab
	Antimyosin	^{111}In-antimyosin

distribution and tissue localization may represent the behavior of only radiolabeled metabolic product and not necessarily that of the intact parent radiopharmaceutical. In addition, the patient's medication and many other factors may significantly alter the biodistribution and tissue localization and retention characteristics of a radiopharmaceutical. The different mechanisms of localization are discussed below, using specific examples of the more common radiopharmaceuticals.

2.5.1 Isotope Dilution

The dilution principle is based on the concept of "diluting" a radiotracer (or tracer) of known activity (or mass) in an unknown volume. By measuring the degree to which the radiotracer was diluted by the unknown volume, one can determine the total volume (or mass) of the unknown volume. The dilution principle is currently used for a quantitative determination of RBC volume (mass), plasma volume, and total blood volume. It is very important that the radiotracer remain only in the blood volume to be measured. Nondiffusible intravascular agents such as ^{51}Cr-RBCs are used to measure RBC mass, while ^{125}I-HSA is used to measure plasma volume. There is no specific mechanism involved other than simple dilution of the radiotracer. The use of ^{99m}Tc-RBCs for the measurement of cardiac ejection fraction and gastrointestinal bleeding studies is another application of the dilution principle.

2.5.2 Capillary Blockade

The technique most commonly used to determine the perfusion to an organ depends on trapping the radiolabeled particles (microembolization) in the capillary bed of an organ such as lung, heart, or brain. Pulmonary capillaries have a mean diameter of about 8 μm and the precapillary arterioles have a diameter of 20–25 μm. ^{99m}Tc-MAA particles generally are in the range of 10 – 50 μm in diameter. Therefore, following intravenous injection, ^{99m}Tc-MAA particles are physically trapped in the arteriocapillary beds of the lung and block the blood flow to the distal regions. Smaller particles pass through the pulmonary capillaries and are extracted by the reticuloendothelial system in the body. Therefore, the mechanism of localization of particles in lungs is purely a mechanical process, called capillary blockade. The gold standard for the determination of perfusion in experimental animal studies is radiolabeled microspheres, with varying physical half-lives and particle diameters.

2.5.3 Physicochemical Adsorption

Bone scanning with ^{99m}Tc-labeled phosphonates (MDP, HDP) is extensively used in nuclear medicine to evaluate osteomyelitis, arthritis, Paget's disease, and the bone involvement or metastatic spread to bone in patients with a wide variety of cancers. The ^{99m}Tc-phosphonates accumulate in hydroxyapatite (HA) crystal (containing Ca^{2+} and phosphate ions) matrix or in the amorphous (noncrystalline) calcium phosphate (ACP). The principal uptake mechanism of the radiotracer appears to be simply "physicochemical adsorption". However, the exact mechanisms involved in the extraction of the radiotracer from the blood through the endothelial cells, extracellular fluid, and finally to HA are not known. In contrast to the P-O-P bond in phosphates, the P-C-P bond in phosphonates is not a substrate for alkaline phosphatase and is very stable in vivo. Primary bone tumors such as osteogenic sarcomas avidly accumulate bone agents because of the production of bone matrix in extraosseous tissue. Metastatic deposits that produce a vigorous osteoblastic response will appear as hot spots in a bone scan, while the lesions that generate osteolytic reactions may not accumulate the bone agent [6]. The bone scanning agents may also be taken up occasionally in soft tissues. The primary underlying factor responsible for the uptake of these tracers is excess calcium in soft tissue. Cell hypoxia and cell death would lead to increased deposition of calcium phosphates in the extracellular fluid. The uptake of ^{99m}Tc-phosphonates in the soft tissues is believed to be due to chemisorption on the surface of calcium salts.

The localization of bone-seeking radiotracers in increased amounts at the tumor-bone interface provides the basis for the use of radionuclides in the treatment of bone pain. Several radiopharmaceuticals (Table 2.3) are indicated for relief of pain (bone pain palliation) in patients with confirmed osteoblastic bone lesions. The exact mechanism of action of relieving the pain of bone metastases is not known, however.

2.5.4 Cellular Migration and Sequestration

^{111}In-oxine- or ^{99m}Tc-HMPAO-labeled autologous mixed leukocytes (predominantly neutrophilic polymorphonuclear leukocytes, PMNs) are routinely used to image various inflammatory diseases and infectious processes. The inflammatory reaction is a well-described sequence of events in response to an infection. In an acute infection, within the first 6 – 12 h the predominant cells infiltrating a site of infection are the PMNs. Following intravenous administration of radiolabeled leukocytes, the labeled cells migrate to the site of infection, similar to the circulating leukocytes. The

leukocytes migrate to the site of infection/inflammation because they are attracted by the immediately generated chemotactic factors, such as complement subcomponents. In a similar manner, ^{111}In-platelet localization at the site of active thrombus formation also involves simple cellular migration, since platelets play a major role in thrombus formation.

Accessory splenic tissue can develop after splenectomy. Heat-damaged ^{99m}Tc-RBCs are more specific for the detection of accessory splenic tissue. Following intravenous administration, the spleen sequesters the heat-damaged RBCs in the same way that old and damaged circulating RBCs are normally removed.

2.5.5 Membrane Transport

The cell membrane consists of a lipid bilayer that is not miscible with either the extracellular fluid or the intracellular fluid and provides a barrier for the transport of water molecules and water-soluble substances across the cell membrane. The transport proteins with in the lipid bilayer, however, provide different mechanisms for the transport of molecules across the membrane. Membranes of most cells contain pores or specific channels that permit the rapid movement of solute molecules across the plasma membrane. Channels are selective for specific inorganic ions, whereas pores are not selective. Plasma membranes contain transport systems (transporters) that involve intrinsic membrane proteins and actually translocate the molecule or ion across the membrane by binding and physically moving the substance. Transporters play important roles in the uptake of nutrients, maintenance of ion concentrations, and control of metabolism. Transport through the lipid bilayer or through the transport proteins may involve simple diffusion, passive transport (facilitated diffusion), or active transport mechanisms. Certain macromolecules may also be transported by vesicle formation, involving either endocytosis or exocytosis mechanisms.

2.5.5.1 Simple Diffusion

The mechanism of localization of many radiopharmaceuticals in target organs involves a simple diffusion process. The direction of movement of the radiotracers by diffusion is always from a higher to a lower concentration, and the initial rate of diffusion is directly proportional to the concentration of the radiotracer. A net movement of molecules from one side to another will continue until the concentration on each side is at chemical equilibrium.

The gases used for ventilation studies, such as ^{133}Xe, ^{127}Xe, and ^{81m}Kr, are inert lipophilic gases. Following their administration through inhalation, these gases are distributed within the lung air spaces by diffusion, proportional to ventilation. The distribution, however, is interrupted in obstructive airways. The gases pass from the lungs into the pulmonary venous circulation and are released through the lungs by the mechanism of alveolar capillary diffusion. Similarly, distribution of ^{99m}Tc-Technegas within the lung also involves diffusion. By contrast, the irregular distribution of ^{99m}Tc-DTPA aerosol preparation within the lung is due mostly to gravity sedimentation depending on particle size.

2.5.5.1.1 Diffusion and Intracellular Metabolism/Binding

The blood-brain barrier (BBB) plays an important role in the mechanism of localization of many radiopharmaceuticals in the brain. The endothelial cells of the cerebral vessels form a continuous layer without gap junctions, preventing diffusion of water-soluble molecules. In certain pathological conditions, the BBB is disrupted, allowing water-soluble molecules to diffuse from the blood into brain tissue. Traditionally, the brain scan was performed with such radiopharmaceuticals as ^{99m}Tc-pertechnetate and ^{99m}Tc-DTPA, that diffuse freely in the extracellular fluid and can accumulate in lesions with defects in BBB. The intact BBB does allow the transport of small molecules across the plasma

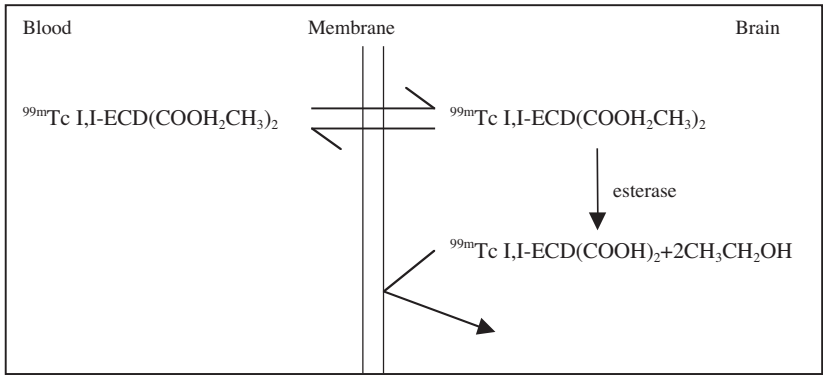

Fig. 2.1. With the labeling of red blood cells (RBCs) with ^{99m}Tc whether in vitro or in vivo, the $^{99m}TcO_4$ freely diffuses in and out of the RBCs, but in the presence of stannous ion it is reduced intracellularly, where it reacts with hemoglobin (HB) to form ^{99m}Tc-Hb. The ^{99m}Tc-Hb does not diffuse out of the RBCs as shown in Fig. 2.2

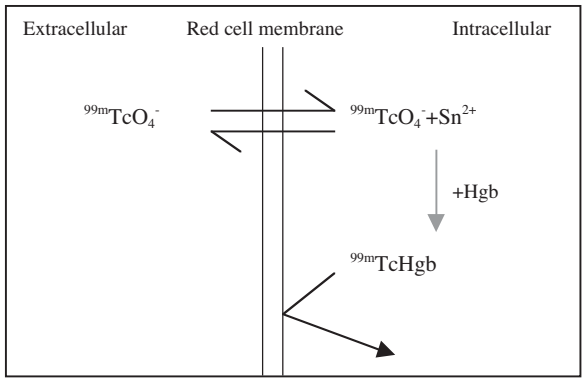

Fig. 2.2. Intracellular binding of $^{99m}TcO_4$ to Hgb

membrane of the neuron by facilitated diffusion. Some small, neutral molecules, however, can cross the BBB depending on their relative lipid solubility. Brain perfusion-imaging agents such as ^{123}I-IMP (N-isopropyl-*p*-iodoamphetamine), ^{99m}Tc-HMPAO (Ceretec), and ^{99m}Tc-ECD (Neurolite) are lipophilic radiotracers that cross the BBB via passive diffusion. The extraction of these tracers by the brain tissue is proportional to regional cerebral blood flow (rCBF). The retention of these tracers within the neuronal tissue following diffusion and extraction is assumed to be due to intracellular binding or metabolic degradation to polar metabolites or charged complexes that cannot be washed out of the cell by back-diffusion as exemplified by the cellular retention of ^{99m}Tc-ECD (Fig. 2.1) and labeling of ^{99m}Tc-pertechnetate with RBC (Fig. 2.2). With ^{99m}TC-ECD the radiotracer freely diffuses into the brain tissue, where it is hydrolyzed by the action of esterase to an acid which is trapped in the brain tissue. For ^{99m}TcO4, the tracer is reduced intracellulary by the circulating stannous ion and the reduced ^{99m}Tc binds to Hgb to form ^{99m}TcHgb that does not diffuse out of the brain tissue.

2.5.5.1.2
Diffusion and Mitochondrial Binding

A number of lipophilic, cationic ^{99m}Tc radiopharmaceuticals (sestamibi, tetrofosmin, and furifosmin) have been developed for imaging myocardial perfusion. Although ^{99m}Tc-sestamibi is cationic, similar to $^{201}Tl^+$, the transport of this agent through the cell membrane involves only passive diffusion since the transport process is temperature dependent and nonsaturable [7]. The myocardial cell uptake of ^{99m}Tc-sestamibi was initially considered to be due to binding of the cell membrane to lipid components. It was later shown that intracellular binding of ^{99m}Tc-sestamibi was associated mainly with mitochondria. Using cultured chicken myocytes, Piwnica-Worms et al. [8] observed that the cellular entry of ^{99m}Tc-sestamibi is related to the mitochondrial metabolism and the negative inner membrane potential of the mitochondria. The mitochondrial retention of ^{99m}Tc-sestamibi, however, is not organ or tumor specific, but appears to be a mechanism common to most types of tissue. The intracellular levels of Ca^{2+} in normal cells are significantly low. However, with irreversible ischemia, extracellular calcium enters the cell and is sequestered in the mitochondria, resulting in mitochondrial destruction. The increased calcium concentration in mitochondria blocks ^{99m}Tc-sestamibi binding to mitochondria.

A number of investigators have reported the diagnostic potential of ^{99m}Tc lipophilic cationic complexes for imaging parathyroid adenomas, osteosarcomas, and tumors of the brain, breast, lung, and thyroid.

The mechanisms of uptake of sestamibi and tetrofosmin have been compared to that of ^{201}Tl in tumor cell lines [9]. While the ^{99m}Tc agents are associated with mitochondria, ^{201}Tl remains in the cytoplasmic compartment. There were significant differences between sestamibi and tetrofosmin regarding intracellular localization based on in vitro studies. While 90% of total sestamibi was associated with mitochondria, most of the tetrofosmin accumulated in the cytosolic fraction [9]. The uptake and retention of lipophilic ^{99m}Tc cationic agents by tumor cells appear to be related to the back-diffusion or efflux of the tracer from the cell. There is now extensive evidence suggesting that the transport of the tracer out of the tumor cell is mediated by P-glycoprotein (Pgp), a 17-kd plasma membrane lipoprotein encoded by the human multidrug resistance (MDR) gene. Piwnica-Worms et al. [10, 11] demonstrated that sestamibi is a transport substrate for Pgp and is useful for imaging Pgp expression.

2.5.5.1.3
Diffusion and Increased Capillary and Plasma Membrane Permeability

^{67}Ga-citrate has been shown to localize in a variety of tumors and inflammatory lesions. In the past three decades, a number of investigators have reported various physical and biochemical factors responsible for the tumor uptake of ^{67}Ga-citrate. However, there is still no general agreement on the exact mechanisms of localization in tumors, as indicated by many review articles [12, 13]. Following intravenous administration of carrier-free ^{67}Ga as gallium citrate, ^{67}Ga is bound exclusively to the two specific metal-binding sites of iron-transport glycoprotein, transferrin in normal plasma, and is transported to normal tissues and tumor sites predominantly as ^{67}Ga-transferrin complex [14]. At a physiological pH of 7.4, gallium may also exist as a soluble gallate ion, $Ga(OH)_4^-$. The volume of distribution of ^{67}Ga in patients is about 23 l, suggesting that gallium is extensively distributed in the extravascular space [13]. While the ^{67}Ga-transferrin complex is slowly

transported through the capillary vessel wall, the non-transferrin-bound, free gallium rapidly leaves the blood compartment and equilibrates with the interstitial fluid of normal and tumor tissue. The increased capillary permeability and the expanded extracellular space of tumor tissue would also augment the transport of macromolecules such as transferrin (80 kd) across the leakier tumor blood vessels. Increased transferrin concentration within the interstitial fluid of the tumors would also lend support to the role of increased capillary permeability in ^{67}Ga tumor localization. The mechanisms involved in the uptake of ^{67}Ga by tumor cells are very complex, since a variety of factors appear to affect transport and retention of ^{67}Ga within the tumor tissue. Based on in vivo studies, Hayes et al. [15] concluded that the initial entry of ^{67}Ga into tumor tissue involves simple diffusion of the unbound or loosely bound form of ^{67}Ga, whereas its uptake by normal soft tissues is strongly promoted by its binding to transferrin. The increased permeability of the tumor cell membrane compared with normal cells may also account for increased diffusion of non-transferrin-bound gallium species into cells. The accumulation of ^{67}Ga within tumor cells is very much dependent upon the intracellular binding of ^{67}Ga to iron-binding proteins such as lactoferrin and ferritin or other higher-molecular-weight molecules which can chelate gallium with greater affinity, thereby preventing back-diffusion of free gallium species [13].

2.5.5.2 Facilitated Diffusion

^{18}F-fluorodeoxyglucose (FDG). All cells use glucose to generate metabolic energy. For brain tissue, glucose is the primary source of energy, but in the heart glucose becomes the primary source of energy for ischemic myocardium. Tumor cells have increased rates of anaerobic and aerobic glycolysis compared with most normal tissues. Glucose is transported into the cell across the plasma membrane by facilitated diffusion, mediated by members of the glucose transporter (Glut) protein family (Glut1 – 6) [16]. Similar to glucose, FDG is also transported into normal and malignant cells by facilitated diffusion.

Hepatobiliary Agents. Evaluation of hepatocyte function using radiopharmaceuticals that are excreted via biliary secretion is another example of a carrier-mediated transport mechanism. Lipophilic organic anions with nonpolar groups (favoring plasma protein binding) having molecular weights in the range of 600 – 1000 are predominantly removed from the body via biliary excretion. Following intravenous administration, ^{99m}Tc-disofenin (Hepatolite) and ^{99m}Tc-mebrofenin (Choletec) diffuse through pores in the endothelial lining of the sinusoids and bind to the anionic membrane-bound carriers on the hepatocyte. The hepatic uptake is facilitated by carrier-mediated, non-sodium-dependent, organic anionic pathways similar to that of bilirubin. Subsequent biliary excretion of the radiotracer is relatively passive and involves following the flow of bile through the biliary tree. The bile may be stored and concentrated temporarily in the gallbladder or excreted directly into the intestine. Since bilirubin is excreted by the same hepatocyte transport system, higher serum bilirubin levels may have a significant effect on the biodistribution and hepatic excretion of radiopharmaceuticals. Of the ^{99m}Tc-iminodiacetate (IDA) derivatives, ^{99m}Tc-mebrofenin combines the best characteristics of high hepatic uptake, low urinary excretion, fast blood clearance and hepatocellular transit, and has the highest degree of resistance to the competitive effects of bilirubin as measured in isolated hepatocytes.

2.5.5.3 Active Transport

Active transport involves translocating a solute molecule through a cell membrane against its concentration gradient and requires the expenditure of some form of energy. Active transport is driven by either hydrolysis of ATP to ADP (primary active transporters) or utilization of an electrochemical gradient of Na^+ or H^+ (secondary active transporters) across the membrane. If the energy source is inhibited or removed, the transport system will not function.

Radioiodide and ^{99m}Tc-Pertechnetate Anions. Thyroid tissue selectively traps certain anions, such as I^-, TcO_4^-, and ClO_4^-, by an active transport mechanism using the same pathway; hence they are the competitive inhibitors of each other. The clinical implication is that iodinated contrast agents or iodine containing medications may interfere with the accumulation of $^{99m}TcO_4$ in the thyroid, thereby leading to poor image quality. However, only iodide is used by the thyroid gland to synthesize thyroid hormones, while the other anions diffuse out of the gland. In addition to thyroid tissue, the salivary glands, stomach, bowel, and genitourinary tract show significant uptake (secretion) of radioiodide and pertechnetate. Radioiodide is rapidly absorbed from the GI tract after oral administration and is accumulated in thyroid tissue over the next 24 h. This uptake may be affected by TSH levels, thyroid and nonthyroid medications, and the total body iodine pool. Normal thyroid tissue has a very high affinity for iodide, while thyroid cancer and metastases accumulate iodide less readily. Papillary and follicular cancers arise from the thyroid follicular cells and retain to a certain extent the ability to trap iodide. By contrast, medullary carcinoma of the thyroid arises from the parafollicular, or C,

cells of the thyroid and does not accumulate radioiodide.

^{201}Thallous Chloride. Since the thallous ion ($Tl(OH)_2^+$) acts as an analogue of the K^+ ion, ^{201}Tl is used to image myocardial perfusion in order to evaluate the extent of myocardial ischemia and/or infarction. Positron emitter ^{82}Rb – a monocation, like potassium – is also useful for imaging myocardial perfusion. The myocardial uptake of thallium and rubidium involves active cation transport mechanisms including both passive diffusion and ATP or energy-dependent pathways [19].

The diagnostic value of ^{201}Tl for imaging brain tumors, osteosarcomas, low-grade lymphomas, Kaposi sarcomas, and parathyroid tumors is well established. Accumulation of ^{201}Tl in the tumor is a function of tumor blood flow and increased cell-membrane permeability. The tumor cell uptake of ^{201}Tl also appears to be due to an active transport system involving the Na^+/K^+ ATPase pump within cell membranes. Based on studies with murine Ehrlich ascites tumor cells, Sessler et al. [20] have demonstrated that the cellular uptake of ^{201}Tl is inhibited by ouabain, digitalis, and furosemide, which block the Na^+/K^+ pump. The drug ouabain blocks only the ATPase-dependent Na^+/K^+ pump while furosemide can also block a chloride co-transport system. Sessler et al. [21] observed that the inhibition of ^{201}Tl uptake by ouabain and furosemide was additive and suggested that ^{201}Tl uptake into the cell may involve two separate transport mechanisms. In addition, even after the blockade of Na^+/K^+ ATPase and chloride transport systems, a minimal amount of ^{201}Tl was taken up by the cells and this transport mechanism may be mediated by the calcium-dependent ion channel [21].

Renal Agents. Each kidney is made up of about 1 million nephrons, each with two components, a glomerulus and a long tubule that has three segments: the proximal tubule, loop of Henle, and distal tubule. One of the major functions of the kidney is excretion of waste materials by glomerular filtration and tubular secretion. Depending on the needs of the body, some of the molecules are subsequently reabsorbed back into the blood. Tubular reabsorption is the movement of fluids and solutes (Na^+ and glucose) from the tubular lumen to the peritubular capillary plasma, while tubular secretion involves transport of molecules (ammonia and hydrogen ions) from the plasma of peritubular capillary to the tubular lumen. Glomerular filtration (GFR) provides the best estimate of functioning renal tissue. The measurement of GFR requires a molecule such as inulin that has a stable plasma concentration and is freely filtered in the glomerulus and not secreted or reabsorbed by the tubule. The radiotracers most commonly used for measurement include ^{125}I-iothalamate, ^{99m}Tc-DTPA or ^{51}Cr-EDTA, since they meet the necessary requirements for glomerular filtration. No specific transport mechanisms are involved in the filtration process, and the GFR is determined by the sum of hydrostatic and colloid osmotic forces across the glomerular membrane. Radiopharmaceuticals such as radioiodinated hippuran and ^{99m}Tc-mercaptoacetyltriglycine (MAG_3) are partly filtered in the glomerulus but mostly excreted by tubular secretion. Compared with radioiodinated hippuran (30% by glomerular filtration), most of ^{99m}Tc-MAG3 is bound to plasma proteins and only about 10% may undergo glomerular filtration. These carboxylate substrates are actively transported by the renal hippurate anionic transport system of the proximal convoluted tubule cells [23].

2.5.5.4 Phagocytosis

Most of the ^{99m}Tc-sulfur colloid (SC) particles are in the range of 0.1 – 1.0 μm. Following intravenous administration, particles are able to leave the circulation via the sinusoidal type capillary structures in the liver, spleen, and bone marrow. Specific serum proteins known as opsonins may interact and provide a proper coating to the particles so that they may be recognized by receptors on the phagocytic cell surface. The cells of the reticuloendothelial system (RES) engulf the colloid particles and remove them from circulation. Kupffer's cells (macrophages in liver sinusoids) and reticular cells (macrophages in spleen) accumulate the particles by phagocytosis. Cold lesions identified on a liver scan with ^{99m}Tc-SC may be due to an intrahepatic tumor displacing the usual distribution of RES cells. Similarly, radiation damage in liver and bone marrow is seen as cold areas due to decreased RES function.

Recently, ^{99m}Tc-SC has been used extensively in lymphoscintigraphy in order to identify a "sentinal node" (first lymph node to receive lymphatic drainage from a tumor site) in patients with breast cancer and melanoma [24]. If radiocolloid is introduced into the interstitial fluid, it drains into the lymphatic vessels and then into regional lymph nodes. Colloid particles smaller than 0.1 μm show rapid clearance from the interstitial space into lymphatic vessels and significant retention in lymph nodes. While normal lymph nodes appear as hot spots, cancerous nodes do not sequester colloids, resulting in false-negative identification. Because of their small particle size, ^{99m}Tc-antimony sulfide-colloid (0.002 – 0.015 μm) and ^{99m}Tc-human serum albumin, or nanocolloid (0.01 – 0.02 μm) are ideal for lymphoscintigraphy studies. Since these agents are not available in the United States, filtered (using a 0.2-μm filter) ^{99m}Tc-SC preparation is being used for sentinal node detection [24].

2.5.5.5 Receptor-Mediated Endocytosis

A common pathway for tumor cell uptake of ^{67}Ga and ^{59}Fe via a transferrin receptor was initially proposed by several investigators [25], who suggested that ^{67}Ga localization in tumors involves endocytosis of the ^{67}Ga-transferrin-receptor complex. In vitro studies clearly demonstrated that transferrin, at low concentrations (< 0.1 mg/ml), stimulated and increased ^{67}Ga uptake by tumor cells. However, in vivo studies with animal tumor models provided conflicting results regarding the role of transferrin receptors in ^{67}Ga localization [12]. In addition, ^{67}Ga tumor uptake was also observed in tumor-bearing mice with congenitally absent transferrin (hypotransferrinemic) [26]. Although there is some evidence that the number of transferrin receptors in tumor cells may be increased tenfold compared with normal cells [13], the exact connection between transferrin receptors and ^{67}Ga tumor uptake in vivo has not been established.

2.5.6. Metabolic Substrates and Precursors

Cancer cells have an altered metabolism compared with normal cells. As a result, cancer cells use more glucose than normal cells. Due to the increased rate of cell proliferation, the protein and DNA synthesis is augmented and the cancer cells need to transport increased amounts of precursors such as amino acids and nucleotides. A number of radiopharmaceuticals were developed based on the increased demand of metabolic substrates of tumor cells.

Metabolic Trapping of FDG. ^{18}F-2-deoxy-2-fluoro-d-glucose (FDG) was developed in 1977 to measure local cerebral glucose utilization using PET [27]. In 1980, Som et al. [28] demonstrated that FDG accumulated in a variety of transplanted and spontaneous tumors in animals. Similar to d-glucose, FDG is transported into the cell by facilitated diffusion and is phosphorylated by hexokinase to FDG-6-phosphate (Fig. 2.3).

In the next step of glycolysis, the enzyme glucose-6-phosphate isomerase does not react with FDG-6-phosphate due to very strict structural and geometric demands. As a result, the very polar FDG-6-phosphate is trapped in the cytoplasm [29]. FDG-6-phosphate may be converted back to FDG, but the enzyme glucose 6-phosphatase, which is responsible for this reaction, is either at very low levels or absent in cancer tissue. FDG-PET is now being extensively used for an increasing number of clinical indications at different stages of cancer, e.g., diagnosis, staging, monitoring of response to therapy, and finally detection of recurrence. In addition, FDG accumulates in granulomatous tissue and macrophages infiltrating the areas surrounding necrotic tumor tissue [30] and may also have a role to play in imaging areas of infection/inflammation.

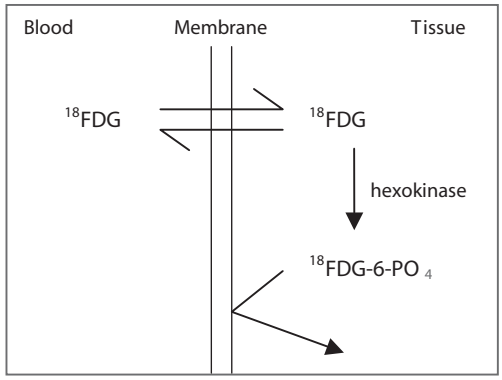

Fig. 2.3. Intracellular phosphorylation of ^{18}FDG to ^{18}FDG-6-PO_4 by hexokinase

2.5.6.1 Precursors: Radiolabeled Amino Acids

Since amino acids are the biological building blocks of proteins, radiolabeled amino acid uptake within tumors may reflect the increased protein synthesis rate of proliferating tumor cells or simply an increased rate of amino acid transport across the tumor cell membrane [31]. Despite its complex biochemistry and in vivo metabolism, methionine has been the most widely used amino acid tracer, in the form of l-[methyl-^{11}C]methionine. The predominant mechanism of methionine tumor uptake reflects the increased rate of active membrane transport process rather than the rate of protein synthesis [32]. Since tyrosine reflects the protein synthesis rate, radiolabeled tyrosine and a number of tyrosine analogs have been evaluated [33]. These include l-[1-^{11}C]tyrosine, l-[2-^{18}F]fluorotyrosine, l-4-[^{18}F]fluoro-m-tyrosine, and l-[3-^{18}F]-a-methyltyrosine (FMT). Among these tracers, FMT is relatively easy to synthesize and displays high in vivo stability, with 75% of the injected dose in the unmetabolized form in the circulation [33].

Recently, the tyrosine analog L-*O*-[2-^{18}F]fluorethyltyrosine (FET), which is not incorporated into proteins but nevertheless transported by an active transport mechanism, was developed [34]. FET is stable in vivo with fast brain and tumor uptake kinetics, and the biodistribution reflects that of an unnatural amino acid [34]. Radiolabeled natural amino acids and analogs also exhibit high uptake in normal brain tissue. A number of unnatural nonmetabolized amino acids can be used as substrates for active transport with minimal accumulation by normal brain tissue. Labeled with positron emitters, these compounds have been investigated as tumor-imaging agents. Among these tracers,

[^{11}C]a-aminocyclobutane carboxylic acid (ACBC) and [^{18}F]FACBC analogs showed intense uptake in such brain tumors as astrocytomas and glioblastomas [33].

2.5.7 Tissue Hypoxia

Imaging. Hypoxia may result from either insufficient regional perfusion (acute or transient hypoxia), as in myocardium, or insufficient oxygen diffusion (chronic hypoxia), as in tumors. Since hypoxia cannot be predicted, noninvasive techniques for identifying hypoxic regions in tumor, myocardium, and brain tissue are being developed. The compound 2-nitro in misonidazole (MISO) is transported into the cell by diffusion. In the cytoplasm, the nitro group (NO_2) undergoes one electron enzymatic reduction to the free radical anion [35]. In normoxic cells, this reaction step is reversed by intracellular oxygen and the oxidized molecule diffuses out of the cell. In hypoxic tissue, the free radical is further reduced to a reactive species, hydroxylamine, and then to an amine [35]. Free radicals are attached irreversibly to cellular macromolecules and are retained within the cell. Reduction of these molecules occurs in all tissue with viable enzymatic processes, but retention occurs only in those tissues with low oxygen tension.

A number of radiolabeled compounds incorporating a 2-nitroimidazole moiety to image tumor hypoxia have been developed. ^{18}F-fluoromisonidazole (FMISO) is probably the most extensively studied hypoxia-selective radiopharmaceutical [36]. In order to develop PET tracers for hypoxia imaging, radiolabeled agents of copper have been investigated, since copper has an amenable coordination and electrochemistry that would lend itself to redox-mediated trapping in cells. One of these compounds, ^{64}Cu-ATSM (Cu-diacetyl-*bis*-(N^4-methylthiosemicarbazone) has been shown to be selectively trapped in hypoxic tissue but rapidly washed out of normoxic cells [37].

Among the iodinated compounds, successful imaging of tumor hypoxia has been reported using a sugar containing the MISO derivative ^{123}I-iodoazomycin arabinoside (IAZA) [38]. Significant in vivo deiodination, however, limits the clinical usefulness of this compound. A ^{99m}Tc-labeled hypoxic imaging agent, a propylene amine oxime (PnAO) derivative of 2-nitroimidazole also known as BMS181321, showed hypoxia selectivity in tumor models but has slow clearance due to high lipophilicity [39]. It was recently reported that a complex of core ligands without the nitroimidazole group labeled with ^{99m}Tc also showed very high tumor-hypoxia selectivity. A prototype formulation of one of these compounds, ^{99m}Tc-HL91 (4,9-diaza-3,3,10,10-tetramethyldodecan-2,11-dione dioxime), has demonstrated uptake in a variety of tumors [40].

Hypoxia and Tumor pH. Increased glucose metabolism of tumor cells was initially recognized in 1925 by Warburg [41], who observed that tumor cells have increased rates of anaerobic and aerobic glycolysis compared with most normal tissues. In glucose metabolism, the initial reaction sequence, known as glycolysis, takes place in the cytoplasm where glucose is converted to two molecules of pyruvate. Under anaerobic conditions (hypoxia), this mechanism is unavailable; pyruvate is converted to lactic acid by lactate dehydrogenase (LDH) and accumulates. Consequently, the pH of the tumor tissue is lightly acidic [41], compared with normal tissue pH of 7.4. The acidic pH of the tumor tissue may possibly play a significant role in the mechanism of ^{67}Ga localization in tumors. The stability of the ^{67}Ga-transferrin complex is very much dependent upon bicarbonate concentration and pH; decreasing either bicarbonate or pH would help more ^{67}Ga to dissociate from transferrin [42] and would help to generate more free gallium species. The pH of the interstitial fluid of tumors is slightly acidic compared with the normal tissue, and reducing tumor pH by enhancing anaerobic glycolysis in tumor-bearing rats actually increased ^{67}Ga uptake by tumors [42].

2.5.8 Cell Proliferation

In normal tissue there is a balance between cell growth and cell death. Within a tumor, growth is favored. Until recently, increased mitotic rate, cell proliferation, and lack of differentiation were regarded as the main factors responsible for accelerated growth of malignant tissue. Most benign tumors grow slowly over a period of years, but most malignant tumors grow rapidly, sometimes at an erratic pace. In general, the growth rate of tumors correlates with their level of differentiation; thus most malignant tumors grow more rapidly than benign tumors do. Therefore, there is increased mitotic activity in tumor tissue. The number of cells in the S-phase of cell cycle is also higher compared with normal cells. As a result, there is an increased requirement of substrates (nucleotides) for DNA synthesis. Nucleotide incorporation into DNA in tumor tissue determined in vitro using [^{3}H]-thymidine (thymidine labeling index) is a measure of tumor proliferation [43]. ^{11}C-Thymidine has been used for many years as a PET tracer to image tumors of the head and neck [44]. Due to the rapid metabolism of this tracer in blood, however, the tumor uptake of ^{11}C-thymidine is not optimal for imaging studies and quantitation is difficult. ^{125}I-5-iodo-2'-deoxyuridine (IudR), an analog of thymidine (TdR), has recently been developed by replacing the 5-methyl group with an iodine atom [45]. Within the tumor cell, IudR is phosphorylated and incorporated in DNA. The therapeutic potential of IudR labeled with

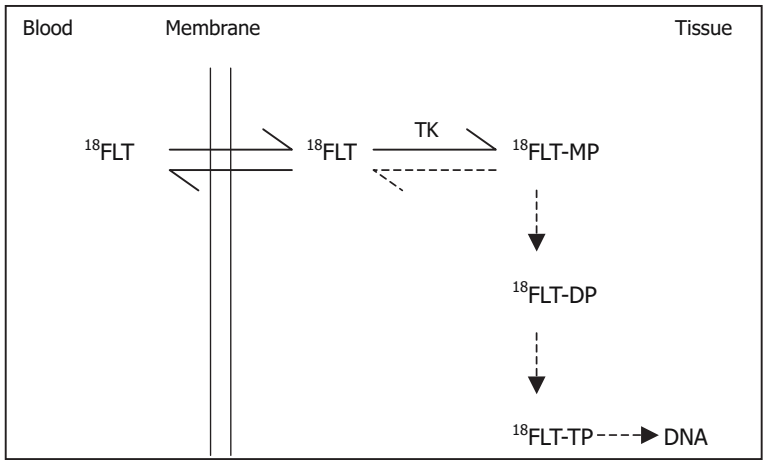

Fig. 2.4. Intracellular phosphorylation of ^{18}FLT to ^{18}FLT monophosphate by thymidine kinase 1

^{125}I has been attributed to the Auger electron emission from this radionuclide [46].

^{18}F-Fluoro-3'-deoxy-3'-l-fluorothymidine (FLT) was developed for imaging cell proliferation [47]. Similar to thymidine, ^{18}FLT is transported into the cell by both passive diffusion and facilitated transport by Na^+-dependent carriers, where it is phosphorylated by thymidine kinase 1 (TK1) into ^{18}FLT-monophosphate that is trapped in the cell (Fig. 2.4). Using ^{3}H-FLT, it has been shown that FLT is not incorporated into DNA because it acts as a chain terminator due to absence of the 3'-hydroxyl group (Fig. 2.4).

^{18}F-FLT is currently being investigated (a) for imaging malignant tumors. However, the uptake of ^{18}F-FLT has been shown to be less than that of ^{18}F-FDG, resulting in a lower sensitivity. Probable explanations include the fluorine substitution in the 3'-position of FLT that results in a decreased affinity for the pyrimidine transporter compared to thymidine [47]. The affinity of FLT for TK is lower than that of thymidine. (b) ^{18}F-FLT is also being investigated as a proliferation tracer because it is phosphorylated by TK, and TK activity is very high throughout the cell cycle in malignant tumors. Hence FLT can be regarded as a tumor specific PET tracer. (c) Finally, ^{18}F-FLT is undergoing evaluation and measurement of the response of anti-cancer therapy.

2.5.9 Specific Receptor Binding

The term receptor is generally used to denote a specific cellular binding site for a small ligand, such as peptide hormones and neurotransmitters. In the case of antigen-antibody interactions, antigen expressed on a cell may be regarded as a receptor for a specific antibody. Antigen molecules may be present either in or on cells but may be also secreted into the extracellular fluid and circulation. Since the mechanism of localization of receptor-binding radiopharmaceuticals is specific and depends on receptor or antigen expression of the tumor tissue, multiple factors representing many characteristics of the radiopharmaceutical will influence the uptake of radiotracer in the target tissue, the image quality, and ultimately the clinical utility of these agents. The major factors include (a) blood clearance, (b) specific activity, (c) affinity of the tracer, (d) immunoreactivity or the relative biological potency, (e) in vivo stability, (f) nonspecific binding, and (g) blood flow and perfusion of the tumor tissue.

2.5.9.1 Radiolabeled Peptides

Somatostatin Receptors. There are two naturally occurring bioactive somatostatin (SST) products, a 14-amino-acid (SST_{14}) and a 28-amino-acid (SST_{28}) form. SST is secreted throughout the body and has multiple physiological functions including the inhibition of secretion of growth hormone, glucagon, insulin, gastrin, and other hormones by the pituitary and gastrointestinal tract. The diverse biological effects of SST are mediated through a family of G-protein-coupled receptors, of which five subtypes have been identified by molecular cloning [47]. Human SST receptors (SSTR) have been identified on many cells of neuroendocrine origin as well as on lymphocytes. In addition, most neuroendocrine tumors, small cell lung cancers, and medullary thyroid carcinomas express SSTRs in high density [48, 49]. The expression of SSTR subtypes in human tumor tissues, however, seems to vary with tumor type [50].

A number of somatostatin analogues (seglitide, octreotide, somatuline, or lanreotide) with greater biological stability than SST_{14} have been synthesized. These derivatives consist of hexapeptide and octapeptide molecules, which incorporate the biologically active core of SST_{14}. Structure-function studies have shown that the amino acid residues Phe^7, Trp^8, Lys^9, and Thr^{10} in SST_{14} are necessary for biological activity,

with residues Trp and Lys being essential whereas Phe and Thr can undergo minor substitutions [47]. It is important to recognize that SST_{14} binds to all five SSTR subtypes with comparable affinity. By contrast, octreotide binds with higher affinity to SSTR 2, 3, and 5 while lanreotide and RC-160 bind to SSTR 1 – 4 with comparable affinity. None of the synthetic peptides show high-affinity binding to SSTR 1.

Radiolabeled SST Analogs. Radioiodinated octreotide was the first radiotracer introduced for imaging SSTR-positive tumors [49]. Due to in vivo dehalogenation and biliary excretion, substantial accumulation of activity was seen in the intestines and bladder, making image interpretation difficult. In order to overcome these difficulties, ^{111}In-DTPA-d-Phe^{1}-pentetreotide or Octreoscan (Mallinckrodt Inc, St. Louis), with a high specific activity (5 – 6 mCi of ^{111}In/10 µg octreotide), was developed. Following intravenous administration, Octreoscan is rapidly cleared from the circulation via the kidneys (about 50% within 5 h), providing an image with less intestinal activity than ^{123}I-tyr^{3}-octreotide. The prolonged residence time of ^{111}In activity in the kidneys suggests that following glomerular filtration, part of the radiolabeled peptide is actively reabsorbed in the renal tubules [49]. Octreoscan binds to SSTR 2 and 5 subtypes with greater affinity than the unlabeled octreotide.

Due to the very specific localization of octreotide analogs in neuroendocrine tumors, radiolabeled SST analogs were also developed for the therapy of neuroendocrine tumors. Structure-activity studies suggest that substitution of Tyr amino acid residue for the Phe^{3} position in the octreotide molecule provides favorable SSTR binding affinity of the octreotide molecule [47]. Based on these chemical and pharmacological advantages, ^{90}Y-DOTA-Tyr^{3}-octreotide (DOTATOC) was developed. Similar to Octreoscan, ^{111}In- or ^{90}Y-labeled DOTATOC also binds with nanomolar affinity to tumor cells expressing the SSTR 2 subtype [51, 52].

Since lanreotide binds to SSTR 2 – 5 subtypes with equal or slightly higher affinity than octreotide, radiolabeled lanreotide analogs have been developed for therapy. Unlike Octreoscan, ^{111}In-DOTA-lanreotide binds to SSTR 2 – 5 subtypes with high affinity (K_d 1 – 10 n*M*) and to SSTR1 with low affinity (K_d 200 n*M*) [53]. The therapeutic potentials of ^{90}Y-DOTATOC and ^{90}Y-DOTA-lanreotide are being investigated in a number of clinical trials.

Biologically active synthetic octreotide analogs have a disulfide bridge between the two cysteine amino acid residues. Labeling these peptide analogs with ^{99m}Tc is problematic, because the reducing agent (stannous ion) used in ^{99m}Tc labeling can reduce (open) the disulfide bond, resulting in considerable loss of SSTR binding affinity. In order to avoid the incompatibility of having a disulfide residue in a molecule, a peptide known as P-829 has been developed (Diatide, Inc, Londonderry, NH) to hold the pharmacophore, i.e., the amino acid residues essential for SSTR binding, in a cyclic configuration that is not susceptible to reductive cleavage [54]. The P829 peptide can be efficiently labeled with ^{99m}Tc by incubating it in a boiling water bath for 15 min. In a rat pancreatic cell membrane assay, the metallocomplex, rhenium-P829 (a molecular surrogate of Tc-P829), has higher affinity than ^{111}In-DTPA-octreotide (0.32 vs. 1.2 n*M*). In preclinical studies, ^{99m}Tc-P829 showed very high specificity for SSTR and, in particular, specific binding to SSTR 2 and 3 subtypes [54]. In a number of clinical studies, ^{99m}Tc-P829 showed potential diagnostic utility for imaging a number of SSTR-expressing tumors. Recently, ^{99m}Tc-P829, NeoTect (Amersham Inc.), was approved by the FDA for imaging lung tumors.

VIP Receptors. Vasoactive intestinal peptide (VIP) is a 28-amino-acid neuroendocrine mediator with a broad range of biological activity in diverse cells and tissues. In addition to being a vasodilator, VIP promotes the growth and proliferation of normal and malignant cells. Cell membrane VIP receptors are widely distributed throughout the gastrointestinal tract, but they are also found on various other cell types. Increased VIP receptor expression has been seen on adenocarcinomas, breast cancers, melanomas, neuroblastomas, and pancreatic carcinomas [55].

^{123}I-VIP. High-specific-activity ^{123}I-VIP (150 – 200 MBq/µg) was prepared by Virgolini et al. [56]. In clinical studies they were able to demonstrate specific uptake in primary tumors as well as in liver, lung, and lymph node metastases of pancreatic adenocarcinoma, colon adenocarcinoma, or gastrointestinal neuroendocrine tumors. In vitro receptor studies with cloned VIP receptors clearly demonstrated that ^{123}I-VIP bound to VIP receptors as well as the unlabeled VIP [57]. In addition, they observed interaction between VIP and SST on various cell types, including primary tumor cells. The high-affinity binding of ^{123}I-VIP to SSTR 3 suggests that the SSTR 3 receptor subtype might be the site of cross-competition between VIP and SST [57].

2.5.9.2 Steroid Hormone Receptors

Sex steroid hormones – estrogen, progesterone and testosterone – bind with high affinity to intracellular receptors. The majority of breast cancers are hormone dependent, as indicated by increased expression of intracellular estrogen or progesterone receptors. Noninvasive quantitative imaging of estrogen or progesterone receptor content in breast cancer may be useful for

predicting the responsiveness of hormonal therapy. Various steroid and nonsteroid estrogen analogs have been radiolabeled with positron-emitting radionuclides, ^{77}Br and 18F. Among these tracers, 16α-[^{18}F]fluoro-17β-estradiol (FES) showed high affinity and selectivity to estrogen receptors and has shown a potential for detecting estrogen receptor-positive metastatic foci [58]. Similarly, 21-[^{18}F]fluoro-16a-ethyl-19-norprogesterone (FENP) has shown a potential for imaging progesterone receptors [58]. Recently, ^{123}I-labeled *cis*-11β-methoxy-17a-iodovinylestradiol (Z-[^{123}I]MIVE) was introduced as a radioligand to image estrogen receptor expression in breast cancers [59]. These radiotracers are transported into the cell by passive diffusion and bind to steroid receptors within the nucleus.

2.5.9.3 Adrenergic Presynaptic Receptors and Storage

Tumors arising from the neural crest share the characteristic of amine precursor uptake and decarboxylation (APUD) and contain large amounts of adrenaline, dopamine, and serotonin within the secretary granules in cytoplasm. Tumors of the adrenergic system include pheochromocytomas (arise in adrenal medulla) or paragangliomas (extra-adrenal tissue). Meta-iodobenzylguanidine (MIBG) is an analog of noradrenaline, originally developed by Wieland et al. [60]. ^{131}I-MIBG was initially used to image pheochromocytoma. It has since been used for imaging neuroblastoma, medullary thyroid carcinoma, retinoblastoma, melanoma, and bronchial carcinoma. Wieland et al. [61] observed that ^{131}I-MIBG accumulated in the chromaffin cells of the adrenal medulla. Since MIBG is structurally similar to noradrenaline, MIBG is believed to be transported into the cell by the reuptake pathways of the adrenergic presynaptic neurons [61]. Within the cells, MIBG is transported into the catecholamine-storing granules by means of the ATPase-dependent proton pump. The major difference between MIBG and noradrenaline is that MIBG does not bind to postsynaptic adrenergic receptors. Reduced ^{131}I-MIBG uptake by the tumors is seen in patients using drugs such as labetolol, calcium channel blockers, and antipsychotic and sympathomimetic agents.

2.5.9.4 LDL Receptors

Plasma low-density lipoprotein (LDL) carries cholesterol to the adrenal glands. Cholesterol is the substrate for adrenal steroid hormone (cortisol and aldosterone) synthesis. ^{131}I-6β-iodomethyl-19-norcholesterol (NP-59) is the agent of choice for imaging patients with adrenal cortical diseases [62]. Two other analogs, ^{131}I-6-iodocholesterol (Iodorin) and ^{75}Se-β-iodomethyl-19-norcholesterol (Scintadren), have also been proven to be clinically useful for imaging the adrenal glands. NP-59 and other radioiodinated cholesterol analogs are transported by plasma LDL and are accumulated in the adrenal cortex via LDL receptors. Subsequently, NP-59 is esterified like cholesterol and stored intracellularly without further metabolism or incorporation into adrenocortical steroid hormones. Normal adrenal glands show bilateral symmetrical uptake of NP-59. Bilateral increased adrenal uptake of NP-59 may be due to Cushing's disease (excess ACTH production by a pituitary adenoma) or to ectopic secretion of ACTH. Adrenal adenoma is identified as intense unilateral uptake while adrenal carcinoma shows no uptake of NP-59. Dexamethasone, which suppresses pituitary ACTH secretion, decreases the uptake of NP-59 by the adrenal cortex, while intramuscular administration of ACTH increases NP-59 accumulation by the adrenal cortex [62].

2.5.9.5 Radiolabeled Antibodies

Antibodies (Ab), also called immunoglobulins (Ig), are a group of glycoprotein molecules produced by B-lymphocytes in response to antigenic stimulation. Each antibody binds to a restricted part of the antigen called an epitope. A particular antigen can have several different epitopes. However, a monoclonal antibody (MAb) is specific for a particular epitope rather than the whole antigen molecule. IgG is the major immunoglobulin in human serum and may be thought of as a typical antibody. It has a molecular weight of 146,000 daltons and a plasma half-life of 21 days. The enzyme pepsin cleaves the IgG molecule to yield the $F(ab')_2$ and Fc' fragments, while the enzyme papain splits the IgG molecule into two Fab fragments and the Fc fragment. The Fab region binds to the antigen, while the Fc region mediates effector functions such as complement fixation and monocyte binding. Almost all MAbs used in nuclear medicine for diagnosis and therapy belong to the IgG class. MAbs derived from mice are called murine MAbs. Since the Fc portion of the murine antibody is antigenic in human beings and induces the formation of human anti-mouse-antibody (HAMA), chimeric antibodies are being developed in which murine variable regions of Fab' are attached to constant regions of human IgG.

The most important requirement in developing radiolabeled antibodies for diagnosis and therapy is to identify an antigen or an epitope specific to a particular type or class of cancer or tissue. Most tumor cells synthesize many proteins or glycoproteins that are antigenic in nature. These antigens may be intracellular, expressed on the cell surface, or shed or secreted from the cell into extracellular fluid or circulation. These tumor-associated antigens (TAA) such as CEA, TAG-72, PSA, and PSMA may also be expressed in small amounts in

normal cells, but tumor cells typically produce them in large amounts. A number of radiolabeled antibodies and antibody fragments specific for TAAs have been developed for both diagnosis and therapy of tumors (Tables 2.2, 2.3). Another important requirement for radiolabeling antibodies is that the radionuclide to be used should match the pharmacokinetics of the antibody. Thus radionuclides with short half-lives such as ^{99m}Tc and ^{123}I are best suited for labeling antibody fragments with faster blood clearance, while ^{111}In and ^{131}I, with comparatively longer half-lives, may be better for labeling intact antibodies. While ^{123}I, ^{99m}Tc, and ^{111}In are preferred radionuclides for imaging studies, a number of beta radionuclides such as ^{131}I, ^{90}Y, and ^{188}Re are attached to antibodies for targeted radioimmunotherapy of cancer. Radiolabeling techniques have been designed to produce high-specific-activity radiolabeled antibodies while preserving the immunoreactivity of the labeled antibody.

Radioiodinated Antibodies. ^{131}I is the most commonly used radionuclide for both diagnostic and therapeutic studies. Its physical half-life of 8 days is ideally suited for labeling the IgG molecule. High-specific-activity (10 – 15 mCi/mg) radioiodinated antibody can be easily prepared using the iodogen method. Since radioiodide atoms label the tyrosine residues in the antibody molecule, it is quite possible that tyrosine residues of the variable region of the IgG molecule are labeled, resulting in significant loss of immunoreactivity and tumor localization of the radiolabeled antibody. ^{131}I-anti B1 antibody (BEXAR) binds specifically to the CD20 antigen on tumor cells and is being evaluated for the treatment of non-Hodgkin's lymphoma [63].

^{99m}Tc-Labeled Antibodies. Antibody molecules can be labeled with ^{99m}Tc using either direct or indirect labeling techniques. The direct labeling technique involves reduction of disulfide groups of the antibody molecule and subsequent labeling of reduced ^{99m}Tc to the sulfide moieties of the antibody. This is the technique most commonly used to label antibody fragments such as CEA-Scan and Verluma. CEA-Scan binds to a 200-kd CEA antigen on tumor cells and is useful for imaging colorectal cancer. Verluma binds to a 40-kd cell surface glycoprotein present in lung tumor cells; it is useful for imaging small-cell lung cancer. The indirect method involves linking ^{99m}Tc to the antibody through a ligand which binds to the amino groups of the lysine and arginine residues of the antibody [63a–c]. Depending on the ligand used, the ^{99m}Tc is bound either to the antibody [63a] or to the ligand [63b,c]. With iminothiolane as the conjugate ligand, and also the reducing agent, the ^{99m}Tc is bound to the antibody through the –SH group [63a], but with N2S2 or N3S tetradentate ligands the ^{99m}Tc is bound to the ligand [63b,c]. The ^{99m}Tc-labeled ligand may be preformed and attached to the antibody as exemplified by ^{99m}Tc-diamide dithiolate (^{99m}Tc-DADS) or the ligand-antibody may first be derivatized, and reduced ^{99m}Tc is added to form the ^{99m}Tc-ligand antibody. The derivatization procedure lends itself to a one-step final preparation because the ligand, antibody and reducing agent, stannous ion, can be lyophilized and ready for use.

^{111}In- and ^{90}Y-Labeled Antibodies. Indirect labeling of antibodies with radiometals such as ^{111}In or ^{90}Y requires a bifunctional chelating agent, which is attached covalently to the antibody molecule. To develop a radiolabeled antibody that is stable in vivo, the choice of a chelating agent depends on the radiometal to be complexed. DTPA or isothiocyanatobenzyl-DTPA chelating agents provide high in vivo stability to ^{111}In-labeled antibodies. However, a major disadvantage of ^{111}In-conjugated antibody is the high concentration of radioactivity in the liver, spleen, bone marrow and intestine, while the major advantages include the possibility of kit formation and the reasonably long physical half-life of ^{111}In.For radiometals such as ^{90}Y and ^{76}Cu, however, macrocyclic bifunctional chelating agents such as DOTA and TETA provide greater in vivo stability. To preserve the immunoreactivity of the antibody, the preferred site for conjugation of the chelating agent is the Fc segment (as in the case of ProstaScint and OncoScint) of antibody since this region does not participate in antigen binding. OncoScint binds to TAG-72 antigen on tumor cells and is useful for imaging colorectal and ovarian cancer. ProstaScint binds to an intracellular epitope of prostate-specific membrane antigen (PSMA) on prostate cancer cells and is useful for imaging prostate carcinoma. Even random attachment of the chelating agent on the antibody appears to provide radiolabeled antibodies with high specific activity and immunoreactivity, as in the case of ^{90}Y-IDEC-Y2B8 [64]. The localization of radiolabeled antibodies and antibody fragments in tumor tissue depends on many factors such as blood clearance, tumor blood flow, tumor mass, and tumor cell viability. For antibodies that are internalized following binding to antigen on the cell surface, radiolabeling with ^{111}In and ^{90}Y provides greater intracellular retention of radioactivity than radioiodinated antibodies.

Radiolabeling Antibodies In Vivo Using Biotin/Streptavidin. The relatively long residence time of radiolabeled antibodies in circulation increases the background and decreases the target/background ratio, as well as increasing the radiation dose to bone marrow. In order to accelerate the clearance of radiolabeled antibodies from the circulation and to improve the delivery of radionuclides to the tumor tissue, biotin and streptavidin have been used in a two- or three-step pro-

cess. Streptavidin and avidin are proteins (60 – 66 kd) with a very high affinity (K_d=$10^{-15}M$) for biotin, a vitamin (244 D) [65]. In a two-step method, patients are first injected with cold biotin-labeled antibodies [66]; 3 – 4 days later radiolabeled avidin is administered, removing the circulating antibodies rapidly as well as binding to the pretargeted biotin-antibody complex at the tumor site. This approach is very effective for both diagnosis and therapy. A three-step method [67], designed specifically for imaging studies, includes the following steps: (a) tumor pretargeting by cold biotin-labeled antibody; (b) subsequent (1 or 2 days later) administration of cold avidin to remove the circulating antibodies and avidinate the biotin-antibody complex at the tumor site; (c) administration of radiolabeled biotin, which clears rapidly from the circulation and binds to the avidin-biotin-antibody complex at the tumor site. A number of clinical studies have demonstrated the advantage of this approach.

2.5.10 Imaging Gene Expression

Following the completion of human genome sequencing, the discovery of molecular mechanisms of carcinogenesis and the significant advances in gene therapy, it may be possible to assess gene function and regulation by radionuclide imaging of gene expression. Radionuclide imaging of gene expression involves two main general methods: either using antisense oligonucleotides targeted towards the mRNA of a particular gene or using reporter genes to track the expression of endogenous or exogenous genes, thus creating new and exciting opportunities for the development of radiopharmaceuticals to image specific genes and gene expression in tumors. Over the next few years, a new generation of positron- and single-photon-emitting radiotracers will be under intense clinical evaluation for imaging gene expression.

Antisense Imaging. Antisense RNA and DNA techniques were developed originally to modulate the expression of specific genes based on studies using bacteria that showed that these organisms are able to regulate gene replication and expression by producing small complementary RNA molecules in an opposite direction (antisense), the rationale being that once one gene sequence is known, its expression can be selectively inhibited, modulated or silenced by the application of synthetic single-strand nucleic acid segments (oligonucleotides) whose sequence is in the opposite direction of replication, transcription, splicing, transportation, or translation of the targeted mRNA of a particular gene. Thus, these antisense oligonucleotides have emerged as highly selective inhibitors or modulators of gene expression. When labeled to an appropriate radionuclide, the antisense ologonucleotide can be used for imaging or therapy. Unfortunately, oligonucleotides are poor pharmaceuticals because of their large size, low stability and poor membrane permeability. Hence, chemically modified oligonucleotides such as phosphorothioate and methylphosphonate peptide nucleic acid oligomers have been developed and labeled with radionuclides. These radiolabeled antisense-oligonucleotides ideally should be easy to synthesize, are stable in vivo, and have high uptake into and accumulation in the cell and minimal interaction with other macromolecules. For imaging the antisense radiopharmaceutical can be used for (a) visualization of the expression of specific genes in vivo; (b) therapeutic monitoring of the effort to block the expression of the specific gene; and (c) gene radiotherapy [68]. A few oligonucleotides have been labeled mostly with ^{99m}Tc [69, 70] and ^{111}In [71, 72]. The in vitro study of vascular smooth muscle cells has shown that ^{99m}Tc-labeled antisense oligonucleotide to proliferating cell nucleus antigen may be useful for in-vivo imaging of atherosclerotic plaque and restenosis [69]. A ^{111}In-labeled antisense oligonucleotide (15 bases long) has demonstrated specific binding to isolated mRNA in vitro, thus indicating that it could be used to image the c-*myc* oncogene [71]. Though an attempt to label antisense oligonucleotide with ^{18}F was successful, the nucleotide was not selective for inducible NO synthease expressing cells [73].

Reporter Gene Imaging. Molecular biologists have used reporter genes to study promoter/promoter elements involved in gene expression, inducible promoters to examine the induction of gene expression, but their methods are not able to invasively determine the locations or magnitude of gene expression in a living human being [74]. However, radionuclide imaging offers such a possibility. For imaging, reporter genes can be classified into two categories: (a) those that lead to the production of an enzyme that is capable of metabolizing or trapping a reporter probe and (b) those that lead to the production of a protein that acts as a receptor for binding intracellularly or extracellularly with the reporter probe. In imaging the herpes simplex virus type 1 thymidine kinase (*HSV1-tk*) reporter gene, various reporter probes such as 9-(4-^{18}F-fluoro-3-[hydroxymethyl]butyl)guanine (FHBG) [75] and 2'-fluoro-2'-deoxy-1B-arabinofuranosyl-5-iodo-uracil (FIAU) [76, 77] have been developed in which the reporter probe is trapped due to phosphorylation by the protein product, HSV1-TK. Imaging gene expression that involves receptor binding is exemplified by using dopamine type2 receptor (D2R) as gene reporter and 3-(2'-^{18}F-fluoroethyl)spiperone as a reporter probe (^{18}F-FESP) [78, 79]. The D2R is expressed primarily in the brain striatum and in the pituitary glands. The ^{18}F-FESP binds with high affinity to D2R. Other reporter

probes for D2R, ^{11}C-raclopride and ^{123}I-iodobenzamine have been developed and tried in animals and humans.

The reporter gene should have ideal characteristics as adequately reviewed by Gambhir et al. [74]. Some of these characteristics include (a) the presence of the reporter gene in mammalian cells but not expressed in order to prevent an immune response; (b) when expressed, the reporter gene protein should produce specific reporter probe accumulation only on those cells in which it is expressed; (c) when not expressed there should not be a significant accumulation of reporter probe in the cells.

References

1. Wagner HN Jr (1995) Nuclear medicine: what it is and what it does. In: Wagner HN Jr, Szabo Z, Buchanan JW (eds) Principles of nuclear medicine. WB Saunders, Philadelphia, pp 1 – 8
2. Virchow R (1958) Disease, life and man. Stanford University Press, Stanford, Calif.
3. McCance KL, Huether SE (1998) Pathophysiology. The biologic basis for disease in adults and children, 3rd edn. Mosby-Year Book, St. Louis
4. Cotran RS, Kumar V, Collins T (1999) Robbins pathologic basis of disease, 6th edn. WB Saunders, Philadelphia
5. Wagner HN Jr (1995) The diagnostic process. In: Wagner HN Jr, Szabo Z, Buchanan JW (eds) Principles of nuclear medicine. WB Saunders, Philadelphia, pp 9 – 17
6. Krasnow AZ, Hellman RS, Timins ME, et al (1997) Diagnostic bone scanning in oncology. Semin Nucl Med 27: 107 – 141
7. Delmon-Moingeon LI, Piwinca-Wormas D, Van den Abbeele AD, Holman BL, Davison A, Jones AG (1990) Uptake of the cation hexakis (2-methoxyisobutylisonitrile)-technetium-99m by human carcinoma cell lines in vitro. Cancer Res 50:2198 – 2202
8. Piwnica-Worms D, Kronauge JF, Chiu ML (1990) Uptake and retention of hexakis (2-methoxyisobutyl isonitrile) technetium (I) in cultured chick myocardial cells. Mitochondrial and plasma membrane potential dependence. Circulation 82:1826 – 1838
9. Arbab AS, Koizumi K, Toyama K, Araki T (1996) Uptake of technetium-99m-tetrofosmin, technetium-99m-MIBI and thallium-201 in tumor cell lines. J Nucl Med 37:1551 – 1556
10. Piwnica-Worms D, Chiu ML, Budding M, Kronauge JF, Kramer R, Croop JM (1993) Functional imaging of multidrug-resistant P-glycoprotein with an organotechnetium complex. Cancer Res 53:977 – 984
11. Hendrikse NH, et al (1998) 99mTc-sestamibi is a substrate for P-glycoprotein and the multi-drug resistance associated protein. Br J Cancer 77:353 – 358
12. Tsan MF, Scheffel U (1986) Mechanism of gallium-67 accumulation in tumors. J Nucl Med 27:1215 – 1219
13. Weiner RE (1996) The mechanism of 67 Ga localization in malignant disease. Nucl Med Biol 23:745 – 751
14. Vallabhajosula SR, Harwig JF, Siemsen JK, et al (1980) Radiogallium localization in tumors: blood binding and transport and the role of transferrin. J Nucl Med 21: 650 – 656
15. Hayes RL, Rafter JJ, Byrd BL, Carlton JE (1981) Studies of the in vivo entry of Ga-67 into normal and malignant tissue. J Nucl Med 22:325 – 332
16. Mueckler M (1994) Facilitative glucose transporters. Eur J Biochem 219:713 – 725
17. Schwenk M (1980) Transport systems of isolated hepatocytes: studies on the transport of biliary compounds. Arch Toxicol 44:113 – 126
18. Okuda H, Nunes R, Vallabhajosula S, et al (1986) Studies of the hepatocellular uptake of the hepatobiliary scintiscanning agent 99mTc-DISIDA. J Hepatol 3:251 – 259
19. Weich HF, Strauss HW, Pitt B (1977) The extraction of thallium-201 by the myocardium. Circulation 56:188
20. Sessler M, Maul FD, Geck P, Munz D, Hor G (1982) Kinetics and mechanism of thallium uptake in malignant tumors in vivo and in vitro. In: Raynaud C (ed) 3rd World Congress of Nuclear Medicine and Biology, August 29–September 2, Paris. Nucl Med Biol Proc 1982:2281 – 2284
21. Sessler MJ, Geck P, Maul FD, et al (1986) New aspects of cellular Tl-201 uptake: co-transport is the central mechanism of ion uptake. Nucl Med 25:24 – 27
22. Eshima D, Taylor A (1992) Tc-99m mercaptoacetyltriglycine (Tc-99m MAG3): update on the new Tc-99m renal tubular function agent. Semin Nucl Med 22:61 – 73
23. Eshima D, Taylor A (1992) Semin Nucl Med 22:61 – 73, and chapter 73, Red Book)
24. Alazraki NP, Eshima D, Eshima LA, et al (1997) Lymphoscintigraphy, the sentinel node concept, and the intraoperative gamma probe in melanoma, breast cancer, and other potential cancers. Semin Nucl Med 27:55 – 67
25. Larson SM, Rasey JS, Allen DR, et al (1980) Common pathway for tumor cell uptake of gallium-67 and iron-59 via a transferrin receptor. J Natl Cancer Inst 64:41 – 53
26. Sohn MH, Jones BJ, Whiting Jr JH, et al (1993) Distribution of gallium-67 in normal and hypotransferrinemic tumor-bearing mice. J Nucl Med 34:2135 – 2143
27. Ido T, Wan C-N, Fowler JS, et al (1977) Fluorination with F2. A convenient synthesis of 2-deoxy-2-fluoro-D-glucose. J Org Chem 42:2341 – 2342
28. Som P, Atkins HL, Bandoypadhyay D, et al (1980) A fluorinated glucose analog, 1-fluoro-2-deoxy-D-glucose (F-18): nontoxic tracer for rapid tumor detection. J Nucl Med 21:670 – 675
29. Gallagher BM, Fowler JS, Gutterson NI, et al (1978) Metabolic trapping as a principle of radiopharmaceutical design: some factors responsible for the biodistribution of [^{18}F]2-deoxy-2-fluoro-D-glucose. J Nucl Med 19:1154 – 1161
30. Kubota R, Yamada S, Kubota K, et al (1992) Intratumoral distribution of fluorine-18-fluorodeoxyglucose in vivo: high accumulation in macrophages and granulation tissues studied by microautoradiographic comparison with FDG. J Nucl Med 33:1872 – 1980
31. Vaalburg W, Coenen HH, Crouzel C, et al (1992) Amino acids for the measurement of protein synthesis in vivo by PET. Nucl Med Biol 19:227 – 237
32. Ishiwata K, Kubota K, Murakami M, Kubota R, Senda M (1993) A comparative study on protein incorporation of L-[methyl-^{3}H]methionine, L-[1-^{14}C]leucine and L-[2-^{18}F]fluorotyrosine in tumor bearing mice. Nucl Med Biol 20:895 – 899
33. Shoup TM, Olson J, Hoffman JM, et al (1999) Synthesis and evaluation of [^{18}F]1-amino-3-fluorocyclobutane-1-carboxylic acid to image brain tumors. J Nucl Med 40:331 – 338
34. Wester HJ, Herz M, Weber W, et al (1999) Synthesis and radiopharmacology of *O*-[2-^{18}F]fluorethyltyrosine for tumor imaging. J Nucl Med 40:205 – 212
35. Nunn A, Linder K, Strauss HW (1995) Nitroimidazoles and imaging hypoxia. Eur J Nucl Med 22:265 – 280
36. Rasey JS, Koh WJ, Evans ML, et al (1996) Quantifying regional hypoxia in tumors with positron emission tomog-

raphy: a pretherapy study of 37 patients. Int J Radiat Oncol Biol Phys 36:417 – 428
37. Lewis JS, McCarthy DW, McCarthy TJ, Fugibayashi Y, Welch MJ (1999) Evaluation of ^{64}Cu-ATSM in vitro and in vivo in a hypoxic tumor model. J Nucl Med 40:177 – 183
38. Parliament MB, Chapman JD, Urtasunn RC, et al (1992) Noninvasive assessment of human tumor hypoxia with ^{123}I-iodoazomycin arabinoside: preliminary report of a clinical study. Br J Cancer 65:90 – 95
39. Ballinger JR, Kee JWM, Rauth AM (1996) In vitro and in vivo evaluation of a technetium-99m-labeled 2-nitroimidazole (BMS181321) as a marker of tumor hypoxia. J Nucl Med 37:1023 – 1031
40. Cook GJR, Houston S, Barrington SF, Fogelman I (1998) Technetium-99m-labeled HL91 to identify tumor hypoxia: correlation with fluorine-18-FDG. J Nucl Med 39:99 – 103
41. Warburg O (1956) On the origin of cancer cells. Science 123:309 – 314
42. Vallabhajosula SR, Harwig JF, Wolf W (1982) Effect of pH on tumor cell uptake of radiogallium in vitro and in vivo. Eur J Nucl Med 7:462 – 468
43. Livingston RB, Ambus U, George SL, Freireich EJ, Hart JS (1974) In vitro determination of thymidine-[^{3}H] labeling index in human solid tumors. Cancer Res 34:1376 – 1380
44. Goethals P, Lameire N, van Eijkeren M, et al (1996) Methylcarbon-11 thymidine for in vivo measurement of cell proliferation. J Nucl Med 37:1048 – 1052
45. Kassis AI, Adelstein SJ (1996) Preclinical animal studies with radioiododeoxyuridine. J Nucl Med 37 [Suppl]:10s–12s
46. O'Donoghue JA (1996) Strategies for selective targeting of Auger electron emitters to tumor cells. J Nucl Med 37 [Suppl]:3s–6s
47. Patel YC, Greenwood MT, Panetta R, Demchyshyn L, Niznik H, Srikant CB (1995) Minireview: the somatostatin receptor family. Life Sci 57:1249 – 1265
47a. Been LB, Suurmeijer AJH, Cobben DCP, et al (2004) [^{18}F]FLT-PET in oncology: current status and opportunities. Eur J Nuc Med Mol Imaging 31:1659 – 1672
48. Reubi JC, Laissue J, Krenning EP, Lamberts SWJ (1992) Somatostatin receptors in human cancer: incidence, characteristics, functional correlates and clinical implication. J Steroid Biochem Mol Biol 43:27 – 35
49. Krenning EP, Kwekkeboom DJ, Bakker WH, Breeman WA, Kooij PP, Oei HY, van Hagen M, Postema PT, de Jong M, Reubi JC (1993) Somatostatin receptor scintigraphy with [^{111}In-DTPA-D-Phe^{1}]- and [^{123}I-Tyr^{3}]-octreotide: the Rotterdam experience with more than 1000 patients. Eur J Nucl Med 20:716 – 731
50. Virgolini I, Pangerl T, Bischof C, Smith-Jones P, Peck-Radosavljevic M (1997) Somatostatin receptor subtype expression in human tissues: a prediction for diagnosis and treatment of cancer? Eur J Clin Invest 27:645 – 647
51. de Jong M, Bakker WH, Krenning EP, Breeman WA, van der Pluijm ME, Bernard BF, Visser TJ, Jermann E, Behe M, Powell P, Macke HR (1997) ^{90}Y and ^{111}In labeling, receptor binding and biodistribution of DOTA^{0}, D-Phe^{1}, Tyr^{3}]octreotide, a promising somatostatin analog for radionuclide therapy. Eur J Nucl Med 24:368 – 371
52. Stolz B, Weckbecker G, Smith-Jones PM, Albert R, Raulf F, Bruns C (1998) The somatostatin receptor-targeted radiotherapeutic [^{90}Y-DOTA-Dphe^{1}-Tyr^{3}]-Octreotide (SMT487) eradicates experimental rat pancreatic CA 20948 tumors. Eur J Nucl Med 25:668 – 674
53. Virgolini I, Szilvasi I, Kurtaran A, Angelberger P, Raderer M, Havlik E, Vorbeck F, Bischof C, Leimer M, Dorner G, Kletter K, Niederle B, Scheithauer W, Smith-Jones P (1998) Indium-111-DOTA-lanreotide: biodistribution, safety and tumor dose in patients evaluated for somatostatin receptor-mediated radiotherapy. J Nucl Med 39:1928 – 1936
54. Vallabhajosula S, Moyer BR, Lister-James J, McBride BJ, Lipszyc H, Lee H, Bastidas D, Dean R (1996) Technetium-99m labeled somatostatin receptor binding peptides for tumor imaging: Preclinical evaluation of ^{99m}Tc-P587 and ^{99m}Tc-P829. J Nucl Med 37:1016 – 1022
55. Reubi JC (1995) In vitro identification of vasoactive intestinal peptide receptors in human tumors: implications for tumor imaging. J Nucl Med 36:1846 – 1853
56. Virgolini I, Raderer M, Kurtaran A, et al (1994) Vasoactive intestinal peptide-receptor imaging for the localization of intestinal adenocarcinomas and endocrine tumors. N Engl J Med 331:1116 – 1121
57. Virgolini I, Yang Q, Li S, et al (1994) Cross-competition between vasoactive intestinal peptide and somatostatin for binding to tumor cell membrane receptors. Cancer Res 54:690 – 700
58. Katzenellenbogen JA (1995) Designing steroid receptor-based radiotracers to image breast and prostate tumors. J Nucl Med 36 [Suppl]:8s–13s
59. Rijks LJM, Boer GJ, Endert E, et al (1996) The stereoisomers of 17α-[^{123}I]iodovinyloestradiol and its 11β-methoxy derivative evaluated for their estrogen receptor binding in human MCF-7 cells and rat uterus, and their distribution in immature rats. Eur J Nucl Med 23:295 – 307
60. Wieland DM, Swanson DP, Brown LE, Beierwalters WH (1979) Imaging the adrenal medulla with an I-131-labeled anti-adrenergic agent. J Nucl Med 20:155 – 158
61. Jaques S Jr, Tobes MC, Sisson JC, Baker JA, Wieland DM (1984) Comparison of sodium dependency of uptake of metaiodobezylguanidine and norepinephrine into cultured bovine adrenomedullary cells. Mol Pharmacol 26:539 – 546
62. Beierwalters WH, Weiland DM, Yu T, Swanson D, Mosley S (1978) Adrenal imaging agents. Rationale, synthesis, formulation and metabolism. Semin Nucl Med 8:5 – 21
63. Kaminski MS, Zasadny KR, Francis IR, et al (1993) Radioimmunotherapy of B-cell lymphoma with [^{131}I]anti-B1 (anti-CD20) antibody. N Engl J Med 329:459 – 465
63a. Goedemans WT, Panek KJ, Ensing GJ, et al (1990) A new simple method for labeling of proteins with Tc-99m 1-imino-4-mercaptobutyl groups. In: Nicolini M, Bandolini G, Mazzi U (eds) Technetium and rhenium in chemistry and nuclear medicine, vol 3. Cortina International, Verona; Raven Press, New York, pp 595 – 604
63b. Joiris E, Bastin B, Thornback JR (1990) A new method for labeling of monoclonal antibodies, fragments and other proteins with technetium-99m. In: Nicolini M, Bandolini G, Mazzi U (eds) Technetium and rhenium in chemistry and nuclear medicine, vol 3. Cortina International, Verona; Raven Press, New York, pp 609 – 614
63c. Fritzberg AR, Abrams PG, Beaunier PC, et al (1988) Specific and stable labeling of antibodies with technetium-99m with a diamidedithiolate chelating agent. Proc Natl Acad Sci USA 85:4025 – 4029
64. Knox S, Goris M, Trisler K, et al (1996) Yttrium-90-labeled anti-CD20 monoclonal antibody therapy of recurrent B-cell lymphoma. Clin Cancer Res 2:457 – 470
65. Stoldt HS, Aftab F, Chinol M, et al (1997) Pretargeting strategies for radioimmunoguided tumor localization and therapy. Eur J Cancer 33:186 – 192
66. Hnatowich DJ, Virzi F, Rusckowski M (1987) Investigations of avidin and biotin for imaging applications. J Nucl Med 28:1294 – 1302
67. Paganelli G, Magnani P, Zito F, et al (1991) Three-step monoclonal antibody tumor targeting in carcinoembryonic antigen-positive patients. Cancer Res 51:5960 – 5966

68. Younes CK, Boisgard R, Tavitian B (2002) Labelled oligonucleotides as radiopharmaceuticals: pitfalls, problems and perspectives. Curr Pharm Des 8:1451 – 1466
69. Zhang YR, Zhang YX, Cao W, Lan XL (2005) Uptake kinetics of 99mTc-MAG3-antisense oligonucleotide to PCNA and effect on gene expression in vascular smooth muscle cells. J Nucl Med 46:1052 – 1058
70. Qin G, Zhang Y, Cao W, et al (2005) Molecular imaging of atherosclerotic plaques with technetium-99m-labelled antisense oligonucleotides. Eur J Nucl Med Mol Imaging 32: 6 – 14
71. Dewanjee MK, Ghafouripour AK, Kapadvanjwala M, et al (1994) Noninvasive imaging of c-*myc* oncogene messenger RNA with indium-111-antisense probes in a mammary tumor-bearing mouse model. J Nucl Med 35:1054 – 1063
72. Suzuki T, Wu D, Schlachetzki F, et al (2004) Imaging endogenous gene expression in brain cancer in vivo with ^{111}In-peptide nucleic acid antisense radiopharmaceuticals and brain drug-targeting technology. J Nucl Med 42: 1766 – 1755
73. de Varies EF, Vroegh J, Dijkstra G, et al (2004) Synthesis and evaluation of a fluorine-18 labeled antisense oligonucleotide as a potential PET tracer for iNOS mRNA expression. Nucl Med Biol 31:605 – 612
74. Gambhir SS, Barrio JR, Herschman HR, et al (1996) Imaging gene expression: Principles and assays. J Nucl Cardiol 6:219 – 233
75. Min JJ, Iyer M, Gamghir SS (2003) Comparison of ^{18}F-FHBG and ^{14}C-FIAU for imaging of HSV1-tk receptor expression: adenoviral infection vs stable transfection. Eur J Nucl Med 30:1547 – 1560
76. Tjuvajev JG, Finn R, Watanabe K, et al (1996) Noninvasive imaging of herpes virus thymidine kinase gene transfer and expression: a potential method for monitoring clinical gene therapy. Cancer Res 56:4087 – 4095
77. Tjuvajev JG, Doubrovin M, Akhurst T, et al (2002) Comparison of radiolabeled nucleoside probes (FIAU, FHBG, FHPG) for PET imaging of HSV1-tk gene expression. J Nucl Med 43:1072 – 1083
78. MacLaren DC, Gambhir SS, Satyamurthy N, et al (1999) Repetitive, non-invasive imaging of the dopamine D2 receptor as a reporter gene in living animals. Gene Ther 6: 758 – 791
79. Kung HF, Sangren P, Kung M-P, et al (1988) In vitro and in vivo evaluation of ^{123}I-IBZM; a potential CNS D-2 dopamine receptor imaging agent. J Nucl Med 30:88 – 94

3 Basis of ^{18}F-FDG Positron Emission Tomography Imaging

Seham Mustafa, Abbas Alavi, Abdelhamid H. Elgazzar

3.1 Introduction

During the past few decades the development of novel radiolabeled tracers and the improvement of instruments for imaging have enabled a functional approach to be taken based on metabolic alterations rather than physiological phenomena [1].

Positron emission tomography (PET) is a unique form of diagnostic imaging that observes in vivo biologic changes using radiopharmaceuticals that closely mimic endogenous molecules. It produces images of the concentration of a radioactive tracer in the body, which has been selected to represent the specific metabolic process under study. PET studies consist of a series of consecutive PET images and contain information about the temporal evolution of the radiotracer concentration.

18-Fluorodeoxyglucose (^{18}F-FDG) is considered the current ideal radiopharmaceutical for PET imaging owing to its low positron energy (0.64 MeV) of 18 F, which results in a low radiation dose rate to the patient and also allows high resolution images [2]. It is the most commonly used tracer because of the practical half-life of ^{18}F of 110 min, compared with other shorter-lived positron emitters. ^{18}F-FDG allows the evaluation of glucose metabolism in several disorders.

3.2 Uptake of Glucose

Glucose is an essential compound for living organisms. It is the most important carbon supplier for the synthesis of tissue ingredients and energy-producing metabolic processes that depend largely on glucose availability. Glucose cannot normally diffuse through the pores of the cell membrane because the maximum molecular weight of substrates for such a process is about 100, whereas glucose has a molecular weight of 180. The uptake of glucose by human cells can take place, however, through two mechanisms of transport. The first method involves facilitative glucose transport (GLUT) and the second method is active transport.

3.2.1 Facilitated Diffusion

Many cell membranes possess specialized transport mechanisms that regulate entry and exit of physiologically important molecules, such as glucose. Facilitated diffusion is also called carrier-mediated diffusion because a substance transported in this manner usually cannot pass through the membrane without a specific carrier protein allowing one entry. That is, the carrier facilitates the diffusion of the substance to the other side. However, the carrier protein transports a specific molecule partly but not all the way through the membrane. The molecule to be transported enters the channel and then becomes bound. Then in a fraction of a second a conformational change occurs in the carrier

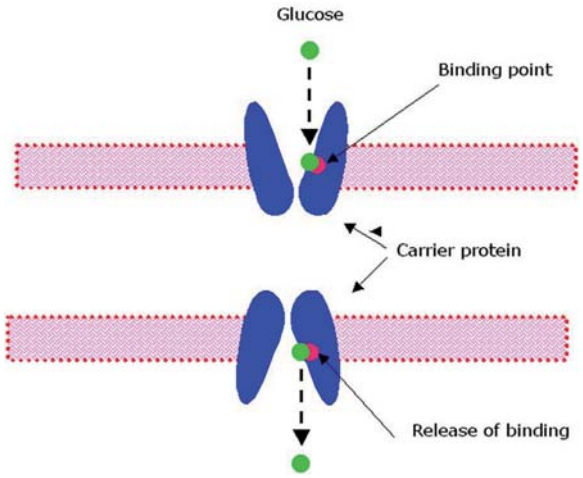

Fig. 3.1. A postulated mechanism for facilitated diffusion

protein so that the channel now opens to the opposite side of the membrane. This mechanism allows the transported molecule to diffuse in either direction through the membrane as shown in Fig. 3.1. Insulin can increase the rate of facilitated diffusion of glucose as much as 10- to 20-fold. This is the principal mechanism by which insulin controls glucose use in the body [3].

Carrier-mediated transport, because it involves a binding step, shows the characteristic of saturation. With simple diffusion, the rate of transport increases directly in proportion to the concentration gradient, whereas with carrier-mediated transport the carrier sites become saturated at high ligand concentrations and the rate of transport does not increase beyond this point. Furthermore, competitive inhibition of transport can occur in the presence of a second ligand that binds to the same carrier. Carrier-mediated transport is important for some drugs that are chemically related to endogenous substances.

Such systems may operate purely passively, without any energy source; in this case they merely facilitate the process of transmembrane equilibration of the transported species in the direction of its electrochemical gradient. If the concentration of glucose is greater on one side of the membrane than on the other side, more glucose will be transported from the high concentration area than in the opposite direction.

Six isoforms of facilitative glucose transporters have been identified so far: GLUT-1 to GLUT-5 and GLUT-7 (Table 3.1). These isoforms share the same transmembrane topology, but they differ in kinetic properties, tissue location, sugar specificities and regulation in states of imbalanced glucose homeostasis [1].

GLUT-1. This transporter is widely expressed at the membranes of many different cells in the human body. The highest concentrations are found in fetal tissue and placenta. Insulin, insulin-like growth factor 1, growth hormone and thyroid hormone induce a higher expression of GLUT-1 [1]. It has been suggested that GLUT-1 belongs to the family of glucose-regulated proteins, which are expressed in situations of cellular stress [4].

Table 3.1. Facilitative glucose transporters and their tissue locations

Transporter	Site of highest concentration
GLUT-1	Fetal tissue and placenta
GLUT-2	Intestine, kidney, liver and β cells of pancreas, brain
GLUT-3	Neurons in the brain
GLUT-4	Brown and yellow adipose tissue and skeletal muscle
GLUT-5	Small intestine
GLUT-7	Endoplasmic reticulum

GLUT-2. This low-affinity transporter can be found in the intestine, kidney, liver β cells of the pancreas and brain. Together with the glycolytic enzyme glucokinase, it constitutes a glucose-sensing system, which signals the differences in glycemia to the liver and the β cells of the pancreas [5].

GLUT-3. High affinity of this transporter for glucose ensures a constant glucose supply to neurons in the brain, even at low extracellular glucose concentrations [6]. In the brain, glucose is transported across the blood-brain barrier by GLUT-1 and, once it reaches the neurons, GLUT-3 is the most efficient transporter in the hypoglycemic conditions of the cerebral interstitial space.

GLUT-4. Expression of this transporter is high in brown and yellow adipose tissue and in skeletal and cardiac muscle. In hyperglycemic states, glucose transport can be increased up to 30 times in response to insulin. Insulin stimulates GLUT-4 transporter [7].

GLUT-5. This transporter is only 40% identical to the other isoforms [8]. It is the main transporter of fructose, and expressed in the small intestine.

GLUT-7. The sequence of GLUT-7, cloned in rat liver, resembles that of GLUT-2. It has a role in the dephosphorylation process of glucose-6-phosphate inside the endoplasmic reticulum [1].

3.2.2 Active Transport

Glucose may be coupled to the electrochemical gradient of Na^+; in this case transport can occur against an electrochemical gradient and is called active transport, which occurs through the gastrointestinal membrane or through the epithelium of the renal tubules. Glucose is transported by the mechanism of active sodium cot-

ransporter, in which active transport of sodium provides energy for absorbing glucose against a concentration difference. This sodium cotransport mechanism functions only in certain special epithelial cells that are specifically adapted for active absorption of glucose.

3.2.2.1 Sodium-Dependent Glucose Transporter

This process requires Na^+ as a co-factor for the active transport of glucose across intestinal and kidney epithelial cells by sodium/glucose transporters. This means that Na^+ enters the cell down its electrochemical gradient, accompanying glucose. The accumulated Na inside the cell is cleared by the Na^+/K^+ ATPase. Two different isoforms are currently known for sodium/glucose transporter (SGLT-1 and SGLT-2). SGLT-1 has a high affinity for glucose and transports Na^+ and glucose in the ratio 2:1, whereas SGLT-2 has a low affinity and the Na^+/glucose ratio is 1:1 [9].

3.3 Fates of Glucose in Normal Cells

3.3.1 Phosphorylation of Glucose

Immediately upon entry in the cells, glucose combines with a phosphate radical. This phosphorylation is promoted by the enzyme glucokinase in the liver or hexokinase in most other cells. Four different types of hexokinase are known. Type I is most abundant in brain and erythrocytes. Type II is predominant in insulin-sensitive tissue, such as skeletal muscle, heart, diaphragm and adipose tissue. Type III is predominant in any tissue and Type IV, also called glucokinase, is predominant in liver cells. The enzymatic activity of all hexokinases except glucokinase is inhibited by glucose-6-phosphate. When glucose is abundant, glucokinase becomes activated in the liver to produce glucose-6-phosphate for the synthesis of glycogen [1].

The phosphorylation of glucose is almost completely irreversible except in the liver cells, the renal tubular epithelium, and the intestinal epithelial cells in which glucose phosphatase is available for reversing the reaction. Therefore, in most tissues of the body phosphorylation serves to capture the glucose in the cell (Fig. 3.2). After absorption into the cells, glucose can either be used immediately for release of energy to the cells or can be stored in the form of glycogen.

3.3.2 Glycolysis

Energy is released from the glucose molecule by this process, which occurs by splitting of the glucose molecule to form two molecules of pyruvic acid. This occurs by ten successive steps of chemical reactions in the cytosol.

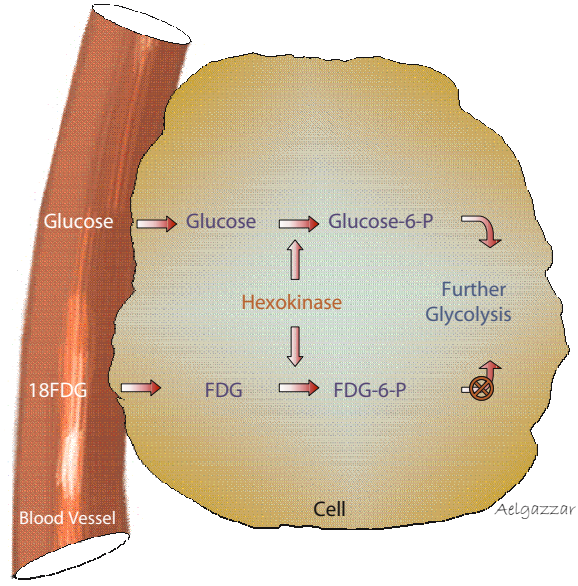

Fig. 3.2. Glucose and FDG are transported into the cell and phosphorylated, but FDG does not undergo further metabolism and accumulates in proportion to glucose utilization (increased in tumors, macrophages and ischemic myocytes)

3.3.3 Storage of Glycogen

Glycogenesis is the process by which glycogen is formed in the cell. Several specific enzymes are required for this process. Glycogenolysis is the breakdown of glycogen to re-form glucose in the cells. Glycogenolysis does not occur by reversal of the same chemical reactions that serve to form glycogen; instead, each succeeding glucose molecule on each branch of the glycogen polymer is split away by a process of phosphorylation, catalyzed by the enzyme phosphorylase. Under resting conditions, the phosphorylase is in an inactive form so that glycogen can be stored but not reconverted into glucose. Two hormones, epinephrine and glucagon, can specifically activate phosphorylase and cause rapid glycogenolysis.

3.4 FDG Localization

The glucose analogue deoxyglucose, which has one oxygen atom less than the glucose molecule (Fig. 3.3), is transported into the cell in the same way as glucose. Once it has reached the cytosol, it is phosphorylated to deoxyglucose-6-phosphate by the enzyme hexokinase,

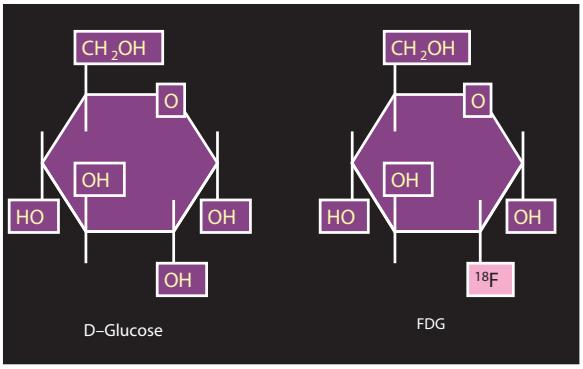

Fig. 3.3. [^{18}F]2-deoxy-2-fluoro-D-glucose (FDG). In FDG the hydroxyl group in the 2-position of D-glucose is replaced by ^{18}F

just like normal glucose. The next reaction in glycolysis, producing deoxyfructose-6-phosphate, in effect a rearrangement of the carbonyl group from the C-1 to C-2 position in the ring structure, is not possible because this would require an oxygen atom at the C-2 position. When it is labeled with ^{18}F, this molecule can be revealed by PET at sites of uptake of this agent. Hence, a high uptake of ^{18}F-fluorodeoxyglucose reflects an increased glucose metabolism, for example in tumor cells [1]. As a result, the very polar FDG-6-phosphate is trapped in the cytoplasm. FDG-6-phosphate may be converted back to FDG, but the enzyme glucose-6-phosphatase, which is responsible for this reaction, is either present at very low levels or absent in cancer tissues [10].

The uptake and retention of FDG as radiopharmaceuticals (metabolic substrates) by different tissues and organs vary substantially depending on the levels of glycolysis at one site (Fig. 3.2). The injury to a cell or tissue significantly alters the morphology and molecular biology compared with that of normal tissue or organs. FDG PET is now being extensively used for an increasing number of clinical indications at different stages of cancer, e.g., diagnosis, staging, monitoring of response to therapy, and finally detection of recurrence. In addition, FDG accumulates in activated white cells and macrophages and as such may also play a role in detecting infection and inflammation.

Biodistribution of ^{18}F-FDG can be affected by various physiologic factors. Blood glucose levels have an impact on ^{18}F-FDG uptake through competition for the sites of high glycolysis. Patients should fast 4 – 6 h to reduce competition with plasma glucose and thus optimize and standardize ^{18}F-FDG uptake. These requirements are especially important in diabetic patients, in whom high glucose levels can alter the distribution of FDG. When plasma glucose levels are greater than reference values, FDG uptake increases in muscles and affects the quality of the images [11]. Muscle relaxants may be used to reduce muscle uptake. Good hydration is required before imaging to encourage urinary excretion. Patients should remain silent during and after injection to reduce laryngeal muscle uptake [12].

3.5 Basis of Specific Clinical Applications of FDG

3.5.1 Cancer: Diagnosis, Staging and Follow-up

3.5.1.1 Pathophysiology of FDG Cancer Uptake

3.5.1.1.1 Basis of Uptake by Cancer Cells

Cancer cells have an altered metabolism compared with normal cells. As a result, cancer cells use more glucose than normal cells. Due to the increased rate of cell proliferation, the protein and DNA synthesis is augmented and the cancer cells need to transport large amounts of precursors and nucleotides. In addition to overproduction of glycolytic enzymes, increased uptake of glucose is seen in tumor cells. The facilitative glucose transporters, the expression and activity of which are regulated by oncogenes and growth factors, are generally held responsible for this increase of glucose taken up. Therefore overexpression of GLUT-1, GLUT-3 and GLUT-5 plays a role in this enhanced transport [13].

The transport and phosphorylation of FDG to FDG-6-phosphate occurs at a higher rate in cancer cells than in normal cells. FDG has become a tumor marker for assessing disease activity in current clinical practice [11].

The glycolytic capacity of a given tumor is generally assumed to be characteristic of its state of differentiation [14]. It was suggested that the promoting force for this increased glycolytic flux is the phosphorylation of glucose, the first reaction of the glycolytic pathway. This step is catalyzed by hexokinase and it is this enzyme that promotes an increased glycolytic activity of tumor cells [15]. At least two factors contribute to this increased activity of hexokinase [1]. One is the difference in binding to the outer membrane of the mitochondrion; the other is the overproduction of this enzyme in malignant cells compared to normal cells. Rempel et al. [15] found that the percentage of membrane-bound hexokinase activity increases with the grade of malignancy. Four different isoenzymes of hexokinase are known and there is a pronounced tissue-specific distribution. In malignant cells, type 11 hexokinase and to a lesser extent type 1 hexokinase are overexpressed [16]. Therefore, it is clear that accumulation of FDG in tumor cells is due to: (1) increased transporter expression and its activity, (2) increased production and activity of hexokinase, (3) absent or low levels of glucose-6-phosphatase.

Tumor perfusion and delivery of ^{18}F-FDG is affected by necrosis and therapy-induced changes. ^{18}F-FDG is a highly sensitive and specific imaging modality in the evaluation of biochemical changes that occur in tumors during or after therapy. Uptake of FDG in tumor cells is influenced by a certain number of factors such as increased expression of glucose transporters and the presence of a highly active hexokinase isoform, hypoxia and the glucose levels in the blood.

3.5.1.1.2 Tumor Hypoxia

Clavo et al. [17] showed that FDG uptake was increased when cells were exposed to a hypoxic environment. The hypoxia was associated with an increased expression of the GLUT-1 glucose transporter and an increased membrane transport of glucose. Wang and Semenza [18] determined the presence of a specific region inducing hypoxia in the promoter of hexokinase. The hypoxic state of a solid tumor may cause upregulation of hexokinase, which enhances the rate of glycolysis, serving as a mechanism for the tumor cell to survive [1]. Many solid tumors develop areas of hypoxia during their evolution. This is primarily caused by unregulated cellular growth, resulting in a great demand on oxygen for energy metabolism [19]. Hypoxia in tumor tissue is an important prognostic indicator of response to either chemotherapy or radiation therapy. Thus, detection of hypoxia in advance of such interventions is important for optimizing the use and outcome of different therapeutic modalities. Several hypoxia-imaging agents have been developed rather than FDG [20]. These compounds diffuse into normally oxygenated and hypoxic cells but are retained substantially in a higher concentration in the hypoxic tissues, which can be detected on images.

3.5.1.1.3 Fed/Fast State

In normal cells, insulin is active in the high glucose level states. Therefore opposing effects on gene expression have been found: insulin activates the transcription of hexokinase and glucagon inhibits this transcription. Both insulin and glucagon activate the promoter of the hexokinase II gene in cancer cells. This can be seen as a strategy of the cancer cell to keep its glycolysis high, even with a limited supply of glucose. If the glucose level in the environment rises, the cancer cell can utilize the available glucose immediately, without a lag period. This means that transcription of hexokinase in tumor cells is independent of the metabolic state of neighboring healthy cells. Thus, cancer cells have an advantage over their cell of origin [19].

FDG uptake into human cancer cells is inhibited by high glucose levels in the medium, because of the competition between FDG and glucose for uptake into malignant cells [21]. It has been demonstrated in vitro and in vivo that tumor uptake of FDG is markedly diminished by acute hyperglycemia. It has also been shown that tumor targeting with FDG is impaired by insulin-induced hypoglycemia. Therefore to optimally evaluate tumor biology by PET, the fasting state seems necessary for FDG. Since glucose represents the preferred fuel for cancer cells, there is some debate about the potential stimulation of tumor metabolism induced by glucose-based total parenteral nutrition (TPN) in cancer patients. It was proven that despite glucose being the preferred fuel for cancer cells, its disproportionately high uptake even in fasting conditions makes the glucose consumption unable to be modulated by a further supply of glucose or lipid [22]. All diabetic patients should have their blood sugar level controlled with oral hypoglycemic or insulin, although some time after the time of FDG injection (>2 h). Insulin injection close to the time of FDG administration induces diffusely increased uptake of FDG in the skeletal muscles [23]. When plasma glucose levels are greater than reference values, FDG uptake increases in muscles. This will lead to blurring of tumor margins [11].

3.5.1.1.4 Degree of Uptake

Intensity of radiopharmaceutical uptake relative to the normal tissue has been used to differentiate benign from malignant lesions. There have been multiple reports of varying degrees of uptake of ^{18}F-FDG in benign conditions demonstrating hypermetabolism on ^{18}F-FDG PET scans, including granulomatous infection, benign tumors, and autoimmune diseases, also bronchiolitis obliterans organizing pneumonia [24]. Accordingly, intensity is not a reliable parameter and dual acquisition and quantitation are helpful in this regard. The intensity of the uptake reflects the viability of the cells in the involved lesion. ^{18}F-FDG directly targets malignant cells anywhere in the body and, therefore, is able to visualize disease activity directly at all anatomic sites.

3.5.1.2 Clinical Utilization in Cancer

The introduction of ultrasonography, magnetic resonance imaging and computed tomography has improved the clinical management of patients with malignant tumors. However, these substantially structurally based techniques assess primary tumors and metastases by size and visual patterns. Furthermore, they lack specificity in characterizing many lesions. The introduction of PET has improved further the diagnosis and

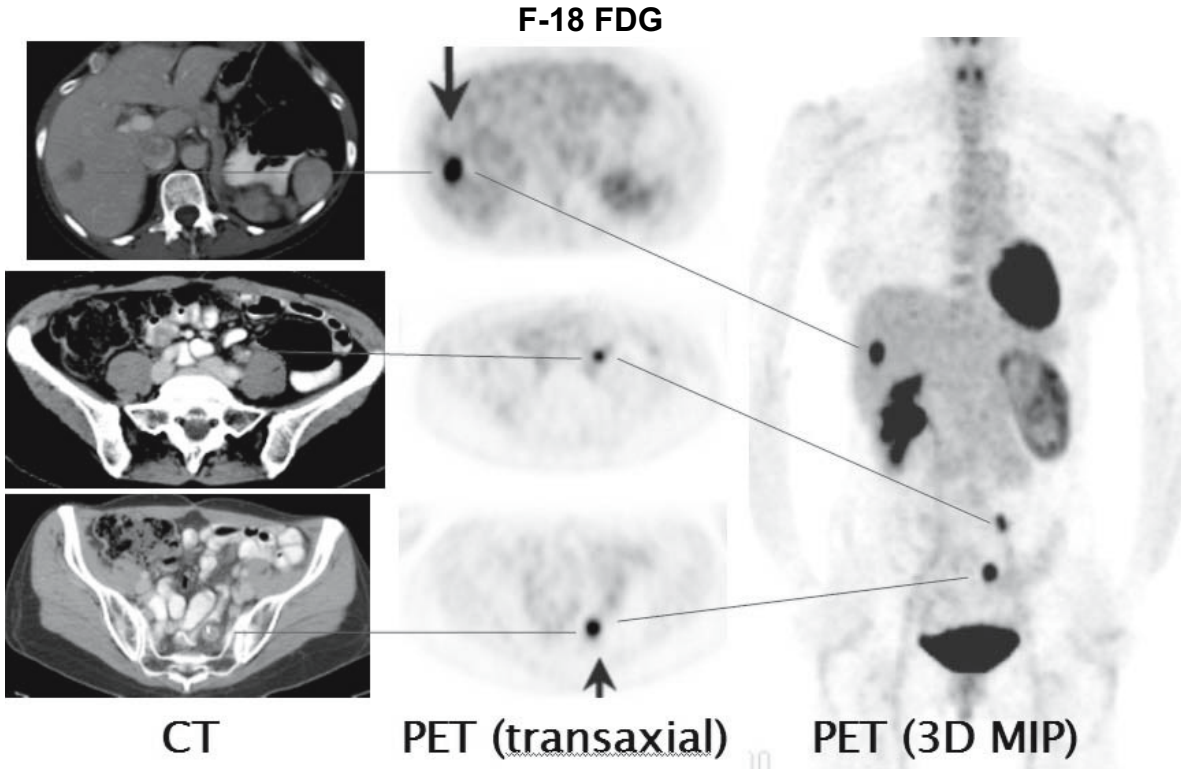

Fig. 3.4. An FDC study of a patient with known colon cancer. The study shows metastases to the liver and abdominal lymph nodes (*arrows*)

Fig. 3.5. FDG study of a patient with osteogenic sarcoma showing intense uptake by the tumor (*arrow*)

management of cancer patients. ^{18}F-FDG PET is useful in detecting, staging, restaging, and assessment of response to treatment of many tumors including lung, colorectal, breast carcinoma, melanoma, lymphoma, head and neck, thyroid, brain, cervical, prostate and ovarian cancers [11, 12, 20, 25 – 35].

3.5.1.2.1 Tumor Detection

FDG PET is valuable in the early detection of tumor (Figs. 3.4, 3.5) and can help in its diagnosis [36]. The indeterminate lung nodule is an important example illustrating this. It is estimated that solitary pulmonary nodules are detected in 52 per 100,000 people in the United States. Thirty percent of these will be considered benign based on an initial examination for history of risk factors and standard radiographs. The remaining 70% are considered indeterminate, requiring further examination – often by X-ray computed tomography (CT). Of the cases sent to CT, 78% are diagnosed indeterminate or malignant, and 75% will be referred to surgery, resulting in approximately 68,000 thoracotomies annually. Twenty percent of these thoracotomies will yield a *benign* diagnosis. Based on published data, PET would reduce the number of unnecessary thoracotomies, resulting in only a 6% yield of benign diagnosis for resected solitary pulmonary nodules [37 – 40].

3.5.1.2.2 Tumor Staging

FDG-PET is particularly valuable in staging cancer and has proven cost effective in avoiding unnecessary costs for surgeries by adding PET FDG studies such as in cases with lung cancer (Fig. 3.6). Accuracy in staging permits selection of the most appropriate treatment. Identification of metastases that are not seen with anatomic imaging (upstaging) avoids the high morbidity and cost of treatments that cannot benefit the patient and permits more effective choices of therapy. Likewise, metabolic reclassification of malignant lesions to benign (downstaging) allows patients with false-posi-

◁ **Fig. 3.6.** ^{18}F-FDG study for staging of a patient recently diagnosed with non-small-cell right lung cancer. CT showed increased sizes of lymph nodes ipsi- and contralaterally. The question was whether the patient had stage N2 or N3 to determine resectability. The FDG study shows only ipsilateral lymph node metastasis, indicating minimal N2, M0 stage. (Courtesy of Professor Osama Sabri, Leipzig)

tive anatomic findings but limited disease to receive potentially curative treatment.

3.5.1.2.3 Evaluation of Therapy and Detecting Recurrence

The most important application of PET in cancer is early and accurate evaluation of therapy (Fig. 3.7) and early detection of recurrence, which has a significant impact on cancer management. Evaluation of the response to therapy and follow-up of tumor patients determining the residual uptake and recurrence provide important prognostic information. For example, in the United States, there are approximately 110,000 new colon cancers and 45,000 new rectal cancers reported every year. Approximately 66% of these cases are cured by surgical resection, while cancer in the remaining 33% recurs generally before 2 years postsurgery. Distinguishing which of these recurrent cases can benefit from additional surgery is challenging, because only one in four of recurrent cases is curable. The incurable cases run the risk of unnecessary and expensive surgery [41] (see Chapter 12 for more details).

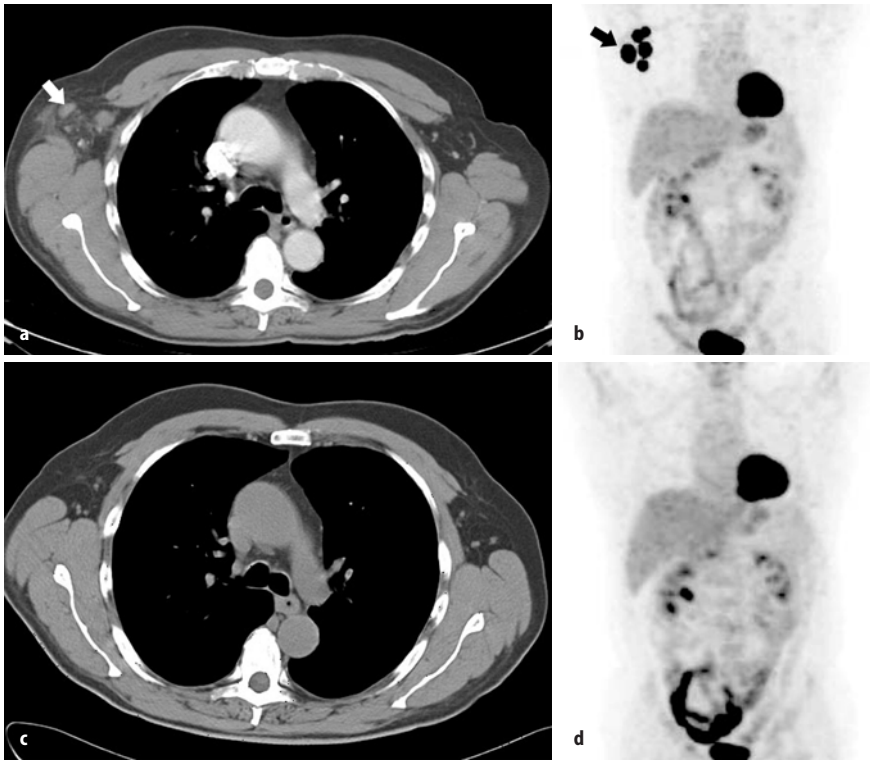

Fig. 3.7a–d. Young male presents with right axillary adenopathy proven to be non-Hodgkin's lymphoma. The CT scan (**a**) shows enlarged nodes (*arrow*). The FDG PET study (**b**) shows intense uptake by the tumor (*arrows*). The postchemotherapy CT scan (**c**) shows a decrease in the size of the nodes while the post-therapy FDG study (**d**) shows no uptake, indicating a definite good response to therapy

3.5.2 Neuropsychiatric Disorders

Under resting conditions, the metabolism of the brain accounts for about 15% of the total metabolism in the body, even though the mass of the brain is only 2% of the total body mass. Therefore, brain metabolism is about 7.5 times the average metabolism in the rest of the body. Most of this excess metabolism of the brain occurs in the neurons. During excessive brain activity, neuronal metabolism can increase severalfold.

The brain cells are quite different from most other cells of the body in that they normally use essentially only glucose as the source of energy, utilizing other substrates, such as fat and ketone bodies, only as a last resort. The brain is also quite different from most other tissues of the body in that insulin has little or no effect on uptake or use of glucose. Instead, the brain cells are even normally permeable to glucose and can use glucose without the mediation of insulin. Therefore, even in patients who have serious diabetes with essentially zero secretion of insulin, glucose still diffuses readily into the neurons [3].

FDG PET is an excellent tool with which to evaluate brain function because the synthesis of over 95% of adenosine triphosphate that is hydrolyzed to fuel cerebral function originates from the catabolism of glucose [42]. For example, in patients with varying severity of dementia, the magnitude and extent of hypometabolism correlates with the severity of dementia [43].

3.5.2.1 Alzheimer's Disease and Related Disorders

In its early stages, the identification and differential diagnosis of dementia is especially challenging, because of the difficulty of distinguishing it from the mild cognitive decline associated with normal aging, and from mild cognitive manifestations associated with neuropsychiatric conditions (i.e., depression).

It is well established that regional cerebral metabolic rates for glucose as assessed by FDG PET in patients in the resting state (eyes and ears covered) provide a sensitive, in vivo metabolic index for diagnosing Alzheimer's disease. The brain hypometabolism revealed by FDG PET is a sensitive marker of disease progression in this disease. Therefore FDG PET can be used to investigate the progression of serious brain disorder [44, 45].

Patients with neurodegenerative disease gain the most from effective therapies that intervene as early as possible. Since several prescription medications for the treatment of mild to moderate Alzheimer's disease are available, early and accurate diagnosis has become more urgent. The drugs which increase acetylcholine levels in the brain are considered efficacious if prescribed early during the course of the disease. Early Alzheimer's disease can be detectable only by metabolic imaging techniques [46–48]. As the disease progresses, metabolic changes may translate into significant cortical atrophy. FDG PET may become the critical test for selecting the appropriate patients for treatment when the disease process is at the molecular level and before structural alterations have taken place [49].

3.5.2.2 Movement Disorders

Kuhl et al. [50] found that in Parkinson's disease, findings on FDG PET were nonspecific. Cerebral glucose metabolism was reduced uniformly throughout the brain (average 18% decrease). Bradykinesia severity was increased associated with mild to moderate dementia. In Parkinson's disease the whole brain metabolism decreases further. Severe parietal cortex hypometabolism was found in one moderately demented patient with Parkinson's disease, and also in Alzheimer's disease. In contrast, mildly to moderately demented patients with Huntington's disease had marked caudate hypometabolism, but cerebral glucose metabolism was normal elsewhere. It appears that some neurotransmitters are decreased or are lost in the nigrostriatal system in the parkinsonian brain, and it is now clear that there is an abnormal metabolic process involving neurons [50].

3.5.2.3 Epilepsy

The use of FDG PET in localizing seizure foci in the temporal lobe for surgical interventions is well established. It has been clearly shown that FDG PET is quite sensitive in detecting such sites, with 85%–90% accuracy [51]. Hypometabolism at the seizure focus is noted when there is clinical evidence for epilepsy while anatomic images remain normal for an extended period [52–54]. It has been realized that longstanding seizure episodes eventually lead to significant atrophy, and also that longstanding metabolic and molecular abnormality eventually will result in significant atrophy in most chronic disorders of the brain [49]. Abnormalities of glucose utilization and metabolic dysfunction will be related to persistent epilepsy ([55], Fig. 3.8, [56]).

3.5.2.4 Other Neuropsychiatric Disorders

There is growing evidence that PET is useful in several other neuropsychiatric disorders including evaluation of severe dysfunction in head injury [57, 58], Huntington's chorea [59, 60], schizophrenia [61, 62], migraine [63] and frontal lobe dementia [64, 65].

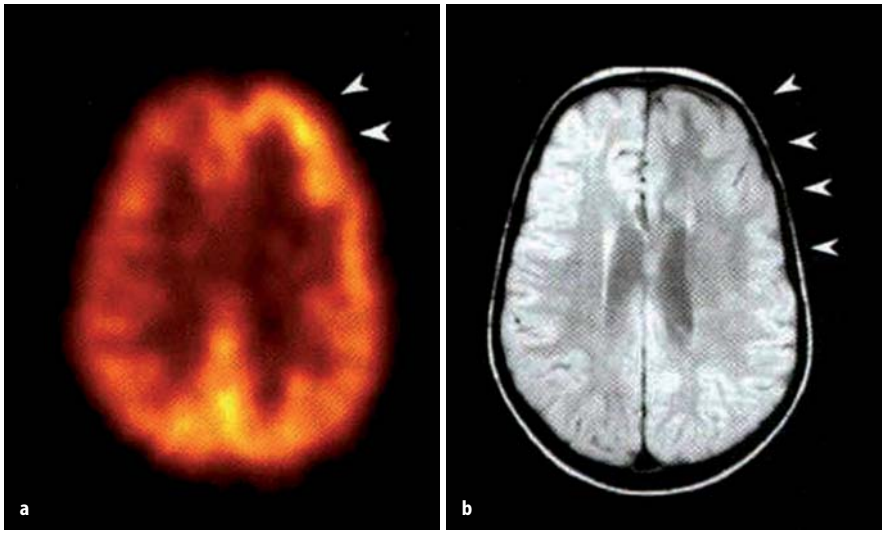

Fig. 3.8a,b. FDG PET (**a**) was performed in a 4-year-old boy with refractory frontal lobe seizures and developmental delay and with extensive left front parietal dysplasia on MRI (**b**, *arrowheads*, transaxial image). The PET study shows increased metabolic activity (**a**, *arrowheads*) associated with virtually continuous epileptiform activity emanating from the left frontal lobe, and normal metabolic activity in the right cerebral hemisphere. On the basis of the PET findings, a decision was made to proceed to surgery, limiting the resection to the hypermetabolic cortex in the left frontal lobe. The child had a significant reduction in seizure frequency, with a marked improvement in cognitive and developmental milestones. (Reprinted with permission from [56])

Encephalitis during the acute phase of the disease manifests itself on ^{18}F-FDG PET as areas of hypermetabolism. However, there can also be large areas of hypometabolism associated with encephalitis. These areas can be the result of active inflammation or seizure activity. EEG monitoring during the PET scan would be essential for ruling out subclinical seizure activity as the cause of the hypermetabolism [66] (see Chapter 18 for more on PET in neuropsychiatric disorders).

3.5.3 Cardiovascular Disease

3.5.3.1 Myocardial Viability

FDG PET has been used to study cardiovascular disorders ranging from hypertrophic and idiopathic dilated cardiomyopathy [67] to unstable angina [68], myocardial infarction [69] and chronic ischemic left ventricular dysfunction [70].

The use of FDG PET to determine myocardial viability remains a very important technique and is considered the gold standard for viability [49].

The myocardium derives energy from a variety of sources such as free fatty acids, glucose, lactate, pyruvate, ketone bodies and amino acids [71]. Under normal resting conditions, metabolism is mainly oxidative, with free fatty acids being the major source of energy, while glycolysis contributes only about 30% to the overall metabolic activity of the heart. Dietary and hormonal conditions markedly alter the selection of substrates. For example, in the fasting state, free fatty acids levels are high and glucose and insulin levels are low. Consequently, the rate of myocardial free fatty acid oxidation is high and inhibits glycolysis. After ingestion of carbohydrates, plasma concentrations of glucose and insulin rise. Insulin reduces peripheral lipolysis, thereby further lowering plasma concentrations of free fatty acids and hence reducing their availability to the myocardial energy production [72].

Myocardial ischemia alters myocardial substrate metabolism, and also results in a dramatic and sustained switch to glucose uptake. Ischemia is also associated with increased glycolysis, with glucose transporters expressed in higher numbers as possible flux-generating steps. Uptake of FDG may remain normal or may even increase in altered myocardial states, such as contractile dysfunction or reduced perfusion resulting from ischemia in patients with stable angina, unstable angina and chronic hibernation [73]. FDG accumulation in such altered myocardium indicates the persistence of metabolic activity and thus the potential for recovery of contractile function (Fig. 3.9) [74].

Myocardial FDG uptake depends quantitatively on plasma concentrations of glucose and insulin. Glucose uptake in peripheral tissues is the most important mechanism of clearance of FDG from blood. Myocardial glucose uptake also depends on myocardial work, plasma level of free fatty acids, insulin, catecholamines and oxygen supply [71].

Under fasting conditions, the normal myocardium primarily utilizes free fatty acids, while glucose utilization, and thus FDG uptake, is minimal. In ischemic myocardium, when glucose becomes an important energy substrate, FDG uptake will be enhanced. Consequently, there will be a marked difference in FDG uptake between normal and ischemic myocardium, which is reflected on the image as a "hot spot". Thus for the

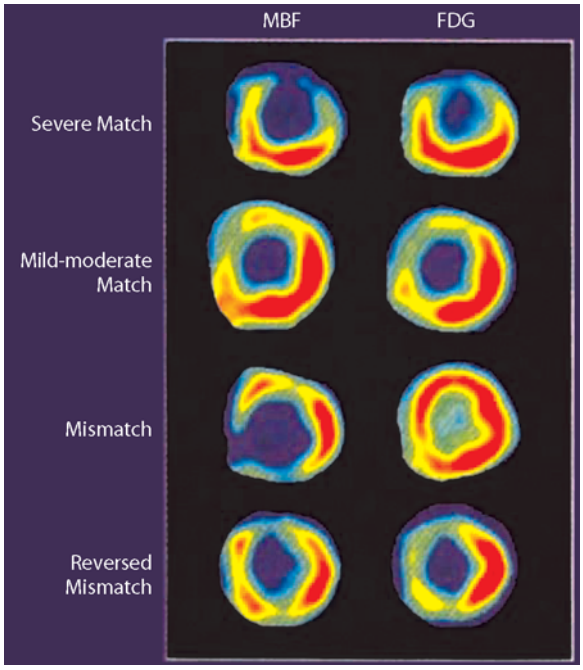

Fig. 3.9. Patterns of myocardial viability by use of myocardial perfusion and FDG PET. Patterns refer to post-glucose-loading FDG PET imaging. (Reprinted with permission from [74])

detection of ischemia, fasting may be preferable. However, FDG distributes heterogeneously throughout the normal myocardium in the fasted state, limiting the specificity for the detection of myocardial ischemia. In addition, uptake of glucose and FDG in both myocardial and skeletal muscle is low, resulting in poor-quality images. Therefore it was proven that small doses of regular, short-acting insulin might improve image quality. It has been demonstrated that oral administration of a nicotinic acid or its derivatives may be such an alternative approach. Nicotinic acid inhibits peripheral lipolysis and thus reduces plasma free fatty acid concentrations. Acipimox is a nicotinic acid derivative, which is 20 times more potent than nicotinic acid [75].

Recently, metabolic aspects, perfusion autoregulation, and receptor-mediated cardiac responses of the orthotopic cardiac transplant have been a priority in research. In one study [76] increased myocardial uptake on FDG PET was explained by inefficient metabolic utilization of glucose by the transplanted myocardium or by the influence of circulating catecholamines, which may stimulate glucose uptake independently of cardiac workload. ^{18}F-FDG regional uptake was approximately threefold higher in the transplanted heart than in the native heart. This largely results from the difference in myocardial tissue viability, as well as probably reflecting functional-metabolic coupling of the transplanted heart as opposed to the native heart [76].

Injured myocardium frequently demonstrates impaired oxidative metabolism, an excess of glucose utilization relative to flow. Stunned myocardium shows preserved flow, and either matched or excessive FDG accumulation [77]. At times, stunning results in impaired FDG accumulation have been obtained, producing an underestimation of viability [78]. Hibernation has been shown to demonstrate decreased perfusion, and relatively preserved or disproportionately increased FDG accumulation. Infarcted myocardium shows a matched decrease in both perfusion and FDG uptake.

Syndrome X has been recognized as a disease that is primarily reflected in the cardiac microvasculature. In syndrome X patients, myocardial FDG uptake is increased extensively, and is strongly associated with narrowed myocardial microvasculature [79].

Coronary artery disease is the most important cause of morbidity and mortality on a global scale. FDG can be used to evaluate accurately the exercise-induced myocardial ischemia [80]. Detection of myocardial viability is most important for patients diagnosed with congestive heart failure, compromised left ventricular function, and end-stage coronary artery disease. For these patients, the goals of therapy include reduction of cardiac mortality and relief of congestive heart failure symptoms (leading to a gain in quality of life years). Options for therapeutic intervention are cardiac transplantation, surgical revascularization, and medical management.

Several approaches for identifying viable myocardium are available. A popular technique is dobutamine (i.e., pharmacologically induced) stress echocardiography, which can show preserved contractile reserve as a key feature of reversible dysfunctional myocardium. A study by Bax et al. [81] emphasized good specificity of stress echocardiography but a low sensitivity. An alternative approach for assessing myocardial viability is the conventional nuclear medicine test: rest-redistribution ^{201}Tl-single photon emission computed tomography (SPECT). Although conceptually sound, ^{201}Tl-SPECT may lack diagnostic accuracy in patients with markedly enlarged left ventricles, and poor myocardial perfusion, and suffer from technique-related problems such as poor image quality (low signal-to-noise and attenuation artifacts) [82].

Compared with ^{201}Tl-SPECT, ^{18}F-FDG PET has substantially better sensitivity, as many studies have reported uncovering substantial amounts of viable myocardium in patients with equivocal SPECT studies or with fixed defects on SPECT. For example, two investigations reported the presence of metabolic activity with FDG PET in 90% [83] and in 52% [84] of patients with ischemic cardiomyopathy and with fixed defects or equivocal findings on ^{201}Tl-SPECT rest-distribution imaging.

3.5.3.2 Atherosclerosis

FDG is taken up in the atherosclerotic vessel wall [85]. This process is quite noticeable in the aorta in its entirety and other major arteries. There is evidence that the uptake is mainly located in the intimae and likely represents high metabolic activity in macrophages, which are abundant in the atherosclerotic plaques [86]. It is also likely that the smooth muscles in the arterial wall are visualized due to high glucose use by this tissue. The uptake in the peripheral vessels, such as the popliteal and the lower femoral arteries, is mostly located in the smooth muscle rather than in the intimae, while FDG is mainly localized in the atherosclerotic plaques in the aorta, and its tributaries in the trunk, neck and upper thighs [49].

There is also evidence that thrombosis and atherosclerosis are associated with increased glucose use, which can be detected with FDG PET [85].

The cellular components of the atherosclerotic plaque, such as macrophages, exhibit high glucose metabolic activity. This vascular uptake might be due to smooth muscle metabolism in the media, subendothelial smooth muscle proliferation from senescence, and the presence of macrophages within the atherosclerotic plaque [86].

3.5.4 Skeletal Disorders

FDG directly targets malignant cells anywhere in the body, including the marrow space, and therefore is able to visualize disease activity directly at all anatomic sites. However, bone imaging displays indirect evidence for the presence of disease. Some aggressive malignancies such as lung cancers may not result in an adequate degree of new bone formation to be detectable by bone scanning. However, they can be visualized directly by FDG PET in the marrow space [49]. FDG-PET can be used for the detection and follow-up of bone tumors when ^{99m}Tc-MDP bone scintigraphy gives negative findings [87].

Positron emission tomography also shows promise in the evaluation and treatment of inflammatory arthropathies. Psoriatic arthritis increases the level of FDG uptake in the joints of the hands. The areas of increased activity correlate well with the regions of symptoms reported by the patient [88]. FDG PET has also shown a potential in the diagnosis of chronic active osteomyelitis. A recent study has shown that FDG-PET has the highest diagnostic accuracy for confirming or excluding the diagnosis of chronic osteomyelitis, particularly in the axial skeleton compared to other modalities including leukocyte scintigraphy [89].

3.5.5 Inflammatory Disorders

FDG has proven to be an excellent tracer for detecting inflammation in the setting of either infectious or noninfectious processes [90]. Activated inflammatory cells appear to have increased rates of glycolysis and accumulate FDG with high concentration [91]. Therefore, FDG can be effectively used to detect sites of infection and inflammation [92].

Orthopedic infections, particularly those related to implanted prostheses [93], and osteomyelitis [91] can be detected successfully by FDG PET. Increasingly, this technique is being used for detecting infection in soft tissues anywhere in the body, including the source of fever of unknown origin [94]. The potential of FDG PET for detecting inflammatory processes in disorders such as regional ileitis [95], sarcoidosis [96], rheumatologic disease [97, 98], and vasculitis [99] and any other disorder is also vast.

PET can be used in the diagnosis of giant cell arteritis. PET revealed diffuse abnormal ^{18}F-FDG arterial uptake in a patient with giant cell arteritis. The patient showed prompt resolution of symptoms after treatment with steroids. A repeat PET scan showed near-complete resolution of the abnormal FDG uptake [100].

Among the large number of positron imaging radiopharmaceuticals that have been synthesized to date, FDG stands out as the most effective preparation for research and clinical applications. This preparation will remain the agent of choice for many years to come. More than 95% of PET procedures performed around the world use FDG as the imaging agent [49].

While uptake of FDG continues to increase at malignant sites for several hours, as can be shown by an incremental increase of the standardized uptake values (SUV), inflammatory lesions peak at approximately 60 min, and their SUV either stabilize or decline thereafter. This difference in the behavior of FDG in malignant versus inflammatory cells can be explained best by the varying levels of enzymes that degrade deoxyglucose-6-phosphate in the respective cells (Fig. 3.10). Glucose-6-phosphatase dephosphorylates intracellular FDG-6-phosphate, allowing it to leave the cell. It has been shown that most tumor cells have low levels of this enzyme, while its expression is high in the mononuclear cells [101, 102]. For this reason, imaging at two time points after administration of FDG may prove to be important in differentiating between these two common disorders.

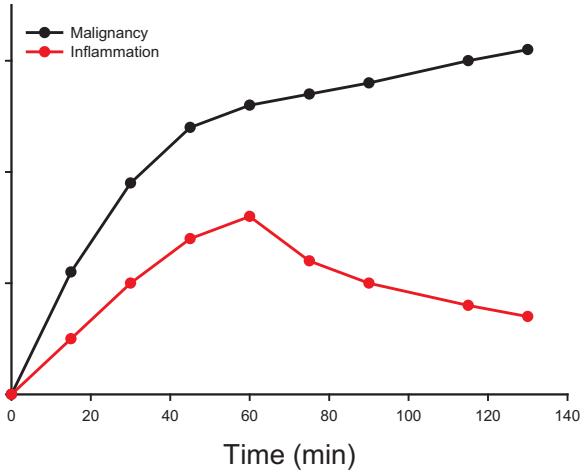

Fig. 3.10. A plot of SUV change over time in malignancy and inflammatory lesions illustrating the decline of SUV in inflammation

3.6 Other PET Radiotracers

More than 30 years after its inception, FDG is still the most widely used radiopharmaceutical for PET studies, but numerous radiotracers have been developed.

There are four positron-emitting radioisotopes that are well suited for standard production by modern cyclotrons. These are fluorine-18 (^{18}F), carbon-11 (^{11}C), nitrogen-13 (^{13}N) and oxygen-15 (^{15}O). The reason these are so commonly used is that they have many attractive properties, one of which is that they can be easily substituted directly into biomolecules. Substitution of ^{11}C for ^{12}C does not alter the biological behavior of one molecule. A similar situation exists for ^{13}N and ^{15}O. ^{18}F can often be substituted for a hydroxyl group on a molecule or placed in a position where its presence does not significantly alter the in vivo biochemical kinetics of the compound. The half-lives of these tracers are: ^{11}C = 20.4 min; ^{13}N = 9.98 min; ^{15}O = 2.03 min and ^{18}F = 109.8 min [103].

Several new more specific tracers will be approved and routinely used in the coming years. The tissue uptake of ^{18}F-FDG is nonspecific. Thus, radiopharmaceuticals that are more specific for tumor imaging are desirable, as well as development of new radiopharmaceuticals that target amino acid and protein synthesis, DNA synthesis and cell proliferation, lipid synthesis, receptor-mediated radioligands, hypoxia, angiogenesis, apoptosis and gene therapy.

Protein synthesis is essential for growth and development. Several amino acids have been labeled with ^{18}F for tumor imaging such as O-(2[^{18}F]fluoroethyl)-l-tyrosine. The incorporation of ^{14}C or ^{3}H-labeled thymidine into cells has been standard for measuring tissue proliferation and growth kinetics. ^{18}F-3-fluoro-3-deoxythymidine ([^{18}F]FLT) measures cell proliferation, [^{18}F]FLT being taken up by cells and phosphorylated by thymidine kinase-1, leading to the 5'-phosphate, which is intracellularly trapped [104]. It is logical to assume that [^{18}F]FLT uptake is specific for malignant lesions since benign tumors do not exhibit cell proliferation. Furthermore, following a favorable response to treatment, an inflammatory reaction may confound the use of FDG but does not affect the use of [^{18}F]FLT in this setting. Thus [^{18}F]FLT may be a better tumor-imaging agent than FDG (Fig. 3.11), although the high uptake of [^{18}F]FLT in liver decreases its usefulness in liver tumors [105, 106].

Choline is one of the components of phosphatidylcholine, an essential element of phospholipids in cell membrane. The levels of choline and choline kinase are elevated in neoplasms [107]. Human studies have indicated that both ^{11}C- and ^{18}F-labeled choline are superior to ^{18}F-FDG for the detection of brain tumors, prostate cancer, lung cancer, and head and neck cancer

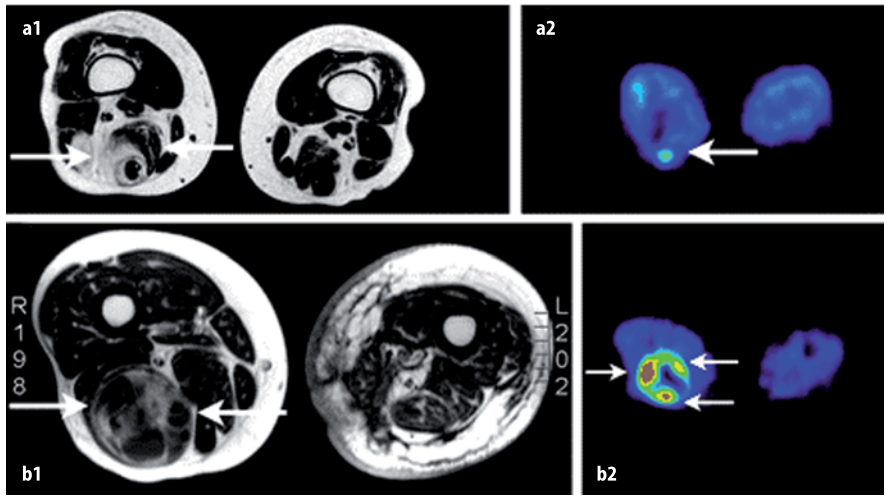

Fig. 3.11. a Magnetic resonance imaging (MRI, **a1**) and 3'-[^{18}F]fluoro-3'-deoxy-l-thymidine-positron emission tomography (FLT-PET, **a2**) images of a low-grade soft tissue sarcoma (STS). **b** MRI (**b1**) and FLT-PET (**b2**) images of a high-grade STS. The MRI images of both patients demonstrate a heterogeneous tumor. However, the FLT uptake in the high-grade STS is higher than in the low-grade STS. (Reprinted with permission from [106])

[108]. ^{18}F-FDG imaging resulted in a broad accumulation of tracer in normal brain as well as the lesion, whereas the accumulation of methionine was more specific, as was the accumulation of choline. ^{11}C-labeled choline was reported to be useful in the detection of clinically localized prostate cancer, while ^{18}F-FDG was not particularly useful (most of the tumors of the prostate are not sufficiently malignant to accumulate FDG) [109].

Acetate also has a high uptake in tumors. Its accumulation in tumor cells seems to be caused by the low oxygen consumption and enhanced lipid synthesis of these cells. Both ^{11}C- and ^{18}F-labeled acetate have been used as tumor imaging agents.

High levels of receptors have been found in certain tumors. For example, ^{18}F-labeled steroid receptor radioligands have been used to image breast cancer and prostate cancer.

Agents that measure regional hypoxia in malignant tumors and possibly in some benign disorders will be frequently employed. Hypoxia in tumor tissue is an important indicator of response to both chemotherapy and radiation therapy. [$^{60/62}$Cu]ATSM is a promising imaging tumor hypoxic agent [110].

Tumor angiogenesis is essential for growth, invasion, and metastasis. These days there are specific radiopharmaceuticals available for imaging angiogenesis.

Detection of cell death (apoptosis) by imaging is an interesting area for assessing both malignant and benign disorders [111]. ^{99m}Tc-labeled annexin V is the first agent used for this purpose. This compound binds to phosphatidylserine, which is externalized in the cell membrane following apoptosis. Because apoptosis mediates regression of both tumor cells and angiogenic vascular endothelial cells, annexin V imaging may provide insight into the therapeutic response to cancer therapy. Labeling annexin V with ^{18}F may permit imaging by PET and substantially improve the quality of scans [41].

Nitrogen-13 ammonia is used as a blood flow tracer in a similar manner to ^{201}Tl, which has been used for perfuse cardiac imaging for 3 decades. ^{15}O-labeled water has also been used for this purpose, although not as commonly as ammonia. The myocardial oxygen consumption is often measured with ^{11}C-labeled acetate. Fatty acid metabolism is often measured with ^{11}C-labeled palmitate.

A variety of PET radiotracers for application in neuroscience have been introduced. These radiotracers are used for studying dopamine, serotonin, opioid, norepinephrine and the cholinergic system and for imaging β-amyloid. ^{18}F-labeled dopa is expected to be used for the diagnosis of Parkinson's disease and will be widely adopted for this purpose. There are several amyloid imaging agents that may become the test of choice in the early diagnosis of Alzheimer's disease [112].

Dopamine plays an important role in regulating movement, cognition, motivation, addiction and reinforcement. Dopamine does not pass the blood-brain barrier. Thus to study brain dopamine metabolism, the labeled derivative of L-dopa or tyrosine that can transport into the brain then converted to dopamine can be used. These radiotracers are 6-[^{18}F]fluoro-dopa, 6-[^{18}F]fluoro-L-*m*-tyrosine and [^{11}C]-L-dopa. There are also dopamine receptor radioligands, dopamine transporter and vesicular monoamine transporter radioligands [105].

Abnormalities in the brain serotonin system have been implicated in various neuropsychiatry disorders including anxiety, depression, eating disorders, sleep disorders and suicide. 5-HT_{1A} and 5-HT_{1B} receptor radioligands and serotonin transporter radioligands have been developed for PET. Abnormalities in norepinephrine have been implicated in cardiac failure, in major depression and in Alzheimer's disease. [^{11}C]methylreboxetine([^{11}C]MeNER) and [^{18}F]MeNER have shown promise as agents in animals. Opioid receptors (μ, δ, κ) mediate the effects of endogenous and exogenous opioids, including respiratory depression, analgesia, sedation, and reward. Radiotracers for the brain opioid system such as [^{11}C]carfentanil, [^{11}C]diprenorphine, [^{11}C]buprenorphine, 6-*O*-[^{18}F]fluoroethyldiprenorphine, [^{11}C]GR89696, and [^{11}C]naltrindole have been used in humans. Benzodiazepine drugs have potent anxiolytic, anticonvulsant, and hypnotic properties. Several benzodiazepine receptor radioligands have been developed such as [^{11}C]RO15 – 1788 ([^{11}C]flumazenil) and [^{11}C]PK11195.

Acetylcholine has been implicated in learning, memory, and Alzheimer's disease. Many PET radiotracers are being used to investigate acetylcholine. These include muscarine-cholinergic receptor radioligands such as [^{11}C]scopolamine and nicotinic-cholinergic receptor radioligands such as [^{18}F]NIDA52189. Acetylcholinesterases include ([^{11}C]physostigmine, ^{11}C-PHY), and vesicular acetylcholine transporter radiotracers include [^{18}F]fluorobenzyltrozamicol ([^{18}F]FBT) [105].

References

1. Pauwels EK, Sturm EJ, Bombardieri E, Cleton FJ, Stokkel MP (2000) Positron-emission tomography with [^{18}F]fluorodeoxy glucose, part 1. Biochemical uptake mechanism and its implication for clinical studies. J Cancer Res Clin Oncol 126:549 – 559
2. Couturier O, Luxen A, Chatal JF, Vuillez JP, Rigo P, Hustinx R (2004) Fluorinated tracers for imaging cancer with positron emission tomography. Eur J Nucl Med Mol Imaging 31:1182 – 1206
3. Guyton AC, Hall JE (2000) Text book of medical physiology, 10th edn, Chap 4 [40 – 51]. WB Saunders, Philadelphia

4. Sviderskaya EV, Jazrawi E, Baldwin SA, Widnell CC, Pasternak CA (1996) Cellular stress causes accumulation of the glucose transporter at the surface of cells independently of their insulin sensitivity. J Membr Biol 149:133 – 140
5. Theorens B, Sarkar HK, Kaback HR, Lodish HF (1988) Cloning and functional expression in bacteria of a novel glucose transporter present in liver, intestine, kidney, and beta-pancreatic islet cells. Cell 55:281 – 290
6. Maher F (1995) Immunolocalization of GLUT1 and GLUT3 glucose transporters in primary cultured neurons and glia. J Neurosci Res 42:459 – 469
7. Rea S, James DE (1997) Moving GLUT4: the biogenesis and trafficking of GLUT4 storage vesicles. Diabetes 46:1667 – 1677
8. Kayano T, Burant CF, Fukumoto H, Gould GW, Fan YS, Eddy RL, Byers MG, Shows TB, Seino S, Bell GI (1990) Human facilitative glucose transporters. Isolation, functional characterization, and gene localization of cDNAs encoding an isoform (GLUT5) expressed in small intestine, kidney, muscle, and adipose tissue and an unusual glucose transporter pseudogene-like sequence (GLUT6). J Biol Chem 265:13276 – 13282
9. Kanai Y, Lee WS, You G, Brown D, Hediger MA (1994) The human kidney low affinity Na^+/glucose cotransporter SGLT2. Delineation of the major renal reabsorptive mechanism for D-glucose. J Clin Invest 93:397 – 404
10. Alavi A, Reivich M (2002) The conception of FDG-PET imaging. Semin Nucl Med 32:2 – 5
11. Nabi HA, Zubeldia JM (2002) Clinical applications of ^{18}F-FDG in oncology. J Nucl Med Tech 30:3 – 9
12. Kostakoglu L, Goldsmith SJ (2003) ^{18}F-FDG PET evaluation of the response to therapy for lymphoma and for breast, lung and colorectal carcinoma. J Nucl Med 44: 224 – 239
13. Merrall NW, Plevin R, Gould GW (1993) Growth factor, mitogens, oncogenes and the regulation of glucose transport. Cell Signal 5:667 – 675
14. Flier JS, Mueckler MM, Usher P, Lodish HF (1987) Elevated levels of glucose transport and transporter messenger RNA are induced by ras or src oncogenes. Science 235:492 – 1495
15. Rempel A, Bannasch P, Mayer D (1994) Differences in expression and intracellular distribution of hexokinase isoenzymes in rat liver cells of different transformation stages. Biochem Biophys Acta 1219:660 – 668
16. Mathupala SP, Rempel A, Pedersen PL (1995) Glucose catabolism in cancer cells. Isolation, sequence, and activity of the promoter for type II hexokinase. J Biol Chem 270: 16:918 – 925
17. Clavo AC, Brown RS, Wahl RL (1995) Fluorodeoxyglucose up-take in human cancer cell lines is increased by hypoxia. J Nucl Med 36:1625 – 1632
18. Wang GL, Semenza GL (1995) Purification and characterization of hypoxia-inducible factor I. J Biol Chem 270: 1230 – 1237
19. Rajendran JG, Krohn KA (2005) Imaging hypoxia and angiogenesis in tumors. Radiol Clin Am 43:169 – 187
20. Alavi A, Kung JW, Zhuang H (2004) Implication of PET based molecular imaging on the current and future practice of medicine. Semin Nucl Med 34:56 – 69
21. Wahl RL (1999) Positron emission tomography in cancer patient management. Cancer J Sci Am 5:205 – 207
22. Bozzetti F, Gavazzi C, Mariani L, Crippa F (2004) Glucose-based total parenteral nutrition does not stimulate glucose uptake by human tumours. Clin Nutr 23:417 – 421
23. Torizuka T, Cavo AC, Wahl RL (1997) Effect of hyperglycemia on in vitro tumor uptake of tritiated FDG, thymidine, l-methionine and l-leucine. J Nucl Med 38:382 – 386
24. Shin L, Katz DS, Yung E (2004) Hypermetabolism on F-18 FDG PET of multiple pulmonary nodules resulting from bronchiolitis obliterans organizing pneumonia. Clin Nucl Med 29:654 – 656
25. Keyes JW Jr, Chen MY, Watson NE Jr, Greven KM, McGuirt WF, Williams DW (1997) FDG PET in head and neck cancer. Am J Roentgenol 169:1663 – 1669
26. Bury T, Dowlati A, Paulus P, Hustinx R, Radermecker M, Rigo P (1996) Staging of non-small cell lung cancer by whole-body fluorine-18 deoxyglucose positron emission tomography. Eur J Nucl Med 23:204 – 206
27. Albes JM, Lietzenmayer R, Schott U, Schulen E, Wehrmann M, Ziemer G (1999) Improvement of non-small-cell lung cancer staging by means of positron emission tomography. Thorac Cardiovasc Surg 47:42 – 47
28. Coleman RE (1999) PET in lung cancer. J Nucl Med 40: 814 – 820
29. Ilknur AK, Stokkel MP, Pauwels EK (2000) Positron emission tomography with 2-[^{18}F]fluoro-2-deoxy-D-glucose in oncology, part II. The clinical value in detecting and staging primary tumors. J Cancer Res Clin Oncol 126:560 – 574
30. Wahl RL (2001) Current status of PET in breast cancer imaging, staging, and therapy. Semin Roentgenol 36:250 – 260
31. Mankoff DA, Dunnwald LK, Gralow JR (2002) Blood flow and metabolism in locally advanced breast cancer (LABC): Relationship to response to therapy. J Nucl Med 43:500 – 509
32. Chander S, Zingas AP, Bloom DA, Zak IT, Joyrich RN, Getzen TM (2004) Positron emission tomography in primary thyroid lymphoma. Clin Nucl Med 29:572 – 573
33. Diehl M, Graichen S, Menzel C, Lindhorst E, Grunwald F (2003) F-18 FDG PET in insular thyroid cancer. Clin Nucl Med 28:728 – 731
34. Park CH, Lee EJ, Kim JK, Joo HJ, Jang JS (2002) Focal F-18 FDG uptake in a nontoxic autonomous thyroid nodule. J Nucl Med 27:136 – 137
35. Zhuang H, Duarte PS, Pourdehand M, Shnier D, Alavi A (2000) Exclusion of chronic osteomyelitis with F-18 fluorodeoxyglucose positron emission tomographic imaging. Clin Nucl Med 25:281 – 284
36. Schoder H, Larson SM, Yeung HW (2004) PET/CT in oncology: integration into clinical management of lymphoma, melanoma, and gastrointestinal malignancies. J Nucl Med 45:72S–81S
37. Bury T, Corhay JL, Duysinx B, Daenen F, Ghaye B, Barthelemy N, Rigo P, Bartsch P (1999) Value of FDG-PET in detecting residual or recurrent nonsmall cell lung cancer. Eur Respir J 14:1376 – 1380
38. Magnani P, Carretta A, Rizzo G, Fazio F, Vanzulli A, Lucignani G, Zannini P, Messa C, Landoni C, Gilardi MC, Del Maschio A (1999) FDG/PET and spiral CT image fusion for mediastinal lymph node assessment of non-small cell lung cancer patients. J Cardiovasc Surg 40:741 – 748
39. Marom EM, McAdams HP, Erasmus JJ, Goodman PC, Culhane DK, Coleman RE, Herndon JE, Patz EF Jr (1999) Staging non-small cell lung cancer with whole-body PET. Radiology 212:803 – 809
40. Gambhir SS, Czernin J, Schwimmer J, Silverman DH, Coleman RE, Phelps ME (2001) A tabulated summary of the FDG PET literature. J Nucl Med 42:S1–S93
41. Abdel-Nabi H, Doerr RJ, Lamonica DM, Cronin VR, Galantowicz PJ, Carbone GM, Spaulding MB (1998) Staging of primary colorectal carcinomas with fluorine-18 fluorodeoxyglucose whole-body PET: correlation with histopathologic and CT findings. Radiology 206:755 – 760
42. Phelps ME (2000) Positron emission tomography provides molecular imaging of biological processes. Proc Natl Acad Sci 97:9226 – 9233
43. Newberg A, Alavi A, Clark C (1998) The metabolic imaging severity rating scale (MISRS) in Alzheimer's disease: comparison with quantitative data. Eur J Nucl Med 25:1068

44. Newberg AB, Alavi A (2005) Role of PET imaging in the management of patients with central nervous system disorders. Radiol Clin Am 43:49 – 65
45. Alexander GE, Chen K, Pietrini P, Rapoport SI, Reiman EM (2002) Longitudinal PET evaluation of cerebral metabolic decline in dementia: a potential outcome measure in Alzheimer's disease treatment studies. Am J Psychiatry 159:738 – 745
46. Alavi A, Dann R, Chawluk J, Alavi J, Kushner M, Reivich M (1986) Positron emission tomography imaging of regional cerebral glucose metabolism. Semin Nucl Med 16:2 – 34
47. Salmon E, Sadzot B, Maquet P, Degueldre C, Lemaire C, Rigo P, Comar D, Franck G (1994) Differential diagnosis of Alzheimer's disease with PET. J Nucl Med 35:391 – 398
48. Van Heertum RL, Tikofsky RS (2003) Positron emission tomography and single photon emission computed tomography brain imaging in the evaluation of dementia. Semin Nucl Med 33:77 – 85
49. Alavi A, Lakhani P, Mavi A, Kung JW, Zhuang H (2004) PET: a revolution in medical imaging. Radiol Clin N Am 42:983 – 1001
50. Kuhl DE, Metter EJ, Riege WH (1984) Patterns of local cerebral glucose utilization determined in Parkinson's disease by the [^{18}F]fluorodeoxyglucose method. Ann Neurol 15:419 – 424
51. Newberg AB, Alavi A, Berlin J, Mozley PD, O'Connor M, Sperling M (2000) Ipsilateral and contralateral thalamic hypometabolism as a predictor of outcome after temporal lobectomy for seizures. J Nucl Med 41(12):1964 – 1968
52. Engle J Jr, Kuhl DE, Phelps ME, Rausch R, Nuwer M (1983) Local cerebral metabolism during partial seizures. Neurology 33:400 – 413
53. Theodore WH, Newmark ME, Sato S, Brooks R, Patronas N, De La Paz R, DiChiro G, Kessler RM, Margolin R, Manning RG, et al. (1983) [^{18}F]flurodeoxyglucose positron emission tomography in refractory complex partial seizures. Am Neurol 14:429 – 437
54. Barrington SE, Koutroumanidis M, Agathonikou A, Marsden PK, Binnie CD, Polkey CE, Maisey MN, Panayiotopoulos CP (1998) Clinical value of "ictal" FDG-positron emission tomography and the routine use of simultaneous scalp EEG studies in patients with partial epilepsies. Epilepsia 39:753 – 766
55. Gaillard WD, Kopylev L, Weinstein S, Conry J, Pearl PL, Spanaki MV, Fazilat S, Venzina LG, Dubovsky E, Theodore WH (2002) Low incidence of abnormal (18)FDG-PET in children with new-onset partial epilepsy: a prospective study. Neurology 58:717 – 722
56. Ollenberger GP, Pyrne AJ, Berlangieri SU, Rowe CC, Pathmaraj K, Reutens DC, Berkovic SF, et al (2005) Assessment of the role of FDG PET in the diagnosis and management of children with refractory epilepsy. Eur J Nucl Med 32:1311 – 1316
57. Alavi A, Newberg AB (1996) Metabolic consequences of acute brain trauma: is there a role for PET? J Nucl Med 37:1170 – 1172
58. Newberg AB, Alavi A (2003) Neuroimaging in patients with head injury. Semin Nucl Med 33:136 – 147
59. Mazziotta JC, Phelps ME, Pahl JJ, Huang SC, Baxter LR, Riege WH, Hoffman JM, Kuhl DE, Lanto AB, Wapenski JA, et al (1987) Reduced cerebral glucose metabolism in asymptomatic subjects at risk for Huntington's disease determined by ^{18}FDG and computed tomography scan. N Engl J Med 316:357 – 362
60. Kuhl DE, Phelps ME, Markham CH, Metter EJ, Riege WH, Winter J (1982) Cerebral metabolism and atrophy in Huntington's disease determined by ^{18}FDG and computed tomographic scan. Ann Neurol 12:425 – 434
61. Lehrer DS, Christian BT, Mantil J, Murray AC, Buchsbaum BR, Oakes TR, Byne W, Kemether EM, Buchsbaum MS (2005) Thalamic and prefrontal FDG uptake in never medicated patients with schizophrenia. Am Psychiatry 162:931 – 938
62. Mitelman SA, Byne W, Kemether EM, Hazlett EA, Buchsbaum MS (2006) Correlations between volumes of the pulvinar, centromedian, and mediodorsal nuclei and cortical Brodmann's areas in schizophrenia. Neurosci Lett 9; 392:16 – 21
63. Fumal A, Laureys S, Di Clemente L, Boly M, Bohotin V, Vandenheede M, Coppola G, Salmon E, Kupers R, Schoenen J (2005) Orbitofrontal cortex involvement in chronic analgesic-overuse headache evolving from episodic migraine. Brain 5 (ahead of print)
64. Newberg A, Cotter A, Udeshi M, Brinkman F, Glosser G, Alavi A, Clark C (2003) Brain metabolism in the cerebellum and visual cortex correlates with neuropsychological testing in patients with Alzheimer's disease. Nucl Med Commun 24:785 – 790
65. Silverman DH, Small GW, Chang CY, Lu CS, Kung De Aburto MA, Chen W, Czernin J, et al (2001) Positron emission tomography in evaluation of dementia: Regional brain metabolism and long-term outcome. JAMA 286:2120 – 2127
66. Lee BY, Newberg AB, Liebeskind DS, Kung J, Alavi A (2004) FDG-PET findings in patients with suspected encephalitis. Clin Nucl Med 29:620 – 625
67. Grover-McKay M, Schwaiger M, Krivokapich J, Perloff JK, Phelps ME, Schelbert HR (1989) Regional myocardial blood flow and metabolism at rest in mildly symptomatic patients with hypertrophic cardiomyopathy. J Am Coll Cardiol 13:317 – 324
68. Araujo LI, Camici P, Spinks TJ, Jones T, Maseri A (1988) Abnormalities in myocardial metabolism in patients with unstable angina as assessed by positron emission tomography. Cardiovasc Drugs Ther 2:41 – 46
69. Schwaiger M, Brunken R, Grover-McKay M, Krivokapich J, Child J, Tillisch JH, Phelps ME, Schelbert HR (1986) Regional myocardial metabolism in patients with acute myocardial infarction assessed by positron emission tomography. J Am Coll Cardiol 8:800 – 808
70. Maddahi J, Schelbert H, Brunken R, Di Carli M (1994) Role of thallium-201 and PET imaging in evaluation of myocardial viability and management of patients with coronary artery disease and left ventricular dysfunction. J Nucl Med 35:707 – 715
71. Camici P, Ferrannini E, Opie L (1989) Myocardial metabolism in ischemic heart disease: basic principles and application to imaging by positron emission tomography. Progr Cardiol Dis 32:217 – 238
72. Knuuti J, Scelbert HR, Bax JJ (2002) The need for standardisation of cardiac FDG PET imaging in the evaluation of myocardial viability in patients with chronic ischaemic left ventricular dysfunction. Eur J Nucl Med 29:1257 – 1266
73. Wijns W, Vatner SF, Camici PG (1998) Hibernating myocardium. N Engl J Med 339:137 – 181
74. Di Carli MF (2004) Advances in positron emission tomography. J Nucl Cardiol 11:719 – 732
75. Musatti L, Maggi E, Moro E, Valzelli G, Tamassia V (1998) Bioavailability and pharmacokinetics of Acipimox, a new antilipolytic and hypolipidaemic agent. J Int Med Res 9: 381 – 386
76. Rechavia E (1999) Images in cardiovascular medicine. Myocardial [^{18}F]fluorodeoxyglucose uptake after heterotopic cardiac transplantation assessed by positron emission tomography. Circulation 99:3322
77. Bolli R (1996) The early and late phases of preconditioning against myocardial stunning and the essential role of oxy-

radicals in the late phase: an overview. Basic Res Cardiol 91:57 – 63
78. Perrone-Filardi P, Bacharach SL, Dilsizian V, Marin-Neto JA, Maurea S, Arrighi JA, Bonow RO (1994) Clinical significance of regional myocardial glucose uptake in regions with normal blood flow in patients with chronic coronary artery disease. J Am Coll Cardiol 23:608 – 616
79. Osamichi S, Kouji K, Yoshimaro I, Tadashi U, Hiroichi T, Seiyu K, Shinji O, Noboru T (2004) Myocardial glucose metabolism assessed by positron emission tomography and the histopathologic findings of microvessels in syndrome X. Circ J 68:220 – 226
80. He ZX, Shi RF, Wu YJ, Tian YQ, Liu XJ, Wang SW, Shen R, Qin XW, Gao RL, Narula J, Jain D (2003) Direct imaging of exercise-induced myocardial ischemia with fluorine-18-labeled deoxyglucose and Tc-99m-sestamibi in coronary artery disease. Circulation 108:1208
81. Bax JJ, Valkema R, Visser FC, Poldermans D, Cornel JH, van Lingen A, Krenning EP, Rambaldi R, Roelandt JR, Visser CA, Fioretti PM (1997) Detection of myocardial viability with F-18-fluorodeoxyglucose and single photon emission computed tomography. G Ital Cardiol 27:1181 – 1186
82. Schelbert HR (2002) ^{18}F-deoxyglucose and the assessment of myocardial viability. Semin Nucl Med 32:60 – 69
83. Akinboboye OO, Idris O, Cannon PJ, Bergmann SR (1999) Usefulness of positron emission tomography in defining myocardial viability in patients referred for cardiac transplantation. Am J Cardiol 83:1271 – 1274, A9
84. Dreyfus GD, Duboc D, Blasco A, Vigoni F, Dubois C, Brodaty D, de Lentdecker P, Bachet J, Goudot B, Guilmet D (1994) Myocardial viability assessment in ischemic cardiomyopathy: benefits of coronary revascularization. Ann Thorac Surg 57:1402 – 1407
85. Yun M, Jang S, Cucchiara A, Newberg AB, Alavi A (2002) ^{18}F FDG uptake in the large arteries: A correlation study with the atherogenic risk factors. Semin Nucl Med 32:70 – 76
86. Vallabhajosula S, Machac J, Knesaurek K (1996) Imaging atherosclerotic macrophage density by positron emission tomography using F-18-fluorodeoxyglucose. J Nucl Med 37:38
87. Kato H, Miyazaki T, Nakajima M, Takita J, Kimura H, Faried A, Sohda M, Fukai Y, Masuda N, Fukuchi M, Manda R, Ojima H, Tsukada K, Kuwano H, Oriuchi N, Endo K (2005) Comparison between whole-body positron emission tomography and bone scintigraphy in evaluating bony metastases of esophageal carcinomas. Anticancer Res 25: 4439 – 4444
88. Yun M, Kim W, Adam L, Alnafisi N, Herman C, Alavi A (2001) F-18 FDG uptake in a patient with psoriatic arthritis: imaging correlation with patient symptoms. J Nucl Med 26:692 – 693
89. Termaat MF, Raijmakers PG, Scholten HJ, Bakker FC, Patka P, Haarman HJ (2005) The accuracy of diagnostic imaging for the assessment of chronic osteomyelitis: a systematic review and meta-analysis. J Bone Joint Surg Am 87: 2464 – 2471
90. Zhuang H, Alavi A (2002) 18-Fluorodeoxyglucose positron emission tomographic imaging in the detection and monitoring of infection and inflammation. Semin Nucl Med 32:47 – 59
91. Zhuang H, Duarte PS, Pourdehnad M, Maes A, Van Acker F, Shnier D, Garino JP, Fitzgerald RH, Alavi A (2001) The promising role of ^{18}F-FDG PET in detecting infected lower limb prosthesis implants. J Nucl Med 42:44 – 48
92. Bakheet SM, Saleem M, Powe J, Al-Amro A, Larsson SG, Mahassin Z (2000) F-18 fluorodeoxyglucose chest uptake in lung inflammation and infection. Clin Nucl Med 25(4):273 – 278
93. Vanquickenborne B, Maes A, Nuyts J, Van Acker F, Stuyck J, Mulier M, Verbruggen A, Mortelmans L (2003) The value of (18)FDG-PET for the detection of infected hip prosthesis. Eur J Nucl Med Mol Imaging 30:705 – 715
94. Blockmans D, Knockaert D, Maes A, De Caestecker J, Stroobants S, Bobbaers H, Mortelmans L (2001) Clinical value of [(18)F]fluoro-deoxyglucose positron emission tomography for patients with fever of unknown origin. Clin Infect Dis 32:191 – 196
95. Neurath MF, Vehling D, Schunk K, Holtmann M, Brockmann H, Helisch A, Orth T, Schreckenberger M, Galle PR, Bartenstein P (2002) Noninvasive assessment of Crohn's disease activity: A comparison of ^{18}F fluorodeoxyglucose positron emission tomography, hydromagnetic resonance imaging and granulocyte scintigraphy with labeled antibodies. Am J Gastroenterol 97:1978 – 1985
96. Ludwig V, Frdice S, Lamar R, Martin WH, Delbeke D (2003) Unsuspected skeletal sarcoidosis mimicking metastatic disease on FDG positron emission tomography and bone scintigraphy. Clin Nucl Med 28:176 – 179
97. Poisson RP, Schoenberg OI, Fischman A, Rubin R, Simon LS, Rosenthal D, Palmer WE (1995) Use of magnetic resonance imaging and positron emission tomography in the assessment of synovial volume and glucose metabolism in patients with rheumatoid arthritis. Arthritis Rheum 38:819 – 825
98. Beckers C, Ribbens C, Andre B, Marcelis S, Kaye O, Mathy L, Kaiser MJ, Hustinx R, Foidart J, Malaise MG (2004) Assessment of disease activity in rheumatoid arthritis with (18)F-FDG PET. J Nucl Med 45:956 – 964
99. Derdelinckx I, Maes A, Bogaert J, Mortelmans L, Blockmans D (2000) Positron emission tomography scan in the diagnosis and follow-up of aortitis of the thoracic aorta. Acta Cardiol 55:193 – 195
100. Fletcher TM, Espinola D (2004) Positron emission tomography in the diagnosis of giant cell arteritis. Clin Nucl Med 29:617 – 619
101. Suzuki S, Toyota T, Suzuki H, Goto Y (1984) Partial purification from human mononuclear cells and placental plasma membranes of an insulin mediator which stimulates pyruvate dehydrogenase and suppresses glucose-6-phosphate. Arch Biochem Biophys 235:418 – 426
102. Nelson CA, Wang JQ, Leav I, Crane PD (1996) The interaction among glucose transport, hexokinase and glucose 6-phosphate with respect to ^{3}H-2-deoxyglucose retention in murine tumor models. Nucl Med Biol 23:533 – 541
103. Schlyer DJ (2004) PET tracers and radiochemistry. Ann Acad Med Singapore 33:146 – 154
104. Kong XB, Zhu QY, Vidal PM Watanabe KA, Polsky B, Armstrong D, Ostrander M, Lang SA Jr, Muchmore E, Chou TC (1992) Comparisons of anti-human immunodeficiency virus activities, cellular transport, and plasma and intracellular pharmacokinetics of 3'-fluoro-3'-deoxythymidine and 3'-azido-3'-deoxythymidine. Antimicrob Agents Chemother 36:808 – 818
105. Shiue CY, Welch MJ (2004) Update on PET radiopharmaceuticals: life beyond fluorodeoxyglucose. Radiol Clin Am 42:1033 – 1053
106. Cobben DC, Elsinga PH, Suurmeijer AJ, Vaalburg W, Maas B, Jager PL, Hoekstra HJ (2004) Detection and grading of soft tissue sarcomas of the extremities with (18)F-3'-fluoro-3'-deoxy-l-thymidine. Clin Cancer Res 10:1685 – 1690
107. Nakagami K, Uchida T, Ohwada S, Koibuchi Y, Suda Y, Sekine T, Morishita Y (1999) Increased choline kinase activity and elevated phosphocholine levels in human colon cancer. Jpn J Cancer Res 90:419 – 424
108. Hara T (2001) ^{18}F-fluorocholine: a new oncologic PET tracer. J Nucl Med 12:1815 – 1817

109. Kumar R, Zhuang H, Alavi A (2005) PET in the management of urologic malignancies. Radiol Clin N Am 42: 1141 – 1153
110. Dehdashti F, Mintun MA, Lewis JS, Bradley J, Govindan R, Laforest R, Welch MJ, Siegel BA (2003) In vivo assessment of tumor hypoxia in lung cancer with ^{60}Cu-ATSM. Eur J Nucl Med 30:844 – 850
111. Blankenberg FG, Strauss HW (2002) Nuclear medicine applications in molecular imaging. J Magn Reson Imaging 16:352 – 361
112. Alavi A (2004) PET imaging I. Radiol Clin N Am 42:xi–xiii

Inflammation

4

Abdelhamid H. Elgazzar, Magda Elmonayeri

4.1 Introduction

Inflammation was described as early as 3000 BC in an Egyptian papyrus [1] and is still a common problem despite continuous advancements in prevention and treatment methods. The delineation of the site and extent of inflammation is crucial to the clinical management of infection and for monitoring the response to therapy [2].

This issue is relevant to nuclear medicine since physiologic along with morphologic imaging has an important role in achieving this goal.

Inflammation is a complex tissue reaction to injury. Injury may be caused not only by living microbes, i.e., bacteria, viruses, or fungi, leading to infection, but also by injurious chemical, physical, immunological, or radiation agents:

- Physical agents
  - Trauma
  - Heat
- Chemical agents
  - Chemotherapy
  - Industrial accidents
- Immunological agents
  - Antigen-antibody reactions
- Radiation
  - Radiation therapy
  - Nontherapeutic radiation exposure

Inflammation is fundamentally a protective reaction against the cause of cell injury as well as the consequence of such injury. However, inflammation is potentially harmful and may even be life threatening. Since most of the essential components of the inflammatory process are found in the circulation, inflammation occurs only in vascularized tissue. Inflammation is generally considered a nonspecific response, because it happens in the same way regardless of the stimulus and the number of exposures to the stimulus [2]. This is different from the immune system, which has memory, and the antigens are specific and induce a specific response.

4.2 Classification of Inflammation

Inflammation may be classified as acute or chronic. Acute inflammation is the immediate or early response to injury and is of relatively short duration. It lasts for minutes, hours, or at most a few days. Chronic inflammation, on the other hand, is of longer duration and may last from weeks to years [3]. The distinction between acute and chronic inflammation, however, depends not only on the duration of the process but also on other pathological and clinical features.

4.3 General Pathophysiological Changes of Inflammation

4.3.1 Local Pathophysiological Changes of Inflammation

4.3.1.1 Acute Inflammation

Acute inflammation continues only until the threat to the host has been eliminated, which usually takes 8 – 10 days, although this is variable. Inflammation is generally considered to be chronic when it persists for longer than 2 weeks [2]. Many regional and systemic changes accompany acute inflammation, are mediated by certain chemicals produced endogenously called chemical mediators and are behind the spread of the acute inflammatory response following injury to a small area of tissue into uninjured sites. These chemical mediators include mediators released from cells such as histamine and prostaglandins and others in plasma which are released by the systems contained in the plasma; these are the four enzymatic cascade systems, the complement system, the kinins, the coagulation factors and the fibrinolytic system, which produce several inflammatory mediators [4 – 6]. Table 4.1 summarizes the main chemical mediators of inflammation.

Acute inflammation is characterized by the following major regional components:

4.3.1.1.1 Local Vascular Changes

1. Vasodilation following transient vasoconstriction is one of the most important changes that accompany acute inflammation and it persists until the end of the process. It involves first the arterioles and then results in the opening of new capillary beds in the area.
2. Increased vascular permeability due to:
   - Contraction of endothelial cells with widening of intercellular gaps
   - Direct endothelial injury, resulting in endothelial cell necrosis and detachment
   - Leukocyte-mediated endothelial injury: Leukocytes adhere to the endothelium, which becomes activated, thereby releasing toxic oxygen species and proteolytic enzymes and causing endothelial injury.
   - Angiogenesis: With inflammation, endothelial cells may proliferate and form new capillaries and venular beds (angiogenesis). These capillary sprouts remain leaky until endothelial cells differentiate.

Table 4.1. Chemical mediators of inflammation

Mediator	Characteristics and role in inflammation
A. Cell factors	
Histamine	Stored in mast cells, basophil and eosinophil leukocytes, and platelets. Release from sites of storage is stimulated by complement components C3a and C5a, and by lysosomal proteins released from neutrophils. Responsible for vasodilatation and the immediate phase of increased vascular permeability
Lysosomal compound	Released from neutrophils and includes cationic proteins, which may increase vascular permeability, and neutral proteases, which may activate complement
Prostaglandins	Long-chain fatty acids derived from arachidonic acid and synthesized by many cell types. Some prostaglandins potentiate the increase in vascular permeability caused by other compounds
Leukotrienes	Synthesized from arachidonic acid, especially in neutrophils, and have vasoactive properties
5-Hydroxytryptamine (serotonin)	A potent vasoconstrictor present in high concentrations in mast cells and platelets
Lymphokines	Released by lymphocytes and may have vasoactive or chemotactic effects
B. Plasma factors	
Products of complement activation:	
C5a	Chemotactic for neutrophils; increases vascular permeability; releases histamine from mast cells.
C3a	Similar to but less active than C5a.
C567	Chemotactic for neutrophils.
C56789	Cytolytic activity.
C4b, 2a, 3b	Facilitates phagocytosis of bacteria by macrophages (opsonization of bacteria)
Kinin system	Bradykinin included in the system is the most important vascular permeability factor, also a mediator for pain which is a major feature of acute inflammation
Coagulation factors	Responsible for the conversion of soluble fibrinogen into fibrin, a major component of the acute inflammatory exudate
Fibrinolytic system	Plasmin included in the fibrinolytic system is responsible for the lysis of fibrin into fibrin degradation products, which have a local effect on vascular permeability

3. Stasis (slowing of circulation): Increased permeability with extravasation of fluid into the extravascular spaces results in concentration of red blood cells in the small vessels and increased viscosity of blood, with slowing of circulation in the local vessels. Figures 4.1 and 4.2 illustrate the main vascular changes.

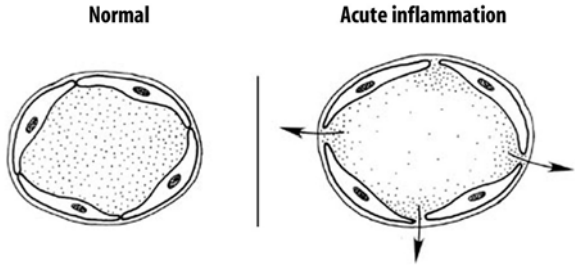

Fig. 4.1. Vasodilation of vessels and opening of the intercellular gaps in inflammation

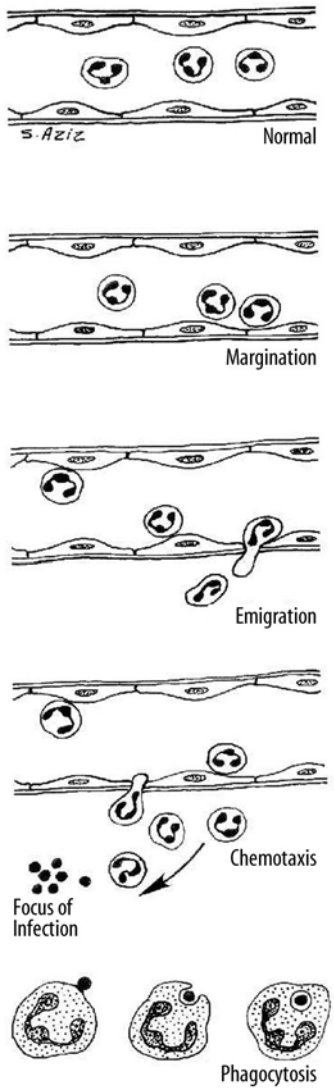

Fig. 4.2. Sequence of cellular changes that accompany inflammation

4.3.1.1.2 Formation of Exudate

Increased permeability of the microvasculature, along with the other changes described, leads to leakage with formation of "exudate", an inflammatory extravascular fluid with a high protein content, much cellular debris, and a specific gravity above 1.020. This is the hallmark of acute inflammation, which may also be called exudative inflammation. It indicates significant alteration in the normal permeability of small blood vessels in the region of injury.

The two components of exudate, fluid and protein, serve good purposes. Fluid increase helps to dilute the toxins. Protein increase includes globulins that provide protective antibodies, while fibrin helps to limit the spread of bacteria and promotes healing. Exudate varies in composition. In early or mild inflammation it may be watery (serous exudate) with low plasma protein content and few leukocytes. In more advanced inflammation, the exudate becomes thick and clotted (fibrinous exudate). When large numbers of leukocytes accumulate (Fig. 4.3), the exudate consists of pus and is called suppurative, while if it contains erythrocytes due to bleeding it is referred to as hemorrhagic. Pus, accordingly, is a variant of exudate that is particularly rich in leukocytes, mostly neutrophils and parenchymal cell debris.

Exudate should be differentiated from "transudate", which is a fluid with low protein concentration and a specific gravity of less than 1.012. Transudation is associated with normal endothelial permeability [3, 5].

4.3.1.1.3 Local Cellular Events

1. Margination
   After stasis develops, leukocytes will be peripherally oriented along the vascular endothelium, a process called leukocytic margination (Fig. 4.2).
2. Diapedesis (emigration)
   Leukocytes emigrate from the microcirculation and accumulate at the site of injury.
3. Chemotaxis
   Once outside the blood vessel, the cells migrate at varying rates of speed in interstitial tissue towards a chemotactic stimulus in the inflammatory focus. Through chemoreceptors at multiple locations on their plasma membranes, the cells are able to detect where the highest concentrations of chemotactic factors are and to migrate in their direction. Granulocytes, including the eosinophils, basophils, and some lymphocytes, respond to such stimuli and aggregate at the site of inflammation. The primary chemotactic factors include bacterial products, complement components C5a and C3a, kalli-

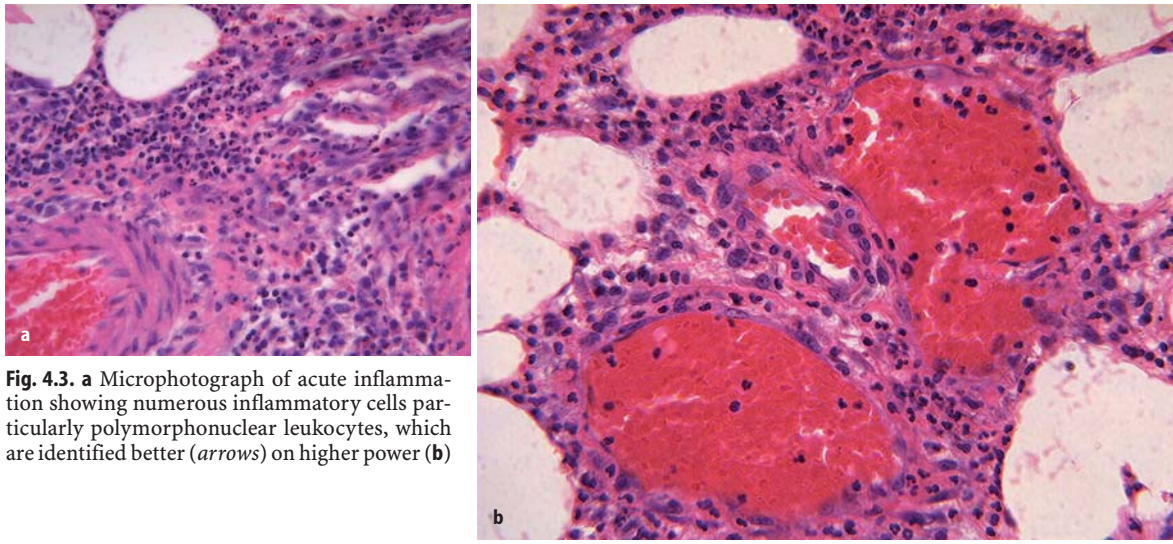

Fig. 4.3. a Microphotograph of acute inflammation showing numerous inflammatory cells particularly polymorphonuclear leukocytes, which are identified better (*arrows*) on higher power (**b**)

krein and plasminogen activators, products of fibrin degradation, prostaglandins, and fibrinopeptides. Histamine is not a chemotactic factor but facilitates the process. Some bacterial toxins, particularly from gram-negative bacteria and streptococcal streptolysins, inhibit neutrophil chemotaxis [2, 3, 5].

4. Phagocytosis
   This defense mechanism is particularly important in bacterial infections. The polymorphonuclear leukocytes and macrophages ingest debris and foreign particles.

4.3.1.2 Local Sequelae of Acute Inflammation

Acute inflammation has several possible local sequelae. These include resolution, suppuration (formation of pus), organization and progression to chronic inflammation. Resolution means complete restoration of tissues to normal. Organization of tissues is their replacement by granulation tissue with formation of large amounts of fibrin, new capillaries growing into fibrin, macrophages migrating into the zone and proliferation of fibroblasts resulting in fibrosis and the consequent organization of exudate.

4.3.1.3 Chronic Inflammation

Acute inflammation may progress to a chronic form characterized by reduction of the number of polymorphonuclear leukocytes but proliferation of fibroblasts with collagen production. Commonly, chronic inflammation may be primary with no preceding acute inflammatory reaction. Chronic inflammation, whether following acute inflammation or not, is characterized by a proliferative (fibroblastic) rather than an exudative response with predominantly mononuclear cell infiltration (macrophages, lymphocytes, and plasma cells) (Fig. 4.4). Vascular permeability is also abnormal, but to a lesser extent than in acute inflammation with formation of new capillaries.

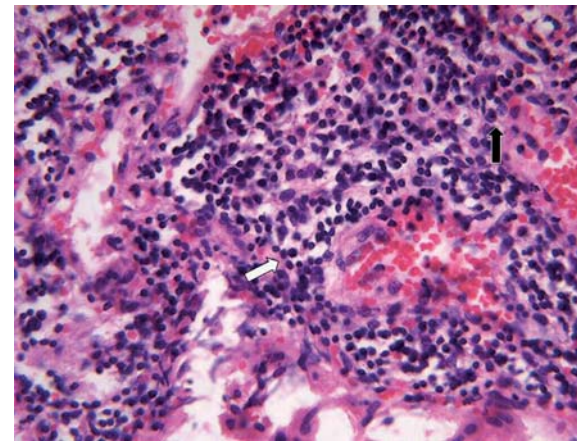

Fig. 4.4. Microphotograph of chronic inflammation illustrating the different types of inflammatory cells, the mononuclear cells including lymphocytes (*arrow*) and plasma cells (*open arrow*)

4.3.1.4 Abscess Formation

Abscess is defined as a collection of pus in tissues, organs, or confined spaces, usually caused by bacterial infection. The abscess formation starts by a phase of cellulitis, characterized by hyperemia, leukocytosis, and edema, without cellular necrosis or suppuration. This stage is also called phlegmon. It may be followed by necrosis, liquefaction and formation of pyogenic membrane surrounding the pus, which results in abscess formation that can be present with both acute and chronic inflammation.

4.3.2 Systemic Pathophysiological Changes of Inflammation

Three major systemic changes are associated with inflammation: leukocytosis, fever, and an increase in plasma proteins. Leukocytosis is an increased production of leukocytes due to stimulation by several products of inflammation such as complement component C3a and colony-stimulating factors. A febrile response is due to the pyrogens. The increase in plasma proteins is due to stimulation of the liver by some products of inflammation, leading to increased synthesis of certain proteins referred to as acute-phase reactants which include C-reactive protein, fibrinogen- and haptoglobin and are anti-inflammatory [2].

4.3.3 Pathophysiological Changes of Healing

Healing of tissue after injury is closely linked to inflammation since it starts by acute inflammation. Healing may lead to restoration of normal structure and function of the injured tissue (resolution) or to the formation of a scar consisting of collagen (repair) when resolution cannot be achieved because the tissue is severely injured or cannot regenerate.

In either case, acute inflammation occurs first and for this reason is considered the defensive phase of healing. Healing (resolution and repair) occurs in two overlapping phases, reconstruction and maturation. The reconstructive phase starts 3 – 4 days after injury, continues for approximately 2 weeks, and is characterized by fibroblasts followed by collagen synthesis. The maturation phase is characterized by cell differentiation, scar formation and remodeling of the scar; it begins several weeks after injury and may take up to 2 years to complete.

4.4 Pathophysiology of Major Soft Tissue Inflammation

4.4.1 Abdominal Inflammation

An abdominal abscess may be formed in an abdominal organ or within the abdomen outside the organs. There are several types of abdominal infection: abscess, cellulitis (phlegmon), i.e., early inflammation of the soft tissue prior to or without formation of an abscess, and peritonitis. Abscesses fall into three categories:

1. Intraperitoneal abscess
   - Subphrenic
   - Midabdominal
   - Right lower quadrant
   - Left lower quadrant
   - Pelvic abscess
2. Retroperitoneal abscess
   - Anterior retroperitoneal
   - Perinephric
3. Visceral abscess
   - Hepatic
   - Pancreatic
   - Splenic

The organisms causing abscesses may reach the tissue by direct implantation such as penetrating trauma, and may spread from contiguous infection, through hematogenous or lymphatic routes from a distant site, or through migration of resistant flora into an adjacent, normally sterile area such as in perforation of an abdominal viscus.

Factors predisposing to abscess formation include impaired host defense mechanisms, trauma/surgery, obstruction of urinary, biliary, or respiratory passages, foreign bodies, chemical or immunological irritation, and ischemia. Abdominal surgery (particularly of the colon, appendix, and biliary tree) and trauma are the most common; less common are appendicitis, diverticulitis, and pelvic inflammatory disease. The formation of fibrin in the abdominal cavity is a common pathophysiological pathway for abdominal abscess formation due to diminished fibrin degradation. Hyaluronan-based agents were found to reduce adhesion formation after surgery and to reduce abscess formation in experimental peritonitis. Possible mechanisms of action of hyaluronan include modulation of the inflammatory response and enhanced fibrinolysis [7]. Low pH, large bacterial inocula, poor perfusion, the presence of hemoglobin, and large amounts of fibrin (which impedes antibiotic penetration) make the abscess a cloistered environment that is penetrated poorly by many antimicrobial therapies. Therefore, management of these infections requires prompt recognition, early localization, and effective drainage, as well as appropriate antimicrobial use. Once the diagnosis is made and the abscess is localized, treatment should begin promptly. Percutaneous or open surgical drainage should be used. Broad-spectrum antibiotics should be given until culture and sensitivity data are obtained. Localization is crucial since for example percutaneous drainage is inappropriate for abscesses in certain locations such as the posterior subphrenic space or in the porta hepatis [8]. In the liver, abscesses occur in the right lobe in approximately 95% of cases, and in 70% of cases the liver abscesses are solitary [9].

Accumulation of leukocytes in the abscess is the pathophysiological basis for using labeled white blood cells for abscess imaging. In the acute phase migration of leukocytes is vigorous. Later, the migration rate slows and the cell type changes from predominantly

neutrophils to mononuclear cells (lymphocytes, plasma cells, and macrophages). This pathophysiological change associated with the chronic state explains the better diagnostic accuracy of labeled leukocyte scans in acute as opposed to chronic abscesses.

Inflammatory bowel disease (IBD) is an idiopathic disease, probably involving an immune reaction of the body to its own intestinal tract. The two major types of IBD are ulcerative colitis (UC) and Crohn's disease (CD). Crohn's disease is also referred to as regional enteritis, terminal ileitis, or granulomatous ileocolitis. IBD is a disease of the industrialized nations and is observed most commonly in northern Europe and North America. Incidence among whites is approximately 4 times that of other races, slightly greater in females and higher in Ashkenazi Jews (those who have immigrated from northern Europe) than in other groups. The risk of developing UC is higher in nonsmokers and former smokers than in current smokers. Incidence peaks in the 2nd and 3rd decades of life. A second smaller peak occurs in patients aged 55 – 65 years. CD and UC can occur in childhood, although the incidence is much lower in children younger than 15 years with some differences in presentation and a more negative effect on quality of life in the younger age group [10].

The etiology of IBD is unsettled. Suspected factors include environmental, infectious, genetic, autoimmune, and host factors. A great deal of research has been performed to discover potential genes linked to IBD. One of the early linkages discovered was on chromosome 16 (*IBD1* gene), which led to the identification of the *NOD2* gene (now called *CARD15*) as the first gene clearly associated with IBD (as a susceptibility gene for Crohn's disease). Studies have also provided strong support for IBD susceptibility genes on chromosomes 5 (5q31) and 6 (6p21 and 19p). None of these mechanisms has been implicated as the primary cause, but they are postulated as potential causes. The lymphocyte population in persons with IBD is polyclonal, making the search for a single precipitating cause difficult. The trigger for the activation of the immune response has not been defined. However, possible triggers include a pathogenic organism (unidentified as yet), an immune response to an intraluminal antigen (e.g., cow's milk protein), or an autoimmune process with an immune response to an intraluminal antigen and a similar antigen present on intestinal epithelial cells. In any case, activation of the immune system leads to inflammation of the intestinal tract, both acute and chronic [11 – 19].

The pathophysiology of IBD is still incompletely understood and is under active investigation, but the common end pathway is inflammation of the mucosal lining of the intestinal tract, causing ulceration, edema, bleeding, and fluid and electrolyte loss. The inflammation of the intestinal mucosa includes both acute inflammation with neutrophilic infiltration and chronic inflammation with mononuclear cell infiltration (lymphocytic and histiocytic) [20].

In UC, inflammation always begins in the rectum, extends proximally a certain distance, and then abruptly stops. A clear demarcation exists between involved and uninvolved mucosa. The rectum is always involved in UC. UC remains confined to the rectum in approximately 25% of cases. In the remainder of cases, UC spreads proximally and contiguously. Pancolitis occurs in 10% of patients. UC primarily involves the mucosa and the submucosa, with formation of crypt abscesses and mucosal ulceration. The mucosa typically appears granular and friable. In more severe cases, pseudopolyps form, consisting of areas of hyperplastic growth with swollen mucosa surrounded by inflamed mucosa with shallow ulcers. In severe UC, inflammation and necrosis can in rare cases extend below the lamina propria to involve the submucosa and the circular and longitudinal muscles.

The small intestine is essentially not involved, except when the distal terminal ileum is inflamed in a superficial manner, referred to as backwash ileitis. Even with less than total colonic involvement, the disease is strikingly and uniformly continuous. As the disease becomes chronic, the colon becomes a rigid foreshortened tube that lacks its usual haustral markings, leading to the lead pipe appearance observed on barium enema. The skip areas (normal areas of the bowel interspersed with diseased areas) observed in CD of the colon do not occur in UC.

Crohn's disease, on the other hand, consists of segmental involvement by a nonspecific granulomatous inflammatory process. The most important pathologic feature is involvement of all layers of the bowel, not just the mucosa and the submucosa, as is characteristic of UC.

Furthermore, CD is discontinuous, with skip areas interspersed between one or more involved areas. Late in the disease, the mucosa develops a cobblestone appearance, which results from deep longitudinal ulcerations interlaced with intervening normal mucosa. The three major patterns of involvement in CD are (1) disease in the ileum and cecum, occurring in 40% of patients; (2) disease confined to the small intestine, occurring in 30% of patients; and (3) disease confined to the colon, occurring in 25% of patients. Rectal sparing is a typical but not constant feature of CD. However, anorectal complications (e.g., fistulas, abscesses) are common. Much less commonly, CD involves the more proximal parts of the GI tract, including the mouth, tongue, esophagus, stomach, and duodenum.

The incidence of gallstones and kidney stones is increased in CD because of malabsorption of fat and bile salts. Gallstones are formed because of increased cholesterol concentration in the bile, caused by a reduced bile salt pool. Patients who have CD with ileal disease or

resection also are likely to form calcium oxalate kidney stones. With the fat malabsorption, unabsorbed long-chain fatty acids bind calcium in the lumen. Oxalate in the lumen normally is bound to calcium. Calcium oxalate is poorly soluble and poorly absorbed; however, if calcium is bound to malabsorbed fatty acids, oxalate combines with sodium to form sodium oxalate, which is soluble and is absorbed in the colon (enteric hyperoxaluria). The development of calcium oxalate stones in CD requires an intact colon to absorb oxalate. Patients with ileostomies do not develop calcium oxalate stones. Extraintestinal manifestations of IBD include iritis, episcleritis, arthritis, and skin involvement, as well as pericholangitis and sclerosing cholangitis.

The most common causes of death in IBD are peritonitis with sepsis, malignancy, thromboembolic disease, and complications of surgery. Malnutrition and chronic anemia are observed in longstanding CD. Children with CD or UC can exhibit growth retardation.

Patients with UC most commonly present with bloody diarrhea, whereas patients with CD usually present with non-bloody diarrhea. Abdominal pain and cramping, fever, and weight loss occur in more severe cases. The presentation of CD is generally more insidious than that of UC. UC and CD are generally diagnosed using clinical, endoscopic, and histologic criteria. However, no single finding is absolutely diagnostic for one disease or the other. Furthermore, approximately 20% of patients have a clinical picture that falls between CD and UC; they are said to have indeterminate colitis. Accordingly, imaging may be needed for the detection and evaluation of the disease activity during its course.

4.4.2 Chest Inflammation

The chest is a common site of various types of infection, acute and chronic. Such infections are frequent in the elderly and in immunosuppressed patients, including cancer patients. Common inflammatory conditions relevant to nuclear medicine include pneumonia, sarcoidosis, diffuse interstitial fibrosis, and *Pneumocystis (jiroveci) carinii* pneumonia (see also Chapter 13).

4.4.2.1 Sarcoidosis

Sarcoidosis is an inflammatory condition of uncertain etiology characterized by the presence of non-caseating granulomas involving multiple organs. The disease is now recognized as a member of a large family of granulomatous disorders and has been reported from all parts of the world. Current evidence points to a genetic predisposition and exposure to as yet unknown transmissible agent(s) and/or environmental factors as etiological agents [21]. The lung is most commonly and usually the first site of involvement, and the inflammatory processes extend through the lymphatics to the hilar and mediastinal nodes [22]. Lung is involved in more than 90% of cases. Pulmonary sarcoidosis starts as diffuse interstitial alveolitis, followed by the characteristic granulomas. Granulomas are present in the alveolar septa as well as in the walls of the bronchi and pulmonary arteries and veins. The center of the granuloma contains epithelioid cells derived from mononuclear phagocytes, multinucleated giant cells, and macrophages. Lymphocytes, macrophages, monocytes, and fibroblasts are present at the periphery of the granuloma [23]. Sarcoidosis represents a challenge to clinical investigation because of its unpredictable course, uncertain response to therapy, and diversity of potential organ involvement and clinical presentations [24]. The diagnosis is based on a compatible clinical and/or radiological picture, histopathological evidence of non-caseating granulomas in tissue biopsy specimens and exclusion of other diseases capable of producing similar clinical or histopathological appearances. Even microscopically, the non-caseating granulomas are not specific [21]. Infection by mycobacterial species other than *Mycobacterium tuberculosis* frequently leads to the production of non-caseating granulomas [25]. The condition is underdiagnosed in some areas. However, owing to increasing awareness, it is being diagnosed more frequently than a few decades ago [26].

The disease runs a benign course with spontaneous remission of the activity though some degree of residual pulmonary function abnormality persists. Only a minority of patients develop complicated disease, which may lead to blindness, renal failure, liver failure and heart involvement.

Corticosteroids remain the mainstay of treatment. Treatment under close clinical monitoring should be tailored to suit the needs of the individual patient; hence the need to evaluate disease activity [26].

Advanced age, the presence of pulmonary symptoms, the presence of parenchymal lesions on the chest radiograph, a previous history of treatment with corticosteroids, and the presence of extrathoracic involvement at the time of detection are possible prognostic factors in patients with sarcoidosis [27]. The mode of onset and the extent of the disease are also related to prognosis. An acute onset with erythema nodosum or asymptomatic bilateral hilar lymphadenopathy usually heralds a self-limiting course, whereas an insidious onset, especially with multiple extrathoracic lesions, may be followed by relentless, progressive fibrosis of the lungs and other organs.

4.4.2.2 Pneumocystis carinii (jiroveci) Pneumonia

Pneumocystis carinii (jiroveci) pneumonia (PCP) is a condition that may be endemic or epidemic. It is caused by *Pneumocystis carinii (jiroveci)*, which was considered as a protozoon and recently as a fungus. The condition is common in premature infants, debilitated children, and in other immunocompromised conditions, particularly the acquired immune deficiency syndrome (AIDS), but it is also seen in congenital immunodeficiency and in patients who are receiving chemotherapy and corticosteroids [28]. It is the most common infection in AIDS patients and it remains an important cause of morbidity and mortality [29]. The introduction of highly active antiretroviral therapy in industrialized nations, however, has led to dramatic declines in the incidence of AIDS-associated complications, including PCP. In the developing countries, no decline has occurred [30]. Transmission is usually airborne. The pathological changes are predominantly in the lungs with an inflammatory reaction consisting of plasma cells of variable amount, monocytes, and histiocytes. This disease has also been reported in immunocompetent patients and in this case the presentation more closely resembles the disease of immunocompromised patients other than AIDS patients [31, 32]. The diagnosis is currently established through identification of the organisms in bronchial secretions obtained by bronchoalveolar lavage or bronchial washings [33]. Gallium-67 is an important imaging modality that helps in the diagnosis and evaluation of the activity of the disease.

4.4.2.3 Idiopathic Pulmonary Fibrosis

Idiopathic pulmonary fibrosis, a sometimes fatal condition, is characterized by parenchymal inflammation and interstitial fibrosis. The pathological changes start with alveolitis; this is followed by derangement of the alveolar-capillary units, leading to the end stage of fibrosis. There is a correlation between the inflammatory activity and the amount of gallium-67 activity in the lungs [34].

4.4.3 Renal Inflammation

Urinary tract infection (UTI) is common particularly in children. There are two main varieties of acute renal infection. Pyelitis, which is confined to the renal pelvis, and pyelonephritis, where the renal parenchyma is also involved. It is not always possible to differentiate between the two conditions on clinical grounds.

The importance of the acute renal infections lies in the fact that recurrent subclinical attacks are believed to be significant in the pathogenesis of chronic pyelonephritis [35]. The number of patients with chronic kidney disease and consequent end-stage renal disease is rising worldwide [36]. End-stage kidney disease defined as the need for dialysis, receipt of a transplant, or death from chronic kidney failure, generally affects less than 1% of the population [37]. Among today's challenges is that of identifying those at greatest risk for end-stage renal disease and of intervening effectively to prevent progression of early chronic kidney disease and conditions leading to chronic disease [37].

Rarely, uncomplicated acute pyelonephritis causes suppuration and renal scarring. However, urinary infections in patients with renal calculi, obstructed urinary tract, neurogenic bladder, or diabetes are frequently much more destructive and have ongoing sequelae [38].

4.4.3.1 Acute Pyelonephritis

The diagnosis and management of this common medical condition are complex. Patients initially diagnosed with pyelonephritis typically exhibit symptoms and laboratory evidence suggesting infected urine, with signs referable to upper urinary tract infection. However, no consistent set of signs and symptoms are sensitive and specific for this diagnosis. Symptoms of acute pyelonephritis generally develop rapidly over a few hours or a day. Symptoms of lower UTI may or may not be present. These include dysuria, urinary frequency, hesitancy, urgency, gross hematuria, suprapubic discomfort, heaviness, pain, or pressure. Additionally, flank pain and tenderness, unilateral or sometimes bilateral, are present. Fever is not always present. When present, it is not unusual for the temperature to exceed 103°F (39.4°C). Rigor, chills, malaise, weakness, anorexia, nausea, vomiting and diarrhea may be present. Most patients have significant leukocytosis, pyuria with leukocyte casts in the urine, and bacteria on a gram stain of unspun urine.

Many conditions and clinical situations are associated with an increased risk of pyelonephritis. Table 4.2 lists common risk factors (adapted from [39] and [40]).

Pyelonephritis is significantly more common in females than in males (more so in white than in black persons). Approximately 10% – 30% of women develop a symptomatic UTI at some point in their lives.

Acute pyelonephritis is a bacterial infection of the kidney with acute inflammation of the pyelocaliceal lining and renal parenchyma centrifugally along medullary rays. This can occur in more than one route. Most often it occurs because of ascending infection from the lower urinary tract. The initial colonization of the walls of the ureter is in areas of turbulent flow, which leads to paralysis of peristalsis. Dilation and

Table 4.2. Common risk factors for pyelonephritis

Mechanical factors
Obstruction
Prostatic infection
Calculi
Urinary diversion procedure
Infected cysts
External drainage with urinary catheters or nephrostomy tubes
Stents
Vesicoureteral reflux
Neurogenic bladder
Bladder or renal abscesses
Fistulae
Recent urinary tract instrumentation
Metabolic and hormonal factors
Diabetes mellitus
Pregnancy
Renal impairment
Malakoplakia
Primary biliary cirrhosis
Immune factors
Transplant recipients
Neutropenia
Congenital or acquired immunodeficiency syndromes
Infectious factors (unusual pathogens)
Yeasts and fungi
Mycoplasma species
Resistant bacteria, including *P. aeruginosa*
Calculi-predisposing bacteria, including *Proteus* species and *Corynebacterium urealyticum*
Other factors
Uncircumcised penis
Old ages
Recent antimicrobial use

functional obstruction result, with subsequent pyelonephritis. Another route is by direct reflux of bacteria. Hematogenous spread to the kidney by gram-positive and less likely by gram-negative organisms is the third route that can occur. This has become less prevalent since the advent of rapid use of antibiotics. Little or no evidence supports lymphatic spread.

Grossly, the kidney is enlarged and edematous. The cut surface may show small abscesses in the cortex, and more often there are wedge-shaped purulent areas streaking upwards from the medulla, with normal areas of kidney tissue intervening in between infected zones (Fig. 4.5). Frequently, the pelvis and calyces are inflamed and dilated. In severe infection, renal papillary necrosis may be present.

Microscopically, there is intense inflammation, with infiltration of polymorphonuclear leukocytes throughout the interstitial tissue and abscess formation. There is destruction of the tubules, but the glomeruli and blood vessels are often unaffected. The disease remains essentially focal in character, with areas of normal tissue. Following treatment and removal of predisposing factors such as obstruction, healing may occur, leaving coarse scars which stretch from the medulla to the capsule of the kidney.

4.4.3.2 Chronic Pyelonephritis

Chronic pyelonephritis is a chronic condition affecting the pelvis and parenchyma and resulting from recurrent or persistent renal infection. It occurs almost exclusively in patients with major anatomic anomalies, including urinary tract obstruction, struvite calculi, renal dysplasia, or, most commonly, vesicoureteral reflux (VUR) in young children. Grossly, the kidney shows normal areas alternating with zones of scarring. Wedge-shaped scars can be seen on the subcapsular surface of the kidney. The appearance differs, depending on the presence or absence of obstruction. Chronic pyelonephritis in the presence of intra- or extrarenal obstruction shows dilatation of the pelvocalyceal system and sometimes peripelvic fibrosis. If no obstruction is present the pelvic change is in the form of peripelvic fibrosis rather than dilatation (Fig. 4.6).

Microscopically, the scarred areas show changes in the interstitium and tubules. The interstitial tissue

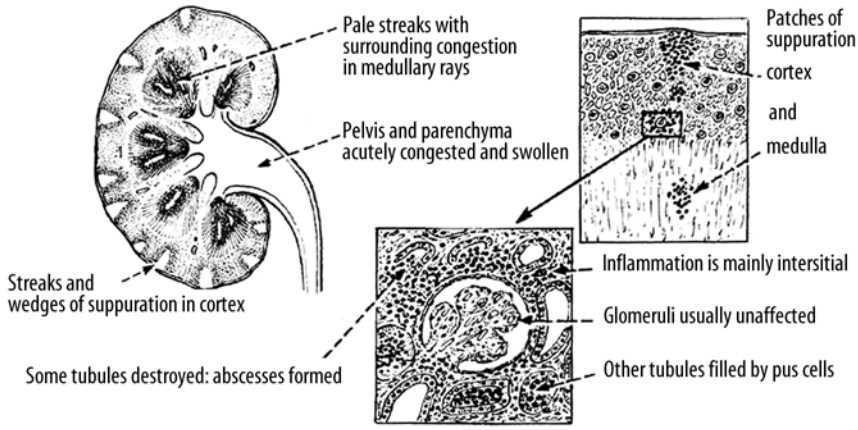

Fig. 4.5. Acute pyelonephritic changes (modified from [41] with permission)

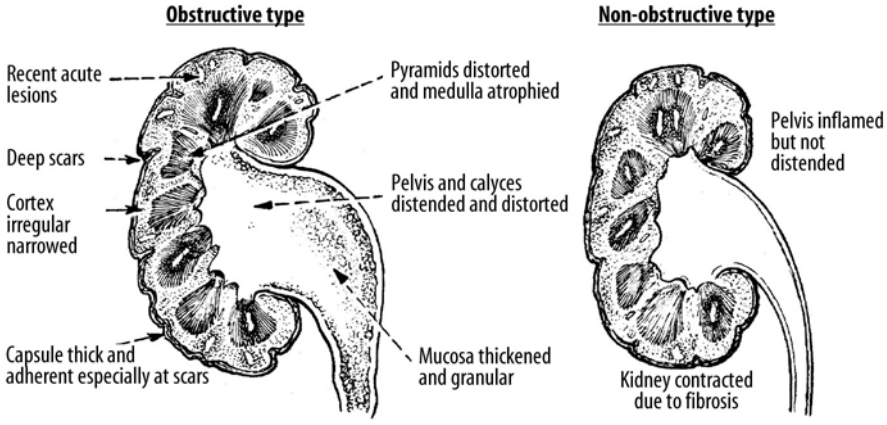

Fig. 4.6. Types of pyelonephritic changes based on whether obstruction is present (from [41] with permission)

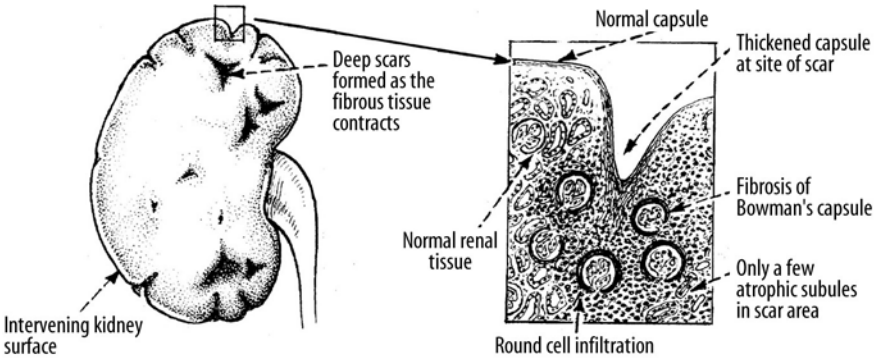

Fig. 4.7. Main pathological changes of chronic pyelonephritis (from [41] with permission)

shows infiltration by predominantly lymphocytes and plasma cells. The tubules become atrophic and may collapse (Fig. 4.7). The glomeruli may be normal in some cases while in others periglomerular fibrosis is present.

4.5 Pathophysiology of Major Skeletal Inflammations

Osteomyelitis indicates an infection involving the cortical bone as well as the marrow (see Chapter 6). It is classified into many types based on several pathological and clinical factors [42–49] including route of infection, patient age, etiology, and onset. Hematogenous osteomyelitis most commonly affects children, and the metaphyses of long bones are the most common sites. Nonhematogenous osteomyelitis, on the other hand, occurs as a result of penetrating trauma, spread of a contiguous soft tissue infection, or inoculation, as in drug addicts [48–54]. Many organisms have been encountered in the pathogenesis of osteomyelitis, particularly gram-positive organisms, the most common being *Staphylococcus aureus* [44–46]. Like many other pathological conditions of bone, infections cause reactive new bone formation which – among other factors, particularly increased blood flow – is the principal reason for the accumulation of bone-seeking radiopharmaceuticals at the site of skeletal infections.

It is difficult to draw the line between acute and chronic osteomyelitis. Chronic osteomyelitis can occur after a duration as short as 5 days or as long as 6 weeks. It is characterized by less marked inflammatory cell infiltrates than acute infection and may exhibit a variable amount of necrotic tissue. Acute septic arthritis is a medical emergency, since it may result in destruction of the articular cartilage and permanent disability if treatment is delayed [55]. See Chapter 6 for more details on skeletal inflammations.

4.6 Radiopharmaceuticals for Inflammation Imaging

Many radioisotopes have been used to detect and localize infection (see Table 4.3). Several mechanisms explain the uptake of these radiotracers at the site of infection:

1. Increased vascular permeability
   - ^{111}In and ^{99m}Tc human polyclonal IgG
   - ^{111}In monoclonal IgM antibody
   - ^{111}In and ^{99m}Tc liposomes

Table 4.3. Radiopharmaceuticals for imaging infection [56–58]

Gallium-67 citrate
Labeled WBCs using ^{111}In-oxime or ^{99m}Tc-HMPAO (^{99m}Tc-hexamethyl propyleneamine oxime)
Labeled particles
Nanocolloid
Liposomes
Labeled large protein
Nonspecific immunoglobulins
Specific immunoglobulins: polyclonal and monoclonal
Antigranulocyte monoclonal antibodies
Anti-E-selectin antibodies
Labeled receptor-specific small proteins and peptides
Chemotactic peptides
Interleukins
Labeled antibiotics: ciprofloxacin
^{18}F-FDG

- ^{111}In biotin and streptavidin
- ^{99m}Tc nanocolloids
- ^{111}In chloride
- ^{67}Ga-citrate

2. Migration of WBCs to the site of infection
   - ^{111}In- and ^{99m}Tc-labeled leukocytes
   - ^{99m}Tc anti-WBC antibodies
3. Binding to proteins at the site of infection, i.e., ^{67}Ga citrate (lactoferrin and other iron-containing proteins)
4. Binding to WBCs at the site of infection
   - Chemotactic peptides
   - Interleukins
5. Binding to bacteria
   - ^{99m}Tc-labeled ciprofloxacin antibiotic
   - ^{67}Ga citrate
6. Metabolic trapping, i.e., ^{18}F-fluorodeoxyglucose

Since there are limitations to the radiopharmaceuticals available for imaging infection, the search continues for better agents with ideal properties [56–59]. They should:

1. Be easy to prepare
2. Have low cost and wide availability
3. Ensure rapid detection and localization of infections (< 3 h)
4. Have low toxicity and produce no immune response
5. Clear rapidly from the blood with no significant uptake in liver, spleen, GI tract, bone, kidneys, bone marrow, or muscle
6. Clear rapidly from the background
7. Have high specificity and sensitivity and be able to differentiate infection from other causes of inflammation and tumors
8. Be able to differentiate acute from chronic infection

Gallium-67 has been used for many years to detect inflammation. The multiple mechanisms of uptake of gallium by inflammatory tissue include the following:

1. Increased vascular permeability
2. Gallium-67 binding substances at site of inflammation
   - Transferrin (due to leakage of plasma proteins)
   - Lactoferrin (secreted with lysosomal contents of stimulated or dead neutrophils)
   - Siderophores produced by bacteria
3. Leukocytes: direct uptake
4. Bacteria: direct uptake

Sfakianakis et al. [60] found that indium-111 leukocyte imaging accuracy was best for relatively acute infections (less than 2 weeks) but yielded a 27% false-negative rate among patients with prolonged infections. On the other hand, ^{67}Ga imaging had its highest sensitivity in long-standing processes, with false-negative results of 19% in relatively acute infections of less than 1 week duration. In a comparative study of rabbits with experimental abscesses, Bitar et al. [61] found that ^{111}In-leukocytes were clearly superior to gallium for imaging early abscesses. Furthermore, they found that the accumulation of ^{111}In-leukocytes in experimental subcutaneous abscesses was inversely proportional to the age of the abscess. In abscesses 1–2 h, 6–8 h, 24 h, and 7 days old, 10.4%, 5.2%, 3%, and 0.73% of the injected dose, respectively, was accumulated. ^{67}Ga uptake, on the other hand, was not significantly affected by abscess age (Table 4.4). In abscesses 7 days old, ^{67}Ga accumulated to a greater extent than did ^{111}In-labeled leukocytes. Thus Bitar et al., based on animal studies, and Stakianakis et al. came independently to the conclusion that ^{111}In-labeled WBCs are more suitable for acute infections of short duration while ^{67}Ga labeling is better for infections of longer duration.

In rats, McAfee et al. [62] showed that as many as 10% of circulating neutrophils accumulate daily at focal sites of inflammation. This high propensity of white blood cells to migrate to an abscess makes positive identification of the abscess likely on an ^{111}In-WBC image. The authors also showed abscess-to-muscle ratios of 3000 to 1 with ^{111}In WBCs at 24 h compared with 72 to 1 with ^{67}Ga and 7 to 1 with ^{111}In chloride. Accordingly, a small dose of only 500 μCi of ^{111}In leukocytes is sufficient for positive identification and localization of abscesses on an image. In ^{67}Ga imaging, a higher administered activity of approximately 5 mCi is needed. There

Table 4.4. Comparison of uptake of ^{111}In-WBC and ^{67}Ga-citrate in experimental abscesses of varying age (from [61])

Abscess age	Percent uptake ^{111}In-WBC	^{67}Ga citrate
1–2 h	10.4	1.5
6–8 h	5.2	1.5
24 h	3	1.4
7 days	0.73	1.1

Table 4.5. Advantages and disadvantages of the main available radiopharmaceuticals for inflammation

	Gallium-67 citrate	Indium-111 WBC	^{99m}Tc-HMPAO WBC
Advantages	Whole-body imaging	Whole-body imaging Highly specific for infection	Whole-body imaging Earlier diagnosis (2 – 4 h) Better physical characteristics of technetium than ^{67}Ga and ^{111}In
Disadvantages	Results after 24 h or more Physiological liver, spleen, and bowel activity Uptake in tumors	Tedious procedure Results at 24 h Physiological liver and spleen activity	Tedious procedure Physiological bowel activity by 2 h Normal urinary activity

is a higher radiation dose to the spleen from 500 μCi of ^{111}In WBC but radiation doses to gonads, marrow, and the whole body are higher with 5 mCi of ^{67}Ga. ^{99m}Tc HMPAO-labeled WBCs could provide fast diagnosis and localization of the abdomen (within 2 – 4 h). Physiological bowel activity, however, is found in 7% at 2 h and in 28% of patients imaged with this agent at 4 h. Leukocytes labeled with ^{111}In or ^{99m}Tc-HMPAO are superior to those labeled with ^{67}Ga for acute infections in terms of sensitivity and specificity [63, 64]. Table 4.5 lists the main advantages and disadvantages of the major radiopharmaceuticals used for inflammation imaging.

Human nonspecific polyclonal immunoglobulin (hIgG, prepared commercially for intravenous therapeutic use) labeled with ^{111}In and administered intravenously has been used for infection imaging. Gamma camera images at 6, 24, and 48 h often demonstrated various foci of infection. The mechanism is poorly understood but may be secondary to increased vascular permeability. ^{99m}Tc IgG yields a sensitivity and specificity similar to the ^{111}In labeled IgG. This procedure gives little nonspecific bowel activity, making the scan useful for detection of abdominal infection. ^{111}In IgG was directly compared with ^{67}Ga-citrate IgG. The former was found to be more sensitive and specific for infection [65]. It was also found to be superior to antigranulocyte antibodies and is as useful as labeled leukocytes in diagnosing infections. Serial ^{111}In IgG scans were found to be useful for monitoring therapy and providing proof of cure. The sensitivity of ^{111}In IgG reported in the literature ranges from 90% to 100% and the specificity from 70% to 100% [66, 67].

Several monoclonal antibodies are also used to detect infections. These antibodies are mainly directed against receptors on inflammatory cells. Anti-CD15 (LeuTech) contains a murine IgM anti-CD15 monoclonal antibody. It binds to CD15 antigens expressed on the surface of human neutrophils. The basis of this is the elevated level of CD15 epitope in activated neutrophils, which should make them good targets for imaging with a monoclonal antibody. The advantages of this tracer include easy preparation since it takes about 30 min. Imaging is begun immediately and diagnostic images are usually obtained within 30 min. The technique accordingly avoids the disadvantages of white blood cell radiolabeling with either ^{99m}Tc-HMPAO or ^{111}In-oxine, including usual preparation times of 2 h or more; potential exposure of technical personnel to bloodborne pathogens; and misadministration of the labeled white blood cells into the wrong patient [68, 69].

Another method is the use of ^{99m}Tc-anti-NCA-90 Fab' fragments (nonspecific cross-reacting antigen), which are preferred because they are easily available, simpler to use, and have less radiation exposure and human antibodies have not been observed. The ^{99m}Tc-anti-NCA-90 Fab' fragments can recognize a specific cross-reacting-antigen (NCA-90) (the surface antigenic glycoprotein) on granulocytes, promyelocytes, and myelocytes [70 – 72]. Leukoscan uptake at the site of infection is explained partly by the migration of circulating antibody-labeled granulocytes to the site of infection. Leukoscan uptake is also explained by the fact that the greater proportion of the labeled antibody fragment is in a free soluble form which can easily cross capillary membranes, binding to the leukocyte once in situ. This mechanism is favored by the increased capillary permeability at the site of infection. An important advantage of Leukoscan is the 5 min preparation time compared with the 2 h 30 min required by a specialized team for labeling leukocytes. Despite the fact that Leukoscan involves the i.v. injection of mouse proteins, no anaphylactic or other hypersensitivity reactions were observed.

^{99m}Tc-ciprofloxacin (Infecton) is also being used to image infection. Ciprofloxacin is a broad-spectrum fluoroquinolone antibiotic. Patients receive ^{99m}Tc-ciprofloxacin 10 mCi and images are obtained at 1, 3 – 4, and, occasionally, 24 h postinjection. ^{99m}Tc-ciprofloxacin may be useful in distinguishing infection from inflammation. Early images of noninfectious rheumatologic inflammatory conditions were positive, but activity decreased with time [73].

^{111}In- and ^{99m}Tc-labeled chemotactic peptide analogs have been used for detecting and localizing infections. Imaging can be performed at less than 3 h post injection, which compares favorably with the 18 – 24 h or more for most other agents [54].

Labeled liposomes have been used for scintigraphic imaging of infection and inflammation [74, 75]. Boer-

man et al. [76] used ^{111}In-labeled sterically stabilized liposomes (long circulating) in rats and showed that the clearance of this agent is similar to that of ^{111}In IgG. The uptake in abscess was twice as high as that of IgG and the abscess was visualized as early as 1 h post injection. ^{99m}Tc nanocolloid has also been tried but has not gained wide acceptance.

^{18}F-fluorodeoxyglucose (FDG PET) has emerged as an important diagnostic agent for infectious and noninfectious soft tissue and skeletal inflammations including inflammatory bowel disease, fevers of unknown origin, rheumatologic disorders, tuberculosis infection, fungal infection, pneumonia, abscess, postarthroplasty infections, chronic and vertebral osteomyelitis, sarcoidosis and chemotherapy-induced pneumonitis) [77 – 93]. Inflammatory conditions show high FDG uptake which is related to increased glucose metabolism that is produced by stimulated inflammatory cells, macrophage proliferation, and healing [94]. While uptake of FDG continues to increase at malignant sites for several hours, as can be shown by an incremental increase of the standardized uptake values (SUV), inflammatory lesions peak at approximately 60 min, and their SUV either stabilize or decline thereafter. This difference in the behavior of FDG in malignant versus inflammatory cells can be explained best by the varying levels of enzymes that degrade deoxyglucose-6-phosphate in the respective cells. Glucose-6-phosphatase dephosphorylates intracellular FDG-6-phosphate, allowing it to leave the cell. It has been shown that most tumor cells have low levels of this enzyme, while its expression is high in the mononuclear cells [95]. For this reason, imaging at two time points after administration of FDG may prove to be important in differentiating between these two common disorders.

4.7 Infection Imaging

Diagnosis and localization of infection by clinical and laboratory methods is often difficult. The results frequently are nonspecific and imaging may be needed. Imaging of infection may be achieved by either nuclear medicine or other strictly morphological methods. Several nuclear medicine modalities are used to diagnose and localize soft tissue and skeletal infections. These include ^{111}In-labeled white blood cells, ^{67}Ga citrate, IgG polyclonal antibodies labeled with ^{111}In or ^{99m}Tc, monoclonal antibodies such as antigranulocyte antibodies, ^{99m}Tc HMPAO-labeled white blood cells, ^{99m}Tc nanocolloid, ^{99m}Tc DMSA, ^{99m}Tc glucoheptonate, ^{99m}Tc MDP multiphase bone scan, ^{111}In-labeled chemotactic peptide analogs, and ^{18}F-FDG. X-ray, CT, MRI, and ultrasonography are other modalities useful in the diagnosis and localization of both soft tissue and skeletal inflammations. These studies are complementary to the physiological modalities of nuclear medicine.

4.7.1 Imaging of Soft Tissue Infections

The strategy for imaging soft tissue infections depends on the pathophysiological and clinical features, including whether localizing signs and symptoms are present and the location and duration of the suspected infection.

4.7.1.1 Localizing Signs Present

4.7.1.1.1 Imaging Abdominal Infections

Abdominal Abscess. Rapid and accurate diagnosis of an abdominal abscess is crucial. The mortality from untreated abscesses approaches 40% and may reach 100% in some series. The mortality among patients treated reaches 11% [96 – 104]. Delayed diagnosis is associated with higher mortality in spite of treatment. If localizing signs suggest abdominal infection, morphological modalities, predominantly ultrasound (Fig. 4.8) and CT (Fig. 4.9) may be used first, depending on the location of suspected infection in the abdomen. Standard radiographs have low sensitivity, although when seen, findings are specific.

The advantages of these modalities are numerous, but most importantly they provide quick results and adequate anatomical details. These studies can be used

Fig. 4.8. Ultrasonographic study of a patient with abdominal pain and malaise. The study helped make the diagnosis of abdominal abscess (*arrow*) and provided accurate localization

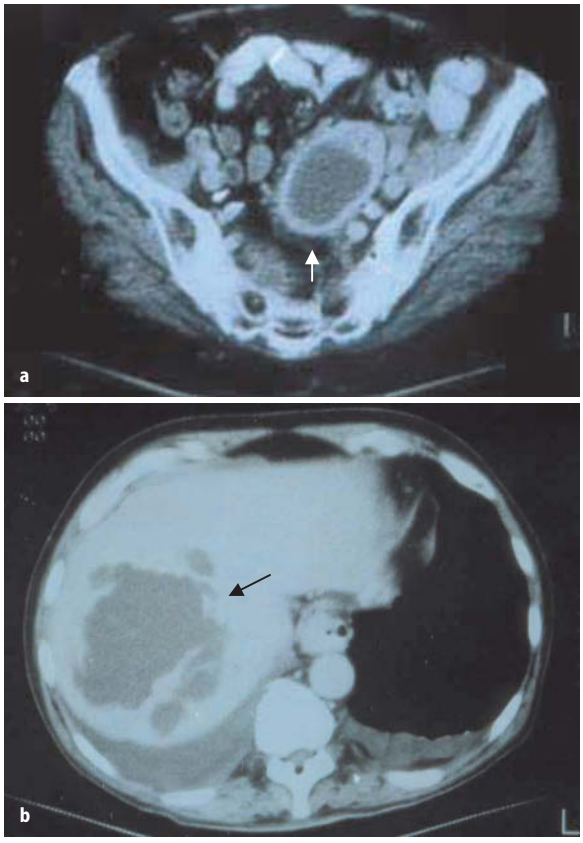

Fig. 4.9. Representative images of CT scans of the abdomen illustrating **a** periappendicular abscess (*arrow*). **b** Hepatic abscess (*arrow*)

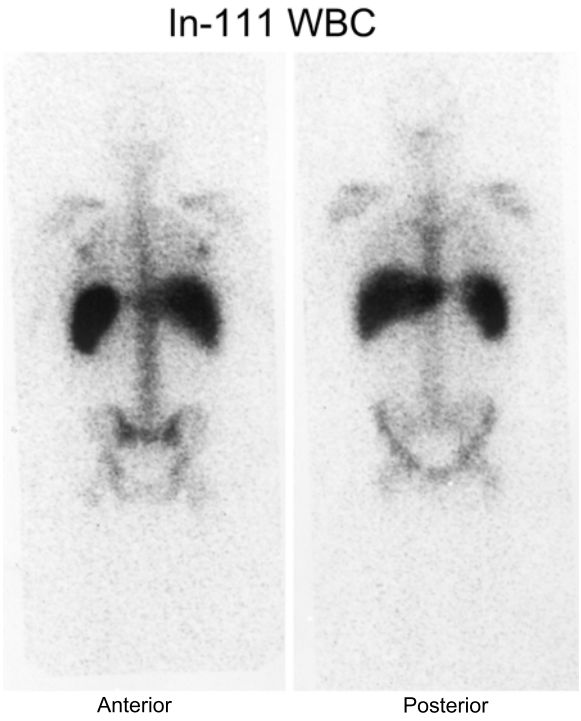

Fig. 4.10. Whole body 24-h ^{111}In-labeled leukocyte scan obtained in a patient with a 10-day history of fever and no localizing signs. Anterior and posterior images reveal physiologic uptake in the bone marrow, liver, and spleen with no abnormal accumulation of labeled cells

to guide needle aspiration and abscess drainage. Ultrasound can be used portably for critically ill patients. One of the major limitations of these modalities is the inability to differentiate infected from noninfected tissue abnormalities, particularly in early stages of infection (phlegmon) before formation of abscesses.

The diagnostic accuracy of these morphological modalities may be compromised in cancer patients, and the evaluation of studies that use these techniques may be difficult. This is because the interpretation of these modalities depends on the presence of normal anatomical markers, which may be altered or obliterated by either the cancer treatment or the cancer itself [105]. For example, both CT and MRI are often of little value in distinguishing post-treatment scarring from recurrent tumor.

When the results of the morphological modalities are inconclusive, nuclear medicine techniques may be used to detect abdominal infections. The ability to image the entire body is the major advantage of nuclear medicine modalities (Fig. 4.10). Hence radionuclide techniques are often used in cases with no localizing signs. In one study, 16% of patients suspected of having abdominal infection in fact had extra-abdominal infections as seen on ^{111}In leukocyte scans [106]. Accordingly, negative morphological modalities, when used first, may be followed by whole-body nuclear imaging. Labeled-WBC studies are the most specific for acute infections (Figs. 4.11, 4.12). Ga-67 is more suitable for infection of longer duration (Fig. 4.13). ^{99m}Tc HMPAO-labeled WBCs frequently used in critically ill patients [39] after US and/or CT have yielded inconclusive results. It is worthy of note that ^{99m}Tc HMPAO-labeled WBCs provide quicker results than ^{67}Ga- or ^{111}In-labeled WBCs. Minoja et al. [108] reported a sensitivity of 95%, a specificity of 91%, and an accuracy of 94% for ^{99m}Tc-labeled WBC scanning in intensive care unit patients with occult infections. The gallium-67 scan has been reported to have a better diagnostic specificity than the C-reactive protein test for abdominal infections [109].

Inflammatory Bowel Disease (IBD). Upright chest radiography and abdominal series, barium enema and upper GI, CT scanning, MRI and ultrasonography are the main imaging modalities used for the diagnosis. CT scanning and ultrasonography are best for demonstrating complications such as intra-abdominal abscesses and fistulas. Evaluation of the extent of the disease and

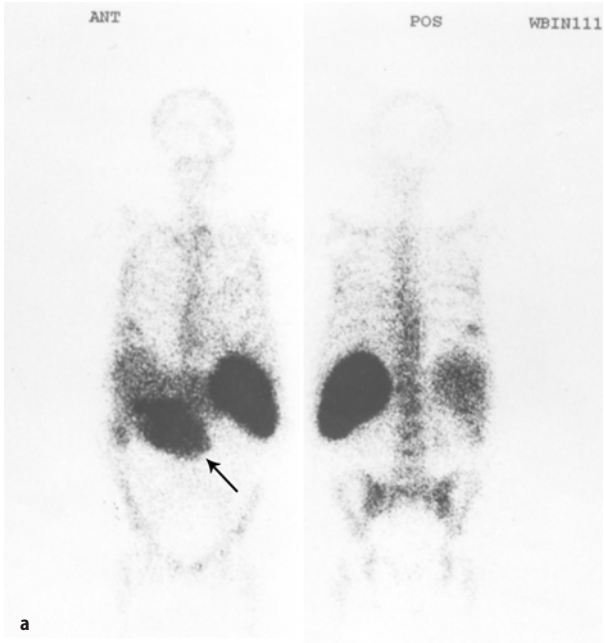

Fig. 4.12. Indium-111-labeled leukocyte scan posterior projection of the abdomen demonstrating two foci (*arrows*) of abnormal accumulation of labeled cells at the ends of a vascular graft indication infection of the graft

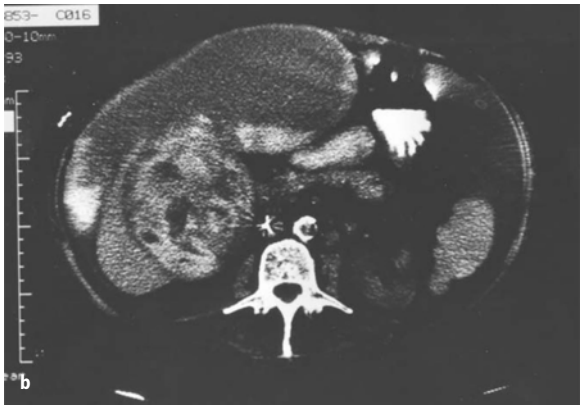

Fig. 4.11a,b. Indium-111-labeled leukocyte study (**a**) shows a large acute abdominal abscess (*arrow*) corresponding to the finding (*arrow*) on CT (**b**)

disease activity is often difficult. A wide variety of approaches depicting the different stages of the inflammatory response have been developed. Non-specific radiolabeled compounds such as ^{67}Ga-citrate and radiolabeled polyclonal human immunoglobulin accumulate in inflammatory foci due to enhanced vascular permeability. Specific accumulation of radiolabeled compounds in inflammatory lesions results from binding to activated endothelium (e.g., radiolabeled anti-E-selectin), the enhanced influx of leukocytes (e.g., radiolabeled autologous leukocytes, anti-granulocyte antibodies or cytokines), the enhanced glucose uptake by activated leukocytes (^{18}F-fluorodeoxyglucose) or direct binding to microorganisms (e.g., radiolabeled ciprofloxacin or antimicrobial peptides). Scintigraphy using autologous leukocytes, labeled with ^{111}In or ^{99m}Tc, is still considered the "gold standard" nuclear medicine technique for the imaging of infection and inflamma-

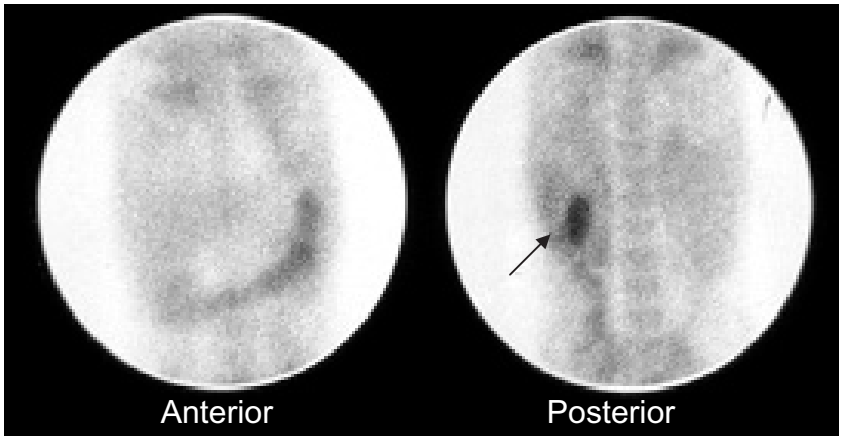

Fig. 4.13. A 72-h gallium-67 image of abdomen anterior and posterior projections for a 21-year-old female with a 6-week history of intermittent fever. No localizing signs were reported. The images demonstrate increased accumulation of gallium-67 in a perirenal abscess (*arrow*) seen in posterior view

tion, including evaluation of IBD activity. Recently, positron emission tomography with ^{18}F-fluorodeoxyglucose has been shown to delineate various infectious and inflammatory disorders with high sensitivity [110–114]. In a recent study [68], gallium, magnetic resonance imaging (MRI), and PET FDG were compared for their ability to detect disease activity. PET FDG showed more than twice as many lesions in the abdomen of patients with Crohn's disease as did gallium. Not all lesions on MRI were FDG positive, suggesting they might represent areas of prior inflammation.

4.7.1.1.2 Imaging Chest Infections

The role of the chest X-ray cannot be overemphasized. The chest X-ray should be used as the initial imaging modality for most chest pathologies. In many instances, however, an additional modality is needed to evaluate certain chest conditions including infections.

Although CT often clearly depicts chest pathology including infections, ^{67}Ga still is commonly used in such cases. ^{111}In leukocytes have limited utility for chest infections. Siemon et al. [115] studied ^{67}Ga imaging in a variety of pulmonary disorders and found excellent sensitivity and specificity (Table 4.6). Gallium-67 has also been widely used in AIDS patients to detect PCP (Fig. 4.14). It is highly sensitive and correlates with the response to therapy. In a study comparing ^{67}Ga, bronchial washing, and transbronchial biopsy in 19 patients with PCP and AIDS, ^{67}Ga and bronchial washing were 100% sensitive compared with 81% for transbronchial biopsy [116]. ^{67}Ga is also valuable in idiopathic pulmonary fibrosis, sarcoidosis and amiodarone toxicity [117, 118]. It is also useful in monitoring response to therapy of other infections including tuberculosis (Fig. 4.15).

^{111}In WBC imaging is less helpful, as the specificity of abnormal pulmonary uptake (either focal or diffuse) is very low. Noninfectious problems that cause abnormal uptake include congestive heart failure, atelectasis, pulmonary embolism, ARDS, and idiopathic conditions [119].

Table 4.6. ^{67}Ga findings in patients with lung pathologies including infections (from [115])

Pathology	Patients (*n*)	Ga negative (%)	Ga positive (%)
Normal	100	100	–
Active tuberculosis	197	3	97
Inactive tuberculosis	32	100	–
Pulmonary abscess	18	–	100
Asbestosis	12	–	100
Cancer	264	10	90

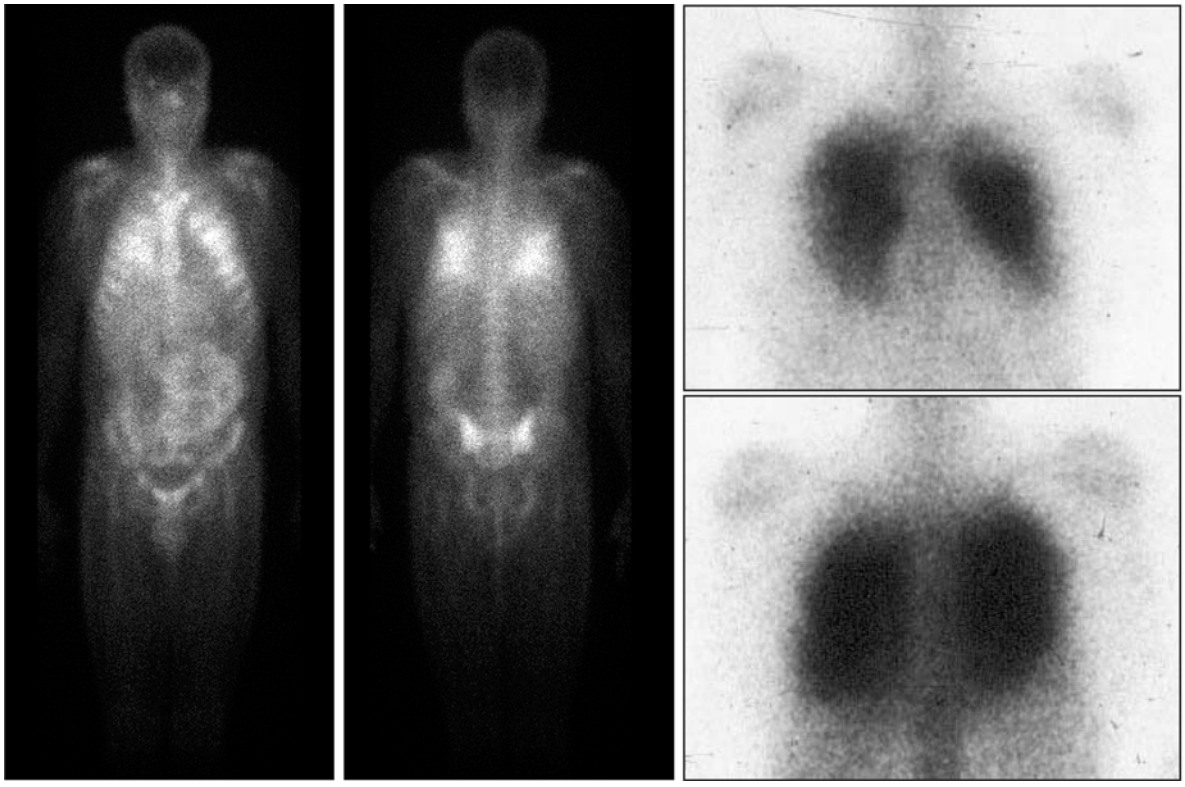

Fig. 4.14. Gallium-67 images of an AIDS patient with a 5-week history of fever. Images show diffuse uptake in both lungs illustrating the typical pattern of gallium-67 in PCP

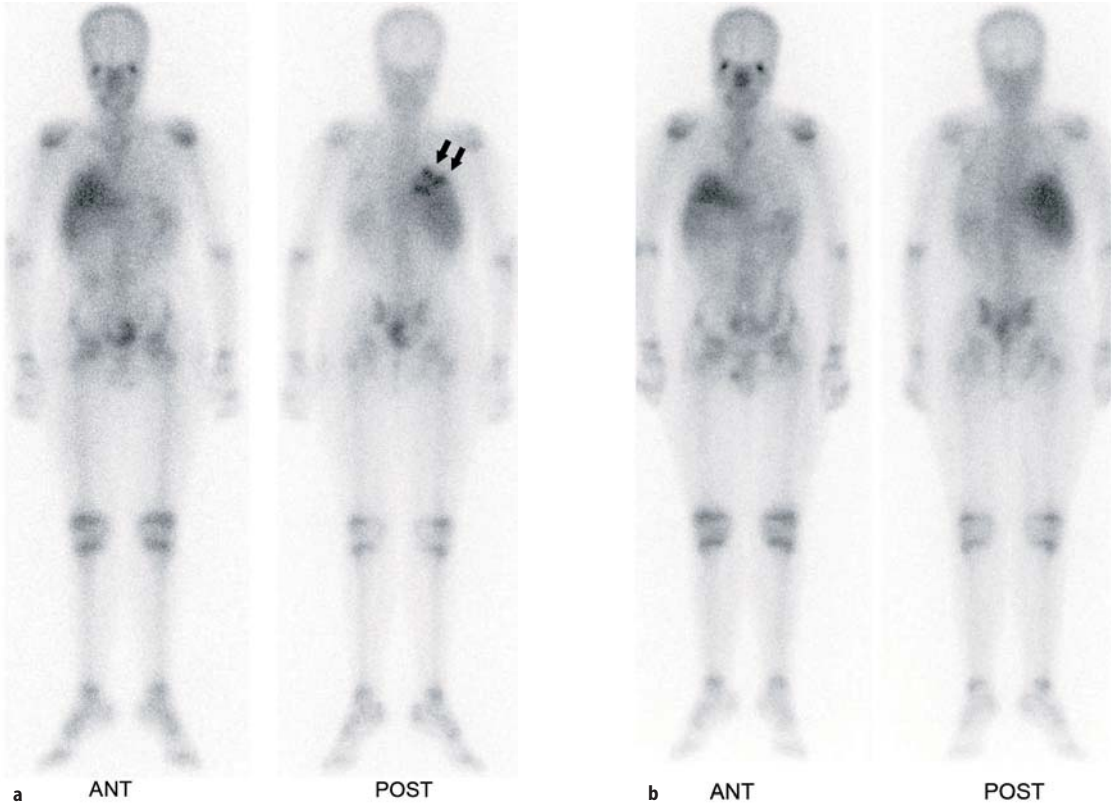

Fig. 4.15a,b. Gallium-67 studies of a patient with tuberculosis. Initial study **(a)** showing abnormal uptake of the right lung (*arrows*) which disappeared on follow-up study **(b)** 3 months after starting therapy, indicating excellent response to treatment

4.7.1.1.3 Imaging Renal Infections

The CT scan has good sensitivity and specificity in the diagnosis of renal infections. IVP has a very limited value when the question is urinary tract infection, with a sensitivity of only 25% [120]. Ultrasound has been used frequently to evaluate the kidneys with suspected infections. The sensitivity of US has been shown to be 40% – 55% [121, 122], which is inferior to the result for cortical scintigraphy (sensitivity of 86%, specificity of 81% using ^{99m}Tc-glucoheptonate). In a comparative study with IVP and US (24% and 42% sensitivity, respectively) [123], cortical scintigraphy was the modality of choice for detecting and following pyelonephritis (Fig. 4.16).

Renal ultrasonography is not sensitive for detecting renal parenchymal infections [124, 125]. To date ^{99m}Tc-DMSA is considered the most sensitive method for the detection of acute pyelonephritis in children. Furthermore it permits the photopenic area to be calculated as the inflammatory volume which correlates with the severity of infection and the possibility of scar formation [126] although some of the defects detected might be too small to be clinically significant [127].

Positive ultrasonography can obviate the need for DMSA; however, because of a large number of false-negative results with reported sensitivities of 42% – 58% and underestimation of the pyelonephritis lesions, ultrasonography cannot replace ^{99m}Tc-DMSA [128, 129].

The pathophysiologic basis of the ability of Doppler sonography in detecting acute pyelonephritis is the fact that the acute phase of pyelonephritis is the focal decrease of renal perfusion due to edema, which causes vascular compression, intravascular granulocyte aggregation or both, leading to capillary and arteriolar occlusion facilitating the detection of these hypovascular areas [130, 131].

Spiral CT and MRI with contrast have been found to be sensitive in detecting acute pyelonephritis [132 – 134]. MRI is not practical because of the cost and the need for sedation for the longer periods required for imaging [128].

4.7.1.2 No Localizing Signs Present

When no localizing clinical signs are present, which is common in cancer and immunosuppressed patients,

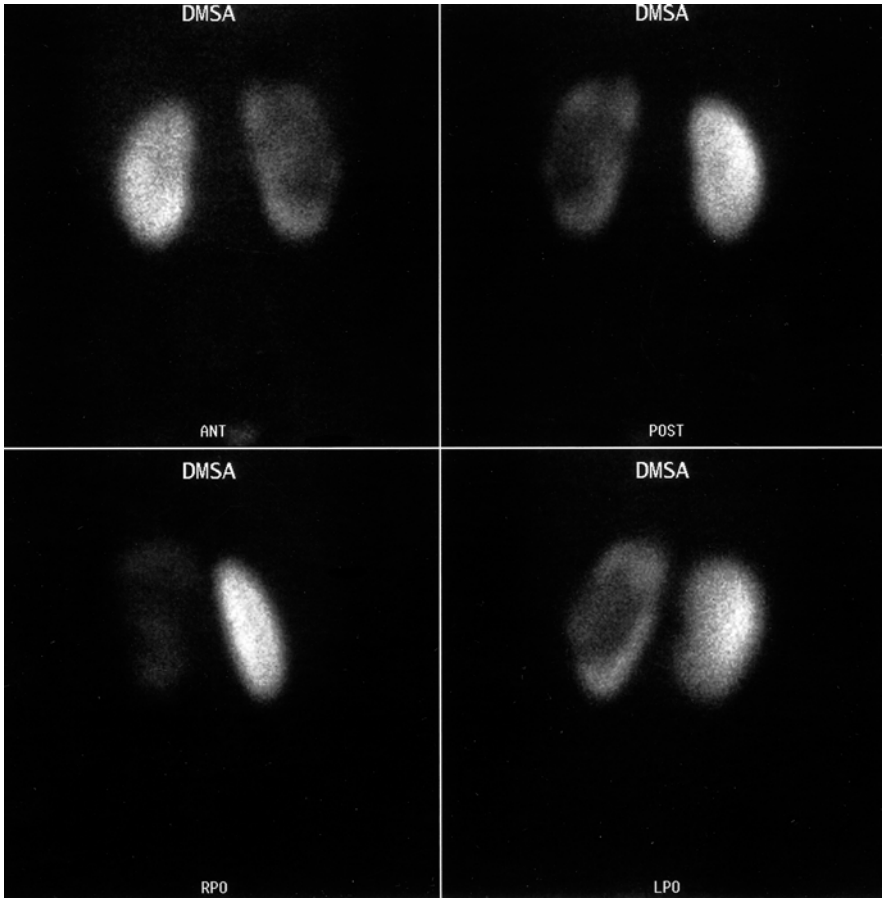

Fig. 4.16. ^{99m}Tc DMSA study in a patient with chronic pyelonephritis and significant urine outflow obstruction. Note the irregularly thinned cortex and the dilated pelvocalyceal system on the left affected kidney

nuclear medicine procedures are often the imaging modalities chosen. The ability to screen the entire body is particularly important for many such cases.

The optimal choice of radiotracer again depends on the duration of infection (Fig. 4.17). Indium-111-labeled white blood cells are the most specific for acute infections, but false-positive results have been reported with some tumors, swallowed infected sputum, GI bleeding, and sterile inflammation. False-negative results have been reported in infections present for more than 2 weeks. More rarely, such false-negative results occur for infections present for only 1 week. Gallium-67 is less specific than labeled WBCs, as it is taken up by many tumors, and by sterile inflammation. Labeled antibodies and peptides have the potential for a specific diagnosis of infection when the localizing signs are present [56]. Correlation with morphological modalities after successful radionuclide localization of infection can be of great help. For example, this correlation provides anatomical information prior to surgical interventions. Morphological modalities are useful in the management of inflammatory diseases particularly if localizing signs are present. They have the very important advantages of better spatial resolution than nuclear medicine modalities. X-rays, CT, MRI, and US usually yield fast results but unfortunately may not distinguish infected from noninfected tissue. Figure 4.17 illustrates suggested algorithms for the diagnosis of soft tissue infections.

4.7.2 Imaging of Skeletal Infection

Several imaging techniques are being utilized for the detection of osteomyelitis including the standard radiograph, computerized tomography, magnetic resonance imaging, and several nuclear medicine modalities. The choice of modality depends on the clinical presentation, particularly its duration, the site of suspected infection, and whether the site of suspected infection has been affected by previous pathology. The pathophysiology of skeletal inflammations and relevant scintigraphic considerations are discussed in detail in Chapter 6, on the musculoskeletal system.

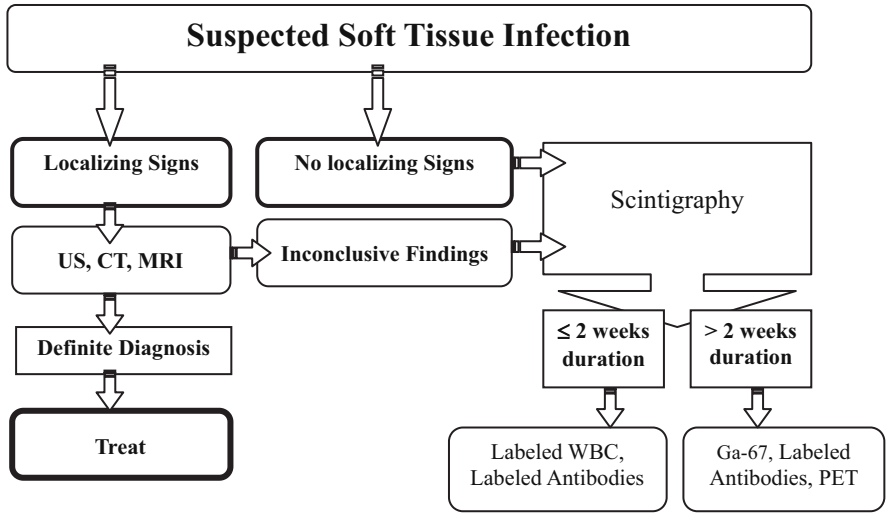

Fig. 4.17. Suggested diagnostic algorithm for soft tissue infections. Note that in case of suspected renal infection, ^{99m}Tc DMSA scan is preferred; in infections of relatively long duration, labeled WBC may be used, but if negative, ^{67}Ga or other labeled antibodies should follow before excluding chronic active infection due to possible false-negative results with labeled WBC

Table 4.7. Correlation of pathophysiological features and scintigraphic findings of infection

Pathological change at the site of infection	Scintigraphic pattern
Hyperemia	Locally increased accumulation of several radiotracers, increased flow and blood pool activity on bone scan; hyperemic pattern on delayed bone images may be present with soft tissue infection
Increased vascular permeability	Increased migration of WBCs, increased accumulation of ^{67}Ga, increased uptake of radiolabeled antibodies
Increased migration of WBCs and chemotaxis	Increased accumulation of labeled WBCs
Increased secretion of iron-containing globulin by injured and stimulated WBCs	Increased accumulation of ^{67}Ga
Localized areas of renal parenchymal damage in pyelonephritis	Areas of reduced or absent DMSA uptake
Dilatation of PC system in pyelonephritis	Prominent pelvocalyceal system on DMSA images
Formation of woven bone	Increased uptake of ^{99m}Tc-MDP with prolonged accumulation of radiotracer
Increased expression of glucose transporters on cell surface	Increased uptake of ^{18}F-FDG

4.8 Summary

Many morphological and functional imaging modalities are available to help diagnose and localize inflammation of soft tissue and bone. It is clear that no single technique is ideal in all situations. The choice depends on several factors, including whether localizing signs are present, the site of possible infection, whether anatomy is normal or altered by surgery or trauma, the duration of symptoms and signs, and the presence of other underlying diseases such as cancer. For physicians, understanding the pathophysiological changes is crucial for deciding on an appropriate diagnostic strategy. Understanding pathophysiological changes also helps the nuclear physician to recognize and explain the scintigraphic patterns of inflammatory conditions (Table 4.7 summarizes common examples). PET is currently undergoing further evaluation in the diagnosis, localization and follow-up of inflammations. Discovery of new radiopharmaceuticals that will be ideal for more specific imaging of inflammation is an important topic for future research.

References

1. Weissman G (1990) Inflammation: historical perspectives. In: Gallin JI, et al (eds) Inflammation: basic principles and clinical correlates, 2nd edn. Raven, New York, pp 5 – 13
2. Rote NSV (1998) Inflammation. In: McCance KL, Huether SE (eds) Pathophysiology, 3rd edn. Mosby, St. Louis, pp 205 – 236
3. Kumar V, Abbas A, Fausto N (1999) Robbins and Cotran, pathologic basis of disease, 7th edn. Saunders, Philadelphia, pp 47 – 86

4. Rankin JA (2004) Biologic mediators of acute inflammation. Clin Issues 15:3 – 17
5. Botting RM, Botting JH (2000) Pathogenesis and mechanisms of inflammation and pain: An overview. Clin Drug Invest 19 (Suppl 2):1 – 7
6. Hernandez-Pando R, Bornstein QL, Aguilar LD, Orozo EH, Madrigal VK, Martinez CE (2000) Inflammatory cytokine production by immunological and foreign body multinucleated giant cells. Immunology 100:352 – 258
7. Reijnen MM, Bleichrodt RP, van Goor H (2003) Pathophysiology of intra-abdominal adhesion and abscess formation, and the effect of hyaluronan. Br J Surg 90:533 – 541
8. Sirinek KR (2000) Diagnosis and treatment of intra-abdominal abscesses. Surg Infect 1:31 – 38
9. Zibari GB, Maguire S, Aultman DF, McMillan RW, McDonald JC (2000) Pyogenic liver abscess. Surg Infect 1:15 – 21
10. Greth J, Torok HP, Koenig A, Folwaczny C (2004) Comparison of inflammatory bowel disease at younger and older age. Eur J Med Res 22:552 – 554
11. Korzenik JR (2005) Past and current theories of etiology of IBD: toothpaste, worms, and refrigerators. J Clin Gastroenterol 39:s59 – 65
12. Inoue S, Nakase H, Chiba T (2005) Etiopathogenesis and aggravating factors of ulcerative colitis. Nippon Rinsho 63:757 – 762
13. Baron S, Turck D, Leplat C, Merle V, Gower-Rousseau C, Marti R, Yzet T, Lerebours E, Dupas JL, Debeugny S, Salomez JL, Cortot A, Colombel JF (2005) Environmental risk factors in paediatric inflammatory bowel diseases: a population based case control study. Gut 54:357 – 363
14. Kolls JK, Zhang Z (2005) Anti-interleukin-12 antibody for active Crohn's disease. N Engl J Med 352:627 – 628
15. Kolls JK, Zhang Z (2004) Anti-interleukin-12 antibody for active Crohn's disease. N Engl J Med 351:2069 – 2079
16. Shanahan F (2005) Physiological basis for novel drug therapies used to treat the inflammatory bowel diseases I. Pathophysiological basis and prospects for probiotic therapy in inflammatory bowel disease. Am J Physiol Gastrointest Liver Physiol 288:G417 – 421
17. Sakamoto N, Kono S, Wakai K, Fukuda Y, Satomi M, Shimoyama T, Inaba Y, Miyake Y, Sasaki S, Okamoto K, Kobashi G, Washio M, Yokoyama T, Date C, Tanaka H; Epidemiology Group of the Research Committee on Inflammatory Bowel Disease in Japan (2004) Dietary risk factors for inflammatory bowel disease: a multicenter case-control study in Japan. Inflamm Bowel Dis 11:154 – 163
18. Regueiro M, Kip KE, Cheung O, Hegazi RA, Plevy S (2005) Cigarette smoking and age at diagnosis of inflammatory bowel disease. Inflamm Bowel Dis 11:42 – 47
19. Pierik M, Yang H, Barmada MM, Cavanaugh JA, Annese V, Brant SR, Cho JH, Duerr RH, Hugot JP, McGovern DP, Paavola-Sakki P, Radford-Smith GL, Pavli P, Silverberg MS, Schreiber S, Taylor KD, Vlietinck R; IBD International Genetics Consortium (2005) The IBD international genetics consortium provides further evidence for linkage to IBD4 and shows gene-environment interaction. Inflamm Bowel Dis 11:1 – 7
20. Hatoum OA, Binion DG (2005) The vasculature and inflammatory bowel disease: contribution to pathogenesis and clinical pathology. Inflamm Bowel Dis 11:304 – 313
21. Zumla A, James DG (1996) Granulomatous infections: Etiology and classification. Clin Infect Dis 23:146 – 158
22. Fink CW, Cimaz R (1997) Early onset sarcoidosis: not a benign disease. J Rheumatol 24:174 – 177
23. Center D, McFadden R (1985) Pulmonary defense mechanisms. In: Sodeman W, Sodeman T (eds) Pathologic physiology, mechanisms of disease. Saunders, Philadelphia, pp 460 – 481
24. Mandel J, Weinberger SE (2001) Clinical insights and basic science correlates in sarcoidosis. Am J Med Sci 321: 99 – 107
25. Medical Section of the American Lung Association (1997) Diagnosis and treatment of disease caused by nontuberculous mycobacteria. Am J Respir Crit Care Med 156:S1 – 25
26. Sharma SK, Mohan A (2002) Sarcoidosis: global scenario and Indian perspective. Ind J Med Res 116:221 – 247
27. Nagai S, Shigematsu M, Hamada K, Izumi T (1999) Clinical courses and prognoses of pulmonary sarcoidosis. Curr Opin Pulmonary Med 5:293 – 298
28. Wazir JF, Ansari NA (2004) *Pneumocystis carinii* infection. Update and review. Arch Pathol Lab Med 128:1023 – 1027
29. Feldman C (2005) Pneumonia associated with HIV infection. Curr Opin Infect Dis 18:165 – 170
30. Morris A, Lundgren JD, Masur H, Walzer PD, Hanson DL, Frederick T, Huang L, Beard CB, Kaplan JE (2004) Current epidemiology of *Pneumocystis* pneumonia. Emerg Infect Dis 10:1713 – 1720
31. Al Soub H, Taha RY, El Deeb Y, Almaslamani M, Al Khuwaiter JY (2004) *Pneumocystis carinii* pneumonia in a patient without a predisposing illness: case report and review. Scand J Infect Dis 36:618 – 621
32. Medrano FJ, Montes-Cano M, Conde M, de la Horra C, Respaldiza N, Gasch A, Perez-Lozano MJ, Varela JM, Calderon EJ (2005) *Pneumocystis jirovecii* in general population. Emerg Infect Dis 11:245 – 250
33. Pinlaor S, Mootsikapun P, Pinlaor P, Phunmanee A, Pipitgool V, Sithithaworn P, Chumpia W, Sithithaworn J (2004) PCR diagnosis of *Pneumocystis carinii* on sputum and bronchoalveolar lavage samples in immuno-compromised patients. Parasitol Res 94:213 – 218
34. Beckerman C, Hoffer PB (1987) The role of gallium-67 imaging in the clinical evaluation of pulmonary disorders. In: Loken MK (ed) Pulmonary nuclear medicine. Appleton & Lange, Norwalk, p 276
35. Kasseh (1966) Pathogenesis of pyelonephritis in the kidney. In: Mostafi FK, Smith DE (eds) Williams & Wilkins, Baltimore, pp 204 – 212
36. Meguid El Nahas A, Bello Aminu K (2005) Chronic kidney disease: the global challenge. Lancet 365:331 – 340
37. White SL, Cass A, Atkins RC, Chadban SJ (2005) Chronic kidney disease in the general population. Adv Chronic Kidney Dis 12:5 – 13
38. Ronald AR, Pattullo AL (1991) The natural history of urinary infection in adults. Med Clin North Am 75:299 – 312
39. Hooton TM, Stamm WE (1997) Diagnosis and treatment of uncomplicated urinary tract infection. Infect Dis Clin North Am 11:551 – 581
40. Ronald and Harding (1997) Complicated urinary tract infections. Infect Dis Clin North Am 11:583 – 592
41. Govan A, Macfarlane P, Callander R (1988) Pathology illustrated, 2nd edn. Churchill Livingstone, Edinburgh
42. Haas DW, McAndrew M (1996) Bacterial osteomyelitis in adults: evolving considerations in diagnosis and treatment. Am J Med 101:550 – 561
43. Cierny G, Mader JT, Pennick H (1985) A clinical staging system of adult osteomyelitis. Contemp Orthop 10:17 – 37
44. Mandell GA (1996) Imaging in the diagnosis of musculoskeletal infections in children. Curr Probl Pediatr 26:218 – 237
45. Mader JT, Dhraminder M, Calhoun J (1997) A practical guide to the diagnosis and management of bone and joint infections. Drugs 54:253 – 264
46. Bonakdar-pour A, Gaines VD (1983) The radiology of osteomyelitis. Orthop Clin North Am 14:21 – 37
47. Trueta J (1959) The three types of acute hematogenous osteomyelitis: a clinical and vascular study. J Bone Joint Surg 41B:671 – 680

48. Elgazzar AH, Abdel-Dayem HM (1999) Imaging skeletal infections: evolving considerations. In: Freeman LM (ed) Nuclear medicine annual. Lippincott Williams & Wilkins, Philadelphia, pp 157 – 191
49. Elgazzar AH, Abdel-Dayem HM, Clark J, Maxon HR (1995) Multimodality imaging of osteomyelitis. Eur J Nucl Med 22:1043 – 1063
50. Torda AJ, Gottlieb T, Bradbury R (1995) Pyogenic vertebral osteomyelitis: analysis of 20 cases and review. Clin Infect Dis 20:320 – 328
51. Song KS, Ogden JA, Ganey T, Guidera KT (1997) Contiguous discitis and osteomyelitis in children. J Pediatr Orthop 17:470 – 477
52. Ring D, Wenger DR, Johnson C (1994) Infectious spondylitis in children. The convergence of discitis and vertebral osteomyelitis. Orthop Trans 18:97 – 98
53. Bauer TM, Pipperet H, Zimmerli W (1997) Vertebral osteomyelitis caused by group B streptococci [streptococcus agalactial] secondary to urinary tract infection. Eur J Microb Infect Dis 16:244 – 246
54. Perrone C, Saba J, Behloul Z, Salmon-Ceron D, Leport C, Vilde JL, Kahn MF (1994) Pyogenic and tuberculous spondylodiskitis [vertebral osteomyelitis] in 80 adult patients. Clin Infect Dis 19:746 – 750
55. Sundberg SB, Savage JP, Foster BK (1989) Technetium phosphate bone scan in the diagnosis of septic arthritis in childhood. J Pediatr Orthop 9:579 – 585
56. Vallabhajosula S (1997) Tc-99m labeled chemotactic peptides: specific for imaging infection. J Nucl Med 38:1322 – 1326
57. Chianelli M, Mather SJ, Martin-Comin J, Signore A (1997) Radiopharmaceuticals for the study of inflammatory process. A review. Nucl Med Commun 18:437 – 455
58. Datz FL, Morton KA (1992) Radionuclide detection of occult infection: current strategies. Cancer Invest 9:691 – 698
59. Corstens FHM, van der Meer JWM (1991) Chemotactic peptides: new locomotion for imaging of infection? J Nucl Med 32:491 – 494
60. Sfakianakis GN, Al-Sheikh W, Heal A, et al (1982) Comparison of scintigraphy with In-111 leukocytes and Ga-67 in the diagnosis of occult sepsis. J Nucl Med 23:618 – 626
61. Bitar RA, Scheffel U, Murphy PA, Bartlett JG (1986) Accumulation of In-111 labeled neutrophils and gallium-67 citrate in rabbit abscesses. J Nucl Med 27:1883 – 1889
62. McAfee JG, Subramanian G, Gagne G (1984) Technique of leukocyte harvesting and labeling: problems and prospectives. Semin Nucl Med 14:83 – 106
63. Peters AM (1994) The utility of Tc-99m HMPAO leukocytes for imaging infection. Semin Nucl Med 24:110 – 127
64. Datz FL (1994) Indium-111 labeled leukocytes for the detection of infection: current status. Semin Nucl Med 24: 92 – 109
65. Rubin RH, Fischman AJ, Callahan RJ, Khan BA, Keech F, Ahmed M, Wilkinson R, Strauss HW (1989) In-labeled nonspecific immunoglobulin scanning in the detection of focal infection. N Engl J Med 321:935 – 940
66. Fishman JA, Strauss HW, Fishman AJ, et al (1991) Imaging of *Pneumocystis carinii* pneumonia with In-111 labeled non-specific polyclonal IgG: an experimental study. Nucl Med Commun 12:175 – 178
67. Rubin RH, Fishman AJ (1994) The use of radiolabeled nonspecific immunoglobulin in the detection of focal inflammation. Semin Nucl Med 24:169 – 179
68. Vehling D, Neurath M, Siessmeier T, Schunk K, Bartenstein P (2000) FDG-PET, antigranulocyte-scintigraphy and hydro-MRI in the determination of bowel wall inflammation in Crohn's disease. The 47th Annual Meeting of the Society of Nuclear Medicine; June 3 – 7, 2000; St. Louis, Missouri. Abstract 41
69. Kampen WU, Jaekel C, Brenner W, Czecj N, Henze E (2000) New indications for immunoscintigraphy with ^{99m}Tc-labeled anti-granulocyte antibody fragments (*LeukoScan*) in routine diagnostics of inflammatory diseases. The 47th Annual Meeting of the Society of Nuclear Medicine; June 3 – 7, 2000; St. Louis, Missouri. Abstract 42
70. Becker W, Goldenberg DM, Wolf F (1994) The use of monoclonal antibody and antibody fragments in the imaging of infectious lesions. Semin Nucl Med 24:142 – 153
71. Becker W, Palestro CJ, Winship J, Feld T, Pinsky CM, Wolf F, Goldenberg DM (1996) Rapid imaging of infections with a monoclonal antibody fragment (Leukoscan). Clin Orthop Relat Res 329:263 – 272
72. Barron B, Hanna C, Passalaqua AM, Lamki L, Wegener WA, Goldenberg DM (1999) Rapid diagnostic imaging of acute, nonclassic appendicitis by leukoscintigraphy with sulesomab, a technetium 99m-labeled antigranulocyte antibody Fab' fragment. LeukoScan Appendicitis Clinical Trial Group. Surgery 125:288 – 296
73. Britton KE, Solanki KK, Das SS, Amaral H, Bhatnagar A, Katamihardja AHS, Malamitsi J, Moustafa H, Soroa VE, Sundram FX, Wareham DW, Padhy AK (2000) Bacterial specific imaging. [abstract] J Nucl Med 41:11P
74. Morgan JR, Williams LA, Howard CB (1985) Technetium labeled liposome imaging for deep-seated infection. Br J Radiol 58:35 – 39
75. O'Sullivan MM, Powell N, French AP, Williams KE, Morgan JR, Williams BD (1988) Inflammatory joint disease: a comparison of liposome scanning, bone scanning and radiography. Ann Rheum Dis 47:485 – 491
76. Boerman OC, Storm G, Oyen WJG, van Bloois L, van der Meer JWM (1995) Sterically stabilized liposomes labeled with In-111 to image focal infection. J Nucl Med 36: 1639 – 1644
77. Brudin LH, Valind SO, Rhodes CG, Pantin CF, Sweatman M, Jones T, Hughes JM (1994) Fluorine-18 deoxyglucose uptake in sarcoidosis measured with positron emission tomography. Eur J Nucl Med 21:297 – 305
78. Yamada S, Kubota K, Kubota R, Ido T, Tamahashi N (1995) High accumulation of fluorine-18-fluorodeoxyglucose in turpentine-induced inflammatory tissue. J Nucl Med 36:1301 – 1306
79. Taylor IK, Hill AA, Hayes M, Rhodes CG, O'Shaughnessy KM, O'Connor BJ, Jones HA, Hughes JM, Jones T, Pride NB, Fuller RW (1996) Imaging allergen-invoked airway inflammation in atopic asthma with [18-F]-fluorodeoxyglucose and positron emission tomography. Lancet 347:937 – 940
80. Ichiya Y, Kuwabara Y, Sasaki M, Yoshida T, Akashi Y, Murayama S, Nakamura K, Fukumura T, Masuda K (1996) FDG-PET in infectious lesions: the detection and assessment of lesion activity. Ann Nucl Med 10:185 – 191
81. Kapucu LO, Meltzer CC, Townsend DW, et al (1998) Fluorine-18-fluorodeoxyglucose uptake in pneumonia. J Nucl Med 39:1267 – 1269
82. Larson SM (1994) Cancer or inflammation? A holy grail for nuclear medicine. J Nucl Med 35:1653 – 1655
83. Jadvar H, Bading JR, Yu X, Conti PS (2002) Kinetic analysis of inflammation and cancer with dynamic 18F-FDG PET. J Nucl Med 43:271P
84. Hustinx R, Smith RJ, Benard F, Rosenthal DI, Machtay M, Farber LA, Alavi A (1999) Dual time point fluorine-18 fluorodeoxyglucose positron emission tomography: a potential method to differentiate malignancy from inflammation and normal tissue in the head and neck. Eur J Nucl Med 26:1345 – 1348

85. Chacko TK, Zhuang HM, Alavi A (2002) FDG-PET is an effective alternative to WBC imaging in diagnosing and excluding orthopedic infections. J Nucl Med 43:126P
86. Chacko TK, Moussavian B, Zhuang HM, Woods K, Alavi A (2002) Critical role of FDG-PET imaging in the management of patients with suspected infection in diverse settings. J Nucl Med 43:126P
87. Love C, Marwin SE, Tomas MB, Palestro CJ (2002) Improving the specificity of 18F-FDG imaging of painful joint prostheses. J Nucl Med 43:126P
88. Chacko TK, Zhuang HM, Alavi A (2002) Increased uptake at the tip of total hip prosthesis on FDG-PET is a non-specific sign. J Nucl Med 43:342P
89. Love C, Bhargava KK, Afriyie MO, Pugliese PV, Palestro CJ (2002) FDG as a screening test in patients with painful joint prostheses: a comparison with 3-phase bone scintigraphy. J Nucl Med 43:343P
90. El-Zeftawy H, LaBombardi V, Dakhel M, Heiba S, Adbel Dayem H (2002) Evaluation of 18F-FDG PET imaging in diagnosis of disseminated *Mycobacterium avium* complex (DMAC) in AIDS patients. J Nucl Med 43:127P
91. Liu RS, Shei HR, Feng CF, Chang CP, Liao SQ, Yeh SH (2002) Combined 18F-FDG and 11C-acetate PET imaging in diagnosis of pulmonary tuberculosis. J Nucl Med 43:127P
92. Liu RS, Shei HR, Chu YK, Liao SQ, Chang CW, Chou KL, Yeh SH (2002) The prognostic value of 18F-fluoromisonidazole PET scan in patients with tuberculosis therapy. J Nucl Med 43:127P
93. Buck AK, Reuter S, Schirrmeister H, Manfras B, Juengling FD, Kotzerke J, Kern P, Reske SN (2002) FDG-PET for assessment of viability of *Echinococcus multilocularis*. J Nucl Med 43:128P
94. Yamada S, Kubota K, Kubota R, Ido T, Tamahashi N (1995) High accumulation of fluorine-18-fluorodeoxyglucose in turpentine-induced inflammatory tissue. J Nucl Med 36:1301 – 1306
95. Nelson CA, Wang JQ, Leav I, Crane PD (1996) The interaction among glucose transport, hexokinase and glucose 6-phosphate with respect to ^{3}H-2-deoxyglucose retention in murine tumor models. Nucl Med Biol 23:533 – 541
96. Men S, Akhan O, Koroglu M (2002) Percutaneous drainage of abdominal abscess. Eur J Radiol 43:204 – 218
97. Petri A, Hohn J, Hodi Z, Wolfard A, Balogh A (2002) Pyogenic liver abscess – 20 years' experience. Comparison of results of treatment in two periods. Langenbecks Arch Surg 387:27 – 31
98. Bulger EM, McMahon K, Jurkovich GJ (2003) The morbidity of penetrating colon injury. Injury 34:41 – 46
99. Capitan Manjon C, Tejido Sanchez A, Piedra Lara JD, Martinez Silva V, Cruceyra Betriu G, Rosino Sanchez A, Garcia Penalver C, Leiva Galvis O (2003) Retroperitoneal abscesses – analysis of a series of 66 cases. Scand J Urol Nephrol 37:139 – 144
100. Wu CW, Hsiung CA, Lo SS, Hsieh MC, Shia LT, Whang-Peng J (2004) Randomized clinical trial of morbidity after D1 and D3 surgery for gastric cancer. Br J Surg 91:283 – 287
101. Haraldsen P, Andersson R (2003) Quality of life, morbidity, and mortality after surgical intensive care: a follow-up study of patients treated for abdominal sepsis in the surgical intensive care unit. Eur J Surg Suppl 23 – 27
102. Kaplan GG, Gregson DB, Laupland KB (2004) Population-based study of the epidemiology of and the risk factors for pyogenic liver abscess. Clin Gastroenterol Hepatol 2:1032 – 1038
103. Tunuguntla A, Raza R, Hudgins L (2004) Diagnostic and therapeutic difficulties in retroperitoneal abscess. South Med J 97:1107 – 1109
104. Morales CH, Villegas MI, Villavicencio R, Gonzalez G, Perez LF, Pena AM, Vanegas LE (2004) Intra-abdominal infection in patients with abdominal trauma. Arch Surg 139:1278 – 1285
105. Rubin RH, Fischman AJ (1996) Radionuclide imaging of infection in the immunocompromised host. Clin Infect Dis 22:414 – 422
106. Datz FL (1996) Abdominal abscess detection: gallium, In-111 and Tc-99m labeled leukocytes and polyclonal and monoclonal antibodies. Semin Nucl Med 26:51 – 64
107. Kao CH, Wang JL, Liao SQ, Wang SJ (1992) Tc-99m HMPAO labeled WBCs in the detection of occult sepsis in the intensive care unit. Intensive Care Med 18:15 – 19
108. Minoja G, Chiaranda M, Fachinetti A, Raso M, Dominioni L, Torre D, De Palma D (1996) The clinical use of Tc-99m labeled WBC scintigraphy in clinically ill surgical and trauma patients with occult sepsis. Intensive Care Med 22:867 – 871
109. Yang MD, Jeng LB, Kao A, Lin CC, Lee CC (2003) C-reactive protein and gallium scintigraphy in patients after abdominal surgery. Hepatogastroenterology 50:354 – 356
110. Bleeker-Rovers CP, Boerman OC, Rennen HJ, Corstens FH, Oyen WJ (2004) Radiolabeled compounds in diagnosis of infectious and inflammatory disease. Curr Pharm Des 10:2935 – 2950
111. Wiesner W, Steinbrich W (2003) Imaging diagnosis of inflammatory bowel disease. Ther Umsch 60:137 – 144
112. Shah DB, Cosgrove M, Rees JIS, Jenkins HR (1997) The technetium white cell scan as an initial imaging investigation for evaluating suspected childhood inflammatory bowel disease. J Pediatr Gastroenterol Nutr 25:524 – 528
113. Papos M, Varkonyi A, Lang J, Buga K, Timar E, Polgar M, Bodi I, Csernay L (1996) HM-PAO-labeled leukocyte scintigraphy in pediatric patients with inflammatory bowel disease. J Pediatr Gastroenterol Nutr 23:547 – 552
114. Kerry JE, Marshall C, Griffiths PA, James MW, Scott BB (2003) Technetium-99m leukoscan imaging in inflammatory bowel disease [abstract]. Nucl Med Commun 24:333
115. Siemon JK, Siegfried GF, Waxman AD (1978) The use of Ga-67 in pulmonary disorders. Semin Nucl Med 3: 235 – 249
116. Woolfenden JM, Corrasquillo JA, Larson SA, Simmons TJ, Masur H, Smith PD, Shelhamer JH, Ognibene FP (1987) Acquired immunodeficiency syndrome: Ga-67 citrate imaging. Radiology 162:383 – 387
117. Tuazon CU, Delaney MD, Simon GL, Witorsch P, Varma PM (1985) Utility of gallium-67 scintigraphy and bronchial washings in the diagnosis and treatment of *Pneumocystis carinii* pneumonia in patients with the acquired immune deficiency syndrome. Am Rev Resp Dis 132: 1087 – 1092
118. Moinuddin M, Rackett J (1986) Gallium scintigraphy in the detection of amiodarone lung toxicity. Am J Radiology 147:607 – 609
119. Coak PS, Datz FL, Disbro MA, Alazaraki N, Taylor A (1984) Pulmonary uptake in indium-111 leukocyte imaging: clinical significance in patients with suspected occult infections. Radiology 150:557 – 561
120. Little PJ, McPherson DR, De Wardener HE (1965) The appearance of the intravenous pyelogram during and after acute pyelonephritis. Lancet 1:1186 – 1188
121. Conway JJ (1988) Role of scintigraphy in urinary tract infection. Semin Nucl Med 18:308 – 319
122. Mackenzie JR (1996) A review of renal scarring in children. Nucl Med Comm 17:176 – 190
123. Traisman ES, Conway JJ, Traisman HS, Yogev R, Firlit C, Shkolnik A, Weiss S (1986) The localization of urinary

tract infection with Tc-99m glucoheptonate scintigraphy. Pediatr Radiol 16:403 – 406
124. Hellerstein S (2000) Long term consequences of urinary tract infections. Curr Opin Pediatr 12:125 – 128
125. Lin KY, Chiu NT, Chen MJ, Lai CH, Huang JJ, Wang YT (2003) Acute pyelonephritis and sequelae of renal scar in pediatric first febrile urinary tract infection. Pediatr Nephrol 18:362 – 365
126. Chiou YY, Wang ST, Tang MJ, Lee BF, Chiu NT (2001) Renal fibrosis: prediction from acute pyelonephritis focus volume measured at 99mTc dimercaptosuccinic acid SPECT. Radiology 221:366 – 370
127. Wang Yu-Tai, Chiu Nan-Tsing, Chen Mei-Ju, Huang Jeng-Jong, Chou Hsin-Hsu, Chiou Yuan-Yow (2005) Correlation of renal ultrasonographic findings with inflammatory volume from dimercaptosuccinic acid renal scans in children with acute pyelonephritis. J Urol 173:190 – 194
128. Bykov S, Chervinsky L, Smolkin V, Helevi R, Garty I (2003) Power Doppler sonography versus Tc99m DMSA scintigraphy for diagnosing acute pyelonephritis in children: are these two methods comparable? Clin Nucl Med 28:198 – 203
129. El Hajjar M, Launay S, Hossein-Foucher C, Foulard M, Robert Y (2002) Power Doppler sonography and acute pyelonephritis in children: comparison with Tc-99m DMSA scintigraphy. Arch Pediatr 9:21 – 25
130. Dacher JN, Pfister C, Monroc M, Eurin D, LeDosseur P (1996) Power Doppler sonographic pattern of acute pyelonephritis in children: Comparison with CT. Am J Roentgenol 166:1451 – 1455
131. Sakarya ME, Arslan H, Erkoc R, Bozkurt M, Atilla MK (1998) The role of power Doppler ultrasonography in the diagnosis of acute pyelonephritis. Br J Urol 81:360 – 363
132. Majd M, Nussbaum Blask AR, Markle BM, Shalaby-Rana E, Pohl HG, Park JS, Chandra R, Rais-Bahrami K, Pandya N, Patel KM, Rushton HG (2001) Acute pyelonephritis: comparison of diagnosis with Tc-99m DMSA SPECT, spiral CT, MR imaging and power Doppler US in an experimental pig model. Radiology 218:101 – 108
133. Pennington DJ, Lonergan GJ, Flack CE, Waguespack RL, Jackson CB (1996) Experimental pyelonephritis in piglets; diagnosis with MRI imaging. J Radiol 201:199 – 205
134. Lonergan GJ, Pennington DJ, Morrison JC, Haws RM, Grimley MS, Kao TC (1999) Childhood pyelonephritis: comparison of gadolinium-enhanced MR imaging and renal cortical scintigraphy for diagnosis. Radiology 207: 377 – 384

5 Nuclear Hematology

Kshitish C. Das

5.1 Introduction

Nuclear hematology deals with the use of radionuclides or radiopharmaceutical agents in the study of the pathophysiology, diagnosis and therapy of hematological diseases arising de novo in the hematopoietic tissues or as a consequence of some systemic diseases. This practice virtually began in 1940, when John Lawrence first used ^{32}P to treat a young patient with chronic myeloid leukemia [1]. This was followed by the use of ^{32}P as a radioactive label for red cells to measure blood volume [2]. From these modest beginnings, nuclear hematology has come a long way and evolved into a contemporary discipline as a very useful and often an essential investigative tool in many areas of hematology. Radionuclides are now widely used to label the formed elements of the blood (random labels) to trace their biological distribution, function and life span in vivo as well as to study the proliferation and differentiation of hematopoietic progenitor and precursor cells in the bone marrow (cohort labels). The other major applications of nuclear hematology include the determination of spleen size, splenic sequestration of blood cells and investigations relating to the absorption, metabolism and utilization of hematopoietic nutrients such as iron, vitamin B_{12} and folate.

Many imaging techniques are being increasingly employed and explored in order to determine the anatomical distribution of hematopoietic tissues in the bone marrow and other organs, and to evaluate their significance in the diagnosis and management of various hematological disorders. This chapter reviews the pathophysiological basis of the important applications of radiopharmaceuticals and radio-isotopes in the practice of hematology.

5.2 Hematopoiesis and Hematopoietic Tissues

Hematopoiesis is a complex biological process which represents a unique paradigm of developmental biology and ontogeny in a replicating mesenchymal cell system – the hematopoietic system. The various blood cells develop from the stem cells by multiplication, differentiation, orderly maturation and release of mature cells from the bone marrow to the peripheral circulation. A dynamic equilibrium is maintained between cell death in peripheral circulation and compensatory production of these cells in the bone marrow, creating a steady state of "normal blood cell numbers" in physiological conditions.

The circulating blood cells, i.e., the red blood cells, leukocytes and platelets, are highly specialized cells with distinctive morphology (structures) and functions. They are end-stage cells of their respective lineages and are destined to be lost from the circulation

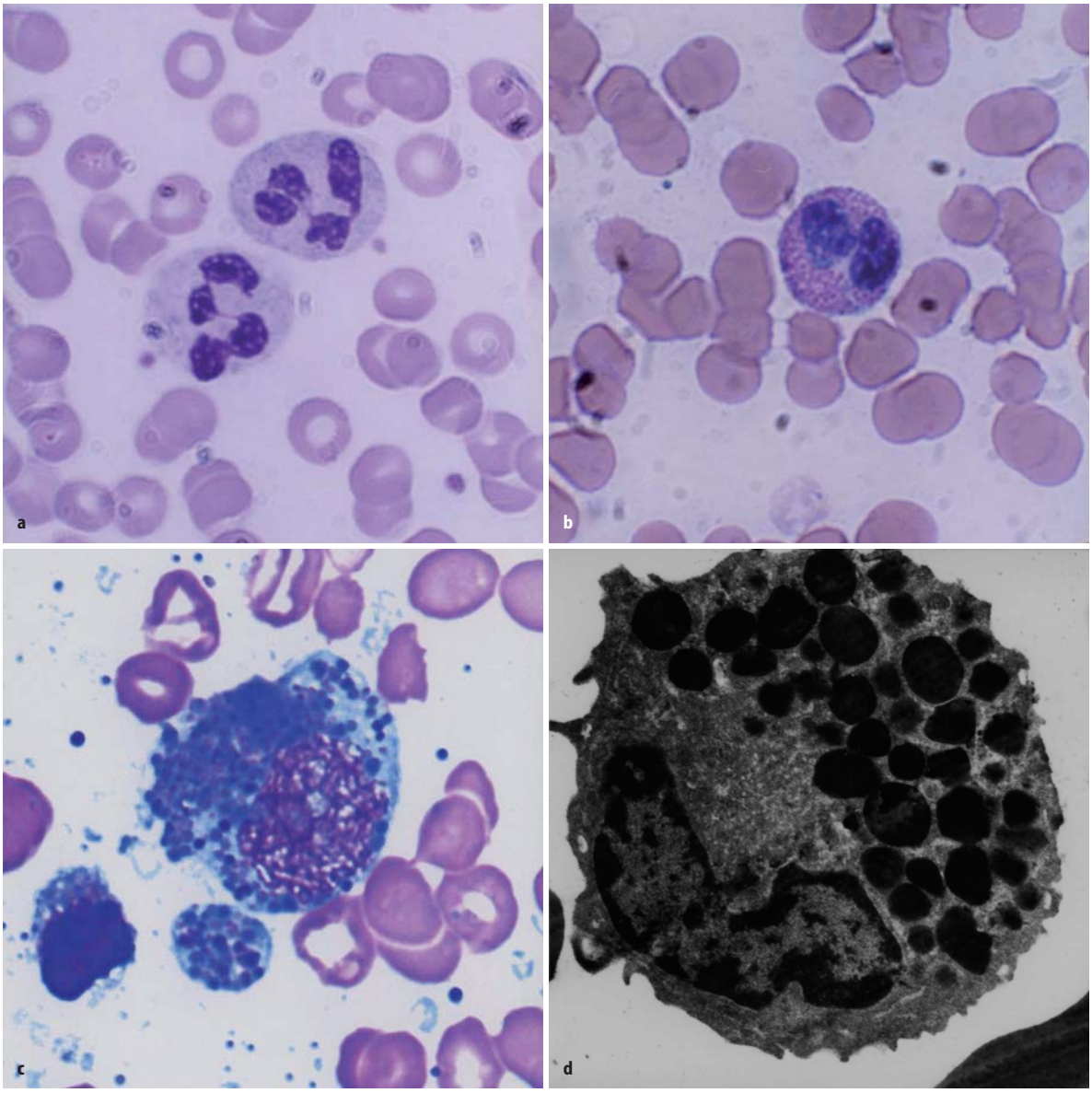

Fig. 5.1. a Neutrophilic polymorphonuclear leukocytes showing predominantly secondary or specific granules, which are fine and neither basophilic nor eosinophilic (neutral). Romanovsky stain. **b** Eosinophil, which is a polymorphonuclear leukocyte containing large eosinophilic prominent granules in the cytoplasm. Romanovsky stain. **c** Basophils, which are granulocytic leukocytes containing dark colored (basophilic) granules in the cytoplasm. Romanovsky stain. **d** Electron microscopic picture of an eosinophil showing a large number of intracytoplasmic granules containing electron dense crystaloid cores surrounded by lighter areas of matrix

after a relatively brief time span of hours, days or weeks. A steady state is attained, however, and the physiological range of their numbers is maintained by a continuous supply of newly formed cells (regeneration) from the blood-forming (hematopoietic) tissues.

The *red blood cells* (mature erythrocytes), each approximately 8 μm in diameter, contain hemoglobin in a reduced (ferrous) state for successful gaseous exchange in the tissues. They circulate in the vascular system as flexible biconcave discs maintaining osmotic equilibrium against high intracellular hemoglobin concentration and differential concentration gradients of intra- and extracellular potassium and sodium. The energy required for this physicochemical stability is provided by ATP generated by the anaerobic glycolytic (Embden-Meyerhoff) pathway and the hexose-monophosphate shunt pathway generating reduced coenzymes NADH and NADPH respectively.

The mature leukocytes (white blood cells) comprise two broad groups: the granulocytes and monocytes (phagocytes), and the lymphocytes (immunocytes). Normally only the mature leukocytes are found in the circulating peripheral blood. These include mature granulocytes (neutrophilic polymorphonuclear leukocytes, eosinophils and basophils) (Fig. 5.1a–c), monocytes (Fig. 5.2a,b) and lymphocytes (Fig. 5.3a,b). Both granulocytes and monocytes have phagocytic functions. With Romanovsky stain, polymorphonuclear neutrophils show faint, but fine granules (neutral) (Fig. 5.1a), eosinophils show larger spherical red or pink granules (Fig. 5.1b), whereas basophils show many dark-staining granules (Fig. 5.1c) in their cytoplasm. The monocytes and all of these granulocytes have variable degrees of phagocytic function.

The *mature neutrophils* (Fig. 5.1a) contain several types of granules and other subcellular organelles. These include *the primary or azurophilic granules and specific granules*. The *primary granules* appear at the promyelocytic stage, gradually decrease as the cells mature and contain many antimicrobial compounds which include myeloperoxidase, defensins, lysozyme, bactericidal permeability-increasing protein (BPI) and several serine proteases such as elastase, cathepsin G, proteinase 3 and others. The primary granules also contain organelles such as lysosomes, which fuse with phagocytic vesicles and deliver antimicrobial contents to the ingested organisms. *Specific granules* also called secondary granules of the neutrophils may fuse with phagocytic vesicles in inflammatory processes. The contents of these granules include lactoferrin, vitamin-B_{12}-binding proteins (transcobalamins I and III), plasminogen activator, collagenase, etc. These granules also play an important part in promoting chemotaxis and antimicrobial activities. The main functions of neutrophils consist in their mounting a protective response of the host to microbial infections. The neutrophils adhere to the endothelial cells (marginate) and then extend their cytoplasmic membrane (pseudopodia) into the endothelial cells lining the capillaries and thus emigrate into the tissues at the site of infection; the energy for this movement is generated by the activation of anaerobic glycolysis in the granulocytes. The plasma membrane of the involved neutrophils envelops the invading organisms or particles by its pseudopodia,

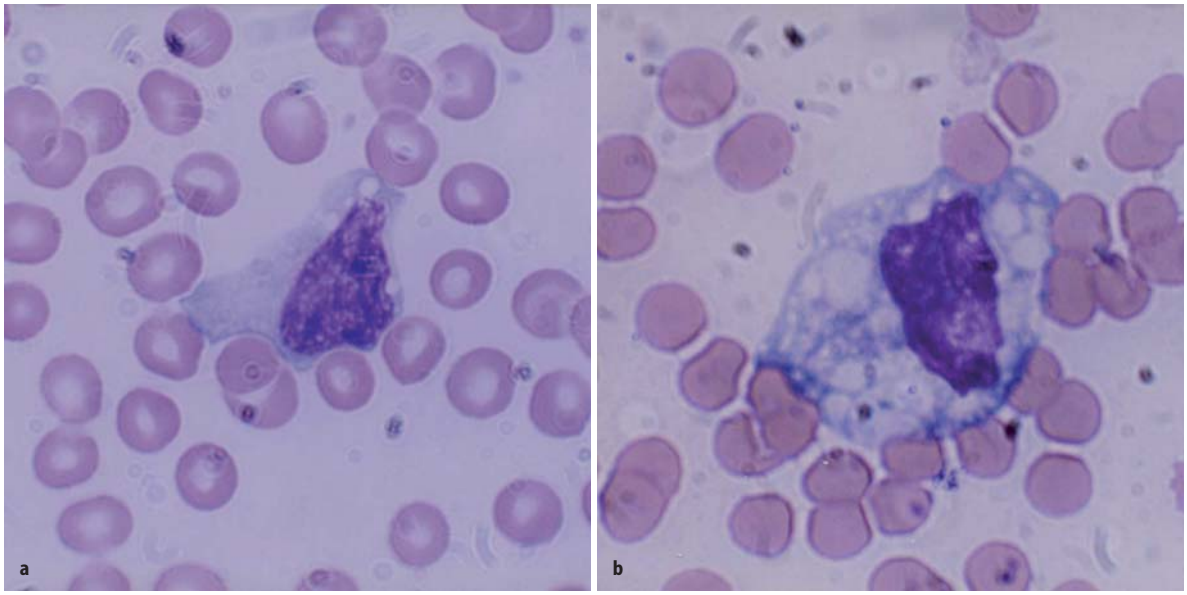

Fig. 5.2a,b. Monocyte; these are generally larger than neutrophils, have delicate fine nuclear chromatin, indistinct nucleoli and thin membrane outline. The cytoplasm is abundant with irregular outline, light blue color and a ground glass appearance

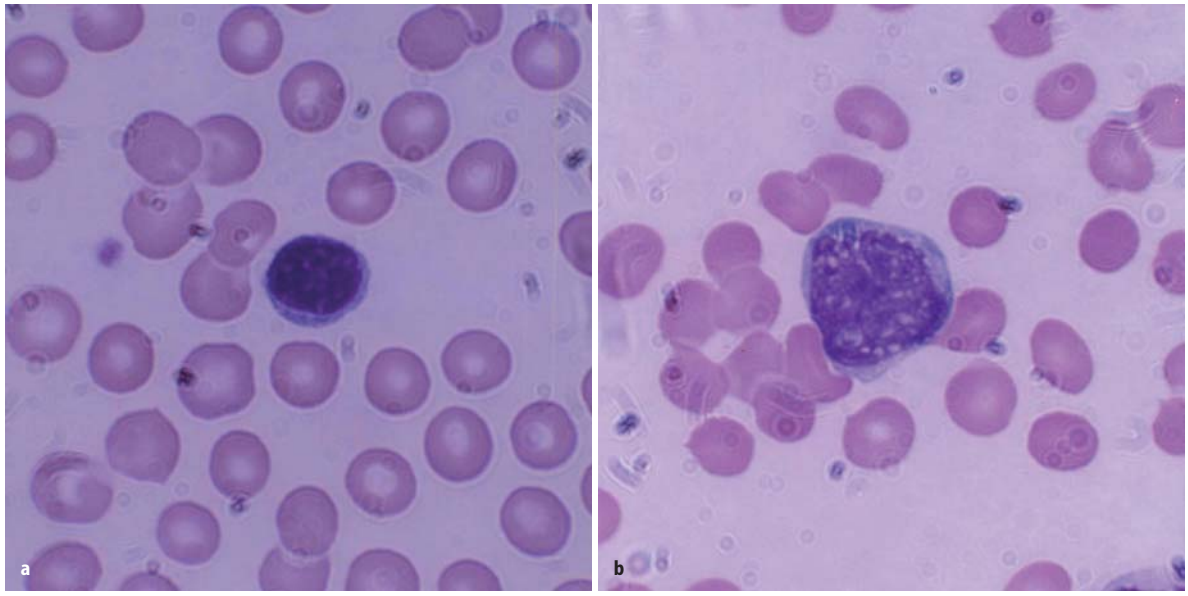

Fig. 5.3. a B-lymphocyte, which is a relatively small round mononuclear cell (8 – 10 μm in diameter), a nucleus occupying almost the whole of the cell usually with no nuclei, and a scanty cytoplasm with a bluish or moderately basophilic narrow rim of cytoplasm. **b** T-lymphocyte, which contains a dense, but uneven prominent chromatin structure with a shallow intranuclear indentation

which fuse around the organisms (phagocytosis) forming phagosomes. The phagosomes fuse with the contents of the azurophilic (primary) and specific (secondary) granules forming phagolysosomes, facilitating microbiocidal activities of the neutroplils. The phagocytosed microorganisms are killed and digested by synergistic oxidative (oxygen-dependent) and non-oxidative (oxygen-independent) reactions [3].

Eosinophils contain highly specialized and unique granules, each granule containing a rectangular or square crystalloid core surrounded by lighter matrix in electron microscopic pictures (Fig. 5.1d). These granules contain a major basic protein (MBP) in the core, several other eosinophilic cationic proteins (ECP) in the matrix and a number of proinflammatory cytokines. Eosinophils participate in allergic reactions, in defense against parasitic infections and removal of antigen-antibody complexes. These cationic proteins and proinflammatory cytokines have been implicated in tissue damage that occurs in asthma and other allergic conditions.

Basophils: Human basophils are round and have irregular short surface projections and many large dark-staining granules (Fig. 5.1c). Basophils are only occasionally seen in normal peripheral blood. The ultrastructure of these mature cells generally shows electron-dense cytoplasmic granules, prominent aggregates of cytoplasmic glycogen and short, blunt irregularly distributed plasma membranes. There is no convincing evidence that mature basophils, whether in the circulation or in the tissues, retain mitotic capability, or that basophils metamorphose into “mast cells” after entering the tissues. The dark cytoplasmic granules of basophils contain heparin, histamine and minor quantities of other biogenic amines. These cells have receptors for IgE attachment.

Monocytes belong to the mononuclear phagocyte system, which comprises monocytes, macrophages and their precursors. These cells have a common origin and share similar basic morphology and functions. Monocytes are released from the bone marrow into the blood and after a variable, yet short stay of 20 – 40 h migrate to different tissues either randomly or in response to chemotactic stimuli. In the tissues, these cells transform into macrophages after activation by microorganisms or other foreign particles. Monocytes are 10 – 12 μm in diameter, generally larger than mature neutrophils. They have a large oval or indented nucleus with delicate nuclear chromatin, indistinct nucleoli and thin membrane. When stained by Romanovsky stain, the cytoplasm appears abundant often with irregular outline and gray or light blue color, giving a ground glass appearance (Fig. 5.2a,b) and may sometimes contain numerous vacuoles, and rarely fine lilac colored azure granules. The monocytes have a strong avidity for attachment to glass surfaces or polystrene beads. Like polymorphonuclear neutrophils, monoctyes are capable of ameboid movement, chemotactic activity and phagocytic and bacteriocidal functions.

Macrophages represent the tissue phase of the monocytes and are believed to arise by differentiation and transformation of emigrated blood monocytes in the tissues. Macrophages are large cells (15 – 80 μm in diameter) and irregular in shape with active ameboid

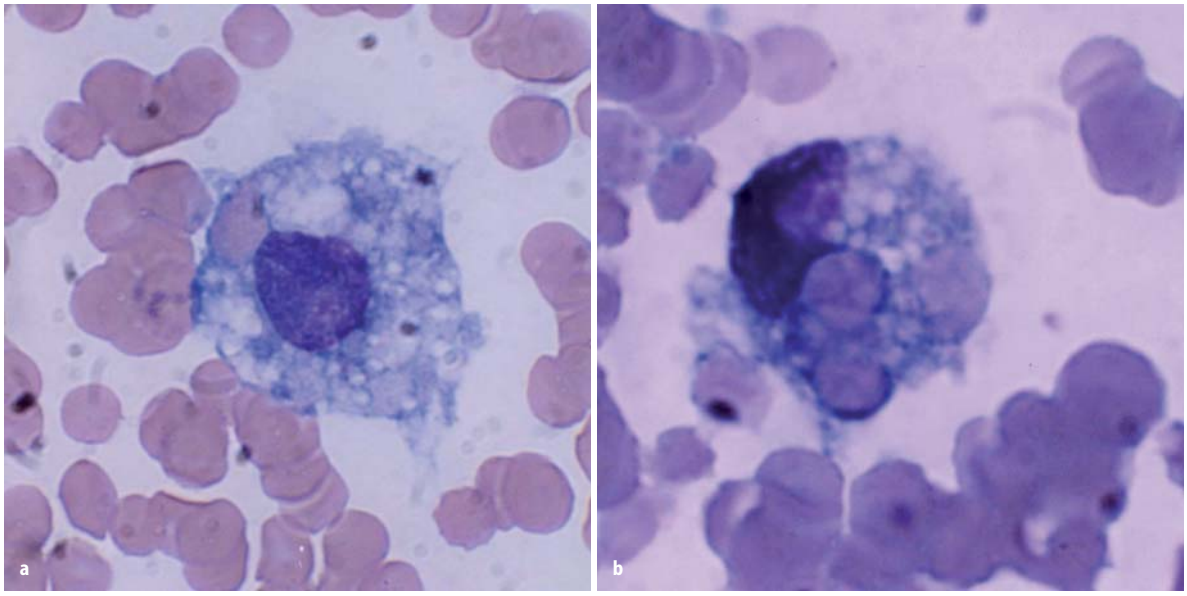

Fig. 5.4a,b. Macrophages; these are large mononuclear cells (15 – 80 μm in diameter) with an irregular cytoplasmic membrane outline suggesting ameboid mobility, finely stippled nuclear chromatin and spongy vesicular nucleus. **a** One macrophage shows phagocytosed red cells; **b** a macrophage shows several phagocytosed red cells (erythrophagocytosis)

mobility of the cytoplasm, which may contain many vacuoles. The nuclear chromatin is finely stippled, spongy and often appears vesicular. They are highly active cells with intensely powerful phagocytic and microbicidal activities. The phagocytic activity often manifests in the presence of ingested red cells inside the phagocytes (Fig. 5.4a,b).

Lymphocytes tend to offer protection to the host by more subtle processes and are also known as immunocytes. These cells are formed from lymphoid stem cells in the primary lymphoid organs (i.e., thymus and bone marrow in postnatal life and yolk sac, liver and spleen in prenatal life) independent of any antigenic stimulation, but under the influence of several non-specific cytokines. They are also formed in secondary or reactive lymphopoietic sites such as lymph nodes, spleen, lymphoid follicles of the alimentary and respiratory tracts and other diffuse lymphoid tissues in response to antigenic challenges. The majority of the blood lymphocytes are small cells (8 – 10 μm in diameter) and have condensed nuclear chromatin occupying almost the whole of the cell. No nucleolus is usually visible (Fig. 5.3a). The cytoplasm is scanty and may appear as a bluish or moderately basophilic narrow rim in a small lymphocyte, but is more abundant in large lymphocytes. When stained by Romanovsky stain, the small lymphocytes show scant or no granules, but in large lymphocytes a small number of lilac colored granules (azurophilic granules) may be seen; these granules are more numerous in the large granular lymphocytes (LGL). The latter cells are larger in size (10 – 12 μm in diameter), have pale blue more abundant cytoplasm containing peroxidase negative (azurophilic) granules and constitute 10% – 12% of the peripheral blood lymphocytes.

The lymphocytes contain some mitochondria (visible under electron microscopy) for the basic energy requirement of the resting cells (Fig. 5.5a). The lymphocytes in the peripheral blood are generally resting cells with mild or poor metabolic activities which are multiplied severalfold when these cells encounter an antigen, mitogen or an infection to which they respond by active transformation into a blastoid form – the "transformed lymphocytes" or "activated lymphocytes". These latter cells are as large as lymphoblasts, show intense pyroninophila (strongly basophilic in Romanovsky stain), prominent nuclear chromatin and one or more nucleoli (Fig. 5.6).

Lymphocytes (immunocytes) are functionally heterogeneous. The different subpopulations of immunologically competent lymphocytes have evolved in order to meet the requirements of diverse immune functions such as antigen recognition (self/non-self-discrimination), clonal selection for antibody production, cell-mediated immune functions, immunological memory and self-regulation. Broadly, B- and T-lymphocytes evolved to subserve these diverse immunological and biological activities. The various subpopulations of lymphocytes are identified and categorized by the presence of specific cell surface receptors (CD; cluster of differentiation antigens), which are detected by fluorescence-tagged specific monoclonal antibodies in a flow cytometer. B-lymphocytes are capable of synthesizing immunoglobulin (Ig) molecules, which in the

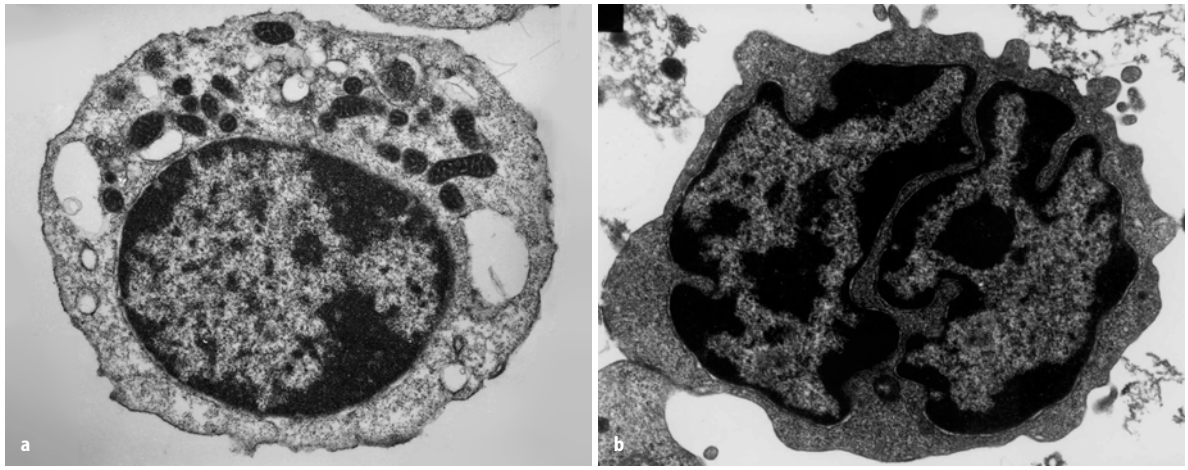

Fig. 5.5. a Transmission electron microscopic picture of a B-lymphocyte. The cell shows a small rim of cytoplasm, condensed nuclear chromatin and several mitochondia in the cytoplasm. **b** Transmission electron microscopic picture of a T-lymphocyte, showing dense heterochomatin along the nuclear membrane and euchromatin in the remaining nuclear surface. The nucleus also shows deep indentations

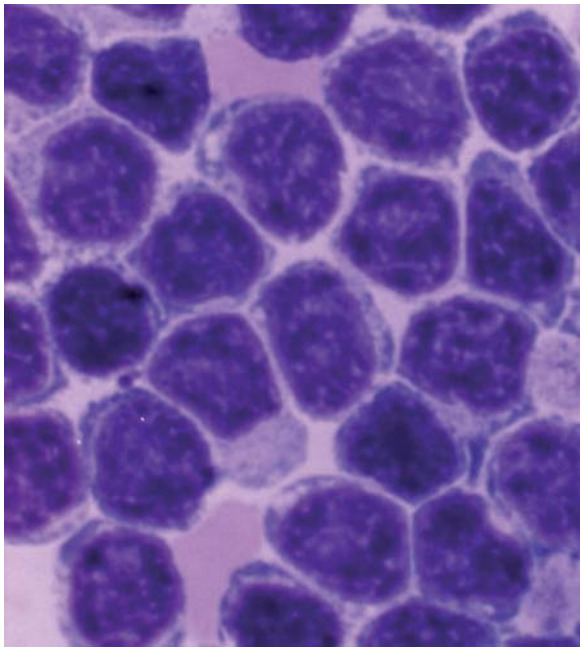

Fig. 5.6. Morphological features of "transformed lymphocytes" that were generated by phytohemagglutinin stimulation of peripheral blood lymphocytes in short-term culture for 72 h. These lymphoyctes became larger, developed cytoplasmic basophilia, and revealed prominent nuclear chromatin and nucleoli

resting phase of the lymphocytes remain attached to the cell membrane and are used as identification markers. The B-lymphocytes are believed to arise from the bone marrow stem cells in the human, whereas in avian species these cells originate in the bursa of Fabricius; an equivalent organ in the human remains unidentified.

T-lymphocytes also originate in the bone marrow stem cells; the prothymocytic T-lymphocytes acquire CD7 antigen on their cell surface and then emigrate to the thymus, where epithelial and dendritic cells provide a microenvironment for their further induction and maturation. A mature T-lymphocyte often contains a dense, but uneven prominent nuclear chromatin structure with one or more intranuclear indentations (Fig. 5.3b). The mature helper T-lymphocytes express CD4 and suppressor cells express CD8; other subpopulations of T-lymphocytes develop many other CD antigens. T-lymphocytes express cell surface receptors, $\alpha\beta$ or $\gamma\varepsilon$. Transmission electron microscopy of these cells reveals prominent basophilic cytoplasm, dense heterochromatin in the nucleus along the nuclear membrane, and euchromatin in the remaining area of the nucleus. There are also one or more deep nuclear indentations (Fig. 5.5b).

Plasma cells are a progeny of B-lymphocytes, actively synthesizing immunoglobulins under appropriate antigenic stimuli, during which they undergo morphological transformation. They can be morphologically distinguished from lymphocytes by their distinctive features. These cells are spherical or ellipsoidal in shape (5 – 25 µm in diameter) with diffusely basophilic deep blue cytoplasm, but may sometimes have a fine granular appearance. The nucleus is round or oval, often eccentrically placed, and has dense prominent, aggregated chromatin giving a "cartwheel" appearance. These cells have a well-defined perinuclear halo (clear zone) that contains the Golgi apparatus (Fig. 5.7a). The ultrastructure of plasma cells shows well developed endoplasmic reticulum, perinuclear space with Golgi apparatus (Fig. 5.7b).

The *bone marrow* is the principal hematopoietic tissue in the adult human being and contains the great majority of the hematopoietic stem cells and the hematopoietic inductive microenvironment that induces dif-

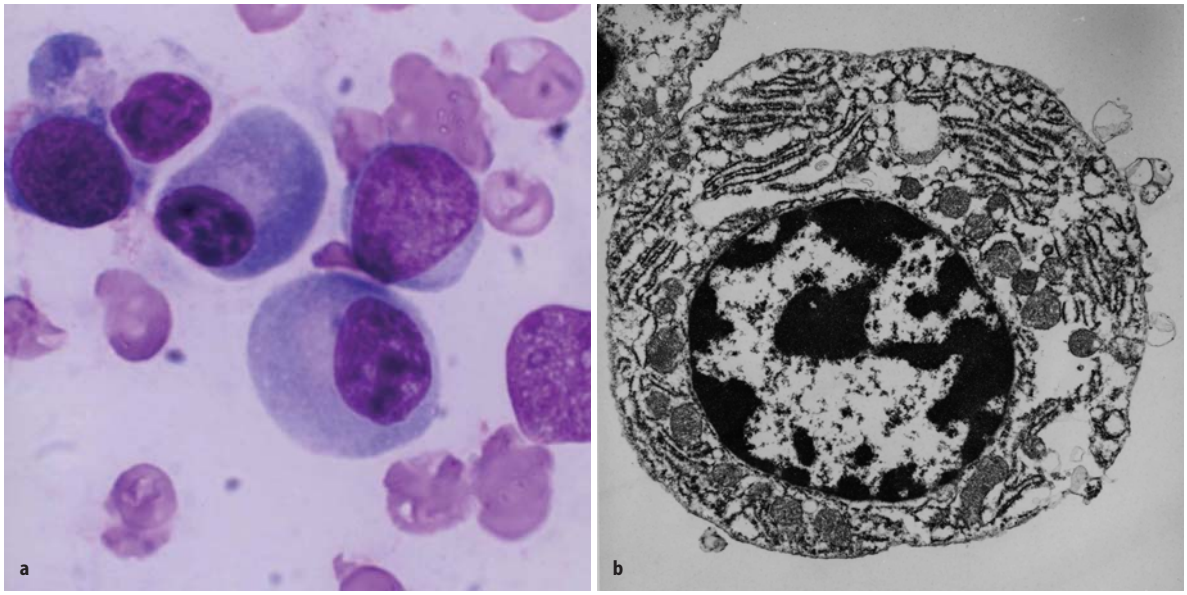

Fig. 5.7. a Light microscopic morphology of a plasma cell in Romanovsky stain. The mature plasma cell shows a strongly basophilic cytoplasm, and an eccentrically placed nucleus showing aggregated nuclear chromatin, suggesting a "cartwheel" appearance. **b** Transmission electron microscopic picture of a plasma cell showing a well-developed endoplasmic reticulum, an eccentrically placed nucleus with condensed chomatin, and a perinuclear zone with the Golgi apparatus

ferentiation of the stem cells into each blood cell type, characteristic of the diverse cell lineages such as myeloid (granulocytic, monocytic, and erythroid cell) and lymphocytic series of cells. Considerable changes are known to occur in the site and the nature of hematopoiesis at different stages of development from the embryo to the adult.

5.3 The Sites and Distribution of Prenatal and Postnatal Hematopoietic Tissue

In the embryo, blood cell formation starts in the yolk sac mesoderm as primitive "blood islands" comprising a cluster of specialized mesodermal cells. These cells align themselves into peripheral endothelial cells and centrally located cells that produce a short-lived first line of primitive hematopoietic cells, the primitive erythroblasts at 2–3 weeks of prenatal life. By the 10th week of prenatal life, a second set of hematopoietic cells develop predominantly in the liver and the spleen from the stem cells that have presumably migrated from the yolk sac mesoderm and then constitute the definitive line of hematopoietic cells (predominantly erythropoietic cells). At this point the fetal liver becomes the main site of blood formation, where erythropoiesis continues and granulopoiesis begins to appear (Fig. 5.8). The spleen is also an important organ for prenatal hematopoiesis, although it makes a much smaller contribution than the liver. Spleen and liver continue to produce blood cells until about 2 weeks before birth and make an important contribution to lymphopoiesis. From 20 weeks of fetal life on, the bone marrow becomes increasingly active in blood cell formation and it constitutes the main hematopoietic organ at birth. During the first 2–3 postnatal years, the bone marrow shows very active hematopoiesis in all bones in the body. During childhood there is a gradual replacement of active, hematopoietic (red) marrow by relatively inactive, fatty (yellow) marrow. This change starts in the diaphyses of long bones and extends towards the epiphyses. In early adulthood, active hematopoietic marrow is confined to the epiphyses of the long bones and all areas of the flat bones (axial skeleton) such as the sternum, ribs, cranium, vertebrae and pelvis. Even in these "active" hematopoietic tissues, fat cells constitute approximately half of the total marrow tissues (Fig. 5.9). The red and yellow marrow each constitutes half of the bone marrow weight. Since half of the red marrow is fatty, 75% of the total bone marrow in the adult human is virtually adipose tissue [4]. The hematopoietic cells in the red marrow gradually recede with advancing age from about 60% in the first decade to about 30% in the eighth decade of life [5]. When there is an increased need for blood cell formation in response to a hematological stress (e.g., hemolytic anemias), there is an expansion of active hematopoietic tissues to the areas containing predominantly fatty, yellow marrow and sometimes to the liver and the spleen causing "extramedullary hematopoiesis". The hematopoietic cells in the extramedullary hematopoietic foci devel-

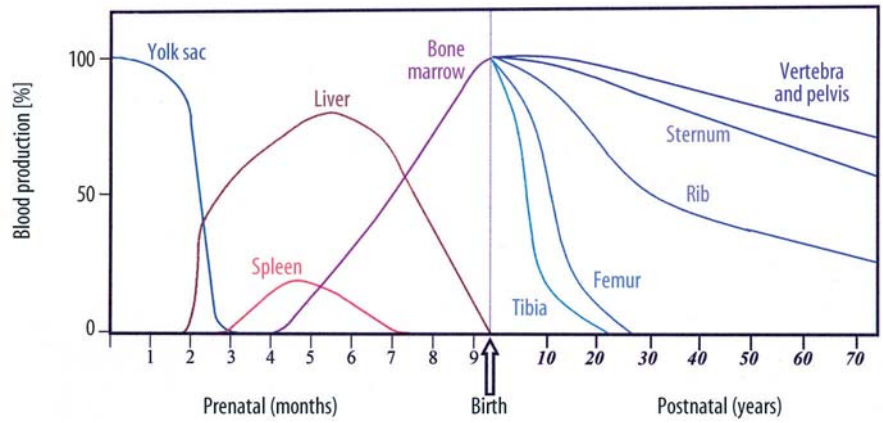

Fig. 5.8. The sites of pre- and postnatal hematopoiesis

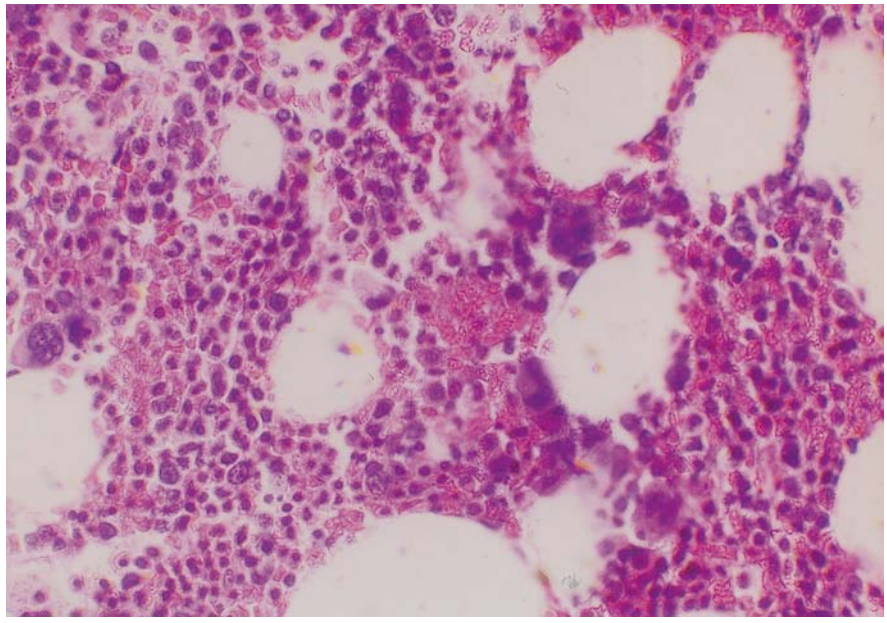

Fig. 5.9. Histological section of a bone marrow biopsy from an adult human being. At least 50% of the marrow tissue shows fat cells and approximately 50% hematopoietic cells. H & E

op from the stem cells which migrate to those sites from the bone marrow via the circulating blood [6]

Bone marrow weighs approximately 3000 g in normal adult men and 2600 g in women. There is a dual blood supply to the bone marrow consisting of a periosteal capillary network and a nutrient artery that penetrates the bony shaft and divides into multiple branches in the marrow tissue. The blood flow through the bone marrow has been estimated to be about 10 ml/min/100 cm^2 in normal volunteers, as assessed with positron emission tomography using a ^{15}O-labeled CO_2 steady-state technique. The blood flow was shown to be 2.5 – 3.5 times higher in patients with polycythemia vera (26.9 ± 4.6), chronic myeloid leukemia (25.2 ± 3.9) and myelofibrosis (35.1 ± 7.3) [6]. Blood flow was found to be in the normal range, however, in patients with aplastic anemia, chronic hemolysis, or chronic lymphatic leukemia, which would suggest that there is no direct correlation between blood flow and bone marrow cellularity [7].

5.4 Hematopoietic Growth Factors

The development of hematopoietic cells depends both on (a) the genetically programmed innate cellular processes such as proliferation and maturation, and (b) the induction and regulation of these processes by hematopoietic growth factors. A large number of these growth factors have been identified, chemically characterized and their amino acid sequences analyzed. The chromosomal locations of the responsible genes for most of them have been identified and cloned. While a comprehensive description of the cytokines is beyond the scope of this review, some general characteristics of these factors are relevant and useful to understand the functioning of the hematopoietic system. The hematopoietic growth factors (cytokines) are all glycoproteins, behave and function as hormones and share a number of common properties.

T-lymphocytes, cells of the monocyte-macrophage system, endothelial cells and fibroblasts are the major cellular sources of these growth factors in the body except for erythropoietin, which is produced predominantly in the kidneys. The biological functions of these growth factors are mediated through specific receptors on their target cells (hematopoietic cells and their precursors). They may act locally at the site of production or after they are absorbed into the circulating blood. One growth factor may act at one or more stages of hematopoietic cell maturation, and multiple factors may act on more than one stage of cell development. Several growth factors appear to exert synergistic action at multiple stages of development in the same lineage or even in more than one lineage, but in a hierarchical manner (Fig. 5.10). The growth factors not only promote the proliferation, maturation and functions of hematopoietic target cells but also inhibit the apoptosis of the target cells. The latter (i.e., apoptosis) represents a genetically programmed process of cell death that normally balances the rate of blood cell production and helps maintain a steady state. A large number of these cytokines are now available as recombinant DNA products for therapeutic and experimental applications.

5.5 Hematopoiesis and Hematopoietic Stem Cells

The factors or processes that induce the undifferentiated mesoderm to be committed to the development of multiple lineages of hematopoietic cells have only recently began to be understood in some measure. The hematopoietic cells constitute a highly efficient system of hierarchical development of multilineage blood cells with specialized structural and functional characteristics (Fig. 5.10). The pluripotent stem cells conceptually develop from the undifferentiated mesodermal cells and are characterized by their capacity for proliferation, self-maintenance or self-renewal. A replicate population of these stem cells gives rise to progenitor cells which become irreversibly committed to differentiation along one or the other hematopoietic cell lineages. These processes of cellular proliferation and differentiation appear to occur in a sequential manner and also possibly as overlapping events under the influence of a large number of hematopoietic growth factors. The flexibility inherent in these processes provides for enormous amplification of the cell systems on demand. The spleen colony-forming unit (CFU-S), a murine

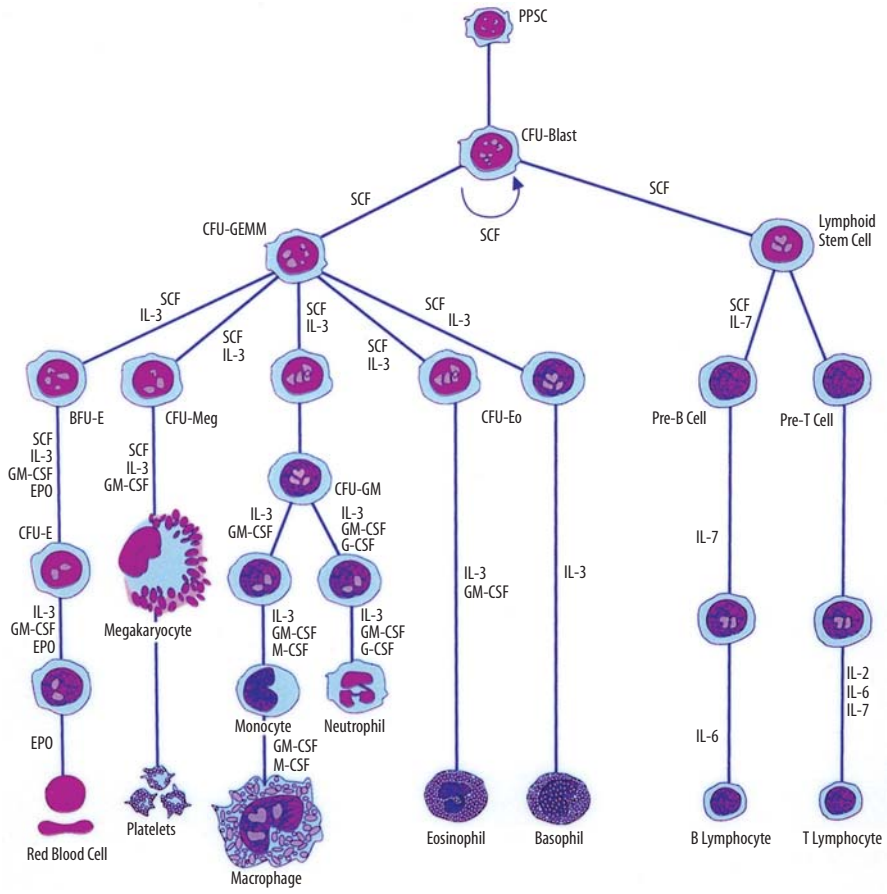

Fig. 5.10. A hematopoietic pluripotent stem cell (*PPSC*), and the different cell lineages that develop from it under the influence of various hematopoietic growth factors (cytokines) (Modified from [110] with permission)

self-renewing transplantable stem cell described by Till and McCullough [8], is conceptually closest to the pluripotent stem cells. The successful development of in-vitro colony-forming units in agar or methylcellulose-based tissue culture media supplemented by biological fluids (which contain hematopoietic growth factors) has provided a very useful system for studying the stem cells. These technical developments led to the identification of several colony-forming units such as CFU-GEMM CFU-GM, CFU-G, CFU-M, and CFU-E. These committed stem cells, in turn, generate the earliest morphologically recognizable cells in different hematopoietic cell lines (lineages) such as myeloblasts in the granulocytic, proerythroblasts in the erythroid cells (red blood cells) and promegakaryocytes in the platelet series. These progenitors, precursors and other more mature cells are held in the hematopoietic microenvironment of the stroma by numerous adhesive molecules for which appropriate receptors are present in the hematopoietic cells and also in the stromal cells (Fig. 5.11). The microenvironment plays an important and perhaps essential function in sustaining hematopoiesis. It is believed that damage to the microenvironment of the bone marrow causes irreversible impairment of growth and proliferation of hematopoietic cells and may be responsible for bone marrow failure in a subset of patients with aplastic anemia and myelofibrosis.

As the hematopoietic cells progressively grow and mature, the receptors for the adhesive protein molecules are downregulated and the cells become less adherent and more mobile. Interestingly, the development of lineage specificity of the hematopoietic cells is associated with loss of some receptors and acquisition of others. Many CFU-S, though multipotent, do not appear to have long-term repopulating capability [9]. A cell or a group of cells that provides long-term hematopoietic reconstitution of radiation-ablated bone marrow including repopulation of all myeloid and lymphoid cell lineages, are referred to as long-term hematopoietic repopulating units. These cells correspond to the totipotent or pluripotent stem cells conceptually or operationally. An in vitro assay system for hematopoietic stem cells can identify and quantify the cells in a test population that are capable of initiating long-term hematopoiesis in culture after seeding them onto irradiated stromal cell monolayers [10, 11]. These cells are referred to as long-term culture-initiating cells (LTC-IC) [10] and have been shown to grow and sustain production of multilineage progenitors of both myeloid and lymphoid series for many weeks in the presence of appropriate hematopoietic growth factors [10, 11]. Some recent reports indicate that human LTC-IC can be expanded substantially in vitro over a culture period of several weeks [12, 13].

5.6 Hematopoietic Cell Lineages

The bone marrow is normally the principal or the only site of blood cell formation in childhood and adult life in the human being. The developing hematopoietic cells grow in the stromal microenvironment outside

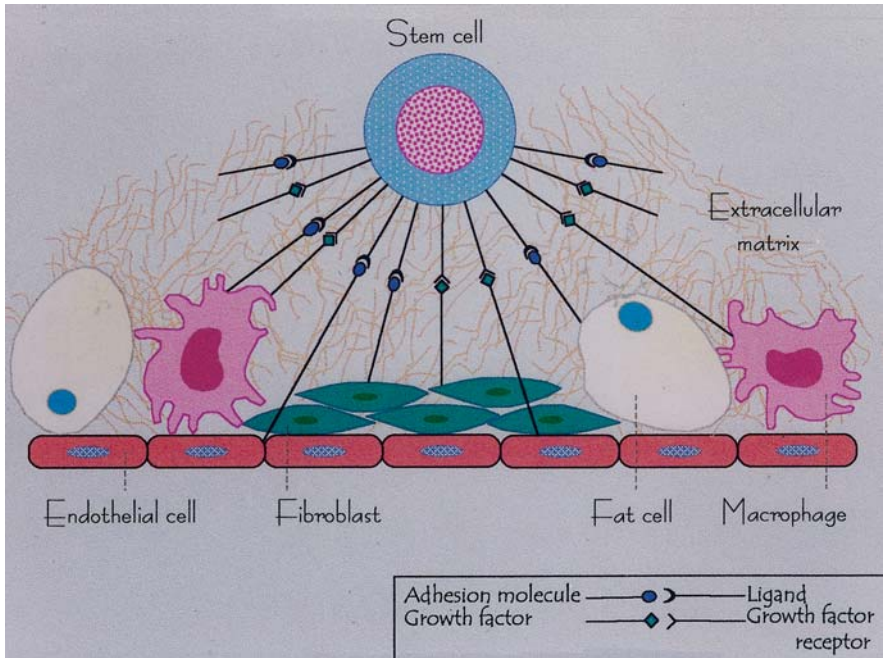

Fig. 5.11. The hematopoietic microenvironment provided by a stromal matrix on which stem cells and other hematopoietic progenitors and precursor cells divide and grow. (Modified with permission from [110])

the sinusoids in the bone marrow and when mature, are released into the sinusoidal space (microcirculation of the bone marrow) and then into the general circulation. The hematopoietic cells comprise at least four lineages: (a) the granulocytic and monocytic, (b) the erythroid, (c) the megakaryocytic and (d) the lymphoid cell lines. All of these cells apparently originate from a common stem cell (totipotent/pluripotent stem cell) which is believed to divide and differentiate initially into the multipotent stem cell – CFU-GEMM (common stem cell for granulocytic, erythroid, monocytic and megakaryocytic series) and the lymphoid stem cell (Fig. 5.10). Further division and maturation of these progenitor cells follow and these cells become irreversibly committed to differentiation along the morphologically and functionally distinctive lines of different blood cells under the influence of a number of hematopoietic growth factors and nutrients.

5.7 Erythropoiesis

The formation of mature red blood cells in the bone marrow occurs in different stages starting with the first stem cell progeny committed to erythroid differentiation and ending with the release of red cells into the circulation. The whole mass of erythroid tissue is conceived as a functional unit and is often referred to as the erythron, comprising the mature red blood cells, the morphologically recognizable erythroid precursor cells and their functionally defined (as erythroid colony-forming units) progenitors in the bone marrow. This functional concept of the erythron has contributed significantly to the understanding of the physiology and pathology of normal and abnormal erythropoiesis respectively [9]. The earliest recognizable erythroid precursor cell in the bone marrow is the proerythroblast (pronormoblast in the normal bone marrow), which in the widely used Romanovsky stain appears as a large cell with dark-blue cytoplasm, a central nucleus and prominent nucleoli. This cell undergoes several divisions (usually four) and progressive maturation to give rise to the basophilic, the polychromatic and the orthochromatic normoblasts respectively. As these cells mature they become smaller, the nuclear chromatin becomes more condensed and the cytoplasm appears increasingly more hemoglobinized. The nucleus is finally extruded from the normoblast at the orthochromatic stage and a reticulocyte is formed, which contains some ribosomal RNA and can still synthesize hemoglobin. The reticulocytes spend about 1 – 2 days in the bone marrow before they are released into the circulation, where they spend another 1 – 2 days mainly in the spleen to mature into red cells. A mature red cell is devoid of RNA and can no longer synthesize hemoglobin.

Normal human peripheral blood contains about 1% – 2% reticulocytes (i.e., 25 – 75'10^9/l) and no normoblasts. Under physiological conditions, erythropoiesis is a well-balanced process in which the rate of red cell production is regulated so as to maintain a steady state and a relatively constant red cell mass. The glycoprotein hormone, erythropoietin, which is a highly glycosylated polypeptide of 165 amino acids, is the major humoral regulator of erythropoiesis. Erythropoietin has been established as the major regulatory growth factor for erythropoiesis and is known to act on the committed erythroid stem cell – CFU-E, as well as on the other erythroid precursor cells, whereas the early stages of erythropoiesis up to the stage of BFU-E (burst-forming unit-erythroid) are independent of erythropoietin or are minimally influenced by this hormone. As cells in the CFU-E proliferate and differentiate into the red cell precursors giving rise to morphologically recognizable normoblasts of various stages (with Romanovsky stain), a number of biochemical events occur in these cells. These include increased synthesis of RNA, induction of globin gene transcription (mainly alpha and beta globin genes), increased uptake of calcium and glucose, synthesis of transferrin receptors, increased iron uptake and synthesis of red cell membrane proteins [9, 14]. Hemoglobin synthesis continues throughout all stages of maturation of erythroblasts and also persists at a very low rate in the reticulocytes after the extrusion of the nucleus.

The process of differentiation of committed erythroid cell, the colony-forming unit-erythroid (CFU-E), into the various stages of erythroid precursors (i.e., pronormoblasts and basophilic, polychromatic, orthochromatic normoblasts, reticulocytes) is associated with activation of genes for hemoglobin synthesis. Thus this process involves genes for at least three different biochemical pathways corresponding to the three essential components of the hemoglobin molecule – globin chains, protoporphyrin and iron.

5.8 Globin Chain Synthesis

There are two distinct unlinked gene clusters for the two groups of globin polypeptide chains of hemoglobin in the human. The β gene cluster (50 kb) (containing the linked genes ∈, Gγ, Aγ, δ, and β) is located on the long arm of chromosome 11, whereas the $\zeta a_2, a_1$ gene cluster is located on the short arm of chromosome 16. Like most mRNAs in the eukaryotic cells, the globin mRNAs are synthesized in a precursor form which is about three times as long as the finally processed template for protein synthesis. These precursor molecules undergo further processing in order to be converted to the final mRNA template including "capping" at the 5'

end of the molecule, polyadenylation at the 3 'end, and "splicing"; the latter process removes the intervening sequences or introns. The finally processed mRNA for globin chain synthesis contains 675 – 750 nucleotides [15]. The rate of globin chain synthesis has been shown to be regulated in a significant measure by heme [16, 17]. The presence of heme is known to stimulate globin chain synthesis in reticulocytes in vivo and in cell-free systems, and this is executed by a major effect exerted on the chain-initiation step in translation and to a smaller extent in transcription of globin mRNA or its processing [18]. In conditions associated with an absence or a deficiency of heme (e.g., iron deficiency), an inhibitor of globin chain synthesis accumulates in the system, which slows down or inhibits the rate of globin chain synthesis and functions as a rate-limiting factor [19 – 21].

5.9 Heme Synthesis

Heme is a ferrous complex of protoporphyrin IX, which is a tetrapyrrole ring compound and synthesized in the body in several sequential steps starting with the condensation of glycine and succinyl coenzyme A to yield δ-aminolevulinic acid (ALA) under the action of the enzyme ALA-synthase (ALAS) with pyridoxal-5-phosphate (vitamin B_6) as a coenzyme. The enzyme ALAS is encoded by a gene located in chromosome 3; in erythroid cells ALA synthesis is catalyzed predominantly by the erythroid-specific ALAS, which is coded by a gene located in the X chromosome. In the next step, two molecules of ALA undergo further condensation to form porphobilinogen, the primary building block for all natural tetrapyrroles. Four molecules of porphobilinogen condense through several steps of enzymatic reactions to form protoporphyrin IX in the mitochondrion, where protoporphyrin IX again combines with ferrous iron to yield ferrous protoporphyrin IX (i.e., heme). The latter reaction is catalyzed by the enzyme heme synthase (ferrochelatase) in the presence of the cofactor – pyridoxal-5-phosphate (vitamin B_6).

5.10 Some Essential Hematopoietic Nutrients

The hematopoietic cells constitute a cell renewal system, which produces a large number of cells daily to maintain the steady state of normal blood cell numbers and to meet the additional demands of increased cell production during stress. The biological processes of proliferation and maturation depend on a succession of carefully regulated biochemical events in the cells, which include turnover of DNA, RNA, and protein. These processes require a number of cofactors such as vitamin B_{12}, folate and vitamin B_6 and also minerals such as iron, cobalt, copper and manganese. While vitamin B_{12}, folate and vitamin B_6 are required for the synthesis of DNA and RNA and for interconversions of amino acids, iron is an essential constituent of hemoglobin and is necessarily for erythropoiesis. Iron is also an important component of many enzyme systems including nucleotide diphosphate reductase, which converts the substrate nucleotide diphosphate to deoxynucleotide diphosphate in the pathway for thymine DNA synthesis.

5.11 Iron Metabolism and Erythropoiesis

Iron metabolism is intimately related to hemoglobin synthesis and thus to erythropoiesis. Iron is the most abundant mineral micronutrient present in the human body. Although iron is one of the most common elements in the earth's crust, iron deficiency anemia is the most common type of anemia all over the world. The total body iron content in normal adult men is approximately 50 mg/kg body wt., and in women this is about 35 mg/kg body wt. Two-thirds of the total body iron exists as hemoglobin in the erythrocytes. Plasma iron is derived mainly from the reticuloendothelial (RE) cells and the macrophages, which acquire iron by engulfing senescent and effete erythrocytes at the end of their life span (erythrophagocytosis) (Fig. 5.4a,b). The iron so obtained as a degradation product of hemoglobin by the RE cells generally becomes deposited as ferritin and hemosiderin (siderotic granules). Although monocytes lack transferrin receptors, these cells express these receptors when they are transformed into macrophages. It is important to mention, however, that a small proportion of plasma iron comes from dietary sources after their absorption through the duodenum and jejunum. The plasma iron pool is the most important source of iron supply to the various body cells. Iron in the blood plasma is bound almost exclusively to the specific binding protein – transferrin, a β-globulin which is synthesized in the liver and has a half-life of 8 – 10 days. Transferrin is the exclusive transport protein for iron, delivering it to the cells of the erythroid series and to a smaller extent to other cells. Each molecule of transferrin can bind two atoms of iron and is normally one-third saturated with iron (i.e., transferrin saturation 33%). Normal plasma contains 2.0 – 4.0 g transferrin per liter. In an average normal subject, the plasma iron concentration is approximately 18 μmol/l (100 μg/dl) and total iron binding capacity (TIBC) is approximately 56 μmol/l (300 μg/dl). The total transferrin-bound iron in the plasma amounts to approximately 4 mg; this cycles seven times each day to provide

about 28 mg of transferrin-bound iron to be reutilized over and over again for hemoglobin synthesis and thus complete the internal iron cycle (Fig. 5.12). Transferrin delivers iron to the red cell precursors (proerythroblasts, early or basophilic normoblasts, intermediate or polychromatic normoblasts, late or orthochromatic normoblasts and reticulocytes) and to a smaller extent to other cells by binding to a specific cell surface receptor (transferrin receptor, CD71) (Fig. 5.13). Like many other receptors, the transferrin receptor is also a disulfide-linked transmembrane glycoprotein. This is encoded by a gene located in chromosome 3q26-qter [22]. Transferrin receptors can bind two types of transferrin molecules: diferric transferrin with a high affinity and monoferric transferrin with a somewhat lower affinity. As a result diferric transferrin has a competitive advantage in delivering iron to the erythrocyte precursors [23]. During erythroid maturation, the number of transferrin receptors on the cell surface increases reaching a peak in the polychromatic or intermediate normoblasts. Only a few are found on BFU-E and a few more on CFU-E. The early or basophilic normoblasts

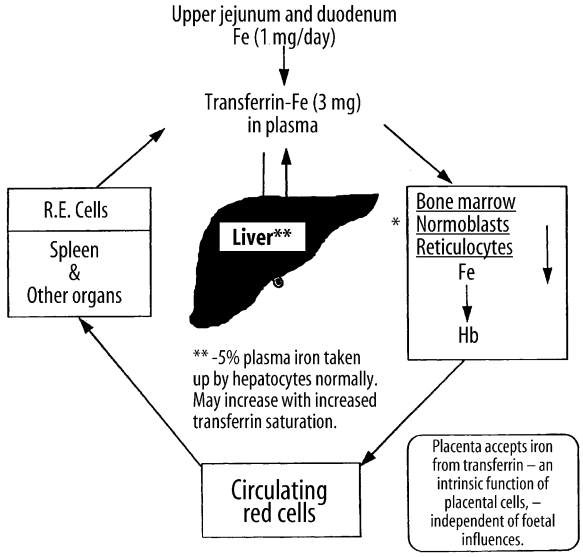

* Membrane-bound ferritin demonstrable in 50% erythroblasts (sideroblasts) by Prussian blue reaction.

Fig. 5.12. The internal metabolic cycle of iron in the human being

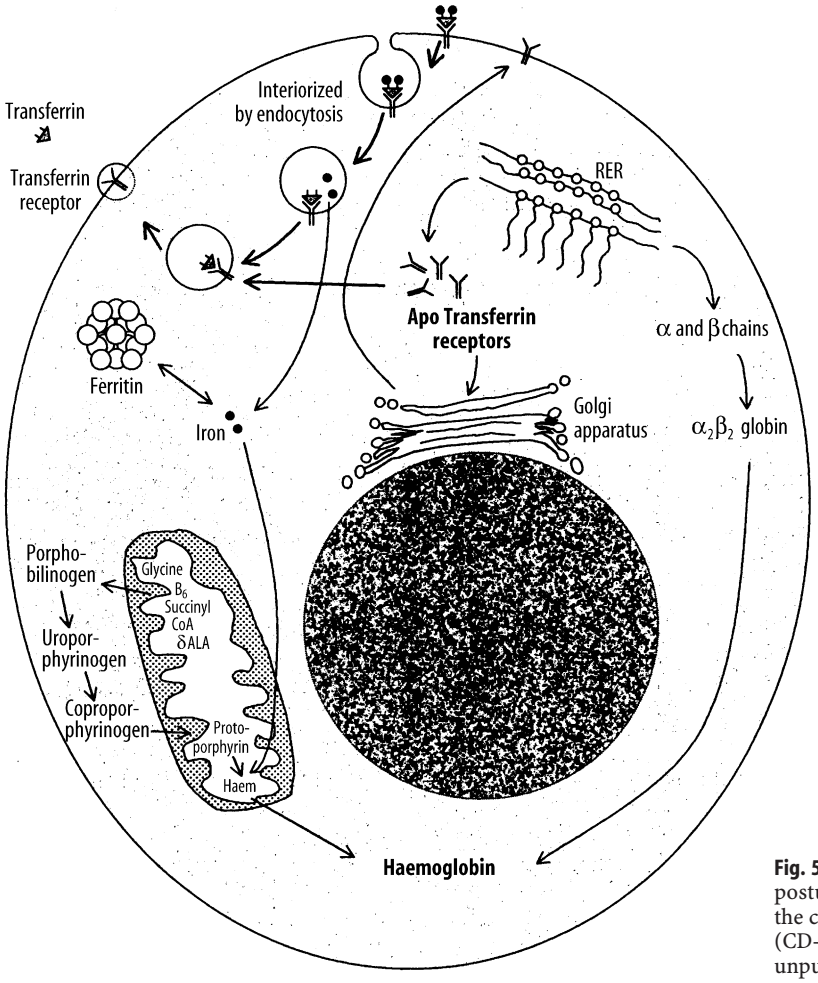

Fig. 5.13. The transferrin-iron cycle with postulated mechanism of iron uptake by the cells that have transferrin receptors (CD-71) on their cell surface (Das K.C., unpublished work)

are reported to have about 300,000 receptors on each cell increasing to about 800,000 at the polychromatic or intermediate stage. This number decreases further to about 100,000 on the reticulocytes, but with considerable variability depending on the degree of maturation of an individual reticulocyte. The rate of iron uptake by the erythroid cells is related to the number of transferrin receptors on their surface. The mature erythrocytes have very few or no transferrin receptor on their surface and, therefore, cannot take up iron from the plasma. The erythroid precursor cells appear to shed their receptors gradually as they mature possibly by proteolytic cleavage [24]. The shed (free) transferrin receptors appear in the plasma in a concentration that correlates with the rate of erythropoiesis [25, 26]. The transferrin receptors in the plasma can be quantitated with considerable accuracy. An increase in the plasma concentration of transferrin receptors is considered to be a sensitive indicator of iron deficiency.

The mechanism of transport of iron from the surface of the erythroid precursors cells to their interior is interesting and subtle. The transferrin molecules with iron bound to them form a complex with the transferrin receptors on the cell surface and are then interiorized by endocytosis into vesicles. The contents of the vesicles are then acidified and the iron is released from the complex leaving the iron-free transferrin still bound to the receptor. The iron then enters the cytosol and the vesicle containing the transferrin-receptor complex is transported back to the surface of the cell, where the neutral pH causes the release of the apotransferrin to the plasma. Normally, 80% – 90% of the iron that enters the cell is taken up by the mitochondria and is incorporated into heme. Most of the remaining iron becomes bound to ferritin and remains in storage as siderotic granules. The overall rate of entry of iron into the erythroid precursor cells is intimately related to the rate of heme synthesis [27].

5.12 Intracellular Regulation of Iron

Intracellular iron metabolism appears to be regulated by a complex mechanism which allows the cells to acquire iron as they need and to avoid the toxic effects of excess iron. They do so by regulating the synthesis of transferrin receptors and apoferritin. Cells containing adequate iron synthesize apoferritin and inhibit the synthesis of transferrin receptors, thereby limiting the cellular entry of iron; on the other hand, iron-deficient cells accelerate the synthesis of transferrin receptors and thus promote the increase of cellular entry of iron but inhibit the synthesis of apoferritin, minimizing its diversion to the storage pool. This is achieved at the transcriptional level. The mRNAs for transferrin receptors and for apoferritin contain stem-loop structures that constitute iron-responsive elements (IREs); five such IREs are present in the mRNA for transferrin receptors and one in the mRNA for apoferritin. The IREs bind the two iron-regulatory proteins (IRPs), IRP1 and IRP2 respectively. This binding produces opposite effects on the two mRNAs. While the stability of mRNA for transferrin receptor increases with consequent increased synthesis of transferrin receptors, the translation of apoferritin is inhibited.

5.13 Investigations to Evaluate the Qualitative and Quantitative Aspects of Erythropoiesis

As stated earlier in this chapter, erythropoiesis entails a number of sequential events such as (a) proliferation and maturation of erythroid cells in the bone marrow, (b) hemoglobin synthesis in these cells including in the reticulocytes and (c) release of mature erythrocytes into the circulation. However, not all erythroid precursor cells develop into mature red cells to be released into the peripheral blood even in normal individuals. It has been shown that about 5%–10% of the total erythroid precursor cells in the normal bone marrow die prematurely during maturation and are engulfed by the macrophages giving rise to ineffective erythropoiesis. These processes of premature intramedullary cell death and ineffective erythropoiesis are significantly increased in a number of hematological diseases:

1. Megaloblastic anemia due to deficiency of vitamin B_{12} and/or folate or caused by their metabolic inhibitors
2. Myelodysplastic syndrome
3. Congenital dyserythropoietic anemias
4. Myelofibrosis
5. Thalassemia major
6. Hypoplastic/aplastic anemia
7. Bone marrow infiltration by metastatic neoplasms
8. Leukemias, lymphomas, myeloma
9. Therapy with cytotoxic, antineoplastic drugs
10. Anemias associated with chronic diseases

They constitute the major pathogenetic mechanism by which anemia and other cytopenias are caused. The apparent increase of cell mass of the erythroid precursor cells in the bone marrow yielding a decreased myeloid: erythroid ratio (often referred to as increased total erythropoiesis) contrasts with the decreased output of mature red cells into the circulation in most of these disorders with a few exceptions: For example, hypoplastic and aplastic anemias are characterized by a marked decrease of bone marrow cells involving all cell lines including erythroid precursor cells with a conse-

quent decreased output of all mature blood cells including red blood cells (i.e., ineffective erythropoiesis). Although the etiology and mechanism(s) of bone marrow failure in these disorders may vary, the final outcome is similar and is manifested as ineffective hematopoiesis (and erythropoiesis) with the development of pancytopenia in the peripheral blood.

There are several biochemical markers of ineffective erythropoiesis which often provide useful indications for diagnosis. These include elevated serum level of unconjugated bilirubin (i.e., breakdown products of hemoglobin), high serum level of lactate dehydrogenase (LDH) with a preponderance of the anodic fraction LDH_1, which is released as a result of increased intramedullary destruction of red cell precursors cells. The morphological examination of the bone marrow shows hyperplasia of erythroid precursor cells (erythroid hyperplasia) with a low reticulocyte count in the peripheral blood indicating ineffective erythropoiesis. These bone marrow changes explain the ferrokinetic findings of rapid plasma iron clearance with poor iron incorporation into the red blood cells. However, in hypoplastic and aplastic anemias plasma iron clearance is slower than normal, but the fraction of injected radioactive iron incorporated into the newly formed red cells is reduced because of the reduced quantum of red cells produced in the bone marrow; this disorder is, therefore, associated with both anatomical and functional reduction or failure of erythropoiesis.

The metabolic cycle of iron is intimately related to hemoglobin synthesis and erythropoiesis. The use of radionuclides in studying iron metabolism helps in tracing the movement of iron in the metabolic cycle, and can monitor the transport of iron, its uptake by hematopoietic tissue in the bone marrow and other organs, and the site, quantum and nature of erythropoiesis. Radioactive iron (^{59}Fe) is used to study the following aspects of iron metabolism and the kinetics of erythropoiesis (ferrokinetics):

1. The gastrointestinal absorption of iron
2. The distribution of ^{59}Fe radioactivity following intravenous injection of a standard dose of radioactive iron
3. The imaging of radioactive iron uptake by the bone marrow and other organs

5.14 Iron Absorption

The assessment of absorption of orally administered iron by the gastrointestinal tract constitutes theoretically a very important component of the study of iron status and iron metabolism in a patient. A small quantity of radioactive iron (^{59}Fe) usually in the form of ferric chloride, mixed and diluted with nonradioactive iron ($FeSO_4$, $7H_2O$) and a reducing agent (such as ascorbic acid) in a known volume of aqueous solution, is administered by mouth to the patient after an overnight fast; the patient is not allowed to take anything by mouth for a further 3 h after the oral test dose of radioactive iron. The subsequent part of the procedure is cumbersome and involves collection of feces passed by the patient during the following 7 days or so and measuring the radioactivity of the radio-iron excreted in the stool in a gamma scintillation counter against a control solution of 1 ml of the radioactive iron solution which is given to the patient to drink at the onset of the test. The absorption of iron is calculated as the difference between the intake of radioactive iron and its excretion in stool collected for a week after the test, and is expressed as the percentage of ingested radio-iron retained.

As stated earlier in this chapter, ingested iron is absorbed by the mucosa of the duodenum and jejunum by mechanisms that are complex and only partially understood. The rate of absorption is affected by a host of factors including the nature of the diet, the presence of chelators, reducing agents, and other interacting factors, intestinal mobility and function, and the state of erythropoiesis. Because of these dietary and biological variables, the interpretation of absorption data based on a small test dose of soluble inorganic iron is difficult in the context of deficiency or disorders of iron metabolism. The average iron absorption in normal subjects is reported to vary between 10% and 30% of the ingested test dose; in iron-deficient states the absorption is markedly increased depending on the severity of deficiency and perhaps the degree of transferrin saturation. The validity of the results of iron absorption tests also depends on the reliability of complete collection of stool samples until $< 1\%$ of the ingested radioactivity is excreted in 1 day's collection of stool samples. For these reasons, the oral absorption test for iron is not considered to be of much clinical convenience and value, and it is sparingly used in clinical conditions.

5.15 Ferrokinetics

Iron-turnover studies with intravenously injected radio-iron (^{59}Fe) provide the best obtainable indications of the movement of iron in the metabolic cycle, of the degree of total erythropoietic activity and of the intensity of effective and ineffective erythropoiesis. However, injected iron is also taken up to some extent by the RE cells in the liver, spleen and bone marrow, where it may be deposited as storage iron in the form of ferritin and hemosiderin, and also by the circulating reticulocytes. The ferrokinetic data yield several types of semiquantitative and quantitative information:

1. Plasma iron clearance (i.e., the clearance of injected radio-iron from the plasma)
2. Plasma iron turnover [28] or plasma iron transport rate (PIT) [29]
3. Iron utilization by newly formed red blood cells (RCU)
4. Surface counting to measure the uptake and turnover of iron by various structures and organs (i.e., sacrum, liver and spleen)
5. Erythrocyte (red blood cell) iron turnover (EIT)

In these studies, approximately 5–10 ml of plasma is obtained aseptically from freshly collected heparinized blood of the patient. Radioactive iron (^{59}Fe) in the form of ferric chloride is added to the plasma, which is then incubated at room temperature for about 15 min. The radio-iron becomes bound to the plasma transferrin, which is then injected intravenously into the patient. A 2-ml sample of blood is collected from the patient at 5 min, and another four to five samples are collected into heparin or EDTA at intervals of 15 min for 1–2 h after the injection of radio-iron, then one sample daily for 10–15 days thereafter with heparin or EDTA as anticoagulant. The ^{59}Fe radioactivity in the plasma and red cells of these samples is measured and the plasma iron concentration and volume of packed red cells (VPRC) are determined.

5.15.1 Plasma Iron Clearance

The radioactivities of ^{59}Fe in the plasma samples collected at different intervals are plotted on the *y*-axis and the time intervals (minutes) on the *x*-axis on log-linear graph paper. The radioactivity at the time of radio-iron injection is derived by extrapolation of the initial slope to zero. The time taken for the plasma radioactivity to decrease to half (50%) of its initial level ($T^1/2$) plasma clearance is derived from this graph (Fig. 5.14). The plasma iron clearance rate is related largely to the mass of erythroid cell population in the bone marrow and, therefore, apparently to the total erythropoietic activity and to some extent to the activity of the RE cell system in the liver, spleen and bone marrow. It has been estimated that approximately 90% of all body transferrin receptors are normally in the erythron and the remaining 10% are mainly in the liver. In normal individuals in the steady state, ^{59}Fe plasma clearance (^{59}Fe T½) varies considerably. Our own studies of 25 clinically and hematologically normal subjects have shown that

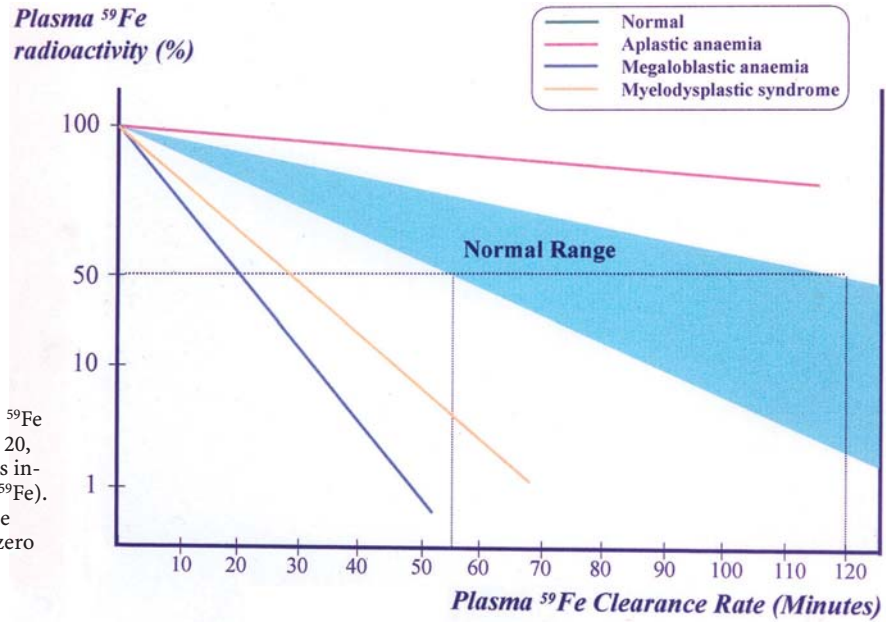

Fig. 5.14. Plasma iron clearance. ^{59}Fe radioactivity in plasma at 5, 10, 20, 30, and 60 min after intravenous injection of a dose of radio-iron (^{59}Fe). The T½ is the time in which ^{59}Fe activity declined to 50% of the zero time radioactivity

Table 5.1. Ferrokinetic patterns in various types of hematological disorders (Das K.C., unpublished data) (*PIT* plasma iron turnover, *RCU* red cell iron utilization, *EIT* erythrocyte iron turnover)

[a] Figures in parentheses indicate average values

	Plasma ^{59}Fe clearance (T½, min)[a]	PIT (mg/day/dl)	Maximum RCU (%)	EIT (mg/day/dl)
Normal	55–125 (75)	0.65–0.76 (0.71)	80–90 (85)	0.51–0.66 (0.58)
Aplastic anemia	180–360 (250)	0.60–0.75 (0.60)	14–20 (14)	0.09–0.25 (0.12)
Megaloblastic anemia	30–45 (35)	4.8–7.5 (6.3)	15–30 (22)	0.95–2.0 (1.5)
Myelodysplastic syndrome	35–50 (40)	5.0–6.9 (6.2)	10–35 (25)	0.68–1.4 (1.1)
Myelofibrosis	30–47 (36)	2.5–6.2 (4.8)	14–20 (18)	0.78–1.5 (1.3)

plasma ^{59}Fe T½ ranges from 55 to 125 min (Table 5.1). A rapid plasma ^{59}Fe clearance (i.e., shorter plasma ^{59}Fe T½) would indicate increased total erythropoietic activity usually associated with an increase of erythroid precursor cell mass as seen in patients with megaloblastic anemia, myelodysplastic syndrome, thalassemia major and iron-deficiency anemia. On the other hand, a slow or delayed plasma iron clearance (i.e., longer plasma ^{59}Fe T½) occurs in patients with aplastic and hyperplastic anemias, which are characterized by reduced erythropoietic activity and depletion of erythroid precursor cell mass in the bone marrow with or without reduction of other cell lineages. In hematological neoplasias including leukemias and in myelofibrosis and myelosclerosis, the plasma iron clearance rate is variable depending on the degree of erythropoietic activity in the bone marrow and the presence or absence of extramedullary erythropoiesis; however, in these conditions, the plasma iron clearance rate is more often high (i.e., plasma ^{59}Fe T½ is shorter; i.e., clearance is rapid) than low or normal (Das K.C., unpublished data).

5.15.2 Plasma Iron Turnover

The parameter of plasma iron turnover (PIT) is also referred to as the plasma iron transport rate [28, 29]. As mentioned above, the plasma iron clearance does not take into account the concentration of plasma iron and at the most yields a semiquantitative concept of the rate of movement of plasma iron to the erythropoietic tissue in the bone marrow and to the RE cell system. In determining the PIT rate, the plasma iron concentration is related with the plasma iron clearance rate to obtain quantitative data on the rate at which iron leaves the plasma per unit time and unit volume of blood. This is expressed as a total daily rate (i.e., mg or μmol of iron/l/day).

The computation of PIT is done according to the following formula:

$$\text{Plasma iron turnover (PIT) (mg/l/day)} = \frac{\text{Plasma iron (mg/l)} \times 10^3\ (\text{I} - \text{PCV})}{\text{Plasma } ^{59}\text{FeT½ (min)}}$$

$$\text{Plasma iron turnover (PIT) (μmol/l/day)} = \frac{\text{Plasma iron (μmol/l)} \times 10^3\ (\text{I} - \text{PCV})}{\text{Plasma } ^{59}\text{FeT½ (min)}}$$

PIT is a frequently used parameter in the ferrokinetic profile of patients with disorders of iron metabolism and anemias. It is considered to be a reasonably good indicator of total erythropoiesis and generally correlates with total nucleated red cell mass. Its clinical usefulness is limited, however, by several physiological constraints: (a) In calculating PIT, the blood volume is assumed to be normal, which can be amended by measuring the blood volume separately and expressing the results incorporating the blood volume in the calculation. (b) PIT does not take into consideration the fact that some iron leaves the plasma pool to enter the extravascular space (i.e., extravascular flux, EVF). (c) As stated earlier in this chapter, the plasma iron pool has both monoferric and diferric transferrins; diferric transferrin has a greater affinity for transferrin receptors and delivers twice as much iron per molecule of transferrin to the cells. For these reasons the PIT rate tends to increase as the serum iron level increases or as the transferrin saturation increases [28, 29]. PIT is generally found to be increased in iron-deficiency anemia, hemolytic anemias, megaloblastic anemia [30], thalassemia major and myelosclerosis. In aplastic anemia the PIT is either normal or decreased, but it may also be increased when the plasma iron concentration is very high. The measurement of PIT has limited clinical usefulness for the reasons stated above and because of the fact that this parameter does not distinguish between effective and ineffective erythropoiesis.

5.16 Red Cell Utilization (RCU) of Radio-iron

The injected radio-iron (^{59}Fe) transits into the bone marrow and becomes incorporated into the hemoglobin of developing red cell precursors and reticulocytes from day 1. This incorporation increases steadily and reaches a peak on the 10th–15th day under the physiological state of erythropoiesis. RCU is measured by collecting samples of whole blood daily or on alternate days for about 2 weeks after the injection of the radio-iron test dose. The radioactivity of ^{59}Fe is measured in 1 ml of whole blood collected as above, and the percentage utilization on each day is calculated according to the following formula:

$$\text{Percentage iron utilization} = \frac{\text{cpm/ml of whole blood sample at zero time}}{\text{cpm/ml/of whole blood sample daily}} \times 100f$$

where f is a PCV correction factor, which is as follows:

$f = 0.9\text{PCV}/(1 - 0.9\ \text{PCV})$ assuming that the body: venous PCV ratio is 0.9; when there is a possibility that this ratio is not 0.9, the red cell volume of the patient is determined by a direct independent method [28], and the percentage utilization on each day is then calculated as follows:

$$\text{Percentage iron utilization} = \frac{\text{Red cell volume (ml) ' cpm/ml red cells}}{\text{Total radioactivity injected (cpm)}} \times 100$$

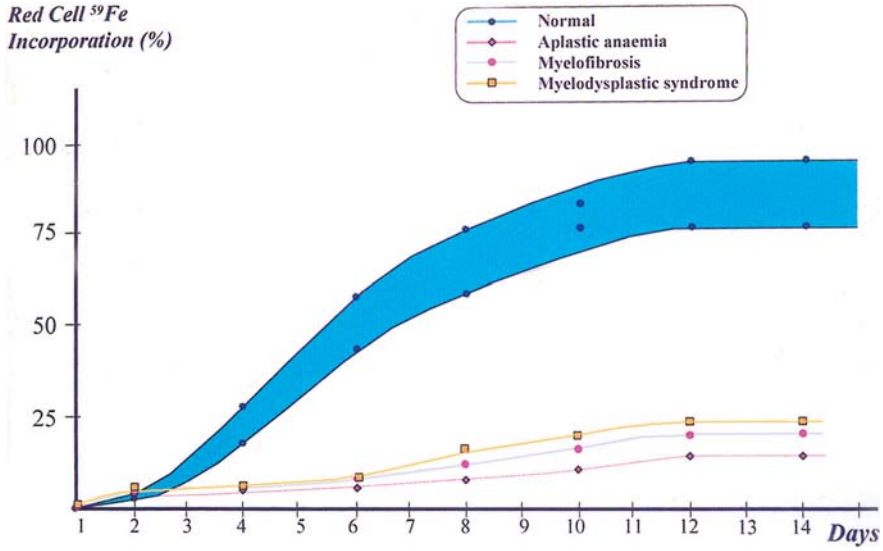

Fig. 5.15. Red cell iron utilization (RCU): ^{59}Fe incorporation into red cells (mature erythrocytes) in (*) normal subjects and patients with (◆) aplastic anemia, (●) myelofibrosis, and (■) myelodysplastic syndrome

The data on RCU provide an objective assessment of effective erythropoiesis. In normal subjects, a maximum RCU (approximately 70% – 80% of injected radio-iron) is reached between the 10th and the 15th day after the injection of ^{59}Fe (radio-iron). In patients with significant dyserythropoiesis and ineffective erythropoiesis with or without increased total erythropoiesis (i.e., erythroid hyperplasia in the bone marrow) such as in megaloblastic anemia and myelodysplastic syndrome, RCU is markedly reduced and may range from approximately 15% to 45%, whereas in aplastic/hypoplastic anemia, in which ineffective erythropoiesis is associated with depleted erythroid precursor cell mass as a striking pathological feature, RCU is further reduced to as low as 10% (Fig. 5.15).

5.17 Erythrocyte Iron Turnover

The erythrocyte or red blood cell iron turnover (EIT) rate is determined from plasma iron turnover and maximum red cell iron utilization (i.e., PIT'RCU) and is expressed as mg/l blood/day. The EIT is a measure of the rate at which iron moves from bone marrow to circulating red cells. It is an index of effective erythropoiesis and correlates well with an appropriately corrected reticulocyte index [29]. In normal subjects, EIT is about 5 mg/l/day; however, this may be underestimated in hemolytic anemias. As would be expected from morphological and biochemical (pathophysiological) evidence of disturbed erythropoiesis, EIT is markedly decreased in most patients with myelodysplastic syndrome, thalassemia major, myelofibrosis, congenital dyserythropoietic anemias, and acute leukemias.

5.18 Surface Counts for ^{59}Fe

Surface counting for ^{59}Fe can be done by placing a collimated probe of a gamma counter over the upper part of the sacrum, liver, spleen and heart with the patient ly-

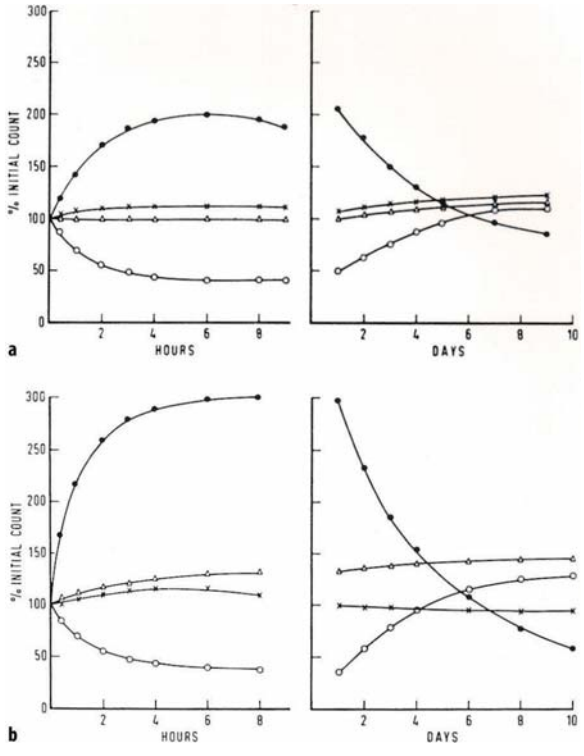

Fig. 5.16a,b. Surface counting patterns following an intravenous injection of ^{59}Fe to a normal subject (**a**) and to a subject with iron-deficiency anemia (**b**). Radioactivity was measured over the heart (○), sacrum (●), spleen (△), and liver (×). The patient with iron-deficiency anemia showed an excessive uptake of ^{59}Fe by the bone marrow.

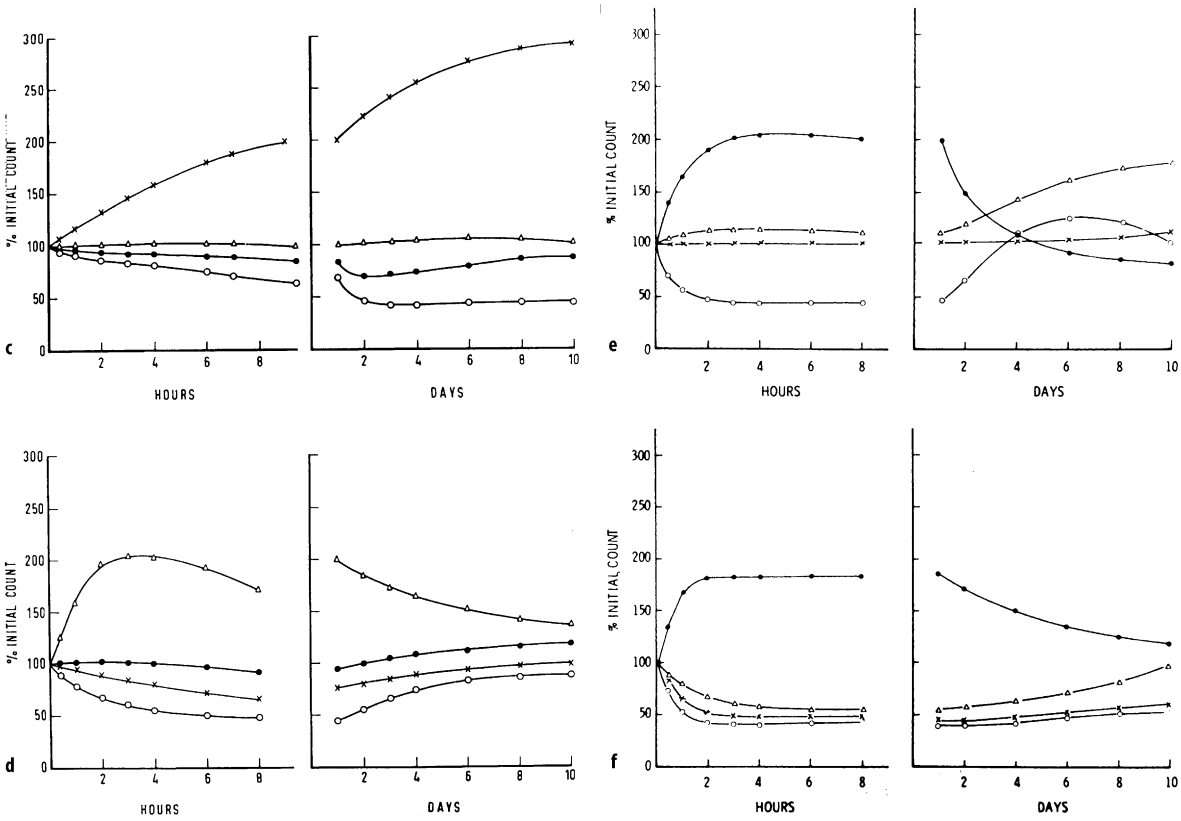

Fig. 5.16. c, d Surface counting patterns following an intravenous injection of ^{59}Fe to patients with aplastic anemia (**c**) and myelosclerosis (**d**): Radioactivity was measured over the heart (○), sacrum (●), spleen (△), and liver (×). In aplastic anemia the rate of clearance of the ^{59}Fe from blood (heart counts) is unusually slow and the bulk of the ^{59}Fe is taken up by the liver. In myelosclerosis there is little or no uptake of ^{59}Fe by the bone marrow but a clear excess uptake by the spleen. The subsequent decrease in radioactivity over the spleen is an indication that iron is being used for erythropoiesis and is not merely being stored in the organ. **e, f** Surface counting pattern following an intravenous injection of ^{59}Fe to patients with hemolytic anemia (**e**) and dyserythropoiesis (**f**). Radioactivity was measured over the heart (○); sacrum (●); spleen (△), and liver (×). In hemolytic anemias there is a delayed excess uptake of ^{59}Fe by the spleen, which is the main site of red cell sequestration. In dyserythropoiesis there is an active uptake of ^{59}Fe by the bone marrow. The subsequent retention of most of the radioactivity in the bone marrow is an indication of ineffective erythropoiesis. (Reproduced from [111, 112] with permission)

ing in the supine position in order to map out the pattern of distribution of the radioactive iron at varying time intervals after the intravenous injection of the iron isotope (^{59}Fe). These counts are generally taken after 5, 10, 20, 40, and 60 min, then hourly for 6–10 h, and then once daily or on alternate days for the next 10–15 days, the initial counts at each site being expressed as 100% and the subsequent counts converted proportionately after correction for the physical decay of the radioactive iron. These counts are then plotted on arithmetic graph paper (Fig. 5.16). The procedures for measuring surface counts have been described in detail in textbooks of practical hematology and nuclear medicine [28, 31]. The procedures are very laborious for both the laboratory physicians and the patients, but they are still useful as an investigative tool for some patients with aplastic anemia, myelofibrosis and myelodysplastic syndrome to make a functional assessment of iron utilization by erythroid precursor cells and of hematopoiesis and in planning therapeutic strategies.

5.19 Imaging of Bone Marrow and Other Organs for Evidence of Erythropoietic Activity

Iron utilization by the erythroid precursor cells in the bone marrow and in other unusual sites can be measured using the positron-emitting radioisotope of iron, ^{52}Fe, which has a short half-life of only several hours. The use of this iron isotope permits direct imaging of the distribution of this radio-iron in tissues and organs with active erythropoiesis. This type of imaging using a positron camera is capable of revealing pictorially the sites of erythropoiesis and the extension of this process into long bones and even into extramedullary sites

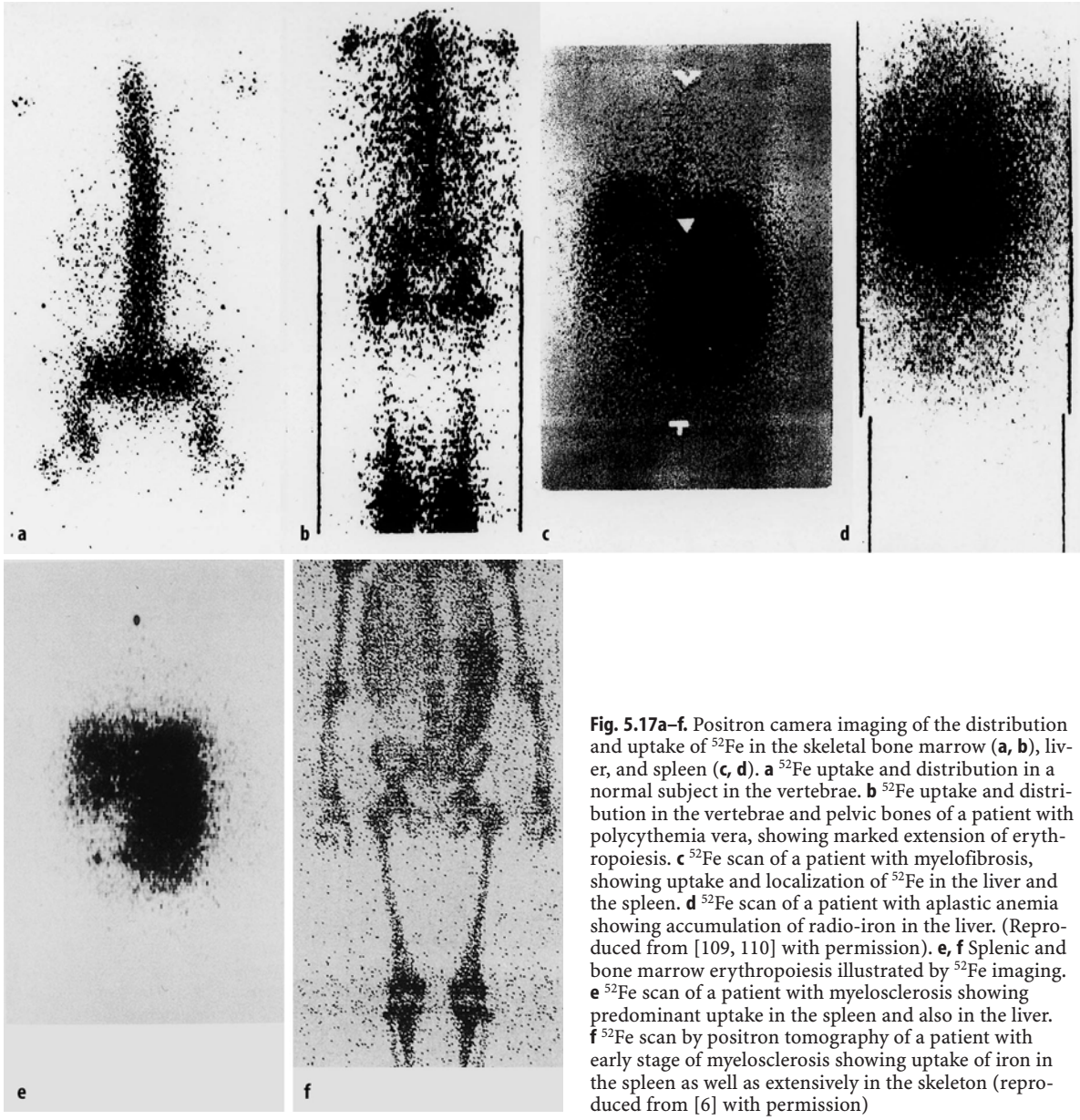

Fig. 5.17a–f. Positron camera imaging of the distribution and uptake of ^{52}Fe in the skeletal bone marrow (**a, b**), liver, and spleen (**c, d**). **a** ^{52}Fe uptake and distribution in a normal subject in the vertebrae. **b** ^{52}Fe uptake and distribution in the vertebrae and pelvic bones of a patient with polycythemia vera, showing marked extension of erythropoiesis. **c** ^{52}Fe scan of a patient with myelofibrosis, showing uptake and localization of ^{52}Fe in the liver and the spleen. **d** ^{52}Fe scan of a patient with aplastic anemia showing accumulation of radio-iron in the liver. (Reproduced from [109, 110] with permission). **e, f** Splenic and bone marrow erythropoiesis illustrated by ^{52}Fe imaging. **e** ^{52}Fe scan of a patient with myelosclerosis showing predominant uptake in the spleen and also in the liver. **f** ^{52}Fe scan by positron tomography of a patient with early stage of myelosclerosis showing uptake of iron in the spleen as well as extensively in the skeleton (reproduced from [6] with permission)

(Fig. 5.17a–d), as may occur in some patients with polycythemia vera, myelofibrosis, and myelosclerosis and in thalassemia major with extension of hematopoietic (mainly erythropoietic) cell mass into the paravertebral tissues, sometime causing compression of the nerve roots. In patients with aplastic anemia the shrinkage or atrophy of erythropoietic tissue can be revealed by this imaging procedure. Thus this imaging technique may validate the results of routine and conventional morphological and biochemical investigations for erythropoiesis, sometime yielding additional information, but it is rarely used in routine clinical hematological practice.

5.20 The Life Spans of Red Blood Cells

The mature red blood cells in the human are highly specialized cells with a relatively simple architecture consisting of a plasma membrane which encloses a solution of proteins, enzymes and electrolytes. More than 90% of the intracellular protein consists of the unique oxygen-carrying chromoprotein – hemoglobin; the remainder contains numerous enzymes including those responsible for anaerobic glycolysis (Embden-Meyerhof pathway) and also those responsible for the hexose monophosphate (HMP) shunt pathway. The biochemical reactions in the anaerobic glyco-

lytic pathway generate high-energy phosphate molecules – ATP and the coenzyme NADH required for methemoglobin reductase to maintain hemoglobin in the ferrous state as well as 2,3-DPG, which regulates the oxygen affinity of hemoglobin molecules. The HMP oxidative pathway causes about 5% – 10% of glycolysis and generates NADPH, which helps in maintaining sulfhydryl groups in the plasma membrane to act as possible antioxidants. The biconcave disk-shaped structure of the red cell is well-suited to its function of gas transfer and renders it more deformable to facilitate its movement within the microvascular circulation. The normal biconcave discoid shape of the red cell yields 40% more membrane than is needed to enclose its cytoplasmic contents. This excess of plasma membrane coupled with the peculiar biological nature of the membrane gives greater resistance to bending forces and relatively less resistance to sheer forces. The plasma membrane is formed by a matrix of double-layered phospholipids (lipid bilayer) with the "fluid-mosaic" model of globular proteins fitted into the lipid bilayer; some of the proteins penetrate the membrane completely, while others penetrate only partially without undergoing extensive remodeling. The erythrocyte membrane withstands rapid elongation and folding in the microcirculation and deformation as the cells pass through the small fenestrations of the splenic sinusoids.

The main functions of the red cells are to carry O_2 as oxyhemoglobin from the lungs to the tissues, where hemoglobin molecules are deoxygenated and also to carry CO_2 from the tissues to the lungs. During the process of deoxygenation, the β-globin chains are pulled apart to accommodate the metabolite 2,3-DPG. This change lowers the oxygen affinity of the hemoglobin molecule, which renders the O_2-dissociation curve into a sigmoid form. The P_{50} (i.e., the partial pressure of O_2 at which hemoglobin is half saturated) of normal blood is 26.6 mmHg. When the O_2 affinity of hemoglobin is lowered, the curve shifts to the right (i.e., the P_{50} rises) and tends to become sigmoid in shape and with increased O_2 affinity the curve shifts to the left (i.e., P_{50} falls). Normally, the arterial blood is about 95% saturated with O_2 and has a mean arterial O_2 tension of 95 mmHg, whereas venous blood is 70% saturated with O_2 with a mean venous O_2 tension of 40 mmHg. The oxygen dissociation curve of blood is influenced not only by 2,3-DPG, but also by H^+ ion concentrations, CO_2 in the red cells and the structure of the hemoglobin molecule. The red cells pass repeatedly through the microcirculation (with an average diameter of 4 μm) of the tissues for gaseous exchanges for a period of about 120 days (average life span). The energy for this active life span of the red cells is provided by the ATP generated by the anaerobic glycolytic pathway, reducing the power of NADH (generated during anaerobic glycolysis) and of NADPH generated by the glucose-6-phosphate dehydrogenase-dependent HMP oxidative pathway.

Measurement of red cell life span can provide useful data in those cases of anemia in which hemolysis remains a possibility but cannot be clearly revealed by other laboratory investigations. This is performed by labeling autologous red cells of patients in-vitro with radioactive chromium (^{51}Cr) – hexavalent sodium chromate ($Na_2\ ^{51}Cr_4$), a γ-ray-emitting isotope. The population of red cells of all ages are randomly labeled with ^{51}Cr-labeled sodium chromate (Na_2Cr_4), which passes through the surface membrane of the red cells and becomes reduced to a trivalent form and binds to proteins, preferentially to the β-polypeptide chains of hemoglobin. The trivalent chromium is not reutilized or transferred to other cells in the circulation [32]. In "cohort labeling" an isotope (e.g., ^{59}Fe) is taken up and incorporated into the newly synthesized hemoglobin of the developing erythroblasts. The radioactivity of the red cells which are freshly released into the circulation is measured as a cohort of closely similar age. Red cell life span can be calculated from the measurement of red cell iron obtained with cohort labeling by ^{59}Fe [33], but the interpretation of the data is difficult because of the reutilization of iron derived from red cells at the end of their life span for fresh heme synthesis. Random labeling with ^{51}Cr is a much more realistic method than cohort labeling with ^{59}Fe. However, there are several disadvantages to the ^{51}Cr random labeling method:

1. ^{51}Cr gradually elutes from the labeled red cells after they are injected. The rate of elution appears to be faster over the first 3 days and uncertain on subsequent days.
2. Chromium is toxic to the red cells probably because of its oxidant action. It inhibits glycolysis in red cells at a concentration of 10 μg/ml or more and blocks glutathione reductase activity at a concentration of greater than 5 μg/ml. It is recommended that <2 μg chromium should be used for 1 ml red cells.

The technique of chromium labeling of red cells with Na_2Cr_4 is the same as for determining red cell volume. However, for red cell survival studies in which surface counting is also done the radio-chromium is used in a higher dose (e.g., 0.4 Mbq or 1 μCi/kg body wt.). The methodology for determining red cell life span and surface counting has been described in detail in textbooks of nuclear medicine and hematology [28, 31]. However, it may not be out of place here to emphasize some important points and precautions:

Since the most important indication for measuring red cell life span is suspected hemolytic anemia, adequate precautions should be taken to prevent lysis of red cells during washing. When a significant number of spherocytes are present in the blood sample, as in he-

reditary spherocytosis or in autoimmune hemolytic anemia, it is advisable to use a slightly hypertonic solution (e.g., 12 g/l NaCl). In patients with autoimmune hemolytic anemias, associated with high-titer, high-thermal-amplitude cold agglutinins, blood should be collected in ACD solution which has been warmed to 37°C and the subsequent procedure should be carried out at 37°C.

Following the injection of ^{51}Cr-labeled red cells, an interval of 10 min (60 min in persons with cardiac failure or splenomegaly) is allowed for the mixing of radiolabeled red cells with the rest of the circulating red cells before a sample of venous blood is collected from a vein other than that used for the initial injection. The ^{51}Cr radioactivity in this sample is taken as the baseline for expressing the radioactivity of samples collected on subsequent days. One part of the labeled cell suspension initially injected into the patient is also retained as a standard for determination of red cell volume or red cell mass, if this was not done earlier. Subsequent samples are collected from the patient daily for 3–4 days and on alternate days for about 10 days; then two specimens are collected per week for another 2 weeks (International Committee for Standardization in Hematology) [34]. Such measurements are performed until the radioactivity has declined to 50% of the baseline value. ^{51}Cr survival on any day (e.g., day "t") is given by the following formula:

$$\text{Percentage survival} = \frac{\text{cpm/ml blood on day 't'}}{\text{cpm/ml blood on day '0'}}$$

If all the samples and the baseline standard are counted on day "t", no adjustment is required for physical decay. Two additional factors are involved in the disappearance of ^{51}Cr radioactivity from the labeled red cells: ^{51}Cr is eluted from intact red cells in the circulation at a rate which varies to a small extent in different individuals but to a greater extent in different diseases, especially in conditions associated with reduced red cell life span [28, 31]. The rate of elution is also believed to be influenced by the anticoagulant solution used: for example with NIH-A ACD solution the rate of elution is about 1%/day [24]. Appropriate corrections for the elution of ^{51}Cr have been suggested and can be incorporated in the computation of the red cell survival [28, 31]. This is achieved by multiplying the % ^{51}Cr radioactivity of red cells on a particular day by the elution factor for that day [28, 31].

Another event that has been observed in this method of determining red cell life span is the early loss of ^{51}Cr from the red cells, amounting to about 10% within the first 24 h. A method of correcting for the early loss of ^{51}Cr from the red cell has been described. This is performed by plotting the data on arithmetic graph paper; the point of intersection is taken as 100%, and then the scale at the ordinate is recalibrated accordingly. The methods for drawing survival curves and for deriving the mean red cell life span have been described in the well-known *Textbook of Practical Hematology* by Dacie and Lewis [28]. The red cell survival curve is drawn by plotting the percentage radioactivity data of whole blood samples obtained on different days, after correction for physical decay and elution, on arithmetic and semilogarithmic graph paper and fitting straight lines passing through the data points. If a straight line can be fitted to the arithmetic plot, the mean red cell life span is given by the point in time at which the line or its extension cuts the abscissa. Usually, a straight line is better fitted to the semologarithmic plot and the mean red cell life span is read off as the exponential, e–1, i.e., the time when 37% of the cells are still surviving, or is calculated by multiplying the half-time of the fitted line by the reciprocal of the natural log of 2 (0.693), i.e., multiplying by 1.44 (Fig. 5.18a–d). A computer program can automate this calculation. However, it is believed that the computer analysis does not improve overall accuracy for clinical purposes [28]. In many laboratories, it is common practice to calculate the T_{50} ^{51}Cr (i.e., the time taken for the ^{51}Cr radioactivity to decline to 50% of its initial value) after correcting for the physical decay factor. The ^{51}Cr data may not be strictly comparable to an Ashby survival curve even after corrections for ^{51}Cr elution and early loss, but this procedure is acceptable for clinical purposes, provided that the findings of survival data are compared with ^{51}Cr survival curves obtained from normal subjects by an identical technique [28, 31] (Fig. 5.18a).

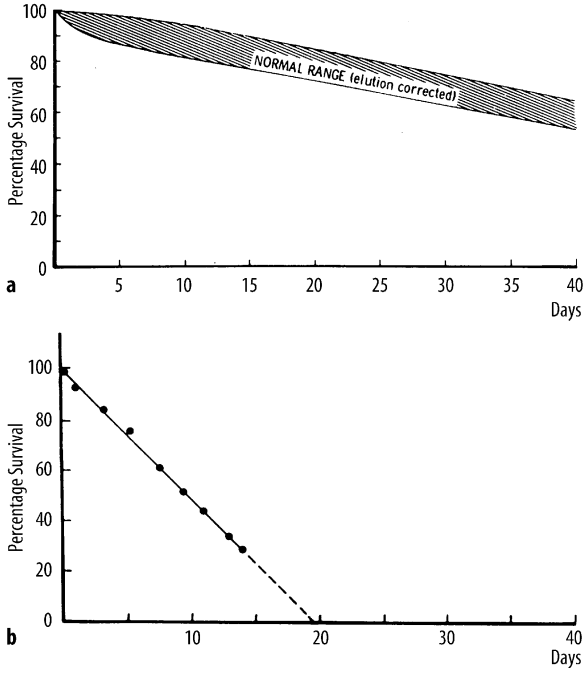

Fig. 5.18a–b. ^{51}Cr red cell survival curves. **a** Normal subjects; **b** a patient with hereditary spherocytosis

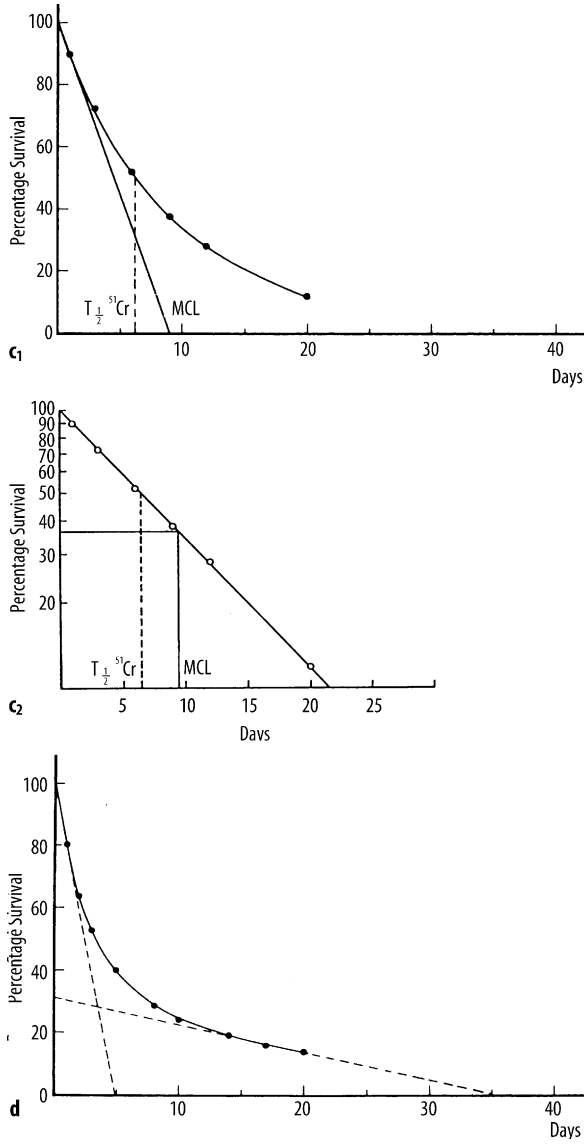

Fig. 5.18. c a patient with autoimmune hemolytic anemia. In the *upper chart* the results have been plotted on arithmetic graph paper and mean cell life span (*MCL*) was deduced by extrapolation of a tangent at the initial slope to the abscissa (9 days). In the *lower chart* the results have been plotted on semilogarithmic graph paper and the MCL was read as the time when 37% of the cells were still surviving (9–10 days). The T_{50}Cr was 6–7 days. **d** Red cell survival curve showing a "double population". The MCL of the entire population was deducted by extrapolation of a tangent at the initial slope to the abscissa (5 days). By extrapolation of the less-steep slope to the ordinate it was deduced that approximately 30% of the red cells belonged to one population, and by extrapolation of the same slope to the abscissa the MCL of this population was calculated as 35 days. The life span of the remaining 70% of red cells was calculated to be 3.6 days. The T_{50} was 3–4 days. (Reproduced from [111, 112] with permission)

In hereditary spherocytosis in which there is a chronic hemolytic anemia, the red cell survival is significantly shortened and the results give a straight line when plotted on arithmetic graph paper (Fig. 5.18b). In patients with autoimmiune hemolytic anemias, the results of ^{51}Cr red cell survival studies, when plotted on arithmetic graph paper, yield a markedly curvilinear graph and indicate a random destruction of red cells, which are eliminated in an exponential manner. The same data give a straight line when plotted on semilogarithmic graph paper (Fig. 5.18c). The mean red cell life span can be read as the time when ^{51}Cr radioactivity declines to 37% of its initial value.

Some types of hemolytic anemia may be associated with more than one population of red cells. For example, in patients with intravascular hemolysis, as in paroxysmal nocturnal hemoglobinuria (PNH), and in some patients with sickle cell anemia, there may be more than one population of red cells with varying life spans. In the survival curves of red cells of such patients, the population of more fragile or short-lived red cells will produce an initial steep slope followed by a much less steep slope or a normal-looking curve. The mean cell life span of the entire population of red cells can be derived by plotting the points on semiligarithmic graph paper. The population of red cells with longer life span can be assessed by plotting the points on arithmetic graph paper and extrapolating the less steep slope of the curve back to the ordinate (Fig. 5.21d); their life span can be estimated by extending the same slope to the abscissa. The life span of the short-lived population can be derived from the following mathematical model [28].

$$\text{MCLs} = \frac{\dfrac{\%\ \text{S}}{100\ \%\ \text{L}}}{\text{MLCT MLCL}}$$

where S = short-lived population, L = longer-lived population, T = entire cell population, MLC = mean cell life-span

5.21 Surface Counts to Determine Sites of Red Cell Destruction Using ^{51}Cr-Labeled Red Cells

Reticuloendothelial cells (cells of the monocyte-macrophage system) engulf senescent and effete red cells mainly in the spleen and to a much smaller extent in the liver of normal subjects who have a steady state of erythropoiesis. In hemolytic anemias, especially chronic hemolytic anemias, this process of sequestration and destruction of red cells is exaggerated and involves red cells at random, irrespective of their chronological age. The exaggerated rate of red cell destruction and the localization of the damaged or dead red cells in organs like the spleen and the liver can be demonstrated and evaluated in quantitative figures by in vivo surface counting using a properly shielded scintillation co-

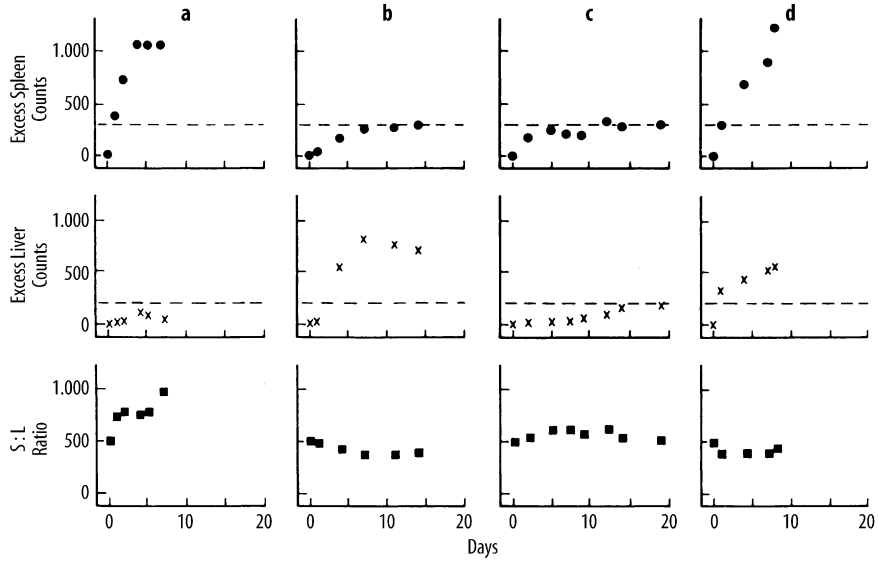

Fig. 5.19a–d. Surface counting patterns following labeling of patients' red cells with ^{51}Cr in various hemolytic anemias. *Interrupted lines* indicate the limits of accumulation in normal subjects. Only excess counts and the spleen:liver ratio are shown. **a** Hereditary spherocytosis; **b** sickle cell disease; **c** pyruvate-kinase deficiency; **d** autoimmune hemolytic anemia. (Reproduced from [111] and [112] with permission)

unter (collimated scintillation detector) placed respectively over the heart, spleen and liver. These counts are recorded over a period of time and are expressed with reference to the counts over the heart taken as 1000 and the differences between the actual counts and the expected counts are taken as the excess counts (as evidence of sequestration or engulfment of damaged or sensitized red cells by the RE cells in these organs). For example, the spleen: the liver count ratio is expressed as an index and reflects the relative accumulation of ^{51}Cr in the spleen and the liver. The ratio between the counts on day 0 is recorded as 100 and all subsequent ratios are related to this. The details of the procedure for surface counts for ^{51}Cr after injection of ^{51}Cr-labeled red cells have been described by Dacie and Lewis [28], who have also illustrated the surface count patterns in normal subjects and in several types of hemolytic anemias. Four patterns of surface counting abnormalities have been described by these authors (Fig. 5.19):

1. Excess accumulation in the spleen as in hereditary spherocytosis (HS), hereditary elliptocytosis, and some patients with autoimmune hemolytic anemias (AIHA).
2. Excess accumulation chiefly in the liver that occurs in sickle cell anemia especially in adult patients.
3. Little or no excess accumulation in either spleen or liver as in some hereditary enzyme-deficiency hemolytic anemia and in PNH.
4. Excess accumulation in both liver and spleen as in some cases of AIHA.

The results of surface counting patterns over the spleen and the liver have some relevance to the observed clinical results of splenectomy in these patients with hemolytic anemias. Splenectomy usually benefits patients with a surface counting pattern in Fig. 5.19a, and to a more limited extent also patients with the pattern in Fig. 5.19d in parallel with the spleen:liver ratio. However, the relationship is not quantitatively direct and the degree of improvement is not closely correlated with the magnitude of the ^{51}Cr accumulation in the spleen [32].

Surface counting studies have many limitations. Minor alterations in the conditions of counting and positioning of the patient may cause significant changes. Among the variables which affect the count rate are the amount of the organ volume counted in relation to its total volume, the distance of the organ from the surface of the body, the absorption of radiation by the overlying tissues and the rate of loss of deposited ^{51}Cr from the organ. Despite these perceivable theoretical problems, surface counting has proved to be of value in the management of patients with some types of hemolytic anemia when used judiciously with other clinical and laboratory data [32, 33].

5.22 Use of Radionuclides in the Investigation of Patients with Megaloblastic Anemia

5.22.1 Etiopathogenetic Basis of Megaloblastic Anemia

Megaloblastic anemia is characterized by a morphologically distinct abnormality of erythropoiesis in which the erythroid precursor cells are transformed into large cells with finely stippled nuclear chromatin and asynchronous nuclear: cytoplasmic maturation [30, 34, 35] (Fig. 5.20). The retarded nuclear maturation in relation to the cytoplasmic maturity is believed to be a morphological expression of deranged DNA synthesis [35–37]. The most common cause of megaloblastosis is deficiency of folate (folic acid) and vitamin B_{12}. Both of these vitamins are essential cofactors for DNA synthesis and

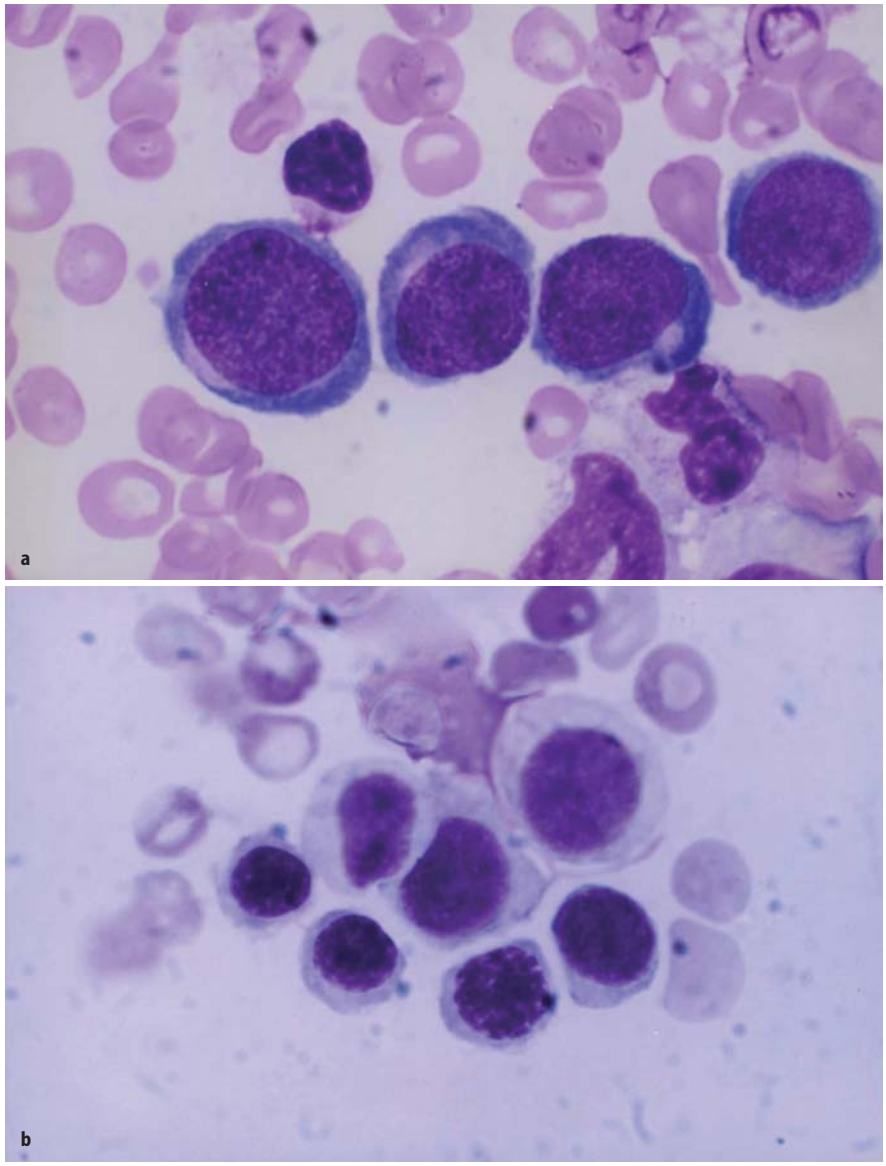

Fig. 5.20a,b. Megaloblastic erythropoiesis in the bone marrow of a patient with vitamin B_{12} deficiency showing **a** finely stippled nuclear chromatin, asynchronous nuclear:cytoplasmic maturation, and retarded nuclear maturity as compared to **b** normal (normoblastic) erythropoiesis

cell replication in all proliferating mammalian cells [30, 35–37]. The deficiency of these vitamins also affects the other hematopoietic cell lineages and frequently causes hypersegmentation of neutrophils (i.e., at least 5% neutrophils having 5 or >5 lobes per cell), leukopenia, granulocytopenia and thrombocytopenia in addition to macrocytic anemia. The peripheral blood pancytopenia is caused predominantly by markedly increased intramedullary death of hematopoietic precursor cells resulting in ineffective hematopoiesis [29, 30, 39]. Examination of a peripheral blood film from a patient with established megaloblastic anemia reveals an appreciable number of macrocytic and macro-ovalocytic red blood cells (MCV >95 fl.), pear-shaped poikilocytes and hypersegmented neutrophils. Megaloblastic changes may also appear in the erythroblasts in some rare hematological disorders such as erythroleukemia and myelodysplastic syndrome. These disorders are unresponsive to treatment with vitamin B_{12} and folic acid. The mechanism of megaloblastic changes in these conditions remains obscure.

The principal markers (i.e., identifiable features) of deficiency of vitamin B_{12} and folate have been traditionally considered to be clinical expressions of anemia and morphological transformation from normoblastic erythropoiesis to megaloblastic erythropoiesis. However, recent advances in analytical biochemical techniques, and successful explorations of various metabolic loops between vitamin B_{12}- and folate-dependent biochemical pathways, have provided the impetus to look beyond these classical expressions of deficiencies of these vitamins. The range of expressions of deficien-

cies currently include the gene nutrient interface, mild preclinical deficiency states, subtle changes in the lymphocytes and related immunological status, varied neurological consequences, the possible contribution of folate insufficiency to birth defects, neoplastic transformations and immunological abnormalities. The application of HPLC and mass spectroscopy has facilitated the estimation of methylmalonic acid and homocysteine in the plasma of patients with deficiencies of these vitamins. Whereas increased plasma or serum concentration of methylmalonic acid is an early feature of vitamin B_{12} deficiency, increased concentration of homocysteine occurs early in both vitamin B_{12} and folate deficiencies. In spite of overlapping functional and metabolic activities of these two vitamins, there are a great many differences in their molecular structures and biochemical activities involving different tissues.

"Folate and folic acid" are used as generic terms for any member of the family of folate compounds, whereas the term "folic acid" has been used as a synonym for pteroylglutamic acid (pteroylmonoglutamate). The structural formula of the parent compound and major coenzymically active forms of folic acid are illustrated in Fig. 5.21. The major portions of the molecule are the pteridine moiety linked by a methylene bridge to *p*-aminobenzoic acid, which itself is joined in amide linkage to glutamic acid. The parent compound, pteroylmonoglutamate, is not normally found in food or in the human body in significant concentrations, nor is it biochemically active unless it becomes reduced in positions 5, 6, 7 and 8, and acquires substitution of one-carbon addicts on the N^5 and N^{10} positions. Folate in circulating blood and tissue fluids is a monoglutamate, usually 5-methyltetrahydrofolate; but intracellular folate occurs as conjugates of two to seven glutamic acid residues (pteroylpolyglutamate) either in methylated or formylate forms. The α-amino group of the second glutamic acid molecule is linked with the γ-carboxyl group of the proximal molecule. The polyglutamate forms of folate are resistant to the action of trypsin, but are hydrolyzed to mono- or diglutamates by conjugases present in plasma and other tissues. The enzymatic reduction of pteroylmonoglutamic acid is catalyzed by the enzyme dihydrofolate reductase. The latter is inhibited by several folate antagonists such as methotrexate, aminopterin, pyrimethamine and triamterene. The simple, yet functional, monoglutamate folate is a reduced compound, tetra-hydropteroylglutamic acid (-THF), which is essentially involved in the transfer of single carbon units in different states of reduction which include formyl (CHO-), methenyl (=CH-), methylene ($-CH_2$), formimino (-CHNH), and methyl ($-CH_3$). These are required for a variety of biosynthetic reactions. Among these compounds, 5-methyltetrahydrofolate (5-CH_3THF) is the most reduced form of folate (Fig. 5.21) and is the most predominant folate compond in the plasma. These folate coenzymes may be identified spectrophotometrically, flourometrically or by their affinity for a anion-exchange column or absorption on Sephadex or cellulose. These may also be identified by microbiological assays.

Vitamin B_{12} is synthesized by microorganisms and not by mammalian cells. It has a complex chemical

	R	OXIDATION STATE
N^5 formyl THFA	-CHO	formate
N^{10} formyl THFA	-CHO	formate
N^5 formimino THFA	-CH=NH	formate
$N^{5,10}$ methenyl THFA	>CH	formate
$N^{5,10}$ methylene THFA	$>CH_2$	formaldehyde
N^5 methyl THFA	$-CH_3$	methanol

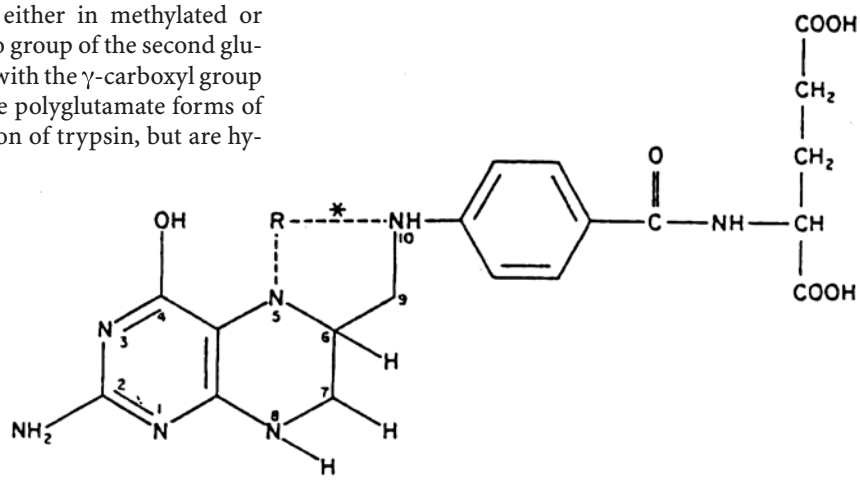

*Broken lines indicate the N^5 and/or N^{10} site of attachment of various 1-carbon units for which THFA acts as a carrier.

5,6,7,8-Tetrahydrofolic Acid (THFA)(FH_4)(R=—H)

Fig. 5.21. The structures and nomenclature of folate derivatives. The table above the formula lists some of the possible 1-carbon adducts with THFA (From Das KC and Herbert V 1976 [36]; by courtesy of Saunders Publications)

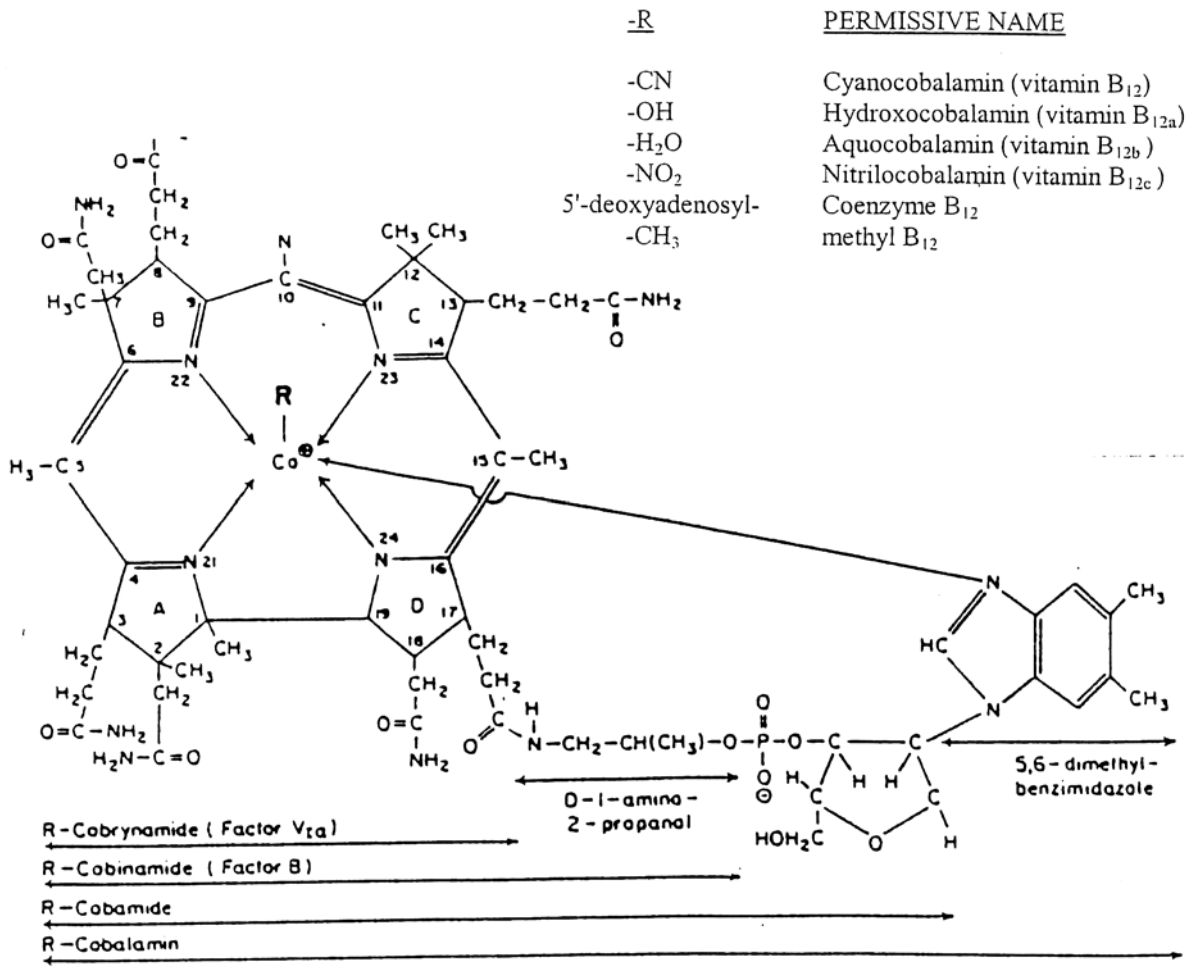

Fig. 5.22. Structural formula of vitamin B_{12} (cyanocobalamin). The numbering system for the corrin nucleus is made to correspond to that of the porphin nucleus by omitting the number 20. The corrin nucleus is in the plane of the page. The R-anionic ligand is above it; the rest of the nucleus is below it. (From Das KC and Herbert V 1976 [36]; by courtesy of Saunders Publications)

structure of corrinoid, a class of compounds which have a core structure resembling that of heme in the hemoglobin molecule (Fig. 5.22). A corrinoid is a tetrapyrrole compound (i.e., consisting of four pyrrole rings) in which two pyrrole rings (A and D) are linked directly, unlike other pyrrole rings, which are linked by alpha-methane bridges. The corrin nucleus (a planar structure) is linked to the ribonucleoside of a "nucleotide" lying at right angles to the plane of the corrin nucleus and linked to it by d-1-amino-2-propanol. The "nucleotide" consists of a base, 5,6-dimethyl-benzimidazole, attached to ribose-3-phosphate by an alpha-glycoside linkage. The corrin ring contains a cobalt atom in the center, which is linked to the four reduced pyrrole rings and to an anionic ligand (-R group). A second bond exists between the major parts of the molecule – the coordinate linkage of the cobalt atom and one of the nitrogen atoms of the "nucleotide" molecule. The part of the vitamin B_{12} molecule without the anionic ligand is often referred to as "cobalamin". The commercially available pharmacological forms of vitamin B_{12} are cyanocobalamin and hydroxocobalamin, which are stable on storage. Cyanocobalamin is not biologically active until the cyanide group is removed in the tissues. Two chemically and biologically active forms of this vitamin are methylcobalamin and 5'-deoxyadenosylcobalamin; both of these compounds are relatively unstable and decompose on exposure to light and undergo photolysis with the formation of aquocobalamin. When vitamin B_{12} is converted into metabolically active coenzyme forms, the cobalt atom is reduced in two steps from a trivalent to a monovalent state, to which the organic anionic ligands are then enzymatically attached. Methylcobalamin is the major form of vitamin B_{12} in the plasma and 5-deoxyadenosylcobalamin in the liver and other tissues.

The development of clinical manifestations of both vitamin B_{12} and folate deficiency is very insidious, and

the sequential changes of developing folate deficiency in human volunteers have been described [40, 41]. In the early stages of deficiency of these vitamins, many of the hematological and biochemical features of established megaloblastosis, including the red cell morphological changes referred to earlier, may not appear. The diagnostic features of a negative balance of the metabolic states of these vitamins can be very subtle and difficult to obtain by routine investigations, and may sometimes be difficult to ascertain even with sensitive analytical biochemical procedures. The development of a vitamin B_{12} deficiency from a vitamin-replete state is gradual and the transitional period can be divided into several stages. The transition from a folate-replete state to one of folate-deficiency anemia also progresses through similar stages. However, this transition in folate status occurs in a shorter time span than in vitamin B_{12}-deficiency state.

There is a close interrelationship between vitamin B_{12} and folate metabolism in man. When large doses of folic acid are given to patients with vitamin B_{12} deficiency, the anemia may significantly improve but neurological manifestations may develop, or if already present may progress further [36, 37, 42, 43]. Both hematological and neuropsychiatric manifestations occur in classical pernicious anemia. The latter is a special variety of megaloblastic anemia which is caused by malabsorption of vitamin B_{12} due to inadequate or absent gastric intrinsic factor (IF). In an overwhelming majority of patients this is caused by an autoimmune process leading to the atrophy of gastric parietal epithelial cells. Antibodies to gastric parietal cells and to gastric IF are commonly found in the sera of patients with pernicious anemia. The neuropsychiatric manifestations of patients with pernicious anemia may precede or develop in the absence of any hematological abnormalities [43 – 45].

A fall in the serum vitamin B_{12} level is usually considered an early sign of developing deficiency of this vitamin and precedes morphological changes in the bone marrow and blood, but it lacks specificity, as it may also be found in severe folate deficiency, normal pregnancy, and transcobalamin 1 (TC-I) deficiency. On the other hand, megaloblastic anemia due to vitamin B_{12} deficiency can occur in the presence of a normal serum vitamin B_{12} level as in TC-II deficiency and in conditions associated with high levels of TC-I such as hepatocellular disorders [46], chronic myeloid leukemia and other myeloproliferative disorders. As stated earlier, vitamin B_{12} has a complex molecular structure consisting of a tetrapyrrole, corrinoid ring with a cobalt atom in the center and a nucleotide side chain. Radiolabeling of vitamin B_{12} is achieved by replacing the native central cobalt atom by a radioactive cobalt atom (^{57}Co, ^{58}Co, ^{60}Co). The two natural forms of this vitamin, methyl (CH_3-) cobalamin and deoxyadenosyl (deoxy ado-) cobalamin, have (CH_3-) and (deoxy ado-) groups attached to the cobalt atom, respectively, whereas the relatively stable pharmacological forms are cyano- (CN) and hydroxo- (OH) cobalamins. Methylcobalamin is the predominant form of vitamin B_{12} in the plasma, and deoxyadenosyl cobalamin is present largely in the tissues. Since vitamin B_{12} is synthesized by neither animals nor plants, but only by certain microorganisms, all or most human dietary vitamin B_{12} is derived from their binding proteins in food by the action of proteolytic enzymes and acids in the gastric juice in the stomach, where this vitamin becomes bound to R-binders (nonspecific binders) in the gastric juice. The gastric IF moves down into the jejunum with R-binders, where pancreatic proteolytic enzymes release vitamin B_{12} from these binders in an alkaline environment. The released vitamin B_{12} then binds to IF, and IF-B_{12} complexes move down to the lumen of the distal ileum, where specific receptors on the ileal epithelial cells bind the complex in the presence of calcium and alkaline pH of the contents. Vitamin B_{12} is dissociated from IF and is transported by facilitated diffusion across the mucosal cells into the portal circulation where it binds to transcobalamin II. The latter transports and delivers vitamin B_{12} to the tissues for participation in relevant metabolic activities. The remaining vitamin B_{12} reappears in the circulation bound to TC-I and TC-III, which act predominantly as long-term storage proteins for vitamin B_{12}.

TC-II bound with vitamin B_{12} is referred to as holo-TCII (holo-transcobalamin II). In normal human subjects, TC-II-bound vitamin B_{12} amounts to about 40 – 50 ng/l. Hereditary deficiency of TC-II is associated with megaloblastic anemia, which is resistant to vitamin B_{12} therapy in the conventional dosage due to deficiency or absence of the delivery protein. Vitamin B_{12} serves as an essential cofactor for at least two important metabolic reactions in the human being:

1. Conversion of methylmalonyl CoA to succinyl CoA catalyzed by the enzyme isomerase in the presence of the cofactor, deoxyadenosyl-cobalamin; vitamin B_{12} deficiency is marked by accumulation of methylmalonic acid in the plasma and its increased excretion in urine.
2. Conversion of homocysteine to methionine, which is dependent on methyl cobalamin; 5-methyl-tetrahydrofolate (5-CH_3-THF) also participates in this reaction as a methyl donor, and this reaction reflects the metabolic interrelationship between vitamin B_{12} and folate. In deficiency of vitamin B_{12} as well as of folate, homocysteine tends to accumulate in the plasma, causing hyperhomocysteinemia.

Diagnostic tests for vitamin B_{12} deficiency should include the following:

1. Serum vitamin B_{12} assay
2. TC-II-bound cobalamin (i.e., holo-TC-II) assay

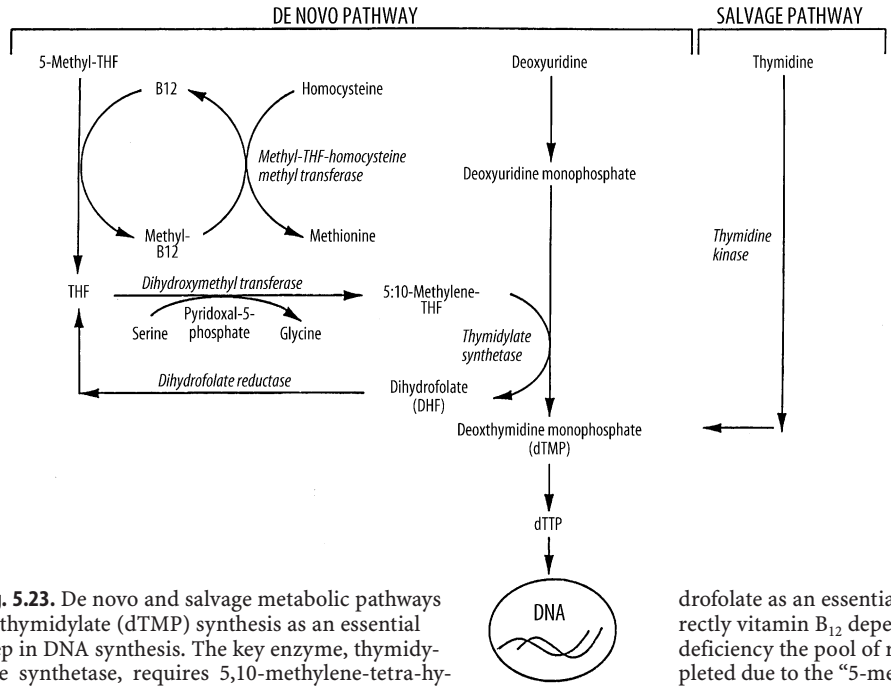

Fig. 5.23. De novo and salvage metabolic pathways of thymidylate (dTMP) synthesis as an essential step in DNA synthesis. The key enzyme, thymidylate synthetase, requires 5,10-methylene-tetra-hydrofolate as an essential cofactor, and is also indirectly vitamin B_{12} dependent, since in vitamin B_{12} deficiency the pool of reduced folate becomes depleted due to the "5-methyl-tetra-hydrofolate trap"

3. Estimation of serum concentrations of methylmalonic acid and serum homocysteine
4. Deoxyuridine (dU) suppression test (i.e., DNA synthetic defect) in bone marrow cells and PHA-stimulated lymphocytes

Folic acid is generally present in green vegetables and foliage, and after being absorbed by the gastrointestinal (mainly jejunal) epithelium accumulates to a small but significant extent in the mammalian liver and spleen in reduced formyl- or methyl-polyglutamate forms. Folate polyglutamates are the physiological forms of tissue folate. The dietary requirement of folate in the human being is approximately 300 µg daily for adults and may be higher for infants and pregnant women. Human body stores of folate are limited and may not last for more than 100 days. Folates are reduced to tetrahydrofolates (THF) predominantly in the liver before these can participate as cofactors in biochemical reactions to donate single carbon groups. The predominant form of folate in the serum is methyl-tetra-hydrofolate (CH_3-THF), and its concentration declines rapidly as the intake of folate is reduced or in conditions associated with negative folate balance without immediate depletion of the tissue stores of folate. The red cell level of folate (which is predominantly reduced folate polyglutamate) rather than the serum folate level reflects the folate status of patients. However, a low red cell folate level may not always indicate true folate deficiency. The red cell folate level may also be low in about 50% of patients with severe vitamin B_{12} deficiency, since tetrahydrofolate is needed as a substrate for polyglutamate synthesis [36, 48, 49]. The red cell folate may be normal despite folate deficiency in patients with marked reticulocytosis and following blood transfusion.

Reduced, formylated or methylated forms of folate act as essential cofactors for several enzymatic reactions in the body relating to purine and pyrimidine biosynthesis, DNA synthesis and amino acid interconversions. The folate coenzyme 5-methyl-THF also interacts with vitamin B_{12} metabolism in homocysteine-methionine interconversion by acting as a methyl donor and the resulting release of THF from 5-methyl-THF makes this single carbon group available for further participation in serine-to-glycine interconversion. THF acquires a methylene group, which is released from serine at this step of interconversion, forming 5,10-methylene-THF. The latter folate compound is an essential cofactor in the cellular synthesis of deoxy-thymidine-monophosphate (dTMP) from deoxyuridine monophosphate (dUMP) and thus promotes the synthesis of one of the four constituent deoxy-nucleotide-triphosphates of DNA molecule [30, 35, 39] (Fig. 5.23).

Diagnostic tests for the detection of folate deficiency include:

1. Serum and red cell folate assays usually by competitive protein-binding radioassays
2. Estimation of serum or plasma homocysteine concentration
3. Bone marrow and lymphocyte dU suppression test

5.23 Vitamin B_{12} Radioassay

The estimation of serum vitamin B_{12} has conventionally been used as a test for identifying the cause of megaloblastic anemia as well as of neuropathy. Competitive protein-binding inhibition radioassays of vitamin B_{12} have virtually replaced microbiological assays [50–52] in almost all laboratories in the world. This is because radioassays are simple, rapid and unaffected by the presence of antibiotics, antimetabolites, and other drugs in the plasma [53, 54]. Antibiotics, antimetabolites and other drugs inhibit the growth of microorganisms, yielding falsely low values in the microbiological assays. Radioisotopic methods (radioisotope dilution assays) using different binders for the vitamin (purified IF) as well as R-binders can distinguish true cobalamin from other corrinoids or vitamin B_{12} analogues [52]. The most commonly used radioassay is based on the principle of the saturation analysis technique, which measures the dilution of a standard amount of radiolabeled vitamin B_{12} (^{57}Co-B_{12}) by the endogenous cobalamin of the serum or plasma (which is released from the binding proteins by lowering the pH); purified gastric IF is used as ligand binding protein and hemoglobin-coated charcoal is used to adsorb the free vitamin B_{12}, in order to separate the bound form of the vitamin from the free form [51, 53]. However, it has been reported that a normal serum vitamin B_{12} level was found in a significant minority of patients with typical or atypical clinical features of deficiency [45, 55], even though very sensitive radioassays were used [52]. On the other hand, many patients with low serum cobalamin levels such as vegetarians and vegans do not show significant clinical evidence of deficiency for a variable length of time [55, 56]. Further, tissue depletion of vitamin B_{12} is not reflected in the estimated serum level of this vitamin in certain disorders such as liver diseases [46], TC-II deficiency [57], myeloproliferative disorders [58] and after exposure to nitrous oxide [59, 60]. Low serum vitamin B_{12} levels are also found in some patients with deficiency of folate as well as in the latter part of apparently normal pregnancy without evidence of tissue depletion of vitamin B_{12} and rarely in an occasional patient with iron-deficiency anemia [61]. On the other hand, some patients with vitamin B_{12} deficiency reveal high serum folate and low red cell folate levels. It is, therefore, desirable that both vitamins be measured in all patients with suspected deficiency of either vitamin.

5.24 Determination of Holo-Transcobalmin-II (Holo-TC-II)

Human plasma or serum contains two major types of vitamin B_{12}-binding proteins: transcobalamin II (TC-II) and haptocorrin (R-binders: TC-I and TC-III). TC-II binds 6%–20% of endogenous vitamin B_{12} and delivers the vitamin to the metabolically active tissues, where it is required as a cofactor. TC-II binds approximately 50–100 ng of endogenous vitamin B_{12}/l. When vitamin B_{12} deficiency occurs, TC-II-bound vitamin B_{12} is the first to be reduced at the early stage of depletion [41, 44, 62, 63]. TC-II containing bound vitamin B_{12} is referred to as holo-TC-II. Studies in patients with untreated pernicious anemia and AIDS with vitamin B_{12} deficiency have shown that a decrease in holo-TC-II is the earliest sign of developing vitamin B_{12} deficiency [62, 63].

A simplified method for estimating vitamin B_{12} on TC-II (i.e., holo-TC-II) has been described by Das et al. [64] as an extension of the competitive inhibition radioassay of vitamin B_{12} in human serum [52]. In this procedure, the TC-II-bound endogenous vitamin B_{12} is separated from endogenous haptocorrin (i.e., TC-I, TC-III)-bound vitamin B_{12} by adsorption with microfine silica gel (Quso G32, or G761). The determination of holo-TC-II by this method involves an additional step in the competitive inhibition radioassay for vitamin B_{12}. The estimation of vitamin B_{12} content on haptocorrin (vitamin B_{12} bound to TCI and TCIII, i.e., vitamin B_{12} content of the serum after absorption with Quso G32 or G761) is subtracted from the vitamin B_{12} content of the untreated or unabsorbed serum. The resultant value provides the vitamin B_{12} content on TC-II (i.e., holo-TC-II). The holo-TC-II level may be subnormal at an early stage of developing vitamin B_{12} deficiency, even though the total vitamin B_{12} level may be within the laboratory range of normal [41, 62–65].

5.25 Identification of the Cause of Vitamin B_{12} Deficiency

Vitamin B_{12} deficiency due to pure dietary inadequacy of this vitamin is very rare and occurs mainly in strict vegetarians and vegans [56]. More often gastrointestinal disorders, atrophic gastritis, pernicious anemia, congenital lack or abnormality of gastric IF or total or partial gastrectomy cause malabsorption and consequent deficiency of this vitamin. Diseases involving the distal ileum such as Crohn's disease, intestinal stagnant loop syndrome and rarely congenital selective ileal malabsorption with proteinuria (Imerslund-Grasebeck syndrome) may also result in malabsorption of vitamin B_{12}.

The malabsorption of vitamin B_{12} is classically detected by the Schilling test.

This procedure uses an oral test dose of radiolabeled cyanocobalamin (usually ^{57}Co-B_{12}) with or without added IF (intrinsic factor). The absorption is most frequently measured indirectly by measuring the urinary excretion of the radiolabeled vitamin B_{12}; the vitamin is flushed out into a 24-h collection of urine sample by a large parenteral dose (1 mg) of nonradioactive vitamin B_{12} injected intramuscularly usually 1 h after administration of the oral test dose. A convenient method is to use two radioisotopes of cobalt, ^{58}Co-labeled cyanocobalamin with IF and ^{57}Co-cyanocobalamin without IF (*often referred to as the dual-isotope method*) [66]. The ratio of excretion of these two radiolabeled vitamin B_{12} is calculated [42]. The dual radioisotope method has several advantages over the classical two stage procedure [67]: (1) the error inherent in incomplete urine collection can be partially obviated since these two isotopes are administered simultaneously, and the ratio of excretion of these isotopes in urine is used to calculate the intestinal absorption of vitamin B_{12} as well as any change in the absorption by the administration of IF (i.e., any correction if the absorption of vitamin B_{12} is subnormal); (2) the total time taken to perfom this test is much shorter than the two phase test. Because of these considerations, many commercial kits for vitamin B_{12} absorption provide for the dual isotope procedure.

Normal subjects (with no abnormality of vitamin B_{12} absorption) show urinary excretion of free radioactive vitamin B_{12} to the extent of 9% or more, with an IF-bound to free cobalamin ratio of between 0.8 and 1.2. In pernicious anemia the urinary excretion of radioactive vitamin B_{12} falls below 8.0% with an IF-bound to free vitamin B_{12} ratio of greater than 1.5. If the urinary excretion of radioactive vitamin B_{12} is decreased (< 8.0%) and the ratio of IF-bound to free radioactive vitamin B_{12} is similar to normal (i.e., 0.8 – 1.2), intestinal malabsorption not due to deficiency of IF would be suspected (Table 5.2).

5.25.1 Food Cobalamin (Vitamin B_{12}) Malabsorption

The Schilling test appears to introduce some degree of artifact from the physiological reality, because it uses a crystalline pharmaceutical form of cobalamin, whereas natural food cobalamin is bound to proteins possibly in reduced forms. Numerous reports have appeared documenting that patients with achlorhydria and other local gastric disorders fail to absorb food vitamin B_{12}, although absorption of crystalline cobalamin by the classical Schilling test is normal [42, 68, 69]. More physiologically designed tests employing cobalamin bound to eggs [70], chicken serum or other proteins have been used especially in cases of atypical cobalamin deficiency. Food cobalamin malabsorption was found in some patients with unexplained low serum B_{12} levels and in subtle cobalamin deficiency states with or without anemia [71, 72] and sometimes with neurological or neuropsychiatric problems relieved by vitamin B_{12} therapy. Some patients with this syndrome have gastric dysfunction consequent to gastritis including that caused by *H. pylori* infection, chronic alcoholism or prolonged use of cimetidine, ranitidine, and omeprazole.

5.25.2 DNA Synthesis and Deoxyuridine (dU) Suppression Test in Megaloblastic Anemia

Megaloblastosis is a morphological abnormality that occurs predominantly in the erythroid precursor cells in the bone marrow and in other replicating cells in human subjects due to deficiency of vitamin B_{12} and folate or metabolic abnormalities involving these vitamins. This pathological change is generally believed to be a morphological expression of deranged DNA synthesis in these proliferaing cells in deficiency of these vitamins and rarely in conditions associated with their metabolic disorders [36, 73]. The abnormality in DNA synthesis resulting from deficiency of these vitamins has been specifically demonstrated as an impaired conversion of deoxyuridine-monophosphate (dUMP) to deoxythymidine-monophosphate (dTMP), a reaction catalyzed by the enzyme thymidylate synthetase, requiring the presence of a reduced folate cofactor, 5,10-methylene-tetrahydrofolate (5,10-CH_2-THF) (Fig. 5.23). This abnormality has been demonstrated in short-term cultures of bone marrow cells and PHA-stimulated lymphocytes from patients with megaloblastic anemia and is referred to as the abnormal deoxyuridine (dU) suppression test.

Percentage radioactivity excreted in urine Groups of subjects	^{57}Co B_{12} + IF (mean + range)	^{58}Co B_{12} (NO IF) (mean + range)	^{57}Co: ^{58}Co ratio (mean + range)
Normal (n = 20)	18.0 (10.0 – 40.0)	17.8 (9.7 – 42.0)	1.0 (0.8 – 1.2)
Pernicious anemia (n = 18)	10.0 (6.0 – 15.0)	3.0 (0.5 – 7.0)	> 1.5
Atrophic gastritis (n = 10)	8.5 (7.0 – 16.0)	4.0 (1.0 – 7.5)	> 1.5
Malabsorption not caused by IF deficiency (tropical sprue) (n = 22)	5.5 (5.0 – 8.0)	6 (4.5 – 7.0)	0.9 (0.8 – 1.2)

Table 5.2. Characteristic results of the Schilling test in normal human subjects and patients with pernicious anemia and other malabsorption syndromes

The biochemical basis of this test is intimately related to the pathways of synthesis of the four constituent deoxynucleotide-triphosphates (dNTPs) of DNA. Cellular DNA synthesis depends on the availability of the four deoxynucleotide-triphosphate building blocks: triphosphates of deoxyadenosine, deoxyguanosine, deoxycytosine and deoxythymidine (dATP, dGTP, dCTP, dTTP) [36, 39] (Fig. 5.23). The introduction of carbon-2 and carbon-8 in the purine ring involves two folate-dependent reactions [36, 37]. Folate coenzymes play a key role in the biosynthesis of pyrimidine nucleotide. A balanced synthesis of purine and pyrimidine nucleotides is an important requirement for DNA synthesis in proliferating cells. The nucleotide pools in the cells are maintained by de novo synthesis as well as by incorporation of exogenous substrates by salvage pathways and interconversions of different nucleotides. The synthesis of dTTP is of particular significance due to the relative specificity of the thymine base for DNA. In mammalian cells, the synthesis of thymidylate (deoxythymidine-monophosphate, dTMP) occurs via the conversion of uridylate (uridine-monophosphate, UMP) to deoxyuridylate (deoxyuridine-monophosphate, dUMP) by an iron-dependent enzyme – ribonucleotide reductase and the subsequent methylation of dUMP to dTMP by the enzyme thymidylate synthetase. The synthesis of dTMP is a rate-limiting step in mammalian DNA synthesis and requires the folate coenzyme 5,10-methylene tertahydrofolate (5,10-CH_2-THF) as an essential cofactor. This step is directly folate dependent and indirectly vitamin B_{12} dependent, since the supply of tetrahydrofolate (THF) is reduced in vitamin B_{12} deficiency due to impaired homocysteine to methionine conversion (methyl folate trap) [40, 74]. When exogenous deoxyuridine (dU) is added to cultures of proliferating cells, this substrate (dU) is also taken up by these cells and phosphorylated to dUMP, which then acts as a substrate for thymidylate synthesis. The synthesis of dTMP from dUMP forms the major de novo pathway of thymine-DNA synthesis in mammalian cells under normal circumstances. However, almost all cells also contain the enzyme thymidine kinase for cellular uptake of preformed or exogenously added thymidine, which provides a "salvage pathway" for thymine-DNA synthesis. This alternative pathway may be of particular significance in bone marrow for possible reutilization of thymidine available from the breakdown or turnover of cells. Cellular DNA synthesis is regulated by a number of feedback loops involving these pathways (Fig. 5.23). The two alternative pathways of thymine-DNA synthesis – the de novo and the salvage pathways – are interrelated by a common end-product (deoxy-thymidine-triphosphate, dTTP), which exerts a regulatory influence on both pathways by a feedback inhibition and presumably maintains a balanced synthesis of cellular DNA [36, 37]. By the simultaneous addition of ^{3}H-deoxyuridine (^{3}H-dU) and ^{14}C-thymidine in short-term cultures of bone marrow cells and PHA-stimulated cultures of lymphocytes, it has been shown that there is a reciprocity between the de novo and the salvage pathway of dTTP synthesis so that increasing concentrations of added dU suppress the incorporation of thymidine and vice versa [74].

5.25.3 Deoxyuridine (dU) Suppression Test

The deoxyuridine (dU) suppression test essentially measures the effective conversion of dUMP to dTMP and the impairment of this reaction in deficiency of vitamin B_{12} and/or folate. In practice, this test is performed by monitoring the extent to which added (exogenous) nonradioactive dU suppresses the incorporation into DNA of ^{3}H-thymidine or its analogue ^{125}I-deoxyuridine [39, 73, 74]. When an excess of deoxyuridine is added to short-term cultures of normal bone marrow cells, the incorporation of ^{3}H-thymidine into DNA via the salvage pathway is reduced or suppressed, but this suppression does not occur (abrogated) in the bone marrow of patients with megaloblastic anemia. It has been further shown that vitamin B_{12} is not directly involved in the de novo pathway of dTMP synthesis and that impaired dTMP synthesis in vitamin B_{12}-deficient bone marrow cultures is due to a block in folate metabolism in vitamin B_{12} deficiency; this block involves the failure or impairment of conversion of homocysteine to methionine, which requires methyl cobalamin as an essential cofactor and 5-methyl THF as a methyl-group donor. In vitamin B_{12} deficiency, methyl THF accumulates in plasma and perhaps in cells as well, causing generalized deficiency of functional folate (i.e., the methyl folate trap hypothesis) [40]. In short-term cultures of bone marrow cells from non-megaloblastic patients, preincubation with excess nonradioactive dU suppresses the incorporation of ^{3}H-thymidine to approximately 10% of control cultures (i.e., replicate cultures of the same marrow to which no dU has been added) and the extent of this suppression is not further increased by the addition of folate or vitamin B_{12}. In folate-deficient megaloblastic anemia, there is an inadequate pool of folate, as a result of which there is inadequate methylation of dUMP to dTMP. In deficiency of vitamin B_{12}, the active folate pool is depleted due to decreased availability of reduced folate, since "folate" is trapped as metabolically inactive 5-methyl THF as a result of failure of vitamin B_{12} (methyl cobalamin)-dependent homocysteine-to-methionine interconversion [37]. The net effect of vitamin B_{12} deficiency on the de novo pathway of thymidylate synthesis (dUMP®dTTP) is similar to that of folate deficiency. Therefore, in deficiency of either vitamin, the synthesis of dTMP via the folate-dependent de novo pathway (by the catalytic ef-

fect of the enzyme thymidylate synthetase) is decreased and this impairment of the de novo pathway appears to be closely related to the severity of the vitamin deficiency. As a result of this abnormality, the alternative salvage pathway of dTMP synthesis (via direct thymidine incorporation) becomes correspondingly more active. This correlates well with increased activity of the salvage pathway enzyme, thymidine kinase in the hematopoietic cells in these vitamin-deficiency states [30, 35, 39, 75, 76, 77]. This promotes increased incorporation of ^{3}H-thymidine into the dTMP pool and finally into DNA. As a result of this, in spite of adding a standardized excess of nonradioactive dU to the cultures of bone marrow cells, ^{3}H-thymidine incorporation into DNA remains proportionately higher than in cultures of normal bone marrow cells (i.e., greater than 10%). In folate deficiency, dU suppression abnormality is completely corrected by folic acid (i.e., pteroylmonoglutamate), 5-methyl THF as well as folinic acid, but not by vitamin B_{12}. On the other hand, in vitamin B_{12} deficiency, the abnormal dU suppression is partially corrected by the addition of vitamin B_{12} alone, but completely corrected by the simultaneous addition of vitamin B_{12} and 5-methyl THF, or by the addition of folic acid or folinic acid alone, and not at all by 5-methyl THF.

The dU suppression test for the diagnosis of vitamin B_{12} and folate deficiency can also be performed with excellent results in cultures of PHA-stimulated lymphocytes from patients with deficiency of these vitamins [77 – 79]. The detailed methodology for performing the dU suppression test has been described by Das et al. [30, 39, 77 – 79], who showed that when performed with appropriate controls, the test is very sensitive and is capable of detecting these vitamin deficiencies even when morphological manifestations of megaloblastosis remain equivocal.

5.26 Visualization and Imaging of the Spleen in Health and Disease

The spleen is an important and interesting organ with diverse functions, some or all of which may be affected in several primary hematological disorders; on the other hand, disorders of the spleen may lead to hematological abnormalities. In both instances evaluation of splenic functions and visualization of the spleen become important for diagnosis, prognosis (including staging) and therapeutic management. The spleen is a unique organ of great relevance to the hematopoietic system in both prenatal and postnatal life. Its development from the embryonic mesoderm becomes apparent at the 5th week of gestation just posterior to the developing stomach. The mesenchymal cells possibly derived from the yolk sac of the embryo differentiate into several functional components of the hematopoietic system such as pluripotent stem cells and colony-forming units, the reticuloendothelial system (RE cell system) and the lymphatic system. It is no wonder that different investigators have classified the spleen differently as being a component of:

- The circulating system
- The hematopoietic system
- The mononuclear phagocytic system
- The lymphatic system

Developmentally, several independent lobules within the mesogastrium appear to fuse to form a multilobulated mass that ultimately becomes structurally organized into the spleen in late fetal life; occasionally a stray lobule failing to coalesce with the main mass forms an independent or accessory mass of functioning splenic tissue. Thus the spleen appears to take its definitive shape after several similar lobular masses of tissue converge and coalesce in both structure and function. The spleen is anatomically disposed between the stomach and the left costal margin of the ribs. Its size varies with age as well as with immunological and nutritional status. The average adult spleen measures 12 × 3.5 cm with a weight of 150 g and a volume of approximately 300 ml. A spleen longer than 14 cm is usually clinically palpable. The spleen enlarges in a variety of hematological as well as non-hematological disorders and may be massively enlarged, weighing more than 2 kg in some hematological disorders.

The spleen is a functionally complex organ and this is reflected in its microstructure. The splenic tissue is supported by a connective-tissue scaffold that also provides the intrasplenic framework. The vascular elements enter the spleen at the hilum, traverse the connective tissue trabeculae and penetrate the interior of the spleen to supply the microcirculation including the red pulp. As the arterial elements enter the splenic tissue, they become surrounded by an aggregate of lymphoid tissue which is distributed along the arterial vasculature in a sheath-like pattern. These lymphoid aggregates are collectively termed the white pulp of the spleen. Sometimes isolated follicles appear at places along the coaxial course of the lymphoid sheath in the parenchyma of the spleen (Malpighian corpuscles). The white pulp forms about one-fourth of the splenic volume and is composed predominantly of lymphocytes. The periarteriolar lymphatic sheath (PALS) is formed by a collection of T-lymphocytes which traverse the splenic tissue following the arterioles in a coaxial fashion until terminal distribution. The follicular collection of lymphoid elements (i.e., Malpighian corpuscles) in the splenic parenchyma are composed mainly of B-lymphocytes [80, 81]. The balance of splenic tissue beneath the capsule formed by the fi-

brous tissue is the red pulp, constituting three-fourths of the splenic volume. It is composed of vascular channels which provide the pathways for splenic microcirculation including the splenic sinusoids. These sinuses are incompletely lined by endothelial and adventitial cells with a highly fenestrated basement membrane. These sinuses are connected by cords (Bilroth cords) which are formed by a reticular meshwork of fibroblast-like cells which are in fact rich in cells of the monocyte-macrophage system (i.e., RE system). The lumen of these splenic cords (Bilroth cords) are packed with circulating elements of blood in transit: erythrocytes, platelets, macrophages, lymphocytes, granulocytes and plasma cells. Thus the spleen acts as a clearing house for circulating cellular elements of blood. Between the white and the red pulp, an intermediate region is found which is known as the marginal zone.

Branches of the splenic arteries such as central arteries continue from the white pulp sheath through the marginal zone and eventually end up in the red pulp giving off additional branches at right angles (lateral) to the arteries. These lateral branches are known as penicillar branches [80]. They may circle back and supply the marginal sinus; they may terminate in the red pulp supplying the splenic cords and a minority may directly terminate into the venous sinuses for direct venous return (closed system). Circulating elements of splenic blood flow return by first entering the splenic sinuses which are the preliminary venous vessels. They may do so directly through the arterial connection in a closed circulatory fashion; alternatively, plasma and blood cells may reach the sinuses only after percolating through the reticulum of the parenchyma in an open circulatory system [81, 82].

The multiplicity of tissues and cell systems present in the spleen indicate the diverse functions of this organ. As stated above, the spleen houses several structural and functional systems in a predominantly single anatomical space (in the absence of accessory spleens). One of the basic functions of the splenic blood flow is to filter blood of aging, senescent and abnormal red cells (culling), and intraerythrocytic inclusions (pitting) as well as extrinsic or foreign particles. The mechanism(s) by which these functions are actually carried out are still poorly understood. There are several theories as to the mechanism underlying the process of recognition and removal of aged and effete red cells which are still of academic interest. These include (a) trapping of aged red cells in the resident macrophages of the cord of Bilroth due to membrane loss and resultant poor deformability of these cells; (b) hemoconcentration created in the splenic cords leading to a limited supply of metabolites, decreased ATP production and failure of the Na^+/K^+ pump with eventual swelling and entrapment of the cells within the meshwork of red pulp macrophages; (c) aged red cells expose their surface antigens to the blood cells, which are recognized by self-directed antibodies [80].

Regardless of the mechanisms involved, it is apparent that red or other cells bound for destruction (aged cells, abnormal cells, etc.) become trapped or held within the meshwork of splenic cords and as the splenic transit time increases, the cells become vulnerable to destruction by resident phagocytic cells. Similar events occur for morphologically abnormal red cells in hereditary spherocytosis, elliptocytosis and sickle cell anemia; this is a common denominator for the spleen's ability to clear these red cells [80].

The ability of the spleen to remove intraerythrocytic inclusions while maintaining the integrity of the red cells is known as the pitting function of the spleen. This process occurs in a variety of pathological states and includes Heinz bodies (denatured hemoglobin), Howell-Jolly bodies (nuclear remnants), and Pappenheimer bodies (iron granules) [82–84]. When these cells pass through the splenic red pulp and try to reenter the circulation through the slit-like fenestrations of the sinus endothelium, the deformable part of the red cell can negotiate and pass through the fenestrations, whereas the nondeformable inclusion is removed or held back by the macrophages [4]. The splenic macrophages are also capable of removing particulate matter from the circulating blood by their phagocytic functions [80, 84].

The spleen subserves important immunological functions. In fact, the cellular composition and peculiar microstructure including the vasculature make it a unique organ for appropriate immune functions. The presence of T- and B-lymphocytes in close proximity to the resident and circulating macrophages as well as the architecture of the splenic pulp and the splenic cord make it ideally suited to play a coordinating role both in the nonspecific and the specific arms of immune responses. The non-specific functions involve the clearance of pathogens, the clearance of opsonized red cells and platelets, production of complement components and perhaps surveillance against malignant cells. The spleen plays an important role in removing bloodborne pathogens such as bacteria, especially encapsulated ones, viruses and circulating immune complexes. It is well known that asplenic or hyposplenic patients or patients – particularly children after splenectomy – are prone to develop fulminant septicemia most often involving encapsulated bacteria (e.g., pneumococci, meningococci, etc.) and overwhelming post-splenectomy sepsis (OPSI) [85].

The specific immune functions of the spleen are of considerable significance. Ninety percent of the blood in the spleen passes through the marginal sinuses and surrounding zones [82, 83]. Foreign antigens present in the blood are exposed to the T- and B-lymphocytes of the PALS and the Malpighian follicles and stimulate a

cascade of responses in both humoral and cellular arms of the immune system, ultimately resulting in the production of IgM, plasma cells and memory cells [82] specific to the exposed antigens.

The spleen is an important reservoir of the blood's cellular elements. Its role as a reservoir of red cells in the human being remains controversial [80]. Recently evidence has been provided that supports the role of the spleen also as a reservoir for white blood cells [82, 85–87]. The spleen can sequester approximately 30% of the body's platelets and release them on demand. A pathologically enlarged spleen as seen in patients with portal hypertension and tropical splenomegaly can sequester up to 90% of the body's reserves and cause severe thrombocytopenia [82]. On the other hand, there is a significant rise in platelet counts following splenectomy which may sometimes be transient, if the RE cell system in other organs including the liver compensates by increasing its ability to sequester platelets [82]. The normal spleen holds only about 2–20 ml of red cells and there is a rapid mixing of circulating red cells and splenic pool of red cells in normal subjects. For these reasons, it is believed that the normal spleen serves no reservoir function in man [80, 82]. The human spleen trabeculae lacks the substantial contractile elements seen in other species and changes in the splenic blood flow are generally due to changes in splenic vascular tone alone in normal human subjects [80].

The spleen is a major site of erythropoiesis from the 5th month of intrauterine life; it loses its ability to do so gradually and at birth it ceases to produce red cells. In postnatal life, the spleen may participate in hematopoiesis in some pathological states such as in myelofibrosis, myelosclerosis with myeloid metaplasia and secondary metastasis of malignant tumors in the bone marrow; for extramedullary hematopoiesis in these pathological conditions, the stem cells are possibly derived from the circulating blood or from displaced bone marrow cells. The spleen may have some undefined role in the recycling of iron obtained from the degraded hemoglobin of red cells after they are destroyed by the macrophages in the spleen, since asplenic patients show lower serum iron concentrations for a considerable period of time after the spleen is lost [82–84].

Visualization of the spleen becomes necessary in pathological conditions associated with enlargement of this organ (splenomegaly) as well as in diseases in which splenic atrophy or asplenia occurs. The determination of spleen size by traditional radiographic techniques remains unsatisfactory and usually fails to detect minor enlargement often undetected on physical examination. Even a moderately enlarged spleen may be difficult to palpate in obese persons. In recent years several imaging techniques have been used very successfully for visualization of the spleen. These include ultrasonic imaging, magnetic resonance imaging (MRI) and computed tomography (CT) scan. Most or all of these procedures yield excellent structural details with little or no information about splenic function. Radionuclear imaging of the spleen, in addition, provides a major advantage in that more reliable information is obtained on the functions of the spleen. The principle of radionuclide scintillation scanning of the spleen involves intravenous injection of radiolabeled autologous red cells of the patients, after these red cells have been subjected to certain procedures to damage them in a manner that when injected, they are rapidly removed from the circulation by the spleen. The red cells of the patient are labeled with ^{51}Cr, ^{111}In or ^{99m}Tc and then heated to a temperature of 49.5°C for precisely 20 min. These radiolabeled heated red cells are injected back into the patient and scintillation scanning is usually done about 1 h later, but it can be performed up to 3–4 h later [28]. This procedure is very useful for map-

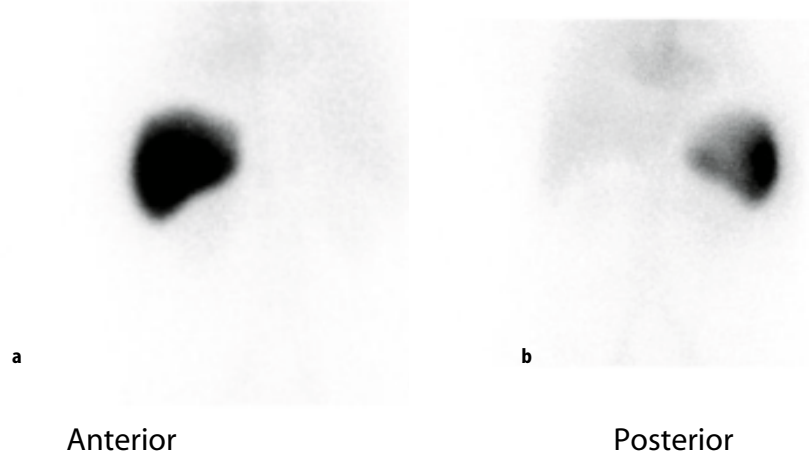

Fig. 5.24. A 47-year-old female with history of persistent thrombocytopenia. A ^{99m}Tc-denatured labeled RBC scan has been performed to rule out functional hyposplenia. The study shows homogeneous radiotracer distribution to the normally located splenic tissue. Findings indicate normally functioning splenic tissue (AHE)

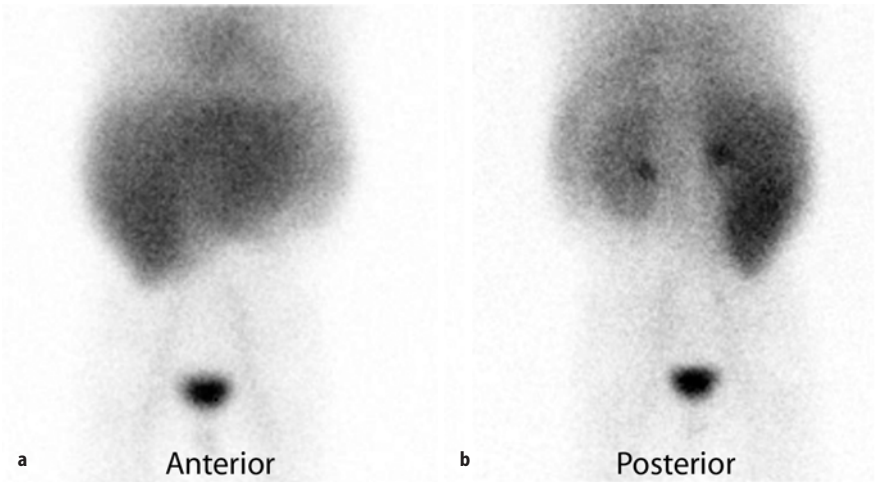

Fig. 5.25. A ^{99m}Tc-denatured red blood cell study of a 9-year-old boy known to have sickle cell anemia with recurrent vaso-occlusive crises. A ^{99m}Tc-sulfur colloid scan previously done showed hepatomegaly with non-visualized spleen. This denatured labeled RBC study was obtained to assess the sequestration function of the spleen. The study shows hepatomegaly with no scintigraphic evidence of sequestrating splenic tissue indicating non-functioning splenic tissue (AHE)

ping out the spleen size and in the diagnosis of splenomegaly (Fig. 5.24), space-occupying lesions such as splenic cysts and tumor deposits, for identifying abnormally disposed spleen and accessory splenic tissue, and for demonstrating asplenia, splenic atrophy or the presence of residual splenunculus (Fig. 5.25a,b). The area of the spleen can be determined from the linear measurements and the volume of the spleen can be obtained from these measurements using an appropriate formula such as [6]:

Spleen volume (ml) = 9.9A – 540,
(where A = measured area of the spleen).

5.26.1 Measurement of Splenic Activity

Splenic activity can be measured by studying the rate of clearance of heat-damaged ^{51}Cr-labeled red cells from the circulation. A sample of blood is collected from the patient exactly 3 min after the midpoint of the injection of heat-damaged ^{51}Cr-labeled red cells and further samples are collected at 5-min intervals for 30 min, then at 45 min and finally at 60 min. The radioactivity in each sample is measured and expressed as a percentage of the radioactivity in the 3-min sample. These are plotted on semilogarithmic graph paper, the radioactivity of the 3-min sample being taken as 100%. The radioactivity curve is generally exponential and the rate of blood flow is calculated as the reciprocal of the time taken for the radioactivity to fall to 50% value (T½). In individuals with normal splenic activity, the T½ ranges from 5 to 15 min. The clearance rate is considerably prolonged in thrombocythemia and in other conditions associated with splenic atrophy such as sickle cell anemia or celiac disease [28, 48, 85–88]. The relevant procedure has been described in great detail by Dacie and Lewis [28].

5.26.2 Bone Marrow Imaging by Scintigraphy

Bone marrow imaging by scintigraphy (BMS) provides a whole-body picture of the functioning hematopoietic tissue. The recently introduced MRI is a highly sensitive technique for imaging normal and abnormal bone marrow and can detect differences between normal bone marrow and fatty, fibrotic, hypercellular and hemosiderotic bone marrow [88, 89]. BMS is equally sensitive and can depict a functional image of the bone marrow with the help of recently introduced new radiopharmaceutical agents that localize in the bone marrow such as ^{99m}Tc-labeled nanocolloid and monoclonal antibody (^{99m}TcMAb).

From the functional aspects BMS should be ideally capable of imaging the pathophysiological changes relating to the different functional cell lineages [90–94] such as: (a) erythropoietic imaging; (b) reticuloendothelial imaging (RE cell imaging); (c) granulopoietic imaging.

The radiopharmaceutical tracers used in these studies vary with the type of cell lineage targeted. Erythropoietic marrow and activity can be analyzed by visualization with ^{52}Fe labeling and positron imaging as indicated earlier in this chapter in connection with studies on erythropoiesis and iron metabolism.

Iron-52 is an ideal radionuclide for measuring the extent of erythropoietic marrow [90–94]. This is produced in a cyclotron, has a half-life of 8.2 h and is thus capable of being transported to locations distant from the site of its production. The erythropoietic bone marrow can be imaged for up to 24 h after this radionuclide has been injected. Due to the possible high radiation burden to the bone marrow (the energy level of the radiation emission by ^{52}Fe is relatively high), the administered dose is usually limited to 100–200 mCi and the image quality may be relatively poor when scanned by

a conventional scintillation camera equipped with a high-energy collimator. However, better-quality images are produced when a positron-emission tomography (PET) scanner is used. One of the advantages of ^{52}Fe over the RE system tracers is that the activity over the liver and the spleen is poor or absent, which makes it convenient to detect pathology in the bone marrow over the thoracic and lumbar areas.

Another radiotracer used in bone marrow imaging is technetium ^{99m}Tc-labeled colloids which, when injected into blood, are rapidly cleared by the phagocytic cells in the blood, bone marrow and liver (Kupffer cells) and by the RE cells in the spleen. In most nuclear medicine laboratories, ^{99m}Tc-sulfur (particle sizes ranging from 100 to 1000 nm) are used. It has been found that in normal adults about 5% of the injected radioactivity is distributed in the RE cells of the bone marrow, 80%–85% in the liver and 10% in the spleen [90, 91]. As a result of this, bone marrow in the lower thoracic and upper lumbar spine cannot be properly visualized by ^{99m}Tc-colloid imaging due to overlapping radioactivity over the liver and the spleen (Fig. 5.26).

Recently ^{99m}Tc-labeled monoclonal antibodies (^{99m}Tc-MAB) directed against nonspecific iron-reacting antigen 95 (NCA-95), a differentiation antigen of granulopoiesis, have been obtained [90, 95–97] and clinically applied for the imaging of granulopoietic marrow [99–101]. Using this complex (^{99m}Tc-Ab), bone marrow scans of much-improved quality have been obtained without significant superimposition of liver and spleen and the radioactivity over the bone marrow was found to be 2–4 times that with ^{99m}Tc microcolloid [100, 101, 103]. High-quality images with homogeneous distribution of ^{99m}Tc-AB in hematopoietic bone marrow have been obtained [90] (Fig. 5.27). Indium-111 chloride has been used as a marrow imaging agent but with indifferent results and the exact target of ^{111}In has not been properly identified. This radiotracer is produced in a cyclotron, has a half-life of 2.8 days and emits photons with energies of 173 and 247 KeV. Approximately 1–5 mCi (37–185 MBq) of ^{111}In chloride is injected intravenously and images are obtained 24–48 h later. Following intravenous injection, ^{111}In is rapidly complexed with serum transferrin and eliminated from the plasma with a half-life of 5 h [89–91]. About 30% of the ^{111}In is distributed to the bone marrow, 20% to the liver, 7% to the kidneys and 1% to the spleen and the remaining all over the body without any specific tissue accumulation. In spite of its strong affinity for transferrin [89, 104, 105], only approximately 4% of the injected ^{111}In activity appears in the peripheral red blood cells after 8–10 days as com-

Fig. 5.26. ^{99m}Tc-sulfur colloid scans. Intense activity in the liver and spleen often obscures bone marrow in the lower thoracic and upper lumber spine regions. (From [90] with permission)

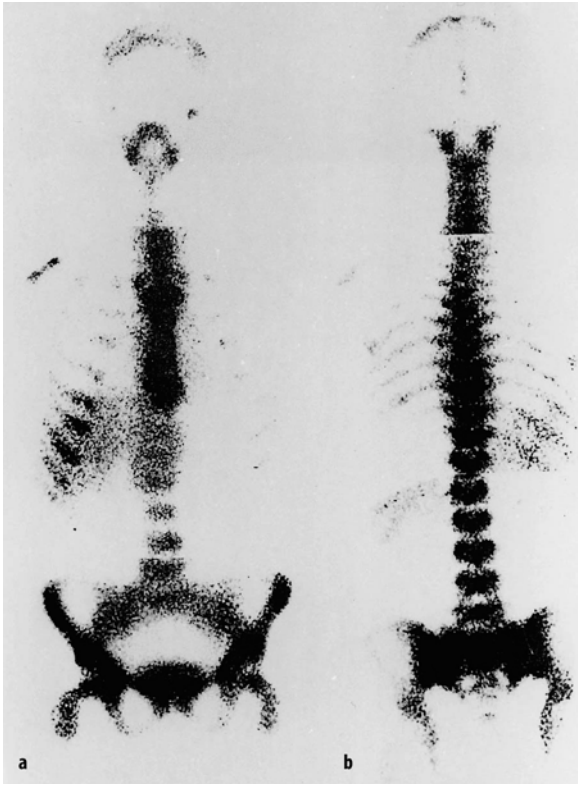

Fig. 5.27a,b. Normal bone marrow scans with ^{99m}Tc-NSAb. **a** anterior, **b** posterior. (From [90] with permission)

pared with 80% of iron [89], but the marrow distribution of its localization remains uncertain. The cellular and subcellular distribution of ^{111}In in the bone marrow needs to be further studied [90, 92, 93]. A scintigraphic scan with ^{111}In shows a distribution of activity similar to that of ^{99m}Tc-labeled colloids in patients with normal bone marrow [90, 92, 93]. However, many reports have appeared, indicating disparity between ^{111}In activity and ^{52}Fe activity (erythropoietic activity) in various conditions [90, 92, 93, 104] (Fig. 5.28).

5.26.3 Leukocyte (WBC) or Granulocyte Labeling for Imaging Bone Marrow

Leukocytes labeled with either ^{111}In or ^{99m}Tc are generally used for the localization of infections or abscesses. This has also been tried in bone marrow imaging [90, 106, 107, 108]. A recent study claimed that ^{99m}Tc-WBC activity (Fig. 5.28a) correlated better with hematopoietic cellularity than ^{111}In-chloride activity [92, 102, 107]. However, tomographic techniques used with ^{111}In-labeled granulocytes showed that the bone marrow:liver activity ratio was higher than that for ^{99m}Tc-WBC, indicating that with ^{111}In-labeled leukocytes the activity over the liver is significantly less than that of colloidal agents [90, 102, 108, 109] (Fig. 5.28b).

5.26.4 Blood Platelets

The blood platelets are the smallest blood cells, measuring 2 – 4 μm in diameter and 5 – 8 fl in volume. These cells are non-nucleated and are formed predominantly in the bone marrow as fragments of cytoplasm of the megakaryocytes. Megakaryocytes develop from pluripotent stem cells through several stages of maturation under the influence of a number of cytokines. These include thrombopoietin, a specific hematopoietic hormone which is now available as a recombinant product for use in some types of thrombocytopenia.

In addition, IL-3, IL-6 and IL-11 have synergistic effects on thrombopoiesis. Morphologically recognizable precursor cells of this series include megakaryoblasts, promegakaryocytes and megakaryocytes. These precursor cells have a large nucleus which develops into multilobulated forms by endomitotic division till megakaryocytes are formed; at this stage mitosis ceases and platelet formation occurs by cleavage of the cytoplasm into fragments. Each megakaryocyte is believed to be capable of giving rise to as many as 3000 or more platelets. Immediately after they are released from the bone marrow, the large platelets or "proplatelets" pass to the microcirculation of the lungs, where the platelets take their final shape probably through a process of mechanical trimming. Platelets are non-nucleated

Fig. 5.28. ^{111}In-WBC (*left*) and ^{99m}Tc-WBC (*right*) scans. The spine is not usually obscured. (From [90] with permission)

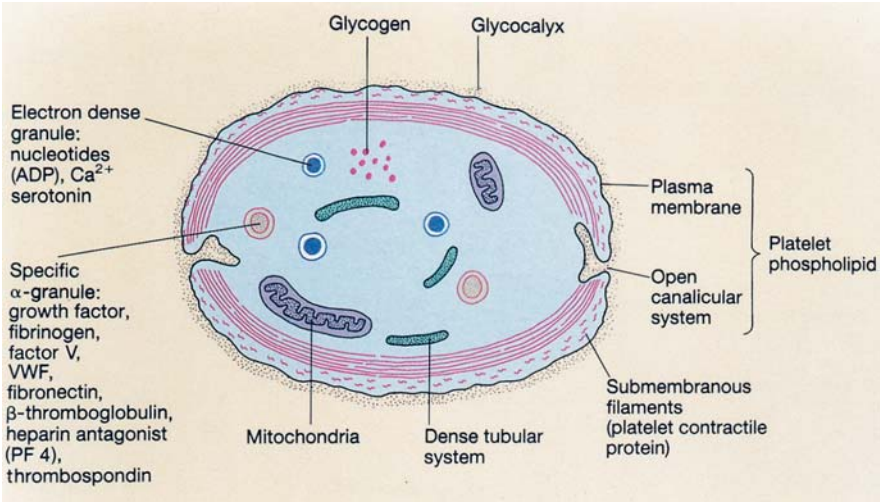

Fig. 5.29. The ultrastructure of a platelet. (Reproduced from [110] with permission)

cells, but possess typical lipid bilayer plasma membrane which is essential for their functional integrity. The plasma membrane contains a number of glycoprotein receptors through which platelets interact with various blood coagulation factors such as von Willibrand Factor (vWF), fibrinogen, thrombin and other aggregating agents such as ADP, ristocetin, epinephrine, collagen and arachidonic acid. The platelet membrane also contains phospholipids which are essential components for the synthesis of prostaglandins and mobilization of calcium within the cells and for the generation of platelet procoagulant activity.

Although platelets do not have a nucleus, they possess organelles and constituents that promote brisk metabolic activity. Transmission-electron microscopy of platelets (Fig. 5.29) demonstrates the presence of the dense microtubular system, the circumferential microfilaments which maintain the discoid shape of these cells. Platelets also possess mitochondria with their complement of enzymes, the electron-dense granules which contain nucleotides (ADP), calcium and serotonin, and the specific a-granules containing platelet-derived growth factor (PDGF), fibrinogen, factor V, vWF, fibronectin, β-thromboglobulin, PF-4 (platelet factor 4 – a heparin antagonist) and thrombospondin. The contractile property of platelets is ensured by the microtubular systems, the circularly disposed microfilaments and the presence of actin, myosin and calmodulin.

Approximately 30% of the circulating platelets are in the splenic pool (or are sequestered in the spleen) and it is generally believed that platelets spend about a third of their life span in the spleen. The splenic pool of platelets is markedly increased in conditions associated with splenomegaly with or without reduction of mean platelet life span. The life span of normal platelets ranges between 9 and 14 days. In immune thrombocytopenias (idiopathic thrombocytopenic purpura, ITP; drug-induced immune thrombocytopenia) platelets sensitized by autoantibodies may be destroyed in the liver and the spleen. The life span of platelets in patients with ITP is appreciably reduced and the measurement of platelet life span in this condition appears to have a clinical relevance, since this may be useful in the diagnosis, prognosis and management of some patients with this autoimmune thrombocytopenia. The majority of patients with ITP respond well to the administration of corticosteroids or intravenous immunoglobulins. Some patients with this disorder may become refractory to these therapeutic measures and splenectomy offers a good alternative therapeutic measure.

5.26.5 Measurement of Platelet Survival

Platelet survival can be studied by in-vitro radioisotopic labeling of platelets using ^{51}Cr as the tracer isotope as in the case of measuring red cell survival [28]. Recently it has been recommended that ^{111}In may replace ^{51}Cr with several advantages. ^{111}In has a shorter half-life, a greater efficiency because of higher photon emissions and a greater affinity for platelets. The use of ^{111}In as a platelet-labeling agent also appears to make it possible to measure platelet pooling in the spleen, liver and other organs and thus to identify the sites of platelet destruction [28]. The details of methodology have been described in monographs of hematology techniques [28] and nuclear medicine [90].

References

1. Lawrence JH (1940) Nuclear physics and therapy: preliminary report on a new method for the treatment of leukemia and polycythemia. Radiology 35:51
2. Hahn L, Hevesy GA (1940) A method of blood volume determination. Acta Physiol Scand 1:3 – 5

3. Paraskevas F (1999) Phagocytosis. In: Lee GR, et al (eds) Wintrobe's clinical hematology, 10th edn, vol 1. Williams and Wilkins, Baltimore, p 415
4. Vogler JB, Murphy WA (1988) Bone marrow imaging. Radiology 168:679 – 693
5. Dunnhill MS, Anderson JH, Whitehead R (1967) Quantitative histological studies on age changes in bone. J Pathol Bacteriol 94:275 – 291
6. Hoffbrand AV, Lewis SM, Tuddenham EGD (1999) Postgraduate haematology, 4th edn. Butterworth-Heinemann, Oxford, pp 1 – 22, 327, 330, 334
7. Martial P, Ferrant A, Cogneau M, et al (1987) Assessment of bone marrow blood flow using positron emission tomography; no relationship with bone marrow cellularity. Br J Haematol 66:307 – 310
8. Till JE, McCullough EA (1961) A direct measurement of the radiation sensitivity of normal mouse bone marrow cells. Radiat Res 14:213 – 222
9. Bondurant MC, Koury MJ (1999) Origin and development of blood cells. In: Lee GR, et al (eds) Wintrobe's clinical hematology, 10th edn, vol 1. Williams and Wilkins, Baltimore, p 149
10. Sutherland HJ, Landsorp PM, Henkelman, et al (1990) Functional characterization of individual human hematopoietic stem cells cultured at limiting dilution on supportive marrow stromal layers. Proc Natl Acad Sci U S A 87:3584 – 3588
11. Murry L, Chen B, Galy A, et al (1995) Enrichment of human hematopoietic stem cell activity in the CD 34^{+}Thy-1 + Lin-subpopulation from mobilised peripheral blood. Blood 85:368 – 378
12. Pelzer A, Hogge DE, Lansdorp PM, et al (1996) Self-renewal of primitive human hematopoietic cells (long-term culture initiating cells) in vitro and their expression in defined medium. Proc Natl Acad Sci U S A 93:1470 – 1474
13. Koller M, Emerson S, Palsson B (1993) Large-scale expansion of human stem and progenitor cells from bone marrow mononuclear cells in continuous perfusion cultures. Blood 82:378 – 384
14. Sawyer ST, Krantz SB (1986) Transferrin receptor number synthesis and endocytoxis during erythropoietin – induced maturation of Friend virus-infected erythroid cells. J Biol Chem 261:9187
15. Perry RP (1976) Processing of RNA. Ann Rev Biochem 45:605
16. Adamson SD, et al (1968) Factors affecting the rate of protein synthesis in lysate systems from reticulocytes. Arch Biochem Biophys 125:671
17. Bruns GP, London IM (1995) The effect of hemin on the synthesis of globin. Biochem Biophys Res Commun 18:236
18. RossJ, Sautner D (1976) Induction of mRNA accumulation by hemin in cultured erythroleukemia cells. Cell 8:513
19. Waxman HS, Rabinovitz M (1966) Control of reticulocyte polyribosome content and hemoglobin synthesis by heme. Biochem Biophys Acta 129:369
20. Rannue RS, et al (1978) Regulation of protein synthesis in rabbit reticulocyte lysates. Proc Natl Acad Sci U S A 75: 745
21. Lohr JB, Friedman HC (1976) New pathway for d-aminolevulinic acid biosynthesis: formation from a-ketoglutaric acid by two partially purified plant enzymes. Biochem Biophys Res Commun 69:908
22. Rabin M, McClelland A, Kuhn L, et al (1985) Regional localisation of the human transferrin receptor gene to $3q^{26-qter}$. Am J Hum Genet 37:1112
23. Huebers H, et al (1982) Basis of plasma iron exchange in the rabbit. J Clin Invest 70:769
24. Chitambar CR, Zivkovic Z (1989) Release of soluble transferrin receptor from the surface of human leukemic HL60 cells. Blood 74:602
25. Flowers CH, et al (1989) The clinical measurement of serum transferrin receptor. J Lab Clin Med 114:368
26. Huebers HA, et al (1990) Intact transferrin receptors in human plasma and their relation to erythropoiesis. Blood 75:102
27. Ponka P, Neuwirt J (1970) Feedback inhibitory effect of heme on iron entry into reticulocytes and on heme synthesis. Br J Haematol 19:593
28. Dacie JV, Lewis SM (1995) Erythrokinetics. In: Practical haematology, 8th edn. Churchill Livingstone, Edinburgh, pp 397 – 416
29. Lee GR, Herbert V (1999) Nutritional factors in the production and function of erythrocytes. In: Lee GR, et al (eds) Wintrobe's clinical hematology, 10th edn, vol 1. Williams and Wilkins, Baltimore, pp 228 – 266
30. Das KC, Mohanty D, Garewal G (1989) Nutritional megaloblastosis: from morphology to molecular biology. In: Sapru RP (ed) Medical research monographs. Malhotra Publishing House, New Delhi, pp 1 – 59
31. Price DC (1996) The hematopoietic system. In: Herbert JC, Eckelman WC, Neumann RD (eds) Nuclear medicine: diagnosis and therapy. Thieme Medical Publishers, New York, pp 764 – 785
32. Ahuja S, Lewis SM, Szur I (1972) Value of surface counting in predicting response to splenectomy in haemolytic anaemia. J Clin Pathol 25:467
33. Ferrant A, Cauwe JL, Michaux C, Beckers C, et al (1982) Assessment of the sites of red cell destruction using quantitative measurement of splenic and hepatic red cell destruction. Br J Haematol 50:591
34. Herbert V, Das KC (1992) Anemias due to maturation defects. In: Hurst JW (ed) Medicine for the practising physician, 3rd edn. Butterworth-Heinemann, Oxford, pp 851 – 857
35. Das KC (1995) Megaloblastosis a morphological expression of molecular derangements in DNA and histone biosynthesis. Immunohematol Bull 26:1 – 24
36. Das KC, Herbert V (1976) Vitamin B12-folate interrelationships. Clin Haematol 5:697 – 725
37. Herbert V, Das KC (1976) The role of vitamin B_{12} and folic acid in haemato- and other cell poiesis. Vitam Horm 34:1 – 30
38. Das KC, Garewal G, Mohanty D (1980) Derangement of DNA synthesis in erythroleukaemia. Normal deoxyuridine suppression and impaired thymidine in corporation in bone marrow culture. Acta Haematol 64:121 – 134
39. Das KC, Herbert V (1989) In vitro DNA synthesis by megaloblastic bone marrow. Am J Hematol 31:11 – 20
40. Herbert V, Zalusky R (1962) Interrelationships of B_{12} and folic acid metabolism: folic acid clearance studies. J Clin Invest 41:1263 – 1276
41. Herbert V (1987) The Herman Award Lecture: Nutrition science as a continually unfolding story: the folate and vitamin B_{12} paradigm. Am J Clin Nutr 46:387 – 402
42. Zittoun J, Zittoun R (1999) Modern clinical testing strategies in cobalamin and folate deficiency. Semin Hematol 36:35 – 46
43. Chanarin I (1979) Pernicious anaemia. In: Megaloblastic anaemias, 2nd edn. Blackwell Scientific, London, pp 316 – 331
44. Herbert V (1985) Biology of disease. Megaloblastic Anaemias Lab 52: 3 – 19
45. Lindenbaum J, Healton EB, Savage DB, et al (1988) Neuropsychiatric disorders caused by cobalamin deficiency in the absence of anemia or macrocytes. N Engl J Med 318:1720 – 1728

46. Kanazawa S, Herbert V (1985) Total corrinoids, cobalamin (vitamin B_{12}) and cobalamin analogue levels may be normal in serum despite cobalamin in liver depletion in patients with alcoholism. Lab Invest 53:108 – 110
47. Mackenzie RE (1986) Summary: pteroylpolyglutamate metabolism. In: Cooper BA, Whitehead VM (eds) Chemistry and biology of pteridines. de Gruyter, Berlin, pp 767
48. Garewal G, Narang A, Das KC (1988) Infantile tremor syndrome: a vitamin B_{12} deficiency syndrome in infants. J Trop Pediatr 34:174 – 178
49. Chanarin I, Deacon R, Lumb, et al (1992) Cobalamin and folate: recent developments. J Clin Pathol 45:277 – 283
50. Anderson BB (1964) Investigations into the Euglena method for the assay of vitamin B_{12} in serum. J Clin Pathol 17:14 – 26
51. Lau KS, Gottlieb C, Wasserman LR, Herbert V (1965) Measurement of serum vitamin B_{12} levels using radioisotope dilution and coated charcoal. Blood 26:202 – 214
52. Kolhouse JF, Kondo H, Allen RH (1978) Cobalamin analogues are present in human plasma and can mask cobalamin deficiency because current radio isotope dilution assays are not specific for true cobalamin. N Engl J Med 299:785 – 792
53. Herbert V, Gottlieb C, Altschule MD (1965) Apparently low serum vitamin B_{12} levels in association with chlorpromazine: an artifact. Lancet 2:1052 – 1053
54. Mollin DL, Anderson BB, Burman JF (1976) The serum vitamin B_{12} level: its assay and significance. Clin Haematol 5:521 – 546
55. Allen RH, Stabler SP, et al (1990) Diagnosis of cobalamin deficiency. 1. Usefulness of serum methyl malonic acid and total homocysteine concentrations. Am J Hematol 34: 90 – 98
56. Kumar S, Ghosh K, Das KC (1989) Serum vitamin B_{12} in an Indian population: on evaluation of three assay methods. Med Lab Sci 46:487 – 492
57. Hakami N, Neiman PE, Cancellos G, Lazerson J (1971) Neonatal megaloblastic anemia due to inherited transcobalamin II deficiency in two siblings. N Engl J Med 285:1163 – 1170
58. Corcino J, Zalusky R, Greenberg M, Herbert V (1971) Coexistence of pernicious anaemia and chronic myeloid leukaemia. An experiment of nature involving vitamin B_{12} metabolism. Br J Haematol 20:511 – 520
59. Amess JAL, Burman JF, Rees GM, et al (1978) Megaloblastic hematopoiesis in patients receiving nitrous oxide. Lancet 2:339 – 342
60. Layzer RB (1978) Myeloneuropathy after prolonged exposure to nitrous oxide. Lancet 2:1227 – 1230
61. Wickramasinghe SN (1999) The wide spectrum and unresolved issues of megaloblastic anemia. Semin Hematol 36:3 – 18
62. Herbert V (1989) Staging nutrient status from too little to too much by appropriate laboratory tests. In: Livingstone (ed) Nutritional status assessment of the individual. Food & Nutrition Press, Trumball, CT
63. Herzlich B, Herbert V (1988) Depletion of serum holotranscobalamin II: an early sign of negative vitamin B_{12} balance. Lab Invest 58:332 – 337
64. Das KC, Manusselis C, Herbert V (1991) Determination of vitamin B_{12} (cobalamin) in serum and erythrocytes by radioassay,and holo-transcobalamin II (holo-TC-II) in serum by adsorbing holo-TC-II on microfine silica. J Nutr Biochem 2:455 – 464
65. Herbert V, Memoli D, McAleer E, et al (1986) What is normal? Variation from the individual's norm for granulocyte "lobe average" and holo transcobalamin II (holo-TC-II) diagnose vitamin B_{12} deficiency before variation from the laboratory norm. Clin Res 34:718A
66. Briedis D, McIntyre PA, Judisch J, Wagner HN Jr (1973) An evaluation of a dual-isotope method for the measurement of vitamin B12 absorption. J Nucl Med 14:135 – 141
67. Krynycki BR, Zuckier LS (1995) Accuracy of measurement of dual-isotope Schilling test to measure urine samples: a multicentric study. J Nucl Med 36:1659 – 1665
68. Belaiche J, Cattan D, Zittoun J, et al (1983) Effects of ranitidine on cobalamin absorption. Dig Dis Sci 28:667 – 668
69. Carmel R (1992) Malabsorption of food folate. In: Megaloblastic anaemia. Baillieres Clin Haematol 8:639 – 655
70. Doscherholmen A, Swaim WR (1973) Impaired assimilation of egg ^{57}Co-vitamin B_{12} in patients with hypochlorhydria and achlorhydria and after gastric resection. Gastroenterology 64:913 – 919
71. Carmel R, Sinow RM, Siegel ME, et al (1988) Food cobalamin malabsorption occurs frequently in patients with unexplained low serum cobalamin levels. Arch Intern Med 148:1715 – 1719
72. Karnaze DS, Carmel R (1990) Neurologic and evoked potential abnormalities in subtle cobalamin deficiency states, including deficiency without anemia and normal absorption of free cobalamin. Arch Neurol 47:1008 – 1012
73. Metz J, Kelly A, Swett VC, et al (1968) Deranged DNA synthesis by bone marrow from vitamin B_{12} deficient humans. Br J Haematol 14:575 – 592
74. Das KC, Manusselis C, Herbert V (1980) In vitro DNA synthesis by bone marrow cells and PHA-stimulated lymphocytes. Suppression of nonradioactive thymidine of the incorporation of ^{3}H-deoxyuridine into DNA: enhancement of incorporation when inadequate vitamin B_{12} or folate is corrected. Br J Haematol 44:51 – 63
75. Wichramasinghe SN, Olsen I, Saunders JE (1975) Thymidine kinase activity in bone marrow cells. Scand J Haematol 15:139 – 144
76. Hooton JW, Hoffbrand AV (1976) Thymidine kinase in megaloblastic anaemia. Br J Haematol 33:527 – 537
77. Das KC, Hoffbrand AV (1970) Lymphocyte transformation in megaloblastic anaemia. Morphology and DNA synthesis. Br J Haematol 19:459 – 468
78. Das KC, Manusselis C, Herbert V (1978) The lymphocyte as a marker of past nutritional status. Peristence of abnormal lymphocyte deoxyuridine(dU) suppression test and chromosomes in patients with past deficiency of folate and vitamin B_{12}. Br J Haematol 38:219 – 233
79. Das KC, Manusselis C, Herbert V (1980) Simplifying lymphocyte culture and the deoxyuridine suppression test by using whole blood instead of separated lymphocytes. Clin Chem 26:72 – 77
80. Bannester LH (1995) Haemolymphoid system. In: Bannester LH, et al (eds) Gray's anatomy, 38th edn. Churchill Livingstone, New York, pp 1399 – 1442
81. Ross MH, Reith EJ, Romrell LJ (1989) The lymphatic system in histology: a text and atlas, 2nd edn. Williams & Wilkins, Philadelphia, pp 324 – 328
82. Chapman WC, Newman M (1999) Disorders of the spleen. In: Lee GR (ed) Wintrobe's clinical hematology, 10th edn, vol 2. Williams and Wilkins, Baltimore, pp 1969 – 1989
83. Ferrant A, Leners N, Michaux JL, et al (1987) The spleen and hemolysis: evaluation of the intrasplenic transit time. Br J Hematol 65:31 – 34
84. Sheldon GF, Croom RD III, Meyer AA (1991) The spleen. In: Sabeston DC Jr, et al (eds) Textbook of surgery, 14th edn. Saunders, Philadelphia, pp 1108 – 1133
85. Bohnsack JF, Brown EJ (1986) The role of spleen in resistance to infection. Annu Rev Med 37:49 – 59
86. Spirer Z, Zakuth V, Tzehoval E et al (1980) Tuftsin stimu-

lates IL-1 production by human mononuclear cells, human spleen cells and mouse spleen cells in vitro. J Clin Lab Immunol 28:27 – 31
87. Pabst R, Westemann J (1991) The role of the spleen in lymphocyte migration. Scan Micro 5:1075 – 1079
88. Toft P, Tonnesen E, Helbo-Hansen HS et al (1994) Redistribution of granulocytes in patients after major surgical stress. APMIS 102:43 – 48
89. Steiner RM, Mitchell DG, Rao VM, et al (1993) Magnetic resonance imaging of diffuse bone marrow disease. Radiol Clin North Am 31:383 – 409
90. Kim CK, Reske SN, Alavi A (1996) Bone marrow scintigraphy. In: Honkin RE, Boles MA, Dillehag GL, et al (eds) Nuclear medicine, vol I. Mosby, St. Louis, pp 1223 – 1249
91. Desai AG, Thakur ML (1985) Radiopharmaceuticals for spleen and bone marrow studies. Semin Nucl Med 15:229 – 238
92. Datz FL, Taylor A Jr (1985) The clinical use of radionuclide bone marrow imaging. Semin Nucl Med 15:239 – 259
93. Mishkin FS, Freeman LM (1984) Miscellaneous application of radionuclide imaging: bone marrow. In: Freeman LM (ed) Freeman and Johnson's radionuclide imaging, 2nd edn. Grune & Stratton, Orlando
94. Van Dyke D, Shkurkin C, Price D, et al (1967) Differences in distribution of erythropoietic and reticuloendothelial marrow in hematologic disease. Blood 30:364 – 374
95. Noworoska A, Hardozinska A, Richter, et al (1985) Nonspecific cross-reacting antigen (NCA) in the individual maturation stages of myeloid cell series. Br J Cancer 51:371 – 377
96. Wahren B, Gahrton G, Hammerstroem S (1980) Non-specific cross-reacting antigen in normal and myeloid cells and serum of leukemic patients. Cancer Res 40:2039 – 2044
97. Wahren B, Gahrton G, Ruden U, et al (1982) Clinical evaluation of NCA in patients with chronic myelocytic leukemia. Int J Cancer 29:133 – 137
98. Engstedt L, Franzen S, Jonsson L, et al (1958) In vivo localization of colloidal Au 198 intravenously injected in polycythemia vera. Acta Radiol (Diagn)(Stockh) 49:66 – 71
99. Reske SN, Buell U (1990) Reduced technetium-99m labelled NCA-95/CEA antibodies (TcNCAA) for immunoscintigraphy of hematopoietic bone marrow in man. Antibody distribution in normal bone marrow. In: Hofer A, Bergmann H (eds) Radioactive Isotope in Klinik und Forschung. Schattauer, Stuttgart
100. Reske SN, Karstens JH, Gloeckner W, et al (1989) Radioimmunoimaging for diagnosis of bone marrow involvement in breast cancer and malignant lymphoma. Lancet 1:299 – 301
101. Reske SN, Sohn M, Karstens JH et al (1990) Immunoscintigraphy of bone marrow with Tc-99m labelled NCA-95/CEA antibodies (TcNCAA). Comparison with bone scanning, plain radiographs and HAMA response. J Nucl Med 31:751
102. Axelsson B, Kalin B (1990) Comparison of ^{111}In granulocytes and Tc-99m albumin colloid for bone marrow scintigraphy by the use of quantitative SPECT imaging. Clin Nucl Med 15:473 – 479
103. Beamish MR, Brown EB (1964) A comparison of the behaviour of ^{111}In and Fe-59 labeled transferrin on incubation with human and rat reticulocytes. Blood 43:703 – 711
104. Chipping P, Klonizakis I, Lewis SM (1980) Indium chloride scanning; a comparison with iron as a tracer for erythropoiesis. Clin Lab Haematol 2:255 – 263
105. Goodwin DA, Goode R, Brown L, et al (1971) ^{111}In labeled transferrin for the detection of tumours. Radiology 100:175 – 179
106. Staub RT, Gaston E (1973) ^{111}In chloride distribution and kinetics in hematologic disease. J Nucl Med 14:456 – 457
107. Aburano T, Yokoyama K, Shuke N, et al (1992) Tc-99 m HMPAO-labeled leukocytes for hematopoietic marrow imaging. Comparison with In-III chloride. Clin Nucl Med 17:938 – 944
108. Palestro C, Charalel J, Vallabhajosula S, et al (1987) In-WBC as a bone marrow imaging agent. J Nucl Med 28:574
109. Bourgeois P, Demoncean G, Stegen M, et al (1991) 99m-Tc-HMPAO-labelled leucocytes for bone marrow scintigraphy and evaluation of skeletal lesions. Comparison with 99m-Tc-HSA colloid results. Nucl Med Commun 12:621 – 627
110. Hoffbrand AV, Pettit JE (1993) Essential haematology, 3rd edn. Blackwell Science, Oxford, pp 3, 4
111. Dacie JV, Lewis SM (1984) Practical haematology, 6th edn. Churchill Livingstone, Edinburgh, pp 293 – 295, 296, 301 – 303, 306, 408
112. Dacie JV, Lewis SM (1989) Practical haematology, 7th edn. Churchill Livingstone, Edinburgh, pp 405 – 411

6 Musculoskeletal System

Abdelhamid H. Elgazzar, Dia Shehab

6.1 Introduction

Bone is a rigid connective tissue which provides support and protection for the organs and tissue of the body. Within certain bones such as the skull, vertebrae, and ribs, marrow cavities serve as sites of blood formation. Bone also has an important function in mineral homeostasis. Scintigraphy plays a crucial role in the diagnosis and management of various skeletal diseases, and the expanding use of this imaging modality in the area of benign bone disorders is particularly notable.

6.2 Anatomical and Physiological Considerations

6.2.1 Bone Structure

The structure of normal adult bone can be summarized in four categories:

Gross Level. The skeleton consists of two major parts, the axial skeleton and the appendicular skeleton (Fig. 6.1). The axial skeleton includes the skull, spine and rib cage (ribs and sternum), while the appendicular skeleton involves the bones of the extremities, pelvic girdle and pectoral girdle (clavicles and scapulae).

Tissue Level. Bone is divided into two types of tissues forming the skeleton: compact or cortical and cancellous, trabecular or spongy bone. The spongy bone has a turnover rate approximately eight times greater than that of cortical bones and hosts hematopoietic cells and many blood cells. In mature bone, compact bone forms

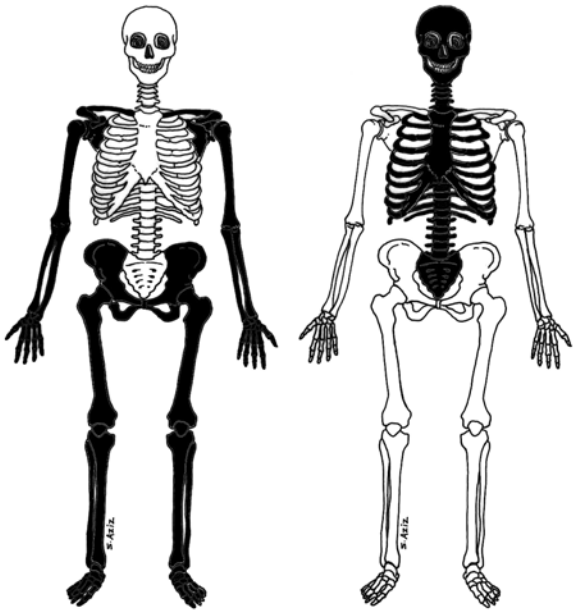

Fig. 6.1. Axial (*right*) and appendicular (*left*) skeletons

an outer layer (cortex) which surrounds an inner layer of loose trabecular, cancellous or spongy bone in the medulla. The architecture is arranged according to the Haversian system. The spongy portion contains hematopoietic cells, which produce blood cells, fat and blood vessels. The compact bone constitutes 80% of the skeletal mass and contains 99% of the total body calcium and 90% of its phosphorus.

The appendicular skeleton is composed predominantly of cortical bone. The cortical bone is thicker in the diaphysis than in the metaphysis and epiphysis of long bones. The blood supply to the metaphysis is also different since it is rich and consists of large sinusoids, which slow down the flow of blood, a feature that predisposes to bacterial proliferation. The spine, on the other hand, is composed predominantly of cancellous bone in the body of the vertebra and compact bone in the endplates and posterior elements.

Cellular Level. Three types of cells are seen in bone: (1) osteoblasts that produce the organic bone matrix, (2) osteocytes that produce the inorganic matrix and (3) osteoclasts, which are active in bone resorption [1]. Osteoclasts are derived from the hemopoietic system in contrast to the mesenchymal origin of osteoblasts. Osteocytes are derived from osteoblasts that have secreted bone around themselves [2].

Molecular Level. At the molecular level, bone matrix is composed primarily of organic matrix (approximately 35%) including collagen and glycoproteins and inorganic matrix (approximately 65%), which includes hydroxyapatite, cations (calcium, magnesium, sodium, potassium and strontium) and anions (fluoride, phosphorus and chloride [3, 4]). Table 6.1 summarizes the major constituents of bone and their function.

Table 6.1. Bone structures and their functions. (Modified from [1])

Major structural elements	Function
Bone cells	
Osteoblasts	Synthesize collagen and proteoglycans, stimulate osteoclast resorptive activity
Osteocytes	Maintain bone matrix
Osteoclasts	Resorb bone, assist with mineral homeostasis
Bone matrix	
Organic matrix:	
Collagen fibers	Provide support and tensile strength
Proteoglycans	Control transport of ionized materials through matrix
Sialoprotein	Promotes calcification
Osteocalcin	Inhibits calcium/phosphate precipitation, promotes bone resorption
Laminin	Stabilizes basement membranes in bone
Osteonectin	Binds calcium to bones
Albumin	Transports essential elements to matrix
Inorganic matrix:	
Calcium	Crystallizes to provide rigidity and compressive strength
Phosphate	Regulates vitamin D and thereby promotes mineralization

6.2.2 Blood Supply

The pattern of the skeletal blood supply varies with the age-group. In children epiphyseal, metaphyseal, and diaphyseal vessels are present. In adults all vessels communicate together. Nutrient and periosteal arteries feed a rich network of vessels to supply the cortex and medulla (Fig. 6.2). This vasculature takes the form of interconnecting capillaries, sinusoids, and veins. It is estimated that blood flow to cancellous bone containing marrow is 5 – 13 times higher than in cortical bone [5].

6.2.3 Bone Remodeling

Within all bones a balance between osteogenesis and bone resorption continuously occurs, even in normal nonviolated bone. Remodeling occurs throughout life, with removal and replacement of bone at different rates in different parts of the skeleton. Bone remodeling is regulated by parathyroid hormone, vitamin D, and numerous other factors. It is estimated that 18% of the skeleton is replaced yearly in adults, indicating that the entire skeleton is replaced every 5 years. The process is more

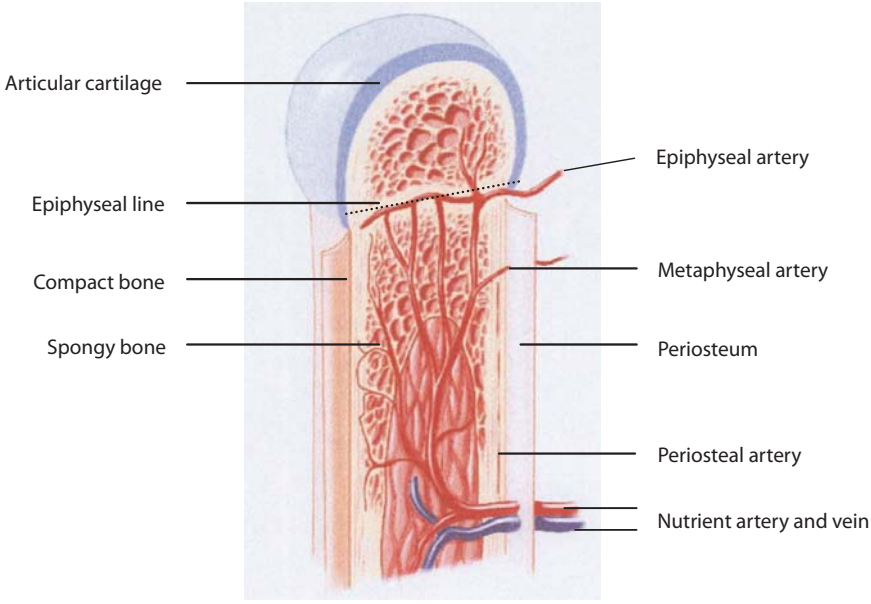

Fig. 6.2. Diagram illustrating blood supply to a long bone

Table 6.2. Inhibitors and stimulators of bone turnover

Bone turnover inhibitors
Estrogens
Estrogen receptor antagonists
Tamoxifen
Raloxifen
Calcitonin
Vitamin D derivatives
Calciferol
Calcitrol
Bisphosphonates
Etidronate
Pamidronate
Alendronate
Tiludronate
Clodronate
Thiazide diuretics
Bone turnover stimulators
Anabolic steroids
Parathyroid hormone and peptides
Fluoride

active in cancellous bone, with a yearly replacement rate of approximately 25% compared with 2% for compact bone [6]. Turnover varies and is affected by many factors including drugs (Table 6.2) and disease. Certain diseases are characterized by an increase in the rate of remodeling, are therefore known as high turnover disorders, and may affect the entire skeleton or a single bone. In this group, both osteoblastic and osteoclastic activity is increased but the amount of bone formed is usually less than the bone removed, resulting in osteopenia. An exception is Paget's disease, during which, in the later stages of its course, osteoblastic exceeds osteoclastic activity. The stress fracture is not as thought due to repeated traumatic microfractures. It is a focal area of increased bone turnover secondary to the repeated stress.

6.2.4 Bone Marrow

Normally, almost the entire fetal marrow space is occupied by red (hematopoietic) marrow at birth. Conversion from red to yellow, nonhematopoietically active marrow, starts in the immediate postnatal period. This process begins in the extremities and progresses in general from the peripheral to the central skeleton and from diaphyseal to metaphyseal regions in individual long bones. By approximately the age of 25 years, marrow conversion to the adult pattern is complete (Fig. 6.3). In adults, hematopoietic bone marrow usually is confined to the skull, vertebrae, ribs, sternum, pelvis, and proximal portions of the humerus and femur. Fatty marrow in other bones may contain islands of hematopoietic tissue, however, and for this reason variations on the normal adult pattern of hematopoietic bone marrow are frequently encountered. Acquired alterations in the distribution of hematopoietic bone marrow may be due to surgery, trauma, infection, and other destructive processes.

Furthermore, with increasing demand for red cells, reconversion of yellow to red marrow may take place. This process follows the reverse order of the initial red-to-yellow marrow conversion. Accordingly, it starts in the axial skeleton, followed by the extremities from proximal to distal [7,8].

6.2.5 Response to Injury

The principal response of bone to injury and disease is reactive bone formation. This reactive bone goes through stages. It is disorganized early but later may re-

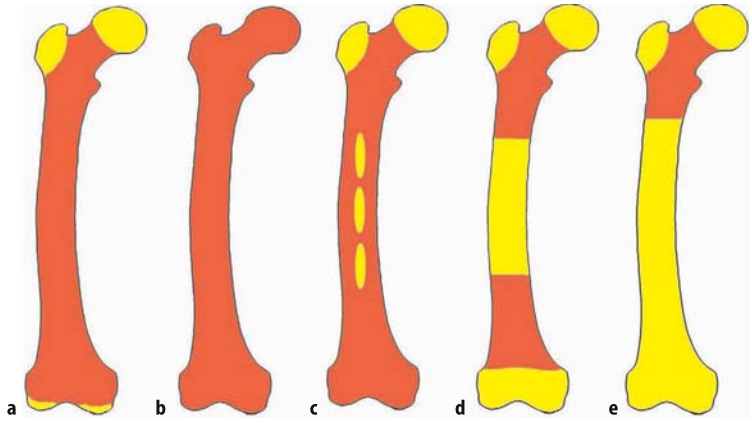

Fig. 6.3a–j. Bone marrow distribution in long bones of the lower extremity illustrating changes during development over the years until the adult pattern is reached by about 25 years of age. **a,f** Birth; **b,g** 7 year-; **c,h** 14 year-; **d,i** 18 year-; **e,j** 25 year-old

model to normal bone. This new disorganized bone is termed woven bone (Fig. 6.4) and is active with no lamellar arrangement.

Technetium-99m-diphosphonates are the radiopharmaceuticals most commonly used for skeletal scintigraphy. These agents concentrate predominantly in the mineral phase of bone, which consists of crystalline hydroxyapatite and amorphous calcium phosphate. Using an in vitro assay, Francis et al. [9] showed that the competitive adsorption of ^{99m}Tc-diphosphonates to pure inorganic hydroxyapatite was 40 times that to pure organic bone matrix. These radiopharmaceuticals do not localize to a significant degree in osteoblasts or in osteoid.

While several factors affect the uptake of diphosphonates in the skeleton, blood flow and extraction efficiency are the most important. Increased flow of blood produces increased uptake. Pathological foci containing woven bone show increased uptake due to higher extraction efficiency.

Other factors also influence diphosphonate uptake:

1. Blood flow
2. Extraction efficiency
3. Vitamin D
4. Parathyroid hormone
5. Corticosteroids
6. Intraosseous tissue pressure
7. Capillary permeability
8. Acid-base balance
9. Sympathetic tone

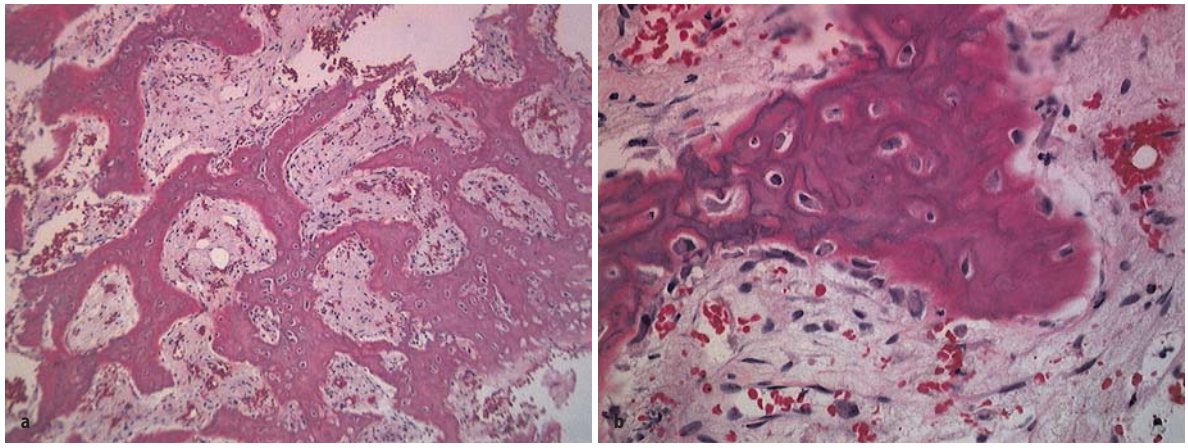

Fig. 6.4a–d. Photomicrographs illustrating the difference between woven and lamellar bone. The irregular and disorganized nature of woven bone at different microscopic magnification levels (**a** × 10; **b** × 40) is easily seen compared to lamellar bone depicted in **c** (× 10) and **d** (× 40). The bony spicules in lamellar structure are even, with occasional lacunae containing osteocytes. Cellular marrow is seen between the spicules of bone

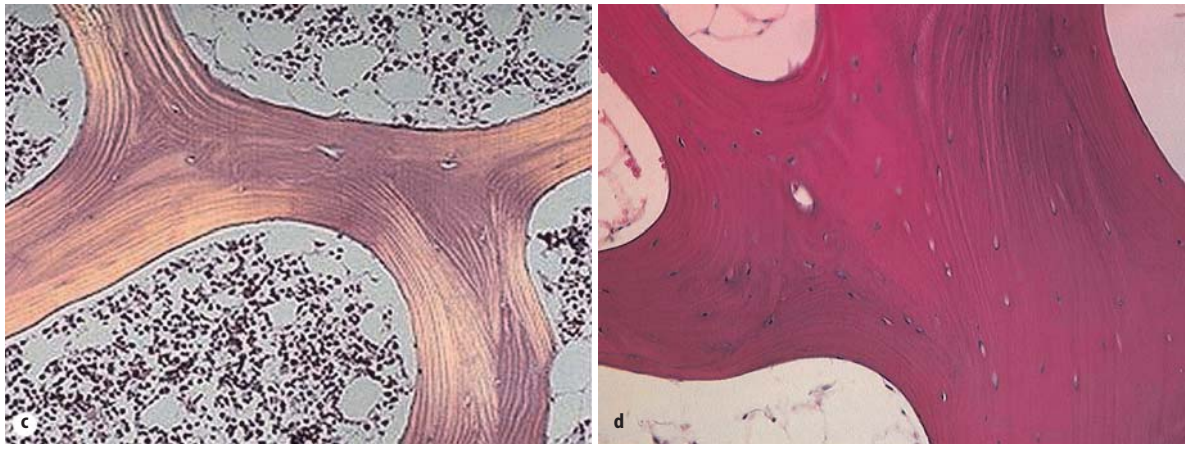

Fig. 6.4. (*Cont.*)

Accordingly, in children prominent uptake of the radiopharmaceutical is seen at the costochondral junctions, at the metaphyseal ends of the normal long bones, and in the facial bones. When the skeleton has matured, this prominent uptake at the costochondral junctions and metaphyseal ends of long bones disappears. Overall, the skeletal accumulation of diphosphonates decreases with age, particularly in the extremities [10].

Bone scintigraphy shows many patterns, some specific, in a variety of benign and malignant bone diseases. Many of these patterns are better understood once the underlying pathophysiological changes are appreciated.

6.3 Non-neoplastic Bone Diseases

6.3.1. Skeletal Infections

6.3.1.1 Definitions: Periosteitis, Osteitis, Osteomyelitis

The term osteomyelitis optimally indicates infection involving the cortical bone as well as the marrow. When infection starts in the periosteum, such as in cases of direct extension bone infection, it produces periosteitis. At this stage, infection may not yet involve the cortex or marrow and the condition is called infectious periosteitis. When infection penetrates the cortex, the term infectious osteitis is used. When marrow is involved as well, the term osteomyelitis is applied (Fig. 6.5).

6.3.1.2 Classification of Osteomyelitis

Osteomyelitis may be classified based on several factors [11, 12] including route of infection, patient age, etiology, or onset (Table 6.3). In hematogenous osteomyelitis, the metaphyses of long bones are the most common site. Nonhematogenous osteomyelitis occurs as a result of penetrating trauma, spread of a contiguous soft tissue infection, or inoculation (as in drug addicts). In these situations infection may occur in any part of the bone. Infantile osteomyelitis refers to that occurring prior to 1 year of age; the juvenile type occurs between 1 year and the age at closure of the physes; adult type occurs after closure of the physes. While gram-positive bacteria such as *Staphylococcus aureus* are the most frequent cause, many different organisms have been encountered in osteomyelitis [13–16] (Table 6.4).

6.3.1.3 Pathophysiological Changes

Acute hematogenous osteomyelitis occurs most commonly in children, affecting males approximately twice as often as females. It has a predilection for the metaphyses of long bones, where blood flow is rich and rela-

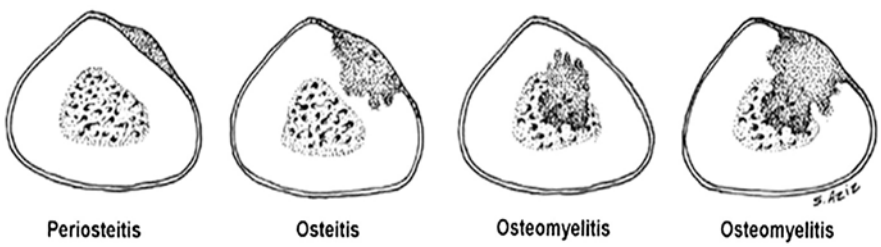

Fig. 6.5. A comparison of the extent of infection in osteomyelitis compared with the extent of infection in periosteitis and in osteitis

Table 6.3. Classifications and staging of osteomyelitis

Basis of classification	Types
Presentation	I. Acute, II. subacute, III. chronic
Route of infection	I. Hematogenous, II. direct extension (nonhematogenous)
Age	I. Infantile (including neonatal), II. juvenile, III. adult
Causative organism	I. Pyogenic, II. nonpyogenic
Location	I. Appendicular skeleton osteomyelitis: metaphyseal, epiphyseal, diaphyseal II. Axial skeleton osteomyelitis (examples: vertebral and bony pelvis osteomyelitis)
Multifactorial (Waldvogel classification):	I. Hematogenous osteomyelitis II. Osteomyelitis secondary to contiguous infection III. Osteomyelitis associated with vascular insufficiency
Anatomy of disease and host physiology (Cierny-Mader classification of adult type)	Anatomic types: I. medullary, II. superficial, III. localized, IV. diffuse Physiological class: A. Normal host B. Compromised host: Systemic compromise Local compromise Local and systemic compromise C. Prohibitive: treatment worse than disease
Prior pathology at the site of interest	I. Violated bone (complicated) osteomyelitis, II. nonviolated bone osteomyelitis

Table 6.4. Organisms associated with osteomyelitis in different clinical settings

Clinical situation	Most likely associated microorganisms causing bone infection
All types of osteomyelitis	*Staphylococcus aureus*
Infantile osteomyelitis	*S. aureus* and group B streptococci
Vertebral osteomyelitis	*S. aureus, Pseudomonas aeruginosa, Escherichia coli*, streptococci
Diabetic foot osteomyelitis	*S. aureus*, enterococcus, enterobacteria
Intravenous drug abusers	*P. aeruginosa, Klebsiella*
Immunosuppressed patients	*Salmonella, Aspergillus, Mycobacterium avium* complex, *Candida albicans*
Sickle cell disease	*Salmonella, S. aureus*
Hospital-acquired infections	*P. aeruginosa, Klebsiella*
Drinking raw milk in brucella-endemic areas	*Brucellosis*
Cat and human bites	*Pasteurella multocida, Eikenella corrodens*
Sharp object passing deep into foot tissue	*P. aeruginosa*
Contamination of open wound by soil	*Clostridia, Nocardia*
Infected catheter-related bone infections	*E. coli, C. albicans*

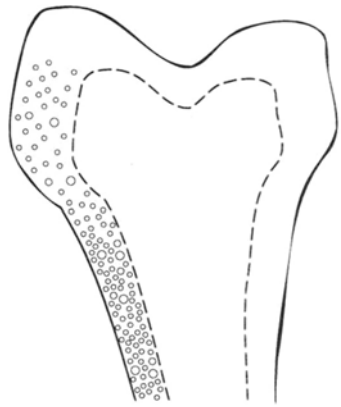

Fig. 6.6. Diagram of part of a long bone illustrating the more porous nature of the metaphysis, the most frequently affected site by hematogenous skeletal infections

tively sluggish and bone is relatively porous in comparison to the diaphysis (Fig. 6.6). Here the blood flows through large intramedullary venous sinusoids, a fertile site for bacterial lodgment and proliferation [12]. The process starts by implantation of organisms in the bone marrow. As infection becomes established in the marrow, it provokes acute suppurative neutrophilic infiltrates and edema with local ischemia, vasospasm, and thrombosis. Infection subsequently spreads, first to the subperiosteal space and often involving the metaphyseal area.

In children between 1 and approximately 16 years of age, the blood supply to the medullary space of bone enters through the nutrient artery and then passes through smaller vessels toward the growth plate. Once these vessels reach the metaphyseal side of the growth plates, they turn back upon themselves in loops to empty into large sinusoidal veins, where the blood flow is slower. The epiphyseal plate separating the epiphyseal and metaphyseal blood supplies acts as a barrier to the spread of infection (Fig. 6.7a, b), making joint involvement less common in this age-group. In this situation, infection must first break through the bone to produce joint infection (Fig. 6.7e). This occurs in the locations where the metaphysis is within the joint capsule (proximal femur in the hip joint, distal tibia in the ankle joint, proximal humerus in the shoulder joint, and rarely proximal radius in the elbow joint). On the other hand, in infants and adults, the terminal branches of the nutrient artery extend into the epiphysis, as there is no growth-plate barrier. This vascular communication between epiphyses and metaphyses facilitates the spread of infection to adjacent joints (Fig. 6.7c, d). In flat bones acute hematogenous osteomyelitis is found mainly at locations with vascular anatomy similar to that of the long-bone metaphyses, such as the bony pelvis, vertebrae, and calcaneus [17].

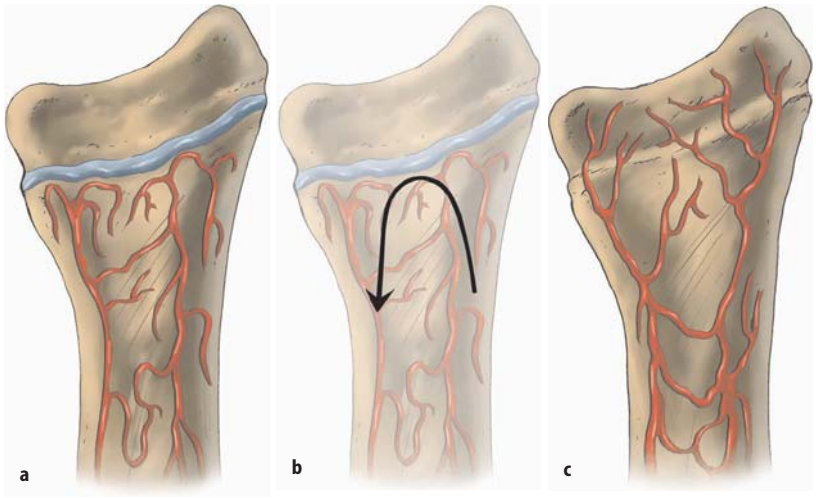

Fig. 6.7a–e. Diagram illustrating the vascular communication between the metaphysis and epiphysis of long bones. When the growth plate (**a**) is present it acts as a barrier and vessels turn on themselves forming loops. This acts to prevent infection that is most commonly present in the metaphysis from extending to epiphysis and adjacent joint (**b**). On the other hand, in neonates after the closure of the growth plate (**c**), infection extends more easily (**d**) to the joint since there is free vascular communication between metaphysis and epiphysis. **e** illustrates the path of severe infection which is able to involve the joint, when the growth plate is present, by breaking through the bone

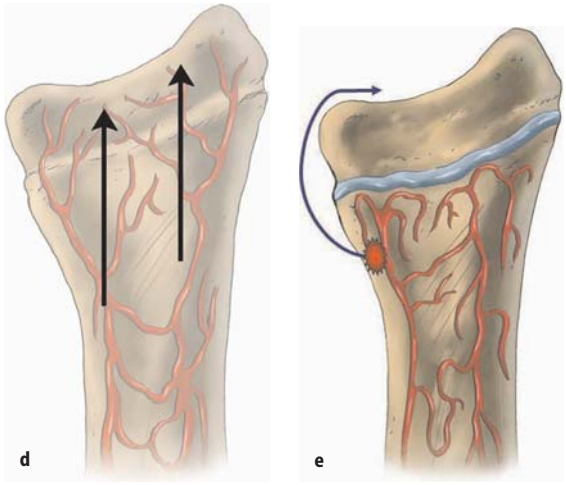

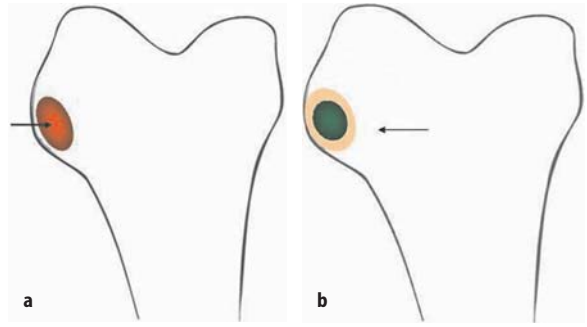

Fig. 6.8a,b. Diagrammatic representation of the sequestrum showing the necrotic segment of bone (*arrow*) and involucrum, which has a layer of new bone formation (*arrow*) surrounding the focal infection

When infection lifts the periosteum the blood supply may be impaired, causing necrosis of bone or sequestrum (Fig. 6.8a). In some cases, infection may stimulate osteoblastic activity, particularly from the periosteum, forming new subperiosteal bone that may envelop the infectious focus (involucrum) (Fig. 6.8b). This osteogenesis may occasionally continue long enough to give rise to a densely sclerotic pattern of osteomyelitis that is referred to as sclerosing osteomyelitis.

It is difficult to draw the line between acute and chronic osteomyelitis. However, it should be noted that cases of clear chronic osteomyelitis need special handling in diagnosis and management. Chronic osteomyelitis has variously been defined as symptomatic osteomyelitis with a duration of symptoms and of signs ranging from 5 days to 6 weeks [18]. Since the pathology of osteomyelitis varies with age, microorganisms, prior therapy, underlying diseases, and other factors, it is somewhat inappropriate to depend only on duration of the disease to define chronicity. Chronic osteomyelitis has less marked inflammatory cell reactions and may occur without preceding acute inflammation. Microscopically, chronic osteomyelitis shows predominantly lymphocytes and plasma cells rather than polymorphonuclears (Fig. 6.9). There is also fibrosis and a variable amount of necrotic tissue, and sequestra may form in some cases. The presence of necrotic tissue may also lead to draining sinuses or organization in the medullary cavity, forming a cystic cavity (Brodie's abscess) (Fig. 6.10). Because these abscesses are avascular, levels of antibiotics sufficient to eradicate the bacteria may not be achieved during treatment. Accordingly, bacteria may remain indolent for a long time (inactive disease). Reactivation of the disease may occur later, even years after the initial episode (active disease). It is important to evaluate patients for possible chronic disease and to either exclude or confirm the presence of chronic active infection: continuation of intravenous antibiotic therapy and/or surgical intervention to eradicate infection will depend on that determination [19].

Vertebral osteomyelitis (spondylodiskitis) is a specific form of osteomyelitis that has some unique fea-

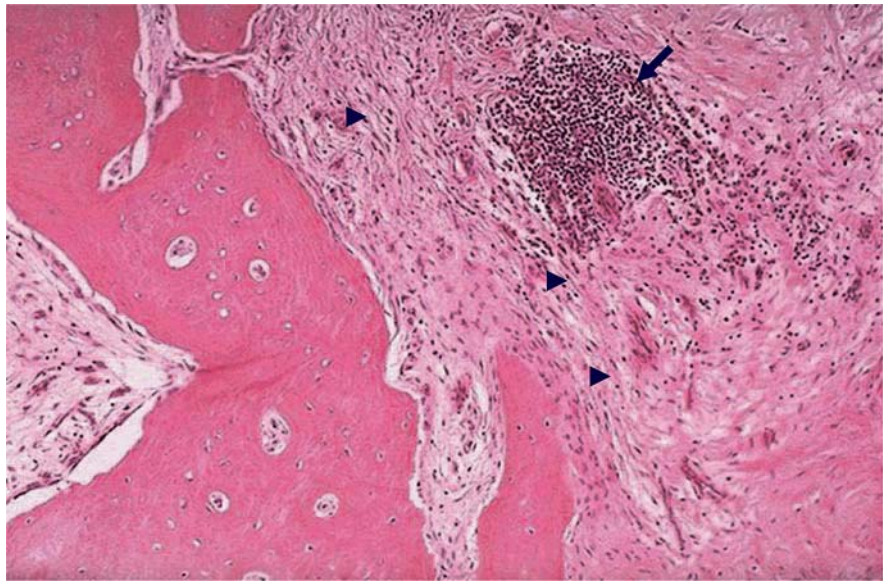

Fig. 6.9. Chronic osteomyelitis. A photomicrograph of a specimen of bone from a patient with long-standing chronic osteomyelitis. Note the presence of numerous lymphocytes (*arrow*) as well as fibrosis (*arrowheads*) within the marrow space

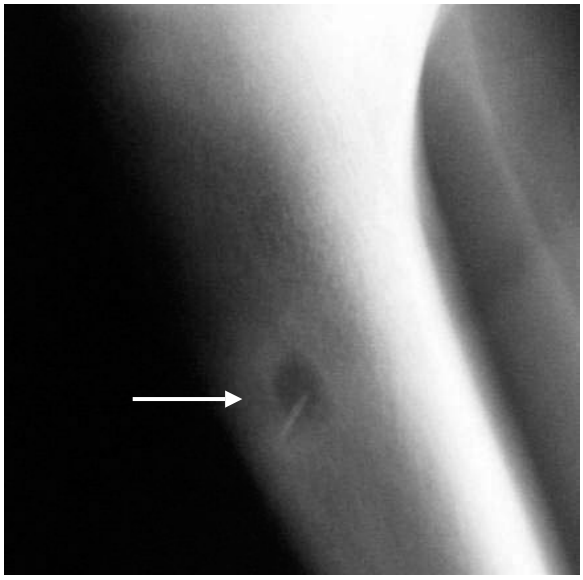

Fig. 6.10. Radiograph showing a Brodie's abscess (*arrow*)

tures. The most common site is the lumbar region, followed by the thoracic and cervical spine. Several factors predispose to vertebral osteomyelitis:

1. Diabetes mellitus
2. Drug addiction
3. Old age
4. Oral steroid therapy
5. Dialysis
6. Urinary tract infection
7. Genitourinary instrumentation
8. Prior back surgery
9. Bacteremia secondary to intravenous cannulation
10. Spinal trauma

The disease occurs most frequently in adults with a mean age of 60 – 70 years, although it also occurs at all other ages, including in children. The pyogenic form most often is caused by *Staphylococcus aureus*, but streptococci and gram-negative bacteria are also involved [20 – 22]. Infection usually originates at a distant site with hematogenous extension to contiguous vertebral bodies and the intervening space via the ascending and descending branches of the posterior spinal artery. Extension to the posterior elements (pedicles, transverse processes, posterior spinous processes, and laminae) has been noted in 3% – 12% of cases. However, involvement of posterior elements only is exceedingly rare, with only 15 cases reported to date. Other causes include extension of infection from adjacent structures and complications from spinal surgery and trauma.

In adults, the causative organism generally settles in the richly vascularized subchondral vertebral end plates with eventual progression of infection into the adjacent intervertebral disk, which is relatively avascular. In childhood, infection often starts at the disks, which are nourished by small perforating vessels. In either case, local spread of infection eventually occurs and causes end-plate destruction, disk space narrowing, and collapse. Figure 6.11 illustrates possible ways of development of vertebral osteomyelitis. These changes may take weeks to be seen on radiographs [18, 19]. Since the disk is almost invariably involved in vertebral infections, the term spondylodiskitis is preferred [20, 21].

Diabetic foot osteomyelitis is a unique clinical and pathological problem. It is a common complication of diabetes, particularly when angiopathy is present. It occurs in 15% of adult diabetic patients and, without prompt diagnosis and treatment, may lead to amputa-

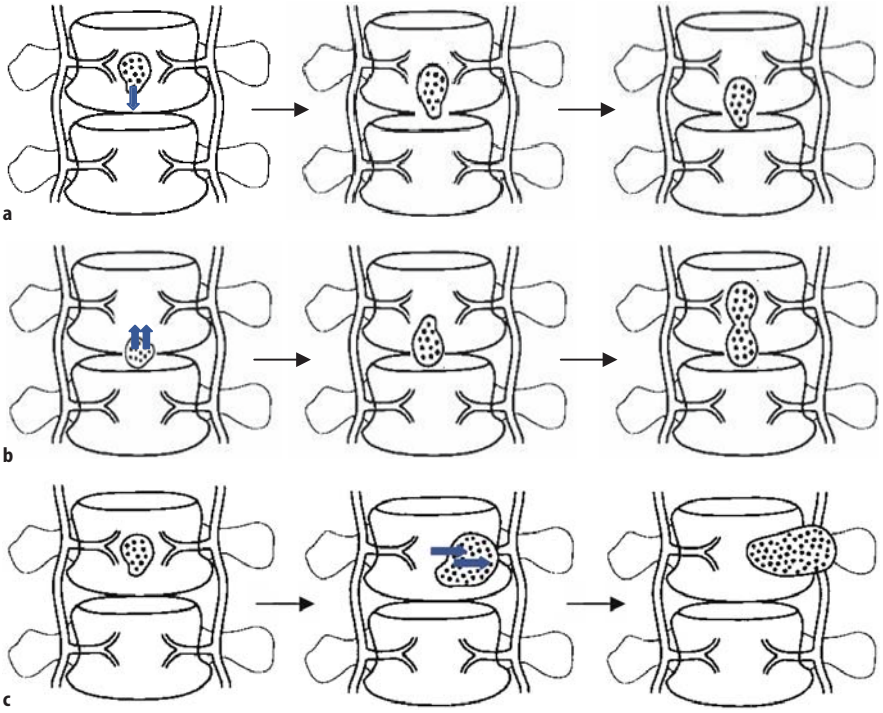

Fig. 6.11a–c. The possible ways of development and extension of infection in hematagenous vertebral osteomyelitis

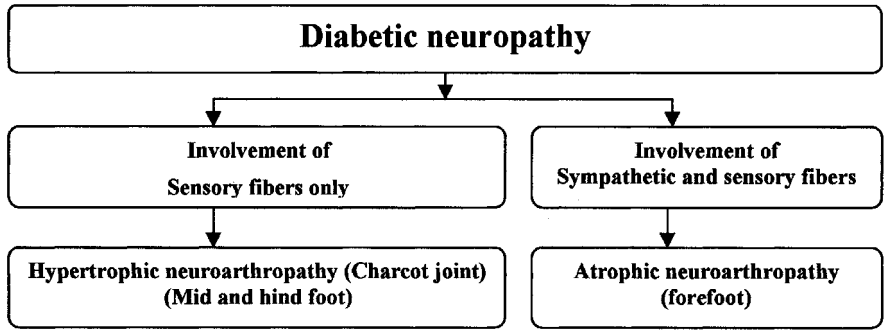

Fig. 6.12. Types of diabetic neuropathy. (From [18], with permission)

tion. Ulceration of the foot is 50 times more common in diabetics, and the incidence of amputation of the lower extremities is 25 times greater than among the general population [27]. More than 90% of osteomyelitis of the foot of diabetic patients occurs as a result of the spread of infection from adjacent foot ulcers [28].

Early diagnosis is difficult, both clinically and radiologically, because of superimposed disease processes, such as neuroarthropathy, chronic soft tissue infection, and edema. There is particular difficulty in differentiating osteomyelitis from neuroarthropathy: the conditions have similar clinical presentations. Neuroarthropathy has a better prognosis than osteomyelitis and is managed differently. Thus, it is critical to make the correct diagnosis.

Neuroarthropathy is characterized by destructive joint changes. A combination of factors is involved (Fig. 6.12). Loss of protective pain and proprioceptive sensation along with hyperemia secondary to loss of vasoconstrictive neural impulses are thought to result in atrophic neuropathy, occurring most frequently in the forefoot [29]. On the other hand, absence of sympathetic fibers in the presence of sensory fiber involvement tends to result in hypertrophic neuroarthropathy, which occurs most frequently in the mid and hind foot. Since the patient continues to walk and traumatize the foot, disuse osteoporosis is usually absent. Unrelenting trauma may also result in rapidly progressive destruction, sometimes with disintegration of one or more tarsal bones within a period of only a few weeks. This is a rapidly progressive form of neuroarthropathy which has more inflammatory reaction than otherwise. A long history of diabetes mellitus with a combination of angiopathy, neuropathy, and immunopathy predisposes to pedal osteomyelitis (Fig. 6.13). Metatarsal bones and the proximal phalanges are the most commonly involved sites [30–32].

In osteomyelitis associated with sickle cell disease erythrocytes become viscous and sickle abruptly when

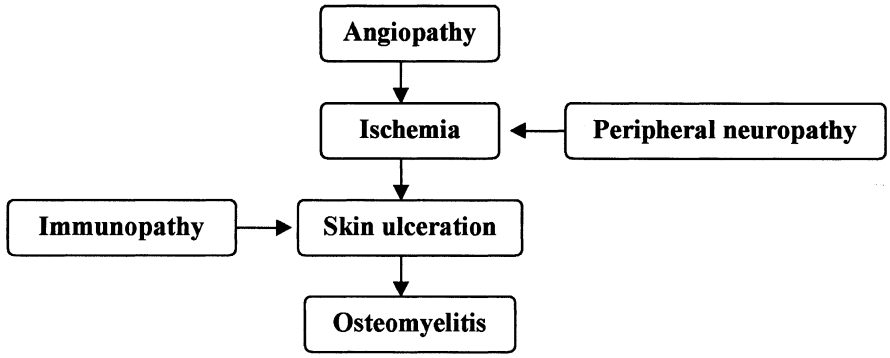

Fig. 6.13. Changes leading to skeletal infections in diabetics. (Modified from [18], with permission)

exposed to hypoxia, since hemoglobin S is sensitive to hypoxemia,. This may compromise the microvascular flow and may cause infarction, the most common skeletal complication of sickle cell disease. For symptomatic sickle cell patients, distinguishing infarction from osteomyelitis is critical. Although less common than infarctions, osteomyelitis is the second most frequent bacterial infection in children with sickle cell disease after pneumonia [13]. Osteomyelitis may occur as a primary event or may be superimposed on infarcts; necrotic bone is a fertile site for such secondary infections. *S. aureus* and *Salmonella* are frequent causative organisms.

Periprosthetic Infections. Hip and knee arthroplasties are two of the most frequent orthopedic procedures, exceeding 600,000 per year in the United States alone [32–34]. Between 10% and 25% of patients experience discomfort within 5 years after hip or knee replacement [35]. This can be due to loosening with or without infection. Loosening is the most common complication after hip replacements, occurring in up to 50% of femoral components and in 15% of acetabular components by 10 years after implantation.

Periprosthetic infection is a clinically important, and increasingly rare, complication after joint replacement. Although the incidence of infection was reported previously to be as high as 4% after the primary surgery and 32% after revision of hip arthroplasty, the currently reported incidence of infection after total hip or knee arthroplasties is only 0.5%–2%, and is less than 3% following revision surgery and occurring mostly within 4 months of operation [36, 37]. Infection occurs mostly within 4 months of operation.

The cementless porous-coated prosthesis depends on bone ingrowth for fixation and induces more reactive bone formation than the cemented prosthesis. Differences between cemented and porous-coated hip prostheses largely explain the scintigraphic patterns noted after hip arthroplasty. Prominent although still, "normal" activity may remain present for years, depending on the location of the finding and type of prosthesis. After knee replacement, on the other hand, the most common complications are fracture, dislocation, and avascular necrosis followed by loosening of the tibial component, with infection occurring less frequently [38].

The incidence of loosening associated with infection is high and is found in up to 80% of infected prostheses [39]. Heterotopic bone formation following arthroplasties is also common and is present in about 50%–55% of hip prostheses and 10% of knee prostheses [34, 40].

Infectious (septic) arthritis refers to the invasion of synovial space by microbes. The synovial space contains synovial fluid, which is produced by a rich capillary network of the synovial membrane. This is a viscous fluid that serves to lubricate, nourish, and cushion the avascular joint cartilage. When the synovial space is infected, bacterial hyaluronidase decreases the viscosity of the synovial fluid. Pain is then felt with stress on the joint capsule.

Acute septic arthritis is normally caused by bacteria, while fungal and mycobacterial pathogens are seen more commonly in chronic arthritis. Acute septic arthritis is a medical emergency. Delay in the diagnosis and treatment may result in destruction of the articular cartilage and permanent disability. The lytic enzymes in the purulent articular fluid destroy the articular and epiphyseal cartilage. Additionally, pus in the joint space increases the intracapsular pressure with epiphyseal ischemia.

Other sequelae include dislocation, deformity, and destruction of the femoral head and neck. Hence drainage and antibiotic therapy must be considered without delay [18, 41].

Microorganisms reach the joint by a hematogenous route, contagiously from an adjacent osseous infection, or through traumatic/surgical inoculation. The joints most commonly involved in children are the hip (35%), knee (35%), and ankle (10%). When the synovium becomes hyperemic in septic arthritis, flow to adjacent extra-articular bone will also increase via anastomoses from the synovial vascular network to juxtaepiphyseal and epiphyseal vessels supplying the epiphysis and metaphysis. Accordingly, increased uptake of bone-seek-

ing radiopharmaceutical typically may be seen in and around affected joints [41–43].

6.3.1.4 Multimodality Imaging of Skeletal Infections

In many clinical practices, skeletal infections are frequently encountered. For example, such infections are commonly seen in cancer patients and in immunosuppressed individuals. Particularly when co-morbidity is present, the clinical presentation may be confusing and the laboratory findings often are not specific. Several imaging modalities are now being utilized for detection of osteomyelitis, including standard radiography, computerized tomography (CT), magnetic resonance imaging (MRI), and nuclear medicine techniques. The choice of modality depends on clinical presentation, duration of symptoms, site of suspected infection, previously known underlying pathology (such as fracture or tumor), and other factors [18].

6.3.1.4.1 Imaging of Acute Osteomyelitis

Standard radiographs are not sensitive for early detection of osteomyelitis, as the changes (Fig. 6.14) are evident only after 10–21 days from the time of infection [44]. Bone scintigraphy is very sensitive in the early diagnosis of osteomyelitis [19] and can show the abnormality as early as 24 h after infection [45]. Typically, there is focally increased flow, blood pool activity, and delayed uptake (Fig. 6.15). When the bone has not been previously affected by other pathological conditions (nonviolated), the bone scan has high accuracy and is a cost-effective modality for diagnosis of osteomyelitis with both sensitivity and specificity of 90%–95% [19].

Fig. 6.14. A radiograph of an adult patient with osteomyelitis showing the typical radiographic changes of bone demineralization, bone lysis and cortical lucency (*arrow*)

However, there have been some reports of proven early acute osteomyelitis demonstrating either reduced or normal accumulation of the radiopharmaceutical, particularly in neonates, although these reports were based on the use of earlier instrumentations. With the use of modern technology, the recent reports show a high accuracy of bone scan (Fig. 6.16) in the diagnosis of neonatal osteomyelitis [46–48]. Tuson et al. [47] found that the positive predictive value of reduced uptake (a "cold" scan) in a selected group of patients was higher (100%) than that of a typical "hot" scan (82%). Cold lesions had a shorter average history (4 days) than did hot scans (7 days) [47] confirming an earlier report [49] that a "cold" scan indicates more virulent disease. A more recent report on seven cases with cold scan osteomyelitis also confirmed the prior data regarding the more aggressive nature of this infection that was also associated with elevated ESR, significantly elevated temperature, and resting pulse, longer hospital stay and higher rate of surgical interventions [50]. Cold foci on bone scan in cases of osteomyelitis are thought to be secondary to increased intraosseous and subperiosteal pressure.

If bone has been affected by a previous pathology (violated), particularly after orthopedic surgical procedures, which can be common in cancer patients specially with orthopedic tumors, the bone scan will still be highly sensitive but the average specificity is only approximately 30% [18]. In such situations, unless the bone scan is unequivocally negative, an additional modality should be used, particularly scanning with leukocytes labeled with ^{111}In-oxine or ^{99m}Tc-hexamethyl propylene amine oxime (HMPAO). Overall, ^{111}In-leukocyte studies have a sensitivity of approximately 88% and a specificity of 84% for osteomyelitis [19]. This modality is particularly useful for excluding infection in previously violated bone sites such as in postsurgical and post-traumatic conditions; ^{99m}Tc-HMPAO-labeled leukocytes have sensitivity and specificity similar to those labeled with ^{111}In and can be used particularly in peripheral locations such as the extremities. Combined labeled leukocytes and bone scans have a better accuracy than labeled-leukocyte scans alone and can help to localize abnormal foci [51–53].

Since labeled-leukocyte scans show uptake by active bone marrow, it may be difficult to differentiate this normal marrow uptake from abnormal uptake due to infection. Furthermore, surgical procedures may alter the bone marrow distribution significantly. Bone marrow scans using ^{99m}Tc-sulfur colloid or nanocolloid may improve the specificity of such studies [54, 55]. Labeled antibodies have also been used in recent years for the diagnosis of osteomyelitis. ^{111}In- or ^{99m}Tc-labeled human nonspecific polyclonal antibodies (IgG) are used more commonly than monoclonal antibodies such as labeled antigranulocyte antibodies. IgG is easi-

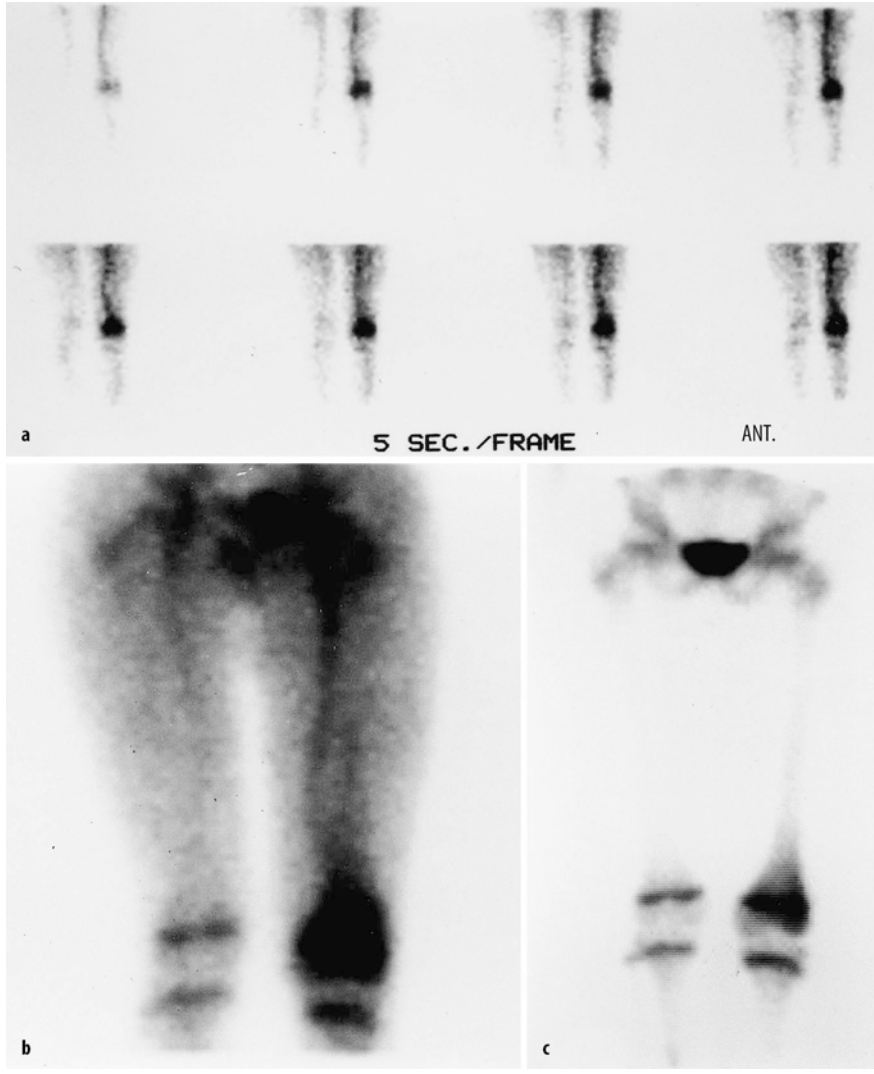

Fig 6.15a–c. A case of osteomyelitis in a nonviolated bone as seen on ^{99m}Tc multiphase bone scan. Regionally increased flow (**a**), blood pool activity (**b**) and delayed uptake is noted in the left distal femur

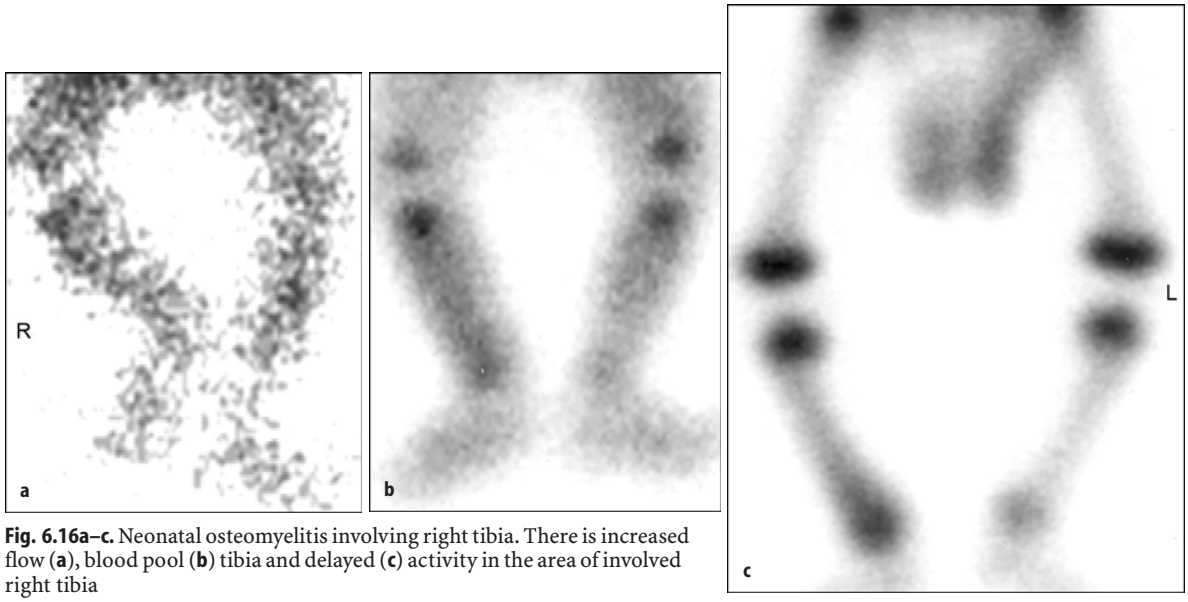

Fig. 6.16a–c. Neonatal osteomyelitis involving right tibia. There is increased flow (**a**), blood pool (**b**) tibia and delayed (**c**) activity in the area of involved right tibia

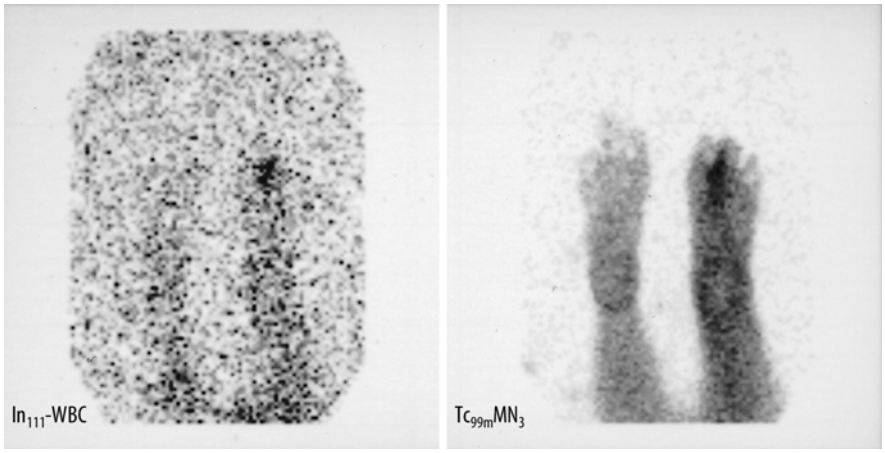

Fig. 6.17. ^{111}In-labeled leukocyte and 6-h MN3 images (plantar views) from a diabetic patient with osteomyelitis of the left 2nd metatarsal. While both studies are positive, the superior image quality of the technetium-labeled compound can be easily appreciated. (Courtesy of Dr. Christopher Palestro, with thanks)

Table 6.5. Accuracy of antigranulocyte antibodies in skeletal infections

Author	Year	Sensitivity	Specificity
Harwood	1999	91%	69%
Devillers	2000	86%	56%
Ryan	2002	85%	77%
Palestro	2003	100%	77%
Rothenberg	2003	85%	67%

er to prepare and use than labeled leukocytes. The results of IgG, with a sensitivity of 95% and a specificity of 83%, are encouraging [56]. Leukoscan (anti-NCA-90) (Fig. 6.17) and fanolesomab (anti-NCA-95) are also used to diagnose skeletal infections. Early studies suggested similar or better accuracy (90%) to WBC scan [57]. However, recent studies have showed variable results (Table 6.5). These studies [58–62] suggest that leukoscan does not achieve the level of accuracy that was suggested earlier and is not accurate enough to replace WBC imaging for orthopedic infection.

Ultrasound is useful in detecting osteomyelitis, particularly in infants and children. Since osteomyelitis in this age-group affects predominantly the end regions of long bones, ultrasound can detect characteristic findings associated with the pathological changes in these areas. Accordingly, ultrasound commonly shows intra-articular fluid collection and subperiosteal abscess formation that may precede the radiological changes by several days [63].

MRI has an important role in the diagnosis of osteomyelitis. Overall, it has a sensitivity of 60%–100% and a specificity of 50%–95% [19]. The average overall accuracy of MRI is similar to that of multiphase bone scans, but compared with bone scanning, MRI is more expensive. In patients with violated bone, MRI has been reported to encounter difficulty in differentiating between those with and without infection [64]. MRI is often used in suspected vertebral osteomyelitis, in complicated cases of chronic osteomyelitis, and in situations where anatomical details are necessary for planning surgical intervention.

Koori et al. [65] studied 16 rabbits in 2 groups of 8; one group was a control, and the other was infected with *S. aureus* directly into the tibia. In the osteomyelitic group, metaphyses were resected and replaced with a preinfected block of bone cement; in the control group the metaphyseal defect was replaced by bone cement injected with sterile saline. Two weeks later, the bone cement in both groups was surgically removed (osteomyelitis was confirmed in the infected group). At 3 and 6 weeks a peripheral CT and ^{18}F-FDG positron emission tomography (PET) were performed. PET images showed not only higher ^{18}F-FDG activity in the osteomyelitic group but also continuous elevated uptake at 6 weeks. Using standardized uptake values, the control group showed a decrease from 1.9 to 1.2 at weeks 3 and 6 respectively whereas the infected group measured 3.1 at week 3 and 5.5 at week 6. The results showed that intact bones have low ^{18}F-FDG uptake, and normal bone healing (seen in the control group) will have a transient increase in uptake just to normalize within a 6-week period. Bone infection, on the other hand, showed a markedly higher constant uptake. This study indicates that ^{18}F-FDG PET can differentiate bone healing from infection. The study also proposes that 3–6 months should be allowed following surgical or traumatic bone healing just to lower the odds of a false positive.

6.3.1.4.2 Imaging of Peculiar Forms of Skeletal Infections

Diabetic Foot Osteomyelitis. Bone scanning is very sensitive but not specific for detecting infection in diabetics. It is positive in cases of neuroarthropathy as well as of infection, with a specificity ranging from 0% to 70% (average 27%) [18]. Accordingly, the three-phase

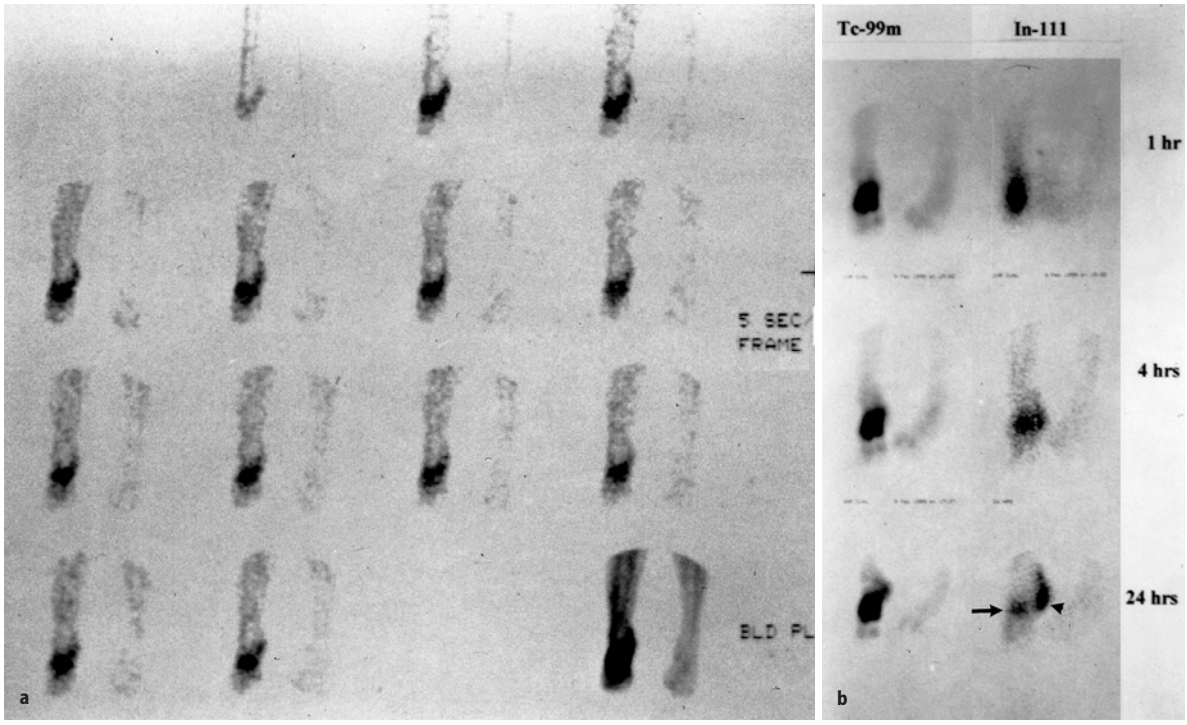

Fig. 6.18a, b. Simultaneous ^{99m}Tc MDP and ^{111}In-labeled leukocyte bone scan illustrating the decreasing leukocyte uptake in the area of neuroarthropathy (*arrow*) and increasing uptake in the area of osteomyelitis at the region of the right heal (*arrow head*)

bone scan cannot reliably distinguish infection from neuroarthropathy. The four-phase bone scan and using the timing of arterial hyperemia on flow studies for scan interpretation for diagnosing osteomyelitis, may improve the specificity. ^{67}Ga is not helpful in resolving the question of osteomyelitis in the diabetic foot, since it is also positive in noninfected neuroarthropathy.

Indium-111 leukocyte imaging has been reported to be both sensitive and specific for diabetic foot infections. However, sensitivities range from 50% to 100% and specificities from 29% to 100% [20]. All ulcers exposing bone were found to be associated with osteomyelitis, and such patients may thus be treated without the need for imaging [66]. Patients with ulcers not exposing bone are recommended to have ^{111}In-leukocyte studies to detect osteomyelitis. False-positive results have been reported in several conditions, including rapidly progressive neuroarthropathy, and the specificity varies in the literature. The vast majority of neuroarthropathies are not rapidly progressive and show no abnormal accumulation of labeled leukocytes. Only in a minority of cases of the rapidly progressive variant does ^{111}In-white blood cell imaging show significantly increased uptake. Combined bone/labeled-leukocyte imaging improves the accuracy of the diagnosis of foot osteomyelitis and its differentiation from soft tissue infection. Grerand [52] reported a sensitivity of 93% and a specificity of 83% for this dual-isotope technique and concluded that it can reliably determine the site and extent of diabetic foot osteomyelitis. False-positive results, however, can still occur in some cases of noninfected neuroarthropathy [67]. A decreasing lesion-to-background ratio of labeled white blood cells between 4 and 24 h helps to differentiate the condition from osteomyelitis, which does not show a decreasing ratio (Fig. 6.18). Because of the poor spatial resolution of labeled-leukocyte studies, uptake in soft tissues could be incorrectly attributed to bone uptake and vice versa. Dual-isotope studies for diabetic foot allow also for better localization of white blood cell activity, and consequently help to increase the accuracy in differentiating osteomyelitis from cellulitis [68, 69].

Combined ^{111}In-labeled-leukocyte and ^{99m}Tc-sulfur colloid marrow scans (Fig. 6.19) further improve the specificity, differentiating marrow uptake of labeled leukocytes from uptake by actual bone infection. Palestro et al. recently found this approach superior to combined bone/leukocyte scintigraphy [67].

MRI can differentiate between soft tissue and bone infections [70]. This is particularly important in diabetics and has been found useful in the diagnosis of diabetic foot osteomyelitis. Several investigators found MRI to be clearly superior to the plain films and bone scintigraphy, with a sensitivity and specificity approaching 100%. These studies, however, involved mostly severe infections with significant pathological

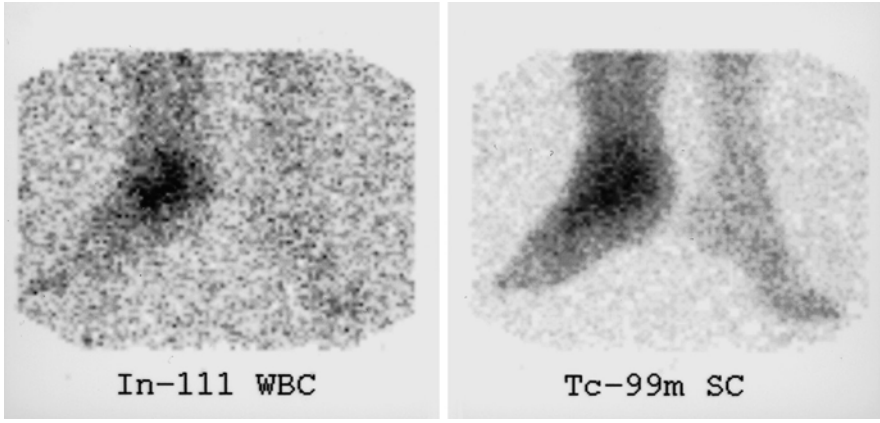

Fig. 6.19. Both labeled leukocyte and ^{99m}Tc sulfur colloid images show increased uptake in the right mid foot of a diabetic patient with a Charcot joint (medical images). (Courtesy of Dr. Christopher Palestro, with thanks)

changes. Newman et al. [71] reported a sensitivity of only 29% for relatively low-grade osteomyelitis compared with 100% for labeled-leukocyte scanning of the same patients. The specificity was similar for both modalities. Cook et al. also recently reported a sensitivity of 91% and a specificity of only 69% [72]. Morrison et al. reported a lower accuracy for diabetic compared with nondiabetic cases, with sensitivity and specificity of 82% and 80%, respectively, for diabetic osteomyelitis compared with 89% and 94% for nondiabetic bone infections. However, these authors found that MRI was clinically useful and cost effective [73]. Beltran [74] reported the characteristic pattern of osteomyelitis as a high signal intensity from the marrow space on T_2-weighted images. However, this finding itself is not specific for osteomyelitis and can be seen with other conditions, including rapidly progressive neuroarthropathy: the pattern may be indistinguishable from that of osteomyelitis.

Labeled antigranulocyte antibody imaging is another alternative for diabetic foot infection and have an advantage of producing earlier results and a less demanding technique [58–60]. The technique has been reported to be very sensitive (91–100%); however, the specificity is again less than adequate (69–77%) [58–60].

A recent study suggests that PET offers high specificity and sensitivity for targeting osteomyelitis in the diabetic foot [75]. A total of 13 diabetic patients (ten men and three women ranging in age from 29 to 70 years) with ulcerations, fever, and other signs of suspected osteomyelitis of the foot were enrolled in the study. Each patient underwent a PET/CT. Results were compared with final diagnoses based on histopathology and bacteriologic assays during the surgery or at clinical and imaging follow-ups. FDG uptake values suggesting infection were detected by PET in eight patients. All findings based on the PET/CT were correctly confirmed at surgery or clinical/imaging follow-up. These included 12 foci of infection (75%) localized to bone in five patients and three foci (19%) localized only to soft tissue in three patients. Mildly diffuse or no FDG uptake was seen in the remaining five patients who had no evidence of foot infection at further clinical and imaging follow-ups. In addition to higher diagnostic sensitivity and more accurate ability to assess the extent of infection and inflammatory activity, PET/CT also provides faster results (typically within 2 h).

Vertebral Osteomyelitis (Spondylodiskitis). Signs and symptoms of vertebral osteomyelitis are usually vague and insidious and thus the diagnosis and treatment may be delayed. Standard radiographs are neither sensitive nor specific for the diagnosis of vertebral infection [76–78]. Bone scanning is also sensitive but is not specific. In cases of proven vertebral osteomyelitis, bone scan results have been negative as late as 2 weeks following the onset of symptoms [79]. More importantly, findings of increased uptake on bone scan are not specific for osteomyelitis as increased uptake may be present in degenerative arthritis or in healing fractures. Furthermore, the increased uptake of the radiotracer does not differentiate inactive from active osteomyelitis since uptake may persist for a long time [80].

The CT scan is quite sensitive for vertebral osteomyelitis but, like the bone scan, it is not specific. However, CT is used to guide needle biopsy [80].

Magnetic resonance imaging, on the other hand, is both sensitive and specific for vertebral osteomyelitis. Modic [77] found MRI to be as sensitive, specific, and accurate as combined ^{99m}Tc and ^{67}Ga isotope scanning. Changes of vertebral osteomyelitis have been reported to be seen on MRI as early as those on bone scan [84], although in one report these changes were late, even later than plain film changes [85].

Gallium-67 has a sensitivity of 90% and a specificity of 100% when combined with ^{99m}Tc-MDP [76, 77, 80, 82–85]. For scan interpretation, the degree of bone uptake is compared with that of ^{67}Ga to achieve the high specificity of this combined approach (Figs. 6.20, 6.21).

Recently, Love reported on a small number of patients with vertebral osteomyelitis and found that SPECT gallium-67 and bone scans were more sensitive and specific than planar gallium and bone scintigraphy (91% and 92% vs. 64% and 85%, respectively). The authors found that gallium-67 SPECT alone has an identical accuracy to combined SPECT Ga and bone and suggested the use of Ga-67 SPECT alone in the diagnosis of vertebral osteomyelitis since it was also sensitive and slightly more specific than MRI in their series [83].

Labeled-leukocyte scanning using both ^{111}In and ^{99m}Tc-HMPAO is neither sensitive nor specific. This low sensitivity is due to different patterns of uptake – normal, decreased, or increased – in cases of proven vertebral osteomyelitis [81, 86–88]. Because the diagnosis of vertebral osteomyelitis is often delayed, most infections are chronic in nature, which explains the low sensitivity of ^{111}In-labeled leukocytes in its diagnosis. In studying 71 patients with suspected vertebral osteomyelitis, Palestro et al. [87] found that ^{111}In-leukocyte scintigraphy demonstrated increased or decreased uptake in patients with proven osteomyelitis. Increased uptake was associated with a high specificity of 98%, but it was only 39% sensitive for the condition. The photopenic pattern was neither sensitive (54%) nor specific (52%) for osteomyelitis. In a study of 91 patients with suspected vertebral osteomyelitis, Whalen et al. [86] reported a sensitivity of 17%, a specificity of 100%, and an accuracy of 31% for ^{111}In-leukocyte imaging. The authors found photon-deficient areas at the sites of proven osteomyelitis in 50% of 18 patients, and they were included in the false-negative scans. Because the diagnosis of vertebral osteomyelitis is often delayed, most infections are chronic in nature, which can explain the low sensitivity of ^{111}In leukocytes in their diagnosis. Photopenic areas on ^{111}In-leukocyte imaging in proven vertebral osteomyelitis could be secondary to secretion of antichemotactic factors by some causative organisms such as *Pseudomonas aeruginosa* and *Klebsiella pneumoniae*, which prevents enough accumulation of labeled cells at the site of infection [88]. Hovi reported three cases of proven infection detected by MRI but none by ^{99m}Tc-HMPAO-labeled leukocytes [89].

In a study performed on 30 consecutive patients showing positive PET scans in all five cases with disc space infection, because none of the patients with degenerated disc space demonstrated FDG uptake, even in the presence of substantial end plate abnormalities, the authors suggested that FDG-PET may be useful for excluding disc space infection in equivocal MR findings [90].

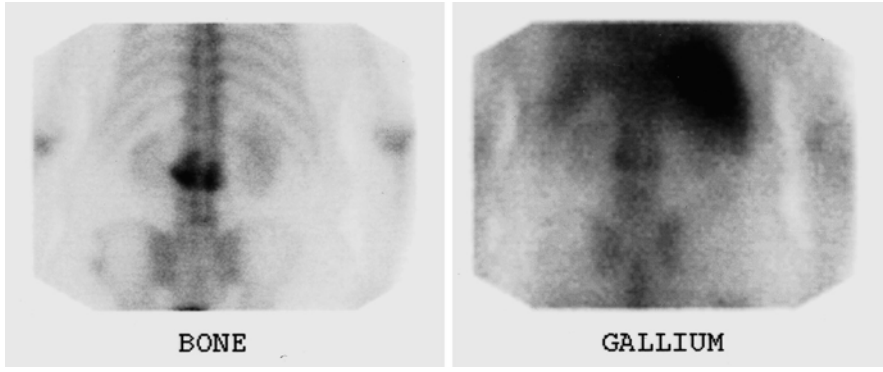

Fig. 6.20. Sequential bone/gallium scans – negative for osteomyelitis in a patient with compression fracture (gallium uptake is less than MDP uptake). (Courtesy of Dr. Christopher Palestro, with thanks)

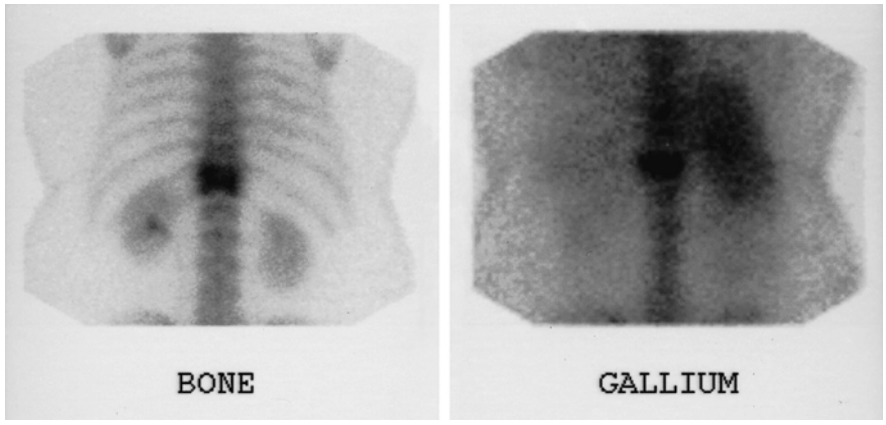

Fig. 6.21. Sequential bone/gallium scans – equivocal for osteomyelitis in a patient with compression fracture. (The uptake on both studies is very similar, in terms of both intensity and spatial distribution.) (Courtesy of Dr. Christopher Palestro, with thanks)

Chronic Osteomyelitis. The radiological diagnosis of chronic active osteomyelitis is neither sensitive nor specific, while bone scintigraphy is very sensitive but not specific. This low specificity is due to the chronic bone repair that is associated with increased bone metabolism and increased uptake on bone scan in the absence of active infection. It is therefore difficult to differentiate healing from chronic active disease, although increased activity on all phases of the bone scan is suggestive of chronic active disease. The bone scan, accordingly, cannot confirm the presence of active disease, but a negative scan excludes it.

Gallium-67 citrate imaging is more specific than bone scanning for chronic osteomyelitis. False positives still occur in conditions such as healing fractures, tumors, and noninfected prostheses. Combined ^{99m}Tc-MDP and ^{67}Ga scans can be helpful in making the diagnosis of active disease. As Tumeh et al. [91] suggested, when ^{67}Ga uptake exceeds ^{99m}Tc-MDP uptake in intensity or differs in spatial distribution, active osteomyelitis is present.

There is controversy regarding the role of ^{111}In-labeled leukocytes in the diagnosis of chronic osteomyelitis. Since the majority of labeled cells are polymorphonuclear cells, the test is usually normal in true chronic osteomyelitis. However, due to the difficulty in making a clinical distinction between acute and chronic disease, results are variable and may be confusing. Tumeh and Tohmeh reported no advantage of ^{111}In-leukocytes over ^{67}Ga, as there was no significant difference between them in the sensitivity and specificity for chronic active osteomyelitis [92]. Krznaric et al. found that ^{99m}Tc-HMPAO leukocyte studies were sensitive and specific for the diagnosis of chronic osteomyelitis except for vertebral osteomyelitis [93]. Determining the presence or absence of sequestra is important, as their presence may require surgical treatment. The CT scan is a sensitive modality for the detection of sequestra. MRI was found to be useful in limited numbers of patients for detecting sequestra and was also useful in identifying the presence and sites of active chronic infection [94].

Sciuk et al. [95] used ^{99m}Tc IgG and ^{99m}Tc monoclonal antigranulocyte antibodies in 25 patients with suspected chronic osteomyelitis. Three-phase bone scanning in the study was 71% sensitive and 50% specific. IgG was 71% sensitive and 100% specific, while monoclonal antibodies had 40% sensitivity and 100% specificity. Both agents were sensitive in peripheral lesions (5/6 for IgG and 6/6 for monoclonal antibodies); in the central skeleton with active bone marrow IgG detected five of eight lesions, while monoclonal antibodies detected none of the eight. This study also confirmed the lack of specificity of multiphase bone scans for chronic osteomyelitis and suggested a possible role for labeled IgG as a more specific agent in both central and peripheral chronic bone infections. Thus, among the commonly used modalities, combined bone and ^{67}Ga scanning is highly recommended for detecting chronic active osteomyelitis. Determining the presence or absence of sequestra is important as their presence needs surgical treatment. MRI or CT scans are complementary procedures found useful in equivocal bone and gallium scans and are particularly helpful in detecting sequestra.

Recently, PET has been found useful for assessing the activity of chronic osteomyelitis [96–100]. De Winter et al. reported on 60 patients with suspected chronic musculoskeletal infection studied with ^{18}F-FDG PET. Twenty-five patients had proven infection and all were correctly identified by two readers with a sensitivity of 100%. There were four false-positive cases and overall specificity was 88% (90% for central skeleton and 86% for peripheral skeleton). The authors concluded that this single technique is accurate and simple, and has the potential to become a standard technique for the diagnosis of chronic musculoskeletal infections [98]. From the studies reported, the overall technique has a sensitivity of 95%–100% and a specificity of 86%–100% [96–99].

Periprosthetic Infection. Making the distinction between mechanical failure of a prosthesis and infection is not easy. Symptoms and signs of early infection are not specific and may even be similar to those of the normal healing process. The erythrocyte sedimentation rate and leukocyte count are not sensitive, and the standard radiographic appearance of infection can mimic that of mechanical loosening. Aspiration arthrograms are more accurate but, again, the sensitivity as reported by Johnson et al. [38] is only 67%. The late stages of infection can be detected more easily on the basis of clinical findings. It is crucial, however, to initiate treatment in the early stage, as progression to a serious infection may occur rapidly [101].

In the case of hip replacement, knowledge of the type of implant is important to plan a diagnostic strategy. In cemented total hip replacements, periprosthetic post operative uptakes are seen on bone scintigraphy during the first 12 months after joint replacement. Focal uptake at the tip of the femoral component is most typical of loosening, while diffuse uptake around the shaft is most typical of infection. These patterns are not specific, however, and there are controversies regarding their value in discriminating loosening from infection. In cementless, porous-coated hip arthroplasty (which depends on bony ingrowth for fixation instead of on cement) postoperative uptake on bone scintigraphy remains for 2 years or longer in asymptomatic patients [102, 103]. In knee replacement, postoperative increased uptake may also be seen on bone scintigraphy in more than 60% of femoral components and about 90% of tibial components for a long time,

even when patients are asymptomatic [104]. Accordingly for both cemented and porous-coated hip and knee replacements a bone scan is most useful in excluding infections when it is clearly negative.

Combined bone and ^{67}Ga scans have better specificity than either scan alone (Fig. 6.22). However, ^{111}In-leukocyte imaging has proven to have better accuracy than combined ^{67}Ga/bone scan. Still, false-positive ^{111}In leukocyte results occur as a result of physiological uptake by cellular bone marrow. Oswald et al. [103] found focal or diffuse accumulation of ^{111}In leukocytes around the prostheses for up to 2 years in 48% of uncomplicated cases. Addition of ^{99m}Tc-sulfur colloid bone marrow to ^{111}In-leukocyte scanning helps improve the specificity and is the recommended modality. The study is considered positive for infection when the ^{111}In-leukocyte uptake exceeds ^{99m}Tc-colloid activity on the bone marrow scan in extent and/or focal intensity (discordant pattern). If the relative intensity and distribution of ^{111}In-labeled leukocyte localization is equal to that of ^{99m}Tc-colloid (concordant pattern of normal marrow), the study is considered negative for infection [54, 105]. Accordingly, the optimal procedure for diagnosing infection of joint replacements is combined labeled-leukocyte/marrow scintigraphy (Figs. 6.23, 6.24), which has a diagnostic accuracy of more than 90% [54].

Antibody imaging (Fig. 6.25) has also been used to diagnose infections in patients with hip and knee prostheses with a sensitivity of 70% – 100% and a specificity of 83% – 100% for ^{99m}Tc-antigranulocyte antibodies [70], and a sensitivity of 92% and a specificity of 88% for ^{111}In-labeled IgG [106].

FDG-PET has been recently shown to be promising in detecting infections and loosening and differentiating both conditions in patients with hip and knee prostheses [107, 108]. The sensitivity and specificity for detecting infection are 90% and 89% for hip and 90% and 72% for knee periarthroplasty infections respectively [108]. Although the intensity of FDG uptake as determined by SUV values is important in making the diagnosis of malignancy, this is not the case with periprosthetic infections. Infected prostheses often show a moderate increased uptake which is not higher than that noted with aseptic loosening [107]. However, the location of the increased uptake is more important in differentiating infection from loosening since infection is characterized by uptake along the interface between bone and the prostheses, while in loosening it is around the neck and head [107].

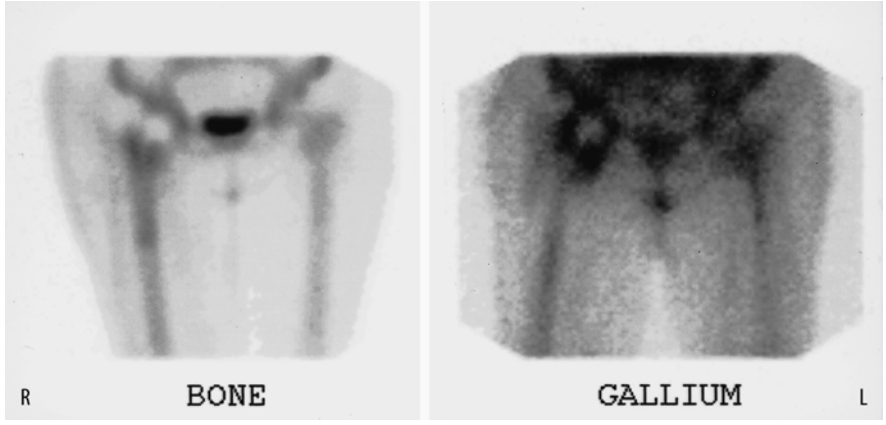

Fig. 6.22. Sequential bone/gallium scan – positive for infection of the right total hip replacement (incongruent distribution of two radiotracers). (Courtesy of Dr. Christopher Palestro, with thanks)

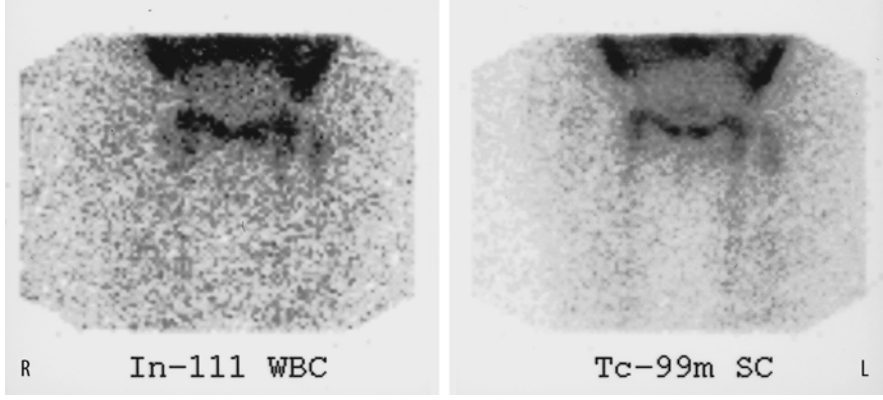

Fig. 6.23. Combined leukocyte/marrow scan with congruent uptake pattern in the left hip region indicating no infection. (Courtesy of Dr. Christopher Palestro, with thanks)

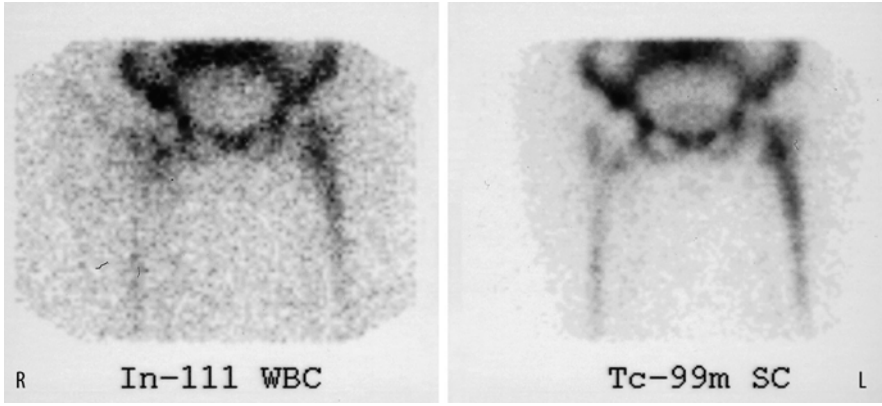

Fig. 6.24. Combined leukocyte/marrow scan. There is focal abnormal ^{111}In-leukocyte accumulation with no corresponding ^{99m}Tc-sulfur colloid uptake indicating infections in the right hip region. (Courtesy of Dr. Christopher Palestro, with thanks)

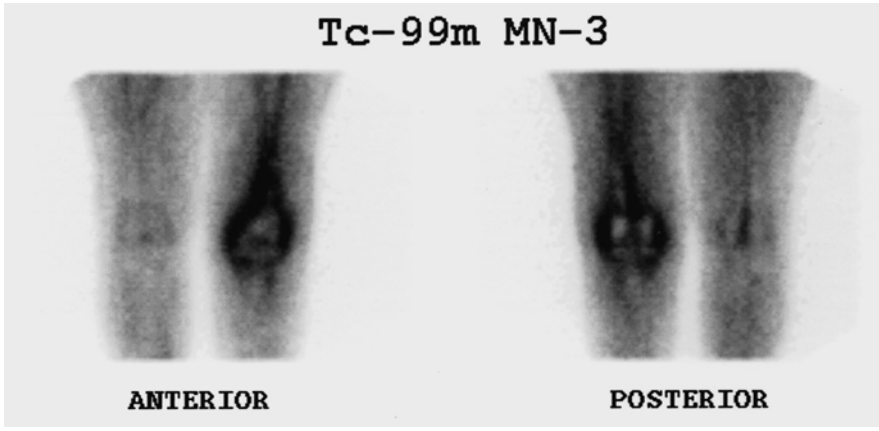

Fig. 6.25. Antigranulocyte antibody uptake indicating infected left knee prosthesis. (Courtesy of Dr. Christopher Palestro, with thanks)

Osteomyelitis in Patients with Sickle Cell Disease. Differentiating bone infarct from osteomyelitis clinically is difficult. Initial radiographs either are normal or show nonspecific changes. On bone scintigraphy the findings vary. If bone scintigraphy is performed a week after the onset of symptoms, healing of the infarct may cause increased uptake rather than the typical pattern of cold defect. To add more difficulty, osteomyelitis may also cause cold defects rather than increased uptake [19, 109, 110]. Addition of ^{67}Ga or ^{99m}Tc-sulfur colloid imaging to bone scans enhances the specificity and can resolve the majority of diagnostic problems related to osteomyelitis in patients with sickle cell disease [110]. If the bone scan shows areas of increased uptake, a bone marrow scan can be added. If a marrow scan in the area of interest is normal, it indicates osteomyelitis, while if radiocolloid photon deficiency is seen it suggests healing infarct. On the other hand, if the bone scan shows a photon-deficient area, ^{67}Ga may help to differentiate osteomyelitis by showing an incongruent pattern spatially or more ^{67}Ga uptake than that on the bone scan. Infarcts will show a congruent pattern [109].

Labeled leukocytes have also been used, although we encountered technical difficulties in labeling cells of sickle cell patients with failed scans. MRI and contrast-enhanced CT scans have also been reported to be of help in patients with nondiagnostic radiographs and bone scans.

Infectious (Septic) Arthritis. It has been reported that identifying joint involvement and distinguishing bone from joint infection can be achieved in up to 90% of cases using bone scintigraphy [111 – 113]. Bone scintigraphy, however, cannot distinguish infectious from noninfectious arthropathy. Detailed clinical information should always be an integral part of bone scan interpretation. Sundberg et al. [112] compared the interpretation of bone scans with and without knowledge of clinical information in 106 children suspected of having septic arthritis. The bone scan interpretation was correct in 13% when read without clinical history and in 70% when clinical information was included. It is possible in the vast majority of cases to make the distinction if certain criteria are followed. Periarticular distribution of the abnormal uptake that is largely limited to the joint capsule and has a uniform pattern indicates septic arthritis. Osteomyelitis, on the other hand, shows abnormal uptake beyond the confines of the joint capsule or shows nonuniform uptake within the joint capsule [112, 113].

To simplify the utilization of the many imaging modalities, Table 6.6 is provided to summarize the strengths and limitations of different modalities in the

Table 6.6. Summary of commonly used imaging modalities for skeletal infection

Modality	Advantages	Disadvantages	Typical findings and overall accuracy
Standard radiograph	Cost effectiveness: no additional imaging needed if positive. Identify other causes of symptoms (fracture). Assess comorbidities such as fractures and arthritis.	Low sensitivity. Findings take up to 2 – 3 weeks to appear, delaying diagnosis. Low specificity to identify infection in violated bone.	Cortical destruction (very sensitive finding). Soft tissue swelling with obliteration of fat planes. Endosteal scalloping; cortical tunneling. III defined radiolucent lesions. Osteopenia. Sensitivity: 28% – 94% (average of 56%). Specificity: 3% – 92% (average of 75%).
Computed tomography	Excellent visualization of the cortex. Multiplanar and thin slice reconstruction enhance ability to evaluate infection and identify sequestra.	Less resolution than plain radiography. Beam hardening artifact.	Increased attenuation of bone marrow. Periosteal reaction and new bone formation. Sequestrum. Intraosseous and/or soft tissue gas.
MRI	Excellent delineation of soft tissue versus bone infections. Evaluation of bone marrow edema. Excellent for suspected vertebral osteomyelitis. Very useful in neonatal pelvic osteomyelitis to identify associated soft tissue abscesses.	Bone marrow edema is nonspecific – can be seen in osteonecrosis, fractures, and metabolic bone disease. Specificity is lower with small bones and in complicated cases of infection.	Cortical destruction. Increased T2 signal (particularly on STIR); Decreased T1 signal and post-gadolinium enhancement. Sensitivity: 60% – 100% (average: 90%) Specificity: 50% – 95% (average: 86%)
Multiphase bone scan	Earlier detection than plain film (24 – 48 h after infection). Very high sensitivity for infections even in the presence of other comorbidities. Whole body imaging allows for detection of infection at other unsuspected sites.	Specificity decreases when other pathologies are present. Scans will stay positive for a long time after infection heals; therefore is not ideal for monitoring response to treatment.	Focal increased uptake on blood flow, blood pool, and delayed images. Sensitivity: 90% – 95%. Specificity: nonviolated bone: 92%; violated bone 0% – 76% (average of 30%).
WBC scan Alone or with bone scan	High specificity for infection. Improves bone scan specificity in the setting of violated bone. Scans normalize as early as a few days, and so may be used to monitor response to therapy.	If used alone, difficult to differentiate bone versus soft tissue infections. A tedious procedure.	Focal increased uptake. Dual imaging will show concordant uptake with bone scan in positive studies. Average sensitivity: 88%. Average specificity: 88% (91% – 94% when combined with bone scan).
Gallium-67 scintigraphy Alone or with bone scan	Early detection of infection. Scans return to normal in 6 weeks with successful therapy, allowing use for monitoring treatment. Useful for chronic active and vertebral osteomyelitis.	Positive findings can be nonspecific, and may be positive in other settings such as tumor and inflammation.	Combined scanning is considered positive when they are spatially incongruent or spatially congruent with greater gallium intensity than bone scan. Average sensitivity: 89%. Average specificity: 70%.
Bone marrow scan as an addition to WBC scan alone or along with bone scan.	Improves specificity for infection versus inflammation in complicated cases, such as postarthroplastic infections.	Adds time and cost to the diagnostic imaging.	Infection is confirmed when no bone marrow activity present corresponding to the positive area on labeled WBC scan. If activity is present, it indicates physiologic bone marrow as a cause of WBC uptake.
Ultrasound	Excellent for rapid and accurate detection of joint effusions. Identify soft tissue and subperiosteal abscesses. No radiation.	Poor modality to visualize bone.	Fluid collection adjacent to the cortex of infected bone with communication to the medullary cavity. Occasionally, superficial local defects and periosteal reactions in advanced cases of osteomyelitis. Absence of joint effusion will rule out septic arthritis.
PET	Useful in chronic active osteomyelitis and periprosthetic infections as a single modality. Can be useful in early assessment of the response to therapy.	Availability. Expense.	Focally increased uptake with moderate to high SUV. Sensitivity: 95% – 100% (chronic osteomyelitis); 90% (preprosthetic infection). Specificity: 86% – 100% (chronic osteomyelitis); 89% hip periprosthetic infection; 72% knee periprosthetic infection

Table 6.7. Correlation of imaging findings and pathophysiologic features of infection

Vasodilation of blood vessels	Increased flow and blood pool activity on bone scan, increased ^{67}Ga- and ^{99m}Tc-nanocolloid accumulation
Pathologic change at the site of infection	Imaging pattern
Increased permeability and chemotaxis	Increased accumulation of ^{111}In- or ^{99m}Tc-labeled WBC
Increased secretion of iron-containing globulin by injured and stimulated WBC	Increased accumulation of Ga-67
Formation of woven bone	Increased uptake of ^{99m}Tc-MDP on delayed images with persistent accumulation beyond 3 – 4 h
Increased expression of glucose transporters	Increased accumulation of ^{18}F-FDG on activated inflammatory cells

diagnosis of skeletal infections, Table 6.7 summarizes the correlation between scintigraphic and pathophysiologic changes in skeletal infections and Fig. 6.26 presents a suggested algorithm for the diagnosis of skeletal infection.

6.3.2 Avascular Necrosis (Osteonecrosis)

Avascular necrosis of bone results from imbalances between the demand and supply of oxygen to osseous tissues. There are many causes for osteonecrosis:

1. Trauma (e.g. fracture or dislocation)
2. Hemoglobinopathies (e.g., sickle cell anemia)
3. Exogenous or endogenous hypercortisolism (e.g., corticosteroid medication, Cushing's syndrome)
4. Renal transplantation
5. Alcoholism
6. Pancreatitis

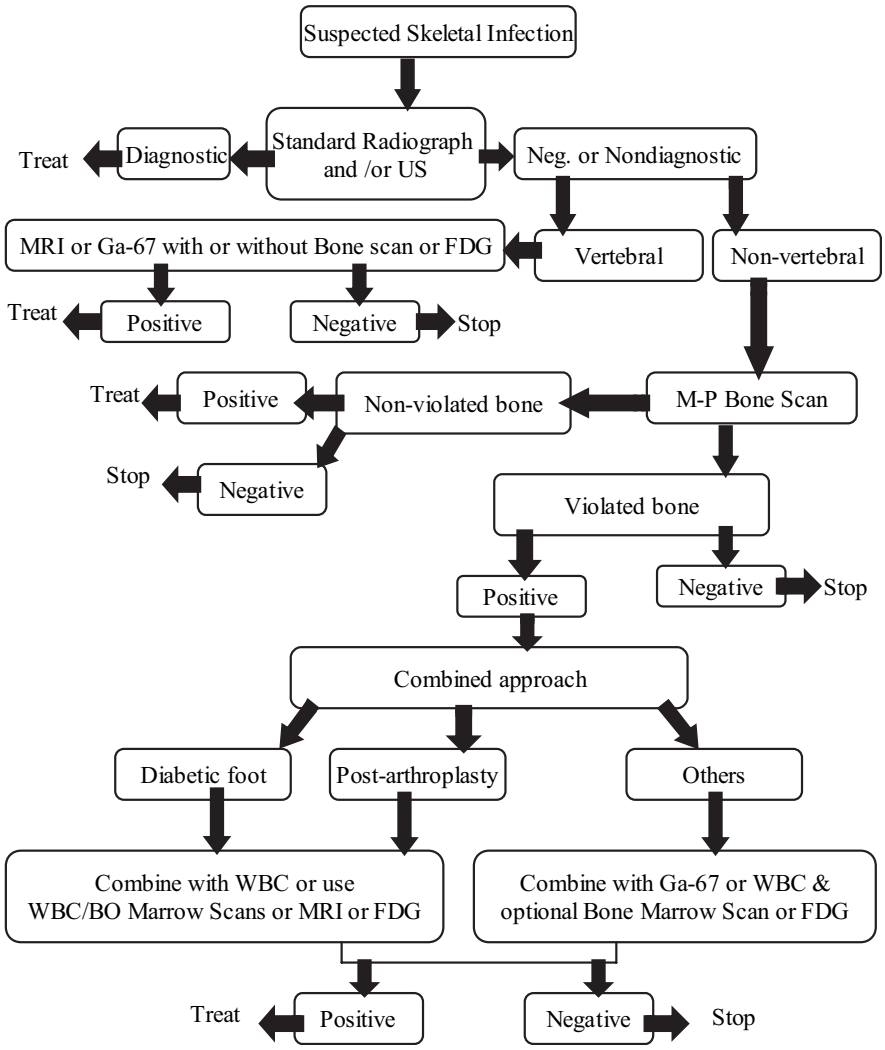

Fig. 6.26. Algorithm for the diagnosis of skeletal infection utilizing multiple modalities based on the location and probable pathophysiology of the suspected infection

7. Dysbaric (e.g., Caisson disease)
8. Small vessel disease (e.g., collagen vascular disorders)
9. Gaucher's disease
10. Hyperuricemia
11. Irradiation
12. Synovitis with elevation of intra-articular pressure (infection, hemophilia)
13. Idiopathic (spontaneous osteonecrosis)

In some cases the underlying cause cannot be determined and in this situation the term primary, idiopathic, or spontaneous osteonecrosis is used.

Following the interruption of blood flow, blood forming and mesenchymal cells of the marrow as well as primitive osteoblasts are involved first and die 6 – 12 h after the interruption of the blood supply. Bone cells including osteocytes and mature osteoblasts die 12 – 48 h later, followed by the fat cells, which are most resistant to ischemia and die 2 – 5 days after the interruption of blood flow. This sequence of events may explain why bone marrow scintigraphic changes of decreased uptake appear earlier than bone scan abnormalities, since the bone marrow is affected earlier than the bone cells, which are relatively more resistant to ischemia [114, 115].

Ischemia does not directly affect the mineralized bone matrix or cartilage. The articular cartilage receives most of its nutrition by direct absorption from synovial fluid. Cartilage, however, cannot resist persistent elevation of intracapsular pressure for more than 5 days, after which time degeneration begins.

The reparative process is initiated and carried out by neovascularization through the collateral circulation, advancing from the periphery of the area of necrosis or by recanalization of occluded vessels. This granulation tissue provides all the elements necessary for the formation of bone matrix and new bone deposition by young osteoblasts. This repair process may be altered. Often bone collapse results from structural weakening and external stress. Bone collapse and cartilage damage can result in significant deformity [115, 116].

The different scintigraphic patterns of femoral head avascular necrosis are correlated with the sequence of pathological events. In stage I, during the first 48 h, the morphology of bone is preserved and the radiographs are normal. Osteoblastic uptake on bone scan varies from being absent to almost normal. This reflects the greater resistance of mature osteoblasts to ischemia. Subsequently, a cold area of necrosis develops on bone scintigraphy. This avascular pattern will be seen immediately if interruption of the blood supply is abrupt and severe.

Stage II begins with the reparative process. Hyperemia is frequent and there is diffuse demineralization of the area surrounding the necrotic tissue. This stage is characterized scintigraphically by increased technetium diphosphonate uptake starting at the boundaries between the site of necrosis and the normal tissue beginning in 1 – 3 weeks. This increased uptake eventually will advance around a central photopenic area and involves the entire femoral head, lasting for several months.

As the reparative process is completed, uptake returns to normal. However, in cases with bone collapse (stage III), increased uptake may persist indefinitely. Stage IV is characterized by collapse of articular cartilage with degenerative changes on both sides of the joint and resultant increased periarticular uptake. Single photon-emission computed tomography (SPECT) should then be included in diagnosing femoral head avascular necrosis. It may detect a center of decreased uptake and increases the sensitivity of bone scanning.

When osteonecrosis occurs in growing skeleton it is included in the group of disorders collectively called osteochondrosis. Osteochondrosis involves the epiphyses or apophyses of the growing bones. The process is due to osteonecrosis in some cases, to trauma or stress in others (Table 6.8). In addition to avascular necrosis, the osteochondroses often demonstrate similar pathological features such as transchondral fractures, reactive synovitis, and cyst formation. Some common forms of osteonecrosis are described below.

Post-traumatic Osteonecrosis. Following a fracture, bone death of variable extent on either side of the fracture line is relatively common. Necrosis of a relatively large segment of bone following fracture or dislocation, however, is generally restricted to sites that possess a vulnerable blood supply with few arterial anastomoses. The femoral head, the body of the talus, scaphoid bone (Fig. 6.27), and the humeral head are such sites [118]. Other locations include the carpal hamate and lunate and the tarsal navicular bone. These bones are characterized by an intra-articular location and limited attachment of soft tissue, in addition to the peculiarities of their blood supply [115].

Table 6.8. Osteochondroses (modified from [117])

Involved bone	Disease
Capital femoral epiphysis	Legg-Calvé-Perthes disease
Metatarsal head	Freiberg's disease
Carpal lunate	Kienböck's disease
Tarsal navicular	Köhler's disease
Capitellum of humerus	Panner's disease
Phalanges of the hand	Thiemann's disease
Tibial tuberosity	Osgood-Schlatter disease
Proximal tibial epiphysis	Blount disease
Vertebral body	Scheuermann's disease
Patella	Sinding-Larsen-Johansson
Calcaneus	Serress disease
Ischiopubic synchondrosis	Van Neck's disease

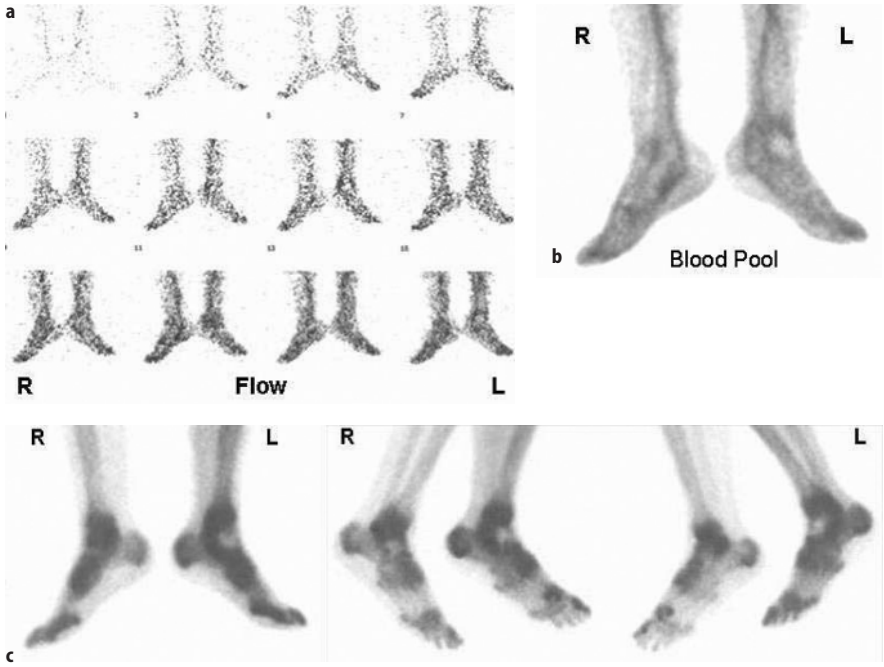

Fig. 6.27a–c. Post-traumatic osteonecrosis. Osteonecrosis of the talus bone in a 34-year-old male with history of foot trauma 2 months earlier. Flow images (**a**) show an ill-defined area of decreased flow in the region of the left talus, better seen on blood pool images (**b**), which also show a rim of increased blood pool activity. On delayed images (**c**) there is a photon-deficient area in the left talus surrounded by a rim of increased activity

Legg-Calvé-Perthes Disease. This condition represents osteonecrosis of the femoral head in pediatric populations, especially boys 4–7 years old. The blood supply to the adult femoral heads is via the circumflex femoral branches of the profunda femorus artery. This adult pattern of femoral head vascularity usually becomes established after closure of the growth plate at approximately 18 years of age. In infancy and childhood variable vascular patterns can be noted. The changing pattern of femoral head vascular supply with age may explain the prevalence of Legg-Calvé-Perthes disease in persons between the age of 4 and 7 years and the high frequency of necrosis following femoral neck injury in children. Fractures of the femoral neck, more often intracapsular than extracapsular fractures, are the most common cause. Others include dislocation of the hip and slipped capital femoral epiphysis. Table 6.9 summarizes the changes that characterize the stages of the disease which vary from the sequence of changes of other types of osteonecrosis as described earlier.

Bone scintigraphy is an integral part of the workup of patients suspected of having the condition. Pinhole imaging must be used routinely in this age group of patients with suspected Legg-Perthes disease rather than the parallel hole. Additionally, since the anterolateral aspect of the femoral head (the principal weight-bearing region) is typically involved, but no region of the head is necessarily spared and involvement is not uniform, pinhole imaging using frog leg and straight anterior position pinhole is recommended for better resolution of the abnormalities of this condition. Pinhole imaging is preferred to SPECT in the diagnosis of this condition in children. Bone scintigraphy is both a sensitive and a specific modality for the diagnosis of this condition, typically showing a cold area with or without a rim of increased uptake (Fig. 6.28). The sensitivity and predictive value of early postoperative bone scans for the detection of early avascular necrosis of the femoral head after surgical treatment of slipped capital

Table 6.9. Stages of Legg-Calvé-Perthes disease

Stage	Presentation
First (incipient stage): several weeks	Edema Hyperemia Joint fluid in many cases Widening of joint space Bulging of joint capsule
Second (necrotic stage): several months to 1 year	Death of femoral head (usually starts in anterior half and may extend to other parts) Softening of the metaphyseal bone at the junction of the femoral neck and capital epiphyseal plate Cysts may be present
Third (regenerative)	Procallus formation replacing dead head Collapse and flattening of the femoral head Femoral neck may become short and wide
Fourth (residual)	Remodeling occurs Newly formed bone becomes organized into a line of spongy bone Restoration of femoral head to normal shape, more likely if only anterior portion is involved

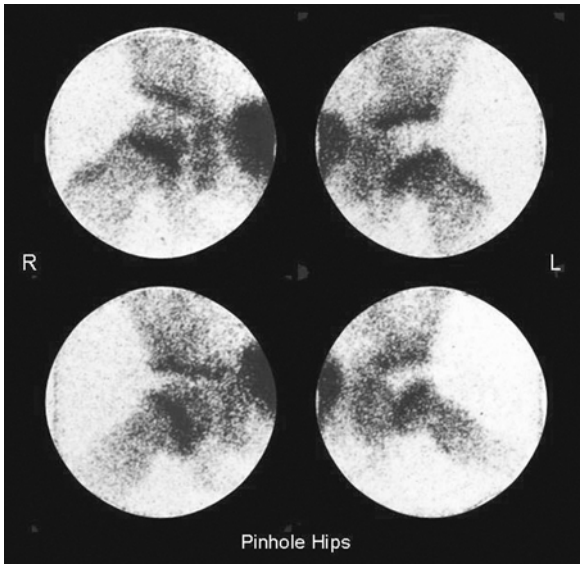

Fig. 6.28. Six-year-old boy with left hip pain and no history of trauma. Pinhole images of the hips in anterior (*upper row*) and frog leg (*lower row*) positions. Left hip shows photon deficiency indicating osteonecrosis of the left femoral head (Legg-Perthes disease)

femoral epiphysis was evaluated by Fragniere et al. [119]. The authors reviewed records of 49 patients (64 hips) operated on between 1980 and 1997 with a mean follow-up of 3 years. Sixty-one out of 64 hips had negative early postoperative bone scan. The three hips that developed AVN showed a significant decrease of radionuclide uptake. There were neither false-positive nor false-negative cases in this series [119]. The authors concluded that bone scintigraphy has an excellent sensitivity and predictive value for detection of AVN after surgical treatment of slipped capital femoral epiphysis.

Bone scintigraphy has proven also to have a prognostic value. Conway introduced a prognostic classification [120] of two pathways: pathway A is defined by the early appearance of a lateral column formation (before any radiologic sign) as activity in the capital femoral epiphysis indicating early and rapid revascularization. This pathway is associated with good outcome. Pathway B is defined by lateral column formation. The value of scintigraphy in predicting the course of the disease using this classification was illustrated by Tsao, who studied 44 consecutive patients treated for Legg-Calvé-Perthes disease and undergoing serial technetium-99m-diphosphonate bone scintigraphy and with a average follow-up period of 4.4 years. Twenty hips were classified as pathway A. The average age at presentation was 6.1 years. At last follow-up, none of the patients of this group had radiographic "head-at-risk" signs or required operative treatment. Twenty hips were classified as pathway B. The average age at presentation was 5.8 years. At last follow-up, 18 patients had head-at-risk signs, with 11 requiring operative treatment. Bone-scintigraphy classification preceded the radiographic head-at-risk signs by an average of 3 months, allowing earlier treatment [121]. The prognostic value of this classification was also more recently reconfirmed by Comte et al. [122], who showed that the presence of lateral column formation (pathway A) has a positive predictive value of 85% for good outcome. On the other hand, pathway B with the absence of lateral column formation has a 97% positive predictive value for poor final outcome [122]. Comte found that the appearance of hyperactivity of the metaphyseal growth plates provides additional prognostic information since it indicates poor outcome. The value of bone scintigraphy in determining the prognosis lies also in the short time in which the prognostic information can be obtained since it may be seen as early as the time of presentation but generally over 5 months duration after the insult. MRI is also very useful in predicting the course of the disease, particularly later during the fragmentation stage.

Dysbaric Osteonecrosis. This type of osteonecrosis occurs in patients subjected to a high-pressure environment, such as deep-sea divers. The exact cause of ischemia is debated. Immobilization of gas bubbles blocking the vascular channels is considered to be the major factor by many investigators. The presence of intravascular gas bubbles is seen even after ultrasound and other techniques [123] have documented asymptomatic decompression. Shoulders, hips, knees, and ankles are commonly involved in this type.

Sickle Cell Disease Necrosis. Sickle cell disease is a relatively common hereditary hematological disorder. The disease is caused by the replacement of the glutamic acid of B-chains with valine. The disease has numerous consequences, one of the most common being injury to bone. Osteonecrosis and osteomyelitis are the most common complications [124]. The bone manifestations occur similarly in other hemoglobinopathies and affect most commonly the femora, tibiae and humeri [125, 126]. Since sickle cell osteonecrosis most commonly involves the femoral and humeral heads although it can affect any bone of the skeleton, it is possible that the increased length of the nutrient arteries supplying the marrow in the long bones makes them more susceptible to occlusion. Necrosis of the femoral head is one of the significant skeletal disorders in sickle cell disease patients. Neonates who have sickle cell disease do not often develop osteonecrosis because of the high fetal hemoglobin level. Although the pathogenesis of the vascular occlusion leading to an infarct is not entirely clear, vaso-occlusion is considered to be one of the main culprits in sickle cell crisis. Since hemoglobin S is sensitive to hypoxemia, erythrocytes become vis-

cous and sickle abruptly when exposed to hypoxia. This may compromise the microvascular flow and may cause infarction [18]. Signs of acute infarction can include warmth, tenderness, erythema, and swelling over the site of vaso-occlusion [126]. However, these clinical signs are nonspecific and may also occur in acute osteomyelitis, which may occur as a primary event or may be superimposed on infarcts; necrotic bone is a fertile site for such secondary infections [125, 126]. Thus, recognition of bone marrow infarction often relies on the use of imaging modalities. MRI has not been found to have the specificity or sensitivity of radionuclide studies [127]. The scintigraphic diagnosis may be straightforward using ^{99m}Tc-MDP scan, which shows photon deficient areas early on. SPECT and pinhole imaging are very valuable, particularly in resolving photon deficient areas in the middle of the increased uptake in the reparative process. In this stage it can be difficult to differentiate osteonecrosis from osteomyelitis and adding gallium-67 or bone marrow scanning may be essential. Acute chest syndrome in sickle cell patients is characterized by chest pain, which can mimic several pulmonary disorders including pulmonary embolism and pneumonia [128]. This condition is believed to be a sequel of osteonecrosis of the ribs and is usually associated with pulmonary infiltrates on chest X-ray. Whole body imaging cannot be overemphasized and should include the ribs in addition to the area of interest if different (Fig. 6.29).

Idiopathic (Primary or Spontaneous) Osteonecrosis. This is a unique entity with cases presenting no clear underlying disorders. Most commonly it affects the femoral head; it is usually bilateral and leads to secondary osteoarthritis. It also affects the femoral condyles, tibial plateau, wrists, and humoral heads.

Spontaneous Osteonecrosis of Femoral Head. Although no specific cause is recognized for this condition, an abnormality of fat metabolism, leading to marrow fatty infiltration or vascular embolization, is the most popular hypothesis [129]. Primary osteonecrosis of the femoral head affects adult men more frequently than women and is usually seen between the fourth and seventh decade of life. Unilateral and bilateral involvement may be detected. The reported incidence of bilateral disease has varied from 35% to 70%, influenced predominantly by the method of examination and the length of follow-up. Despite the high frequency of bilateral involvement, the condition usually first manifests as a unilateral symptomatic that can be related to osseous collapse in the more severely affected sites. The pathological findings are virtually identical to those in other varieties of osteonecrosis. To demonstrate photopenia in the femoral heads, SPECT (85%) is more sensi-

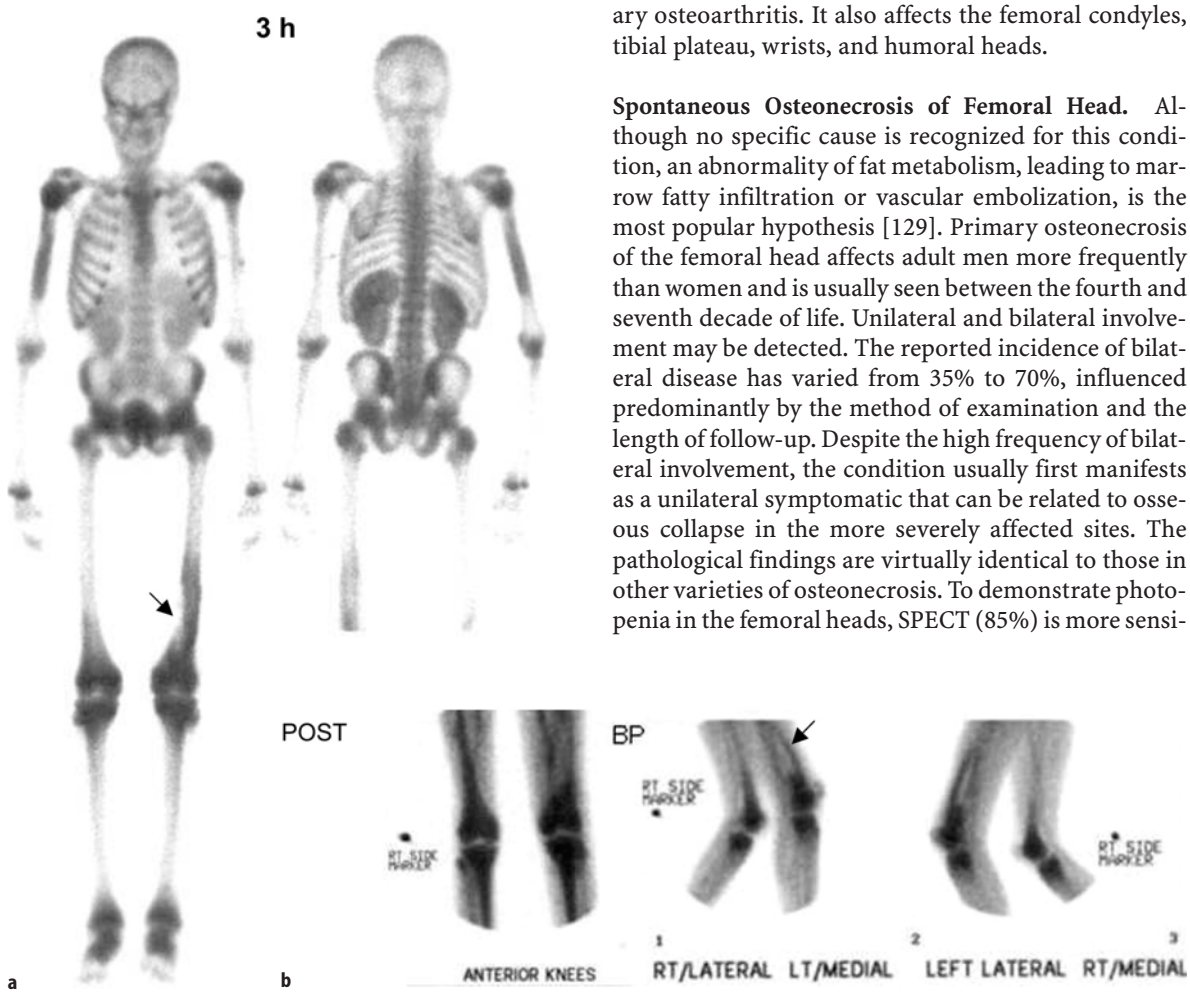

Fig. 6.29a,b. ^{99m}Tc-MDP whole body (**a**) and spot images including blood pool image of the knee regions (**b**) of a 17-year-old female with sickle cell disease complaining of left thigh bony pain. Note the photon deficient linear area in the medial aspect of the left distal femur (*arrow*) indicating acute infarction while the multiple areas of increased uptake in the humeri and femora particularly distal left represent older infarcts in healing phase. Note also periarticular uptake throughout the skeleton representing the pattern of bone marrow expansion associated with the underlying condition of sickle cell anemia. Another associated finding of the disease is the prominent kidney uptake diffusely on the delayed images as seen in this example

tive than planar imaging (55%) [130]. Figure 6.30 illustrates the value of SPECT in the diagnosis of the condition.

Spontaneous Osteonecrosis of the Knee. Although osteonecrosis around the knee is observed in association with steroid therapy, sickle cell anemia, other hemoglobinopathies, and renal transplantation, it may also occur in a spontaneous or idiopathic fashion. This entity occurs most characteristically in the medial femoral condyle. It can also affect the medial portion of the tibial plateau, the lateral femoral condyle, or the lateral portion of the tibial plateau alone or in combination with the medial femoral condyle. It characteristically affects older women and is characterized by abrupt onset of knee pain. Localized tenderness, stiffness, effusion, and restricted motion may also be present. Unilateral involvement predominates over bilateral involvement. Initially, radiographs are normal. Weeks or months pass before changes in the weight-bearing articular surface of the medial femoral condyle are seen. The pathogenesis of this condition is not clear. Vascular insufficiency associated with age is a proposed etiology. Traumatic microfractures in the subchondral bone with secondary disruption of the local blood supply have also been suggested. A predominant role of me-

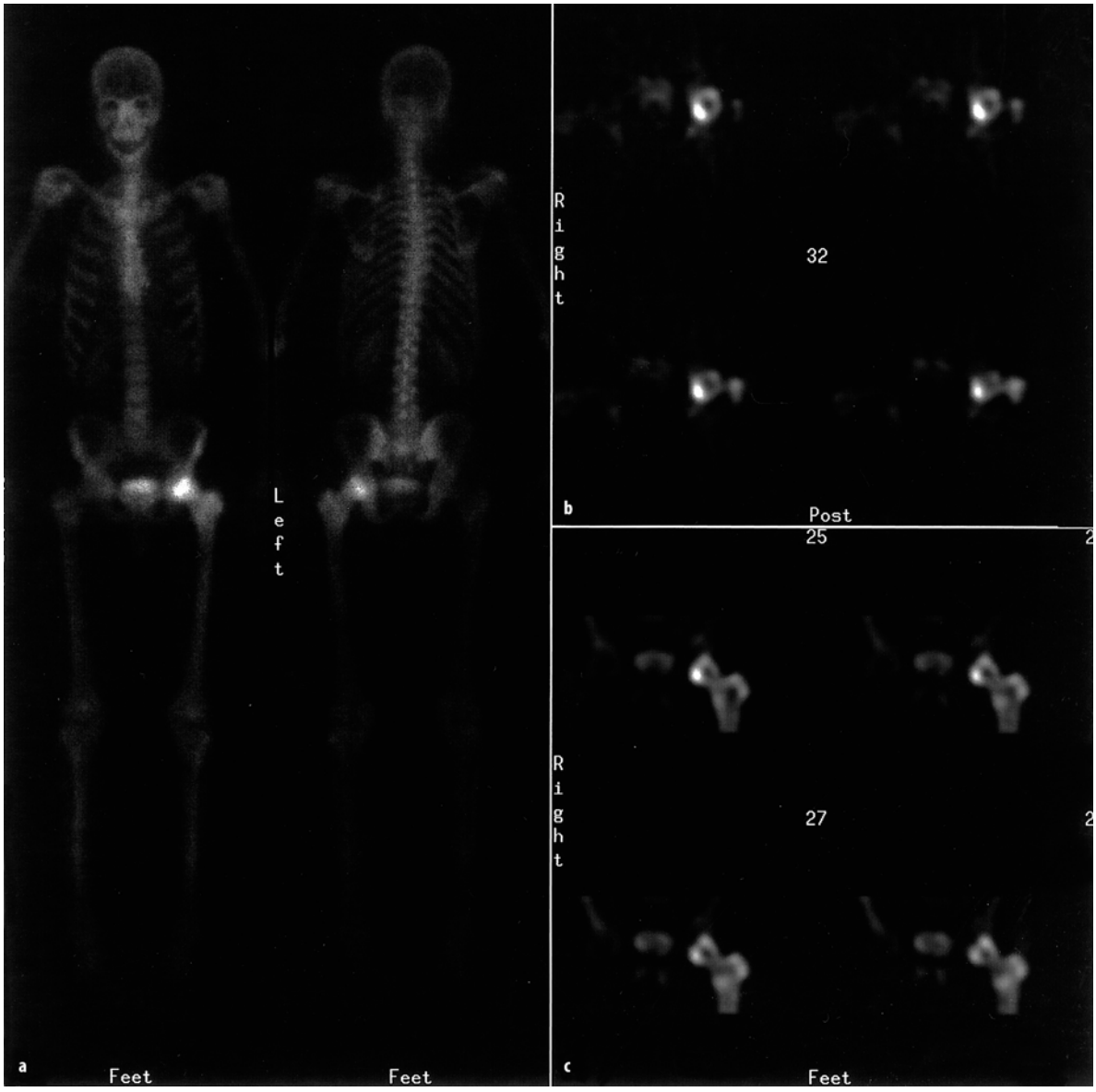

Fig. 6.30a–c. Bone scan from a case of osteonecrosis of the femoral head. SPECT images show a central cold area, confirming the diagnosis

niscus injury in the pathogenesis has also been proposed. X-rays are usually normal at the time of presentation and may even remain so for the entire course of the disease. Scintigraphy is a more sensitive modality and will be helpful in early detection. Scintigraphy may reflect the likely pathogenesis of microfractures with vascular disruption. In the first 6 months there is increased flow, blood pool activity, and uptake on delayed images (Fig. 6.31). From 6 months to approximately 2 years, blood flow decreases as well as the blood pool activity, while delayed uptake may persist. After 2 years the bone scan tends to return to normal except in patients who develop joint collapse and secondary osteoarthritis [130, 131]. Osteochondritis dissecans (which affects young patients and does not classically involve the weight-bearing surface of the femoral condyle) should not be confused with spontaneous osteonecrosis. Also osteoarthritis, commonly affecting the knee, is usually limited to the subchondral bone, whereas osteonecrosis tends to involve the adjacent shaft.

6.3.3 Complex Regional Pain Syndrome-1 (CRPS-1) or Reflex Sympathetic Dystrophy

Complex regional pain syndrome (CRPS I), is a clinical syndrome which has been defined according to the criteria of the International Association for the Study of Pain (IASP); it is a clinical syndrome characterized by pain, allodynia, hyperalgesia, edema, abnormal vasomotor and pseudomotor activity, movement disorder, joint stiffness, regional osteopenia and dystrophic soft tissue changes [132–136]. The pathophysiology of reflex sympathetic dystrophy (RSD) is not well understood. It is believed that an imbalance between the sympathetic and neuroceptive sensory systems occurs after an event usually trauma. Normally, afferent C and A delta fibers carry information from skin neuroceptors to the neurons in the dorsal horns of the spinal cord. From this region, information is transferred to higher central nervous system levels and also directed through sympathetic neurons and their efferent fibers. These sympathetic fibers control the tone of distal arterioles and capillaries. It is postulated that trauma, which could be trivial or minor or nerve injury, causes an alteration or imbalance of these nociceptive-sympathetic contact sites, resulting in vasomotor disturbances, pain, and dystrophic changes which form the features of this condition. It is now believed that the pathophysiology of this syndrome is, at least in part, a

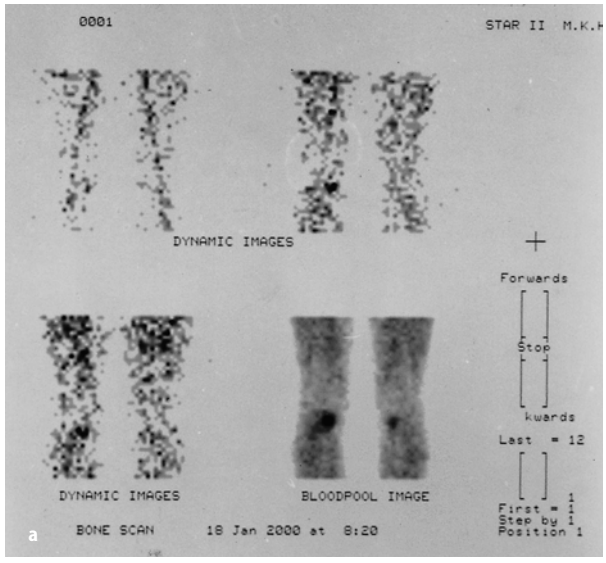

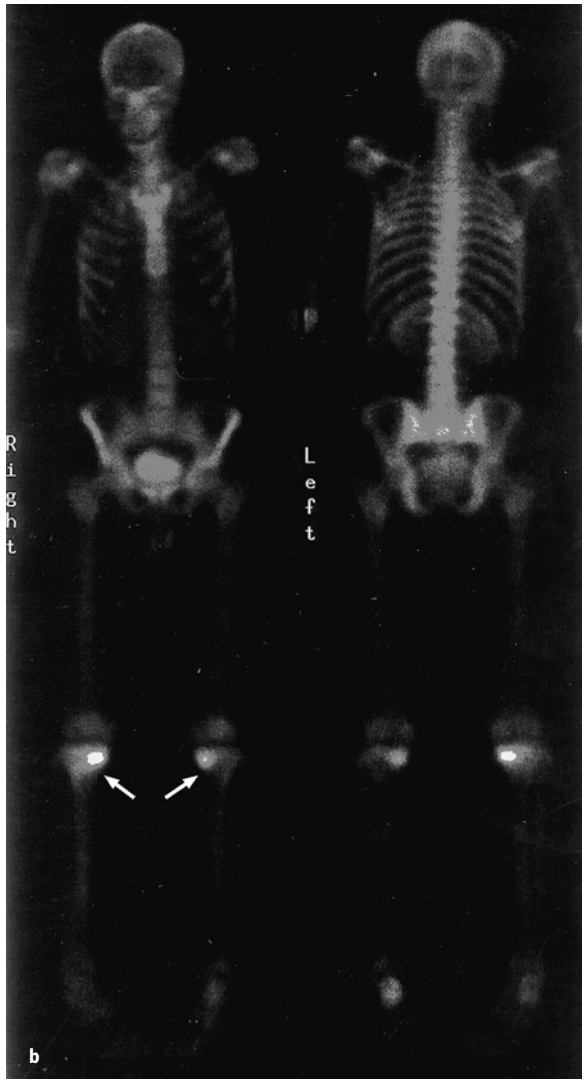

Fig. 6.31a,b. A case of bilateral osteonecrosis of the knee, illustrating the typical pattern on bone scintigraphy. Note the focal increased flow and blood pool with corresponding focally increased uptake on delayed image

disease of both the central and peripheral nervous system [134, 135]. Synovial histopathological changes have been found in patients with RSD. The most common changes are proliferation of synovial cells, subsynovial fibrosis, and vascular proliferation.

Vascular changes can be demonstrated on ^{99m}Tc-diphosphonate blood pool images, which show increased periarticular activity. A unifying pathophysiological mechanism in RSD can be proposed, related to an initial triggering injury causing an imbalance between the nociceptors and the autonomic nervous system (sympathetic and parasympathetic) to the affected area. As a result, vasomotor disturbances take place with vasodilatation as a prominent feature, leading to increased blood flow to the synovial and osseous tissues. The synovium reacts with cell proliferation and eventually secondary fibrosis. There is a lack of inflammatory cellular infiltration. The adjacent bone undergoes increased turnover locally, with some resorption. This explains the presence of radiographic and bone scintigraphic changes typical of RSD, as well as the changes at the level of the synovium. The clinical course of the condition, which may be underrecognized and could vary with the location, consists of three stages: acute, dystrophic, and atrophic [137].

The first stage is characterized by pain, stiffness, tenderness, and swelling of the involved joint. In stage 2, there is still pain, tenderness, and wasting of subcutaneous tissues and muscles. Thickened fascia and loss of color with cold skin are also seen. Stage 3 may last for months or becomes chronic. This stage is characterized by pronounced wasting of the muscles and subcutaneous tissue. The skin is atrophic and smooth-appearing contractures are frequent.

The scintigraphic pattern depends on the duration or stage of the disease [43, 114]. In the first or acute stage (20 weeks), all three phases of bone scan show increased activity (Fig. 6.32). After 20 and up to 60 weeks during the dystrophic phase, the first two phases are normalized, while the delayed-phase images show increased periarticular uptake. After 60 weeks (atrophic phase), the flow and blood pool images show decreased perfusion, with normal uptake on delayed images. In children with RSD, decreased perfusion and uptake are the most common manifestations (Table 6.10). A unilateral decrease in the metaphyseal band of activity may be the most striking feature.

Radiopharmaceuticals other than ^{99m}Tc-MDP have also been reported to have potential in the diagnosis. These include ^{99m}Tc-labeled human serum albumin [138], combined ^{13}N-ammonia and 6-[^{18}F]-fluorodopamine [139], ^{99m}Tc-sestamibi [140], ^{111}In-octreatides and ^{123}I-MIBG [141]. ^{13}N-ammonia radioactivity has been reported to be less in the affected side than in the unaffected side while the ^{18}F-FDG activity is symmetrical. Accordingly, the perfusion adjusted FDG activity is high in the affected side [139]. ^{123}I-MIBG on the other hand was found to be decreased in the affected side, reflecting the impaired sympathetic dysfunction with congruent reduction in perfusion [141].

Table 6.10. Scintigraphic patterns of reflex sympathetic dystrophy (modified from [43] with permission)

Pattern on bone scans	Flow on angiogram	Blood pool	Uptake in delayed images
Typical	Increased	Increased	Increased
Atypical RSD of children and adolescents	Decreased	Decreased	Increased
Paralysis, immobilization	Decreased	Decreased	Increased
Subacute	Normal	Normal	Increased
Late phase of RSD	Normal, decreased	Normal, decreased	Variable
Persistent use of painful limb	Decreased	Decreased	Decreased

Different modalities were used to treat CRPS I including oral or parenteral medications or sympathetic blocks and physical therapy with varying degrees of success, the main aim of the treatment being to restore the function of the affected limb. Bone scintigraphy can be used not only to help in the diagnosis but also to monitor the disease with treatment.

6.3.4 Fibrous Dysplasia

Fibrous dysplasia is a benign, developmental, noninherited condition. It is relatively common, although the etiology is not known. The condition may involve one bone (monostotic) or many bones (polyostotic) and results in enlargement and deformity of the involved bone. Pathologically it is characterized by slow, progressive replacement of the medullary cavity of bone by fibrocollagenous tissue containing poorly formed and randomly arranged trabeculae of woven bone, islands of cartilage, and cystic formations of varying size. The cytoplasm of osteogenic cells within the bone spicules and of the stellate and spindle-shaped cells in the stroma stains histochemically for alkaline phosphatase. A recent study using ^{11}C-methionine PET in two cases of fibrous dysplasia indicated the presence of viable tumor-like cells [142]. Elevated serum alkaline phosphatase levels have been observed in about one-third of patients, usually with the polyostotic form. Alkaline phosphatase is not a sensitive indicator of the disease but correlates with its extent and severity [43].

The lesions are monostotic in 70% – 80% of patients and polyostotic in up to 30% of cases [115]. Typically, multiphase bone scans show intense uptake (Fig. 6.33).

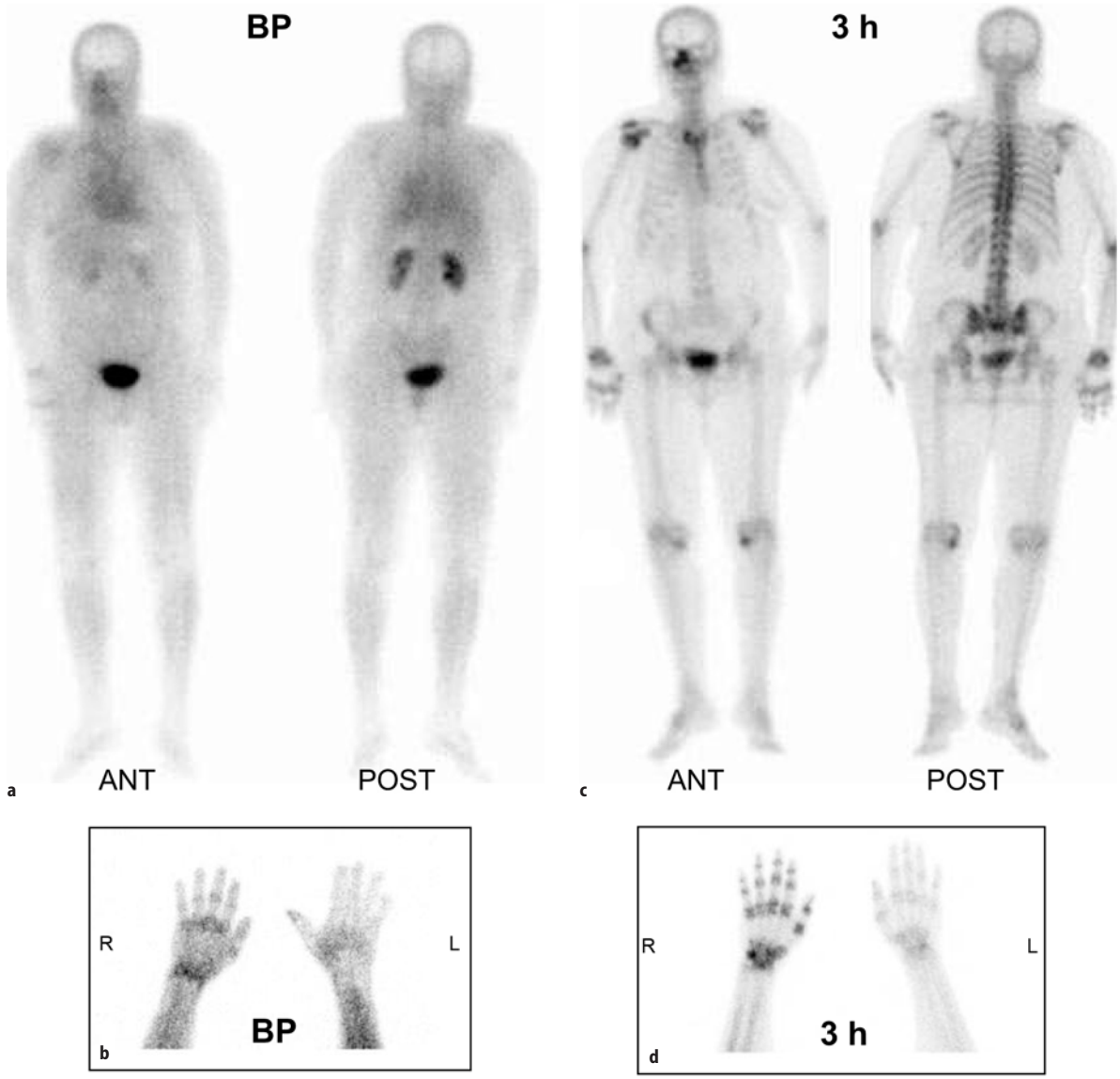

Fig. 6.32a–d. ^{99m}Tc-MDP whole body and spot images of a 40-year-old male with CRPS-1 (RSD) involving the right upper extremity. Whole body blood pool images (**a**) and blood pool spot image of the hands (**b**) show increased activity in the right shoulder wrist and hand. Delayed whole body and spot images (**c, d**) show periarticular increased uptake in the right shoulder, elbow, wrist and hand

However, rarely barely increased uptake probably due to concurrent bone infarct may be seen [143]. The condition may be associated with an endocrine abnormality (McCune-Albright syndrome), which includes precocious puberty and abnormal skin pigmentation in the form of café au lait spots [144].

6.3.5 Trauma

Trauma to the musculoskeletal system may affect bone, cartilage, muscles, and joints. To each of these structures, trauma may cause immediate damage and late changes.

6.3.5.1 Fractures

A fracture is defined as a break in the continuity of a bone. Fractures can be classified according to several features (Table 6.11). Based on the extent of the break, fractures are classified as complete or incomplete. A complete fracture breaks the bone all the way through, while with incomplete fracture the bone is broken but stays as one piece. Fractures are also classified as open (previously called compound) if the skin is broken and closed (previously called simple) when the skin at the site of fracture is not broken [145].

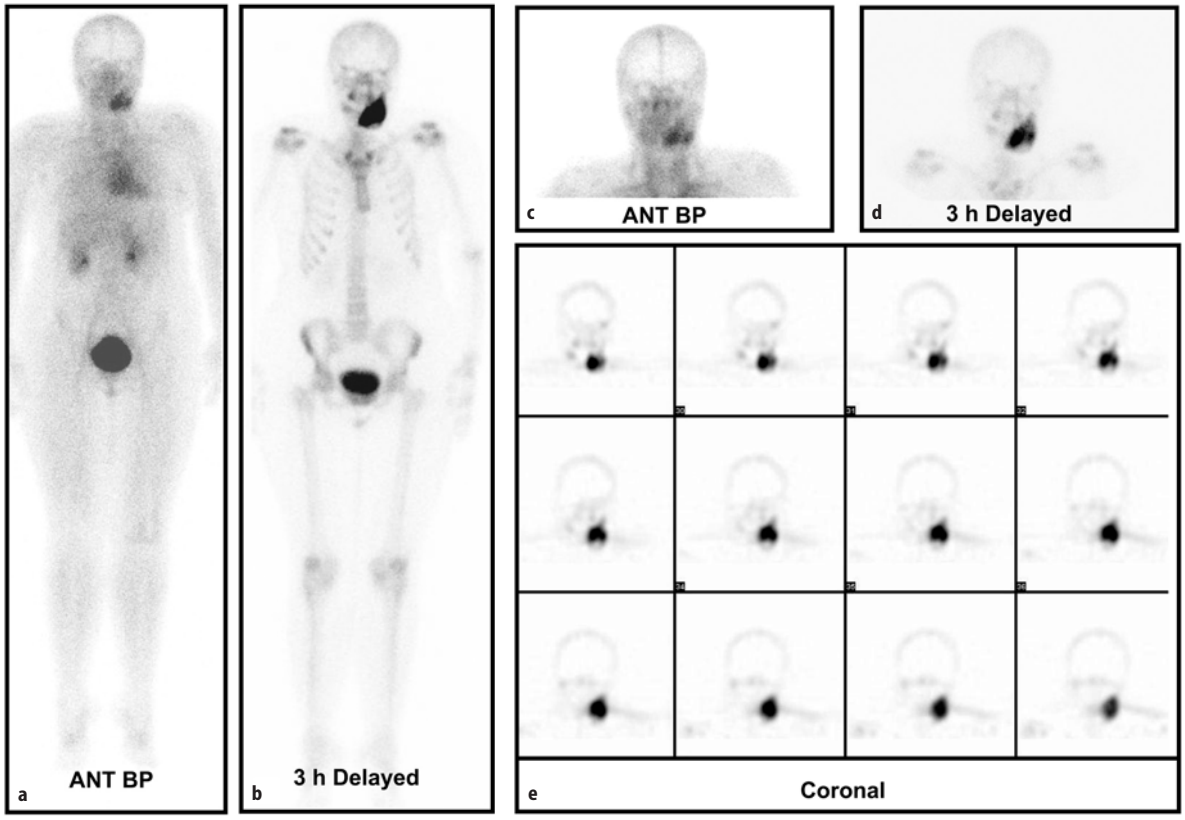

Fig. 6.33a–e. Whole body blood pool and delayed images, spot blood pool and 3-h images of the head and representative images of the SPECT study of the skull (**a–e**) show increased blood pool activity and intensely delayed uptake in the left mandible illustrating the scintigraphic pattern of fibrous dysplasia on multiphase bone scan

The fracture pattern depends on the mechanism of injury. Compression load produces a compaction or oblique fracture. Bending load has a tendency to produce a flat transverse fracture. However, bending load on one side is associated with compression on the other side, which may affect the pattern of the fracture. Torsional force tends to produce a spiral fracture.

Other classifications are based on the number of bone pieces, the direction of the fracture line, and other factors (Table 6.11). Pathological fractures occur at the sites of preexisting abnormalities that weaken bone. A minimal force that usually would not cause the fracture of a normal bone may produce a pathological fracture. A transchondral fracture (osteochondritis dissecans) represents fragmentation and separation of portions of cartilage or cartilage and bone. This type is most prevalent in adolescents and occurs typically in the head of the femur, ankle, kneecap, elbow, and wrist [145].

The role of scintigraphy in fracture diagnosis is limited to cases of radiologically occult fractures and fractures of the small bones of the hands and feet.

Stress Fractures. Stress fractures are due to repeated stress, each episode of which is less forceful than re-

Table 6.11. Classification of fractures

Based on extent of the break:
1. Complete: bone is broken all the way through
2. Incomplete: bone is still in one piece

Based on skin condition:
1. Open: broken skin
2. Closed: intact skin

Based on resulting number of bone fragments:
1. Comminuted: multiple bone fragments
2. Noncomminuted: only two fragments

Based on direction of fracture line:
1. Linear: line is parallel to the long axis of bone
2. Oblique: line is at oblique angle to the shaft of the bone
3. Spiral: line encircles the bone
4. Transverse: line is perpendicular to the long axis of bone

Based on cause of fracture:
1. Excessive force on normal nonviolated bone: classic traumatic fracture
2. Pathological fracture: break at the site of preexisting pathology
3. Stress fractures:
   - Fatigue fractures: Abnormal stresses applied to normal bones
   - Insufficiency fractures: Usual stresses to abnormal bones
4. Transchondral fracture (osteochondritis dissecans)

quired to fracture the bony cortex. The stress fracture is not as thought due to repeated traumatic microfractures. It is a focal area of increased bone turnover secondary to the repeated stress. The process starts with resorption cavities before being coupled to an osteoblastic response to replace the absorbed bone. The process of rarefaction is faster than the osteoblastic process and will progress if the individual continues with stressful activity and trauma. Complete fracture through the zone of rarefaction may occur.

If this occurs in normal bones, the resulting fractures are called fatigue fractures, while if they occur on abnormal bones, as in osteoporosis, they are termed insufficiency fractures. Fatigue fractures are common in athletes, military recruits, and dancers (Table 6.12). Bone scintigraphy is much more sensitive than standard radiographs in detecting stress fractures. If scintigraphy is performed in the acute phase of less than 4 weeks, the flow and blood pool images show increased activity. Later, only delayed uptake will be seen. The delayed uptake is typically focal or fusiform, involving less than one-fifth of the bone (Fig. 6.34). This is different from the pattern of a shin splint, which is another consequence of stress and occurs in the same patient population as fatigue fractures. Shin splints typically show normal flow and blood pool images, with an elongated linear pattern of increased uptake on delayed images. They are most commonly found in the tibiae and may coexist with fatigue fractures in the same patient. The pattern seen with shin splints is due to subperiosteal bone formation [146].

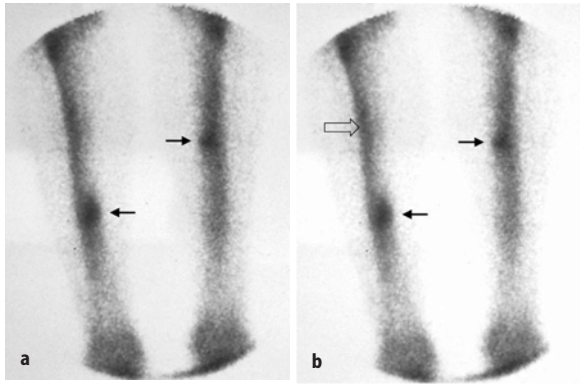

Fig. 6.34. Recent bilateral tibial stress (fatigue) fractures in an athletic young man. Note the typical focally increased uptake (*arrows*) at the site of fractures. Another example shows bilateral tibial stress (fatigue) fractures (*arrows*) with a linear pattern of increased uptake (*open arrow*) illustrating the scintigraphic pattern of shin splint

Spondylolysis. Spondylolysis is a condition in which there is a loss of continuity of bone of the neuroarch of the vertebra due to trauma, or more likely to stress. The gap or loss of continuity most commonly occurs at the junction of the lamina when the vertebra is viewed from above, or between the superior and inferior articular processes (pars interarticularis or facetal joints) when viewed from the side. This condition most frequently affects the fourth and fifth lumbar vertebra, may or may not be symptomatic, and usually does not result in any neurological deficit but is a common cause of low back pain, particularly in children and young adults. The diagnosis is principally radiological, and

Location	Activity or event
Sesamoids of metatarsal bones	Prolonged standing
Metatarsal shaft	Marching; stamping on ground; prolonged standing; ballet; postoperative bunionectomy
Navicular	Stamping on ground; marching; long-distance running
Calcaneus	Jumping; parachuting; prolonged standing; recent immobilization
Tibia: mid and distal shaft	Long-distance running
Proximal shaft (children)	Running
Fibula: distal shaft	Long-distance running
Fibula: proximal shaft	Jumping; parachuting
Patella	Hurdling
Femur: shaft	Ballet; long-distance running
Femur: neck	Ballet; marching; long-distance running; gymnastics
Pelvis: obturator ring	Stooping; bowling; gymnastics
Lumbar vertebra (pars interarticularis)	Ballet; lifting heavy objects; scrubbing floors
Lower cervical, upper thoracic spinous process	Clay shoveling
Ribs	Carrying heavy pack; golf; coughing
Clavicle	Postoperative radical neck
Coracoid of scapula	Trap shooting
Humerus: distal shaft	Throwing a ball
Ulna: coronoid	Pitching a ball
Ulna: shaft	Pitchfork work; propelling wheelchair
Hook of hamate	Holding golf club, tennis racquet, baseball bat

Table 6.12. Location of stress fracture by activity (from [147] with permission)

scintigraphy is reserved for detection of radiologically occult conditions and for assessing metabolic activity of the condition. Typically, a focal area of increased uptake is seen in the region of the pars interarticularis (Fig. 6.35). SPECT is much more sensitive than planar imaging in detecting the abnormality. The treatment of this condition is usually conservative, with the use of back support, and usually corrects the problem.

Spondylolysthesis is the forward or occasionally backward movement of one vertebra over another (Fig. 6.36a–c) which may result from fracture of the neuroarch. It is again most commonly seen in the fifth lumbar vertebra, in which there is a forward shift of L-5 on the sacrum. It is less commonly seen at L-4. In addition to parallel-hole high-resolution acquisition, pin hole and/or SPECT is needed, along with correlation with the plain radiographs of the lumber spine.

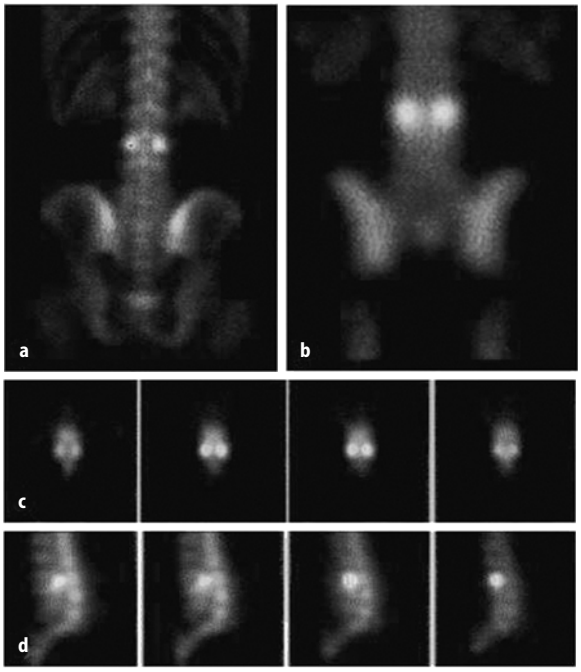

△

Fig. 6.35a–d. Planar (**a**), representative coronal cut (**b**), transaxial (**c**) and sagittal (**d**) cuts of SPECT study of a young male athlete complaining of low back pain. The study shows focally increased uptake in both sides of L-3 seen in both planar and SPECT images in a case of spondylolysis

6.3.5.2 Fracture Healing

Fracture union is simply defined as sufficient growth of bone across the fracture line. The healing process of a fracture is outlined as follows:

1. Formation of hematoma following the fracture event: When a fracture disrupts the periosteum and blood vessels in the cortex, marrow and the adjacent soft tissue, bleeding occurs and a hematoma forms between the bony fracture ends, beneath the periosteum and within the medullary cavity.
2. Invasion of granulation tissue into the hematoma: Necrosis of the bone tissue adjacent to the fracture takes place immediately. This necrotic tissue along with the effect of the traumatic force induces inflammatory response with features of acute nonspecific inflammation including vasodilatation, ex-

▽

Fig. 6.36. a Spondylolisthesis without spondylolysis. Degenerative anterior spondylolithesis. Apophyseal joint osteoarthritis allows the inferior articular processes to move anteriorly, producing forward subluxation of the superior vertebra on the inferior vertebra. **b** Spondylolisthesis without spondylolysis but with backward subluxation of the superior vertebra. **c** Spondylolisthesis with spondylolysis. The bilateral defects through the pars interarticularis allow anterior displacement of vertebral body on its neighbor but the alignment of the apophyseal joints is normal. (Adapted from Resnick [117])

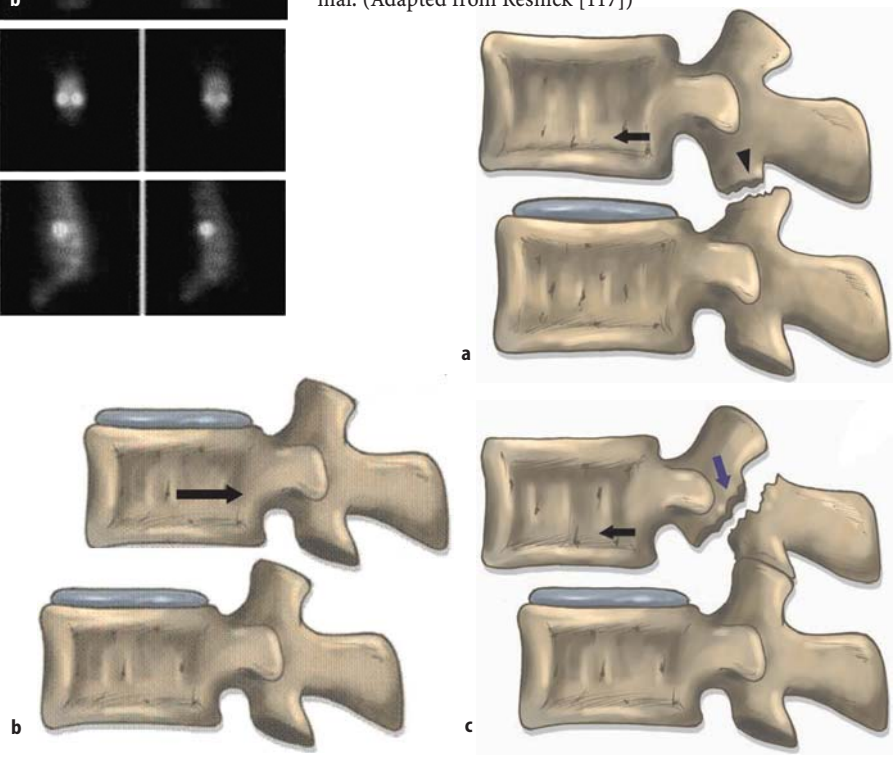

travasation of plasma and leukocytes and infiltration with leukocytes. Within 48 h, blood flow to the entire bone increases with organization of the hematoma around the broken ends of bone into a fibrous network.
3. Procallus is formed along the outer surface of the shaft and over the broken ends of bone by the bone forming cells in the periosteum, endosteum and marrow.
4. Callus starts to form with synthesis of collagen and matrix by osteoblasts. Mineralization with calcium deposition follows to complete the formation of callus (woven bone).
5. Remodeling: The unnecessary callus is resorbed as the process of healing continues, trabeculae are formed, and remodeling leads to alignment of the cortical bony margins and marrow cavity. Bone accordingly heals by forming new tissue rather than scar tissue.
6. Modeling: reshaping of cortex.

Several factors affect the fracture healing and if disturbances occur, delayed, non- or malunion could result (Table 6.13). *Delayed union* indicates that union does not occur at the expected time, which is difficult to determine objectively and varies with the site of fracture although overall it is usually 3–4 months after the fracture. *Nonunion* indicates failure of the bone ends to grow together. Instead of new bone, dense fibrous tissue, or uncommonly fibrocartilaginous tissue, fills the gap between the broken ends. Necrotic tissue is not seen unless infection is present in the area of nonunion. Delayed and nonunion are commonly seen in tibia, fibula and scaphoid bones. Less common sites are humerus, radius, ulna, and clavicle [9]. Occasionally, the gap between the bone ends contains a space filled with fluid. In this case, the term false joint or *pseudoarthrosis* is applied and persistent uptake of ^{99m}Tc-MDP continues to be seen after the usual period of healing or postoperative changes. The fracture is considered nonunited after 6 months although in certain locations such as in the case of cantral fracture of the femoral neck it is considered nonunited after only 3 months. Nonunion is classified predominantly according to the radiologic appearance into hypervascular (hypertrophic) and avascular (atrophic) and is based on the capability of biologic reaction. Hypertrophic nonunion is rich in callus as seen on standard radiographs and has a rich blood supply in the ends of the fragments with the potential to heal under the correct stable environment [147]. Atrophic nonunion, on the other hand, is considered relatively avascular at the ends of the fragments, acellular and inert and consequently lacks the ability to heal under the correct and stable environment [147]. This type is typically seen in tibial fractures treated by plate and screws. Both types contain fibrous tissue, hyaline cartilage, fibrocartilage and areas of bone formation. However, the amount and type of bone formation differ between the two types. As expected, the hypertrophic type contains more areas of new bone, which ossifies by both endochondral and intramembranous ossification. Atrophic nonunion on the other hand has only few areas of bone formation, which forms predominantly by endochondral ossification [147]. Radiographs show most of these changes but do not reflect the biologic changes that were recently studied by Reed and associates [147], who found that hypertrophic nonunion shows increased apoptosis or programmed cell death in both types. *Malunion* describes healing of a bone in a nonanatomic orientation.

Table 6.13. Factors affecting fracture healing

1. Patient age: Non-union is rare in children unless there is other condition present as neurofibromatosis, infection, or extensive soft tissue damage
2. Weight bearing: stimulates healing of fractures
3. Fixation: Stimulates union but does not accelerate repair itself
4. Nerve damage: Is associated with rapid union with unknown mechanism
5. Damage of intramedullary canal and nailing: this may lead to delayed repair or to extensive reactive osteogenic activity
6. Blood supply: interrupted blood supply may cause delayed healing
7. Infection: May lead to delayed healing
8. Excessive use of steroids can cause delayed healing
9. Extent of fracture: severely displaced fractures, open fractures, loss of fragments and extensive soft tissue damage cause delayed healing

Scintigraphy plays no role in the diagnosis and management of most fractures. Exceptions include occult fractures of the small bones of the hands and feet, fractures of abused children [148], and delayed union or nonunion of fractures. Bone scintigraphy often is used to detect stress fractures and can also play a role in the follow-up of these injuries, as noted above. Scintigraphy also has a role in assessing the healing of fractures and bone grafts.

6.3.5.3 Trauma to Bone-Adjacent Structures

Skeletal muscle damage in variable degrees is common with fractures. The incidence of sepsis and other fracture-related complications is significantly influenced by the severity of muscle and soft tissue damage. The classical criteria for assessing skeletal muscle damage – color, consistency, bleeding, and contractility – are subjective. Research on animals and humans shows the feasibility of more accurate objective methods to assess

skeletal muscle damage using radionuclide imaging techniques. Since muscle injury causes release of the muscle protein myosin from the injured cells, ^{111}In-labeled anti-myosin antibodies can be used to detect and assess the extent of skeletal muscle damage [149, 150].

Tears to tendons are called sprains, while ligament tears are called strains. These injuries usually do not cause abnormal uptake on bone scintigraphy. On the other hand, complete separation of tendons or ligaments from their attachments are called avulsions, and these do cause abnormal uptake on bone scans.

6.3.6 Growth Plate Injury

The physis, or growth plate, is recognized as the site of endochondral ossification and is responsible for a bone's growth in length. Although the band of increased uptake seen on scintigraphic bone images is referred to as the growth plate, it actually does not correspond to the lucent band present on a bone radiograph that is also referred to as the growth plate. The radionuclide growth plate corresponds to the dense band of bone in the metaphysis adjacent to the radiographic growth plate and is described in radiographic anatomy as the zone of provisional calcification. Physiological status of the growth plate is difficult to evaluate using morphologic imaging. Scintigraphic imaging complements anatomic studies by reflecting the physiological status of the growth plate (Fig. 6.37) and has the advantage of quantitation. It can also detect the abnormalities earlier than morphologic modalities and can help particularly in detecting segmental growth plate arrests that are difficult to determine by these modalities [151–153]. Two- or three-phase imaging is recom-

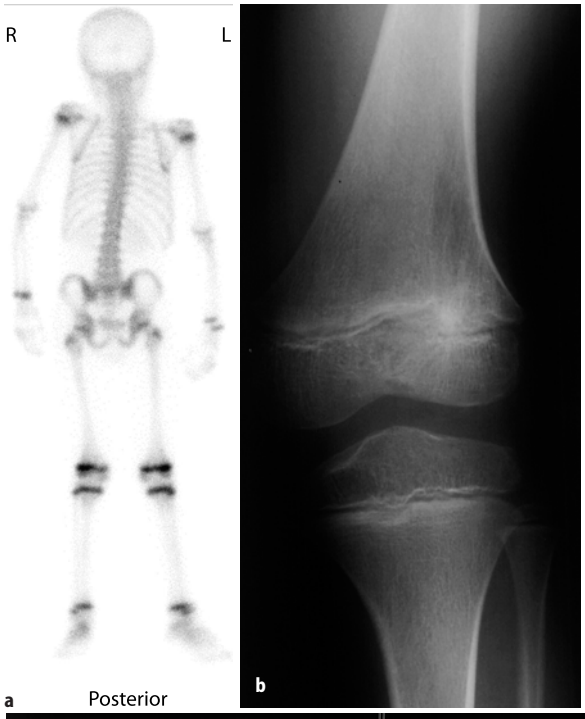

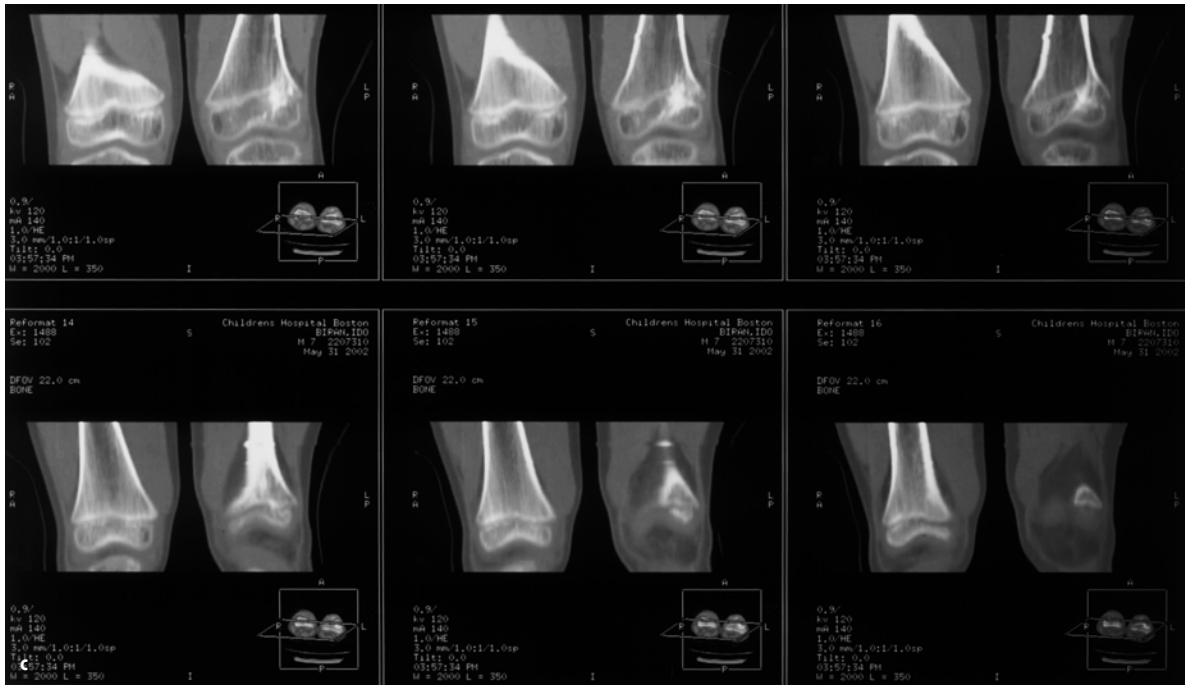

Fig. 6.37a–c. Growth plate injury. Whole body anterior (**a**) and posterior bone scan of a 4-year-old boy with pain in his left knee. The scan shows increased uptake in the lateral aspect of the left distal femoral growth plate. Standard radiograph (**c**) and MRI images of the same patient illustrating the same injury

mended in growth plate evaluation. Both flow and blood pool images show information on plate activity. They often show differences in plate function more clearly than the delayed images [154]. The normal physis scintigraphic appearance of the growth plate changes with age. In the infant and young child the physis has a thicker, oval-shaped appearance. With maturation it becomes linear, and in adolescence the closing physis shows progressively decreasing activity. Growth plates in different areas of the skeleton close at different times. Based on quantitative data in normal children, greater activity presents in the medial half of the distal femoral growth plate than the lateral half, while in the proximal tibial growth plate, the lateral half shows more activity than the medial half [155]. Skeletal maturation occurs earlier in females than in males. In addition to conditions, such as trauma and infection, which directly affect the physis, the plate can be influenced by mechanical stresses such as differential weight bearing and conditions producing regional hyperemia. Rheumatoid arthritis, chronic synovitis, and lesions such as fibrous dysplasia can accelerate closure or a growth plate located in the involved region.

Injury to the physis or growth plate in children may lead to growth arrest and/or angular deformities in the limbs. Segmental closure can be better identified using the pinhole view and quantitation [154, 155]. In addition to asymmetric and segmental differences in uptake, blurred growth plate appearance can also be seen with adjacent epiphyseal and/or metaphyseal injuries [154]. These findings are not permanent as shown by Etchebehere et al. [156], who studied 18 children with uncomplicated femoral fractures by multiphase bone scintigraphy at three different time intervals (2 – 5 months, 6 – 12 months and 18 – 24 months). Visual analysis of the blood flow, equilibrium and delayed images showed increased activity in the distal femoral growth plates during the first and second time intervals, but not during the third [156]. Scintigraphy is considered the only imaging modality capable of assessing the magnitude of physeal stimulus caused by femoral fractures and of predicting a favorable or unfavorable outcome of leg length by semiquantitative analysis. SPECT imaging was found useful to detect and locate decreased metabolism associated with post-traumatic closure of the physeal plate, which predicts growth arrest and deformities [151, 155, 157]. However, pinhole magnification imaging is superior to SPECT and is the preferred method of imaging [153 – 155].

Stress factors and mechanical loading influence the scintigraphic uptake at the growth plate. For example, when an extremity is placed at rest, as with prolonged immobilization, activity in the growth plate decreases in comparison with the contralateral weight-bearing extremity. This can occur also in ambulatory patients with a gait disturbance, which results in differential weight bearing. On the other hand, increased growth plate uptake can occur on a regional basis in response to trauma, infection, and any condition that relates to increased metabolic activity in the skeleton. Systemic and metabolic diseases can result in a generalized increase in growth plate uptake throughout the skeleton. Trauma and infection may result in uniform increased activity in the plate or segmental abnormal uptake. Fractures and slipped capital femoral epiphysis result in uniformly increased plate activity at the involved location. Segmental increase and decrease in a growth plate is of particular importance, since it is associated with the development of angular deformities. In insults such as trauma and infection directly involving the growth plate or if such injury occurs near the plate, the segmental abnormal uptake will be seen and deformity may follow. A fracture in the metaphysis of a long bone can, for example, provoke angular deformity by stimulating an adjacent growth plate. Harcke described the increased growth plate activity with metabolic bone disease and documented a return to normal after successful treatment. Such injuries, particularly fractures, may cause permanent closure of segments of growth plates [158]. Partial arrest of the growth plate occurs when an osseous or cartilaginous bridge forms across the plate. If this occurs laterally, the relative accelerated activity of the medial growth plate will result in valgus deformity, while if the bar is located in the medial side and normal physis continues to grow laterally, it will cause varus deformity [159]. These angular deformities could also occur secondary to contiguous chronic hyperemia of a metaphysis or epiphysis such as after a fracture to these locations which stimulates the activity of the adjacent part of the physis, resulting in unequal growth with subsequent deformity [160]. Computed tomography and magnetic resonance imaging are accurate in identifying segmental closure [161].

6.3.7 Metabolic Bone Diseases

The osseous bone response to injury, regardless of the type, is characterized by increased remodeling and new bone formation in an attempt to repair the damage or to contain the noxious insult. This process is evidenced by focal increased uptake of bone-seeking agents. In contrast, in metabolic bone disease, a general imbalance of the processes of bone formation and resorption is present. The net effect resulting from these two processes determines the scintigraphic patterns observed in metabolic bone disease.

Metabolic bone disease, however, is usually linked to alterations of the calcium metabolism by one or more

of a number of physiologic factors [43]. Increased rates of bone turnover are present in most metabolic bone disorders often associated with decreasing calcium content of the affected bone. This explains why most metabolic disorders result in generalized increased radiopharmaceutical uptake on bone scintigraphs, reflecting this increased bone turnover.

The regulation of calcium and bone metabolism is multifactorial and complex. Parathyroid hormone (PTH) plays an important role in these mechanisms by acting on two major target organs, bone and kidney. Its effects on the kidney are closely related to those of vitamin D. The two main actions are (1) to increase resorption of calcium and magnesium, and (2) to decrease phosphate reabsorption. The effect of PTH on bone is also modulated by vitamin D and is mainly to promote efflux of calcium from bone, acting through osteoclasts [162].

In some disorders, however, abnormal bone formation has a more localized character as is the case in hypertrophic osteoarthropathy, the pathogenesis of which is still poorly understood, although neurovascular abnormalities may be present.

6.3.7.1 Paget's Disease (Osteitis Deformans)

Paget's disease of bone is common in temperate areas, where the prevalence is estimated to be 3% – 4% among individuals over the age of 55 years and 10% among those above 80 years of age. It is uncommon among persons under the age of 55 and in areas with warm weather such as the Middle East. The disease is asymptomatic in 90% of affected subjects.

The etiology of Paget's disease is not known; viral infection has been suggested, although direct recovery of a virus has not been made. It was proposed that a slow virus is the causative agent. It is postulated that the primary residence of the virus is the osteoblast, while the osteoclast represents a site of viral assembly. The infected osteoblasts produce excessive interleukin-6, which stimulates bone resorption and activates c-*fos* proto-oncogenes, which interfere with normal bone development.

The skeletal distribution of Paget's disease suggests that the disease predominates in bones containing red marrow and may be dependent on the blood supply. Normal hematopoietic bone marrow may be replaced by loose fibrous connective tissue. With time, the increased osteoblastic and osteoclastic activity ceases, marrow abnormalities return to normal, and the affected bones become sclerotic [130].

The disease simply represents a state of increased metabolic activity in bone with abnormal and excessive bone resorption and formation. The chronic acceleration of remodeling may lead to enlargement and softening of the bones affected.

Paget's disease begins with active and excessive resorption (resorption or lytic phase), which may progress rapidly and results in softening of bone. Pathological fractures frequently occur, particularly of the femur and tibia. In this phase the bone trabeculae are slender and very vascular. Giant osteoclasts are present and have been shown to take up ^{67}Ga [163]. This is followed by a mixed phase characterized by accelerated formation as well as resorption of bone. If bone formation predominates, this can be called the osteoblastic phase and the term mixed can be reserved for those with approximately equal resorption and formation. The final phase (the sclerotic or burned-out phase) is characterized predominantly by new bone formation, more disorganized structure, thick trabeculae, and less prominent vascular sinusoids [164].

The morphology of the resorptive phase of Paget's disease is characterized by the presence of increased numbers of large multinucleated osteoclasts that may assume bizarre shapes and contain as many as 100 nuclei; normal osteoclasts have 5 to 10 nuclei (Fig. 6.38a,b). In the mixed phase, a profusion of osteoblasts and osteoclasts, evidence of high bone turnover, coexist in a matrix of highly vascularized fibrous tissue. This may facilitate the development of microfractures in long bones and basilar invagination when the base of the skull is diffusely involved. The late sclerotic phase is characterized by a disordered mosaic pattern of thickened lamellae containing irregular patterns of cement lines where waves of bone formation have succeeded in areas of previous bone resorption.

Although Paget's disease is diagnosed economically with standard radiographs, other modalities are needed, particularly scintigraphy, given the limitations of the standard radiographs. The early radiologic lesions of Paget's disease reflect severe localized osteolysis. These are typically "flame-shaped" or inverted "V" lesions that most commonly occur proximal to the distal epiphysis of a long bone and that gradually progress to the opposite end of the bone. Osteoporosis circumscripta is the term applied to osteolytic lesions in the skull. In the vertebrae, osteolytic lesions may simulate malignancy. As the disease evolves, the ingrowth of fibrovascular tissue "mixed stage" and a high rate of bone remodeling may lead to deformity of the skull, enlarged dense vertebral bodies, and slowly progressive deformities of weight bearing bones. Microfractures may occur on the convex side of the femur or tibia, increasing the degree of deformity and leading to the transverse or "banana" fracture that is typical of Paget's disease. Pelvic involvement may be limited to the ilia and pubic rami, but it may involve the acetabulum or both the acetabulum and the femur. It should be noted that radiologically the pagetic process may be seen to involve subchondral bone but not to cross the joint space. In addition, Paget's patients are also susceptible

to the development of inflammatory arthritis: gouty arthritis, rheumatoid arthritis, psoriatic arthritis, and ankylosing spondylitis have each been reported in association with Paget's disease. However, it is osteoarthritis that most often is the most common source of chronic joint pain and limited mobility.

MRI imaging can demonstrate the presence and extent of several characteristic disease complications, including basilar impression, spinal stenosis, and secondary neoplasm [165]. MRI can also add diagnostic value to other imaging modalities used for the diagnosis of Paget's disease including radiographs, computed tomography, and bone scintigraphy, by demonstrating marrow changes when present, and can contribute to a noninvasive diagnosis of Paget's disease in atypical presentations [166].

Although bone densitometry studies have little to do with the diagnosis of Paget's disease, the bone density pattern should be known to avoid misinterpretation of density data. Although bone density may be increased in bone that is affected by Paget's disease, density in noninvolved bones is unaffected. High density values may alert to the possibility of Paget's disease, especially if the value deviates from the expected normal sequence in lumbar vertebrae. Osteoporotic vertebrae may be overlooked if the average value of bone mineral

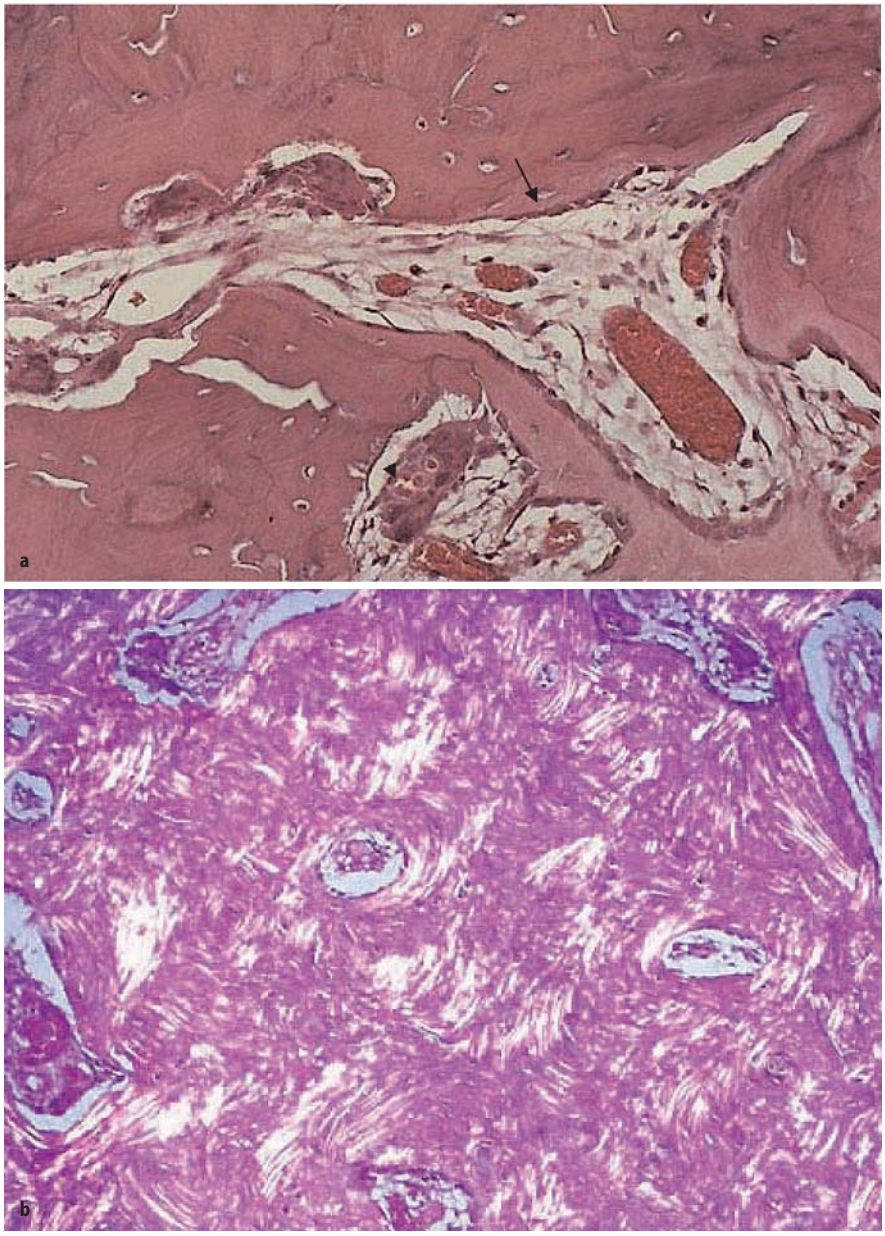

Fig. 6.38. a A microscopic picture of mixed osteoblastic-osteoclastic stage of Paget's disease. A line of osteoblasts is present at the *center right* forming new bone (*arrow*), and lacunae containing multinucleate osteoclasts are seen at the *center left* and *lower center* (*arrowhead*). The result is a patchwork mosaic of bone without an even lamellar structure. This phase is preceded by a predominantly lytic phase and is followed by a "burnt out" sclerotic phase. **b** Under polarized light, the irregularities of the bony lamellae are apparent

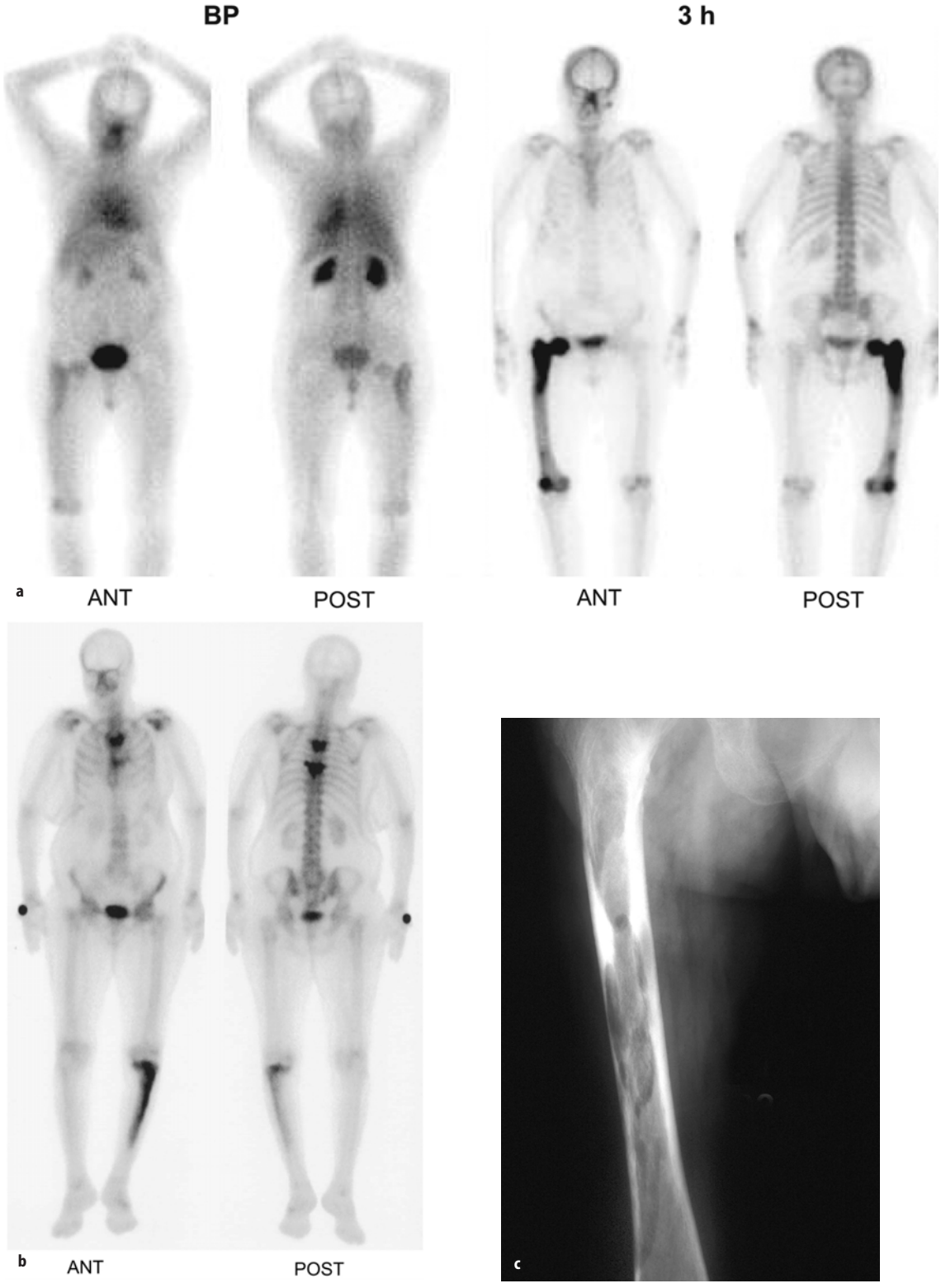

Fig. 6.39. a Seventy-six-year-old female with lytic lesion in the right tibia. Monostotic Paget's disease. Diffusely increased blood pool activity in the right tibia is more obvious proximally with corresponding increased delayed uptake. The increased uptake involves the entire tibia but with grades of uptake from mild to intense representing uptake patterns in early active phase and later phases. **b** demonstrates a polystotic type of the disease affecting more than one location (thoracic spine and left tibia). **c** Radiograph of a femur affected with Paget's disease demonstrating the typical osteolytic pattern (flame-shaped) of the disease

density is taken in the lumbar spine without reviewing each vertebra [167]. On multiphase bone scan, dynamic flow and early static images show varying degrees of hyperemia at the sites of involvement depending on the stage of the disease; the earlier the phase the more the hyperemia. On delayed static images, Paget's disease appearance depends on the stage of the disease. During the active lytic phase, involvement of Paget's disease is characteristically seen as intense increased uptake which is uniformly distributed throughout the region affected (Fig. 6.39a–c). An exception to this characteristic pattern of the early phase is the skull pagetic lesion, which shows intense uptake at the periphery of the lesion, while the center is cold, which is referred to as osteoporosis circumscepta [168]. With time, the disease activity gradually decreases towards the sclerotic phase and uptake of the bone imaging agents decrease as well. With time the sclerotic phase may show practically no abnormal uptake of the radiopharmaceuticals and hence the disease can be detected by X-ray and missed by bone scanning. This is in contrast to the early lytic phase when bone scan is much more sensitive than radiographs. The bone scan will identify approximately 15% – 30% of lesions not visualized on X-rays [168, 169]. An advantage of bone scan could be contributing partly to this, which is its ability to detect abnormalities in bones that are difficult to explore by radiographs such as sternum, ribs and scapula [170]. Conversely, in about 5% of cases, the radiograph may demonstrate diffuse pagetic involvement, for example, of the pelvis, whereas the bone scan reveals little uptake of the isotope. In this circumstance, the alkaline phosphatase level may be normal or only slightly elevated, reflecting lesions that are sclerotic, relatively inactive, or "burned out". Affected bones may also appear increased in size but with preservation of the normal configuration. The transition between the affected bone and adjacent normal bone is characteristically narrow during this active phase. Renier and Audran reported in a large series of 200 patients with Paget's disease, 169 (85%) with polyostotic involvement, with data suggesting that the disease process spreads across a joint in some patients. The authors reported several cases with extensive pagetic lesion seen on one side of a joint and a considerably smaller lesion on the other side. The study also found that Paget's disease may involve paired bones and involvement could be symmetrical [171].

The disease is often nonuniform within the skeleton. Individual involved bones can simultaneously present more than one stage of the disease process, reflecting variations of the duration of the disease at different sites.

Paget's disease may show absent and expanded bone marrow uptake or a mixture of both. This can be explained by the presence of areas of advanced, sclerotic disease with active bone marrow and areas of earlier active disease with replaced bone marrow. Since ^{111}In-WBCs are taken up by hematopoietic bone marrow, uptake is therefore seen in areas of Paget's disease with active marrow. This can mimic the uptake in infection, particularly when it is focal [105].

6.3.7.2 Osteoporosis

Bone mass gradually increases during childhood and increases rapidly once the skeleton approaches maturity and longitudinal skeletal growth slows [172] till it reaches the peak bone mass in the 2nd decade, although this is somewhat controversial [173]. At maturity, black men have a denser skeleton than white men and black women (Fig. 6.40), whereas white women have the least dense bones [174]. Generally men have on average 20% greater peak bone mass than women [175]. Peak bone mass appears to be a major factor in determination of the risk of developing osteoporosis.

After reaching its peak, bone mass begins to decrease at a rate of 0.25% – 1% per year. Men demonstrate a gradual rate of bone loss that persists throughout the remainder of adult life. Women on the other hand undergo a rapid rate of bone loss in the perimenopausal and postmenopausal periods [176]. Loss of trabecular bone exceeds that of compact bone. Some investigators have determined that 50% of trabecular bone and 30% of compact bone will eventually be lost [176]. Generally lifetime bone losses for men are 20% – 30% while some women may lose 50% or more [174]. In the postmenopausal period, women show a normal age related annual bone loss of 1% – 2% in appendicular bone and about 4% – 6%, or even 8%, in the spinal trabecular bone [177, 178]. The factors related to bone loss in the perimenopausal and postmenopausal

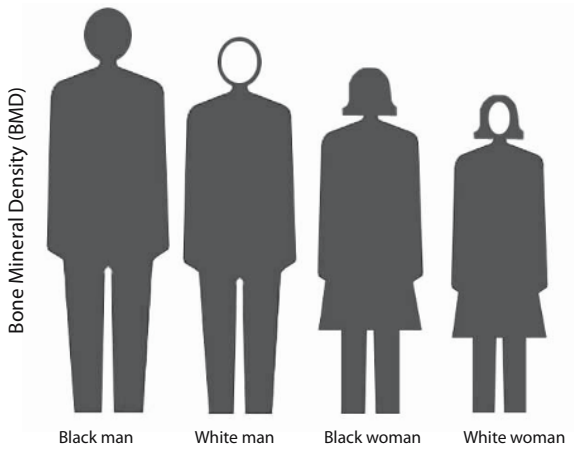

Fig. 6.40. Histogram illustrating the peak BMD among men and women. Note that white women have the lowest value

periods include age related factors, estrogen deficiency, calcium deficiency and other factors such as physical activity, smoking, alcohol consumption and medications.

Remodeling has a crucial role in maintaining the integrity of normal bone and altering the bone architecture in response to stress. Trabecular bone is remodeled more rapidly than cortical bone [174]. Trabecular bone has a turnover rate approximately 4–8 times as high as that of compact bone and is highly responsive to metabolic stimuli [176, 179]. This high turnover rate in trabecular bone makes it a primary site for detecting early bone loss and for monitoring the response to interventions [180].

Osteoporosis is the most common metabolic disorder of the skeletal system. It affects approximately 20 million older Americans, 90% of whom are postmenopausal [181]. Osteoporosis is "a condition in which bone tissue is reduced in amount increasing the likelihood of a fracture" [182, 183]. In other words the bone is qualitatively normal but quantitatively abnormal.

Osteoporosis is characterized by abnormal reduction in bone density and hence a decrease in the amount of calcified bone mass per unit volume of skeletal tissue. The basic mechanism behind this condition is decreased bone formation (osteoid formation), even though calcium deposition may be normal. The disease develops when the process of bone resorption and formation (remodeling cycle) is disrupted, leading to an imbalance. The complete remodeling cycle that consists of activation of basic multicellular units, bone resorption, and bone formation normally takes about 4 months in adults. In patients with osteoporosis this remodeling cycle may require up to 2 years. This can be attributed to an increase in the number of activated basic multicellular units, leading to resorption at more sites, increased rate of resorption, increased frequency of activation of basic multicellular units, and delay in bone formation. Osteoporosis also occurs when the numbers of osteoblasts and osteoclasts in bone are inadequate.

There are numerous causes of osteoporosis, many of which are metabolic in nature (Table 6.15). Types of osteoporosis not considered metabolic in nature include juvenile osteoporosis, which affects younger individuals and is idiopathic rather than metabolic. The disease may be generalized, involving the major portions of the axial skeleton, or regional, in one segment of the appendicular skeleton. Both compact and spongy bones are lost, but loss of spongy bone exceeds that of compact bone.

Senile osteoporosis, which is the most common type, often produces increased susceptibility to fractures in old age. Since men have greater peak bone mass than women, men are affected by senile osteoporosis later in life. It is estimated that women lose about 50% of their spongy bones while men lose 25% when affected by the disease. Postmenopausal osteoporosis is also common; deficiency of estrogen leads to decreased bone formation. Estrogen is necessary to stimulate production of new osteoblasts, which otherwise fail to lay down sufficient bone matrix. Prolonged use of steroids or steroid overproduction, as in Cushing's syndrome, may cause osteoporosis. This hormone increases the ability of the body to resorb bone [184]. Smoking lowers circulating estrogen levels in premenopausal women and accelerates the onset of menopause and these are risk factors for osteoporosis. Smoking is also a risk factor for osteoporosis in men. Osteoporosis has also been reported to be prevalent among patients with liver cirrhosis. In one study, the prevalence of spinal osteoporosis was 20% in cirrhotic patients compared with 10% in controls [185].

Since the condition results in brittle or porous bone, patients suffer more than normal from fractures. Compression fractures of the spine, distal radius, and femo-

Table 6.14. Etiology and classification of osteoporosis

Primary
1. Involutional
Type I: postmenopausal
Type II: age related (senile)
2. Idiopathic
Juvenile
Adult
Secondary
1. Prolonged immobilization
2. Steroid therapy
3. Diabetes mellitus
4. Prolonged heparin administration
5. Sickle cell disease
6. Cushing's syndrome
7. Rheumatoid arthritis
8. Scurvy
9. Multiple myeloma
10. Osteogenesis imperfecta (brittle bone disease)
11. Disuse or immobilization of a limb (regional osteoporosis)

Table 6.15. Risk factors for primary involutional osteoporosis

1. Sex (female)
2. Age, advancing
3. Positive family history
4. Race, Caucasian or Asian
5. Slender body habitus
6. Early or surgical menopause
7. Late menarche
8. Calcium deficiency
9. Alcohol, smoking, caffeine
10. Medications: steroids, heparin, thyroid hormones, anticonvulsants
11. Sedentary lifestyle
12. Hypogonadism in men
13. Anorexia nervosa
14. Hyperparathyroidism
15. Hyperthyroidism
16. Primary or secondary amenorrhea

ral neck are more common in the presence of osteoporosis. Repeated and multiple vertebral fractures, commonly in the thoracic spine, may lead to kyphosis and other spinal deformities [184, 186, 187]. Fractures of ribs, sternum, pelvis and feet are also common in osteoporotic patients.

Regional and transient osteoporosis occurs in a segment of the appendicular skeleton when there is disuse or immobilization of a limb, such as would happen with paralysis or healing of a fracture in a cast. Osteoporosis usually appears after about 8 weeks of immobilization but can develop earlier in individuals younger than 20 or older than 50 years.

Osteoporosis sometimes is obvious on plain radiographs. Quantification of bone density from plain radiographs is difficult and inaccurate. Dual-photon absorptiometry, X-ray absorptiometry, and computed tomography scans are all used to measure bone mineral density and evaluate osteoporosis. The goal of treatment is to slow down the rate of calcium and bone loss and to avoid the complications that can be disabling and life threatening.

Bone densitometers measure the radiation absorption by the skeleton to determine bone mass of the peripheral, axial, and total skeleton. Common techniques include single-photon absorptiometry (SPA) of the forearm and heel, dual-photon (DPA) and dual-energy X-ray absorptiometry (DXA) of the spine and hip, quantitative computed tomography (QCT) of the spine or forearm, and radiographic absorptiometry (RA) of the hand. Although osteoporosis sometimes is obvious on plain radiographs, quantification of bone density from plain radiographs is difficult and inaccurate. Quantitative bone densitometry is now well established in clinical practice. DXA, however, is the most widely used technique and is considered the gold standard method for the measurement of bone mineral density (BMD). It has the advantages of good precision, short scan times and stable calibration.

Bone loss measurement is performed by various methods of densitometry. Densitometry is used to: (1) assess patients with a high risk for metabolic bone disease and estimate the status and severity of osteoporotic bone loss in perimenopausal women, (2) estimate fracture risk for the spine, hip and wrist and (3) monitor the effectiveness of treatment. The goal of the treatment is to slow down the rate of calcium and bone loss and avoid the complications that can be life threatening.

A measurement of hip BMD has been shown to be the most reliable in the risk of hip fracture [188, 189], while the spine is considered the optimum site for monitoring response to therapy [190] because vertebrae are rich in the metabolically active trabecular bone. The radiation dose to the patient from a DXA scan is very low (1 – 10 μSv) [191], which is comparable to the average daily radiation dose of 7 μSv from natural background. For the interpretation of DXA, T-score and, to a lesser extent, Z-score are used. T-score relates the individual's density to that of young healthy adults and Z-score relates to that of the same age group. T-score is calculated by determining the difference between a patient's measured BMD and the mean BMD of healthy young adults, matched for gender and ethnic group, and expressing the difference relative to the young adult population SD.

Based on the T-score values, the WHO has defined osteoporosis and osteopenia [192]. An individual with a T-score = –2.5 or below at the spine, hip or forearm is classified as having osteoporosis, a T-score between –2.5 and –1 is classified as osteopenia, while a T-score = –1 or higher is regarded as normal (Figs. 6.41, 6.42).

Instead of comparing the patient's BMD with the young adult mean, the Z-score compares the bone density of the individual with the mean BMD expected for the patient's peers (age matched). Although Z-score is not as widely used as T-score, it remains a useful concept since it expresses the patient's risk of having an osteoporotic fracture relative to their peers. It is estimated that for every reduction of 1 SD in BMD the likelihood of fracture increases by 1.5 – 2.5. Accordingly, patients with a Z-score –1 are at a substantially increased risk of fracture compared to their peers with a Z-score = 0. Presenting bone density results using T- and Z-scores is advantageous since it avoids the confusion present when using the actual BMD values that differ between different items of equipment [193].

6.3.7.3 Osteomalacia and Rickets

Osteomalacia is due to abnormal mineralization of bone, predominantly as a result of vitamin-D deficiency, with a decrease in bone density secondary to lack of both calcium and phosphorus. Note that in osteomalacia the amount of osteoid (bone formation) is normal, while osteoid is decreased in osteoporosis. In other words, there is inadequate and delayed mineralization of osteoid in spongy and compact bones, which have a normal remodeling cycle as opposed to delayed cycles in osteoporosis. Simply put, in osteomalacia the osteoid tissue is normal in amount but soft since it lacks calcium, while in osteoporosis there is a lack of osteoid tissue as a whole.

If osteomalacia occurs in growing bones prior to closure of the growth plate, it is called infantile osteomalacia, or rickets. Growing bones fail to mineralize and become soft, with resultant deformities. Growth plates and metaphysis are disorganized in patients with rickets, with a decrease in the length and width of the growth plates. Nutritional (vitamin D deficiency) rickets is now a rarity in the industrial world because of food fortification. Most cases result from hereditary in-

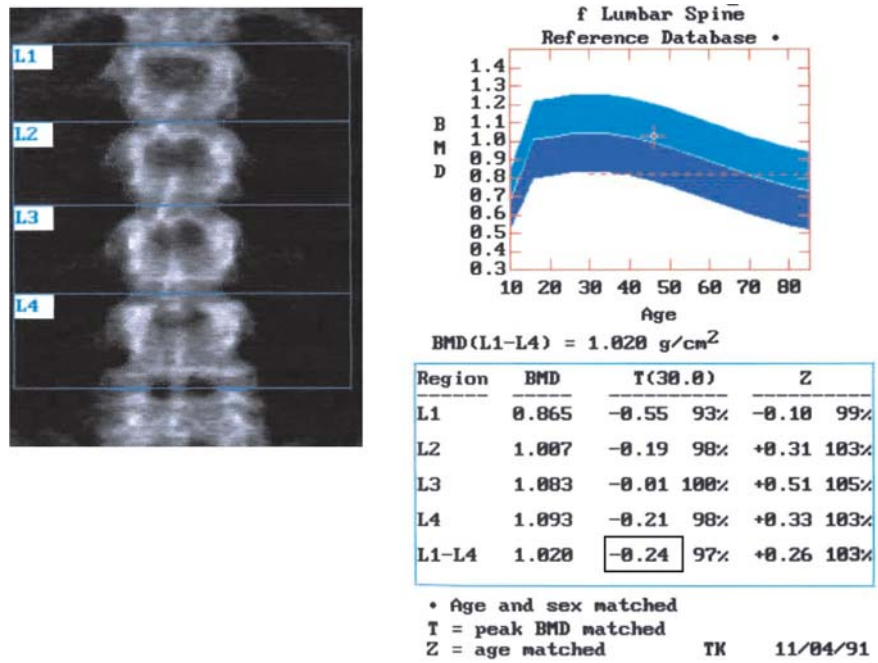

Fig. 6.41. A bone densitometry study with normal T-scores of ≥ 1 SD

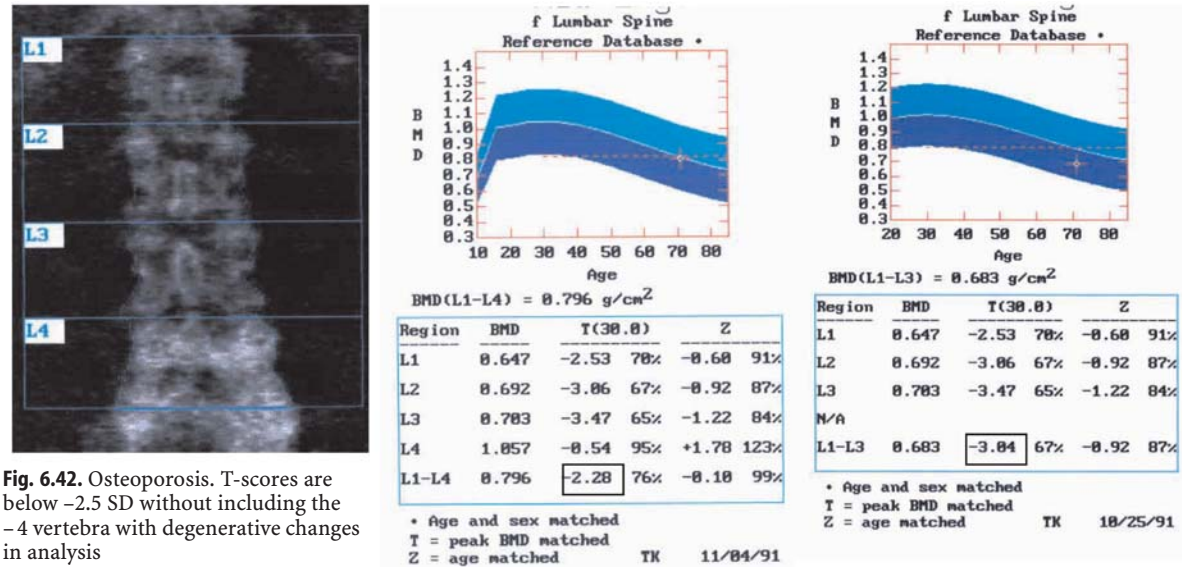

Fig. 6.42. Osteoporosis. T-scores are below –2.5 SD without including the – 4 vertebra with degenerative changes in analysis

born errors of vitamin D metabolism or end-organ unresponsiveness as is exemplified in the case of hypophosphatemic rickets.

Clinically, osteomalacia is manifested by progressive generalized bone pain, muscle weakness, hypocalcemia, pseudofractures, and, in its late stages, a waddling gait. Osteomalacia due to vitamin D depletion appears not to be suspected or diagnosed promptly in susceptible patients, probably because physicians are not sufficiently aware of this rare condition. In a study of 17 patients with osteomalacia due to vitamin D depletion, only 4 were suspected by the referring physicians, although a gastrointestinal disorder that can lead to vitamin D depletion was present in every patient [194]. Osteomalacia is usually neglected when compared with other metabolic bone diseases and may present with a variety of clinical and radiographic manifestations mimicking other musculoskeletal disorders [195]. Eight women aged 17 – 72 years, six with osteomalacia and two with primary hyperparathyroidism, were studied by bone scans and ^{99m}Tc (V) DMSA scans. Many of the fracture and pseudofracture (Fig. 6.43) sites detected on bone scans were also visualized on ^{99m}Tc (V) DMSA scans, which was suggested by the authors to have a potential as a screening method in patients with metabolic bone disease [196, 197].

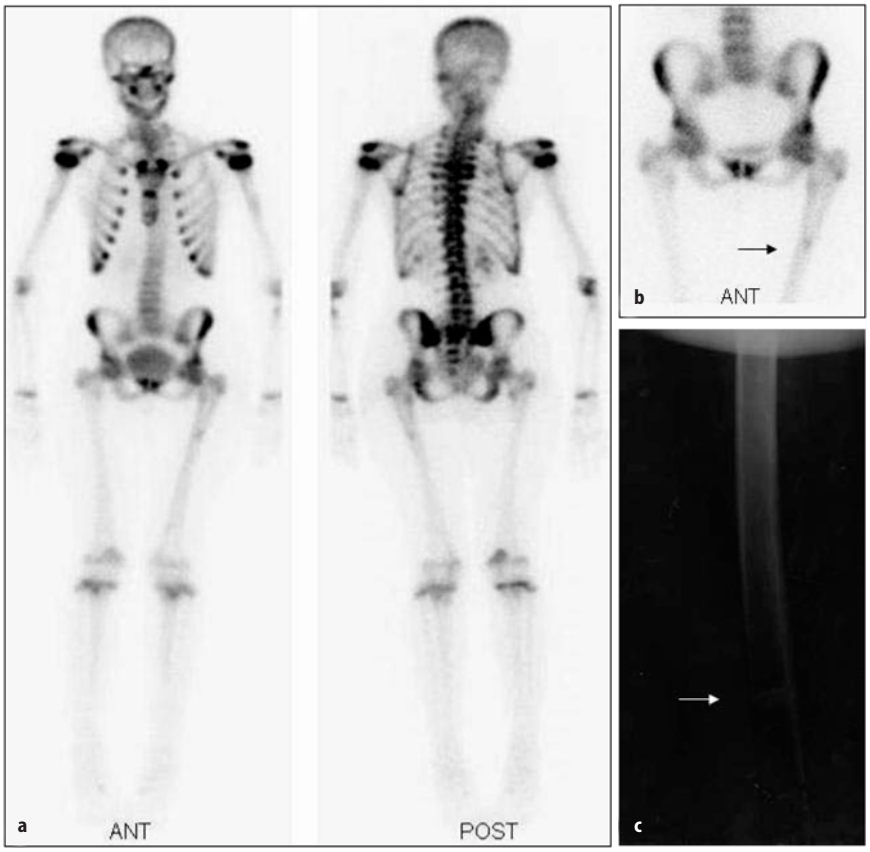

Fig. 6.43a–c. Osteomalacia. Whole body bone scan of a 19-year-old patient with osteomalacia. Note the increased uptake in the costochondral junctions, spine, mandible and the fracture of the left femur seen better on the spot image of the pelvis (b) and on the radiograph (c)

6.3.7.4 Bone Changes of Hyperparathyroidism

Overactivity of the parathyroid gland(s) results in excess secretion of parathyroid hormone, which promotes bone resorption and consequently leads to hypercalcemia and hypophosphatemia. Primary, secondary, and tertiary hyperparathyroidism all share elevated serum calcium and parathyroid hormone but show different scintigraphic patterns.

Primary hyperparathyroidism is caused by benign adenoma in approximately 80% of cases. Hyperplasia is generally the cause in the remainder of cases, and carcinoma is a very rare cause. Secondary hyperparathyroidism is due to compensatory hyperplasia in response to hypocalcemia. For example, this may occur in long-standing renal failure. Reduced renal production of 1,25-dihydroxyvitamin D_3 (active metabolite of vitamin D) leads to decreased intestinal absorption of calcium, resulting in hypocalcemia. Failure of the tubules to excrete phosphate results in hyperphosphatemia. Hypocalcemia is compensated for by parathyroid hyperplasia and excess production of parathyroid hormone [186, 187, 198]. Tertiary hyperparathyroidism describes a condition of persistent parathyroid hormone overproduction (even after a low calcium level has been corrected) as a result of autonomous hyperplastic parathyroid tissue.

In all forms of hyperparathyroidism there is increased bone resorption associated with increased osteoblastic activity, leading to increased uptake of bone-seeking radiopharmaceuticals. This is least prominent in primary compared with the other forms of hyperparathyroidism.

6.3.7.5 Renal Osteodystrophy

Renal osteodystrophy is a metabolic condition of bone associated with chronic renal failure. It is a frequent complication of renal insufficiency that became more prevalent recently due to the improved survival of patients with renal failure. This led to an increased number of patients with the condition, changed our understanding and defined the forms of the disease [199, 200]. The pathogenesis of renal osteodystrophy is incompletely understood. However, two mechanisms predominate: secondary hyperparathyroidism and abnormal vitamin D metabolism following reduced renal function. Renal insufficiency results in decreased excretions of phosphate leading to hyperphosphatemia, which in turn causes a decrease of serum calcium and

consequently secondary hyperparathyroidism. On the other hand, since renal tissue is the site of activation of 25-hydroxycholecalciferol into the 1,25-dihydroxy form of vitamin D, which is the active form of the vitamin, chronic renal failure causes a decrease of the formation of the active form. This leads to reduced gastrointestinal absorption of calcium, producing hypocalcemia.

The major skeletal changes of the disease include osteitis fibrosa, osteitis fibrosa cystica, rickets, osteomalacia, osteosclerosis and extraosseous calcification including tumoral calcinosis. Slipped capital femoral epiphysis, avascular necrosis including Legg-Perthes disease in children and brown tumors are other associated pathologic features [200 – 205]. Osteitis fibrosa is characterized by extensive medullary fibrosis and increased osteoclastic resorption linked to PTH hypersecretion. When cystic lesions are present it forms cystitis fibrosa cystica. Osteomalacia is mainly due to vitamin D insufficiency, hypocalcemia, acidosis, aluminum toxicity and exceptionally hypophosphatemia. It should be mentioned that aluminum overload directly inhibits the osteoblast.

The clinical presentation of renal osteodystrophy is influenced by the patient's age at onset of renal failure, the etiology of the renal disease, geographic location, dietary contents (protein, phosphate and calcium) and treatment modalities. The reported prevalence of each bone change mentioned varies and does not correlate well with the clinical findings and laboratory data. Currently the disease is believed to occur in three major types: high turnover disease, low turnover disease and mixed disease [105, 206 – 211]. The additional terms of "dynamic" or "aplastic" bone disease have also emerged recently and have been used synonymously with low turnover disease but should actually be considered as extreme variants of the low turnover type [112 – 213]. The prevalence of different forms of the disease has changed significantly over the last decade. The high turnover form is the most common, presents typically with osteitis fibrosa and is linked to the development of secondary hyperparathyroidism; hence it is sometimes described as "predominant hyperparathyroid bone disease".

High turnover renal osteodystrophy is usually associated with tubular interstitial nephritis as an underlying disease of renal failure since it is a slowly progressing form of renal pathology compared to glomerular disease, which has a rapidly progressive course with a lower risk of developing high turnover disease [208].

The low turnover type may present with osteomalacia and osteoporosis, which can also occur in the high turnover disease. The mixed form shows both osteomalacia and osteitis fibrosa. Differentiation of different forms is usually based on clinical data, laboratory findings and standard radiographs although it can be difficult.

Radiologically, skeletal deformities, thickening of cortical bone, thickened irregular trabeculae, osteonecrosis, extraosseous calcification and brown tumors can all be seen with variable frequency. Brown tumor presents as well defined lytic lesions that may cause expansion on standard radiographs since they may involve the cortical bone.

Scintigraphically, diffusely increased uptake with increased skeletal to renal uptake ratio occurs in the high turnover form. This uptake may be homogeneous or heterogeneous, with focal findings depending on the predominant pathophysiologic process (Fig. 6.44). One or more of the typical findings of metabolic bone disease on bone scan may be seen (Table 6.16). The low turnover form shows typically decreased uptake unless it is complicated by a focal pathology. A mixture of these findings are seen in the mixed form. Accordingly there is no consistency in the patterns seen on standard

Fig. 6.44. Renal osteodystrophy. A whole body bone scan of a patient with long-standing renal failure. The scan illustrates diffusely increased skeletal uptake. Note the typical sites of abnormal uptake in the mandible, sternum and costochondral junctions of this case of renal osteodystrophy

Table 6.16. Bone scan findings in metabolic bone disease

Generalized increased uptake with increased contrast between bone and soft tissue
Generalized decreased uptake
Increased uptake in long bones
Increased uptake in axial skeleton
Increased uptake in periarticular areas
Increased uptake in the calvaria
Increased uptake in the mandible
Increased uptake in the costochondral junctions (beads)
Increased uptake in the sternum (tie sternum)
Foci of increased uptake due to fractures, pseudofractures and Brown tumor
Faint or absent kidney

radiographs and bone scans in patients with renal osteodystrophy [214].

6.3.7.6 Hypertrophic Osteoarthropathy

Hypertrophic osteoarthropathy is a rheumatic disorder characterized by bone pain, joint pain and nearly always clubbing of fingers and/or toes. Two types of hypertrophic osteoarthropathy are recognized: primary and secondary. The primary type (also called pachydermoperiostosis) is less common and occurs in adolescence, with spontaneous arrest of the process in young adulthood. A variant has been reported in a family [215]. The secondary form follows a variety of pathological conditions, predominantly intrathoracic. Lung cancer and other intrathoracic malignancies, benign lung pathologies, and cyanotic heart disease are common causes. Abdominal malignancies, hepatic and biliary cirrhosis, and inflammatory bowel disease are less common causes [216, 217]. Nasopharyngeal carcinoma has also been reported as a cause [218]. Pathologically, the condition is a form of periostitis and may be painful. Additionally, clubbing of fingers and toes, sweating, and thickening of skin may also be seen. In the tubular bones there is periosteal new bone formation. This pathological feature explains the typical scintigraphic pattern of diffusely increased uptake along the cortical margins of long bones, giving the appearance of "parallel tracks".

The scintigraphic abnormalities are usually confined to diaphyseal regions, although they may also occur in the epiphyseal bone (Fig. 6.45). The changes are usually bilateral but can be unilateral in approximately 15% of cases [217]. The tibiae and fibulae are affected most commonly, followed by the distal femur, radius, ulna, hands, feet, and distal humerus. Scapula, patella, maxilla, mandible, and clavicle are less frequently affected and rarely the ribs and pelvis. The condition has no prognostic significance as there was no significant difference in survival between lung cancer patients with and others without hypertrophic osteoarthropathy [219]. The changes disappear following successful treatment of the lung cancer or other inciting pathology and scintigraphy is useful in evaluating the response to treatment of this paraneoplastic syndrome [220].

Fig. 6.45. Hypertrophic osteoarthropathy in a patient with lung cancer. Note the diffusely increased uptake in all bones of the lower extremities with a parallel track pattern in the femurs and tibiae

6.3.8 Arthropathy

Arthritides may begin primarily with synovial and intra-articular disease or with bone involvement. There is often some overlap with primary periarticular bone disease since synovitis may be associated with bone erosion, and primary bone disease may have an element of synovitis [221]. No unified classification for the many types of joint diseases is available. Arthropathies are grouped into two main categories: inflammatory and noninflammatory [222, 223] (Table 6.18). The inflammatory joint diseases are further classified into infectious and noninfectious. The infectious type is

Table 6.17. High turnover disorders

Generalized disorders
Primary hyperparathyroidism
Renal osteodystrophy (certain forms)
Type 1 (postmenopausal) osteoporosis
Localized disorders
Focal osteoporotic syndromes
Disuse atrophy
CRPS-1 (RSD)
Transient osteoporosis
Paget's disease
Stress fractures

Table 6.18. Main types of joint disease with major examples

A. Inflammatory joint disease
1. Infectious
Infectious arthritis
2. Noninfectious
Rheumatoid arthritis
Crystal deposition arthropathies (gouty arthritis, CPPD)
Sacroiliitis
Neuropathic joint disease
Spondyloarthropathies
Ankylosing spondylitis
Psoriatic arthritis
Reactive arthritis (formerly Reiter's disease)
Inflammatory bowel disease associated arthritis
B. Noninflammatory joint disease
1. Primary osteoarthritis
2. Secondary osteoarthritis

caused by bacteria, mycoplasmas, fungi, viruses, or protozoa while the noninfectious type is caused by immune reactions such as rheumatoid arthritis and ankylosing spondylitis or deposition of crystals in and around the joint as in gout, which is caused by deposition of monosodium urate crystals. Alternatively, the group of inflammatory joint diseases can also be subclassified into immunoinflammatory diseases such as rheumatoid arthritis, infectious diseases, crystal deposition, arthritis associated with connective tissue disease such as in systemic lupus erythematosus and those diseases associated with vasculitis such as Behçet's disease. The noninflammatory joint disease is exemplified by the common osteoarthritis or degenerative joint disease, which can be idiopathic (primary) or secondary. It should be noted that certain conditions such as neuroarthropathy and sacroiliitis have multiple overlapping pathogenetic features including immunologic, vascular and degenerative [222].

6.3.8.1 Rheumatoid Arthritis

Rheumatoid arthritis, an autoimmune disease, causes inflammation of connective tissue, mainly in the joints. It is thought that microvascular injury and mild synovial cell proliferation occur first, along with obliteration of small blood vessels. Synovial inflammatory response is triggered by immune complexes in the blood and synovial tissue through activation of plasma protein complement. This complement activation stimulates release of kinin and prostaglandin, which causes an increase in vascular permeability in the synovial membranes and attracts leukocytes out of the circulation to the synovial membrane. Inflammation eventually may spread from the synovial membrane to the articular cartilage, the joint capsule, and the surrounding tendons and ligaments with resultant pain, loss of function, and joint deformity [223]. The small joints of the hands and joints in the feet, wrists, elbows, ankles, and knees are the most commonly affected. On bone scintigraphy, there is increased perfusion and delayed uptake periarticularly in the areas of the joints affected, commonly the small joints of the hand, wrists, feet, and elbows, ankle and knees. ^{99m}Tc-polyclonal human immunoglobulin-G (HIG) has been shown to be a successful agent in the depiction of active inflammation in rheumatoid arthritis [224].

Scintigraphy is more sensitive but less specific than radiography in the depiction of abnormal joints in rheumatoid arthritis, especially in the peripheral joints. Active disease may be detected scintigraphically before becoming clinically evident [225–227].

The pattern of symmetric peripheral joint involvement can usually be distinguished scintigraphically from that of the rheumatoid variants (ankylosing spondylitis, psoriasis, Reiter's syndrome, etc.), which tend to have more central skeletal involvement and asymmetric peripheral articular uptake. While bone scintigraphy cannot always distinguish progressive disease from joints responding to therapy with osteoblastic repair, radiolabeled IgG and leukocytes have considerable prognostic sensitivity [228, 229].

6.3.8.2 Ankylosing Spondylitis

Stiffening and fusion (ankylosis) of the spine and sacroiliac joints causing most frequently low back pain and stiffness characterize the chronic inflammatory joint disease ankylosing spondylitis, which is the most common type of the seronegative spondyloarthropathies. It affects predominantly the axial joints, particularly the sacroiliac joints. Other joints such as the hips, knees, and shoulders are involved in approximately 30% of patients. The condition usually affects boys and begins in adolescence with inflammation of fibrocartilage in cartilaginous joints (primarily in the vertebrae) along with infiltration of inflammatory cells (mainly macrophages and lymphocytes) in the fibrous tissue of the joint capsule, cartilage, and periosteum. This process is followed by repair of cartilaginous structures by proliferation of fibroblasts that secrete collagen, which

later becomes organized into fibrous scar. This scar eventually undergoes calcification and ossification, causing loss of flexibility and fusion of joints [230]. Scintigraphically, patterns vary with the disease stage; in early stage scintigraphy reveals typical although not always symmetrical intense tracer uptake in both sacroiliac joints. Later as the spine becomes involved scintigraphy particularly pinhole reveals patchy uptake in apophysial joints, and horizontal band like uptake in the discovertebral junctions [231].

6.3.8.3 Gouty Arthritis

Uric acid crystallizes when it reaches certain concentrations in fluids, forming insoluble crystals that can precipitate in the connective tissue of different parts of the body. When this process involves the synovial fluid, it causes acute inflammation of the joints. Although the effect is the same, classic gouty arthritis is caused by deposition of monosodium urate crystals, while deposition of calcium pyrophosphate dihydrate crystals causes pseudogout [232].

The disease is rare in children and premenopausal women and uncommon in men under 30 years of age. Gout is closely linked to purine metabolism and kidney function. An accelerated rate of purine synthesis may occur in some individuals leading to overproduction of uric acid, since the latter is a breakdown product of purine nucleotides. In other individuals, the rate of breakdown (rather than synthesis) of purine nucleotides is accelerated, resulting also in overproduction of uric acid.

Uric acid is eliminated predominantly through the kidney. Urate excretion by the kidney may be sluggish due to a decrease in glomerular filtration of urate or an acceleration of urate reabsorption. Sluggish excretion of urate occurs in primary gout. Urate crystals are deposited in the renal interstitium, causing impaired renal flow, and may also precipitate to cause renal stones.

Monosodium urate crystals trigger an acute inflammatory response in the synovial membrane and other tissues of the joints. Leukocytes, particularly neutrophils, are attracted out of the circulation to phagocytose the crystals. Trauma is the most common aggravating factor. Therefore, because of the chronic strain during walking, the great toe is a common presenting site (50% of initial attacks).

On bone scan, there is increased flow, blood pool activity and delayed uptake in the areas of the joint involved. The first metatarsophalangeal joint, ankle, and the knee are the joints most often affected [233, 234] on bone scintigraphy, with the most typical being that of the metatarsophalangeal joint of the great toe, called podagra. Recently a case of gouty tophus of the patella was evaluated by positron emission tomography (PET) using a combination of an amino-acid analog emitter, l-[^{3}F18]-alpha-methyltyrosine (FMT), which does not accumulate in malignancies and shows increased metabolic activity, while the glucose analog emitter ^{18}F-fluoro-2-deoxy-d-glucose (FDG), which essentially accumulates in malignancies and does not show appreciable activity, suggests that PET may be useful for the preoperative evaluation of gouty tophus including detection and differentiation from malignant tumors [235].

6.3.8.4 Osteoarthritis

Idiopathic osteoarthritis is the most common type of noninflammatory joint disease. The idiopathic and the secondary form of osteoarthritis have the same pathological characteristics. Although it affects any joint, those most commonly involved are in the hands, wrists, lower cervical spine, lumbar spine, sacroiliac joint, hips, knees, ankles, and feet. Aging is an important risk factor, although the cause of osteoarthritis is unknown. Premature cartilage degeneration due to an inherited genetic defect encoding for the structural components of articular cartilage has been suggested as the etiology of this condition.

Primary or osteoarthritis of unknown cause progresses with age. Secondary osteoarthrosis occurs when the predisposing cause is known, e.g., following intraarticular fracture, rheumatoid diseases, neurogenic and metabolic disorders, drugs, and recurrent hemarthrosis as may occur among hemophilic patients. The pain of osteoarthrosis is caused by intracapsular tension, muscle spasm, abnormal stress on the bone, and increased intraosseous venous pressure [236–238].

Osteoarthritis starts with changes in the articular cartilage. The ability of articular cartilage to repair is very limited. Intrinsic repair occurs in infants, as chondrocytes are still able to proliferate. Extrinsic repair occurs by granulation tissue growing from the adjacent bone. Granulation tissue changes to fibrocartilage, which is inferior to normal cartilage in its mechanical properties.

The changes of articular cartilage in osteoarthritis progress from fibrillation to erosion and then, at the advanced stage, to complete loss of cartilage. With loss of articular cartilage the exposed bone takes increased stress, becomes more compressed, and shows subarticular hardening (sclerosis) [238].

Thus, the pathological features of osteoarthritis include gradual loss of articular cartilage, thickening and sclerosis of the bone underneath the cartilage, and formation of osteophytes (spurs). As the articular cartilage erodes, cartilage-coated osteophytes often grow into the joint. Small pieces of osteophyte may break off and become free within the synovial cavity. These pieces, called joint mice, irritate the synovial mem-

Table 6.19. Typical scintigraphic findings of major joint diseases

Disease	Scintigraphic findings
Rheumatoid arthritis	Symmetric uptake involving small and large joints
Gouty arthritis	Uptake of metatarsophalangeal joint of the great toe and large joints, commonly symmetric
Ankylosing spondylitis	Symmetric intense tracer uptake in both sacroiliac joints and spine
Osteoarthritis	Uptake of large joints, symmetric in primary type
Reactive arthritis	Asymmetric uptake of large and small joints and spine
Psoriatic arthritis	Asymmetric uptake of large and small joints typically of upper extremity including fingers and spine
Infectious arthritis	Uptake involving a large joint
Enteropathic arthritis	Uptake of large joints (asymmetric), sacroiliac joints (symmetric) and spine

brane, resulting in synovitis and joint effusion. In addition, the joint capsule may thicken and in some cases adhere to the underlying bone, causing limitation of movement.

Pathologic features of arthropathies are translated into various patterns of findings on scintigraphic imaging modalities. Table 6.19 summarizes the typical scintigraphic findings seen on bone scans in major arthropathies.

6.3.9 Soft Tissue Calcification

Pathological calcification is classified mainly into three types, as detailed below.

6.3.9.1 Dystrophic Calcification

Dystrophic calcification is calcification of dying or dead tissue. The mechanism appears to be increased calcium-binding capacity of the exposed denatured proteins of the injured cells which preferentially bind with phosphate ions which in turn react with calcium and form calcium deposits. Examples include calcification in infarcted myocardial muscle, in atheromas, in amyloid tissue, and in the centers of tumors (Fig. 6.46).

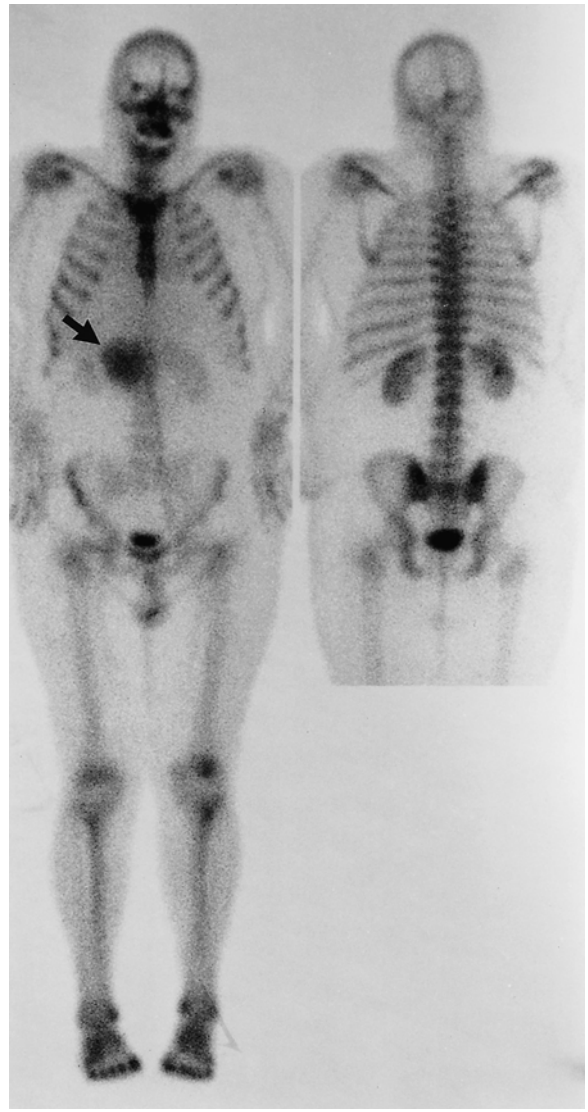

Fig. 6.46. ^{99m}Tc-MDP uptake as an example of dystrophic calcification in a case of hepatoma (*arrow*)

6.3.9.2 Metastatic Calcification

Metastatic calcification describes calcification of viable, undamaged, normal tissue (Fig. 6.47) as a result of hypercalcemia associated with increased calcium phosphate product, locally or systemically. This can be due to metabolic abnormalities as with renal failure, hypervitaminosis D, and hyperparathyroidism or to increased bone demineralization from bone tumors or disseminated metastases [43].

6.3.9.3 Heterotopic Bone Formation

Heterotopic bone formation, or increased ectopic osteoblastic activity, is defined as the presence of bone in soft tissue, where it does not normally exist. In the vast majority of cases the condition is acquired. Rarely it can be congenital. The pathogenesis of heterotopic bone formation is still debated. However, it is believed

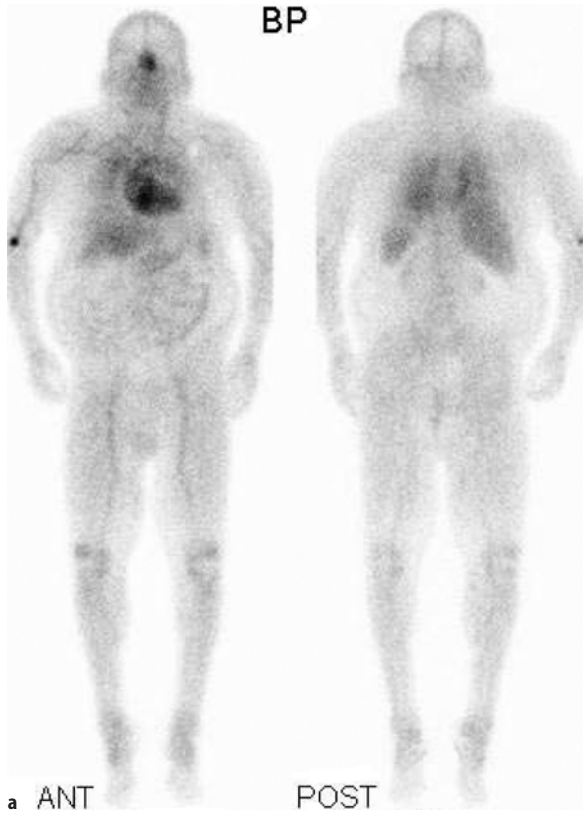

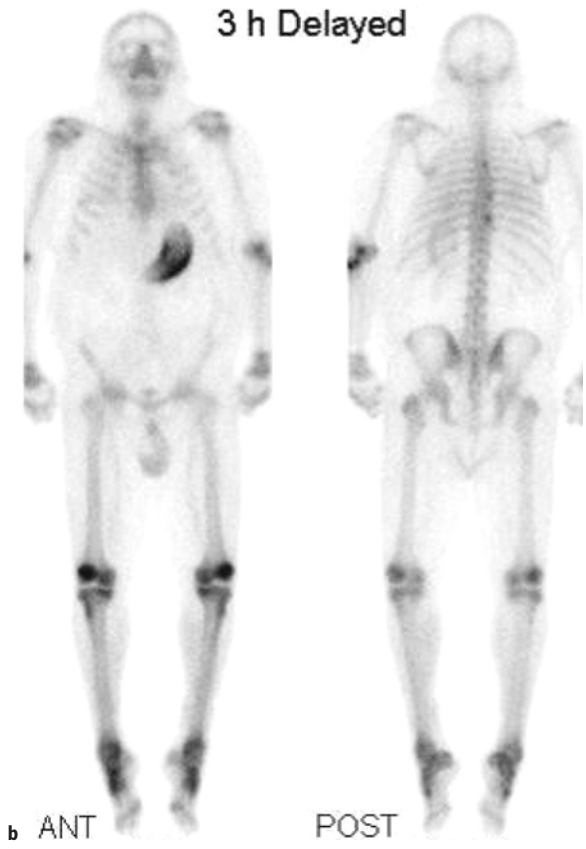

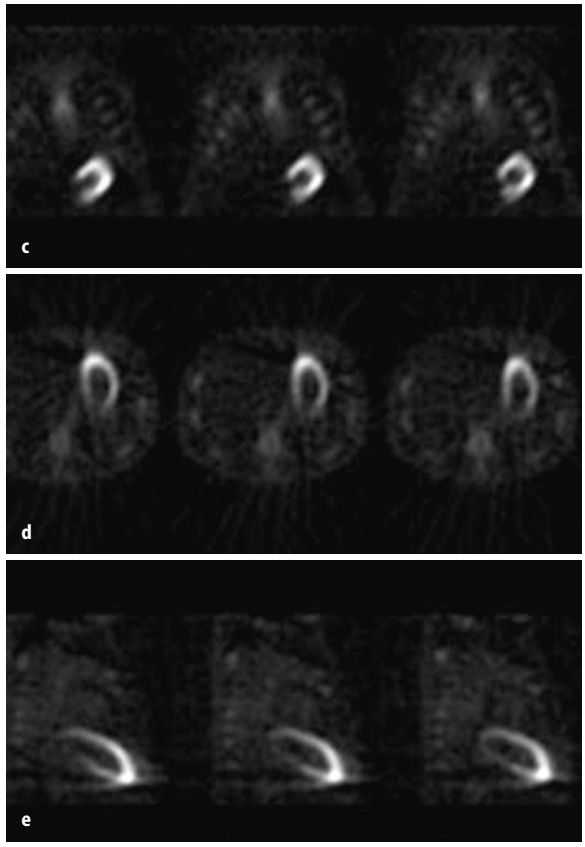

Fig. 6.47a–e. ^{99m}Tc-MDP whole body blood pool (a) and delayed scans and selected SPECT cuts of the chest of a 57-year-old male with a history of chronic renal failure and coronary artery disease presenting with chronic progressive motor demyelinating polyneuropathy. Rule out osteosclerotic melanoma. The patient is thought to have POEMS syndrome. Increased activity in the T spine is likely due to degenerative disease, and may represent osteophyte formation. Increased activity in the knees has the appearance of arthropathy. Increased activity in the left elbow is consistent with known olecranon bursitis. Poor visualization of the kidneys is consistent with known chronic renal failure. Intense visualization in the stomach is most likely due to metastatic calcification, which can be seen secondary to numerous metabolic disorders including hyperparathyroidism, which in this patient may be secondary hyperparathyroidism due to chronic renal failure. This is also likely the cause of the increased visualization of the long bones

to be secondary to transformation of pluripotent mesenchymal cells, present in the connective tissue septa within muscle, into the osteogenic cell line.

The acquired form of heterotopic bone formation often occurs after trauma. Other associated conditions include burns, sickle cell disease, hemophilia, tetanus, poliomyelitis, multiple sclerosis, toxic epidermal necrolysis, and cancer. It also occurs infrequently in the absence of a precipitating event or condition. Heterotopic bone formation includes the specific entity myositis ossificans: a post-traumatic skeletal muscle ossification usually occurring next to long bones. In many clinical practices, myositis ossificans is usually seen among patients who have sustained trauma such as operative procedures (e.g., total hip arthroplasty), fractures, dislocations, and direct trauma to muscle groups (mainly quadriceps femoris and brachialis muscles). Additional reported sites include abdominal incisions, wounds, and the gastrointestinal tract. The other acquired traumatic form follows trauma to the nervous system, i.e., neurogenic, and is most commonly seen following spinal cord injury. Patients are typically adolescents or adults, with 75% younger than age 30. There is no sex predominance. This subtype often occurs following closed head injuries, strokes and central nervous system infarctions, and tumors [239, 240]. Anatomically, HBF is always extra-articular, but it may be attached to the joint capsule without disrupting it. Occasionally, HBF may be attached to the cortex of adjacent bone with or without cortical disruption (Fig. 6.49). Tumoral calcinosis describes heterotopic bone formation that has large amounts of bone formation resembling tumor masses (Fig. 6.50).

The incidence of heterotopic bone formation varies greatly in different patient populations. It has been reported to be between 20% and 25% among spinal cord injury patients, while 10% – 20% of closed head injury patients develop heterotopic bone formation. The onset of heterotopic bone formation has been reported to range from 4 to 12 weeks after injury, most commonly at 2 months, but it has also been reported to occur as early as 20 days post injury. The most commonly involved areas, in decreasing order, are the hips, knees, shoulders, and elbows. Rarely, it can occur in the foot.

The course of acquired heterotopic bone formation is relatively benign in 80% or more of cases. The remaining patients often develop significant loss of motion, and ankylosis occurs in up to 10%. Clinical, laboratory, radiographic, and scintigraphic criteria have been used to follow the course of heterotopic bone formation and to assist in treatment.

The most sensitive imaging modality for early detection of heterotopic bone formation is multiphase bone scintigraphy. Blood flow and pool images have detected incipient heterotopic bone formation as early as 2.5 weeks after injury, with delayed scintigraphs becoming positive about 1 week later. These scintigraphic findings precede positive radiographs by 1 – 4 weeks [241]. The condition is classified as immature when flow and blood pool activity are increased (Fig. 6.48). When flow and blood pool patterns normalize or stabilize after showing decreasing activity, the condition is considered to be mature. As heterotopic bone progresses from immature to mature, the three-phase bone scan typically shows progressive reduction in the activity of all three phases. The majority of bone scans re-

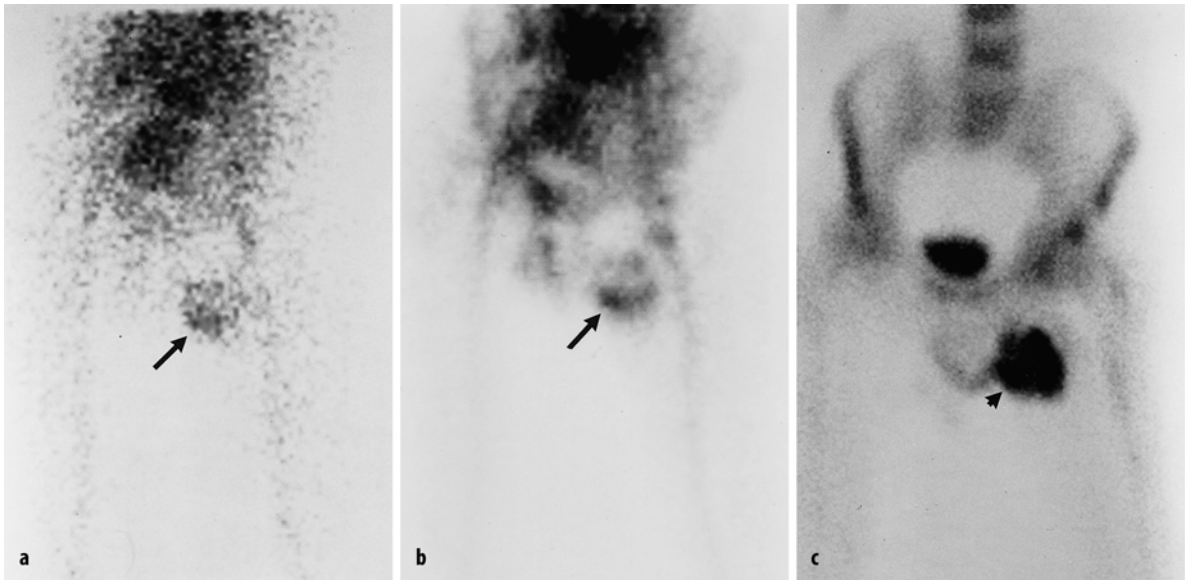

Fig. 6.48a–c. Multiphase bone scan showing increased flow (a), blood pool (b), and delayed (c) soft tissue uptake in the left thigh and illustrating the finding of immature heterotopic bone formation

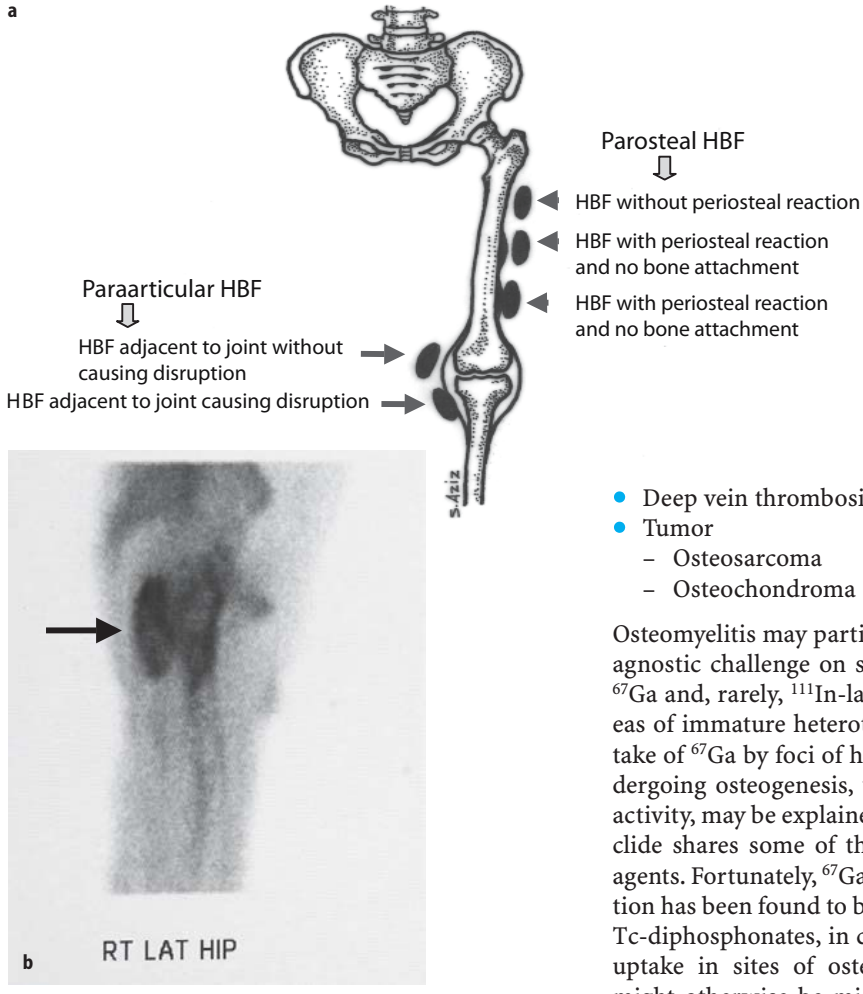

Fig. 6.49. a Illustration of the relation of heterotopic bone formation to the bone cortex and joints. Heterotopic bone formation is always extra-articular, but may be attached to the cortex of adjacent bone with or without cortical destruction. **b** A spot delayed image of a bone scan obtained using ^{99m}Tc-MDP showing a focus of hetertopic bone formation adjacent to the posterior surface of the upper right femur

turn to baseline within 12 months, although many patients reach the mature phase much earlier or much later. Since surgical intervention during the immature phase often leads to recurrence, serial bone scans are useful in monitoring the activity of the disease, so as to determine the appropriate time for surgical removal of heterotopic bone with minimal risk of recurrence. In several reported series, preoperative serial bone scans with quantitation of the uptake ratios between heterotopic and normal bone have successfully identified those patients who remained free of heterotopic ossification following surgery (i.e., those patients with decreasing or stable scintigraphic activity as measured by this quantitative technique).

Several pathological conditions can clinically mimic the scintigraphic appearance of early heterotopic ossification:

- Infection
- Osteomyelitis
- Cellulitis
- Thrombophlebitis
- Deep vein thrombosis
- Tumor
  - Osteosarcoma
  - Osteochondroma

Osteomyelitis may particularly represent a difficult diagnostic challenge on scintigraphy, particularly since ^{67}Ga and, rarely, ^{111}In-labeled WBCs accumulate in areas of immature heterotopic bone formation. The uptake of ^{67}Ga by foci of heterotopic bone formation undergoing osteogenesis, with considerable osteoblastic activity, may be explained by the fact that this radionuclide shares some of the properties of bone-imaging agents. Fortunately, ^{67}Ga uptake in heterotopic ossification has been found to be proportional to the uptake of Tc-diphosphonates, in contrast to its relatively greater uptake in sites of osteomyelitis. Since ^{67}Ga uptake might otherwise be mistaken for infection or tumor, this proportionality can help to differentiate heterotopic ossification from osteomyelitis. Therefore, in the appropriate clinical setting, heterotopic ossification is a diagnostic consideration for patients with a positive ^{67}Ga scan [240].

The rare congenital form of heterotopic ossification is called myositis ossificans progressiva, or fibrodysplasia ossificans progressiva [242]. This autosomal dominant congenital disease is often associated with other skeletal abnormalities including malformation of the great toes and shortening of digits, as well as other clinical features such as deafness and baldness. Although symptoms have been reported to develop in patients with this disease prior to 4 years of age, the diagnosis is frequently missed. The soft tissue ossification present may be mistakenly attributed to bruising or even to a sarcoma. Initial failure to appreciate the significance of the toe and other digit malformations also is common. Progression to severely impaired joint mobility with ankylosis by early adulthood is the hallmark of this disease.

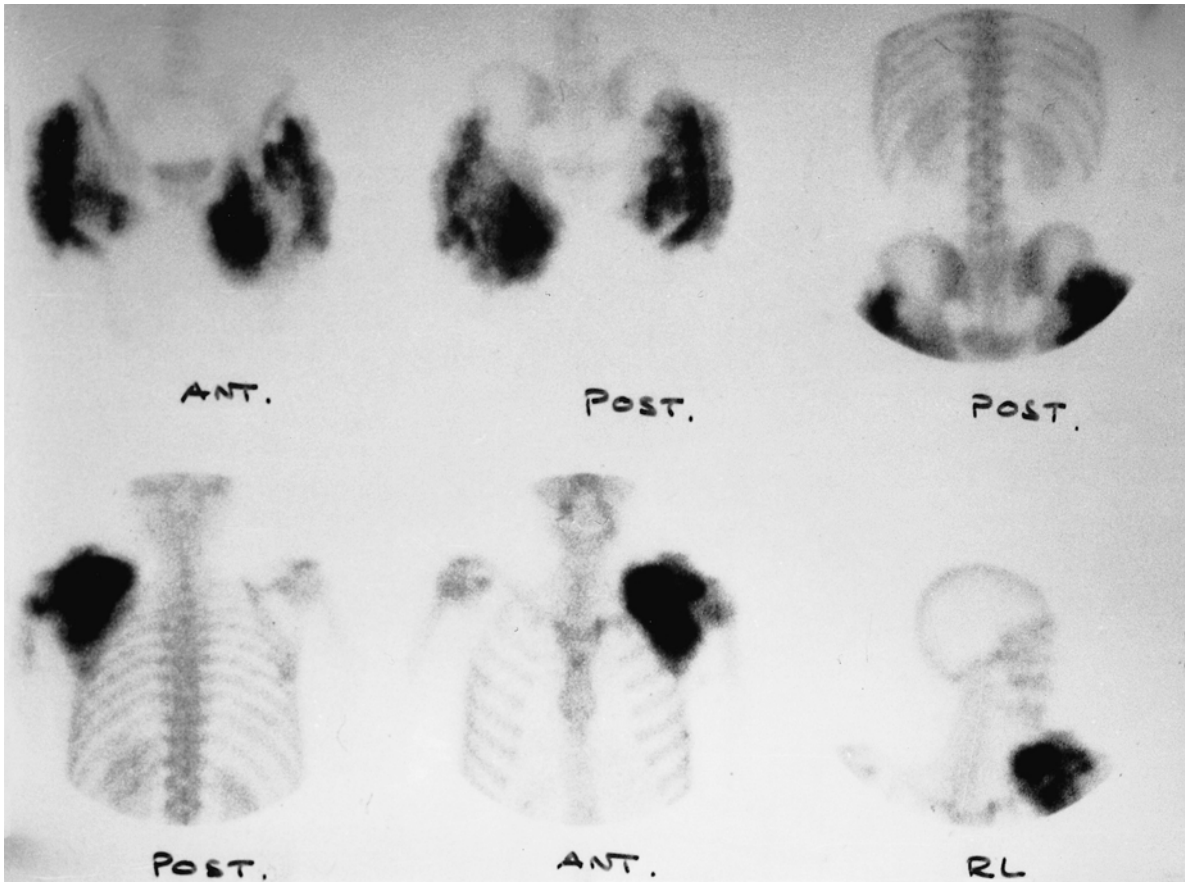

Fig. 6.50. Spot images of ^{99m}Tc bone scan of a case of tumoral calcinosis. Note the rather large amount of soft tissue calcification

6.3.9.4 Calcinosis Cutis

Calcinosis cutis describes a group of disorders in which calcium deposits form in the skin, subcutaneous tissue and connective tissue sheaths around the muscles. Etiologically, dystrophic, metastatic, iatrogenic, and idiopathic varieties may be identified. Some rare types may even be variably classified as dystrophic or idiopathic. These include calcinosis cutis circumscripta and calcinosis cutis universalis. Most lesions of calcinosis cutis develop gradually and are asymptomatic. However, the history and evolution of the lesions depend upon the etiology of the calcification.

6.3.9.4.1 Calcinosis Cutis Universalis

This entity describes diffuse calcium deposits in the skin, subcutaneous tissue and connective tissue sheaths around the muscles but not within the muscles as is the case with myositis ossificans. It is seen mostly in association with scleroderma and polymyositis. On bone scintigraphy it shows uptake of variable degrees in a diffuse fashion in large areas of the skin and subcutaneous regions.

6.3.9.4.2 Calcinosis Cutis Circumscripta

This condition is a form of localized calcium deposition in the skin. If dystrophic it is secondary to localized causes of dystrophic calcification such as trauma, insect bites, acne and certain skin tumors. If metastatic or associated with systemic causes of dystrophic calcifications, it generally occurs earlier and tends to involve the extremities, whereas calcinosis universalis occurs later and usually is more widespread.

6.3.9.4.3 Calciphylaxis

This is a condition of soft tissue calcification affecting mainly patients with chronic renal failure. The calcification involves the media of small and medium sized cutaneous arterioles with extensive intimal hyperplasia and fibrosis. There is also subcutaneous calcification

and necrosis, which may lead to sepsis, the main cause of morbidity which may be significant.

6.3.9.4.4 Rhabdomyolysis

Rhabdomyolysis, also called myoglobulinuria, is a condition that follows muscle damage secondary to infectious and noninfectious injuries including viral infections, electrical injury, certain drugs, and trauma as in runners and military recruits. The condition can be severe and life threatening. The most severe form is sometimes called crush syndrome. Milder forms are called compartment syndromes. There is excess myoglobulin in the urine since intracellular muscle protein is released with muscle damage and appears in urine. Since variable degrees of muscle death occur, this will increase calcium content, which is sensitively identified by ^{99m}Tc-MDP bone scan, showing increased uptake in the damaged muscle. Bone scan can be useful to evaluate the degree of muscle necrosis [243].

6.4 Neoplastic Bone Disease

6.4.1 Primary Bone Tumors

Various primary tumors originate from the bone. Based on the cell of origin, primary tumors can be classified as osteogenic, chondrogenic, collagenic, or myelogenic (Fig. 6.51).

6.4.1.1 Osteogenic Tumors

Osteogenic tumors originate from bone cell precursors, the osteoblasts, and are characterized by formation of bone or osteoid tissue. These tumors include osteoid osteomas, osteosarcomas, and osteoblastomas.

Osteoid Osteoma. This benign tumor is most common in children, particularly boys. Typically, it presents in the lower extremities, the pelvis, or less commonly the spine. Patients frequently report nocturnal pain which is relieved by aspirin. It is characterized by its small nidus size of less than 2 cm, self-limited growth, and the tendency to cause extensive reactive changes in the surrounding bone tissue. The lesion classically presents with severe pain at night that is dramatically relieved by nonsteroidal anti-inflammatory drugs (NSAIDs). The tumor has been shown to express very high levels of prostaglandins, particularly PGE_2 and PGI_2. High local levels of these prostaglandins are presumed to be the cause of the intense pain seen in patients with this lesion. Studies have shown strong immunoreactivity to cyclo-oxygenase-2 (COX-2) in the nidus of the tumor but not in the surrounding reactive bone. COX-2 is one of the mediators of increased production of prostaglandins by the tumor [244].

Osteoblastoma is a tumor related to osteoid osteoma and has an almost identical histologic appearance, but the nidus is larger in size, measuring more than 2 cm. It is commonly seen in the spine and can occur in any other location. For the appendicular skeleton, the lower extremity is the most common location for osteoblastoma where 35% of the lesions occur.

Osteogenic Sarcoma. Osteogenic sarcoma is an osteogenic tumor with sarcomatous tissue. It is the most common malignant bone-forming tumor and has the appearance of callus containing compact or cancellous bone produced by anaplastic cells and sometimes chondroid and fibrinoid tissue (Fig. 6.52). The male to female ratio is 3/2. Sixty percent of cases occur before the age of 20. A secondary peak incidence is found be-

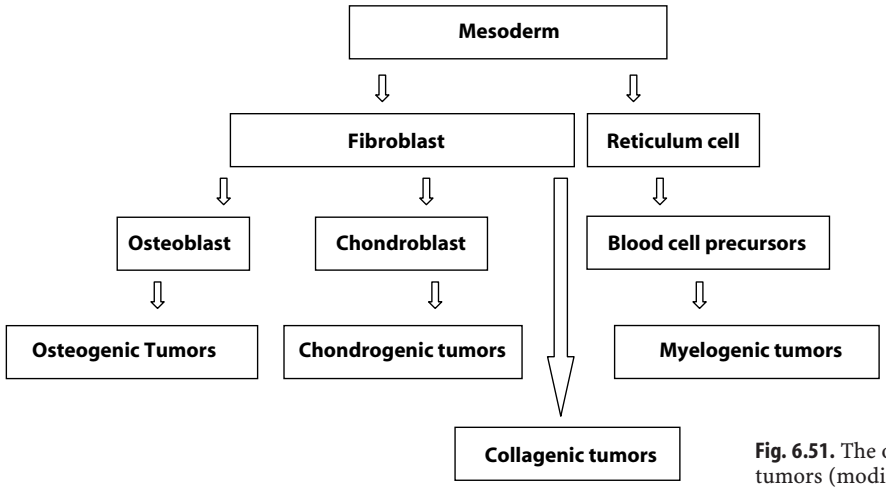

Fig. 6.51. The origin of various primary bone tumors (modified from [1], with permission)

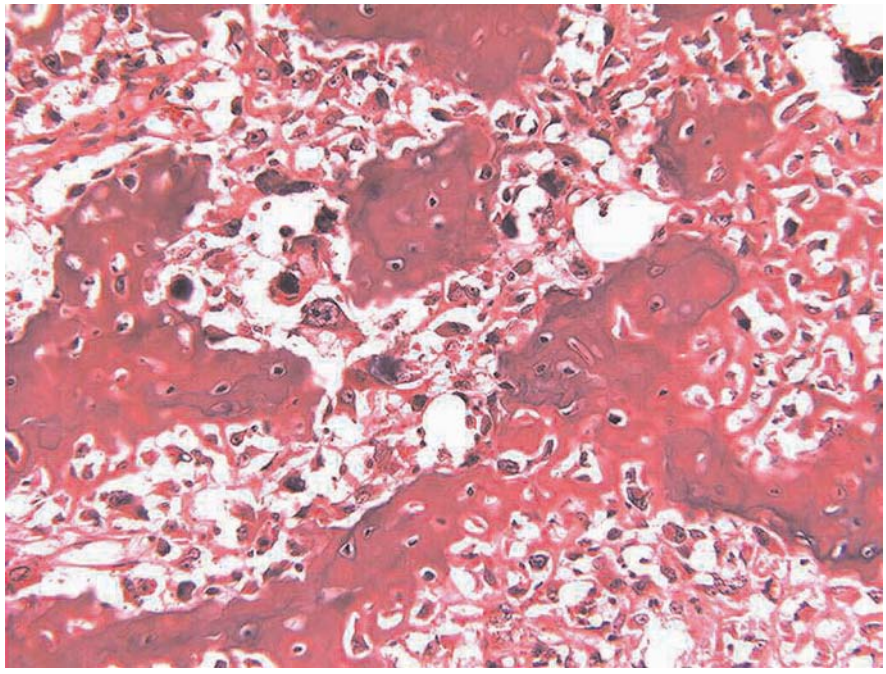

Fig. 6.52. Osteogenic sarcoma pathology

tween 50 and 60 years of age, mainly in patients with a history of prior radiation therapy years earlier [245]. The vast majority of the tumors involve the metaphyses of long bones particularly in the distal femur, with 50% around the knee region (Fig. 6.53).

6.4.1.2 Chondrogenic Tumors

All tumors that produce cartilage, primitive cartilage, or cartilage like substance are called chondrogenic. The most common malignant chondrogenic tumor is chondrosarcoma. Two types of this malignant tumor are recognized: (a) primary chondrosarcoma, occurring mainly in patients aged 50 – 70 years; and (b) secondary chondrosarcoma, which is derived from the benign chondrogenic tumor enchondroma and occurs more frequently in patients aged 20 – 30 years. Chondrosarcoma is more common in men than in women, often arising in the metaphysis or diaphysis of long bones (Fig. 6.53), particularly the femur and in the pelvis. The neoplasm consists of hyaline cartilage with bands of anaplastic cells and fibrous tissue. The tumor may infiltrate the joint spaces located near the end of the long bone. Osteochondroma represents one third of chondragenic lesions and is the most common benign bone tumor formed of a cartilage surrounding canallous bone. Chondroma is an uncommon benign chondrogenic tumor that characteristically forms mature cartilage. The tumor is encapsulated with a lobular growing pattern. It is formed of chondrocytes (cartilaginous cells) that resemble normal cells and produce cartilaginous matrix. It is found mostly in the small bones of the hand and/or feet, although it can also occur in long, tubular bones, primarily the humerus, femur and ribs. Occasionally, focal areas of myxoid degeneration may result in a mistaken diagnosis of chondrosarcoma. Chondromas are classified according to their location into enchondroma within the medullary cavity of bone, periosteal chondroma found on the surface of the bone, and soft tissue chondroma found in the soft tissue. The primary significance of enchondroma is related to its complications, most notably pathologic fracture, and a small incidence of malignant transformation. Enchondromas are usually solitary but may be multiple. Multiple enchondromas occur in three distinct disorders: Ollier's disease, which is a nonhereditary disorder characterized by multiple enchondromas with a predilection for unilateral distribution (Fig. 6.54). Maffucci's syndrome is another nonhereditary disorder which is less common than Ollier's disease. This syndrome features multiple hemangiomas in addition to enchondromas. The third form is metachondromatosis, which consists of multiple enchondromas and osteochondromas, and is the only one of the three disorders that is hereditary as autosomal dominant [246].

6.4.1.3 Collagenic Tumors

Collagenic tumors are primary bone tumors that produce fibrous connective tissue. A fibrosarcoma is a malignant collagen-forming tumor that occurs most fre-

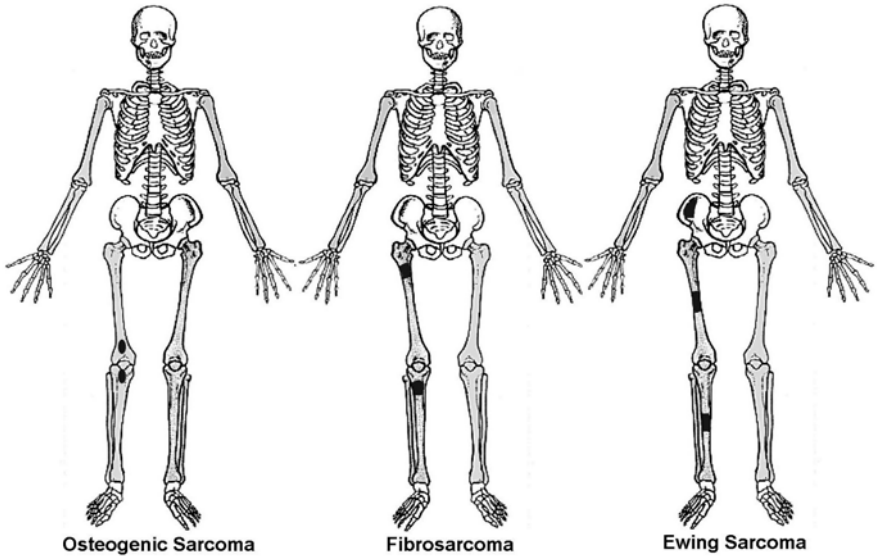

Fig. 6.53. The most common sites of the major primary bone tumors

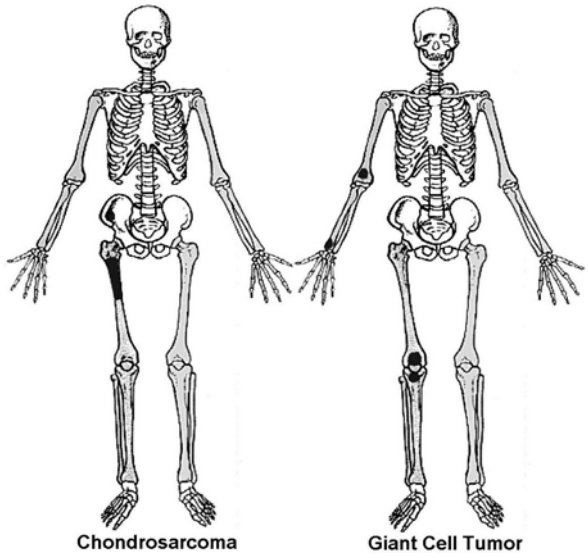

quently in patients between 30 and 50 years of age but also is encountered in younger and older age-groups. It is slightly more common among women. A secondary form may occur following Paget's disease, radiation therapy, and long-standing osteomyelitis. The tumor is most frequently located in the metaphysis of the femur or tibia. It begins in the marrow cavity and infiltrates the trabeculae. Histological examination typically reveals collagen, malignant fibroblasts, and occasionally giant cells.

6.4.1.4 Myelogenic Tumors

Myelogenic tumors originate from various cells in the bone marrow.

Myeloma. A myeloma originates from the plasma cells of the reticuloendothelial element of the bone marrow and may be solitary (85%) or multifocal (multiple myeloma). It is a highly malignant tumor that occurs more commonly in patients above 40 years of age and more frequently in men and blacks. It affects mainly the spine, pelvis, ribs, skull, and proximal bones of the extremities. Pain progresses over time during the course of the disease, and pathological fractures may take place. Patients may develop renal failure, anemia, and thrombocytopenia, and their urine shows Bence-Jones protein. The tumor has a poor prognosis, and radiation and chemotherapy have limited success.

Ewing's Sarcoma and Primitive Neuroectodermal Tumor (PNET). Ewing's sarcoma and PNET are small round cell malignant tumors of bone and soft tissue. The origin of the tumors is not certain but both tumors have a similar neural phenotype and share identical chromosome translocation; hence they are viewed as the same. Ewing's sarcoma occurs most commonly between the ages of 5 and 15 years and it is rare after the age of 30. It is more common in males and in whites. It is characterized by chromosomal translocation between chromosomes 11 and 22. Typically, it occurs in the diaphysis of long bones such as the femur and tibia and in flat bones such as the pelvis; however, any bone may be involved. After arising from marrow, Ewing's sarcoma breaks though the bone cortex to form a soft tissue mass which does not contain osteoid. The tumor metastasizes early to the lung, other bones, lymph nodes, bone marrow, liver, spleen, and central nervous system. Often the prognosis is poor, particularly if the tumor involves the pelvis rather than the long bones.

Morphological imaging modalities play a major role in evaluating the local extent of the primary tumors of

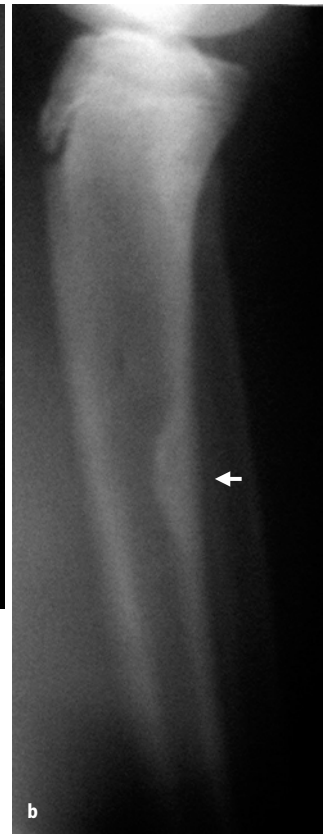

Fig. 6.54a–e. Seventeen-year-old boy presenting at the age of 12 years with swollen and painful right hand after playing boxing. Was diagnosed with a benign enchondroma of the third right metacarpal bone. At the age of 14 years, had a recurrent pain of the upper third of the right leg, and was also diagnosed with a benign enchondroma. Follow-up radiography of the right hand (**a**) revealed no changes in the size or characters of the previously diagnosed enchondroma of the middle metacarpal bone (*arrow*). Left leg (**b**) demonstrated a mixed density scalloped eccentric lesion (*arrow*) in the upper half of left tibia believed to be mostly benign. The patient was referred to the Nuclear Medicine Department for an annual follow-up. A three-phase bone scan was obtained 3 h after IV injection of 25.3 MCI of ^{99m}Tc-MDP. The blood pool images (**c**) of both hands show moderate focal increase uptake in the mid right hand. The delayed images of the hands (**d**) show intense focal uptake in the third right metacarpal bone. The whole body images (**e**) shows two foci of increased uptake in the left tibia, one in the upper third and one in the lower third representing multiple enchondromas

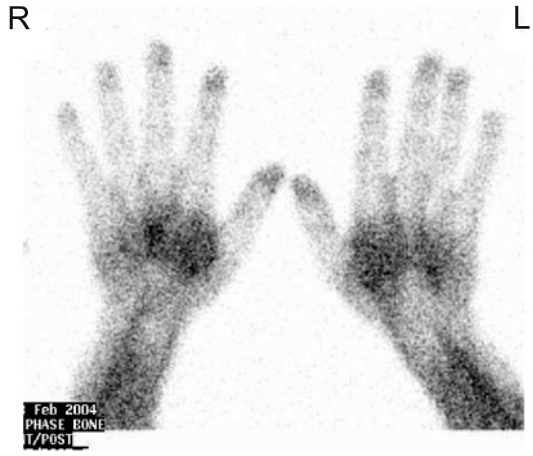

c

d

e

bone. MRI has become the examination of choice for local staging. Bone scintigraphy, on the other hand, has a limited role in local staging but is still the modality of choice for detecting distant metastases. Thallium-201 also plays a role in evaluating the response to therapy and in differentiating benign from malignant lesions [247]. Positron emission tomography (PET) is used on an individual basis, particularly to evaluate the response to therapy.

Giant Cell Tumor. This is difficult to classify although many practitioners include it with myelogenic tumors since it is believed to originate from the fibrous tissue of the bone marrow. While giant cell tumor may occur in persons between 10 and 70 years of age, it is more commonly encountered in those between 20 and 40 years old, with women afflicted more often than men from the metaphyseal-epiphyseal region of long bones. The tumor occurs mainly around the knee (50%), in the radius, and in the humerus. It has a high recurrence rate, often extending locally into adjacent soft tissues; distant metastases, however, occur more rarely. It consists particularly of osteoclast-like giant cells and anaplastic stromal cells, with a minor component of osteoid and collagen [248].

Chordoma is a rare slowly growing neoplasm arising from notochordal remnants in the midline of the neural axis and involving the adjacent bone. The main malignant potential of chordomas resides in their critical locations adjacent to important structures, their locally aggressive nature, and their extremely high rate of recurrence. CT and MRI are essential for accurate evaluation. Myelography is used to determine intraspinal extension.

Bone hemangiomas are benign, malformed vascular lesions, overall constituting less than 1% of all primary bone neoplasms. They occur most frequently in the vertebral column (30% – 50%) and skull (20%), but can occur anywhere in the body, and thus any bone can be affected including the long bones, short tubular bones, and ribs. They are multiple in approximately one-third of cases particularly within the vertebral column. Osseous hemangioma generally occurs more commonly in females than males, with a ratio of 3:2. The peak incidence is in the 5th decade, although osseous hemangiomas can be encountered at any age. Bone hemangiomas usually occur in the medullary cavity, but uncommonly surface-based hemangiomas are encountered in the cortex, periosteum, and subperiosteal regions. The rare periosteal and other surface-based hemangiomas tend to occur in younger patients. Bone hemangiomas are usually asymptomatic lesions discovered incidentally on imaging or postmortem examination and mostly encountered in the middle-aged. Vertebral hemangiomas are the most common benign tumor of the spinal column, and they occur most frequently in the lower thoracic and upper lumbar spine. They are usually localized to the vertebral body, less frequently extending into or exclusively affecting the posterior arch. Long-bone hemangiomas are uncommon and are found mainly in the tibia, femur, or humerus. They have a predilection for the metaphyseal or diaphyseal regions but can involve the epiphyses and even extend across the joint space. Skull hemangiomas affect most commonly the frontal bone. Gross pathology usually reveals well-demarcated, unencapsulated lesions with cystic red cavities. Microscopic examination shows hamartomatous proliferations of vascular tissue within endothelial-lined spaces.

There are four histologic variants of hemangioma, classified according to the predominant type of vascular channel: cavernous, capillary, arteriovenous, and venous. These types can coexist. Bone hemangiomas are predominantly of the cavernous and capillary varieties. Cavernous hemangiomas most frequently occur in the skull, whereas capillary hemangiomas predominate in the vertebral column; overall, the former type is most common in bone [249 – 250].

Multiphase ^{99m}Tc (MDP bone scintigraphy may also reveal increased tracer uptake in all phases – perfusion, blood pool and delayed), with a progressive increase in uptake, most marked in the delayed static images. Single-phase bone scintigraphy, though, has a far lower specificity since hemangiomas vary in their aggressiveness and hence in the degree of bone turnover, and may demonstrate either increased or decreased uptake or even normal uptake and therefore generally add minimal information. SPECT may be helpful in vertebral hemangiomas [251], and ^{99m}Tc-labeled red cells will show accumulation by the tumor as is the case with hemangiomas at other sites.

6.4.1.5 Imaging of Primary Bone Tumors

Functional nuclear medicine imaging plays a minor role in evaluating the local extent of the primary bone tumors. However, utilization of several radiotracers including ^{99m}Tc-MDP, thallium-201, ^{99m}Tc-MIBI, gallium-67 and ^{18}F-FDG helps in making the diagnosis, grading and evaluating the response to chemotherapy. Thallium-201, ^{99m}Tc-MIBI and ^{18}F-FDG can help in differentiating malignant from benign bone lesions [246 – 248, 252 – 253].

PET FDG plays an important role in evaluating prognosis and response to therapy. A recent study of 17 patients with primary bone tumors (11 osteosarcomas, 5 Ewing's sarcomas), for instance, has shown that patients with increasing tumor-to-nontumor ratios of FDG uptake or decreasing ratios of less than 30% have poor responses [254].

In comparison to bone scan, which may detect metastases and other lesions as small as 2 mm [255], some

studies suggest that PET scanning may be more sensitive. In one study, FDG PET has been compared to the ^{99m}Tc-MDP bone scan in the detection of osseous metastases in 70 patients with histologically proved malignant primary bone tumors (32 osteosarcomas, 38 Ewing's sarcomas). FDG PET showed a higher sensitivity of 90%, a specificity of 96% and an accuracy of 95% in the detection of bone metastases (49 from Ewing's sarcomas and 5 from osteosarcomas) more than bone scan, which showed a limited sensitivity of 71%, a specificity of 92% and an accuracy of 88%. Similarly, accuracy of FDG-PET in patients with Ewing's sarcoma was found to be higher than that of bone scan (97% and 82%, respectively). In contrast, in patients with osteogenic sarcoma, FDG PET detected none of the five cases of osseous metastases detected by bone scan, indicating a lower sensitivity of FDG PET than bone scan in detection of osteosarcoma induced osseous metastases [256].

6.4.1.6 Imaging of Major Specific Tumors

6.4.1.6.1 Osteoid Osteoma

Characteristically these lesions are intracortical and diaphyseal in location, although they occasionally involve the metaphysis. On standard radiographs, the characteristic appearance is a small, less than 1.5–2 cm, cortically based radiolucency (nidus) surrounded by marked sclerosis and cortical thickening, combined with the classic clinical history of pain, which is worse at night, that is relieved by aspirin. On CT, an area of increased bone density surrounding a lucent nidus is typical of this tumor. Scintigraphically there is a focal area of increased flow, increased blood pool activity and increased delayed uptake [242]. A specific scintigraphic pattern of double density may be seen as more intense uptake corresponding to the nidus and a peripheral less intense activity (Fig. 6.55). Symptoms of osteoid osteoma are cured by removing the nidus. The nidus of the tumor must also be removed during surgery to avoid regrowth. SPECT may help to localize an osteoid osteoma before surgery, and a gamma probe is a useful operating room tool for localizing this tumor [257].

'En-bloc' resection is often not successful because the nidus is hard to find and remove totally. Since the nidus is best localized with CT [258], surgery under CT control using standard equipment usually available in the operating room has been recently used successfully for CT-guided removal of the nidus [259]. MRI also shows intramedullary high intensity areas on T2-weighted images in the nidus and this was suggested to be due to a high level of cyclo-oxygenase-2 (COX-2) expression in neoplastic osteoblasts in the nidus [260].

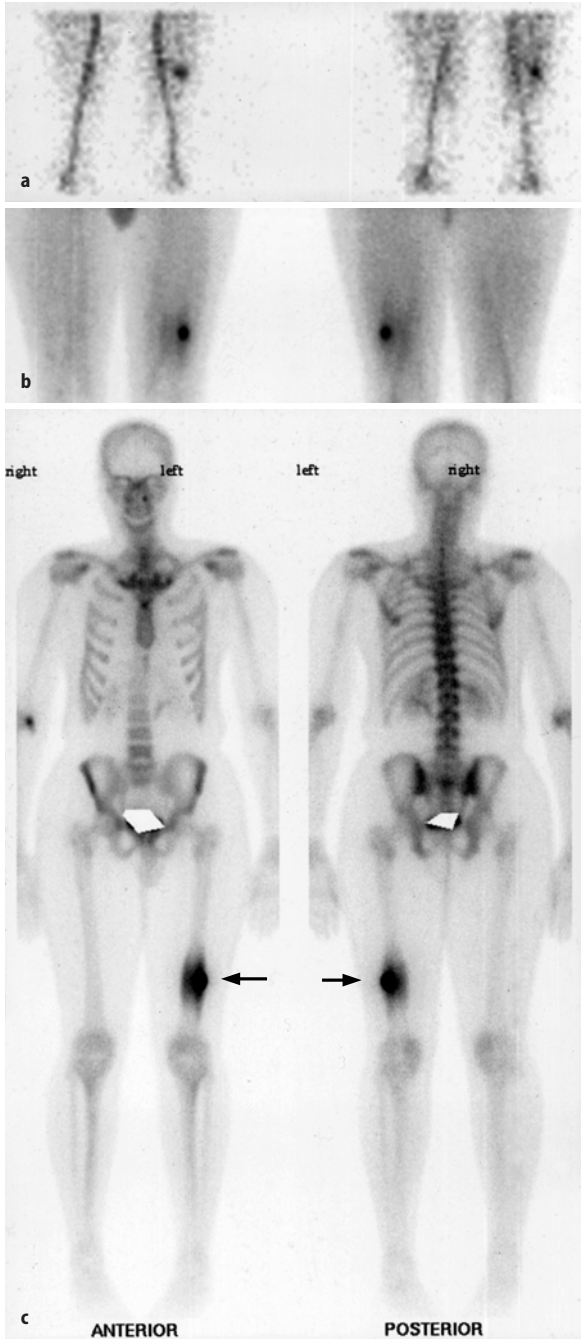

Fig. 6.55a–c. Flow (**a**), blood pool (**b**) and delayed (**c**) images of a patient with osteoid osteoma of the left femur showing intense flow and blood pool activity and on delayed images the specific pattern of double intensity (*arrow*)

Intra-articular and intramedullary osteoid osteomas present special problems. Joint effusion and lymphoproliferative synovitis, similar to that seen in rheumatoid arthritis, are often seen with intra-articular lesions and may suggest an arthritic condition, as may the relatively nonspecific symptoms often seen with these lesions and diagnosis may be delayed.

Fig. 6.56. Osteochondroma. Fourteen-year-old athletic male with pain and swelling of the left distal thigh for 1 week. The patient was referred to rule out trauma or heterotopic bone formation. The scan shows increased blood pool activity in the lateral aspect of the distal left femur representing the typical pattern of pedunculated osteochondroma

6.4.1.6.2 Osteoblastoma

As stated earlier this tumor is related to osteoid osteoma and affects most commonly the spine and lower extremities. Scintigraphically, osteblastoma shows intense uptake similar to osteoid osteoma. Radiographically, a pattern of lysis with or without a rim of surrounding sclerosis is characteristic. Extensive surrounding sclerosis is usually absent; however, surrounding inflammatory changes are often identified on MRI.

6.4.1.6.3 Osteochondroma

This tumor could appear as sessile/pedunculated (exostosis) or asessile. The lesions particularly the pedunculated have a central core of cancellous bone surrounded by a shell of cortical bone and covered by a cap of hyaline cartilage. It can be familial and multiple, forming the entity of hereditary multiple exostosis that is discovered in childhood. We encountered a case of this condition where the patient had more than 300 lesions, which showed a variable degree of uptake on bone scintigraphy [261]. Standard radiographs and CT scan usually are enough to detect the lesions; however, bone scan is particularly useful to detect multiplicity and to follow up patients with hereditary disease since there is a risk of malignant transformation in up to 30% of cases [262]. MRI delineates and assesses the thickness of cartilage cap and is useful in planning biopsy of the lesions. A cartilage cap 1.5 – 2 cm thick in a skeletally mature person is highly suggestive of malignant transformation. Scintigraphically a variable degree of uptake (Fig. 6.56) is seen, which may reflect the lesion's activity; however, active peripheral lesions particularly if small may not show enough uptake to be detected on bone scans [263 – 265].

6.4.1.6.4 Osteogenic Sarcoma

Scintigraphically, osteogenic sarcoma presents as an area of intense uptake (Fig. 6.57). Rarely, the tumor may present as a cold lesion [266]. CT and particularly MRI are superior to bone scan in evaluating the extent of the tumor. Bloem [267] evaluated the relative value of MRI, CT, ^{99m}Tc bone scintigraphy and angiography prospectively in local tumor staging in 56 patients with a primary bone sarcoma. MRI was significantly superior to CT and scintigraphy in defining intraosseous tumor lengths and as accurate as CT in demonstrating cortical bone and joint involvement. Additionally, MRI was superior to CT in demonstrating involvement of skeletal muscle. Bone metastases are extremely rare at presentation. McKillop et al. [268] found only one, out of 55 patients, presenting with bone metastases. On the other hand, during follow-up bone metastases developed in 20 patients who developed abnormal bone scan, but approximately half were asymptomatic. The authors concluded that initial bone scan yield is small but it is a justified procedure on presentation because the results may profoundly alter the treatment of the patient; it is indicated in all patients routinely during follow-up even if they are asymptomatic.

Bone scintigraphy is useful in detecting tumor recurrence. FDG-PET does not have an advantage over the bone scan in this task. However, it is more helpful and particularly useful in the follow-up of the response of the tumor to therapy [30, 31, 269, 270] (Fig. 6.58) ^{99m}Tc-MIBI and thallium-201 are also useful for this purpose and to predict the prognosis. Studies have suggested that P-glycoprotein (Pgp) expression is a prog-

Fig. 6.57. ^{99m}Tc-MDP whole body bone scan demonstrating osteogenic sarcoma, which showed intensely increased uptake (*arrow*)

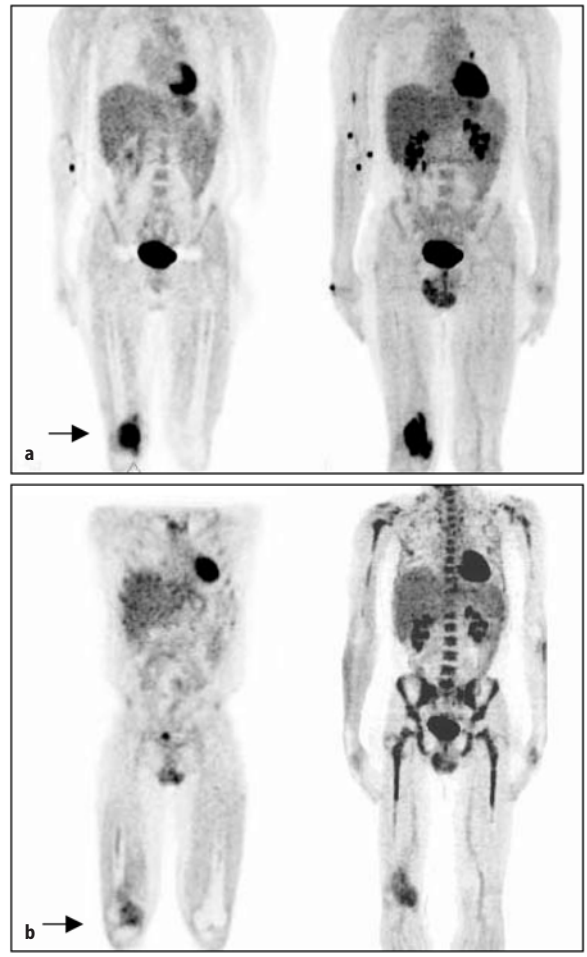

Fig. 6.58a,b. ^{18}F-FDG PET study of a patient with osteogenic sarcoma of the distal right femur showing increased uptake and SUV value of 9.6. **b** Follow-up study obtained after chemotherapy shows a significant decrease of the initial uptake with a drop of SUV to 4.2, indicating a good response

nostic factor for patients with osteosarcoma. Some investigators found a relationship between the wash-out rate of ^{99m}Tc-MIBI and the Pgp score, with a significant difference in wash-out rate being observed between patients with high and patients with low Pgp expression [271]. Others found that ^{99m}Tc-MIBI imaging is not an effective predictor of prognosis since the ^{99m}Tc-MIBI half-life and uptake ratio showed no correlation with histological necrosis following induction chemotherapy and did not correlate with P-glycoprotein expression [272]. Using thallium-201, the pattern of doughnut uptake was found to be a predictor of lower event-free survival in patients with extremity osteogenic sarcoma, but does not correlate with histologic response to therapy [273].

Since initial glucose metabolism of primary osteosarcoma is measured by ^{18}F-FDG PET using tumor to nontumor ratios, FDG-PET imaging provides prognostic information related to grading and estimating biologic aggressiveness. High ^{18}F-FDG uptake correlates with poor outcome and ^{18}F-FDG uptake may be complementary to other well-known factors in judging the prognosis in osteosarcoma [274].

6.4.1.6.5 Myeloma

Traditional staging of myeloma depends partially on the extent of the disease evaluated by full skeletal survey. The tumor presents on radiographs as osteolytic areas due to demineralization of bone by the tumor. ^{99m}Tc-MDP, ^{99m}Tc-MIBI and thallium-201 have all been used to image multiple myeloma as well as measurement of bone mineral density by dual energy X-ray absorptiometry [275, 276]. Bone scan is in general viewed to be unreliable for staging although a recent study reviewing the literature comparing the usefulness of conventional skeletal radiography and bone scans in diagnosing the osteolytic lesions of myeloma shows that bone scintigraphy,

considered by many to have no role in the detection of osteolytic lesions of myeloma, is in fact more sensitive than radiography in detecting lesions in the ribs, scapula, and spine [67]. Radiographs are also known to underestimate the extent of bone and bone marrow involvement [277]. Although cold areas are commonly seen on bone scans, increased uptake (Fig. 6.59) is the most common scintigraphic pattern [278, 279]. This should not contradict the fact that myeloma is the most common tumor to cause cold lesions on bone scan. For following up the disease, CT scan and MRI are the most useful but cannot determine the activity of the disease, ^{201}Tl- and ^{99m}Tc-MIBI have no clear role while PET has a promising role in this tumor.

6.4.1.6.6 Ewing's Sarcoma

As with other primary bone tumors, morphologic modalities including CT and MRI are the primary imaging modalities for assessing local extent of this primary tumor. Bone scan, however, is indicated when metastases need to be excluded. The detection of osseous metastases of Ewing's sarcoma, therapy monitoring and the diagnosis of recurrences are potentially useful clinical indications for FDG-PET [280]. FDG-PET was reported to detect more lesions of metastatic Ewing's sarcoma than bone and gallium scans, especially for those with bone marrow involvement [281]. ^{99m}Tc-MIBI was also used in this tumor to provide an imaging assessment of multiple-drug resistance. The presence or absence of ^{99m}Tc-MIBI uptake at diagnosis or after therapy was found to have no prognostic significance. ^{99m}Tc-MIBI was present in the two tumors that were P-glycoprotein positive and in only one of four tumors that were P-glycoprotein negative. ^{99m}Tc-MIBI imaging does not appear to be useful in Ewing's sarcoma [282].

6.4.2 Metastatic Bone Disease

Metastasis means "the transfer of disease from one organ or part to another not directly connected with it" [201]. In general, several events are required for the metastatic spread of tumors (Fig. 6.60). The sequence of these events is as follows:

1. Neoplastic cells separate from primary tumors.
2. They gain access to an efficient lymphatic channel or blood capillary.
3. They survive the transport.
4. They attach to the endothelium of a distant capillary bed.
5. They exit the vessel.
6. They develop a supporting blood supply for the cells at the new site.

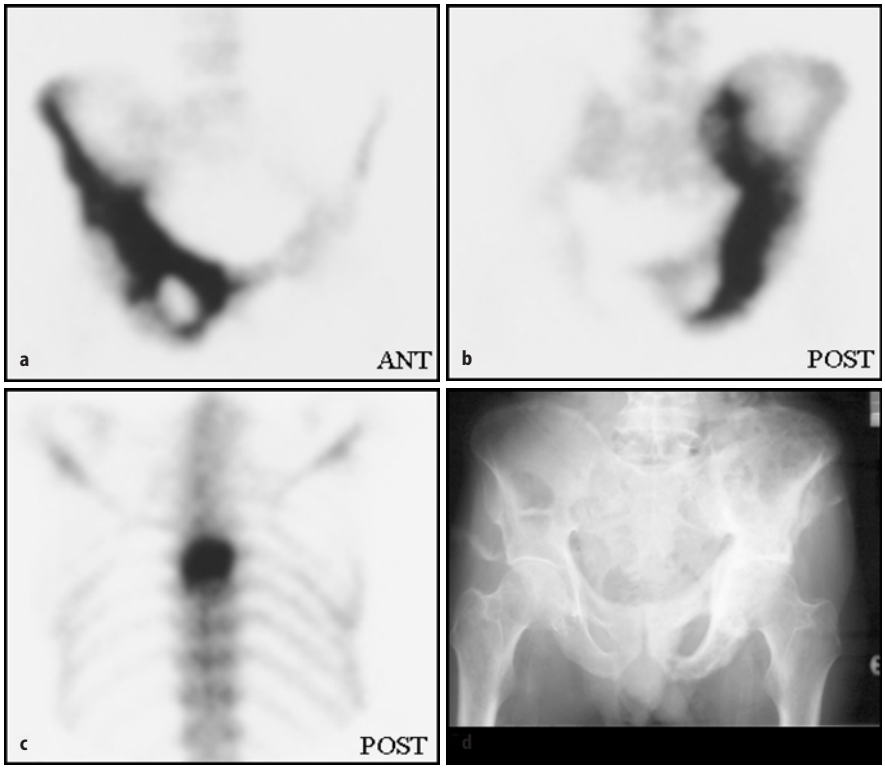

Fig. 6.59a–d. Selected spot images (**a–c**) of a bone scan of a patient with known multiple myeloma show areas of increased uptake at the sites of tumor. X-ray of the pelvis (**d**) shows the tumor corresponding to the increased uptake of the left iliac bone. Note that all lesions depicted have increased uptake and the patient had no history of trauma or pathologic fractures

The pathophysiology of skeletal metastases includes two major events, transport of viable tumor cells to bone and interaction of these cells with osseous tissue.

6.4.2.1 Methods of Tumor Cell Transport

In addition to direct extension, tumor cells are transported to produce metastases by:

Lymphatic Spread. Lymphatic spread is relatively unimportant for the transport of tumor cells to distant bones. However, metastases in regional draining lymph nodes may secondarily involve the adjacent bones.

Hematogenous Spread. Hematogenous spread is a major way of transporting malignant cells to the skeleton; it may happen through the arterial system or through the venous system, particularly the vertebral plexus of the veins of Batson [284]. The relative roles of the arterial and venous systems in the spread of tumor to bone are difficult to define. Metastases occur predominantly in the axial skeleton (specially the spine) and may be present in the absence of pulmonary and other organ involvement, a combination of findings which supports the significance of Batson's vertebral plexus in tumor spread. This vertebral plexus consists of an intercommunicating system of thin-walled veins with low intraluminal pressure. These veins frequently are without valves and lie outside the thoracoabdominal cavity. The plexus has extensive communication with veins (Fig. 6.61) in the spinal canal and with the caval, portal, intercostal, pulmonary, and renal systems [285].

Intraspinal Spread. Intraspinal dissemination allows secondary deposits in the spinal canal to develop in patients with intracranial tumors. This occurs by subarachnoid spread, secondary to fragmentation of a tumor bathed with cerebrospinal fluid, shedding of portions of the tumor at the time of surgery, ependymal breaching by the primary intracranial tumor, or fissuring secondary to hydrocephalus [285]. Dissemination of intracranial neoplasms via the cerebrospinal fluid represents only one of the mechanisms of spread of metastatic foci to the spinal cord. Arterial, venous, and direct extension pathways are additional routes.

6.4.2.2 Bone Response to Metastases

Hematogenous metastasis in human beings generally begins in the medullary cavity and then involves the cortex. Accordingly, intramedullary injection of tumor cell suspension is used experimentally. There are two types of osseous response to metastasis:

1. Bone resorption
   There is increased bone resorption secondary to malignant disease. Osteoclasts, tumor cells, tumor cell extracts, monocytes, and macrophages may all be involved in the process [286, 287].

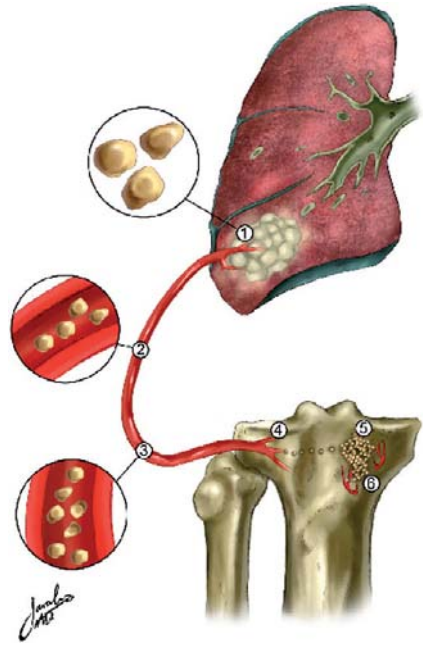

Fig. 6.60. Events required for metastatic spread: *1* separation of cells from primary tumor; *2* access of separated cells to an efficient lymph channel or blood cap; *3* survival of cells during transport; *4* successful attachment of cells to the endothelium of a distant cap bed; *5* exit of cells from vessel at new site; *6* successful development of a supporting blood supply

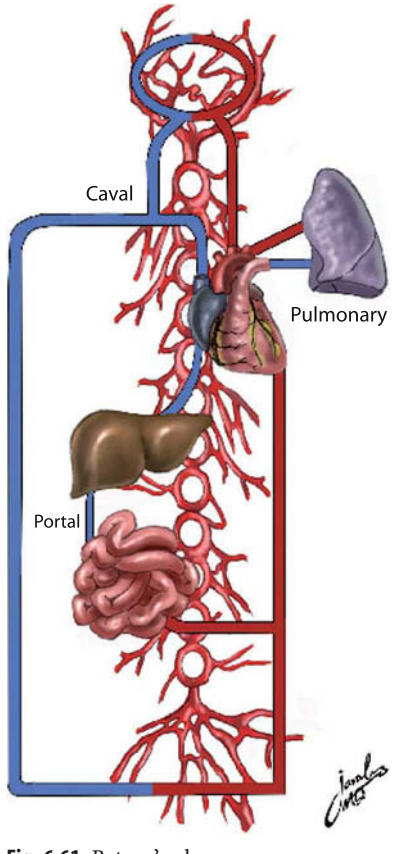

Fig. 6.61. Batson's plexus

2. Bone formation
   This response to tumor occurs in two ways:
   a) Stromal bone formation is the earlier, and quantitatively less important, mechanism of bone formation associated with metastasis. In this type of bone formation intramembranous ossification takes place in areas of fibrous stroma within the tumor. This occurs only in those skeletal metastases which are associated with the development of fibrous stroma, such as carcinoma of the prostate. Highly cellular tumors have little or no stroma and are not accompanied by this type of bone formation.
   b) Reactive bone formation occurs in response to bone destruction. Immature woven bone is deposited and subsequently converted to lamellar bone. In highly anaplastic, rapidly growing tumors, lymphomas, myelomas, or leukemias, the active bone formation may be only minor or insignificant [287].

6.4.2.3 Distribution of Bone Metastases

The distribution of skeletal metastases varies with the type of primary malignant tumor and age (Fig. 6.62). However, metastases typically involve the axial skeleton, which is the region rich in red bone marrow (Fig. 6.63). Factors favoring the predominant involvement of the red marrow include a large capillary network, a sluggish blood flow, and the suitability of this tissue for the growth of tumor emboli. It is estimated that blood flow is 5 – 13 times higher to cancellous bone containing marrow than to cortical bone [288]. In decreasing order, the usual locations of bone metastases are the vertebral column, pelvic bones, ribs, sternum, femoral and humeral shaft, and skull. Less common sites of skeletal metastases include the mandible, patella, and the bones of the extremities distal to the elbows and knees.

The involvement of the spine as the most common site by metastasis can be explained by:

- The fact that Batson's venous plexus provides direct communication between the spine and numerous other locations in the body
- The large amount of bone mass

Within the spine, the thoracic and cervical areas involving the lumbar region are the most commonly affected. Within the vertebra, metastases are more common in the vertebral body than in the posterior elements. Possible explanations for the low frequency of metastases in the distal portion of the extremities are:

1. The blood supply, which is essentially limited to the arterial route
2. The relative absence of red marrow, which is a suitable soil for the growth of metastatic tumor cells

6.4.2.4 Classification of Bone Metastases

Bone metastases can be classified on the basis of several factors, including number of lesions, location, calcium content (as seen on radiographs), and patterns of bone response. The skeleton might at times respond to the various metastatic foci of a tumor in a uniform manner. However, this is not constant. Sometimes bone metastases show, for example, purely osteoblastic or mixed osteoblastic/osteolytic lesions in certain sites and pure-

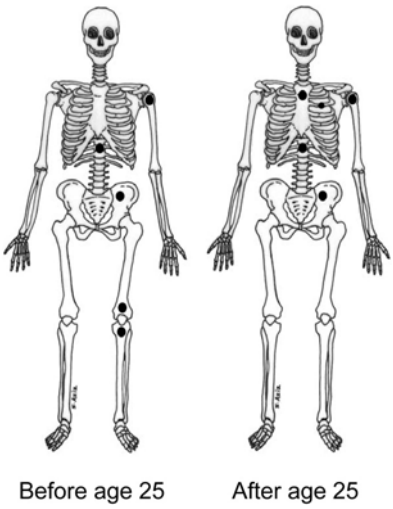

Fig. 6.62. Distribution of bone metastases according to age

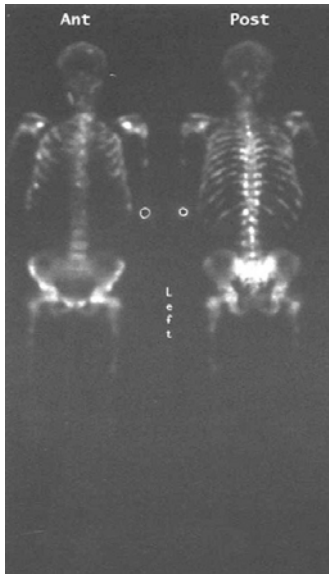

Fig. 6.63. A whole body bone scan with metastatic bone disease distributed axially illustrating the most common sites and corresponding to the axial skeleton

ly osteolytic lesions in others. Based on the pattern of bone response, metastases can be classified as:

- Purely osteolytic: typically arising from carcinomas of the thyroid, kidney, adrenal, uterus, and gastrointestinal tract
- Purely osteoblastic: arising from carcinoma of the prostate and less often from bronchial carcinoid, carcinoma of the nasopharynx and stomach, neuroblastomas, and medulloblastomas
- Mixed osteolytic/osteoblastic: arising from carcinomas of the breast, lung, cervix, ovary, and testis

6.4.2.5 Sources of Bone Metastases

Since the vast majority of metastatic bone lesions appear in the middle and older age-groups, certain tumors are known to be common sources of bone metastases. The following primary tumors are the most common to metastasize to bone: prostate, breast, kidney, lung, and thyroid. Bladder and uterine carcinomas are less common sources.

In children, skeletal metastases come from neuroblastoma, Ewing's sarcoma, and osteosarcoma. In men, carcinoma of the prostate accounts for 60% of bone metastases while in women, breast cancer accounts for 70% of such metastases. The following is a brief presentation of the relevant pathological considerations concerning the major sources of skeletal metastases.

Breast Cancer. Breast cancer is a common source of skeletal metastases. The average incidence of metastases is low at less than 5% in clinical stages 1 and 2, although it ranges from 0% to 40%. In clinical stage 3, the incidence of bone metastases is 20% – 45%. The tumor usually produces osteolytic or mixed osteolytic/osteoblastic lesions. Rarely, breast cancer gives rise to only osteoblastic lesions. The bone metastases develop most rapidly during the first 2 years. Pain is not a good predictor of bone metastases, since such metastases are found in asymptomatic breast cancer patients and in only 60% of patients with constant pain [289 – 292].

Prostate Cancer. Prostate cancer is also a common source of bone metastases that are characteristically osteoblastic. Metastases to bone are found in 8% – 35% of patients at the time of diagnosis. Bone scintigraphy has a crucial role in detecting metastases since it is more sensitive than other imaging and laboratory modalities. Pain has a low predictive value in their detection.

Lung Cancer. Lung cancer produces skeletal metastases in three ways: (a) via lymphatic spread to mediastinal nodes with direct extension to bone; (b) via lymphatic spread to para-aortic nodes, followed by direct extension to bone; (c) via invasion of pulmonary veins, followed by transport of tumor through the arterial circulation to any part of the skeleton, including the appendicular. The lesions are predominantly osteolytic and mixed, although only osteoblastic lesions can occur in a minority of cases, particularly those with small cell and adenocarcinoma. Among the four major types of lung cancer, small cell is the most aggressive, followed by large cell and adenocarcinoma, squamous cell being the least aggressive [285].

Renal Cell Carcinoma. Renal cell carcinoma produces skeletal metastases rather commonly. Although symptoms related to metastases might be the presenting feature, these symptoms are inconsistent and pain is not a reliable predictor. The tumor produces skeletal metastases through: (a) lymphatic channels to para-aortic, hilar, paratracheal, and/or mediastinal nodes with invasion of bone later; (b) invasion of renal veins which lead to the inferior vena cava, right atrium, and then pulmonary vessels, to be disseminated to bones. The metastatic lesions are predominantly osteolytic and in some cases expansile [292, 293].

6.4.2.6 Sequelae of Skeletal Metastases

Local consequences include:

1. Pathological fractures
   Metastases cause weakening of the involved bones and may lead to fractures in the vertebrae (compression fractures) or long bones, most commonly affecting the proximal portion of the femur [293].
2. Periosteal new bone formation
   In general, periosteal reaction due to metastases is minimal if present compared with significant new bone formation in association with primary bone tumors.
3. Soft tissue extension
   Soft tissue masses may infrequently present regionally in association with metastases. This occurs particularly with rib lesions in association with myeloma and in the pelvis in association with colon cancer.
4. Bone expansion
   This occur with both osteolytic and osteoblastic lesions. Carcinomas of the prostate, kidney, and thyroid and hepatocellular carcinoma are particularly known to cause expansile metastatic lesions.

Generalized or metabolic consequences include:

1. Hypercalcemia
   This can be associated with metastases due to destruction of bone, but also with primary tumors not associated with skeletal metastases. Hypercalcemia occurs in up to 20% of cancer patients.

2. Hypocalcemia
   An unidentified humoral substance capable of stimulating osteoclasts in some cancer patients with skeletal metastases is proposed to be the underlying mechanism behind the presence of hypocalcemia in up to 16% of cancer patients.
3. Osteomalacia
   In some patients with skeletal metastases, depressed levels of 1,25-hydroxyvitamin D_3, hypocalcemia, and hypophosphatemia are recognized and associated with generalized weakness and pain of bones and muscles (oncogenic osteomalacia).

6.4.2.7 Imaging of Metastatic Bone Disease

In general, four main modalities are routinely utilized clinically to assess bone, the third most common site of metastatic diseases, for existence of metastatic lesions. These modalities include standard radiography, CT scan, bone scintigraphy and MRI [294].

6.4.2.7.1 Appearance of Bone Metastases on Bone Scan

Bone scan is the most widely used modality and is the most practical and cost effective screening technique for assessing the entire skeleton. In addition, bone scan is very sensitive in detecting the disease. However, there is a variable false-negative rate in assessing lesions in certain locations particularly in the spine and in those confined to bone marrow [295]. On bone scans, metastases have different patterns:

Typical Pattern. The most common and typical pattern of bone metastases is that of multiple, randomly distributed foci of increased uptake (Fig. 6.64), usually in the axial skeleton, following the distribution of certain bone marrow including the shoulder girdle, with relatively less extensive involvement of the ribs. Multiple fractures and multifocal infection may simulate this pattern. The following hematogenously disseminated infections of bone and other pathologic conditions [296] can cause a pattern that may mimic metastases:

1. Tuberculosis
2. Atypical mycobacteria
3. Coccidioidomycosis
4. Tertiary syphilis
5. Brucellosis
6. Sarcoidosis
7. Multiple fractures

Atypical patterns include:

1. Solitary lesions
   These occur in the axial and in the appendicular skeleton in a variable percentage of patients (Fig. 6.65). The incidence of malignancy in solitary lesions varies with the location. The incidence is highest in the vertebrae. These lesions are commonly asymptomatic and are not suspected clinically. Less than half of these lesions are evident on

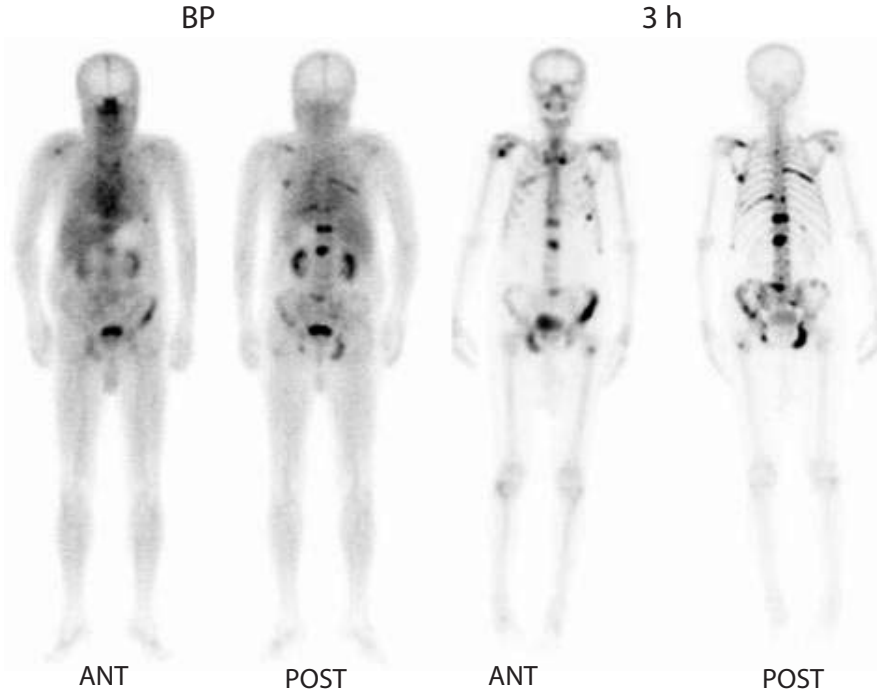

Fig. 6.64. Whole body blood pool and delayed scans of a 77-year-old male with advanced carcinoma of the prostate. PSA 99 ng/µl. Patient was referred to rule out metastases. The scan shows the typical pattern of metastatic bone diseases of randomly distributed foci of increased uptake

X-rays. These facts further emphasize the importance of obtaining a bone scan of the entire skeleton routinely in patients with cancer.

2. Cold lesions
   Aggressive tumors may cause cold lesions at the time of presentation (Fig. 6.66). This is seen frequently in multiple myeloma and renal cell carcinoma, although the most common pattern of multiple myeloma on bone scan is hot spots [297].
3. Equilibrium pattern
   Hot lesions may have a relatively normal appearance with time, reflecting a point of equilibrium between osteoblastic activity and the bone destruction by the tumor. It appears that some skeletal lesions may evolve through increased uptake, the equilibrium phase, and then decreased uptake. The second phase can result in minimal abnormalities of focal, nonuniform, minimally increased uptake, or even near normal patterns that can be missed on scan. This phenomenon has been observed and studied particularly in rib lesions [298].
4. Diffuse pattern
   With advanced metastatic disease, the entire axial skeleton may be involved by a load of tumor cells causing increased extraction of radiopharmaceutical. This pattern may be interpreted as normal depending on the display intensity and should also be differentiated from other causes of diffusely increased uptake in the skeleton (superscan) such as hyperparathyroidism, and other metabolic bone diseases (Fig. 6.67) such as Paget's disease (Table 6.20).

A superscan secondary to metastases shows increased uptake that is usually confined to the axial skeleton with common sparing of the skull, while in the case of metabolic disorders it also involves the skull, mandible, sternum, and metaphyses of long bones. Preferential increase of uptake at the osteochondral junctions and joint renal activity are additional features of metabolic disease on superscans.

5. Flare pattern
   Therapy producing healing at the tumor site results in several pathological changes as seen on scintigraphy. As the term healing implies, inflammatory changes with increasing blood flow occur early after therapy. Since the tumors are in bones, reactive bone formation increases with successful therapy [299].

Following radiation therapy increased activity on blood pool images and delayed images may be seen early on due to inflammatory reaction. Later, these changes disappear and decreased uptake is typically seen. It should be noted that the effects of therapeutic radiation depend on the time after treatment and the dose.

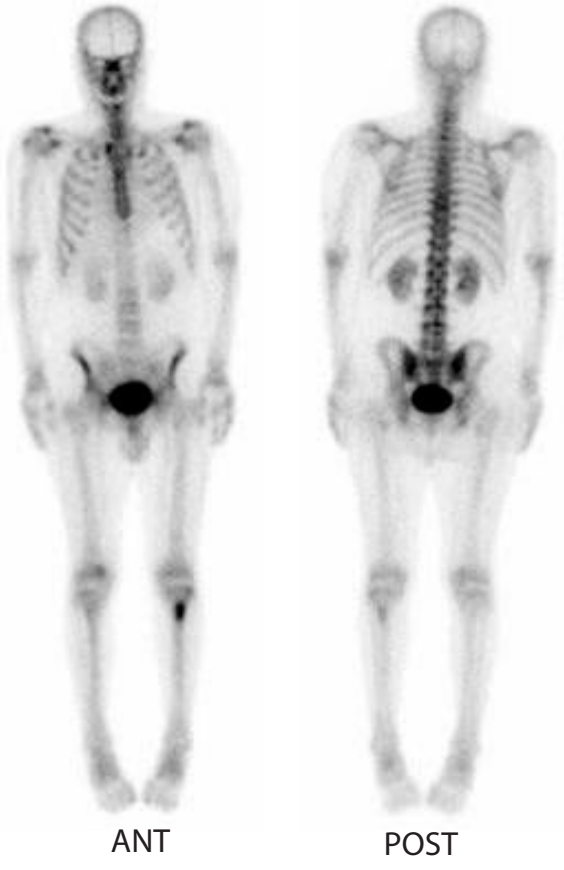

Fig. 6.65. Sixty-three-year-old male with increased alkaline phosphatase and fever. Solitary bone lesion in the left tibia proven to be metastatic

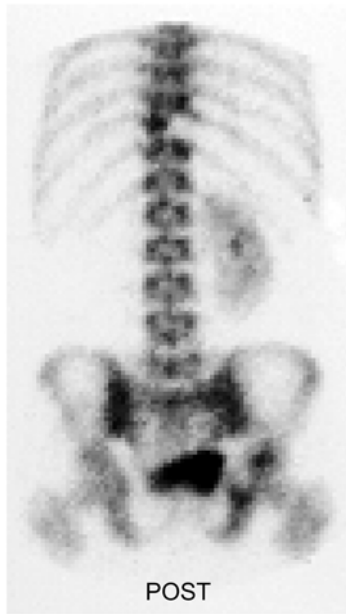

Fig. 6.66. A spot image of a patient with renal cell carcinoma. There is a focus of absent uptake in the right side of T-11 representing "cold" metastatic pattern that is common with certain aggressive tumors including renal cell carcinoma

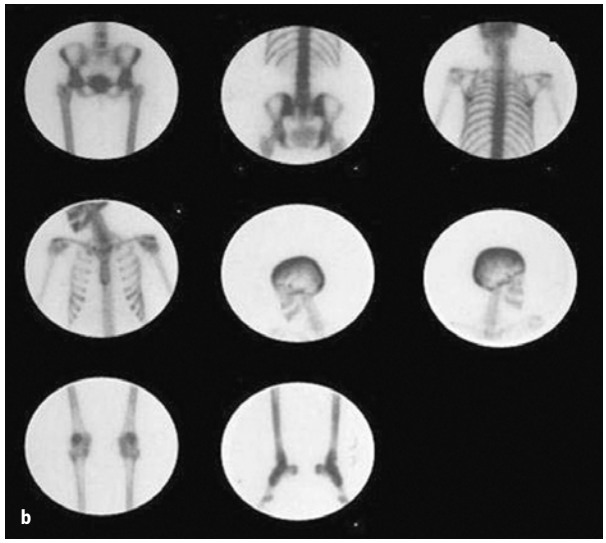

Fig. 6.67. a A whole body bone scan illustrating the pattern of diffuse metastases (superscan). Note that the appendicular bones are essentially not involved compared to the pattern of superscan secondary to metabolic bone disease as illustrated in a patient with renal failure (**b**). In this case the increased uptake extends to appendicular bones even distally

Table 6.20. Causes of diffuse increase of radiopharmaceutical uptake by the skeleton

1. Advanced metastatic bone disease
2. Metabolic bone disease
   - Primary and secondary hyperparathyroidism
   - Hypertrophic osteoarthropathy
   - Renal osteodystrophy
   - Paget's disease
3. Others
   - Acromegaly
   - Aplastic anemia
   - Hyperthyroidism
   - Leukemia
   - Waldenström's macroglobulinemia
   - Myelofibrosis
   - Hypervitaminosis D

Follow-up scans are more frequently obtained after chemotherapy than after radiation therapy and the changes that are seen continue for longer periods. Early increased activity on blood pool and delayed images are noted, followed by decreasing activity that can be normalized. Increasing activity may be significant and continue for several months even with successful therapy. This phenomenon may include the appearance of small, new lesions due to healing at the sites of preexisting small or cold lesions that were not resolved on earlier scans

6. Symmetrical pattern
   Occasionally symmetrical uptake due to metastases is seen in certain tumors as neuroblastoma and in the case of bone marrow involvement in leukemia. This pattern is particularly seen in distal femoral and proximal tibial metaphyses.

Table 6.21 summarizes the important correlation between common pathological changes of bone and the scintigraphic findings on bone scan.

Table 6.21. Scintigraphic pathological correlation

Pathological etiology	Scintigraphic pattern on bone scan
Osteoblastic response	Increased uptake
Increased vascularity	Increased flow and blood pool activity
Angiogenesis	Increased blood pool activity
Bone destruction (infarction, rapidly growing aggressive metastasis)	Cold areas
Large destructive lesion with a rim of new bone formation	Doughnut pattern
Paget's disease, some primary or metastatic tumors	Bone expansion
Arthritis, reflex sympathetic dystrophy	Periarticular increased uptake
Equilibrium of bone destruction and bone formation	Near normal appearance

6.4.2.7.2 Imaging Metastases with Other Modalities

MRI has been found to detect more vertebral metastases than bone scan [300, 301]. PET is increasingly being evaluated for detection of bone metastases (Fig. 6.68) and the initial experience is promising; it has been shown by several studies to be more sensitive than bone scan, though not fully supported [302–305]. In a comparative study, the diagnostic accuracy of whole-body MR imaging, bone scintigraphy, and FDG PET for the detection of bone metastases in children was determined. Twenty-one patients exhibited 51 bone metastases. Sensitivities for the detection of bone metastases were 90%, 82% and 71% for FDG PET, whole-body MR imaging and bone scintigraphy, respectively. False-

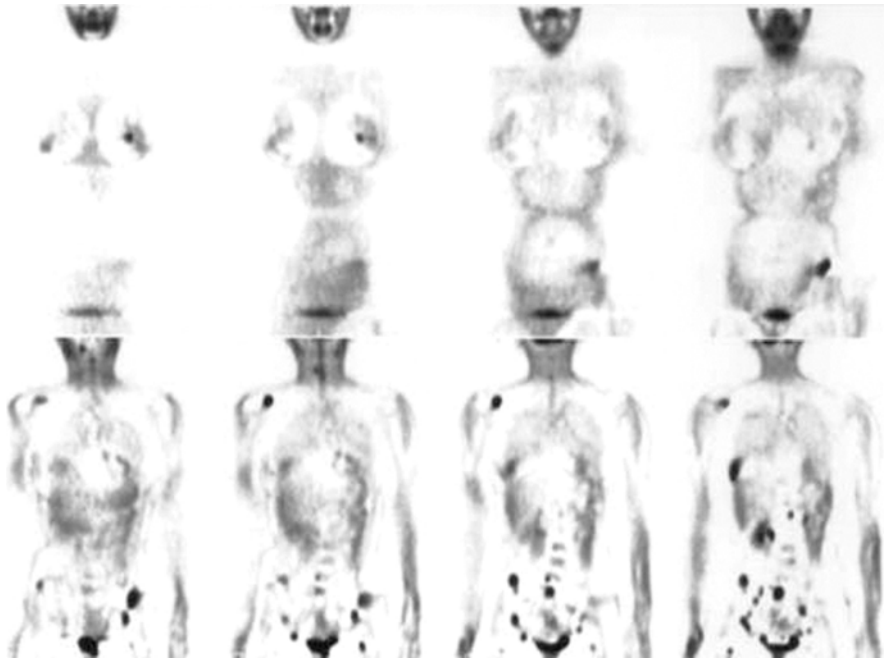

Fig. 6.68. ^{18}F-FDG PET scan showing multiple metastases in the axial skeleton in a patient with recurrent breast cancer

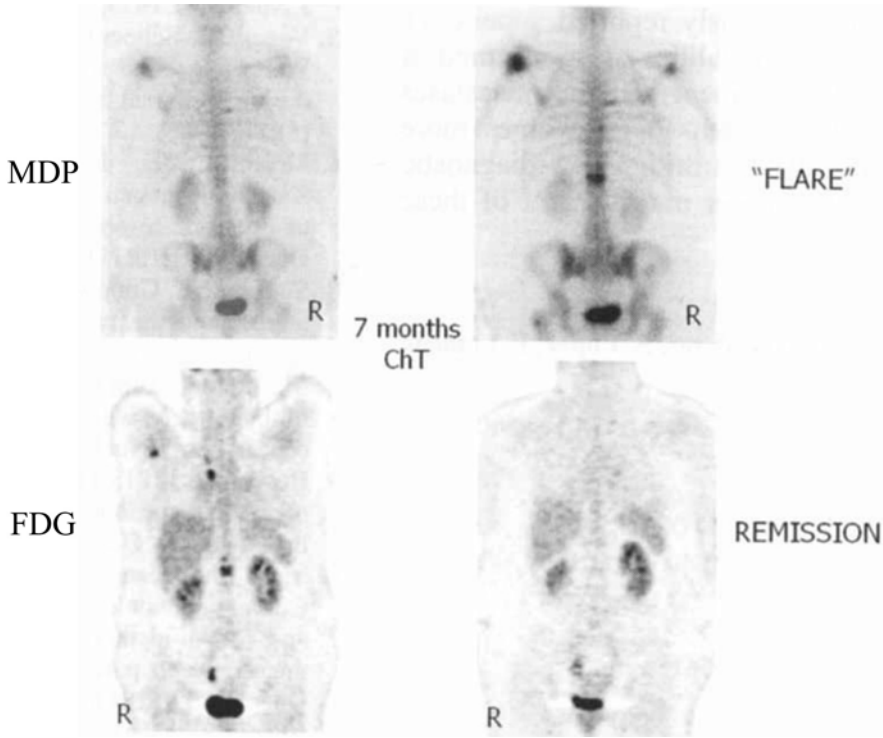

Fig. 6.69. A 49-year-old woman with breast cancer (N1M0) who had undergone mastectomy and axillary lymph node dissection on the right side. The patient had had no evidence of disease for 3 years. She presented with an in CA 15.3 tumor marker. BS showed uptake in the left humeral head suspicious of necrosis on the basis of long-term corticotherapy and nonspecific uptake in the spine (*top left*). PET showed intense FDG uptake in both the humeral head and the seventh right costovertebral junction and first lumbar vertebra (*bottom left*). The patient was treated with chemotherapy. Seven months after treatment, BS showed persistent uptake in the left humeral head with increased activity in the right humeral head, seventh right costovertebral junction and first lumbar vertebra (*top right*). PET scan showed resolution of the previous lesions (*bottom right*). On the basis of the PET findings, the results on BS should be interpreted as representing a flare phenomenon. (From [306] with permission)

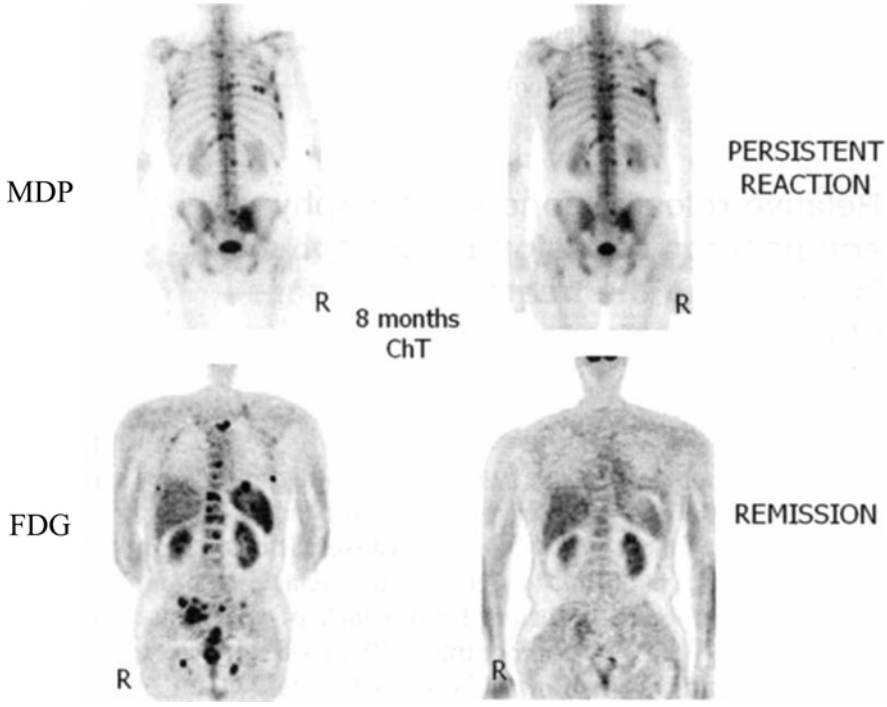

Fig. 6.70. A 55-year-old man recently diagnosed with non-small right lung cell cancer. BS (*top left*) and PET (*bottom left*) in the staging showed multiple bone metastases, with a different distribution, probably due to the lytic/blastic behavior. The patient was treated with chemotherapy. Eight months after treatment, BS remained similar (*top right*). PET scan showed resolution of previous lesions (*bottom right*). On the basis of the PET findings, BS results should be interpreted as representing a persistent bone reaction, not active metastatic disease. (Figure printed with permission from [306])

Table 6.22. Summary of the role of PET in malignant bone disease

1. Evaluate response to therapy of primary or metastatic bone disease
2. Detection of recurrence of primary bone malignancies
3. Early differentiation of progression and flare of metastatic bone disease seen on bone scan
4. Evaluate solitary bone-lesion
5. Detection of metastatic bone disease

negative lesions were different for the three imaging modalities, mainly depending on lesion location. Most false-positive lesions were seen with FDG PET [302]. Another study of 56 patients with malignant lymphoma also showed that FDG PET is more sensitive but, in contrast, more specific than bone scintigraphy [304]. It is important to remember that PET provides direct visualization of metastases while bone scan visualizes the reactive bone in response to the presence of metastases. FDG PET can help differentiate flare from progression and evaluate the tumor status when bone scan is stable [306] (Figs. 6.69, 6.70). Table 6.22 summarizes the role of PET in primary and metastatic bone disease.

References

1. Mourad LA (1998) Structure and function of the musculoskeletal system. In: McCane KL, Huether SE (eds) Pathophysiology, 3rd edn. Mosby, Philadelphia, pp 1405 – 1434
2. Suzuki R, Domon T, Wakita M (2000) Some osteocytes released from their lacunae are embedded again in the bone and not regulated by osteoclasts during remodeling. Anat Embryol 202:119 – 128
3. Gillespy T III, Gillespy MP (1991) Osteoporosis. Radiol Clin North Am 29:77 – 84
4. Boskey AL (1981) Current concepts of the physiology and biochemistry of calcification. Clin Orthop 157:225
5. Tondevold E, Eliasen P (1982) Blood flow rates in canine cortical and cancellous bone measured with Tc99m labeled human albumin microspheres. Acta Orthop Scand 53:7 – 11
6. McCarthy EF (1997) Histopathologic correlates of positive bone scan. Semin Nucl Med 27:309 – 320
7. Dalinka MK, Aronchick JM, Haddad JG (1983) Paget's disease. Orthop Clin North Am 4:3 – 19
8. Vogler JB, Murphy WA (1988) Bone marrow imaging. Radiology 168:679 – 693
9. Francis MD, Horn PA, Tofe AJ (1981) Controversial mechanism of technetium-99m deposition on bone (abstract). J Nucl Med 22:72
10. Francis MD, Slough CL, Tofe AJ, Silberstein EB (1976) Factors affecting uptake and retention of technetium-99m-diphosphonate and technetium 99m pertechnetate in osseous, connective and soft tissues. Calcif Tissue Res 20:303 – 311
11. Haas DW, McAndrew M (1996) Bacterial osteomyelitis in adults: evolving considerations in diagnosis and treatment. Am J Med 101:550 – 561
12. Cierny G, Mader JT, Pennick H (1985) A clinical staging system of adult osteomyelitis. Contemp Orthop 10:17 – 37
13. Mandell GA (1996) Imaging in the diagnosis of musculoskeletal infections in children. Curr Probl Pediatr 26:218 – 237
14. Mader JT, Dhraminder M, Calhoun J (1997) A practical guide to the diagnosis and management of bone and joint infections. Drugs 54:253 – 264
15. Bonakdar-pour A, Gaines VD (1983) The radiology of osteomyelitis. Orthoped Clin North Am 14:21 – 37

16. Lee DP, Waldvogel FA (2004) Osteomyelitis. Lancet 364: 369 – 379
17. Trueta J (1959) The three types of acute hematogenous osteomyelitis: a clinical and vascular study. J Bone Joint Surg 41B:671 – 680
18. Elgazzar AH, Abdel-Dayem HM (1999) Imaging skeletal infections: evolving considerations. In: Freeman LM (ed) Nuclear medicine annual. Lippincott Williams and Wilkins, Philadelphia, pp 157 – 191
19. Elgazzar AH, Abdel-Dayem HM, Clark J, Maxon HR (1995) Multimodality imaging of osteomyelitis. Eur J Nucl Med 22:1043 – 1063
20. Torda AJ, Gottlieb T, Bradbury R (1995) Pyogenic vertebral osteomyelitis: analysis of 20 cases and review. Clin Infect Dis 20:320 – 328
21. Song KS, Ogden JA, Ganey T, Guidera KT (1997) Contiguous discitis and osteomyelitis in children. J Pediatr Orthop 17:470 – 477
22. Ring D, Wenger DR, Johnson C (1994) Infectious spondylitis in children. The convergence of discitis and vertebral osteomyelitis. Orthop Trans 18:97 – 98
23. Waldvogel FA, Vasey H (1980) Osteomyelitis: the past decade. N Engl J Med 303:360 – 370
24. Babinchak TJ, Riley DK, Rotheram EB (1997) Pyogenic vertebral osteomyelitis of the posterior elements. Clin Infect Dis 25:221 – 224
25. Bauer TM, Pipperet H, Zimmerli W (1997) Vertebral osteomyelitis caused by group B streptococci [streptococcus agalactial] secondary to urinary tract infection. Eur J Microbial Infect Dis 16:244 – 246
26. Perrone C, Saba J, Behloul Z, Salmon-Ceron D, Leport C, Vilde JL, Kahn MF (1994) Pyogenic and tuberculous spondylodiskitis [vertebral osteomyelitis] in 80 adult patients. Clin Infect Dis 19:746 – 750
27. Forrest RD, Jacobson CA, Yudkin JS (1986) Glucose intolerance and hypertension in north London: the Islington diabetes survey. Diabet Med 3:338 – 342
28. Bamberger DM, Daus GP, Gerding DN (1987) Osteomyelitis in the feet of diabetic patients: long term results, prognostic factors, and the role of antimicrobial and surgical therapy. Am J Med 83:653 – 660
29. Schwartz GS, Berenyi MR, Siegel MW (1969) Atrophic arthropathy and diabetic neuritis. AIR 106:523 – 529
30. Horwitz SH (1993) Diabetic neuropathy. Clin Orthop 296:78 – 85
31. Gold RH, Tang DTF, Crim JR, Seeger LL (1995) Imaging the diabetic foot. Skeletal Radiol 24:563 – 571
32. Rand JA (1995) Preoperative planning for total knee arthroplasty. In: Callaghan JJ, Dennis DA, Paprosky WG, Rosenberg AG (eds) Orthopedic knowledge update. Hip and knee reconstruction. American Academy of Orthopedic Surgeons, Rosemont, IL
33. American Academy of Orthopaedic Surgeons (1995) Proceedings of the American Academy of Orthopaedic Surgeons. AAOS, Rosemont, IL, pp 255 – 263
34. Griffiths HJ (1995) Orthopedic complications. Radiol Clin North Am 33:401 – 410
35. Seabald JE, Nepola JV (1999) Imaging techniques for evaluation of postoperative orthopedic infections. Q J Nucl Med 43:21 – 28
36. Harris WH, Sledge CB (1990) Total hip and total knee replacement, part I. N Engl J Med 323:725 – 731
37. Harris WH, Sledge CB (1990) Total hip and total knee replacement, part II. N Engl J Med 323:801 – 807
38. Johnson JA, Christle MJ, Sandler MP, Parks PF Jr, Horma L, Kayle JJ (1988) Detection of occult infection following total joint arthroplasty using sequential technetium-99m HDP bone scintigraphy and indium-111 WBC imaging. J Nucl Med 29:1347 – 1353
39. Hendrix RW, Anderson TM (1981) Arthrographic and radiologic evaluation of prosthetic joints. Radiol Clin North Am 19:349 – 364
40. Griffiths HJ, Lovelock JE, Evarts CM (1984) The radiology of total hip replacement. Skel Radiol 12:1 – 11
41. Barton LL, Dunkle LM, Habib FH (1987) Septic arthritis in childhood: a 13-year review. Am J Dis Child 141:898 – 900
42. Welkon CJ, Long SS, Fisher MC, Alburger PD (1986) Pyogenic arthritis in infants and children: a review of 95 cases. Pediatr Infect Dis 5:669 – 676
43. Silberstein EB, Elgazzar AH, Fernandez-Uloa M, Nishiyama H (1996) Skeletal scintigraphy in non-neoplastic osseous disorders. In: Henkin RE, Bles MA, Dillehay GL, Halama JR, Karesh SM, Wagner PH, Zimmer AM (eds) Textbook of nuclear medicine. Mosby, New York, pp 1141 – 1197
44. Waldvogel FA, Medoff G, Swartz MN (1970) Osteomyelitis: a review of clinical features, therapeutic considerations and unusual aspects, part I. N Engl J Med 282:198 – 206
45. Handmaker H. Leonards R (1976) The bone scan in inflammatory osseous disease. Semin Nucl Med 6:95 – 105
46. Connolly LP, Connolly SA, Drubach LA, Jaramillo D, Treves ST (2002) Acute hematogenous osteomyelitis of children: assessment of skeletal scintigraphy-based diagnosis in the era of MRI. J Nucl Med 43:1310 – 1316
47. Tuson GE, Hoffman EB, Mann MD (1994) Isotope bone scanning for acute osteomyelitis and septic arthritis in children. J Bone Joint Surg (Br) 76B:306 – 310
48. Handmaker H, Giammona ST (1984) Improved early diagnosis of acute inflammatory skeletal – articular diseases in children: A two radiopharmaceutical approach. Pediatrics 73:661-669
49. Sfakianakis GN, Scoles P, Welch M, et al (1978) Evolution of the bone imaging findings in osteomyelitis. J Nucl Med 19:706
50. Pennington WT, Mott MP, Thometz JG, Sty JR, Metz D (1999) Photopenic bone scan osteomyelitis: A clinical perspective. J Ped Orthoped 19:695 – 698
51. Johnson JE, Kennedy EJ, Shereff MJ, Patel NC, Collier BD (1996) Prospective study of bone, In-111 labeled white blood cell and gallium scanning for the evaluation of osteomyelitis in the diabetic foot. Foot Ankle Int 17:10 – 16
52. Grerand S, Dolan M, Laing P, Bird M, Smith ML, Klenerman L (1996) Diagnosis of osteomyelitis in neuropathic foot ulcers. J Bone Joint Surg (Br) 78B:51 – 55
53. Ezuddin S. Yuille D, Spiegelhoff D (1992) The role of dual bone and WBC scan imaging in the evaluation of osteomyelitis and cellulitis using both planar and SPECT imaging. J Nucl Med 33:839
54. Seabold JE, Nepola JV, Marsh JL et al (1991) Postoperative bone marrow alterations: potential pitfalls in the diagnosis of osteomyelitis with In-111-labeled leukocyte scintigraphy. Radiology 180:741 – 747
55. Palestro CJ, Swyer AI, Kim CK et al (1991) Infected knee prosthesis: diagnosis with In-111 leukocyte, Tc-99m sulfur colloid and Tc-99m MDP imaging. Radiology 1179:645 –648
56. Bihl H, Rossler B, Borr U (1992) Assessment of infectious conditions in the musculoskeletal system: experience with Tc-99m HIG in 120 patients. J Nucl Med 33:839
57. Hakki S, Harwood SJ, Morrissey MA, et al (1997) Comparative study of monoclonal antibody scan in diagnosing orthopedic infection. Clin Orthop 335:275 – 285
58. Harwood SJ, Valsivia S, Hung GL, et al (1999) Use of Saluesomab, a radiolabeled antibody fragment to detect osteomyelitis in diabetic patients with foot ulcers by leucoscintigraphy. Clin Infect Dis 28:1200 – 1205
59. Devillers A, Garin E, Polard JL, Poirier JY, Arvieux C, Girault S, Moisan A, Bouruet P (2000) Comparison of Tc-

99m-labeled antileukocyte fragments Fab' and Tc-99m-HMPAO-labeled leukocyte (HMPAO-LS) scintigraphy in the diagnosis of bone and joint infections: a prospective study. Nucl Med Commun 21:747 – 753
60. Ryan PJ (2002) Leukoscan for orthopaedic imaging in clinical practice. Nucl Med Commun 23:707 – 714
61. Palestro CJ, Caprioli R, Love C, Richardson HL, Kipper SL, Weiland FL, Thomas MB (2003) Rapid diagnosis of pedal osteomyelitis in diabetics with technetium-99m labeled monoclonal antigranulocyte antibody. J Foot Ankle Surg 42:2 – 8
62. Rothenberg TV Schaffstein J, Ludwig J, Vehling D, Koster O, Schmid G (2003) Imaging osteomyelitis with Tc99m-labeled antigranulocyte antibody Fab fragments. Clin Nucl Med 28:643 – 647
63. Riebel T, Nasir R, Nazarenko OC (1996) The value of sonography in the detection of osteomyelitis. Pediatr Radiol 26:291 – 197
64. Berquist TH, Brown ML, Fitzgerald RH et al (1985) Magnetic resonance imaging: application in musculoskeletal infection. Mag Res Imaging 3:219 – 230
65. Koort J, Makinen TJ, et al (2004) Comparative 18F-FDG PET of experimental *S. aureus* osteomyelitis and normal bone healing. J Nucl Med 45:1406 – 1411
66. Newman LG, Waller J, Palestro CJ, Schwantz M, Klein MJ, Hermann G, Harrington E, Harrington M, Roman SH, Stagnaro-Green A (1991) Unsuspected osteomyelitis in diabetic foot ulcers: diagnosis and monitoring by leukocyte scanning with In-111 oxyquinoline. JAMA 266:1246 – 1251
67. Palestro CJ, Mehta HH, Patel M, Freeman SJ, Harrington WN, Tomas MB, Marwin SE (1998) Marrow versus infection in Charcot joint: indium-111 leukocyte and technetium 99m sulfur colloid scintigraphy. J Nucl Med 39:349 – 350
68. Tailji S, Yacoub TY, Abdella N, Albunni A, Mahmoud A, Doza B, Loutfi I, Al-Za'abi K, Heiba S, Elgazzar A (1999) Optimization of simultaneous dual In-111 labeled leukocytes (WK) and Tc-99m MDP bone scans in diabetic foot. Eur J Nucl Med 26:1201
69. Poirier JY, Garin E, Derrien C, Devillers A, Moisan A, Bourguet P, Maugendre D (2002) Diagnosis of osteomyelitis in the diabetic foot with a 99mTc-HMPAO leucocyte scintigraphy combined with a 99mTc-MDP bone scintigraphy. Diabetes Metabol 28:485 – 490
70. Mason MD, Zlatkin MB, Esterhai IL, et al (1989) Chronic complicated osteomyelitis of the lower extremity: evaluation with MR imaging. Radiology 173:355 – 359
71. Newman LG, Waller J, Palestro CJ, Hermann G, Klein MJ, Schwatrz M, Harrington E et al (1992) Leukocyte scanning with 111-In is superior to magnetic resonance imaging in diagnosis of clinically unsuspected osteomyelitis in diabetic foot ulcers. Diabetes Care 15:1527 – 1530
72. Cook TA, Rahim N, Simpson HC, Galland RB (1996) Magnetic resonance imaging in the management of diabetic foot infection. Br J Surg 83:245 – 248
73. Morrison W, Schweitzer ME, Wapner KL, Hecht PJ, Gannon FH, Behm WR (1995) Osteomyelitis in diabetics: clinical accuracy, surgical utility and cost effectiveness of MR imaging. Radiology 196:557 – 564
74. Beltran J, Campanini DS, Knight C, McCalla M (1990) The diabetic foot: Magnetic resonance imaging. Skeletal Radiol 19:37 – 41
75. SNM 51st Annual Meeting: Abstract 217. Presented June 21, 2004
76. Abbey DM, Hosea SW (1989) Diagnosis of vertebral osteomyelitis in a community hospital by using computed tomography. Arch Intern Med 149:2029 – 2035
77. Meyers P, Wiener S (1991) Diagnosis of hematogenous pyogenic vertebral osteomyelitis by magnetic resonance imaging. Arch Intern Med 151:683 – 687
78. Modic MT, Feiglin DH, Piraino DW (1985) Vertebral osteomyelitis: assessment using MR. Radiology 157:157 – 166
79. Schlaeffer F, Mikolich DJ, Mates SM (1987) Technetium-99m diphosphonate bone scan. False-normal findings in elderly patients with hematogenous vertebral osteomyelitis. Arch Intern Med 147:2024 – 2026
80. Kern RZ, Houpt TB (1984) Pyogenic vertebral osteomyelitis: diagnosis and management. Can Med Assoc J 130: 1025 – 1028
81. Rubin RH, Fischman AJ, Callahan RJ (1989) Indium-111 labeled nonspecific immunoglobulin scanning in the detection of focal infection. N Engl J Med 321:935 – 940
82. Lisbona R, Derbekyan V, Novales-Diaz J et al (1993) Gallium-67 scintigraphy in tuberculosis and non-tuberculosis infectious spondylitis. J Nucl Med 34:853 – 859
83. Love C, Petel M, Lonner BS, Tomas MB, Palestro CJ (2000) Diagnosing spinal osteomyelitis: A comparison of bone and Ga-67 scintigraphy and magnetic resonance imaging. Clin Nucl Med 25:963 – 977
84. Quinn SF, Murray W, Clark RA (1988) MR imaging of chronic osteomyelitis. J Comput Assist Tomogr 12:113 – 117
85. Cahill DW, Love LC, Rechtine GR (1991) Pyogenic osteomyelitis of the spine in the elderly. J Neurosurg 74:878 – 886
86. Whalen IL, Brown ML, McLeod R et al (1991) Limitations of indium leukocyte imaging for the diagnosis of spine infections. Spine 16:193 – 197
87. Palestro Cl, Kim CK, Swyer Al et al (1991) Radionuclide diagnosis of vertebral osteomyelitis: indium-111-leukocyte and technetium-99m-methylene diphosphonate bone scintigraphy. J Nucl Med 32:1861 – 1865
88. Fernandez-Ulloa M, Vasavada Pl, Hanslits MJ et al (1985) Vertebral osteomyelitis imaging with In-111-labeled white blood cells and Tc-99m bone scintigrams. Orthopedics 8:1144 – 1150
89. Hovi I (1996) Complicated bone and soft tissue infections: imaging with 0.1 MR and Tc99m HMPAO labeled leukocytes. Acta Radiol 37:870 – 876
90. Stumpe KDM, Zanetti M, Weishaupt D, Hodler J, Boos N, Schulthess GK (2002) FDG positron emission tomography for differentiation of degenerative and infectious end plate abnormalities in the lumbar spine detected on MR imaging. AJR 179:1151 – 1157
91. Tumeh SS, Aliabadi P, Weissman BN, McNeil BJ (1986) Chronic osteomyelitis: bone and gallium scan patterns associated with active disease. Radiology 158:685 – 688
92. Tumeh SS, Tohmeh AG (1991) Nuclear medicine techniques in septic arthritis and osteomyelitis. Rheum Dis Clin North Am 17:559 – 583
93. Krznaric E, De Roo M, Verbruggen A, Stuyck J, Mortelinans L (1996) Chronic osteomyelitis: diagnosis with technetium 99m d,1-hexamethylpropylene amine oxime labeled leukocytes. Eur J Nucl Med 23:792 – 797
94. Erdman WA, Tamburro F, Jayson HT, Weatherall PT, Ferry KB, Peshoch RM (1991) Osteomyelitis: characteristics and pitfalls of diagnosis with MR imaging. Radiology 180:533 – 539
95. Sciuk J, Brandau W, Vollet B, Stucker R, Erlemann R, Bartenstein P et al (1991) Comparison of technetium-99m polyclonal human immunoglobulin and technetium-99m monoclonal antibodies for imaging chronic osteomyelitis. Eur J Nucl Med 18:401 – 407
96. Guhlmann A, Brecht-Krauss D, Sugar G, Glatting G, Kotzerke J, Kinzi L, Reske SN (1998) Chronic osteomyelitis: detection with FDG PET and correlation with histopathologic findings. Radiology 206:749 – 753
97. Zhuang HM, Duarte PS, Poudehnad M, et al (2000) The exclusion chronic osteomyelitis with F-18 fluorodeoxy-

glucose positron tomography imaging. Clin Nucl Med 25:281 – 284
98. De Winter F, Dierckx R, De Bondt P, et al (2000) FDG PET as a single technique is more accurate than the combination bone scan/white blood cell scan in chronic orthopedic infection (COI). J Nucl Med 41:59 (Abstract)
99. De Winter F, Van de Wiele C, Vandenberghe S, de Bondt P, de Clercq D, D'Asseler Y, Dierckx R (2001) Coincidence camera FDG for the diagnosis of chronic orthopedic infections: A feasibility study. J Comput Assist Tomogr 25:184 – 189
100. Zaknun JJ, Zangerle R, Gabriel M, Virolini I (2005) F18 FDG-PET for monitoring disease activity in an HIV-1 positive patient with disseminated chronic osteomyelitic brucellosis due to *Brucella melitensis*. Eur J Nucl Med Mol Imaging 32:630
101. Love CH, Tomas MB, Marwin SE, Pugliese PV, Palestro CHF (2001) Role of nuclear medicine in diagnosis of the infected joint replacement. Radiographics 21:1229 – 1238
102. Oswald SG, VanNostrand D, Savory CG, Callaghan JJ (1989) Three phase bone scan and indium white blood cell scintigraphy following porous-coated hip arthroplasty: a prospective study of the prosthetic hip. J Nucl Med 30:1321 – 1331
103. Oswald SG, VanNostrand D, Savory CG, Anderson JH, Callaghan JJ (1990) The acetabulum: a prospective study of three-phase bone and indium white blood cell scintigraphy following porous coated hip arthroplasty. J Nucl Med 31:274 – 280
104. Rosenthal L, Lepanto L, Raymond F (1987) Radiophosphate uptake in asymptomatic knee arthroplasty. J Nucl Med 28:1546 – 1549
105. Elgazzar AH, Yeung HW, Webner PJ (1996) Indium-111 leukocyte and technetium 99m sulfur colloid uptake in Paget's disease. J Nucl Med 37:858 – 861
106. Oyen WJG, VanHorn JR, Claessens RAMJ, Slooff JJH, Van der Meer JWM, Corstens HM (1992) Diagnosis of bone, joint and joint prosthesis infections with In-111-labeled nonspecific human immunoglobulin G scintigraphy. Radiology 182:195 – 199
107. Zhuang H, Durate PS, Pourdehnad M, et al (2001) The promising role of F-18-FDG PET in detecting infected lower limb prosthesis implants. J Nucl Med 42:44 – 48
108. Chacko TK, Zhuang H, Stevenson K, Moussavian B, Alavi A (2002) The influence of the location of fluodeoxyglucose uptake in periprosthetic infection in painful hip prostheses. Nucl Med Commun 23:851 – 855
109. Mandell GA (1996) Imaging in the diagnosis of musculoskeletal infections in children. Curr Probl Pediatr 26:218 – 237
110. Amunden TR, Siegel MJ, Siegel BA (1984) Osteomyelitis and infarction in sickle cell hemoglobinopathies: differentiation by combined technetium and gallium scintigraphy. Radiology 153:807 – 812
111. Jaramillo D, Treves ST, Kasser JR, Harper M, Sundel R, Laor T (1995) Osteomyelitis and septic arthritis in children. Appropriate use of imaging to guide treatment. AJR 165:399 – 403
112. Sundberg SB, Savage JP, Foster BK (1989) Technetium phosphate bone scan in the diagnosis of septic arthritis in childhood. J Pediatr Orthop 9:579 – 585
113. Gilday DL, Paul DJ, Paterson J (1975) Diagnosis of osteomyelitis in children by combined blood pool and bone imaging. Radiology 117:331 – 335
114. Greyson ND, Tepperman PS (1984) Three-phase bone studies in hemiplegia with reflex sympathetic dystrophy and the effect of disuse. J Nucl Med 25:423 – 429
115. McAffe JG, Roba RC, Majid M (1995) The musculoskeletal system. In: Wagner HN (ed) Principles of nuclear medicine, 2nd edn. Saunders, Philadelphia, pp 986 – 1020
116. Graham J, Wood SK (1976) Aseptic necrosis of bone following trauma. In: Davidson JK (ed) Aseptic necrosis of bone. Excerpta Medica, Amsterdam, p 101
117. Resnick D (1989) Bone and joint imaging. Saunders, Philadelphia, pp 979 – 999
118. Fragniere B, Chotel F, Vargas Barreto B, Berard J (2001) The value of early postoperative bone scan in slipped capital femoral epiphysis. J Pediatr Orthopaed B 10:51 – 55
119. Conway JJ (1993) A scintigraphic classification of Legg-Calvé-Perthes disease. Semin Nucl Med 23:274 – 295
120. Tsao AK, Dias LS, Conway JJ, Straka P (1997) The prognostic value and significance of serial bone scintigraphy in Legg-Calvé-Perthes disease. J Pediatr Orthoped 17:230 – 239
121. de Sanctis N, Rondinella F (2000) Prognostic evaluation of Legg-Calvé-Perthes disease by MRI, part II: pathomorphogenesis and new classification. J Pediatr Orthoped 20:463 – 470
122. Comte F, De Rosa V, Zekri H, Eberle MC, Dimeglio A, Rossi M, Mariano-Goulart D (2003) Confirmation of the early prognostic value of bone scanning and pinhole imaging of the hip in Legg-Calvé-Perthes disease. J Nucl Med 44:1761 – 1766
123. Resnick D, Niwayama G (1998) Osteonecrosis: diagnostic techniques and complications. In: Resnick D, Niwayama G (eds) Diagnosis of bone and joint disorders, 2nd edn. Saunders, Philadelphia, p 3268
124. Smith JA (1996) Bone disorders in sickle cell disease. Hematol Oncol Clin North Am 10:1345 – 1346
125. Kim SK, Miller JH (2002) Natural history and distribution of bone and bone marrow infarction in sickle cell hemoglobinopathies. J Nucl Med 43:896 – 900
126. Keeley K, Buchanan GR (1982) Acute infarction of long bones in children with sickle cell anemia. J Pediatr 101:170 – 175
127. Skaggs DL, Kim SK, Green NW, Harris D, Miler JH (2001) Differentiation between bone infarct and acute osteomyelitis in children with sickle-cell disease with use of sequential radionuclide bone-marrow and bone scans. J Bone Joint Surg Am 83:1810 – 1813
128. Sisayan R, Elgazzar AH, Webner P, Religioso DG (1996) Impact of bone scintigraphy on clinical management of a sickle cell patient with recent chest pain. Clin Nucl Med 21:523 – 526
129. Kawai K, Maruno H, Watanabe Y, Hirohata K (1980) Fat necrosis of osteocytes as a causative factor in idiopathic osteonecrosis inheritable hyperlipemic rabbits. Clin Orthop Relat Res 153:273
130. Collier BD, Carrera GF, Johnson RP, Isitman AT, Hellman RS, Knobel J et al (1985) Detection of femoral head avascular necrosis in adults by SPECT. J Nucl Med 26:979 – 987
131. Greyson ND, Lotem MM, Gross AE (1982) Radionuclide evaluation of spontaneous femoral osteonecrosis. Radiology 142:729 – 735
132. Holder LE, Cole LA, Myerson MS (1992) Reflex sympathetic dystrophy in the foot: clinical and scintigraphic criteria. Radiology 184:531 – 535
133. Kozin F (1994) Reflex sympathetic dystrophy syndrome. Curr Opin Rheumatol 6:210 – 216
134. Schwartzman RJ, Popescu A (2002) Reflex sympathetic dystrophy. Curr Rheumatol Rep 4:165 – 169
135. Janig W, Baron R (2003) Complex regional pain syndrome: mystery explained? Lancet Neurol 2:687 – 697

136. Stanton-Hicks M, Janig W, Hassenbusch S, Haddox JD, Boas R, Wilson P (1995) Reflex sympathetic dystrophy: changing concepts and taxonomy. Pain 63:127 – 133
137. Shehab D, Al-Jarralah K, Al-Awadhi A et al (1999) Reflex sympathetic dystrophy: an under-recognized entity in Kuwait. APLAR J Rheumatol 3:343 – 347
138. Blockx P, Driessens M (1991) The use of Tc-99-m-HSA dynamic vascular examination in the staging and therapy monitoring of reflex sympathetic dystrophy. Nucl Med Commun 12:725 – 731
139. Goldstein DS, Tack C, Li TS (2000) Sympathetic innervation and function in reflex sympathetic dystrophy. Ann Neurol 48:49 – 59
140. Sankaya A, Sankaya I, Pekindil G, Firat MF, Pekindil Y (2001) Technetium-99m sestamibi limb scintigraphy in post-traumatic reflex sympathetic dystrophy: preliminary results. Eur J Nucl Med 28:1517 – 1522
141. Haensch C, Jorg J, Lerch H (2002) I-123 metaiodobenzylguanidine uptake of the forearm shows dysfunction of sympathetic mediated neurovascular transmission in complex regional pain syndrome 1 (CRPS 1). J Neurol 249:1742 – 1743
142. Tsuyuguchi N, Ohata K, Morino M, Takami T, Goto T, Nishio A, Hara M, Sunada I (2002) Magnetic resonance imaging and [11c] methyl-l-methionine positron emission tomography of fibrous dysplasia – two case reports. Neurologia Medico-Chirurgica 42:341 – 345
143. Han J, Ryu JS, Shin MJ, Kang GH, Lee HK (2000) Fibrous dysplasia with barely increased uptake on bone scan: a case report. Clin Nucl Med 25:785 – 788
144. Kairemo KJ, Verho S, Dunkel L (1999) Imaging of McCune Albright syndrome using bone single photon emission computed tomography. Eur J Pediatr 158:123 – 126
145. Mourad A (1998) Alterations of musculoskeletal function. In: McCance KL, Huether SE (eds) Pathophysiology, 3rd edn. Mosby, Philadelphia, pp 1435 – 1485
146. Holder LE, Michael RH (1984) The specific scintigraphic pattern of shin splints in the lower leg: concise communication. J Nucl Med 25:865 – 869
147. Reed A, Joyner C, Brawnlow H, Simpson H (2001) Radiological classification of human nonunions does not reflect biological activity. Proceeding of the 47th annual meeting, Orthopedic Research Society, San Francisco, pp 971
148. Sty JR, Starshak RJ (1983) The role of bone scintigraphy in the evaluation of the suspected abused child. Radiology 146:369 – 375
149. Malki A, Elgazzar A, Ashqar T, Owunwanne A, Abdel-Dayem AH (1992) New technique for assessing muscle damage after trauma. J R Coll Surg Edin 37:131 – 133
150. Malki A, Owunwanne A, Elgazzar A, Abdel-Dayem AH (1999) Assessment of skeletal muscle damage in experimental animal using In-111 antimyosin. J Surg Invest 1:99 – 105
151. Sharkey CA, Harcke HT, Mandell GA, et al (1986) SPECT techniques in the evaluation of growth plate abnormalities about the knee. J Nucl Med Tech 14:Ab13
152. Harcke HT, Zapf SE, Mandell GA, et al (1987) Angular deformity of the lower extremity: Evaluation with quantitative bone scintigraphy. Radiology 164:437 – 440
153. Harcke HT (1978) Bone imaging in infants and children: A review. J Nucl Med 19:324 – 329
154. Mandell GA (1998) Nuclear medicine in pediatric orthopedics. Semin Nucl Med 28:95 – 115
155. Harcke HT, Mandell GA (1993) Scintigraphic evaluation of the growth plate. Semin Nucl Med 23:266 – 273
156. Etchebehere EC, Caron M, Pereira JA, Lima MC, Santos AO, Ramos CD, Barros FB, Sanches A, Santos-Jesus R, Belangero W, Camargo EE (2001) Activation of the growth plates on three-phase bone scintigraphy: the explanation for the overgrowth of fractured femurs. Eur J Nucl Med 28:72 – 80
157. Etchebehere EC, Etchebehere M, Gamba R, Belangero W, Camargo EE (1998) Orthopedic pathology of the lower extremities: scintigraphic evaluation in the thigh, knee, and leg. Semin Nucl Med 28:41 – 61
158. Wioland M, Bonnerot V (1993) Diagnosis of partial and total physeal arrest by single photon emission computed tomography. J Nucl Med 34:1410 – 1415
159. Peterson HA (1984) Partial growth plate arrest and its treatment. J Pediatr Orthoped 4:246 – 258
160. DeCampo JF, Boldt DW (1986) Computed tomography in partial growth plate arrest: Initial experience. Skeletal Radiol 183:119 – 123
161. Jaramillo D, Hoffer EA, Shapiro F, et al (1990) MR imaging of fracture of the growth plate. AJR 155:1261 – 265
162. Khan A, Bilezikian J (2000) Primary hyperparathyroidism: pathophysiology and impact on bone. CMAJ 163:184 – 718
163. Mills BG, Masuoka LS, Graham CC Jr et al (1988) Gallium-67 citrate localization in osteoclast nuclei of Paget's disease of bone. J Nucl Med 29:1083
164. Lander PH, Hadjipavlou AG (1986) A dynamic classification of Paget's disease. J Bone Joint Surg [Br] 68B:431 –438
165. Boutin RD, Spitz DJ, Newman JS, Lenchik L, Steinbach LS (1998) Complications in Paget disease at MR imaging. Radiology 209:641 – 651
166. Vande Berg BC, Malghem J, Lecouvet FE, Maldague B (2001) Magnetic resonance appearance of uncomplicated Paget's disease of bone. Semin Musculoskeletal Radiol 5:69 – 77
167. Cherian RA, Haddaway MJ, Davie MW, McCall IW, Cassar-Pullicino VN (2000) Effect of Paget's disease of bone on areal lumbar spine bone mineral density measured by DXA, and density of cortical and trabecular bone measured by quantitative CT. Br J Radiol 73:720 – 726
168. Serafini AN (1976) Paget's disease of bone. Semin Nucl Med 6:47 – 58
169. Fogelman I, Carr D (1980) A comparison of bone scanning and radiology in the evaluation of patients with metabolic bone disease. Clin Radiol 31:321 – 326
170. King MA, Maxon HR (1984) Paget's disease: The role of nuclear medicine in diagnosis and treatment. In: Silberstein EB (ed) Bone scintigraphy. Futura, Mount Kisco, New York, pp 333 – 346
171. Renier JC, Audran M (1997) Polyostotic Paget's disease. A search for lesions of different durations and for new lesions. Revue du Rhumatisme (English edition) 64:233 – 242
172. Kaplan FS (1987) Osteoporosis: Pathophysiology and prevention. Chin Sympozia 39:2
173. Matkovic V, De Kanic D (1989) Developing strong bones: The teenage female. In: Kleerehoper M, Krane SM (eds) Clinical disorders of bone and mineral metabolism. Mary Ann Liebert, New York, pp 165
174. Gillespy T, Gillespy MP (1991) Osteoporosis. Radial Clin North Am 29:77 – 84
175. Christiansen C, Riis BJ (1989) Optimizing bone mass in the premenopause. In: Kleerehoper M, Krane SM (eds) Clinical disorder of bone and mineral metabolism. Mary Ann Liebert, New York, pp 189
176. Lang P, Steiger P, Faulkner K, et al (1991) Current techniques and recent developments in quantitative bone densitometry. Rad Clin North Am 29:49 – 76
177. Snyder W (1975) Report of the task group on reference man. Pergamon Press, Oxford
178. Recker RR, Heaney RP (1989) Effects of age, sex and race on bone remodeling. In: Kleerekoper MJ, Krane SM (eds)

Clinical disorders of bone and mineral metabolism. Mary Ann Liebert, New York, p 59
179. Heaney RP (1989) Optimizing bone mass in the premenopause: calcium. In: Kleerehoper MJ, Krane SM (eds) Clinical disorders of bone and mineral metabolism. Mary Ann Liebert, New York, p 181
180. Frost HM (1964) Dynamics of bone remodelling. In: Frost HM (ed) Bone biodynamics. Little, Brown, Boston, pp 315–334
181. Ettinger B, Genant HK (eds) (1987) Osteoporosis update. Radiology Research and Education Foundation, San Francisco
182. Schwivitz S, Djukic S, Genant HK (1990) The current status of bone densitometry. Appl Radiol June 1990, pp 20–25
183. Cooper C, Aihie-Sayer A (1994) Osteoporosis: recent advances in pathogenesis and treatment. Q J Med 87:203–209
184. Simon SR (1994) Osteoporosis: orthopedic basic science. American Academy of Orthopedic Surgeons, Chicago
185. Chen CC, Wang SS, Jeng FS, Lee SD (1996) Metabolic bone disease of liver cirrhosis: is it parallel to the clinical severity of cirrhosis? J Gastroenterol Hepatol 11:417–421
186. Fogelman I (1987) The bone scan in metabolic bone disease. In: Fogelman I (ed) Bone scanning in clinical practice. Springer, Berlin Heidelberg New York, pp 73–88
187. Lack CA, Rarber JL, Rubin E (1999) The endocrine system. In: Rubin E, Farber JL (eds) Pathology, 3rd edn. Lippincott-Raven, Philadelphia, pp 1179–1183
188. Marshall D, Johnell O, Wedel H (1996) Meta-analysis of how well measures of bone mineral density predict occurrence of osteoporotic fractures. BMJ 312:1254–1259
189. Cummings SR, Black DM, Nevitt MC, et al. (1993) Bone density at various sites for prediction of hip fractures. Lancet 341:72–75
190. Eastell R (1998) Treatment of postmenopausal osteoporosis. N Engl J Med 338:736–746
191. Njeh CF, Fuerst T, Hans D, Blake GM, Genant HK (1999) Radiation exposure in bone mineral assessment. Appl Rad Isotope 50:215–236
192. WHO Technical Report Series 843 (1994) Assessment of fracture risk and its application to screening for postmenopausal osteoporosis. World Health Organization, Geneva
193. Genant HK, Grampp S, Glüer C-C, et al (1994) Universal standardization for dual x-ray absorptiometry: patient and phantom cross-calibration results. J Bone Miner Res 9:1503–1514
194. Basha B, Rao DS, Han ZH, Parfitt AM (2000) Osteomalacia due to vitamin D depletion: A neglected consequence of intestinal malabsorption. Am J Med 108:296–300
195. Reginato AJ, Falasca GF, Pappu R, McKnight B, Agha A (1999) Musculoskeletal manifestations of osteomalacia: report of 26 cases and literature review. Semin Arthritis Rheumat 28:287–304
196. Akbunar AT, Orhan B, Alper E (2000) Bone-scan-like pattern with 99mTc(V)-DMSA scintigraphy in patients with osteomalacia and primary hyperparathyroidism. Nucl Med Commun 21:181–185
197. Leitha T (1998) Rapid changes in the scintigraphic pattern in Tc-99m DPD whole-body scanning in metabolic bone disease. Clin Nucl Med 23:784–578
198. Sy WM, Mittal AK (1975) Bone scan in chronic dialysis patients with evidence of secondary hyperparathyroidism and renal osteodystrophy. Br J Radiol 48:878–884
199. Olmastroni M, Seracini D, Lavoratti G, Marin E, Masi A, Vichi G (1997) Magnetic resonance imaging of renal osteodystrophy in children. Pediatr Radiol 27:865–868
200. Goen G, Mazzaferro S (1994) Bone metabolism and its assessment in renal failure. Nephron J 67:383–401
201. Olmastroni M, Seracini D, Lavoratti G, Marin E, Masi A, Vichi G (1997) Magnetic resonance imaging of renal osteodystrophy in children. Pediatr Radiol 27:865–868
202. Rosenberg AE (1991) The pathology of metabolic bone disease. Radiol Clin North Am 29:19–36
203. Dabbagh S (1998) Renal osteodystrophy. Curr Opin Pediatr 10:190–196
204. Cicconetti A, Maffeini C, Piro FR (1999) Differential diagnosis in a case of brown tumor caused by primary hyperparathyroidism. Minerva Stomatologica 48:553–558
205. Loder RT, Hensinger RN (1997) Slipped capital femoral epiphysis associated with renal failure osteodystrophy. J Pediatr Orthoped 17:205–211
206. Savaci N, Avunduk MC, Tosum Z, Hosnuter M (2000) Hyperphosphatemic tumoral calcinosis. Plastic and Reconstruct Surg 105:162–165
207. Rosenberg AE, Salusky IB, Ramirez JA, Goodman WG (1994) Disorders of bone and mineral metabolism in chronic renal failure. In: Holliday MA, Barrett TM, Arner ED (eds) Pediatric nephrology. Williams & Wilkins, Baltimore, pp 1287–1304
208. Yalcinkaya F, Ince E, Tumer N, Ensari A, Ozkaya N (2000) Spectrum of renal osteodystrophy in children on continuous ambulatory peritoneal dialysis. Pediatr Int 42:53–57
209. Jorgetti V, Lopez BD, Caorsi H, Ferreira A, Palma A, Menendez P, Douthat W, Olaizola I, Ribeiro S, Jarava C, Moreira E, Cannata J (2000) Different patterns of renal osteodystrophy in IberoAmerica. Am J Med Sci 320:76–80
210. Sanchez CP, Salusky IB (1996) The renal bone diseases in children treated with dialysis. Adv Ren Replace Ther 3:14–23
211. Olaizola I, Aznarez A, Jorgetti V, Petroglia A, Caorsi H, Acuna G, Fajardo L, Ambrosoni P, Mazzuchi N (1998) Are there any differences in the parathyroid response in the different types of renal osteodystrophy? Nephrol Dialysis Transplant 13 Suppl:15–18
212. Fukagawa M, Akizawa T, Kurokawa K (2000) Is a plastic osteodystrophy a disease of malnutrition? Curr Opin Nephrol Hypertens 9:363–367
213. Alon US (2001) Preservation of bone mass in pediatric dialysis and transplant patients. Adv Ren Replace Ther 8:191–205
214. Kim CD, Kim SH, Kim YL, Cho DK, Lee JT (1998) Bone marrow immunoscintigraphy (BMIS): a new and important tool for the assessment of marrow fibrosis in renal osteodystrophy. Adv Periton Dialysis 14:183–187
215. Seggewiss R, Hess T, Fiehn C (2003) A family with a variant form of primary hypertrophic osteoarthropathy restricted to the lower extremities. Joint Bone Spine Revue Rhumatisme 70:230–233
216. Howell DS (1985) Hypertrophic osteoarthropathy. In: McCarty DJ (ed) Arthritis and allied conditions, 10th edn. Lea and Febiger, Philadelphia, pp 1195–1201
217. Ali A, Tetalman MR, Fordham EW et al (1980) Distribution of hypertrophic pulmonary osteoarthropathy. AJR 134:771–780
218. Wang CJ, Huang CH, Leung SW, Chen HC, Huang EY (1998) Hypertrophic osteoarthropathy in nasopharyngeal carcinoma patients: two case reports. Changgeng Yi Xue Za Zhi 21:222–226
219. Morgan B, Coakley F, Finlay DB, Belton I (1996) Hypertrophic osteoarthropathy in staging skeletal scintigraphy for lung cancer. Clin Radiol 51:694–697
220. Albrecht S, Keller A (2003) Postchemotherapeutic reversibility of hypertrophic osteoarthropathy in a patient with bronchogenic adenocarcinoma. Clin Nucl Med 28:463–466
221. Rosenthall L (1991) Nuclear medicine techniques in arthritis. Rheum Dis Clin North Am 17:585–597

222. McCarthy D (ed) (1984) Arthritis and allied conditions. Lea and Fabiger, Philadelphia
223. Goldenberg DL, Cohen AS (1978) Synovial membrane histopathology in the differential diagnosis of rheumatoid arthritis, gout, pseudogout, systemic lupus erythematosus, infectious arthritis and degenerative joint disease. Medicine 57:239 – 252
224. Cindas A, Gokce-Kustal Y, Kirth PO, Caner B (2001) Scintigraphic evaluation of synovial inflammation in rheumatoid arthritis with (99m) technetium-labelled human polyclonal immunoglobulin G. Rheumatol Int 20:71 – 77
225. De Bois M, Arndt J, van der Velde EA et al (1992) ^{99m}Tc human immunoglobulin scintigraphy – a reliable method to detect joint activity in rheumatoid arthritis. J Rheumatol 19:1371 – 1376
226. Weissberg DI, Resnick D, Taylor A et al (1978) Rheumatoid arthritis and its variants: analysis of scintiphotographic, radiographic and clinical examination. AJR 131: 665 – 673
227. Waxman AD, Ducker S, McKee D (1977) Evaluation of ^{99m}Tc diphosphonate kinetics and bone scan in patients with Paget's disease before and after calcitonin treatment. Radiology 125:761 – 764
228. Al-Janabi MA, Solanki K, Critchley M et al (1992) Radioleukoscintigraphy in osteoarthritis. Is there an inflammatory component? Nucl Med Commun 13:706 – 712
229. Berna L, Torres G, Diez C et al (1992) Technetium-99m human polyclonal immunoglobulin G studies and conventional bone scans to detect active joint inflammation in chronic rheumatoid arthritis. Eur J Nucl Med 19:173 – 176
230. Rupani HD, Holder LE, Espinola DA et al (1985) Three-phase radionuclide bone imaging in sports medicine. Radiology 156:187 – 196
231. Bahk Y (2000) Combined scintigraphic and radiographic diagnosis of bone and joint diseases, 2nd edn. Springer, Berlin
232. Kaye JJ (1990) Arthritis: roles of radiography and other imaging techniques in evaluation. Radiology 177:601 – 608
233. Mijiyawa M (1995) Gout in patients attending the rheumatology unit of Lome Hospital. Br J Rheumatol 34:843 – 846
234. Koh WH, Seah A, Chai P (1998) Clinical presentation and disease associations of gout: a hospital-based study of 100 patients in Singapore. Ann Acad Med Singapore 27:7 – 10
235. Sato J, Watanabe H, Shinozaki T, Fukuda T, Shirakura K, Takagishi K (2001) Gouty tophus of the patella evaluated by PET imaging. J Orthoped Sci 6:604 – 607
236. George E, Creamer P, Dieppe PA (1994) Clinical subsets of osteoarthritis. J Musculoskeletal Med 11:14
237. Gelber AC, Hochberg MC, Mead LA, Wang NY, Wigley FM, Klag MJ (2000) Joint injury in young adults and risk of subsequent knee and hip osteoarthritis. Ann Intern Med 133:321 – 328
238. Garland D (1991) A clinical perspective on common forms of acquired heterotopic ossification. Clin Orthop Relat Res 263:13 – 29
239. Nagaraj N, Elgazzar AH, Fernandez-Ulloa M (1995) Heterotopic ossification mimicking infection: scintigraphic evaluation. Clin Nucl Med 20:763 – 766
240. Orzel JA, Redd TG (1985) Heterotopic bone formation: clinical, laboratory and imaging correlation. J Nucl Med 26:125 – 132
241. Elgazzar AH, Martich V, Gelfand MJ (1995) Advanced fibrodysplasia ossificans progressiva. Clin Nucl Med 20:519 – 521
242. Smith FW, Gilday DL (1980) Scintigraphic appearance of osteoid osteoma. Radiology 137:191 – 195
243. Hod N, Fishman S, Horne T (2002) Detection of rhabdomyolysis associated with compartment syndrome by bone scintigraphy. Clin Nucl Med 27:885 – 886
244. Kawaguchi Y, Hasegawa T, Oka S, Sato C, Arima N, Norimatsu H (2001) Mechanism of intramedullary high intensity area on T2-weighted magnetic resonance imaging in osteoid osteoma: a possible role of COX-2 expression. Pathol Int 51:933 – 937
245. Dahlin DC, Coventry MB (1967) Osteosarcoma: a study of 600 cases. J Bone Joint Surg Am 49:101 – 110
246. Robbin MR, Murphey MD (2000) Benign chondroid neoplasms of bone. Semin Musculoskelet Radiol 4:45 – 58
247. Elgazzar AH, Fernandez-Ulloa M, Silberstein EB (1993) Thallium 201 as a tumor imaging agent: current status and future consideration. Nucl Med Commun 14:96 – 103
248. Huvos AG (1991) Bone tumors; diagnosis, treatment and prognosis, 2nd edn. Saunders, Philadelphia
249. Resnik D, Kyriakos M, Greenway GD (2002) Tumors and tumor-like lesions of bone. Diagnosis of bone and joint disorders, 4th edn. Saunders, Philadelphia, pp 3979 – 3985
250. Choi JJ, Murphey MD (2000) Angiomatous skeletal lesions. Semin Musculoskelet Radiol 4:103 – 112
251. Han BK, Ryu JS, Moon DH, Shin MJ, Kim YT, Lee HK (1995) Bone SPECT imaging of vertebral hemangioma: correlation with MR imaging and symptoms. Clin Nucl Med 20:916 – 921
252. Aoki J, Watanabe H, Shinozaki T, Takagishi K, Ishijima H, Oya N, Sato N, Inoue T, Endo K (2001) FDG PET of primary benign and malignant bone tumors: standardized uptake value in 52 lesions. Radiology 219:774 – 777
253. Dimitrakopoulou-Strauss A, Heichel TO, Lehner B, Bernd L, Ewerbeck V, Burger C, Strauss LG (2001) Quantitative evaluation of skeletal tumors with dynamic FDG PET: SUV in comparison to Patlak analysis. Eur J Nucl Med 28:704 – 710
254. Franzius C, Sciuk J, Brinkschmidt C, Jurgens H, Schober O (2000) Evaluation of chemotherapy response in primary bone tumors with F-18 FDG positron emission. Clin Nucl Med 25:874 – 878
255. Ell PJ, Dixon HJ, Abdullah AZ (1980) Unusual spread of juxtacortical osteosarcoma. J Nucl Med 21:190 – 191
256. Franzius C, Sciuk J, Daldrup-Link HE, Jurgens H Schober O (2000) FDG-PET for detection of osseous metastases from malignant primary bone tumors: comparison with bone scintigraphy. Eur J Nucl Med 27:1305 – 1311
257. Yildiz C, Erler K, Atesalp AS, Basbozkurt M (2003) Benign bone tumors in children. Curr Opin Pediatr 15:58 – 67
258. Miller SL, Hoffer FA (2001) Malignant and benign bone tumors. Radiol Clin North Am 39:673 – 699
259. Buhler M, Binkert C, Exner GU (2001) Osteoid osteoma: technique of computed tomography-controlled percutaneous resection using standard equipment available in most orthopaedic operating rooms. Arch Orthopaed Trauma Surg 121:458 – 461
260. Kawaguchi Y, Hasegawa T, Oka S, Sato C, Arima N, Norimatsu H (2001) Mechanism of intramedullary high intensity area on T2-weighted magnetic resonance imaging in osteoid osteoma: a possible role of COX-2 expression. Pathol Int 51:933 – 937
261. Ossiani M, Elgazzar AH (2003) Multiple osteochondroma (unpublished data)
262. Moser RP Jr, Masewell JF (1987) An approach to primary bone tumors. Radiol Clin North Am 25:1049 – 1093
263. Woerthler K, Linder N, Gosheger G, Brinkschmidt C, Heindel W (2000) MR imaging of tumor-related complications. Eur Radiol 10:832 – 840

264. Brian WE, Mirra JM, Luck JV Jr (1999) Benign and malignant tumors of bone and joint: their anatomical and theoretical basis with an emphasis on radiology, pathology and clinical biology II. Juxtacortical cartilage tumors. Skeletal Radiol 28:1 – 20
265. Moody EB, Classman SB, Hansen AV, Lawrence SK, Delbeke D (1992) Nuclear medicine case of the day. AJR 158:1382 – 1386
266. Siddiqui RA, Ellis JH (1982) "Cold spots" on bone scan at the site of primary osteosarcoma. In: Rossleigh MA, Smith J, Yeh SDJ, et al (1987) Case reports: A photopenic lesion in osteosarcoma. Br J Radiol 60:497 – 499
267. Bloem JL, Taminiau AHM, Eulderink F, Hermans J, Pauwels EKJ (1988) Radiologic staging of primary bone sarcoma: MR imaging, scintigraphy, angiography, and CT correlated with pathologic examination. Radiology 169:805 – 810
268. McKillop JH, Etcubanas E, Goris ML (1981) The indications for and limitations of bone scintigraphy in osteogenic sarcoma. Cancer 48:1133 – 1138
269. Franzius C, Daldrup-Link HE, Wagner-Bohn A, Sciuk J, Heindel WL, Jurgens H, Schober O (2002) FDG-PET for detection of recurrences from malignant primary bone tumors: comparison with conventional imaging. Ann Oncol 13:157 – 160
270. Abdel-Dayem (1997) The role of nuclear medicine in primary bone and soft tissue tumors. Semin Nucl Med 27:355 – 363
271. Burak Z, Ersoy O, Moretti JL, Erinc R, Ozcan Z, Dirlik A, Sabah D, Basdemir G (2001) The role of 99mTc-MIBI scintigraphy in the assessment of MDR1 overexpression in patients with musculoskeletal sarcomas: comparison with therapy response. Eur J Nucl Med 28:1341 – 1350
272. Gorlick R, Liao AC, Antonescu C, Huvos AG, Healey JH, Sowers R, Daras M, Calleja E, Wexler LH, Panicek D, Meyers PA, Yeh SD, Larson SM (2001) Lack of correlation of functional scintigraphy with (99m)technetium-methoxyisobutylisonitrile with histological necrosis following induction chemotherapy or measures of P-glycoprotein expression in high-grade osteosarcoma. Clin Cancer Res 7:3065 – 3070
273. Kaste SC, Billips C, Tan M, Meyer WH, Parham DM, Rao BN, Pratt CB, Fletcher BD (2001) Thallium bone imaging as an indicator of response and outcome in nonmetastatic primary extremity osteosarcoma. Pediatr Radiol 31:251 – 256
274. Franzius F, Bielack S, Flege S, Sciuk J, Jürgens H, Schober O (2002) Prognostic significance of ^{18}F-FDG and ^{99}Tc-methylene diphosphonate uptake in primary osteosarcoma. J Nucl Med 43:1012 – 1017
275. Murthy NJ, Rao H, Friedman AS (2000) Positive findings on bone scan in multiple myeloma. Southern Med J 93:1028 – 1029
276. Waxman AD, Steimsen JK, Levine AM, et al (1981) Radiographic and radionuclide imaging in multiple myeloma: The role of gallium scintigraphy. Concise communication. J Nucl Med 22:232 – 236
277. Watanabe N, Shimizu M, Kageyama M, Tanimura K, Kinuya S, Shuke N, Yokoyama K, Tonami N, Watanabe A, Seto H, Goodwin DA (1999) Multiple myeloma evaluated with Tl-201 scintigraphy compared with bone scintigraphy. J Nucl Med 40:1138 – 1142
278. Alexandrakis MG, Kyriakou DS, Passam F, Koukouraki S, Karkavitsas N (2001) Value of Tc-99m sestamibi scintigraphy in the detection of bone lesions in multiple myeloma: comparison with Tc-99m methylene diphosphonate. Ann Hematol 80:349 – 353
279. Kusumoto S, Jinnai I, Itoh K, et al (1997) Magnetic resonance imaging patterns in patients with multiple myeloma. Br J Hematol 99:649 – 655
280. Connolly LP, Drubach LA, Ted Treves S (2002) Applications of nuclear medicine in pediatric oncology. Clin Nucl Med 27:117 – 125
281. Hung GU, Tan TS, Kao CH, Wang SJ (2000) Multiple skeletal metastases of Ewing's sarcoma demonstrated on FDG-PET and compared with bone and gallium scans. Kaohsiung J Med Sci 16:315 – 318
282. Bar-Sever Z, Cohen IJ, Connolly LP, Horev G, Perri T, Treves T, Hardoff R (2000) Tc-99m MIBI to evaluate children with Ewing's sarcoma. Clin Nucl Med 25:410 – 413
283. Dorland's (1988) Illustrated medical dictionary, 27th edn. Saunders, Philadelphia, p 1016
284. Batson OV (1940) The function of the vertebral veins and their role in the spread of metastases. Ann Surg 112:138
285. Resnick D, Niwayama G (1998) Skeletal metastases. In: Resnick D, Niwayama G (eds) Diagnosis of bone and joint disorders, 2nd edn. Saunders, Philadelphia, pp 3945 – 4010
286. Resnick D, Niwayama G, Galasko CSD (1981) Bone metastasis studied in experimental animals. Clin Orthop Rel Res 155:269
287. Galasko CSD (1982) Mechanisms of lytic and blastic metastatic disease of bone. Clin Orthop Relat Res 169:20
288. Tondevold E, Eliasen P (1982) Blood flow rates in canine cortical and cancellous bone measured with Tc-99m, labeled human albumin microspheres. Acta Orthop Scand 53:7 – 11
289. O'Connell MJ, Wahner HW, Ahmann DL et al (1978) Value of preoperative radionuclide bone scan in suspected primary breast carcinoma. Mayo Clin Proc 53:221 – 226
290. Baker RR (1978) Preoperative assessment of patients with breast cancer. Surg Clin North Am 58:681 – 691
291. Shutte H (1979) The influence of bone pain on the results of bone scans. Cancer 34:2039 – 2043
292. Massie JD (1984) Bone scanning and metastatic disease. In: Proceedings of 35th annual meeting, South Eastern Chapter, Society of Nuclear Medicine, pp V1–V20
293. Wilner D (1982) Radiology of bone tumors and allied disorders. Saunders, Philadelphia, p 3641
294. Rybak LD, Rosenthal DI (2001) Radiological imaging for the diagnosis of bone metastases. Q J Nucl Med 45:53 – 64
295. Ron IG, Striecker A, Lerman H, Bar-Am A, Frisch B (1999) Bone scan and bone biopsy in the detection of skeletal metastases. Oncol Rep 6:185 – 188
296. Elgazzar AH, Abdel-Dayem HM, Shible O (1991) Brucellosis simulating metastases on Tc99m MDP bone scan. Clin Nucl Med 16:162 – 164
297. Goris ML, Basso LV, Etcubanas E (1980) Photopenic lesions in bone scintigraphy. Clin Nucl Med 5:299 – 301
298. Sy WM, Westring DW, Weinberger G (1975) Cold lesions on bone imaging. J Nucl Med 16:1013 – 1016
299. Galasko CSD (1980) Mechanism of uptake of bone imaging isotopes by skeletal metastases. Clin Nucl Med 12:565
300. Steinborn MM, Heuck AF, Tiling R, Bruegel M, Gauger L, Reiser MF (1999) Whole-body bone marrow MRI in patients with metastatic disease to the skeletal system. J Computer Assist Tomogr 23:123 – 129
301. Taoka T, Mayr NA, Lee HJ, Yuh WT, Simonson TM, Rezai K, Berbaum KS (2001) Factors influencing visualization of vertebral metastases on MR imaging versus bone scintigraphy. Am J Roentgenol 176:1525 – 1530
302. Daldrup-Link HE, Franzius C, Link TM, Laukamp D, Sciuk J, Jurgens H, Schober O, Rummeny EJ (2001) Whole-body MR imaging for detection of bone metastases in children and young adults: comparison with skeletal scintigraphy and FDG PET. AJR 177:229 – 236

303. Kao CH, Hsieh JF, Tsai SC, Ho YJ, Yen RF (2000) Comparison and discrepancy of 18F-2-deoxyglucose positron emission tomography and Tc-99m MDP bone scan to detect bone metastases. Anticancer Res 20:2189 – 2192
304. Moog F, Kotzerke J, Reske SN (1999) FDG PET can replace bone scintigraphy in primary staging of malignant lymphoma. J Nucl Med 40:1407 – 1413
305. Schirrmeister H, Guhlmann A, Elsner K, Kotzerke J, Glatting G, Rentschler M, Neumaier B, Trager H, Nussle K, Reske SN (1999) Sensitivity in detecting osseous lesions depends on anatomic localization: planar bone scintigraphy versus F18 PET. J Nucl Med 40:1623 – 1629
306. Garcia JR, Simo M, Soler M, Perez G, Lopez S, Lomena F (2005) Relative roles of bone scintigraphy and positron emission tomography in assessing the treatment response of bone metastases. Eur J Nucl Med Mol Imaging 32:1243 – 1244

Thyroid Gland

7

Salil D. Sarkar

7.1 Thyroid Anatomy

The thyroid gland develops from the foramen cecum of the tongue, to which it is connected by the thyroglossal duct. It descends during fetal life to reach the anterior neck by about the seventh week, and absent or aberrant descent results in ectopic locations, including the sublingual region and superior mediastinum (Fig. 7.1). The thyroglossal duct undergoes atrophy, though remnant duct tissue frequently is visualized by scintigraphy as an upper midline neck structure following thyroidectomy and TSH stimulation. The duct remnant occasionally may form a cyst.

The normal adult thyroid gland in iodine-sufficient regions weighs about 14 – 18 g. It is generally smaller in women than in men, and is barely palpable [1, 2]. The thyroid is located in the mid to lower anterior neck, with the isthmus in front of the trachea, usually just below the cricoid cartilage, and the lobes on the sides of the trachea. In older individuals with shorter necks, the thyroid may lie at or just above the suprasternal notch, and it is often partly substernal. The thyroid gland moves cephalad during swallowing, a characteristic that aids in palpation and in distinction of thyroid from nonthyroid neck masses.

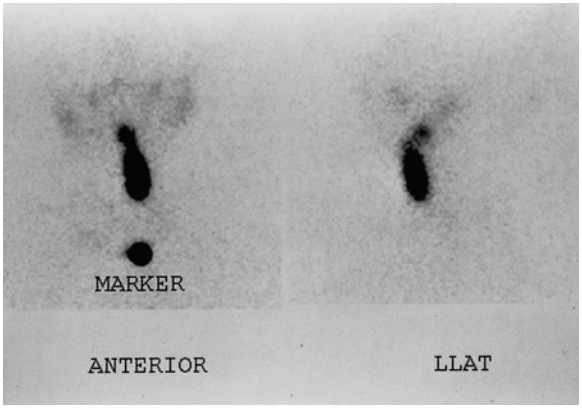

Fig. 7.1. Scintigraphic images in the anterior and left lateral projections show partly descended thyroid gland extending from the sublingual region to the upper neck

7.2 Hormone Synthesis and Secretion

7.2.1 Iodide Transport

The thyroid follicle consists of a colloid center, which acts as a storage site for thyroid hormone, surrounded by epithelial cells. The thyroid epithelial cell has a transport mechanism, also referred to as "trapping" or "uptake", that enables thyroid concentration of iodide far in excess of that in the plasma [3, 4]. A plasma membrane protein, the sodium/iodide symporter (NIS), is responsible for iodide transport. Symporter activity is influenced primarily by pituitary thyrotropin, also called thyroid stimulating hormone (TSH), which increases the transport of iodide. The trapped iodide subsequently undergoes organification and incorporation into thyroid hormones.

Iodide is accumulated, though not organified, in other organs including the salivary glands, stomach, mucous glands, skin, breast, and placenta, which may be associated with undesirable consequences for the clinical use of radioiodine. After therapeutic administration of ^{131}I for thyroid cancer, uptake in the salivary glands and gastric mucosa may cause sialitis and gastritis respectively, while activity in the skin and mucous secretions may increase environmental contamination and interfere with image interpretation [5–7]. Iodide uptake by the placenta and mammary glands exposes the fetus and the nursing child to unacceptable amounts of radiation from both the therapeutic and diagnostic use of ^{131}I [8, 9].

Other anions, including pertechnetate, thiocyanate, and perchlorate, also are accumulated by the thyroid gland. The uptake of pertechnetate is the basis for ^{99m}Tc-pertechnetate scintigraphy. Thiocyanate, derived from certain foods, decreases thyroid accumulation of iodine and may exacerbate iodine deficiency. Perchlorate has diagnostic and therapeutic applications, which are discussed later.

7.2.2 Hormone Synthesis

Iodide transported via NIS at the basolateral cell membrane is converted to an oxidized form at the apical surface of the cell by thyroid peroxidase (TPO) in the presence of hydrogen peroxide. Oxidation of iodide permits its binding to the amino acid tyrosine. Synthesis of hormone takes place in thyroglobulin, a glycoprotein, which is produced in the thyroid cell and extruded into the colloid. Iodine combines with tyrosine in thyroglobulin to form monoiodotyrosine (MIT) and diiodotyrosine (DIT). Subsequently, the iodotyrosines are coupled, with the formation of thyroxine (T_4) and triiodothyronine (T3). The coupling reaction also is mediated by peroxidase.

Decrease in peroxidase, associated with certain congenital and acquired thyroid disorders, impairs organic iodination and increases the proportion of unbound intrathyroidal iodine. Potassium perchlorate in pharmacological doses discharges unbound iodine from the thyroid. This is the basis for its use in the "Perchlorate Discharge Test" to detect an organification defect [10–12], and in the treatment of thyroid dysfunction caused by amiodarone, an iodine-rich drug (see later).

7.2.3 Release of Hormone and Thyroglobulin

In response to TSH, a small amount of colloid is engulfed by the epithelial cell and proteolyzed, with release of T_3 and T_4, which diffuse into the circulation. Thyroglobulin not undergoing proteolysis also enters the circulation in small quantities. The serum thyroglobulin has been used as a tumor marker in differentiated thyroid cancer. Thyroglobulin becomes undetectable following thyroidectomy and ^{131}I ablation, and its subsequent rise indicates a recurrence. TSH stimulation, by promoting colloid endocytosis, increases the amount of thyroglobulin released. Consequently, the serum thyroglobulin is a more reliable tumor marker at high TSH levels [13, 14].

7.2.4 T_3 and T_4

Most of the circulating thyroid hormones are bound to plasma proteins, the free fraction comprising about 0.05% of T_4 and 0.2% of T_3. Only the free hormone has metabolic effects, and it is a more accurate measure of thyroid function than the total hormone, which varies with plasma proteins levels.

T_3 is considered the active hormone. About 20%–30% of the circulating T_3 is secreted by the thyroid gland and the remainder is produced by monodeiodination of T_4 in extrathyroid tissues, notably the liver, kidney, brain, and pituitary [14]. Decrease in the peripheral conversion of T_4 to T_3 is a basis for the use of some antithyroid drugs (see below).

Synthetic forms of thyroid hormones are commonly used for replacement and/or suppressive therapy. Thyroxine is preferred for this purpose because it has a longer biological half-life (6–7 days) compared with T_3 (about 1–2 days). However, T_3 has a more rapid onset of action and may be useful in selected clinical situations.

7.2.5 Antithyroid Drugs

Most antithyroid drugs generally block one or more steps in the synthesis and metabolism of thyroid hor-

mone. The thiourea derivatives ("thionamides"), including propylthiouracil (PTU) and methimazole, are the most common antithyroid agents in use [14, 15]. Both decrease hormone synthesis primarily by blocking iodine organification, while PTU alone decreases the monodeiodination of T_4 to T_3. These drugs also lower serum levels of thyrotropin receptor autoantibodies (TRAB), which are responsible for Graves' hyperthyroidism. Methimazole or PTU may be used to control hyperthyroidism in Graves' disease and toxic nodular goiter before treatment with ^{131}I. In selected patients, these drugs also may be used as primary therapy for Graves' disease. Remission occurs in a minority of patients after thionamide treatment for 1 – 2 years.

Other drugs used for their antithyroid actions include glucocorticoids, iodides, lithium, and potassium perchlorate [14]. Glucocorticoids have a rapid inhibitory effect on the peripheral conversion of T_4 to T_3, and are a useful adjunct in thyroid storm. Their anti-inflammatory and cell membrane stabilizing actions have been utilized in Graves' ophthalmopathy and protracted subacute thyroiditis. Iodide in pharmacological amounts decreases the synthesis of thyroid hormones, permitting rapid control of hyperthyroidism in thyroid storm (see "Thyroid Autoregulation"). It also blocks thyroid uptake of radioiodine, and is recommended as a prophylactic measure after a nuclear reactor accident [16]. Lithium blocks the release of thyroid hormone, and may be used as an adjunct for the control of severe hyperthyroidism. Lithium prolongs iodine retention in thyroid tissue, and increases the absorbed radiation dose from ^{131}I, an advantage in the treatment of differentiated thyroid cancer [17]. Potassium perchlorate decreases thyroid iodine uptake and discharges unbound iodine. It may be used for the treatment of thyroid dysfunction caused by amiodarone, a drug with a high iodine content, and after accidental exposure to radioactive iodine.

7.2.6 Summary

Synthesis and secretion of thyroid hormone are regulated primarily by thyrotropin. Circulating iodide is trapped by the thyroid epithelial cell, oxidized, and bound to tyrosine. Coupling of iodotyrosines yields T_3 and T_4. Thyroid peroxidase promotes oxidation of iodide, a necessary step for iodination of tyrosine, as well as coupling of iodotyrosines. Thyroid hormone action is mediated by T_3. About 20% – 30% of the circulating T_3 is secreted by the thyroid, and the remainder is derived from the peripheral monodeiodination of T_4. Among the drugs with antithyroid actions, PTU and methimazole are most commonly used. Both drugs decrease hormone synthesis and TRAB levels, while PTU alone decreases the conversion of T_4 to T_3.

7.3 Thyroid Handling of Radiotracers

7.3.1 Technetium-99m-pertechnetate

Technetium-99m-pertechnetate is widely used for imaging the thyroid gland [18, 19]. The popularity of this radiotracer stems from its easy availability (from portable molybdenum-99 generators) and low absorbed radiation dose (short half-life of 6 h and absence of beta emissions).

^{99m}Tc-pertechnetate is trapped by the thyroid, but unlike iodine, it does not undergo organification and remains in the gland for a relatively short period. Therefore, imaging is done about 20 – 30 min after administration of the radiotracer. Approximately 5 – 10 mCi (185 – 370 MBq) is used. The thyroid-to-background activity ratio is not as high as that with radioiodine, so that ^{99m}Tc-pertechnetate is unsuitable for imaging of metastatic thyroid carcinoma, which usually functions poorly compared with normal tissue. Imaging of ectopic mediastinal thyroid tissue also may be suboptimal due to high blood and soft tissue background activity.

7.3.2 Iodine-123

Iodine-123 has ideal characteristics for imaging the thyroid gland, with a short physical half-life of 13 h, absence of beta emissions, and high uptake in thyroid tissue relative to background. However, it is less readily available and more expensive than ^{99m}Tc-pertechnetate. ^{123}I undergoes organic binding in the thyroid gland, and imaging is usually done 4 – 24 h after the administration of 200 – 400 μCi (7.4 – 14.8 MBq) of radiotracer [18, 19]. Because of its superior biodistribution characteristics, ^{123}I is preferred over ^{99m}Tc-pertechnetate for imaging of poorly functioning and ectopic thyroid glands. ^{123}I also may be used for whole body imaging in differentiated thyroid cancer (see below). Approximately 2 – 4 mCi (74 – 148 MBq) of the radiotracer are used for this purpose.

7.3.3 Iodine-131

Iodine-131 may be used for the measurement of thyroid uptake, which requires only small amounts of radiotracer. It is no longer used for routine imaging of the thyroid gland because of a high absorbed radiation dose related to the long physical half-life of 8 days and beta emissions. ^{131}I, however, continues to be valuable for the detection of metastases and recurrences in differentiated thyroid cancer [13, 19, 20]. Following appropriate patient preparation to increase TSH levels

(see "Manipulation of Thyrotropin Levels"), 2 – 4 mCi (74 – 148 MBq) of ^{131}I is administered and imaging is performed 48 – 96 h later. Radioiodine imaging has diagnostic as well as prognostic value. Iodine-avid tumors tend to have well-differentiated histological features and a favorable prognosis, whereas tumors that do not accumulate iodine are likely to be less differentiated and more aggressive [13, 21, 22].

Iodine-131 delivers a high radiation absorbed dose to the thyroid, with relative sparing of non-thyroid tissues. It is therefore ideal for the treatment of thyroid disease, and used extensively in the management of Graves' disease, toxic nodular goiter, and differentiated thyroid cancer.

7.3.4 Fluorine-18-fluorodeoxyglucose

Positron emission tomography (PET) with ^{18}F-fluorodeoxyglucose (FDG) is used in evaluating a variety of neoplasms including differentiated thyroid cancer. Imaging is possible for two reasons. First, malignant tumors derive energy from a higher rate of glycolysis, so that the uptake of glucose (and FDG) is increased. Second, unlike glucose, FDG is not metabolized completely and retained longer within the tumor. In differentiated thyroid cancer, FDG may be used to identify metastases not visualized at radioiodine imaging, and to assess prognosis. Lesions that accumulate FDG tend to follow a more aggressive course than lesions that are not FDG-avid [23, 24]. Whole body FDG-PET, therefore, is useful in evaluating high-risk thyroid cancer. Patient preparation is similar to that for radioiodine scintigraphy, since the uptake and diagnostic sensitivity of FDG are increased by TSH stimulation [25, 26]. Focal uptake of FDG within the thyroid gland, an occasional finding at evaluation of non-thyroid cancers, may be related to a benign or malignant pathology.

7.3.5 Summary

^{99m}Tc-pertechnetate is trapped but not organified by thyroid tissue. Imaging with this radiotracer is limited to the intact thyroid gland. ^{123}I and ^{131}I are trapped and organified, and provide higher thyroid-to-background uptake ratios. Both tracers are used to detect thyroid cancer metastases, while ^{123}I is also used for imaging the thyroid gland. ^{131}I delivers a high absorbed radiation dose to thyroid tissue, and is a mainstay in the management of Graves' disease, toxic nodular goiter, and differentiated thyroid cancer. Imaging and treatment of thyroid cancer metastases with ^{131}I require high TSH levels. ^{18}F-FDG, a glucose analogue, is accumulated in various malignant tumors including differentiated thyroid cancer. FDG-PET is particularly useful in high risk thyroid cancer, where it may detect metastases not visualized at radioiodine imaging and provide prognostic information. Tumor uptake of FDG is increased by TSH stimulation.

7.4 TSH and Thyroid Function

7.4.1 TSH Secretion

Thyrotropin-releasing hormone (TRH), a tripeptide originating from the hypothalamic median eminence, stimulates the secretion and synthesis of thyroid stimulating hormone (TSH, thyrotropin), a glycoprotein, by the anterior pituitary. TSH comprises an alpha unit, also present in other anterior pituitary hormones (FSH, LH), and a beta unit responsible for its specific actions. It acts on specific membrane-bound receptors of the thyroid epithelial cell, activating the adenylate cyclase system and increasing sodium/iodide symporter expression. As a result, the transport of iodide, synthesis of hormone, and release of T_3, T_4, and thyroglobulin are increased.

The production and release of TSH are influenced by the concentration of T_3 within the pituitary. When the T_3 concentration falls below a "set point", TSH secretion increases, and synthesis and release of thyroid hormones are accelerated. Conversely, when the T_3 level rises above the set point, TSH release is inhibited. In addition to its pituitary effect, T_3 inhibits hypothalamic TRH release. Other mechanisms reported more recently include the inhibitory actions of the released TSH on TRH secretion, and on TSH receptors in the pituitary itself. In sum, TSH secretion is influenced by thyroid-to-pituitary, thyroid-to-hypothalamus, pituitary-to-hypothalamus, and pituitary-to-pituitary feedback control mechanisms, which combine to reduce fluctuations in circulating T_3 and T_4 [14, 27 – 28]. In the rare condition of partial tissue resistance to thyroid hormone, the pituitary fails to respond to increasing T_3 levels, so that TSH continues to be secreted and serum TSH and thyroid hormones are both elevated. Individuals with this condition may become hyperthyroid if tissue resistance is limited to the pituitary or remain euthyroid if resistance is generalized [29].

In addition to regulation of thyroid function, TSH promotes thyroid growth. If thyroid hormone synthesis is chronically impaired, as in iodine deficiency and autoimmune thyroid disease, chronic TSH stimulation eventually may lead to the development of a goiter.

7.4.2 Serum TSH in Thyroid Disorders

The serum TSH is a sensitive marker of thyroid function. Normal serum TSH is about 0.45 – 4.5 μunits/ml,

and levels up to 20 μunits/ml are considered normal in newborns because of the contribution of maternal TSH. During early gestation, TSH tends to be at low normal (at times below normal) levels, which coincide with a surge in human chorionic gonadotropin (hCG) release. Serum TSH is increased in primary hypothyroidism and decreased in hyperthyroxinemia of all etiologies except for the uncommon entity of thyrotropin-induced hyperthyroidism.

The availability of high sensitivity assays, which can accurately measure very low TSH levels, has significantly improved the ability to diagnose mild hyperthyroidism. Third-generation assays can detect levels as low as 0.01 – 0.03 μunits/ml and are particularly helpful in establishing subclinical hyperthyroidism in nodular goiter and athyrotic persons receiving replacement levothyroxine therapy [27, 30]. Subclinical hyperthyroidism in older individuals has been associated with adverse effects on the heart and bone mineral density [31 – 34].

The serum TSH is also a sensitive marker of hypothyroidism. As such it is commonly used to detect hypothyroidism in Hashimoto's disease, newborns, and hyperthyroid patients treated with ^{131}I. The TRH Stimulation Test measures the TSH response to TRH. It was used in the past for the diagnosis of subtle thyroid dysfunction including central hypothyroidism, but has been largely abandoned with the emergence of high-sensitivity TSH assays [35].

7.4.3 Manipulation of TSH Levels

7.4.3.1 Suppressing TSH Levels

The secretion of TSH is suppressed with exogenous thyroid hormone to avoid stimulation of tumor growth in patients with differentiated thyroid cancer, and to decrease thyroid size or arrest thyroid growth in the early stages of goiter development. While levothyroxine (T_4) is the traditional thyroid hormone preparation for this purpose, regimens combining T_4 and T_3 are currently under investigation. Not infrequently, patients receiving levothyroxine are referred for a nuclear uptake and scan, requiring hormone withdrawal to allow the recovery of the hypothalamus-pituitary-thyroid axis. It may take as long as 8 weeks for recovery and for return of radioiodine uptakes to baseline values; however, shorter periods of up to 3 weeks may suffice for evaluating nodular function.

7.4.3.2 Increasing TSH Levels

Stimulation with TSH increases thyroid function and thyroid uptake of radioiodine. This principle is used in differentiated thyroid cancer for the detection and treatment of thyroid remnants and thyroid cancer metastases with radioiodine [13, 19, 36]. Thyroid stimulating hormone levels are allowed to rise to 30 – 50 μunits/ml or higher after withholding thyroid hormone supplements, or after administering recombinant human TSH. The latter is gaining in popularity since it shortens the preparation time and avoids a period of hypothyroidism [37 – 41]. Currently, recombinant TSH is approved primarily for diagnostic use, i.e., prior to scintigraphy and serum thyroglobulin measurement. It appears to be effective in monitoring thyroid cancer, especially the low-risk papillary type, though the radioiodine uptake and serum thyroglobulin usually are lower than after hormone withdrawal. As noted earlier, PET with fluorodeoxyglucose is optimal at high TSH levels, and it may be combined with radioiodine imaging and thyroglobulin measurement in selected patients [23 – 26].

Recombinant human TSH may have the potential to facilitate the treatment of large nodular goiters with ^{131}I. Radioiodine uptake in these goiters is usually low and heterogeneous. As a result, large and multiple therapeutic ^{131}I doses may be needed to reduce goiter volume and cure the associated hyperthyroidism. In recent studies, a small dose of recombinant TSH resulted in a more uniform ^{131}I distribution, a higher 24-h uptake, and increased therapeutic efficacy [42, 43].

7.4.4 Summary

Thyroid stimulating hormone (thyrotropin) promotes iodide transport, and the synthesis and release of thyroid hormone and thyroglobulin. The secretion of TSH is modulated by the hypothalamus-pituitary-thyroid axis. The serum TSH level is a sensitive and specific marker of primary hyperthyroidism and hypothyroidism, and is particularly valuable for diagnosing subclinical thyroid dysfunction. Suppression of TSH secretion with exogenous thyroid hormone may help reduce goiter size and limit the growth of thyroid cancer. In athyrotic patients with differentiated thyroid cancer, a high serum TSH is needed for radioiodine/FDG imaging, thyroglobulin measurement, and ^{131}I treatment. The serum TSH may be increased by withdrawing thyroid hormone, or by administering recombinant human TSH.

7.5 Iodine Intake and Thyroid Function

7.5.1 Iodine Deficiency

The daily requirement for iodine is about 150 μg, increasing to roughly 200 – 250 μg during pregnancy. Iodine deficiency is most prevalent in the mountainous

regions of the Himalayas, Alps, and Andes, and in some low lands remote from the ocean. Iodine deficiency alone or in combination with goitrogens present in certain foods results in decreased thyroid hormone synthesis [44, 45]. Selenium deficiency may be a contributing factor. Reduced synthesis of thyroid hormone is compensated, at least in part, by increased TSH secretion, resulting eventually in goiter formation. Because an adequate supply of thyroid hormone is needed for fetal neurological development, maternal and fetal hypothyroidism resulting from iodine deficiency is associated with varying degrees of neuropsychological deficits including cretinism [46 – 50].

7.5.2 Iodine Excess

7.5.2.1 Thyroid Autoregulation

Thyroid hormone homeostasis is maintained by an intrathyroid autoregulatory mechanism in addition to the hypothalamus-pituitary-thyroid axis. When intrathyroid iodine concentrations are significantly increased, the rate of thyroid hormone synthesis is decreased, with a reduction in iodothyronine synthesis and decrease in the DIT/MIT ratio. This response is referred to as the Wolff-Chaikoff effect [51].

The amount of intrathyroid iodine needed to trigger the Wolff-Chaikoff effect varies, depending on prior long-term iodine intake and thyroid function. Barring other mechanisms, continued exposure to large amounts of iodine would eventually lead to hypothyroidism, with compensatory increase in TSH and development of goiter. While this does occur occasionally (see below), adaptation or "escape" from the effects of chronic iodide excess is more likely. Adaptation appears to be the result of an absolute decrease in iodide transport, so that intrathyroid iodine is reduced to levels that allow resumption of hormone synthesis.

The inhibitory effect of iodides on thyroid function is utilized clinically for prompt control of severe hyperthyroidism and thyroid storm. In Graves' disease, large doses of iodide decrease not only hormone synthesis but also hormone release [52]. Since escape from the inhibitory effect is likely, iodide therapy is only a short-term measure for lowering thyroid hormone levels rapidly.

7.5.2.2 Thyroid Dysfunction

Iodine excess may lead to hyperthyroidism or hypothyroidism [51 – 54]. Iodine-induced hyperthyroidism, referred to as jodbasedow, characteristically occurs in persons with nodular thyroid glands. Hyperthyroidism occurring after iodine supplementation in endemic goiter areas is a classical example. Iodine-containing medical products, including amiodarone, radiographic dyes, and kelp, also have the potential to cause jodbasedow [51, 55 – 58]. Amiodarone, a cardiac antiarrhythmic drug, is perhaps the commonest source of iodine today. Each 200 mg tablet yields about 7 mg free iodine, while the daily requirement is only 0.15 mg [55, 56]. Amiodarone-related hyperthyroidism may be related to another mechanism. The drug may cause thyroiditis, which is discussed later (see "Destructive (Subacute) Thyroiditis"].

Hypothyroidism related to increased iodine intake results from the inability to escape from the Wolff-Chaikoff effect. It is more frequent in iodine-sufficient areas, where autoimmune disease is more common than nodular disease [53, 54]. In the past, "iodide goiter" with or without hypothyroidism was related to the use of iodine solutions as mucolytic agents in bronchial asthma, often with reversal of clinical manifestations after stopping the drug. A similar condition has been reported from ingestion of large quantities of (iodine-rich) seaweed in the coastal regions of Japan [59].

7.5.2.3 Iodine and Autoimmune Thyroid Disease

Iodine appears to have another, more insidious effect on the thyroid. In regions that were previously iodine-deficient, a rise in autoimmune thyroid disease has been observed after the institution of iodine supplementation in foods [60]. Experimental work in animals confirms an association between iodine and autoimmunity, probably related in part to the greater antigenic potential of highly iodinated thyroglobulin [61]. Autoimmune thyroid disease and associated disorders are discussed under "Hashimoto's Disease".

7.5.3 Summary

Excessive amounts of iodine may cause hypothyroidism or hyperthyroidism. A significant increase in thyroid concentration of iodine may initiate an autoregulatory response, the Wolff-Chaikoff effect, which decreases hormone synthesis. Although this effect is usually temporary, occasionally it may be sustained and lead to hypothyroidism. Iodine-induced hypothyroidism is more frequent in iodine-replete regions with a high prevalence of autoimmune thyroid disease. Excessive iodine also may lead to hyperthyroidism. This may occur in individuals with nodular thyroid glands, and it is more common in iodine-deficient areas. In addition to its effects on thyroid function, iodine is believed to promote the development of autoimmune thyroid disease, a view supported by epidemiological and experimental evidence.

7.6 Endemic Goiter

Endemic goiter is attributed primarily to iodine deficiency, possibly in association with selenium deficiency or goitrogens. Goitrogens are present in certain foods and chemicals and cause either decreased synthesis or increased metabolism of thyroid hormone.

7.6.1 Goitrogens

Certain foods including cassava and bamboo shoots contain cyanogenic compounds, which may interfere with thyroid accumulation of iodine and exacerbate iodine deficiency [62]. Other foods with goitrogenic potential include pearl millet and plants from the brassica family [63].

Various chemicals may alter thyroid hormone metabolism and lead to the development of goiter. Contamination of drinking water with ammonium perchlorate from discarded rocket fuel is a concern. However, the suggested regulatory limit for perchlorate concentration in water is well below the amount needed to block iodine uptake [64]. Cigarette smoking has been linked to thyroid disease and aggravation of Graves' ophthalmopathy. The effects presumably are mediated in part by thiocyanate [65]. Other industrial chemicals and drugs may induce hepatic enzymes that accelerate the metabolic elimination of thyroid hormone [66, 67].

7.6.2 Pathophysiology

The thyroid enlarges primarily in response to TSH stimulation resulting from inefficient hormone synthesis. There is natural heterogeneity in cellular growth and response to TSH, and rapid proliferation of thyrocytes with a growth advantage leads eventually to the development of nodules. An additional mechanism for nodule formation involves the activation of the adenylate cyclase system, usually by somatic mutations of the TSH receptor, with increase in cell replication rates [68 – 71]. Evidence of such mutations has been found in both solitary nodules and nodules associated with multinodular goiters. The development of toxic nodular goiter occurs over a period of years, if not decades, with gradual transition of cell clones to micronodules, and subsequently to macronodules of sufficient size to cause hyperthyroidism. The disorder, therefore, is typically seen in older individuals.

Hyperthyroidism associated with nodular goiter is often subclinical, with a suppressed TSH and a normal free T4. Nonetheless, treatment with ^{131}I or surgery is generally recommended in the elderly because of increased risk of osteopenia, and of adverse cardiovascular sequelae including atrial fibrillation [31 – 34]. Suppressive levothyroxine therapy is often attempted to arrest nodular growth in euthyroid patients, but is rarely successful since the nodules are largely independent of TSH control [72].

Hyperfunctioning nodules may become "cold" or non-functional due to hemorrhage and necrosis. Cold nodules also may be caused by the failure of iodide transport with aging, rapid proliferation of cells with decreased function, and malignant transformation.

7.6.3 Radionuclide Procedures

Toxic multinodular goiters typically show irregular distribution of radioiodine or technetium pertechnetate, and a normal or mildly elevated 24-h radioiodine uptake. The irregular tracer distribution is consistent with heterogeneity in cell function and growth, and the presence of micro- and macronodules (Fig. 7.2). Large and discrete hyperfunctioning nodules may be associated with poor uptake in the extranodular thyroid tissue. The latter consists of "suppressed" normal tissue, and/or small autonomous nodules with relatively less tracer accumulation. Following ^{131}I treatment, the areas that were previously "cold" may appear more active. A dominant nonfunctioning nodule may be related to a number of causes, but may require additional diagnostic work-up to exclude malignancy.

Nodular disease may be treated with ^{131}I or surgery. For large multinodular goiters, the goal of ^{131}I treatment is to reduce thyroid volume and cure hyperthyroidism. But the treatment may fail because radioiodine distribution is heterogeneous and the 24-h uptake is not significantly elevated. Stimulation with recombinant human TSH causes a global increase in thyroid uptake of ^{131}I, and appears to improve the therapeutic outcome [42, 43].

7.6.4 Summary

Endemic goiter is the result of iodine deficiency, occasionally in association with goitrogens, with decrease in hormone production and compensatory increase in TSH secretion. Hyperfunctioning nodules may result from a growth advantage of some cells or gain-of-function mutations of the TSH receptor. Nodular thyroid disease is a common cause of subclinical hyperthyroidism in the elderly, and it may be associated with atrial fibrillation and osteopenia. Radionuclide studies typically show heterogeneous tracer distribution in the thyroid gland, with a normal or mildly elevated 24-h radioiodine uptake. Recombinant human TSH increases the thyroid uptake globally, and may facilitate the treatment of nodular goiters with ^{131}I.

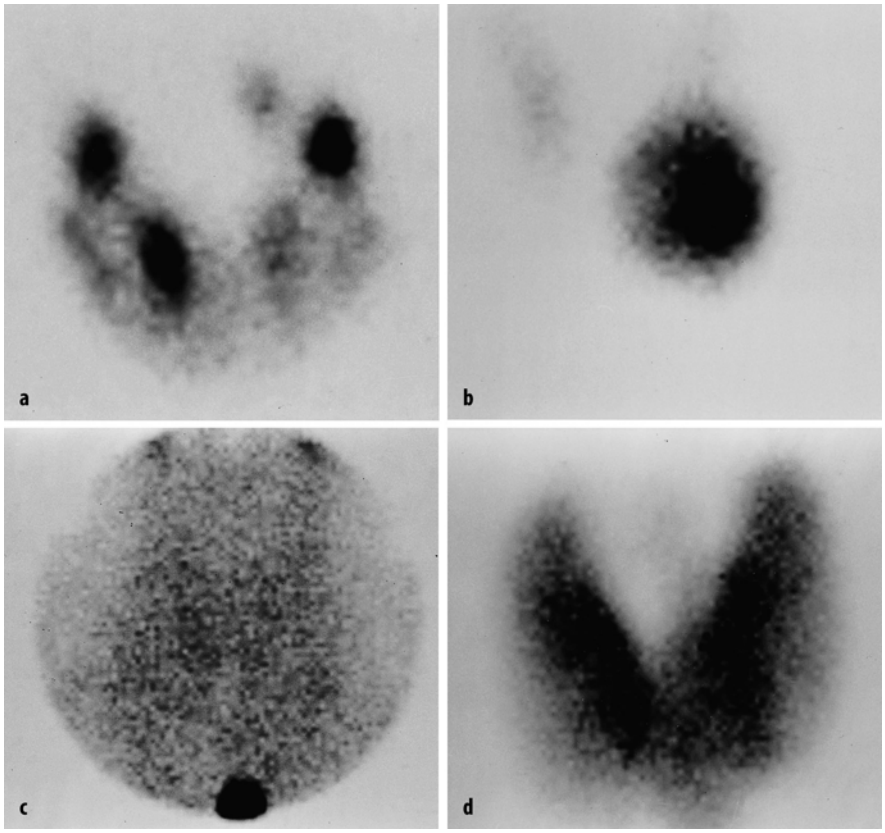

Fig. 7.2a–d. Scintigraphic images in four types of hyperthyroidism show: **a** multinodular goiter, **b** solitary hyperfunctioning thyroid nodule, **c** thyroiditis, **d** Graves' disease

7.7 Destructive ("Subacute") Thyroiditis

Destructive thyroiditis, also referred to as "subacute thyroiditis" or simply "thyroiditis", is characterized by cell membrane breakdown and release of excessive amounts of thyroid hormone into the circulation. Serum thyroglobulin levels also are increased. The usual causes are autoimmune thyroid disease, viral infection, and amiodarone treatment. These are discussed below. Less commonly, thyroiditis may be related to treatment with interferon alpha, interleukin-2, lymphokine-activated killer (LAK) cells, and lithium. These therapeutic agents probably exacerbate existing autoimmune thyroid disease [73–77]. Bacterial thyroiditis is rarely encountered today.

Thyroiditis tends to resolve spontaneously. Hyperthyroidism in the active phase is followed by transient hypothyroidism before restoration of the euthyroid state, usually in 6–12 months. Treatment usually consists of β-adrenergic blockers in the hyperthyroid phase, with analgesics for pain. Protracted thyroiditis may require glucocorticoids.

7.7.1 Postpartum Thyroiditis

Postpartum thyroiditis, also known as "painless" or "subacute lymphocytic" thyroiditis, is the principal thyroid disorder in postpartum women. It may be considered an accelerated form of autoimmune thyroid disease, attributed to suppression of immune-related disorders during pregnancy with a rebound after childbirth [78–82]. For the same reason, Graves' disease also may occur in the postpartum period, though less frequently, and a strong association with insulin-dependent diabetes mellitus, an autoimmune condition, has been noted.

Postpartum thyroiditis, like other forms of destructive thyroiditis, is a self-limited disease, but tends to reoccur in subsequent pregnancies. Permanent hypothyroidism occurs in 20%–25% of patients over a period of 5 years. The incidence is greater in iodine-replete regions with a higher prevalence of autoimmune thyroid disease. Elevated thyroid peroxidase ("anti-microsomal") antibodies during pregnancy are associated with a sharp increase in postpartum thyroiditis.

7.7.2 Viral Thyroiditis

Viral subacute thyroiditis, also known as "de Quervain's" thyroiditis, usually occurs after an upper respiratory tract infection. The disorder tends to be seasonal and may occur in clusters, occasionally causing mini epidemics [83]. It usually presents as a painful and tender goiter, associated with general malaise and possibly fever. Inflammation frequently begins in one lobe of the thyroid and gradually spreads to involve the entire gland. Permanent hypothyroidism is uncommon.

7.7.3 Thyroiditis and Other Effects of Amiodarone

Amiodarone is an iodine-rich benzofuran derivative used to treat and prevent cardiac arrhythmias. It may precipitate a number of thyroid conditions including thyroiditis, which appears to be related to a cytotoxic effect [55, 56]. Since amiodarone and its metabolite desethylamiodarone have long half-lives of up to 100 days, the thyroid-related effects can be protracted and occasionally may begin after stopping the drug. Amiodarone-induced thyroiditis generally requires treatment with a glucocorticoid. Permanent hypothyroidism is uncommon.

Other side effects of amiodarone stem from its high iodine content (see Sect. 7.5, "Iodine Intake and Thyroid Function"). Thyroid hormone synthesis may increase or decrease. Increased hormone synthesis (jodbasedow) typically occurs in nodular thyroid glands, which are common in iodine-deficient areas. Decreased hormone synthesis, resulting from a persistent Wolff-Chaikoff effect, is more frequent in iodine-sufficient regions with a higher incidence of autoimmune thyroid disease.

Treatment of amiodarone-induced hyperthyroidism depends on the cause, although this may be difficult to determine. Thyroiditis, as noted earlier, responds to glucocorticoid therapy. Jodbasedow is treated with a thionamide, and if needed with potassium perchlorate to deplete thyroid iodine content. A clear distinction between thyroiditis and jodbasedow is frequently not possible, and treatment should be initiated with both a glucocorticoid and a thionamide. In resistant cases, ^{131}I treatment may be feasible if the radioiodine uptake is adequate. Thyroidectomy may be an alternative in refractory cases, or when continued amiodarone treatment and prompt relief of hyperthyroidism are required.

Other actions of amiodarone are worth noting. It blocks peripheral conversion of T4 to T3, binding of T3 to its receptors, and thyroid release of T3 and T4. These effects may permit the use of amiodarone in very selected cases of hyperthyroidism [84].

7.7.4 Radionuclide Procedures

Poor radioiodine/^{99m}Tc-pertechnetate uptake in the thyroid gland is the hallmark of subacute thyroiditis of any etiology (Fig. 7.2). Decreased tracer uptake is related to TSH suppression by excessive thyroid hormone released from damaged follicles, and to decreased hormone synthesis in the damaged gland. The thyroid uptake and scan normalize with resolution of thyroiditis.

The nuclear study is frequently used in hyperthyroid individuals to differentiate thyroiditis, with low uptake, from Graves' disease, with high uptake. A thyroid uptake/scan also may be worthwhile in amiodarone-related hyperthyroidism, which may be due to jodbasedow or thyroiditis. A suppressed thyroid uptake is non-diagnostic, while a normal or high uptake suggests that jodbasedow is likely. The thyroid uptake measurement also helps determine the feasibility of ^{131}I treatment in refractory cases.

7.7.5 Summary

Subacute thyroiditis is usually caused by exacerbation of autoimmune disease, viral infection, and amiodarone therapy. It is characterized by an initial thyroid-destructive phase, with release of stored hormone into the circulation. Nuclear studies in this phase show poor radiotracer uptake, and help differentiate thyroiditis from other causes of hyperthyroidism. The disorder is self-limited and treated symptomatically, though amiodarone-related thyroiditis tends to last longer and generally requires a glucocorticoid. Amiodarone may be associated with other thyroid disorders related to its high iodine content, including jodbasedow (iodine-induced hyperthyroidism) and hypothyroidism.

7.8 Autoimmune Thyroid Disease

7.8.1 Etiological Factors

Autoimmune thyroid disease comprises two major entities, Hashimoto's disease (also known as chronic autoimmune thyroiditis) and Graves' disease. Variants of Hashimoto's disease include "subacute" thyroiditis, which occurs typically in the postpartum period, and atrophic thyroiditis. There is a genetic predisposition to the disease, with contribution from environmental factors [65, 85–89]. As discussed earlier, iodine excess has been associated with autoimmune thyroid disease. Cigarette smoking has been linked to exacerbation of autoimmune thyroid conditions including Graves' ophthalmopathy, and increased occurrence in women im-

plies a role of sex steroids. The relationship between psychological stress and Graves' disease presumably is related to immune suppression and rebound. A similar mechanism is believed to apply to postpartum thyroid dysfunction. The occasional occurrence of Graves' disease in couples suggests that infection may be a precipitating factor. In support of this hypothesis, antibodies to certain microbial proteins have been found to cross-react with the human TSH receptor. Rarely, Graves' disease may be precipitated by ^{131}I treatment of nodular goiter in patients with underlying autoimmune thyroid disease [90]. Follicular disruption and release of thyroid antigens is believed to be the initiating event in these instances. Onset of Graves' disease after subacute thyroiditis probably represents an analogous situation [91, 92].

7.8.2 Pathophysiology

Elevation of thyroid peroxidase antibodies is characteristic of Hashimoto's disease. Antithyroglobulin antibodies also may be elevated. Hormone synthesis is impaired with compensatory increase in TSH secretion, which stimulates thyroid function and growth. Eventually, many patients become hypothyroid. Both overt and subclinical hypothyroidism related to autoimmune disease are widely prevalent in iodine-sufficient regions [93–95]. Exacerbation of Hashimoto's disease, frequently occurring in the postpartum period, is a cause of subacute thyroiditis (see "Postpartum Thyroiditis"). Graves' disease is associated with high levels of thyrotropin receptor autoantibodies (TRAB) that stimulate thyroid growth, and thyroid hormone synthesis and release [86–89]. Most organ systems are affected by Graves' disease, the cardiovascular manifestations being the most apparent [31–33]. Increased heart rate and contractility increases the cardiac output. These effects are related to a direct inotropic effect of T3, decreased systemic vascular resistance, increased preload related to a higher blood volume, and heightened sensitivity to sympathetic stimulation. Blood volume is increased by activation of the renin-angiotensin-aldosterone system caused by the reduction in systemic vascular resistance, and by increased erythropoietin activity. Overt cardiac failure may result from severe and prolonged hyperthyroidism, but is rarely seen today. Atrial fibrillation is not an uncommon complication, occurring in up to 15% of patients with hyperthyroidism.

7.8.3 Radionuclide Procedures

Nuclear studies are non-specific in Hashimoto's disease. The thyroid gland is usually symmetrically enlarged with uniform tracer distribution, and the 24-h uptake is normal. In subacute thyroiditis resulting from exacerbation of Hashimoto's disease, tracer uptake is typically absent or very low.

Graves' disease typically shows uniformly increased tracer uptake in a diffusely enlarged thyroid gland, frequently with visualization of a pyramidal lobe (Fig. 7.2). However, atypical appearances, particularly in Graves' disease superimposed on nodular goiter, are occasionally encountered. If needed, TRAB measurement may assist in confirming the diagnosis. The 24-h uptake is elevated and, on average, much higher than in toxic nodular goiter. ^{131}I treatment and antithyroid drugs remain the primary means of management of Graves' disease.

7.8.4 Summary

Autoimmune thyroid disorders, including Hashimoto's disease and Graves' disease, are related primarily to genetic susceptibility, with contributions from environmental factors including chronic iodine excess. Elevated serum anti-TPO antibodies are characteristic of Hashimoto's disease. Exacerbation of Hashimoto's disease, usually observed in postpartum women, may cause subacute thyroiditis with hyperthyroidism. Scintigraphy in such cases shows poor tracer uptake in the thyroid gland. Graves' disease is characterized by elevated TSH receptor antibodies (TRAB). It affects most organ systems, but the cardiovascular manifestations generally are the most pronounced, and cardiac complications are not uncommon. The thyroid uptake and scan may be used to confirm the diagnosis of Graves' disease and differentiate it from a destructive thyroiditis.

7.9 Thyroid Dysfunction During Gestation

7.9.1 Hyperthyroidism

Hyperthyroidism during pregnancy is usually caused by gestational transient thyrotoxicosis (GTT) or Graves' disease [48, 49]. Gestational transient thyrotoxicosis appears to be related to the TSH-like effects of human chorionic gonadotropin (hCG), which increases in early gestation. The condition resolves spontaneously in the second half of pregnancy. The incidence and severity of GTT are variable. It is occasionally associated with hyperemesis gravidarum. As in other hyperthyroid conditions, the serum TSH is low and free T4 may be elevated, but thyroid autoantibodies including TSH receptor antibodies (TRAB) are absent, since GTT is not an autoimmune condition.

Graves' disease in pregnancy is a more serious condition associated with significant maternal and fetal risks, including pre-eclampsia, premature delivery, low infant birth weight, neonatal Graves' disease, and central congenital hypothyroidism [48, 49, 96]. Characteristically, TRAB levels are elevated. Management of gestational Graves' disease poses several challenges. Iodine-131 therapy is contraindicated, and thyroidectomy is inherently risky for both the mother and the fetus. Left untreated or inadequately treated, Graves' disease in pregnancy increases the risk of fetal hyperthyroidism because of the transplacental passage of maternal TRAB. Of the available treatment options, thionamides – either PTU or methimazole – appear to be the safest. These drugs help control hyperthyroidism and reduce TRAB levels, but should be used only in small doses since they cross the placenta and may decrease fetal thyroid function [15, 49]. Graves' disease tends to improve in the later stages of pregnancy, probably due to immune suppression, allowing thionamides to be tapered or discontinued. But therapy should be resumed after childbirth because of the risk of recurrence related to postpartum immune rebound.

7.9.2 Hypothyroidism

Normal neurological development is dependent on adequate maternal and fetal thyroid function, and on thyroid hormone sufficiency in the early neonatal period [45 – 50, 97]. Iodine deficiency, present in regions of endemic goiter, may be associated with hypothyroidism in both the mother and the fetus, and may cause varying severities of neurological and growth retardation including cretinism. Fortunately, the incidence of these disorders has declined due to iodine supplementation programs.

Maternal thyroid hormone is increasingly recognized as an important factor in fetal development in the second and third trimesters. Maternal hypothyroidism alone, i.e., without fetal hypothyroidism, has been linked to neuropsychological deficits in the offspring, and to increased risk of fetal loss and preterm delivery. Autoimmune thyroid disease is the most frequent cause of hypothyroidism in the mother. While overt iodine deficiency is relatively uncommon today, iodine intake has gradually declined in many "iodine-sufficient" areas and may actually fall short of requirement during pregnancy. This may have the potential to aggravate autoimmune hypothyroidism.

7.9.3 Summary

Hyperthyroidism in pregnancy is generally caused by GTT or Graves' disease. Management of Graves' disease remains a challenge, with thionamide treatment as the best option. Patients should be monitored closely because undertreatment, with persistently high maternal TRAB, increases the risk of fetal hyperthyroidism, while overtreatment may cause fetal hypothyroidism. Gestational hypothyroidism is usually related to autoimmune thyroid disease, and less frequently to iodine deficiency. The latter may be associated with fetal hypothyroidism as well. Neurological development is influenced by maternal thyroid function, fetal thyroid function, and thyroid hormone levels in the newborn.

References

1. Pankow BG, Michalak J, McGee MK (1985) Adult human thyroid weight. Health Physics 49:1097 – 1103
2. Mochizuki Y, Mowafy R, Pasternack B (1963) Weights of human thyroids in New York City. Health Physics 9: 1299 – 1301
3. Wolff J (1964) Transport of iodide and other anions in the thyroid gland. Physiol Rev 44:45
4. De la Vieja A, Dohan O, Levy O, Carrasco N (2000) Molecular analysis of the sodium/iodide symporter: Impact on thyroid and extrathyroid pathophysiology. Physiol Rev 80:1083 – 1105
5. Alexander C, Bader JB, Shaefer A, et al (1998) Intermediate and long-term side effects of high-dose radioiodine therapy for thyroid carcinoma. J Nucl Med 39:1551 – 1554
6. Kappes RS, Sarkar SD, Har-El G, et al (1994) Iodine-131 therapy of thyroid cancer: extensive contamination of the hospital room in a patient with tracheostomy. J Nucl Med 35:2053 – 2054
7. Mitchell G, Pratt BE, Vini L, et al (2000) False positive 131I whole body scans in thyroid cancer. Br J Radiol 73:627 – 635
8. Romney B, Nickoloff EL, Esser PD (1989) Excretion of radioiodine in breast milk. J Nucl Med 30:124 – 126
9. Stoffer SS, Hamburger JI (1975) Inadvertent I-131 therapy for hyperthyroidism in the first trimester of pregnancy. J Nucl Med 17:146 – 149
10. Roti E, Minelli R, Gardini E, et al (1994) The iodine perchlorate discharge test before and after one year of methimazole treatment of hyperthyroid Graves' disease. J Clin Endocrinol Metab 78:795 – 799
11. Bijayeswar V, Coffey R, Coyle R et al (1999) Concurrence of Pendred syndrome, autoimmune thyroiditis, and simple goiter in one family. J Clin Endocrinol Metab 84:2736 – 2738
12. Frills J (1987) The perchlorate discharge test with and without supplement of potassium iodide. J Endocrinol Invest 10:581 – 584
13. Sarkar SD, Savitch I (2004) Management of thyroid cancer. Applied Radiol November:34 – 45
14. Sarkar SD (1996) Thyroid pathophysiology. In: Sandler MP, Coleman RE, Th. Wackers FJ (eds) Diagnostic nuclear medicine. Williams and Wilkins, Baltimore, pp 899 – 909
15. Cooper DS (2005) Antithyroid drugs. N Engl J Med 352:905 – 917
16. Schneider AB, Becker DV, Robbins J (2002) Protecting the thyroid from accidental or terrorist-instigated ^{131}I releases. Thyroid 12:271 – 272
17. Koong S, Reynolds JC, Movius EG et al (1999) Lithium as a potential adjuvant to I-131 therapy of metastatic, well-differentiated thyroid carcinoma. J Clin Endocrinol Metab 84:912 – 916

18. Sarkar SD (2006) Benign thyroid disease, in lifelong learning and self-assessment program (LLSAP), Society of Nuclear Medicine (www.snm.org)
19. Sarkar SD, Becker DV (1995) Thyroid uptake and imaging. In: Becker KL (ed) Principles and practice of endocrinology and metabolism. Lippincott, Philadelphia, pp 307 – 313
20. Sarkar SD, Kalapparambath T, Palestro CJ (2002) Comparison of I-123 and I-131 for whole body imaging in thyroid cancer. J Nucl Med 43:632 – 634
21. Casara D, Rubello D, Saladini G, et al (1993) Different features of pulmonary metastases in differentiated thyroid cancer: Natural history and multivariate statistical analysis of prognostic variables. J Nucl Med 34:1626 – 1631
22. Ward LS, Santarosa PL, Granja F, et al (2003) Low expression of sodium iodide symporter identifies aggressive thyroid tumors. Cancer Lett 200:85 – 91
23. Hooft L, Hoekstra OS, Deville W, et al (2001) Diagnostic accuracy of ^{18}F-fluorodeoxyglucose positron emission tomography in the follow-up of papillary or follicular thyroid cancer. J Clin Endocrinol Metab 86:3779 – 3786
24. Wang W, Larson SM, Fazzari M, et al (2000) Prognostic value of ^{18}F-fluorodeoxyglucose positron emission tomographic scanning in patients with thyroid cancer. J Clin Endocrinol Metab 85:1107 – 1113
25. Chin BB, Patel P, Cohade C, et al (2004) Recombinant human thyrotropin stimulation of fluoro-D-glucose positron emission tomography in well-differentiated thyroid carcinoma. J Clin Endocrinol Metab 89:91 – 95
26. Moog F, Linke R, Manthey N, et al (2000) Influence of thyroid stimulating hormone levels on uptake of FDG in recurrent and metastatic differentiated thyroid carcinoma. J Nucl Med 41:1989 – 1995
27. Freitas J, Gross MD, Sarkar SD (2003) Laboratory (in vitro) assessment of thyroid function. In: Sandler MP et al (eds) Diagnostic nuclear medicine, 4th edn. Lippincott Williams and Wilkins, Philadelphia, pp 591 – 606
28. Prummel MF, Brokken LJS, Wiersinga WM (2004) Ultra short-loop feedback control of thyrotropin secretion. Thyroid 14:825 – 829
29. Refetoff S, Weiss RE, Usala SJ (1993) The syndromes of resistance to thyroid hormone. Endocr Rev 14:348 – 399
30. Burmeister LA, Goumaz MO, Mariash CN, Oppenheimer JH (1992) Levothyroxine dose requirements for thyrotropin suppression in the treatment of differentiated thyroid cancer. J Clin Endocrinol Metab 75:344 – 350
31. Klein I, Ojamaa K (2001) Thyroid hormone and the cardiovascular system. N Engl J Med 344:501 – 509
32. Kahaly GJ, Dillmann WH (2005) Thyroid hormone action in the heart. Endocrine Rev, July, e-publication
33. Parle JV, Maisonneuve P, Sheppard MC, et al (2001) Prediction of all-cause and cardiovascular mortality in elderly people from one low serum thyrotropin result: a 10-year cohort study. Lancet 358:861 – 865
34. Bauer DC, Ettinger B, Nevitt MC, et al (2001) Risk for fracture in women with low serum levels of thyroid-stimulating-hormone. Ann Intern Med 134:561 – 568
35. Hartoft-Nielsen M-L, Lange M, Rasmussen AK, et al (2004) Thyrotropin-releasing hormone stimulation test in patients with pituitary pathology. Horm Res 61:53 – 57
36. Sarkar SD, Torres MA, Manalili E et al (1998) Iodine-131 effects on thyroid remnant function: influence of serum TSH levels. Radiology 209P:404
37. Ladenson PW, Braverman LE, Mazzaferri EL et al (1997) Comparison of administration of recombinant human thyrotropin with withdrawal of thyroid hormone for radioactive iodine scanning in patients with thyroid carcinoma. N Engl J Med 337:888 – 896
38. Haugen BR, Pacini F, Reiners C, et al (1999) A comparison of recombinant human thyrotropin and thyroid hormone withdrawal for the detection of thyroid remnant or cancer. J Clin Endocrinol Metab 84:3877 – 3885
39. Mazzaferri EL, Robbins RJ, Spencer CA, et al (2003) A consensus report of the role of serum thyroglobulin as a monitoring method for low-risk patients with papillary thyroid carcinoma. J Clin Endocrinol Metab 88:1433 – 1441
40. Sarkar SD, Afriyie MO, Palestro CJ (2001) Recombinant human thyroid-stimulating-hormone-aided scintigraphy: Comparison of imaging at multiple times after I-131 administration. Clin Nucl Med 26:392 – 395
41. Rudavsky AZ, Freeman LM (1997) Treatment of scan-negative, thyroglobulin-positive metastatic thyroid cancer using radioiodine I-131 and recombinant human thyroid stimulating hormone. J Clin Endocrinol Metab 82:11 – 14
42. Huysmans DA, Nieuwlaat W-A, Hermus AR (2004) Towards larger volume reduction of nodular goitres by radioiodine therapy: a role for pretreatment with recombinant human thyrotropin? Clin Endocrinol 60:297 – 299
43. Albino CC, Junior M, Olandoski M, et al (2005) Recombinant human thyrotropin as adjuvant in the treatment of multinodular goiters with radioiodine. J Clin Endocrinol Metab 90:2775 – 2780
44. Dunn JT (2002) Guarding our nation's thyroid health. J Clin Endocrinol Metab 87:486 – 488
45. Aghini-Lombardi F, Antonangeli L, Martino E et al (1999) The spectrum of thyroid disorders in an iodine-deficient community. The Pescopagano Survey. J Clin Endocrinol Metab 84:561 – 566
46. Boyages SC (1993) Iodine deficiency disorders. J Clin Endocrinol Metab 77:587 – 591
47. Haddow JE, Palomaki GE, Allan WC et al (1999) Maternal thyroid deficiency during pregnancy and subsequent neuropsychological development of the child. N Engl J Med 341:549 – 555
48. Lazarus JH (2002) Epidemiology and prevention of thyroid disease in pregnancy. Thyroid 12:861 – 865
49. Glinoer D (2003) Management of hypo- and hyperthyroidism during pregnancy. Growth Horm IGF Res 13 Suppl A:S45 – 54
50. American Academy of Pediatrics (1993) Newborn screening for congenital hypothyroidism: recommended guidelines. Pediatrics 91:1203 – 120
51. Fradkin JE, Wolff J (1983) Iodide-induced thyrotoxicosis. Medicine 62:1 – 20
52. Wartofsky L, Ransil BJ, Ingbar SH (1970) Inhibition by iodine of the release of thyroxine from the thyroid glands of patients with thyrotoxicosis. J Clin Invest 49:78 – 86
53. Pedersen IB, Knudsen N, Jorgensen T, et al (2002) Large differences in incidences of overt hyper- and hypothyroidism associated with a small difference in iodine intake: A prospective comparative register-based population survey. J Clin Endocrinol Metab 87:4462 – 4469
54. Laurberg P, Pedersen KM, Hreidarsson A et al (1998) Iodine intake and the pattern of thyroid disorders: a comparative epidemiological study of thyroid abnormalities in the elderly in Iceland and in Jutland, Denmark. J Clin Endocrinol Metab 83:765
55. Bogazzi F, Bartalena L, Gasperi M, et al (2001) The various effects of amiodarone on thyroid function. Thyroid 11: 511 – 519
56. Daniels GH (2001) Amiodarone-induced thyrotoxicosis. J Clin Endocrinol Metab 86:3 – 8
57. Livadas DP, Koutras DA, Souvatzoglou A, et al (1977) The toxic effects of small iodine supplements in patients with autonomous thyroid nodules. Clin Endocrinol 7:121 – 127

58. Laurie AJ, Lyon SG, Lasser EC (1992) Contrast material iodides: potential effects on radioactive iodine thyroid uptake. J Nucl Med 33:237 – 238
59. Konno N, Makita H, Yuri K et al (1994) Association between dietary iodine intake and prevalence of subclinical hypothyroidism in the coastal regions of Japan. J Clin Endocrinol Metab 78:393 – 397
60. Beierwaltes WH (1969) Iodine and lymphocytic thyroiditis. Bull All-India Institute Med Sci 3:145
61. Bagchi N, Sundick RS, Hu LH et al (1996) Distinct regions of thyroglobulin control the proliferation and suppression of thyroid-specific lymphocytes in obese strain chickens. Endocrinology 137:3286 – 3290
62. Chandra AK, Mukhopadhyay S, Lahari D, et al (2004) Goitrogenic content of Indian cyanogenic plant foods & their *in vitro* anti-thyroidal activity. Indian J Med Res 119:180 – 185
63. Elnour A, Hambraeus L, Eltom M, et al (2000) Endemic goiter with iodine sufficiency: a possible role for the consumption of pearl millet in the etiology of endemic goiter. Am J Clin Nutr 71:59 – 66
64. Hershman JM (2005) Perchlorate and thyroid function: What are the environmental issues? Thyroid 15:427 – 431
65. Vestergaard P, Rejnmark L, Weeke J, et al (2002) Smoking as a risk factor for Graves' disease, toxic nodular goiter, and autoimmune hypothyroidism. Thyroid 12:69 – 75
66. Curran PG, DeGroot LJ (1991) The effect of hepatic enzyme-inducing drugs on thyroid hormones and the thyroid gland. Endocr Rev 12:135 – 150
67. Gaitan E (1988) Goitrogens. Ballieres Clin Endocrinol Metab 2:683 – 702
68. Studer H (1989) Natural heterogeneity of thyroid cells: the basis for understanding thyroid function and nodular goiter growth. Endocr Rev 10:125 – 135
69. O'Sullivan C, Barton CM, Staddon SL, et al (1991) Activating point mutation of the gsp oncogene in human thyroid adenomas. Mol Carcinog 4:345 – 349
70. Tonacchera M, Chiovato L, Pinchera A et al (1998) Hyperfunctioning thyroid nodules in toxic multinodular goiter share activating thyrotropin receptor mutations with solitary toxic adenoma. J Clin Endocrinol Metab 83:492 – 498
71. Krohn K, Fuhrer D, Bayer Y, et al (2005) Molecular pathogenesis of euthyroid and toxic multinodular goiter. Endocr Rev 26:504 – 524
72. Castro MR, Gharib H (2005) Continuing controversies in the management of thyroid nodules. Ann Intern Med 142:926 – 931
73. Atkins MB, Mier JW, Parkinson DR et al (1988) Hypothyroidism after treatment with interleukin-2 and lymphokine-activated killer cells. N Engl J Med 318:1557 – 1563
74. Vialettes B, Guillerand MA, Viens P, et al (1993) Incidence rate and risk factors for thyroid dysfunction during recombinant interleukin-2 therapy in advanced malignancies. Acta Endocrinol 129:31 – 38
75. Fernandez-Soto L, Gonzalez A, Escobar-Jimenez F et al (1998) Increased risk of autoimmune thyroid disease in hepatitis C vs hepatitis B before, during, and after discontinuing interferon therapy. Arch Intern Med 158:1445 – 1448
76. Mazziotti G, Sorvillo F, Stornaiuolo G, et al (2002) Temporal relationship between the appearance of thyroid autoantibodies and development of destructive thyroiditis in patients undergoing treatment with two different type-1 interferons for HCV-related chronic hepatitis: A prospective study. J Endocrinol Invest 25:624 – 630
77. Dang AH, Hershman JM (2002) Lithium-associated thyroiditis. Endocr Pract 8:232 – 236
78. Amino N, Tada H, Hidaka Y et al (1999) Screening for postpartum thyroiditis. J Clin Endocrinol Metab 84:1813
79. Stagnaro-Green A (2002) Postpartum thyroiditis. J Clin Endocrinol Metab 87:4042 – 4047
80. Premawardhana LDKE, Parkes AB, John R, et al (2004) Thyroid peroxidase antibodies in early pregnancy: Utility for prediction of postpartum thyroid dysfunction and implications for screening. Thyroid 14:610 – 615
81. Parker RH, Beierwaltes WH (1961) Thyroid antibodies during pregnancy and in the newborn. J Clin Endocrinol Metab 21:792
82. Sarlis NJ, Brucker-Davis F, Swift JP, et al (1997) Graves' disease following thyrotoxic painless thyroiditis. Analysis of antibody activities against the thyrotropin receptor in two cases. Thyroid 7:829 – 836
83. De Bruin TWA, Riekhoff FPM, de Boer JJ (1990) An outbreak of thyrotoxicosis due to atypical subacute thyroiditis. J Clin Endocrinol Metab 70:396 – 402
84. Brusco F, Gonzalez G, Soto N, et al (2004) Successful treatment of hyperthyroidism with amiodarone in a patient with propylthiouracil-induced acute hepatic failure. Thyroid 14:862 – 865
85. Fountoulakis S, Tsatsoulis A (2004) On the pathogenesis of autoimmune thyroid disease: a unifying hypothesis. Clin Endocrinol 60:397 – 409
86. Weetman AP (2000) Graves' disease. N Engl J Med 343: 1236 – 1248
87. Rees-Smith B, Bolton J, Young S, et al (2004) A new assay for thyrotropin receptor autoantibodies. Thyroid 14:830 – 835
88. Rees-Smith B, McLachlan SM, Furmaniak J (1988) Autoantibodies to the thyrotropin receptor. Endocr Rev 9:106 – 121
89. Gupta M (1992) Thyrotropin receptor antibodies: advances and importance of detection techniques in thyroid disease. Clin Biochem 25:193 – 199
90. Nygaard B, Knudsen JH, Hegedus L et al (1997) Thyrotropin receptor antibodies and Graves' disease, a side-effect of I-131 treatment in patients with nontoxic goiter. J Clin Endocrinol Metab 82:2926 – 2930
91. Wartofsky L, Schaaf M (1987) Graves' disease with thyrotoxicosis following subacute thyroiditis. Am J Med 83:761 – 764
92. Litaka M, Morgenthaler NG, Momotani N, et al (2004) Stimulation of thyroid-stimulating hormone (TSH) receptor antibody production following painless thyroiditis. Clin Endocrinol 60:49 – 53
93. Sawin CT, Castelli WP, Hershman JM (1985) The aging thyroid: thyroid deficiency in the Framingham study. Arch Intern Med 145:1386 – 1388
94. Surks MI, Ortiz E, Daniels GH, et al (2004) Subclinical thyroid disease: scientific review and guidelines for diagnosis and management. JAMA 291:228 – 238
95. Cooper DS (2004) Subclinical thyroid disease: consensus or conundrum? Clin Endocrinol 60:410 – 412
96. Kempers MJE, van Tijn DA, van Trotsenburg ASP, et al (2003) Central congenital hypothyroidism due to gestational hyperthyroidism: detection where prevention failed. J Clin Endocrinol Metab 88:5851 – 5857
97. Stagnaro-Green A, Chen X, Bogden JD, et al (2005) The thyroid and pregnancy: A novel risk factor for very preterm delivery. Thyroid 15:351 – 357

8 Parathyroid Gland

Abdelhamid H. Elgazzar

8.1 Introduction

The last organ to be recognized in man, the parathyroid glands, was discovered in 1880 by Ivar Sandstrom, a Swedish medical student. The discovery attracted little attention initially. Later, with the uncovering of the relationship of the glands to significant bone disease, interest quickened. In the early 1900s, Jacob Erdheim demonstrated that the four parathyroid glands were enlarged in osteomalacia and in rickets and thought it was a compensatory phenomenon. Subsequently, occasional cases of bone disease were encountered in which only a single gland was enlarged. In 1915, Friedrich Schlaugenhaufer suggested that enlargement of a single parathyroid gland might be the cause of the bone disease, not its result. The first parathyroidectomy for von Recklinghausen's disease of bone was performed by Felix Mandl in 1925 in Vienna. Subsequently, the parathyroid glands were shown to be affected by a number of primary pathological processes – neoplasia (adenoma and carcinoma) and hyperplasia (wasserhelle-cell and chief-cell types) – that resulted in overactivity and required surgical removal of one or more of them [1].

The frequency of hyperparathyroidism has been increasing in the past few decades. It has also been recognized that this condition has various clinical presentations and can be associated with normocalcemia or borderline hypercalcemia. The condition, even with atypical laboratory findings, is known to be associated with an increasing number of complications, including the more recent findings of the resultant neuromuscular and psychiatric disorders. Accordingly, the management of hyperparathyroidism by the proper surgical approach is crucial. Although the success rate of surgical excision of abnormal parathyroid glands is high, certain factors and new developments favor preoperative identification of abnormal glands [2–7]. Exploring the pathophysiology of the parathyroids can help to enhance our understanding of the currently used preoperative localization procedures and their future modifications. Optimal parathyroid scintigraphy requires an understanding of (a) the embryologic, anatomic, and physiologic features of the parathyroid glands and (b) the properties of the two common imaging agents, ^{99m}technetium-sestamibi and ^{99m}Tc-tetrofosmin. Normal parathyroid glands are too small to be visualized, but parathyroid disease often produces visibly enlarged glands. Enlarged parathyroid glands may be found near the thyroid gland or outside their expected locations. Characteristic abnormal scintigraphic patterns may be described as focal or multifocal, usual or ectopic in location, and associated with a normal or abnormal thyroid gland. Patients who are referred for parathyroid imaging should have an abnormal biochemical profile. The first step in evaluating images of a patient suspected of having parathyroid disease is to correlate the normal or abnormal scintigraphic patterns with the clinical and surgical history. By integrating the interpretative, pathophysiologic and technical data of parathyroid scintigraphy, the interpreting physician can be more confident of establishing a correct diagnosis and

can precisely guide the surgeon to a single parathyroid adenoma, multiple parathyroid adenomas, or multigland hyperplasia [8].

8.2 Anatomical and Physiological Considerations

Normal parathyroid glands are derived from the pharyngeal pouches, the upper glands from the endoderm of the fourth pouch and the lower glands from the third pouch. The parathyroid glands are typically located on the thyroid gland (Fig. 8.1). Occasionally one or more glands may be embedded in the thyroid [9]. The normal position of the superior parathyroids is at the cricothyroid junction, above the anatomic demarcation of the inferior thyroid artery and the recurrent laryngeal nerve [10, 11]. The inferior parathyroids are more widely distributed, with most of them anterolateral or posterolateral to the lower thyroid gland [11]. The accessory glands that can be variously located in human beings, from the cricoid cartilage down into the mediastinum [12, 13], are derived from the numerous dorsal and ventral wings of the pouches. Normally, human beings have four glands, but more or fewer than this number are found in some individuals [2]. Among healthy adults, 80% – 97% have four parathyroids, approximately 5% have fewer than four glands, and 3% – 13% have supernumerary glands [11].

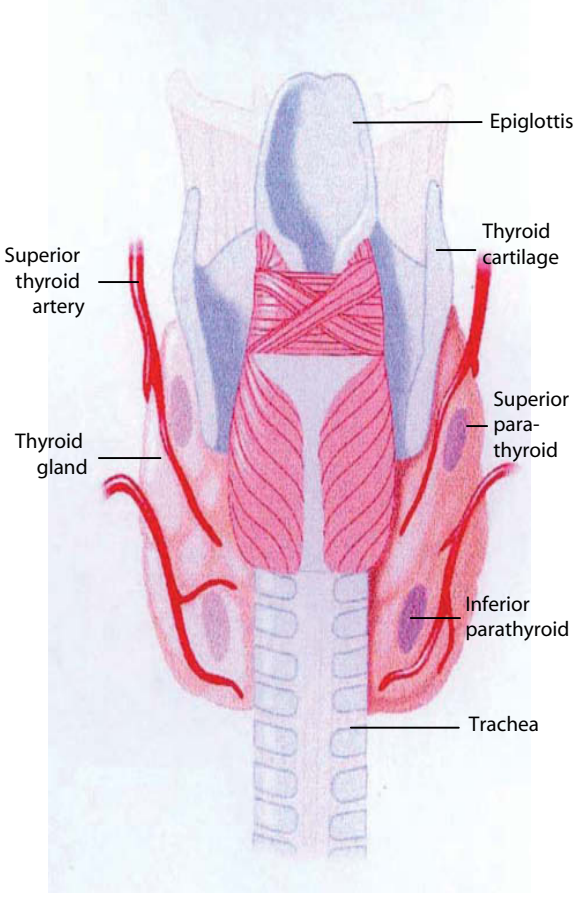

Fig. 8.1. Diagram showing typical locations of parathyroid glands

The normal glands vary considerably in shape and size between individuals and within the same individual. Because of the variable shapes of the parathyroids, the diameters vary. The normal glands usually measure 4 – 6 mm in length, 2 – 4 mm in width, and 0.5 – 2 mm in thickness. The glands are usually ovoid or bean-shaped but may be elongated, flattened into a leaf-like structure, or multi-lobulated [3]. The weight of the glands is therefore a better estimate of the glandular tissue; they are usually 30 mg each, with the largest normal gland not exceeding 70 mg. The relatively new important parameter, the weight of the functioning parenchyma, can be calculated from the glandular weight and the relative proportions of the two main glandular components, parenchymal and fat cells. The total weight of the glands is less than 210 mg and the total parenchymal cell weight is less than 145 mg [3]. The proportion of fat cells in the parathyroid glands varies with age, since they are sparse up to adolescence and increase gradually to constitute 10% – 25% of the glandular volume by the age of 30: the proportion remains fairly constant except when the individual suffers from obesity, which causes a larger amount of fat cells, as opposed to cachectic persons who have essentially no fat cells. In normal glands, parenchymal cells are predominantly chief cells which contain cytoplasmic fat droplets. Oxyphilic and transitional oxyphilic cells are sparsely present in children and young adults and increase to 4% – 5% of the parenchymal cells in old age. These cells tend to form nodules if they increase in number and have a very small amount of fat or no fat at all in their cytoplasm. Ultrastructurally, oxyphil cells are characterized by the presence of closely packed mitochondria while chief cells contain moderate to high mitochondrial content, but also prominent Golgi body and endoplasmic reticulum. Water-clear cells are vacuolated with distended organelles. Each of the three cell types may contain varying amounts of lipid droplets and residual bodies.

Table 8.1 summarizes the types of parathyoid cells and their function.

Parathyroid hormone has four principal actions: (a) to increase calcium absorption from the gastrointestinal tract; (b) to stimulate osteoclastic activity, resulting in resorption of calcium and phosphate from bone; (c) to inhibit phosphate reabsorption by the proximal renal tubules; and (d) to enhance renal tubular calcium reabsorption. Parathyroid hormone secretion is controlled mainly by the extracellular calcium concentra-

Table 8.1. Cells of the parathyroid glands and their functions

Cell type	Major ultrastructural feature	Function
Chief cell	Slightly eosinophilic cytoplasm, few mitochondria	The active endocrine cell, producing the parathyroid hormone
Oxyphil cell	Rich eosinophilic cytoplasm, tightly packed mitochondria	May be able to produce parathyroid hormone
Transitional oxyphil cell	Less eosinophilic cytoplasm	Variant of oxyphil cell
Clear cell	Foamy and water-clear cytoplasm	Unknown, fundamentally inactive

tion. The parathyroid cell surface is thought to be equipped with a cation-sensitive receptor mechanism through which ambient calcium regulates the cytosolic calcium ($Ca^{2+}i$) concentration and parathyroid hormone secretion. Activation of this receptor also causes activation of protein kinase C [3]. 1,25-Dihydroxycholecalciferol reduces the secretion of parathyroid hormone independent of any changes in calcium concentration. Parathyroid hormone is metabolized in Kupffer's cells of the liver.

In patients with hyperparathyroidism, pathological parathyroid cells show defective sensing of ambient calcium. The cellular basis of this abnormality is unknown, although increased protein kinase C activity within abnormal parathyroid cells may be the mechanism. Pathological parathyroid glands also have an increased parenchymal cell content, although the extent of hypercalcemia appears more closely related to the defective secretory regulation than to increased parenchymal cell mass [5, 14].

8.3 Hyperparathyroidism

Hyperparathyroidism has been diagnosed with increasing frequency in recent years due to awareness of the disease and to the laboratory advancement that allowed for routine chemistry screening. The condition is characterized by excess secretion of parathyroid hormone. The resulting biochemical changes, including increased levels of serum calcium and increased urinary excretion of calcium, may result in calcium wastage, nephrocalcinosis, urolithiasis, bone disease, and neuropsychiatric disturbances. Hyperparathyroidism may occur as a primary, secondary, or tertiary disease. It can also occur as eutopic and ectopic disease. In addition, it may have a familial origin, as in multiple endocrine neoplasia (MEN).

8.3.1 Primary Hyperparathyroidism

Primary hyperparathyroidism occurs due to neoplastic or hyperplastic parathyroid glands or when nonparathyroid tumors such as bronchogenic or renal cell carcinomas secrete ectopically parathyroid hormone or a biologically similar product. The incidence in the USA has been estimated at approximately 27.7 cases per 100,000 population per year [15]. The condition is more prevalent in females than males by a ratio of 3 to 1. More than 80% of patients with primary hyperparathyroidism have a solitary adenoma. Hyperplasia – predominantly of chief cells – occurs in less than 20% of patients. Parathyroid carcinoma is the cause in less than 1% of patients, and very rarely the condition is due to ectopic secretion of parathyroid hormone such as with renal cell carcinomas.

Primary hyperparathyroidism occurs as part of MEN. MEN is a hereditary syndrome that involves hyperfunctioning of two or more endocrine organs. Primary hyperparathyroidism, pancreatic endocrine tumors, and anterior pituitary gland neoplasms characterize type 1 MEN. MEN 2A is defined by medullary thyroid carcinoma, pheochromocytoma (about 50%), and hyperparathyroidism caused by parathyroid gland hyperplasia (about 20%). MEN 2B is defined by medullary thyroid tumor and pheochromocytoma. Both MEN 1 and MEN 2 are inherited autosomal dominant cancer syndromes. The gene responsible for MEN 1 is a tumor suppressor gene located on chromosome 11.

Primary hyperparathyroidism is the most common manifestation of MEN-1 (80% occurrence) and is caused by hyperplasia of all four parathyroid glands. This is followed by pancreatic islet cell tumors and involvement of the pituitary gland [16–19]. There is a high frequency of carcinoid tumors of foregut origin with male predominance for thymic involvement and female predominance for bronchial lesions [17, 20]. Type 1 MEN has a potentially lethal outcome with hemorrhagic peptic ulcer disease and metastatic pancreatic neoplasms [17]. Primary hyperparathyroidism is also associated with thyroid pathology in 15%–70% of patients [21–28]. This includes thyroid carcinoma, which has been reported in the range of 1.7%–6.2% (Table 8.2) of patients with primary hyperparathyroidism [21–31].

8.3.2 Secondary Hyperparathyroidism

Secondary hyperparathyroidism occurs when there is a condition causing chronic hypocalcemia such as chronic renal failure, malabsorption syndromes, dietary rickets, and ingestion of drugs such as phenytoin, phenobarbital, and laxatives, which decrease intestinal

Table 8.2. Incidence of thyroid cancer among patients with primary hyperparathyroidism: cumulative literature data

Author	Year	No. of patients	% with thyroid cancer
Ogburn [29]	1956	230	4 (1.7%)
Nishiyama [22]	1979	420	13 (3%)
Prinz [23]	1982	351	16 (4.6%)
Hedman [30]	1984	426	25 (5.8%)
Attie [24]	1992	948	31 (3.3%)
Burmeister [25]	1997	700	18 (2.6%)
Sidhu [26]	2000	65	4 (6.2%)
Bentrem [27]	2002	580	12 (2%)
Beus [31]	2004	101	3 (3%)
Total		3821	126 (3.3%)

absorption of calcium. Secondary hyperparathyroidism is simply a compensatory hyperplasia in response to hypocalcemia. In this condition, reduced renal production of 1,25-dihydroxyvitamin D_3 (active metabolite of vitamin D) leads to decreased intestinal absorption of calcium, resulting in hypocalcemia. Tubular failure to excrete phosphate results in hyperphosphatemia. Hypocalcemia along with hyperphosphatemia is compensated for by hyperplasia of the parathyroids to overproduce PTH [32].

8.3.3 Tertiary Hyperparathyroidism

Tertiary hyperparathyroidism describes the condition of patients who develop hypercalcemia following long-standing secondary hyperparathyroidism due to the development of autonomous parathyroid hyperplasia, which may not regress after correction of the underlying condition, as with renal transplantation.

8.3.4 Eutopic Parathyroid Disease

Parathyroid disease with typical location of glands (eutopic) represents 80% – 90% of all cases [33]. There is a relatively fixed location for the superior parathyroids and they are found close to the dorsal aspect of the upper thyroid [10, 11]. On the other hand, inferior parathyroids have a more widespread distribution, which is closely related to the migration of the thymus. Inferior parathyroids are mostly located inferior, posterior, or lateral to the lower thyroid [10]. They may be very close to the thyroid and may be covered by or attached to the thyroid capsule and are sometimes adjacent to or surrounded by remnant thymic tissue. Interestingly, the parathyroid glands demonstrate a remarkably constant symmetry, which is helpful in the surgical exploration of eutopic disease [11].

8.3.5 Ectopic Parathyroid Disease

Superior parathyroid adenoma may have an abnormal superoposterior mediastinal position, such as a retropharyngeal, retroesophageal, or paraesophageal site or the tracheo-esophageal groove. The frequency of ectopia (up to 39%) is similar for the right and left superior parathyroids [33]. Intrathyroid superior parathyroid adenomas are rare.

The more common ectopic inferior parathyroids are a well-established entity responsible for 10% – 13% of all cases of hyperparathyroidism [33]. Ectopic tissue can occur from the angle of the mandible to the mediastinum according to the developmental and migratory aberrations. These sites include the mediastinum, thymus, aortopulmonary window, carotid bifurcation and rarely thyroid, carotid sheath, vagus nerve, retroesophageal region, thyrothymic ligament, and pericardium [33 – 36].

8.3.6 Parathyroid Adenoma

Parathyroid adenoma is a benign tumor that is usually solitary, although multiple adenomas have been reported in a low percentage. The tumor varies in weight from less than 100 mg to more than 100 g. The most commonly found adenomas, however, weigh 300 mg–1 g. The size was found to correlate to the degree of hypercalcemia [5].

Microscopically, the vast majority of typical adenomas are formed predominantly of chief cells, although a mixture of oxyphil cells and transitional oxyphil cells is also common. Adenomas formed of water-clear cells are very rare. A rim of parathyroid tissue is usually present outside the capsule of the adenoma and can serve to distinguish it from parathyroid carcinoma. The chief cells in adenomas are usually enlarged, and their nuclei are larger and more variable in size than in normal chief cells. Nuclear pleomorphism may be prominent; this is not considered a sign of malignancy but a criterion for discriminating adenoma from hyperplasia, which lacks this feature. The following variants of parathyroid adenoma may be recognized:

8.3.6.1 Solitary Adenoma

Solitary adenoma is found in 80% – 85% of patients with primary hyperparathyroidism [11]. There is no significant predominance in location among the four parathyroids with each responsible for approximately 25% of all solitary adenomas [33]. The remainder of parathyroid glands associated with single adenomas usually have lower weight and parenchymal cell mass

than the average normal glands and show signs of secretory inactivity on electron microscopy [3].

8.3.6.2 Double or Multiple Adenomas

Double or multiple adenomas occur in up to 12% of cases of primary hyperparathyroidism [37, 38]. Double adenomas are bilateral in 55%–88% of cases and are seen predominantly in patients beyond the 6th decade of life [39]. These patients have more prominent symptoms and usually have higher parathyroid hormone and alkaline phosphatase levels than those with a solitary parathyroid adenoma or hyperplasia. However, symptoms and laboratory values do not enable the diagnosis of double adenoma. Preoperative detection of double or multiple adenomas with any imaging modality is not reliable [40]. ^{99m}Tc-sestamibi scintigraphy has a sensitivity of less than 37% for detection of multisite disease [41, 42].

8.3.6.3 Cystic Adenoma

Cystic adenomas are thought to represent central necrosis or cystic degeneration of adenomas and account for less than 9% of all parathyroid adenomas [43]. Contrary to the asymptomatic true parathyroid cysts, which are due to embryologic vestiges of the third and fourth pharyngeal pouches or enlargement of microcysts within the parathyroid as a manifestation of colloid retention [43, 44], cystic adenomas are frequently associated with hyperparathyroidism. Cystic adenoma may not be visualized on sestamibi studies.

8.3.6.4 Lipoadenoma

Parathyroid lipoadenoma, composed of hyperfunctioning parathyroid tissue and fatty stroma [45], is a rare entity that occurs in patients beyond the 4th decade of life [45]. Compared to typical adenoma, there is no gender predilection and no difference in terms of symptoms. On ^{99m}Tc-sestamibi studies, the target-to-background signal ratio of lipadenoma may be low due to the high adipose content of the tumor [45].

8.3.6.5 Oncocytic Adenoma

In contrast to the typical adenoma that is composed of chief cells or a mixture of chief, oxyphil or transitional oxyphil cells, oncocytic adenoma is formed of exclusively oxyphil cells or of more than 80% of such cells. It is a rare subtype and has been reported to be associated with hyperparathyroidism. It is found in the sixth or seventh decades and like the typical adenomas is more common in women [46].

Table 8.3. Classification of parathyroid hyperplasia

Type	Major pathological features
Primary hyperplasia	Uniform chief cells with some oxyphil and transitional oxyphil cells
Secondary hyperplasia	
Diffuse (classic) type	Cords, sheets, or follicular arrangement of cells replacing the stromal fat cells. Oxyphil cells are more frequent in this type. This type is indistinguishable from the primary type
Adenomatous-nodular type	Cells are grouped in large islands or nodules. Necrosis is seen more frequently than in diffuse type

8.3.7 Parathyroid Hyperplasia

Parathyroid hyperplasia affects the glands to varying degrees, and commonly one or two glands are of normal size even though microscopic signs of endocrine hyperfunction, described later, are present, at least focally, in all glands. Chief cell hyperplasia is the most common and is composed of chief cells or a mixture of chief cells and to a lesser extent oxyphil cells. The cells are arranged diffusely, in nodules, or there is a mixture of both patterns. Water-clear cell hyperplasia is rare and is characterized by substantial enlargement of most parathyroid glands. The large water-clear cells are usually arranged in a diffuse pattern.

In primary hyperparathyroidism, hyperplasia affects the glands asymmetrically. In secondary hyperparathyroidism, the hyperplastic glands are more uniformly enlarged than with primary chief cell hyperplasia, with two histological types (Table 8.3). In the tertiary form, the glands are more often markedly and asymmetrically enlarged with frequent prominent parenchymal cell nodules.

Pathologically, it is difficult to differentiate primary chief cell hyperplasia of only one gland from adenoma. Both contain large numbers of active chief cells with cells characterized by aggregated arrays of rough endoplasmic reticulum and a large, complex Golgi apparatus with numerous vacuoles and vesicles. Secretory granules are frequently present in these cells. These changes indicate that most of these cells are in the more active phases of parathyroid hormone synthesis and secretion [47]. Molecular biology techniques used on pathological parathyroid tissue have shown that cell proliferation is monoclonal in many sporadic adenomas and in the largest glands of multiple endocrine neoplasia type I. This monoclonality has not been found in the smaller parathyroid glands of multiple endocrine neoplasia or in sporadic hyperplasia. Additionally, rearrangement of

parathyroid hormone gene in chromosome 11 was observed in sporadic adenomas [48].

8.3.8 Parathyroid Carcinoma

Parathyroid carcinoma is a rare cause of hyperparathyroidism which can arise in any parathyroid gland, including ectopic and mediastinal, although the usual site of involvement is the normally located parathyroids. The tumor is found predominantly in patients between the ages of 30 and 60 years, with no sex preference, and is usually functioning. The tumors tend to be larger than adenomas and appear as lobulated, firm, and uncapsulated masses that often adhere to the surrounding soft tissue structures [49]. The involved glands usually weigh more than 1 g and the diagnosis is restricted histologically to the lesions displaying infiltrative growth into vessel or capsule, since pleomorphism can be seen in many adenomas.

8.3.9 Hyperfunctioning Parathyroid Transplant

Autotransplantation of parathyroid tissue is performed in cases of recurrent, persistent type 1 MEN and symptomatic secondary hyperparathyroidism [19] in association with total parathyroidectomy. After total parathyroidectomy, the most normal glands, usually one or two, are used for the graft. They are diced into small fragments approximately 1–2× 1× 1 mm, with each fragment placed in an individual bed beneath the muscle sheath and between muscle fibers [19, 50]. The graft consists of a cluster of 10–25 parathyroid fragments. The remainder of the healthy gland (or glands) is cryopreserved for potential retransplantation [19, 40, 50]. Graft may be placed into the brachioradial muscle or flexor muscle group of the forearm or into the sternocleidomastoid muscle. A graft site in the forearm is preferred for accessibility for laboratory work-up of parathyroid hormone levels and surgical reexploration in cases of recurrent hyperparathyroidism [19]. The graft may be functional in 8–9 days after surgery [39].

After autotransplantation, recurrent hyperparathyroidism occurs in approximately 14% of cases [51]. The hyperfunctioning transplant is a possible cause as is residual or ectopic diseased parathyroid tissue. A hyperfunctioning graft in the forearm is easily demonstrated with Doppler US or ^{99m}Tc-sestamibi scintigraphy [19, 52].

8.4 Consequences of Hyperparathyroidism

Excess secretion of parathyroid hormone promotes bone resorption and consequently leads to hypercalcemia and hypophosphatemia. The clinical presentation and complications of hyperparathyroidism depends on the rapidity of development and the degree of hypercalcemia. The following abnormalities may occur:

- Genitourinary: nephrolithiasis, nephrocalcinosis, renal insufficiency, polyuria, nocturia and decreased urine concentrating ability.
- Gastrointestinal: Nausea, vomiting, constipation, increased thirst, loss of appetite, abdominal pain, peptic ulcers, heartburn (hypercalcemia causes increased gastric acidity) and pancreatitis.
- Musculoskeletal: myopathy, muscle weakness, osteoporosis, osteomalacia, bone and joint pains, renal osteodystrophy and pseudogout. In all forms of hyperparathyroidism there is increased bone resorption associated with increased osteoblastic activity, leading to increased uptake of bone-seeking radiopharmaceuticals. See also Chapter 6.
- Neuropsychiatric: Memory loss, anxiety, sleepiness, confusion, lassitude, coma, depression, impaired thinking and psychosis.
- Others: Fatigue, hypertension, pruritis, metastatic calcification including cardiocalcinosis and band keratopathy (present in the medial and lateral aspects of the cornea).

The five disease specific symptoms are muscle weakness, polydipsia, dry skin and itching, memory loss and anxiety. Overall the symptoms, particularly the disease specific ones, show significant decline after successful parathyroidectomy [53].

8.5 Management of Hyperparathyroidism

Routine blood chemistry screening has been behind the recent increase in the recognition of hyperparathyroidism. Surgery is the major and only current curative modality in treating primary hyperparathyroidism. It is recommended for all patients who are operative candidates and for many asymptomatic patients. Parathyroidectomy is successful in more than 90% of cases in experienced hands, based on intraoperative localization by the surgeon. Identifying the glands can be difficult, however, particularly with removal of multiple glands and with reoperation [54]. Three important factors contribute to successful surgical explorations: correct preoperative diagnosis, accurate preoperative localization of abnormal glands, and meticulous surgical technique [2]. Although the success rate is high in experienced hands, up to 25% of the initial explorations fail because the abnormal glands cannot be located. Prolonged exploration was also found to result in a high incidence of recurrent laryngeal nerve damage [54]. Surgical reexploration with violated anatomy is even more

difficult and hazardous, and can often be unrewarding. Preoperative localization of parathyroid lesions is thus desirable to reduce the incidence of missed lesions and to help avoid prolonged neck exploration. Since surgeons' experience with neck exploration is dwindling due to the reduced incidence of thyroid surgery with the expanding use of iodine-131 for therapy of hyperthyroidism, preoperative localization of parathyroid lesions is even more important than before.

In recent years, minimal access parathyroid surgery(small incisions with gamma probe or endoscopic assistance) is increasingly becoming the operation of choice for single parathyroid adenomas [55]. Compared with bilateral neck exploration it has a shorter hospital stay, less morbidity, and better cosmetic result [56]. The development of this minimally invasive surgical technique has placed an even greater emphasis on preoperative localization [57]. The forms that preoperative localization can take include computed tomography (CT), ultrasound, magnetic resonance imaging (MRI), arteriography, selective venous sampling, ^{99m}Tc-sestamibi (MIBI) scintigraphy, ^{18}F-fluorodeoxyglucose positron emission tomography (FDG PET) and ^{11}C-methionine PET.

8.6 Preoperative Localization

Several imaging and nonimaging modalities have been used to localize the abnormal glands and guide the surgeon. Invasive techniques include arteriography and selective venous sampling via neck vein catheterization. Although these techniques are reliable, they are expensive, time consuming, technically difficult, and involve some risks. Noninvasive techniques are many, indicating that none is ideal. In general, older noninvasive techniques such as barium swallow, thermography, ultrasound, computerized tomography, and scintigraphy using selenomethionine-75 have not been considered very useful for preoperative localization. The morphologic imaging modalities, such as CT, ultrasound and MRI, have the disadvantage that they cannot distinguish functional parathyroid tissue from other types of tissue. However, they provide excellent image resolution and contrast. Overall their accuracy is inadequate and varies. Ultrasound, for example, has a wide range of accuracy, with a range of sensitivity between 36% and 76%. Computed tomography has a similar range, between 46% and 76%. More recently, MRI has also been used with a reported sensitivity of 50% – 78% [58 – 62]. The most sensitive technique is the use of MIBI scintigraphy, with reported sensitivities of approximately 90% [63]. Several other nuclear medicine techniques have been used including thallium-201, ^{99m}Tc-pertechnetate, ^{99m}Tc-tetrofosmin (Myoview), ^{99m}Tc-sestamibi and PET. Some advocate the use of both ^{99m}Tc-sestamibi and ultrasound to confirm abnormal parathyroid tissue [64 – 66]. When the use of both techniques is comprehensive, this may not be a cost-effective approach for primary hyperparathyroidism [67]. Many, including our institution, use only ^{99m}Tc-sestamibi if this test localizes the site of parathyroid hyperactivity.

8.6.1 Scintigraphic Imaging Localization

Since a single parathyroid adenoma is the underlying pathology in more than 80% of cases of primary hyperparathyroidism, there would be no need to explore both sides of the neck with potentially increased morbidity if a sensitive imaging modality could localize the abnormal gland preoperatively. Although experienced neck surgeons can achieve a high success rate of parathyroidectomy after bilateral neck exploration without prior localizing study [2, 3], a preoperative localization study would decrease operative time and morbidity and is frequently needed for the minimally invasive surgical approach that is currently practiced with increasing frequency.

Scintigraphy using ^{99m}Tc-sestamibi is currently the preferred nuclear medicine method for parathyroid imaging. It is the most sensitive and cost-effective modality for preoperative localization of hyperfunctioning parathyroid tissue [4 – 6]. If a single parathyroid adenoma is detected, a unilateral scan-directed neck exploration can be performed. Due to a wide variation in scintigraphic techniques [7, 14], the reported sensitivities of MIBI scan range from 80% to 100%. This radiopharmaceutical is a cationic and lipophilic isonitril derivative that was shown to be taken up by abnormal parathyroid cells. Although the exact mechanism is not fully understood, mitochondria have been implicated in its uptake by parathyroid cells [68]. P-glycoprotein, a membrane transport protein encoded for by the multidrug resistance (MDR) gene, may also be additionally responsible for uptake, since it transports other products with structural similarity to ^{99m}Tc-sestamibi [69]. The uptake and retention of ^{99m}Tc-sestamibi by the abnormal neoplastic and hyperplastic lesions are probably due to the alterations in the biology of the abnormal parathyroid cells, as noted earlier, and mitochondria are probably the site of retention. The size of the lesions is also an important factor in their visualization but cannot alone explain the uptake and retention. This rationale is strengthened by the observation that some large adenomas are occasionally not visualized while small ectopic implants are seen by the technique [68]. In a recent study, Takebayashi et al. found the size and the cellularity of the abnormal gland to correlate with its sestamibi uptake [70]. The authors found a significantly higher count ratio in high cellular glands than in low cellular

ones on either early or delayed images. Bénard et al. [71] reported a large adenoma which was missed on MIBI scan seemingly due to a rapid washout along with the presence of a few oxyphil cells. One study which correlated thallium-201 scintigraphy with ultrastructural alterations in hyperfunctioning parathyroid lesions, has suggested that the ability of this scan to localize the abnormal glands might depend upon the amount of mitochondria-rich oxyphil cells [72]. Generally speaking, the uptake mechanisms of thallium-201 and ^{99m}Tc-MIBI differ significantly. That of thallium depends predominantly on Na^+ and K^+ ATPase pump while ^{99m}Tc-MIBI uptake has been related to the mitochondria. Accordingly, the findings regarding the correlation of thallium uptake by parathyroid adenomas and ultrastructural changes may not be applicable to ^{99m}Tc-MIBI.

Carpentier et al. [73] reported positive correlation between MIBI uptake on delayed images with oxyphil cells in parathyroid adenomas. Other studies did not find a correlation between the degree of hypercellularity of oxyphil cell and MIBI uptake [74] or a relation between the percentage of chief and oxyphil cells and scintigraphic findings [75].

Parathyroid lesions detected by ^{201}Tl scintigraphy have been shown to have significantly higher numbers of mitochondria-rich oxyphil cells compared with nonvisualized lesions, indicating further that the uptake depends in part on the metabolic activity of the lesion [76]. Recently our group found that the amount of mitochondria (Fig. 8.2) in adenoma cells correlates with the degree of uptake [77]. Significant P-glycoprotein or multidrug resistance-related protein expression was reported to limit the sensitivity of

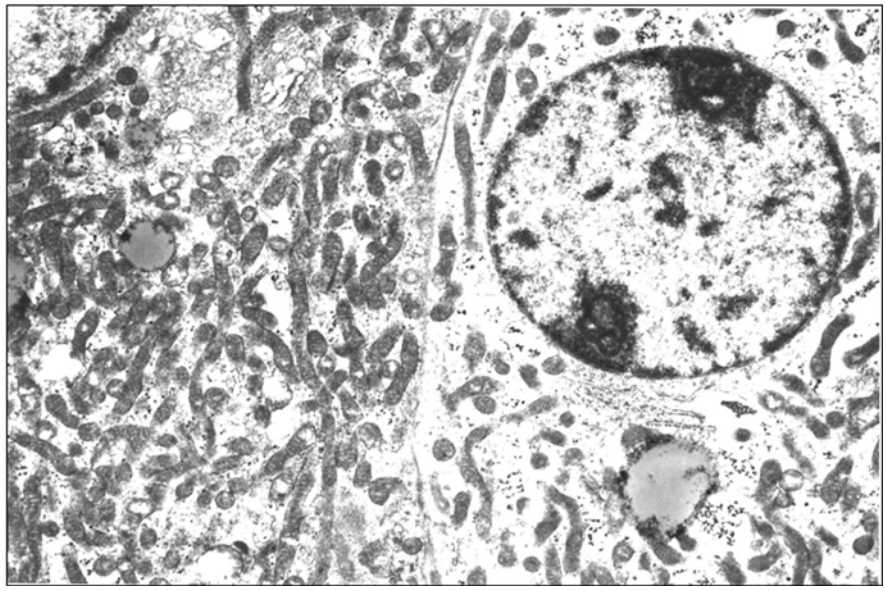

Fig. 8.2. Electron microscopic photograph of a parathyroid adenoma showing cell packed with mitochondria

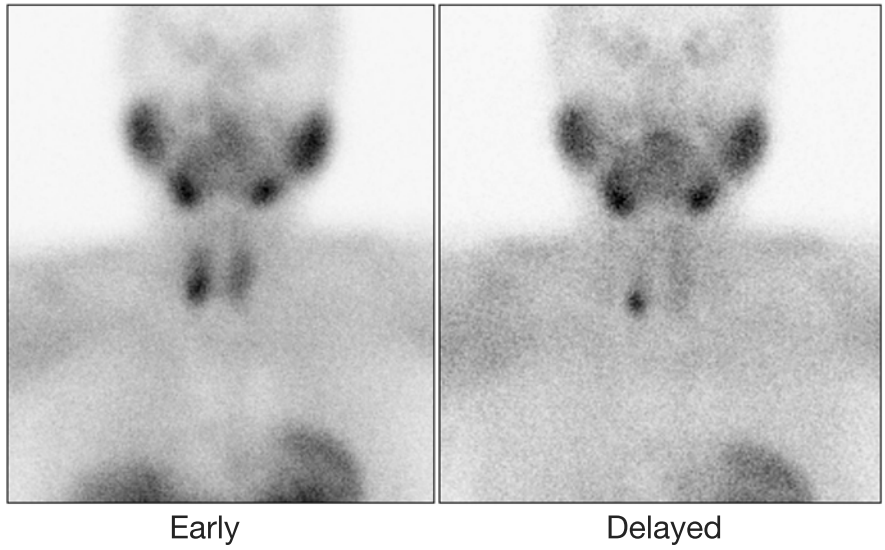

Fig. 8.3. ^{99m}Tc-sestamibi study acquired 15 min and 90 min post-injection. The delayed image shows differential clearance of activity from the thyroid gland with retained and intense uptake by a large parathyroid adenoma of the same patient in Fig. 8.2

^{99m}Tc-MIBI imaging in localizing parathyroid adenomas [78].

Although the activity per gram of tissue in thyroid and parathyroid gland is higher with ^{201}Tl- than with ^{99m}Tc-sestamibi, the slower washout of sestamibi from parathyroid lesions results in a higher target-to-nontarget ratio than with ^{201}Tl [68]. Since the activity in the lesion compared with that in the surrounding tissue affects image contrast, one would expect to distinguish parathyroid lesion from thyroid tissue (Fig. 8.3) better with sestamibi [79] and allow for smaller gland localization. In our experience, switching from ^{201}Tl to ^{99m}Tc-sestamibi resulted in a significant improvement of the accuracy in localizing parathyroid lesions preoperatively.

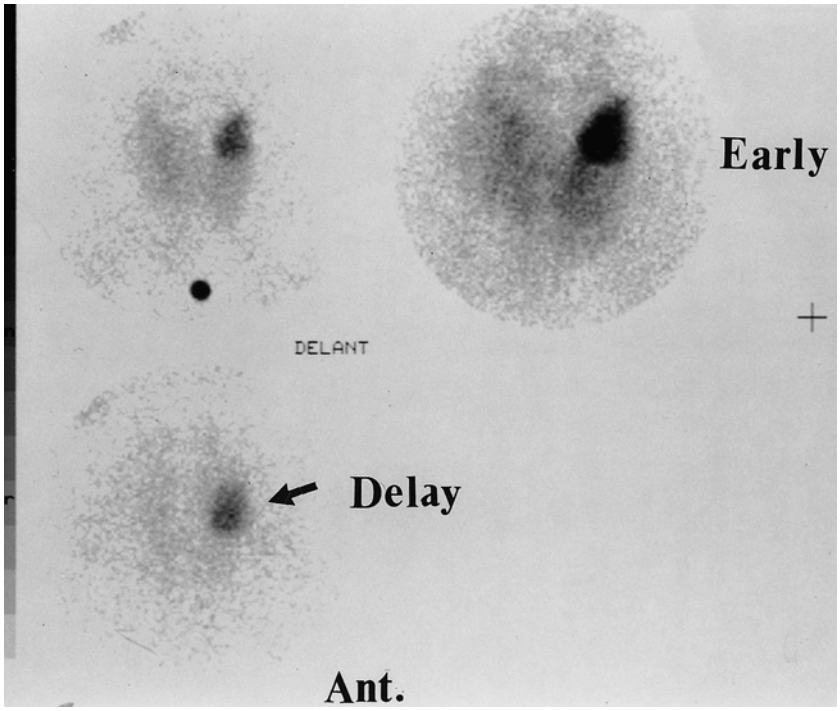

Fig. 8.4. ^{99m}Tc-sestamibi parathyroid localization study showing retained activity in a large parathyroid adenoma (*arrow*) located in left superior position

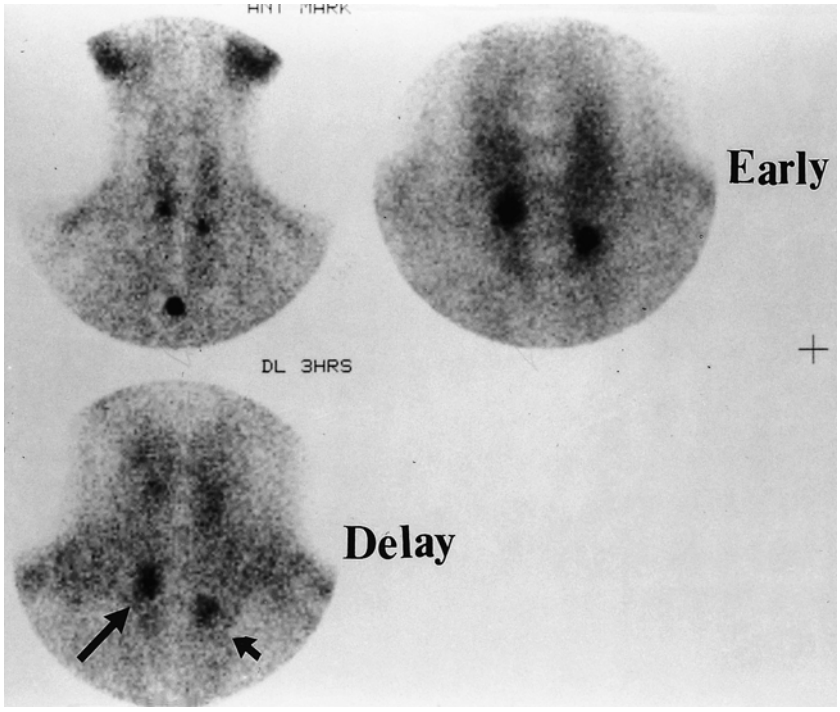

Fig. 8.5. Hyperplastic parathyroid glands (*arrows*) with persistent uptake on delayed ^{99m}Tc-sestamibi image

Parathyroid scintigraphy is not a screening study to be used in each patient with hypercalcemia of unknown etiology. It should be reserved for localization in patients with biochemically proven hyperparathyroidism. Since parathyroid glands can be found ectopically, the search for abnormal parathyroid lesions should include the mediastinal area. Techniques that are based on subtraction such as ^{201}Tl-/^{99m}Tc-pertechnetate are not currently preferred, due to the technical problems associated with subtraction [80, 81]. With the use of ^{99m}Tc-sestamibi, the radiopharmaceutical is injected intravenously and planar images of the neck and chest are obtained at 15 min post-injection with markers of the suprasternal notch, thyroid cartilage, and xiphosternum. Based on the findings, pinhole images of the neck and possibly other areas suspected of having an abnormality are acquired (Figs. 8.4 – 8.6). Images are repeated at 2 – 3 h post-injection, and SPECT is an option when needed for better localization of an abnormality at the discretion of the physician (Fig. 8.7). For planar imaging pinhole collimation is superior to parallel hole collimation [82]. This early and delayed imaging technique is preferred, since the initial uptake by normal thyroid tissue clears while the radiopharmaceutical is usually retained by the abnormal parathyroid cells. This also obviates the need for additional thyroid images using ^{99m}Tc-pertechnetate or ^{123}I with or without subtraction, which are reserved for occasional cases. ^{99m}Tc-tetrofosmin is also being used for scintigraphic localization [83].

Recently PET has been investigated for localizing parathyroid glands. Initial studies using FDG showed conflicting results in imaging the parathyroid glands in primary hyperparathyroidism [84, 85]. ^{11}C-methionine PET was suggested to be more promising than FDG in parathyroid localization. Sundin et al. [86] studied 32 patients with primary hyperparathyroidism, and reported a sensitivity of 85% for proper localization with C-11 methionine. Cook et al. [87] in 8 patients with persistent or recurrent hyperparathyroidism after surgery found that ^{11}C-methionine PET showed all the abnormal parathyroid glands correctly.

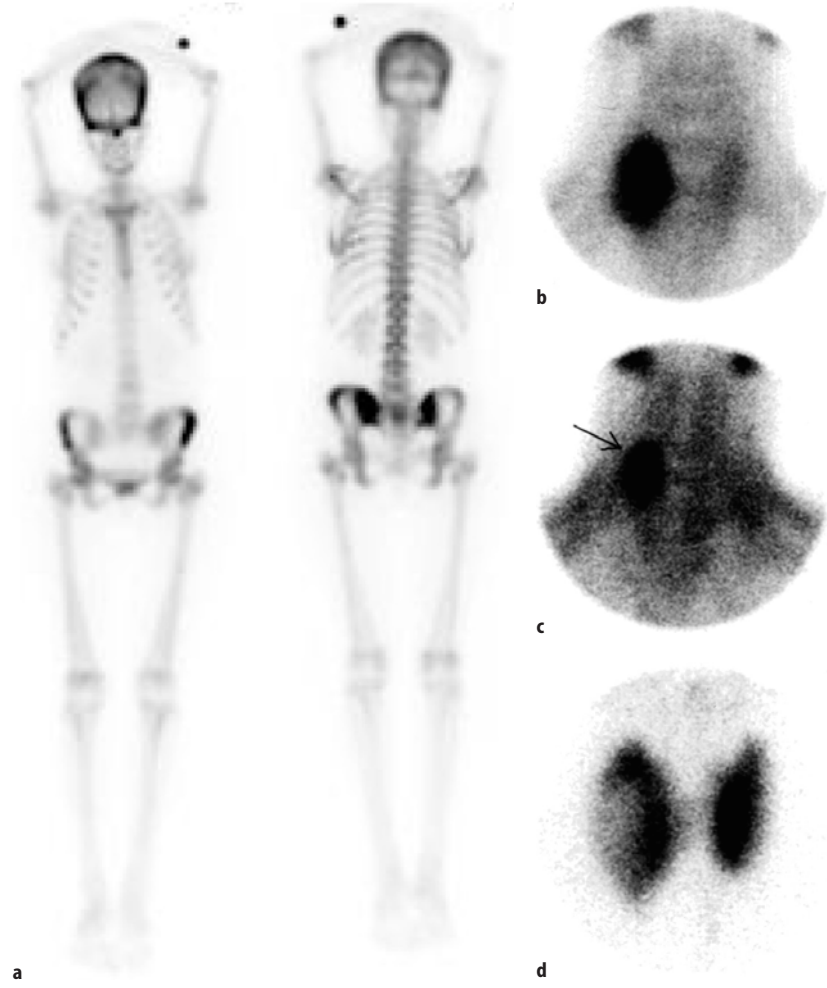

Fig. 8.6a–d. Functioning parathyroid carcinoma. A 45-year-old female was referred for bone scan to evaluate the cause of generalized bony pains. The study (**a**) showed generalized increased bone uptake particularly in the calvarium, indicating metabolic bone disease. Parathyroid hormone was found to be high and ^{99m}Tc-sestamibi (**b-d**) was obtained and showed a focus of increased uptake on early image (**b**) with retention of activity on delayed image (**c**). ^{99m}Tc-pertechnetate thyroid scan (**d**) shows a solitary cold nodule corresponding to the finding on sestamibi study and was proved to be parathyroid carcinoma

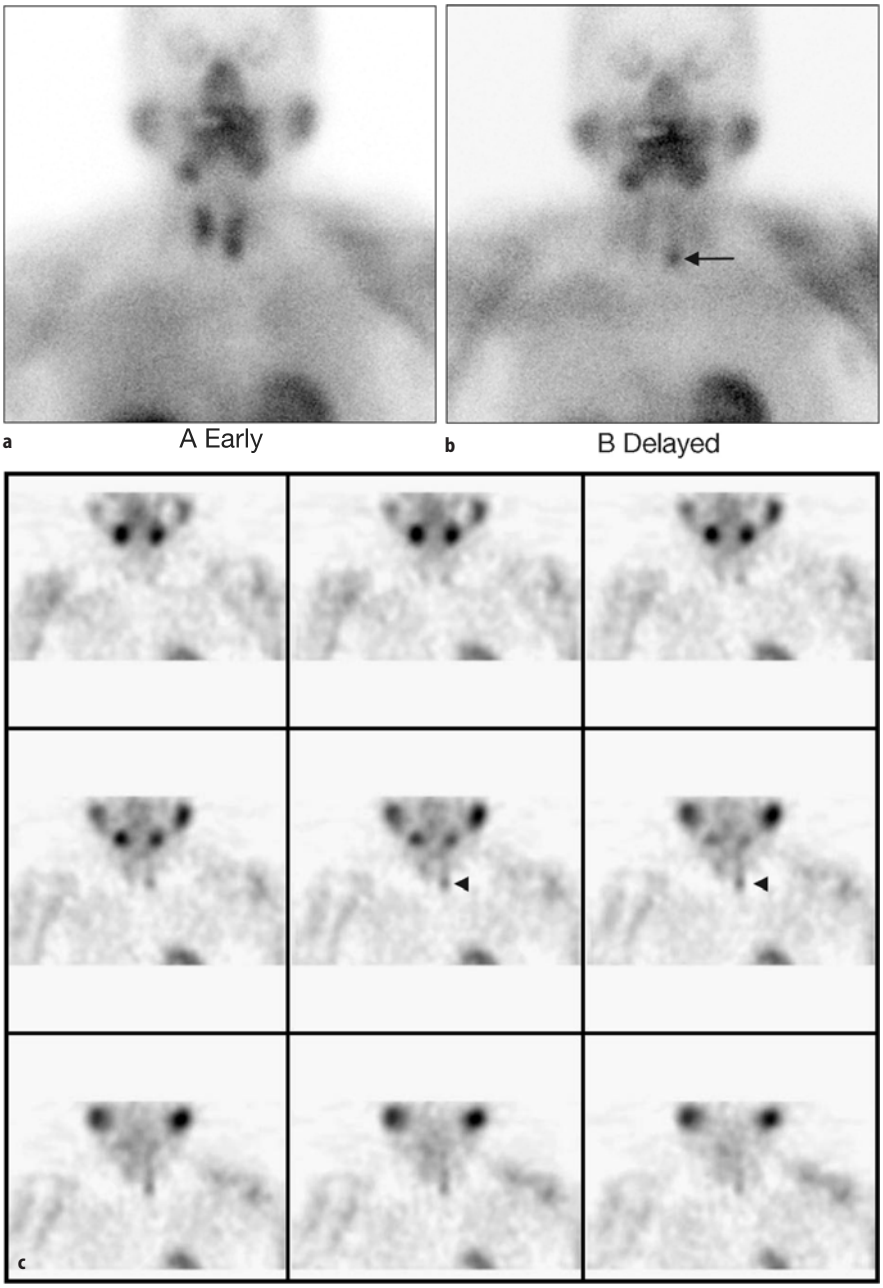

Fig. 8.7a–c. ^{99m}Tc-Sestamibi parathyroid localization study showing retained activity in a parathyroid adenoma (*arrow*) in the left lower pole. SPECT study was obtained. Representative coronal images illustrate the abnormal uptake at the adenoma seen on planar images (*arrowheads*)

More recently Beggs reported a sensitivity of 83%, a specificity of 100% and an accuracy of 88% in successfully locating parathyroid adenomas among 51 patients presenting with hyperparathyroidism, and in whom other imaging techniques including ^{99m}Tc-MIBI had failed to definitely identify the site of adenoma. Most false negatives were due to adenomas in the lower mediastinum that was outside the area of scanning [88].

The protocol for the most popular imaging study ^{99m}Tc-sestamibi parathyroid scintigraphy varies, but in general the technique currently accepted by most researchers is to acquire early static imaging 15 min following injection of 20 mCi ^{99m}Tc-MIBI using a pinhole collimator for the anterior neck and a parallel hole collimator for imaging the mediastinum. This is repeated 2 – 3 h later. Some may still use early dynamic imaging (one frame/min for 60 min) upon i.v. injection of 20 mCi ^{99m}Tc-MIBI using a large-field-of-view gamma camera and a parallel hole collimator. The field should include the neck and mediastinum up to the upper margins of the heart. This dynamic imaging is then followed by planar static images of neck and mediastinum every 20 min until the complete or significant clearance of the radiotracer from the thyroid gland. Advocates of

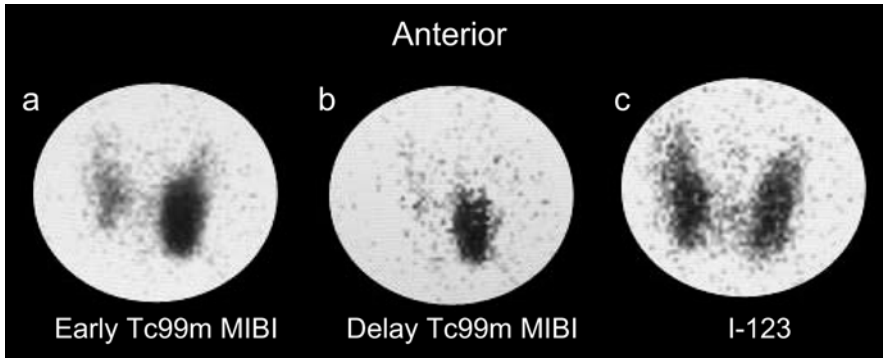

Fig. 8.8a–c. ^{99m}Tc-Sestamibi study shows increased uptake in the left inferior lower pole on early image (**a**) with retention of activity on delayed image (**b**). Iodine-123 4-h study (**c**) acquired on the same day following the sestamibi study shows no thyroid abnormalities. This example illustrates the occasional difficulty in differentiating parathyroid pathology from thyroid abnormalities on sestamibi studies

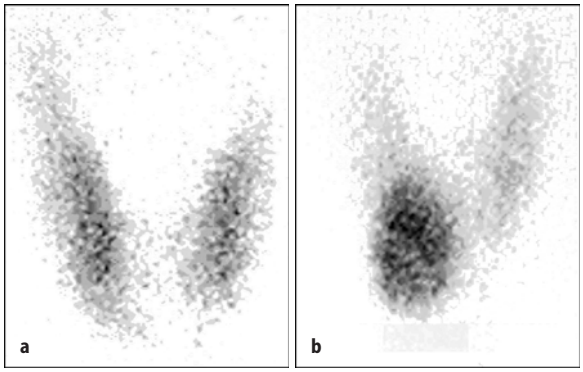

Fig. 8.9a,b. Dual tracer study using ^{99m}Tc-pertechnetate for thyroid scan (a) followed next day by ^{99m}Tc-Myoview acquired as a single early acquisition (**b**). Comparing the two images clearly shows right sided localized accumulation of Myoview with no matching finding on pertechnetate scan. A large parathyroid adenoma was found. This method was reported in a preliminary experience to be easy for interpretation and has high accuracy. (Courtesy of Dr Sahar A-Sobaie)

this protocol think that uptake in some abnormal parathyroid glands shows fast clearance in less than 2 h post-injection. The variable behavior of abnormal parathyroid glands is due to the varying ultrastructure of the cells, the various combinations of cell types, and their biological activity. ^{123}I (Fig. 8.8) or pertechnetate (Fig. 8.6) thyroid imaging for comparison or subtraction is only occasionally needed on an individual basis (e.g., presence of thyroid nodule). If the presence of thyroid pathology is known or suspected clinically, one starts with a thyroid scan to define the morphology and localize the thyroid by injecting 1 mCi ^{99m}Tc-pertechnetate i.v., and the neck is imaged 15 min later.

SPECT imaging has been used routinely or as optional. The study is usually performed acquiring 64 frames (32 × 2 in case of using dual head camera), 30 s each using a matrix of 128× 128 with a circular orbit of 360 degrees. The field of view encompasses the neck and thorax [39]. The additive value of SPECT is controversial [89]. Studies using SPECT showed sensitivities of 53%, 87%, 81%, 57% and 73% respectively [84, 90–93]. It is difficult to know why reported sensitivities differ so much. The low sensitivity reported by De Feo et al. [92] may be secondary to the use of low-dose sestamibi (240 MBq (6.5 mCi) compared with 370–740 MBq (10–20 mCi) for other studies), although Neumann et al. [84] used 740 MBq (20 mCi). The timing of imaging after sestamibi injection may affect sensitivity, but there is no consensus in the literature about optimal timing. Neumann et al. [84] imaged at 10 min, Bonjer et al. [91] at 30 min, De Feo et al. [92] at 10 and 90 min, Kliegler and O'Mara [94] at 30 min and 2 h, Mazzeo et al. [95] at 30 min and 3 h and Slater at 2 h [93]. Tertrofosmin has been also used in a 2-day protocol using ^{99m}Tc-pertechnetete imaging of thyroid and single acquisition of ^{99m}Tc-Myoview next day. Comparing the activity of both scans (Fig. 8.9) obtained 15 min post-injection facilitates detecting focal activity of parathyroid adenomas and hyperplastic glands with high accuracy.

A recent study found that parathyroid sestamibi SPECT scan interpretation by a nuclear medicine physician with an endocrine surgeon resulted in improved accuracy of gland localization and lateralization compared to a nuclear medicine physician reading alone. This improvement may be due to increased awareness of clinical data and head-and-neck anatomy [93].

8.6.2 Intraoperative Probe Localization

Localization using intraoperative gamma probe (Fig. 8.10) has recently gained popularity [96]. The patient is injected 2 h before surgery and the probe is used to detect the higher level of activity after exploration by the surgeon. On the day of surgery, the patients receive the same dose of MIBI as for imaging and are taken to the operating room. Prior to skin incision, counts over four quadrants in the neck as well as over the mediastinum are obtained using a gamma probe [97].

8.6.3 Atypical Washout of Radiotracer

As outlined the diagnosis of parathyroid tumor with ^{99m}Tc-sestamibi scintigraphy is based on the differential washout rate between the thyroid and diseased

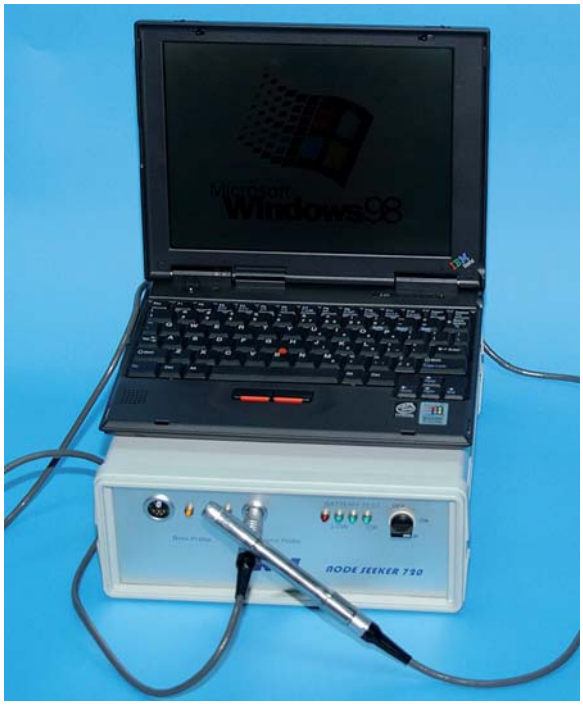

Fig. 8.10. The gamma probe used for intraoperative localization of parathyroid glands in patients with biochemically proven hyperparathyroidism

parathyroids. Atypical radiotracer clearance whether fast parathyroid or delayed thyroid gland washout will limit the efficacy of detection of parathyroid disease with dual-phase ^{99m}Tc-sestamibi scintigraphy as well as using the intraoperative probe.

Early parathyroid washout is frequently seen in parathyroid hyperplasia; the detection rate for this entity is approximately half of that for parathyroid adenoma [52]. Scintigraphy performs worse in cases of multisite hyperplasia, in which only the most prominent radiotracer-avid gland is visualized. In addition, rapid washout from a parathyroid adenoma has been attributed, without unanimous confirmation, to the histologic composition of the adenoma [25, 52]. Modifying the imaging protocol with additional interval scanning between the standard 15-min and 2 – 4-h acquisitions may be helpful in demonstrating rapid washout.

Delayed radiotracer washout from the thyroid parenchyma makes dual-phase scintigraphic assessment difficult. It was observed that the delay varies and significant washout may not occur even several hours after injection of the radiotracer. This retention of ^{99m}Tc-sestamibi occurs in thyroid diseases such as multinodular goiter, Hashimoto thyroiditis, thyroid adenoma, and thyroid carcinoma owing to the hypermetabolic characteristics of these diseases [41, 98, 99]. Extended delayed-phase imaging of ^{99m}Tc-sestamibi along with in-depth clinical examination may be useful in diagnosis of concomitant thyroid and parathyroid disease [100].

Table 8.4. Causes of false-positive ^{99m}Tc-sestamibi [41, 52, 101, 102]

Lymph nodes
Supraclavicular
Axillary
Hyperplastic thymus[a]
Sarcoidosis[b]
Carcinoid tumor
Malignant tumors

[a] Confused with an intrathymic or mediastinal parathyroid adenoma
[b] Thorax

As rapid washout and small size of parathyroid glands would cause false negative localization studies, several pathologies can also cause false positive studies (Table 8.4).

8.7 Summary

To understand the various scintigraphic patterns of parathyroid disease, it is important to understand parathyroid embryology and anatomy. Although experienced neck surgeons can achieve a high success rate of parathyroidectomy after bilateral neck exploration without prior localizing study [2, 3], a preoperative localization study would decrease operative time and morbidity and is frequently needed for the minimally invasive surgical approach that is currently practiced with increasing frequency. The most commonly used and most cost effective modality for preoperative localization is ^{99m}Tc-sestamibi and alternatively ^{99m}Tc-Myoview. The technique is being used before the initial surgery but is most clearly indicated for the preoperative evaluation of recurrent or persistent hyperparathyroidism. SPECT and particularly pinhole acquisition are valuable to improve the accuracy of localization. Intraoperative gamma probe localization is increasingly used also along with the minimally invasive surgical approach. The spectrum of parathyroid disease demonstrated with ^{99m}Tc-sestamibi scintigraphy includes eutopic disease, ectopic disease, solitary adenoma, double or multiple adenomas, cystic adenoma, lipoadenoma, multiple endocrine neoplasia, hyperfunctioning parathyroid transplant and others. The diagnosis of parathyroid tumors with ^{99m}Tc-sestamibi scintigraphy is based on the difference in clearance rates between the thyroid and diseased parathyroid glands, and any condition that interferes with radiotracer clearance will limit the effectiveness of the study. Atypical washout is one of the known entities that can limit the accuracy of these stuidies and it is probably related to the mitochondrial contents of the cells of the abnormal glands.

Adding thyroid scan and ultrasonography improves results but is not cost effective enough to be a routine practice.

Subtraction ^{99m}Tc-sestamibi, iodine-123 scintigraphy or more recently PET may be helpful in difficult cases.

References

1. Carney JA (1996) The glandulae parathyroideae of Ivar Sandstrom. Contributions from two continents. Am J Surg Pathol 20:1123 – 1144
2. Maxon HR, Elgazzar AH (1988) Parathyroid imaging. In: Gelfand G, Thomas S (eds) Effective use of computers in nuclear medicine. McGraw Hill, New York, pp 485 – 496
3. Akerstrom G, Grimelius L, Johansson H, Lundquist H, Pertoft H, Bergstrom R (1981) The parenchymal cell mass in normal human parathyroid glands. Acta Pathol Microbiol Immunol Scand 89(A):367
4. Grimelius L, Ackerstrom Goran, Bonderson L, Juhlin C, Johnsson H, Ljunghall S, Rastad J (1991) The role of the pathologist in diagnosis and surgical decision making in hyperparathyroidism. World J Surg 15:698 – 705
5. Akerstrom G, Rastad J, Ljunghall S, Johnsson H (1990) Clinical and experimental advances in sporadic primary hyperparathyroidism. Acta Chir Scand 156:23 – 28
6. Birkenhager JC, Bouillon R (1996) Asymptomatic hyperparathyroidism. Postgrad Med J 72:323 – 326
7. Mitchell BK, Merrell RC, Kinder BK (1995) Localization studies in patients with hyperparathyroidism. Endocr Surg 75:483 – 498
8. Smith JR. Oates ME (2004) Radionuclide imaging of the parathyroid glands: patterns, pearls, and pitfalls. Radiographics 24:1101 – 1115
9. Berland T, Smith SL, Huguet KL (2005) Occult fifth gland intrathyroid parathyroid adenoma identified by gamma probe. Am Surg 71:264 – 266
10. Wang CA (1976) The anatomic basis of parathyroid surgery. Ann Surg 183:271 – 275
11. Akerstrom G, Malmaeus J, Bergstrom R (1984) Surgical anatomy of human parathyroid glands. Surgery 95:15 – 21
12. Delaney SE, Wermers RA, Thompson GB, Hodgson SF, Dinneen SF (1999) Mediastinal parathyroid carcinoma. Endocr Pract 5:133 – 136
13. Quiros RM, Warren W, Prinz RA (2004) Excision of a mediastinal parathyroid gland with use of video-assisted thoracoscopy, intraoperative 99mTc-sestamibi scanning, and intraoperative monitoring of intact parathyroid hormone. Endocr Pract 10:45 – 48
14. Akerstrom G, Rudberg C, Grimelius L, et al (1986) Histologic parathyroid abnormalities in an autopsy series. Hum Pathol 17:520 – 527
15. Heath H III (1991) Clinical spectrum of primary hyperparathyroidism: evolution with changes in medical practice and technology. J Bone Miner Res 6:S63–S70
16. Fitzpatrick LA (1989) Hypercalcemia in the multiple endocrine neoplasia syndromes. Endocrinol Metab Clin North Am 18:741 – 752
17. Skogseid B, Rastad J, Oberg K (1994) Multiple endocrine neoplasia type 1. Endocrinol Metab Clin North Am 23:1 – 17
18. Herfarth KK, Wells SA (1997) Parathyroid glands and the multiple endocrine neoplasia syndromes and familial hypocalciuric hypercalcemia. Semin Surg Oncol 13:114 – 124
19. Mallette LE (1994) Management of hyperparathyroidism in multiple endocrine neoplasia syndromes and other familial endocrinopathies. Endocrinol Metab Clin North Am 23:19 – 36
20. Duh QY, Hybarger CP, Geist R, Gamsu G, Goodman PC, Gooding GA, Clark OH (1987) Carcinoids associated with multiple endocrine neoplasia syndromes. Am J Surg 154:142 – 148
21. Beus KS, Stack BC (2004) Synchronous thyroid pathology in patients presenting with primary hyperparathyroidism. Am J Otolaryngol 25:308 – 312
22. Nishiyama RH, Farhi D, Thompson NW (1979) Radiation exposure and the simultaneous occurrence of primary hyperparathyroidism and thyroid nodules. Surg Clin North Am 59:65 – 75
23. Prinz RA, Barbato AL, Braithwaite SS (1982) Simultaneous primary hyperparathyroidism and nodular thyroid disease. Surgery 92:454 – 458
24. Attie JN, Vardhan R (1993) Association of hyperparathyroidism with nonmedullary thyroid carcinoma: Review of 31 cases. Head Neck 15:20 – 23
25. Burmeister LA, Sandberg M, Carty SE (1997) Thyroid carcinoma found at parathyroidecomy: Association with primary, secondary and tertiary hyperparathyroidism. Cancer 79:1611 – 1616
26. Sidhu S, Campbell P (2000) Thyroid pathology associated with primary hyperparathyroidism. Aust N Z J Surg 70: 285 – 287
27. Bentrem DJ, Angelos P, Talamonti MS (2002) Is preoperative investigation of the thyroid justified in patients undergoing parathyroidectomy for hyperparathyroidism? Thyroid 12:1109 – 1112
28. Arem R, Lim-Abrahan MA, Mallette LE (1986) Concomitant Graves' disease and primary hyperparathyroidism. Influence of hyperthyroidism on serum calcium and parathyroid hormone. Am J Med 80:693 – 698
29. Ogburn P, Black B (1956) Primary hyperparathyroidism and papillary adenocarcinoma of the thyroid: Report of four cases. Mayo Clin Proc 31:295 – 298
30. Hedman IL, Tisell LE (1984) Associated hyperparathyroidism and non-medullary thyroid carcinoma: The etiological role of radiation. Surgery 95:392 – 397
31. Beus KS, Stack BC Jr (2004) Synchronous thyroid pathology in patients presenting with primary hyperparathyroidism. Am J Otolaryngol 25:308 – 312
32. Sy WM, Mittal AK (1975) Bone scan in chronic dialysis patients with evidence of secondary hyperparathyroidism and renal osteodystrophy. Br J Radiol 48:878 – 884
33. Thompson NW, Eckhauser FE, Harness JK (1982) The anatomy of primary hyperparathyroidism. Surgery 92: 814 – 821
34. Simeone DM, Sandelin K, Thompson NW (1995) Undescended superior parathyroid gland: a potential cause of failed cervical exploration for hyperparathyroidism. Surgery 118:949 – 956
35. Shen W, Duren M, Morita E, Higgins C, Duh QY, Siperstein AE, Clark OH (1996) Reoperation for persistent or recurrent primary hyperparathyroidism. Arch Surg 131:861 – 869
36. Doppman JL, Skarulis MC, Chen CC, et al (1996) Parathyroid adenomas in the aortopulmonary window. Radiology 201:456 – 462
37. Tezelman S, Shen W, Shaver JK, et al (1993) Double parathyroid adenomas: clinical and biochemical characteristics before and after parathyroidectomy. Ann Surg 218: 300 – 309
38. Bartsch D, Nies C, Hasse C, et al (1995) Clinical and surgical aspects of double adenoma in patients with primary hyperparathyroidism. Br J Surg 82:926 – 929

39. Nguyen BD (1999) Parathyroid imaging with Tc-99m sestamibi planar and SPECT scintigraphy. Radiographics 19:601 – 614
40. Clark OH, Duh QY (1989) Primary hyperparathyroidism: a surgical perspective. Endocrinol Metab Clin North Am 18:701 – 714
41. McHenry CR, Lee K, Saadey J, et al (1996) Parathyroid localization with technetium-99m-sestamibi: a prospective evaluation. J Am Coll Surg 183:25 – 30
42. Bergenfelz A, Tennvall J, Valdermarsson S, et al (1997) Sestamibi versus thallium subtraction scintigraphy in parathyroid localization: a prospective comparative study in patients with predominantly mild primary hyperparathyroidism. Surgery 121:601 – 605
43. Rogers LA, Fetter BF, Peete WPJ (1969) Parathyroid cyst and cystic degeneration of parathyroid adenoma. Arch Pathol 88:476 – 479
44. Fallon MD, Haines JW, Teitelbaum SL (1982) Cystic parathyroid gland hyperplasia-hyperparathyroidism presenting as a neck mass. Am J Clin Pathol 77:104 – 107
45. Turner WJD, Baergen RN, Pellitteri PK, Orloff LA (1996) Parathyroid lipoadenoma: case report and review of the literature. Otolaryngol Head Neck Surg 114:313 – 316
46. Cummings C et al (2005) Otolaryngology: head and neck surgery, 4th edn. Mosby, Philadelphia
47. Rinsho N (1995) Primary hyperparathyroidism, pathologic findings and ultrastructure. Jpn J Clin Med 53:861 – 863
48. Baglin A, Junien C, Prinseau J (1991) Mechanism of parathyroid cell proliferation in primary hyperparathyroidism. Presse Med 20:803 – 808
49. Lack CA, Rarber JL, Rubin E (1999) The endocrine system. In: Rubin E, Farber JL (eds) Pathology, 3rd edn. Lippincott-Raven, Philadelphia, pp 1179 – 1183
50. Kilgore EJ, Teigen EL, Cowan RJ (1996) Imaging of transplanted parathyroid tissue in a patient with recurrent hyperparathyroidism. Clin Nucl Med 21:383 – 386
51. Chen CC, Premkumar A, Hill SC, Skarulis MC, Spiegel AM (1995) Tc-99m sestamibi imaging of a hyperfunctioning parathyroid autograft with Doppler ultrasound and MRI correlation. Clin Nucl Med 20:222 – 225
52. Lee VS, Spritzer CE, Coleman RE, Wilkinson RH Jr, Coogan AC, Leight GS Jr (1995) Hyperparathyroidism in high-risk surgical patients: evaluation with double-phase technetium-99m sestamibi imaging. Radiology 197:627 – 633
53. Walker RP, Paloyan E, Gopalsami C (2004) Symptoms in patients with primary hyperparathyroidism: muscle weakness or sleepiness. Endocrine Pract 10:404 – 408
54. Wang CA (1977) Parathyroid re-exploration: a clinical and pathological study of 112 cases. Ann Surg 186:140
55. Assalia A, Inabnet WB (2004) Endoscopic parathyroidectomy. Otolaryngol Clin North Am 37:871 – 886
56. Thomas SK, Wishart GC (2003) Trends in surgical techniques. Nucl Med Commun 24:115 – 119
57. O'Doherty MJ, Kettle AG (2003) Parathyroid imaging: preoperative localisation. Nucl Med Commun 24:125 – 131
58. Erdman WA, Breslau NA, Weinreb JC, Weatherall P, Setiawan H, Harrell R, Snyder W (1989) Noninvasive localization of parathyroid adenomas: a comparison of X-ray computerized tomography, ultrasound, scintigraphy and MRI. Magn Reson Imaging 7:187 – 194
59. Auffermann W, Gooding GA, Okerlund MD, Clark OH, Thurnher S, Levin KE, Higgins CB (1988) Diagnosis of recurrent hyperparathyroidism: comparison of MR imaging and other imaging techniques. Am J Roentgenol 150: 1027 – 1033
60. Peck WW, Higgins CR, Fisher MR, Ling M, Okerland MD, Clark OH (1987) Hyperparathyroidism: comparison of MR imaging with radionuclide scanning. Radiology 163:415 – 420
61. Levin KE, Gooding GA, Okerlund M, Higgins CB, Norman D, Newton TH, Duh QY, Arnaud CD, Siperstein AE, Zeng QH, et al. (1987) Localizing studies in patients with persistent or recurrent hyperparathyroidism. Surgery 102:917 – 925
62. Miller DL, Doppman JR, Shawker TH, Krudy AG, Norton JA, Vucich JJ, et al (1987) Localization of parathyroid adenomas in patients who have undergone surgery, part I. Noninvasive imaging methods. Radiology 162:133 – 137
63. Coakley AJ (2003) Nuclear medicine and parathyroid surgery: a change in practice. Nucl Med Commun 24:111 – 113
64. Van Vroonhoven TJ (2000) Minimally invasive adenomectomy: An alternative for patients with primary hyperparathyroidism. Ann Surg 231:559 – 565
65. Haciyanli M, Lal G, Morita E (2003) Accuracy of preoperative localization studies and intraoperative parathyroid hormone assay in patients with primary hyperparathyroidism and double adenoma. J Am Coll Surg 197:739 – 746
66. Bentrem DJ, Angelos P, Talamonti MS (2002) Is preoperative investigation of the thyroid justified in patients undergoing parathyroidectomy for hyperparathyroidism? Thyroid 12:1109 – 1112
67. Ruda JM, Stack BC Jr, Hollenbeak CS (2004) The cost-effectiveness of sestamibi scanning compared to bilateral neck exploration for the treatment of primary hyperparathyroidism. Otolaryngol Clin North Am 37:855 – 870
68. O'Doherty MJ, Kettle AG, Wells P, Collins RE, Coakley AJ (1992) Parathyroid imaging with technetium 99m-sestamibi: preoperative localization and tissue uptake studies. J Nucl Med 33:313 – 318
69. Piwnica-Worms D, Chiu ML, Budding M, Kronauge JF, Kramer RA, Croop JM (1993) Functional imaging of multidrug resistant P-glycoprotein with an organotechnetium complex. Cancer Res 53:977 – 984
70. Takebayashi S, Hidai H, Chiba T, Takaga Y, Nagatani Y, Matsubara S (1999) Hyperfunctional parathyroid glands with Tc-99m MIBI scan: semiquantitative analysis correlated with histologic findings. J Nucl Med 40:1792 – 1797
71. Bernard F, Lefebvre B, Beuvon F, Langlois MF, Bisson G (1995) Rapid washout of technetium 99m MIBI from a large parathyroid adenoma. J Nucl Med 36:241 – 243
72. Sandrock D, Merino MJ, Norton JA, Neumann RD (1993) Ultrastructural histology correlates with results of thallium-201/Tc-99m parathyroid subtraction scintigraphy. J Nucl Med 34:24 – 29
73. Carpentier A, Jeannotte S, Verrault J, Lefebvre B, Bisson G, Mongeau CJ, et al (1998) Preoperative localization of parathyroid lesions in hyperparathyroidism: relationship between technetium-99m-MIBI and oxyphil cell count. J Nucl Med 39:1441 – 1444
74. Ishibashi M, Nishida H, Okuda S, Suekane S, Hayabuchi N (1998) Localization of parathyroid glands in hemodialysis patients using Tc-99m sestamibi imaging. Nephron 78:48 – 53
75. Pinero A, Rodriguez JM, Ortiz S, Soria T, Bermejo J, Claver MA, et al (2000) Relation of biochemical, cytologic, and morphologic parameters to the result of gammagraphy with technetium 99m sestamibi in primary hyperparathyroidism. Otolaryngol Head Neck Surg 122:851 – 855
76. Sandrock D, Merino MJ, Norton JA, Neumann RD (1993) Ultrastructural histology correlates with results of thallium-201/technetium-99m parathyroid subtraction scintigraphy. J Nucl Med 34:24 – 29
77. Naddaf S, Anim JJ, Farghaly MM, Behbehani AE, Alshomar KA, Elgazzar AH (2005) Ultrastructure of hyperfunctioning parathyroid glands: does it explain various patterns of sestamibi uptake JNM 45:P
78. Kao A, Shiau YC, Tsai SC, Wang JJ, Ho ST (2002) Technetium-99m methoxyisobutylisonitrile imaging for parathy-

roid adenoma: relationship to P-glycoprotein or multidrug resistance-related protein expression. Eur J Nucl Med Mol Imaging 29:1012 – 1015
79. Goris ML, Basso LV, Keeling C (1991) Parathyroid imaging. J Nucl Med 32:887 – 889
80. Elgazzar AH, Maxon HR, Hertzberg V, et al (1985) Parathyroid scintigraphy with and without thyroid hormone suppression. Proceedings of the Eastern Great Lakes Chapter, Society of Nuclear Medicine, Niagara Falls, New York
81. Thule P, Thakore K, Vansant J, McGarity W, Weber C, Phillips LS (1993) Preoperative localization of parathyroid tissue with technetium-99m sestamibi I-123 subtraction scanning. J Clin Endocrinol Metab 78:77 – 82
82. Dontu VS, Kettle AG, O'Doherty MJ, Coakley AJ (2004) Optimization of parathyroid imaging by simultaneous dual energy planar and single photon emission tomography. Nucl Med Commun 25:1089 – 1093
83. Al-Sobaei S (2005) Proceedings of the first gulf nuclear medicine congress. Riyadh, Saudi Arabia, March 1 – 3
84. Neumann DR, Esselstyn CB, MacIntyre WJ, Go RT, Obuchowski NA, Chen EQ, et al (1996) Comparison of FDG-PET and sestamibi SPECT in primary hyperparathyroidism. J Nucl Med 37:1809 – 1815
85. Melon P, Luxen A, Hamoir E, Meurisse M (1995) Fluorine-18-fluorodeoxyglucose positron emission tomography for preoperative parathyroid imaging in primary hyperparathyroidism. Eur J Nucl Med 22:556 – 558
86. Sundin A, Johansson C, Hellman P, Bergstrom M, Ahlstrom H, Jacobson GB, et al (1996) PET and parathyroid L-[carbon-11]methionine accumulation in hyperparathyroidism. J Nucl Med 37:1766 – 1770
87. Cook GJR, Wong JCH, Smellie WJB, Young AE, Maisey MN, Fogelman I (1998) [^{11}C]Methionine positron emission tomography for patients with persistent or recurrent hyperparathyroidism. Eur J Endocrinol 139:195 – 197
88. Beggs AD, Hain SF (2005) Localization of parathyroid adenomas using ^{11}C-methionine positron emission tomography. Nucl Med Commun 26:133 – 136
89. Melton GB, Somervell H, Friedman KP, Zeiger MA, Cahid CA (2005) Interpretation of ^{99m}Tc sestamibi parathyroid SPECT scan is improved when read by the surgeon and nuclear medicine physician together. Nucl Med Commun 26:633 – 638
90. Civelek AC, Ozalp E, Donovan P, Udelsman R (2002) Prospective evaluation of delayed technetium-99m sestamibi SPECT scintigraphy for preoperative localization of primary hyperthyroidism. Surgery 131:149 – 157
91. Bonjer HJ, Bruining HA, Valkema R, Lameris JS, de Herder WW, van der Harst E, Pols HA (1997) Single radionuclide scintigraphy with 99m-technetium-sestamibi and ultrasonography in hyperparathyroidism. Eur J Surg 163:27 – 32
92. De Feo ML, Colagrande S, Biagini C, Tonarelli A, Bisi G, Vaggelli L, Borrelli D, Cicchi P, Tonelli F, Amorosi A, Serio M, Brandi ML (2000) Parathyroid glands: combination of ^{99m}Tc MIBI scintigraphy and US for demonstration of parathyroid glands and nodules. Radiology 214:393 – 402
93. Slater A, Gleeson FV (2005) Increased sensitivity and confidence of SPECT over planar imaging in dual-phase sestamibi for parathyroid adenoma detection. Clin Nucl Med 30:1 – 3
94. Klieger P, O'Mara R (1998) The diagnostic utility of dual phase Tc-99m sestamibi parathyroid imaging. Clin Nucl Med 23:208 – 211
95. Mazzeo S, Caramella D, Lencioni R, Molea N, De Liperi A, Marcocci C, Miccoli P, Iacconi P, Bossio GB, Viacava P, Lazzeri E, Bartolozzi C (1996) Comparison among sonography, double-tracer subtraction scintigraphy, and double-phase scintigraphy in the detection of parathyroid lesions. AJR Am J Roentgenol 166:1465 – 1470
96. Berland T, Smith SL, Huguet KL (2005) Occult fifth gland intrathyroid parathyroid adenoma identified by gamma probe. Am Surg 71:264 – 266
97. Ugur O, Bozkurt MF, Hamaloglu E, Sokmensuer C, Etikan I, Ugur Y, Sayek I, Gulec SA (2004) Clinicopathologic and radiopharmacokinetic factors affecting gamma probe-guided parathyroidectomy. Arch Surg 139:1175 – 1179
98. Bergenfelz A, Tennvall J, Valdermarsson S, et al (1997) Sestamibi versus thallium subtraction scintigraphy in parathyroid localization: a prospective comparative study in patients with predominantly mild primary hyperparathyroidism. Surgery 121:601 – 605
99. Taillefer R, Boucher Y, Potvin C, Lambert R (1992) Detection and localization of parathyroid adenomas in patients with hyperparathyroidism using a single radionuclide imaging procedure with technetium-99m-sestamibi (double-phase study). J Nucl Med 33:1801 – 1807
100. Caixas A, Berna L, Hernandez A, Tebar FJ, Madariaga P, Vegazo O, Bittini AL, Moreno B, Faure E, Abos D, Piera J, Rodriguez JM, Farrerons J, Puig-Domingo M (1997) Efficacy of preoperative diagnostic imaging localization of technetium 99m-sestamibi scintigraphy in hyperparathyroidism. Surgery 121:535 – 541
101. Mudun A, Kocak M, Unal S, Cantez S (1995) Tc-99m MIBI accumulation in remnant thymus: a cause of false-positive interpretation in parathyroid imaging. Clin Nucl Med 20:379 – 380
102. Desai S, Yuille DL (1993) Visualization of a recurrent carcinoid tumor and an occult distant metastasis by technetium-99m-sestamibi. J Nucl Med 34:1748 – 1750

9 Adrenal Gland

Sleiman Naddaf, Abdelhamid H. Elgazzar

9.1 Anatomical and Physiological Considerations

The adult adrenal glands weigh 8–10 g and lie above and slightly medial to the upper pole of both kidneys. The outer cortex comprises 90% of the adrenal weight, the inner medulla about 10%. The cortex is rich with vessels and receives its main blood supply from branches of the inferior phrenic artery, renal arteries, and the aorta. These small arteries form an arterial plexus beneath the capsule and then enter a sinusoid system that penetrates the cortex and medulla, draining into a single central vein in each gland [1].

Histologically, the adult adrenal cortex is composed of three zones: an outer zona glomerulosa which produces aldosterone, a zona fasciculata, and an inner zona reticularis. The zona fasciculata is the thickest layer and produces cortisol and androgens; its cells are large and contain more lipid and thus are termed clear cells. The zona reticularis produces weak androgens. The zonae fasciculata and reticularis are regulated by adrenocorticotropic hormone (ACTH).

Cholesterol within the adrenal cortex is the starting point for synthesis of multiple adrenal hormones. Therefore, a radioactive cholesterol is useful in evaluating the functional status of adrenocortical lesions. The

Table 9.1. Adrenal hormones and their effects

Structure	Secreted hormone	Functions
Adrenal cortex		
Zona glomerulosa	Mineralocorticoids, especially aldosterone	Conserves blood volume through reabsorption of sodium (and water) from distal tubules
Zona fasciculata	Glucocorticoids, especially cortisol	Increases blood glucose level, stimulates protein catabolism and lipolysis, and increases resistance to stress
Zona reticularis	Androgens, especially dehydroepiandrosterone	Sustains normal pubic and axillary hair and stimulates RBC production, protein synthesis and growth
Adrenal medulla		
Epinephrine		More β-receptor effects, e.g., relaxation of musculature of gastrointestinal tract, uterus, bronchi, and urinary bladder
Norepinephrine		More β-receptor effects, e.g., vasoconstriction and contraction of sphincters and uterus

adrenal medulla is composed histologically of chromaffin cells, which are large ovoid columnar cells arranged in clumps or cords around blood vessels and surrounded by capillaries and sinusoids. They have large nuclei and a well-developed Golgi apparatus; they have a large number of granules containing catecholamines. The adrenal medulla also contains some sympathetic ganglia. The cells of the adrenal medulla are innervated by preganglionic sympathetic fibers. Most of the blood supply to the hormonally active cells of the medulla is derived from a portal vascular system arising from the capillaries in the cortex. There is also a network of lymphatics that drain into a plexus around the central vein [2]. The adrenals provide adjustment of heart performance and vascular tone. Epinephrine is found essentially only in the adrenal medulla, and constituting greater than 80% of its output. Norepinephrine is synthesized by adrenergic neurons and cells of the adrenal medulla; therefore, a radioactive norepinephrine analog is used to evaluate adrenomedullary lesions.

9.2 Adrenal Cortex

9.2.1 Pathophysiology

9.2.1.1 Primary Aldosteronism (Conn's Syndrome)

In primary aldosteronism (Conn's syndrome), there is increased production of aldosterone by abnormal zona glomerulosa (adenoma or hyperplasia) leading to hypertension through the increased reabsorption of sodium and water from the distal tubules. A benign adenoma accounts for 75% of cases of this syndrome; it is usually small, ranging from 0.5 to 1.5 cm in diameter. It is more common in women than in men (3:1) and usually occurs between the ages of 30 and 50 years. Bilateral, or rarely unilateral, micro- or macronodular adrenal hyperplasia accounts for most of the remaining cases. Two types of familial hyperaldosteronism have recently been identified: Type I is glucocorticoid suppressible and associated with bilateral hyperplasia, and type II is associated with adrenocortical adenoma. Adrenal carcinoma is a very rare cause of this syndrome. The patients typically come to medical attention because of clinical signs of hypokalemia or detection of previously unsuspected hypertension during the course of a routine physical examination. The diagnosis is principally a biochemical one (low plasma renin activity and a high level of aldosterone); imaging is required to localize the lesion and identify its multiplicity. The diagnostic information provided by CT or MRI in localizing adenomas is both accurate and practical and they are the initial approach of choice. Some smaller adenomas which are not clearly visualized by CT can be depicted by scintigraphy.

9.2.1.2 Cushing's Syndrome

The most common (60% – 70% of cases) pathological cause of this syndrome is the stimulation of the zona fasciculata by excess ACTH from the pituitary gland (Cushing's disease) or, less commonly, the ectopic production of ACTH (as in small cell lung cancer and neural crest tumors) or corticotropin-releasing factor (CRF) (as in bronchial carcinoid and prostate cancer). Stimulating this zona may lead to bilateral adrenocortical hyperplasia, which is nodular in 25% and diffuse in 75% of cases. Cushing's syndrome may also be due to autonomous adrenal cortisol production (30% – 40% of cases) due to adrenal adenoma, or hyperfunctioning adrenal carcinoma. ACTH-induced Cushing's disease is more common in adults (25 – 45 years) and is at least three times more common in women than in men. Cushing's disease resulting from ectopic ACTH secretion is more common in older adults, particularly men. Adrenal tumors rather than pituitary tumors are more common in children, especially girls. Twenty percent of nonfunctional adrenocortical carcinomas tend to be highly malignant, with weights exceeding 1 kg.

9.2.1.3 Hyperandrogenism

Hyperandrogenism can be the result of hypersecretion of androgens (causing virilization) or estrogens (causing feminization) from the zona reticularis of the adrenal cortex by primary adrenocortical hyperplasia and rarely by adrenal tumors, though the most common cause of this syndrome is polycystic ovary disease (POD). In POD, the chronic anovulation associated with increased circulating LH levels results in increased ovarian stromal stimulation, which leads to increased ovarian androgen production. A testosterone-secreting adrenal adenoma may contain the crystalloids characteristic of Leydig's cells [3].

9.2.2 Scintigraphy: NP-59

NP(^{131}I-6-iodomethyl-19-norcholesterol)-59 is the nuclear medicine study used to evaluate some disease processes related to the adrenal cortex. Its main uses are documented cases of adrenal excess secretion and negative or equivocal CT or MRI findings. This radiopharmaceutical is a cholesterol analog that is bound to and transported by low-density lipoproteins (LDL) to specific LDL receptors on adrenocortical cells; therefore, endogenous hypercholesterolemia may limit the number of receptors available for radiocholesterol localization through competitive inhibition. Once liberated from LDL, NP-59 is esterified but is not further

converted to steroid hormones [4]. This scan should be done only on patients with clinically hyperfunctioning adrenal cortex verified by lab results, CT, or MRI.

Patient Preparation

1. Suppression of normal adrenal cortex is achieved by oral administration of 1 mg dexamethasone q.i.d. beginning 7 days before and for the duration of the study. This is not required in patients with hypercortisolism.
2. The following medications should be stopped for at least 48 h: diuretics, spironolactone, and antihypertensive drugs, if feasible.
3. To suppress the thyroid uptake of free radioiodine, saturated solution of kallium iodide (SSKI) is given orally in a dose of one drop t.i.d. starting 2 days before and continuing for 14 days. Patients allergic to iodine can take potassium perchlorate (200 mg every night after meals), starting 1 day before injection of NP-59, for 10 days.
4. To diminish bowel activity, a laxative should be given starting 48 h prior to imaging and continuing till final imaging. Enemas may be required. The dose of ^{131}I-NP-59 is 1 mCi, to be strictly injected i.v. through a secured i.v. line over 2 min. NP-59 background clearance and accumulation in the adrenals occurs slowly, but by day 5, accumulation in the normal adrenals is greater than in other organs. Suppressed patients should be imaged on days 3, 4, 5, and 7. If the adrenals are not seen by day 7, dexamethasone should be stopped and the patient imaged on day 10; nonsuppressed patients are imaged on days 5 and 7. Anterior and posterior projections of the adrenals are obtained; in case of hyperandrogenism, the pelvis and genitalia should be included.

The normal distribution is seen in the liver, gallbladder, and colon. In 90% of cases, the right adrenal gland is more cephalad and deeper than the left adrenal gland. In two-thirds of normal subjects, the activity in the right adrenal appears greater than that in the left in the posterior projection; this is because the right adrenal occupies a more posterior location than the left adrenal. In some instances the gallbladder can be confused with the right adrenal. In the lateral view, the gallbladder is located anterior. In difficult cases, cholecystokinin can clear the gallbladder activity. Interfering colonic activity can be reduced by cathartics. Although count rates are low, single photon-emission computed tomography (SPECT) can be performed and may separate adrenals from gut and liver activity. The radiation-absorbed dose (rad/mCi) is 26, 8.0, and 2.3 to the adrenals, ovaries, and testes, respectively.

In primary aldosteronism, early unilateral increased uptake indicates adrenal adenoma, whereas bilateral increased uptake suggests bilateral adrenal hyperplasia. Pituitary ACTH-producing adenoma or ectopic ACTH secretion can result in bilateral adrenal hyperplasia manifested by bilateral symmetric increased uptake, with ectopic causes producing more uptake of NP-59; this pattern may be asymmetric in the macronodular form of hyperplasia. Adrenal adenoma causes unilateral increased uptake, whereas adrenocortical carcinoma gives rise to bilateral nonvisualization. In hyperandrogenism, early bilateral uptake is compatible with hyperplasia, and early (< 5 days) unilateral uptake or a marked asymmetric visualization is indicative of adrenal adenoma.

9.3 Adrenal Medulla

9.3.1 Pathophysiology

9.3.1.1 Pheochromocytoma

Pheochromocytoma is a rare tumor arising from chromaffin cells of the adrenal medulla. Most pheochromocytomas produce excessive amounts of norepinephrine, attributable to autonomous functioning of the tumor, although large tumors secrete both norepinephrine and epinephrine [5] and in some cases also dopamine. Releasing the catecholamine into the circulation causes hypertension and other signs. Other catecholamine-producing tumors (e.g., chemodectoma and ganglioneuroma) may also cause a syndrome similar to that seen with pheochromocytoma. Furthermore, they also produce some active peptides such as somatostatin, ACTH, and calcitonin. Pheochromocytomas vary in size from less than 1 g to several kilograms; in general, they are small, most weighing under 100 g. They are vascular tumors, tend to be capsulated, and commonly contain cystic or hemorrhagic areas. The cells tend to be large and contain typical catecholamine storage granules. Multinucleated cells, pleomorphic nuclei, mitosis, and extension into capsule and vessels are sometimes seen but do not indicate that the tumor is malignant. The chromogranin existing within secretory granules in the tumor tends to form *Zellballen* (cell balls); these structures are surrounded by sustentacular cells. Five to 10% of cases are malignant, and malignancy is determined only by the biological behavior of the tumor. It is estimated that 0.1% of hypertensive patients have pheochromocytoma. More than 90% of patients with pheochromocytoma exhibit hypertension, which is sustained in two-thirds of patients. These tumors are observed somewhat more frequently in women than in men and at all ages, including infancy; they are most common in the 5th and 6th decades [5].

Although most patients with functioning tumors have symptoms (sweating, palpitation, headache, dyspnea, and anxiety), most of the time these vary in intensity and in about half of the patients they are paroxysmal. Pheochromocytomas are sporadic, but about 10% – 20% of cases are familial and arise alone or as part of several hereditary syndromes including: multiple endocrine neoplasia (MEN) type IIa and type IIb, neuroectodermal disorders (tuberous sclerosis, von Hippel-Lindau disease, and neurofibromatosis type I), Carney's syndrome (pulmonary chondroma, gastric epithelioid leiomyosarcoma, and paraganglioma), and McCune-Albright syndrome. Pheochromocytoma can be found anywhere in the sympathetic nervous system from the neck to the sacrum; it is subdiaphragmatic in about 98% of cases. In 85% – 90% of these cases, it is found in the adrenal medulla. In sporadic cases of pheochromocytoma, 80% of the tumors are unilateral, 10% bilateral, and 10% extra-adrenal (paraganglioma). By contrast, two-thirds of those occurring in the context of MEN are bilateral. In children, it is extra-adrenal in 30% of cases. These extra-adrenal locations are: para-aortic sympathetic chain (8%), organ of Zuckerkandl at origin of inferior mesenteric artery (2% – 5%), gonads, scrotum, and urinary bladder (1%). Fewer than 10% of these tumors are malignant and metastasize by lymphatic or hematogenous routes; metastases are usually found in the skeleton, liver, lymph nodes, and lungs [6]. The differential diagnosis includes thyrotoxicosis, migraine, sympathomimetic drug use, menopausal hot flushes, and anxiety disorders. Patients with persistent symptoms and hypertension may develop complications such as nephropathy, retinopathy, myocardial infarction, cerebrovascular accidents, and congestive heart failure.

The diagnosis is confirmed by assay of catecholamines and their metabolites, followed by MRI or CT to localize the lesion; predominant production of epinephrine, when present, suggests an adrenal location. Dopamine excretion is a sensitive indicator of tumor aggressiveness, and a rising plasma or urinary dopamine level is regarded as a poor prognostic indicator.

MRI is somewhat more successful in locating extra-adrenal tumors and has the advantage of providing bright images of pheochromocytoma with T_2 weighting in contrast to most other adrenal tumors. Only the smallest tumors or those shielded by clips and other metal objects from previous surgery cannot be detected; in these cases, an MIBG study is indicated.

9.3.1.2 Neuroblastoma

Neuroblastoma is a malignant tumor of the sympathetic nervous system, accounting for up to 10% of childhood cancers and 15% of cancer deaths among children. Seventy-five percent of neuroblastoma patients are younger than 4 years. The tumor is usually more than 5 cm in the largest diameter and tends to extend across the midline; it has the potential to mature into pheochromocytoma or ganglioneuroma. Metastases are the first manifestation in up to 60% of cases. The electron-microscopic appearance of neuroblastoma cells is distinctive. The malignant neuroblasts exhibit peripheral dendritic processes containing longitudinally oriented microtubules, neurosecretory granules, and filaments in the cytoplasm. Neuroblastomas readily infiltrate the surrounding structures and metastasize to regional lymph nodes, liver, lungs, and bones; metastases to the orbit may result in proptosis [7]. Areas of necrosis, hemorrhage, calcification, and cystic changes are frequently present. Around one-third of cases are found in the adrenal gland, another third in other abdominal sites, and 20% in the posterior mediastinum. More than 90% of these tumors produce catecholamine in excess but they rarely cause typical clinical syndromes. Severe diarrhea may be caused by secretion of vasoactive intestinal peptides by the neuroblastoma.

9.3.1.3 Ganglioneuroma

Ganglioneuroma is a benign tumor found in older children and young adults, with no sex predilection. Forty percent of the patients are over 20 years of age. Up to 30% of these tumors occur in the adrenal medulla and 43% in the posterior mediastinum. Histologically, the tumor consists of mature ganglion cells and is well encapsulated; it is frequently calcified and rarely hormone active.

9.3.2 Scintigraphy

9.3.2.1 Metaiodobenzylguanidine

Metaiodobenzylguanidine (MIBG) is a guanethidine analog chemically similar to noradrenaline. Following i.v. injection, MIBG is rapidly cleared from the vascular compartment; however, a small amount remains in the thrombocytes. It localizes in storage granules of adrenergic tissue (referred to as synaptosomes) by means of energy- and Na-dependent mechanisms (type 1) and it is not metabolized to any appreciable extent [8]. Neural crest tumors have these synaptosomes in abundance.

Preparation. The patient should be given Lugol solution orally (3 drops b.i.d. for 4 – 5 days, starting 2 days before injection to block the thyroid uptake of free ^{131}I). The patient should stop taking reserpine, imipramine,

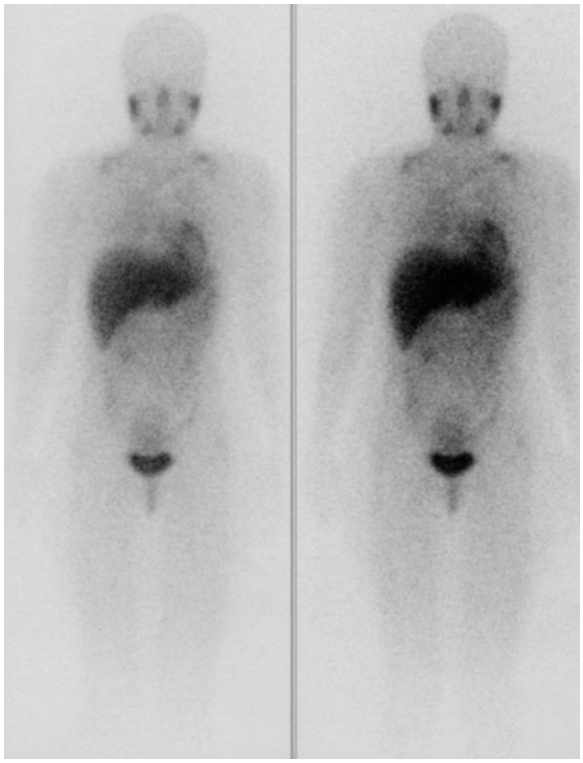

Fig. 9.1. Thirty-two-year-old male with suspected pheochromocytoma. Anterior ^{131}I-MIBG whole body image with different intensity are shown. There is increased uptake at the supraclavicular region bilaterally. This pattern is due to uptake by brown fat. The remainder of the study shows also physiologic distribution of the radiotracer with no abnormalities

calcium channel blockers, cocaine, labetalol, amphetamine-like drugs and others.

The dose of ^{131}I-MIBG is 0.5 – 1.0 mCi and results in a radiation dose of 50 – 100 rads/mCi to the adrenal medulla. The dose of ^{123}I-MIBG is 3 – 10 mCi, with a radiation dose of 0.80 rads/mCi to the adrenal medulla. The normal distribution of ^{123}I-MIBG (Fig. 9.1) is to the salivary gland, liver, urinary bladder, gastrointestinal tract, lung, myocardium, normal adrenal gland, thyroid, spleen, uterus [9 – 11]; and particularly in small children, uptake may also be seen in the nape of the neck, which is currently believed to be related to accumulation in brown adipose tissue [12].

Eighty-five percent of the injected dose is excreted unchanged by the kidneys. Imaging is performed at 24 and 48 h after injection of ^{131}I-MIBG and at 6 and 24 h after injection of ^{123}I-MIBG. When ^{123}I-MIBG SPECT is used (Figs. 9.2, 9.3), increased certainty is achieved in interpreting the studies [9]. It is worthy of mention that ^{123}I is better than ^{131}I, especially in the pediatric population, because of the lower radiation exposure to the adrenals in addition to the superior image quality of the former (Fig. 9.4). The sensitivity of ^{131}I-MIBG in pheochromocytoma is 80% – 90% and specificity is more than 90%; positive MIBG uptake in benign solitary pheochromocytoma (Fig. 9.5) occurs in about 90% of patients [13]; tumors as small as 1 – 2 cm in diameter were detected especially with ^{123}I [14].

Moreover, metastatic and recurrent tumors can also be located (Fig. 9.6). Adrenal medullary hyperplasia found in MEN IIa is difficult to diagnose with CT or MRI. MIBG scintigraphy is uniquely suited to detect this condition. Occasionally, however, some large tumors are not visualized because of extensive tumor necrosis.

MIBG is localized in other neuroendocrine tumors to a lesser degree, including carcinoid, medullary thyroid carcinoma, and paraganglioma. Indium-111 octreotide (a somatostatin analog) is less accurate in the detection of pheochromocytoma, probably due to normal physiological uptake in liver, spleen and kidneys and blocking of somatostatin receptors by endogenous somatostatin.

Radiolabeled MIBG imaging is now a well-established examination in the diagnostic evaluation of neuroblastoma. ^{123}I is preferred especially in pediatric patients (dose 3 – 5 mCi) due to its favorable dosimetry and superior image quality; scintigraphy can be performed as early as 4 h after injection. Elevated catecholamine levels are not necessary for the detection of NB by MIBG. The sensitivity of MIBG in NB is 91%. So-

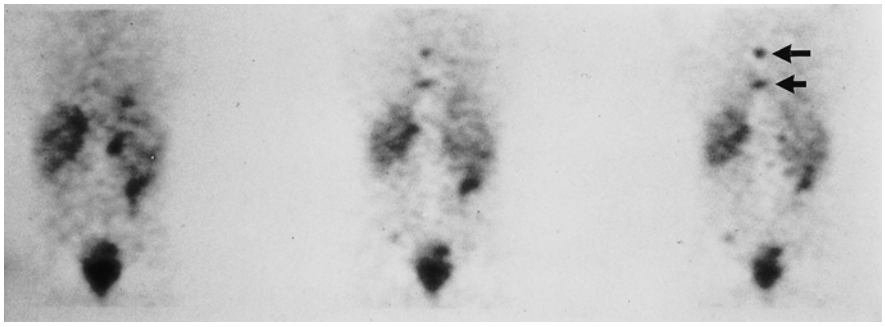

Fig. 9.2. Representative coronal images from a SPECT ^{123}I-MIBG study for a patient with neuroblastoma, showing metastases to the spine (*arrows*)

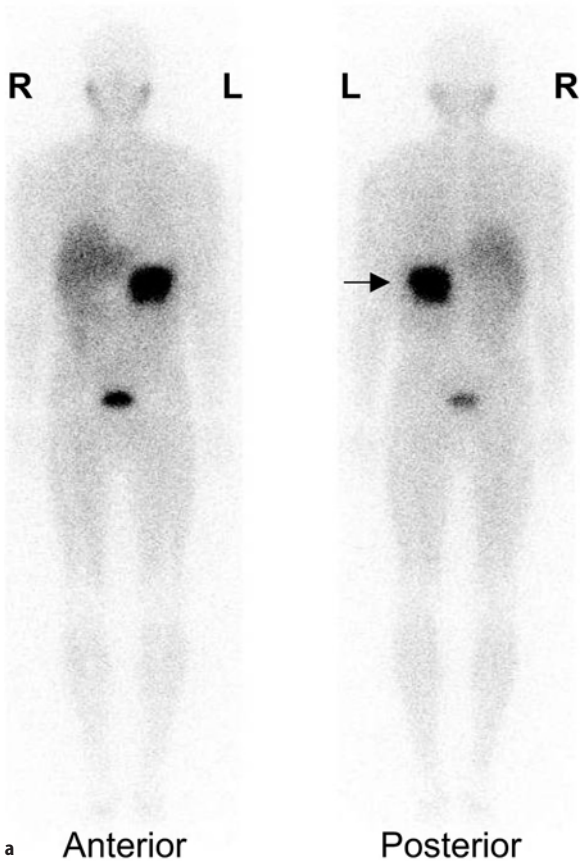

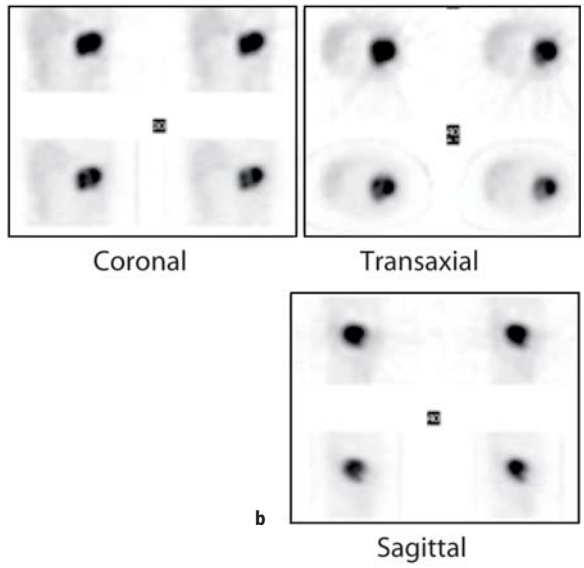

Fig. 9.3a–c. ^{123}I-MIBG whole body (**a**), SPECT (**b**) and CT scan (**c**) of a patient with a large pheochromocytoma (*arrow*)

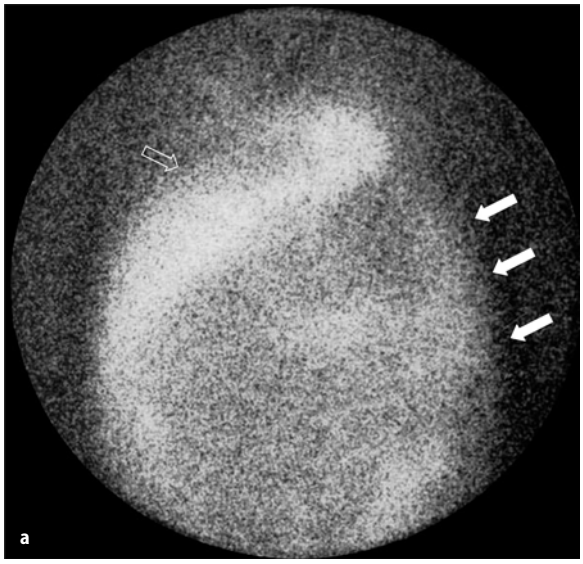

Fig. 9.4. a ^{123}I-MIBG of a 2-year-old boy with a large neuroblastoma (*arrows*) occupying the abdominal cavity and pushing the liver (*open arrow*) superolaterally. **b** CT scan of the abdomen of the same patient showing the tumor (*arrow*)

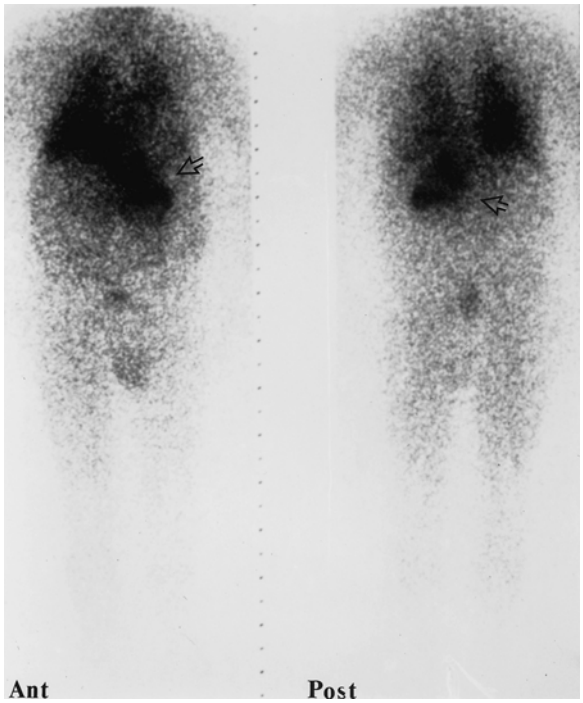

matostatin analog scintigraphy has been reported to visualize MIBG-negative tumor sites in patients with NB. MIBG is essential as a prelude to ^{131}I-MIBG therapy.

9.3.2.2 Indium-111 Octreotide

In healthy human beings, somatostatin, a natural neuropeptide, is produced in various tissues, including the nervous system, endocrine pancreas, and gasrointestinal tract. Somatostatin inhibits the secretion of several hormones, most importantly GH and TSH.

Neuroendocrine (including adrenal medulla) and non-neuroendocrine organs have surface receptors that bind to somatostatin. Octreotide, a somatostatin analog with a half-life of 120 min, is used to evaluate the tumors that contain these receptors, in which case it binds to somatostatin receptor subtypes 2 and 5.

◁

Fig. 9.5. ^{123}I-MIBG anterior and posterior whole-body planar images showing a large pheochromocytoma (*arrowheads*)

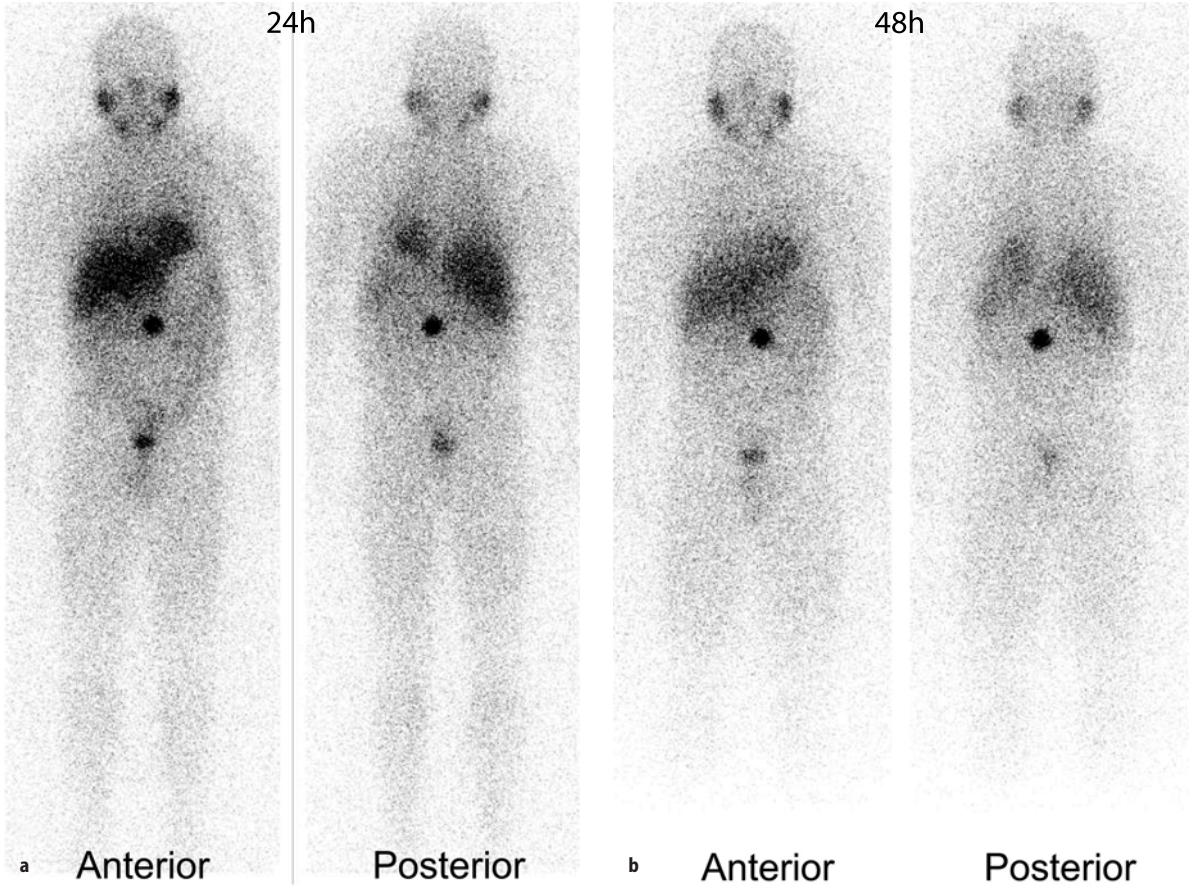

Fig. 9.6a–g. ^{123}I-MIBG whole body (**a,b**) of a patient with known pheochromocytoma who was referred for back pain. The study shows a focal area of increased uptake in the midline of the abdomen. Forty-eight-hour spot image (**c**) was acquired and

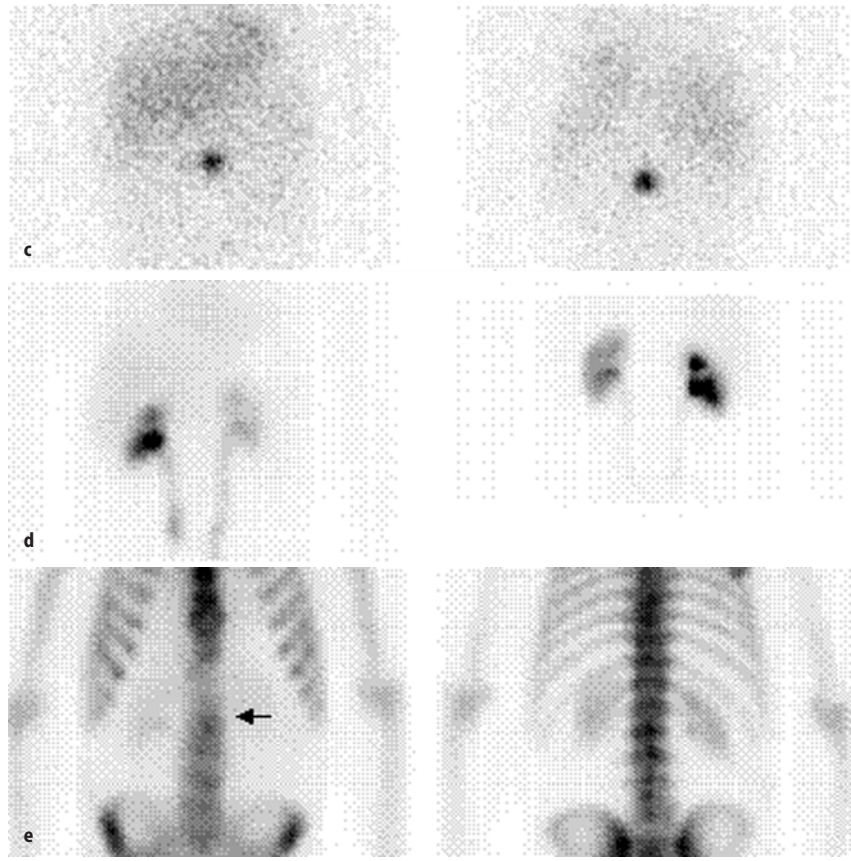

Fig. 9.6 (Cont.) ^{99m}Tc-DTPA study (**d**) was also obtained for comparison and lesion appeared away from the kidneys. The study was correlated with ^{99m}Tc-MDP spot images thoracolumbar spine (**e**) which showed questionable focal abnormality in the mid lumber spine corresponding to the location of I-123 abnormal uptake. MRI (**f**) and CT (**g**) scans were obtained and show a lesion in L-3 representing metastatic pheochromocytoma

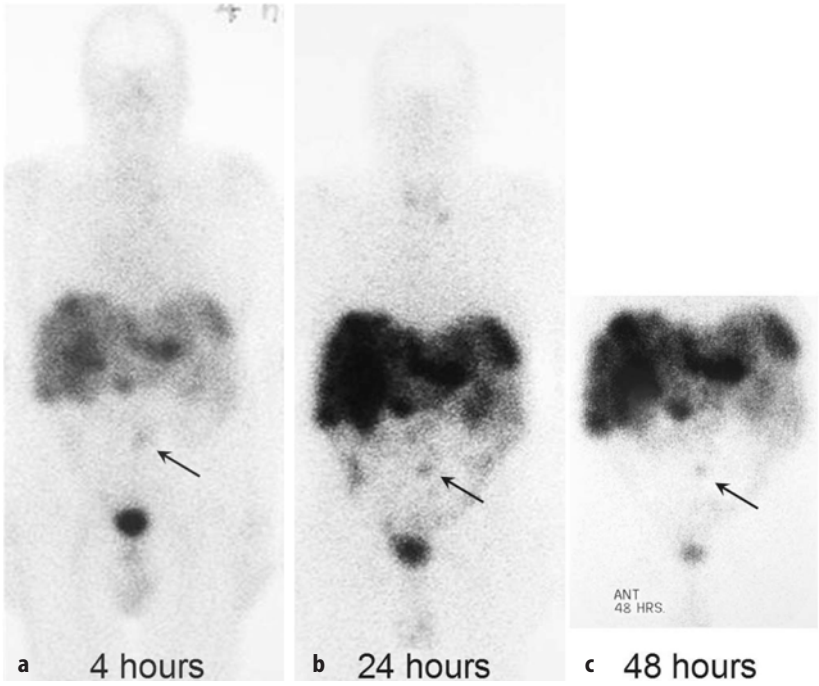

Fig. 9.7a–c. ^{111}In-octreotide imaging study obtained at 4, 24 and 48 h after i.v. injection of 6 mCi of the radiopharmaceutical. The images illustrate – in addition to the foci of metastatic carcinoid to the liver – the physiological uptake in the liver, spleen, kidneys, bowel and urinary bladder. Note that delayed imaging (**c**) and/or SPECT may be needed to differentiate physiologic activity such as in bowel from true disease (*arrow*) such as in this case

Among these tumors are pheochromocytoma, neuroblastoma, and paraganglioma, and others including pancreatic tumors and carcinoid.

Octreotide is usually tagged with ^{111}In, although ^{123}I has also been used in the past. It is recommended that octreotide therapy be withheld for at least 72 h prior to the injection of the radiopharmaceutical. Following i.v. injection of a standard dose of 6 mCi, static images are obtained at 4 h and 24 h (Fig. 9.7). SPECT images through the region of interest are then obtained at 4 h, and at 24 h if needed. This radiopharmaceutical is excreted via glomerular filtration. In a normal patient, octreotide activity is identified in the thyroid, kidneys, liver, spleen, pituitary, and gallbladder, and, to a lesser extent, the bowel on delayed images. The kidney and spleen receive the highest absorbed dose. A focal area of intense early radiotracer uptake is considered to be pathological, indicating primary neoplasm or metastasis. A false-negative scan is seen in cases where the tumor is small, has few somatostatin receptors, or both. ^{111}In-octreotide scanning is highly sensitive for detecting tumors greater than 1.5 cm. Since the expression of somatostatin receptors in neuroblastomas is variable with less receptors in more advanced disease, an accurate sensitivity of ^{111}In-octreotide is not readily definable. In children, several studies have compared ^{111}Inoctreotide with MIBG scintigraphy for imaging neuroblastoma; the sensitivity of the former ranged from 55% to 70%, and that of the latter from 83% to 94% [15–23]. Several studies reported MIBG-negative tumor sites detected by ^{111}In-pentetreotide in patients with neuroblastomas [16, 19, 23]. High affinity of octreotide for the MIBG-negative neuroblastoma cell line has been found [20]. Tenenbaum et al. recommended the use of octreotide to detect somatostatin receptors when results from MIBG scans are negative [19]. Pashankar suggested that neuroblastoma can be imaged by either ^{111}In-octreotide or MIBG depending on local expertise, as they have a complementary role in the initial diagnostic workup particularly since ^{111}In-octreotide additionally correlates with prognosis [22].

^{111}In-octreotide is currently the agent of choice for nuclear medicine imaging of head and neck paraganglioma, though it is insensitive for lesions less than 1 cm. The recent introduction of SPECT/CT has greatly improved the sensitivity of ^{111}In-octreotide scintigraphy [24].

Anderson et al. suggested that ^{111}In-DTPA-D-Phe 1-octreotide might be useful for radiation therapy of patients with surgically incurable tumors having high somatostatin receptor densities such as carcinoid [25].

9.3.2.3 Positron Emission Tomography

PET has been used to evaluate adrenal masses (Fig. 9.8). The higher spatial resolution of PET scanners enables the detection of small pheochromocytomas not seen with ^{123}I-MIBG. Malignant adrenal tumors can be detected with FDG PET, but its use in these cases is limited due to the low specificity. ^{11}C-hydroxyephedrine, the first available positron-emitting tracer of the sym-

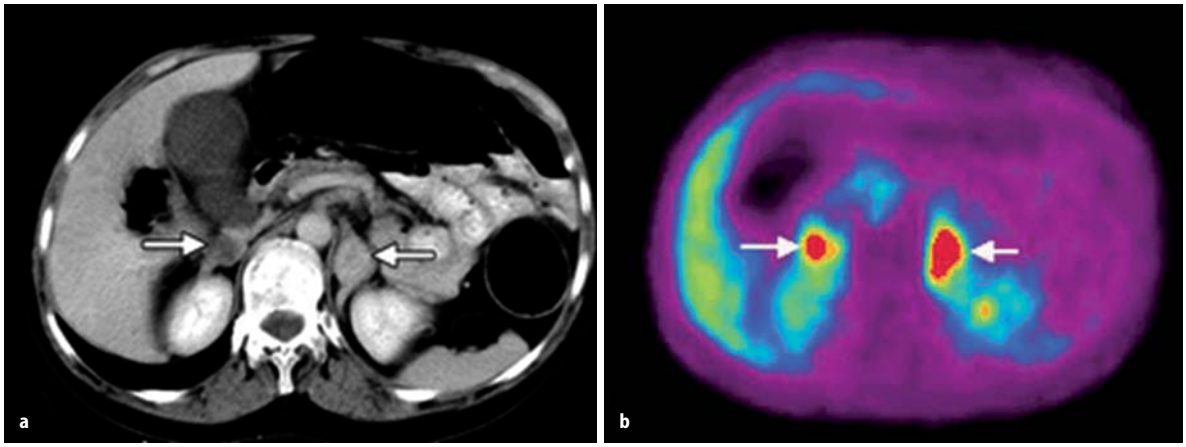

Fig. 9.8a,b. Transverse images obtained in a patient with multiple endocrine neoplasia type 2 and an increase in urinary catecholamine levels. **a** CT image shows bilateral adrenal tumors (*arrows*), a 2-cm-diameter tumor on the right side, and a 4-cm-diameter tumor on the left side adrenal lesions (*arrows*). HED PET image (**b**) shows intense uptake in both. Surgery revealed bilateral pheochromocytomas (from [26] with permission)

pathetic nervous system, was found useful in the detection of pheochromocytomas, with a high level of accuracy [26]. Its uptake reflects catecholamine transport and storage and neuronal reuptake. In detecting metastatic pheochromocytomas, ^{18}F-dopamine was found to be superior to ^{131}I-MIBG [27, 28].

9.4 Imaging of Incidental Adrenal Masses

Incidental adrenal masses are detected in about 2% – 5% of contrast-enhanced abdominal CT examinations, making the diagnosis of adrenal incidentaloma a common clinical problem [29]. In these cases the patients should be screened for pheochromocytoma clinically and biochemically. Adrenal incidentalomas are uncommon in patients younger than 30 years but increase in frequency with age; they occur equally in males and females. Adrenocortical adenoma accounts for 36% – 94% of incidentalomas detected in patients without a history of malignancy [30, 31]. Only about 10% of incidental adrenal masses are functional [30]. Accordingly, NP-59 would not be an appropriate radiotracer for adrenal incidentaloma because 90% of adrenal masses cannot incorporate NP-59 in their cells. Metomidate is an inhibitor of 11β-hydroxylase, a key enzyme in the biosynthesis of cortisol and aldosterone by the adrenal cortex. ^{11}C-metomidate is a promising PET tracer to identify incidentalomas of adrenocortical origin [32, 33]. Khan et al. reported on the value of ^{11}C-metomidate in evaluation of adrenocortical cancer [34].

References

1. Aron DC, Tyrrell JB (1997) Glucocorticoids and adrenal androgens. In: Greenspan FS, Strewler GJ (eds) Basic and clinical endocrinology, 5th edn. Appleton and Lange, Norwalk, Conn, p 318
2. Goldfien A (1997) Adrenal medulla. In: Greenspan FS, Strewler GJ (eds) Basic and clinical endocrinology, 5th edn. Appleton and Lange, Norwalk, Conn, p 382
3. Ryan JJ, Rezkalla MA, Rizk SN, Peterson KG, Wiebe RH (1995) Testosterone-secreting adrenal adenoma that contained crystalloids of Reinke in an adult female patient. Mayo Clin Proc 70:380 – 383
4. Lynn MD, Gross MD, Shapiro B, Bassett D (1986) The influence of hypercholesterolemia on the adrenal uptake and metabolic handling of I-131 6-beta-iodomethyl-19-norcholesterol (NP-59). Nucl Med Comm 1:631 – 635
5. Omura M, Saito J, Yamaguchi K, Kakuta Y, Nishikawa T (2004) Prospective study on the prevalence of secondary hypertension among hypertensive patients visiting a general outpatient clinic in Japan. Hypertens Res 27:193 – 202
6. Huether SE, Tomky D (1998) Alterations of hormonal regulation. In: McCance KL, Huether SE (eds) Pathophysiology, the biologic basis for disease in adults and children, 3rd edn. Mosby, St Louis, p 700
7. Spencer RP (1998) Tumor-seeking radiopharmaceuticals: nature and mechanisms. In: Murray IP, Ell PJ (eds) Nuclear medicine in clinical diagnosis and treatment, 2nd edn. Churchill Livingstone, Hong Kong, p 764
8. Hoefnagel CA, de Kraker J (1998) Childhood neoplasia. In: Murray IP, Ell PJ (eds) Nuclear medicine in clinical diagnosis and treatment, 2nd edn. Churchill Livingstone, Hong Kong, p 1002
9. Elgazzar AH, Gelfand MJ, Washburn LC, Clark J, Nagaraj N, Cummings D, Hughes J, et al (1995) I-123 MIBG scintigraphy in adults, a report of clinical experience. Clin Nucl Med 20:147
10. Gelfand MJ, Elgazzar AH, Kriss VM, Masters PR, Golsch GJ (1994) Iodine-123 MIBG SPECT versus planar imaging in children with neural crest tumors. J Nucl Med 35:1753 – 1756
11. Parisi MT, Sandler ED, Hattner RS (1992) The biodistribution of metaiodobenzylguanidine. Semin Nucl Med 22: 46 – 48

12. Okuyama C, Ushijima Y, Kubota T, Yoshida T, Nakai T, Kobayashi K, Nishimura T (2003) ^{123}I-Metaiodobenzylguanidine uptake in the nape of the neck of children: likely visualization of brown adipose tissue. J Nucl Med 44:1421 – 1425
13. Shapiro B, Copp JE, Sisson JC, Eyre PL, Wallis J, Beierwaltes WH (1985) Iodine-131 metaiodobenzyl-guanidine in the locating of suspected pheochromocytoma: experience in 400 cases. J Ncl Med 26:576
14. Paltiel HJ, Gelfand MJ, Elgazzar AH, Washburn LC, Harris RE, Masters PR, Golsch GJ (1994) Neural crest tumors: I-123 MIBG imaging in children. Radiology 190:118
15. Limouris GS, Giannakopoulos V, Stavraka A, Toubanakis N, Vlahos L (1997) Comparison of In-111 pentetreotide, Tc-99m (V)DMSA and I-123 mIBG scintimaging in neural crest tumors. Anticancer Res 17:1589 – 1592
16. Shalaby-Rana E, Majd M, Andrich MP, Movassaghi N (1997) In-111 pentetreotide scintigraphy in patients with neuroblastoma. Comparison with I-131 MIBG, N-Myc oncogene amplification, and patient outcome. Clin Nucl Med 22:315 – 319
17. Schilling FH, Bihl H, Jacobsson H, Ambros PF, Martinsson T, Borgstrom P, Schwarz K, et al (2000) Combined (111)In-pentetreotide scintigraphy and (123)I-mIBG scintigraphy in neuroblastoma provides prognostic information. Med Pediatr Oncol 35:688 – 691
18. Kropp J, Hofmann M, Bihl H (1997) Comparison of MIBG and pentetreotide scintigraphy in children with neuroblastoma. Is the expression of somatostatin receptors a prognostic factor? Anticancer Res 17:1583 – 1588
19. Tenenbaum F, Lumbroso J, Schlumberger M, Mure A, Plouin PF, Caillou B, Parmentier C (1995) Comparison of radiolabeled octreotide and meta-iodobenzylguanidine (MIBG) scintigraphy in malignant pheochromocytoma. J Nucl Med 36:1 – 6
20. Manil L, Perdereau B, Barbaroux C, Brixy F (1994) Strong uptake of ^{111}In-pentetreotide by an MIBG-negative, xenografted neuroblastoma. Int J Cancer 57:245 – 246
21. Sautter-Bihl ML, Dorr U, Schilling F, Treuner J, Bihl H (1994) Somatostatin receptor imaging: a new horizon in the diagnostic management of neuroblastoma. Semin Oncol 21(5 Suppl 13):38 – 41
22. Pashankar FD, O'Dorisio MS, Menda Y (2005) MIBG and somatostatin receptor analogs in children: current concepts on diagnostic and therapeutic use. J Nucl Med 46 Suppl 1:55S–61S.
23. Manil L, Edeline V, Lumbroso J, Lequen H, Zucker JM (1996) Indium-111-pentetreotide scintigraphy in children with neuroblast-derived tumors. J Nucl Med 37:893 – 896
24. Krausz Y, Keidar Z, Kogan I, Even-Sapir E, Bar-Shalom R, Engel A, Rubinstein R, et al (2003) SPECT/CT hybrid imaging with ^{111}In-pentetreotide in assessment of neuroendocrine tumours. Clin Endocrinol (Oxf) 59:565 – 573
25. Andersson P, Forssel-Aronsson E, Johanson V, Wangberg B, Nilsson O, Fjalling M, Ahlman H (1996) Internalization of indium-111 into human neuroendocrine tumor cells after incubation with indium-111-DTPA-D-Phe 1-octreotide. J Nucl Med 37:2002 – 2006
26. Trampal C, Engler H, Juhlin C, Bergstrom M, Langstrom B (2004) Pheochromocytomas: detection with C-11 hydroxyephedrine PET. Radiology 230:423 – 428
27. Pacak K, Eisenhofer G, Carrasquillo JA, Chen CC, Li ST, Goldstein DS (2001) 6-[^{18}F]Fluorodopamine positron emission tomographic (PET) scanning for diagnostic localization of pheochromocytoma. Hypertension 7:6 – 8
28. Ilias I, Yu J, Carrasquillo JA, Chen CC, Eisenhofer G, Whatley M, McElroy B, et al (2003) Superiority of 6-[^{18}F]-fluorodopamine positron emission tomography versus [^{131}I]-metaiodobenzylguanidine scintigraphy in the localization of metastatic pheochromocytoma. J Clin Endocrinol Metab 88:4083 – 4087
29. Brunt LM, Moley JF (2001) Adrenal incidentaloma. World J Surg 25:905 – 913
30. Mantero F, Masini AM, Opocher G, Giovagnetti M, Arnaldi G (1997) Adrenal incidentaloma: an overview of hormonal data from the National Italian Study Group. Horm Res 47:284 – 289
31. Bertherat J, Mosnier-Pudar H, Bertagna X (2002) Adrenal incidentalomas. Curr Opin Oncol 14:58 – 63
32. Minn H, Salonen A, Friberg J, Roivainen A, Viljanen T, Langsjo J, Salmi J, et al. (2004) Imaging of adrenal incidentalomas with PET using C-11 metomidate and ^{18}F-FDG. J Nucl Med 45:972 – 979
33. Zettinig G, Mitterhauser M, Wadsak W, Becherer A, Pirich C, Vierhapper H, Niederle B, et al (2004) Positron emission tomography imaging of adrenal masses: (18)F-fluorodeoxyglucose and the 11β-hydroxylase tracer C-11 metomidate. Eur J Nucl Med Mol Imaging 31:1224 – 1230
34. Khan TS, Sundin A, Juhlin C, Langstrom B, Bergström M, Eriksson B (2003) ^{11}C-metomidate PET imaging of adrenocortical cancer. Eur J Nucl Med Mol Imaging 30:403 – 410

Basis of Renal Scintigraphy

10

Salil D. Sarkar, Pravin C. Singhal

10.1 Introduction

Scintigraphy has provided a unique tool for the noninvasive evaluation of renal pathophysiology, and the past two decades have witnessed a rapid increase in the scope and number of radionuclide renal studies. This chapter is intended to familiarize nuclear medicine physicians with the pathophysiological basis of renal scintigraphy. To this end, a general review of relevant renal physiology and scintigraphic techniques is followed by detailed discussions of specific disorders frequently encountered in nuclear medicine. These include renovascular hypertension, urinary tract obstruction, acute pyelonephritis, and renal transplant complications.

10.2 General Physiology

10.2.1 The Nephron

The principal functions of the kidneys are the maintenance of water, electrolyte, and acid-base balance, elimination of waste products, and regulation of blood pressure. The functional unit of the kidney is a nephron, which consists of a glomerulus and a tubule, and urine is formed as a result of glomerular filtration, tubular reabsorption, and tubular secretion [1].

The *glomerulus* consists of a network of capillaries derived from the afferent glomerular arteriole. The glomerular capillary tuft acts as a filter for plasma. It is encased by two epithelial layers, the inner layer becoming part of the outer capillary wall and the outer layer lining Bowman's space (capsule), which receives the filtered fluid. The glomerular filtration rate (GFR) is dependent largely on the hydrostatic and colloid osmotic pressure in the glomerular capillaries and the hydrostatic pressure in Bowman's space. Filtered fluid from Bowman's space enters the *tubule*, which can be broadly divided into several portions: the proximal tubule, loop of Henle, distal tubule, collecting tubule, and collecting duct system (Fig. 10.1).

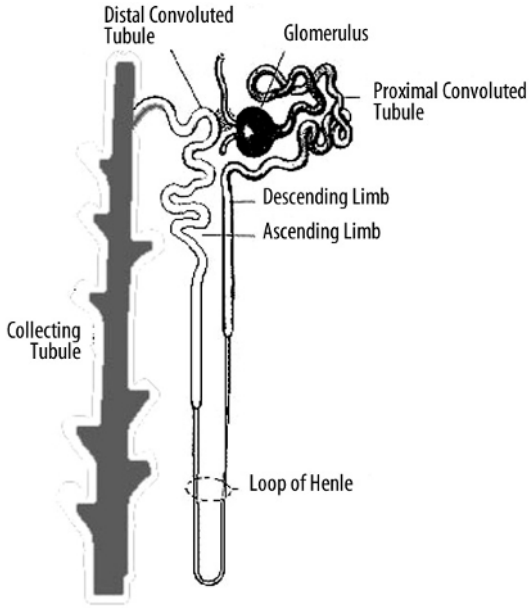

Fig. 10.1. The components of the nephron. (Adapted from Brundage D (1992) Renal disorders. Mosby, St. Louis)

The *proximal tubule* plays a key role in reabsorbing filtered solutes. About half to two-thirds of the sodium, chloride, and potassium are reabsorbed in this segment. Reabsorption of solutes is accompanied by passive osmotic diffusion of water.

The *loop of Henle*, consisting of a descending limb and an ascending limb, is the site of reabsorption of about 25% of the filtered solutes. Reabsorption occurs primarily in the "thick" ascending limb, where the epithelial cells are thick and metabolically very active. It is in this section that "loop" diuretics such as furosemide exert their effects (see later). The reabsorbed solutes enter the medullary interstitium and contribute to its hypertonicity.

The *distal tubule* transports sodium, chloride, and potassium, but not water, from its proximal part, similar to the loop of Henle. The terminal distal tubule shares similar functions with the collecting tubules (see later). At the very beginning of the distal tubule is the *macula densa*, a region of specialized cells in close proximity to the juxtaglomerular (JG) cells in the afferent arteriole that store renin. In response to changes in sodium and chloride concentration in this portion of the tubule, the macula densa sends signals to the JG cells to release renin.

The *collecting tubule* and terminal distal tubule are under the influence of *aldosterone* and *antidiuretic hormone* (ADH). Aldosterone, released from the zona glomerulosa of the adrenal cortex in response to angiotensin II, increases potassium secretion and sodium reabsorption. The latter promotes water reabsorption by osmosis and raises blood volume. ADH, originating in the hypothalamus and posterior pituitary and released in response to a rise in osmotic pressure of extracellular fluids or low blood pressure, increases the permeability of the cortical collecting ducts to water, which helps to maintain body fluid osmolality and effective plasma volume and to form concentrated urine. A hyperosmotic medullary interstitium, primarily the result of reabsorption of solutes from the thick ascending limb of the loop of Henle, also contributes to the reabsorption of fluid and the formation of concentrated urine.

10.2.2 Loop Diuretics

Furosemide, used for the scintigraphic evaluation of urinary tract obstruction, and other loop diuretics block the reabsorption of sodium, chloride, and potassium in the thick ascending limb of the loop of Henle. Increased tubular sodium decreases water reabsorption by an osmotic effect. Additionally, decreased sodium reabsorption into the medullary interstitium reduces its osmolarity, which in turn reduces water reabsorption from the collecting tubules.

10.2.3 Renal Vasculature

The renal artery enters through the hilum of the kidney and branches successively into the interlobar arteries, arcuate arteries, interlobular arteries, and afferent arterioles. Each afferent arteriole eventually branches into the glomerular capillaries. The distal glomerular capillaries merge to form the efferent arteriole. Efferent arterioles subdivide to form peritubular capillaries in the cortex or the vasa recta in the medulla. As discussed later, changes in the afferent or efferent arteriolar tone play an important role in regulating the GFR.

10.2.4 Juxtaglomerular Apparatus

The afferent arteriole has specialized smooth muscle cells called juxtaglomerular (JG) cells that store renin and stretch receptors that respond to changes in arteriolar pressure. Renin is released as a result of decreased stretch of the arteriolar wall when arteriolar pressure is decreased. Another stimulus for renin comes from the macula densa, which consists of specialized cells in the first part of the distal tubule, and is located close to the JG cells. The macula densa signals the JG cells to release renin when the sodium and chloride content of this part of the tubule is low. Finally, the sympathetic nervous system can stimulate renin release in response to systemic baroreceptor stimuli. These mechanisms are discussed further under Sect. 10.4, "Renovascular Hypertension".

10.3 Renal Scintigraphy

10.3.1 Radiopharmaceuticals

Based on kinetics, renal radiopharmaceuticals can be divided into two broad classes – those that are excreted rapidly into the urine and those that are retained for prolonged periods in the renal parenchyma. In the first category are ^{99m}Tc-mercaptoacetyltriglycine (MAG3), ^{99m}Tc-diethylenetriamine pentaacetic acid (DTPA), and ^{131}I-orthoiodohippurate (OIH), and in the second category, ^{99m}Tc-dimercaptosuccinic acid (DMSA) and ^{99m}Tc-glucoheptonate.

10.3.1.1 Rapidly Excreted Radiopharmaceuticals

The rapidly excreted radiopharmaceuticals are used to assess individual renal function [2–5]. ^{99m}Tc-MAG3, the agent of choice, is 90% protein bound and excreted almost exclusively by the renal tubules. High renal-to-background count ratios provide excellent images and permit visualization of poorly functioning kidneys that may not be adequately visualized by ^{99m}Tc-DTPA or ^{131}I-OIH. The renal extraction fraction for MAG3 (about 70%) is lower than that for OIH (80%–90%). Although this characteristic is not ideal for precise quantification of renal blood flow, reasonable estimates can be made with the use of correction factors.

^{99m}Tc-DTPA was the most popular radiopharmaceutical in its category prior to the introduction of ^{99m}Tc-MAG3. It shows little protein binding (about 5%) and is excreted exclusively by glomerular filtration. Renal uptake of ^{99m}Tc-DTPA is limited because only 20% of the renal blood flow is filtered by the glomeruli. The 20% extraction fraction is considerably lower than that of ^{99m}Tc-MAG3 and yields lower renal-to-background uptake ratios. However, ^{99m}Tc-DTPA is less costly and may be used as an alternative to ^{99m}Tc-MAG3, particularly if a quantitative estimate of GFR is also needed. Functional assessment with ^{99m}Tc-MAG3 and ^{99m}Tc-DTPA generally is concordant. However, differences may be noted with glomerular-tubular dissociation in some cases of tubulointerstitial disease.

Orthoiodohippurate is about 70% protein bound. Approximately 15%–20% of the radiotracer is excreted by glomerular filtration and the remainder by tubular secretion. The use of ^{131}I-OIH for scintigraphy has been largely abandoned because of the limitations of a higher radiation exposure [6] and poor image quality related to a lower administered dose (1/15th that of ^{99m}Tc-MAG3). Radiation exposure with ^{123}I-labeled OIH is lower, and better images can be obtained using larger amounts of radiotracer. However, this radiopharmaceutical is expensive and not readily available. The extraction fraction of OIH, while not optimum (since it is not completely extracted by the kidneys), is the highest among the radiopharmaceuticals in use today. Therefore, it can be used for the quantification of renal blood flow.

10.3.1.2 Slowly Excreted Radiopharmaceuticals

Prolonged cortical retention of the slowly excreted radiopharmaceuticals allows the assessment of parenchymal morphology, and since accumulation occurs only in functioning tubules, uptake can be quantified to assess differential renal function [2, 3]. Technetium-99m-DMSA, the preferred agent, is 90% protein bound and accumulates in functioning tubules. Since very little of the radiotracer is excreted, interference from collecting system activity, particularly on delayed images, is minimal. A total of about 40% of the administered amount is accumulated in the renal cortex, versus about 20% for Tc-99m glucoheptonate. Additionally, significant amounts of ^{99m}Tc-glucoheptonate are excreted by glomerular filtration, resulting in interfering activity in the collecting system.

10.3.2 Interpretation

10.3.2.1 Rapidly Excreted Radiopharmaceuticals

Renal scintigraphy using the rapidly excreted radiopharmaceuticals generally involves dynamic acquisition over a period of approximately 30 min after radiotracer administration. Images are usually grouped in 2-min frames and a time-activity histogram is obtained. Assessment of function is based on a number of criteria, including initial cortical uptake of the radiotracer, cortical retention, first visualization of the collecting system, and time to peak cortical activity. It is cautioned, however, that these parameters also may be affected by the state of hydration. An adequate assessment should include analysis of both the images and the time-activity curves.

10.3.2.1.1 Cortical Uptake

The first minute after radiotracer administration represents the vascular delivery phase. The next 2 min constitute the "parenchymal phase". Uptake in the kidney during this interval, i.e., between 1 and 3 min after radiotracer injection, is proportional to its function, using either tubular or glomerular agents. In practice, renal counts are obtained over a 1-min period, typically between 1 and 2 min for ^{99m}Tc-MAG3, and expressed as a percentage of the combined renal counts.

10.3.2.1.2 Cortical Retention

The cortical retention of radiotracer, quantified by expressing renal counts at 20 – 30 min on the time-activity curve as a percentage of the peak uptake, is a measure of the rapidity with which the radiotracer is excreted by the kidney. As renal function deteriorates, the percentage retained increases. An apparent increase in retention may occur with urine stasis in the collecting system. Hence the need for evaluating the time-activity curve in conjunction with the images.

10.3.2.1.3 First Visualization of Collecting System

The interval between radiotracer administration and excretion of activity into the collecting system, i.e., the pelvis and/or calyces, is a measure of *cortical* function. This interval, needless to say, is obtained from the sequential images. Delayed appearance of the collecting system is associated with renal insufficiency.

10.3.2.1.4 Time to Peak

The interval between radiotracer administration and maximum cortical activity is another parameter of function. It is more easily measured from the time-activity curve, although an accurate estimate may not be possible in the absence of a peak, which is often the case in significant renal dysfunction.

A 1-min dynamic flow study, with images grouped in 3-s frames, is frequently combined with the functional evaluation. These images reflect renal perfusion and generally are concordant with the functional study. Sophisticated quantitative techniques have been developed to quantify perfusion [7]. These may have a potential role, particularly for the transplanted kidney, but are not widely used.

10.3.2.2 Slowly Excreted Radiopharmaceuticals

Scintigraphy with ^{99m}Tc-DMSA and ^{99m}Tc-glucoheptonate is done between 4 and 24 h after radiotracer administration. It is usually used to detect renal parenchymal defects such as pyelonephritis, scars, and infarcts. Since only functioning tubular cells accumulate these radiopharmaceuticals, the total renal uptake is a measure of individual renal function. Thus, relative renal function can be measured as with the rapidly excreted radiopharmaceuticals.

10.4 Renovascular Hypertension

10.4.1 Introduction

The teleological function of the renin-angiotensin system, i.e., maintenance of systemic blood pressure, is well served in such conditions as hypotension and shock. In significant renal artery stenosis, however, activation of the renin-angiotensin system is a mixed blessing, limiting a fall in GFR but causing systemic (renovascular) hypertension. Systemic blood pressure is maintained primarily by increase in vascular tone and retention of sodium and water, while a sharp reduction in GFR is prevented by increase in the glomerular capillary hydrostatic pressure.

Glomerular capillary hydrostatic pressure is modulated by the tone of the afferent and efferent glomerular arterioles. Increased tone in the efferent arteriole or decreased tone (increased flow) in the afferent arteriole raises capillary hydrostatic pressure and GFR, while decreased tone in the efferent arteriole or increased tone (decreased flow) in the afferent arteriole lowers GFR.

10.4.2 Activation of Renin-Angiotensin System

The first step in the activation of the renin-angiotensin system is the release of *renin* by the renal JG cells. The following mechanisms are involved [8, 9]:

1. Signals from *baroreceptors* (“stretch” receptors) in the afferent arteriole, stemming from decreased arteriolar pressure due to systemic hypotension/decreased effective blood volume or significant renal artery stenosis. Baroreceptor signals are modulated by prostaglandins.
2. Chemoreceptor signals from the *macula densa* (located in the initial portion of the distal tubule) related to decreased sodium and chloride in the distal tubule (reduction in GFR leads to slower flow and greater reabsorption of sodium and chloride in the loop of Henle). Macula densa signals are modulated by prostaglandins and adenosine.
3. Increased *sympathetic activity* due to activation of systemic cardiopulmonary and carotid sinus baroreceptors by hypotension. The renal baroreceptor signals are modulated by prostaglandins and the macula densa signals by adenosine and prostaglandins.

Renin released as a result of the above stimuli converts circulating *angiotensinogen*, an α_2-globulin produced by the liver, to *angiotensin I*, a decapeptide. Angiotensin I is then converted to the active octapeptide form, *angiotensin II*, by *angiotensin-converting enzyme*

(ACE), found in vascular endothelium, and the bulk of this conversion occurs in the pulmonary vascular bed. Angiotensin II is also produced in the kidney.

10.4.3 Effects of Angiotensin II

10.4.3.1 Systemic Effects

Angiotensin II raises systemic blood pressure primarily by increasing vascular tone and stimulating the synthesis and secretion of aldosterone from the zona glomerulosa of the adrenal cortex, which promotes sodium and water reabsorption from the renal tubules.

10.4.3.2 Intrarenal Effects

The intrarenal effects of angiotensin II help counter a fall in GFR due to decreased afferent arteriolar and glomerular capillary hydrostatic pressure [8, 9]. First, angiotensin II raises GFR by preferential constriction of the efferent glomerular arteriole. Second, angiotensin II increases tubular reabsorption of sodium and water directly and indirectly (increased tone in efferent arteriole decreases hydrostatic pressure in peritubular capillaries with resultant increase in sodium and water reabsorption). In unilateral renal artery stenosis, GFR remains unchanged in the contralateral normal kidney, because increased efferent arteriolar tone is offset by an increase in afferent arteriolar tone in response to a higher systemic blood pressure.

The effects of angiotensin II eventually lead to *inhibition of renin release*. In unilateral renovascular disease, sodium retention is offset by pressure natriuresis (decreased sodium chloride reabsorption in the proximal tubule) by the normal kidney. This limits the expansion in blood volume, so that pressure in the afferent arteriole of the stenotic kidney continues to be low. In bilateral renovascular disease, however, blood volume expansion may be sufficient to increase afferent arteriolar pressure and decrease (but not necessarily normalize) renin secretion. Angiotensin II also has a direct inhibitory effect on the JG cells.

10.4.4 Scintigraphy in Renovascular Hypertension

10.4.4.1 Principles

The scintirenographic diagnosis of renovascular hypertension is based on the demonstration of changes in renal physiology following the administration of an ACE inhibitor [10–16]. As noted above, angiotensin II, formed by the activation of the renin-angiotensin system, helps maintain GFR by increasing the tone of the efferent glomerular arteriole which, in turn, raises the glomerular capillary hydrostatic pressure. These changes are reversed by ACE inhibitors, which block the conversion of angiotensin I to angiotensin II. Consequently, there is a sharp drop in GFR and in proximal tubular urine flow.

Decreased GFR and tubular flow after the administration of an ACE inhibitor will result in decreased uptake and prolonged cortical retention of ^{99m}Tc-DTPA, a radiopharmaceutical excreted by glomerular filtration. Since renal blood flow generally is not significantly changed, a blood flow agent such as ^{99m}Tc-MAG3 shows only prolonged cortical retention without decreased uptake. Rarely, uptake of ^{99m}Tc-MAG3 may actually decrease, presumably due to a fall in blood pressure below a critical level required to maintain perfusion in the stenotic kidney. The general principles of ACE-inhibitor renography also apply to patients receiving chronic treatment with angiotensin II (AT1) receptor antagonists [17].

10.4.4.2 Interpretation

Scintigraphic studies are generally interpreted by comparing a baseline examination with one performed after the administration of ACE inhibitor. Both the images and the time-activity curves are evaluated using the traditional parameters of function discussed earlier, and the following changes after ACE inhibition are considered significant for renovascular hypertension [14, 15]:

1. Increase in cortical retention by at least 15%
2. Delay in collecting system visualization by at least 2 min
3. Decrease in initial cortical uptake by at least 10%
4. Increase in time to peak by at least 2 min

10.4.4.3 Factors Influencing ACE Inhibitor Scintigraphy

Because of the complexity of the renin-angiotensin system, ACE inhibitor renography is subject to a number of variables that may result in false-positive or false-negative studies.

1. Hypotension or a marked change in blood pressure after ACE inhibitor administration is often associated with *bilateral symmetrical* renal retention of radiotracer. Presumably, this is related to compensatory mechanisms triggered by hypotension that promote fluid reabsorption from the tubules and reduce urine flow. This finding should not be mistaken for bilateral renal artery stenosis, which characteristically responds *asymmetrically* to ACE inhibition.

2. Diuretics may cause dehydration, with resultant decrease in tubular flow and increase in cortical radiotracer retention [18]. Here again, the abnormality is *symmetrical*. Diuretics also increase the likelihood of hypotension after ACE inhibition. Therefore, adequate hydration is particularly important for patients receiving diuretic treatment.
3. Chronic ACE inhibitor therapy potentially may lower scintigraphic sensitivity, and should be discontinued before the test. Alternatively, if the ACE inhibitor cannot be discontinued, scintigraphy may be performed while the patient is on therapy. If renal function appears symmetrical, renovascular hypertension is unlikely and a baseline study need not be done. However, if function is asymmetrical, the ACE inhibitor should be discontinued before the baseline study.
4. Aspirin and such other nonsteroid anti-inflammatory agents as indomethacin may decrease the sensitivity of the test. As described earlier, renin release by the juxtaglomerular apparatus in response to baroreceptor and chemoreceptor stimuli is mediated by prostaglandins. Aspirin and indomethacin decrease prostaglandin activity and therefore indirectly decrease renin-angiotensin activity. Consequently, their effect on scintigraphy is the same as that of chronic ACE inhibitor therapy. It interesting that a single dose of aspirin may cause scintigraphic changes in a stenotic kidney, not unlike those seen after captopril [19].
5. Calcium channel blocking drugs are commonly used in renovascular hypertension. Although their effect on GFR is not as pronounced as that of ACE inhibitors, these drugs have been implicated as a cause of false-positive studies [20, 21]. The mechanisms responsible for this finding are not entirely clear. It appears that the effect of angiotensin II on efferent arteriolar constriction requires the presence of extracellular calcium and therefore can be attenuated by calcium channel blockers. Perhaps a marked decrease in GFR resulting from the combined effect of both calcium channel blockers and captopril may explain the above findings.

10.4.4.4 Relationship of Renal Artery Stenosis to Renovascular Hypertension

Approximately 3% of hypertension is renovascular in origin. The incidence is higher in a selected hypertensive population and may be as high as 30% – 40%. Renal artery stenosis generally is due to atherosclerotic plaques or fibromuscular dysplasia, the latter occurring in younger individuals. "Significant" stenosis, i.e., one that would trigger the activation of the renin-angiotensin system and lead to the development of renovascular hypertension, has been defined as a reduction in intraluminal diameter by 50% or greater. However, the degree of anatomically defined renal artery stenosis does not always correlate with the presence of renovascular hypertension.

In an autopsy study, 17% of individuals who had been normotensive had ≥50% renal artery stenosis [22]. In another study, half of the patients undergoing aortography for reasons other than hypertension had ≥50% stenosis [23]. Thus, the characterization of "significant stenosis" by anatomical criteria remains uncertain.

Ideally, a test for the diagnosis of renovascular hypertension should allow the prediction of therapeutic outcome. In other words, those with positive studies should derive benefit from revascularization and vice versa. Follow-up studies after ACE inhibitor renography have indeed shown good correlation with outcome after angioplasty, though additional prospective studies are clearly needed for corroboration [24 – 27]. The emergence of high-resolution, noninvasive imaging techniques, notably contrast-enhanced magnetic resonance angiography, has considerably improved our ability to detect renal artery stenosis [28 – 33]. However, additional studies are needed to define their place in the diagnostic algorithm.

10.5 Urinary Tract Obstruction

10.5.1 Introduction

Urinary tract obstruction may be complete or partial, and it may occur at various locations including the ureteropelvic junction (UPJ), ureterovesical junction (UVJ), and bladder outlet. The clinical consequences are quite dramatic and predictable in an acute and complete obstruction, but not in a partial and chronic one, exemplified by UPJ obstruction in children. Chronic UPJ obstruction, however, may eventually lead to renal cortical atrophy. Hence the need for diagnostic markers to identify those patients at risk of progressive renal insufficiency.

Despite a large body of literature on the diagnostic evaluation of urinary tract obstruction, the identification of "significant obstruction", i.e., one that would result in progressive renal failure, remains somewhat elusive. This is because significant obstruction is probably much more a functional entity than an anatomical one, and left untreated, similar types of obstruction may have markedly dissimilar outcomes. This section is devoted primarily to chronic (partial) UPJ obstruction in infants and young children, an entity frequently encountered by the nuclear medicine physician, and its relationship to hydronephrosis and renal function.

10.5.2 Ureteropelvic Junction Obstruction

UPJ obstruction may be extrinsic or intrinsic, and both conditions may exist in the same patient. *Extrinsic* obstruction is usually caused by adventitial bands compressing the upper ureter. Typically, this type of obstruction is intermittent and brought on by increased diuresis, which dilates the pelvis and increases the constrictive pressure of the adventitial bands. As might be expected, pressure-flow studies of the renal pelvis are not linear in this condition. More importantly, the diuretic renogram may be negative if adequate diuresis, i.e., adequate dilatation of the pelvis, is not achieved because of dehydration, inadequate diuretic dosage, improper timing of diuretic administration, or renal dysfunction.

Intrinsic obstruction may be related to luminal narrowing of a segment of the upper ureter, or to an adynamic segment. This type of obstruction generally exhibits a linear pressure-flow relationship, and although considered "fixed", the obstruction is not necessarily permanent and does not invariably cause progressive renal deterioration.

10.5.3 Hydronephrosis

Hydronephrosis may be due to obstruction or to such nonobstructive conditions as vesicoureteral reflux, congenital dysmorphism, and urinary tract infection. It may be temporary with spontaneous resolution in infants and young children, or intermittent, or progressive with eventual stabilization. Such variability is related to the multifactorial etiology of hydronephrosis [34–36]. These factors include the following:

1. Compliance and capacity of the renal pelvis, which determine intrapelvic pressure.
2. Renal function, which determines the rate of urine flow.
3. Degree of obstruction.

Progression or stabilization of hydronephrosis depends on the degree of balance between these factors. *Pressure in the renal pelvis*, though not measurable by diuretic renography, is a critical component in the pathogenesis of hydronephrosis and renal dysfunction. Pressure-flow studies suggest that the pelvis fills at low pressures initially until a critical volume ("capacity") is reached, above which the pelvic pressure rises. Subsequent development of hydronephrosis tends to relieve pelvic pressure. A low-capacity pelvis is more likely to have higher pelvic pressures with progressive hydronephrosis. In this instance, cortical atrophy eventually occurs, with decrease in urine formation and reduction of pelvic pressure.

10.5.4 Diuretic Renography

Diuretic renography [35–39] is based on the premise that increased urine flow resulting after furosemide administration causes rapid "washout" of radiotracer from the unobstructed collecting system (Fig. 10.2), but delayed washout if obstruction is present (Fig. 10.3). While furosemide generally is administered intravenously after filling of the pelvocalyceal system, administration at the time of or prior to radiotracer administration also has been advocated. The washout half-time following diuretic injection is determined from the time-activity curve. A half time of 10 min or less is considered normal, 10–20 min equivocal, and more than 20 min abnormal. Given the dynamic nature of UPJ obstruction, however, a number of factors may influence the diuretic renogram and must be taken into consideration for a proper assessment.

10.5.4.1 Rate of Urine Flow

Inadequate rate of urine flow after diuretic administration may prolong washout time and render the study falsely positive. This may be related to renal dysfunction, dehydration, or inadequate furosemide dosage. Thus, proper methodology is critical, and an abnormal washout time in a kidney with decreased function should be held to greater scrutiny.

10.5.4.2 Pelvic Capacity and Tone

Radiotracer washout tends to be delayed if the pelvis is atonic and large, and rapid if the pelvis is small, with good tone. Pelvic compliance, unfortunately, cannot be determined by diuretic renography and remains an unknown variable.

10.5.4.3 Disease Fluctuation

As noted earlier, significant obstruction cannot be defined anatomically and may be best characterized as one that results in progressive renal dysfunction. However, the factors that combine to cause significant obstruction are not constant, and a single diuretic renogram may therefore provide misleading information. In fact, hydronephrosis may stabilize or improve spontaneously, even in patients with positive diuretic renograms, questioning the prudence of early pyeloplasty in infants [40–42].

The foregoing concerns notwithstanding, a number of steps may be taken to optimize the radionuclide eval-

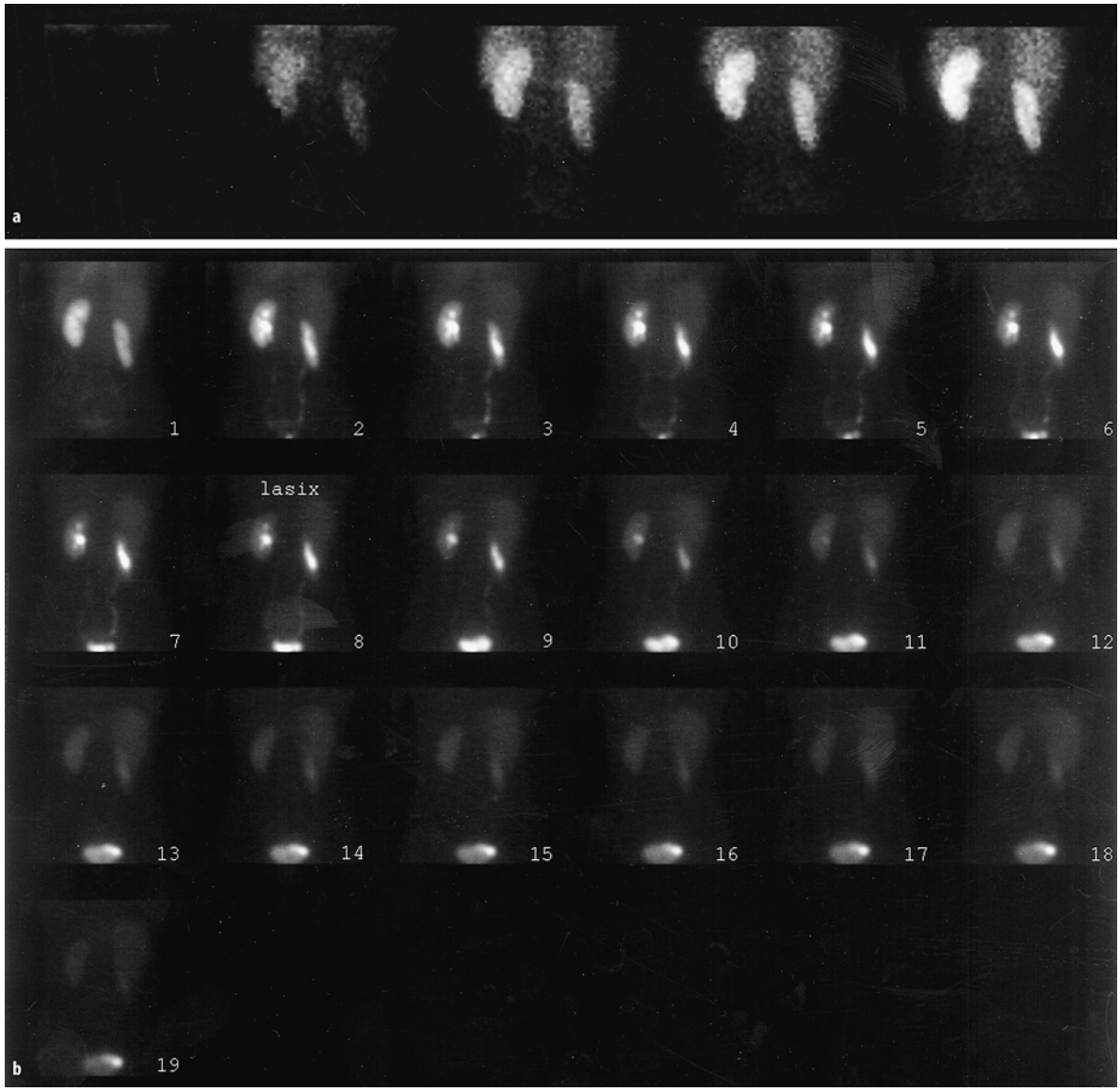

Fig. 10.2a–c. Nonobstructive hydronephrosis: Flow (**a**), sequential (**b**) images and renogram (**c**) of a 14-year-old girl with right hydronephrosis (sonogram). Rapid washout of right renal collecting system following administration of Lasix (furosemide), with washout T1/2 of 3 min

uation of urinary tract obstruction. Since preservation of renal function is the overriding concern, it has been suggested that evaluation of renal cortical function should be the primary focus of scintigraphic assessment [40]. Additionally, since renal impairment or its progression is unpredictable, a single study in the infant with UPJ obstruction is of limited value. Instead, *periodic scintigraphic assessments* at intervals of 1–3 months are more desirable. Undue reliance on a single postdiuresis washout half-time also appears unwarranted because of the changing pathophysiology. If methodology is standardized, periodic evaluation as for functional assessment may improve the predictive ability of the washout parameter as well. An increasing

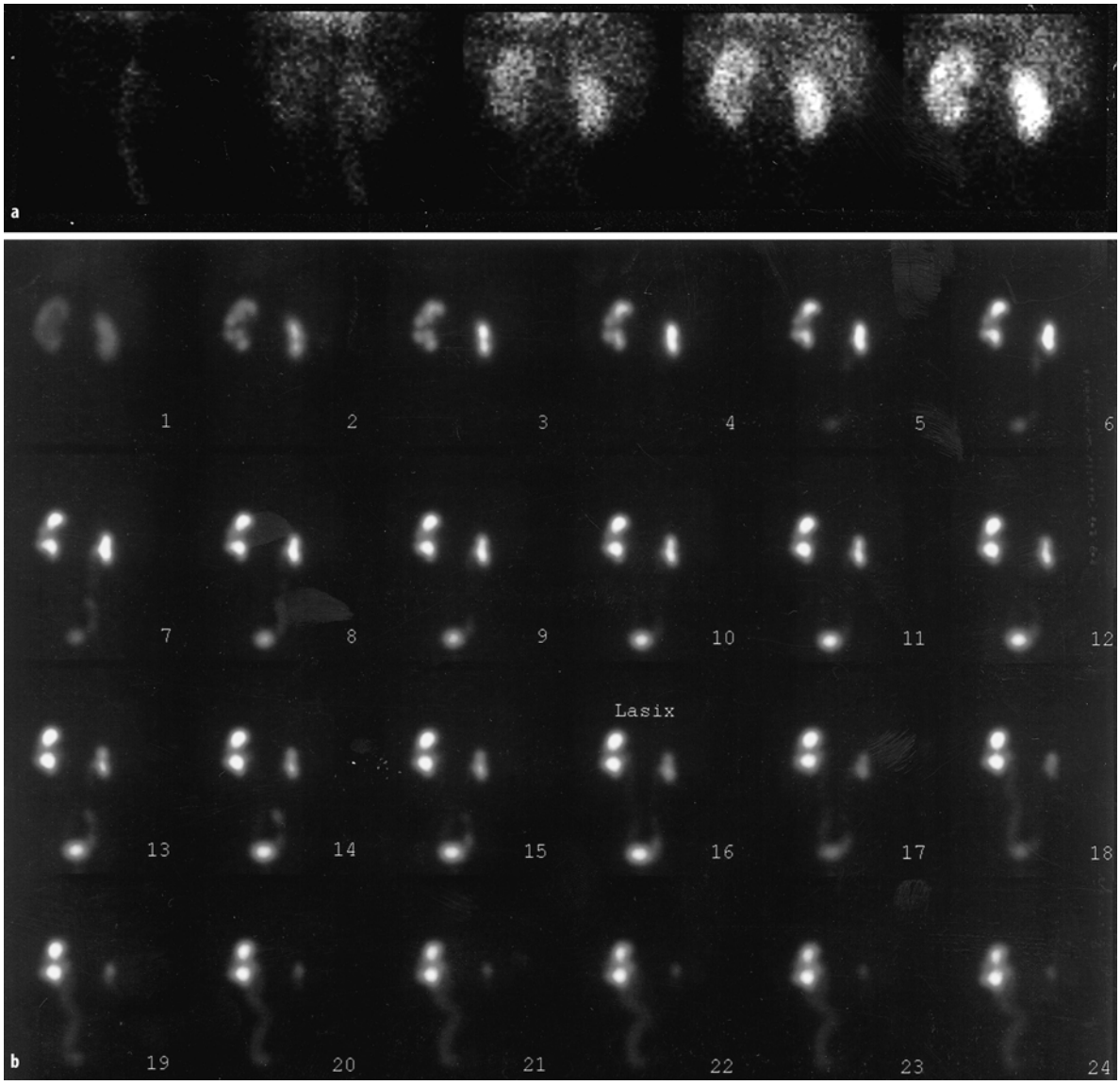

Fig. 10.3a–c. Left hydronephrosis in an 8-month-old boy, first detected in the womb. Renal images with MAG-3 flow (**a**) and sequential (**b**) 2 min/frame show obstruction of hydronephrotic left kidney, with washout T1/2 of 47 min after Lasix administration (**c**)

washout time probably is more meaningful than a single "positive" study.

Preliminary data suggest another method of evaluating UPJ obstruction using ACE inhibitors [43]. Urinary tract obstruction is associated with alterations in renal blood flow and GFR, mediated in part by the renin-angiotensin system, and changes in these parameters induced by ACE inhibitors may constitute additional evidence of significant UPJ obstruction. In addition, the evaluation of hydronephrosis with non-scintigraphic techniques, including dynamic contrast enhanced magnetic resonance imaging, is currently under investigation [44].

10.6 Acute Pyelonephritis

10.6.1 Introduction

This section deals primarily with pyelonephritis in children, the group most likely to benefit from radionuclide renal studies. Pyelonephritis refers to infection of the renal tubules, pelvis, and interstitium, and it has a wide spectrum of clinical presentations. While the clinical diagnosis is obvious when characteristic manifestations of flank or back pain, fever, and bacteriuria are present, pyelonephritis may be missed if symptoms are absent or referable only to the lower urinary tract. Acute pyelonephritis requires more vigorous treatment than lower urinary tract infection, and, left untreated, it can lead to scarring and renal insufficiency. Consequently, identification of renal involvement is critical in children with suspected urinary tract infection, and parenchymal scintigraphy with the tubular agent, ^{99m}Tc-dimercaptosuccinic acid (DMSA), can play an important role in their diagnostic evaluation.

10.6.2 Pathogenesis

Ascending infection from the lower urinary tract is the usual mechanism for pyelonephritis [45, 46]. The infection appears to originate in the urethra or the vaginal introitus, which are colonized by enteric flora, predominantly *Escherichia coli*, and it is more common in females, presumably due to their shorter urethra. Structural abnormalities of the urinary tract, such as vesicoureteral reflux and bladder outlet obstruction (which exacerbates reflux), are predisposing factors, though often not demonstrable. Another predisposing factor appears to be an inborn increase in uroepithelial cell susceptibility to bacterial adherence, which facilitates bacterial ascent to the upper urinary tract. Lastly, catheterization and sexual intercourse can allow urethral bacteria to enter the bladder. Ascending infection eventually reaches the renal calyces, from which microorganisms enter the parenchyma through the papillae by intrarenal reflux.

Scarring of the renal parenchyma may result from pyelonephritis [47 – 49]. It is a common cause of hypertension and, if sufficiently extensive, it can lead to progressive renal insufficiency and end-stage renal disease. Although vesicoureteral reflux is frequently associated with scarring, it is not a prerequisite for this condition.

10.6.3 Scintigraphy

Imaging of the renal parenchyma with ^{99m}Tc-DMSA offers a simple and accurate method for detecting acute pyelonephritis in the child with urinary tract infection [50 – 52]. ^{99m}Tc-DMSA localizes in functioning proximal tubular cells and is not excreted in significant amounts, so that imaging at 4 – 24 h after radiopharmaceutical administration reveals primarily cortical uptake without interfering activity in the collecting system. A cortical defect due to pyelonephritis is characterized by preservation of renal contour, whereas scarring (from a previous infection) typically results in volume contraction, although the two may be indistinguishable. Such distinction may become less relevant as scarring declines with the routine use of ^{99m}Tc-DMSA imaging in children with urinary infection.

In addition to imaging during the acute phase of the disease, follow-up studies are done to confirm resolution of the pyelonephritic defect(s) and absence of cortical scarring. Patients with scars are followed periodically with imaging and measurement of relative function for assessment of progressive renal insufficiency.

Magnetic resonance imaging (MRI) and spiral CT are other modalities that may be helpful in the evaluation of pyelonephritis [52].

10.7 Renal Transplantation

10.7.1 Introduction

Advances in our understanding of the pathophysiology of renal transplants over the past several years have resulted in significant improvement in graft survival and an increase in the number of transplantations. The key factors influencing survival are *donor-recipient histocompatibility* (matching of HLA-A, HLA-B, HLA-DR antigens) and *donor status* (living related, living unrelated, cadaver). Graft survival is best when the donor is an HLA-identical sibling, and better for living-related than for cadaver donors with similar HLA matches. A host of other factors, including harvesting and transplantation technique, cold ischemia time (between harvest and transplantation), donor/recipient age, recurrence of primary renal disease, and race, also play an important role in graft survival. The surgical and medical complications of renal transplantation are considered below [53 – 57].

10.7.2 Surgical Complications

10.7.2.1 Urine Extravasation, Ureteral Obstruction

Extravasation of urine ("urinoma") may result from ischemic injury related to devascularization during harvesting, or from leakage at the ureterovesical anastomosis. It may predispose to infection and therefore requires a timely diagnosis. While scintigraphy performed routinely after transplantation may detect urine extravasation, it is often used to confirm a leak suspected clinically or sonographically. The scintigraphic appearance is that of an area of increased radiotracer activity, although such an increase may not be apparent for up to 2 – 3 h after radiotracer administration in some instances.

Ureteral obstruction is thought to be usually due to ischemia or postischemic scarring. Extrinsic compression by a lymphocele or hematoma is another cause. If needed, dilatation of the ureter or stent placement/reoperation may be done. Scintigraphy, with furosemide-induced diuresis if needed, may be helpful in the diagnosis and post-treatment evaluation of this condition.

10.7.2.2 Hematoma, Lymphocele

Hematomas are generally perinephric or intravesical in location. The scintigraphic appearance is that of a photopenic collection, i.e., with activity less than background. Hematomas are usually self-limited.

Lymphoceles are extrarenal collections of lymphatic fluid from the kidney, occurring most frequently about 2 – 3 months after transplantation. They may be exacerbated by rejection, which increases renal lymph flow. Most lymphoceles are inconsequential, though some may be associated with ureteral compression, as noted earlier, or iliac vein compression resulting in lower extremity edema. Treatment consists of sclerotherapy, drainage, or creation of a peritoneal window. The characteristic scintigraphic finding with lymphoceles is a perinephric photopenic region, which is easier to visualize if a high-intensity image is obtained at the end of the study to accentuate the body background. The same consideration holds for hematomas, which are also photopenic (see above). It should be noted, however, that lymphoceles occasionally may become isointense with the background or exceed background activity on later images [55].

10.7.2.3 Renal Artery Stenosis

Hypertension is usually due to pathology in the native kidneys, transplant rejection, or cyclosporine/tacrolimus treatment, and less frequently to renal artery stenosis. The stricture is generally at the anastomotic site or distal to it, and blood pressure response has been shown following angioplasty. The pathophysiological consequences of renal artery stenosis in the transplanted kidney are somewhat different than those of unilateral stenosis in a patient with two kidneys. In the latter, elimination of sodium is decreased on the stenosed side, but increased sodium excretion by the normal kidney helps keep the blood volume from increasing. In the case of a transplanted kidney with renal artery stenosis, however, a normal kidney is not available for elimination of excess sodium. Therefore, depending on the level of salt intake, the initial renin-dependent hypertension develops into a volume-dependent hypertension. Consequently, the fall in GFR in response to an ACE inhibitor may be less than expected and inapparent on the scintigraphic study. It is fortuitous, however, that most of these patients are on diuretics and/or a salt-restricted diet, which helps to limit a rise in blood volume.

10.7.3 Medical Complications

10.7.3.1 Acute Tubular Necrosis

Acute tubular necrosis (ATN), characterized by ischemic necrosis of the tubular epithelial cells and decreased GFR, is frequently associated with cadaver renal transplants. Possible causes are hypotension/hypovolemia in the donor and prolonged interval between harvest and transplantation. Urine output usually starts to decrease within the first 24 h or so and improves spontaneously after a few days, although ATN may occasionally last a few weeks. It is often difficult to make a clinical distinction between ATN and rejection in the post-transplantation period. A clear scintigraphic distinction between these two conditions also has remained elusive, for two reasons. First, the scintigraphic diagnosis of ATN rests on the premise that graft perfusion is preserved despite decreasing function (Fig. 10.4), in contrast to rejection, where both perfusion and function decrease in parallel (Fig. 10.5). However, depending on the severity/stage of ATN, graft perfusion may vary. Second, ATN and acute rejection may coexist.

From a clinical standpoint, a cadaver transplant with impaired function is assumed to have ATN, and an aggressive search/treatment for rejection is initiated if the expected recovery in graft function fails to occur. Such recovery can best be ascertained by serial scintigraphy, a sensitive measure of graft function.

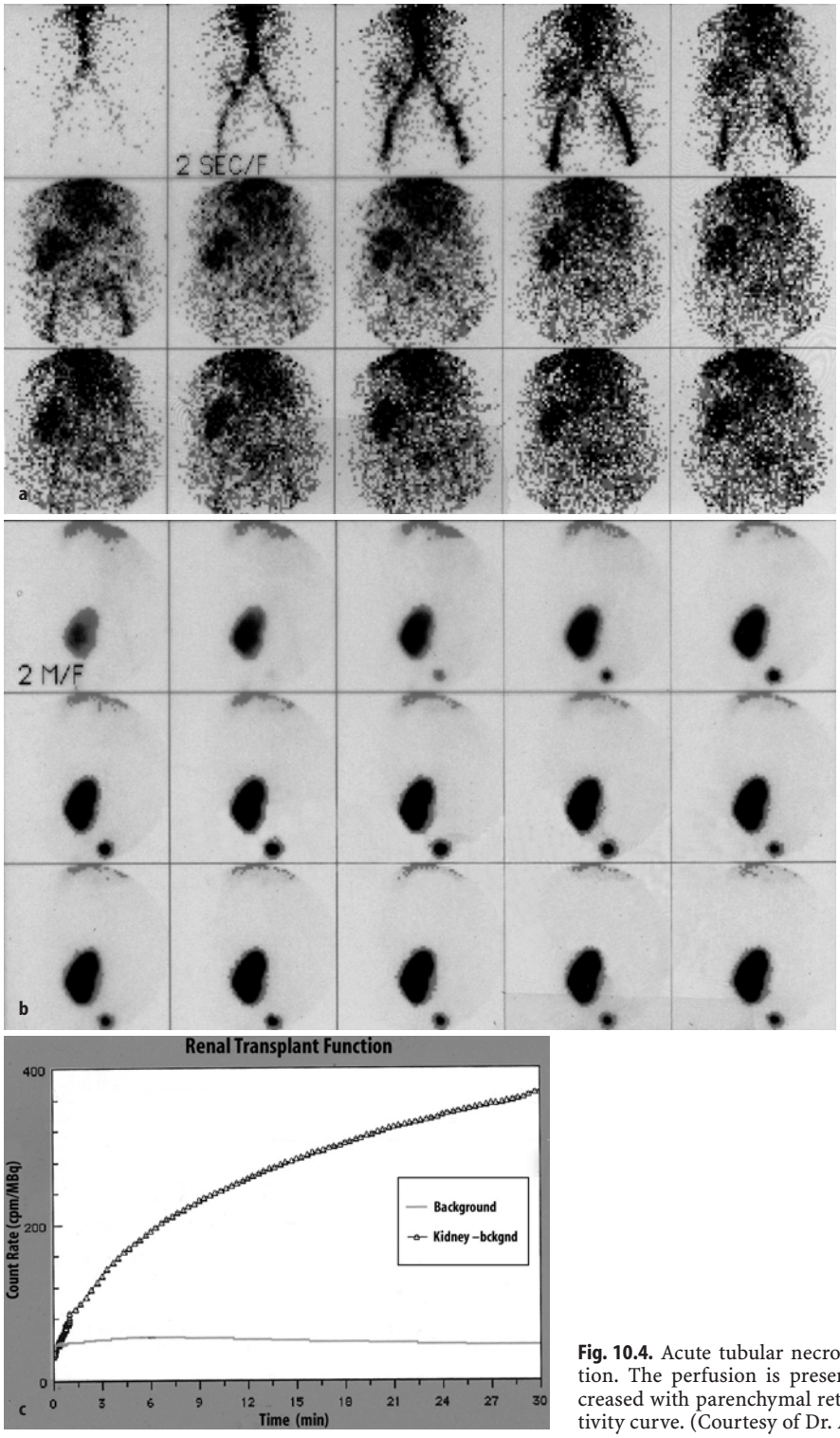

Fig. 10.4. Acute tubular necrosis following renal transplantation. The perfusion is preserved, while the function is decreased with parenchymal retention as noted on the time-activity curve. (Courtesy of Dr. A. Omar)

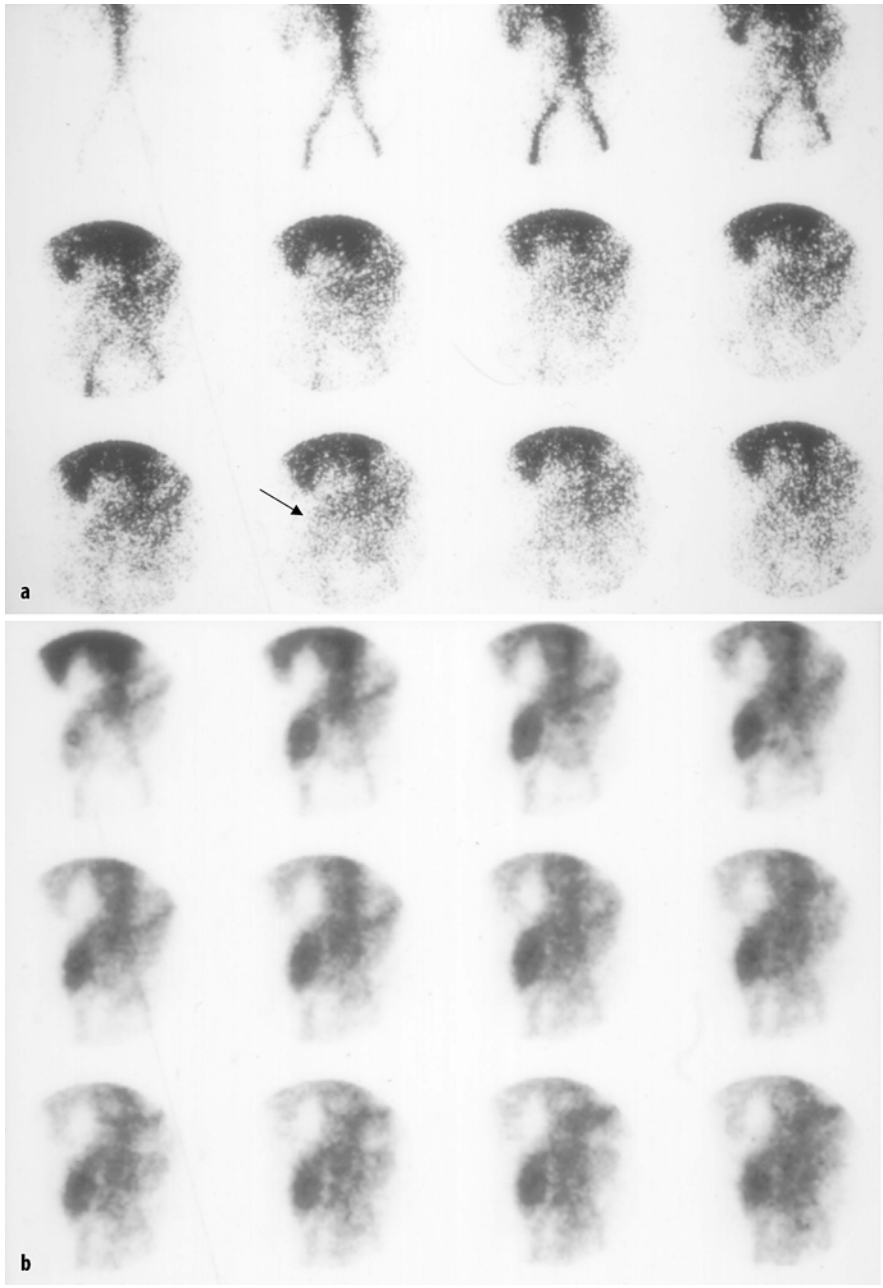

Fig. 10.5a,b. Forty-five-year-old male referred for a radionuclide renography to rule out rejection 1 month status post renal transplant because of a rising creatinine and decreased urine output. The flow (**a**) and sequential imaging (**b**) studies show poor flow to the transplanted kidney in the right iliac fossa (*arrow*) and decreased uptake by the transplanted kidney with delayed transit indicating rejection

10.7.3.2 Rejection

The histopathological criteria for the diagnosis and classification of rejection have improved significantly in recent years and continue to evolve [53, 58, 59]. From a large body of literature, a consensus referred to as the Banff Classification has emerged. The new classification shifts the focus from diagnosis of rejection to prognosis, to facilitate patient management. Distinction is made between rejection with *tubulointerstitial* changes, representing milder disease, and rejection with *vasculitis*, where the outcome is poorer. The types of rejection are discussed below.

1. Antibody-mediated rejection:
   Two types of antibody-mediated rejection are described, immediate or hyperacute, and delayed or accelerated acute. *Hyperacute rejection* is caused by preformed anti-donor antibodies and characterized by intense vasculitis, fibrin-platelet thrombi, and infarction of the renal cortex, with graft loss. Rejection may begin within minutes or hours and is usually apparent during surgery. Scintigraphy

shows a *photopenic* region corresponding to the avascular graft. Fortunately, hyperacute rejection is rare nowadays and largely preventable by appropriate screening tests.

Accelerated acute rejection may be considered a "slow" variant of hyperacute rejection, mediated primarily by anti-donor antibodies. It usually occurs on the second or third day following transplantation, after allograft function has been established. Clinical manifestations include fever, pain, swelling, or tenderness in the transplant region, hypertension, and oliguria or anuria. Scintigraphy generally shows poor radiotracer uptake in the graft.

2. Acute/active rejection:
   Acute rejection is the most frequent type of rejection confronting the nuclear medicine physician. It is most common in the first 4 weeks following transplantation but may occur at any time between 3 days and 10 or more years. Clinical findings generally are not as dramatic as in accelerated rejection. Acute rejection is predominantly a cell-mediated process with mononuclear cell infiltration and tubulitis, although the more severe forms are associated with a humoral component with various degrees of vasculitis. Accordingly, the Banff system grades acute rejection from I to III, with subdivisions for severity of changes. The lowest grade represents interstitial infiltration and moderate tubulitis, while the highest grade is associated with transmural arteritis and/or arterial fibrinoid change and necrosis of medial smooth muscle cells.
3. Chronic/sclerosing allograft nephropathy:
   Chronic/sclerosing nephropathy generally occurs 6 months to years after transplantation. It may be related to a number of causes including chronic rejection, hypertension, an infectious/noninfectious inflammatory process, and effects of medications (see below). Rejection, if present, may respond to treatment, though the diagnosis may not be apparent on biopsy. Histopathological changes in the condition also can be graded, depending on the severity of interstitial fibrosis and tubular atrophy.

10.7.3.3 Nephrotoxicity of Drugs

Cyclosporine and more recently tacrolimus (FK506) have been used routinely as immunosuppressive agents. Clinically, nephrotoxicity resulting from these drugs may be difficult to distinguish from rejection, and the conditions may be superimposed. Toxicity is generally associated with elevated blood levels of the drug and it improves after reduction of the dose. Histopathological findings of microvascular injury, with fibrin thrombi in the glomerular arterioles and capillaries, have been noted but unfortunately are not diagnostic for cyclosporine or tacrolimus toxicity [60].

References

1. Cotran AS, Kumar V, Collins T (1999) The kidney. In: Robbins pathologic basis of disease. WB Saunders, Philadelphia, pp 930 – 996
2. Eshima D, Fritzberg AR, Taylor A (1990) Tc-99m renal tubular function agents: current status. Semin Nucl Med 20:28 – 40
3. Blaufox MD (1991) Procedures of choice in renal nuclear medicine. J Nucl Med 32:1301 – 1309
4. Rutland A (1985) Comprehensive analysis of DTPA renal studies. Nucl Med Commun 6:11 – 30
5. Jafri RA, Britton KE, Nimmon CC, et al (1988) Technetium-99m-MAG3: a comparison with iodine-123 and iodine-131 orthoiodihippurate in patients with renal disorders. J Nucl Med 29:147 – 158
6. Stabin M, Taylor A, Eshima D, Wooter W (1992) Radiation dosimetry for technetium-99m-MAG3, technetium-99m-DTPA, and I-131-OIH based on human biodistribution studies. J Nucl Med 33:33 – 40
7. El-Maghraby TAF, de Fijter JW, van Eck-Smit BLF, et al (1998) Renographic indices for evaluation of changes in graft function. Eur J Nucl Med 25:1575 – 1586
8. Safian SD, Textor SC (2001) Renal-artery stenosis. N Engl J Med 344:431 – 442
9. Martinez-Maldonado M (1991) Pathophysiology of renovascular hypertension. Hypertens 17:707 – 719
10. Fine EJ, Sarkar SD (1989) Differential diagnosis and management of renovascular hypertension through nuclear medicine techniques. Semin Nucl Med 19:101 – 115
11. Miyamori I, Shuichiro Y, Takeda Y, et al (1986) Effects of converting enzyme inhibition on split renal function in renovascular hypertension. Hypertension 8:415 – 421
12. Hricik DE, Browning PJ, Kopelman R, et al (1983) Captopril-induced functional renal insufficiency in patients with bilateral renal artery stenosis or renal artery stenosis in a solitary kidney. N Engl J Med 308:373 – 376
13. Mann SJ, Pickering TG, Sos TA, et al (1991) Captopril renography in the diagnosis of renal artery stenosis. Am J Med 90:30 – 40
14. Sarkar SD (1994) Captopril renography. Pocket lecture series. Society of Nuclear Medicine, Reston, Virginia
15. Taylor A, Nally J, Mattias A, et al (1996) Consensus report on ACE inhibitor renography for detecting renovascular hypertension. J Nucl Med 37:1876 – 1882
16. Lagomarsino E, Orellana P, Munoz J, et al (2004) Captopril scintigraphy in the study of arterial hypertension in pediatrics. Pediatr Nephrol 19:66 – 70
17. Picciotto G, Sargiotto A, Petrarulo M, et al (2003) Reliability of captopril renography in patients under chronic therapy with angiotensin II (AT1) receptor antagonists. J Nucl Med 44:1574 – 1581
18. Kopecky RT, Deaver TF, McAfee JG (1987) Furosemide augments the effects of captopril on nuclear studies in renovascular stenosis. Hypertens 10:181 – 188
19. Imanishi M, Yano M, Hayashida K, et al (1994) Aspirin renography to detect unilateral renovascular hypertension. Kidney Int 45:1170 – 1176
20. Claveau-Tremblay R, Turpin S, De Braekeleer M, et al (1998) False-positive captopril renography in patients taking calcium antagonists. J Nucl Med 39:1621 – 1626
21. Ludwig V, Martin WH, Delbeke D (2003) Calcium channel blockers: a potential cause of false-positive captopril re-

nography. Clin Nucl Med 28:108 – 112
22. Holley KE, Hunt JC, Brown AL Jr, et al (1964) Renal artery stenosis: a clinicopathologic study in normotensive and hypertensive patients. Am J Med 37:14 – 22
23. Dustan HP, Humphries AW, de Wolfe VG, Page IH (1964) Normal arterial pressure in patients with renal artery stenosis. JAMA 187:1028 – 1029
24. Dondi M, Fanti S, De Fabritiis A, et al (1992) Prognostic value of captopril renal scintigraphy in renovascular hypertension. J Nucl Med 33:2040 – 2044
25. Fommei E, Ghione S, Hilson AJW, et al (1993) Captopril radionuclide test in renovascular hypertension: a European multicenter study. Eur J Nucl Med 20:625 – 644
26. Setaro JF, Saddler MC, Chen CC, et al (1991) Simplified captopril renography in diagnosis and treatment of renal artery stenosis. Hypertens 18:289 – 298
27. Mann SJ, Pickering TG (1992) Detection of renovascular hypertension. Ann Int Med 117:845 – 853
28. Leung DA, Hoffmann U, Pfammater T, et al (1999) Magnetic resonance angiography versus duplex sonography for diagnosing renovascular disease. Hypertens 33:726 – 731
29. Radermacher J, Chavan A, Bleck G, et al (2001) Use of Doppler ultrasonography to predict the outcome of therapy for renal artery stenosis. N Engl J Med 344:410 – 417
30. Sarkar SD, Siegel DN (2000) Imaging of renovascular hypertension: Respective value of renal Doppler ultrasound, renal scintigraphy, and magnetic resonance angiography. Invited commentary. Radiographics 20:1368 – 1371
31. Vasbinder GBC, Nelemans P, Kessels AGH, et al (2004) Accuracy of computed tomographic angiography and magnetic resonance angiography for diagnosing renal artery stenosis. Ann Intern Med 141:674 – 682
32. Textor SC (2004) Pitfalls in imaging for renal artery stenosis: Editorial. Ann Intern Med 141:730 – 731
33. Knipp BS, Dimick JB, Eliason JL, et al (2004) Diffusion of new technology for the treatment of renovascular hypertension in the United States: Surgical revascularization versus catheter-based therapy, 1988 – 2001. J Vascular Surg 40:717 – 723
34. Koff SA (1983) Determinants of progression and equilibrium in hydronephrosis. Invest Urol 21:496 – 500
35. Kekomaki M, Rikalainen H, Ruotsalainen P, Bertenyi C (1989) Correlates of diuretic renography in experimental hydronephrosis. J Urol 141:391 – 394
36. Koff SA, Thrall JH (1981) Diagnosis of obstruction in experimental hydronephrosis. Urology 17:570 – 577
37. Sarkar SD (1992) Diuretic renography: concepts and controversies. Urol Radiol 14:79 – 84
38. McCarthy CS, Sarkar SD, Izquierdo G, et al (1994) Pitfalls and limitations of diuretic renography. Abdom Imaging 19:78 – 81
39. Pohl HG, Rushton HG, Park JS, et al (2001) Early diuresis renogram findings predict success following pyeloplasty. J Urol 165:2311 – 2315
40. Koff SA, Campbell KD (1994) The nonoperative management of unilateral neonatal hydronephrosis: natural history of poorly functioning kidneys. J Urol 152:593 – 595
41. Arnold AJ, Rickwood AMK (1990) Natural history of pelviureteric obstruction detected by prenatal sonography. Br J Urol 65:91
42. MacNeily AE, Maizels M, Kaplan WE, et al (1993) Does early pyeloplasty really avert loss of renal function? A retrospective review. J Urol 150:769 – 773
43. Homsy YL, Tripp BM, Lambert R, et al (1998) The captopril renogram: a new tool for diagnosing and predicting obstruction in childhood hydronephrosis. J Urol 160: 1446 – 1449
44. Perez-Brayfield MR, Kirsch AJ, Jones RA, et al (2003) A prospective study comparing ultrasound, nuclear scintigraphy, and dynamic contrast enhanced magnetic resonance imaging in the evaluation of hydronephrosis. Pediatric Urol 170:1330 – 1334
45. Scholes D, Hooton TM, Roberts PL, et al (2005) Risk factors associated with acute pyelonephritis in healthy women. Ann Intern Med 142:20 – 27
46. Reid G, Sobel JD (1987) Bacterial adherence in the pathogenesis of urinary tract infection. A review. Rev Infect Dis 9:470 – 481
47. Naseer SR, Steinhardt GF (1997) New renal scars in children with urinary tract infection, vesicoureteral reflux and voiding dysfunction: a prospective evaluation. J Urol 158:566 – 568
48. Ditchfield MR, Summerville D, Grimwood K, et al (2002) Time course of transient cortical scintigraphic defects associated with acute pyelonephritis. Pediatr Radiol 32:849 – 852
49. Taskinen S, Ronholm K (2005) Post-pyelonephritic renal scars are not associated with vesicoureteral reflux in children. Pediatric Urol 173:1345 – 1348
50. Clarke SEM, Smellie JM, Prescod N, et al (1996) Technetium-99m-DMSA studies in pediatric urinary tract infection. J Nucl Med 37:823 – 828
51. Craig JC, Wheeler DM, Irwig L, et al (2000) How accurate is dimercaptosuccinic acid scintigraphy for the diagnosis of acute pyelonephritis? A meta-analysis of experimental studies. J Nucl Med 41:986 – 993
52. Majd M, Blask ARN, Markle BM, et al (2001) Acute pyelonephritis: Comparison of diagnosis with ^{99m}Tc-DMSA SPECT, spiral CT, MR imaging, and power Doppler US in an experimental pig model. Radiology 218:101 – 108
53. Kirkpatrick CH (1987) Transplantation immunology. JAMA 258:2993 – 3000
54. Dubovsky EV, Russell CD, Erbas B (1995) Radionuclide evaluation of renal transplants. Semin Nucl Med 25:49 – 59
55. Fortenbery EJ, Blue PW, Van Nostrand D, Anderson JH (1990) Lymphocele: the spectrum of scintigraphic findings in lymphoceles associated with renal transplant. J Nucl Med 31:1627 – 1631
56. Shamlou KK, Drane WE, Hawkins IF, Fennell RS (1994) Captopril renography and the hypertensive renal transplantation patient: a predictive test of therapeutic outcome. Radiology 190:153 – 159
57. Tulchinsky M, Dietrich TJ, Eggli DF, et al (1997) Technetium-99m-MAG3 scintigraphy in acute renal failure after transplantation: a marker of viability and prognosis. J Nucl Med 38:475 – 478
58. Nickeleit V, Vamvakes EC, Pascual M (1998) The prognostic significance of significant arterial lesions in acute allograft rejection. J Am Soc Nephrol 7:1301 – 1308
59. Racusen LC, Solez K, Colvin RB, et al (1999) The Banff 97 working classification of renal allograft pathology. Kidney Int 55:713 – 723
60. Randhawa PS, Tsamandas AC, Magnone M, et al (1996) Microvascular changes in renal allografts associated with FK506 (tacrolimus) therapy. Am J Surg Pathol 20:306 – 312

11 Basis of Tumor Imaging 1: Principles of Tumor Pathology and Biology

Ezzeldin M. Ibrahim, Jaudah A. Al-Maghrabi

During the past century, there has been a gigantic evolution in our understanding of the perplexing concepts of the biology of human tumors. This chapter is intended to address only the knowledge that has had the most significant impact in this field. Owing to the constraints of space, this chapter is not to be considered all-inclusive. We will deal with the pathological basis of tumorigenesis and the basic principles of pathological classification of tumors.

11.1 Tumor Pathology

The classification and typing of tumors depends mainly on the histopathological diagnosis, which is made on the basis of gross and microscopic examination of tissues. The surgical pathologist's task is to provide a specific and comprehensive diagnosis to enable the clinician to develop an optimal plan of treatment and help him or her to predict prognosis.

Tumor classification is based on histogenesis, degree of cellular differentiation (i.e., well or poorly differentiated), and biological behavior (benign versus malignant). All tumors, whether benign or malignant, have two components: (1) proliferating neoplastic cells and (2) supportive stroma, which is host derived and made up of connective tissue and blood vessels. While the neoplastic cells determine the nature of the tumors, tumor growth and evolution depend on the stroma [1].

In the past, the general concept was that neoplasms of certain phenotypes arise from their normal cell counterpart. However, evidence that accumulated over the years has proven the inaccuracy of this histogenetic assumption. It is now believed that most tumors arise from immature cells that can transform and acquire phenotypic features similar to those of one or more normal cell types. For example, rhabdomyosarcomas are tumors that show rhabdomyoblastic differentiation rather than tumors that arise from striated muscle cells [2]. In some instances, the immature cells can undergo divergent differentiation into two cell types, as in the case of mixed tumors of the salivary gland (Fig. 11.1), or they have the capacity to differentiate into any adult cell type, as in teratoma.

11.1.1 Biological Behavior

The categorization of tumors into benign and malignant is an oversimplification of the wide behavioral range of neoplasms. There are tumors that exhibit intermediate behavior. This has led to the introduction of a third category designated as "borderline or undetermined", which represents low-grade malignant tumors that can mostly be managed by conservative therapeutic approach. The best examples are borderline tumors of the ovary and uterine smooth muscle of low malignant potential [3–5]. Currently, the malignant category is restricted to tumors that have metastatic properties.

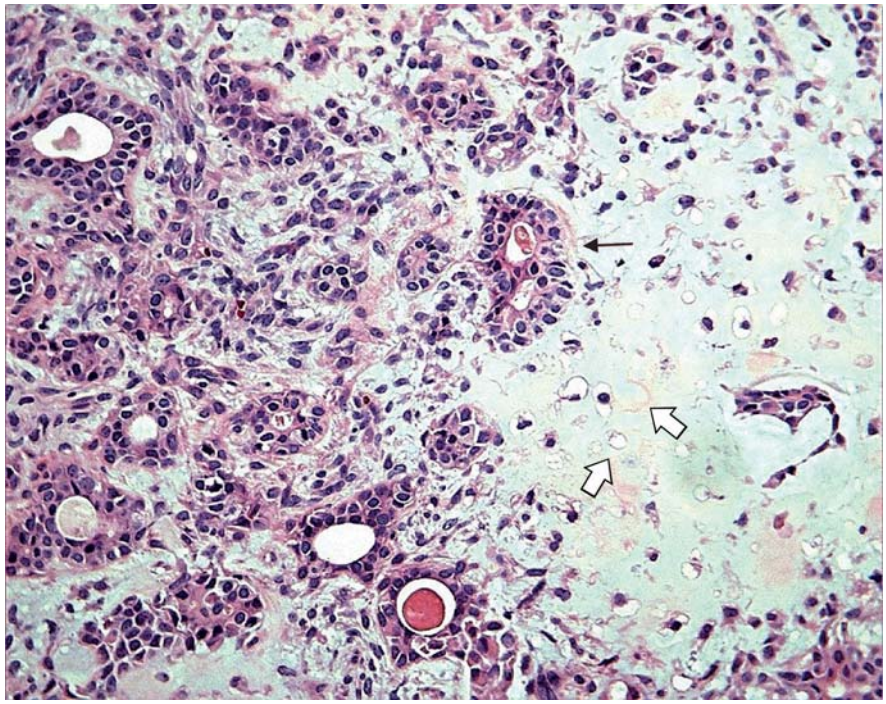

Fig. 11.1. Benign mixed tumor of salivary gland (pleomorphic adenoma). The tumor consists of an epithelial component "glands" (*arrow*) and a mesenchymal component "cartilage" (*open arrows*)

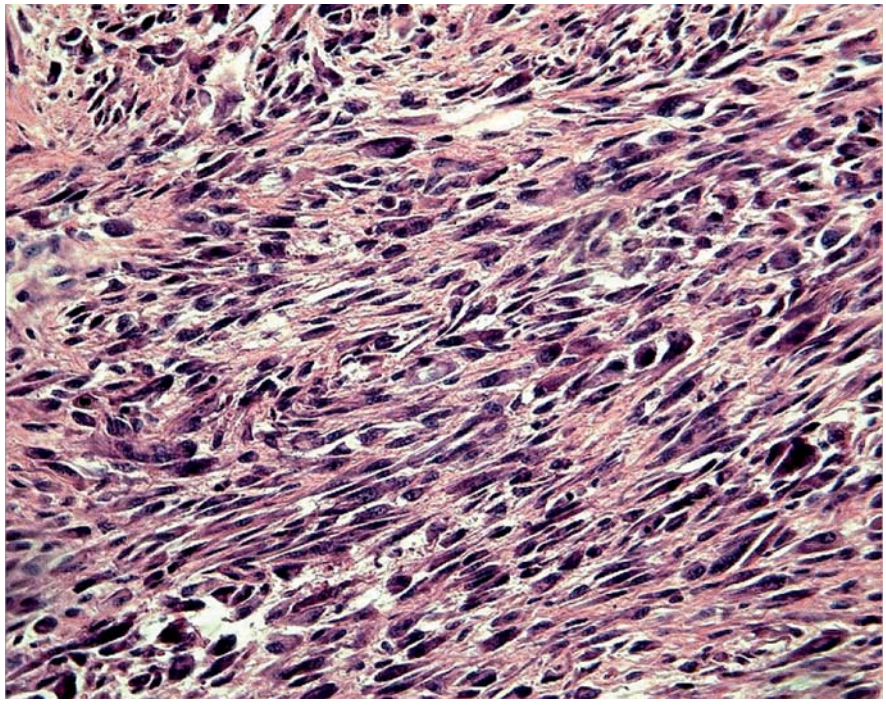

Fig. 11.2. Soft tissue sarcoma consisting of pleomorphic spindle cells, illustrating the features of malignancy as variable cell size and shapes and increased nuclear/cytoplasmic ratio

11.1.1.1 Benign Tumors

In general, the addition of the suffix "-oma" to the cell of origin describes benign tumors; for example, adenoma indicates a benign tumor of epithelial cell origin. Tumors that arise from mesenchymal tissues are designated according to their putative cell of origin (e.g., fibroma, chondroma, lipoma, and leiomyoma). Benign tumors can also be classified on the basis of their macroscopic pattern; for example, papillomas are benign epithelial tumors with certain growth characteristics, such as exophytic or finger-like projections. In general, a benign tumor is composed of well-differentiated cells that resemble their normal counterpart. A tumor is

considered benign when its gross and microscopic characteristics are relatively innocent, implying that it will remain localized and cannot spread to other sites. However, it should be noted that benign tumors can produce more than a localized mass and sometimes cause serious disease.

11.1.1.2 Malignant Tumors

The classification of malignant tumors essentially follows that of benign tumors, with some exceptions. Malignant neoplasms arising from epithelial cells are termed carcinomas (Fig. 11.3). Carcinomas are further classified on the basis of the type of epithelium, for example, glandular as adenocarcinoma, squamous as squamous carcinoma, and transitional as transitional cell carcinoma. Malignant epithelial tumors that have not extended through the underlying basement membrane are described as in situ carcinoma. Malignant tumors arising from mesenchymal tissue are broadly designated as sarcomas. These are further subclassified on a histogenetic basis according to the normal tissue they resemble or its embryonal counterparts, for example, fibrosarcoma, chondrosarcoma, leiomyosarcoma, and rhabdomyosarcoma.

There are tumors that do not follow any classification scheme, and they have been identified by trivial names, such as seminoma and melanoma. Other tumors carry eponyms, such as Hodgkin's disease, and Ewing's sarcoma.

Tumors within a single organ or single type of epithelium are further subclassified into different types; each has its own characteristics, prognosis, and response to therapy. A comprehensive and detailed histological classification of tumors of various organ systems is presented in several reviews and monographs [6, 7]. Malignant tumors are neoplasms that extend into surrounding tissue without respecting normal tissue boundaries, are capable of invading lymphatics and blood vessels, and can be transported to distant sites. Several salient abnormalities are helpful to the pathologist in making the morphological diagnosis of such tumors, and they are expressed in two ways: First, there are abnormalities that affect individual cells in the form of cytological features and increased mitotic activity. Cytological features of malignancy include cell enlargement, increased ratio of nuclear to cytoplasmic area, pleomorphism (variation in size and shape), clumping of nuclear chromatin, and big nucleoli (Fig. 11.2). Second, there are abnormalities that affect intercellular relationship, i.e., altered orientation of neoplastic cells and stroma leading to disorganization [8].

11.1.2 Grading

Grading is a scheme that attempts to determine the degree of malignancy and is based on the evaluation of certain parameters that vary according to the system used. These broadly include: degree of tumor cellularity, resemblance of tumor cells to their normal forebears

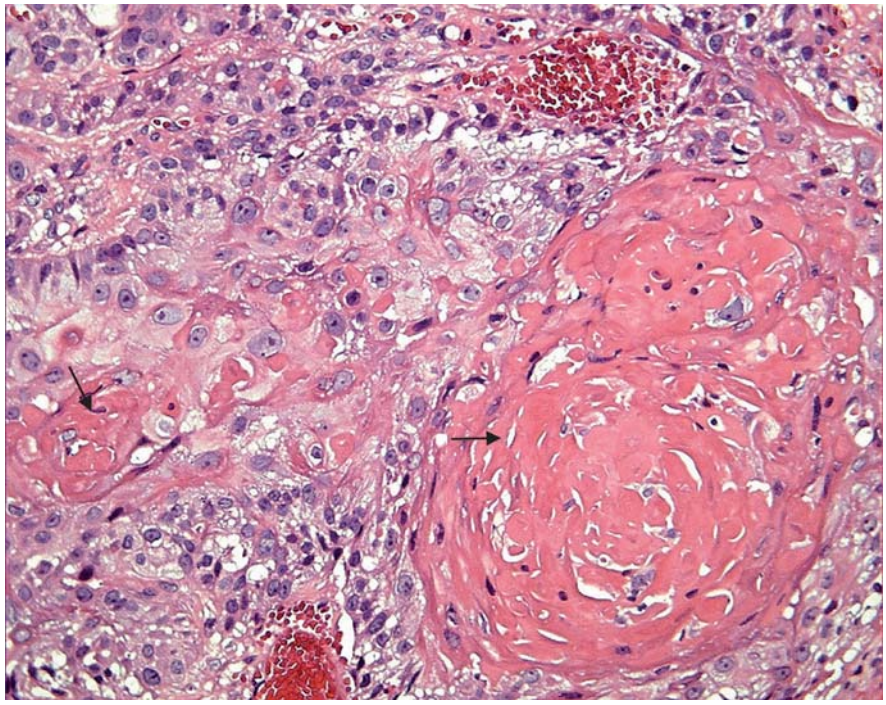

Fig. 11.3. Squamous cell carcinoma. The tumor consists of well-differentiated squamous cells forming keratin pearls (*arrows*)

morphologically and functionally, cellular pleomorphism or anaplasia, mitotic activity (number and abnormality), and necrosis [9]. In general, a three-grade system has proven to be the most reproducible; well, moderately, and poorly or undifferentiated, or grades I, II, and III, where grade III represents the least-differentiated tumor. Certain tumor types are defined as high grade, for example rhabdomyosarcoma, Ewing's sarcoma, and synovial sarcoma. Nonetheless, tumor grading has a few shortcomings: First, grading is subjective and depends on the pathologist's judgement. Second, tumors are heterogeneous, and accurate grading requires microscopic examination of representative tissue. In these cases, the least-differentiated area of the tumor should determine the grade. Thus, the tumor grade is a qualitative assessment of the differentiation of the tumor expressed as the extent to which a tumor resembles the normal tissue at that site, expressed in numerical grades from most differentiated to least differentiated.

11.1.3 Tumor Staging

Staging of cancer depends on the size of the primary neoplasm, its extent to regional lymph nodes and the presence or absence of metastasis. Cancer care is a cooperative, multidisciplinary endeavor; therefore, if the medical disciplines involved in cancer care are to work well together, they must be able to communicate with precision. The TNM system has been developed by the American (American Joint Committee on Cancer, AJCC) and European (Union International Contre le Cancer, UICC) commissions on cancer to allow systematic categorization and description of cancer patients. In this fashion, disease progression patterns natural history, and treatment outcome can be more reliably documented when applied to the individual patient.

The AJCC classification is based on the premise that cancers of similar histological type or site of origin share similar patterns of growth and extension. Obviously, cancers exhibit a variety of growth and extension patterns based upon unique features of either the host or the tumor. A classification scheme must therefore encompass all potential manifestations of both the tumor and its host. The objectives of a staging system can be briefly summarized as follows: (a) to aid the clinician in planning treatment, (b) to give some indication of prognosis, (c) to assist the evaluation of end results, (d) to facilitate the exchange of information between treatment centers, and (e) to assist in the continuing investigation of cancer. To meet the stated objectives, a system of classification is needed that has basic principles applicable to all anatomical sites regardless of treatment, and in which clinical appraisal can be supplemented by later information from surgery, histopathology, and/or other technologies. The TNM system meets these requirements. It is an expression of the anatomical extent of disease and is based on the assessment of three components:

T The extent of primary tumor
N The absence or presence and extent of regional lymph node metastases
M The absence or presence of distant metastases

Temporal variables are defined in the TNM classification scheme to allow an update to occur after certain data have been obtained: TNM clinical-diagnostic staging allows for pretreatment characterization via clinical examination and specific diagnostic studies. TNM surgical-evaluative staging is applied following a major surgical exploration or biopsy. TNM post-surgical treatment–pathological staging characterizes the extent of the cancer following thorough examination of the resected surgical specimen. TNM retreatment staging is applied in instances where the initial therapy has failed and additional treatment decisions are being considered. TNM autopsy staging is the final staging, done after the post-mortem study.

11.1.4 Rate of Growth

Most benign neoplasm grow slowly, and most malignant neoplasms grow much faster. There are many exceptions to this generalization, however, and some benign neoplasm grow more rapidly than some cancers. For example uterine leiomyomas (benign smooth muscle tumors) may increase rapidly in size during pregnancy (hormonal effect). The rate of growth of malignant tumors correlates in general with their level of differentiation. Rapidly growing malignant neoplasms often contain central areas of ischemic necrosis because the tumor blood supply, derived from the host, fails to keep pace with the oxygen needs of the expanding mass of cells [1].

11.1.5 Angiogenesis in Neoplasia

Neovascularization is a feature of neoplasia. Neovascularization supplies nutrients and oxygen and endothelial cells stimulate the growth of adjacent tumor cells by secreting different factors, such as insulin-like growth factors, platelet-derived growth factor (PDGF), granulocyte-macrophage colony-stimulating factor (GM-CSF), and interleukin (IL)-1. Angiogenesis is required not only for continued tumor growth but also for metastasis [1].

Tumor-associated angiogenic factors may be produced by tumor cells or may be derived from inflammatory cells (e.g., macrophages) that infiltrate tumors. The two most important tumor-associated angiogenic

factors are vascular endothelial growth factor (VEGF) and basic fibroblast growth factor. The tumor cells not only produce angiogenic factors but also induce antiangiogenesis molecules. The molecular basis of the angiogenesis is not entirely clear but may involve increased production of angiogenic factors or loss of angiogenesis inhibitors. Hypoxia within the growing tumor favors angiogenesis by release of hypoxia-inducible factor-1 (HIF-1) [1]. HIF-1 controls transcription of VEGF. The transcription of VEGF also is under the control of RAS oncogene, and RAS activation upregulates the production of VEGF. The wild-type TP53 gene seems to inhibit angiogenesis by inducing the synthesis of the antiangiogenic molecule thrombospondin-1. With mutational inactivation of both TP53 alleles (a common event in many cancers), the levels of thrombospondin-1 drop precipitously, tilting the balance in favor of angiogenic factors.

Because of the important role of angiogenesis in tumor growth, extensive publications have concentrated on antiangiogenesis therapy, and the results are very promising [34–41].

11.2 Tumor Biology

11.2.1 Cell Cycle

The cell cycle is a complex circuit composed of positive and negative protein regulators, the role of which is to duplicate DNA specifically during S phase and to segregate it evenly into two identical progeny during M phase. When a cell leaves the dormant state of G0 and enters a metabolically active phase during G1, the destiny of the cell cycle pivots in the equilibrium as the decision to undergo division must be made at the restriction point [10]. Because G1 is such an essential phase of the cell cycle, it is not astonishing that many oncogenic perturbations have been found as targeted amplifications or mutations of G1-specific protein regulators.

11.2.2 Distinguishing Features of Tumor Cells and Tumorigenesis

Cancer is a genetic disease resulting from multiple, sequential genetic changes affecting oncogenes, tumor suppressor genes, and modifiers [10–14]. Because of this multistep process, most human malignancies show various degrees of genetic heterogeneity even if they originate from single cells. Although most human leukemias and lymphomas carry consistent chromosomal rearrangements, principally chromosomal translocations or inversions that activate specific oncogenes or cause loss of function of specific tumor suppressor genes, thereby initiating the process of malignant transformation, it is not known what the initiating events are for some of the most common human malignancies, the malignant epithelial tumors such as lung, breast, and prostate cancer.

During the past several decades, basic cancer research has focused primarily on unraveling the mystery of how cancer cells can acquire distinctive novel phenotypes. The multistep progression model determines that cells pass through a number of distinctive intermediate stages of evolution from normalcy to full malignancy [15]. The evolved tumor cells vary significantly from their normal counterparts. Although, as shown in experimental animal models and human beings, the number of these stages may be only small, the number of cellular changes linked with malignant transformation is significantly large.

Tumor cells have distinguishing morphological and structural features that are different from those of the cells of origin. Moreover, the abnormal cells show altered interaction with neighboring cells. Normal cells have an ordered growth pattern and a predicted relationship with their neighboring cells, and that growth pattern is predominantly two-dimensional. Further normal cell division is inhibited by contacts made with other cells; this is the phenomenon of contact inhibition [16]. In contrast, tumor cells exhibit loss of contact inhibition and continue to display a disordered growth pattern. While the mechanism that maintains contact inhibition in normal cells is not entirely understood, it definitely involves the transfer of small molecules between adjacent cells. During tumor growth, however, it seems that the intercellular communication may be impaired; therefore, contact inhibition will continue to be violated [17, 18].

Another feature that distinguishes normal growth from malignant proliferation is the reduced dependence of the latter on the presence of the known stimulatory and inhibitory growth factors. The diversion from the control of the growth regulatory factors can be explained, in part, by the discovery of biochemical changes within cancer cells resulting from some genetic alterations. Thus, when normal cells are grown in culture they continue to divide for a limited number of generations and then experience a senescent crisis, in which most cells stop dividing and die, and no cells survive to establish permanent cell lines. On the other hand, human tumor cells usually have an unlimited potential for growth and are thus immortalized [19]. While this immortalization may be an essential requirement for tumorigenesis, it is not the only requirement, as confirmed by the studies of some oncogenic viruses. It is known that the genes carried by these tumor viruses can promote the establishment of immortal cell lines; however, these immortalizing genes are not capable of converting an infected cell to the fully tumorigenic states unless other cellular changes are also present.

Recently, this distinctive growth factor independence or autonomy has been attributed to at least four different mechanisms. First, tumor cells have the ability to secrete mitogenic growth factors that have a growth-stimulatory ability on the same cell that has released them, resulting in an autocrine positive-feedback loop [20]. Second, normal cells display growth factor receptors on their surfaces. These receptors release growth-stimulatory signals into the cell when they bind their cognate ligands. Alteration in number or structure can result in the release of mitogenic signals into the cell, even in the absence of any growth-factor signals [21]. Therefore, these aberrantly expressed or structured receptors then operate as oncogene proteins. The best example of this mechanism is illustrated by the overexpression of *HER-2/neu* proto-oncogene in mammary carcinoma [22]. Third, there is a cytoplasmic signaling pathway responsible for picking up signals from cell surface receptors and transducing them to central growth-regulatory switches within the cell. It appears that proteins of such genes as *ras* participate in signal-transducing events in these pathways [23]. Finally, the growth factor independence of tumor cells may also be attributed to the behavior of nuclear proto-oncogenes that are normally regulated through a wide range of expression [22, 23].

Another characteristic feature of human malignancy is its ability to escape the human immune surveillance pathways. It is known that human tumor cells express on their surfaces novel antigens that are not present on the surfaces of their untransformed progenitors. One type of novel antigen may be common to many different types of malignancy and may be recognized by the natural killer lymphocytes even without specific prior immunization [24]. In other instances, novel antigens specific to a particular type of tumor may be displayed. According to one theory of tumorigenesis, all individuals develop abundant transformed cells over the course of their lives, but most of these cells are recognized and destroyed by one or another module of the host's immune mechanisms. Support for this theory stems from the observation of the substantial increase in the incidence of malignancy in patients with acquired immune deficiency syndrome, in patients with organ transplants receiving intensive immunosuppressive agents, and in patients with other immune deficiency disorders [25, 26]. It has been proven that tumor cells may escape the host immune system by downregulating the expression of HLA antigens, which normally assist lymphocyte recognition of the target cells.

Tumor cells exhibit a vast array of metabolic differences distinguishing them from their untransformed counterparts. This is illustrated primarily in simplified metabolic activities and by an increased synthesis of material necessary for cell division. Some of the most striking metabolic alterations include the utilization of anaerobic pathways and the increased utilization of glucose transport [27].

Despite all these aspects that distinguish tumor cells from normal cells, many tumor cells exhibit some characteristic differentiated features of the normal lineage cells. This partially differentiated state of most tumor cells suggests that the initial transformation event leading to tumor formation occurs in a dividing but still undifferentiated stem cell. However, a partial or complete block in the normal developmental pathway toward full differentiation occurs and leads to the formation of a partially differentiated cell trapped in a relatively undifferentiated and highly proliferative cell compartment. In addition, many tumor cells express proteins that are not found in the mature tissue but are part of the normal pattern of protein expression from the corresponding embryonic tissue. For example, the embryonic liver cells secrete alpha-fetoprotein, which is not found in mature hepatic tissue except when injury and regeneration occur. However, alpha-fetoprotein is found both in the tumor cells and in the circulation of patients with hepatocellular carcinoma [28]. Another example is choriocarcinoma, which arises from the placenta and releases into the circulation human chorionic gonadotropin, which is a normal product of the placenta [29].

11.2.3 Invasion and Metastasis

Malignant neoplasms disseminate by one of three pathways: (1) seeding within body cavities; an example of this is carcinoma of the colon that may penetrate the wall of the gut and reimplant at distant sites in the peritoneal cavity; (2) lymphatic spread, which is the preferred way of spread by carcinomas in general; or (3) hematogenous spread, which is favored by sarcomas. The ability of a tumor to metastasize is a multifaceted phenomenon which requires several prerequisites [30]: (1) invasion by tumor cells through adjacent structures, (2) entrance of tumor cells into blood or lymphatic vessels, (3) survival of tumor cells within the circulation and avoidance of the immune system, and (4) implantation in a foreign tissue with establishment of a new tumor locus.

Most carcinomas arise in epithelial cell layers with an underlying basement membrane. Invasive tumors frequently secrete enzymes, including collagenases, heparanase, and stromelysin, that are capable of degrading this type of physical barrier [31]. Once a tumor has eroded through the wall of a blood or lymphatic vessel, individual tumor cells may detach and circulate through the body as an embolus. Encasing these cells in cots of fibrin or in aggregates of platelets may protect them from destruction by the immune system. The

presence of tumor cells in the circulation does not necessarily lead to metastases [32]. However, these circulating cells have to "home" preferentially to a specific target organ. This pattern has been described as the "seeds" and "soil" model and has been demonstrated experimentally and observed consistently in oncological practice. It is not clear how these patterns of metastases arise, but some evidence suggests that tumor cells can respond to specific chemotactic signals. Moreover, specific receptors have recently been identified on the surfaces of metastasizing tumor cells that cause them to adhere to complementary structures displayed by endothelial cells in certain organs [33].

11.2.4 Genetic Mutations and Cellular Oncogenes

Enormous scientific evidence has accumulated over more than half a century to indicate that neoplastic transformation occurs as a direct consequence of alterations to the cell genome.

Four basic approaches have been used to identify genes involved in cancer: (1) the study of cancer-causing viruses, (2) bioassays for cancer genes in tissue culture systems, (3) localization of genes at sites of chromosomal alteration in tumor specimens, and (4) isolation of genes for cancer-predisposing familial syndromes.

Two steps are required to convert the information stored in DNA into protein [42, 43]. In the first step, transcription, the DNA is used as a template for the synthesis of a complementary messenger ribonucleic acid (mRNA). After the primary transcript is processed to the mature mRNA form, the information in the mRNA is converted into protein during translation. Two distinct sets of sophisticated macromolecular polymerization machinery are responsible for each of these processes. In the case of most protein-encoding genes, RNA is synthesized by RNA polymerase II (RNA Pol II) and its associated proteins. RNA Pol I and III synthesize two other classes of RNA, the transfer or tRNAs and the ribosomal or rRNAs, respectively. Unlike the mRNAs, the rRNAs and tRNAs do not encode proteins, but instead function directly as part of the translation machinery.

It is well known that agents that induce damage of the DNA (mutagens) have potential carcinogenic effects. The DNA found in the nucleus of every living cell encodes the heritable or genetic information necessary to direct the development of that organism from a single fertilized cell to the mature organism. Therefore, the progenitor tumor cells that sustain genetic alterations are said to undergo somatic mutations that promote the multistep process of neoplastic development. That is distinguishable from germline mutations that are transmitted from one individual to his or her offspring. Initial progress in our understanding of these mutant cancer-causing genes came from studies of several tumor viruses, among them the DNA-containing viruses SV40, and polyomavirus. These viruses were found to be capable of infecting and transforming cultured rodent cells into a tumorigenic state through the induction of a large number of complex cellular changes. Therefore, it was postulated that a small number of mutant cellular genes could also act as oncogenes to induce the many behavioral aberrancies associated with malignant cells. Indeed, the existence of such cellular genes was indicated by work on RNA-containing tumor viruses (retroviruses), such as the Rous sarcoma virus of chickens. This led to the understanding that the chicken genome must contain a normal gene that can be converted into an active, transformation-inducing oncogene by a retrovirus. By extension, the mammalian genome might contain a gene or a number of such genes, each of which could become activated as a potent oncogene [44].

Earlier studies to examine oncogenesis were very informative. In order to detect oncogenes within the nonviral tumors, DNA was extracted from cells and then introduced into normal, nontransformed recipient cells (transfection). Through these experiments it was very clear that some of the information encoding cancerous behavior of the donor cells could be passed to the recipient cells via DNA molecules. It was not until the early 1980s, with the advent of gene cloning, that it was possible to isolate these cellular oncogenes (Table 11.1).

Many of the oncogenes originally detected by virtue of their association with various retroviruses were then found to be activated through nonviral mutational mechanisms in human cancers. The *myc* oncogene that was discovered in the context of the avian myelocytomatosis virus genome was then seen in activated form in many Burkitt's lymphomas. Another example is the Ha-*ras* oncogene; associated initially with a rat sarcoma retrovirus, it was seen in association with EJ/T24 bladder carcinoma oncogene. In addition, in approximately 30% of human cancers, including a substantial proportion of pancreatic and colon adenocarcinomas, mutated *ras* genes produce mutated proteins that remain locked in an active state, thereby relaying uncontrolled proliferative signals [23]. *Ras* undergoes several post-translational modifications that facilitate its attachment to the inner surface of the plasma membrane. A growing body of data suggests that disruption of *ras* signaling pathways, either directly through mutations or indirectly through other genetic aberrations, is important in the pathogenesis of a wide variety of cancers. Molecules such as farnesyl transferase inhibitors that interfere with the function of *ras* may be exploitable in leukemia (as well as in solid tumors) as novel antitumor agents.

Table 11.1. Cellular oncogenes implicated in human cancer

Category	Proto-oncogene	Mode of Activation	Associated human tumor
Growth factors			
PDGF-β chain	*S/S*	Overexpression	Astrocytoma Osteosarcoma
Fibroblast growth factors	*HST-1* *INT-2*	Overexpression Amplification	Stomach cancer Bladder cancer Breast cancer Melanoma
TGFa	*TGF*a	Overexpression	Astrocytomas Hepatocellular carcinomas
HGF	*HGF*	Overexpression	Thyroid cancer
Growth factor receptors			
EGF-receptor family	*ERB-B1* *(ECFR)* *ERB-B2*	Overexpression	Squamous cell carcinomas of lung, gliomas Breast and ovarian cancers
CSF-1 receptor	*FMS*	Point mutation	Leukemia
Receptor for neutrotrophic factors	*RET*	Point mutation	Multiple endocrine neoplasia 2A and B, familial medullary thyroid carcinomas
PDGF receptor	*PDGF-R*	Overexpression	Gliomas
Proteins involved in signal transduction			
GTP-binding	*K-RAS* *H-RAS* *N-RAS*	Point mutation Point mutation Point mutation	Colon, lung, and pancreatic tumors Bladder and kidney tumors Melanomas
Nonreceptor tyrosine kinase	*ABL*	Translocation	Chronic myeloid leukemia
WNT signal transduction	β-*catenin*	Point mutation Overexpression	Hepatoblastomas, hepatocellular carcinoma
Nuclear regulatory proteins			
Transcriptional activators	*C-MYC*	Translocation	Burkitt's lymphoma
Cell-cycle regulators			
Cyclins	*CYCLIN D*	Translocation Amplification	Mantle cell lymphoma Breast and esophageal cancers
	CYCLIN E	Overexpression	Breast cancer
Cyclin-dependent kinase	*CDK4*	Amplification or point mutation	Glioblastoma, melanoma

Activation of cellular oncogenes is a complex process that involves a variety of somatic mutational mechanisms. The c-*myc* oncogene develops its malignant properties through mechanisms that affect the level of expression of its encoded proteins without any associated alteration in its protein structure. Recently, the prognostic significance of c-*myc* in lymphoma has also been described [45].

On the other hand, a quantitative change in the structure of the encoded proteins may be responsible for oncogene activation. In chronic myelogenous leukemia, for example, the *abl* gene undergoes fusion with a fully unrelated gene, *bcr*. The bcr-abl hybrid protein encoded by these fused genes differs substantially in structure and function from the normal *abl* proto-oncogene protein [46, 47].

It was clear, however, that single oncogenes were not capable of inducing transformation of fully normal cells into totally malignant cells. Instead, the action of a single oncogene usually induces only partial progression to malignancy. Fortunately, this has served as a protective mechanism to prevent the development of cancers in response to single oncogenes that arise through isolated genetic mishaps. Therefore, it appears that each step through which cells pass in the progression from normalcy to malignancy (multistep carcinogenesis) is characterized by a distinct genetic change, often one that creates an oncogene. However, the precise number of the distinct steps for most human tumors is poorly understood.

There is a remarkable proliferation of literature on the molecular basis of cancer [48, 49]. Nonlethal genet-

ic damage may be acquired by the action of environmental agents, such as chemicals, radiation, or viruses, or it may be inherited in the germ line. The current hypothesis implies that cancer forms as a result of clonal expansion of a single progenitor cell that has incurred the genetic damage (i.e., tumors are monoclonal). This theory has been supported by many studies that revealed clonality in neoplasm that have been assessed readily in women who are heterozygous for polymorphic X-linked markers, such as the enzyme glucose-6-phosphate dehydrogenase or X-linked restriction fragment length polymorphisms or in clonality assessed in lymphoid neoplasm. Mutant alleles of proto-oncogenes are called oncogenes.

Three classes of normal regulatory genes – growth-promoting proto-oncogenes; growth-inhibiting cancer suppressor genes (anti-oncogenes); and genes that regulate programmed cell death, or apoptosis – are the principal targets of genetic damage [1]. They are considered dominant because they transform cells despite the presence of their normal counterpart. In contrast, both normal alleles of tumor suppressor genes must be damaged for transformation to occur, so this family of genes sometimes is referred to as recessive oncogenes. Genes that regulate apoptosis may be dominant, as are proto-oncogenes, or they may behave as cancer suppressor genes. In addition to the three classes of genes mentioned earlier, a fourth category of genes, those that regulate repair of damaged DNA, is pertinent in carcinogenesis.

11.2.4.1 Growth-Promoting Proto-oncogenes

Genes that promote autonomous cell growth in cancer cells are called oncogenes. They are derived by mutations in proto-oncogenes and are characterized by the ability to promote cell growth in the absence of normal growth-promoting signals. Their products, called oncoproteins, resemble the normal products of proto-oncogenes except that oncoproteins are devoid of important regulatory elements, and their production in the transformed cells does not depend on growth factors or other external signals.

All normal cells require stimulation by growth factors to undergo proliferation. Many cancer cells acquire growth self-sufficiency, however, by acquiring the ability to synthesize the same growth factors to which they are responsive. Such is the case with platelet-derived growth factor (PDGF) and transforming growth factor α (TGF-α) [50]. Many glioblastomas secrete PDGF, and sarcomas make TGF-α.

11.2.4.2 Growth Factor Receptors

There are several oncogenes that encode growth factor. Those oncogenes represent either mutation or overexpression of normal forms of growth factor receptors. Mutant receptor proteins can send continuous mitogenic signals to cells, even in the absence of the growth factor in the environment [1]. Overexpression can render cancer cells hyperresponsive to normal levels of the growth factor, a level that would not normally trigger proliferation. Among the examples of overexpression is the receptor, called HER2 (ERBB2), which is present in 30% of breast cancers and is present in variable percentages in other human cancers. Breast cancers which are positive for Her are more sensitive to the mitogenic effects of small amounts of growth factors, and a high level of HER2 protein in breast cancer is associated with poor prognosis. The clinical significance of HER2 in breast cancers is clearly evident by the treatment of breast cancer with anti-HER2 antibodies which block the extracellular domain of this receptor [51, 52].

11.2.4.3 Signal-Transducing Proteins

Mutations in genes that encode various components of the signaling pathways are a common process in cancer. These signaling molecules couple growth factor receptors to their nuclear targets. The most important members in this category are RAS and ABL.

Approximately 30% of all human tumors contain mutated versions of the *RAS* gene. In some tumors, such as colon and pancreatic cancers, the incidence of *RAS* mutations is even higher [1]. The activated *RAS* in turn activates downstream regulators of proliferation, including the *RAF-MAP* kinase mitogenic cascade, which flood the nucleus with signals for cell proliferation. In chronic myeloid leukemia and certain acute leukemias, this activity is unleashed because the *ABL* gene is translocated from its normal abode on chromosome 9 to chromosome 22, where it fuses with part of the breakpoint cluster region (*BCR*) gene. The *BCR-ABL* hybrid gene has potent tyrosine kinase activity, and it activates several pathways, including the *RAS-RAF* cascade just described. The crucial role of *BCR-ABL* in transformation has been confirmed by the dramatic clinical response of patients with chronic myeloid leukemia after therapy with an inhibitor of *ABL* kinase called STI 571 (Gleevec); this is another example of rational drug design emerging from an understanding of the molecular basis of cancer.

11.2.4.4 Nuclear Transcription Factors

Growth autonomy in neoplasm may occur as a consequence of mutations affecting genes that regulate transcription of DNA such as *MYC* oncogene that has been localized to the nucleus. The *MYC* proto-oncogene is expressed in virtually all cells, and the *MYC* protein is induced rapidly when quiescent cells receive a signal to divide. The MYC protein binds to the DNA, causing transcriptional activation of several growth-related genes, including cyclin-dependent kinases (CDKs), whose product drives cells into the cell cycle. In normal cells, *MYC* levels decline to near basal level when the cell cycle begins. In contrast, oncogenic versions of the *MYC* gene are associated with persistent expression or overexpression, contributing to sustained proliferation. The classic example is the dysregulation of the *MYC* gene resulting from a t(8;14) translocation which occurs in Burkitt's lymphoma [1].

11.2.5 Tumor Suppressor Genes and Tumor Progression

The existence of tumor suppressor genes, predicted in the 1970s by the elegant epidemiological studies of Knudson [53] and by subsequent cell fusion studies [54], finally became a reality with the discovery of the retinoblastoma (*Rb*) gene and later the role of the *p53* gene in the 1980s [55].

While oncogenes play a critical role in tumorigenesis, another group of genes known as tumor suppressors appears to be equally significant. These tumor suppressor genes, as the name implies, function in the normal cells to restrict cellular proliferation. However, tumor suppressor genes are involved in tumorigenesis when they suffer genetic inactivation or loss-of-function mutations, affecting the two redundant copies of these genes and resulting in elimination of that important barrier to cell growth.

The loss of wild-type tumor suppressor genes such as *Rb* and *p53* is associated with a wide variety of human tumors. Many proto-oncogenes transform in model systems in which the wild-type gene is overexpressed or expressed in the wrong cell type; similarly, overexpression or inappropriate expression of some proto-oncogenes, such as c-*myc*, is thought to be tumorigenic in some human tissues.

Inactive alleles of tumor suppressor genes can be acquired in two ways. First, they may be created through somatic mutation occurring in a target organ. Second, this inactivation or mutation may be passed through the germline, present in all body tissues. The second mechanism may lead to a congenital predisposition to cancer because one of the required mutational events needed to knock out both homologous copies of the gene has already occurred in all cells of the target organ.

The best example of the two mechanisms is associated with the inactivation of the tumor suppressor gene *Rb*. In 1970, DeMars postulated that persons prone to development of the familial form of retinoblastoma are heterozygous for a cancer-predisposing gene, and that cancer develops because of a somatic mutation at the remaining normal allele [56]. Later, Knudson developed a mathematical model based on differences in the incidence and age of onset of unilateral and bilateral cases of familial retinoblastoma [40]. The higher incidence of bilateral tumors and earlier age of onset in familial cases than in sporadic cases indicated that a single additional mutation is the rate-limiting step in the development of tumors in familial cases, but two events are needed in nonfamilial cases. By this model, individuals predisposed to retinoblastoma would inherit one inactive and one functional copy of the *Rb* gene. Somatic mutation to eliminate the functional allele by mutation or loss of heterozygosity would eliminate Rb function. In nonfamilial cases, both alleles would be inactivated somatically; hence the requirement for two independent events. This model has helped explain the epidemiological and molecular findings for a number of human cancers, including familial adenomatous polyposis, Wilms' tumor, Li-Fraumeni syndrome, and von Recklinghausen's neurofibromatosis. It is likely that Rb suppresses tumor formation by virtue of its biological activities [57].

The most commonly mutated tumor suppressor gene in human cancer is *p53*, with at least 50% of tumors having abnormal *p53* genes [58]. The gene participates in a cell cycle checkpoint signal transduction pathway that causes either a G1 arrest or apoptotic cell death following DNA damage. Loss of *p53* function during tumorigenesis can thus result in both inappropriate progressions through the cell cycle after DNA damage and survival of a cell that might otherwise have been destined to die. It is easy to conceive how this would cause both increased genetic instability and decreased apoptosis and contribute to malignant transformation. Some tumors also develop other mechanisms of inactivating *p53* function by overexpression of the *p53*-binding protein, mdm2, or by infection with high-risk human papilloma virus and expression of the HPV E6 protein, which binds to *p53* and enhances its degradation. Thus, many tumors appear to inactivate *p53* function by these mechanisms, rather than by mutation of the *p53* gene itself. In some tumor types, these *p53* mutations are associated with poor prognosis and treatment failure.

Another newly discovered tumor suppressor gene is the *p16*. Since its discovery as a CDKI (cyclin-dependent kinase inhibitor) in 1993, the tumor suppressor *p16* has gained widespread importance in tumor biolo-

gy [59]. The frequent mutations and deletions of *p16* in human cancer cell lines first suggested an important role for *p16* in carcinogenesis. This genetic evidence for a causal role was significantly strengthened by the observation that *p16* was frequently inactivated in familial melanoma kindreds. Since then, a high frequency of *p16* gene alterations has been observed in many primary tumors. In human neoplasms, *p16* is silenced in at least three ways: homozygous deletion, methylation of the promoter, and point mutation. The first two mechanisms comprise the majority of inactivation events in most primary tumors. Additionally, the loss of *p16* may be an early event in cancer progression, because deletion of at least one copy is quite high in some premalignant lesions. *p16* is a major target in carcinogenesis, rivaled in frequency only by the *p53* tumor suppressor gene.

The absence of APC, another tumor suppressor gene, is responsible for the development of familial adenomatous polyposis coli [49, 60]. the loss of APC is common in colon cancer. APC is a cytoplasmic protein whose function in normal cells is to bind another protein called β-catenin and bring about its degradation. β-Catenin is a transcriptional factor and if APC function is defective by mutation, accumulated levels of β-catenin occur in the cells, driving cell proliferation. Individuals born with one mutant allele develop hundreds to thousands of adenomatous polyps in the colon during their teens or 20s. If the cells develop a second mutation of the normal inherited gene on the other allele, it leads to development of carcinoma of the colon.

11.2.6 Apoptosis

Each day, approximately 50 – 70 billion cells die in the average adult because of programmed cell death. The morphological ritual cells go through when experiencing programmed cell death has been termed apoptosis and is executed by a family of intracellular proteases, called caspases [61]. These physiological deaths culminate in fragmentation of cells into membrane-encased bodies, which are cleared through phagocytosis, by neighboring cells without inciting inflammatory reactions or tissue scarring. Defects in the processes controlling apoptosis can extend cell life span, contributing to neoplastic cell expansion independent of cell division [62]. Moreover, failures in normal apoptosis pathways contribute to carcinogenesis by creating a permissive environment for genetic instability and accumulation of gene mutations, by promoting resistance to immune-based destruction, by allowing neglect of cell cycle checkpoints that would normally induce apoptosis, by facilitating growth factor/hormone-independent cell survival, by supporting anchorage-independent survival during metastasis, by reducing dependence on oxygen and nutrients, and by conferring resistance to cytotoxic anticancer drugs and radiation. Exposition of the genes that constitute the core machinery of the cell death pathway has provided new insights into tumor biology, revealing novel strategies for combating cancer. A large family of genes that regulate apoptosis has been identified. Apoptosis occurs as an end result of signaling through the death receptor CD95 (Fas) and by DNA damage [1]. When CD95 is bound to its ligand, CD95L, it attracts the intracellular adaptor protein FADD, which in turn recruits procaspase 8. Caspase 8 activates downstream caspases such as caspase 3 that cleave DNA and other substrates to cause cell death. The other pathway of apoptosis is initiated by DNA damage, for example from radiation or chemical factors. This will lead to cytochrome *c* from mitochondria, which in turn forms a complex with apoptosis-inducing factor 1 (APAF-1), procaspase 9, and ATP. Caspase 9 triggers caspase 3 (where the two pathways join). The release of cytochrome is believed to be a key event in apoptosis, and it is regulated by genes of the *BCL2* family [57, 63]. Some members of this family (e.g., *BCL2, BCL-*X_L) inhibit apoptosis by preventing release of cytochrome *c*, whereas others, such as *BAD, BAX*, and *BID*, promote apoptosis by favoring cytochrome *c* release [1]. The role of *BCL2* in protecting tumor cells from apoptosis is well documented in the literature. The vast majority of B-cell lymphomas of the follicular type carry a characteristic t(14;18) (q32;q21) translocation that causes overexpression of the BCL2 protein, which in turn protects lymphocytes from apoptosis and allows them to survive for long periods; there is a steady accumulation of B lymphocytes, resulting in lymphadenopathy and marrow infiltration.

TP53 is an important proapoptotic gene that induces apoptosis in cells that are unable to repair DNA damage. The actions of *TP53* are mediated in part by activation of *BAX*. Two novel mechanisms by which tumor cells evade apoptosis have recently been discovered. Certain melanoma cells show loss of APAF-1, blocking the mitochondrial-cytochrome *c* pathway [64 – 67]. These cells are resistant to *TP53*-induced apoptosis. Finally, in some tumors, there is transcriptional upregulation of inhibitors of apoptosis that inactivate caspases. This upregulation occurs in certain lymphomas of mucosal lymphoid tissue (so-called MALT lymphomas) as a result of the t(11;18) translocation [68].

The challenge presently facing cancer research is to convert information gained about mechanisms of aberrant cell death control in tumors into new therapeutic opportunities that essentially change the course of cancer treatment as we recognize it today. The path for accomplishing this has been illuminated by basic research. The task now is to implement those strategies which hold the greatest potential.

11.2.7 Hereditary Cancer

The evidence now indicates that for many types of cancer, including the most common forms, there exist not only environmental influences but also hereditary predispositions. Our list of genes whose mutations can account for hereditary cancer is increasing. Hereditary forms of cancer can be divided into three categories :

11.2.7.1 Inherited Cancer Syndromes

Inherited cancer syndromes include several well-defined cancers in which inheritance of a single mutant gene greatly increases the risk of a person's developing a tumor. The predisposition to these tumors shows an autosomal dominant pattern of inheritance. Childhood retinoblastoma is the most striking example of this category.

Familial adenomatous polyposis is the other classic example. For most the development of the clinical features is age dependent, and that development may be early in life, as with hereditary retinoblastoma, or relatively later in life as with colorectal carcinoma. A major problem facing the cancer geneticist at present is the construction of age-specific penetrance curves that can serve as a guide to counseling.

11.2.7.2 Familial Cancers

Almost all the common types of cancers that occur sporadically have been reported to occur in familial forms. Examples include carcinomas of colon and breast. Inherited susceptibility to breast cancer has been an area of intensive investigation for the past 10 years. Early work focused on identifying modes of transmission, which culminated in the identification of chromosome 17q12 – 21 as the first human genomic region that harbored an autosomal dominant susceptibility gene for breast cancer (*BRCA1*) in 1990. *BRCA1* was subsequently identified, followed shortly by the identification of *BRCA2* [69 – 72]. Research has elucidated much about the mutation spectrum and mutation frequency of these genes in specific populations in the past 3 years and is beginning to identify potential functions. Whereas progress in this area has been rapid and much is now known about inherited susceptibility to breast cancer, much more needs to be done to make these discoveries useful in the diagnosis, treatment, and ultimately prevention of breast cancer.

11.2.7.3 Autosomal Recessive Syndromes of Defective DNA Repair

One of the best-studied examples is xeroderma pigmentosum, in which DNA repair is defective. It is a rare autosomal recessive disease characterized by deficiency of endonuclease, the enzyme partly responsible for repair of DNA damage. Children with this disorder develop multiple squamous cell carcinomas [49].

References

1. Kumar V, Cotran RS, Robbins SL (2003) Basic pathology, 6th edn. Saunders, Philadelphia
2. Devita VT, Hellman S, Rosenberg SA (1993) Cancer: principles and practice of oncology, 4th edn. Lippincott, Philadelphia
3. Kennedy AW, Hart WR (1996) Ovarian papillary serous tumors of low malignant potential (serous borderline tumors). A long-term follow-up study, including patients with microinvasion, lymph node metastasis, and transformation to invasive serous carcinoma. Cancer 78:278 – 286
4. Riopel MA, Ronnett BM, Kurman RJ (1999) Evaluation of diagnostic criteria and behavior of ovarian intestinal-type mucinous tumors: atypical proliferative (borderline) tumors and intraepithelial, microinvasive, invasive, and metastatic carcinomas. Am J Surg Pathol 23:617 – 635
5. Bell SW, Kempson RL, Hendrickson MR (1994) Problematic uterine smooth muscle neoplasms. A clinicopathologic study of 213 cases. Am J Surg Pathol 18:535 – 558
6. Rosai J, Sobin LH (1998) Atlas of tumor pathology, 3rd series. Armed Forces Institute of Pathology, American Registry of Pathology, Washington DC
7. World Health Organization (1967 – 2000) International histological classification of tumors, 2nd edn. WHO, Geneva
8. Holland JF, Bast RC, Morton DL, Frei E III, Kufe DW, Weichselbaum RR (1997) Cancer medicine, 4th edn. Williams and Wilkins, Baltimore
9. Collan Y (1989) General principles of grading lesions in diagnostic histopathology. Pathol Res Pract 185:539 – 543
10. Heichman KA, Roberts JM (1994) Rules to replicate by. Cell 79:557 – 562
11. ar-Rushdi A, Nishikura K, Erikson J, Watt R, Rovera G, Croce CM (1983) Differential expression of the translocated and the untranslocated c-*myc* oncogene in Burkitt lymphoma. Science 28:390 – 393
12. Arakawa H, Nakamura T, Zhadanov AB, Fidanza V, Yano T, Bullrich F, Shimizu M, Blechman J, Mazo A, Canaani E, Croce CM (1998) Identification and characterization of the ARP1 gene, a target for the human acute leukemia ALL1 gene. Proc Natl Acad Sci U S A 95:4573 – 4578
13. Naylor SL, Johnson BE, Minna JD, Sakaguchi AY (1987) Loss of heterozygosity of chromosome 3p markers in small-cell lung cancer. Nature 329:451 – 454
14. Tsujimoto Y, Cossman J, Jaffe E, Croce CM (1985) Involvement of the bcl-2 gene in human follicular lymphoma. Science 21:1440 – 1443
15. Foulds L (1969) Neoplastic development, vol 2. Academic, London
16. Abercrombie M, Heaysman JE (1954) Observations on the social behaviour of cells in tissue culture. II. Monolayering of fibroblasts. Exp Cell Res 6:293 – 306

17. Loewenstein WR (1979) Junctional intercellular communication and the control of growth. Biochim Biophys Acta 560:1 – 65
18. Weinstein RS, Merk FB, Alroy J (1976) The structure and function of intercellular junctions in cancer. Adv Cancer Res 23:23 – 89
19. Todaro GJ, Green H (1963) Quantitative studies of the growth of mouse embryo cells in culture and their development into established lines. J Cell Biol 17:299 – 313
20. Sporn MB, Todaro GJ (1980) Autocrine secretion and malignant transformation of cells. N Engl J Med 303:878 – 880
21. Downward J, Yarden Y, Mayes E, Scrace G, Totty N, Stockwell P, Ullrich A, Schlessinger J, Waterfield MD (1984) Close similarity of epidermal growth factor receptor and *v-erb-B* oncogene protein sequences. Nature 307:521 – 527
22. Ross JS, Fletcher JA (1998) The HER-2/neu oncogene in breast cancer: prognostic factor, predictive factor, and target for therapy. Oncologist 3:237 – 252
23. Rowinsky EK, Windle JJ, Von Hoff DD (1999) Ras protein farnesyltransferase: A strategic target for anticancer therapeutic development. J Clin Oncol 17:3631 – 3652
24. Herberman RB, Ortaldo JR (1981) Natural killer cells: their roles in defenses against disease. Science 2:24 – 30
25. Knowles DM (1999) Immunodeficiency-associated lymphoproliferative disorders. Mod Pathol 12:200 – 217
26. Spina M, Vaccher E, Carbone A, Tirelli U (1999) Neoplastic complications of HIV infection. Ann Oncol 10:1271 – 1286
27. Warburg OH (1930) The metabolism of tumors: investigations from the Kaiser Wilhelm Institute for Biology. Constable, London
28. Johnson PJ (1999) Role of alpha-fetoprotein in the diagnosis and management of hepatocellular carcinoma. J Gastroenterol Hepatol 14 (Suppl):32 – 36
29. Nishimura R, Koizumi T, Yokotani T, Taniguchi R, Morisue K, Yoshimura M, Hiranmoy D, Yamaguchi S, Nakagawa T, Hasegawa K, Yasui H (1998) Molecular heterogeneity of hCGbeta-related glycoproteins and the clinical relevance in trophoblastic and non-trophoblastic tumors. Int J Gynaecol Obstet 60(Suppl 1):29 – 32
30. Yokota J (2000) Tumor progression and metastasis. Carcinogenesis 3:497 – 503
31. Recklies AD, Tiltman KJ, Stoker TA, Poole AR (1980) Secretion of proteinases from malignant and nonmalignant human breast tissue. Cancer Res 40:550 – 556
32. Fisher ER, Fisher B (1959) Experimental studies of factors influencing hepatic metastases. I. The effect of number of tumor cells injected and time of growth. Cancer 12:929 – 932
33. Gunthert U, Hofmann M, Rudy W, Reber S, Zoller M, Haussmann I, Matzku S, Wenzel A, Ponta H, Herrlich P (1991) A new variant of glycoprotein CD44 confers metastatic potential to rat carcinoma cells. Cell 65:13 – 24
34. Kerbel RS (2000) Tumor angiogenesis: past, present and the near future. Carcinogenesis 21:505 – 515
35. Cristofanilli M, Charnsangavej C, Hortobagyi GN (2002) Angiogenesis modulation in cancer research: novel clinical approaches. Nat Rev Drug Discov 1:415 – 426
36. Leach MO, Brindle KM, Evelhoch JL, Griffiths JR, Horsman MR, Jackson A, Jayson GC, Judson IR, Knopp MV, Maxwell RJ, McIntyre D, Padhani AR, Price P, Rathbone R, Rustin GJ, Tofts PS, Tozer GM, Vennart W, Waterton JC, Williams SR, Workman P (2005) The assessment of antiangiogenic and antivascular therapies in early-stage clinical trials using magnetic resonance imaging: issues and recommendations. Br J Cancer 92:1599 – 1610
37. Abdollahi A, Lipson KE, Sckell A, Zieher H, Klenke F, Poerschke D, Roth A, Han X, Krix M, Bischof M, Hahnfeldt P, Grone HJ, Debus J, Hlatky L, Huber PE (2003) Combined therapy with direct and indirect angiogenesis inhibition results in enhanced antiangiogenic and antitumor effects. Cancer Res 63:8890 – 8898
38. Takano S, Kamiyama H, Tsuboi K, Matsumura A (2004) Angiogenesis and antiangiogenic therapy for malignant gliomas. Brain Tumor Pathol 21:69 – 73
39. Rege TA, Fears CY, Gladson CL (2005) Endogenous inhibitors of angiogenesis in malignant gliomas: nature's antiangiogenic therapy. Neurooncology 7:106 – 121
40. Gately S, Kerbel R (2003) Therapeutic potential of selective cyclooxygenase-2 inhibitors in the management of tumor angiogenesis. Prog Exp Tumor Res 37:179 – 192
41. Herbst RS, Onn A, Sandler A (2005) Angiogenesis and lung cancer: prognostic and therapeutic implications. J Clin Oncol 23:3243 – 3256
42. Watson JD, Cummings B (1987) Molecular biology: the gene, 4th edn. Menlo Park, NJ
43. Mitchell PJ, Tjian R (1989) Transcriptional regulation in mammalian cells by sequence-specific DNA binding proteins. Science 28:371 – 378
44. Stehelin D, Varmus HE, Bishop JM, Vogt PK (1976) DNA related to the transforming gene(s) of avian sarcoma viruses is present in normal avian DNA. Nature 11:170 – 173
45. Knutsen T (1998) Cytogenetic changes in the progression of lymphoma. Leuk Lymphoma 31:1 – 19
46. Faderl S, Talpaz M, Estrov Z, Kantarjian HM (1999) Chronic myelogenous leukemia: biology and therapy. Ann Intern Med 131:207 – 219
47. Thijsen S, Schuurhuis G, van Oostveen J, Ossenkoppele G (1999) Chronic myeloid leukemia from basics to bedside. Leukemia 13:1646 – 1674
48. Underwood JCE (2000) General and systemic pathology, 3th edn. Churchill Livingstone, London
49. Stevens A, Lowe JS (2000) Pathology, 2nd edn. Mosby, London
50. Derynck R, Akhurst RJ, Balmain A (2001) TGF-beta signaling in tumor suppression and cancer progression. Nat Genet 29:117 – 129
51. Eisenhauer EA (2001) From the molecule to the clinic – inhibiting HER2 to treat breast cancer. N Engl J Med 344:841 – 842
52. Harari D, Yarden Y (2001) Molecular mechanisms underlying ErbB2/HER2 action in breast cancer. Oncogene 19:6102 – 6114
53. Knudson AG Jr (1971) Mutation and cancer: statistical study of retinoblastoma. Proc Natl Acad Sci U S A 68:820 – 823
54. Stanbridge EJ (1976) Suppression of malignancy in human cells. Nature 4:17 – 20
55. Weinberg RA (1991) Tumor suppressor genes. Science 22:1138 – 1146
56. DeMars R (1970) Fundamental cancer research, 23rd annual symposium. Williams and Wilkins, Baltimore
57. Zheng L, Lee WH (2001) The retinoblastoma gene: a prototypic and multifunctional tumor suppressor. Exp Cell Res 264:2 – 18
58. Kirsch DG, Kastan MB (1998) Tumor-suppressor p53: implications for tumor development and prognosis. J Clin Oncol 16:3158 – 3168
59. Liggett WH Jr, Sidransky D (1998) Role of the p16 tumor suppressor gene in cancer. J Clin Oncol 16:1197 – 1206
60. Fearnhead NS, Britton MP, Bodmer WF (2001) The ABC of APC. Hum Mol Genet 10:721 – 733
61. Reed JC (1999) Dysregulation of apoptosis in cancer. J Clin Oncol 17:2941 – 2953
62. Eichhorst ST, Krammer PH (2001) Derangement of apoptosis in cancer. Lancet 4:345 – 346
63. Adams JM, Cory S (2001) Life-or-death decisions by the Bcl-2 protein family. Trends Biochem Sci 26:61 – 66

64. Baldi A, Santini D, Russo P, Catricala C, Amantea A, Picardo M, Tatangelo F, Botti G, Dragonetti E, Murace R, Tonini G, Natali PG, Baldi F, Paggi MG (2004) Analysis of APAF-1 expression in human cutaneous melanoma progression. Exp Dermatol 13:93 – 97
65. Dai DL, Martinka M, Bush JA, Li G (2004) Reduced Apaf-1 expression in human cutaneous melanomas. Br J Cancer 91:1089 – 1095
66. Fujimoto A, Takeuchi H, Taback B, Hsueh EC, Elashoff D, Morton DL, Hoon DS (2004) Allelic imbalance of 12q22 – 23 associated with APAF-1 locus correlates with poor disease outcome in cutaneous melanoma. Cancer Res 64:2245 – 2250
67. Soengas MS, Capodieci P, Polsky D, Mora J, Esteller M, Opitz-Araya X, McCombie R, Herman JG, Gerald WL, Lazebnik YA, Cordon-Cardo C, Lowe SW (2001) Inactivation of the apoptosis effector Apaf-1 in malignant melanoma. Nature 11:207 – 211
68. Hosokawa Y (2005) Anti-apoptotic action of API2-MALT1 fusion protein involved in t(11;18)(q21;q21) MALT lymphoma. Apoptosis 10:25 – 34
69. Blackwood MA, Weber BL (1998) BRCA1 and BRCA2: from molecular genetics to clinical medicine. J Clin Oncol 16:1969 – 1977
70. Miki Y, Swensen J, Shattuck-Eidens D, Futreal PA, Harshman K, Tavtigian S, Liu Q, Cochran C, Bennett LM, Ding W, et al (1994) A strong candidate for the breast and ovarian cancer susceptibility gene BRCA1. Science 7:66 – 71
71. Newman B, Austin MA, Lee M, King MC (1988) Inheritance of human breast cancer: evidence for autosomal dominant transmission in high-risk families. Proc Natl Acad Sci U S A 85:3044 – 3048
72. Williams WR, Anderson DE (1984) Genetic epidemiology of breast cancer: segregation analysis of 200 Danish pedigrees. Genet Epidemiol 1:7 – 20

12 Basis of Tumor Imaging 2: Scintigraphic and Pathophysiologic Correlation

Suman Jana, Hussein M. Abdel-Dayem

12.1 Introduction

The enormous progress made in molecular biology, molecular genetics, and targeted drug design in the twentieth century has led to dramatic advances in understanding the biology of cancer and the detection of many genetic abnormalities responsible for the initiation and progression of cancer. This progress is also responsible for the development of new molecular strategies in cancer treatment including gene therapy [1, 2]. These revolutionary advances have led to an increasing awareness of the importance of the role of imaging, the only noninvasive method to detect the extent of cancer and detect how it responds to a newer treatment modality. Cancer imaging is an increasing component of the general workload of the radiology and nuclear medicine departments in the 21st century. These demands largely result from the increasing incidence of many cancers in a growing geriatric population and the aggressive approach to therapy that places huge demands on imaging resources. Although the overall 5-year survival rate for cancer remains at approximately 40% in the Western world, many patients are achieving a sustained remission with multi-modality therapy in many different tumors, and in some cancers such as testicular cancer and lymphoma, dramatic improvements in survival have been achieved [3].

To keep pace with the developments in oncology, major developments have taken place in nuclear medicine (in instrumentation and in radiopharmaceuticals) as well as other competitive imaging modalities. During the past few years there have been periods of enthusiasm for nuclear medicine physicians and other times of concern over competition with other imaging modalities. In the past 10 years four major developments have given a bright future to nuclear oncology [4–8]. These have come in response to the powerful effect that fluorine-18 fluorodeoxyglucose (FDG) has been shown to have in the management of patients with various malignant diseases. The first and the most important of these developments was the approval by the Food and Drug Administration (FDA) in the United States of the regulations for production and distribution of fluorine-18 FDG commercially. F-18 FDG has a half-life of 110 min. Doses of F-18 FDG could be delivered to application sites within 2–3 h of delivery time from the production site. The second development was the recognition by the FDA of the important role of F-18 FDG in the management of cancer patients. Subsequently, in January 1998, the Health Care Finance Administration (HCFA) approved reimbursement for F-18 FDG PET studies for patients with primary pulmonary nodules for the purpose of differentiating benign from malignant disease and for staging of malignant lung disease. This was followed in April 1999 by the second approval for reimbursement for the purposes of evaluating patients with Hodgkin's and non-Hodgkin's malignant lymphoma (replacing gallium-67 citrate scans), recurrent colorectal cancer, and recurrent malignant melanoma. Thereafter, head and neck cancer in September 2000, esophageal cancer in July 2001, breast cancer in October 2002, carcinoma with unknown primary in March 2003, thyroid cancer in December 2003, and recently in February 2005 cervical carcinoma were included in this list for reimbursement. It is likely that in the coming years there will be inclusion of more and more cancers. As a result of these approvals, not only is FDG PET now used as a clinical tool rather than a re-

search tool but also there is a new enthusiasm for the development of F-18 label PET tracers so that in the near future it can be used like FDG. A few examples of such tracers are ^{18}F-fluoride to evaluate bone, ^{18}F-fluorodeoxythymidine to measure cell proliferation (DNA synthesis), ^{18}F-fluoro-l-tyrosine to assess the rate of protein synthesis, ^{18}F-fluoromisonidazole (^{18}F-FMISO) to assess tumor hypoxia and ^{18}F-fluorocholine to assess the rate of cell proliferation (cell membrane synthesis) [9]. The concept of a PET isotope that could be delivered to a PET imaging center not possessing a cyclotron led to the development of ^{62}Cu (generator produced, 9.74 min half-life)-labeled ligands for imaging and possible therapy with ^{64}Cu (12.7 h half life)-labeled ligands, which can also be delivered. The third important development was the introduction of multifunctional gamma cameras that are capable of performing the routine and common single photon nuclear medicine studies including SPECT and coincidence positron emission tomography (PET). The FDA approved this technology, and the HCFA does not differentiate for the purpose of reimbursement between F-18 FDG PET studies acquired by using dedicated PET systems or multifunctional gamma cameras. This third development led to a more widespread use of F-18 FDG PET imaging; this system can potentially play a very important role in small community hospitals of developing countries [10]. However, this will require strict guidelines for operating the systems and specific quality control recommendations in order to produce higher quality images compared with dedicated PET systems. Currently with the decreasing prices of PET systems, the need for higher accuracy and short acquisition time and the relatively new lower reimbursement for these systems, most of the commercial industrial companies have stopped producing these systems. The fourth important development was the introduction of PET/CT scanners that are capable of performing PET scans and high resolution X-ray computed tomography (CT). This scanner provides the best possible image-fusion technique and, therefore, an image with combined anatomy and physiology. PET/CT studies allow for the first time a direct comparison between functional and morphological changes, both acquired in the same setting within a few minutes from each other. Currently, oncology is one of the main clinical indications for combined morphologic and functional imaging [11, 12]. Abnormal uptake of radiopharmaceutical in the presence of an abnormal CT finding increases the confidence in interpreting both studies and differentiating pathological from physiological F-18 FDG uptake [13]. One of the advantages is that if an abnormal uptake can be localized by CT to one of the sites of physiologic distribution of radiopharmaceutical, then it not only excludes the disease but also saves the further cost of investigation or possible treatment by mistake. The immense potential of this technology has not been fully realized and at this time data is accumulating in the literature to prove its value. However, in the coming decade we will realize its impact much more.

It is expected that nuclear oncology will grow at a rate of more than 10% annually in the coming decade of the 21st century. Further, it is believed that in next decade not only F-18 FDG will continue to play an important and more extended role in oncology, but also other F-18-labeled PET tracers will be available commercially similar to FDG. ^{67}Ga citrate, ^{201}Tl chloride, and ^{99m}Tc-sestamibi and similar compounds for the purpose of tumor imaging will be used only in those hospitals that have no access to a PET imaging facility (dedicated or multifunctional system). It is worth mentioning here that in the case of pediatric imaging FDG is under evaluation and due to the lack of dedicated pediatric PET units, ^{201}Tl chloride, ^{67}Ga citrate, and ^{99m}Tc-sestamibi in conjunction with ^{111}In-octreotide, and ^{131}I- or ^{123}I-MIBG still play a major role in pediatric oncology [14–16]. In the coming years PET/CT will play a major role in the management of cancer patients. During last 2 years in the US, 90% of newly purchased systems have been PET/CT rather than dedicated PET scanners.

The objective of this chapter is to assess the clinical realities related to the objectives of the pathological diagnosis and staging of primary tumors, predicting treatment response and drug resistance, radiotherapy planning, evaluation of treatment response and differentiation of recurrent tumor or metastatic disease from postoperative changes, fibrosis, and/or necrosis. General guidelines for the clinical role of nuclear medicine in the management of patients with malignant tumors are also presented. Any chapter on tumor imaging will be incomplete without a mention of PET/CT and image fusion; this modality has the potential to play a very important role in the near future in the management of cancer patients particularly in radiotherapy planning.

12.2 Uptake Mechanisms of Tumor-Avid Radiopharmaceuticals

There are similarities and differences in the mechanisms of uptake of all the radiopharmaceuticals currently used for tumor imaging; these should be recognized by the physicians. The choice of radiopharmaceutical depends on the location, pathology, and availability of the radiopharmaceutical and the equipment used. Gallium-67 citrate is still more commonly used in centers where a PET service is not available than any other tumor imaging agent in spite of its poor physical characteristics, relatively poor sensitivity, and lack of specificity. This is due primarily to its lower cost and long half-life of 3 days, which makes it suitable for

worldwide delivery. Today, those centers that have access to F-18 FDG PET imaging do not recommend ^{67}Ga citrate studies for tumor imaging, but it is still used for infection localization.

The choice between ^{201}Tl-chloride, ^{99m}Tc-sestamibi, and F-18 FDG is a matter of controversy. Although PET offers better resolution and its biodistribution is better than that of ^{201}Tl-chloride or ^{99m}Tc-sestamibi, it might not be as good as ^{201}Tl-chloride for follow-up of a patient who has been previously treated for intracranial malignant lesions. This is primarily due to the normally high FDG uptake in the normal cerebral cortex [9]. ^{201}Tl-chloride has the advantage of no uptake in the normal brain tissue and very low uptake in the choroid plexus and the pituitary gland. This feature makes ^{201}Tl-chloride the agent of choice in spite of its poor resolution compared with F-18 FDG or ^{99m}Tc-sestamibi. The latter has more intense uptake in the choroid plexus and pituitary gland [9]. The use of F-18-FDG for intracranial tumor imaging always requires image registration with MRI for increased accuracy of the reading of the studies.

The mechanisms of uptake of the various radiopharmaceuticals have similarities and differences. However, most radiopharmaceuticals share an important characteristic, which is that the intensity of the uptake reflects the viability of the cells in the involved lesion. ^{201}Tl-chloride has a mechanism of uptake in the cell related to the sodium pump, ATP-ase activity, angiogenesis, and ill-formed and well-formed new blood vessels [17–19]. ^{99m}Tc-sestamibi uptake is related to the electrical gradient difference across the cell membrane and mitochondrial uptake. Retention of this radiopharmaceutical inside the cell, on the other hand, is thought to be inversely proportional to the multidrug resistance of its glycoprotein content and its activation in the cell [20–26]. ^{99m}Tc-tetrofosium or ^{99m}Tc-Q-12 have similar mechanisms, except that they are more affected by the multidrug resistance activity in the cell. They are characterized by faster washout in the delayed images, which might make delayed imaging impossible. ^{67}Ga citrate uptake is slightly more complicated. It is trapped on the transferrin or lactoferrin receptors, then passes through the cytoplasm intracellularly [27–29]. Therefore, when transferrin-binding sites in the plasma are saturated by iron, gallium stays in free form in plasma; it will not bind to the transferrin and will not pass across the cell membrane. As a result in these conditions of transferrin saturation, ^{67}Ga citrate uptake will be less sensitive for detection of inflammatory and malignant disease. Background activity will be high and the quality of the scan will be poor.

F-18 FDG uptake in the cell is related to several glucose transporters in the cell membrane which allow active F-18 FDG passage across the membrane to the cytoplasm and trapping without further metabolization. The transport of glucose into a cell is mediated by a family of structurally related glucose transporter proteins [30]. One of the biochemical characteristics of malignant cells is an enhanced rate of glucose metabolism due to an increased number of these cell surface glucose transporter proteins (such as Glut-1 and Glut-3) and increased intracellular enzyme levels of hexokinase and phosphofructokinase which promote glycolysis [31–33]. This enhanced glycolytic rate of malignant cells facilitates their detection utilizing FDG PET imaging. The most common glucose transport protein overexpressed on the tumor cell membranes is Glut-1, which is insulin independent [34]. In-vitro studies have shown that FDG uptake is also determined by the number of viable tumor cells within a lesion (tumor-cell density) [32, 34]. Nontumoral tissue such as necrotic and fibrotic tissue may reduce tracer uptake [32]. Increased cell proliferation in tumors (assessed by the mitotic rate) also results in increased glucose utilization [34]. Tumor hypoxia will also increase FDG uptake through hypoxia-inducible factor-1-alpha that upregulates Glut-1 receptors [34]. In summary, FDG accumulation within a tumor is likely related to a complex interaction between the cellular energy demand and the tumoral microenvironment [35]. Once inside the cell, FDG is phosphorylated by hexokinase into FDG-6-phosphate. FDG-6-phosphate does not enter into further metabolism and accumulates intracellularly [31]. Decreased levels of glucose-6-phosphatase (an enzyme which metabolizes FDG-6-phosphate back to FDG) within tumor cells compared to normal cells permit longer intracellular retention of FDG-6-phosphate [36]. The signal derived from tumors represents an average of the FDG uptake throughout the lesion [32].

^{18}F-Fluoride is a bone imaging agent used for PET [37]. After diffusing into the extracellular fluid of bone, the fluoride ion is exchanged for a hydroxyl group in the bone crystal and forms fluoroapatite, which then deposits on the bone surface [37]. Uptake of the fluoride ion is twofold higher than that of ^{99m}Tc-polyphosphonates and there is faster blood clearance (resulting in a better target-to-background ratio) [37]. The spatial resolution of ^{18}F-fluoride is also superior to standard bone scanning [37]. ^{18}F-Fluoride is very sensitive for the detection of both lytic and sclerotic bone lesions; however, benign bone lesions (degenerative change, fractures, Paget's disease, enchondroma, and osteoma) will also demonstrate increased tracer uptake [37]. Improved specificity is seen when the ^{18}F-fluoride scan is interpreted with a fused CT exam [37].

^{18}F-fluorodeoxythymidine (^{18}F-FLT) is an amino acid agent labeled with ^{18}F that can be used to measure tumor cell proliferation [38, 39]. The agent is transported into the cell by the same nucleoside carrier as thymidine [40]. The agent is then phosphorylated within the cell by thymidine kinase-1 (TK_1), which is upregulated

in rapidly dividing tumor cells (thymidine kinase activity is a marker of cellular proliferation) [38, 41]. Because ^{18}F-fluorodeoxythymidine is resistant to catabolism by thymidine phosphorylase, there is prolonged intracellular retention of the agent [38].

^{11}C-choline (^{11}C-CHOL) is an agent that is incorporated into tumor cells by conversion into ^{11}C-phosphorlycholine, which is trapped inside the cell. This is followed by synthesis of ^{11}C-phosphatidylcholine, which constitutes a main component of cell membranes [42]. Because tumor cells duplicate very quickly, the biosynthesis of cell membranes is also very fast and there is increased uptake of choline and upregulation of the enzyme choline kinase [42]. Essentially, the uptake of ^{11}C-CHOL in tumors represents the rate of tumor cell proliferation [43]. ^{11}C-CHOL is very rapidly cleared from the blood, and optimal tumor-to-background contrast is reached within 5 min [42, 44].

Hypoxic cells are more resistant to radiation therapy and therefore require additional radiation to achieve adequate cell killing, which might exceed the tolerance of the surrounding normal tissues, called the tumor bed [45, 46]. ^{18}F-fluoromisonidazole (^{18}F-FMISO) acts as a bioreceptor molecule and is incorporated into cell constituents under hypoxic conditions [45]. Unfortunately, there is slow cellular uptake and slow washout from nonhypoxic tissues, which limit the effectiveness of this agent [45]. ^{62}Cu-ATSM is another tumor hypoxia agent, which accumulates in hypoxic tissues, where it is reduced, trapped, and has the advantage of rapid clearance from nonhypoxic tissue [45, 46].

Another important area of current interest, which goes hand in hand with hypoxia, is angiogenesis. Inhibition of angiogenesis is a current target for the development of new anti-cancer medication against the solid tumors. The alpha(v)beta3 integrin is an important cell adhesion receptor involved in tumor-induced angiogenesis and tumor metastases. The RGD-containing glycopeptide cyclo(-Arg-Gly-Asp-d-Phe-Lys(sugar amino acid)-) with 4-nitrophenyl 2-[^{18}F]fluoropropionate has been studied in vitro as well as in tumor mouse models (xenotransplanted human tumors on nude mouse) [47, 48]. These studies suggested that this F-18-labeled compound is suitable for noninvasive PET imaging of angiogenesis status of a tumor and subsequent monitoring of treatment response, especially when the primary target of the therapy was angiogenesis.

Cell transplantation has evolved from transfusional medicine, using blood and other products derived from the human body, toward a highly technical, clinical grade approach using thoroughly controlled human cells [49, 50]. The cell therapy concept originated in diseases associated with loss of cell, which cannot divide to make up the loss (i.e., loss of dopamine secreting cells in Parkinson's disease, loss of insulin secreting cells in type-I diabetes). Stem cells are defined as undifferentiated, pluripotent cells with prolonged self-renewal capacity and the ability to proliferate extensively [50]. Stem cells can be derived from fetal tissue, bone marrow, olfactory area of brain, and skin of adults. Moreover, stem cells can differentiate into the lost cell type that is able to produce the substance of desire, such as dopamine in Parkinson's disease or insulin in type-I diabetes. Recently, stem cell transplantation has been gaining popularity in oncology. Though oncology deals with the problem of excessive unwanted cells at the beginning, the major limiting factor for aggressive chemo-radiotherapy is loss of normal cells, and stem cell transplantation can potentially broaden the horizon of very high dose chemo-radiotherapy. In aggressive lymphoma it is now a commonly used modality in conjunction with high dose chemo-radiotherapy. During this process the patient's own normal hemopoietic stem cells are collected and harvested before high dose chemo-radiotherapy, which literally kills most of the hemopoietic cells along with cancer cells, and subsequently harvested cells are transfused to the patient to repopulate the bone marrow to produce normal blood cells. The concept of cell therapy is now being introduced for solid tumors (still experimental), one such hypothetical example being inoperable hepatocellular cancer. Normal liver cells can be collected and harvested before very high dose radiotherapy to the liver to kill all normal and cancer cells followed by intraportal vein infusion of harvested normal liver cell to repopulate the liver [51]. The success of cell/stem cell therapy depends on localization of the transfused cells to the required position, survival of these cells at this location, proliferation of cells and then differentiation to the appropriate cell line (if required) to function as lost cells. Therefore, transplanted cells need to be followed to evaluate their anatomic position (tracking), proliferation and functional status.

Reporter gene labeling is a common concept in cell tracking [52]. Most commonly used genes are coding regions for alkaline phosphatase, firefly luciferase, and chloramphenicol acetyltransferase. The corresponding gene product (a protein) can metabolize a substrate into a detectable product (a color, fluorescence, or chemical). Hence, the reporter gene label enables cell detection by an assay [52]. The great disadvantage of these tracking methods is the requirement of a biopsy or even animal sacrifice for the performance of cell tracking. Several methods have been developed to track transplanted cells/stem cells in vivo. Iron oxide-labeled cells (for MRI) [53], fluorescently labeled cells (for optical imaging), and combinations of these techniques [54] were demonstrated to be feasible for cell tracking in the host. MRI has the advantage over fluorescent methods of its ability to be used in humans and larger animals. However, disadvantages are the low sensitivity and the limited number of probes available [55]. In

contrast, methods using radioisotopes combine both the opportunity of imaging humans and larger animals with a larger sensitivity. Radioactively labeled cells can serve as a tool to track the fate of the transplanted cells noninvasively and therefore hold future promise. One such example is In-111-labeled cells [56, 57]. Once the anatomic position of the transplanted cells is known the next question is to determine the functionality of those cells. A variety of methods has been and still is to be developed or has to be adapted for cell functionality assessment. ^{99m}Tc-sestamibi imaging for cardiac metabolic function can be adapted as a functional test for transplanted stem cells for the imaging of cardiac cell function [58]. These can theoretically be used in combination with the tracking methods to evaluate the anatomy of the transplant in relation to its function.

All chemotherapeutic agents and radiation therapies induce programmed cell death called apoptosis. Detection of apoptosis by noninvasive imaging is another interesting area [59]. Annexin V, an endogenous protein labeled with technetium-99m, has led the way to the detection of apoptosis [60]. The mechanism of Tc-99m-annexin uptake is through its binding with phosphatidylserine, which is normally present in the inner aspect of a normal cell membrane becoming externalized during the process of apoptosis [61]. Labeling annexin V with F-18 has been reported [62, 63]. The capability of PET to provide better quantification may further increase the utility of this promising method in the near future and may provide a greater insight into the therapeutic response in patients with cancer [59].

Advances in molecular genetics have made it possible to introduce gene therapy as a treatment option in the near future in conjunction with other treatment modalities in cancer patients. The success of gene therapy depends on several steps like delivery of the gene to the targeted tumor cells, then the gene needs to be incorporated into the native gene of the tumor cells and afterwards the delivered gene should get translated into a final product. The difficulties faced during gene therapy are: (1) variability of uptake of the gene of interest by the targeted cells, (2) uncertainty of incorporation of this gene to the native gene, and (3) variable expression of this gene after incorporation. A noninvasive imaging modality to identify and quantify the extent of success of these steps of gene therapy is essential to the implemention of gene therapy in clinical practice for cancer patients. Currently, PET gene therapy imaging studies with radio-labeled probes use *HSV1-tk* as the reporter gene [64–66] and other several PET tracers, which are analogues of uracil and thymidine, are being developed [67, 68].

Also affecting tumor uptake of the radiopharmaceutical compounds are the tumor-proliferating factors. High mitosis is one of the characteristics of malignant tumors which is unusual for benign lesions. It can be determined by flow cytometry. It provides an indicator of the ratio of tumor undifferentiation and of prognosis. There is a relationship between tumor undifferentiation and prognosis; i.e., tumors with a low grade of mitosis have a better prognosis [69]. It is essential to understand the cell cycle and the various proteins and other factors associated with cell proliferation and the various immunohistochemical staining techniques used to identify them. Analysis of precursors of DNA, RNA, or proteins by autoradiography yields valuable information for a greater understanding of the cell cycle. The use of ^{3}H- and ^{14}C-thymidine can distinguish the cells in the G0 noncyclic phase from the cells in the reproductive phase. Accordingly, the tumor growth factor can be determined. Proteins in the cell cycle can be divided into those that have regulatory proteins such as oncogenes, anti-oncogene products, signal transduction messengers, and protein kinases. Other proteins are constituents of cell replication but have no apparent regulatory function such as peptides and other structural proteins [70–74]. Antibodies against many of these proteins are now commercially available and can be identified by immunohistochemical straining. Ki-67 and proliferating cell nuclear antigen (PCNA) are both indicators of the number of cells in mitosis [75, 76].

Ki-67 is the most widely recognized marker of proliferating cells [75]. The antigen detected by this antibody is localized primarily in the nuclei and is present only in proliferating cells. Its content increases during S and G2 phases. It is degraded after mitosis and is not detected in G0 resting cells. Accordingly, the fraction of proliferating cells in tumors can be estimated based on the percentage of cells labeled with Ki-67 antibody. This technique has minor problems, which prevent its use as an accurate estimate of the growth fraction. However, it is easier than other techniques, such as flow cytometry.

Proliferating cell nuclear antigen is an S-phase-specific nuclear protein which has led to a better understanding of cell kinetic measurement [76]. Its intracellular accumulation is not necessarily dependent on DNA synthesis. Cells in G1–S phase continue to produce PCNA at high levels. Pharmacological inhibition of DNA synthesis does not depress the synthesis of PCNA. It accumulates in a punctate dispersion pattern within the neoplasm, except in the nucleoli in the early S phase, independent of DNA synthesis. In mid S phase, DNA synthesis is a dependent event. It dissipates with a half-life of approximately 20 h, so that by the G2 phase it is present only in trace amounts. PCNA scoring in axillary nodes in breast cancer, for example, is potentially valuable as an indicator for prognosis; i.e., higher PCNA scores are associated with shorter disease-free survival and overall shorter survival [77, 78].

Apoptosis is a process of cell death, which occurs when the signal for cell cycle progression is aborted. It

occurs through a sequence of events programmed within the cell, which when triggered will eventually lead to cell death [79]. It complements mitosis in regulating the cell during development and in the self-renewal of the tissues. Differences between apoptosis and cell division control tumor growth. The in-depth study of this phenomenon could be the basis for future cancer diagnosis and therapy. The *Bcl-2* oncogene was found in experimental systems to extend cellular viability by blocking programmed cell death. Several other oncogenes that are also involved in viability and apoptosis are capable of reading anti-apoptotic signals. The expression of *Bcl-2* can render tumor cells resistant to a number of physical and chemical agents that normally act to involve apoptosis.

Angiogenesis is the process of formation of new blood vessels and is essential for tumor growth and proliferation. It is triggered by soluble factors that induce motility, proteolysis, and growth. The endothelial cells living in the parent vessel are stimulated, leading to degradation of the endothelial basement membrane. This is followed by migration into the perivascular stroma, initiating new capillary growth associated with degradation and lysis of the extracellular matrix in a manner similar to the cancer cells during their invasion of the extracellular matrix [80]. These newly formed capillary sprouts expand and assume the tubular structure. Endothelial proliferation is responsible for the microvascular tubules that develop into loops and subsequently into a functioning circulatory network. Stimulated endothelial cells can produce degradative proteinases such as type IV collagenase and other members of the matrix metalloproteinase family. The balance between proteinases and inhibitors regulates the morphology of the capillary tubules. There is a relationship between the number of microvessels formed and the incidence of metastasis in breast cancer. Therefore, patients with a high rate of angiogenesis could be selected for more aggressive therapy [77, 78].

Omar et al. as well as other groups have previously reported that when benign lesions were compared with malignant lesions in breast cancer all benign lesions had well-formed blood vessels while grade III malignant tumors had ill-formed blood vessels [69]. The latter were associated with ill-formed blood vessels in 100% of the cases, while 83% of benign lesions had well-formed blood vessels. All patients who had high ^{201}Tl-chloride retention or build-up also showed a high percentage of ill-formed blood vessels. In the study by Omar et al. Ki-67 and S-phase specific PCNA antibodies were looked at in benign and malignant breast lesions. All cases with negative washout, i.e., build-up activity, had high-density staining for both Ki-67 (all cells in mitosis) and PCNA (cells in specific S-phase), indicating a high mitotic rate. All these cases involved grade II or III lesions. Omar et al. concluded that ^{201}Tl-chloride could be a reliable method for detecting high-grade malignant tumors by measuring the washout index; however, this needs further verification.

When Omar et al. looked at *Bcl-2*, which produces cell anti-apoptotic signals to prevent programmed cell death, no definite conclusion could be reached, and they did not find a significant correlation between *Bcl-2* expression and ^{201}Tl chloride or ^{99m}Tc-Sesta-MIBI uptake in breast tumors. *Bcl-2* is not fully understood and requires more work.

In summary, benign lesions had a low rate of mitosis as reflected by *Ki-67* and *PCNA* expression, a low percentage of ill-formed blood vessels, moderate *Bcl-2* expression, and a high percentage of well-formed blood vessels. Malignant lesions are characterized by a high rate of mitosis, a high percentage of ill-formed blood vessels, and a low percentage of well-formed blood vessels which is more evident in grade-III lesions.

12.3 Objectives of Tumor Imaging

The following questions are usually faced in clinical practice by both the medical and the surgical oncologist. Undiagnosed lesions must be established as benign or malignant. For diagnosed malignant lesions accurate staging is very important to decide which treatment is most useful to the patient. Additional information is required regarding (a) the grade of differentiation, (b) prediction of prognosis and prediction of treatment response, (c) defining Planning Target Volume (PTV) for radiotherapy, (d) evaluation of preoperative chemo- and/or radiotherapy response, (e) early recognition of local recurrence following surgical treatment, and (f) differentiation of local recurrence from fibrosis and/or necrosis. We will discuss the role of nuclear medicine in these various indications.

12.4 Differentiation of Benign from Malignant Disease

Early diagnosis provides the best chance for cure. Histopathology is the gold standard to differentiate between benign and malignant lesion. Therefore, if any tumor is superficial or accessible for any form of biopsy, biopsy should be the next investigation of choice if not contraindicated rather than wasting time and money on imaging. Various imaging modalities play a role in tumors which are not accessible easily for biopsy, or there is a high chance of sampling error (i.e., for deep seated lesions a needle may sample an area which is not involved by tumor or already necrosed), or when needle biopsy is associated with serious consequences

(e.g., adrenal tumor if pheochromocytoma can precipitate acute crisis, and highly vascular tumor can bleed which could be difficult to control). The goal of an imaging modality is to identify a pathological process correctly noninvasively at the earliest, so that curative treatment (most often surgery) can be offered. Since the late 1970s tremendous developments in molecular biology and genetics have provided medical science with an unprecedented chance to understand the molecular basis of disease. Disease can now be defined on the basis of abnormal deviation from normal regional biochemistry. Molecular derangement occurs at the very beginning of the disease process, and the final result of anatomically detectable abnormalities occurs much later [81].

CT, the most frequently used imaging modality, relies on the differentiation between benign and malignant lesions on the basis of certain criteria involving the size of the lesion and the interval increase in size over a short period of time detected by repeated imaging, the regular/irregular margins of the lesion, the presence of capsular demarcation, the heterogeneity, and the presence of microcalcification [82–86]. Similar criteria are used in mammography for breast cancer screening [87, 88]. All these parameters are nonspecific, and too many patients are therefore sent for unnecessary biopsy [89–93].

On the other hand, functional imaging is unique in that it can provide unperturbed physiologic information. It usually uses a molecular probe for imaging. The probe could be already existing in the tumor, like MR spectroscopy, to detect concentration of ATP/ADP, thereby measuring tumor energy metabolism in a tissue by imaging the ^{31}P of ATP/ADP [81]. The probe can be introduced from outside like F-18 FDG for PET scanning to measure the glucose metabolism in tissue. In this case the administered quantity is so small (< 10 μg) that while portraying the pathway of interest, it leaves that pathway completely intact [81].

Nuclear medicine radiopharmaceuticals used for the differentiation of benign from malignant lesions include gallium-67 citrate, thallium-201 chloride, ^{99m}Tc-sestamibi; more recently, fluorine-18 fluorodeoxyglucose (FDG) has been approved for routine use [94]. PET imaging using F-18 FDG will eventually replace all other single photon emission radiopharmaceuticals because of its more favorable body distribution and higher resolution [10]. There has been interest in reducing the number of unnecessary biopsies performed by using nuclear medicine imaging procedures. For such procedures sensitivity as high as 97% is not enough to substantiate biopsy. The clinical reality is that from any test a negative predictive value of 100% is needed in order to replace biopsy. Having a false-positive nuclear medicine study is not a major disadvantage. It is like a false alarm. It would not prevent the patient from having the proper biopsy. Dual acquisition using early and delayed imaging with quantitation using thallium-201, ^{99m}Tc-MIBI and PET-FDG as well as the use of image fusion or a combined modality such as PET/CT helps further decrease the false-positive results. Its disadvantage is the addition of unnecessary costs, social and psychological impact and exposure to unnecessary radiation of the patients. The real and major problem has always been the false-negative tests. The sensitivity of any nuclear medicine procedure depends on the size of the lesion, the intensity of uptake, and the target-to-nontarget ratio. These are dependent on the resolution and the sensitivity of current nuclear medicine imaging systems. At the present time the resolution of single photon-emission tomography studies for ^{67}Ga-citrate, ^{201}Tl-chloride, or ^{99m}Tc-sestamibi is somewhere between 8 and 12 mm. Currently the best possible resolution of positron-emission tomography systems for imaging patients is between 4 and 7 mm. In order to successfully detect a lesion with 100% accuracy its size has to be at least two times the resolution of the imaging systems, because of the partial volume effect. For a primary lung nodule less than 1 cm, the likelihood that this nodule be detected by SPECT radiopharmaceuticals is much lower than if it is being imaged by F-18 FDG PET radiopharmaceutical. However, if the lesions are more than 1.0 cm, the likelihood that this lesion would be missed by using single photon imaging radiopharmaceuticals still exists, while the chance of being detected by a F-18 FDG PET study is very high (Fig. 12.1). This is an important issue to consider when dealing with patients with primary malignant tumors whether they are in the lungs, the breast, or other parts of the body. If the size of the lesion is below the resolution of the imaging systems, we should not avoid biopsy, relying only on a negative nuclear medicine study. In this case we will be missing the chance of an early diagnosis and early treatment. If the size of the lesions is more than two times the resolution of the systems (particularly when SUV is used) and the nuclear medicine study is negative, then it might be safe in certain diseases to give the patient the choice of either undergoing biopsy or staying under follow-up. Often, a CT scan will leave doubt as to whether a solitary pulmonary nodule (SPN) is benign or malignant. Institutions differ in their approach to SPNs: some will surgically remove such lesions; others may sample them, or monitor them over time. One ideal use of F-18 FDG PET would be to avoid an invasive sampling procedure/lesion removal, if PET could confirm that a lesion is benign, in a patient with low risk for cancer. Hence, PET's negative predictive value (NPV) is of paramount importance. When the prior probability is low, such as in young patients with no history of smoking, then the NPV of F-18 FDG PET is quite high. At a prevalence of lung cancer of 20%, the NPV of F-18 FDG PET is over 98% [95]. Cur-

rently, FDG-PET has been approved for evaluating solitary pulmonary nodule to determine the likelihood of cancer in this nodule before any intervention and has not been approved to evaluate any other tumors for similar purposes.

In PET studies standardized uptake value (SUV) is used to determine if a lesion has increased FDG activity. The SUV normalizes the amount of FDG accumulation in a region of interest (ROI) to the total injected dose and the patient's body weight. It provides a means of comparison of FDG uptake between patients [96]. An SUV greater than 2.5 has been reported to be sensitive and specific for malignant lesions [97]. Visual analysis also been shown to be effective in differentiating benign from malignant lesions [97, 98]. An uptake of more than blood pool activity indicates a malignant lesion [98]. Visual analysis may be more sensitive for nodules smaller than 1.5 cm in size as the partial volume effect will falsely decrease the SUV (however, the improved sensitivity comes at a decreased specificity) [98]. In a prospective multicenter study for the evaluation of pulmonary nodules (>7 mm) when CT findings were indeterminate for malignancy, FDG PET had a sensitivity of 92% and a specificity of 90% using SUV data [98]. Visual analysis of the images demonstrated a sensitivity of 98%, but a lower specificity of 69% [98]. Problems with calculating SUV values in small lesions have been solved by newer software programs that cal-

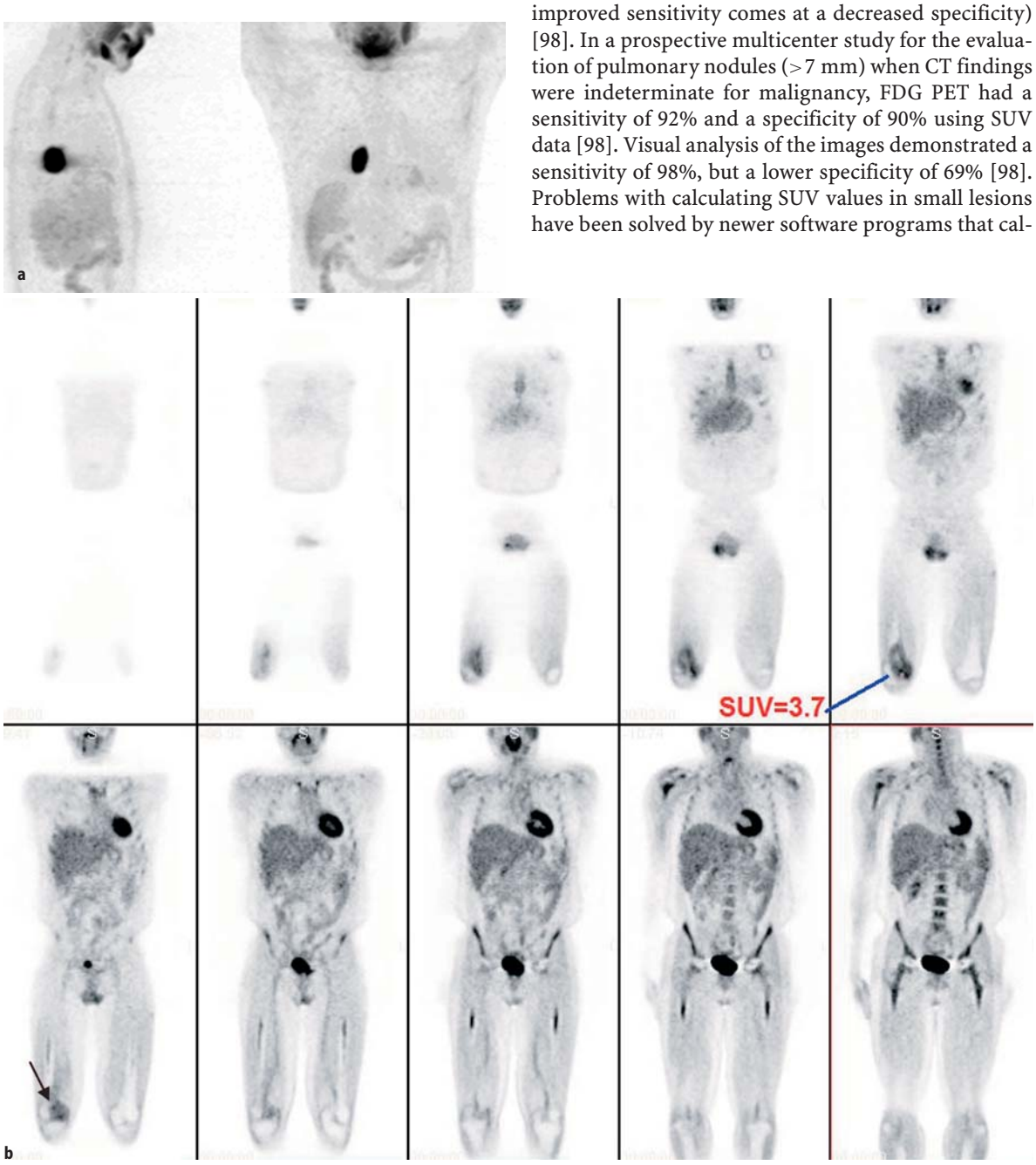

Fig. 12.1. Examples of F-18 FDG uptake by two malignant tumors. **a** An FDG PET image of a patient showing intense uptake of a right lower lobe lung tumor (NSCLC). **b** F-18 FDG study of a patient with osteogenic sarcoma of the right distal femur (*arrow*)

culate the SUV automatically, drawing the margins in three dimensions and the volume of the lesion, and changing the drawing edge calculated as a percentage, usually 20% – 30% from the maximum tumor uptake.

A lesion that presents high SUV values on PET study should be considered malignant until proven otherwise. A lesion that is PET negative has a low probability for being a malignancy (under 5% [99]). However, one must consider all characteristics of a lesion prior to discounting its malignant potential. Follow-up exams with CT should be performed on PET negative nodules to ensure stability [99]. If the lesion grows, further evaluation with tissue diagnosis should be obtained [99]. Patients who have a negative FDG PET exam but are subsequently shown to have lung cancer may have an overall better survival compared to patients with positive FDG exams [100]. However, SUV criteria to diagnose malignancy should be used very cautiously, as there are several factors (mentioned under Sect. 12.8, "Evaluation of Treatment Response") which can influence the value of SUV. Therefore, a specific cutoff value of one center may not be true for others, and before adopting a specific cutoff value each nuclear medicine facility should standardize its imaging and processing protocol [101].

A similar scenario is the case for breast masses. Although mammography has been the accepted method of breast screening for women above the age of 50 and for those at high risk for breast cancer under that age, the criteria used for differentiating benign from malignant disease are not specific and, as a result, the number of biopsies that result in confirmation of malignant lesions varies from 20% to 25% from the total number of biopsies in various locations. The goal of cutting the costs of biopsy for benign lesions by using nuclear medicine procedures has been unsuccessful. Mammography detects lesions under 0.5 cm that can be easily biopsied by mammotomes, and their histological nature is verified pathologically. The sensitivity of all nuclear medicine procedures including PET in lesions under 1 cm is only about 65% – 70%; for lesions that are 0.5 cm it is quite disappointing [102 – 110].

If PET is not available other options are as follows: for lung cancer thallium when the lesion is larger than 2 cm in size, for breast cancer, brain tumors, bone and soft tissue tumors thallium-201 or Tc-99m-sestamibi should be considered.

12.5 Staging of Malignant Disease

Accurate staging of malignant lesions at the time of initial presentation is of utmost importance to provide appropriate management for a particular patient. Overstaging can inappropriately deprive a patient from receiving curative treatment. On the other hand, understaging can subject a patient to undergo a futile but drastic treatment that can even increase the morbidity and mortality (e.g., pneumonectomy in the case of stage III or IV lung cancer) without any increase in the chance of cure. Imaging plays a significant role in staging. Even though the ideal staging is a microscopic process, often it is not possible to biopsy each and every lesion to find out whether they are malignant or not. Therefore, an oncologist has to rely on some type of imaging to figure out the clinical staging rather than microscopic staging. Compared to the problems of differentiation of benign from malignant lesions, the most important factor is the very high NPV, so that none of the cancer patients is missing the correct diagnosis and treatment; for staging purposes there is need for a high sensitivity and specificity to avoid too many overstagings or too many understagings.

Presently, staging is performed according to the findings of noninvasive imaging modalities such as CT or MRI, in addition to other guided invasive procedures for the purpose of biopsy [111]. CT criteria for staging lymph node involvement depend mostly on the size of the lymph nodes. If they are more than 1 cm in the mediastinum or less than 1.5 – 2 cm in the abdomen, the lymph nodes are considered to be positive for malignant involvement [112 – 117]. However, microscopic involvement of these lymph nodes is not related to their size. Metastatic malignant cells can involve small lymph nodes. Large lymph nodes can be due to inflammatory response without metastatic involvement. For the same reasons that have been mentioned with regard to primary lesions, the accuracy of the staging depends on the resolution of the systems, the location of the lymph nodes, and the intensity of uptake of the radiopharmaceutical in the adjacent regions. Nuclear medicine procedures, especially F-18 FDG PET, have a higher degree of accuracy compared with X-ray CT or MRI, with the advantage of functionally verifying and determining whether the draining lymph nodes are involved in metastatic invasion. For example, the accuracy of X-ray CT in staging mediastinal disease in lung cancer is approximately 70%; MRI is slightly higher at around 80%, while F-18 FDG accuracy is better than 90% [118 – 120]. Proper staging always requires surgical, pathological, and microscopic verification. Even with nuclear medicine procedures, however, certain invasive procedures cannot be avoided. For example, in patients with primary pulmonary nodules, if the CT scan does not show evidence of enlargement of mediastinum nodes and the F-18 FDG PET study shows that there is unilateral or bilateral mediastinal lymph node increased uptake, this will be considered as metastatic nodal involvement until proven otherwise. The patient will be upstaged to stage II or III, and other invasive procedures such as mediastinoscopy are needed.

In the presence of enlarged mediastinal lymph nodes on the CT scan, the absence of FDG uptake is not necessarily an indicator that these lymph nodes are free of microscopic involvement, and verification is needed either before or at the time of surgery. FDG uptake in the lymph node could be due either to metastatic disease, with high intensity, or to inflammatory reaction, with low intensity. At no time will the accuracy be 100%. The surgeons have to weigh the results of these studies in order to decide whether to completely avoid invasive staging procedures and be satisfied with the results of the PET studies or to go ahead and perform guided biopsy. All nuclear medicine studies are good only for upstaging malignant disease. Any downstaging has to be verified microscopically.

The same problem holds for the staging of axillary nodal involvement, which is one of the most important factors for the prognosis of breast cancer. The sensitivity of any nuclear medicine procedure, including F-18 FDG PET studies, is never more than 85% – 90% [121 – 125]. Although sentinel node imaging does not image the cancer, it can identify the lymph node/nodes where the primary tumor drains. Excision followed by immunohistological staining for cytokeratin of the sentinel node can identify micrometastases. Staging of breast cancer is a microscopic process, and at the present time sentinel lymph node localization by either the radionuclide or the blue dye technique is the most acceptable alternative to total axillary node dissection [126 – 129].

In summary: Of the TNM stagings, due to lack of anatomical details, nuclear medicine tracers are not preferred for T-staging, which will change in the era of PET/CT when we have both the functional and anatomical information needed for T staging; however, due to the superior ability to detect lymph node (N) and distant metastases (M), nuclear medicine techniques particularly FDG PET will play a significant role and are approved by Medicare for N & M staging of the following cancers: lungs, head and neck, esophagus, colorectal, lymphoma, and melanoma (updated information is available on the following website: http://www.bcbsma.com/common/en_US/medical_policies/358.htm).

12.6 Prediction of Tumor Grade and Prognosis

Once the staging of a cancer is established, the management of that particular patient is mainly based on the stage and associated clinical factors (co-morbid conditions). However, for most of the stage III and IV solid tumors the response rate to the first line treatment is approximately 30% – 40%, with few exceptions such as lymphoma, testicular tumor, etc. Therefore, a significant number of patients will not response to the first line chemotherapy and will require more aggressive second line treatment, which is usually associated with more bone marrow toxicity. In that case patients have already received the first line treatment with associated toxicities leading to a decrease of the bone marrow reserve, so the oncologist has to wait until the patient's bone marrow reserve comes back to a near normal level so that the patient can tolerate the second line treatment. It is possible that during this waiting period the treatment resistant tumor burden increases further and potentially decreases the chance for a response to the second line treatment. On the other hand, if the oncologist can identify those tumors which are less likely to respond to the first line of chemotherapy, probably shifting and changing the treatment of these patients to other alternatives might potentially increase the chance of a complete response. This fact is well known in lymphomas. There are several factors that can directly or indirectly ultimately influence the response to treatment; after stage of tumor, the next most important factor is the tumor grade (i.e., aggressiveness of the tumor) and probably the third important factor is drug resistance. The grade of the primary tumor is best determined by histological evaluation of the biopsy specimens. But, it is not rare that the metastatic lesion is of a different grade from the primary and more aggressive than the primary tumor. In this case, it is not always feasible to do a biopsy on all lesions. A noninvasive imaging modality that can predict the grade of the lesions and thereby can predict the chance of response to the first line treatment will be of immense help in the management. Tumor grade is an intrinsic characteristic and it can be detected indirectly by evaluating the metabolic rate or cell proliferation rate. It is difficult to assess tumor grade by size only. The only way to predict tumor grade by measuring the size is 2 point imaging and looking at the rate of increase; however, this requires a significant waiting period of at least 3 – 4 months without treating the tumor, which is not ethical. Therefore, imaging modalities that can assess the metabolic status of a tumor with single point imaging are preferable than imaging that measures size like CT or MRI. Nuclear medicine, particularly PET, by the virtue of assessing the tumor physiology has this advantage [9].

Early detection of nonresponders to first line treatment and starting more aggressive treatment protocol not only increases the likelihood of complete response to the treatment but also at the same time potentially decreases the incidence of long term complications associated with tumorocidal treatments. This is very important particularly when more and more new treatment regimens are invented to increase the long-term disease free survival. Recently, there is not only an increase in the cure rate for some cancers like lymphoma and testicular tumors, but also these cured patients are living longer (more than 10 – 15 years, when they can

experience the long term toxicities related to the treatment). It is well known that chemotherapeutic agents (e.g., alkylating agents) and radiotherapy, 10 – 15 years post-treatment can cause late complication like solid tumors (lung cancer, breast cancer, melanoma, sarcomas, salivary and thyroid cancer), leukemias, non-Hodgkin's lymphomas, cardiac diseases (myocardial infarction, cardiomyopathy, pericarditis, etc.), pulmonary fibrosis, gonadal problems (oligospermia, azospermia, premature ovarian failure, etc.), and thyroid disorders (thyroiditis, thyroid nodules, hypo- and hyperthyroidism) [130]. These effects are found to be dose dependent. They are not only more likely to occur but also more likely to occur earlier in patients who received first line treatment followed by second line treatment compared to the patients who received the second line treatment at the beginning and did not require any other treatment.

Glucose serves as one of the major metabolites for tumor cells. Correlation studies with histology showed that high mitotic counts tend to be associated with higher glycolytic rates, which tend to have poor prognosis [131]. Higher glycolytic rates, determined by FDG uptake, were shown to be associated with high-grade tumors and poor prognosis [132]. Studies in head and neck cancer patients showed that an SUV higher than 10 is associated with a poorer prognosis [134]. Brunn et al. [135] found that a low pre-therapy FDG uptake (metabolic rate of glucose [MRgl] <20 mmol/min/100 g tissue) predicated a complete local response. Kitagawa et al. [136] reported that an increase in SUV correlated with an increase in tumor proliferative potential (MIB-1 and PCNA), cellularity and overall advanced stage as well as shorter survival compared to the low SUV group. A similar finding has also been reported by Minn et al. [137]. A study by Kunkel et al. [138] found that an SUV of less than 4 predicted 80% survival at 3 years after treatment and the similar number for SUV >4 was only 43%. Other PET tracers capable of assessing the rate of cell proliferation by imaging the rate of DNA synthesis or the rate of protein synthesis or the rate of cell membrane synthesis when labeled with thymidine or methionine or choline respectively also look promising in the near future. This field of tumor imaging is still under evaluation and needs further studies before any definite conclusions can be drawn [9].

12.7 Imaging and Prediction of Drug Resistance

Drug resistance is a major problem in the treatment of cancer. One of the reasons for this is the overexpression of the P-glycoprotein pump and other associated multidrug resistant glycoproteins which are the product of the multidrug resistance gene *MDR* [139]. These glycoproteins are responsible for the outward cellular transport of a variety of chemotherapeutic agents (such as daunorubicin, vincristine, and Adriamycin) [140, 141]. In man there are two closely related genes – *MDR1* and *MDR3*. They have similar structures. *MDR1* has been labeled P-glycoprotein (*Pgp*), or *p170*, because of its molecular weight of 170 kD. It consists of 12 transmembrane domains and two binding sites for ATP, which provides the necessary energy for drug transport [142]. The *Pgp* appears to function as an efflux pump that removes a variety of toxins from the cell, not confined only to chemotherapy. Several facts support the hypothesis that *Pgp* is the molecule responsible for the *MDR* phenomenon. These include the facts that *Pgp* overexpression has been consistently associated with the *MDR* phenomenon, that *Pgp* genes are amplified in multidrug resistance cell lines, that transfection of resultant overexpression of *Pgp* genes into drug-sensitive cells confirm *MDR*, that alteration of *Pgp* structure results in an altered *MDR* phenotype in cells transferred with mutant *Pgp*, and that the structural features of *Pgp* are characteristic and energy dependent on the plasma membrane pump. However, numerous other mechanisms of drug resistance have been determined. These include defective drug transport into the cells, enhanced drug elimination from the cells, decreased metabolic activation of drugs, increased drug inactivation, altered target proteins with reduced affinity for cytotoxic agents, and overproduction of specific target proteins [139]. A noninvasive imaging may have a potential role in the selection of patients in whom the modulation of *Pgp* may be beneficial before and after chemotherapy. As well this imaging could be helpful to evaluate the efficacy of the *Pgp* modulation therapy. ^{99m}Tc-sestamibi is a substrate for the P-glycoprotein pump and a correlation exists between the efflux rate of ^{99m}Tc-sestamibi and the expression of P-glycoprotein in breast cancer [140, 141]. By performing early and delayed ^{99m}Tc-sestamibi imaging of patients with breast cancer the washout rate of sestamibi can be determined. Lack of significant tracer washout indicates a low risk for chemoresistance [140]. On the other hand, a high washout rate was associated with a high probability for chemoresistance (sensitivity 100%, specificity 80%, and positive predictive value 83%) [140]. In these patients, the use of chemorevertant or chemomodulator agents could be justified [140].

^{99m}Tc-tetrofosium and ^{99m}Tc-Q-12 possess similar properties, except that they are more affected by the multidrug resistance activity in the cell. They are characterized by faster washout in the delayed images, which might make delayed imaging impossible.

The multi-drug-resistant energy dependent P-glycoprotein pump system (*MDR-Pgp*) may play a role in the resistance of lung cancer to certain chemotherapeutic

agents. Determination of *MDR-Pgp* at time of diagnosis may provide information regarding which treatment protocol would be best for each individual patient. P-glycoprotein recognizes certain chemotherapy agents as substrates (such as paclitaxel – a taxane agent) and is involved with their transport out of the cell. P-glycoprotein also works to prevent intracellular accumulation of some lipophilic cationic radiopharmaceuticals such as Tc-tetrofosmin. Cancers with low uptake of Tc-tetrofosmin likely have overexpression of *MDR-Pgp* and are more likely to be associated with a poor response to certain chemotherapy agents [143].

PET tracers can be used in this purpose for better quantitation. ^{11}C-verapamil [144], ^{11}C-daunorubicin [145], and ^{11}C-colchicine [146] have been used as *Pgp* probes. These tracers require onsite cyclotron and are, therefore, mainly confined to research. On the other hand, Tc-99m-labeled SPECT radiopharmaceuticals are more likely to be used due to their easy availability and ease of handling. An F18-labeled ligand can potentially obviate the requirement of onsite cyclotron. On the horizon such a hope is F-18-paclitaxel (FPAC), which has been shown to indicate *Pgp* function in tissues from rhesus monkey [147].

12.8 Evaluating Response to Therapy and Differentiation of Tumor Recurrence from Necrosis

Patients can respond differently to the same treatment protocol, and accordingly individualization of therapy should be more appropriate in the future. However, as tumors and their hosts are heterogeneous, there are many crucial secondary problems related to the individualization of therapy. As yet it is not possible, in general, to define precise histology and to establish prognosis entirely noninvasively or to assess responses to therapy rapidly. After initial treatment, methods for early discrimination of tumor recurrence from post-treatment changes are insensitive. These are all areas in which new imaging applications have been developed and are promising [81]. The most important element in individualization of therapy is to be able to rapidly assess whether a chosen treatment strategy is effective. In the past, only semiquantitative methods were generally used for assessment of tumor growth. It has become feasible to consider measurement of size and shape changes with great precision using MR imaging [81]. Tumor volume changes observed during follow-up studies in principle can be used for evaluation of response to anti-tumor therapy. However, it is not early enough before the patient develops considerable toxicity and side effects from the prescribed chemotherapy.

There are problems in developing methods that are sensitive to early changes during the course of treatment and for the discrimination of tumor tissue from surrounding normal tissue, fibrous tissue and necrotic tissue in the post-therapy period. Adding to the problem is that tumors have heterogeneous pathology that is not always clearly distinct from those of normal tissue and the induction of complex deformations in the surrounding tissues after treatment. There is a whole list of functional imaging modalities currently available for clinical and research purposes which include optical imaging, magneto imaging, different types of MR imaging (diffusion weighted imaging, tensor imaging, MR spectroscopy, etc.), and also several methods of radionuclide imaging [11, 81, 148 – 150]. MR spectroscopy provides biochemical information on steady-state processes, and the information from MR spectroscopy has not replaced the kinetic and metabolic information from nuclear medicine techniques [150].

The role of imaging viable tumors is increasing because of the problems encountered by MRI and CT, especially after surgical, radiation, or chemotherapy treatment in differentiating post-therapy changes from residual viable tumor tissue, local recurrence, or necrosis [151]. As a result, different radiopharmaceuticals play an important role in different malignancies for evaluation of treatment response and for detection of recurrence. Radiopharmaceutical agents like gallium (in lymphoma) and FDG (in lymphoma, head and neck cancer, breast cancer and others) have shown good results in predicting response to a treatment regimen as early as after 1 – 3 cycles of chemotherapy [9].

Quantification of radiopharmaceutical uptake in tumors is an important factor for evaluating treatment response and for other purposes as well. In nuclear medicine, intensity of radiopharmaceutical uptake relative to the normal tissue has been used to differentiate benign from malignant lesions [152 – 153]. This has been calculated using different approaches, such as tumor-to-background ratio and standard uptake value. Comparison between early and delayed tumor-to-background ratio of ^{201}Tl-chloride has been proposed in order to differentiate false-positive ^{201}Tl-chloride uptake due to inflammatory lesions or postoperative changes from true-positive uptake due to the malignant lesion [69, 154 – 155]. It is presumed that with delayed images there will be lower background activity and, accordingly, the ^{201}Tl-chloride uptake ratio in malignant lesions increases in the delayed images compared with the early images. Conversely, with benign lesions lesion-to-background ratio in the delayed images is lower due to washout of ^{201}Tl-chloride activity from the benign cells and extravascular and intravascular components of the lesion. It is also believed that malignant cells retain ^{201}Tl-chloride longer, with less washout. They might even continue to accumulate ^{201}Tl-chloride in the delayed images, leading to a higher tumor-to-background ratio. Calculations have been

made by subtracting the delayed from early ratios in order to calculate the washout index. If the product of this subtraction is positive, it means washout of thallium from the lesion, indicating its possible benign nature, while if the result of the subtraction is negative it indicates build up of thallium concentration with time and the possible malignant nature of the lesion. The reverse has also been proposed, i.e., subtracting the early from the delayed ratio to calculate the washout or build-up ratios.

Attempts are being made with F-18 FDG comparing early (starting acquisitions 40 – 45 min following injections), SUV and lesion-to-background ratios with the same SUV or ratios calculated from the delayed images (starting acquisitions 3 – 4 h following i.v. injection). The same observations regarding FDG numbers are now being reported in the early steps of these trials. It is important to realize that there are many reservations to applying these principles in the initial diagnosis for the purpose of differentiation between benign and malignant disease and for follow-up purposes. The following is a review of the problems:

1. For early and delayed imaging, it may not be practical to image the patient twice in one day. This is due in part to the fact that each set of images requires more than 1 h to complete, especially if both planar and SPECT images have to be performed. Further, it causes problems in scheduling studies in a busy service. We should always attempt to provide an answer to the patient problem with the least inconvenience to the patient. This might be successfully dealt with in the future with high sensitivity and high speed, and short acquisition times with newer PET detectors such as LSO and GSO.
2. Early and delayed images might be suitable for radiopharmaceuticals with a half-life of about 3 days, such as ^{201}Tl-chloride or ^{67}Ga-citrate, or of a few hours, such as ^{99m}Tc-sestamibi. F-18 FDG with a half-life of 110 min at 60 min and 2 – 3 h has been successful in differentiating malignant tumors from benign conditions as infections using the most recently available PET imaging systems.
3. There is no litmus imaging procedure that will differentiate malignant lesions from benign lesions, for the following reasons:
   a) All radiopharmaceuticals used do not have specific uptake for malignant cells. Other viable nonmalignant lesions share the same mechanism of uptake. Even with monoclonal antibodies and with receptor imaging, both malignant cells and other normal cells, such as in the liver, share the same radiopharmaceutical binding and receptor sites. This applies to most of the radiopharmaceuticals used for tumor imaging. The only exception is the iodine radioisotopes used for thyroid imaging due to its organification in the thyroid.
   b) Any malignant lesion is histologically a mixture of malignant cells, with various grades of differentiation or undifferentiation, plus a matrix and stroma that include benign cells due to immune and inflammatory response from the surrounding tissues.
4. For the purpose of evaluating the ratios and their use in differentiating benign from malignant lesions, the question is whether the patient is presenting with a new, undiagnosed lesion or whether the lesion has been biopsied and proven to be malignant. If the lesion is proven to be malignant, the task is to stage the disease, so that the appropriate treatment for the patient can be determined. In this case we will be looking for uptake in the lymph nodes that has either increased or does not show any change. We will be looking for a slight increase of uptake in the lymph nodes. We should not wait for higher uptake with nodes-to-background ratios in order to diagnose metastatic disease because this is waiting for advanced disease. Therefore, as previously mentioned, we require the highest system resolution and the highest accuracy from any test to be routinely used clinically.
   The problem is even more complicated if the patient has been previously treated. We should not wait until the lesion-to-background ratio is more than 1.7 or the SUV is more than 2.4 in order to recognize it as local recurrence. This will be a very late diagnosis. We recommend that any uptake at the site of the treated lesion that persists on the delayed images should be suspicious for tumor recurrence until proven otherwise, especially if it has been a new change from a previous negative study.
5. There is no universal approach to calculating tumor-to-background ratios by drawing a region of interest from the area of increased tumor uptake and from the background region. This is particularly controversial in cases of midline lesions or when the contralateral normal side contains organs with high normal physiological uptake such as the heart, liver, or choroid plexus. The operators are given the authority to use their judgment for the selection of areas of normal background. Different ratios can be calculated by the same operator or by different operators. The regions are drawn manually. We recommend that for each department the operator follows certain criteria for drawing the region of interest. The physician interpreting the study preferably should be the person to draw the regions of interest. Ratios calculated from the SPECT images are higher than those calculated from the planar images, especially when overlaid by adjacent organs with relatively high uptake [17].

Calculated ratio can reflect either the mean or average pixel uptake in the ROI or the highest pixel uptake. The choice depends on the objective and the appearance of the lesion. For solid lesions mean pixel ratios are enough to differentiate benign from malignant. Maximum pixel uptake or even a histogram of the distribution of the counts per pixels might help in displaying the heterogeneity of the tumor. In necrotic lesions or in postoperative, post-chemo- and/or radiotherapy follow-up, maximal pixel uptake is more meaningful than average pixel uptake.

6. It is important to remember that there are several factors affecting SUV values [101]. Some of these factors are (a) a high plasma glucose level at the time of injection (diabetes, steroid used during chemotherapy, etc.) can falsely decrease the SUV [32, 108]; (b) time between injection and imaging can influence the SUV (it is assumed that after 45 min the tumor uptake curves reach a plateau but it may not be always true, so comparison of pre-therapy SUV with post-therapy SUV requires attention for this time and preferably should not be more than 5 min of difference [156–157]; (c) a significant change in body weight is not unlikely after chemo- + radiotherapy, so attention should be paid to adjustment of SUV so that pre- and post-treatment SUVs are comparable (as fat has a very low FDG uptake, SUV corrected to either lean body mass or surface area is preferable)[158]; (d) other factors that can affect the SUV include (i) patient motion (due to lesion blurring also during breathing in a long lesion particularly located at the anterior and lower lung fields), (ii) partial-volume effects in lesions smaller than two and half times the scanner resolution at full width half-maximum [159], appropriate recovery coefficients, which represent the ratio of apparent to true isotope concentration in the structure of interest, can be used to correct for partial volume effects. SUVs are obtained by placing a region of interest on the PET images, (iii) image reconstruction (SUV measurements from filtered back projection (FBP) images underestimate the true activity concentration by about 20% – this is much greater than iterative reconstruction (IR) images, which underestimate activity concentration by about 5% [160], (iv) the size of the region of interest affects the radioactivity measurements: the larger the region of interest, the lower the mean SUV. In the clinical setting, the maximum SUV within the region of interest, which represents the highest radioactivity concentration in one voxel within the tumor, is frequently used for comparison between PET studies, and (v) method of attenuation correction methods used (particularly with the growing popularity of the PET/CT scanner, if CT data is used for attenuation, correction SUV value could be 10–15% higher compared to Cs-137 or Ge-68 attenuation corrections) [161–162].

Follow-up studies using a variety of radiopharmaceuticals including ^{67}Ga (Fig. 12.2), ^{201}Tl (Fig. 12.3), and F-18 FDG provide useful information regarding the response to therapy, and consequently about prognosis [9].

FDG-PET in Evaluating Tumor Response. FDG PET imaging can evaluate tumor response to therapy before anatomic changes are observed [163]. PET imaging is currently the most sensitive and specific imaging

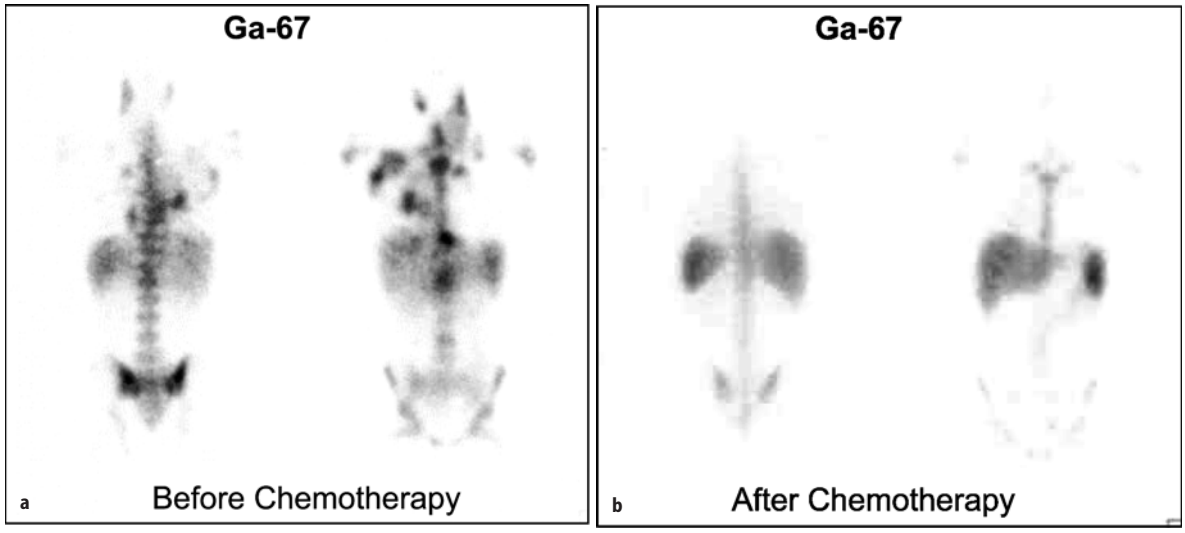

Fig. 12.2. Ga-67 (**a**) and post therapy (**b**) studies of a patient with non-Hodgkin's lymphoma showing excellent response to chemotherapy since the pretherapy significant uptake das disappeared on the follow-up study.

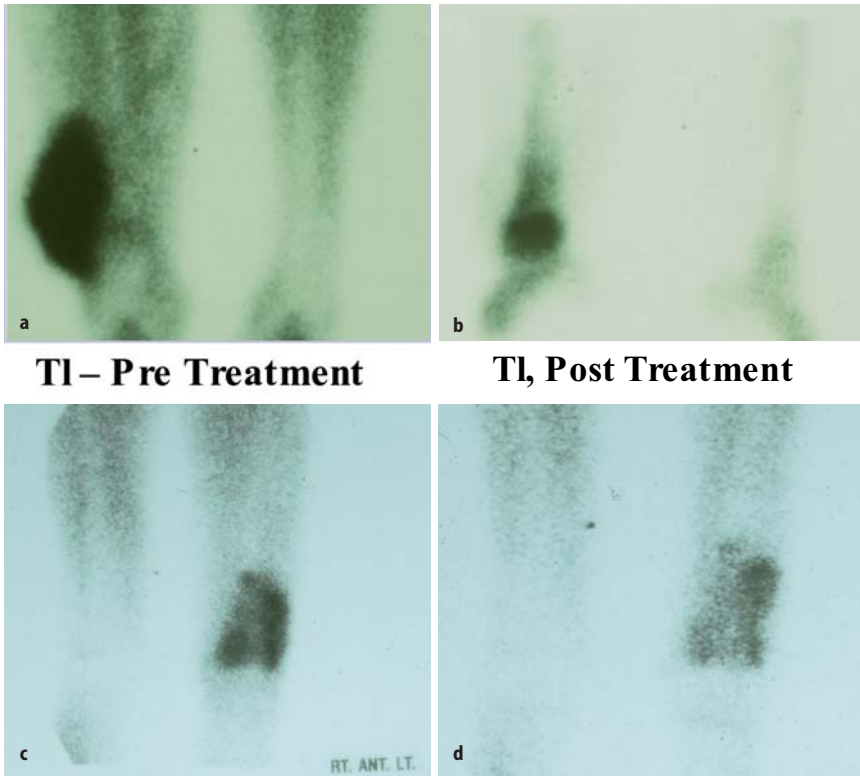

Fig. 12.3a–d. Tl-201 study of a patient with Ewing's sarcoma of the right distal tibia. (**a**) Prechemotherapy study with significant radiotracer accumulation. Follow-up (**b**) post-therapy study shows significantly decreasing uptake at the site of the tumor reflecting the response to therapy. A case of osteogenic sarcoma of the left distal femur is also shown (**c, d**), with Tl-201 showing clearly deceasing uptake, indicating good response to chemotherapy

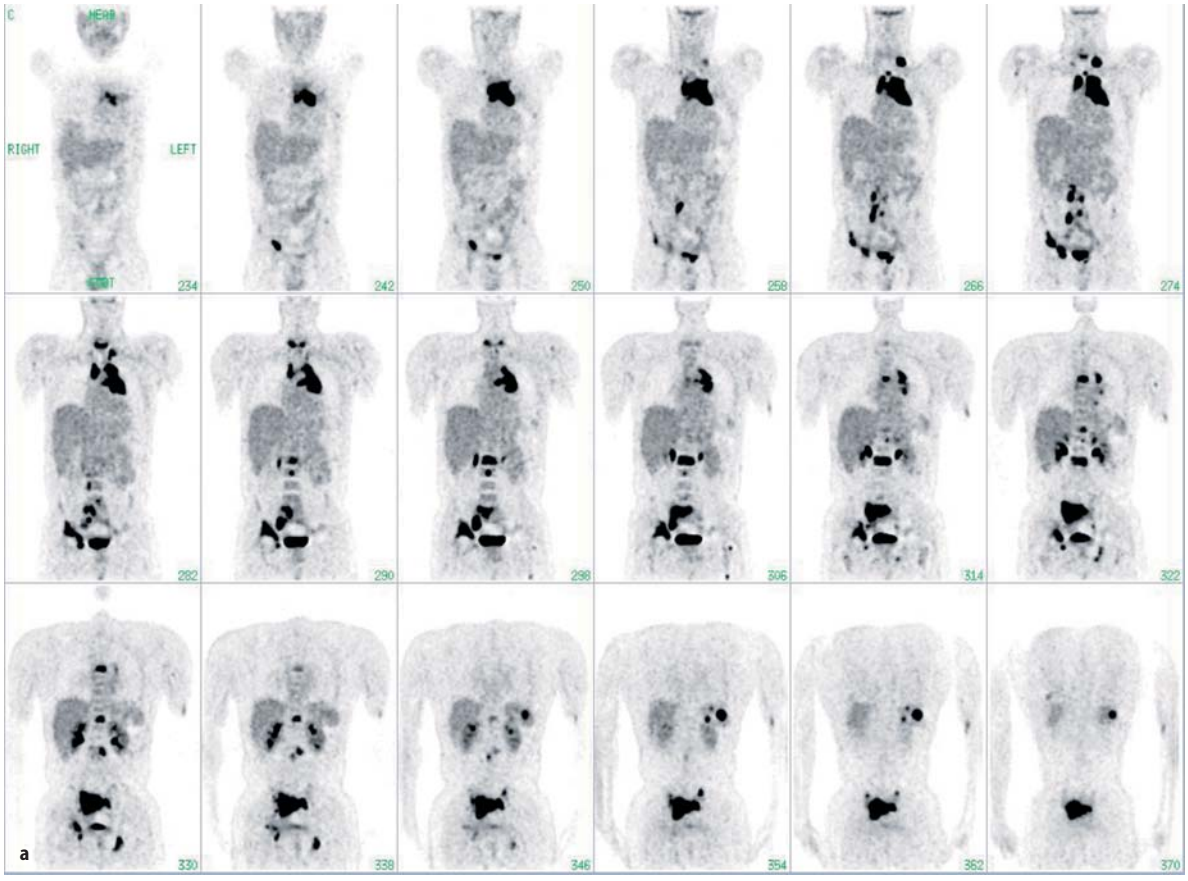

Fig. 12.4. a 42 year old male with B-cell lymphoma, pre-therapy scan (*baseline*); shows extensive disease (Stage IVB).

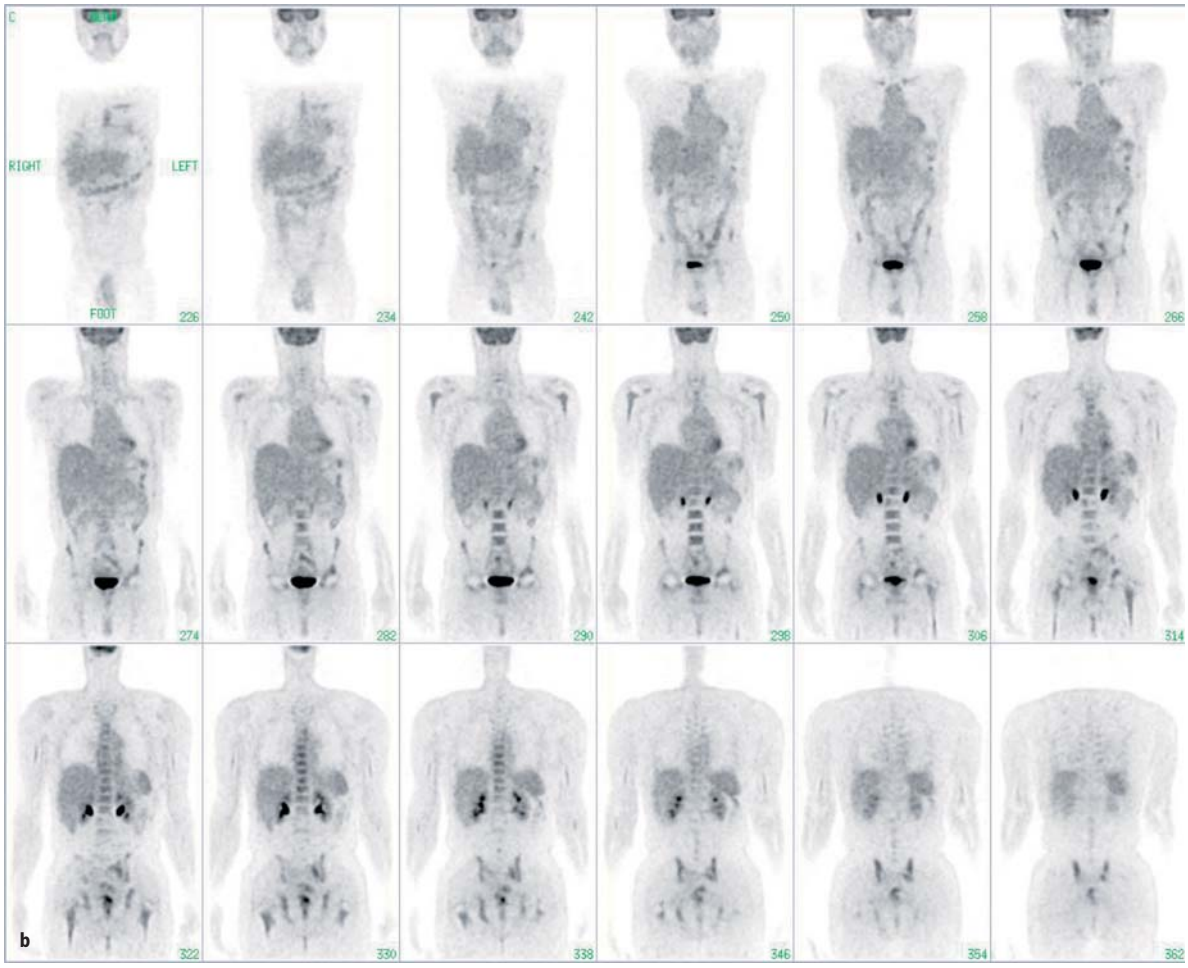

Fig. 12.4. b Same patient as **a**, FDG-PET scan 2 weeks after the 3rd cycle of chemotherapy showing good response. Note the extensive bone marrow uptake which is suggestive of hyperplasia

method to obtain information about tumor physiology [163]. By providing a more timely and accurate assessment of treatment efficacy (Fig. 12.4), PET imaging can have a significant impact on clinical treatment decisions [163].

PET Parameters Used To Monitor Tumor Response

FDG net influx constants (*Ki*), SUV, and lesion to background ratios have been used. Lesion to background ration is the simplest one to use and does not require any other data except the image. SUV is more complex than lesion to background ratio and requires at least the following information (i) injected dose (activity in the syringe before injection minus activity after injection), (ii) time of injection, and (iii) body weight of the patient. SUV corrected to blood glucose level and lean body mass or body surface area can provide better results during monitoring response. On the other hand, FDG net influx is the most complex parameter. It requires dynamic imaging with a variable number of arterial or arterialized venous or venous blood samplings depending on which kinetic model is followed [101]. Studies have demonstrated that SUV and simplified tracer kinetic modeling, using the Patlak-Gjedde analysis, provide highly reproducible parameters of tumor glucose use [164–165]. Weber et al. [164] studied 16 patients twice within 10 days with FDG-PET while they were receiving no therapy. FDG net influx constants (*Ki*), SUVs, normalized to blood glucose (SUV-gluc and Ki-gluc) were determined for 50 separate lesions in these 16 patients. The precision of repeated measurements was determined on a lesion-by-lesion and a patient-by-patient basis. The differences of repeated measurements were approximately normally distributed for all parameters with a standard deviation of the mean percentage difference of about 10%. Changes of a parameter of more than 20% are outside the 95% range for spontaneous fluctuations and can be considered to reflect true changes in glucose metabolism of a tumor mass. There was no clear advantage in using tracer ki-

netic approaches compared with SUV measurements. It seems feasible to use SUV measurements for the evaluation of therapy response. No patients with overt diabetes mellitus were included. Because diabetes mellitus may affect the blood clearance and whole-body distribution of FDG by multiple mechanisms, tracer kinetic approaches may be preferable to SUV measurements in this group of patients [167]. The use of SUVs for serial measurements of short-term changes in tumor glucose use during therapy is also supported by another study in 57 patients with advanced non-small cell lung cancer [167]. In this study patients were studied by FDG-PET before platinum-based chemotherapy and 3 weeks after initiation of therapy. Changes in the SUV of the primary tumor were closely correlated with changes of the FDG-net influx as determined by Patlak analysis. In addition, changes of both parameters 3 weeks after initiation of chemotherapy were significantly correlated with subsequent reduction of tumor size and patient survival. Failure to achieve a measurable reduction in tumor FDG-uptake after 3 weeks of therapy was associated with a 96% risk of not achieving an objective response with the first-line chemotherapy regimen. No responders in FDG-PET were characterized by a three times shorter time to tumor progression and a 1.7 times shorter overall survival.

Although these and other studies indicate that SUVs may be used to determine quantitatively changes in tumor glucose use over time, it is important to note that a strict PET protocol is required to minimize the variation between FDG-PET studies [156–157]. The time between FDG injection and imaging needs to be standardized and should vary by less than 5 min between baseline and follow-up [157]. The radioactivity in the syringe should be measured before and after injection and appropriately corrected for radioactive decay to determine accurately the dose of FDG injected. Extravasations of the radiotracer during injection also influence quantification. Finally, the patient's blood glucose levels should be comparable between the scans and ideally less than 150 mg/dl at the time of tracer injection [156]. The specific method for calculation of SUVs (e.g., normalization to body weight or the lean body mass) is also important for the purpose of therapy monitoring because a significant change in weight is not uncommon during high dose chemo-/radiotherapy. Normalization to body surface area or lean body mass may provide better results.

Early Prediction of Response After Initiation of Therapy. Most in vitro and in vivo studies in tumor-bearing animals suggest a good correlation between tumor viability and FDG uptake. Other nonhuman studies, however, found an increase in FDG uptake of tumor cells after initiation of therapy. The concept of using FDG-PET for monitoring therapeutic response is based on the decrease of tumor glucose use and its correlation with the effectiveness of treatment and ultimately with the reduction of viable tumor cells. In tumors responding to treatment a reduction of glucose use occurs early in the course of therapy. Serial PET scans during treatment should allow prediction of response [156].

In 1993, Wahl et al. [168] studied sequential FDG-PET imaging in 11 newly diagnosed locally advanced primary breast cancers undergoing chemohormotherapy. Patients underwent a baseline and four follow-up PET scans during the first three cycles of treatment. Tumor response was determined histopathologically after nine cycles of treatment. The FDG uptake in eight patients with partial or complete pathologic responses decreased promptly with treatment, whereas the tumor diameter did not significantly decrease. On day 8 of therapy, tumor FDG uptake was 78% of baseline and decreased further to 68% at day 21, 60% at day 42, and 52% at day 63. In contrast, three patients with nonresponding tumors did not show a significant decrease in FDG uptake. The authors concluded that FDG-PET has substantial promise as an early noninvasive metabolic marker of the efficacy of cancer treatment. Similar findings were also observed by Jansson et al. [169] in locally advanced or metastatic breast cancer treated with chemotherapy. Romer et al. [69] studied the changes in metabolic activity over time in non-Hodgkin's lymphoma and compared pretreatment FDG-PET with day 7 and day 42 after initiation of therapy. In successfully treated patients, FDG uptake decreased by 60%–67% from baseline to day 7. This study showed that in responding non-Hodgkin's lymphoma, two-thirds of the metabolic effect of chemotherapy occurred within the first 7 days of treatment. In addition, the long-term prognosis could be predicted early after initiation of chemotherapy by the change in glucose metabolism. These studies suggest that serial FDG-PET imaging can be a valuable tool for monitoring response to therapy early in the course of treatment and numerous studies have proved the hypothesis that changes in tumor glucose metabolism predict the outcome of therapy [156].

Timing of PET Imaging To Predict/Evaluate Treatment Response. It is important to have a baseline examination for proper interpretation of tumor response [163]. Tumors could be FDG negative either due to low FDG uptake secondary to slow metabolic rate, and less expression of Glut-1 (prostate and differentiated thyroid cancer), or abundance of glucose-6-phosphatase enzyme (hepatic tumor) converting FDG-6-phosphate back to FDG and expulsion from the cell. Imaging 4–6 weeks after completion of chemotherapy is recommended to avoid transient fluctuations in FDG metabolism, particularly a decrease in FDG uptake immediately after chemotherapy possibly due to stunning [163]. To predict response early after the initiation of therapy 1–3 cycles of chemotherapy can be used. However, to

decrease false negative results possible due to stunning again it is preferable to perform the PET scan just 1 or 2 days prior to the beginning of 2nd or 4th cycle.

For radiation therapy a longer delay may be required (up to more than 60 days) prior to imaging after completion [156]. Generally, FDG uptake 6 months after radiotherapy is associated with tumor recurrence [75]. At the initial phase of radiotherapy particularly below 20 Gy there can be an increase in FDG uptake due to intense inflammatory response. However, after 40 Gy FDG uptake usually decreases. If the FDG uptake is absent 4 weeks after completion of radiotherapy a repeat PET scan should be performed after 16 – 24 weeks to confirm the findings [9].

After surgery there could be an increased FDG uptake at the surgical bed and, therefore, PET scans after 3 – 4 months are more useful than within a couple of weeks after surgery. This increased FDG uptake could persist even 6 months after surgery and the scan should be read cautiously. Usually, this increase in FDG uptake is diffuse and distinguishable from focal increased uptake suggestive of local recurrence and residual tumor. In the case of core biopsy a waiting period of 2 weeks is preferable to decrease the false-positive results.

Assessment of tumor response to therapy can be determined by visual assessment of the images or by quantitative analysis using standard uptake values [163]. There are currently no universal criteria to evaluate tumor response using PET, and RECIST (Response Evaluation Criteria In Solid Tumors) do not include PET [9, 101]. In 1999, Young et al. [101] reviewed the possibility of including PET in the RECIST in the near future. SUV was preferred over all the other available PET parameters as *Ki* (influx constant) was too complex to be used in daily practice [101]. In this review a change of 25% in SUV was proposed as a cutoff to determine a response, with the idea that a change in SUV up to 20% could be related to the intrinsic variation. It was also suggested that to consider SUV as a parameter of standardized patient preparation, image acquisition and processing protocol are of the utmost importance. In the PET literature a change from 35% to 70% has been used in different cancers [156]. There is no single cutoff used uniformly even for a particular type of cancer. There is a need for large multicenter trial. It may be possible that there will be a need for different cutoffs for different tumors according to their likelihood of responding to a particular therapy; however, this should be established by a large study. For example, a 50% decrease in FDG uptake after three cycles of chemotherapy may not be a good indicator for good response (to permit continuation of current treatment alone) in a lymphoma patient [170]. It seems that a complete absence of FDG uptake is required to predict a good response in lymphoma. This may be related to the fact that lymphoma responds extremely well to the current treatment modality. There is a more than 90% cure rate for advanced stage Hodgkin's disease and at least a more than 50% response rate in non-Hodgkin's lymphoma compared to the advanced stage; other solid tumors have a cure rate of 30 – 40% at the best.

The timing between the last treatment and FDG-PET imaging for assessment of tumor response is of crucial importance. There are no clinical data indicating that chemotherapy causes a metabolic flare phenomenon of tumor tissue, which would lead to an initial increase in FDG uptake after initiation of therapy as it was indicated by in vitro results [171 – 172]. In these in vitro studies, the FDG uptake was assayed in surviving cells after chemotherapy or radiation therapy. This differs from the clinical situation, where the PET signal in a mass is determined by a combination of decreased FDG uptake because of tumor necrosis and cancer cell death plus potentially increased FDG uptake by surviving tumor cells. In most of the clinical studies published so far, the specificity of FDG-PET for detection of viable residual tumor tissue after completion of chemotherapy has been found to be higher than the sensitivity. Of note, as described previously a metabolic flare phenomenon has been observed in metastatic breast cancer as an indicator of good response to antiestrogen therapy [173 – 174].

Radiotherapy often causes a severe inflammatory reaction, which has raised concerns about using FDG-PET for assessment of tumor response to radiotherapy or chemoradiotherapy. It has frequently been recommended that FDG-PET should only be performed several months after completion of radiotherapy. There is a surprising lack of data, however, to support this recommendation. Although there is no doubt that radiation-induced inflammation accumulates FDG, the intensity of FDG uptake is often in most of the cases considerably lower than that of the untreated primary tumors. Furthermore, the configuration of increased FDG uptake in radiation-induced inflammation is frequently markedly different from the configuration seen in a malignant tumor. In the clinical setting it is often possible to differentiate between radiation-induced inflammation and residual tumor tissue, especially when comparing a pretreatment with a post-treatment PET scan. Wieder et al. [175] systematically studied the time course of changes in tumor FDG uptake in 38 patients with locally advanced squamous cell carcinomas of the esophagus treated by preoperative chemoradiotherapy. Patients were imaged before chemoradiotherapy, 2 weeks after initiation of therapy, at completion of therapy, and another 4 weeks later before surgery. None of the serial PET scans demonstrated an increase in tumor FDG uptake, indicating that radiation-induced inflammatory reactions are quantitatively less relevant than the decrease of FDG uptake in viable tumor cells. Of note, the decrease in FDG uptake after

2 weeks of therapy was significantly correlated with subsequent histopathologic tumor regression and patient survival [175]. In addition, there are now several studies on head and neck cancer [176], lung cancer [177], and esophageal cancer [178–180] showing a high specificity of FDG-PET for the detection of viable tumor tissue following chemoradiotherapy. In contrast, Arslan et al. [181] found that in patients with esophageal cancer radiation-induced inflammation could not be differentiated from viable tumor tissue. It is important to note, however, that this study included less advanced tumors, which accordingly demonstrated relatively low FDG uptake in the baseline scan. Even in responding tumors relative changes in tumor FDG uptake are necessarily smaller than in tumors with higher FDG uptake in the baseline scan.

Using FDG-PET for restaging after completion of treatment relies on the metabolic activity of tumor tissue. As a result of treatment, only small amounts of residual viable tumor may be present and lead to disease recurrence.

Metabolic stunning of tumor cells by chemotherapy or radiotherapy has to take into account which tumor cells are still viable, but exhibit a low metabolic activity because of the recent treatment. To achieve the highest sensitivity for detection of residual tumor tissue FDG-PET should be performed as late as possible after completion of therapy to enhance the detection of residual tumor tissue. In the authors' experience, a waiting period of 4–6 weeks after completion of therapy is a reasonable compromise. Imaging at later time points probably improves the accuracy of FDG-PET for detection of residual tumor tissue, and short-term follow-up is recommended in equivocal cases.

In summary, individual tumors will vary widely in their response to a particular form of therapy [162]. Early, particularly after 1–3 cycles of chemotherapy, identification of tumors that are not responding to conventional therapies would permit the timely institution of alternative treatment that may be more effective [163]. Anatomic changes often lag behind tumor cell mortality [163]. FDG PET imaging can evaluate tumor response to therapy before anatomic changes are observed [163]. PET imaging is currently the most sensitive and specific imaging method to obtain information about tumor physiology [163]. FDG-PET imaging can have significant impact on clinical treatment decisions by providing a more timely and accurate assessment of treatment efficacy [163]. It is important to have a baseline pre-therapy scan for proper interpretation of tumor response [131]. Imaging 1–2 weeks after completion of chemotherapy is recommended to avoid transient fluctuations in FDG metabolism [162]. For radiation therapy a longer delay may be required (up to 60 days) prior to imaging. Generally, FDG uptake 6 months after radiotherapy is associated with tumor recurrence [163]. Assessment of tumor response to therapy can be determined by visual assessment of the images or by quantitative analysis using standard uptake values [163]. For uniform use of SUV, standardization and periodic quality control of the imaging and image processing protocols are very important.

12.9 PET/CT and Image Fusion: Radiotherapy Planning

Computed tomography (CT) has a high diagnostic ability by visualizing lesion morphology and by providing the exact localization of sites, but it is unable to provide information about functional status (Fig. 12.5). In contrast, positron emission tomography (PET) with fluorine-18 fluorodeoxyglucose (FDG) provides information about the metabolism and viability of the lesions but fails to provide precise topographic localization. Technical and clinical advances in medicine have led to the understanding that one modality cannot be a substitute for the other; they are complementary to each other. A fused image of PET and CT overcomes the inherent limitations of both modalities, resulting in a precise topographic localization of valuable physiologic information. Image fusion data have been shown to be useful for diagnosis, staging, monitoring response to treatment and follow-up for detection of early recurrence in cancer patients. Fusion of independently done CT and PET is time-consuming, difficult for realignment and involves complex computations. The development of the new technology of PET/CT that allows for combined functional and anatomic data acquisition sequentially has the potential to make fusion an everyday clinical tool. However, this technology is not yet used widely because of its recent arrival on the market.

Fused images from FDG-PET and CT may correctly identify areas of increased FDG uptake as related to normal, physiologic biodistribution and exclude the presence of disease in the suspected sites (Fig. 12.3). Initial reports have assessed the value of combined devices having the ability of sequential acquisition of FDG-PET studies and CT in cancer patient management [11, 182]. In a study of 32 patients, Charron et al. reported that combined imaging indicated the increased FDG uptake to be in sites of physiologic activity and thus excluded the presence of malignancy in a third of patients [182]. In 24% of lesions, it allowed for better localization of disease on PET [182]. Data published in an editorial article suggest that combined imaging resulting in "true" registration may improve patient management in about 20% of patients who undergo whole-body PET [13]. These assumptions are in good correlation with preliminary reports on the use of the combined camera-based PET/CT device in 167 patients [183–184]. PET/CT using FDG improved the accuracy

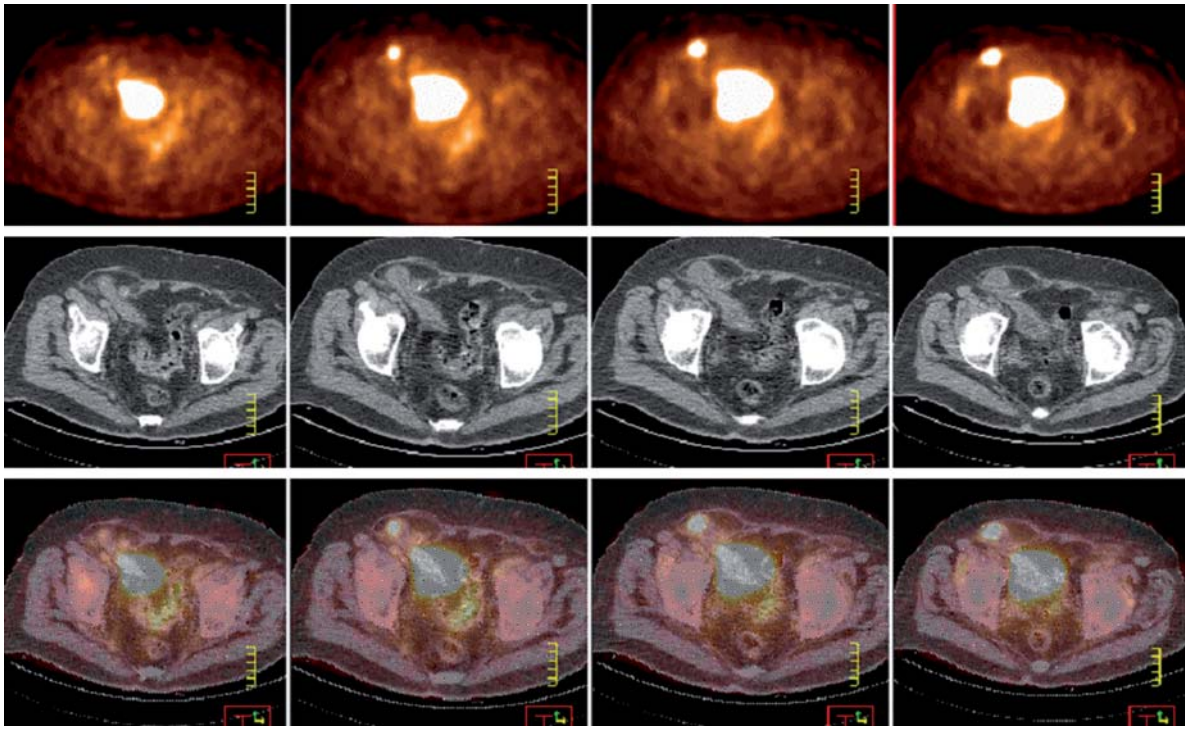

Fig. 12.5. Example of a physiologic activity in abnormal location, however, with the help of PET/CT, diagnosed correctly. This is a patient with history of lymphoma after chemotherapy. *Top panel* showed PET images of the pelvis with a hot activity at the right inguinal region was thought to be recurrent lymphoma when only PET images were evaluated, subsequently when CT images (*middle panel*) were displayed an inguinal hernia was obvious and the fused images (*bottom panel*) showed that the increased uptake is inside the hernia sack, therefore, the final impression was no FDG avid disease

of PET or CT interpretation in 45% of patients. On PET, it was useful in correct localization of malignant lesions and in excluding cancer as the cause of FDG uptake. It also retrospectively identified sites of disease that were missed on the initial CT reading in 7% of patients. Combined acquisition of FDG and CT had an impact on clinical management in 29 patients (17%). Re-staging and early detection of recurrence lead to a change in treatment planning, referral to previously unplanned surgery, sparing of unnecessary surgery, and administration of additional chemotherapy or radiotherapy. In a study of 75 patients, 25% of the suspected sites that showed only an abnormal mass with no FDG uptake were malignant. In contrast, 68% of lesions showing only FDG uptake without a mass were viable cancer sites [185].

In last couple of decades there have been tremendous developments taking place in radiotherapy in the form of 3D-conformation radiotherapy and intensity modulated radiotherapy (IMRT). These modalities can deliver radiation to the tumor not only more precisely with regard to the three-dimensional size and shape of the tumor but can also deliver a different intensity of radiation at different sites of the tumor. Radiotherapy is used with curative intent in tumors of the following organs: head and neck, female genital organs, lymphomas, breast, primary brain tumors, prostate, unresectable sarcomas and skin. However, in spite of the development of RT the commonest type of recurrence for solid tumors is local recurrence. This fact led to the concept of using fused metabolic and anatomic images to define target volume for RT. This image not only will allow inclusion of the metabolically active tumor and spare the normal structure from radiation but will also allow the provision of an extra boost of radiation to the part of the tumor with very high metabolic activity or which is hypoxic (seen by metabolic imaging with misonidazole PET).

Preliminary studies showed that FDG PET can be useful for radiotherapy planning. In a study of 202 patients, Dizendorf et al. [186] found that ^{18}F-FDG PET has a major impact on the management of patients for RT, influencing both the stage and the management in 27% patients. In a prospective study on 26 patients using fused images, Bradley et al. [187] found that radiation targeting with fused PET and CT images altered radiation-therapy planning in more than 50% of patients compared to CT image alone used for targeting. Herone et al. [188] reported that in head and neck cancer PET/CT provides valuable information, resulting in more accurate delineation of normal tissues from tumor bearing areas at high risk for recurrence compared

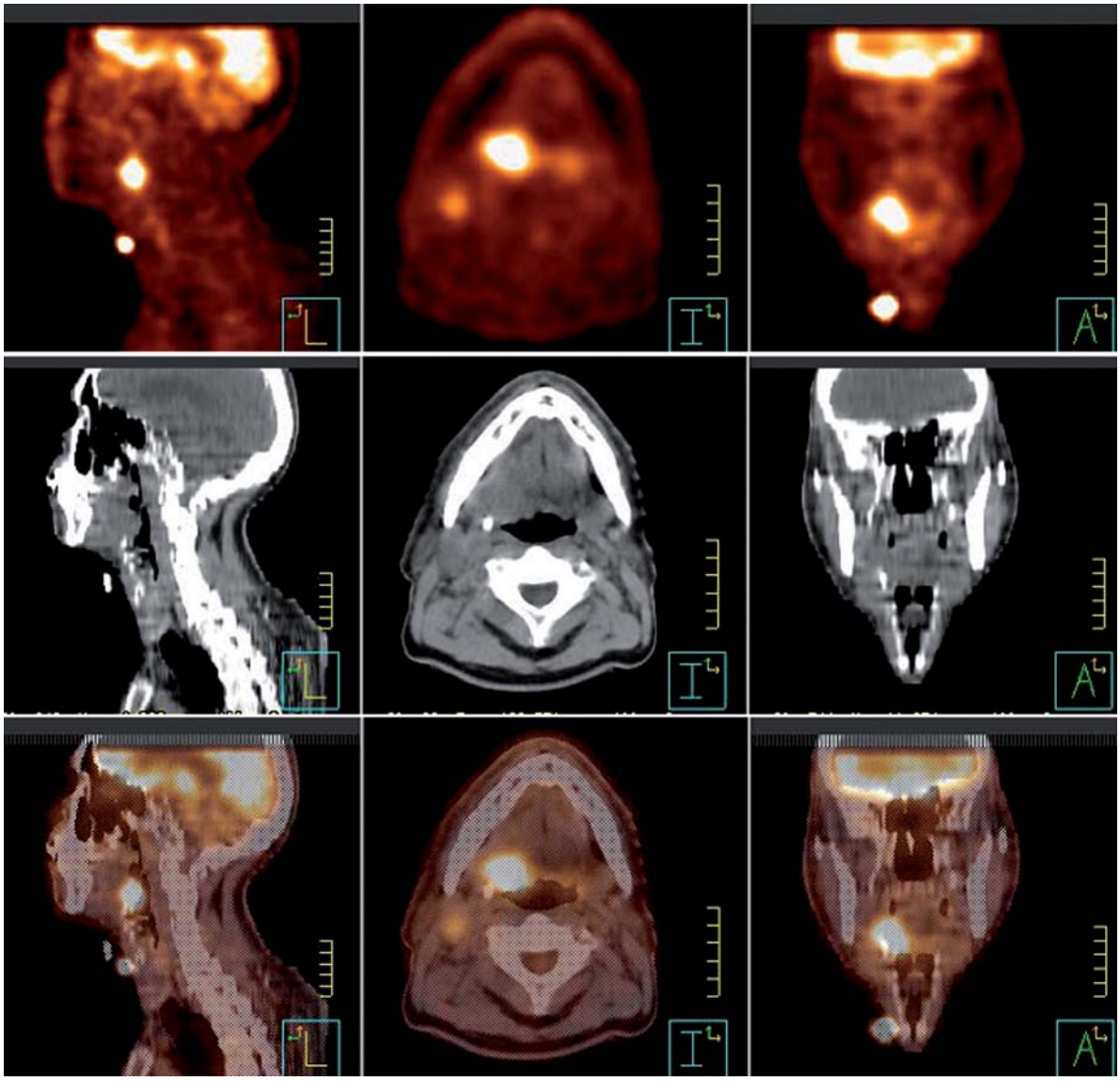

Fig. 12.6. Example of RT planning PET-CT scans for head and neck cancer patients. Upper panel is PET scan, middle panel is corresponding CT scan and lower panel is fused Images. The hot circular activity in front of the patient's neck below the chin outside on the skin is a dual PET and CT marker. This is a Sodium-22 coin (a positron emitter). Therefore, seen in both PET (as hot) and CT (as metallic density in the middle panel) images. The fused images were used in this patient to draw the gross tumor volume which included both the tumor at the right base of the tongue and a right sided cervical lymph node as seen in the lower panel trans-axial image.

with CT alone and PET/CT can improve the therapeutic window for IMRT in head and neck cancers. Image fusion has also been reported to increase the confidence of the radiation oncologist while drawing target volumes and thereby reduces the interobserver variation (Fig. 12.6).

In summary, the advantages of PET during RT planning are: (1) the ability to detect systemic metases thereby helping to avoid unnecessary/aggressive RT, (2) the delineation of metabolically active tissue not picked up on CT, thereby modifying the planned target volume and reducing the risk of geographical misses, (3) accurate target delineation in RT helping to protect vital normal structures, and (4) a decrease in the interobserver variability in drawing target volumes for RT. However, there is no outcome study in the literature in terms of role of PET/CT on the impact on response rates or disease free survival rates. Long term prospective randomized studies within a large population in this direction are very essential before any final conclusions are drawn.

12.10 Summary

A detailed knowledge of image interpretation in different tumors, and of the advantages and limitations of different imaging techniques, is essential. In this rapidly changing field of medicine, the radiologist has to have a good understanding of new developments in all imaging modalities [9].

Nuclear medicine imaging studies have limitations with respect to resolution. It is important that we know the limitations of these procedures so that we do not promise the patient or the referring physician what we cannot deliver. Specificity of uptake in malignant tumors is quite variable, according to the populations studied in various reports and the location of the lesions. Although in some cases the sensitivity and specificity are quite high, the negative predicted value is never 100%. For this reason nuclear medicine studies are not intended to replace surgical confirmation of the primary lesions concerned. Staging of malignant disease is a microscopic process. Nuclear medicine imaging procedures are good only for upstaging malignant disease, while downstaging malignant disease always requires pathological confirmation. For the purposes of patient follow-up, and to evaluate treatment response, the absence of uptake at the site of malignant disease does not mean that there is no evidence of microscopic disease. The chances of recurrence may be quite high if negative scans are obtained shortly after the end of treatment. Negative scans after several months or years of treatment are indicative of a complete local cure. An emerging field is the prediction of tumor response and evaluation of response to chemotherapy by using sequential scans of various radiopharmaceuticals, especially ^{201}Tl-chloride, ^{99m}Tc-sestamibi, ^{67}Ga-citrate, and more recently F-18 FDG. This area is gaining clinical importance in malignant lymphoma, brain tumors, bone and soft tissue sarcomas, esophageal cancer, and head and neck cancers and should be expanded to other locations. Other specific areas of imaging such as monoclonal antibody and receptor imaging are discussed elsewhere in this book. The future for research and growth in nuclear oncology is wide open and very promising.

PET using fluorine-18-fluorodeoxyglucose (FDG) provides more sensitive and more specific information about the extent of disease than morphologic-anatomic imaging alone and it is a powerful modality for determination of response to treatment. The metabolic information from FDG-PET is also superior compared with anatomic imaging in detecting residual viable tumor tissue after completion of treatment. Recent developments in instrumentation and the use of new tracers targeting cell proliferation and amino acid transport and synthesis hold promise to augment the application of PET in cancer patients in the future.

References

1. Liotta LA, Liu ET (2001) Essentials of molecular biology: basic principles. In: Deviate VT, Hellmann S, Rosenberg SA (eds) Cancer: principles and practice of oncology, 6th edn. Lippincott, Williams & Wilkins, Philadelphia, pp 3 – 16
2. Liotta LA, Liu ET (2001) Essentials of molecular biology: genomics and cancer. In: DeVita VT, Hellman S, Rosenberg SA (eds) Cancer: principles and practice of oncology, 6th edn. Lippincott, Williams & Wilkins, Philadelphia, pp 17 – 30
3. Husband J, Reznek R (1998) An overview of imaging in oncology. In: Husband JES, Reznek RH (eds) Imaging in oncology. Isis Medical Media, Oxford, pp 1 – 10
4. Coleman RE (1998) Clinical PET in oncology. Clin Pos Imaging 1:15 – 29
5. Maisey MN, Dakin M (1998) The first 5 years of a dedicated clinical PET centre. Clin Pos Imaging 1:59 – 69
6. Tesar R, Papatheofanis J, Valk P (1998) Reimbursement and technology assessment for positron imaging. Clin Pos Imaging 1:51 – 58
7. Phelps M, Cherry S (1998) The changing design of positron emission tomography. Clin Pos Imaging 1:31 – 45
8. Wagner H (1998) Multi-energy imaging in nuclear oncology. Clin Pos Imaging 1:47 – 50
9. Jana S, Abdel-Dayem HM (2004) Role of nuclear medicine in evaluating treatment response in oncology. Nuclear Medicine Annual 1 – 59
10. Abdel-Dayem H, Luo JQ, El-Zeftawy H, Sadek S (1999) Clinical experience with dual head gamma camera coincidence imaging. Clin Pos Imaging 2:31 – 38
11. Israel O, Keidar Z, Iosilevsky G, Bettman L, Sachs J, Frenkel A (2001) The fusion of anatomic and physiologic imaging in the management of patients with cancer. Semin Nucl Med 31:191 – 205
12. Wahl RL (1999) Imaging cancer in the New Millennium: forms follows function. Radiology 213:25
13. Shreve PD (2000) Adding structure to function. J Nucl Med 41:1380 – 1382
14. Schuetze SM, Rubin BP, Vernon C, Hawkins DS, Bruckner JD, Conrad EU 3rd, Eary JF (2005) Use of positron emission tomography in localized extremity soft tissue sarcoma treated with neoadjuvant chemotherapy. Cancer 103:339 – 348
15. Yeung H, Sanches A, Squire O, Macapinlac H, Larson S, Erdi Y (2002) Standardized uptake value in pediatric patients: an investigation to determine the optimum measurement parameter. J Nucl Med 43:61 – 66
16. Hawkins DS, Rajendran JG, Conrad EU III, Bruckner JD, Eary JF (2002) Evaluation of chemotherapy response in pediatric bone sarcomas by [F-18]-fluorodeoxy-d-glucose positron emission tomography. Cancer 94:3277 – 3284
17. Gehring PJ, Hammond PB (1967) The interrelationship between thallium-201 chloride and potassium in animals. J Pharmacol Exp Ther 155:187 – 201
18. Britten JS, Blank M (1968) Thallium-201 chloride-201 chloride activation of the (Na^+ K^+) activated ATPase of rabbit kidney. Biochim Biophys Acta 159:160 – 166
19. Sessler MJ, Geck P, Maul FD, Hor G, Munz DL (1986) New aspects of cellular thallium-201 chloride-201 chloride uptake: Tl^+-Na^+-2Cl-cotransport is the central mechanism of ion uptake. Nucl Med 23:24 – 27

20. Piwnica-Worms D, Kronauge JF, Chiu ML (1991) Enhancement of tetraphenylborate of technetium-99m-MIBI uptake kinetics and accumulation in cultured chick myocardial cells. J Nucl Med 32:1992 – 1999
21. Piwnica-Worms D, Holman BL (1990) Noncardiac applications of hexakis-(alkylisonitrile) technetium-99m complexes. J Nucl Med 31:1166 – 1167
22. Chiu ML, Kronauge JF, Piwnica-Worms D (1990) Effects of mitochondrial and plasma membrane potentials on accumulation of jexalos (2-methoxyisobutyl isonitrile)technetium (I) in cultured mouse fibroblasts. J Nucl Med 31:1646 – 1653
23. Chiu ML, Herman LW, Kronauge JF, Piwnica-Worms D (1992) Comparative effects of neutral dipolar compounds and lipophilic anions on technetium-99m-hexakis (2-methoxyisobutyl isonitrile) accumulation in cultured chick ventricular myocytes. Invest Radiol 27:1052 – 1058
24. Piwnica-Worms D, Chiu ML, Budding M, Kronauge JF, Kramer RA, Croop JM (1993) Functional imaging of multidrug-resistant P-glycoprotein with an organotechnetium complex. Cancer Res 53:977 – 984
25. Bae KT, Piwnica-Worms D (1997) Pharmacokinetic modeling of multidrug resistance P-glycoprotein transport of gamma-emitting substrates. Q J Nucl Med 41:101 – 110
26. Ballinger JR, Sheldon KM, Boxen I, Erlichman C, Ling V (1995) Differences between accumulation of 99mTc-MIBI and 201Tl-thallous chloride in tumour cells: role of P-glycoprotein. Q J Nucl Med 39:122 – 128
27. Larson SM, Rasey JS, Allen DR, Nelson NJ (1979) A transferrin-mediated uptake of gallium-67 by EMT-6 sarcoma. I. Studies in tissue culture. J Nucl Med 20:837 – 842
28. Larson SM, Rasey JS, Allen DR, Nelson NJ (1979) A transferrin-mediated uptake of gallium-67 by EMT-6 sarcoma. I. Studies in tissue culture. J Nucl Med 20:837 – 842
29. Berry JP, Escaig F, Poupon MF, Galle P (1983) Localization of gallium in tumor cells. Electron microscopy, electron probe microanalysis and analytical ion microscopy. Int J Nucl Med Biol 10:199 – 204
30. Ak I, Stokkel MP, Pauwels EK (2000) Positron emission tomography with 2-[18F]fluoro-2-deoxy-d-glucose in oncology, part II. The clinical value in detecting and staging primary tumours. J Cancer Res Clin Oncol 126:560 – 574
31. Delbeke D (1999) Oncological applications of FDG PET imaging: brain tumors, colorectal cancer, lymphoma and melanoma. J Nucl Med 40:591 – 603
32. Avril N, Menzel M, Dose J, Schelling M, Weber W, Janicke F, Nathrath W, Schwaiger M (2001) Glucose metabolism of breast cancer assessed by 18F-FDG PET: histologic and immunohistochemical tissue analysis. J Nucl Med 42:9 – 16
33. Ak I, Stokkel MP, Pauwels EK (2000) Positron emission tomography with 2-[18F]fluoro-2-deoxy-d-glucose in oncology, part II. The clinical value in detecting and staging primary tumours. J Cancer Res Clin Oncol 126:560 – 574
34. Bos R, van Der Hoeven JJ, van Der Wall E, Van Der Groep, Van Diest PJ, Comans EF, Joshi U, Semenza GL, Hoekstra OS, Lammertsma AA, Molthoff CF (2002) Biologic correlates of (18)fluorodeoxyglucose uptake in human breast cancer measured by positron emission tomography. J Clin Oncol 20:379 – 387
35. Jerusalem G, Beguin Y, Fassotte MF, Najjar F, Paulus P, Rigo P, Fillet G (1999) Whole-body positron emission tomography using 18-F-fluorodeoxyglucose for posttreatment evaluation in Hodgkin's disease and non-Hodgkin's lymphoma has higher diagnostic and prognostic value than classical conventional tomography scan imaging. Blood94: 429 – 433
36. Higashi K, Ueda Y, Sakuma T, Seki H, Oguchi M, Taniguchi M, Taki S, et al. (2001) Comparison of [(18)F]FDG PET and (201)Tl SPECT in evaluation of pulmonary nodules. J Nucl Med 42:1489 – 1496
37. Even-Sapir E, Metser U, Flusser G, Zuriel L, Kollender Y, Lerman H, Lievshitz G, et al. (2004) Assessment of malignant skeletal disease: initial experience with 18F-fluoride PET/CT and comparison between 18F-fluoride PET and 18F-fluoride PET/CT. J Nucl Med 45:272 – 278
38. Rasey JS, Grierson JR, Wiens LW, Kolb PD, Schwartz JL (2002)Validation of FLT uptake as a measure of thymidine kinase-1 activity in A549 carcinoma cells. J Nucl Med 43:1210 – 1217
39. Buck AK, Halter G, Schirrmeister H, Kotzerke J, Wurziger I, Glatting G, Mattfeldt T, et al. (2003) Imaging proliferation in lung tumors with PET: ^{18}F-FLT versus ^{18}F-FDG. J Nucl Med 44:1426 – 1431
40. van Waarde A, Cobben DC, Suurmeijer AJ, Maas B, Vaalburg W, de Vries EF, Jager PL, et al. (2004) Selectivity of ^{18}F-FLT and ^{18}F-FDG for differentiating tumor from inflammation in a rodent model. J Nucl Med 45:695 – 700
41. Cobben DC, Jager PL, Elsinga PH, Maas B, Suurmeijer AJ, Hoekstra HJ (2003) 3'-(18)F-Fluoro-3'-deoxy-l-thymidine: a new tracer for staging metastatic melanoma? J Nucl Med 44:1927 – 1932
42. Pieterman RM, Que TH, Elsinga PH, Pruim J, van Putten JW, Willemsen AT, Vaalburg W, Groen HJ (2002) Comparison of (11)C-choline and (18)F-FDG PET in primary diagnosis and staging of patients with thoracic cancer. J Nucl Med 43:167 – 172
43. Hara T, Inagaki K, Kosaka N, Morita T (2000) Sensitive detection of mediastinal lymph node metastasis of lung cancer with 11C-choline PET. J Nucl Med 41:1507 – 1513
44. Torizuka T, Kanno T, Futatsubashi M, Okada H, Yoshikawa E, Nakamura F, Takekuma M, Maeda M, Ouchi Y (2003) Imaging gynecologic tumors: comparison of ^{11}C-choline PET with ^{18}F-FDG PET. J Nucl Med 44:1051 – 1056
45. Kostakoglu L, Goldsmith SJ (2004) PET in the assessment of therapy response in patients with carcinoma of the head and neck and of the esophagus. J Nucl Med 45:56 – 68
46. Bradley JD, Perez CA, Dehdashti F, Siegel BA (2004) Implementing biologic target volumes in radiation treatment planning for non-small cell lung cancer. J Nucl Med 45 Suppl 1:96S–101S
47. Haubner R, Wester HJ, Weber WA, Mang C, Ziegler SI, Goodman SL, Senekowitsch-Schmidtke R, Kessler H, Schwaiger M (2001) Noninvasive imaging of alpha(v)beta3 integrin expression using 18F-labeled RGD-containing glycopeptide and positron emission tomography. Cancer Res 61:1781 – 1785
48. Haubner R, Wester HJ, Burkhart F, Senekowitsch-Schmidtke R, Weber W, Goodman SL, Kessler H, Schwaiger M (2001) Glyosylated RGD-containing peptides: tracer for tumor targeting and angiogenesis imaging with improved biokinetics. J Nucl Med 42:326 – 336
49. Boersma HH, Tromp SC, Hofstra L, Narula J (2005) Stem cell tracking: reversing the silence of the lambs. J Nucl Med 46:200 – 203
50. Rebulla P, Giordano R (2004) Cell therapy: an evolutionary development of transfusion medicine. Int J Cardiol 95(Suppl 1):S38–S42
51. Takahashi M, Deb NJ, Kawashita Y, Lee SW, Furgueil J, Okuyama T, Roy-Chowdhury N, Vikram B, Roy-Chowdhury J, Guha C (2003) A novel strategy for in vivo expansion of transplanted hepatocytes using preparative hepatic irradiation and FasL-induced hepatocellular apoptosis. Gene Ther 10:304 – 313
52. Herschman HR (2004) PET reporter genes for noninvasive imaging of gene therapy, cell tracking and transgenic analysis. Crit Rev Oncol Hematol 51:191 – 204

53. Jendelova P, Herynek V, Urdzikova L, Glogarova K, Kroupova J, Andersson B, Bryja V, Burian M, Hajek M, Sykova E (2004) Magnetic resonance tracking of transplanted bone marrow and embryonic stem cells labeled by iron oxide nanoparticles in rat brain and spinal cord. J Neurosci Res 76:232 – 243
54. Modo M, Cash D, Mellodew K, Williams SC, Fraser SE, Meade TJ, Price J, Hodges H (2002) Tracking transplanted stem cell migration using bifunctional, contrast agent-enhanced, magnetic resonance imaging. Neuroimage 17:803 – 811
55. Adonai N, Nguyen KN, Walsh J, Iyer M, Toyokuni T, Phelps ME, McCarthy T, McCarthy DW, Gambhir SS (2002) Ex vivo cell labeling with ^{64}Cu-pyruvaldehyde-bis(N4-methylthiosemicarbazone) for imaging cell trafficking in mice with positron-emission tomography. Proc Natl Acad Sci USA 99:3030 – 3035
56. Brenner W, Aicher A, Eckey T, Massoudi S, Zuhayra M, Koehl U, Heeschen C, Kampen WU, Zeiher AM, Dimmeler S, Henze E (2004) 111In-labeled CD34+ hematopoietic progenitor cells in a rat myocardial infarction model. J Nucl Med 45:512 – 518
57. Chin BB, Nakamoto Y, Bulte JW, Pittenger MF, Wahl R, Kraitchman DL (2003) 111In oxine labelled mesenchymal stem cell SPECT after intravenous administration in myocardial infarction. Nucl Med Commun 24:1149 – 1154
58. Yau TM, Tomita S, Weisel RD, Jia ZQ, Tumiati LC, Mickle DA, Li RK (2003) Beneficial effect of autologous cell transplantation on infarcted heart function: comparison between bone marrow stromal cells and heart cells. Ann Thorac Surg 75:169 – 176
59. Kumar Rakesh, Jana Suman (2004) Positron emission tomography: an advanced nuclear medicine imaging technique from research to clinical practice. Methods Enzymol 385:3 – 19
60. Blankenberg FG, Strauss HW (2001) Will imaging of apoptosis play a role in clinical care? A tale of mice and men. Apoptosis 6:117 – 123
61. Blankenberg FG, Katsikis PD, Tait JF, Davis RE, Naumovski L, Ohtsuki K, Kopiwoda S, et al. (1998) In vivo detection and imaging of phosphatidylserine expression during programmed cell death. Proc Natl Acad Sci USA 95:6349 –6354
62. Toretsky J, Levenson A, Weinberg IN, Tait JF, Uren A, Mease RC (2004) Preparation of F-18 labeled annexin V: a potential PET radiopharmaceutical for imaging cell death. Nucl Med Biol 31:747 – 752
63. Grierson JR, Yagle KJ, Eary JF, Tait JF, Gibson DF, Lewellen B, Link JM, Krohn KA (2004) Production of [F-18]fluoroannexin for imaging apoptosis with PET. Bioconjug Chem 15:373 – 379
64. Blakey DC, Burke PJ, Davies DH (1995) Antibody-directed enzyme prodrug therapy (ADEPT) for treatment of major solid tumour disease. Biochem Soc Trans 23:1047 – 1050
65. Weissleder R (1999) Molecular imaging: Exploring the next frontier. Radiology 212:609 – 614
66. Wunderbaldinger P, Bogdanov A Jr,Weissleder R (2000) New approaches for imaging in gene therapy. Eur J Radiol 34:156 – 165
67. Tjuvajev JG, Avril N, Oku T, Sasajima T, Miyagawa T, Joshi R, Safer M, et al. (1998) Imaging herpes virus thymidine kinase gene transfer and expression by positron emission tomography. Cancer Res 58:4333 – 4341
68. Gambhir SS, Barrio JR, Phelps ME, Iyer M, Namavari M, Satyamurthy N, Wu L, et al. (1999) Imaging adenoviral-directed reporter gene expression in living animals with positron emission tomography. Proc Natl Acad Sci USA 96:2333 – 2338
69. Omar WS, Eissa S, Moustafa H, Farag H, Ezzat I, Abdel-Dayem HM (1997) Role of thallium-201 chloride and Tc-99m methoxy-isobutyl-isonitrite (sestaMIBI) in evaluation of breast masses: correlation with the immunohistochemical characteristic parameters (Ki-67, PCNA, Bcl, and angiogenesis) in malignant lesions. Anticancer Res 17:1639 – 1644
70. Kubota K, Ishiwata K, Kubota R, Yamada S, Tada M, Sato T, Ido T (1991) Tracer feasibility for monitoring tumor radiotherapy: a quadruple tracer study with fluorine-18-fluorodeoxyglucose or fluorine-18-fluorodeoxyuridine, l-[methyl-^{14}C]methionine, [6-^{3}H]thymidine, and gallium-67. J Nucl Med 32:2118 – 2123
71. Willemsen A, Waarde A van, Paans A (1995) In vivo protein synthesis rate determination in primary or recurrent brain tumors using l-[1-C11]tyrosine and PET. J Nucl Med 36:411 – 419
72. Minn H, Clavo AC, Grenman R, Wahl RL (1995) In vitro comparison of cell proliferation kinetics and uptake of tritriated fluorodeoxyglucose and L-methionine in squamous-cell carcinoma of the head and neck. J Nucl Med 36:252 – 258
73. Warburg O (1931) The metabolism of tumors. Smith, New York, pp 254 – 270
74. Hiraki Y, Rosen O, Birnbaum M (1988) Growth factors rapidly induce expression of the glucose transporter gene. J Biol Chem 27:13655 – 13662
75. Gerdes J, Lemke H, Baisch H, Wacker HH, Schwab U, Stein H (1984) Cell cycle analysis of cell proliferation associated human nuclear antigen defined by mononuclear antibody Ki-67. J Immunol 133:1710 – 1715
76. Bravo R (1986) Synthesis of the nuclear protein cyclin (PCNA) and its relationship with DNA replication. Exp Cell Res 163:287 – 293
77. Tahan SR, Neuberg DS, Dieffenbach A, Yacoub L (1993) Prediction of early relapse and shortened survival in patients with breast cancer by proliferating cell nuclear antigen score. Cancer 71:3552 – 3559
78. Ottman R, Pike MC, King MC, Henderson BE (1983) Practical guide for estimating risk for familial breast cancer. Lancet 2:556 – 558
79. Reed Jc, Stein C, Subasinghe C, et al (1992) Anti-sense mediated inhibition of Bcl-2 proto-oncogene expression and leukemia cell growth and survival: comparison of phosphodiester and phosphothiote digoneocleotides. Cancer Res 50:6565
80. Weidner N, Semple JP, Welch WR, Folkman J (1991) Tumor angiogenesis and metastasis – correlation in invasive breast carcinoma. N Engl J Med 324:1 – 8
81. Weissleder R, Mahmood U (2001) Molecular imaging. Radiology 219:316 – 333
82. Shaffer K (1997) Radiologic evaluation in lung cancer: diagnosis and staging. Chest 112:235S–238S
83. Itouji E, Kono M, Adachi S, Kusumoto M, Mimura F, Zhang M (1997) The role of CT and MR imaging in the diagnosis of lung cancer. Gan To Kagaku Ryoho 24 [Suppl 3]:353 –358
84. Sandrasegaran K, Robinson PJ, Selby P (1994) Staging of lymphoma in adults. Clin Oncol 94:149 – 161
85. Marglin SI, Castellino RA (1985) Selection of imaging studies for the initial staging of patients with Hodgkin's disease. Semin Ultrasound CT MR 6:380 – 393
86. DeVita VT, Hellman S, Jaffe ES (1993) Hodgkin's disease. In: DeVita VT, Hellman S, Rosenberg S (eds) Cancer principles and practice of oncology. Lippincott, Philadelphia, pp 1819 – 1859
87. Rogers JV, Powell RW (1972) Mammographic indications for biopsy of clinically normal breasts: correlation with pathologic findings in 72 cases. AJR Am J Roentgenol 115:794 – 800

88. Homer MJ (1984) Non-palpable breast abnormalities: a realistic view of the accuracy of mammography in detecting malignancies. Radiology 153:831 – 832
89. Bassett LW, Liu TH, Giuliano AE, Gold RH (1991) The prevalence of carcinoma in palpable vs impalpable, mammographically detected lesions. AJR Am J Roentgenol 157:21 – 24
90. Kopans DB (1992) The positive predictive value of mammography. AJR Am J Roentgenol 158:521 – 526
91. Mann BD, Giuliano AE, Bassett LW, Barber MS, Hallauer W, Morton DL (1983) Delayed diagnosis of breast cancer as a result of normal mammograms. Arch Surg 118:23 – 24
92. Feig SA, Shaber GA, Patchefskly A (1977) Analysis of clinically occult and mammographically occult breast tumors. AJR Am J Roentgenol 128:403 – 408
93. Kalisher L (1979) Factors influencing false negative rates in xeromammography. Radiology 133:297 – 301
94. Conti P, Lilien D, Hawley K, et al (1996) PET and 18F in oncology: a clinical update. Nucl Med Biol 23:717 – 735
95. McCain TW, Dunagan DP, Chin R Jr, Oaks T, Harkness BA, Haponik EF (2000) The usefulness of positron emission tomography in evaluating patients for pulmonary malignancies. Chest 118:1610 – 1615
96. Lowe VJ, Naunheim KS (1998) Current role of positron emission tomography in thoracic oncology. Thorax 53: 703 – 712
97. Erasmus JJ, McAdams HP, Patz EF Jr, Goodman PC, Coleman RE (1998) Thoracic FDG PET: state of the art. Radiographics 18:5 – 20
98. Lowe VJ, Fletcher JW, Gobar L, Lawson M, Kirchner P, Valk P, Karis J, et al. (1998) Prospective investigation of positron emission tomography in lung nodules. J Clin Oncol 16:1075 – 1084
99. Patz EF (2000) Evaluation of focal pulmonary abnormalities with FDG PET. Radiographics 20:1182 – 1185
100. Marom EM, Sarvis S, Herndon JE 2nd, Patz EF Jr, et al. (2002) T1 lung cancers: sensitivity of diagnosis with fluorodeoxyglucose PET. Radiology 223:453 – 459
101. Young H, Baum R, Cremerius U, Herholz K, Hoekstra O, Lammertsma AA, Pruim J, et al (1999) Measurement of clinical and subclinical tumour response using [18F]-fluorodeoxyglucose and positron emission tomography: review and 1999 EORTC recommendations. European Organization for Research and Treatment of Cancer (EORTC) PET Study Group. Eur J Cancer 35:1773 – 1782
102. Waxman AD, Aktolun C (1999) Breast cancer. Nuclear oncology. Springer, Berlin Heidelberg New York, pp 143 – 162
103. Waxman A, Nagaraj N, Ashok G, Khan S, Yadegar J, Memsic L, Silberman A, et al (1994) Sensitivity and specificity of Tc-99m methoxy isobutyl isonitrile (MIBI) in the evaluation of primary carcinoma of the breast: comparison of palpable and nonpalpable lesions with mammography (abstract). J Nucl Med 35:22P
104. Burak Z, Argon M, Memis A, Erdem S, Balkan Z, Duman Y, Ustun EE, et al. (1994) Evaluation of palpable breast masses with 99Tcm-MIBI: a comparative study with mammography and ultrasonography. Nucl Med Commun 15:604 – 612
105. Waxman AD, Ashok G, Kooba A (1993) The use of Tc-99m methoxyisobutyl isonitrile (MIBI) in evaluation of patients with primary carcinoma of the breast: comparison with T1 – 201 (abstract). J Nucl Med 34 [Suppl]:139
106. Khalkhali I, Mena I, Jouanne E (1993) Technetium-99m sestamibi MIBI prone breast imaging in patients with suspicion of breast cancer (abstract). J Nucl Med 34 [Suppl]:140
107. Khalkhali I, Mena I, Jouanne E, Diggles L, Venegas R, Block J, Alle K, Klein S (1994) Prone scintimammography in patients with suspicion of carcinoma of the breast. J Am Coll Surg 178:491 – 497
108. Taillefer R, Robidoux A, Lambert R, Turpin S, Laperriere J (1995) Technetium-99m-sestamibi prone scintimammography to detect primary breast cancer and axillary lymph node involvement. J Nucl Med 36:1758 – 1765
109. Khalkhali I, Cutrone J, Mena I, Diggles L, Venegas R, Vargas H, Jackson B, et al. (1995) Technetium-99m sestamibi scintimammography of breast lesions, clinical and pathological follow-up. J Nucl Med 36:1784 – 1789
110. Palmedo H, Biersack HJ, Lastoria S, Maublant J, Prats E, Stegner HE, Bourgeois P, et al. (1998) Scintimammography with technetium-99m methoxyisobutyl isonitrile results of a prospective European multicentre trial. Eur J Nucl Med 25:375 – 385
111. Rosen EL, Turkington TG, Soo MS, Baker JA, Coleman RE (2005) Detection of primary breast carcinoma with a dedicated, large field of view FDG PET mammography device: initial experience. Radiology 234:527 – 534
112. Mentzer SJ, Swanson SJ, DeCamp MM, Bueno R, Sugarbaker DJ (1977) Mediastinoscopy, thoracoscopy, and video-assisted thoracic surgery in the diagnosis and staging of lung cancer. Chest 112:239S–241S
113. Edell ES (1997) Diagnostic tests for lung cancer. Curr Opin Pulm Med 3:247 – 251
114. White PG, Adams H, Crane MD, Butchart EG (1994) Preoperative staging of carcinoma of the bronchus: can computed tomographic scanning reliably identify stage III tumors? Thorax 49:951 – 957
115. Webb WR, Gatsonis C, Zerhouni EA, Heelan RT, Glazer GM, Francis IR, et al. (1991) CT and MR imaging in staging non-small cell bronchogenic carcinoma: report of the Radiologic Diagnostic Oncology Group. Radiology 178: 705 – 713
116. Bonomo L, Ciccotosto C, Guidotti A, Storto ML (1996) Lung cancer staging: the role of computed tomography and magnetic resonance imaging. Eur J Radiol 23:35 – 45
117. Hanson JA, Armstrong P (1997) Staging intrathoracic non-small-cell lung cancer. Eur Radiol 7:161 – 172
118. Moog F, Bangerter M, Diederichs CG, Guhlmann A, Merkle E, Frickhofen N, Reske SN (1998) Extranodal malignant lymphoma: detection with FDG PET versus CT. Radiology 206:475 – 481
119. Steinert HC, Hauser M, Allemann F, Engel H, Berthold T, von Schulthess GK, Weder W (1997) Non-small cell lung cancer: nodal staging with FDG PET versus CT with correlative lymph node mapping and sampling. Radiology 202:441 – 446
120. Bury T, Dowlati A, Paulus P, Corhay JL, Hustinx R, Ghaye B, Radermecker M, et al. (1997) Whole-body 18 FDG positron emission tomography in the staging of non-small lung cancer. Eur Respir J 10:2529 – 2534
121. Valk PE, Pounds TR, Hopkins DM, Haseman MK, Hofer GA, Greiss HB, Myers RW, et al. (1995) Staging non-small cell lung cancer by whole-body positron emission tomographic imaging. Ann Thorac Surg 60:1573 – 1582
122. Waxman AD (1997) The role of Tc-99m methoxyisobutyl isonitrile in imaging breast cancer. Semin Nucl Med 27:40 – 54
123. Kao CH, Wang SJ, Yeh SH (1994) Technetium-99m MIBI uptake in breast carcinoma and axillary lymph node metastases. Clin Nucl Med 19:898 – 900
124. Kubota K, Matsuzawa T, Amemiya A, Kondo M, Fujiwara T, Watanuki S, Ito M, et al. (1989) Imaging of breast cancer with (18F) fluorodeoxyglucose and positron emission tomography. JCAT 13:1097 – 1098

125. Tse NY, Hoh CK, Hawkins RA, Zinner MJ, Dahlbom M, Choi Y, Maddahi J (1992) The application of positron emission tomographic imaging with fluorodeoxyglucose for the evaluation of breast disease. Ann Surg 216:27 – 34
126. Adler LP, Crowe JP, al-Kaisi NK, Sunshine JL (1993) Evaluation of breast masses and axillary lymph nodes with (F-18)-2-deoxy-D-glucose PET. Radiology 181:743 – 750
127. Giuliano AE, Kirgan DM, Guenther JM, Morton DL (1994) Lymphatic mapping and sentinel lymphadenectomy for breast cancer. Ann Surg 220:391 – 398
128. Gunther JM, Krishnamoorthy M, Tan LR (1997) Sentinel lymphadenectomy for breast cancer in a community managed care setting. Cancer J Sci Am 3:336 – 340
129. Koller M, Barsuk D, Zippel D, Engelberg S, Ben-Ari G, Papa MZ (1998) Sentinel lymph node involvement – a predictor for axillary node status with breast cancer. Has the time come? Eur J Surg Oncol 24:166 – 168
130. Barnwell JM, Arredondo MA, Kollmorgen D, Gibbs JF, Lamonica D, Carson W, Zhang P, et al. (1998) Sentinel node biopsy in breast cancer. Ann Surg Oncol 5:126 – 130
131. Kogel KE, Sweetenham JW (2003) Current therapies in Hodgkin's disease. Eur J Nucl Med Mol Imaging 30 Suppl 1:S19 – 27
132. Okada J, Oonishi H, Yoshikawa K, Itami J, Uno K, Imaseki K, Arimizu N (1994) FDG-PET for predicting the prognosis of malignant lymphoma. Ann Nucl Med 8:187 – 191
133. Kunkel M, Forster GJ, Reichert TE, Jeong JH, Benz P, Bartenstein P, Wagner W, et al. (2003) Detection of recurrent oral squamous cell carcinoma by [18F]-2-fluorodeoxyglucose-positron emission tomography: implications for prognosis and patient management. Cancer 98:2257 – 2265
134. Halfpenny W, Hain SF, Biassoni L, Maisey MN, Sherman JA, McGurk M (2002) FDG-PET. A possible prognostic factor in head and neck cancer. Br J Cancer 86:512 – 516
135. Brun E, Ohlsson T, Erlandsson K, Kjellen E, Sandell A, Tennvall J, Wennerberg J, et al (1997) Early prediction of treatment outcome in head and neck cancer with 2 – 18FDG PET. Acta Oncol 36:741 – 747
136. Kitagawa Y, Sano K, Nishizawa S, Nakamura M, Ogasawara T, Sadato N, Yonekura Y (2003) FDG-PET for prediction of tumour aggressiveness and response to intra-arterial chemotherapy and radiotherapy in head and neck cancer. Eur J Nucl Med Mol Imaging 30:63 – 71
137. Minn H, Lapela M, Klemi PJ, Grenman R, Leskinen S, Lindholm P, Bergman J, et al (1997) Prediction of survival with fluorine-18-fluoro-deoxyglucose and PET in head and neck cancer. J Nucl Med 38:1907 – 1911
138. Kunkel M, Forster GJ, Reichert TE, Kutzner J, Benz P, Bartenstein P, Wagner W (2003) Radiation response non-invasively imaged by [18F]FDG-PET predicts local tumor control and survival in advanced oral squamous cell carcinoma. Oral Oncol 39:170 – 177
139. Luker GD, Luker KE, Sharma V, et al (1999) Assessment of multidrug resistance. Nuclear oncology. Springer, Berlin Heidelberg New York, pp 371 – 382
140. Sciuto R, Pasqualoni R, Bergomi S, Petrilli G, Vici P, Belli F, Botti C, Mottolese M, Maini CL (2002) Prognostic value of ^{99m}Tc Sestamibi washout in predicting response to locally advanced breast cancer to neoadjuvant chemotherapy. J Nucl Med 43:745 – 751
141. Britz-Cunnignham SH, Adelstein SA (2003) Molecular targeting with radionuclides: state of the science. J Nucl Med 44:1945 – 1961
142. Gottesman MM, Pastan I (1993) Biochemistry of multidrug resistance mediated by the multidrug transporter. Annu Rev Biochem 62:385 – 427
143. Kao CH, Hsieh JF, Tsai SC, Ho YJ, Changlai SP, Lee JK (2001) Paclitaxel-based chemotherapy for non-small cell lung cancer: Predicting the response with 99mTc-tetrofosmin chest imaging. J Nucl Med 42:17 – 20
144. Elsinga PH, Franssen EJ, Hendrikse NH, Fluks L, Weemaes AM, van der Graaf WT, de Vries EG, Visser GM, Vaalburg W (1996) Carbon-11-labeled daunorubicin and verapamil for probing P-glycoprotein in tumors with PET. J Nucl Med 37:1571 – 1575
145. Hendrikse NH, Franssen EJ, van der Graaf WT, Vaalburg W, de Vries EG (1999) Visualization of multidrug resistance in vivo. Eur J Nucl Med 26:283 – 293. Review
146. Levchenko A, Mehta BM, Lee JB, Humm JL, Augensen F, Squire O, Kothari PJ, et al (2000) Evaluation of ^{11}C-colchicine for PET imaging of multiple drug resistance. J Nucl Med 41:493 – 501
147. Kurdziel KA, Kiesewetter DO, Carson RE, Eckelman WC, Herscovitch P (2003) Biodistribution, radiation dose estimates, and in vivo Pgp modulation studies of 18F-paclitaxel in nonhuman primates. J Nucl Med 44:1330 – 1339
148. Pamper GM (2001) Functional and metabolic imaging. In: DeVita VT, Hellman S, Rosenberg SA (eds) Cancer: Principles and practice of oncology, 6th edn. Lippincott-Williams & Wilkins, Philadelphia, pp 679 – 689
149. Matthews PM, Wylezinska M, Cadoux-Hudson T (2001) Novel approaches to imaging brain tumors. Hematol Oncol Clin North Am 15:609 – 630
150. Coleman RE, Hoffman JM, Hanson MW, Sostman HD, Schold SC (1991) Clinical application of PET for evaluation of brain tumors. J Nucl Med 32:616 – 622
151. Wallner KE, Galieich JH, Malkin MG, Arbit E, Krol G, Rosenblum MK (1989) Inability of computed tomography appearance of recurrent malignant astrocytoma to predict survival following reoperation. J Clin Oncol 7: 1492 – 1496
152. Cook GJ, Fogelman I, Collier BD, Krasnow AZ, Tauxe WN (1999) Bone tumors. In: Aktolun C, Tauxe WN (eds) Nuclear oncology. Springer, Berlin Heidelberg New York, pp 227 – 244
153. Abdel-Dayem HM, Scott AM, Macapinlac HA, El-Gazzar AH, Larson SM (1994) Role of thallim-201 chloride in tumor imaging. In: Freeman LM (ed) Nuclear medicine annual. Raven, New York, pp 181 – 234
154. Ganz WI, Nguyen TW, Benedetto MP, Friden A, Topchik S, Serafini A, Sfakianakis G (1993) Use of early, late and SPECT thallium-201 chloride imaging in evaluating activity of soft tissue and bone tumors (abstract). J Nucl Med 34:32P
155. Chen DCP, Ma GQ, Anasari A (1993) Optimum imaging time for thallium-201 chloride as a tumor agent in patients with lymphoma (abstract). J Nucl Med 33:A44
156. Avril NE, Weber WA (2005) Monitoring response to treatment in patients utilizing PET. Radiol Clin North Am 43:189 – 204
157. Coleman RE (1999) PET in lung cancer. J Nucl Med 40: 814 – 820
158. Zasadny KR, Wahl RL (1993) Standardized uptake values of normal tissues at PET with 2-[fluorine-18]-fluoro-2-deoxy-D-glucose: variations with body weight and a method for correction. Radiology 189:847 – 850
159. Jana S, Mahadeo S, Heller S, Isasi CR, Blaufox MD (2005) Influence of PET scanners, lesion size, and attenuation correction methods on SUV in FDG-PET imaging. (Abstract) J Nucl Med 46:328
160. Schoder H, Erdi YE, Chao K, Gonen M, Larson SM, Yeung HW (2004) Clinical implications of different image reconstruction parameters for interpretation of whole-body PET studies in cancer patients. J Nucl Med 45:559 – 566

161. Kinahan PE, Hasegawa BH, Beyer T (2003) X-ray-based attenuation correction for positron emission tomography/computed tomography scanners. Semin Nucl Med 33:166 – 179
162. Wu TH, Huang YH, Lee JJ, Wang SY, Wang SC, Su CT, Chen LK, Chu TC (2004) Radiation exposure during transmission measurements: comparison between CT- and germanium-based techniques with a current PET scanner. Eur J Nucl Med Mol Imaging 31:38 – 43
163. Kostakoglu L, Goldsmith SJ (2003) 18F-FDG PET evaluation of the response to therapy for lymphoma and for breast, lung, and colorectal carcinoma. J Nucl Med 44:224 – 239
164. Minn H, Zasadny KR, Quint LE (1995) Lung cancer: reproducibility of quantitative measurements for evaluating 2-[F-18]-fluoro-2-deoxy-D-glucose uptake at PET. Radiology 196:167 – 173
165. Weber WA, Ziegler SI, Thodtmann R (1999) Reproducibility of metabolic measurements in malignant tumors using FDG PET. J Nucl Med 40:1771 – 1777
166. Torizuka T, Clavo AC, Wahl RL (1997) Effect of hyperglycemia on in vitro tumor uptake of tritiated FDG, thymidine, l-methionine and l-leucine. J Nucl Med 38:382 – 386
167. Weber WA, Petersen V, Schmidt B (2003) Positron emission tomography in non-small-cell lung cancer: prediction of response to chemotherapy by quantitative assessment of glucose use. J Clin Oncol 21:2651 – 2657
168. Wahl RL, Zasadny K, Helvie M (1993) Metabolic monitoring of breast cancer chemohormonotherapy using positron emission tomography: initial evaluation. J Clin Oncol 11:2101 – 2111
169. Jansson T, Westlin JE, Ahlstrom H (1995) Positron emission tomography studies in patients with locally advanced and/or metastatic breast cancer: a method for early therapy evaluation? J Clin Oncol 13:1470 – 1477
170. Romer W, Hanauske AR, Ziegler S (1998) Positron emission tomography in non-Hodgkin's lymphoma: assessment of chemotherapy with fluorodeoxyglucose. Blood 91:4464 – 4471
171. Higashi K, Clavo AC, Wahl RL (1993) In vitro assessment of 2-fluoro-2-deoxy-D-glucose, l-methionine and thymidine as agents to monitor the early response of a human adenocarcinoma cell line to radiotherapy. J Nucl Med 34:773 – 779
172. Haberkorn U, Morr I, Oberdorfer F (1994) Fluorodeoxyglucose uptake in vitro: aspects of method and effects of treatment with gemcitabine. J Nucl Med 35:1842 – 1850
173. Dehdashti F, Flanagan FL, Mortimer JE (1999) Positron emission tomographic assessment of "metabolic flare" to predict response of metastatic breast cancer to antiestrogen therapy. Eur J Nucl Med 26:51 – 56
174. Mortimer JE, Dehdashti F, Siegel BA (2001) Metabolic flare: indicator of hormone responsiveness in advanced breast cancer. J Clin Oncol 19:2797 – 2803
175. Wieder H, Brucher BL, Zimmerman F (2004) Time course of tumor metabolic activity during chemoradiotherapy of esophageal squamous cell carcinoma and response to treatment. J Clin Oncol 22:900 – 909
176. Greven KM, Williams DW III, McGuirt WF Sr (2001) Serial positron emission tomography scans following radiation therapy of patients with head and neck cancer. Head Neck 23:942 – 946
177. MacManus MP, Hicks RJ, Matthews JP (2003) Positron emission tomography is superior to computed tomography scanning for response-assessment after radical radiotherapy or chemoradiotherapy in patients with non-small-cell lung cancer. J Clin Oncol 21:1285 – 1292
178. Brucher B, Weber W, Bauer M (2001) Neoadjuvant therapy of esophageal squamous cell carcinoma: response evaluation by positron emission tomography. Ann Surg 233:300 – 309
179. Flamen P, Van Cutsem E, Lerut A (2002) Positron emission tomography for assessment of the response to induction chemotherapy in locally advanced esophageal cancer. Ann Oncol 13:361 – 368
180. Downey RJ, Akhurst T, Ilson D (2003) Whole body 18FDG-PET and the response of esophageal cancer to induction therapy: results of a prospective trial. J Clin Oncol 21:428 – 432
181. Arslan N, Miller TR, Dehdashti F (2002) Evaluation of response to neoadjuvant therapy by quantitative 2-deoxy-2-[18F]fluoro-D-glucose with positron emission tomography in patients with esophageal cancer. Mol Imaging Biol 4:301 – 310
182. Charron M, Beyer T, Bohnen NN, Kinahan PE, Dachille M, Jerin J, Nutt R, et al (2000) Image analysis in patients with cancer studied with a combined PET and CT scanner. Clin Nucl Med 25:905 – 910
183. Front D, Israel O, Mor M, Keidar Z, Gaitini D, Epelbaum R, Engel A, et al (2000) A new technology of combined transmission (CT) and F-18 fluorodeoxyglucose (FDG) emission tomography (TET) in the evaluation of cancer patients. J Nucl Med 41:284(abstr)
184. Israel O, Mor M, Guralnik L, Gaitini D, Zachs Y, Keidar Z, Kuten A (2000) The new technology of transmission and emission F-18 FDG tomography (FDG-TET) in the diagnosis and management of cancer patients. Clin Positron Imaging 3:143 (Abstr)
185. Israel O, Keidar Z, Iosilevsky G, Bettman L, Sachs J, Frenkel A (2001) The fusion of anatomic and physiologic imaging in the management of patients with cancer. Semin Nucl Med 31:191 – 205
186. Dizendorf EV, Baumert BG, von Schulthess GK, Lutolf UM, Steinert HC (2003) Impact of whole-body ^{18}F-FDG PET on staging and managing patients for radiation therapy. J Nucl Med 44:24 – 29
187. Bradley J, Thorstad WL, Mutic S, Miller TR, Dehdashti F, Siegel BA, Bosch W, et al (2004) Impact of FDG-PET on radiation therapy volume delineation in non-small-cell lung cancer. Int J Radiat Oncol Biol Phys 59:78 – 86
188. Heron DE, Andrade RS, Flickinger J, Johnson J, Agarwala SS, Wu A, Kalnicki S, Avril N (2004) Hybrid PET-CT simulation for radiation treatment planning in head-and-neck cancers: A brief technical report. Int J Radiat Oncol Biol Phys 60:1419 – 1424

Respiratory System

13

Abdelhamid H. Elgazzar, Moussa Khadada

13.1 Anatomic and Physiologic Characteristics

The pulmonary system consists of the lungs, airways, pulmonary and bronchial circulation, and chest wall. The lungs consist of lobes, three in the right (upper, middle, and lower) and two in the left lung (upper and lower). Each lobe is again divided into segments and lobules (Fig. 13.1). The airway system consists of upper airways (nasopharynx and oropharynx) and lower airways (trachea, bronchi, bronchioles, and alveolar ducts) connected by the larynx (Fig. 13.2).

13.1.1 Respiratory Airways

The *upper airways* are lined by a ciliated mucosa, richly supplied with blood, which warm and humidify the inspired air and get rid of foreign particles. The air normally flows by way of the nose, nasopharynx, and oropharynx to the lower airways. When the nose is obstructed or additional flow of air is needed, as during exercise, air flows via the mouth and oropharynx to the lower airways. Foreign particle removal and humidification are not efficient with mouth breathing as compared with the usual breathing through the nose.

The *lower airways* are formed of a conducting system and a gas exchange system (Fig. 13.3). The trachea divides into two main bronchi at the carina, and each bronchus enters the corresponding lung at the hilum along with the pulmonary blood vessels and lymphatic channels. The trachea measures up to 25 cm in length and 2.5 cm in diameter. The right main bronchus extends to the right lung more vertically than the left bronchus to the left lung. This explains the more frequent aspiration of foreign material in the right side. At the hila the bronchi divide into lobar bronchi, then segmental and subsegmental bronchi, then into smaller bronchioles, and at the 16th division, the tracheobronchial tree ends in the tiny terminal bronchioles which form the ends of the conducting airways and are followed by the gas exchange airways. The lung segments are individual units with their bronchovascular supply; hence, they can be individually resected. The airways responsible for conducting air from outside the body into the lungs are lined by ciliated mucous membranes. The cilia, which are hairlike projections, act as sweepers to prevent dust and foreign particles from passing distally into the lungs. Damage to the respiratory epithelium and its cilia allows bacteria and viruses to proliferate and induce infection.

The gas exchange airways start where the terminal bronchioles divide further into smaller, respiratory bronchioles which include increasing numbers of alveoli as the division progresses. By the 23rd division, the respiratory bronchioles end in alveolar ducts that lead to alveolar sacs which are made up of numerous alveoli.

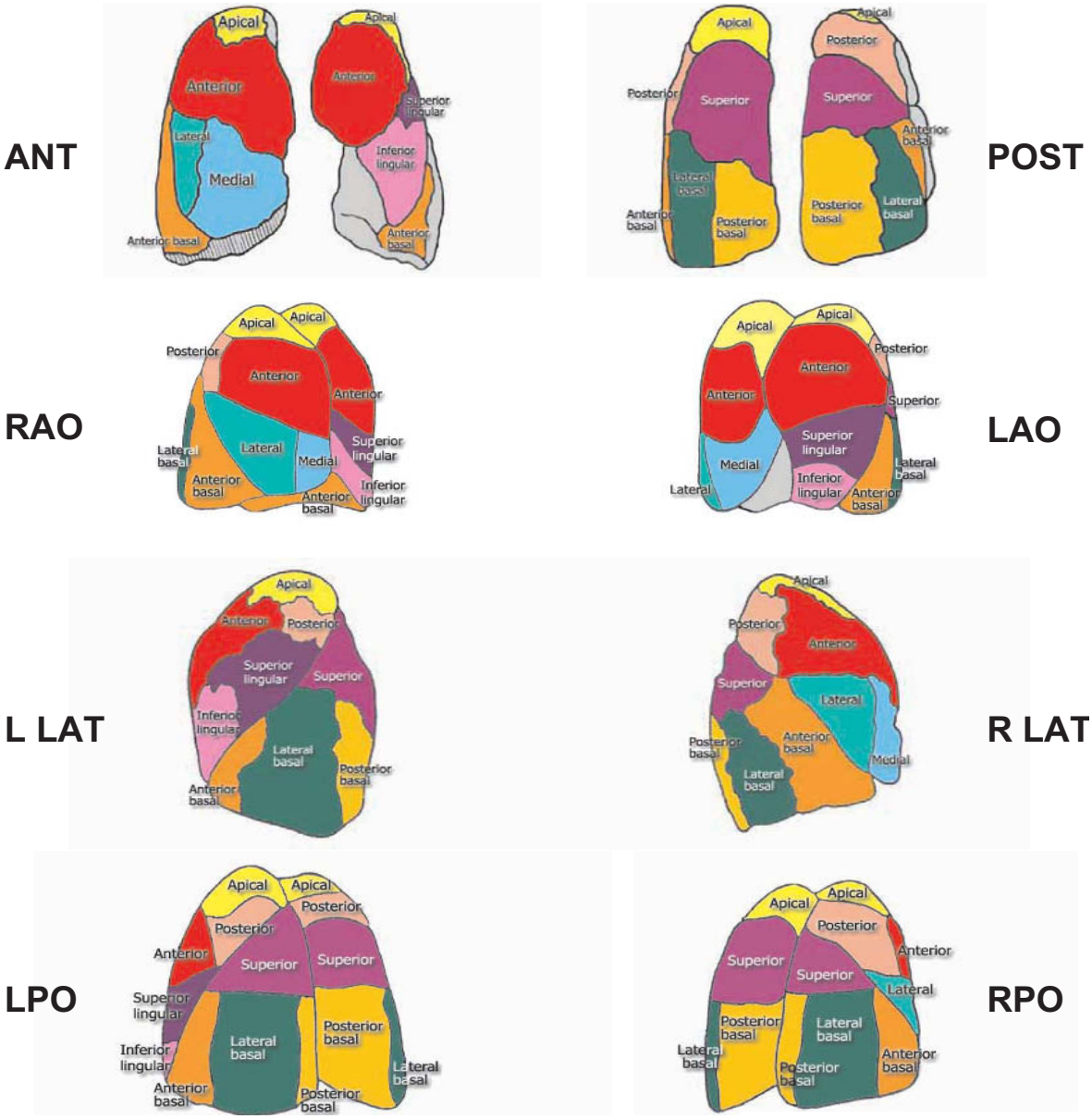

Fig. 13.1. Diagram of the lobes and segments of the lungs

The alveoli are extremely thin walled sacs surrounded by capillaries, and are the primary site of gas exchange. At birth there are approximately 25 million alveoli; this increases to 300 million in adults. The alveoli are lined by type I alveolar cells that provide structure to the alveolar wall and type II cells that secrete a lipoprotein, the surfactant which coats the alveolar inner surface and aids its expansion during inspiration [1].

Ventilation describes the process by which air flows in and out of the gas exchange airways. Ventilation is involuntary most of the time and is controlled by the sympathetic and parasympathetic autonomic nervous systems, which adjust the caliber of the airway via con-

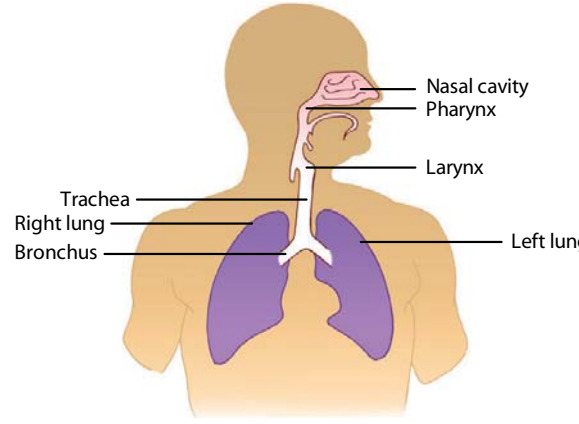

Fig. 13.2. Simple diagram of the upper and lower airways

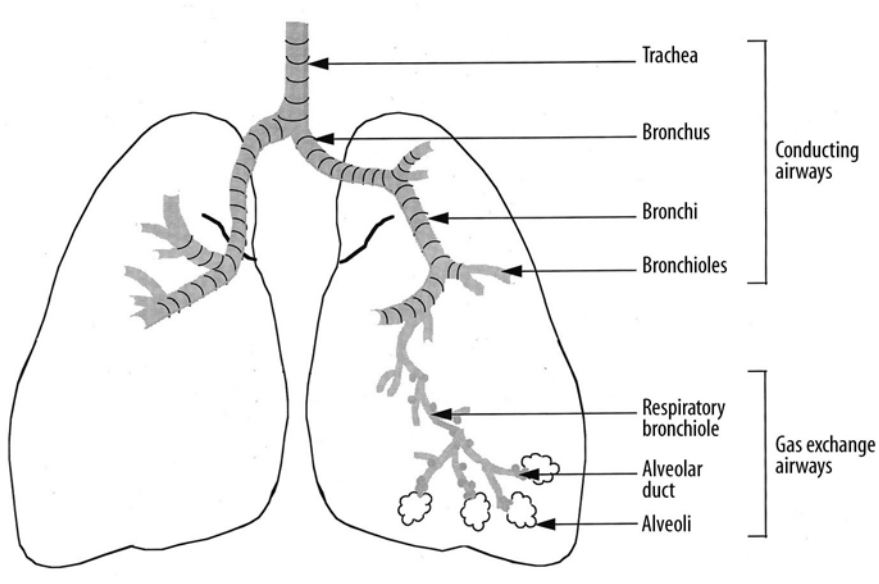

Fig. 13.3. The trachea, bronchi, and bronchioles form the tracheobronchial tree, so called since it resembles an inverted tree. The conducting system is composed of the trachea, bronchi, and bronchioles up to the 16th division and is lined by ciliated mucosa. The gas exchange system consists of the more distal bronchioles (respiratory) and the alveoli that are lined by nonciliated mucus membrane

traction and relaxation of the bronchial smooth muscle and control the depth and rate of ventilation.

The nose and trachea trap most particles more than 10 µm in diameter while the cilia of the bronchi and bronchioles pick up particles 2 – 10 µm in diameter that are deposited in these airways. Smaller particles remain airborne till they are deposited in the alveoli and removed by macrophages. Extremely small particles behave as a gas and are breathed out. This is the basis of scintigraphic ventilation studies using radioactive aerosols and gases. The flow of oxygen through the ^{99m}Tc-DTPA reservoir should create small aerosol particles to be airborne and deposited distally in the alveoli. Larger particles are deposited in the more proximal airways and influence the quality of ventilation studies. This also explains the longer biological clearance of aerosols compared with radioactive gases, which are breathed out without deposition.

13.1.2 Pulmonary Vasculature

The lung is supplied by two different blood circulations. The pulmonary circulation is a low-pressure, low-resistance system through which oxygen enters and carbon dioxide is removed. The bronchial circulation is a part of the high pressure systemic circulation that supplies oxygenated blood to the lung tissue itself.

The pulmonary circulation contains the vast majority of blood present in the lung, and since it has lower pressure than systemic circulation its vessels have a thinner muscle layer. The mean pulmonary artery pressure is 18 mmHg, compared with 90 mmHg for the aorta. The gas exchange airways are served by this pulmonary circulation, which is considered a separate division of the circulatory system. The pulmonary circulation is carried through the pulmonary artery, which branches out to two main pulmonary arteries, one to each lung, entering at the hilum. It then divides progressively into smaller branches, following the branches of the bronchial tree to the smallest, precapillary arterioles, which divide to form a capillary network surrounding the alveoli. The membrane that surrounds the alveoli and contains the capillaries is called the alveolocapillary membrane [2].

The precapillary arterioles are approximately 35 µm in diameter and number approximately 300 million in adults. The capillaries, 7 – 10 µm in diameter, number 300 billion in adults. The more proximal terminal arterioles have a diameter of approximately 100 µm. This basic anatomical fact is important in determining the size of particles injected for perfusion studies; they should be less than 100 µm to prevent blocking of the terminal arterioles [3].

Although the pulmonary circulation is innervated by the autonomic nervous system, vasodilation and vasoconstriction are controlled mainly by local and humoral factors, particularly arterial oxygenation and acid-base balance. Vasoconstriction of the pulmonary arterial system occurs secondary to alveolar hypoxia and acidemia and by the presence of inflammatory mediators such as histamine, bradykinin, serotonin, and prostaglandin.

The bronchial circulation, on the other hand, carries approximately 5% of the blood coming to the lungs and is part of the systemic circulation. In contrast to the pulmonary circulation, it does not participate in gas exchange. It supplies the tracheobronchial tree, large pulmonary vessels, and other structures of the lungs, including the pleurae, with blood.

13.1.3 Respiratory Function

The major function of the respiratory system is to oxygenate the blood and remove waste products of the body in the form of carbon dioxide. Oxygen in the inhaled air diffuses from the alveoli into the surrounding blood in the capillaries, where it attaches to hemoglobin molecules and red blood cells and is carried to the various tissues of the body. Carbon dioxide, on the other hand, as a waste product of cellular metabolism, diffuses in the opposite direction, from the blood in capillaries into the alveoli, and is removed from the body during expiration.

The respiration is controlled by the respiratory center in the medulla at the base of the brain. The respiratory center in the brain stem sends impulses to respiratory muscles to contract and relax. The respiratory center also receives impulses from two main types of peripheral receptors, neuro- and chemoreceptors. Neuroreceptors (lung receptors) monitor the mechanical aspects of ventilation such as the need to expel unwanted substances and expansion of the lungs. The chemoreceptors in the brain circulatory system monitor the pH status of the cerebrospinal fluid and arterial oxygen content (PO_2) to regulate ventilation accordingly.

Any change in the carbon dioxide in the blood will affect the rate and depth of respiration. A slight increase in carbon dioxide concentration in the blood increases the rate and depth of respiration, such as when the individual exercises, since the accumulated waste gas must be removed from the body.

This increase in respiratory rate and depth is secondary to the stimulation of the muscles of respiration, which include the diaphragm and the intercostal muscles, by the respiratory center. Contraction of these muscles causes the volume of the chest cavity to increase, with a consequent drop in the pressure within the lungs, and forces air to move into the tracheobronchial tree. When these respiratory muscles relax the volume of the chest cavity decreases, the pressure increases, and the air is pushed out of the lungs. When breathing is difficult, or in patients with obstructive airway disease, special muscles of expiration, abdominal and internal intercostal muscles, may be additionally needed.

13.1.4 Distribution of Ventilation and Perfusion

Normally, the lower zones of the lungs are better perfused and ventilated because of the effect of gravity. This gradient is more pronounced in perfusion than in ventilation (Fig. 13.4). This physiological fact will usually cause the perfusion to appear less than the ventilation in the lung apices on scintigraphy. This should not be confused with a mismatching pattern. ^{99m}Tc Macro aggregated albumin (MAA) is injected for perfusion imaging while the patient is in the supine position to minimize the gradient. Injection while the patient is taking a deep breath also helps.

13.2 Pulmonary Embolic Disease

Pulmonary embolism is potentially fatal and the most common pathological condition involving the lungs of hospitalized patients. The majority of fatal emboli are not recognized or suspected prior to death.

13.2.1 Pathogenesis and Risk Factors

The vast majority of pulmonary emboli are thromboemboli originating from deep veins. Fat, air, or tumor emboli are rare [4]. Fat emboli are reported with long bone fractures and liposuction while air emboli are associated with cardiac and neurosurgeries. Renal cell carcinoma with invasion reaching the inferior vena

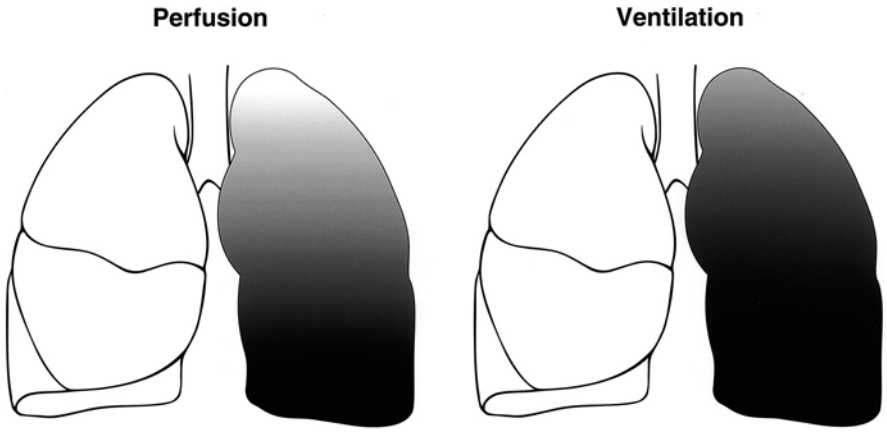

Fig. 13.4. The gradient pattern in perfusion and ventilation of the lungs. (From [21] with permission)

cava is a clinical setting that may lead to tumor emboli. Data indicate that 90% of pulmonary thromboemboli originate from the lower extremities and pelvis. The remainder come from thrombi that occur in the right side of the heart or in bronchial or cervical veins. Embolization and symptomatology are proportional to how proximal is the vein that contains the thrombus. The vast majority of pulmonary thromboemboli originating from thrombi of the lower extremities come more frequently from the thigh and pelvis (75%) than from smaller veins of the calf and feet [5, 6]. Septic embolus refers to an infected thromboembolus which occurs either on site or secondary to detachment of an infected vein thrombus of the lower extremities. The risk of pulmonary embolus is also directly related to the presence of a residual clot at the site of a venous thrombus [7].

13.2.2 Deep Venous Thrombosis

The best solution to the problem of embolism is to prevent it. However, prevention requires identification of those at risk. Perhaps the most important step in defining who is at risk for this disorder has been the recognition that pulmonary emboli arise from sites of deep venous thrombosis, almost exclusively in the lower extremity veins. Therefore, those at risk for deep venous thrombosis are those at risk for pulmonary embolism. The classical risk triad elucidated by Virchow in the nineteenth century includes venous stasis, intimal injury, and alteration in coagulation. These are the primary factors in the pathogenesis of venous thrombosis. Deficiencies of antithrombin III, protein C, protein S, and protein Z are clearly important, as is the presence of lupus anticoagulant. There are other rarer conditions such as homocystinuria and deficiencies of the fibrinolytic system. More factors are being identified, but at the present time up to 90% of all patients with thromboembolism have no identifiable coagulopathy. Thus, in most patients, some clinical states associated with venous stasis, intimal injury, or both are the basis for an increased risk of deep venous thrombosis. These clinical states include injury to the pelvis or lower extremities, surgery involving the lower extremities, all surgical procedures requiring prolonged (at least 30 min) general anesthesia, burns, pregnancy and the postpartum state, previous venous thrombosis with residual obstruction, right ventricular failure of any cause, occupations in which prolonged venous stasis is involved, and any cause of immobility. Other risk factors are age (particularly above 70 years), obesity, cancer and the use of estrogen-containing medications, neoplasm, infection in the immediate area of veins, and hypercoagulability (Table 13.1).

An important point to note is that risk factors should be regarded as cumulative, not independent. These factors allow the establishment of a "risk profile" for a given patient, a profile that conditions the intensity of prophylactic initiatives. The anatomical location of the deep venous thrombosis affects as well the likelihood of extending into a pulmonary embolism as noted earlier.

Table 13.1. Risk factors for deep vein thrombosis and pulmonary thromboembolism

1. Postoperative state especially following operations on the abdomen and pelvis
2. Trauma, including fractures, particularly of the lower extremities
3. Neoplasms
4. Prior history of thromboembolic disease
5. Venous stasis
6. Vascular spasm
7. Intimal injury
8. Hypercoagulability states
9. Immobilization
10. Infection of the area in the immediate vicinity of veins
11. Heart disease, especially:
    Myocardial infarction
    Atrial fibrillation
    Cardiomyopathy
    Congestive heart failure
12. Pregnancy
13. Polycythemia
14. Hemorrhage
15. Obesity
16. Old age
17. Varicose veins
18. Certain drugs such as oral contraceptives, estrogens
19. Following cerebrovascular accidents

Venous thrombi appear to begin either in the vicinity of a venous valve, where eddy current arises, or at the site of intimal injury. Platelet aggregation and release of mediators initiate the sequence. With stasis, there is local accumulation of coagulation factors; the coagulation cascade is activated, and the characteristic red fibrin thrombus develops. Pathologically there will be a platelet nidus from which a large fibrin thrombus extends.

Regarding the natural history, one of three events can happen after the formation of the thrombus. First, the red thrombus grows explosively and obstructs the vein completely. This can happen even within a few minutes. Second, partial venous obstruction may occur. Blood flow therefore continues over the thrombus surface. Under this circumstance, thrombus growth tends to occur by the progressive layering of platelets and fibrin on the clot surface, pathologically seen as the lines of Zahn. Third, probably the most common scenario, a small thrombus is swept away before it reaches an appreciable size. It lodges in the pulmonary vasculature without symptoms.

Unless fibrinolytic resolution is prompt, organization of the thrombus begins within hours of formation. What was a thrombus is slowly replaced by granulation tissue. This process anchors the thrombus to the venous wall.

The dynamic battle between fibrinolysis and thrombus formation is fought out over a period of 7 – 10 days, at the end of which time either complete resolution has occurred or an endothelialized residual is present. At any time during this period, a portion or all of the thrombus can detach as an embolus. This risk is highest early, before significant dissolution or organization occurs [6].

13.2.3 Pulmonary Thromboembolism

13.2.3.1 Consequences

Pulmonary thromboemboli occur more commonly in the lower lobes because of the preferential blood flow to these regions. This also applies to the right lung because of the straighter course of the pulmonary artery. Immediately after acute embolism, there is a decrease of perfusion distal to the occluded vessel along with a transient decrease of ventilation to the affected segment. The blood flow is diverted to the other portions of the lung and pulmonary artery pressure may increase, although cardiac output usually remains stable. The resultant tissue ischemia disturbs certain metabolic functions of the lung such as the production of surfactant. Reduction of the surfactant concentration reduces the alveolar surface tension and may cause the atelectasis that often accompanies embolism. If the embolus completely occludes an artery or an arteriole and the collateral bronchial circulation is insufficient to sustain tissue viability, infarction occurs over 24 – 48 h. Pulmonary infarction with coagulative necrosis results in an area of radiographic opacity that requires an average of 20 days to resolve but occurs in less than 10% – 15% of patients with pulmonary embolism. There is a significant inflammatory component in pulmonary infarcts which is the basis behind the significant FDG uptake in recent lung infarcts as reported recently and can cause a false positive interpretation for lung malignancy [8]. More frequently, incomplete infarction with hemorrhage but without necrosis occurs. This type of injury resolves quickly and produces only transient radiographic opacities. Infarction always involves the pleural surface of the lung (peripheral) and more frequently involves the lower lobes than other sites.

The regional decrease in ventilation is due to local bronchoconstriction with a tendency for redistribution of ventilation away from the hypoperfused segment. This probably occurs due to decreased regional alveolar and airway carbon dioxide tension, which is the usual stimulus for bronchodilation. This hypocapnia is corrected quickly, since patients inhale carbon dioxide-rich tracheal "dead space air" into the alveolar zones after the embolic event, raising the alveolar pCO_2 [6]. Release of neurohumoral factors, most importantly serotonin and thromboxane A_2, also causes bronchoconstriction. These factors are released after embolization by activated platelets and mediate bronchospasm of small airways through their effects on the smooth muscles [9]. The ventilation of the hypoperfused areas returns to normal within several hours after acute embolism [10, 11]. This concept is the pathophysiological basis for the scintigraphic interpretation of ventilation and perfusion scans, which show segmental perfusion defects with preserved ventilation as a typical scintigraphic pattern for pulmonary embolism. Those showing only regions of matched perfusion and ventilation defects carry a low probability of pulmonary embolism if no chest X-ray abnormalities are noted at the same sites, since this pattern is more likely associated with nonembolic conditions and is more typical of parenchymal lung disease. Because patients with pulmonary emboli usually arrive at the hospital after normalization of the ventilation at the site of pulmonary emboli, the mismatching pattern is typical of pulmonary emboli. However, inpatients may have their V/Q scans within a short time after presentation and matching abnormalities may be associated with pulmonary emboli. This has to be borne in mind, and the duration of symptoms should be a factor in decision-making regarding the management of pulmonary embolism.

Some degree of arterial hypoxemia may also occur, one reason being the widening of the arteriovenous oxygen difference caused by acute right ventricular failure. Another reason is the enhanced perfusion of poorly ventilated or nonventilated lung zones. Loss of pulmonary surfactant may add to the hypoxemia. Hyperventilation almost always occurs and may partly explain the normal levels of oxygen arterial pressure seen in 10% – 25% of patients with pulmonary emboli.

An increase in the resistance of the pulmonary arterial circulation, due primarily to mechanical blockage by numerous small emboli in the pulmonary vasculature and also to humorally mediated vasoconstriction, may follow pulmonary emboli. These hemodynamic consequences may include increased pulmonary arterial resistance with elevated pulmonary arterial and right ventricular systolic pressures and hypoxemia. When pulmonary hypertension occurs it indicates at least 25% obstruction of pulmonary vascular tree as assessed by angiography [12]. The higher the degree of obstruction the more severe the abnormalities of the cardiopulmonary hemodynamics become. When over 50% of the pulmonary vasculature is included (massive pulmonary embolism), acute pulmonary hypertension and/or right ventricular failure (cor pulmonale) occur [12]. Systemic hypoxemia results from pulmonary arteriovenous shunting and from perfusion of hypoventilated lung segments (V-P imbalances). The AV shunting accounts for the clinical observation that adminis-

tration of 100% oxygen will only partially correct hypoxemia induced by pulmonary emboli [11].

The physiological consequences of pulmonary embolism depend on the size of the embolic mass and the general status of the pulmonary circulation. In young individuals with good cardiovascular function and good collateral circulation, thrombi of a large central vessel may be associated with only minimal functional impairment if any. On the other hand, in patients with cardiovascular or severely debilitating diseases, pulmonary embolism may lead to infarction.

13.2.3.2 Resolution

Pulmonary emboli may, spontaneously or with treatment, fragment into smaller portions that travel distally and block smaller arterioles (Fig. 13.5). This may create new, smaller perfusion defects that are more peripherally located in comparison to the original defect caused by the original embolus. This pattern should not be mistaken for recurrent pulmonary emboli on a follow-up scan. If this pattern is the only interval change with no other defects seen in areas other than those in the vicinity of the distribution of the original embolus, it does not suggest recurrent emboli [11].

Resolution of pulmonary thromboembolus may start within hours. It can be seen on perfusion scans as early as 24 h and is progressively noted up to 3 months, with insignificant change after 6 months (Fig. 13.6). This is the basis of the recommendation that follow-up ventilation and perfusion scans are performed 3 months after the initial incident for evaluation of resolution and function as a baseline for future incidents to differentiate between acute and unresolved old emboli. This resolution is dependent on the age of the patient, with complete resolution in young age-groups and less complete and less significant resolution in older age-groups [13, 14]. Other factors include age of the thromboembolus or length of time between formation of the embolus and the institution of proper anticoagulation. This is the basis behind the relatively recent trend of starting anticoagulant therapy in most patients with pulmonary emboli who have no contraindication for anticoagulation immediately when a pulmonary thromboembolus is suspected before finishing the workup for the condition. Anticoagulant therapy may then be stopped if the condition is excluded. When thromboemboli do not resolve, they become chronic and can lead to pulmonary hypertension [15].

13.2.3.3 Recurrence

Pulmonary thromboemboli recur in up to 50% of patients [16], although the incidence in treated PIOPED

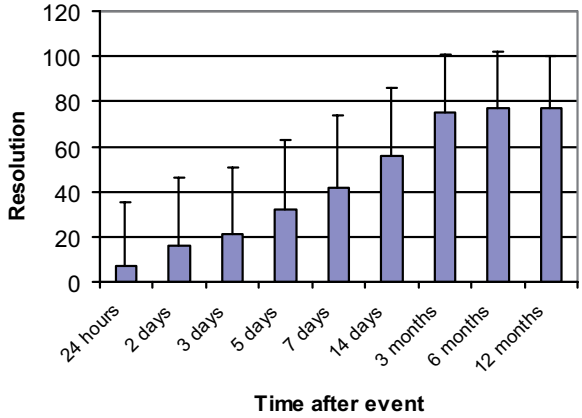

Fig. 13.6. Histogram illustrating the percent resolution of pulmonary emboli. Note that there is progressive increase of the percentage overtime until 3 months after the event with no significant increase afterwards. These data are based on the Urokinase Study [13, 14]

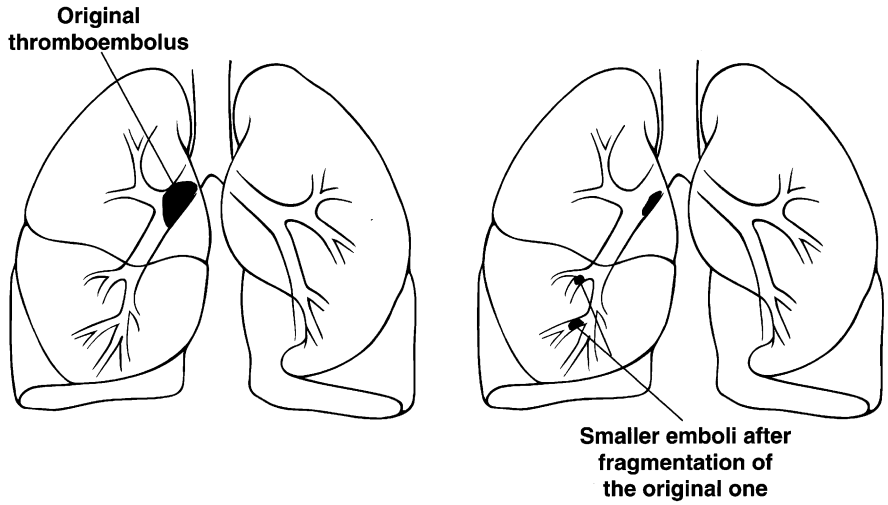

Fig. 13.5. The phenomenon of fragmentation of the thromboemboli. (From [26] with permission)

patients was only 8.3% [17]. The vast majority of deaths among pulmonary embolism patients are due to recurrent emboli. In the PIOPED study population, it was found that nine of ten people who died had a recurrent pulmonary embolus [18]. Recurrence has been reported to occur at the same site as the original thromboembolus [19].

13.2.3.4 Clinical and Scintigraphic Considerations

The clinical diagnosis of pulmonary thromboembolism is difficult and unreliable, due to the nonspecificity of its symptoms and signs as well as the laboratory and chest X-ray findings [20, 21]. Chest X-ray, however, must be obtained since it may show many parynchymal diseases [22] and must be available for lung scan interpretation. Familiarity with different normal structures is important for explaining the scintigraphic patterns (Fig. 13.7). Pulmonary embolism may also be asymptomatic. In a study using spiral CT, 24% of pulmonary emboli were asymptomatic among patients with moderately to severely injured patients [23]. Furthermore the presentation is commonly more difficult and atypical in older age groups compared to younger patients [24, 25]. Accordingly, only 24% of fatal emboli were diagnosed antemortem (Table 13.2) [26]. Data indicate that the mortality of pulmonary embolism is more than 30% if untreated. Promptly diagnosed and treated, emboli have a mortality of 2.5% – 8% [13, 14, 18]. The mortality of PE

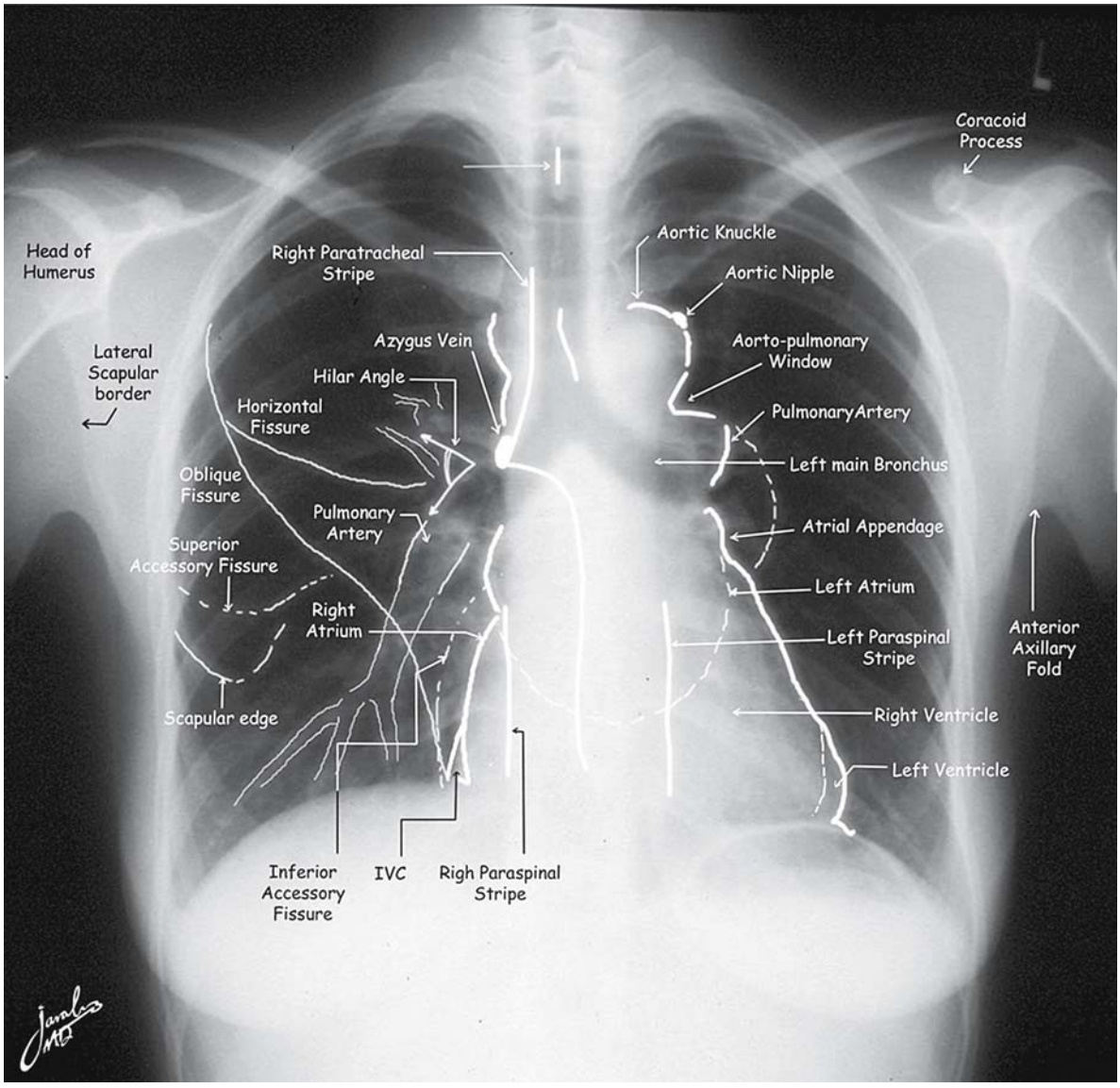

Fig. 13.7. Normal chest X-ray illustrating the important structures that may show variants on perfusion scans

Table 13.2. Cases with antemortem PE diagnosis

Author	Year	No. (%) of cases with antemortem PE diagnosis
Stein and Henry [47]	1995	6/20 (30)
Morgenthaler and Ryu [48]	1995	29/92 (32)
Morpurgo and Schmid [49]	1991	26/92 (28)
Sperry et al. [50]	1990	275/812 (34)
Karwinski and Svendsen [51]	1989	267/1450 (18.4)
Gross et al. [52]	1988	7/18 (39)
Dismuke and Wagner [53]	1986	41/203 (20)
Goldhaber et al. [54]	1982	16/54 (30)
Total		667/2741 (24)

was found to vary among patients with or without cardiac disease. Paraskos et al. [27] reported survival rates at a mean follow-up period of 29 months of 19% among patients with prior congestive heart failure and 86% for those with no prior congestive heart failure. Pulmonary angiography is the most accurate modality for the diagnosis of pulmonary emboli, with an accuracy of 96% [28]. However, angiography is invasive and is not suitable as a screening imaging modality for the disease.

Scintigraphy remains the most cost-effective noninvasive screening modality. The major advantages include its ability to provide regional and quantitative information useful for the diagnosis, as well as for mapping, to guide selective angiography if needed for the diagnosis, after noninvasive methods including Doppler and Duplex studies for deep venous thrombosis have been exhausted. Additionally it determines the disease severity and monitors its progress [29]. Noninvasive DVT studies are useful in decision making in equivocal cases. Positive DVT studies increase probability to up to 93%. Furthermore incorporating DVT studies in algorithms for managing patients suspected of having pulmonary thromboembolism decreases angiograms by 50% [30]. Normal study with low probability V/Q and low clinical probability is associated with a 1% – 2% 3-month risk of venous thromboembolism in patients left without anticoagulants [31]. Spiral CT is another complementary modality that can help with nondiagnostic studies in minimizing the number of patients undergoing pulmonary angiography. It is useful in detecting central emboli but data are controversial for peripheral emboli [32 – 35]. Several studies have shown that this modality cannot be reliable to withhold the anticoagulant therapy based on a negative spiral CT and it needs to be explored further before being accepted as a replacement for V/Q scans [36]. It was found that it has no added value in patients with high probability V/Q scans and has a comparable diagnostic value with SPECT V/Q scans [35]. Spiral CT also as a single study is not cost effective [37].

MRI pulmonary angiography will play a greater role [38]. In a recent experimental study reversible PE was induced by inflating a nondetachable silicon balloon in the left pulmonary artery of five New Zealand White rabbits. MR V/Q scans were obtained prior to, during, and after balloon deflation. High-resolution contrast-enhanced MR pulmonary angiography was also used to confirm the occlusion of the pulmonary artery. Similar to radionuclide ventilation/perfusion technique, acute PE produced a mismatched defect in the MR V/Q scan. MRA verified the occlusive filling defect in the left pulmonary artery. The study suggests that high-resolution MRA and MR V/Q imaging of the lung is feasible and allows comprehensive assessment of pulmonary embolism in one imaging session [39].

Table 13.3. Ventilation agents

Agent	Advantages and limitations
Aerosols	
^{99m}Tc-DTPA aerosol	Lung half clearance time = 58 min Pre or post perfusion Multiple projections
^{99m}Tc-pyrophosphate aerosol	Post perfusion Suitable for SPECT
Technegas	Multiple projections Good peripheral deposition
Gases	
Xenon-133	Ability to obtain single breath, equilibrium and washout images Very sensitive for obstructive airway disease Only posterior view is possible in most patients Low energy of 81 keV Pre-perfusion acquisition
Krypton-81m	Expensive – available only in some areas Energy: 190 keV Half-life: 13 s Multiple views Pre or post perfusion

Several agents have been used for ventilation (Table 13.3). Every agent has certain advantages and limitations. Xenon-133 (Fig. 13.8) is useful in evaluating obstructive airway disease. Krypton-81 (Fig. 13.9), ^{99m}Tc-DTPA (Fig. 13.10) and Technegas (Fig. 13.11) provide the ability to perform ventilation studies after the perfusion, particularly krypton-81. ^{99m}Tc-Macroaggregated albumin is used for perfusion. For proper interpretation of lung perfusion/ventilation study, chest X-ray must be available and should be obtained within 12 h of the time of the scans.

The particle size of ^{99m}Tc-macroaggregated albumin (^{99m}Tc-MAA) is generally between 10 and 90 μm (90% of particles), and no particles should be larger than 150 μm. ^{99m}Tc-MAA is injected slowly IV and lodges in percapillary arterioles, obstructing approximately 0.1% of their total number. The particles clear by enzymatic hydrolysis and are phagocytized by RE cells (the

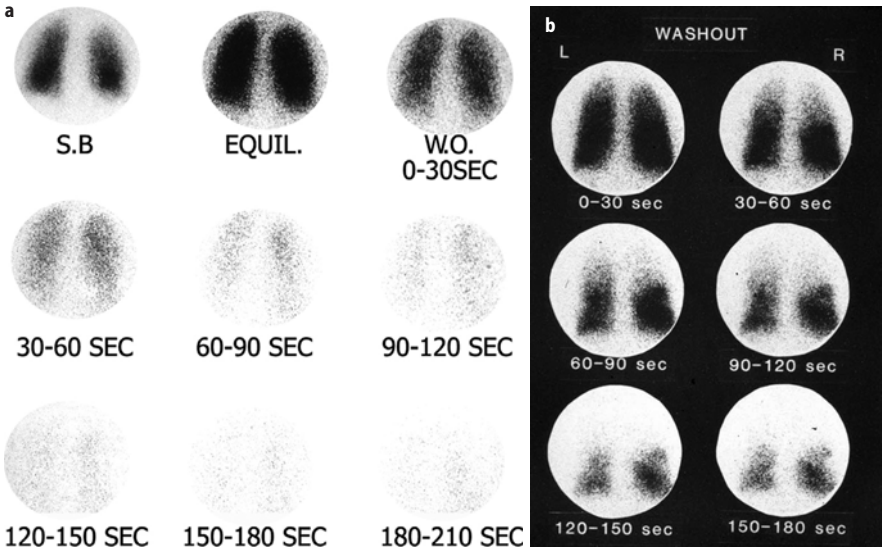

Fig. 13.8a,b. Xenon-133 ventilation studies. **a** Normal study with uniform distribution of the radiotracer in both lungs on single breath and equilibrium images. The washout images reveal prompt clearance with no significant retained activity. **b** Washout images of a patient with obstructive airway disease showing retained activity in lower zones of both lungs by the end of the study

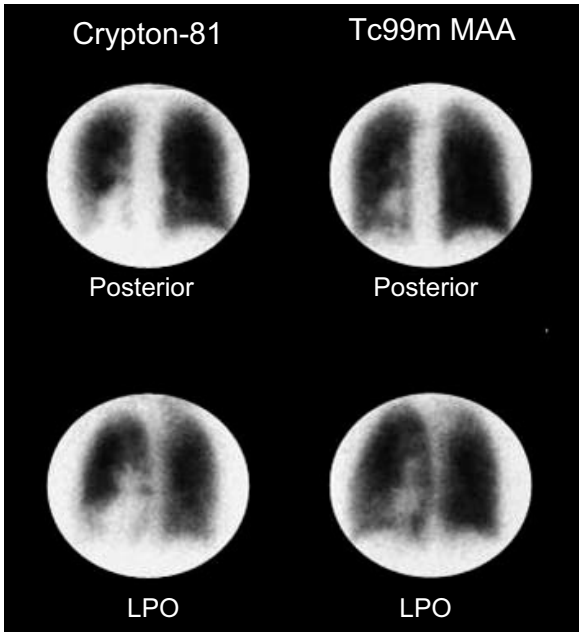

Fig. 13.9. Representative images of krypton-81 ventilation study obtained post perfusion. Note the good quality of images and two projections obtained to evaluate the ventilation status at the regions of the perfusion abnormalities seen on the same projections

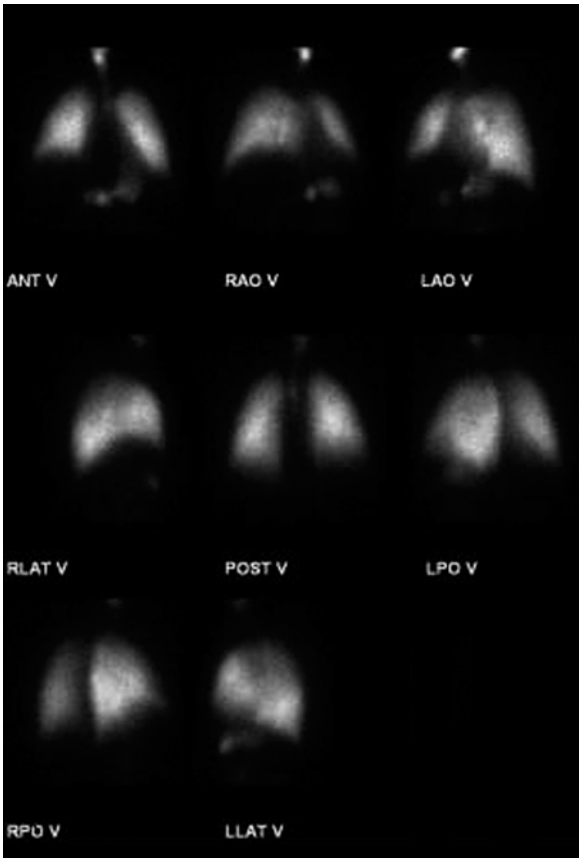

Fig. 13.10. ^{99m}Tc-DTPA aerosol ventilation study. Images show no abnormalities. Observe the activity in the esophagus and stomach due to swallowed activity

agent has a biologic half-life in the lungs of between 6 and 8 h. Normally, only 3% – 6% of the injected ^{99m}Tc-MAA will bypass the pulmonary vasculature. The critical organ is the lungs, which receive a dose of about 1 rad (1 cGy) from a typical 5 mCi dose. The kidneys and bladder receive moderate exposure largely from the excretion of degraded albumin.

^{99m}Tc-DTPA aerosol is commonly used for ventilation studies worldwide. Using an aerosol delivery system that generates submicronic particles, 30 mCi of Tc-DTPA in 3 ml of saline (3 – 5 min of rebreathing on the system with the oxygen at 8 – 10 l/min) delivers about 500 – 750 μCi of tracer to the lungs. This dose yields 100K count images in about 2 min on a standard

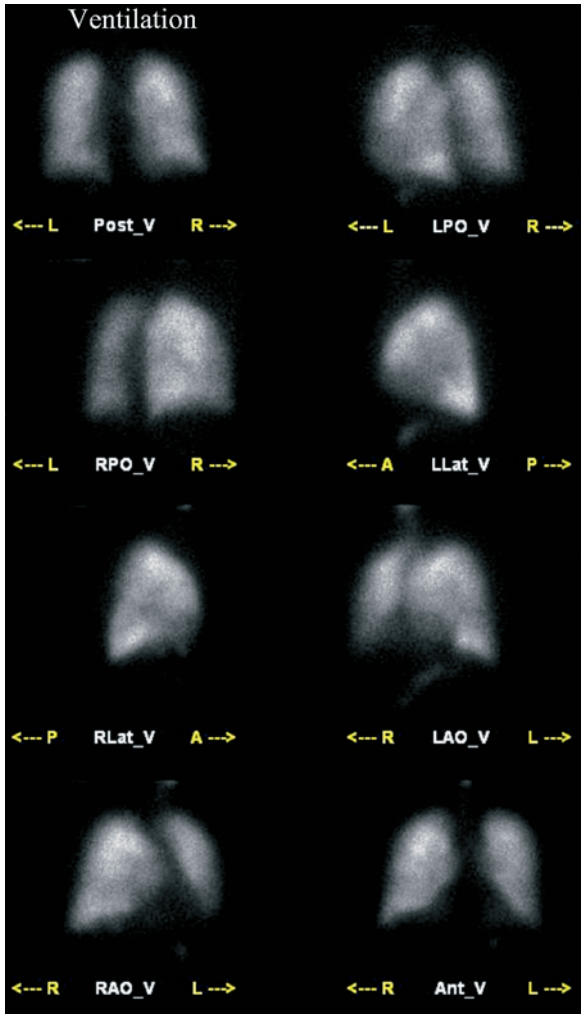

Fig. 13.11. ^{99m}Tc-Technegas ventilation study for a patient suspected of having pulmonary embolism. The study shows no abnormalities and illustrates the good quality of ventilation studies obtained using this agent. The perfusion on the other hand reveals perfusion defects in both lungs and no matching ventilation or X-ray abnormalities, indicating a high probability of pulmonary embolism

gamma camera with a low energy general purpose collimator. The typical radiation exposure to the lungs is about 100 mrad. This is less than the several hundred millirad exposure from a typical Xe-133 rebreathing ventilation exam. The dose to the lungs is also less than that from Kr-81. Images should be acquired for 100K counts or 5 min. Exposure to personnel is usually less than that delivered by a xenon study.

Technegas is a ventilation aerosol agent that has gained popularity recently. It is ultrafine labeled carbon particles produced by heating ^{99m}Tc-pertechnetate to very high temperatures of approximately 2500°C in the presence of 100% argon gas. An ash material is produced that acts like a gas with good peripheral deposition because the particles are so small, with a median size of 0.05 – 0.15 µm. Technegas has a half-clearance time of 4 – 6 h. Since the material produced is not filtered and contains up to 50% of the initial radioactivity, a large number of appropriately sized particles are inhaled with each breath. Thus, only a few inspirations (typically two to ten) are needed to reach an adequate dose. Usually about 1 mCi is deposited in the lung. Extrapulmonary activity in the oropharynx, trachea, and stomach can be seen in about 30% of patients. The exam may be technically inadequate in up to 15% of patients particularly in severely ill patients that cannot be instructed for inhalation, or in patients with very shallow or rapid breathing. If the Technegas portion of the exam is performed following the perfusion study, a counting rate of at least two times the count rate of the perfusion exam is considered adequate.

Table 13.4. Characteristics of ^{99m}Tc-Macro-aggregated albumin (Tc99m-MAA)

• Size	10 – 90 µm (mostly 20 – 50)
• Minimum number of particles to be used in adults	100,000 unless pulmonary hypertension or right to left shunt is present
• Ideal number of particles	200,000 – 500,000
• Biologic half-life	4 – 8 h
• Injection	Care should be taken not to cause particle aggregates that can produce hot spots
• Safety	Particles block < 1/1000 of the capillaries and precapillary arterioles

Another agent, pertechnegas, which is a vapor of pertechnetate, is prepared similarly but in the presence of 2 – 5% oxygen, has a shorter clearance time, and shows excellent deposition in the lungs. Table 13.4 summarizes the essential information relevant to its use in obtaining adequate perfusion scans.

V/Q Scan in Pregnancy. When indicated, low activity of 1 mCi (37 MBq) is used for perfusion. If the perfusion study is abnormal then ventilation and chest X-ray (if not obtained earlier) are obtained as needed. Based upon the available data, there are no apparent short or long term consequences to the fetus from the radiation received as a result of diagnostic ventilation-perfusion scintigraphy. For a V/Q scan, fetal dose would mostly come from tracer accumulating in the bladder, with some internal scatter from the lungs. To minimize radiation exposure to the fetus, a smaller dose of the perfusion tracer ^{99m}Tc-MAA as mentioned earlier will be used for exam (as long as the patient can hold still for the longer imaging times). Frequent voiding will be encouraged if the patient's clinical status permits. Either

xenon-133 or Tc99m agents can be used safely for the ventilation portion of the exam. Xenon-133 has the advantage of not being excreted via the urine.

Normal perfusion study (Fig. 13.12) rules out any clinically significant pulmonary emboli. Since the ventilation and perfusion lung scans lack specificity (Table 13.5), probabilities are used for the interpretation of abnormal studies. Based on the pathophysiological changes and scintigraphic observations, several scintigraphic features of perfusion abnormalities are known to affect the probability of a scan for pulmonary emboli (Table 13.6). One of the important features is the size of segmental perfusion defects. A small defect occupies up to 25% of the segment, a moderate defect between 25% and 75%, while a large defect takes up 75% or more. Using these features, several retrospective and prospective studies were conducted to refine the interpretation of ventilation and perfusion scans and assess their value in managing patients suspected of having embolic disease [40, 41]. The most popular retrospective study is that by Biello et al. [40], which compared the ventilation and perfusion scans and chest X-rays with angiography to produce a set of cri-

Table 13.5. Causes of abnormal perfusion lung scintigraphy

Emphysema
Inflammatory diseases
Pneumonia
Abscess
Granulomatous disease (sarcoidosis, tuberculosis)
Pulmonary fibrosis
Bronchial obstruction
Infection
Neoplasm
Acute and chronic asthma
Mucus plug
Foreign body
Rib fractures (reduced lung excursion)
Congenital hypoplasia or absence of the pulmonary arteries
Peripheral pulmonary artery stenosis
Thromboembolic disease
Thrombus
Tumor embolism
Fat embolism
Air embolism
Extrinsic vessel compression (tumor, inflammation)
Left ventricular failure
Mitral valve disease
Veno-occlusive disease
Prior lung resection
Radiation

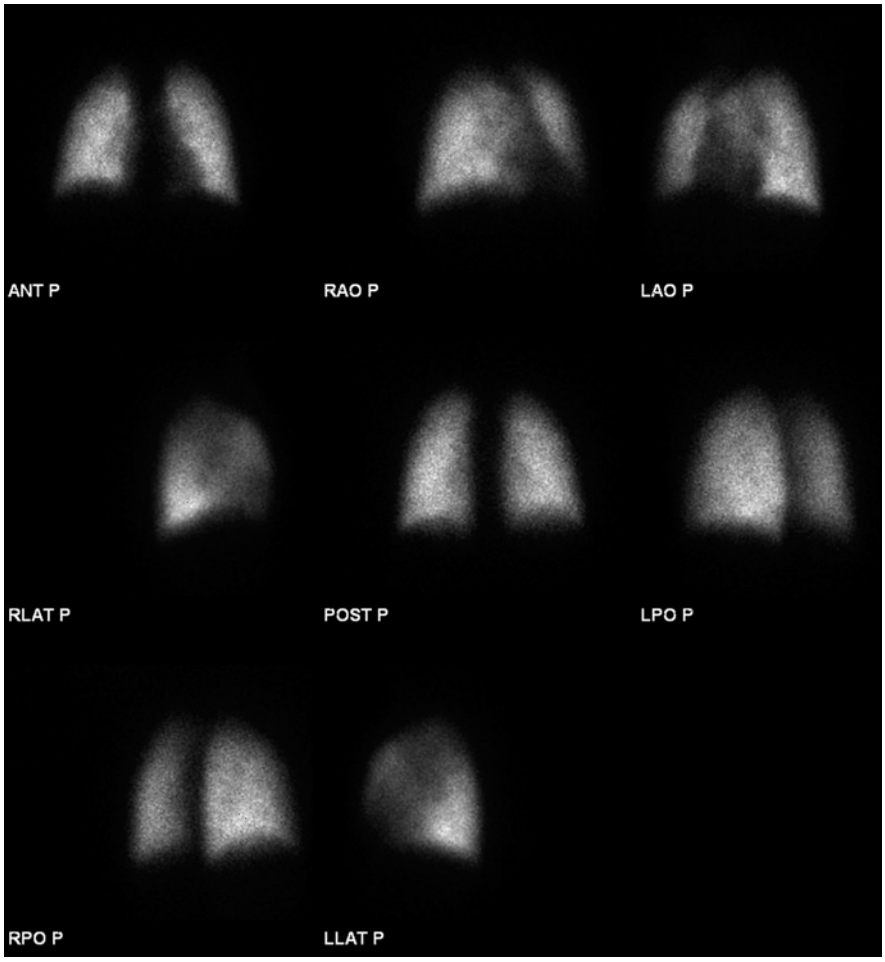

Fig. 13.12. Normal perfusion study. A ^{99m}Tc-MAA perfusion scan of a patient suspected of having pulmonary embolism. The perfusion study reveals uniform perfusion throughout both lungs with no defects. Note the parallel medial borders of both lungs on the posterior view and the sharp delineation of the costophrenic angles

Table 13.6. Features of perfusion defects associated with higher probability of pulmonary emboli

Size	Moderate and large Larger relative size compared with that of chest X-ray densities
Location	Pleural based defects Lower lobes
Shape	Wedge-shaped
Type	Segmental
Relation to ventilation pattern	Mismatching
Number	Multiple

teria for interpreting ventilation and perfusion studies. The most recent and largest prospective study is the PIOPED [17]. Despite its shortcomings, which originated mainly from the use of a pre-established nonstandard set of criteria for interpretation of ventilation and perfusion scans, the PIOPED provided a wealth of information. The study established the value of normal and high probability scans in excluding and diagnosing pulmonary embolism. It validated the segment equivalent concept (Fig. 13.13) and clarified the use of Bayesian analysis utilizing the clinical pre-scan and scan probabilities to figure the post-scan or diagnostic probability. The study showed clearly that when the clinical odds agree with the scan probability in the low and high probability categories, pulmonary embolism can be ruled out or confirmed with a high degree of certainty.

Based on the modifications of PIOPED criteria and the other validated criteria, a simplified set is shown in Table 13.7. Small perfusion defects indicate low probability of pulmonary emboli as well as matching perfusion and ventilation defects regardless of size with no matching X-ray abnormalities (Fig. 13.14). Nonsegmental defects also indicate low probability. When perfusion defects match the X-ray abnormalities it may indicate low, intermediate or high probability based on the relative size of perfusion compared to the X-ray densities (Table 13.7). When the perfusion defect is of the same approximate size as the matching X-ray density (Fig. 13.15), it indicates intermediate probability (approximately 25%). However, Worley et al. suggested that when the perfusion defect matches the chest X-ray density in the upper or intermediate lung zones it indicates low probability while if it is in the lower zones it indicates intermediate probability [42]. Other studies, however, did not support this categorization and it is debatable [43]. Size of pleural effusion also was interpreted as low probability if large and intermediate if small by Worsley et al. [44], but this was not proved by Goldberg et al. [45].

The minimum number of mismatching perfusion defects is two segment equivalent defects with no matching chest X-ray abnormalities to make a high probability interpretation (Fig. 13.16). However, a study analyzing PIOPED data indicated that defects equivalent of 1.5 segments indicate high probability among patients with no prior cardiopulmonary diseases [46].

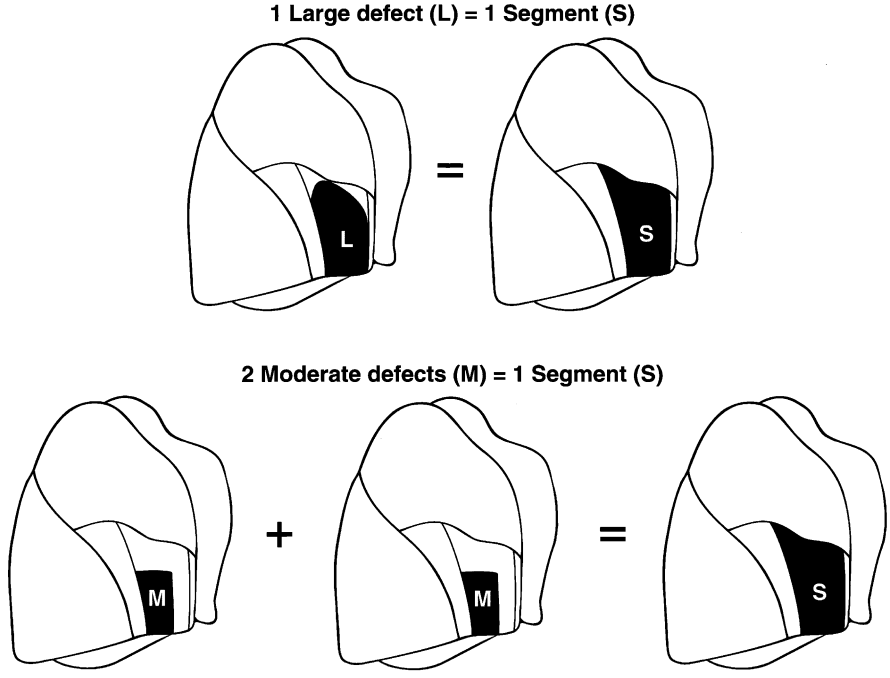

Fig. 13.13. The segment equivalent concept. (From [26] with permission)

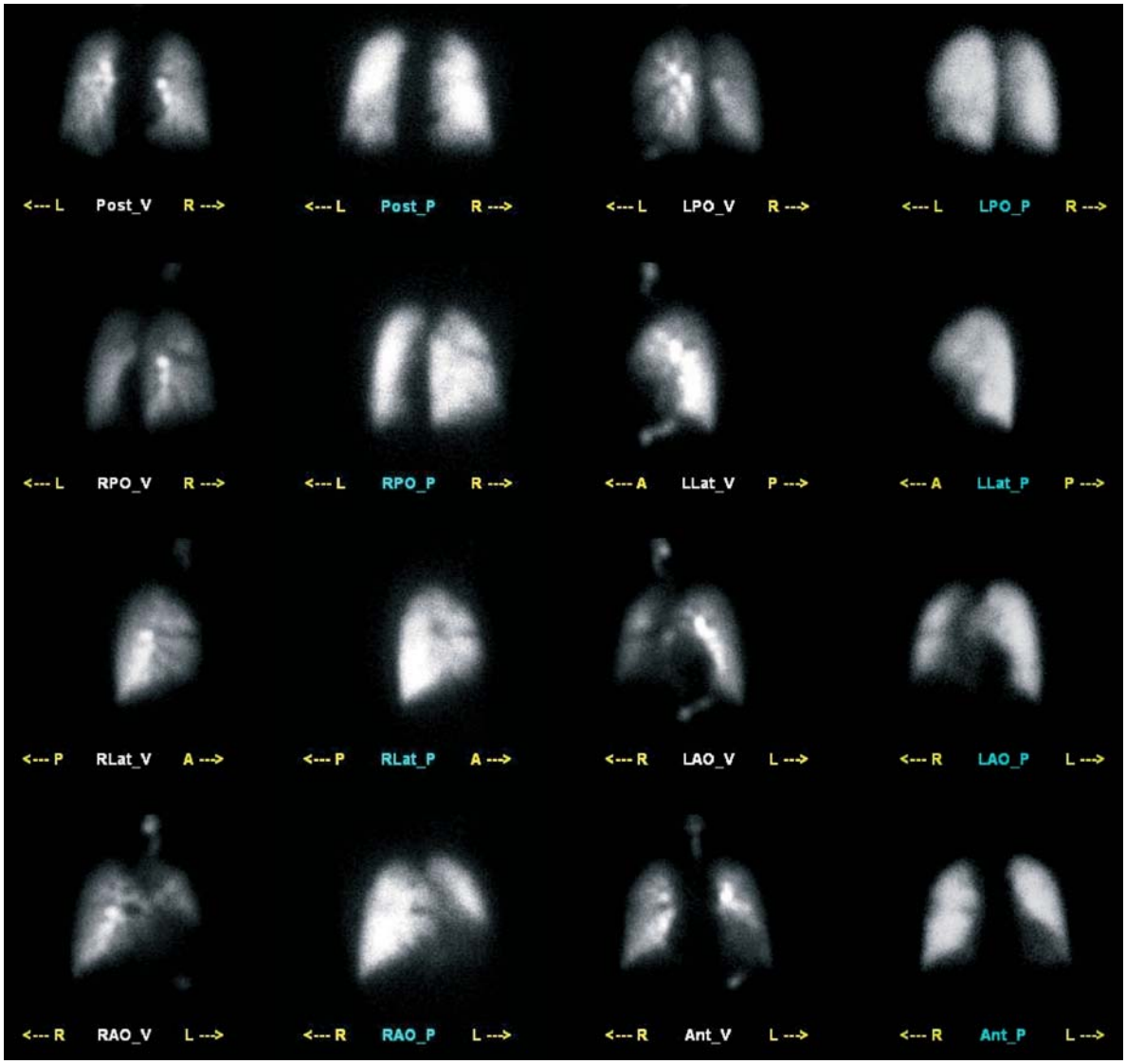

Fig. 13.14. ^{99m}Tc-DTPA aerosol ventilation and ^{99m}Tc-MAA perfusion studies of a patient suspected of having pulmonary embolism. The X-ray was normal. The perfusion study shows multiple small perfusion defects matching the ventilation pattern indicating low probability of pulmonary emboli

Category	Pattern on V/Q images
Normal	No perfusion defects. Allow for impressions explained by enlarged heart or other hilar structures as seen on chest X-ray
Near normal	Nonuniform uptake with no definite segmental or subsegmental perfusion defects
Low	– Nonsegmental perfusion defects other than those explained by cardiomegaly or other prominent hilar structures – Matching V/Q defects with no corresponding CXR abnormalities – Any number of only small defects regardless of ventilation and CXR patterns – Stripe sign – Perfusion defect substantially smaller than CXR abnormality
High	– Two[a] or more large mismatching defects or their equivalent (4 moderate or 1 large plus 2 moderate defects) with no corresponding CXR abnormalities – Perfusion defect substantially larger than CXR abnormality
Intermediate	– Perfusion defect matching chest X-ray abnormality and of the same approximate size – Single moderate up to less than 2 segmental mismatching defects with no corresponding chest X-ray abnormalities – Difficult to categorize as low or high

Table 13.7. Criteria for interpretation of ventilation/perfusion lung scans

[a] 1.5 in patients with no prior cardiopulmonary disease can be considered high probability

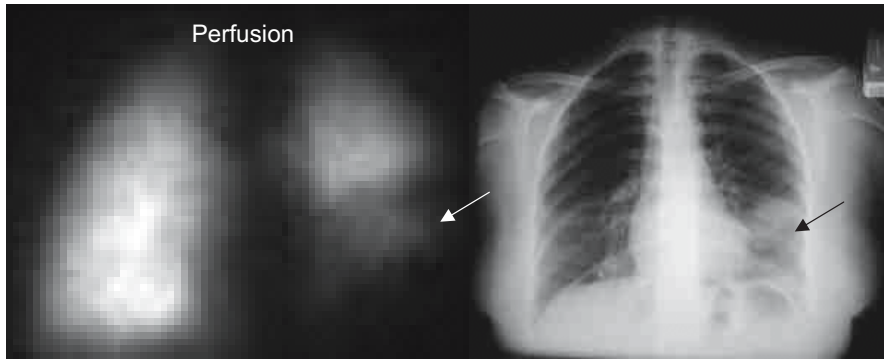

Fig. 13.15. Chest X-ray of a patient referred to rule out pulmonary embolism with a density in the left lower lobe matching the perfusion defect on ^{99m}Tc-MAA scan and is of the same approximate size indicating intermediate probability of pulmonary emboli

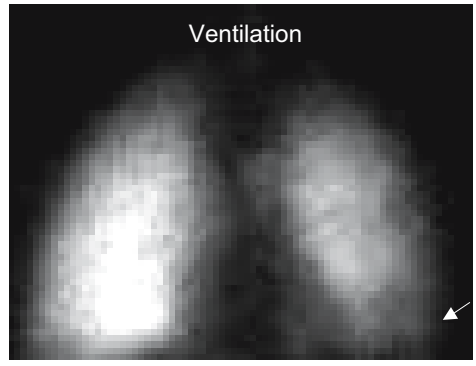

Fig. 13.16. Ventilation and perfusion scans of a 74-year-old man with a history of fracture of left femur treated with internal fixation 3 days earlier. The patient was referred to rule out pulmonary emboli because of acute onset of shortening of breath. Perfusion study shows multiple perfusion defects equivalent to more than two segments with no matching abnormalities on ventilation study and no corresponding changes in the chest X-ray, which was normal. This illustrates a typical pattern of high probability of pulmonary emboli on ventilation/perfusions scans

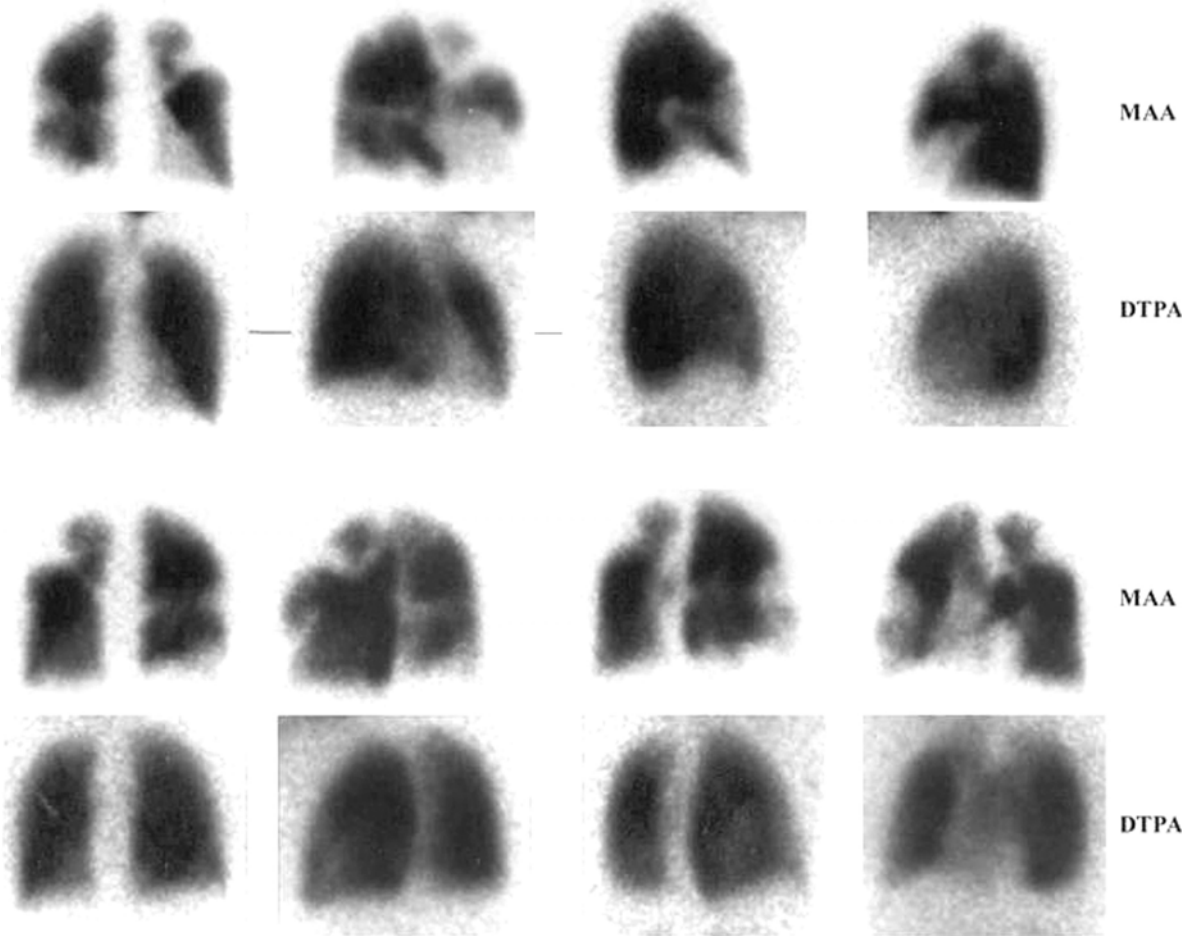

Until further development, proper utilization of V/Q scans along with the DVT tests and spiral CT will solve most diagnostic problems and decreases the need for angiograms

13.3 Pulmonary Hypertension

Normal pulmonary artery systolic pressure at rest is 18 – 25 mmHg, with a mean pulmonary pressure ranging from 12 to 16 mmHg. This low pressure is due to the large cross-sectional area of the pulmonary circulation, which results in low resistance. An increase in pulmonary vascular resistance or pulmonary blood flow results in pulmonary hypertension. It is defined as a pulmonary artery systolic pressure higher than 30 mmHg or a pulmonary artery mean pressure higher than 20 mmHg.

Pulmonary hypertension may have no cause (primary), which is rare or may follow cardiac or pulmonary disorders (secondary). Pathphysiologically, three predominant mechanisms may be involved in the pathogenesis of secondary pulmonary hypertension: (1) hypoxic vasoconstriction, (2) decreased area of the pulmonary vascular bed, and (3) volume/pressure overload.

Chronic hypoxemia such as due to COPD causes pulmonary vasoconstriction by a variety of actions on pulmonary artery endothelium and smooth muscle cells.

A variety of causes may decrease the cross-sectional area of the pulmonary vascular bed, primarily due to disease of the lung parenchyma. Examples of these conditions include collagen vascular diseases, particularly systemic scleroderma or CREST (calcinosis cutis, Raynaud phenomenon, esophageal motility disorder, sclerodactyly, and telangiectasia) syndrome and acute and chronic pulmonary emboli [15]. When pulmonary emboli do not resolve they become organized and incorporated into the pulmonary arterial wall as an epithelialized fibrous mass. This may lead to chronic pulmonary thromboembolism. This condition presents with chronic pulmonary hypertension and right ventricular failure (cor pulmonale) secondary to stenosis of the central pulmonary arterioles sue to the presence of the above mentioned thromboembolic masses.

Disorders of the left heart may cause secondary pulmonary hypertension, resulting from volume and pressure overload. Pulmonary blood volume overload is caused by left-to-right intracardiac shunts, such as in patients with atrial or ventricular septal defects. Left atrial hypertension causes a passive rise in pulmonary arterial systolic pressure in order to maintain a driving force across the vasculature. Ventilation/perfusion lung scans are used to differentiate pulmonary hypertension of chronic thromboemboli from other types. The scans are interpreted as the case for acute pulmonary emboli. High and intermediate probability patterns suggest pulmonary emboli as the underlying reason for pulmonary hypertension (100 % sensitivity and 86 % specificity) while low probability pattern has not been found to be associated with pulmonary emboli as a cause of the pulmonary hypertension [15].

13.4 Pneumocystis carinii (jiroveci) Pneumonia

Pneumocystis carinii (jiroveci) is an opportunistic pathogen currently classified as a fungus [55]. It is a significant cause of morbidity and mortality in human immunodeficiency virus and non-human immunodeficiency virus-associated immunosuppressed patients [56, 57] although it also occurs in nonimmunocompromised patients [58, 59]. Highly effective active antiretroviral therapy in industrialized nations, however, has led to dramatic declines in the incidence of AIDS-associated complications, including PCP, but no decline has occurred in the developing countries [56, 57]. The organism attaches to the alveolar macrophages through a mechanism that involves fibronectin. The trophozoite develops into cysts that produce daughter trophozoites. As the number of organisms increase, the permeability of the alveolar capillary endothelium increases, producing respiratory distress. Typically, infection with *P. carinii* produces a patchy or lobar interstitial pneumonia or, rarely, a bronchopneumonia pattern. Severe infections produce diffuse alveolar damage. The classical histological findings consist of alveolar exudates having a granular or foamy appearance that represent nonstaining clusters of the cysts and trophozoites of *P. carinii* within an eosinophilic staining background of the organism's filopodia and host cellular debris. Atypical pulmonary reactions include the formation of granulomas, focal pulmonary infection, and cavitary lesions. In extremely immunosuppressed persons, the inflammatory reaction may be minimal and consist only of sparse collections of alveolar macrophages. Since clinical manifestations of *P. carinii* pneumonia (PCP) in AIDS patients may precede X-ray changes by at least 2 weeks and as long as 18 months, ^{67}Ga has an important role in the diagnosis of early PCP. ^{67}Ga is more sensitive than chest X-ray for early PCP and is more accurate in measuring the extent of inflammation. The pattern of uptake is typically diffuse and bilateral (Fig. 13.17), although other patterns may be noted [60, 61]. Localized lung uptake and perihilar uptake patterns can be seen in addition to the diffuse pattern, which may be further classified into homogeneous and heterogeneous diffuse patterns. The heterogeneous pattern has the highest positive predictive value, which is even more specific when it is of high-grade uptake and when accompanied by normal chest radiograph.

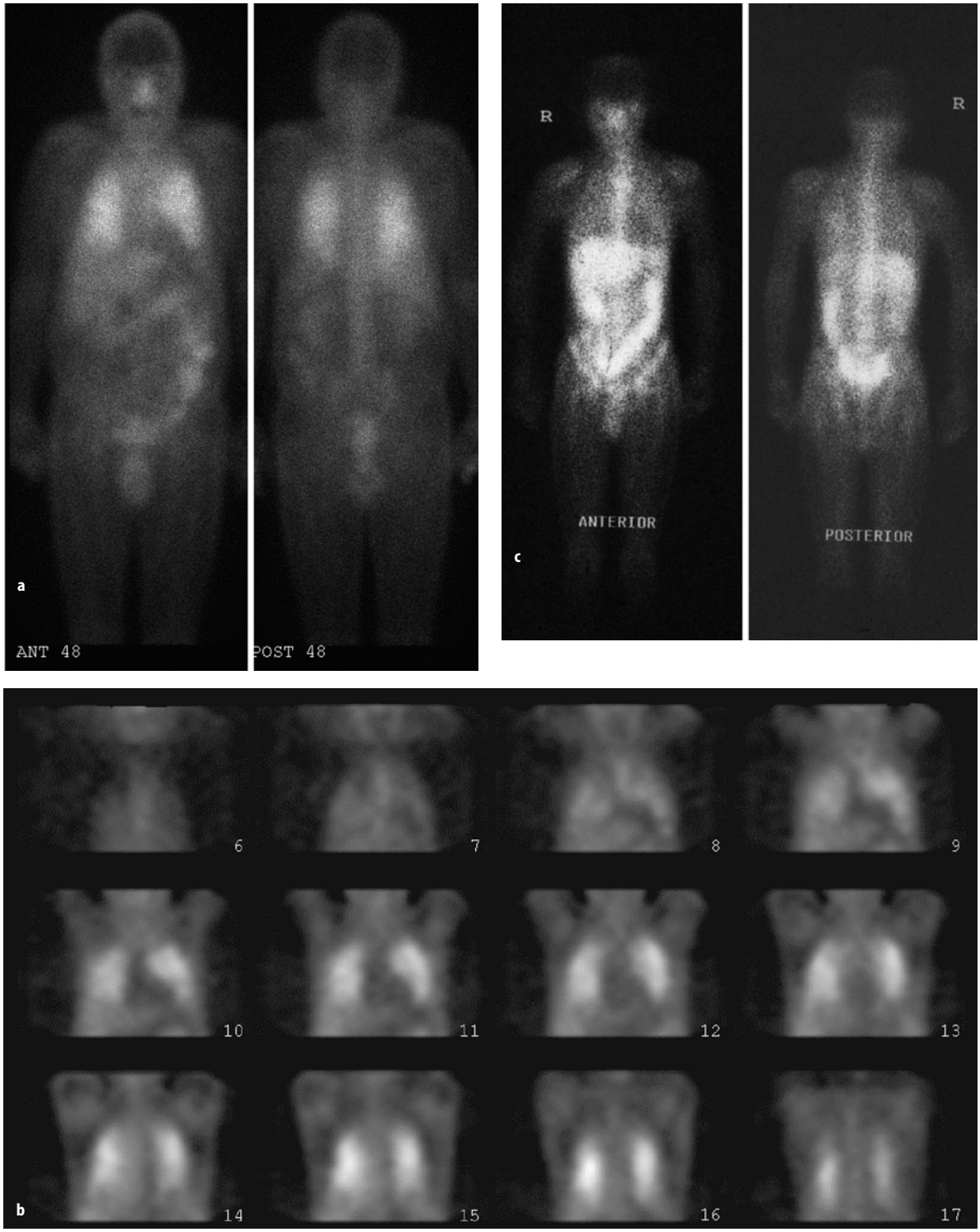

Fig. 13.17a–c. Gallium-67 images of two AIDS patients with PCP obtained 48 h post injection. Planar (**a**) and SPECT (**b**) of one patient show significantly increased accumulation of the radiotracer illustrating severe infection. Planar image of the other patient (**c**) shows slightly increased accumulation of the radiotracer in both lungs diffusely illustrating mild form of PCP infection

13.5 Idiopathic Pulmonary Fibrosis

Idiopathic pulmonary fibrosis (IPF) is characterized by parenchymal inflammation and interstitial fibrosis that may eventually be fatal. The inciting factors in the development of IPF remain unknown [62]. A widely held hypothesis is that this disorder occurs in susceptible individuals following some unknown stimuli. The inciting agent initiates a cascade of events that involve factors controlling inflammatory, immune, and fibrotic processes in the lung. Viral, immunological, and genetic (supported by finding familial cases) factors appear to play an important role. The main feature in IPF is alveolitis, which is chronic inflammation of the alveolar unit followed by fibrosis. The destruction is mediated by inflammatory (neutrophils and macrophages) and immune (immune complex disease) processes, where immune effector cells injure lung cells and induce connective tissue proliferation. The chronic active inflammation is important and directs the investigations for diagnosis. The fibrotic and destructive changes distort the normal lung architecture and result in morbidity.

The major histopathological findings vary from active alveolitis and minimal fibrosis in early cases to severe fibrosis and honeycombing with minimal alveolitis in late stages. The alveolitis is characterized by an outpouring of mononuclear cells, macrophages, and lymphocytes into the alveolar space, with relatively intact alveolar walls which will be deranged by edema, fibrinous exudate, mononuclear cell infiltration, and fibroblast proliferation [63]. Connective tissue alteration occurs later in the process. Recent classification of the type of fibrosis depends on the predominant cell type. Patients with more cellular findings respond to treatment favorably and have a better long-term prognosis compared with those with more fibrotic changes. ^{67}Ga has an important role in evaluating the activity of the disease and in following up the response to treatment. The degree of ^{67}Ga uptake correlates with the degree of interstitial and alveolar cellularity as seen on lung biopsies. Accordingly, it helps to evaluate the extent and activity of the disease by visual assessment and/or quantitation of the uptake.

13.6 Pulmonary Sarcoidosis

Sarcoidosis, a multisystem granulomatous disorder, occurs most commonly in young adults, more commonly in blacks and in temperate areas. A second peak is known to occur in the older age group (over age 60 years) [64]. The exact etiology of the disease is unknown, but it is believed to be due to exaggerated cellular immune response on the part of helper/inducer T lymphocytes to exogenous or autoantigens. It presents most frequently as bilateral hilar adenopathy, pulmonary infiltrates, and skin and eye lesions. It may be acute or chronic. The acute variant has an abrupt onset and may commonly show spontaneous remission within 2 years; the response to steroids is excellent. The chronic variant has an insidious onset and is more likely to cause progressive disease with fibrosis. The disor-

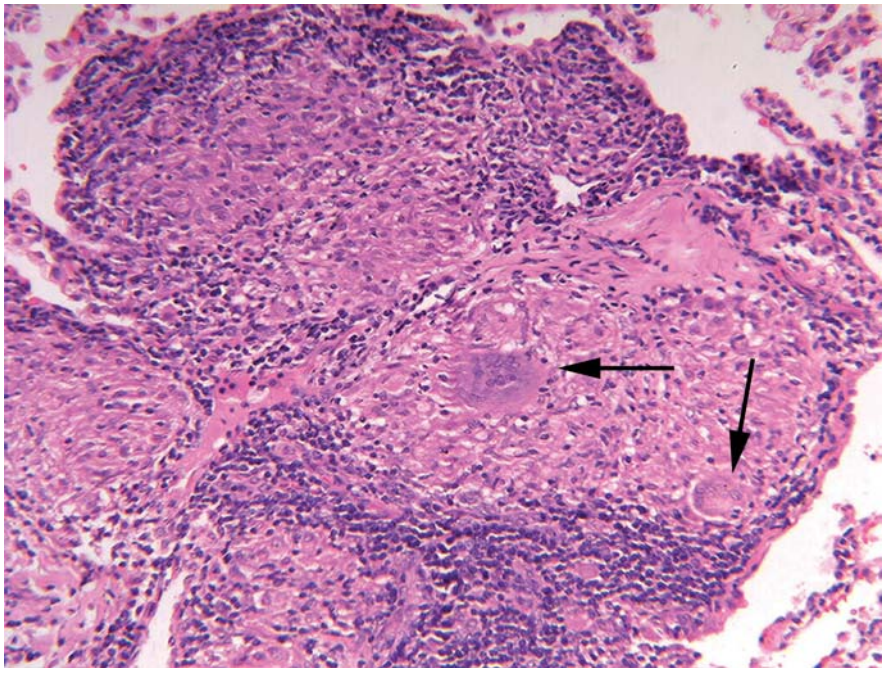

Fig. 13.18. Microphotograph of a noncaseating granuloma of a case of sarcoidosis. Note multinucleated giant cells (*arrows*)

der is characterized by the presence of epithelioid granuloma in affected organs that may lead to fibrosis and organ dysfunction. Granulomas of sarcoidosis often exist diffusely throughout the body despite lack of clinical evidence of disease. Histological features are usually quite typical, but not specific. The architecture of the lesion is that of multiple similar granulomas, consisting of whorls of elongated cells (fibroblasts and epithelioid cells) with mononuclear inflammatory cells at their periphery. Giant cells are located within the granulomas (Fig. 13.18) and multinucleated cellular inclusion bodies are frequently found. Scarring with fibrosis suggests chronicity. Epithelioid cells secrete a number of cytokines and other mediators including angiotensin converting enzyme (ACE), which is suggested to reflect the granuloma burden in sarcoidosis and may play a role in its pathophysiology. Lung is involved in more than 90% of cases. Pulmonary sarcoidosis starts as diffuse interstitial alveolitis, followed by the characteristic granulomas. Granulomas are present in the alveolar septa as well as in the walls of the bronchi and pulmonary arteries and veins. The center of the granuloma contains epithelioid cells derived from mononuclear phagocytes, multinucleated giant cells, and macrophages. Lymphocytes, macrophages, monocytes, and fibroblasts are present at the periphery of the granuloma [60]. Sarcoidosis represents a challenge to clinical investigation because of its unpredictable course, uncertain response to therapy, and diversity of potential organ involvement and clinical presentations [65].

The diagnosis is based on a compatible clinical and/or radiological picture, histopathological evidence of non-caseating granulomas in tissue biopsy specimens and exclusion of other diseases capable of producing similar clinical or histopathological appearances [64]. Patients with pulmonary sarcoidosis may have no symptoms and are discovered by chest X-ray obtained for nonpulmonary reasons. When symptomatic, dyspnea, chest pain and cough are the most common chest symptoms [66]. For many years pulmonary sarcoidosis has been staged into four stages (Table 13.8) based on chest X-ray findings [67]. The distinction between sarcoidosis and tuberculosis can be difficult at times, and the two diseases may coexist in the same patient. Similar granulomas may occur in a wide variety of other diseases, such as with malignancy or immune deficiencies, berylliosis, and foreign-body reactions. ^{67}Ga is useful in evaluating the activity of the disease and the response to therapy. Semi-quantitative and quantitative methods of grading ^{67}Ga uptake can be helpful. Diffuse lung uptake and bilateral hilar uptake (Figs. 13.19, 13.20) are the most common patterns seen, but they lack specificity [68]. The major value of ^{67}Ga is in evaluating the activity of the disease, in detecting extrathoracic sites of involvement, and in evaluating the response to therapy. Ventilation and perfusion scans do not have a specific role in sarcoidosis. However, it should be known that a mismatching pattern is among those seen in the disease and can be falsely interpreted as indicating a high probability of pulmonary emboli.

Table 13.8. Radiologic staging of pulmonary sarcoidosis

Stage 1	Hilar adenopathy alone
Stage 2	Adenopathy plus infiltrates
Stage 3	Infiltrates only
Stage 4	Fibrosis

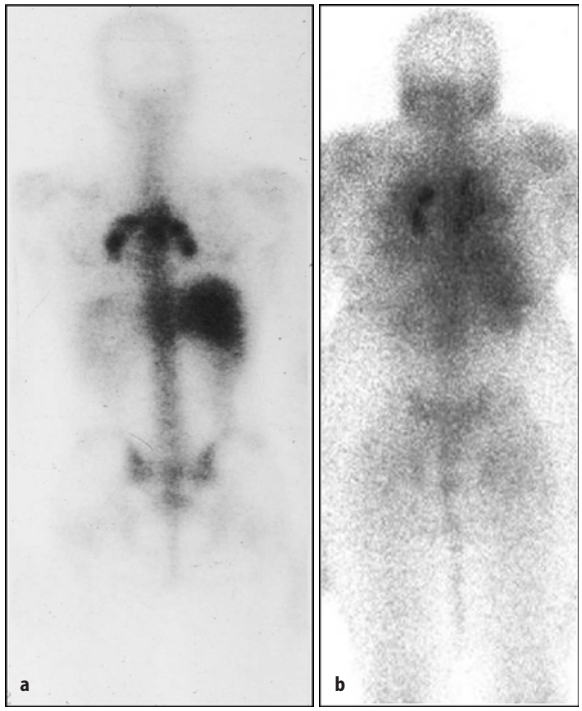

Fig. 13.19a,b. Forty-eight-hour Ga-67 posterior image of a patient with sarcoidosis showing uptake in the hilar nodes bilaterally (**a**). Another patient's study is shown (**b**), illustrating hilar adenopathy and diffuse lung uptake

13.7 Obstructive Airway Disease

Chronic bronchitis, emphysema, and bronchial asthma are collectively known as obstructive airway disease. Chronic bronchitis and emphysema are common among smokers but are also caused by air pollutants. In chronic bronchitis the walls of the bronchi and bronchioles are inflamed with edema, cellular infiltrates, fibrosis, and an increase in the mucus glands and bronchial secretions and thickening of the bronchial walls. All of these changes result in progressive narrowing of the lumina of the bronchi and bronchioles.

Emphysema indicates irreversible dilatation of the alveoli, and destruction of their septa can occur alone

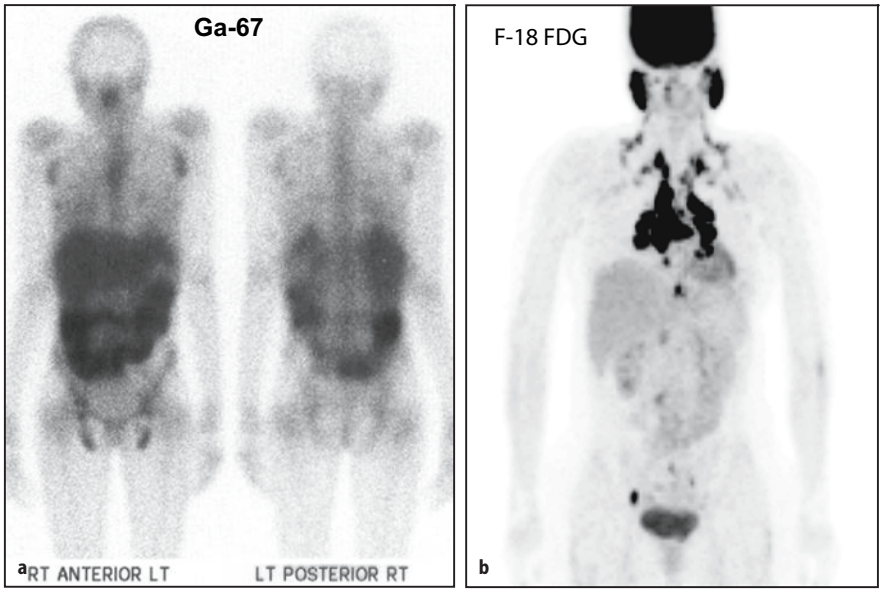

Fig. 13.20. a Gallium-67 images for a patient with sarcoidosis illustrating uptake in the axillary and inguinal lymph nodes as well as mild diffuse accumulation of the radiotracer in the lungs. **b** F-18 FDG image of a 35-year-old female with proven sarcoidosis. The study shows uptake in the areas of active inflammation in mediastinum, pulmonary hilus, salivary glands, cervical, supraclavicular, axillary, para-aortic, iliac and inguinal lymph nodes. (Courtesy of Professor Osama Sabry)

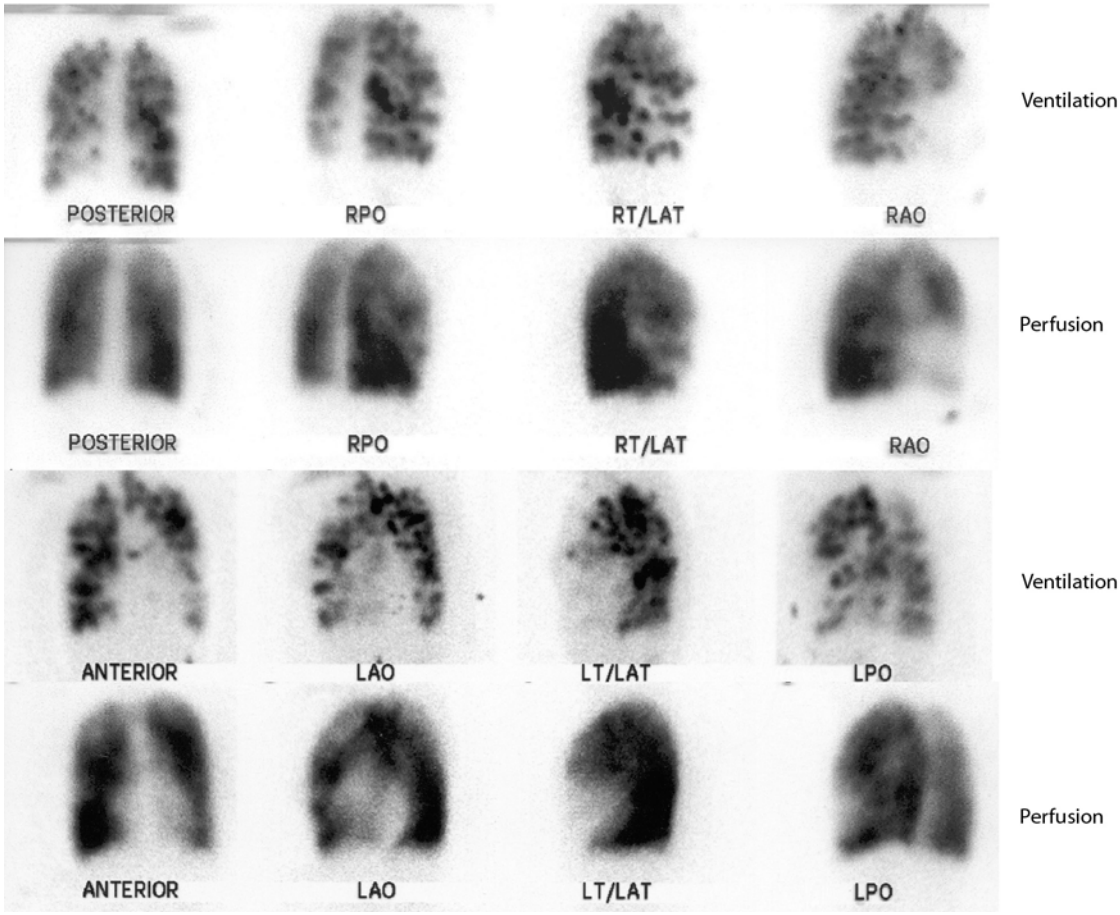

Fig. 13.21. ^{99m}Tc-DTPA aerosol image of a patient with severe obstructive airway disease. Note the central deposition of the radiotracer at the sites of the narrowed openings of the bronchi and bronchioles

or, commonly, in association with chronic bronchitis as part of chronic obstructive airway disease. Hyperinflation of the alveoli and septal destruction may lead to formation of large air spaces (bullae). Air spaces formed adjacent to the pleura are called blebs. There are three types of emphysema:

1. In centrilobular emphysema the central areas of the lungs are affected by alveolar dilatation. This type is most commonly associated with chronic bronchitis in smokers. It affects more the upper lobes and usually spares the alveoli
2. Panlobular emphysema involves an entire lobule with randomly distributed damage. It involves more the lower lobes of the lungs, older individuals, and patients with α_1-antitrypsin deficiency.
3. Localized (previously paraseptal) emphysema is characterized by emphysematous changes in only one or at most a few locations, with the remainder of the lung normal. It is usually of no clinical significance; however, the rather common subpleural bullae may rupture and cause spontaneous pneumothorax.

Bronchial asthma is characterized by episodes of airflow obstruction, which affect both large and small airways. Decreased ventilation and perfusion can be seen on ventilation and perfusion scans within moments of the asthma attack.

Obstructive airway disease can cause an abnormal ventilation scan with or without abnormal perfusion. Xenon-133 is the most sensitive agent for detecting the ventilation abnormalities, particularly in the washout phase. ^{99m}Tc-DTPA aerosol studies show nonuniformity with varying degrees of central deposition of the particles, depending on the severity of bronchial narrowing (Fig. 13.21). The associated perfusion abnormalities range from minimal nonuniformity to complete absence of perfusion, matching the ventilation defects. Obstructive airway disease is commonly seen among patients suspected of having pulmonary emboli. This may pose difficulty in interpreting the ventilation and perfusion images to establish whether a matching pattern is present [69], but the same criteria of interpretation are applied to determine the probability of pulmonary emboli as in patients with no obstructive airway disease.

13.8 Pleural Effusions

Many etiologies can cause pleural effusion, including inflammatory, traumatic, and neoplastic diseases, and disturbance in organ functions. Pulmonary embolism is not uncommonly associated with pleural effusion. Based on the underlying cause, pleural effusion may consist of transudate, exudate, pus, or blood. With pleural effusions, there is diminished ventilation and perfusion, which is proportional to the amount of effusion [70]. Elevated hemidiaphragm causes a similar pattern. The appearance of pleural effusion may change with the position of the patient when effusion is freely mobile, or may not change when the effusion is loculated or encapsulated.

13.9 Pneumonia

Pneumonia is an acute inflammation of the lung parenchyma, which often impairs gas exchange. The condition is prevalent in infants, old individuals, and immunocompromised patients. It is the leading secondary cause of death in the United States. Three major types can be recognized: lobar, lobular (bronchopneumonia), and interstitial. Lobar pneumonia is usually bacterial and involves the alveoli of one lobe or more, but not the bronchi. Chest X-ray and other imaging modalities show varying degrees of abnormalities based on the amount of inflammatory exudate. X-ray will show opacities of different degrees, while nuclear medicine procedures such as labeled WBC or ^{67}Ga (Fig. 13.22) show abnormalities correlating in size and intensity with the severity of inflammation and its duration (see Chapter 4). Lobular pneumonia (bronchopneumonia) shows inflammation of bronchi, bronchioles, and alveoli in a patchy manner. Interstitial pneumonia, also called pneumonitis or viral pneumonia, is a milder form that usually accompanies other viral conditions such as measles. Typically, no exudates are present in the alveoli.

13.10 Bronchiectasis

Bronchiectasis simply indicates weakened and dilated bronchi affecting predominantly the lower zones of the lungs. This may be caused by chronic inflammation, and the resultant dilatation is permanent. Three types are recognized:

1. The varicose type is so named because it is characterized by irregular dilatation and narrowing, similar to varicose veins.
2. The cylindrical type is characterized by uneven dilatation of the bronchi.
3. The saccular or cystic type is characterized by dilatations at the ends of the bronchi.

Fig. 13.22a,b. Gallium-67 48-h study (a) shows two areas of increased accumulation of the radiotracer in the right lower and left mid lung zones in a patient with pneumonia. Chest X-ray (**b**) of the same patient shows infiltrates

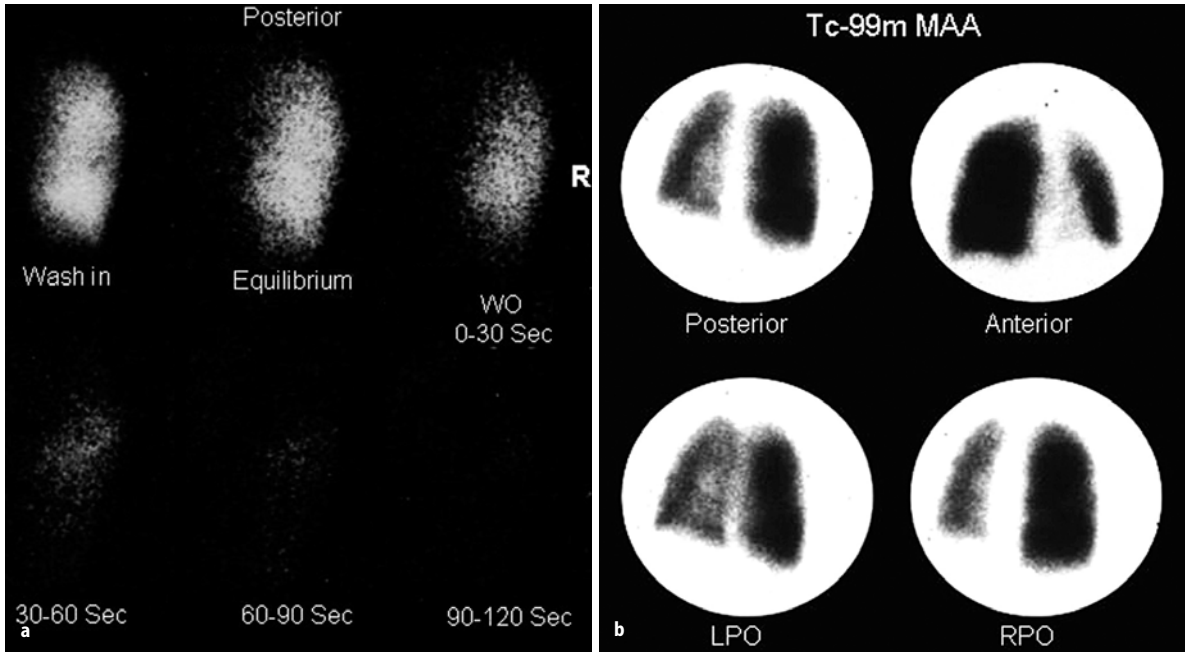

Fig. 13.23a,b. Xenon-133 washout images of a patient complaining of severe shortness of breath. The images reveal nonvisualized left lung. ^{99m}Tc-MAA perfusion study of the same patient shows decreased perfusion to same lung diffusely. This pattern suggests bronchial obstruction with reflex vasoconstriction. The patient has a mucus plug obstructing the left main bronchus

13.11 Bronchial Obstruction

Bronchial obstruction may be caused by obstruction from within or from outside the bronchi. It may be acute, such as obstruction due to a foreign body or mucus plug, or gradual, as in some patients with bronchial compression by an adjacent mass. Depending on the level and severity of obstruction, the ventilation and perfusion are affected. Usually the ventilation is affected more severely than the perfusion and may be totally absent with complete obstruction (Fig. 13.23).

13.12 Cystic Fibrosis

Cystic fibrosis causes most of the progressive pulmonary diseases in children. The most relevant pathological change is the production of thick mucus that is also sticky and then cannot be removed by the cilia. This mucus accumulates in the bronchi and bronchioles, causing obstruction, and predisposes to lung infections. Perfusion and ventilation scans show abnormalities in both perfusion and ventilation that correlate with the severity of the disease; their sensitivity is superior to that of chest radiographs in detecting the presence and extent of early pulmonary involvement by the disease. The scans can also be useful in quantitating the regional function before surgery is performed as a treatment.

13.13 Lung Cancer

Lung cancer is currently the leading cause of cancer death among both men and women. Histologically, lung cancer may be squamous (epidermoid), adenocarcinoma (bronchogenic carcinoma), small cell carcinoma, adenosquamous carcinoma, and anaplastic carcinoma. The role of nuclear medicine lies in detection of the primary tumor in some patients, and more importantly staging of the tumor, and evaluating the response to therapy and sometimes predicting its success [71, 72]. When pneumonectomy is planned for lung cancer, postoperative lung function can be predicted with optimal accuracy by a preoperative perfusion scan in the upright or supine positions. The ventilation scan is less accurate [73]. The role of scintigraphy in detecting the primary tumor, staging, evaluating its response to therapy, and locating its metastases using other radiopharmaceuticals such as ^{18}F-FDG, ^{67}Ga, thallium-201, and ^{99m}Tc-sestamibi is discussed elsewhere. PET-FDG is particularly useful in staging the disease (Fig. 13.24) and determines the best treatment choice. See Chapters 11 and 12.

References

1. Brashers BL, Davey SS (1998) Structure and function of the pulmonary system. In: McCance KL, Huether SE (eds) Pathophysiology, the biologic basis for disease in adults and children, 3rd edn. Mosby, St Louis, pp 1131 – 1157
2. Thibodeau GA, Patton KI (1996) Anatomy and physiology, 3rd edn. Mosby, St Louis
3. De Nardo GL, De Nardo SJ (1984) The lungs. In: Freeman LM, Johnson PM (eds) Clinical radionuclide imaging, 3rd edn. Grune and Stratton, Orlando, FL, pp 1051 – 1139
4. Frieman DG, Suyemoto J, Wessler S (1965) Frequency of pulmonary thromboembolism in man. N Engl J Med 272: 1278 – 1280
5. McLachlin J, Patterson JC (1961) Some basic observations on venous thrombosis and pulmonary embolism. Surg Gynecol Obstet 93:1 – 8
6. Moser KM (1990) Venous thromboembolism: state-of-the-art. Am Rev Respir Dis 141:235 – 249
7. Palevsky HI, Alavi A (1991) Noninvasive strategy for management of patients suspected of pulmonary embolism. Semin Nucl Med 21:325 – 331

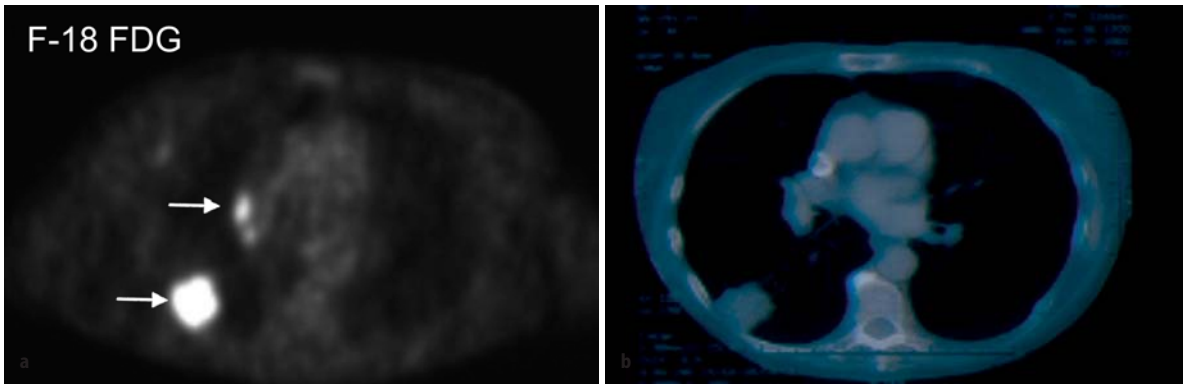

Fig. 13.24a,b. FDG-PET study illustrating right lung nodule with intense uptake and a mediastinal involvement (*arrows*) corresponding to lesions seen on CT scan. These represent non-small cell lung cancer. The example demonstrates the value of FDG in determining the nature of morphologic findings of nodules and in staging the disease

8. Kamel E, Mckee T, Calcagni M, Schmidt S, Markl S, Bischof Delaloye A (2005) Occult lung infarction may induce false interpretation of F-18 FDG PET in primary staging of pulmonary malignancies. Eur J Nucl Med Mol Imaging 32:641 – 646
9. Manny J, Hechtman HB (1985) Vasoactive humoral factors. In: Goldhaber SZ (ed) Pulmonary embolism and deep venous thrombosis. Saunders, Philadelphia, PA, p 283
10. Bass H, Heckscher T, Anthonisen NR (1967) Regional pulmonary gas exchange in patients with pulmonary embolism. Clin Sci 33:355 – 364
11. Smith R, Alderson PO (1987) Ventilation perfusion scintigraphy in pulmonary embolism in pulmonary nuclear medicine. In: Loken MK (ed) Pulmonary nuclear medicine. Appleton and Lange, Norwalk, Connecticut, pp 51 – 79
12. Wolfe MW, Skibo LK, Goldhaber SZ (1993) Pulmonary embolic disease: diagnosis, pathophysiologic aspects and treatment with thrombolytic therapy. Curr Probl Cardiol XVIII:587 – 633
13. National Heart, Lung and Blood Institute (1970) Urokinase pulmonary embolism trial – phase I results. JAMA 214:2163 – 2172
14. National Heart, Lung and Blood Institute (1974) Urokinase pulmonary embolism trial – phase II results. JAMA 229:1606 – 1613
15. Worsley DF, Palesky HI, Alavi A (1994) Ventilation-perfusion lung scanning in the evaluation of pulmonary hypertension. J Nucl Med 35:793 – 796
16. Elgazzar AH, Jobalia R, Subramanian P, Ryan J, Hughes JA (1994) Multiple ventilation and perfusion (V/Q) scans in patients with and without pulmonary emboli (PE). J Nucl Med 35:239
17. PIOPED Investigators (1990) Value of the ventilation/perfusion scan in acute pulmonary embolism: results of the prospective investigation of pulmonary embolism diagnosis (PIOPED). JAMA 263:2753 – 2759
18. Carson JL, Kelley MA, Duff A, Weg JG, Fulkerson WJ, Palevsky HI, Schwartz JS, Thompson BT, Popovich J Jr, Hobbins TE, et al (1992) The clinical course of pulmonary embolism. N Engl J Med 326:1240 – 1245
19. Schober B (1980) Do pulmonary emboli lodge preferentially in prior foci? J Nucl Med 21:659 – 661
20. Hoffman JM, Lee A, Grafton S, Bellamy P, Hawkins RA, Webner M (1994) Clinical signs and symptoms in pulmonary embolism. A reassessment. Clin Nucl Med 19:803 – 808
21. Stein PD, Terrin ML, Hales CA, Palevsky HI, Saltzman HA, Thompson BT, Weg JG (1991) Clinical, laboratory, roentgenographic, and electrocardiographic findings in patients with acute pulmonary embolism and no pre-existing cardiac or pulmonary disease. Chest 100:598 – 603
22. Coche E, Verschuren F, Hainaut P, Goncette L (2004) Pulmonary embolism findings on chest radiographs and multislice spiral CT. Eur Radiol 14:1241 – 1248
23. Schultz DJ, Brasel KJ, Washington L, Goodman LR, Quikkel RR, Lipchik RJ, Clever T, Weigelt J (2004) Incidence of asymptomatic pulmonary embolism in moderately to severely injured trauma patients. J Trauma 56:727 – 731
24. Timmons S, Kingston M, Hussain M, Kelly H, Liston R, (2003) Pulmonary embolism: differences in presentation between older and younger patients. Age Ageing 32: 601 – 605
25. Berman AR, Arnsten JH (2003) Diagnosis and treatment of pulmonary embolism in the elderly. Clin Geriatr Med 19:157 – 175
26. Elgazzar AH (1997) Scintigraphic diagnosis of pulmonary embolism: unraveling the confusion seven years after PIOPED. Nucl Med Ann, pp 69 – 101
27. Paraskos JA, Adelstein SJ, Smith RE, Rickman FD, Grossman W, Dexter L, Dalen JE (1973) Late prognosis of acute pulmonary embolism. N Eng J Med 239:55 – 58
28. Stein PD, Athanasoulis C, Alavi A, Greenspan RH, Hales CA, Saltzman HA, Vreim CE, Terrin ML, Weg JG (1992) Complications and validity of pulmonary angiography in acute pulmonary embolism. Circulation 85:462 – 468
29. Kawamoro M, Ogura Y, Honda N, Satoh K, Suga K, Mori Y, Imai T, Inoue T, Narabayashi I (2002) Present diagnostic strategies for acute pulmonary thromboembolism; results of a questionnaire in a retrospective trial conducted by the respiratory nuclear medicine working group of the Japanese Society of Nuclear Medicine. Ann Nucl Med 16: 549 – 555
30. Ahmad M, Fletcher JW, Pur-Shahriari AA, George EA, Donati RM (1979) Radionuclide venography and lung scanning: Concise communication. J Nucl Med 20:291 – 293
31. Perrier A (2001) Pulmonary embolism: from clinical presentation to clinical probability assessment. Semin Vasc Med 1:147 – 154
32. Langan CT, Weingart S (2006) New diagnostic and treatment modalities for pulmonary. One path through the confusion. The mount Sinai Journal of Medicine; 73:528 – 541
33. Radan L, Mor M, Gips S, Schlang-Eisenberg D, Lurie Y, Dickstein K, Bitterman H, Ben-Haim S (2004) The added value of spiral computed tomographic angiography after lung scintigraphy for the diagnosis of pulmonary embolism. Clin Nucl Med 29:255 – 261
34. Aviram G, Levy G, Fishman JE, Blank A, Graif M (2004) Pitfalls in the diagnosis of acute pulmonary embolism on spiral computed tomography. Curr Probl Diagn Radiolol 33:74 – 84
35. Reinartz P, Wildberger JE, Schaefer W, Nowak B, Mahnken AH, Buell U (2004) Tomographic imaging in the diagnosis of pulmonary embolism: A comparison between V/Q lung scintigraphy in SPECT technique and multislice spiral CT. J Nucl Med 45:1501 – 1508
36. Velmahos GC, Toutouzas KG, Vassiliu P, Rhee P, Wilcox A, Hanks SE, Chan LS, Tillou A, Demetriades D (2004) Can we rely on computed tomographic scanning to diagnose pulmonary embolism in critically ill surgical patients? J Trauma 56:518 – 525
37. Perrier A, Nendaz MR, Sarasin FP, Howarth NM Bounameaux H (2003) Cost effectiveness analysis of diagnostic strategies for suspected pulmonary embolism including helical computed tomography. Am J Respiratory Crit Care Med 167:39 – 44
38. Kanne JP, Lalani TA (2004) Role of computed tomography and magnetic resonance imaging for deep venous thrombosis and pulmonary embolism. Circulation 109:115 – 121 (Suppl)
39. Altes TA, Mai VM, Munger TM, Brookeman JR, Hagspiel KD (2005) Pulmonary embolism: Comprehensive evaluation with MR ventilation and perfusion scanning with hyperpolarized helium-3, arterial spin tagging, and contrast-enhanced MRA. J Vasc Interv Radiol 16:999 – 1005
40. Biello DR, Mattar AG, McKnight RC, Siegel BA (1979) Ventilation-perfusion studies in suspected pulmonary embolism. AJR 133:1033 – 1037
41. Hull RD, Hirsh J, Carter CJ, Jay RM, Dodd PE, Ockelford PA, Coates G, Gill GJ, Turpie AG, Doyle DJ, Buller HR, Raskob GE (1983) Pulmonary angiography, ventilation lung scanning, and venography for clinically suspected pulmonary embolism with abnormal perfusion lung scan. Ann Intern Med 98:891 – 899
42. Worsley DF, Kim CK, Alavi A, Palevsky HI (1993) Detailed analysis of patients with matched ventilation-perfusion defects and chest radiographic opacities. J Nucl Med 34:1851 – 1853

43. Goldberg SN, Palmer EL, Scott JA, Fisher R (1994) Pulmonary embolism: prediction of the usefulness of initial ventilation-perfusion scanning with chest radiographic findings. Radiology 193:801 – 805
44. Worsley DF, Alavi A (1995) Comparative analysis of the results of the PIOPED study. J Nucl Med 36:2380 – 2387
45. Goldberg SN, Richardson DD, Palmer EL, Scott JA (1996) Pleural effusion and ventilation/perfusion scan interpretation for acute pulmonary embolus. J Nucl Med 37:1310 – 1313
46. Stein PD, Coleman ER, Gottscalk A, Saltzman H, Terrin ML, Weg JG (1991) Diagnostic utility of ventilation/perfusion lung scans in acute pulmonary embolism is not diminished by pre-existing cardiac or pulmonary disease. Chest 100:604 – 606
47. Stein PD, Henry JW (1997) Prevalence of acute pulmonary embolism in central and subsegmental pulmonary arteries and relation to probability interpretation of ventilation/perfusion lung scans. Chest 111:1246 – 1248
48. Morgenthaler TI, Ryu JH (1995) Clinical characteristics of fatal pulmonary embolism in a referral hospital. Mayo Clin Proc 70:417 – 424
49. Morpurgo M, Schmid C (1995) The spectrum of pulmonary embolism. Clinicopathologic correlations. Chest 107:18S–20S
50. Sperry KL Key CR, Anderson RE (1990) Towards a population-based assessment of death due to pulmonary embolism in New Mexico. Hum Pathol 21:159 – 165
51. Karwinski B, Svendsen E (1989) Comparison of clinical and postmortem diagnosis of pulmonary embolism. J Clin Pathol 42:135 – 139
52. Gross JS, Neufeld RR, Libow LS, Gerber I, Rodstein M (1988) Autopsy study of the elderly institutionalized patient: Review of 234 autopsies. Arch Intern Med 1:173 – 176
53. Dismuke SE, Wagner EH (1986) Pulmonary embolism as a cause of death. JAMA 225:2039 – 2042
54. Goldhaber SZ, Hennekens CH, Evans DA, Newton EC, Goldleski JJ (1982) Factors associated with correct antemortem diagnosis of major pulmonary embolism. Am J Med 73:822 – 826
55. Wazir JF, Ansari NA (2004) *Pneumocystis carinii* infection: Update and review. Arch Pathol Lab Med 128:1023 – 1027
56. Feldman C (2005) Pneumonia associated with HIV infection. Curr Opin Infect Dis 18:165 – 170
57. Morris A, Lundgren JD, Masur H, Walzer PD, Hanson DL, Frederick T, Huang L, Beard CB, Kaplan JE (2004) Current epidemiology of *Pneumocystis* pneumonia. Emerg Infect Dis 10:1713 – 1720
58. Medrano FJ, Montes-Cano M, Conde M, de la Horra C, Respaldiza N, Gasch A, Perez-Lozano MJ, Varela JM, Calderon EJ (2005) *Pneumocystis jirovecii* in general population. Emerg Infect Dis 11:245 – 250
59. Al Soub H, Taha RY, El Deeb Y, Almaslamani M, Al Khuwaiter JY (2004) *Pneumocystis carinii* pneumonia in a patient without a predisposing illness: case report and review. Scand J Infect Dis 36:618 – 621
60. Kramer EL, Sanger JJ (1989) Detection of thoracic infections by nuclear medicine techniques in the acquired immunodeficiency syndrome. Radiol Clin North Am 27: 1067 – 1075
61. Woolfenden JM, Carrasquillo JA, Larson SM, Simmons JT, Masur H, Smith PD, Shelhamer JH, Ognibene FP (1987) Acquired immunedeficiency syndrome: Ga-67 citrate imaging. Radiology 162:383 – 387
62. Noble PW, Homer RJ (2004) Idiopathic pulmonary fibrosis: new insights into pathogenesis. Clinics Chest Med 25:749 – 758
63. Line BR, Fulmer JD, Reynolds HY, Roberts WC, Jones AE, Harris EK, Crystal RG (1978) Gallium-67 citrate scanning in the staging of idiopathic pulmonary fibrosis: correlation with physiologic and morphologic features and bronchoalveolar lavage. Am Rev Respir Dis 118:355 – 365
64. Baughman RP (2004) Pulmonary sarcoidosis. Clin Chest Med 25:521 – 530
65. Mandel J, Weinberger SE (2001) Clinical insights and basic science correlates in sarcoidosis. Am J Med Sci 321:99 – 107
66. ACCESS Research Group (1999) Design of a case control etiologic study of sarcoidosis (ACCESS). J Clin Epidemiol 52:1173 – 1186
67. Scadding JG (1961) Prognosis of intrathoracic sarcoidosis in England. BJM 4:1165 – 1172
68. Gupta RG, Beckerman C, Silcian L, et al (1982) Gallium citrate scanning and serum angiotensin converting enzyme levels in sarcoidosis. Radiology 144:895 – 899
69. Elgazzar AH, Silberstien EB, Hughes J (1995) Perfusion and ventilation scans in patients with diffuse obstructive airway disease: utility of single breath (wash in) xenon-133. J Nucl Med 36:64 – 67
70. Anthonisen NR, Martin RR (1977) Regional lung function in pleural effusion. Am Rev Respir Dis 116:201 – 207
71. Masayuki M, Kuwabra Y, Ichiya Y, Yoshida T, Nakagawa M, Hiroyasu S, Kenji S, Maehara Y, Masuda K (1999) Prediction of the chemosensitivity of lung cancer by Tc-99m-hexakis-2-methoxyisobutyl isonitrile SPECT. J Nucl Med 40:1778 – 1783
72. Hassan IM, Sahweil A, Constantinides C, Mahmoud A, Nair M, Omar YT, Abdel-Dayem HM (1989) Uptake and kinetics of Tc-99m hexakis-2-methoxyisobutyl isonitrile in benign and malignant lesions in the lungs. Clin Nucl Med 14:333 – 340
73. Kristersson S (1974) Prediction of lung function after lung surgery. A Xe-133 radiospirometric study of regional lung function in bronchial cancer. Scand J Thorac Cardiovasc Surg 18 [Suppl]:5 – 44

14 Basis of Cardiac Imaging 1: Myocardial Contractility and Assessment of Cardiac Function

Sherif I. Heiba, Mohammad Zubaid

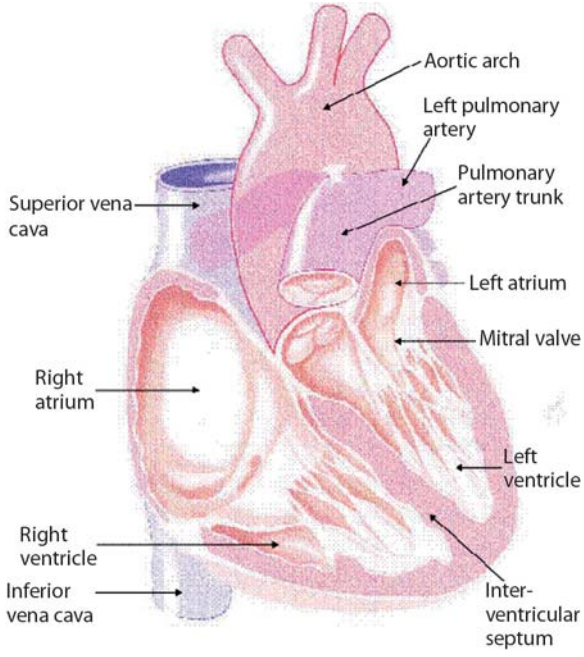

Fig. 14.1. Cutaway view of the heart (AHE)

14.1 Anatomical Considerations

The heart consists of muscle, valves, specialized tissue, coronary arteries, and pericardium. In the embryo, during the first month of gestation, a primitive straight cardiac tube is formed. The tube comprises the sinoatrium, the bulbus cordis, and the truncus arteriosus. In the second month of gestation this tube doubles over on itself to form two parallel pumping systems, each with two chambers and a great artery. The two atria develop from the sinoatrium; the right and left ventricles develop from the bulbus cordis. Differential growth of myocardial cells causes the straight cardiac tube to bear to the right, and the ventricular portion of the tube doubles over on itself, bringing the ventricles side by side (Fig. 14.1) [1].

The coronary arteries originate from the left and right coronary sinuses of the aorta (Fig. 14.2). The left main coronary artery, which comes off the left coronary sinus, continues for a variable distance before it divides into two major arteries, the left anterior descending and circumflex arteries [2]. The left anterior descending artery (LAD) descends in the anterior interventricular groove and, most of the time, continues to the apex, supplying the apical and inferior apical portion. The LAD gives off septal branches that course deep into the interventricular septum. The septal

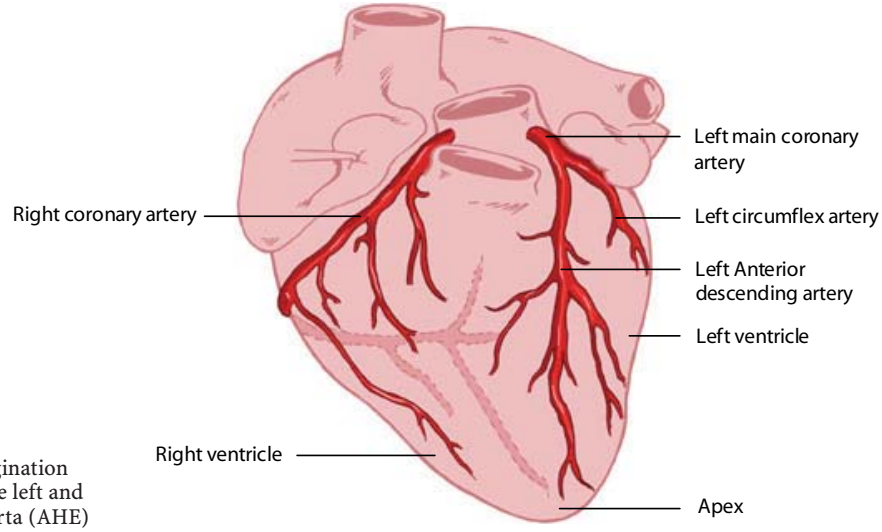

Fig. 14.2. Heart showing the origination of the coronary arteries from the left and right coronary sinuses of the aorta (AHE)

branches vary in size and number. The anterior two-thirds of the septum derives its supply from the septal LAD branches, while the rest of the septum is supplied by the perforator branches from the posterior descending branch of the right coronary artery. The LAD provides also diagonal branches, which run on the epicardial surface diagonally to supply the lateral wall of the left ventricle. Usually, the first one or two diagonal branches are large enough for angioplasty or bypass consideration.

The left circumflex artery (LCx) branches off from the left main artery and runs in the left atrioventricular groove. It then continues to the left and posteriorly. It supplies several posterolateral ventricular branches, which in turn supply the posterior lateral surface of the left ventricle and parallel the diagonal branches of the LAD. In most cases the LCx continues as a small terminal posterior left ventricular branch.

The right coronary artery (RCA) arises from the right coronary sinus and descends in the right atrioventricular (AV) groove. Its first supply is to the proximal pulmonary conus and right ventricular outflow region. Normally, there are also two or three large right ventricular branches that course diagonally over the right ventricle and supply the right ventricular myocardium. Most of the time the RCA continues along the diaphragmatic surface of the heart in the AV groove to reach the crux. At the crux the RCA divides into a posterior descending artery (PDA) and posterior left ventricular branch. The PDA branch is usually a large artery that runs in an anterior direction in the inferior interventricular groove. The PDA supplies the inferior third of the septum. The PDA septal branches can provide a rich collateral pathway via septal perforating arteries of the LAD. The other terminal branch of the RCA, the posterior left ventricular branch, continues in the AV groove and communicates with the terminal branch of the LCx.

14.2 Physiological Considerations

Cardiac muscle has two essential properties: electrical excitability and contractility.

14.2.1 Electrical Excitation

The conduction system is composed of modified cardiac cells. The sinoatrial and atrioventricular nodes have cells with high electrical impulse automaticity while the His bundle and the Purkinje system cells have higher rapid impulse conductivity. The contraction of the heart is normally initiated by an impulse in the sinoatrial node, then spreads over the atrial muscles to the atrioventricular node. The impulse then runs through the His bundle and the Purkinje system to reach all areas of both ventricles at approximately the same time [1].

14.2.2 Contraction

The ability of myocardial muscles to shorten and generate the force necessary to maintain blood circulation is a fascinating property of the heart. This is achieved primarily through the unique contractile function of two proteins of the sarcomere (actin and myosin) of the syncytially arranged myocardial fibers. The two main mechanisms that can alter cardiac muscle performance are a change in initial muscle length (Frank-Starling mechanism) and a change in contractile state. In the intact heart, these are determined by preload status, afterload status, the contractile state under a given set of loading conditions, and the heart rate. There is a passive exponential relationship between the length and

the tension of muscle fibers. Cardiac muscle tissue, like other body tissue, is not entirely elastic. Thus, this relationship does not exist beyond certain muscle stretch limits. Additionally, there is an active proportional relationship between the initial length of myocardial muscle and the force generated by this muscle, again up to certain length limits [1].

Unlike skeletal muscles, cardiac muscle cells are connected to each other by intercalated disks and do not run the length of the whole muscle. Also, heart muscle has a rich supply of the high-energy phosphate needed for the contraction. Therefore, it may not easily develop an oxygen deficit as skeletal muscle does when its work exceeds its oxygen supply. Cardiac sarcomeres are limited by the fact that they can be extended only to a certain limit (the optimum length of 2.2 μm) whereas sarcomeres of skeletal muscles can be stretched out beyond that. Finally, cardiac muscle has all-or-none twitch contraction and cannot be physiologically tetanized as skeletal muscle can.

14.3 Determination of Left Ventricular Performance

14.3.1 Left Ventricular Function Curve

The left ventricular function curve usually refers to plotting of some of the LV performance measurements such as stroke volume or work against some of the preload indices such as pulmonary capillary wedge pressure [2]. This analysis requires invasive measurements and is useful not only for providing prognostic information in acute cardiac conditions but also for monitoring response to therapeutic interventions.

14.3.2 Ejection Fraction

The ejection fraction is the most useful single number of the LV performance, defined as the stroke volume divided by the end-diastolic volume. This functional index can be measured by both invasive and noninvasive techniques. Ejection fraction is closely related to the LV function curve; however, it is very sensitive to loading conditions [2].

14.3.3 Pressure-Volume Relationship Measurement

By studying the pressure-volume relationship a stroke work index can be obtained [2]. This is defined as stroke volume X (mean LV systolic ejection pressure–mean LV diastolic pressure). It is a very sensitive index since it is affected by all factors that may alter LV performance.

14.3.4 Regional Wall Motion Assessment

Assessment of regional wall motion is extremely useful in confirming and locating the site of coronary artery disease (CAD). As with LV ejection fraction measurement, it can be studied using both invasive and noninvasive methods.

14.3.5 Diastolic Function

Diastolic function is usually assessed by studying the relationship between LV passive pressure and volume, and by examining the rate of relaxation after contraction. Several important measurements have been derived from various invasive and noninvasive techniques that can be used for both evaluating and monitoring the changes in diastolic function [2].

14.4 Pathophysiological Considerations

Heart failure is considered a pathophysiological condition rather than a specific disease. In such a condition, the heart fails to supply enough blood to meet the metabolic demand of the tissues. Most cases of heart failure are due to primary myocardial dysfunction or intrinsic abnormalities, which include hypertensive myocardial hypertrophy, ischemic heart disease, valvular heart disease, pulmonary hypertension, pericardial disease, and other cardiomyopathies (Table 14.1). Various extrinsic abnormalities can cause heart failure as well, despite normal ventricular function; this is referred to as secondary heart failure. Heart failure in this situation could have many reasons: inadequate blood volume as in hemorrhage, inadequate oxygen delivery as in anemia, inadequate venous return as in tricuspid stenosis, profound capillary vasodilatation as in toxic shock, and peripheral vascular abnormalities as in arteriovenous shunts.

Table 14.1. Causes of heart failure

Systolic dysfunction
1. Ischemic heart disease (e.g., chronic ischemia, myocardial infarction)
2. Valvular heart disease (e.g., mitral regurgitation, aortic regurgitation)
3. Dilated cardiomyopathy (idiopathic and nonidiopathic)
4. Chronic uncontrolled arrhythmia
Diastolic dysfunction
1. Hypertension
2. Ischemic heart disease (e.g., acute ischemia)
3. Infiltrative myocardial disease (e.g., amyloid)
4. Left ventricular outflow tract obstruction, e.g., hypertrophic obstructive cardiomyopathy, aortic stenosis
5. Uncontrolled arrhythmia

14.4.1 Hypertension

The main consequence of hypertension on the heart is an increase of the afterload pressure. Myocyte hypertrophy is the usual result, to add more new contractile proteins and mitochondria in order to maintain a normal cardiac output opposing the pressure overload [3]. On the level of molecular biology, stretching of myocytes by hemodynamic overload was observed to induce specific genes with a known growth regulatory effect such as proto-oncogenes [4]. These genes expand the myocyte capacity of protein synthesis, thus leading to concentric hypertrophy of the left ventricle (LV) without chamber enlargement. This process is often asymmetric in the various walls of the LV. In hypertrophic hearts, the increase in intracapillary distance and higher intracavitary pressure render the heart more susceptible to ischemia [5, 6].

14.4.1.1 Changes in LV Function

LV Diastolic Dysfunction. Relaxation of the ventricles following contraction is not a purely passive process, as it requires energy to remove calcium ions from the myocardial cells [7, 8]. Diastolic dysfunction is usually evident long before the development of systolic dysfunction. A decrease in early peak filling rate and prolongation of the time to peak filling rate are seen in the majority of hypertensive patients [9]. Accordingly, a greater than usual atrial contraction contribution to the late diastolic filling is noticed as an effort to maintain a normal LV diastolic volume. A high LV filling pressure is thus seen in these patients and is then transmitted to the arterioles and capillaries of the lung. Therefore, hypertensive patients will start developing signs and symptoms of pulmonary congestion despite their normal ventricular ejection fraction [10].

LV Systolic Dysfunction. Long-standing LV pressure overload and the associated myocardial ischemia in the abnormally hypertrophic myocardium will eventually lead to a decrease in the heart's ability to contract [11]. Congestive heart failure is the end result seen in almost all uncontrolled hypertensive patients.

Arrhythmia. In addition to total cardiac pump dysfunction, there is a significant increase in sudden cardiac death among patients with hypertrophic hearts. Both simple and complex ventricular arrhythmias develop more frequently than in nonhypertrophic myocardium, and this cannot be explained only by the usual coexistence of CAD in these patients [12].

14.4.2 Pulmonary Hypertension

The degree of pulmonary blood flow is affected mainly by the lumen size of pulmonary vessels [13]. Further, the pulmonary vascular resistance is defined as the difference of mean alveolar pressure and left atrial (LA) pressure divided by pulmonary blood flow. A change in any of these factors may therefore give rise to pulmonary hypertension. Pulmonary hypertension can be either primary, or secondary to many other causes. In congenital heart diseases, increased medial thickening and atherosclerotic changes of the pulmonary vasculature are observed [14]. Such changes are also seen in patients with systemic to pulmonary collateral circulation. The sudden rise of PA pressure with irreversible RV failure and the usual significant decrease in LV systolic function association in acute pulmonary embolization are the cause of high mortality within the first hour in these patients [15]. Conversely, intimal fibrosis due to thrombus organization is the reason behind the cor pulmonale in chronic pulmonary embolization [16]. Pulmonary hypertension can also develop due to a rise of pulmonary venous pressure caused by LV diastolic dysfunction or high LA pressure. If such a condition persists long enough, medial thickening and arterialization of pulmonary veins will develop, which results in pulmonary fibrosis and destruction of alveolar capillaries [13]. The most common chronic lung disease associated with cor pulmonale is chronic bronchitis. The increased pulmonary vascular resistance in this case is caused by a reduction in the total area of the pulmonary vascular tree as well as mild thickening of the pulmonary arterioles [17, 18].

Unlike the LV, the RV is a high-volume, low-pressure pump. Consequently, as pulmonary vascular resistance increases, a decrease in RV stroke volume and EF is observed [19]. An increase in heart rate does not usually provide enough compensation, and a decrease in cardiac output is inevitable. Additionally, signs and symptoms of systemic venous congestion are seen due to high pressure transmission from the RV. Diastolic LV dysfunction due to RV failure could be caused by the decrease in both the LV distensibility and the myocardial blood flow from the accompanied elevation in coronary venous pressure [20].

14.4.3 Valvular Heart Disease

The valvular destruction in acute rheumatic fever is related to both humoral and cell-mediated immunologic reactions, since the cell membrane of group A streptococcus antigens share common determinants with the heart [21]. Mitral valve regurgitation is the most common presentation of acute valvulitis while mitral steno-

sis is the usual chronic sequel of this disease. Varieties of autoimmune valvular lesions have also been described in many connective tissue disorders. Of the infectious causes, cardiovascular syphilis and infectious endocarditis are still recognizable. Other uncommon causes of valvular heart disease include congenital heart disease, ischemic heart disease, and cardiomyopathies.

14.4.3.1 Functional Changes

Mitral Valve Stenosis. The increase in LA size and pressure is related to the severity of mitral valve stenosis. As the LA enlarges, the incidence of all types of atrial arrhythmias, particularly atrial fibrillation, increases, which may predispose to pulmonary edema and thromboembolism. The increase in pulmonary venous pressure is another outcome that has a direct adverse impact on pulmonary vascular resistance and eventually results in RV failure. LV diastolic dysfunction is frequently observed, mainly due to the change of diastolic inflow pattern and pressure gradient across the mitral valve as well as to the absence of atrial kick. Systolic LV dysfunction can also occur due to prolonged LV pressure rise time, in addition to abnormal LV filling as the atrial systole extends into early ventricular systole [22].

Mitral Regurgitation. Early on in chronic mitral regurgitation, the LA gradually dilates as some of the LV ejected blood returns to the LA. This in turn will result in a gradual increase of the LV diastolic volume. Adaptive increase in diastolic compliance is the reason behind effective maintenance of a relatively normal diastolic LV and both systolic and diastolic LA pressures until the late stage, when both chambers develop dysfunction [23, 24]. In acute mitral regurgitation, however, an early increase in both LA and LV diastolic pressures is evident. The lack of adaptive dilatation, like that seen in chronic regurgitation, will result in a significant increase in pulmonary venous pressure and acute pulmonary edema. Moreover, a marked decrease in LV stroke volume will lead to a decrease in cardiac output and tissue hypoperfusion [23].

Aortic Valve Stenosis. As a result of the increased pressure gradient across the aortic valve, both LV systolic and diastolic pressure increase. A sustained and prolonged LV ejection time is usually seen, along with concentric ventricular hypertrophy [25]. Congestive heart failure usually develops due to both systolic and diastolic dysfunction. As the hypertrophic myocardium fails to eject enough blood across the valve, an increase in diastolic volume and pressure will take place to compensate. This will further increase the diastolic dysfunction and a rapid deterioration of symptoms will then be noticed. In addition, a significant reduction in coronary artery as well as systemic arterial pressures will be manifested as angina and syncope, respectively.

Aortic Regurgitation. In chronic regurgitation, LV volume is overloaded. The end-diastolic volume increase is proportional to the regurgitant volume of blood [26]. LV compliance is initially normal but decreases later on as diastolic pressure increases; this has a deleterious effect on the pulmonary veins and capillaries and results in pulmonary congestion. On the other hand, LV systolic pressure and thickness increase to compensate for the increase in the afterload. This will eventually fail if not surgically corrected. A sudden rise of LV diastolic pressure is seen, if the aortic regurgitation is acute, as the LV does not have enough time to dilate. Therefore, acute pulmonary edema will soon occur, in addition to angina from the reduction in coronary blood flow [26].

Tricuspid Valve Stenosis. Since the tricuspid is the largest valve orifice, severe stenosis is required before a significant pressure gradient can develop across the valve [27]. Systemic venous congestion is the expected finding. Atrial fibrillation is seen more as RA pressure and volume increase.

Tricuspid Regurgitation. Chronic regurgitation results in RV volume and pressure overload. The increase of diastolic pressure cannot be effectively compensated for because of the anatomical structure of the RV. As such, signs and symptoms of RV failure usually develop faster than those of LV failure, if both ventricles are subjected to similar situations. Unlike mitral valve regurgitation, acute tricuspid regurgitation produces no significant acute hemodynamic compromise and is well tolerated in most cases [27].

Pulmonary Valve Stenosis. Pulmonary valve stenosis produces RV pressure overload, which is counteracted by myocardial hypertrophy. RV failure develops much later, as this condition is better tolerated by the RV than the increase pressure in this case of tricuspid regurgitation [27].

Pulmonary Regurgitation. Pulmonary regurgitation is rarely seen; the findings are similar to those of tricuspid valve regurgitation.

14.4.4 Cardiomyopathies

14.4.4.1 Dilated Cardiomyopathy

Dilated cardiomyopathy is not a single disease but rather the final result of various types of myocardial insults. These insults can be viral or other infectious processes, exposure to cardiotoxins such as lithium, anthracyclines, and alcohol abuse, hypertension, pregnancy, and immune-mediated myocarditis. The dilated ventricles also show some degree of hypertrophy but not proportional to the degree of dilatation [28]. Occasional transmural scars, mural thrombi, and a variable degree of increased interstitial fibrous connective tissue can be seen. Mitral and tricuspid regurgitation are frequently noticed due to annular dilatation, lack of sphincteric contraction, and malalignment of the papillary muscle. Reduced systolic function with dilatation of one or both ventricles is the criterion for recognition. Symptoms appear when cardiac output cannot be compensated for or LV filling pressure becomes high.

14.4.4.2 Hypertrophic Cardiomyopathy

Hypertrophic cardiomyopathy is an idiopathic process that affects mainly the LV myocardium, but the right ventricle may also be involved. Other causes of myocardial hypertrophy such as systemic hypertension and aortic valve stenosis must first be excluded. The hypertrophy is asymmetric in most cases but it can be concentric. This process commonly involves the whole septum but it may be localized to the subaortic region. Extension into the anterolateral wall is occasionally seen. An apical hypertrophy variation is seen mainly in Japan. Rarely, only mid-ventricular hypertrophy is seen. Extensive myocardial fiber disarray with myocardial fibrosis involving mainly the septum is the typical histopathological feature. Patients with hypertrophic cardiomyopathy often have an ischemic myocardium due to the generalized arteriolar dysfunction. Sudden death from ventricular arrhythmias is common during the first decade of their life. Those who survive develop progressive LV diastolic dysfunction. Outflow obstruction and increased residual volume with a drop in ejection fraction and stroke volume will lead to a further increase in the LV filling pressure. Increases in LA pressure and size usually result in atrial fibrillation, which further decreases the stroke volume. Mitral regurgitation is occasionally observed due to structural changes in mitral leaflets.

14.4.4.3 Restrictive Cardiomyopathy

Two types of restrictive cardiomyopathy are observed: a rare, noneosinophilic or primary restrictive cardiomyopathy, and a more common eosinophilic type. Of the eosinophilic restrictive cardiomyopathy, endomyocardial fibrosis is described in the tropical zones while Löffler's endocarditis is seen in the temperate zones. The morphological features of the eosinophilic type include myocardial hypertrophy and significant endocardial thickening with plaques of collagen-rich fibrosis that vary in size. The eosinophilic myocardium will first show areas of necrosis, that will progress to scarring with possible superimposed thrombi and finally end as thick myocardial fibrosis [28]. Typically, the venous pressure is exceedingly high due to stiffness of the ventricles that prevents dilatation in the diastolic phase of the cardiac cycle, but systolic myocardial function is well preserved until later stages of the disease. The fibrotic healing process usually starts at the apex and may obliterate the cavity at this region. As the mitral valve becomes embolized, mitral regurgitation develops that cannot be compensated for, since the LV dilatation is impaired. Therefore, an increase in LV filling pressure is usually observed. Similar changes take place in the right heart with manifestation of systemic venous congestion. The infundibulum usually dilates to compensate for the loss of volume and increased filling pressure; this results in tricuspid regurgitation and an increase in pulmonary pressure.

14.4.5 Pericardial Effusion

Pericardial effusion is considered to be present when the amount of fluid in the pericardial space exceeds 50 ml. Pericardial effusion can be associated with generalized processes not related to the pericardium, such as congestive heart failure, hypoalbuminemia, volume overload, and pulmonary hypertension. In most cases, however, it is related to a pericardial disease. The most common causes are post-myocardial infarction and uremic, neoplastic, and idiopathic pericarditis. The hemodynamic consequences of pericardial effusion depend on the rate at which the effusion is developing and the compliance of both the pericardium and the ventricles. With significant increase in the pericardial fluid pressure, the filling pressure of both ventricles may decrease, which subsequently leads to a decrease in cardiac output. This condition is called pericardial tamponade and in severe cases is associated with a high mortality. Echocardiography is an excellent tool for the diagnosis and follow-up of pericardial effusion. The condition is also invariably seen with equilibrium radionuclide angiography (ERNA); however, an effusion of

more than 400 ml is usually needed to be well recognized. The identification of pericardial effusion is important to be able to start an appropriate workup for this potentially lethal condition.

14.5 Scintigraphic Evaluation of Cardiac Function

Radionuclide techniques provide both accurate and noninvasive means of evaluating cardiac function. Their role and clinical utility over the past 20 years are well established in the initial diagnosis of patients with suspected heart disease as well as in monitoring and deciding on prognosis in patients with known heart disease.

Although most ventricular function studies are performed with the patient at rest, exercise functional studies can be also done to assess regional and global myocardial contraction changes with stress. Two distinct types of studies can be performed either at rest or under stress: in the first-pass method a bolus of radioactivity is dynamically imaged as it passes through the various vascular pathways of the heart; in the equilibrium methods the heart is imaged over several hundred heart beats after an intravascular space radioactive tracer has reached equilibrium. The cardiac information obtained by these methods is summarized in Table 14.2 [29].

In the first part of this section, the radiopharmaceuticals, imaging techniques, and methods of RNA analysis are reviewed. This is followed by a description of the common clinical applications of these types of studies.

14.5.1 Imaging Techniques and Interpretation

14.5.1.1 Equilibrium Radionuclide Angiography

Radiopharmaceuticals. Studies with radiopharmaceuticals require the use of an intravascular tracer that equilibrates within the blood pool. The ease with which ^{99m}Tc-pertechnetate can be attached to the patient's own red blood cells (RBCs) makes labeled RBCs the preferred technique over labeled pooled human serum albumin. The usual adult dose is about 30 mCi. Three methods of labeling the RBCs are commonly used: in vivo, modified in vitro, and in vitro. The characteristics of each method are described below. All three methods allow the ^{99m}Tc to bind irreversibly to the hemoglobin and remain in the intravascular space, allowing serial studies to be performed for up to 6–8 h following labeling of the RBCs [32].

Table 14.2. Information obtained by radionuclide evaluation of ventricular function

1. Global right and left ventricular ejection fraction
2. Regional right and left ventricular function
3. Absolute ventricular volumes
4. Systolic emptying and diastolic filling rates
5. Detection and quantitation of cardiac shunts

In Vivo Technique. The patient first receives stannous pyrophosphate intravenously. The stannous ion (tin) enters the RBCs and creates the optimal oxidation-reduction environment for reduction and binding of the ^{99m}Tc-pertechnetate, which is injected intravenously 15–20 min later. Once the ^{99m}Tc-pertechnetate is in the RBCs, it is trapped inside by strong binding to the beta chain of the hemoglobin. Approximately 70%–80% of the ^{99m}Tc is attached to RBCs, but in some patients as little as 50% or less may be attached. This makes identifying the edges of the blood pool during processing and analysis more difficult. In some laboratories, this method is used only when a first-pass study precedes ERNA or the patient has limited venous access. The major advantages of this method are the simplicity of use, shorter labeling time, and lower cost.

Modified In Vitro Technique. This technique is used by many laboratories because it is easier to perform than the in vitro technique and results in a higher labeling efficiency than the in vivo method. As in the previous method, stannous pyrophosphate is first injected intravenously. Blood is then drawn from the patient into an anticoagulant acetate dextrose solution (ACD) or a heparin-treated, lead-shielded syringe containing ^{99m}Tc-pertechnetate. Subsequently, the syringe is placed in a mechanical rocker or rotated slowly by the technician for 10–15 min, and the RBCs are then reinjected into the patient. Labeling efficiency is usually greater than 90%. This method offers the best compromise between ease of use and high labeling efficiency. Total labeling time averages 30 min.

In Vitro Technique. The labeling efficiency of this method approaches 100%. Patient blood is drawn and the RBCs are separated, washed with saline, and incubated first with stannous pyrophosphate and then with ^{99m}Tc-pertechnetate. The cells are washed with normal saline before and after each step to eliminate unbound material. Finally, the labeled cells are reinjected into the patient with very little or no free ^{99m}Tc-pertechnetate. The average labeling time is slightly more than 30 min. This technique also requires handling blood during multiple steps and using needles to inject blood into sealed vials.

RBCs from patients receiving heparin therapy are sometimes difficult to label and in such cases the use of ACD as an anticoagulant is preferred to increase the labeling efficiency. Inadequate anticoagulation or too ag-

gressive shaking of cells may cause thrombus formation and result in hot spots in the lungs. Likewise, stannous pyrophosphate can be oxidized by water in glucose solutions, and this may lead to poor RBC labeling.

14.5.1.2 Image Acquisition

Assessing ejection fraction and regional wall motion requires measurement of volume changes and wall motion at different intervals throughout the cardiac cycle. Acquisition of multiple timed images of the blood pool activity in the heart will then be triggered by each R-wave (Fig. 14.3). The duration of every frame may be 1–60 ms. Multiple beats are acquired to obtain adequate counts in each frame and typically a complete radionuclide ventriculographic study will consist of 200–800 summed beats for each of the three planar views [29].

A minimum of three different views of the heart are needed to assess all walls of the LV as well as all four cardiac chambers. The best septal views are left anterior oblique (LAO), anterior (ANT), which is 45° to the right from LAO, and left lateral (LLT), which is 45° to the left of LAO. Following labeling of the RBC pool, the LAO view is obtained first, as this view allows the best quantitation of the ejection fraction. In the LAO view, the camera is positioned so that the RV and LV are well separated. The other views are obtained for a similar number of counts as the LAO view. The closer the head of the camera is to the patient, the better the spatial resolution of the images. A 10° caudal tilt is used in the LAO view to minimize overlap of the left atrium (LA) and LV counts. Alternatively, a slanted hole collimator may be used to give optimal separation, while allowing the camera head to be closer to the patient on the LAO view. The general all-purpose (GAP) collimator offers a compromise between the high-resolution and high-sensitivity collimators and is the one most frequently used in clinical imaging. A dedicated computer system is required to acquire, store, and process the information.

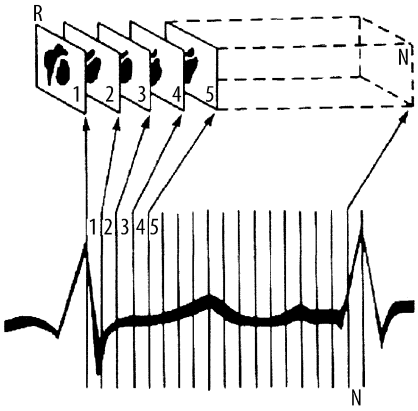

Fig. 14.3. Method by which the computer generates multiple gated images. The cardiac cycle is divided into a preselected number of frames of equal duration. Scintigraphic data from successive beats are placed into separate parts of the computer memory, depending on the temporal relation of the scintigraphic data to the R wave marker (*R*). For each frame (*1...N*), scintigraphic data from successive beats are accumulated either until a preset time is reached (e.g., 2 min for exercise scintigraphy) or until the average cardiac image contains a predetermined number of counts (e.g., 200,000 counts for typical resting studies). (Reproduced with permission from Berman D, *Clinical Nuclear Cardiology:* Saunders, Philadelphia, 1981 [33])

Studies may be acquired for a fixed number of heartbeats or for the total counts in the complete study. Fixed beat studies usually acquire 200–800 individual beats and the time of acquisition is dependent on the heart rate. Fixed-count studies usually require 6 million counts for the entire study, or they may be acquired until a fixed number of counts is reached within each image or in the LV region.

14.5.1.3 Modes of Acquisition

There are three possible modes of acquiring ERNA: list, frame, and dynamic arrhythmia filtration. Each method has its advantages and disadvantages, as described below and summarized in Table 14.3.

List Mode. During acquisition the computer records the spatial location of each photon, the ECG gating signal and rimming markers, usually every millisecond. Following acquisition, each individual beat can be reviewed to eliminate atrial or ventricular premature beats that exceed a determined R-R interval duration

Table 14.3. Comparison between the different modes of computer acquisition

Mode of acquisition	Advantages	Disadvantages
List mode	Optimal temporal resolution Excellent arrhythmia rejection	Intensive memory requirement Longer processing time
Frame mode	Easy setup Minimum memory	Count drop-off Fixed temporal resolution Poor arrhythmia rejection
Dynamic arrhythmia (buffered beat) mode	Flexible temporal resolution and arrhythmia rejection Less memory than list Accurate systole/diastole	Longer setup for greater options

(arrhythmia rejection). The acceptable beats can then be framed in the most appropriate timing interval for the type of analysis that is needed.

Frame Mode. Prior to starting frame mode acquisition, the patient's heart rate is sampled for 10 – 20 s and the mean R-R interval is used to set the time limits or window for acceptable sinus beats. For clinical studies, beats 10% shorter or longer than the mean R-R interval are rejected as possible premature beats. The beat following the early rejected beat is also rejected, as it has a prolonged filling interval and will result in a higher ejection fraction. Frame mode studies are generally acquired for 16 – 32 frames. It is extremely important that patients be in a resting state during the heart rate sampling prior to starting acquisition and throughout acquisition. Major shifts in heart rate will cause many beats to be rejected and prolong the acquisition.

Dynamic Arrhythmia Filtration. This technique allows the acquisition parameters (duration of each frame, percent R-R variability allowed for beat rejection, and total number of frames) to be set at the beginning of acquisition. Once acquisition starts, each beat is placed in a temporary memory buffer where it is examined with regard to the preset parameters. If it meets all criteria, it is accepted and included in the final data set. If it does not meet all the criteria, it is rejected. Thus, greater flexibility in beat selection is possible than with frame mode, but without the memory requirements and longer processing time required by list mode acquisition.

Regardless of the method of acquisition used, it is important to confirm that only the R wave from the ECG signal is detected as the trigger signal and as appropriately gating the acquisition. This can be done by examining an ECG rhythm strip and identifying the triggering signal. Gating may sometimes occur incorrectly on the P, T, or R' wave signal as well as muscle artifact and pacing spikes from artificial pacemakers. If this occurs, the lead placement needs to be changed or the voltage amplitude adjusted to avoid inappropriate gating [33].

Simple LV ejection fraction calculations usually require time intervals of 40 – 50 ms to adequately define the end-systolic point in the heart cycle, where the heart has the smallest volume. For analysis of diastolic function, timing intervals of 10 – 20 ms give the most reliable information for the ventricular filling portion of the heart cycle. Even with list mode and dynamic arrhythmia filtration, there is still slight R-R interval variability that can lower the counts and distort the last few frames of the time-activity curve. This count drop-off does not affect ejection fraction calculation but is deleterious for diastolic function analysis. This limitation can be overcome by generating separate forward and backward time-activity curves and combining them in a final curve for analysis.

Patients in atrial fibrillation have variable diastolic filling intervals and this results in a different ejection fraction for each beat. LV ejection fraction measurement by ERNA during atrial fibrillation has been shown to be an accurate reflection of the summed ejection fraction of each of the individual bats. Thus, it is an accurate reflection of overall ventricular systolic function [29]. Contrast ventriculography and echocardiography will sample only a few beats for ejection fraction calculation and may be less representative of true function.

14.5.1.4 Image Processing

Because of the random nature of radionuclide disintegration, nuclear medicine images are subject to statistical variation. Filtering is used to remove these statistical fluctuations by modifying (smoothing) the data points. Smoothing can be accomplished by spatial (within each frame) or temporal (between frames) filtering. Spatia1 filtering corrects each pixel by using information from surrounding pixels within the same image, while temporal filtering uses pixel information from the preceding and subsequent images.

Identification of the edges of the ventricles is the next step. This can be done manually or using one of several edge-detection computer algorithms provided in most commercially available nuclear cardiology computer systems. When using these automated edge-detection programs, it is important to visually review each frame for accurate definition of edges.

Appropriate background subtraction must be also performed to obtain an accurate estimation of chamber volumes. A time-activity curve of the LV volume at each frame or time point in the cardiac cycle is next generated. This approximates the changes in ventricular volume over time, from which LV ejection fraction can be easily calculated [32].

14.5.1.5 Image Analysis

Assessment of each heart chamber can be performed using an endless-loop cine display in which the beating heart is observed in at least three projections to adequately view all regions. The most commonly used views are the LAO, ANT, and LLT. A complete evaluation should focus on the four heart chambers and include assessment of the size, global contraction, and regional function of each chamber. In addition, all parts of the great vessels, lungs, liver, and spleen that are included in the field of view should be reviewed for abnormalities. Although ventricular and atrial size are

usually assessed visually, more accurate measurements can be obtained by placing lead shielding or radioactive ^{57}Co markers of known dimensions in the field of view and comparing the size of the heart with these standards [29].

14.5.1.6 Qualitative Assessment

Right Atrium. The right atrium (RA) is best seen in the ANT or RAO views (Fig. 14.4). It also can be seen in the LAO view. The tricuspid valve plane appears as a photopenic area between the atria and ventricles that moves downward and to the left during contraction. In older patients a photopenic region may be seen superior to the valve plane; this represents a thrombosed, calcified atrial appendage and may attenuate the blood pool radioactivity. Movement of the lateral RA wall toward the RV is better appreciated than the movement of the rest of the RA. The atrium may appear enlarged in the absence of anatomical enlargement in patients who have had cardiac surgery, where it becomes adherent to the lung serosa, or in patients who are in a nonsinus rhythm. True anatomical RA enlargement is more likely and of greater clinical significance in the presence of RV enlargement.

Right Ventricle. The right ventricle is normally best seen in the ANT and LAO views (Fig. 14.4). Usually the apex and lateral and inferior walls can be seen and assessed for regional wall motion abnormalities. On the LAO view, the lateral RV walls may appear to have decreased contractility. This is due, in part, to the fact that as the RV contracts and empties, the RA is filling with

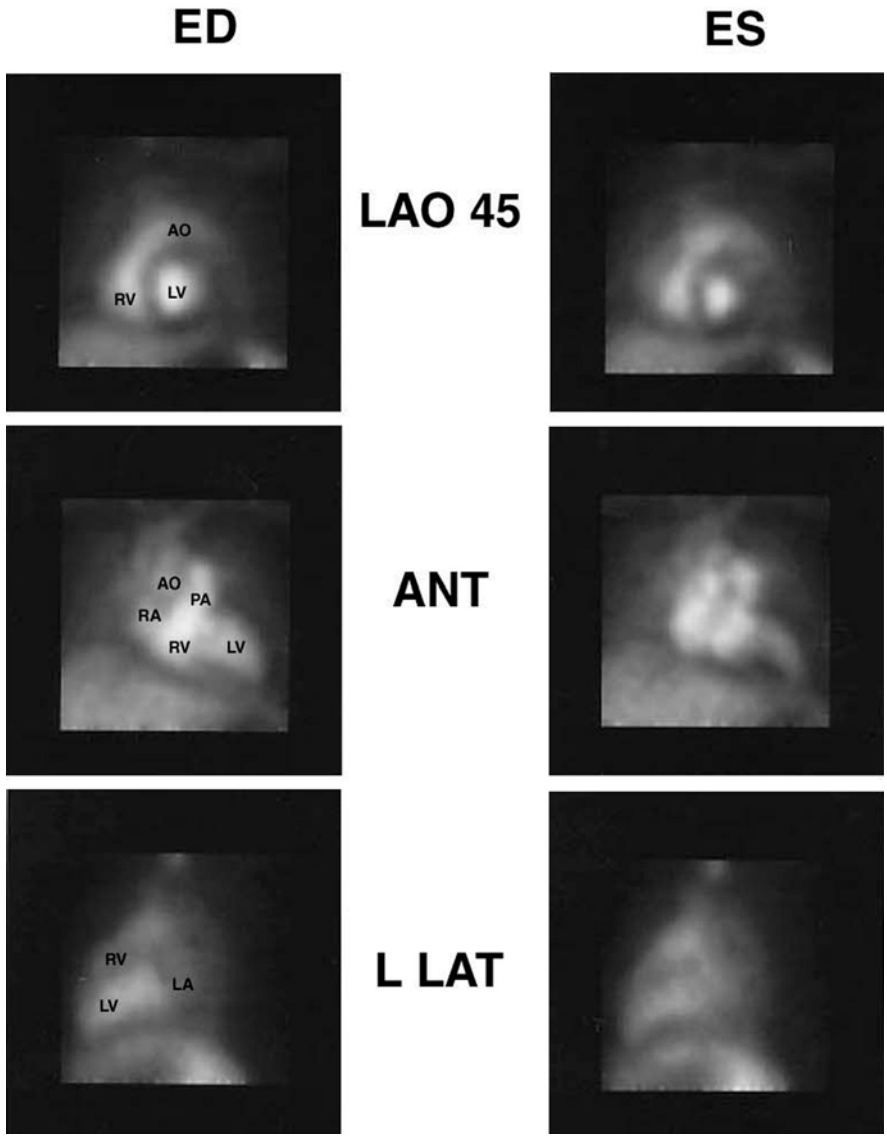

Fig. 14.4. Example of a normal gated blood pool study. The pictures on the *left* represent end-diastolic (ED) frames, while the images on the *right* represent end-systolic (ES) frames. The main structures are identified in each projection: *AO* aorta, *RV* right ventricle, *LV* left ventricle, *RA* right atrium, *PA* pulmonary artery, *LA* left atrium. (Courtesy of Professor A.H. Elgazzar)

blood and "fills in" the lateral wall area. If the RV is visualized in the LLT view, it implies RV dilatation or clockwise rotation of the heart. The pulmonary artery is anterior to the aortic root. It can be clearly seen in all individuals and is especially prominent in patients with pulmonary hypertension.

Left Atrium. The LA is best defined in the LLT or left posterior oblique views (Fig. 14.4). It also can be seen superior to the LV at end-systole in the LAO view in patients with vertical hearts. In patients with horizontal hearts, such an appearance should raise concerns about true anatomical enlargement.

Left Ventricle. The LV is clearly seen on all three views and is normally smaller than the RV in the LAO view (Fig. 14.4). In general, patients with normal global and regional LV contractility will have normal chamber size and volumes. Patients with cardiac enlargement and normal ejection fraction include those with valvular heart disease, especially aortic and mitral regurgitation, and some with high-output heart failure. In such patients, the apex may become hypokinetic in the absence of muscle damage, due to altered contractility and volume loading.

All three views need to be examined visually, and a subjective determination of global LV ejection fraction should be made. Although this measurement is more accurate and reliable by quantitative means, errors in quantitative measurement are possible due to technical limitations. If there is a major discrepancy between the visually assessed and calculated values, the quantitative technique needs to be carefully inspected for possible technical problems.

Assessment of regional wall motion is performed by dividing the LV walls into segments and commenting about the contractility of each segment. Abnormal wall motion in any particular segment can be linked to a disease in the blood-supplying coronary artery. Patients with prior cardiac surgery, bundle branch block, or RV dilatation may have paradoxical septal motion in the absence of reduced coronary blood flow.

LV aneurysm can be accurately identified by this technique (Fig. 14.5). An aneurysm is classically shown as an akinetic or dyskinetic segment with contour deformity, both in systolic and diastolic frames, and normal contraction of the adjacent myocardium. An indentation in an aneurysm or in an area of dyskinesis is highly suspicious for the presence of a thrombus. However, an indentation in a normally moving wall, especially the lateral and inferior walls, is often caused by the attachment of normal or hypertrophic papillary muscles.

A localized photopenic or low-count region surrounding the heart may also be seen in some patients. The differential diagnosis includes myocardial hypertrophy, pericardial effusion, or a prominent fat pad. Of these possibilities, the most common is myocardial hypertrophy due to systemic hypertension or valvular heart disease. Hypertrophy should include enlargement of the septum on the LAO view as well as a prominent "halo" surrounding the entire anterior wall and apex on the ANT view. Large pericardial effusions in the absence of clinical symptoms or suspicion are rare. ERNA is not a sensitive technique for detection of pericardial effusions and only effusions greater than 400 ml are consistently identified. The septum appears to be of normal thickness in patients with effusions as well as in those with a prominent epicardial fat pad, and this is one way to differentiate these two conditions from true ventricular hypertrophy [33].

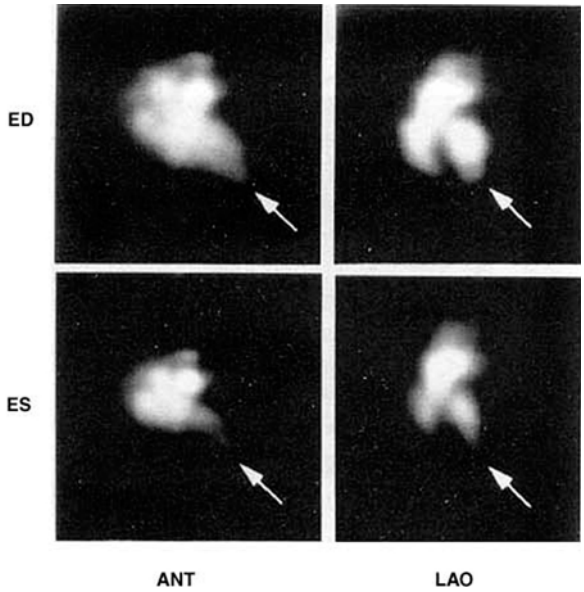

Fig. 14.5. Radionuclide ventriculographic images of a patient with an apical and distal anterior wall aneurysm following myocardial infarction (*arrow*). Note the deformity of the left ventricular apex at end-diastole and end-systole on the LAO view. Despite the normal movement of the rest of the left ventricular walls, ejection fraction was depressed because of the large akinetic aneurysm. *ANT* anterior, *LAO* left anterior oblique, *ED* end-diastole, *ES* end-systole. (From Manuel D. Cerqueira (ed) *Nuclear Cardiology*: Blackwell Scientific Publications, 1999, by permission)

Noncardiac Structures. Extracardiac vascular structures normally visualized include the great vessels, lungs, liver, spleen, and stomach. Focal dilatation of the aorta signifying an aneurysm can be seen in the ascending aortic arch and descending portions. These should be carefully looked for in patients with long-standing hypertension. When lung blood pool activity is increased, particularly in the upper lung zone, it usually indicates LV dysfunction. Pleural effusions and lung masses (tumor, infection with consolidation, or

infarction) may also appear as photopenic areas in the lung fields.

The liver and spleen are also seen in the field of view as highly vascular structures. Focal defects in areas of normal blood pool may be caused by metastasis, cysts, infection, or infarction. The stomach appears as a photopenic region medial to the spleen, except when free pertechnetate has been injected. It then appears as an area of increased radioactive uptake. A hiatal hernia can sometimes be diagnosed by ERNA. In such cases the stomach is seen as a photopenic area near and superior to the LV. This finding is suspicious but not totally diagnostic for a large hiatal hernia.

14.5.1.7 Quantitative Evaluation

Ejection Fraction Calculations. Radioactive counts detected in a ventricle are proportional to its volume. Thus, by measuring counts at end-diastole and end-systole, one can calculate the stroke volume and accurately measure ejection fraction for the RV or LV. To measure LV ejection fraction, calculations are routinely performed on the best septal-view LAO projection, because this provides the best separation of the RV and LV blood pools (Fig. 14.6). In addition, in this view most counts from the LA, which is at least 10 – 15 cm from the gamma camera crystal, are attenuated before reaching the detector. Thus, LV counts or volume in the LV alone can be measured for each frame or time point in the cardiac cycle [29]. Since the LV wall is approximately 1 cm thick, it produces a photopenic region surrounding the LV that allows excellent detection of the ventricular blood pool edge. Thus, LV ejection fraction calculation by this method is easy, reproducible, and accurate.

Poor edge detection of the cavity may result from high background activity due to poor RBC labeling, abnormally increased soft tissue attenuation due to obesity or large breasts in women, and patient movement during acquisition. Heart rotation in a vertical, horizontal, clockwise, or counterclockwise direction requires modifications of the detector angle to adequately separate the RV and LV blood pools. LA enlargement may add considerable counts to the LV region of interest at end-systole, resulting in underestimation of the ejection fraction [34].

If problems develop with ECG gating during acquisition, the heart may appear globally akinetic in the cine movie. This can be distinguished from biventricular dysfunction by the fact that both atria will be akinetic in the former but not in the latter condition. Photon-attenuating artifacts such as metallic electrode leads on the chest wall and automatic implanted cardiac defibrillator (AICD) pads may affect ejection fraction calculation. Breast implants may also cause attenuation artifacts in part of or the whole image. Inappropriate image manipulation including filtering and background subtraction can also influence the accuracy of the ejection fraction calculation [29].

Phase Analysis. Phase analysis is a process whereby each pixel in the heart is evaluated with respect to count

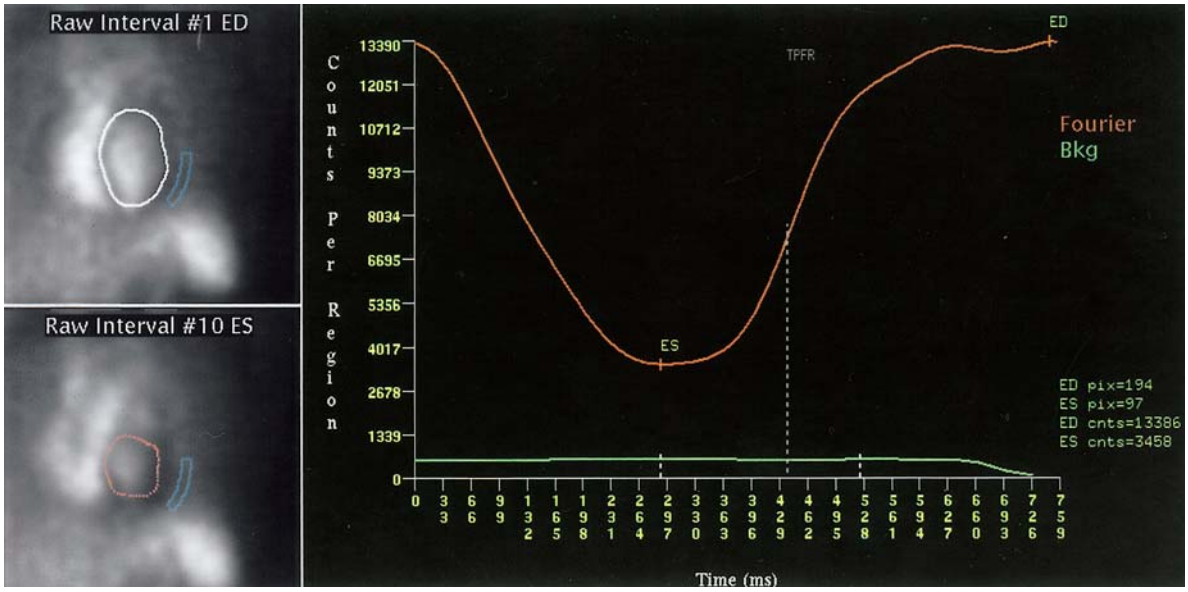

Fig. 14.6. Ejection fraction calculation of an LAO radionuclide ventriculogram. Shown are left ventricular edges as determined by an automated computer algorithm for end-diastole (*top left*) and end-systole (*bottom left*), chosen area for background subtraction, volume curve (*right*) and ejection fraction (60%) of the left ventricle. Specific information on heart rate and time/frame is also provided. (Courtesy of Professor A.H. Elgazzar)

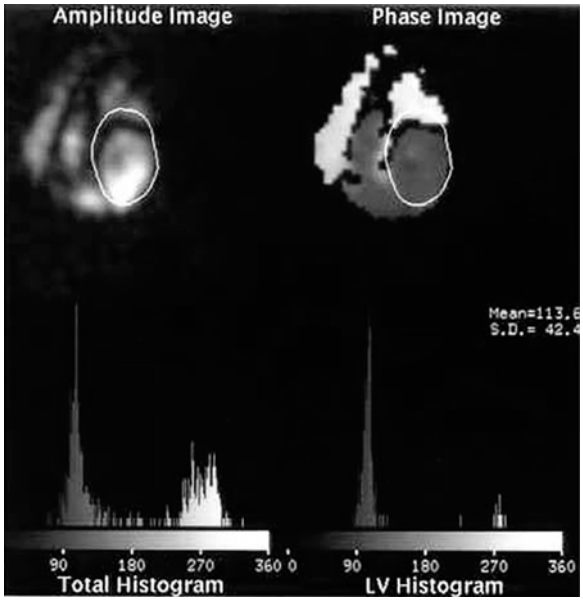

Fig. 14.7. Example of amplitude and phase images. Note the normal pattern of activity in the amplitude image and the uniform activity in the ventricles on the phase image. (Courtesy of Professor A.H. Elgazzar)

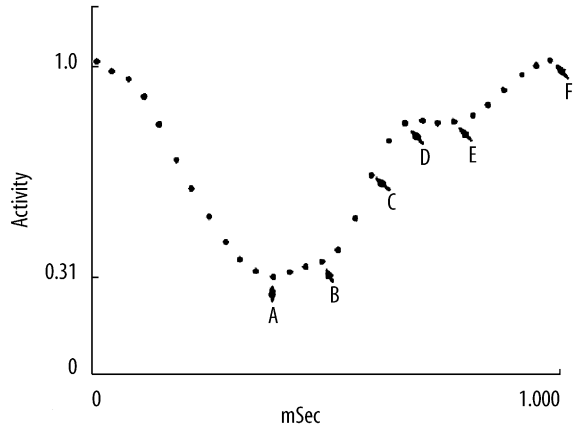

Fig. 14.8. Smoothed raw data of activity (*y* axis) plotted against time in milliseconds (*x* axis) to show important points on filling curve: *A* onset of filling, *B* end of isovolumic period, *C* point of peak filling rate, *D* end of rapid filling phase, *E* end of slow filling phase, *F* end of atrial filling phase. (Reproduced by permission from Sinak U, Clements IP (1989) Influence of age and sex on left ventricular filling at rest in subjects without clinical cardiac disease. *Am J Cardiol* 1989:646–650)

changes over time and a computer-generated image is produced (Fig. 14.7). The phase image readily identifies abnormal timing of ventricular contraction. The atria and ventricles contract at different times, approximately 180° apart. Areas of ventricular dyskinesis are closer in phase to atrial contraction, and will therefore be assigned a color similar to the atria. Areas of akinesis also demonstrate no change and also appear black. Asynchronous contraction in the RV or LV is usually caused by conduction abnormalities, such as bundle branch block and Wolf-Parkinson-White syndrome, or by mechanical abnormalities, such as pulmonary valve stenosis, RV pressure or volume overloading [34].

Amplitude Analysis. Amplitude analysis is a process whereby each pixel in the heart is evaluated with respect to movement changes over time and a computer-generated image of the movement is produced (Fig. 14.6). The amplitude image shows the magnitude of blood ejected from each pixel within the ventricular chamber. Areas of hypokinesis or akinesis display lower values than normal contracting regions. These images are generally less sensitive than visual analysis in detecting regional dysfunction, as errors can be introduced due to heart or patient motion [34].

Diastolic Function Evaluation. Diastole of the ventricles is an energy-dependent process that has four distinct phases: isovolumic relaxation, rapid early filling, diastasis, and atrial filling. All four phases can be recognized and measured on the LV time-activity curve generated from ERNA (Fig. 14.8). Because abnormalities in diastolic function may be present before a detectable decrease in systolic function is seen, measurement of diastolic variables may be potentially more sensitive for detection of heart pathology [32].

The type of diastolic and systolic quantitative information generated from the ERNA time-activity curve consists of peak rates and the time at which these peak rates occur. Conventionally, these rates are normalized to the volume or counts present at end-diastole and expressed as end-diastolic volumes/s (EDV/s). The peak filling rate (PFR), which represents the early and most rapid ventricular rate, has been found to be the most clinically useful measure, and normal values range between 2.4 and 3.5 EDV/s. The time to the PFR should be less than 180 ms (this is the time from end-systole until the peak filling rate is achieved). Ideally, filling rates as measures of diastolic function would be altered in a predictable manner only by the presence of ischemia, myocardial damage, or some other pathological process such as aortic stenosis or regurgitation, or restrictive, hypertrophic, or congestive cardiomyopathies [29]. Unfortunately, heart rate, medications, age, and loading conditions cause changes in filling rates that may be greater than the changes caused by cardiac pathology, and accurate interpretation of diastolic evaluation must take these values into account [34]. Compared with other methods, ERNA offers a rapid and accurate assessment of diastolic function by obtaining information from 200–800 beats and assessing the entire ventricle, rather than a limited number of slices.

Echocardiography and contrast ventriculography are the alternative methods for obtaining diastolic

function information. Contrast ventriculographic evaluation with frame-by-frame digitizing of the ventricular contour throughout a single beat is time consuming and may not be truly representative of general ventricular function. M-mode echocardiographic measurement by digitizing the endocardial contours has similar limitations. The use of Doppler echocardiography to measure flow across the mitral valve overcomes many of these limitations and is the most commonly used measurement of diastolic function. Its only limitation is that the sampling region must be directly below the mitral annulus and the smallest angle between the cursor and the assumed blood row direction obtained. Failure to do so will result in inaccurate information.

14.5.2 Exercise Radionuclide Angiography

Exercise radionuclide angiography is performed during supine or upright bicycle exercise. Bicycle exercise is necessary because treadmill exercise causes movement of the chest, and this does not allow acquisition of movement-free images for analysis. In the supine or upright bicycle position, the patient's chest is placed against the camera in the best septal-separation LAO view and the camera and patient are strapped together to further minimize movement during acquisition [32]. The patient is prepared for blood pressure and continuous ECG monitoring. Two or three ERNA are acquired in the resting state. Exercise is started at a workload of 25 W (150 kpm/min) and increased by 25 W at the end of each 3- or 4-min exercise stage. After the first minute of exercise, image acquisition is started and it continues for 2 or 3 min until the start of the next stage. As in treadmill ECG testing, exercise is terminated by symptom-limiting fatigue, angina, dyspnea, or observed life-threatening signs such as arrhythmia, hypotension, or marked ST segment depression. Slow bicycle pedaling against no load will help prevent post-exercise hypotension and leg cramps. At the end of exercise, two or three studies are obtained to document recovery of function [29].

Images are processed and ejection fraction is calculated using the same technique as rest ERNA. Serial ejection fraction is calculated for rest, each stage of exercise, and recovery. Visual assessment for both segmental wall motion and global function and size of the LV is an essential part of this examination.

14.5.3 First-Pass Radionuclide Angiography

Examination of the initial transit of a radionuclide bolus through the different major vascular compartments can provide information about the function of each chamber. This is probably the most accurate method of calculating RV ejection fraction and it is excellent for calculating LV ejection fraction as well. Optimal performance is achieved using a high-count-rate gamma camera interfaced to a high-speed computer. Multicrystal gamma camera systems offer the highest count rate capabilities but are not widely available [32]. Newer single-crystal systems with the ability to handle high count rates are now available in many nuclear medicine departments and can be used instead to perform these types of studies. First-pass techniques are more technically demanding than ERNA, and attention must be paid to all aspects of bolus injection, acquisition, and processing.

The preferred radiopharmaceutical for rapid bolus injection is any ^{99m}Tc compound in a volume less than 1 ml and a dose of 15 – 30 mCi. Good-quality studies require that the radioactivity remain as a compact bolus to avoid overlapping of chambers' radioactivity at any given time. If serial studies are essential, for example, at rest and following peak exercise, the initial resting study is done using an agent cleared rapidly by the kidneys (^{99m}Tc-DTPA or glucoheptonate) or liver (^{99m}Tc-sulfur colloid). The second study at peak exercise can then be performed using ^{99m}Tc-pertechnetate, which will allow in vivo labeling of the RBC pool and acquisition of ERNA views for assessment of regional wall motion during recovery [35].

Immediately following the bolus injection, 25 – 100 frames/s are acquired in the ANT or 30° RAO position. With newer multihead cameras, two or more projection images of the chest can be assessed simultaneously. The transit of the bolus can be evaluated either by ECG gating or continuous dynamic cine display. Using the gated first-pass technique, four to five individual beats can be summed to increase the number of counts in each frame; this provides better definition of valve planes and the lateral contours of the ventricle, which must be defined for ejection fraction calculation. Unlike equilibrium studies, cardiac chambers, especially the atria, can be studied individually with minimal interference from background or overlapping chambers. Because ERNA studies have difficulty in separating the RV from the RA due to overlap, the first-pass technique is considered the method of choice for accurate RV evaluation. Moreover, it is the only radionuclide method for detection and quantitation of left-to-right cardiac shunts [29].

14.5.4 Nuclear Probe and VEST

Nuclear probe and VEST are two systems that can be used in the acute care setting. The nuclear probe is a portable nonimaging device that allows calculation of beat-to-beat ejection fraction, as well as diastolic function assessment that is comparable in accuracy to ER-

NA. It consists of a small sensitive radiation detector, a single-bore collimator, and a microprocessor. A major advantage of this probe is that it allows continuous cardiac function monitoring in the coronary care unit and for high-risk patients undergoing surgery or procedures that may affect cardiac function. Nonetheless, simultaneous visual examination of all cardiac chambers cannot be obtained [32].

The VEST is a similar nonimaging detector that can be attached to the patient's chest over the heart and provides continuous beat-to-beat ejection fraction and ECG information that is recorded on a tape recording system similar to that used for Holter monitoring. Patients can ambulate and perform normal activities while their ejection fraction is being recorded. At a later time the tape is scanned, and the ejection fraction changes associated with symptoms, ECG changes, and activity level can be observed. Newer VEST systems provide immediate, on-line ejection fraction measurements that allow identification of acute changes, and this makes possible the initiation of immediate treatment [29].

14.5.5 SPECT Gated Equilibrium Radionuclide Angiography

In recent years, there has been growing interest in acquiring ERNA studies using single photon emission computed tomography (SPECT) technique rather than the planar one. This has been largely facilitated by the rapid advancement in the computer technology, particularly in the disk space required to store the large amount of data and the time required for data processing.

The advantages of this technique over the usual planar method include the ability to visualize each cardiac chamber without counts contamination from adjacent structures. Regional wall motion can be also viewed in any projection. Additionally, the need for customizing the camera position to obtain the various planar views is overcome as patient has to be positioned once in the SPECT technique. Unlike planar ERNA studies, accurate computation of RVEF may be possible with SPECT ERNA due to the removal of chamber overlap and the 3D nature of SPECT. Finally, ERNA SPECT can be performed in approximately half the time used to acquire a 3-view planar ERNA series.

On the other hand, counts are manipulated during the tomographic image reconstruction. Thus, the basic relationship between the LV counts and volume on planar ERNA is altered in the SPECT one. Consequently, many investigators used geometric assumptions to calculate the number of voxels in the cardiac chambers in order to estimate EF [36].

Acquisition and Processing. The images can be acquired with any SPECT gamma camera, preferably a 90 degree dual head one. Sixty-four projections (32 per head) over a 180-degree rotation (RAO to LPO) at approximately 30 s per view are usually used. Cardiac cycles are preferably sampled by 16 frames/cycle. A 64 by 64 matrix size of 16-bit word pixels is employed with a zoom that results in a pixel size of about 4 – 5 mm/pixel. It is critical that the entire cardiac blood pool be in the field of view in all projections.

In processing SPECT gated ERNA images are first reconstructed usually by filtered back projection followed by applying standard image filters. Subsequently, each of the 16 gated frames transverse reconstructions is reoriented in short axis oblique slices, long axis coronal and long axis sagittal slices. EF can be calculated by a count based method with end diastolic and end systolic ROI drawn over slices and summed to include the entire chamber. Alternatively, a geometric based method may be used to compute total number of voxels in a chamber. Voxel volume and hence chamber volume can then be calculated. Subsequently, EF is estimated from end diastolic and end systolic volumes. LVEF obtained from SPECT ERNA is likely to be higher than LVEF values determined from planar ERNA method due to the elimination of left atrium activity. Preliminary results indicate that SPECT gated ERNA LVEF is about 7% – 10% higher than planar studies. Caution, therefore, is needed when comparing an LVEF value obtained with SPECT gated ERNA to a prior LVEF performed with planar technique particularly during chemotherapy cardio toxicity evaluation [37]. RVEF methods to date have not been validated. One report found that SPECT gated ERNA significantly overestimated both RVEF and RV volumes [38].

14.6 Clinical Applications

Nuclear medicine techniques are accurate and reproducible for cardiac function evaluation. They provide much important information that is useful in the diagnosis and management of the following clinical situations.

14.6.1 Assessment and Prognosis of Congestive Heart Failure

In many patients, the severity of global ejection fraction impairment can be suggested on the basis of clinical and physical examination findings. In some, however, it is not always easy to separate right from left heart failure or the existence of both. Thus, the accuracy and reproducibility of serial measurements by ERNA are valuable and offer several advantages over other investigations, both for the initial workup and for the follow-up of these patients. This monitoring is especially im-

portant in patients with moderate to severe decrease in ventricular function. Such patients are less able to compensate for alterations in preload, afterload, or contractility state.

In general, LV dysfunction with regional wall motion abnormalities, especially in the presence of normal RV function, is most consistent with an ischemic cardiomyopathy [33]. Such patients may benefit from antianginal therapy or evaluation for the presence of hibernating myocardium. Further evaluation with coronary arteriography, positron emission tomography, or thallium-201 perfusion imaging may be indicated in these patients. Nonetheless, the etiology can be difficult to determine in patients with long-standing LV failure, and the coexistence of pulmonary hypertension with RV failure or RV infarction. Patients with severe biventricular enlargement and global dysfunction are less likely to have an ischemic etiology, and inflammation caused by viruses, exposure to cardiotoxins such as alcohol and Adriamycin, or valvular disease should be considered.

ERNA is useful to differentiate between RV and LV heart failure. It is surprising how often clinical factors and physical examination findings do not allow a clear differentiation. Older patients with a history of smoking have an increased risk of both pulmonary and heart disease. Orthopnea, paroxysmal nocturnal dyspnea, pedal edema, rales, and neck vein distention can be seen in both. ERNA allows visual and quantitative assessment of both ventricles and technically optimal studies can be performed in nearly all patients [29]. Technically adequate echocardiographic studies are not always obtainable in patients with lung disease.

Diastolic function assessment can be important in the management of these patients. In general, patients will have heart failure symptoms due to systolic dysfunction. However, patients with acute myocardial infarction and normal systolic function can have severe congestive heart failure (CHF) due to impaired ventricular filling. Diminished early rapid ventricular filling has a greater impact on producing failure symptoms. In patients who already have a reduced ejection fraction, the consequences of these diastolic abnormalities are even greater [39].

Finally, with the accurate functional information obtained from ERNA, particularly LV ejection fraction, more precise prognostic information about CHF patients is provided. Such information is also valuable for monitoring these patients under the different management plans now available.

14.6.2 Monitoring Drug Therapy and Exposure to Cardiotoxins

Injury to myocytes for any reason results in myocardial fibrosis, which impairs ventricular relaxation and decreases peak filling rate and ejection fraction. Such damage may be due to ischemic infarction, toxins such as alcohol or chemotherapeutic drugs such as Adriamycin, or inflammation.

14.6.2.1 Cardiotoxin Monitoring

Early in the clinical use of Adriamycin, some patients receiving treatment developed a transient cardiomyopathy. Adriamycin also has a direct, dose-dependent cardiotoxicity that is progressive and sometimes fatal. This is seen particularly in patients with prior radiation therapy, concurrent cyclophosphamide treatment, and older age. The individual variation in susceptibility and preexisting cardiac function made the exact prediction of this serious adverse reaction after a certain given dose difficult. Several series showed that doses higher than 1000 mg/m^2 in certain groups of patients did not increase the incidence of cardiomyopathy while toxicity developed in some patients at 300 mg/m^2. Serial monitoring of ventricular function with resting ERNA was shown to be an accurate way of detecting early evidence of cardiotoxicity and allowed changes in therapy to prevent progression, and in some cases to reverse the toxicity [40]. Endomyocardial biopsy is another accurate but expensive and invasive alternative for monitoring toxicity [41].

For Adriamycin monitoring, a baseline study should be obtained prior to treatment to exclude clinically unsuspected heart disease. Patients with LV ejection fraction less than 30% are at extremely high risk for toxicity and should probably not be started on Adriamycin. Patients with ejection fraction between 30% and 50% should have sequential studies before each dose. In these patients, an absolute decrease of ejection fraction greater than 10% and/or a follow-up ejection fraction less than 30% should be regarded as cardiotoxicity, and no further Adriamycin should be given. With a baseline ejection fraction of greater than 50%, a repeat study is recommended when the cumulative Adriamycin dose exceeds 300 mg/m^2, and before each subsequent dose when the cumulative dose exceeds 450 mg/m^2. If there is a decrease in ejection fraction of less than 10%, but the measured value remains more than 45%, this is considered mild toxicity and therapy can be continued. Moderate toxicity is indicated by a more than 15% decrease or a final ejection fraction less than 45%, and Adriamycin should be stopped. Repeat studies showing an improvement in ejection fraction may allow therapy to be restarted in these patients [29].

A limited number of reports has shown that exercise ERNA and diastolic function evaluation are very sensitive in early detection of myocardial damage. Nonetheless, both exercise and diastolic function evaluation are not widely used clinically to date.

14.6.2.2 Other Types of Monitoring

ERNA can be used successfully to monitor treatment for coronary artery disease, chronic CHF, and arrhythmias. Thus, monitoring aggressive treatment of CHF or the use of certain antiarrhythmic drugs with negative inotropic effects has clinical value.

14.6.3 Diagnosis of Coronary Artery Disease

Patients with high-grade stenosis or multivessel coronary artery disease may have normal global and regional function at rest, and it is only because of the increased oxygen demands imposed by maximal exercise or pharmacological stress that these functional parameters become abnormal. Patients with prior myocardial infarction will have regional wall motion abnormalities when studies are performed at rest. Exercise studies may be performed using the first-pass method or by exercise and rest ERNA.

14.6.3.1 Exercise Radionuclide Angiography

Several parameters can be measured from these studies: resting and maximal exercise ejection fraction, the absolute difference in ejection fraction between rest and maximal exercise, the development of regional wall motion abnormalities, and end-systolic and end-diastolic ventricular volumes at peak exercise [42]. All of these parameters have been proven to be valuable, both for diagnostic accuracy and for prognosis. The criteria for an abnormal test are summarized in Table 14.4.

At rest, the LV ejection fraction in a patient without prior infarction should be 50% or higher, and at maxima1 exercise there should be an absolute increase in ejection fraction of at least 5%. A drop or failure to augment ejection fraction by 5% is considered an abnormal response. This has a sensitivity of 85% – 95% and a specificity of 75% – 85% for diagnosis of CAD. The lower specificity is attributed to certain types of patients with no ischemic heart disease who may have an abnormal exercise response in the absence of coronary artery disease. Patients with a high normal ejection fraction, greater than 75%, and patients over the age of 60 may not increase their LV ejection fraction normally with stress in the absence of coronary artery disease [42]. It has also been shown that patients with valvular heart disease or a nonischemic cardiomyopathy may fail to show an appropriate augmentation in ejection fraction with exercise. Other conditions that may result in a false-positive study include mitral valve prolapse, hypertension, left bundle branch block, syndrome X (angina with normal coronaries), and severe anxiety.

Table 14.4. Criteria for abnormal exercise radionuclide angiography

1. Inappropriate ejection fraction response to exercise
   Decrease from baseline
   No change from baseline
   Failure to increase ejection fraction by at least 5%
2. Development of new segmental wall motion abnormalities
3. Transient increase in pulmonary blood pool activity
4. Transient left ventricular cavity dilatation

The development of new regional wall motion abnormalities at peak exercise is highly specific for coronary disease, but it is not very sensitive. The number and location of segments with abnormal movement reflect the extent and location of ischemia, while the degree of functional abnormalities, time of their start, and disappearance reflect the severity of the coronary disease. The apex and inferior wall are difficult to evaluate in the LAO projection. Therefore, an additional ANT view after exercise or a simultaneous LPO view with a dual-head camera are recommended for complete evaluation.

If the ischemia is sufficiently severe, diastolic change may be detected at rest. Abnormalities may also be provoked by exercise and detected as a decreased filling rate for the entire ventricle or for a particular coronary distribution myocardium using regional diastolic analysis. These diastolic changes may be present even when systolic function is completely normal. A decrease in early ventricular filling associated with increasing age is not related to the development of coronary artery disease, but rather to myocardial fibrosis, and there is greater dependence on the atrial component to diastolic filling. Improvements in global and regional diastolic function have been observed in patients with successful percutaneous transluminal coronary angioplasty or coronary artery bypass grafting. This suggests that ischemia was relieved. Diastolic evaluation may also have applications in the assessment of hibernating myocardium.

14.6.3.2 First-Pass Radionuclide Angiography

This is an alternative method to the previously described exercise ERNA. This method also allows evaluation of RV function with exercise. Two separate studies are performed at rest and peak exercise. As mentioned previously, an initial bolus injection using a radiopharmaceutical that is cleared by the kidney or liver is administered at rest. A second bolus is given at peak exercise using a different radiopharmaceutical. ^{99m}Tc-pertechnetate is usually chosen for this second bolus if a traditional radionuclide ventriculogram will follow, because this agent can be used for in vivo labeling of the

RBCs. Another radiopharmaceutical that is more often used now clinically for this study is ^{99m}Tc-sestamibi, which is a myocardial perfusion tracer. A first pass using this agent during stress will help to obtain both functional and perfusion information of the myocardium at stress. If perfusion images, which are usually obtained around 1 h from stress, are performed as gated SPECT images, then a rest functional evaluation will be also provided, all with one radiotracer injection [43].

14.6.4 Assessment and Prognosis of Myocardial Infarction

ERNA has an important role in evaluating patients with myocardial infarction during the acute phase and for long-term follow-up.

14.6.4.1 Acute-Phase Assessment

The development of regional wall motion abnormalities is a manifestation of ischemia or infarction that precedes ECG changes and is a specific but not a very sensitive method. Thus, the presence of hypokinesis by ERNA in a patient with chest pain is consistent and specific for ischemia even in the absence of ECG changes. Although the presence of normal segmental wall motion argues against a large area of ischemia, the intermittent nature of ischemia or the involvement of a small area beyond the resolution limits of the technique can account for the low sensitivity. Preexisting dysfunction, especially in patients with prior myocardial infarction, may confuse the interpretation unless previous ERNA or other functional studies are available for comparison [32].

In general, patients with myocardial infarctions show decreased global LV function that is directly related to the size of infarction [30]. Additionally, in patients with CAD, the degree of resting LV cavity dilatation reflects mainly the extent of infarcted tissue and is closely related to the resting LV ejection fraction [31]. It has been shown that ejection fraction measured during the first 24 h following infraction is the best predictor of in-hospital mortality. Patients with an ejection fraction less than 30% have the highest mortality secondary to cardiac failure and arrhythmias. On the other hand, patients with normal or only mildly reduced ejection fraction have a much lower incidence of complications.

Evaluation may also assist in the diagnosis and management of a unique group of patients with infarctions. RV infarction, infrequently associated with RV failure, requires distinctive management to prevent the associated low cardiac output status. ERNA can help to confirm the diagnosis by showing both the abnormal regional wall motion and the exact RV ejection fraction.

14.6.4.2 Late-Phase Assessment

In patients who have suffered an acute myocardial infarction, the lower the ejection fraction at the time of discharge from the hospital, the shorter the long-term survival. This has been clearly documented using radionuclide and contrast measurements of ejection fraction and is true in the pre- and post-thrombolytic era. Thus, patients with an ejection fraction of 30% or less may benefit from more aggressive techniques such as coronary arteriography, especially if there is recurrence of chest pain or early congestive heart failure. Identification of these high-risk patients and treatment started early while they are asymptomatic, as well as frequent follow-up of their ventricular function, offer the best chance for survival [29].

Visual interpretation of the ERNA can help identify several post-infarction complications, notably ventricular aneurysms. ERNA can help to differentiate between true aneurysms and pseudoaneurysms. True aneurysms, which result from thinning and bulging of scar tissue, have a wide neck and dyskinetic or akinetic wall motion. When the aneurysm is large enough to reduce ejection fraction significantly despite hyperkinesis of normal walls, then aneurysmectomy may help to improve cardiac performance. On the other hand, pseudoaneurysm, caused by a localized rupture of the myocardial tissue, which is contained within the pericardial space, is visualized as a saccular aneurysm connected to the heart by a narrow neck. If pseudoaneurysm is suspected, prompt surgical repair is mandatory because of the tendency to rupture and the associated high mortality [32].

Ventricular thrombosis is another serious problem that can be recognized by ERNA. Intracavitary ventricular thrombi displace the radioactive blood pool and appear as photopenic areas next to akinetic or dyskinetic wall segments. Thrombi never occur in areas adjacent to normally contracting wall segments. If thrombi are suspected on the basis of ERNA, confirmation should be made using echocardiography or radiolabeled platelets [29].

14.6.5 Preoperative Cardiac Risk Assessment

The widely used screening tests utilize the readily available clinical and physical examination findings of poor ventricular function. Congestive heart failure, rales, and an S3 gallop are the factors associated with the highest surgical risk by the Goldman and Detsky criteria. Because in some patients these findings are not adequately appreciated, an accurate, objective, and reproducible measure of function is desirable. It is well established that complications are increased during and fol-

lowing surgery in patients with a diminished LV ejection fraction.

The Coronary Artery Surgery Study also demonstrated that LV function was the best predictor of postoperative cardiac events in patients undergoing bypass surgery. In other studies, vascular surgery patients with an ejection fraction less than 35% had increased cardiac complications and increased 30-day and 1.5-year mortality [44]. The increased surgical risk is due to the frequent coexistence of coronary artery disease. This risk is manifest as an increase in ischemic events as well as an increase in heart failure, arrhythmias, and management complications in those patients with prior myocardial infarction. The incidence of cardiopulmonary complications in high-risk patients rises from 12% to 58% in those with reduced radionuclide ventriculographic ejection fraction. Abnormal LV ejection fraction is an independent risk factor beyond the detection of myocardial ischemia with myocardial perfusion imaging [45].

The measurement of LV ejection fraction can be used effectively in the workup of these patients as follows: If the patient has no symptoms or cardiac risk factors, or is undergoing a minor surgical procedure, there is no need to obtain a ventricular function measurement. This is because of the low postoperative cardiac event in such a group of patients. If, however, the patient is to undergo major surgery and is found to have a markedly reduced LV ejection fraction then it is advisable to cancel the surgery or modify it to a less hazardous procedure if possible, or to revascularize any significant ischemic myocardium prior to the procedure. The probability of postoperative mortality from cardiac causes in these patients was found to be higher than that caused by their surgical disease. But if the resting LV ejection fraction is significantly reduced and the patient's surgery is an emergency, then it is important to monitor the patient extensively during the procedure [46]. Intraoperative monitoring with a Swan-Ganz catheter and an arterial line are indicated, in addition to the use of i.v. nitrates to reduced the perioperative cardiac complications.

14.6.6 Cardiac Transplant Evaluation

Initial ERNA evaluation of transplant candidates is essential to document the severity of ventricular dysfunction and the response to aggressive medical management, as well as to determine priority for transplantation based on the severity of impairment. Although all patients undergo cardiac catheterization, many do not receive contrast medium for ventriculograms. This is due to concerns with contrast media-induced acute tubular necrosis in patients who will develop some degree of renal failure after transplantation secondary to immunosuppressive drugs. Subsequent radionuclide ventriculograms are also helpful to monitor rejection and detect other postoperative problems.

Transplanted hearts have images different from those seen in regular subjects. The best septal view (LAO) is usually shifted leftward. Therefore, subsequent views (ANT, LLT) should be taken perpendicular to the long axis of the heart [47]. Because the donor heart is attached to remaining portions of the recipient RA and LA, this may give the appearance of atrial enlargement and hypokinesis. Paradoxical movement of the septum may be present and is usually related to the postpericardiotomy state as well as to the placement of a normal-size heart into a large pericardial sac. This usually resolves with time.

Depression of ventricular contractility in the immediate postoperative period is thought to be due to ischemia and surgical changes. Thus, baseline ventricular function should be measured for at least 4 days following transplantation. Cardiac rejection, on the other hand, becomes evident during the first month. Since most episodes of rejection are asymptomatic until late in their course, periodic screening is important. Endomyocardial biopsy remains the gold standard for rejection, but is an invasive procedure and is also subject to sampling error. ERNA has an important role in the evaluation of transplant rejection. Drop of LV ejection fraction below 50% has low sensitivity (40%) but a very high specificity (98%) for acute rejection. The sensitivity is higher (80%) for moderate and severe rejection, however [48]. Other investigators have found that LV volumes measured by ERNA may be a better marker of early rejection [49].

Acute isolated RV impairment is also an infrequent finding early after surgery, particularly in patients with increased pulmonary vascular resistance, which resolves spontaneously in most cases. ERNA, particularly first-pass, is useful for diagnosis and follow-up in this setting.

To summarize, ERNA has a role in the initial evaluation of patients being considered for cardiac transplantation. Additionally, it is a specific test for rejection of any severity. Other uncommon causes of functional deterioration in cardiac transplant patients should first be excluded: progressive fibrosis, significant infection, and coronary atherosclerosis. This test also has a good sensitivity for detection of moderate or severe rejection.

14.6.7 Monitoring Valvular Heart Disease

Patients with chronic valvular heart disease tolerate pressure or volume overload for extended periods without the development of myocardial dysfunction or clinical symptoms. However, once a patient becomes

symptomatic, changes in the myocardium are present that may or may not reverse with relief of the pressure or volume overloading. On the other hand, valve replacement is not a totally benign procedure to be performed on all valvular heart disease patients. Tissue prosthetic valves, which do not require anticoagulation in many cases, show more rapid deterioration than mechanical valves, but the latter require long-term anticoagulation to reduce the risk of embolization. Valve replacement does not reverse the myocardial damage, and there may actually be more rapid deterioration following the procedure. Thus, determination of preclinical cardiac reserve function could be helpful in choosing the appropriate timing for valve replacement surgery.

Exercise ERNA is a very sensitive and noninvasive method to assess asymptomatic patients with aortic regurgitation and, to a lesser extent, mitral regurgitation for the preclinical detection of myocardial damage as manifested by a decrease in cardiac functional reserve [39]. A patient without myocardial damage will have a normal ejection fraction at rest and show increased ejection fraction by at least 5% at peak exercise. Younger patients without clinical symptoms should have serial studies done every few years. Older patients or those with mild symptoms should be evaluated more frequently. Patients who remain mildly symptomatic, even if they show a mild decrease in resting or exercise functional response, should be followed more closely. At one time, valve replacement was considered for asymptomatic patients with preclinical detection of deterioration by ERNA, as it was felt that further delays would result in permanent myocardial damage. However, several studies have shown improvement in function in most patients with mild clinical symptoms and evidence of diminished cardiac reserve. If exercise-induced LV dysfunction is mild, these patients can probably continue to be managed medically. If the dysfunction is severe or there is resting LV dysfunction, however, then patients should be considered candidates for surgery. Additionally, resting LV ejection fraction is also a major predictor of postoperative survival, with a 96% 5-year survival for patients with a normal preoperative LV ejection fraction compared with 60% for patients with an abnormal value.

In aortic stenosis, patients develop LV hypertrophy early in the course of the disease, and the LV ejection fraction is often normal or even elevated due to a decrease in end-diastolic volume. However, an increase in afterload imposed by the stenosis may cause a decrease in LV ejection fraction during exercise. Exercise-induced ischemia may also occur with insufficient coronary blood flow, which is limited by the stenosis. Patients with aortic stenosis and an abnormal resting LV ejection fraction have a less favorable prognosis following aortic valve replacement.

Immediately following valve replacement, resting ERNA usually demonstrates improvement of the LV function. However, a decrease in ejection fraction can also be a normal finding due to the decrease in LV preload. Gradual improvement can be observed over time.

A regurgitation fraction can be calculated from resting ERNA by comparing the stroke counts from each ventricle. Although this value correlates well with contrast ventriculography, accurate measurements are difficult to obtain. As with contrast ventriculography, this measurement is not used widely for clinical decision-making.

14.6.8 Myocardial Hypertrophy Evaluation

Myocardial hypertrophy due to hypertension, pressure/volume overloading or idiopathic, e.g., hypertrophic, cardiomyopathy is associated with a decrease in early rapid ventricular filling. In patients with hypertension, such decreases may be observed before the development of obvious echocardiographic hypertrophy and may be an early sign of damage. Such changes can also be observed in aortic stenosis, but they are not clinically useful to monitor the need for valve replacement [29].

Hypertrophic cardiomyopathy causes a marked decrease in isovolumic relaxation and in early rapid ventricular filling. It has also been shown that there is improvement in these measurements when patients are treated with calcium channel blockers; the changes are related to clinical improvement in symptoms and exercise duration [50].

LV ejection fraction is usually in the higher normal value in these patients. This is presumably a compensation mechanism to maintain a normal stroke volume, as the hypertrophic LV is stiff and has smaller end-diastolic volume than normal LV.

14.6.9 Cardiac Shunt Evaluation

Two distinctive types of studies can be obtained to both qualitatively and quantitatively evaluate cardiac shunts, depending on the type of shunt suspected.

Left-to-Right Shunt. A first-pass study should be performed to assess patients with this type of shunt. Subsequently, a time-activity curve is generated from a region of interest drawn in the lung field. The pulmonary transit time is normally shown as a narrow spike, with symmetric limbs that represent the pulmonary blood flow of the radioactivity. However, this curve, particularly the descending limb, is distorted in left-to-right shunts due to early recirculation of pulmonary blood from the shunt. Calculation of the pulmonary-to-sys-

temic flow ratio can be obtained by subtracting the fitted shunt curve from the pulmonary one. This is a sensitive method for detecting pulmonary-to-systemic blood flow shunts between 1.2 and 3.0, provided that the patient has no pulmonary hypertension, congestive heart failure, or tricuspid regurgitation [29].

Right-to-Left Shunt. This can be suggested from visual examination of a first-pass study, where there will be early visualization of the LV. A more accurate and quantitative method of assessing these types of shunt is to inject ^{99m}Tc-macroaggregated albumin. The small particles of this radiopharmaceutical, used mainly in perfusion lung scan, are trapped in the capillary beds as they pass through the pulmonary arteries. However, in the presence of a right-to-left shunt, the pulmonary capillary system is bypassed and the particles enter the systemic circulation, where they are trapped in end organs such as the brain and the kidneys. Qualitative as well as quantitative analysis of activity within the body can be accurately obtained. A significant right-to-left shunt is present if the organ counts are greater than 7% of the total lung uptake [32]. Complication because of capillary blockage is not a clinical concern with this procedure, as the number of particles used is very small compared with the number of capillaries in any organ.

References

1. Parmley WW, Wikman-Coffelt J (1991) Physiology of cardiac muscle contraction. In: Parmley WW, Chatterjee K (eds) Cardiology. Lippincott, Philadelphia, PA, pp 1 – 26
2. Parmley WW (1991) Ventricular function. In: Parmley WW, Chatterjee K (eds) Cardiology. Lippincott, Philadelphia, PA, pp 1 – 20
3. Hall WD Jr, Gravanis MB (1991) Cardiac hypertrophy and hypertensive heart disease. In: Parmley WW, Chatterjee K (eds) Cardiology. Lippincott, Philadelphia, pp 118 – 138
4. Izumo S, Nadal-Ginard B, Mahvadi V (1988) Proto-oncogene induction and reprogramming of cardiac gene expression produced by pressure overload. Proc Natl Acad Sci USA 85:339
5. Levy D, Garrison RJ, Savage DD, et al (1990) Prognostic implications of echocardiographically determined left ventricular mass in the Framingham study. N Engl J Med 322:1561
6. Harrison DG, Florentine MS, Brooks LA, et al (1988) The effect of hypertension and left ventricular hypertrophy on the lower range of coronary autoregulation. Circulation 77:1108
7. Smith V-E, Weisfeldt ML, Katz AM (1986) Relaxation and diastolic properties of the heart. In: Fozzard HA, Haber E, Jennings RB, et al (eds) The heart and cardiovascular system, vol 2. Raven, New York
8. Grossman W (1991) Diastolic dysfunction in congestive heart failure. N Engl J Med 325:1557
9. Smith V-E, Schulman P, Karimeddini MK, et al (1985) Rapid ventricular filling left ventricular hypertrophy. II. Pathologic hypertrophy. J Am Coll Cardiol 5:869
10. Topol EJ, Traill TA, Fortuin NJ (1985) Hypertensive hypertrophic cardiomyopathy of the elderly. N Engl J Med 312:277
11. Conrad GH, Brooks WW, Robinson KG, et al (1987) Impaired myocardial function in the spontaneously hypertensive rate with heart failure. J Mol Cell Cardiol 19 [Suppl 4]:565
12. McLenachan JM, Dargie HJ (1990) Ventricular arrhythmia in hypertensive left ventricular hypertrophy: relationship to coronary artery disease, left ventricular dysfunction, and myocardial fibrosis. Am J Hypertens 3:735
13. Franch RH, Gravanis MB (1993) Pulmonary hypertension and core pulmonale. In: Gravanis M (ed) Cardiovascular disorders: pathogenesis and pathophysiology. Mosby, St Louis, MO, pp 139 – 177
14. Haworth SG (1987) Pulmonary vascular disease in ventricular septal defect: structural and functional correlations in lung biopsies from 85 patients with outcome of intracardiac repair. J Pathol 152:157 – 168
15. Sharma GV, McIntyre KM, Sharma S, et al (1984) Clinical and hemodynamic correlates in pulmonary embolism. Clin Chest Med 5(421):37
16. Palevsky HI, Weiss DW (1990) Pulmonary hypertension secondary to chronic thromboembolism. J Nucl Med 31:1 – 9
17. Fishman AP (1988) Pulmonary hypertension and cor pulmonale. In: Fishman AP (ed) Pulmonary diseases and disorders, 2nd edn. McGraw-Hill, New York
18. Dunnill MS (1961) An assessment of the anatomical factor in cor pulmonale in emphysema. J Clin Pathol 14:246
19. Berger HJ, Matthay RA, Lake J, et al (1978) Assessment of cardiac performance with quantitative radionuclide angiocardiography: right ventricular ejection fraction with reference to findings in chronic obstructive pulmonary disease. Am J Cardiol 41:897 – 905
20. Grossman W (1991) Diastolic dysfunction in congestive heart failure. N Engl J Med 325:1557 – 1567
21. Boudoulas H, Gravanis MG (1991) Valvular heart disease. In: Parmley WW, Chatterjee K (eds) Cardiology. Lippincott, Philadelphia, PA, pp 64 – 117
22. Wooley CF, Sparks EA, Boudoulas H (1991) Mitral stenosis. The anatomic lesion and physiologic state. In: Bashore TM, Davidson CJ (eds) Percutaneous balloon valvuloplasty and related techniques. Williams and Wilkins, Baltimore
23. Boudoulas H, Wooley CF (1991) Mitral regurgitation chronic versus acute. Implications for timing of surgery. In: Bowen JM, Mazzaferri EL (eds) Contemporary internal medicine. Plenum, New York
24. Carabello BA (1988) Mitral regurgitation, part 1. Basic pathophysiological principles. Mod Conc Cardiovasc Dis 57:53 – 64
25. Danielsen R, Nordrehaug JE, Vik-Mo H (1989) Clinical and hemodynamic features in relation to severity of aortic stenosis in adults. Eur Heart J 12:791 – 795
26. McGoon MD, Fuster V, Shub C, et al (1991) Aortic regurgitation. In: Giuliani ER, et al (eds) Cardiology: fundamentals and practice, 2nd edn. Mosby Year Book, St Louis
27. Braunwald E (1992) Valvular heart disease. In: Braunwald E (ed) Heart diseases, 4th edn. Saunders, Philadelphia
28. Oakley CM, Gravanis MB, Ansari AA (1993) Cardiomyopathies. In: Gravanis M (ed) Cardiovascular disorders: pathogenesis and pathophysiology. Mosby, St Louis, pp 210 – 253
29. Heiba SI, Cerqueira MD (1994) Evaluation of cardiac function. In: Cerqueira MD (ed) Nuclear cardiology. Blackwell Scientific, Cambridge, pp 53 – 117
30. Gibbons OJ, Verani MS, Behrenbeck T, et al (1989) Feasibility of tomographic Tc-99m hexakis-2-methoxy-2-meth-

yl-propyl-isonitrile imaging for the assessment of myocardial area at risk and the effect of treatment in acute myocardial infarction. Circulation 80:1277
31. Heiba SI, Cerqueira MD, Jacobson AF, Ferreira MJ (1998) The value and correlates of left ventricular cavity assessment in dipyridamole ^{201}Tl SPET studies. Nucl Med Commun 19:443 – 449
32. Berger HJ, Zaret BL (1984) Radionuclide assessment of cardiovascular performance. In: Freeman L (ed) Freeman and Johnson's clinical radionuclide imaging. Saunders, Philadelphia
33. Berman DS, Maddahi J, Garcia EV, et al (1981) Assessment of left and right ventricular function with multiple gated equilibrium cardiac blood pool scintigraphy. In: Berman DS, Mason DT (eds) Clinical nuclear cardiology. Grune and Stratton, New York
34. Garcia EV, Bateman TM, Berman DS, et al (1988) Computer techniques for optimal radionuclide assessment of the heart. In: Gottschalk A, Hoffer PB, Pothen El (eds) Diagnostic nuclear medicine. Williams and Wilkins, Baltimore
35. Borges-Neto S, Coleman RE (1993) Radionuclide functional analysis. Radiol Clin North Am 31:817 – 830
36. Port SC (2004) Tomographic equilibrium radionuclide angiography: Has its time arrived? J Nucl Cardiol 11:242 – 244
37. DePuey EG, Garcia EV (eds) (2001) Updated imaging guidelines for nuclear cardiology procedures, part 1. J Nucl Cardiol 8:G5–G58
38. De Bondt P, Vandenberghe S, De Mey S, et al (2003) Validation of planar and tomographic radionuclide ventriculography by a dynamic ventricular phantom. Nucl Med Commun 24:771 – 777
39. Port SC (1994) Radionuclide angiography. Am J Cardiac Imaging 8:240 – 248
40. Schwartz RG, McKenzie WB, Alexander J, et al (1987) Congestive heart failure and left ventricular dysfunction complicating doxorubicin therapy: seven-year experience using serial radionuclide angiocardiography. Am J Med 82:1109 – 1118
41. Druck MN, Gulenchyn KY, Evans WK, et al (1984) Radionuclide angiography and endomyocardial biopsy in the assessment of doxorubicin cardiotoxicity. Cancer 53:1667 – 1674
42. Rosanski A (1990) Applications of exercise radionuclide ventriculography in the clinical management of patients with coronary artery disease. J Thorac Imaging 5:37 – 46
43. Borges-Neto S, Coleman RE, Potts JM, Jones RH (1991) Combined exercise radionuclide angiography and single photon emission computed tomography perfusion studies for assessment of coronary artery disease. Semin Nucl Med 21:223 – 229
44. Kazmers A, Moneta GL, Cerqueira MD, Healy DA, Zierler RE, Harley JD (1990) The role of preoperative radionuclide ventriculography in defining outcome after revascularization of the extremity. Surg Gynecol Obstet 171:481 – 488
45. Heiba SI, Jacobson AF, Cerqueira MD, Shattuc S, Sharma S (1999) The additive values of radionuclide ventriculography and extent of myocardium at risk to dipyridamole thallium-201 imaging for optimal risk stratification prior to vascular surgery. Nucl Med Commun 20:887 – 894
46. Pedersen T, Kelbaek H, Munck O (1990) Cardiopulmonary complications in high-risk surgical patients: the value of preoperative radionuclide cardiography. Acta Anaethesiol Scand 34:183 – 189
47. Dietz RR, Patton DD, Copeland JH, McNeill GC (1987) Characteristics of the transplanted heart in radionuclide ventriculogram. J Heart Transplant 5:113 – 121
48. Follansbee WP, Kieman JM, Curtiss El, Zerbe TR, Mock C, Kormos RL (1991) Changes in left ventricular systolic function that accompany rejection of the transplanted hearts: a serial radionuclide assessment of fifty-three consecutive cases. Am Heart J 121:548 – 556
49. Novitzky D, Cooper DKC, Boniaszczuk J (1988) Prediction of acute cardiac rejection by changes in left ventricular volume. J Heart Transplant 7:453 – 455
50. Clements IP, Sinak LJ, Gibbons RJ, Brown ML O'Connor MK (1990) Determination of diastolic function by radionuclide ventriculography. Mayo Clin Proc 65:1007 – 1019

15 Basis of Cardiac Imaging 2: Myocardial Perfusion, Metabolism, Infarction, and Receptor Imaging in Coronary Artery Disease and Congestive Heart Failure

Josef Machac (Co-author 1st edition: Milena J. Henzlova)

15.1 Introduction

This chapter will review the role of radionuclide imaging in the diagnosis and management of coronary artery disease, acute ischemic syndromes, and heart failure. The pathophysiology of coronary artery disease and its complications, pertinent radiotracers and imaging instruments, and the clinical circumstances under which these tools are applied to clinical decision-making will be reviewed.

15.2 Pathophysiology of Coronary Artery Disease

Coronary artery disease is thought to arise from normal repair processes in response to chronic injuries to the arterial endothelium. It is often the result of heightened local shear stress, often at bending points and bifurcations of the arterial tree [1, 2]. These stresses, probably enhanced by hypertension, lead to accumulation of lipids and macrophages, abetted by hypercholesterolemia, glycation end-products of diabetes, chemical irritants, tobacco smoke, and other circulating vasoactive amines, immune complexes, and possibly infectious agents [3–5].

Figure 15.1 is a schematic of the life of an atherosclerotic plaque. The stages are detailed in Table 15.1. An early atherosclerotic lesion, the so-called fatty streak or type II lesion, features a dynamic balance of entry and exit of lipoproteins, as well as the development of an extracellular matrix. This occurs in the first several decades of life. Decreased lipoprotein entrance, through modification of risk factors, results in a predominance of lipoprotein exit, and thus in healing and scarring. Lipoprotein entry predominating over lipoprotein exit can result in a type IV or type Va lesion. Type IV and type Va plaques are soft, rich in lipids, contained by a discrete extracellular matrix (Fig. 15.2). Such an atheroma is prone to disruption [6].

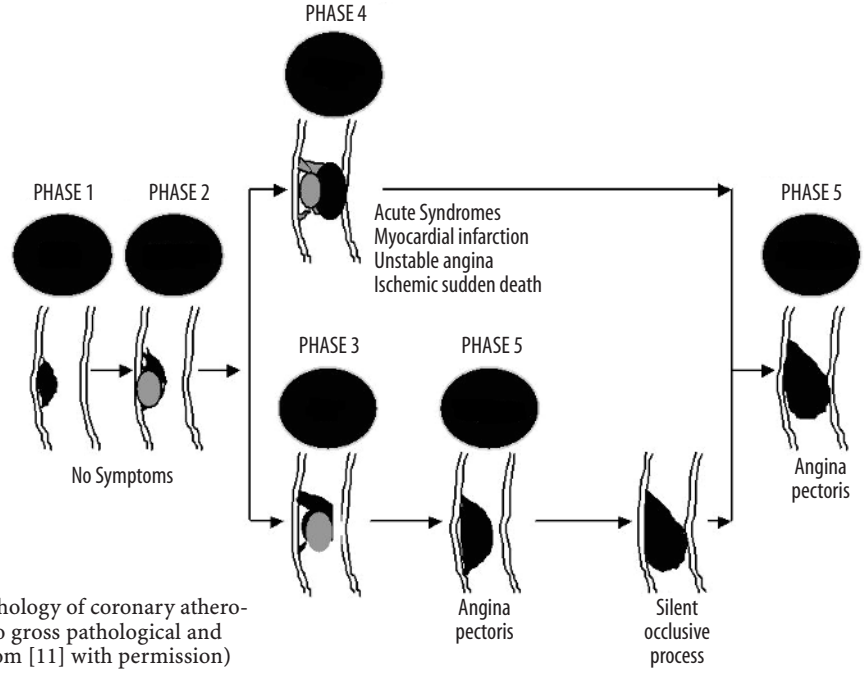

Fig. 15.1. Phases and lesion morphology of coronary atherosclerosis progression according to gross pathological and clinical findings. (Reproduced from [11] with permission)

Table 15.1. Atherosclerotic lesion types. (Adapted [13] from the Committee on Vascular Lesions of the Council on Atherosclerosis, American Heart Association [14])

Plaque type	Characteristics of plaque	Associated clinical syndrome
I	Intimal thickening, macrophages, isolated foam cells	Asymptomatic
II, "fatty streak"	Accumulation of intracellular lipid in infiltrating macrophages and smooth muscle cells	Asymptomatic
III	As above, plus incipient extracellular lipid and connective tissue deposition	Asymptomatic
IV, "atheroma"	Large extracellular intimal lipid core; inflammatory cell infiltration, including macrophages, foam cells, and T cells	Usually asymptomatic; can also be associated with stable angina
Va	Atheroma with fibrous layer or layers	Same as type IV
Vb	Atheroma with extensive calcification in the lipid core or elsewhere in the lesion	Stable angina pectoris; can also be asymptomatic
Vc	Fibrosed atheroma or organized mural thrombus with minimal or absent lipid component	Same as type Vb
VI, "complicated lesion"	Disrupted type IV or V lesion with intramural hemorrhage and/or overlying thrombus	Acute coronary syndrome or asymptomatic lesion progression

The atherosclerotic plaque tends to grow in fits and starts, rather than in a continuous fashion. Sudden plaque growth occurs when the plaque ruptures, resulting in intracoronary thrombosis [7, 8] (Fig. 15.3). Even mildly or moderately stenotic arteries can acutely progress to severely or totally occlusive lesions [6] (Fig. 15.4). They account for many acute coronary syndromes (unstable angina, acute infarction) but also may remain asymptomatic.

Plaque disruption occurs not only in advanced stenotic plaques, but independently of lesion size and degree of stenosis [8]. Most acute coronary syndromes actually result from disruption of lesions which are initially not flow limiting, due to rapid progression to severe stenoses [9, 10]. Culprit lesions in acute coronary syndromes tend to have less calcification and fibrous tissue, which implies softness and vulnerability to shear forces [15] (Fig. 15.3).

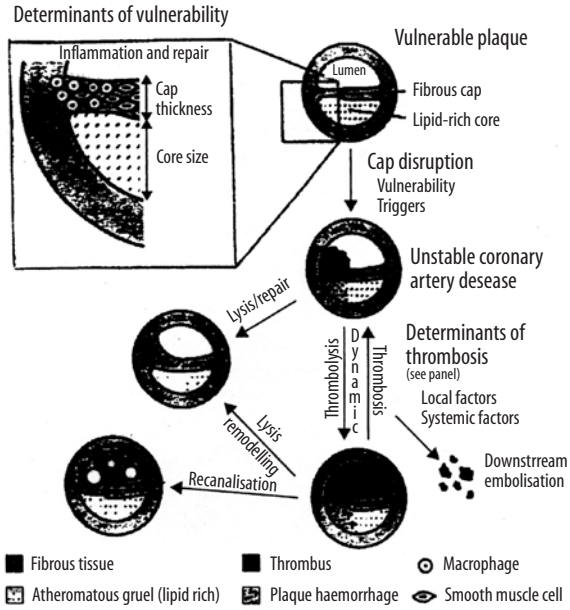

Fig. 15.2. Plaque vulnerability, disruption, and thrombosis: anatomical changes leading to acute coronary syndromes and subsequent plaque remodeling. (Reproduced from [11] with permission)

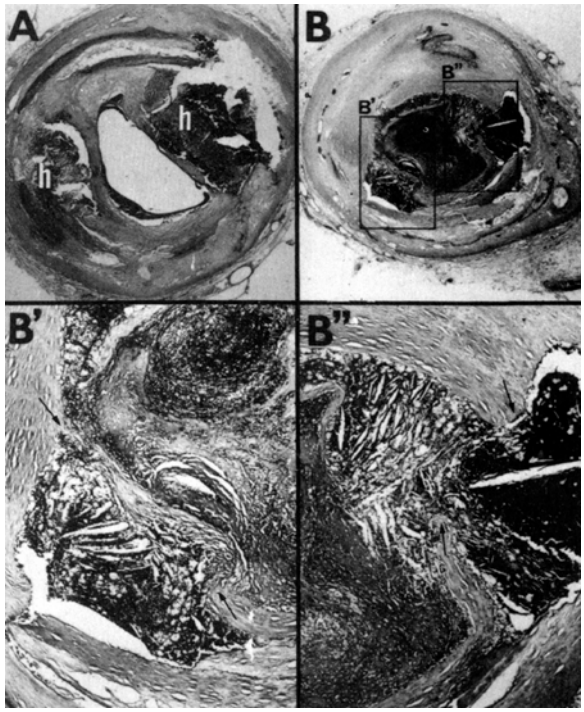

Fig. 15.3A,B. Two consecutive segments of atherosclerotic coronary arteries, 1 cm apart: **A** plaque hemorrhage (*h*); **B** plaque rupture with extrusion of atheromatous debris inducing thrombosis. *Areas boxed* in **B** are shown at higher magnification in **B′** and **B″**. Note extruded cholesterol/fatty acid material, through breaks (*arrows*) in intimal lining of lumen, admixed with thrombus. (Reproduced from [12] with permission)

Nevertheless, lipid composition of a disrupted lesion can vary. Disrupted and thrombosed plaques with little lipid content are described in a recent autopsy report of plaque morphology in sudden cardiac death [16].

The unstable phase of plaque development may be followed by a chronic phase with a calcified type Vb or fibrotic type Vc lesion (Fig. 15.4). It is often marked by stable angina pectoris. Severely stenotic plaques can occlude without plaque rupture due to stasis, leading to a thrombus. Occlusion of such a vessel is often clinically silent, as distal myocardium is frequently supplied by collateral flow [17].

The primary and secondary prevention of acute coronary syndromes includes aggressive cholesterol-lowering therapy, demonstrated to significantly improve prognosis following acute coronary syndromes and in hypercholesterolemic patients without a history of coronary disease [18–20]. The change does not appear to involve only a minimal regression of the atherosclerotic

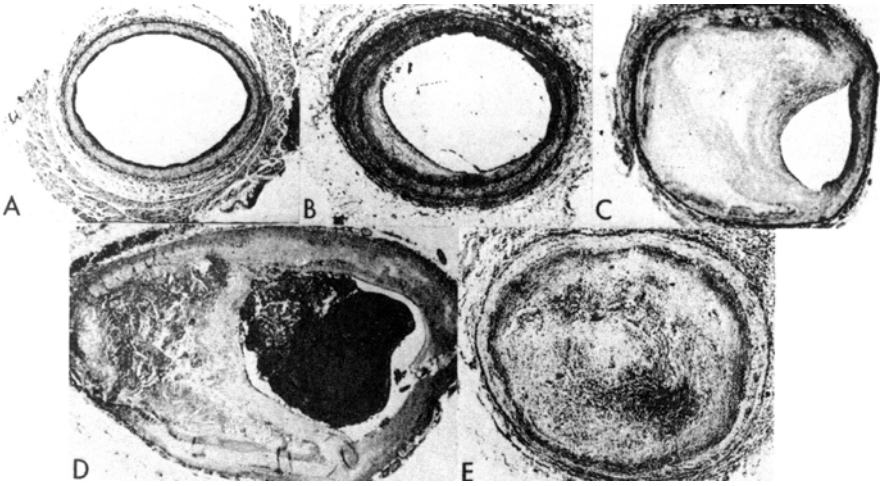

Fig. 15.4A–E. Slow progression of coronary atherosclerosis: **A** normal artery; **B** fatty streak with fibrosis; **C** advanced fibrous plaque. Rapid progression of coronary atherosclerosis: **D** occlusion by thrombus formation; **E** thrombus during process of fibrotic organization. (Reproduced from [12] with permission)

plaque, as demonstrated in a number of angiographic studies [21, 22]. Rather, lowering of cholesterol plus the more recently appreciated anti-inflammatory effects of statins stabilizes the atheromatous plaque by increasing the net efflux of lipid from the plaque, thereby decreasing the lipid content, decreasing the number of macrophages and lowering of indices of inflammation such as local temperature, uptake of FDG, and formation of a thicker fibrous cap. This helps make the plaque more resistant to disruption [23–26], Furthermore, the anti-inflammatory effects of statin therapy independent of cholesterol lowering appear to promote the stabilization of lesions in acute coronary syndromes [27].

15.3 Myocardial Perfusion SPECT Imaging

Clinical manifestations of coronary artery disease include angina pectoris, myocardial infarction, congestive heart failure, and sudden death. It may be asymptomatic until advanced in severity or complications. Most diagnostic methods, both invasive and noninvasive, depend on detection of luminal narrowing of the epicardial coronary vessels. Vessel narrowing of up to 75% of the cross-section area (or < 50% of luminal narrowing) does not affect resting coronary flow. Increase of coronary flow caused by exercise or pharmacological stress exaggerates flow nonuniformity, through either increased metabolic demand or vasodilation [28] (Fig. 15.5). The easiest method of increasing coronary flow is physical exercise, using a motorized treadmill or a stationary bicycle. In patients who are unable to exercise adequately, pharmacological agents (adenosine, dipyridamole, dobutamine, and arbutamine) are used for transient elevation of coronary flow.

Myocardial perfusion imaging (MPI) maps the relative distribution of coronary flow, which is normally almost uniform in the absence of prior infarction or fibrosis. In the presence of luminal narrowing, flow nonuniformity corresponds to anatomical location of the coronary stenoses and to the cumulative severity of the obstructions along the coronary arterial tree and the size of its watershed [29]. Therefore, MPI can diagnose not only the presence of coronary artery disease, but also its extent, severity, and physiological impact, thereby providing great prognostic power.

15.3.1 SPECT Tracers

The ideal tracer of coronary flow would be extracted by the myocardium with 100% efficiency, like microspheres. Its myocardial uptake would be linearly related to coronary flow, and the tracer isotope would have optimal emission photon energy for imaging with a gamma camera. Currently, two classes of tracers are widely used for conventional MPI: thallium-201 and the Tc-99m-labeled tracers. Three agents are approved for clinical use in the USA: thallium-201, Tc-99m-sestamibi and Tc-99m-tetrofosmine. None of the available

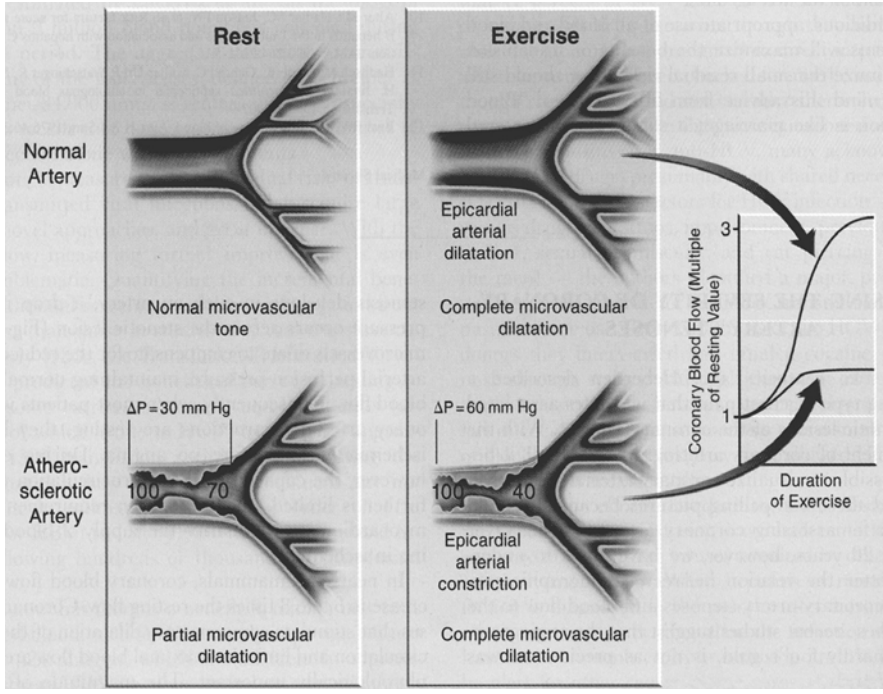

Fig. 15.5. Regulation of blood flow in normal and stenosed coronary arteries: In the normal artery, the epicardial and microvascular vessels dilate with exercise or pharmacological stress. In the atherosclerotic artery, when the patient is resting, there is a drop in pressure across the stenosis in the epicardial artery. During exercise or vasodilation, the pressure drop across the stenosis increases, and the microcirculation has limited additional capacity for dilation, resulting in blood flow not adequate to meet the metabolic demand of exercise, or to keep up with increased blood flow in the normal regions. As a result, the fractional flow reserve is reduced. (Reproduced from [30] with permission)

conventional agents has all the characteristics of an ideal myocardial perfusion agent.

15.3.1.1 Thallium-201

Thallium-201 (Tl-201) has been in clinical use for more than two decades. Tl-201 is a metal in group III-A of the periodic table and as an isotopic cationic tracer has properties similar to those of potassium. Tl-201 is extracted with a high extraction fraction by the ATPase-dependent Na^+/K^+ channels (Table 15.2). Diagnostic and prognostic data on Tl-201 are extensive. Another advantage of Tl-201 is the ease of use. Only one injection is needed [31]. Among the conventional tracers, Tl-201 is the one preferred for evaluation of myocardial viability. Major drawbacks of Tl-201 include low energy of its principle X-ray photons (69 – 80 keV) and its long half-life (72 h), which limits the injected dose. The latter leads to suboptimal image quality due to noise. The former property leads to a high scatter fraction in the imaging energy window, and susceptibility to attenuation, especially in obese and female subjects. Compared with competing modalities (stress echo, Tc-99m-based tracers), a Tl-201 study is relatively long (4 – 6 h) in duration.

A dose of 3 – 4 mCi of Tl-201 is injected intravenously at peak stress (exercise or pharmacological). Stress SPECT imaging starts 10 – 15 min following the injection. Tl-201 uptake in the myocytes requires active metabolic transport; i.e., only viable myocytes take up and retain the tracer. Washout of Tl-201 from the myocardium starts immediately after initial uptake. Initial tracer uptake is a function of the coronary flow and of the integrity of the myocytes. Early (post-stress) images reveal the degree of regional uniformity of the coronary flow, i.e., demonstrate presence or absence of coronary artery disease. Washout of Tl-201 from the myocardium is faster from areas with higher initial uptake (and higher regional flow) and is slower from hypoperfused but viable areas supplied by arteries with inadequate flow during stress. This leads to a "filling in" or "redistribution" of initial defects (Fig. 15.6). The customary time for delayed imaging is 3 – 4 h after tracer injection. Tl-201 redistribution is consistent with presence of viable, but hypoperfused (or ischemic) myocardium. Delayed imaging (up to 24 h) may reveal redistribution in some defects which appeared "fixed"

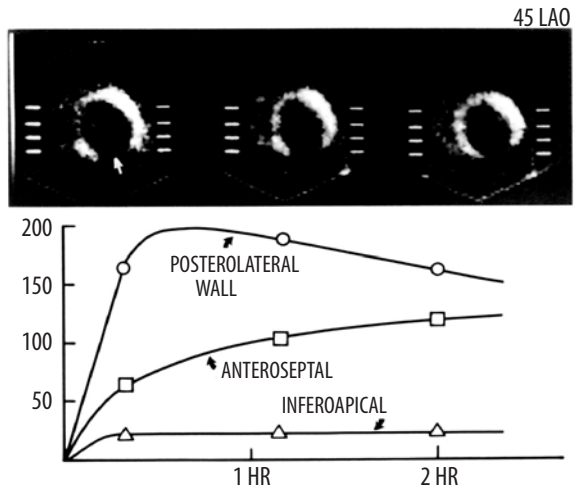

Fig. 15.6. Sequential LAO planar images obtained 10 min, 1 h, and 2 h after low-level treadmill exercise, 10 days after a myocardial infarction. There is a persistent defect involving the inferoapical segment (*white arrow*) compatible with scar. The posterolateral wall shows normal uptake and washout, while the anteroseptal region demonstrates an initial defect with delayed redistribution indicative of ischemia. (Reproduced from [37]with permission)

Table 15.2. Tracers for SPECT myocardial perfusion imaging

	Thallium-201	Tc-99m-sestamibi	Tc-99m-tetrofosmine
Brand name	N/a	Cardiolite	Myoview
Class	K^+ analogue	Isonitrile	Diphosphine
Preparation	Cyclotron	Kit (heated)	Kit (cold)
Charge	Cation	Cation	Cation
Lipophilicity	Low	High	High
Redistribution	Yes	Minimal	Minimal
Tissue clearance	50%/4 h	>6 h	>6 h
Excretion	Renal	GI (renal)	GI (renal)
Time of imaging	5 – 10 min	20 – 60 min	10 – 45 min
Completion time	4 – 6 h	3 – 4 h	3 – 4 h
Counts	Adequate	High	High
SPECT	Yes	Yes	Yes
Extraction	0.85	0.39	0.24
Gating	±	Yes	Yes
Heart:liver(1 h)	2.6	1.2	1.4
TEDE	2.1 rem/3.5 mCi	1.1 rem/30 mCi	0.8 rem/30 mCi
Clinical use			
Diagnosis	Yes	Yes	Yes
Prognosis	Yes	Yes	Yes
Viability	Yes	Yes	Yes

at 3–4 h. In addition, or alternatively, reinjection of a small booster dose of Tl-201 (1 mCi) at rest may reveal improved uptake in regions with "fixed" defects [32–36]. On the other hand, regions with old infarction, where viable myocardial mass, not vessel diameter, is the flow-limiting factor, do not demonstrate redistribution, i.e., replacement of contractile myocardium by fibrotic tissue. Figure 15.7 shows typical Tl-201 SPECT stress and redistribution images and both types of myocardial behavior.

The widespread utilization of multiple headed SPECT gamma cameras has allowed gated thallium-201 images with acceptable quality. Overall sensitivity of Tl-201 SPECT imaging for detection of CAD is >80%. Sensitivity for detection of multivessel CAD is higher than for detection of single-vessel disease. Sensitivity for detection of left anterior descending and right coronary artery disease is higher than for detection of circumflex disease [38]. Specificity of the findings is 50%–80%, depending on the degree of catheterization and laboratory referral bias. Specificity is lower in patients with LBBB, left ventricular dysfunction, end-stage congestive heart failure, left ventricular hypertrophy, and/or marked obesity [39].

15.3.1.2 Tc-99m-Sestamibi, Tc-99m-Tetrofosmine

The technetium-99m-based tracers, Tc-99m-sestamibi (Cardiolite) and Tc-99m-tetrofosmine (Myoview), have

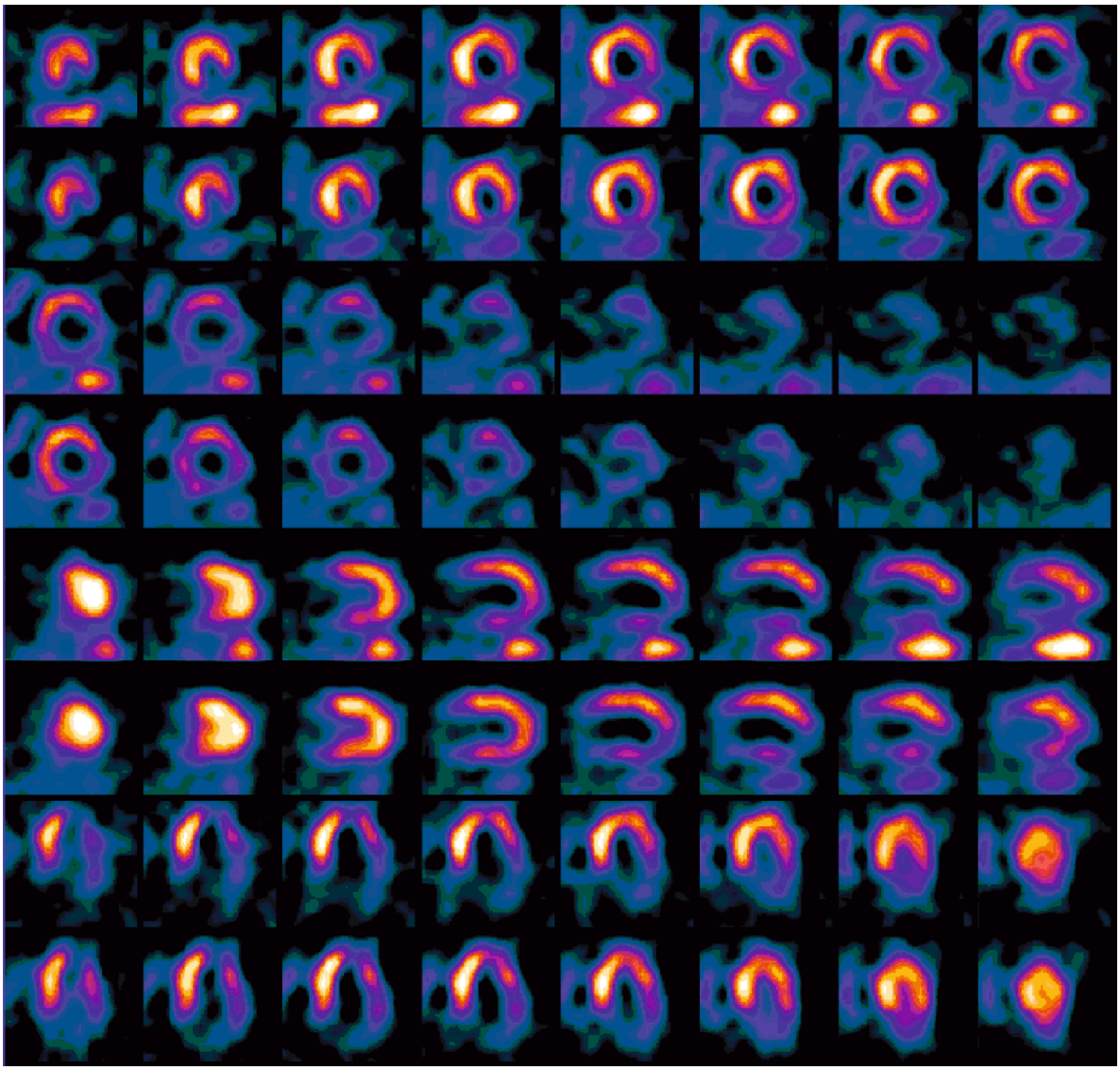

Fig. 15.7. Thallium-201 stress and redistribution images of a patient showing a severe fixed inferolateral defect, a severe, partially reversible basal inferolateral defect, a reversible basal inferoseptal defect, and a mild to moderate reversible anterolateral defect

more similarities than differences (Table 15.2). A shorter physical half-life of Tc-99m (6 h) allows the use of higher tracer doses (up to 50 mCi/day). Combined with more optimal photon energy for gamma camera imaging (140 keV) compared with Tl-201, image quality is less noisy, and frequency and severity of attenuation artifacts is decreased. Negligible washout of Tc-99m-based tracers [40] (Fig. 15.8) necessitates the use of two separate tracer injections: one for rest imaging and one for stress imaging. SPECT imaging is usually started 20 – 60 min after tracer injection. The delay is needed for blood pool clearance and partial liver clearance (Fig. 15.8). Gating of Tc-99m-sestamibi or -tetrofosmine images, made possible because of the high photon flux, allows simultaneous evaluation of perfusion and resting function. Widely available commercial software is used for quantification of left ventricular ejection fraction, left ventricular volumes, left ventricular mass, and for semiquantitative evaluation of myocardial systolic thickening [42] (Fig. 15.9). In laboratories equipped with a suitable gamma camera positioned at the side of the treadmill or upright bicycle, first-pass blood pool imaging can be performed for evaluation of left and right function during exercise stress [43].

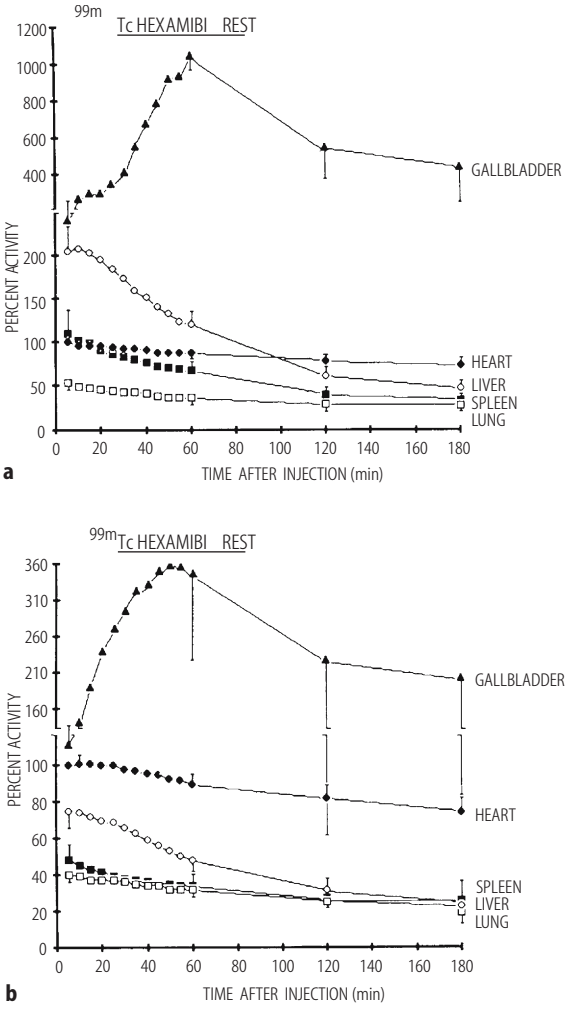

Fig. 15.8. a Organ time-activity curves after injection of Tc-99m-sestamibi at rest in five normal volunteers (mean ± SD). The data are normalized to cardiac activity at 5 min after injection. **b** Organ time-activity curves in five normal volunteers after injection of Tc-99m-sestamibi during exercise. (Reproduced from [41] with permission)

Tc-99m-sestamibi and -tetrofosmine can also be used in the setting of acute coronary syndromes. Patients with recent or current episodes of chest pain can be injected with the tracer at rest, medically stabilized or treated with thrombolysis or percutaneous revascularization, and imaged for diagnostic or prognostic purposes several hours later [44]. Patients in whom an acute infarction has been excluded, and at low risk for unstable angina, can be referred from the emergency department or chest pain unit to undergo stress and rest imaging.

Excretion of the Tc-99m tracers is hepatobiliary and, to a lesser extent, renal [45]. High subdiaphragmatic uptake in the liver or intestines occasionally interferes with evaluation of cardiac perfusion. The average total length of the rest-stress imaging and stress-rest sequence is 3 – 4 h. In direct comparisons, the diagnostic accuracy of sestamibi and tetrofosmine is similar to that of Tl-201 [46, 47]. However, the linearity between flow and uptake of Tc-99m-sestamibi or Tc-99m-tetrofomine is suboptimal at high flow rates (Fig. 15.10), due to the lower extraction fraction, which is achieved with coronary vasodilators (adenosine and dipyridamole) [48 – 50].

In an attempt to utilize advantages of both types of tracers, dual-tracer protocols were developed: Tl-201 is injected at rest, and rest imaging is started within 15 min. Exercise or pharmacological stress is followed by Tc-99m-MIBI or Tc-99m-tetrofosmine injection at peak stress. The test is completed in less than 3 h [51]. A potential drawback derives from different pharmacokinetic properties of the tracers, resulting in nonparallel flow-uptake relationships and different spatial contrast due to different isotope energies.

Tc-99m-teboroxime (Cardiotec) was another FDA approved perfusion agent that was marketed about a decade and a half ago. This highly lipophilic agent readily crosses myocardial cellular membranes but, unlike MIBI, rapidly diffuses out of the cells in 6 – 10 min, allowing only a few minutes for imaging [52]. It requires a separate rest and stress injection. There is some evidence that the differential washout rate of Tc-99m-teboroxime obtained from stress-redistribution images can differentiate between ischemic and infarcted myocardium as well as stress-rest imaging [53]. One advantage of teboroxime is its very high extraction fraction,

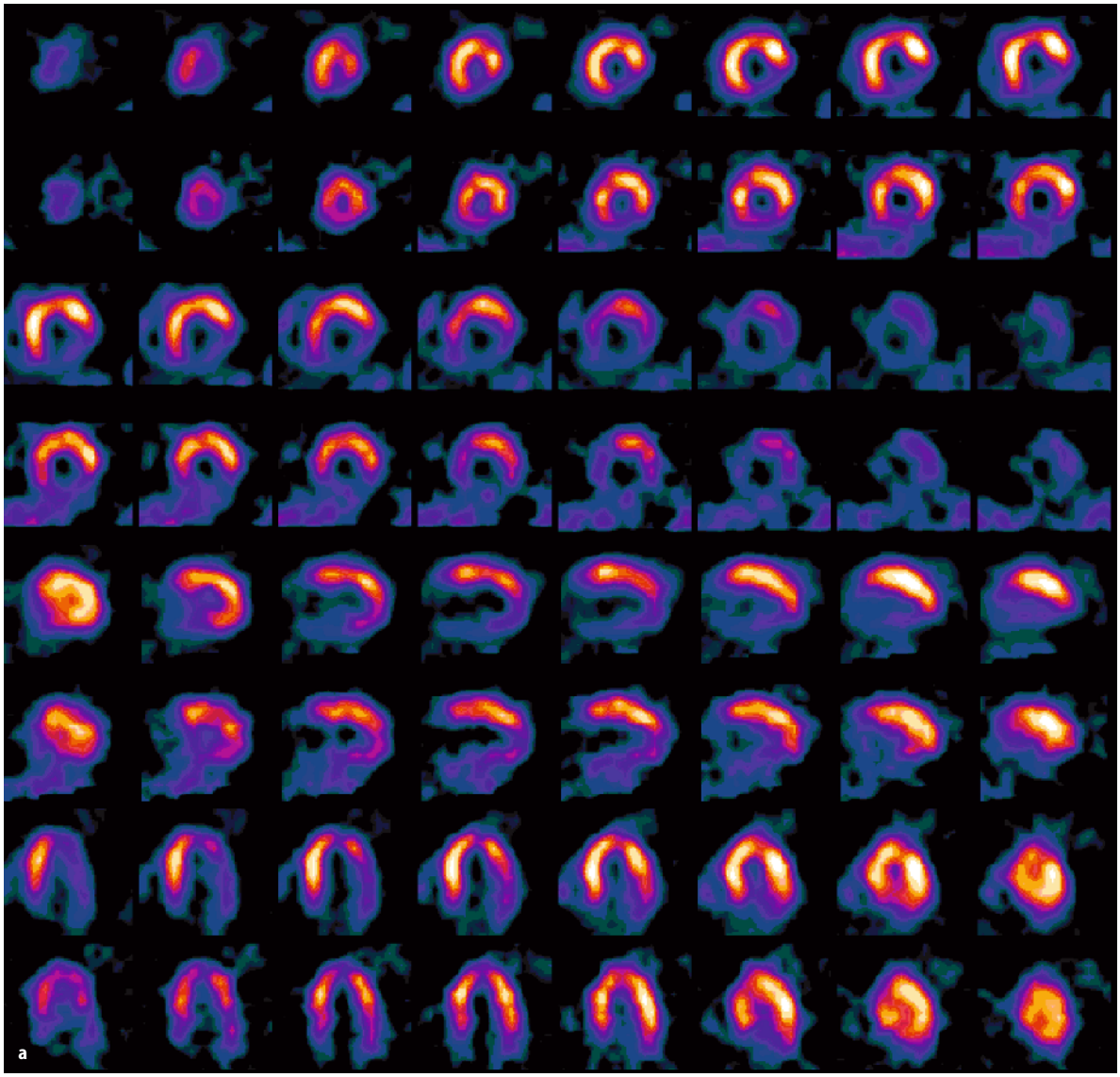

Fig. 15.9a,b. Stress and rest gated Tc-99m-sestamibi imaging study. **a** Stress and rest Tc-99m-sestamibi SPECT images showing severe inferolateral and posterolateral defects at stress with improvement in the inferoapical and lateral walls at rest, and persistence of the inferior and posterior defects

which is higher than any of the other conventional agents at high flow rates during pharmacological vasodilation. Due to the demanding rapid-imaging protocol required, its use never became extensively applied, in spite of examples of good-quality images obtained with either multi-headed or single-headed gamma cameras in some laboratories. Its commercial availability ceased over a decade ago.

15.3.1.3 Investigational Perfusion Radiotracers

Several new perfusion tracers have been developed and are under investigation. One type includes the so-called Q compounds (Q3 and Q12) labeled with Tc-99m. They are mixed cationic ligands, consisting of monophosphate ligands complexed to a Schiff-base ligand. Radiolabeling requires boiling in a water bath with Tc-99m-pertechnetate. The Q agents have a rapid clearance from the blood by hepatobiliary and renal excretion. Myocardial uptake of Q12 is stable without redistribution. However, the first-pass extraction is only 29%, a limitation with high-level exercise and pharmacological stress [35].

Another promising agent was Tc-99m-N-Noet. It is a nitrido dithiocarbamate, a neutral lipophilic compound. It also requires boiling a precursor tri-sulfophenyl phosphine with Tc-99m-pertechnetate, followed by

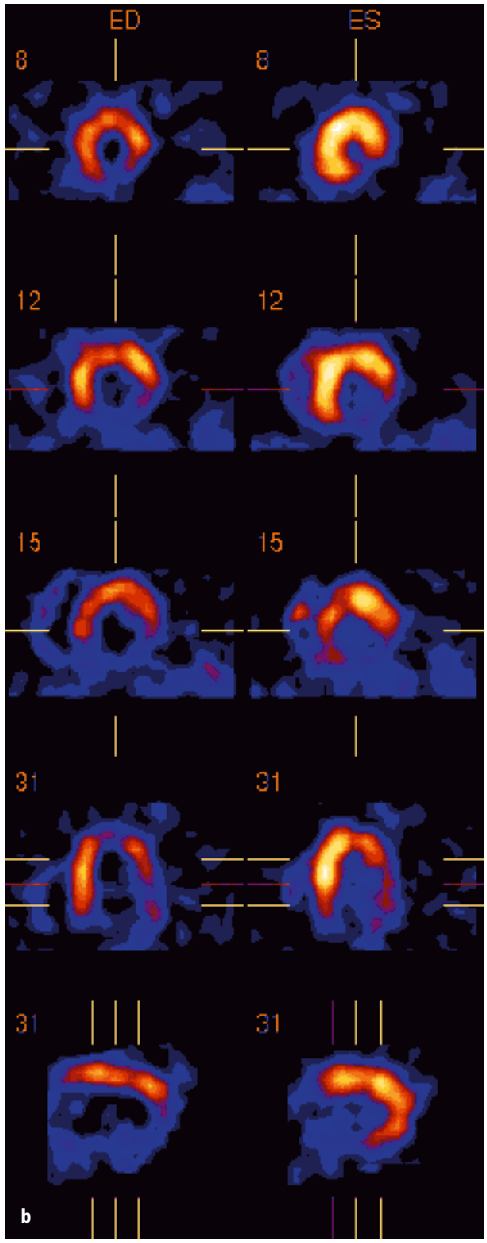

Fig. 15.9. b Stress Tc-99m-sestamibi imaging with gating of the same patient as in **a**, showing end-diastolic and end-systolic gated images. There is excellent wall thickening in the septum and anterior wall, absence of uptake or thickening in the inferolateral and posterolateral walls, and decreased thickening in the basal septum

compounding with dithiocarbamate. Blood activity clearance by hepatobiliary excretion is slower than for Tl-201 or Tc-99m-MIBI or -tetrofosmine. The agent's features are a high extraction fraction, followed by significant washout [45]. However, high lung uptake in some patients has discouraged its clinical application [55].

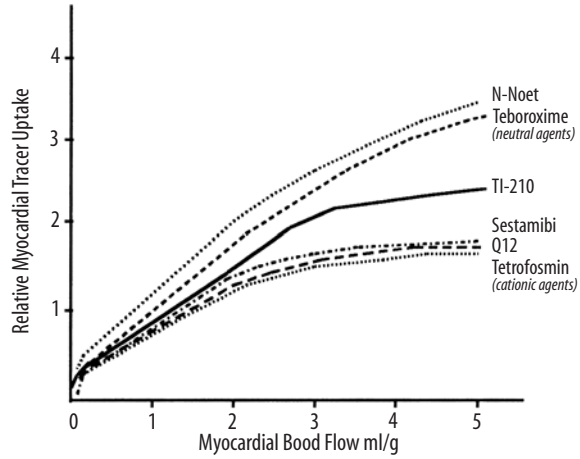

Fig. 15.10. Relationship between myocardial blood flow and uptake of various perfusion tracers. (Reproduced from [54] with permission)

15.3.2 Stressors

15.3.2.1 Exercise

Exercise treadmill stress testing (ETT) is the most frequently used test for noninvasive diagnosis of coronary artery disease. Sensitivity of a symptom-limited ETT for diagnosis of CAD is 65%–70% [56]. When combined with myocardial perfusion imaging, sensitivity increases to 85%–90%, while specificity is increased as well [57]. Motorized treadmill exercise is almost universally used in the USA, while the upright stationary bicycle is more popular in Europe. All monitored parameters (i.e., ECG, blood pressure, patient's appearance, and symptoms) are valuable not only for diagnosis, but also for prognosis. Using a Bayesian approach, pre- and post-test probability for presence of the disease can be reliably estimated. Short-term prognosis for major cardiovascular events can also be derived from easily obtained parameters. The most powerful single predictor in both men and women is exercise capacity (length of the exercise) [58, 59].

15.3.2.2 Pharmacological Stress Testing

Patients who cannot exercise for noncardiac reasons (e.g., orthopedic, neurological, peripheral vascular) or are unable to exercise adequately (for a meaningful period of time and/or to an adequate heart rate) are candidates for pharmacological stress testing. Four agents are currently approved for use in conjunction with MPI: adenosine, dipyridamole, dobutamine, and arbutamine. Adenosine and dipyridamole are coronary vasodilators. Dobutamine and arbutamine are beta-adrenergic agonists and increase myocardial oxygen de-

mand. They also have some direct vasodilatory effect [60]. Pharmacological stress makes possible evaluation of patients unable to exercise for noncardiac reasons, including sick and debilitated patients. However, physiologically useful parameters derived from an exercise test, valuable for a comprehensive evaluation, are lost.

15.3.2.2.1 Adenosine

Adenosine is an endogenous coronary vasodilator produced from ADP and AMP in myocardial and vascular smooth muscle cells. Adenosine affects two kinds of receptors: A1 and A2. Activation of the A1 receptor slows A-V conduction. Activation of the A2 receptor leads to coronary vasodilatation (Fig. 15.11, Table 15.3). The half-life of adenosine is extremely short (seconds only). Perfusion tracers are therefore injected during continuous adenosine infusion (140 µg/kg/min for 6 min). Side effects of adenosine include flushing in 37% patients, chest pain in 35%, shortness of breath in 35%, and gastrointestinal symptoms in 15%. Chest pain is not indicative of myocardial ischemia. Vasodilatation causes a modest blood pressure drop, usually accompanied by compensatory tachycardia, although transient 2nd degree A-V block is seen in 3% – 4% of patients and 3rd degree A-V block in < 1% of tested patients. All side effects and hemodynamic changes are transient and reversible. Use of an antidote (i.v. aminophylline) is very rarely needed. Most situations can be controlled by decreasing the infusion rate and/or by shortening the duration of the infusion. Adenosine may trigger bronchospasm and should not be used in patients with bronchospastic disease, particularly those who have clinical asthma and/or are being treated with bronchodilators. Caffeine, theophylline, and their metabolites competitively block adenosine receptors. Therefore, patients should abstain from caffeine-containing beverages and medication for 12 – 24 h prior to the test [62].

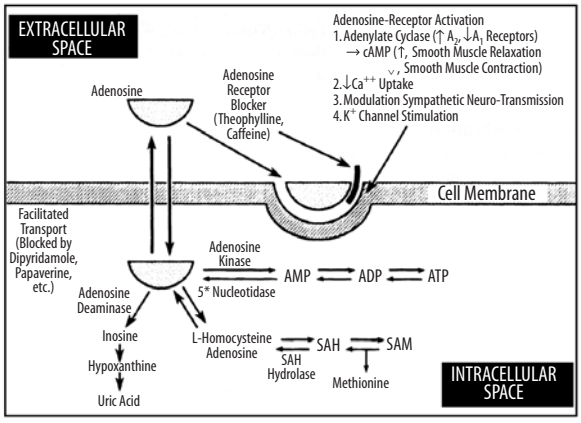

Fig. 15.11. Mechanisms of the vasodilating stress agents. Adenosine is synthesized intracellularly and leaves the cells to act on surface membrane receptors. Dipyridamole blocks adenosine reentry into the cell, increasing extracellular adenosine that can bind to the receptor. Methylxanthines, such as theophylline and caffeine, competitively block the receptor sites. (Reproduced from [61] with permission)

Table 15.3. Coronary vasodilators

	Adenosine	Dipyridamole
Effect	Direct	Indirect
Half-life	< 10 s	Minutes
Onset of action	Seconds	Minutes
Time to peak effect	ca. 1 min	ca. 7 min
A-V block	3% – 4%	0%
Diagnostic utility	Same as dipyridamole	Same as adenosine
Contraindications	Bronchospasm, dipyridamole usage	Bronchospasm

15.3.2.2.2 Dipyridamole

Dipyridamole is an indirect vasodilator: It increases intravascular concentration of endogenously produced adenosine by blocking its cellular reuptake (Fig. 4.11). Dipyridamole has a longer half-life than adenosine and does not affect A-V conduction. Dipyridamole is usually infused for 4 min. The perfusion tracer is injected at 7 min. In some laboratories, the patient is asked to perform low-level exercise or handgrip exercise to enhance its effects. Contraindications for dipyridamole use are similar to those for adenosine, although chest pain is less frequent. An effective antidote is i.v. aminophylline (50 – 100 mg i.v.), which can be used to normalize hemodynamic changes, relieve ischemia, and/or treat side effects [62, 63]. Dipyridamole potentiates the effects of exogenously infused adenosine. Therefore, oral dipyridamole, when being taken for its antiplatelet effects, should be discontinued on the day of the stress test.

15.3.2.2.3 Dobutamine and Arbutamine

Dobutamine is a synthetic catecholamine with predominantly β1 affinity and short plasma half-life (approximately 2 min). In the presence of significant epicardial coronary artery stenosis, the increase in oxygen demand caused by positive inotropic and chronotropic effects of dobutamine can induce myocardial ischemia. Additionally, dobutamine at higher doses induces coronary vasodilation. The infusion rate used for diagnostic imaging (40 – 50 µg/kg/min) is higher than the customary therapeutic infusion rate of dobutamine (10 – 20 µg/kg/min) used for inotropic support in the intensive care units. Side effects of dobutamine in our

patient series included supraventricular and ventricular arrhythmia (6% of patients), palpitations (40%), chest pain (20%), shortness of breath (17%), headache (15%), and GI symptoms (5%). Dobutamine is used mostly in patients who are unable to exercise and have bronchospastic disease [64].

Arbutamine is also a synthetic catecholamine. It has been marketed with a computerized feedback system between arbutamine infusion rate and the heart rate. This approach attempts to minimize the time required to reach a selected peak heart rate. However, the added complexity and expense of this approach make its widespread use unlikely [64].

15.3.2.3 Combined Pharmacologic and Exercise Stress Testing

Many laboratories have found it useful to combine low level treadmill exercise with either adenosine or dipyridamole. This has been found to reduce the unpleasant side effects of flushing, headache, dizziness or nausea due to either stressor. Image quality is also improved through a decrease in hepatic and gut uptake of the technetium-99m perfusion tracers, which is more common with adenosine or dipyridamole, compared to exercise [65, 66]. On the other hand, the incidence of stress-inducible ischemia is more common due to increased myocardial demand, leading to a higher prevalence of ischemic chest pain and ischemic ECG changes. The combination of adenosine and symptom-limited exercise in patients who can exercise but where it is not certain that they can attain maximal heart rate, has been found safe and useful to achieve maximal level of stress [67]. Combined exercise with pharmacological stress should be avoided in patients with left bundle branch block or RV pacemaker, since the likelihood of false positive myocardial perfusion stress images is increased with exercise.

15.3.2.4 Investigational Pharmacological Stress Agents

The currently used vasodilator stress agents, adenosine and dipyridamole, are effective and useful, but they do have significant side effects, making stress testing an unpleasant experience in many patients, and are contraindicated in patients with bronchospastic disease. It has been established that there are four adenosine receptor subtypes: A_1, A_{2A}, A_{2B}, and A_3. Selective activation of A_{2A} receptors leads to coronary vasodilation, while A_1 are responsible for decreased AV conduction and chest pain, while stimulation of A_{2B} receptors leads to peripheral vasodilation, mast cell degranulation, and bronchiolar constriction, and stimulation of A_3 leads to ischemic pre-conditioning and mast cell degranulation [68]. A number of very effective selective A_{2A} receptor agonists have been developed and tested. They include CGS-21680, MRE-0470 (Binodisine), CVT-3146, and ATL-193 and ATL-146e. They all share the ability for selective A_{2A} receptor stimulation and decreased side effects of decreased AV conduction and chest pain, peripheral vasodilation, and bronchospasm. They are administered as a bolus. These properties and increased safety make these agents highly desirable for pharmacologic stress testing.

15.3.3 Methods of SPECT Imaging

15.3.3.1 SPECT Imaging

Single photon emission computed tomography (SPECT) has by now been well standardized and optimized for either thallium-201, Tc-99m-sestamibi or Tc-99m-tetrofosmine imaging as well as optimized for each imaging system manufacturer. This includes timing of acquisition, choice of collimators, choice of step-and-shoot vs contiguous acquisition, circular vs elliptical orbits, filtered vs iterative reconstruction, filtering, display, quantification, and correction for movement artifact. The greatest area of concern and therefore undergoing the greatest evolution is the challenge of addressing inaccuracies in diagnoses and inefficiencies in patient management arising from mistaking soft-tissue attenuation artifacts from true perfusion defects.

Solutions to the problem of soft tissue attenuation include training in recognition by the technologist and interpreting physician and the utilization of various compensation strategies, prone imaging, ECG gating, image quantification, and the use of attenuation correction hardware and corrective reconstruction.

Inspection of the original multiplanar images allows one to detect movement artifact, as well as ascertain the presence of overlapping soft tissue likely to cause attenuation artifact, either due to an overlapping diaphragm, causing inferior wall defects, or in women and obese men, overlapping breast tissue, causing anterior, anteroseptal, or anterolateral defects. This allows the interpreting physician to properly evaluate the obtained images and avoid an unnecessarily false positive reading.

If an inferior wall defect is recognized early, while the patient is still in the laboratory, it has been demonstrated that inferior wall defects due to attenuation artifact seen in the standard supine position resolve after repeat imaging in the prone position, which improves diagnostic accuracy. Limitations of this approach include the creation of a new anterior wall attenuation defect, and the apparent lack of efficacy in anterior wall attenuation artifacts [69, 70]. Nevertheless, this strategy is useful when other means are not available, or in combination with gated SPECT imaging.

15.3.3.2 Gated SPECT Imaging

ECG gating of the SPECT myocardial perfusion images provides, independently from the perfusion information, important information on global LV and RV function, the LV ejection fraction, and regional wall motion and thickening. This information provides information that incrementally adds to the value of myocardial perfusion imaging alone. It can also help enhance the accuracy of perfusion imaging. The presence of a wall motion abnormality corresponding to a perfusion abnormality, and the presence of disease, can be seen with greater confidence, resulting in enhanced accuracy [71]. However, normal wall motion associated with a reversible perfusion defect does not exclude reversible ischemia. Normal wall motion in the presence of mild to moderate fixed perfusion abnormality could be due to non-transmural wall injury, insufficient to cause a discernible wall motion abnormality.

15.3.3.3 Quantification

Quantitative analysis of myocardial perfusion images compares the patient's distribution at rest and during stress, after normalization to an area of best tracer uptake, against an aggregate profile obtained from patients with known absence of disease. Software developed for this purpose provides indices of the extent and severity of perfusion abnormalities outside the normal limits, at arrest and stress, plus an index of change between stress and rest. These indices are expressed for the entire myocardium, for each of the coronary vascular territories, or arbitrary segments (e.g., quadrants). These normal limits reflect the average differences between men and women, as well as a range of regional variation commonly seen in low risk subjects. The use of this technique has been shown to enhance the accuracy of interpretation for a single reader, or for readers who are less than expert [72]. The use of one of the commercially available software packages also provides standard indices that provide objective indices that can be utilized for serial studies. It also provides an index of LV cavity size, which is of prognostic usefulness (see below). Quantification of gated SPECT images provides a global LVEF, plus indices of regional wall motion and wall thickening, useful in evaluation of function.

Nevertheless, quantification of relative distribution of tracer at rest and stress does not express absolute uptake, thus being unable to alert for a diffusely uniform decrease in uptake during stress, indicating diffuse or extensive disease, which can be obtained only from quantitative PET imaging. In addition, quantification does not help one decide if a defect is due to disease or attenuation artifact [72, 73].

15.3.3.4 Attenuation Correction

Commercial SPECT attenuation correction systems determine the distribution of nonuniform attenuation in the chest utilizing an external source of radiation, with either external collimated radionuclide sources [74, 75], or x-ray CT offered on hybrid SPECT/CT systems [76, 77]. The former systems use collimated stationery or moving line sources of gadolinium-153 (Gd-153), which has a physical half-life of 242 days, with photon energies of 97 and 103 kev [78]. Emission and transmission information is separated with physical collimation of the radiation sources and electronic masking of the field of view of the detector during simultaneous emission-transmission imaging, or in some systems, by sequential imaging. In other systems, separation is achieved during simultaneous acquisition of emission and transmission information with either Gd-153 or, alternatively, using barium-133 (Ba-133) (physical half-life of 10.5 years, gamma energy 356 kev) [79] by energy separation.

For the external radiation source transmission scans, limitations include limited source strength, and therefore additional introduced noise, crossover between emission and transmission data. Sequential emission-transmission imaging has the disadvantage of a greater chance for misalignment of the two scans due to body movement or changed respiratory pattern.

Hybrid SPECT/CT systems, combining a multidetector SPECT gamma camera with a single slice, and most recently, multislice CT, developed for oncology and bone imaging, have been applied for cardiac imaging with attenuation correction. The attenuation map is provided by a low-dose non-contrast CT scan, performed after the emission scan [76, 77]. An advantage of CT transmission imaging is greater photon flux, and thus less noise. A disadvantage is the production of unique artifacts from metallic objects, such as stents, pacemakers, and ECG leads [80].

Regardless of the type of manufacturer, careful attention is required to minimize additional image noise introduced by the attenuation correction by good quality control and the use of iterative reconstruction. Care is needed to minimize and compensate for truncation and its artifacts, and minimize misregistration. Attenuation-corrected images are sensitive to artifact stemming from intense subdiaphragmatic activity close to the heart, particularly activity that is changing or in motion in the course of the acquisition [81].

In spite of inauspicious results with early attenuation correction that did not take into account scatter and depth-dependent resolution blur, attenuation correction has been shown to achieve significant improvement in the specificity of detection of coronary disease, across a wide spectrum of multiple centers with differ-

ent methods of attenuation correction [82, 83]. ECG gating and attenuation correction appear to provide synergistic and complementary improvement in diagnostic accuracy [84, 85]. The improvements in specificity as a result of attenuation correction were seen in all patients, but particularly in obese individuals [86]. This has enabled the use of a single normal database for both men and women [87]. The improved detection of patients with disease and identification of patients with normal perfusion has also facilitated the practice of stress-only imaging, thereby saving time and cost of SPECT imaging [88].

15.3.4 Clinical Utility of Myocardial Perfusion Imaging

Initially, myocardial perfusion imaging was a primarily diagnostic method for noninvasive detection of coronary artery disease. Over the past decade and a half, the emphasis has shifted from diagnosis to evaluation of prognosis. Analysis of extensive clinical, angiographic, and perfusion databases has identified patients who are at high risk for adverse outcome (death or nonfatal cardiac events) [89, 90]. Advances in surgical, percutaneous, and medical therapy of CAD have fundamentally changed the natural history of the disease. Thus, appropriate identification of high-risk patients, followed by appropriate therapy, favorably modifies prognosis. Conversely, identification of low-risk patients with a benign prognosis reduces the need for costly and potentially detrimental invasive testing and therapy. A normal SPECT myocardial perfusion imaging study has been shown to be extremely effective in predicting a good prognosis in a variety of settings.

15.3.4.1 Diagnosis

Appropriate candidates for stress testing with MPI are patients with intermediate pre-test probability for the presence of coronary artery disease. The pre-test probability is determined from easily obtained parameters: age, gender, symptoms, and the presence of hypertension, diabetes, smoking, hyperlipidemia and family history [91]. Such patients might be chronically symptomatic patients with some atypical features at presentation. MPI is inappropriate for patients with a low pretest probability due to the high rate of false-positive results. Patients with several risk factors for CAD and typical symptoms with a high probability of CAD do not gain so much from MPI for diagnosis, as the diagnosis is nearly certain on clinical grounds. However, such patients would benefit from MPI for risk stratification. Exercise stress testing without MPI is inadequate for diagnostic purposes in patients who are unable to exercise adequately and in those with nondiagnostic baseline ECG, such as LBBB, paced rhythm, left ventricular hypertrophy, or users of digoxin [94]. In other patients, MPI adds to the diagnostic accuracy of ECG stress testing alone.

Average sensitivity and specificity of MPI for diagnosis of CAD have been reported close to 90% and 70%, respectively. The gold standard for diagnosis of CAD remains coronary angiography, despite its known limitations and likely systematic underestimation of the extent of disease. True sensitivity and specificity with each new tracer and each new imaging protocol has been difficult to ascertain because of post-test angiographic referral bias. Patients with negative results on MPI are rarely referred for coronary angiography. This practice is justified because of the known excellent prognosis of patients with a normal MPI study [92]. Nevertheless, this limits the usefulness of retrospective validation studies using a clinical test population.

15.3.4.2 Prognosis

Several distinct patient groups are commonly referred for MPI:

1. Patients with stable CAD evaluated for prognosis
2. Patients with acute chest pain syndromes
3. Patients after an acute myocardial infarction
4. Patients followed after revascularization procedures (CABG, PTCA, coronary stenting)
5. Patients evaluated prior to noncardiac surgery
6. Patients surveyed after cardiac transplantation for presence of transplant vasculopathy

15.3.4.2.1 Risk Stratification in Stable CAD

Recent technological advances in image acquisition and processing such as tomographic imaging (SPECT), gating, attenuation correction, and Tc-99m-based tracers allow for more accurate simultaneous evaluation of myocardial perfusion and function. Perfusion abnormalities can be classified according to size, localization, severity, and reversibility. Left ventricular volumes, systolic wall thickening, segmental wall motion, and ejection fraction can be quantified. Right ventricular size and function can be assessed.

Retrospective and prospective observations have defined patterns which are compatible with high-risk prognosis as well as benign prognosis. A normal perfusion pattern in patients with an adequate level of stress and with high quality study is consistent with an excellent short-term prognosis, regardless of coronary anatomy [92]. Extent of perfusion abnormalities characterized by number of abnormal segments, severity of defects, and extent of reversibility (ischemia) define prognosis. When integrated with results of the exercise

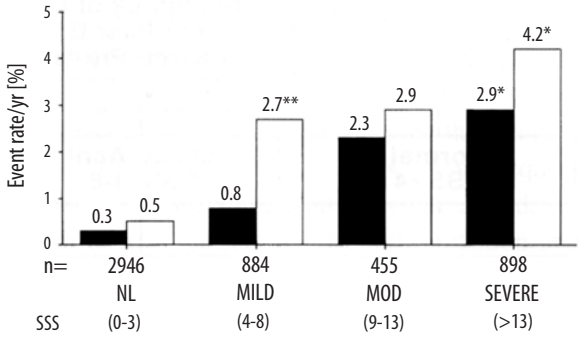

Fig. 15.12. Rates of cardiac death (*solid bars*), and MI (*open bars*) per year, as a function of scan result. The number of patients within each category is shown underneath each pair of bars. *NL* normal, *MILD* mildly abnormal, *MOD* moderately abnormal, *SEVERE* severely abnormal. (Reproduced from [90] with permission)

stress test and parameters of left and right ventricular function, combined information has a prognostic value which exceeds prognostication based on performance of coronary angiography [90] (Fig. 15.12). The average annual cardiac event rate in patients with abnormal images is 12-fold that in patients with normal images. Both fixed and reversible defects are prognostically significant. Fixed defects are a predictor of death, whereas reversible defects are an important predictor of nonfatal myocardial infarction [93]. The event rate is significantly greater in patients with severe than in those with mild abnormalities (10.6% annual hard event rate vs 3.5%) [94]. Incorporation of other SPECT variables, such as LV dilation, LVEF, and LV volumes, further enhances the prognostic power of SPECT imaging [94–96]. A high likelihood of multivessel (hence surgical) CAD is indicated by the presence of perfusion defects in each of the three coronary artery territories: diffuse slow washout of Tl-201, prominent pulmonary Tl-201 activity, transient LV dilation, and the "left main pattern" of anterior, septal, and posterolateral defects [97].

15.3.4.2.2
Acute Chest Pain Syndromes

Acute chest pain may be due to myocardial ischemia as a result of a coronary artery plaque rupture and may be potentially life threatening. However, in only 40% of emergency department (ED) visits for chest pain is the pain of cardiac origin. Rapid and reliable triage is needed for speedy diagnosis of acute myocardial infarction, and to prevent unnecessary hospitalizations and inappropriate discharges from the ED [98]. Current diagnostic tools include clinical observation, serial ECGs, ST segment monitoring, serial measurements of serum markers of myocardial necrosis (such as CK-MB, troponins), and noninvasive cardiac imaging. Many medical centers have recently established dedicated chest-pain evaluation units, usually adjacent to the ED. Some centers perform MPI at rest. Abnormal results lead to hospital admission. Others perform stress testing, with or without MPI, 6–12 h after a negative workup for an acute MI [99, 100]. Based on the results of MPI, a patient's short-term prognosis can be determined. Safety of early stress testing has been well documented. In several cost analyses, up to a 50% decrease in hospital charges and a 50% shorter hospital stay can potentially be realized [101]. In another study, a cost saving of $800 per patient was reported [102]. In still another, a cost saving of $4,000 per patient was realized if patients with normal resting myocardial perfusion images were discharged home from the emergency department [103].

15.3.4.2.3
MPI After an Acute Myocardial Infarction

The purposes of early or pre-discharge MPI evaluation after an acute myocardial infarction are (a) to assess the extent of sustained damage, including determination of the ejection fraction, and (b) to detect residual ischemia, both in the infarct-related territory and in the other vascular territories using either exercise MPI (Fig. 15.13) or pharmacological stress (Fig. 15.14). In the era of acute interventions (i.e., thrombolysis, PTCA), the urge to perform invasive assessment (by angiography) is often irresistible. However, recent reports support a less aggressive approach: Patients with a limited amount of ischemia after an acute myocardial infarction can be risk stratified noninvasively and, if found to have a low-risk profile, treated medically with the same results as those treated with interventions [106–108].

15.3.4.2.4
MPI in Patients After Revascularization Procedures

In view of the possibility of re-stenosis after percutaneous revascularization and of aortocoronary bypass graft closure after coronary artery bypass surgery, and the frequent absence of reliable symptoms, MPI is an efficient means to determine the need for additional and/or repeat interventions [109–111].

15.3.4.2.5
MPI Prior to Noncardiac Surgery

Preoperative evaluation for noncardiac surgery depends partly on a patient's risk factors. These include severity and/or stability of known heart disease, the presence of concomitant conditions such as diabetes mellitus, peripheral vascular disease, renal insufficiency, pulmonary disease, urgency of the surgery (emergency vs. elective), and type of surgery planned. Several principles for preoperative evaluation are summa-

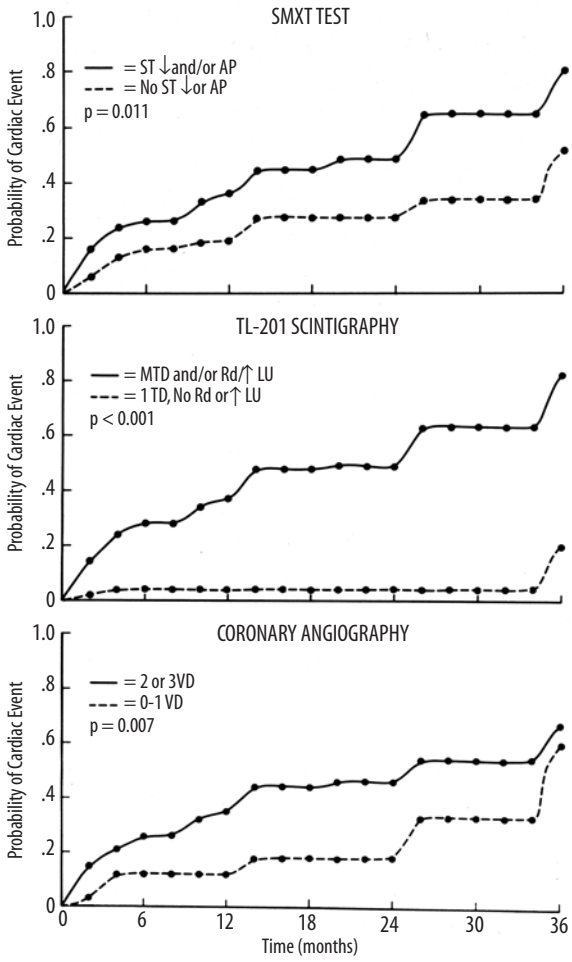

Fig. 15.13. Cumulative probability of cardiac events as a function of time for different subgroups formed by exercise test response (*top*), scintigraphic findings (*middle*), or angiographic findings (*bottom*) before hospital discharge following myocardial infarction. The *solid* and *dashed lines* represent the high-risk and low-risk cumulative probability, respectively. (Reproduced from [104] with permission)

rized in the 2002 AHA/ACC Task Force guideline update recommendations [75]:

1. In case of life-saving surgery, no cardiac evaluation is needed and it should be performed, if necessary, after the surgery.
2. No evaluation is needed in stable patients with a history of revascularization in the past 5 years.
3. Cancellation or delay of elective surgery should be considered for patients with unstable angina, decompensated CHF, significant arrhythmia, and/or severe valvular disease (major predictors).
4. Patients with mild angina, history of myocardial infarction, compensated CHF, diabetes mellitus (intermediate predictors) and those with abnormal ECG at rest, advanced age, nonsinus rhythm, low functional capacity, history of stroke, and uncontrolled arterial hypertension (mild predictors) should be triaged according to their functional capacity and according to the risk of planned surgery to noninvasive stress testing (MPI or stress echocardiography).

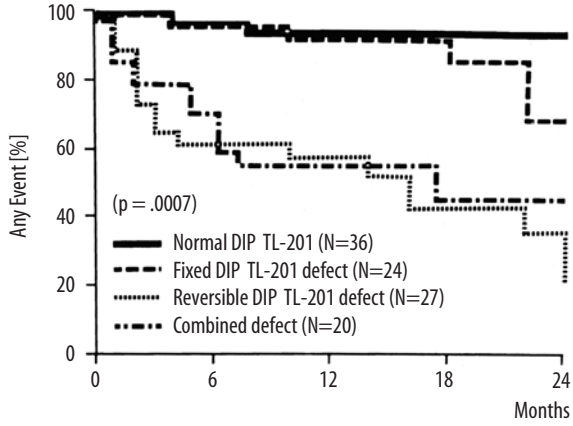

Fig. 15.14. Incidence of cardiac events (cardiac death, nonfatal myocardial infarction, unstable angina pectoris, or occurrence of functional class III or IV angina or the need for a revascularization procedure) in 107 asymptomatic patients with coronary artery disease stratified by intravenous dipyridamole (*DIP*) thallium (*TL*) results. *N* number of patients at entry. (Reproduced from [105] with permission)

There is currently no evidence that preoperative revascularization alters the outcome of noncardiac surgery. However, risk stratification based on preoperative testing can help the patient and physician choose the best type and timing of surgery, perioperative care, and long-term postoperative management.

15.3.4.2.6 MPI After Cardiac Transplantation

Long-term survival after heart transplantation, in excess of 80% after 1 year, is now common [113, 114]. Immunologically mediated obstructive coronary vasculopathy has emerged as the most devastating late complication. Pain symptoms of myocardial ischemia are absent because of denervation of the transplanted heart. Frequent invasive (angiographic) evaluation is not practical. MPI (and perhaps stress echocardiography) are emerging as surveillance methods for detection of asymptomatic myocardial ischemia [115, 116].

15.4 Myocardial Perfusion PET Imaging

In spite of its high diagnostic accuracy and prognostic value, conventional myocardial imaging suffers from limitations of attenuation artifact and spatial nonuni-

formity, only partially mitigated by gated acquisition or attenuation correction [117], limited resolution, and decreased tracer extraction fraction during stress [118]. Limitation is posed in some patients by inadequate exercise level, and by an occasional inadequate effect of pharmacological stress.

15.4.1 Principles of PET Imaging

PET myocardial perfusion imaging offers an alternative for patients with these difficulties. PET imaging utilizes tracers containing isotopes which decay by the emission of positrons; these undergo annihilation together with a local electron to produce two simultaneous high-energy 511 keV photons, 180° apart. Positron emission tomography (PET) gamma cameras are able to document these events through coincidence detection. Localization is achieved electronically, rather than through collimation, greatly enhancing sensitivity. Resolution is also significantly improved (4–6 mm) compared with SPECT or planar imaging (1.5–2.5 cm). The attenuation fraction of the coincident pair of photons is high but uniform along any given path. Attenuation correction is achieved with a separate PET acquisition for each subject using an external source of coincident photons. This is done either by a rotating rod sources containing germanium-68, or more frequently now, with a CT scan contained within a hybrid PET-CT scanner. This transmission acquisition yields an attenuation map, which is used to correct the emission images.

Limitation on resolution comes from: (a) the mean distance that the positron travels before undergoing annihilation [119–121]; (b) the deviation from 180° of the angle between the two coincident photons, depending on the positron momentum at the time of annihilation, producing an error of about 1.7 mm [122]; (c) the proportion of coincident photons which undergo scatter; (d) random coincidences [123, 124]; (e) the noise of acquisition and that introduced by the attenuation correction; and (f) the intrinsic resolution limit of the gamma camera itself. Modern PET cameras achieve an intrinsic resolution of 3–5 mm [125].

15.4.2 Cardiac PET Perfusion Tracers

The most common PET myocardial perfusion tracers include N-13 ammonia, rubidium-82, and O-15 water (Table 15.4). Only rubidium-82 and N-13 ammonia are approved for clinical use. Both N-13 ammonia and O-15 water require an on-site cyclotron and a chemistry laboratory equipped to produce the tracer. Excellent timing between production and patient use is required, due to their short half-lives. Rubidium-82 is produced on site by a commercially available generator consisting of an alumina column containing strontium-82, which decays to rubidium-82, which is eluted with saline. Its availability is reestablished within 6–8 min after each use. The generator is changed every 4 weeks.

Table 15.4. Positron-emitting tracers of myocardial blood flow

Agent	Physical half-life	Mean positron range	Production
N-13 ammonia	9.8 min	0.7 mm	Cyclotron
Rubidium-82	75 s	2.4 mm	Generator
O-15 water	2.0 min	1.1 mm	Cyclotron

The imaging session begins with a short scout perfusion acquisition or a scout transmission CT scan, in order to position the patient within the scanner properly. The perfusion tracer is injected intravenously at rest, followed by a PET acquisition, and again during pharmacological stress with intravenous dipyridamole, adenosine, or dobutamine/arbutamine. The rest and stress perfusion studies can and should be gated, if possible, providing valuable information about LV function at rest and during stress. In the case of a dedicated PET scanner, a pin-source transmission scan is usually performed between the rest and the stress perfusion scan. With a PET-CT scanner, a CT transmission scan with each of the rest and stress perfusion scans is performed. It is possible to perform supine bicycle exercise on the imaging table, but this has been the exception. Except for N-13 ammonia, the half-life of Rb-82 and O-15 is too short to allow imaging with exercise on a treadmill. On the other hand, the short half-lives allow a quick succession of resting and stress acquisition and multiple interventions, including vasodilation, hand grip, hand ice immersion, or mental effort [132].

15.4.2.1 N-13 Ammonia

In the blood stream, N-13 ammonia consists of the neutral NH_3 molecule in equilibrium with NH_4^+. At normal pH, NH_4^+ is the predominant form. The neutral, lipid-soluble NH_3 readily crosses cell membranes by diffusion. Inside the cell, the NH_3 converts into NH_4^+ and is trapped in the cell as glutamine in a reaction catalyzed by glutamine synthase [129]. Egress from the cell is slow, mostly through catabolism of proteins and amino acids. N-13 ammonia has been used as a PET myocardial perfusion agent since 1972 [133] with either pharmacological or exercise stress. Its extraction fraction remains high even with high flows during pharmacological vasodilation, although under severe metabolic derangement, the glutamine synthase pathway can be blocked and the uptake of N-13 ammonia can become low [134]. Its half-life allows high-quality image acquisition and gating. In dogs, Gould et al. demonstrated

Reference	Agent	Stress	No. subjects	Sensitivity (%)	Specificity (%)
CAD patients					
Tamaki et al. [127]	NH_3	Exercise	19	95	95
Allan et al. [128]	Rb-82	Exercise	25	–	96
Schelbert et al. [129]	NH_3	Dipyridamole	32	90	97
Gould et al. [130]	NH_3, Rb-82	Dipyridamole	50	–	95
Normal subjects					
Tamaki et al. [127]	NH_3	Exercise	6	–	100
Deanfield et al. [131]	Rb-82	Exercise	16	–	100
Schelbert et al. [129]	NH_3	Dipyridamole	13	–	100

Table 15.5. Detection of coronary artery disease with PET perfusion imaging [126]

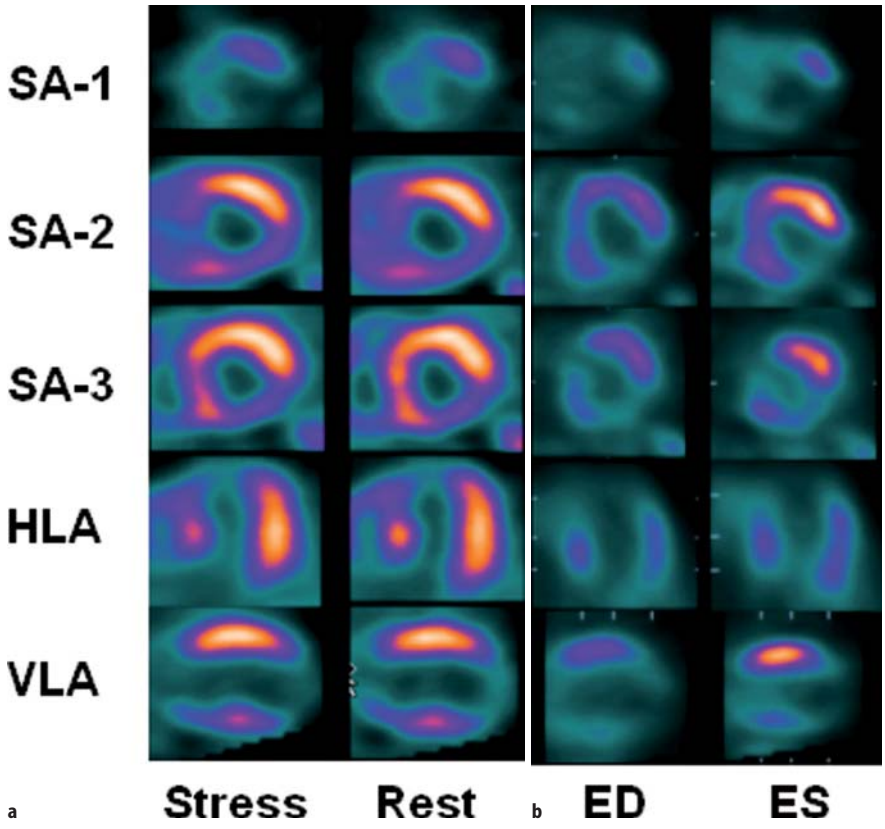

Fig. 15.15. a Stress and rest of Rb-82 PET images demonstrating severe extensive apical, septal, and inferior scarring and only minimal basal septal ischemia. **b** Resting end-diastolic and end-systolic gated images, showing poor or absent contractility in the scarred regions, and poor overall LV function

that coronary stenoses of 47% or greater can be detected by perfusion imaging with N-13 ammonia in conjunction with i.v. dipyridamole [135]. In human beings, Schelbert et al. correctly identified 52 of 58 stenosed vessels (90% sensitivity per vessel) and correctly diagnosed the presence of CAD in 31 of 32 patients (97% sensitivity) [129]. Tamaki et al. [136] demonstrated a sensitivity of 95% for N-13 ammonia rest and exercise stress imaging (Table 15.5).

15.4.2.2 Rubidium-82

Rubidium-82 is a potassium analogue. Like Tl-201, Rb-82 is transported into cells by the Na^+/K^+ ATPase pump. Like Tl-201, Rb-82 extraction decreases at high blood flow [95, 96] and can be altered by drugs, severe acidosis, hypoxia, and ischemia [139–141]. With ischemia, segmental reduction of Rb-82 uptake can persist following exercise, even after symptoms and ECG abnormalities have resolved, for up to 30 min. Owing to its short half-life (75 s), Rb-82 is injected at a high dose (30–60 mCi); this is followed by a short acquisition lasting 4–6 min. The imaging sequence can be fast and efficient. An example of rest and stress Rb-82 PET myocardial perfusion images and gated resting images is shown in Fig. 15.15. In chronically instrumented dogs, Mullani et al. detected coronary stenoses of 50% or greater with Rb-82 imaging and dipyridamole stress [142]. Gould et al. [130] compared Rb-82 rest and dipyridamole-hand grip stress imaging with a validated quantitative flow reserve index obtained from contrast

angiograms. The results showed a sensitivity of 95% and a specificity of 100% for impaired flow reserve.

The rubidium-82 generator needs to be replaced 13 times per year. Its advantage is 24-h availability in PET centers that do not have a cyclotron, or where the cyclotron is preoccupied with production of other isotopes. The disadvantage of Rb-82 is the high fixed cost of the generator, which rivals the yearly costs of a PET camera or cyclotron. It is thus feasible only in centers with a high volume of cardiac PET perfusion imaging. Generally, centers that have an on-site cyclotron perform perfusion imaging with N-13 ammonia, due to the already built-in overhead costs of the cyclotron. Due to the high energy of the positron emitted by Rb-82, the mean travel of the positron is higher compared with the other positron-emitting isotopes, making resolution slightly worse than for F-18 FDG or N-13 ammonia. Due to the short half-life of Rb-82, the images tend to be noisier, especially on older PET instruments with lower sensitivity. This disadvantage is mitigated with the higher sensitivity of 3D PET imaging, but which has to contend with dead-time and high rate of random coincidences and scatter.

15.4.2.3 Oxygen-15 Water

The use of O-15 water is limited to quantification of coronary blood flow. Water enters all cells by diffusion, with a high extraction fraction even at high myocardial flow. Owing to the very short half-life of O-15, the tracer must be produced by an on-site cyclotron. The images tend to be noisy, and the rapid equilibration between blood pool and the myocardium prevents good quality imaging of the myocardial phase. Routine clinical use could tie up a cyclotron just for this indication in a large number of patients. Therefore, for combined clinical use and quantification of blood flow, N-13 ammonia has been used more extensively in centers equipped with a cyclotron.

15.4.3 Applications of Cardiac PET Perfusion Imaging

PET myocardial perfusion imaging offers reliable attenuation correction, thus avoiding the attenuation artifacts seen frequently in SPECT imaging, although caution needs to be exercised to recognize and correct for PET emission-transmission misregistration artifacts. PET imaging also offers higher resolution, although if used without gating, the higher resolution is not fully taken advantage of. The high energy of the positrons from Rb-82 also prevents a full utilization of the inherent high resolution of PET. Because clinically useful risk stratification needs to detect significant myocardial mass with disease risk, spatial resolution is not critical in deciding to use PET vs SPECT imaging. The higher resolution is definitely helpful in children with anomalies of coronary arteries, or after repair procedures, such as the switch operation [143, 144]. The high extraction fraction of the PET tracers, especially N-13 ammonia and O-15 water, assures higher sensitivity for disease at high flows during pharmacological stress, resulting in the ability to reliably detect coronary disease down to about 50% occlusion [147, 148] (Table 15.5). A number of studies have shown a higher accuracy of coronary disease detection by stress PET imaging compared with SPECT Tl-201 imaging [145–147, 149] (Table 15.6). Comparisons of sestamibi and PET perfusion imaging showed that adenosine stress MIBI SPECT imaging significantly underestimates ischemia and defect severity compared with N-13 ammonia PET [150]. More recent studies indicate that the most up-to-date PET imaging achieves both higher sensitivity and specificity for detection of coronary artery disease compared to gated Tc-99m-sestamibi SPECT imaging, both with [151] and without SPECT attenuation correction [152]. Figure 15.16 illustrates such a case. The gating of MPI at rest and during stress with PET imaging allows the additional diagnostic and prognostic relevant information about the severity of disease. Positron emission tomography for myocardial perfusion is an expensive option, due to the high cost of a PET or PET-CT camera ($1–2 million) and of either cyclotron produced isotopes or the Rb-82 generator. Patterson et al. [153] have modeled the clinical use of Rb-82 perfusion imaging, stress ECG, Tl-201 SPECT perfusion imaging, and coronary angiography in the diagnosis of CAD. Using published data for accuracy and costs of procedures, assumptions of some cost savings from making the right diagnosis, and costs incurred when the diagnosis is missed, they found PET perfusion imaging to be more cost-effective (lowest cost/deltaQALY) than the other modalities in populations with a low to intermediate probability of CAD. Savings were realized through reductions of costs of missing disease and reduction in costs from unnecessary additional diagnostic and therapeutic procedures. A preliminary study came to the same conclusions when comparing PET myocardial perfusion imaging with stress echocardiography and

Table 15.6. Comparison of PET and conventional perfusion imaging for CAD detection

Reference	Tracer	Accuracy (%)	Sensitivity (%)	Specificity (%)
Schelbert et al. [129]	NH_3		90	
	Tl-201		58	
Go et al. [145]	Rb-82	92	95	82
	Tl-201	78	79	76
Stewart et al. [146]	Rb-82	84	88	85
	Tl-201	84	53	79

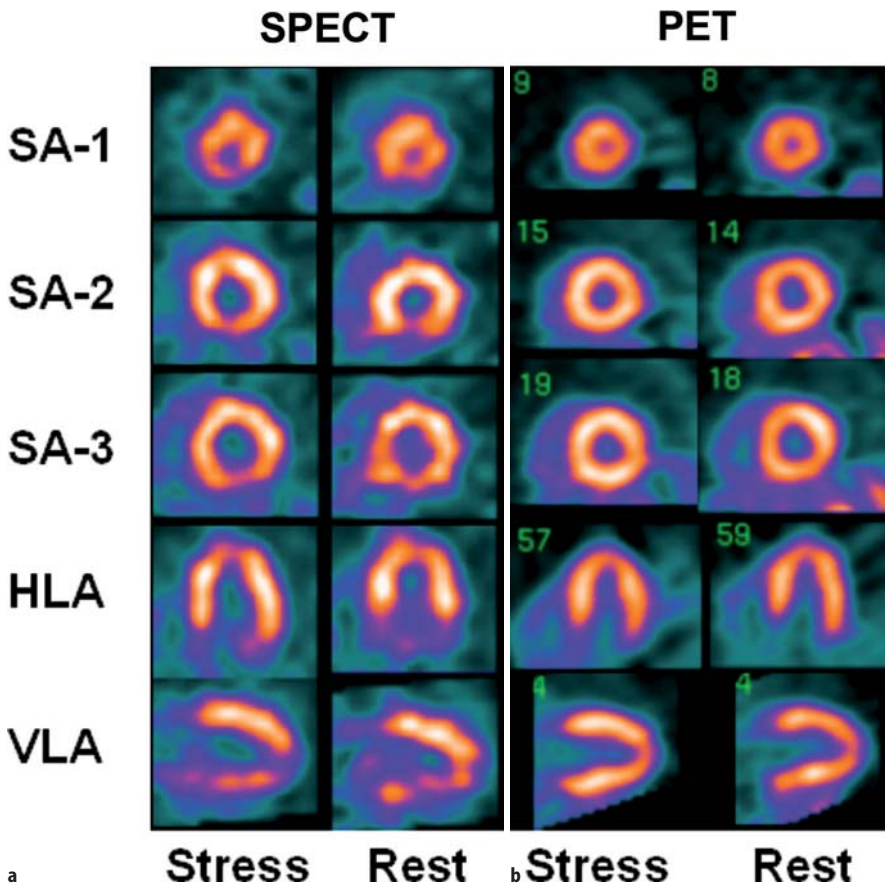

Fig. 15.16. a Stress and rest attenuation-corrected (AC) Tc-99m-sestamibi SPECT images of a 290-lb, 51-year-old male. The SPECT image shows mild to moderate inferior and apical ischemia and partial scarring. **b** The stress and rest PET images show normal distribution

coronary angiography [154]. This model was verified by clinical cost-effectiveness in 1,582 patients with intermediate risk of CAD, with a 25% reduction in management costs due to reduced rate of angiography and CABG surgery [155]. Myocardial PET perfusion imaging has been approved by the CME for reimbursement by Medicare and is reimbursed by most insurance plans. From a more conservative point of view, PET perfusion stress imaging is justified in cases where conventional methods are inconclusive or conflicting, or where technical artifacts, e.g., obesity or breast attenuation artifact, are likely to limit the accuracy of conventional imaging.

The ready availability of Rb-82 from a generator allows the PET scanner to be used in patients with acute chest pain [156–159] where logistics and location permit. Goldstein et al. studied 14 patients with Rb-82 within 96 h of onset of symptoms. Positron emission tomography correctly identified segmental blood flow reduction in all instances of myocardial infarction [160]. PET imaging has been shown to be more reliable than ECGs in distinguishing transmural from nontransmural infarction and in the localization of infarction [161].

PET MPI, similarly to SPECT MPI, has great prognostic value, although the literature with PET imaging is less well developed. Marvick et al. noted that defect severity with PET was related to outcome [162]. Work by Yoshinaga et al. supports these findings [163]. Recent work by Chow et al. [164] indicates that patients with normal ribidium-82 PET MPI have good prognosis, regardless of ECG changes during stress. Work by Nemirovsky et al. supports these findings [165]. Even though this field needs to be developed, it is expected that the prognostic value of PET MPI is expected to, at a minimum, match the results with SPECT perfusion imaging.

From the beginning, PET perfusion rest and stress imaging has shown its value in basic and clinical research endeavors, based on its ability to measure absolute myocardial perfusion. Conventional methods of expressing blood flow reduction pose significant difficulties. Regional blood flow reduction is usually expressed as a ratio of abnormal to maximal uptake, without consideration of the nonlinearity of the relation of the blood flow response and uptake of all diffusible tracers (Fig. 15.10). The same ratio may describe widely different relations in flow reductions.

The high degree of uniformity through attenuation correction in PET allows calibration of the PET imaging system, so that the absolute activity in the myocar-

dium can be measured. Unlike routine myocardial perfusion imaging, which requires only a single "snapshot" of tracer distribution at rest and again at stress, quantification of blood flow requires a dynamic acquisition of both blood pool and myocardial activity. Combined with a suitable compartmental model and a method of measuring or estimating the concentration of tracer in arterial blood, myocardial perfusion can be regionally quantified with N-13 ammonia, Rb-82, or O-15 water [128, 166–169]. Using beta probes and an open-chest dog model, Mullani et al. validated their method of flow quantification using first-pass bolus imaging of Rb-82 [170–172]. This was also validated using PET imaging with either N-13 ammonia or Rb-92 and a compartmental model in dogs. Compared with coronary flow and flow-reserve measurement using coronary electromagnetic flow probes, Yoshida et al. obtained correlation coefficients of 0.94 for N-13 ammonia and 0.88 for Rb-82. A simplified, more practical imaging protocol yielded a correlation of 0.98 and 0.94 between the simplified model and the complete compartmental model for Rb-82 and N-13 ammonia, respectively [173].

Quantification of blood flow at rest and during maximal pharmacological stress allows measurement of flow reserve in various hypertrophies and cardiomyopathies, post-transplant CAD [174], syndrome X, and other vascular endothelial disorders, and to study the effects of smoking, various medications [175–177], and lipid control [178–181].

Ultimately, utilization of PET for perfusion imaging will be determined by a combination of complex factors such as clinical needs, availability and cost of PET gamma cameras and tracers, and reimbursement for outpatients and inpatients. At this time, the number of available PET cameras is rapidly growing, fueled by the acceptance of PET imaging in clinical oncological applications and making its availability for myocardial imaging, at least on a part-time basis, easier than in the past. It is for these reasons that PET MPI has witnessed rapid growth recently.

15.5 Hybrid Myocardial Perfusion and CT Imaging

15.5.1 CT Attenuation Correction

Combined PET and CT imaging in a single combined PET-CT unit has become the preferred approach for PET imaging in oncology. For cardiac PET imaging, the scout CT checks the position of the patient in a few seconds. The CT transmission scan, lasting 10–30 s, saves a significant amount of time compared to transmission imaging using radiation pin-sources. The CT transmission scan is relatively noise-free, compared to the dedicated PET transmission scan. It enables one to perform an entire rest and pharmacological stress PET perfusion imaging study with rubidium-82 in 30–40 min, compared to 45–60 min for a dedicated PET scanner.

PET-CT imaging holds both challenges and solutions for attenuation correction. There is potential for transmission emission scan misregistration, particularly for the stress perfusion study, which is susceptible to changes in heart and diaphragm position due to changes in respiratory pattern during stress. This occurs about 10% of the time, with a potential significant impact in about 5% of patient studies [182]. The CT transmission and PET emission images can be easily displayed using existing software. It has become standard practice in some labs to perform a separate CT transmission scan at rest and during stress.

The lower energy high resolution (80–120 kev) x-rays of the CT attenuation correction scan are also more susceptible to artifacts produced by metallic implants or pacemakers than the 511 kev gamma photons of the pin-source transmission scans. The shorter amount of time (10–30 s) taken by the CT transmission scans makes it more vulnerable to diaphragm motion artifact, compared to the much longer time required for the pin-source transmission scan, which averages the heart and diaphragm motion over several minutes.

The hybrid SPECT-CT imaging system was originally designed for oncology and bone imaging. Following a SPECT emission acquisition, a CT transmission scan can be obtained, which is less noisy than radioactive-source transmission scans. In a study using chest phantoms, O'Conner et al. found that the imaging system with SPECT attenuation correction with a CT transmission scan produced more accurate attenuation correction than other systems with either fixed or moving radioactive moving line sources [183]. On the other hand, sequential emission-transmission imaging is more susceptible to misregistration artifact. Other manufacturers have more recently developed SPECT-CT hybrid systems with higher quality 2–16 slice CT scanners. These multislice CTs are capable of more than just attenuation correction.

15.5.2 Calcium Scoring

Another application of PET-CT and SPECT-CT is the possibility of obtaining coronary calcium scores in the same imaging session as the PET or SPECT MPI, which is feasible with an 8- or 16-slice multidetector CT scanner. Calcium scoring requires gating and a higher current from the CT scanner than a transmission scan, resulting in higher patient radiation exposure, but still lower than diagnostic CT imaging.

The clinical value of coronary calcium scoring is at this time still an open question in clinical practice.

Shaw et al. showed in a large observational data series that coronary calcium scoring provides independent incremental information in addition to traditional risk factors in the prediction of all-cause mortality [184]. Berman et al. [185] and Kim et al. [186] showed that while there is a general relationship between the severity of coronary calcifications and the prevalence and severity of myocardial perfusion abnormalities with SPECT or PET imaging, respectively, there was still a small but substantial proportion of patients with no coronary calcifications but abnormal myocardial perfusion findings, and normal myocardial perfusion even in the presence of very high coronary calcium scores. Thus, regional coronary disease and calcium deposition provide different, even if complementary, information. In patients with risk factors but few symptoms being screened for CAD, calcium scoring can add specificity when the calcium score is low and the perfusion results are equivocal or abnormal due to endothelial dysfunction. The calcium score can add sensitivity in the detection of pre-clinical CAD, even in the presence of a normal MPI. The optimal selection of patients for the acquisition of myocardial perfusion and calcium scoring in the same session remains to be determined.

15.5.3 CT Coronary Angiography

An intriguing possibility is the potential value of CT coronary angiography performed together with PET or SPECT MPI in selected patients. Multislice (16 or greater) CT scans have been found to have sufficient temporal resolution to image, with intravenous contrast, coronary arteries with a diameter of 1.5 mm or greater with 16-slice CT with a sensitivity of 86% – 92%, a specificity of 93% – 99%, and an accuracy of 93%, and an even better performance in smaller vessels with 32- or 64-slice CTs [187, 188]. There are limitations in visualizing lesions in the smallest distal vessels, and in the presence of heavy calcifications. The latter limitations can be overcome with the aid of MPI [189].

It is conceivable that patients with known or suspected disease could be studied with sequential stress-rest perfusion and function imaging and CT angiography, allowing the acquisition of superimposable images of coronary artery anatomy, perfusion, wall motion, and viability [190]. This complete set of spatially mapped information could add precision and ease to decision-making for interventions in multivessel disease, or in patients with physiologically abnormal perfusion but anatomically normal coronary arteries. This proposition needs to be tested in clinical studies.

15.6 Infarct-Avid Imaging

15.6.1 Introduction

The diagnosis of myocardial infarction is made on the basis of clinical history, the ECG, and myocardial enzymes. In the 1970s and earlier, there was a role for myocardial infarct imaging, due to lack of sufficiently sensitive and specific diagnostic methods. The introduction of specific CK-MB myocardial enzyme assays and assays for myoglobin and troponin has markedly improved clinical diagnosis of acute infarction [191].

One indication for infarct-avid imaging has persisted. It occurs in a patient who has a prolonged episode of chest pain and does not present to the hospital until several days later, by which time the value of serial cardiac enzyme measurement has passed. If the patient has an ECG in which diagnosis of infarction is difficult (LBBB, pacemaker, IVCD, marked LVH), infarct-avid imaging can be useful to confirm an MI event. On the other hand, the greatest clinical danger from the MI itself has passed, and the urgency of diagnosis has decreased. Clinical attention is then focused on evaluation of prognosis and the need for further intervention, using the various stress perfusion or wall motion techniques discussed before. Therefore, even for this indication, the use of infarct-avid imaging has been rare.

A second look at myocardial infarct avid imaging is indicated by an increasing need to make a rapid diagnosis, driven by economic considerations and new developments in infarct-avid imaging. One method has been myocardial perfusion imaging in the ER or chest pain unit, an approach that has been implemented in numerous institutions [158, 192]. This works successfully in patients who do not have a history of prior myocardial infarction. However, perfusion imaging is not expected to be successful in patients with prior myocardial damage. Therefore, rapid "hot-spot" imaging, in the setting of prior myocardial damage and dysfunction, would be potentially useful.

15.6.2 Pathophysiology of Myocardial Infarction

Myocardial infarction occurs in the setting of an acute coronary vessel occlusion due to plaque rupture plus thrombosis [193, 194], with a variable amount of spasm [195] and increased myocardial demand as contributing factors. Figure 15.17 shows the peri-infarct zone to be a complex collection of regions in different states of injury, depending on the amount of blood flow reduction, myocardial metabolic demand, and the rate of onset and duration of flow reduction. Myocardial necrosis and severe acute ischemia lead to cellular membrane disruption and increased permeability. Both types of

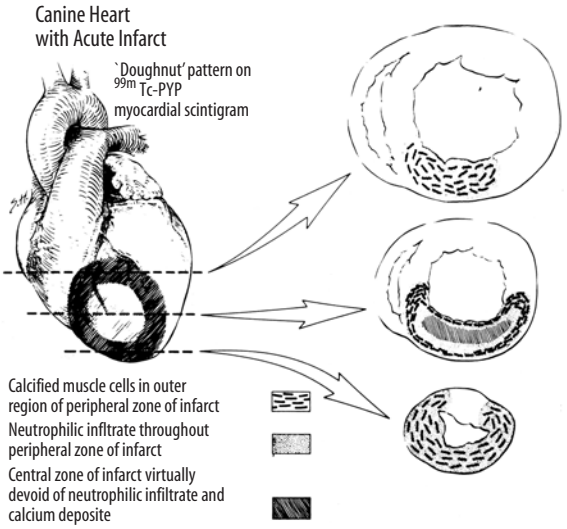

Fig. 15.17. Correlation of scintigraphic and histological features of a typical acute myocardial infarction produced in dogs by occlusion of the proximal left anterior descending coronary artery. Histopathological sections of transverse ventricular slices through the infarct reveal a large peripheral zone infiltrated by neutrophils that surround the subendocardial central zone devoid of neutrophils. An area of extensive calcification (and T-99m-pyrophosphate deposition) is limited to the outer region of the peripheral zone of the infarct. (Reproduced from [197] with permission)

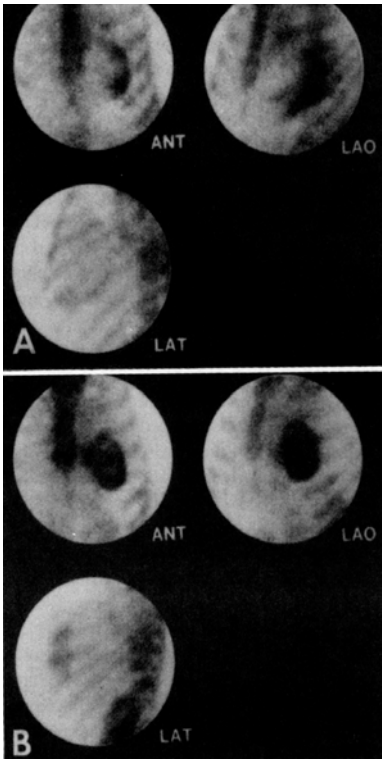

Fig. 15.18A,B. "Hot-spot" imaging with Tc-99m-pyrophosphate. **A** Focal intense uptake in the lateral and inferolateral myocardium. **B** Focal intense uptake in the anterior myocardium. *ANT* anterior, *LAO* left anterior oblique, *LAT* lateral. (Reproduced from [205] with permission)

injury result in leakage of a number of intracellular molecules used to detect tissue injury [191] and in large, exogenous-labeled molecules being able to penetrate and concentrate in these zones. Another zone may consist of ischemia and/or hibernation, where myocardial contraction has ceased or diminished in response to decreased perfusion, but where cellular viability and membrane integrity are intact. Still another zone may have experienced severe ischemic injury, with partial or total spontaneous or therapeutic restoration of myocardial blood flow, but continued dysfunction due to ischemia-induced oxidative stress, or "stunned" myocardium. Finally, there may be a larger zone which is functional and perfused, but jeopardized by being supplied by a partially occluded artery. These various myocardial tissue states could be present in layers, or closely interdigitated with each other, seen pathologically as islands of viable tissue in the midst of fibrosis, or vice versa [196].

The time course of coronary thrombosis is variable, with endogenous thrombotic and thrombolytic factors in competition in an unstable dynamic state [198]. The presence of collaterals, available immediately or gradually through the recruitment or development of new collaterals, has been shown to make a big difference between the amount of infarcted and/or injured myocardium and its potential recovery [196]. Spontaneous or therapeutic thrombolysis or acute revascularization plays an important role in the salvage of myocardium that has managed to survive following acute ischemic occlusion [199, 200]. All of these factors greatly influence the relative proportions of these zones of tissues and the likelihood that one turns into the other [196].

15.6.3 Infarct-Imaging Agents

An early and the most extensively used infarct-avid imaging agent in the past is Tc-99m-pyrophosphate, a bone-imaging agent [201, 202]. It is imaged at 4 h after intravenous injection. This tracer binds to microscopic calcium deposits in dead or dying cells [203] and in severely ischemic cells. Consequently, it tends to overestimate infarct size [204]. The technique was found to have a sensitivity of 59% – 100% [206, 207], depending on infarct type. This was sensitive enough for acute transmural infarction (94%), but its sensitivity was limited for subendocardial infarction (42%) [208]. Its peak sensitivity is at 48 h after the infarction, with a useful range of 12 h to 8 days after infarction [209] (Fig. 15.18). Tc-99m-pyrophosphate imaging may remain positive for up to several months in very large infarcts. Clearly, its use is limited to the rare patient who

presents several days after the event when the ECG and serum markers cannot help in diagnosis, and to patients in whom the age of the infarction, discovered on a routine ECG while screening for noncardiac surgery, is unknown. The method is poor in detecting very small infarctions. Its use declined to a virtual zero level in the 1980s and thereafter.

In-111-labeled antimyosin Fab antibody imaging has been studied for the past two decades and was approved by the FDA for acute myocardial infarction several years ago, although it was then withdrawn from the market. Antimyosin antibody imaging is sensitive and specific for the diagnosis of myocardial necrosis. Myocytes with disruption of cellular and sarcolemmal membranes expose the insoluble intracellular myosin to the antibodies, which are normally limited to the extracellular and intravascular space [210]. The antimyosin antibodies can be administered any time after the onset of chest pain, but a delay of 12 – 24 h is needed in order to image the resulting distribution, due to required blood pool clearance [211, 212]. In-111-antimyosin antibody imaging was found to have a 96% sensitivity and a very high specificity [212] (Figs. 15.19, 15.20). In a comparison with Tc-99m-pyrophosphate, the sensitivity of antimyosin antibody imaging for detection of myocardial infarction was similar (90%), but its ability to delineate the myocardial infarct area was more accurate [213, 214]. SPECT imaging with In-111-antimyosin antibodies yields high accuracy in determination of infarct size, especially when combined with Tl-201 perfusion imaging [216]. The time delay required for imaging has prevented this agent from becoming routinely used in clinical decision-making in the ER.

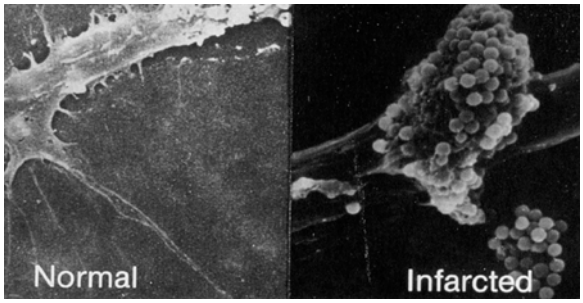

Fig. 15.19. Electron micrographs demonstrating microspheres bound to antimyosin antibodies binding to areas of myocyte cell membrane disruption. Higher magnification shows specific binding of antimyosin microspheres to exposed myofibrils. (Reproduced from [211] with permission)

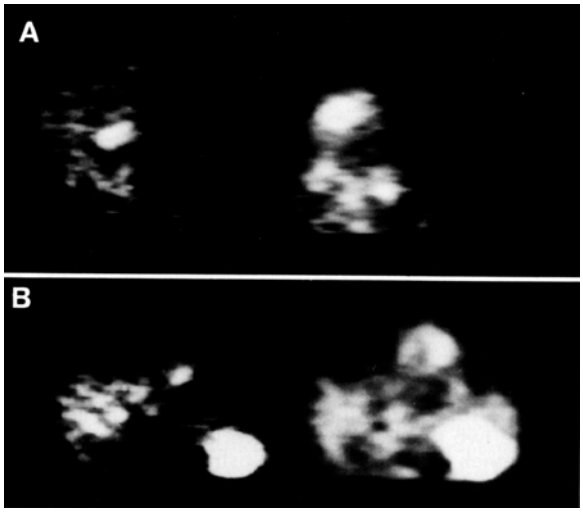

Fig. 15.20A,B. Long-axis views (**A**) and short-axis views (**B**) obtained with indium-111 antimyosin (*left*) and thallium-201 (*right*) in a patient with acute inferior infarction. In both projections, there is I-111 antibody uptake and a Tl-201 defect in the inferior wall. (Reproduced from [215] with permission)

The need for rapid diagnosis has stimulated the search for other infarct-avid agents. Tc-99m-glucaric acid is a dicarboxylic sugar. It was found to detect experimental myocardial infarcts very rapidly after administration, in part due to rapid clearance from the blood [217]. Tc-99m-glucaric acid binds to nuclear histones in the nucleus exposed by membrane disruption [218] (Fig. 15.21). Uptake of Tc-99m-glucarate is highly specific for myocardial infarction, as distinct from ischemic myocardium [219] or noninfarcted reperfused myocardium. Its distribution closely correlates with the distribution of In-111-antimyosin Fab localization [218]. However, its uptake in infarcted myocardium can be imaged as early as after 3 – 4 h of reperfusion in rats, increasing for the first 24 – 48 h, and resolving by 7 – 10 days [221]. In clinical trials, a large acute MI was visualized as early as 1 h after administration of Tc-99m-glucarate. Small MIs required 2 – 3 h for detection. By the time peak CK levels were reached at 13 h after onset of chest pains, the Tc-99m-glucarate images were already negative. In patients with unstable angina, the images were consistently negative [222].

Given the need for rapid diagnosis of acute MI, Tc-99m-glucarate is a promising agent. Further trials are needed to demonstrate its potential role in clinical decision-making under current conditions.

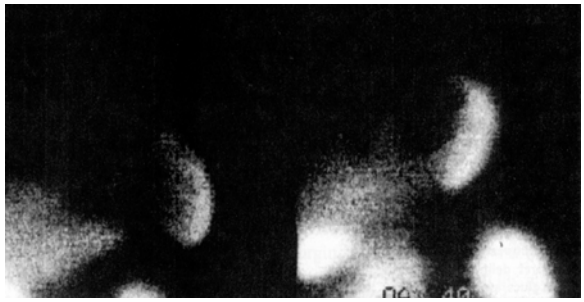

Fig. 15.21. Anterior and LAO planar images from a patient with reperfused myocardial infarction injected with Tc-99m-glucarate, obtained 3.5 h after i.v. administration of the tracer. (Reproduced from [220] with permission)

15.7 Congestive Heart Failure

15.7.1 Introduction

Congestive heart failure (CHF) is a leading cause of mortality and morbidity in the industrialized world [223, 224]. The primary causes are ischemic heart disease and hypertension. Other etiologies include valvular disease, viral, idiopathic, and alcoholic cardiomyopathy, and, less commonly, thyroid disease and hemochromatosis [225, 226] (see also Chap. 13).

CHF stems from inadequate cardiac output, due to systolic or diastolic left ventricular (LV) dysfunction. This results in inadequate flow to the peripheral tissues at rest and with exertion, leading to compensatory responses designed to maintain perfusion pressure to vital organs. The neurohumoral systems include the sympathetic nervous system, the renin-angiotensin system, and circulating plasma vasopressin [227, 228]. The model accepted today is that inadequate flow activates vasoconstrictor forces that eventually cause excessive impedance to left ventricular ejection and further reduction in cardiac output, allowing a vicious cycle to ensue (Fig. 15.22).

Despite, or because of, neuroendocrine activation, patients with CHF have a blunted sympathetic and vasopressin response to orthostatic tilt or exercise. This abnormality appears to be related to the severity of the resting hemodynamic abnormality [229–234], suggesting that sympathetic system responsiveness is a useful index of the progression of CHF.

The diagnosis of CHF is usually made on the basis of symptoms of dyspnea, orthopnea, paroxysmal nocturnal dyspnea, and edema, but these are relatively nonspecific [235] and may be misleading in many patients [236, 237]. The diagnosis is aided by the more specific physical signs of third heart sound, elevated jugular venous pressure, and the presence of pulmonary crackles on auscultation [235]. The chest radiograph is helpful in correlating signs and symptoms with heart enlargement and pulmonary venous distention [238]. To distinguish CHF secondary to LV systolic dysfunction from that resulting from diastolic dysfunction [239], echocardiography or radionuclide gated blood pool imaging are commonly employed.

15.7.2 Therapy

The standard therapy for CHF is diuretics [240–242] and ACE inhibitors [243]. Digoxin was recently shown not to reduce mortality, but it did lower hospitalization rates [244]. Beta-blocker therapy results in increased ejection fraction and reduces the risk of dying by some 30%. Benefit was noted especially in patients with the lowest LVEF [245–249] in spite of the possibility of exacerbation of the heart failure, bradycardia, and AV block in some patients. The combined alpha/beta blocker carvedilol produced a 65% reduction in total mortality caused by both progressive CHF and sudden death [250].

Sudden death accounts for about half of all CHF deaths [251, 252]. The class-3 drug amiodarone reduces

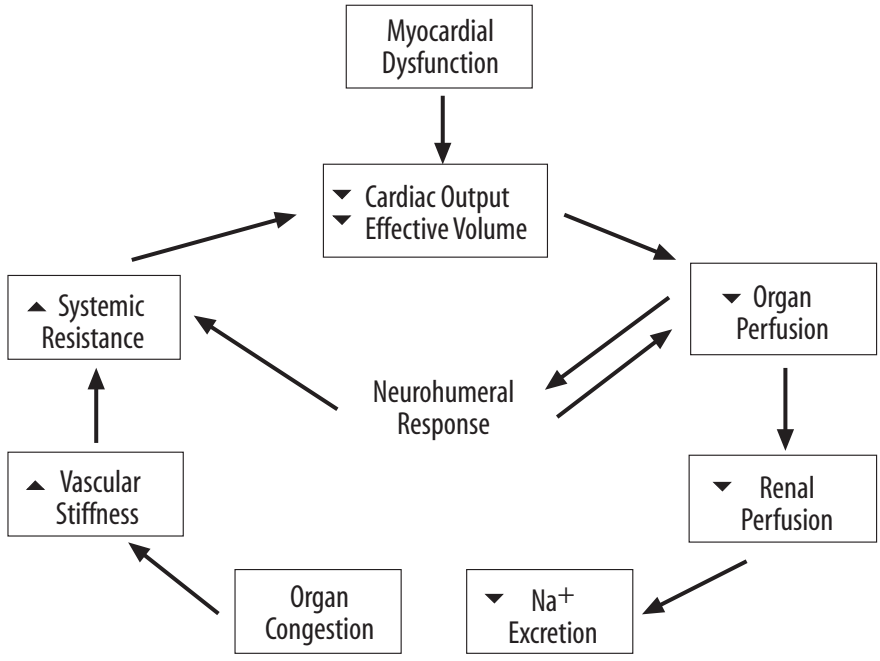

Fig. 15.22. The pathophysiology of congestive heart failure

mortality from sudden death by 29% and overall mortality by 15% [253]. Another option is prophylaxis with an implantable defibrillator in patients with nonsustained VT and CAD [254].

A further cause of morbidity and mortality is embolic stroke, particularly with atrial fibrillation. Warfarin reduces the risk of embolic stroke by 68% in patients with nonvalvular atrial fibrillation. The benefit outweighs the risk of a serious hemorrhage [255].

Some patients with ischemic heart disease benefit from revascularization, using either percutaneous methods or coronary artery bypass surgery (CABG), by controlling symptoms of ischemia, improving function, and preventing further deterioration. Heart transplantation provides a last resort for some patients with severe CHF. Exciting research is being conducted in the new field of induction of angiogenesis [256], laser transmyocardial revascularization, and implantation of bone marrow stem cells.

Much of the treatment of CHF is based on the hemodynamic paradigm, which predicts that interventions that improve the LVEF or its surrogates (exercise time, symptoms) should improve survival. However, a lack of direct connection between inotropism and survival is shown by the lack of life prolongation with digoxin therapy [244] and the increased mortality with milrinone, amrinone, and enoximine, despite improvements in hemodynamics and symptoms [257–259].

15.7.3 Clinical Risk Stratification

Only a small number of patients actually benefit from transplantation [260]. The high mortality in CHF poses a challenge to devise effective risk stratification which would optimally steer patients for revascularization, implantation of pacemakers-defibrillators, or heart transplantation.

Therapy of CHF is based on the response to initial empirical therapy, evaluation of disease severity, and an estimation of the patient's prognosis. The risk of mortality and sudden death increases with advancing LV dysfunction and higher NYHA class [261, 262]. The annual mortality among ambulatory patients approaches 10%–20% [263–265]. Older patients with severe CHF have 1-year survival rates of less than 50% [266]. Risk is particularly high in those with a history of sustained VT or syncope [267, 268] or the combination of low LVEF, frequent ventricular ectopy, and a positive signal-averaged electrocardiogram [269].

15.7.4 Ventricular Function

The single most important measurement in CHF is the assessment of LV function (ejection fraction). It separates patients with systolic dysfunction from those with other causes of CHF and is an important index of survival [270]. This can be done with 2D echocardiography, radionuclide gated blood pool imaging, gated myocardial perfusion imaging, MRI ventriculography, or contrast ventriculography. Assessment of LV size and diastolic dimension is also useful. As important as the LVEF is, it correlates poorly with the extent of disability as measured by exercise tolerance tests [271, 272]. Repeat measurements of LVEF are justified if the patient has an important change in clinical status or has received an intervention that might have a significant effect on LV function [273]. RV function also is an important independent prognostic indicator [274].

15.7.5 Selection for Bypass

Coronary artery bypass surgery (CABG) plays an important role in the control of medically intractable ischemia and improves mortality in some groups of patients with CAD, particularly those with multivessel disease and LV dysfunction. The CASS registry showed that patients with CHF and three-vessel CAD who underwent CABG had a 9% incidence of sudden cardiac death at 5 years, compared with 31% for patients who did not undergo CABG [275]. Lansman et al. showed that it was possible to perform CABG safely (mortality of 4.8%) even in patients with LVEFs less than 20% [276]. Reduced survival was noted for patients with an RVEF of less than 30%.

15.7.6 Assessment of Ischemia

Myocardial stress perfusion SPECT imaging is very useful for prognostic risk stratification. Patients with clinical CHF usually present with already severe LV dysfunction and, if due to CAD, with extensive areas of hypoperfusion on rest or stress perfusion imaging. Therefore, these patients already belong to the high-risk category. The value of rest and stress imaging lies in establishing (a) LV vs RV dysfunction; (b) the presence of normal LV function or only mild to moderate LV dysfunction, the presence of extensive stress-induced ischemia, which clinically presents as heart failure, a high risk combination that indicates need for CABG; (c) the presence of severe LV dysfunction, and the presence of stress-induced ischemia that helps clarify vague symptoms or document silent ischemia. Myocardium which is functional and well perfused at rest but becomes ischemic with stress, the so-called jeopardized myocardium, contributes to diastolic and systolic dysfunction during ischemia. (d) It also helps to distinguish ischemic from nonischemic heart disease.

15.7.7 Assessment of Viability

The need for making the diagnosis of resting ischemia, hibernation, or stunning stems from their role in exacerbating LV dysfunction, CHF symptoms, sudden death, and hemodynamic deterioration and from the need to decide between revascularization and cardiac transplantation. Nonfunctioning but viable myocardium includes stunned and hibernating myocardium:

1. Stunned myocardium shows decreased contractility after an episode of prolonged ischemia, but intact blood flow at the time of observation [277]. Oxygen-derived free radicals contribute to post-ischemic dysfunction [278]. Stunned myocardium generally improves without further intervention. In most cases of exercise-induced ischemia, this may take a few minutes or, uncommonly, several hours. Following an acute coronary occlusion and thrombolysis, most of the improvement takes place over 7 – 10 days, but it may take longer in the presence of residual stenosis and/or repeated stunning [279]. Patients may experience repeated episodes of ischemia, often silent, in the same territory, and the stunned myocardium may not be able to recover, leading to a quasi-permanent state of stunning [222, 281] and progressing to hibernation [282]. When superimposed on an already severely dysfunctional heart, it may become dangerous, and the patient may require hemodynamic support. Restoration of vessel patency or prevention of ischemic episodes due to coronary spasm or thrombosis is required to reverse this precarious state.
2. Hibernation occurs in myocardium that has undergone a down-regulation of contractile function, thus reducing cellular demand for energy, in response to chronic ischemia [283]. Hibernation, by definition, requires the restoration of blood flow in order to improve function. Benefit also may be expected from reduced metabolic demand via hemodynamic support.

Studies have found that the majority (72%) of dysfunctional but viable segments are in fact due to stunning, with only a minority (28%) due to hibernation [284]. The definition of either stunning or hibernation requires the recovery of function, either spontaneously or after intervention. This hemodynamic paradigm ignores other potential benefits from the reversal of stunning or hibernation, including prevention of remodeling or arrhythmias. The above definitions also ignore the possibility that the different tissue types may coexist with each other and with inducible ischemia and scarred tissue in the same or adjacent myocardial segments. Melon et al. showed that dysfunctional but "viable" myocardium is a heterogeneous condition [285]. This may partially explain the limitations in predictive abilities for all imaging techniques.

How prevalent is dysfunctional but viable myocardium? Up to 50% of patients with previous infarction may have areas of dysfunctional viable myocardium mixed with scar tissue, even in areas with Q-waves on the ECG [286] and in 24% – 82% of all dysfunctional segments [287]. Therefore, the importance of this subject cannot be overemphasized when dealing with the management of CHF.

Resting wall motion imaging identifies myocardium which is thickening and moving well and that which is not. It cannot differentiate dysfunctional and recoverable (viable) myocardium from permanently scarred myocardium, except by documenting serial changes in function over time. Stimulation by exercise, catecholamines, or nitrates, or post-exercise and post-PVC potentiation are all evidence of viability, albeit with limited sensitivity. Low-dose dobutamine (LDDE) and high-dose dobutamine echocardiography showed that both a biphasic response (improvement at low dose and deterioration at high dose) and sustained improvement of wall motion (improvement at both low dose and high dose) in dysfunctional segments were highly predictive of reversible dysfunction [288], with a combined sensitivity of 84% and specificity of 81% [287] (Table 15.8).

The uptake and retention of myocardial perfusion agents is good evidence of myocardial viability. However, impaired retention of perfusion tracers can be seen in dysfunctional, stunned myocardium, while decreased uptake due to decreased perfusion is often seen in hibernation [289]. Simple stress-redistribution imaging with Tl-201 has been shown to underestimate the presence of viability. Augmentation with late (12 – 24 h) imaging and/or resting reinjection was found to increase sensitivity for viability [289 – 293]. The latter approach yielded a combined mean sensitivity of 86% but at the cost of a lower specificity of 47% [287]. In patients who cannot exercise owing to poor LV function and clinical CHF, rest-redistribution Tl-201 imaging has shown a combined sensitivity of 90% and a specificity of 54% [287]. Comparisons showed LDDE to be slightly less sensitive but more specific. Rest-dobutamine MRI wall motion imaging was shown to be slightly less sensitive (50%) but specific (81%) compared with Tl-201 imaging [294].

Myocardial perfusion imaging with Tc-99m-sestamibi has yielded a slightly lower sensitivity of 83% but a higher specificity of 69% [287, 295]. Tc-99m-sestamibi imaging combined with nitrate administration has yielded an improved sensitivity of 91% and a specificity of 88% [287]. Gated Tc-99m-sestamibi imaging with nitroglycerin (NTG) administration can be used successfully as an alternative to rest-redistribution Tl-201 SPECT imaging [296]. Tc-99m-tetrofosmine showed performance similar to that of Tl-201 stress-redistribu-

tion imaging and slightly lower sensitivity than rest-late redistribution Tl-201 imaging [294].

It is evident that neither myocardial perfusion imaging nor LDDE imaging can supply both high sensitivity and high specificity. Sequential testing by Tl-201 and LDDE imaging in patients with intermediate probability of viable myocardium by either test alone enhances the prediction of post-revascularization improvement of the LVEF [297].

Another strategy is the addition of metabolic imaging to perfusion imaging using analogues of either free fatty acids or glucose imaging. Injured myocardium frequently demonstrates impaired oxidative metabolism, impaired free fatty acid utilization, and an excess of glucose utilization relative to flow. F-18-fluorodeoxyglucose (FDG) is an analogue of glucose, which is transported into cells via a specific glucose membrane transporter and is phosphorylated by hexokinase. Unlike glucose, FDG is trapped and is not metabolized further (Fig. 15.23). Its accumulation is an index of glucose utilization [298]. Myocardial flow can be imaged with N-13 ammonia or Rb-82 with PET imaging, or Tl-201, Tc-99m-sestamibi, or Tc-99m-tetrofosmine imaging using SPECT.

Stunned myocardium shows preserved flow, and either matched or excessive FDG accumulation [299, 300]. At times, stunning results in impaired FDG accumulation, producing an underestimation of viability [301]. Hibernation has been shown to demonstrate decreased perfusion, and relatively preserved or disproportionately increased FDG accumulation [302, 303] (Fig. 15.24). Infarcted myocardium shows a matched decrease in both perfusion and FDG uptake (Fig. 15.25) (Table 15.7).

Early studies with FDG PET imaging required a cyclotron and a dedicated PET scanner. PET imaging with FDG yielded a combined 88% sensitivity and 73% specificity [287] for viability. More recently, F-18-FDG has been imaged as a SPECT study with specially de-

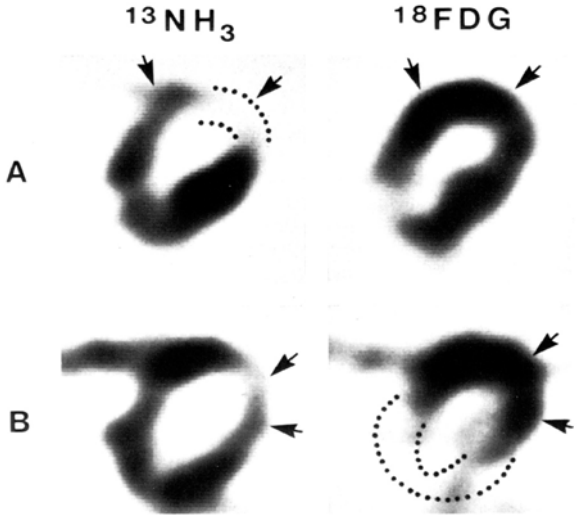

Fig. 15.24. Comparison between regional blood flow (assessed with N-13-labeled ammonia, *left panel*) and exogenous glucose utilization (assessed with F-18 FDG, *right panel*) in two patients with ischemic heart disease and segmental wall motion abnormalities. Patient A, who was imaged in the nonfasting state, shows marked reduction in blood flow in the anteroseptal and anterior wall (*arrows*) and normal or increased uptake of exogenous glucose. Patient B, who was imaged in the fasting state, shows a marked defect in anterior and anterolateral perfusion. The F-18 FDG image shows enhanced glucose utilization in the underperfused segments, and little utilization in the normally perfused segments. (Reproduced from [333] with permission)

Table 15.7. Value of Tl-201/F-18 FDG match and mismatch in predicting improvement in wall motion [308]

Pattern	% Improvement
Normal	75
Mild match	15
Mild mismatch	70
Severe match	5
Severe mismatch	70

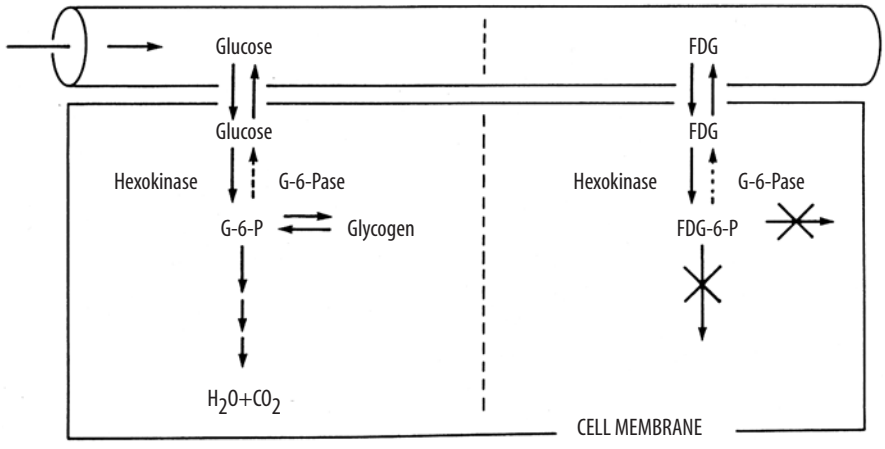

Fig. 15.23. Mechanism transport and metabolism of glucose and of its analogue, F-18-fluorodeoxyglucose (*FDG*). *G-6-P* glucose-6-phosphate, *G-6-Pase* glucose-6-phosphatase

signed high-energy collimators for conventional SPECT gamma cameras, together with Tl-201 or Tc-99m-sestamibi [305] (Fig. 15.26). Several groups have shown the sensitivity and specificity of FDG/Tl-201 SPECT imaging to be 87% and 78%, respectively, similar in magnitude to corresponding studies using PET imaging [305–307] (Table 15.8). Hybrid coincidence cameras with attenuation correction, newly developed in the past few years, can image both the coincident gamma photons of FDG, similar to PET but at a lower cost, while able to perform, sequentially or simultaneously, SPECT imaging of perfusion with Tl-201 or Tc-99m-sestamibi. Nonetheless, only imaging with a dedicated PET or PET-CT scanner is approved for reimbursement in the U.S. The need for an on-site cyclotron has lessened with the establishment of commercial FDG production and distribution centers in most major metropolitan regions in the U.S. FDG metabolic/perfusion imaging has become a clinical tool in many centers around the world and should no longer be considered an investigational technique.

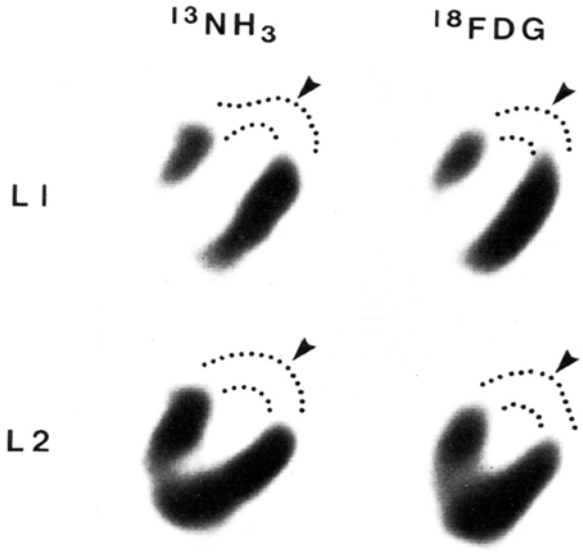

Fig. 15.25. Comparison between myocardial blood flow (assessed by intravenous N-13-ammonia) and exogenous glucose utilization (assessed by F-18 FDG) in a patient with recent myocardial infarction. Two contiguous cross-sectional images are shown (L1 and L2), which demonstrate a matched decreased in perfusion and glucose utilization. This concordant pattern is consistent with irreversible tissue injury. (Reproduced from [304] with permission)

Table 15.8. Sensitivity and specificity of various methods of imaging for myocardial viability [287]

Method	No. of patients	Sensitivity (%)	Specificity (%)
Tc-99m-MIBI	207	83	69
Tc-99m-MIBI + NTG	55	91	88
Tl-201 reinjection	209	86	47
Tl-201 rest-redistribution	145	90	54
LDDE	448	84	81
F-18 FDG PET	332	88	73

A somewhat different approach uses labeled free fatty acid (FFA) analogues. Myocardial FFA uptake is proportional to blood flow. FFA beta-oxidation is reduced in the presence of ischemia, stunning, and hibernation, which increases the proportion of FFAs accumulating in the triglyceride pool. Myocardial imaging with iodine-123-labeled FFAs shows uptake and rapid clearance in normal myocardium, and delayed clearance or accumulation in the presence of impaired oxidation. Thus impaired FFA clearance represents recoverable myocardium [309, 310]. Because the image quality with labeled FFAs is poor, the situation was remedied by using another labeled FFA analogue with an extra methyl group at the beta carbon of the FFA chain, which blocks beta-oxidation. One such analogue is BMIPP. It shows prolonged retention in normal myocardium, thus achieving good image quality. With oxidative impairment, BMIPP retention is reduced. Thus, a disproportionately reduced BMIPP retention relative to flow is an indicator of stunning or hibernation [311, 312]. This pattern predicts improvement in left ventricular function and recovery of oxidative metabolism [313]. Labeled FFAs are only investigational in the U.S. BMIPP is approved for clinical use in Japan. Where FDG production and PET imaging equipment is unavailable, ^{123}I-labeled FFA imaging is a feasible alternative to FDG imaging.

How much impaired but viable tissue is needed in order to result in functional improvement after revascularization? Bax et al. conducted ROC analysis on the results of Tl-201/FDG SPECT imaging in 32 patients. The extent of viable myocardium was closely related to the magnitude of LVEF improvement after revascularization. An LVEF improvement greater than 5% could be expected when three or more impaired but viable segments (out of 13 segments) were present [314]. This

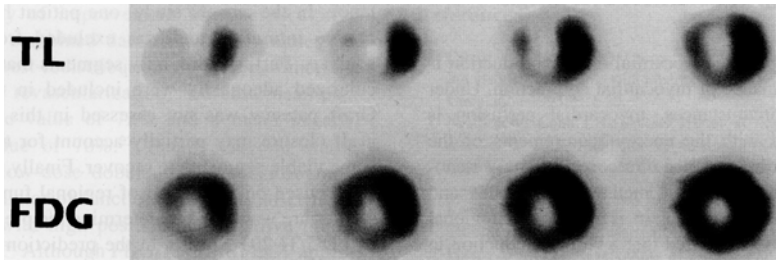

Fig. 15.26. Short-axis slices of a patient with a severe Tl-201 defect in the anterior, septal, and inferior regions, showing preserved FDG uptake in these regions. (Reproduced from [306] with permission)

supports findings in the earlier pioneering study by Tillisch et al. [315].

The ultimate utility of myocardial viability imaging appears to lie in its prognostication value, rather than in mere prediction of increased LVEF after revascularization. Pasquet et al. showed that the presence of ischemic myocardium (determined by thallium scintigraphy) and viable myocardium (determined by LDDE) are independent predictors of subsequent mortality [316]. Layher et al. showed a higher risk of arrhythmic death in patients with PET mismatch patterns [317]. Huiting et al. showed that patients who had Tl-201/FDG mismatched defects ($n = 39$) experienced 19 cardiac events (deaths, reinfarction, late revascularizations, and unstable angina) vs one event (one death) in the matched-defect group ($n = 20$) [318]. Patients with substantial viability on LDDE demonstrated not only improvement in LVEF and NYHA functional class after revascularization but also a favorable prognosis after revascularization [319].

In some patients, a low LVEF can discourage surgery. Several centers have demonstrated that patients with severe LV dysfunction can undergo surgery with acceptable risk (< 10% mortality) even in the absence of consistent screening for the presence of viable myocardium before surgery [320 – 322]. The presence of viable myocardium appears to predict a more favorable outcome [323 – 325]. Viability studies promise to help in the selection of patients at low risk for serious perioperative complications [326, 327]. These studies suggest that revascularization brings a survival benefit beyond wall motion enhancement or an increase in LVEF, possibly due to protection against sudden death, or protection from further remodeling and dilatation. The question of possible survival benefit from CABG even in the absence of an increase in LVEF needs to be ascertained.

Some patients with angina undergo CABG even without hope of likely improvement in LVEF [328]. Documentation of ischemia in patients with symptoms, or episodes of exacerbation of CHF and prediction of resolution of ischemic episodes after even limited revascularization, is a desirable aim.

15.7.8 Selection for Transplantation

Despite the reduction of mortality in CHF patients as a result of ACE inhibitor and beta-blocker therapy, and in spite of advances in selecting patients for CABG and technical advances in performing CABG, the prognosis of patients suffering from end-stage CHF remains grim. While heart transplantation can substantially modify the prognosis for these patients, leading to a prolonged and potentially productive life [329], only a small proportion of patients actually undergo transplantation [330]. Many patients die while undergoing evaluation for heart transplantation and waiting for a donor heart. Therefore, an effective triage of pretransplant patients is desirable.

The severity of heart failure is routinely evaluated on the basis of symptoms, clinical findings, hemodynamic measurements, exercise tolerance [331 – 335], and assessment of the degree of activation of the neurohormonal system [263, 336 – 338]. Despite these efforts, an accurate risk stratification system that would predict survival or mortality has been elusive to date.

15.7.8.1 Neuroendocrine Evaluation

There have been important advances in the in vivo evaluation of function of autonomic innervation and receptors in the heart that offer the potential of improved risk stratification and more specific therapy by manipulating the autonomic milieu. These methods are still being evaluated in clinical trials in patients with CHF.

The heart is richly supplied with autonomic sympathetic and parasympathetic innervation. Sympathetic innervation originates from the right and left stellate ganglia; their neuronal fibers travel along the epicardial coronary vessels to reach the myocardium. Sympathetic nerves synthesize and store norepinephrine, which is released during stimulation into the neuromuscular synaptic junction (Fig. 15.27). Presynaptic receptors mediate neurotransmitter reuptake. Postsynaptic membrane receptors are linked with their effector mechanisms. The neurotransmitters are metabolized within the synapse, the nerve terminals, and in the liver.

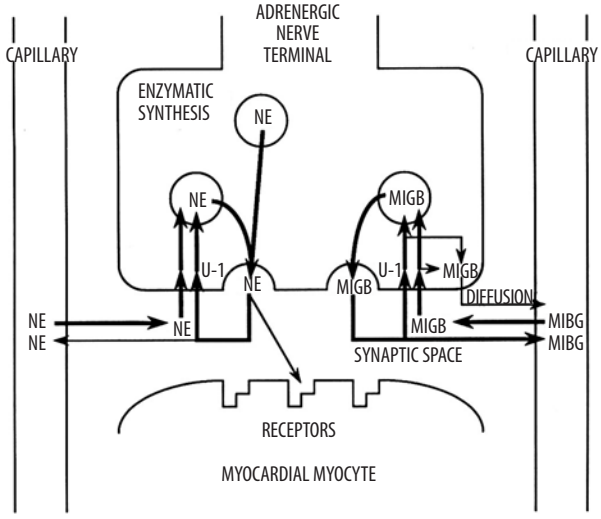

Fig. 15.27. Schematic of an adrenergic neuron and synaptic space within the heart, and the transport and release of norepinephrine (*NE*) and I-123-metaiodobenzylguanidine (*MIBG*) *U-1* uptake-1 mechanism. (Reproduced from [337] with permission)

Activation of the sympathetic nervous system and parasympathetic withdrawal play an important part in the progression of CHF. An elevated plasma norepinephrine is one of several independent prognostic indicators in heart failure [336]. There is also decreased clearance of norepinephrine by sympathetic neurons in the myocardium, resulting in increased synaptic norepinephrine levels. The post-synaptic adrenergic receptors become desensitized to catecholamine stimulation due to decoupling of receptors from effector systems, as well as loss of beta (B1) receptors [240]. Myocardium from hearts with idiopathic cardiomyopathy shows a greater degree of B1 receptor downregulation. Ischemic disease leads to a greater degree of uncoupling [341]. However, this differential response has not resulted in different approaches in beta-blocker therapy.

The loss of responsiveness to catecholamines may be overcome through short-term administration of beta-receptor agonists. Long-term catecholamine inotropes administration may lead to further desensitization, myocardial injury, and increased incidence of arrhythmias. In contrast, cautious use of beta-blocking agents can restore responsiveness of the beta-receptor system, through protection against excess levels of circulating and local catecholamines and restoration of response to direct stimulation [342]. Treatment with beta blockers has emerged as a successful approach for some patients.

15.7.8.2 Sympathetic Receptor Imaging

A number of radiotracers can be used to study cardiac presynaptic autonomic neuronal function. The norepinephrine analog I-123-metaiodobenzyl-guanidine (MIBG) has been widely used in studies with conventional planar and SPECT imaging [343, 344], and C-11-hydroxyephedrine with PET imaging [345]. Postsynaptic beta-adrenergic receptors have been studied with the nonselective beta antagonists C-11-CGP-12177 and PET imaging [346], and I-123-cyanopindolol with SPECT imaging [347].

MIBG is an analog of the adrenergic-neuron-blocking agent guanethidine. MIBG is taken up and stored by the same mechanism as norepinephrine, but it is not metabolized by catechol-*o*-methyltranferase or monoamine oxidase [348] (Fig. 15.26). Initial accumulation in the heart consists of both specific intravesicular (uptake-1 system) and nonspecific, nonvesicular accumulation (uptake-2 system). Imaging at 4 h after injection allows assessment of specific neuronal accumulation of MIBG in various pathological conditions [349].

Uptake of MIBG in the heart, measured by the heart-to-mediastinum activity ratio (H/M) and the heart-to-lung ratio, is inversely related to the level of circulating plasma catecholamines, although it is not known if this

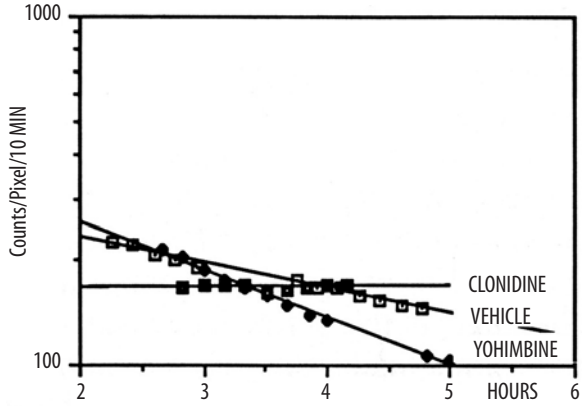

Fig. 15.28. Rates of loss of MIBG from the heart of a lightly anesthetized dog. Data were acquired by scintigraphic camera between 2 and 6 h after injection of I-123-MIBG for each of three experiments featuring administration of control vehicle (*VEHICLE*), yohimbine (*YOHIMBINE*), and clonidine (*CLONIDINE*) given 2 h after administration of MIBG. Yohimbine, an alpha-2-antagonist that increases sympathetic nerve traffic, resulted in accelerated nerve loss of MIBG, while clonidine, an alpha-2-antagonist that slows neuron traffic, resulted in inhibition of MIBG loss. (Reproduced from [339] with permission)

is due to direct competition or secondary to sympathetic nerve dysfunction [350]. Increased cardiac sympathetic nervous system activity has been associated with increased myocardial MIBG clearance [351, 352] (Fig. 15.28).

Studies showed poor cardiac retention of MIBG in patients with idiopathic cardiomyopathy (IDC), in proportion to the severity of LVEF impairment [353, 354] (Fig. 15.29). Schofer et al. demonstrated that scintigraphically and biopsy-measured cardiac MIBG activity was significantly related to myocardial norepinephrine concentration and LV ejection fraction (Fig. 15.30), but that elevated circulating catecholamines in CHF do not directly affect cardiac norepinephrine and MIBG content [355]. Merlet et al. showed that a poor inotropic response to dobutamine infusion correlated with both increased plasma norepinephrine (NE) concentration and diminished cardiac MIBG concentration, suggesting that the desensitization is related to both. A subset of patients with moderate CHF showed diminished cardiac MIBG uptake but normal plasma NE levels, suggesting that neuronal dysfunction is an early mechanism of desensitization in IDC [357].

In patients with dilated cardiomyopathy (CMP) treated with either beta blockers or ACE inhibitor therapy, the LVEF improved only after they had received beta blockers, but not with ACE inhibitor therapy. NYHA score and MIBG retention improved in both groups, but more in the group treated with beta blockers [358]. In a small, randomized trial, patients who received carvedilol showed an increase in LVEF after 1 year. Initial cardiac MIBG uptake showed an inverse

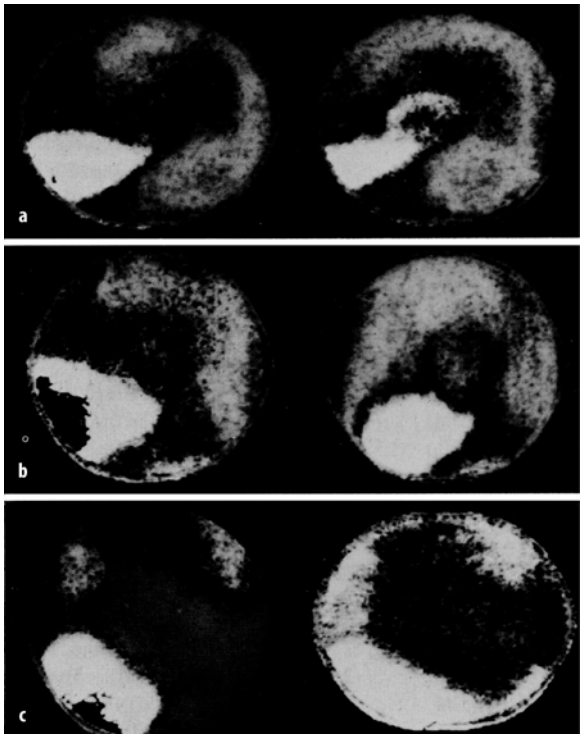

Fig. 15.29. a MIBG scintigram in a patient with normal (79%) left ventricular ejection fraction. There is intense and homogeneous tracer uptake in the myocardium. **b** MIBG scintigram of a patient with an abnormal (44%) left ventricular ejection fraction. There is a low heart-versus-background ratio, and myocardial uptake defects are present. **c** MIBG scintigram in a patient with severe (class IV) heart failure and low left ventricular ejection fraction (20%). The myocardium is not visible. The MIBG uptake in the lungs is high in patients with LV dysfunction. (Reproduced from [356] with permission)

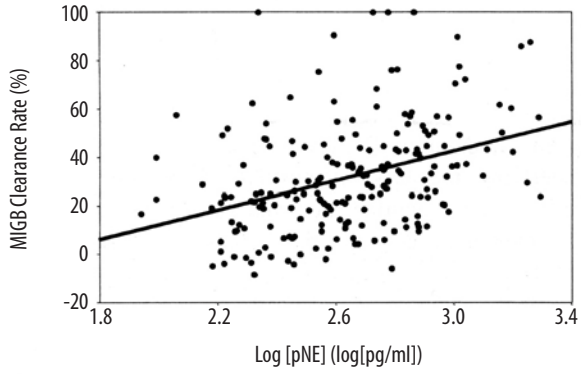

Fig. 15.30. Relation between myocardial norepinephrine (*NE*) content and the myocardial versus mediastinal MIBG activity ratio in 28 patients with dilated cardiomyopathy. (Reproduced from [356] with permission)

relationship with future improvement in LVEF. MIBG predicted which patients would improve after carvedilol therapy [359].

Merlet et al. tested the ability of MIBG to predict survival in 112 patients with CHF due to IDC, in comparison with circulating plasma NE, LVEF, peak VO_2, X-ray cardiothoracic ratio, M-mode echo end-diastolic diameter, and right-sided heart catheterization parameters. After a follow-up of 27 months, the only independent predictors for mortality were low MIBG uptake and LVEF. MIBG uptake and plasma NE were the only independent predictors for life duration. MIBG was a better discriminator between high- and low-risk patients than LVEF or plasma NE [360] (Figs. 15.31 – 15.33). In another preliminary study, Agostini et al. analyzed NYHA functional class, LVEF, peak VO_2, and cardiac MIBG uptake in predicting cardiac events in 89 patients with CHF. VO_2 and MIBG uptake ratio had the higher risk odds ratio independently. Patients with greater than 50% maximal predicted VO_2 or MIBG uptake > 125% had a risk of cardiac events of less than 10%, while pa-

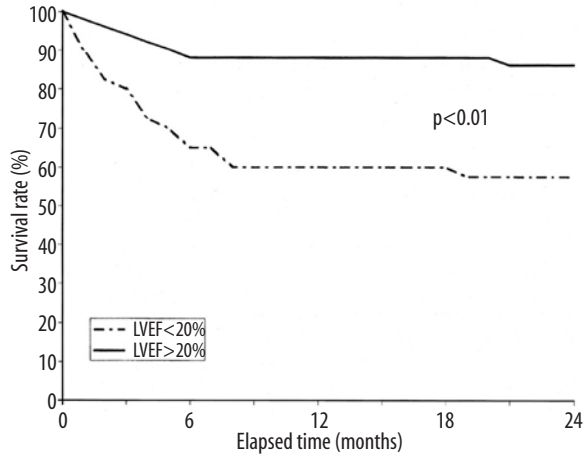

Fig. 15.31. Survival curves obtained from life-table analysis using LVEF for prognostication. Patient subset with LVEF > 20% (*solid line*) shows better survival than patient subset with LVEF < 20% (*dashed line*). (Reproduced from [360] with permission)

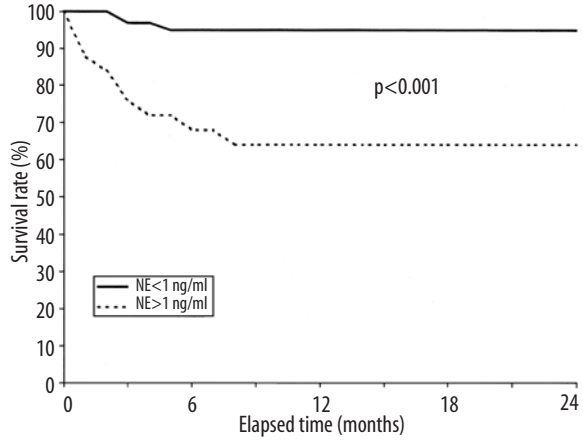

Fig. 15.32. Survival curves obtained from life-table analysis using plasma norepinephrine (*NE*) concentration for prognostication. Patients with NE values > 1.0 ng/ml (*solid line*) had better survival than those with NE values < 1.0 ng/ml (*dashed line*). (Reproduced from [360] with permission)

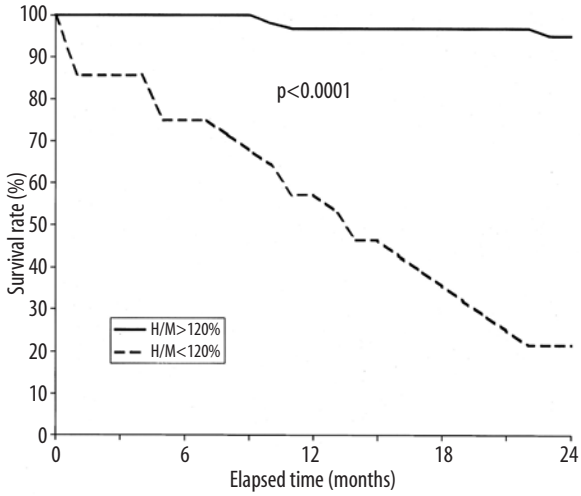

Fig. 15.33. Survival curves obtained from life-table analysis using scintigraphic index of cardiac MIBG uptake (*H/M*) for prognostication. MIBG imaging permits clear delineation between high- and low-risk subsets when using a threshold value of 120% for H/M ratio. Patients with low MIBG uptake (*dashed line*) had poor prognosis compared with patients with high MIBG uptake (*solid line*). (Reproduced from [360] with permission)

tients with VO_2 < 50% or MIBG uptake < 125% had a cardiac event rate of > 60% [361].

Thus, MIBG is a powerful predictor of a high risk for cardiac events in those who would be least likely to survive waiting for cardiac transplantation. Alone or in combination, this index can predict a low cardiac event rate in patients who can survive with medical therapy. In order for this approach to be accepted, it needs to be tested in a larger trial. Such a trial is currently under way. Although neuroendocrine imaging techniques remain investigative, they have a promising potential for developing and selecting more specific management strategies in the treatment of patients with heart failure.

The regional distribution status of cardiac sympathetic neuron dysfunction is also of relevance. In ischemic myocardial disease, myocardial infarction produces sympathetic denervation in noninfarcted myocardium distal to the infarct site. Since the sympathetic nerves run along the epicardial vessels, denervation occurs distal to proximal myocardial injury. This viable apical tissue demonstrates denervation supersensitivity to exogenous norepinephrine and isoproterenol [362, 363], presumably due to the absence of local sympathetic stimulation and lack of removal of exogenous catecholamines. Stanton et al. showed that ten of 12 patients with spontaneous ventricular tachyarrhythmias after myocardial infarction exhibited regions of Tl-201 uptake, indicating viable and perfused myocardium with no MIBG uptake, indicating regional denervation. Eleven of these 12 patients had ventricular tachycardia induced by programmed stimulation. This induction could not be prevented by beta blockers. Sympathetic denervation was seen in only two of seven patients without ventricular tachycardia. Normal subjects showed a normal perfusion and MIBG uptake pattern. This study suggested that some patients susceptible to tachyarrhythmias could be identified noninvasively [364], although this has not been replicated successfully.

Other tracers have been used to study postsynaptic receptor function noninvasively. Merlet et al. demonstrated a 53% decrease in the number of beta-adrenergic receptors in patients with congestive heart failure, which was concordant with in vitro biopsy studies [365]. It has been appreciated that receptor density changes dynamically with presynaptic function and neurotransmitter level [366, 367]. Buja et al. found that beta-receptor density increases during the early stages of myocardial ischemic injury and decreases in cells irreversibly injured. The initial increase in reversibly injured myocytes was reversed on withdrawal of the insulting agent. Changes in circulating catecholamines are not required to cause changes in sensitivity to catecholamines [368].

At this time and the foreseeable future, quantification of postsynaptic receptors, employing cyclotron-produced tracer-labeled neurotransmitter ligands imaged with PET, is limited to a few experimental centers, although other postsynaptic tracers such as I-123-cyanopindolol can be imaged with conventional instrumentation. Interestingly, Qing et al. found a concordant relationship of beta-receptor density in the lung and mononuclear leukocytes and the myocardium after albuterol treatment in normal subjects [369]. Although the reduction of receptor density by the B2-agonists was less in the myocardium than those in the leukocytes, presumably due to differential B2 and B1 concentrations, these findings suggested that it would be possible to monitor the beta-receptor milieu remotely by in vitro assays available in most laboratories. To date, it is not known to what extent monocyte sampling misdiagnoses the influence of the local myocardial milieu. In RV heart failure due to pulmonary hypertension, only right ventricular beta-adrenergic receptors are decreased [340].

15.7.9 Imaging of Cardiac Transplant Rejection

With aggressive use of immunosuppression and tissue matching, post cardiac transplantation survival has been in excess of 80% at 1 year [370]. Application of immunosuppressive therapy requires an accurate diagnosis of cardiac allograft rejection. The current method of diagnosing rejection is endomyocardial biopsy and the pathological finding of myocyte necrosis [371].

Electrocardiography, and M-mode and 2D echocardiography, have been shown to be too nonspecific [371–373]. Radionuclide imaging with labeled WBC imaging has shown increased deposition in the myocardium during rejection, but was found to be nonspecific, as lymphocyte infiltration is not considered a sufficient criterion for rejection [374–376]. Since myocyte necrosis is the criterion of rejection by biopsy, myocardial infarct-avid In-111-antimyocin antibody imaging has been studied for its potential value in diagnosing rejection noninvasively. In dogs, rejection led to increased uptake even when there was no ECG evidence of rejection. In chronically transplanted hearts without active rejection, In-111-antimyosin antibody uptake was low [377].

Several small patient series were studied: 18 recipients underwent 20 imaging studies, using planar imaging within 24 h of biopsy. Cardiac uptake greater than skeletal uptake gave 16/20 concordant results with biopsies, eight true-positives and eight true-negatives, two false-positives and two false-negatives, for an overall accuracy of 80% [378].

In spite of its early promise, the technique has not become a standard method of evaluating rejection. The time lag between injection and imaging is a disadvantage. The need for serial imaging is made difficult by HAMA (human anti-murine antibody) development, raising the possibility of either allergic reaction or decreasing imaging effectiveness after more than one imaging session. Given the stakes, even 80% accuracy may not be high enough to replace invasive biopsies.

References

1. Fuster V, Badimon L, Badimon JJ, et al (1992) The pathogenesis of coronary artery disease and the acute coronary syndromes. Parts I and II. N Engl J Med 326:1062–1088
2. Fuster V (1994) Mechanisms leading to myocardial infarction: insights from studies of vascular biology. Circulation 90:2126–2146
3. Fuster V, Gotto AM, Libby P, et al (1966) Matching the intensity of risk factor management with the hazard for coronary artery disease events. Pathogenesis of coronary artery disease: the biologic role of risk factors. J Am Coll Cardiol 27:964–976
4. Saikku P, Leinonen M, Mattila K, et al (1988) Serological evidence of an association of a novel Chlamydia, TWAR, with chronic coronary heart disease and acute myocardial infarction. Lancet 2:983–986
5. Markus HS, Sitzer M, Carrington D, et al (1999) *Chlamydia pneumoniae* infection and early asymptomatic carotid atherosclerosis. Circulation 100:832–837
6. Falk E, Shah PK, Fuster V (1995) Coronary plaque disruption. Circulation 92:657–671
7. Gotto AM (1997) Cholesterol management in theory and practice. Circulation 96:4424–4430
8. Davies MJ (1995) Stability and instability: two faces of coronary atherosclerosis. Circulation 94:2013–2019
9. Richardson PD, Davies MJ, Born GV (1989) Influence of plaque configuration and stress distribution on fissuring of coronary atherosclerotic plaques. Lancet 2:1462–1363
10. Ambrose JA, Tannenbaum M, Alexopoulos D, et al (1988) Angiographic progression of coronary artery disease and the development of myocardial infarction. J Am Coll Cardiol 12:56–62
11. Fuster V, Fayad ZA, Badimon JJ (1999) Acute coronary syndromes: biology. Lancet 353 [Suppl II]:5–9
12. Fuster V, Kottke BA (1987) Atherosclerosis A. Pathogenesis, pathology, and presentation of atherosclerosis. In: Brandenburg RO, Fuster V, Giuliani ER, McGoon DC (eds) Cardiology: fundamentals and practice. Year Book Medical Publishers, Chicago, p 981
13. Gutstein DE, Fuster V (1999) Pathophysiology and clinical significance of atherosclerotic plaque rupture. Cardiovasc Res 41:323–333
14. Stary HC, Chandler AB, Dinsmore RE, et al (1995) A definition of advanced types of atherosclerotic lesions and a histologic classification of atherosclerosis: a report from the Committee on Atherosclerosis. American Heart Association. Circulation 92:1355–1374
15. Mintz GS, Pichard AD, Popma JJ, et al (1997) Determinants and correlates of target lesion calcium in coronary artery disease: a clinical, angiographic and intravascular ultrasound study. Am Coll Cardiol 29:268–274
16. Burke AP, Farb A, Malcolm GT, et al (1997) Coronary risk factors and plaque morphology in men with coronary disease who died suddenly. N Engl J Med 226:1276–1281
17. Guststein DE, Fuster V (1999) Pathophysiology and clinical significance of atherosclerotic vessel rupture. Cardiovasc Res 41:323–333
18. Shepherd J, Cobbe SM, Ford I, et al (1995) Prevention of coronary heart disease with pravastatin in men with hypercholesterolemia: West of Scotland Coronary Prevention Study. N Engl J Med 333:1301–1307
19. Scandinavian Simvastatin Survival Study Group (1994) Randomized trial of cholesterol lowering in 444 patients with coronary artery disease: the Scandinavian Simvastatin Survival Study. Lancet 344:1383–1389
20. The Cholesterol and Recurrent Events (CARE) Trial Investigators (1996) The effect of pravastatin on coronary events after myocardial infarction in patients with average cholesterol levels. N Engl J Med 335:1001–1009
21. Fuster V, Badimon JJ (1995) Regression or stabilization of atherosclerosis means regression or stabilization of what we don't see in the arteriogram. Eur Heart J 16:6–12
22. Waters D (1996) Review of cholesterol-lowering therapy: coronary angiographic and events trials. Am J Med 101: 34S–39S
23. Gotto AM (1997) Cholesterol management in theory and practice. Circulation. 96:4424–4430
24. Fuster V, Fallon JT, Badimon JJ, et al (1997) The unstable atherosclerotic plaque: clinical significance and therapeutic intervention. Thromb Haemost 78:247–255
25. Corti R, Fayad ZA, Fuster V, et al (2001) Effects of lipid-lowering by simvastatin on human atherosclerotic lesions: a longitudinal study by high-resolution, noninvasive magnetic resonance imaging. Circulation 104:249–252
26. Rudd JHF, Warburton EA, Fryer TD, et al (2002) Imaging atherosclerotic plaque inflammation with 18-fluorodeoxyglucose positron emission tomography. Circulation 105: 2708–2711
27. Ray KK, Cannon C (2005) The potential relevance of the multiple lipid-independent (pleiotropic) effects of statins in the management of acute coronary syndromes. J Am Coll Cardiol 46:1425–1433
28. Gould KL, Lipscomb K, Hamilton GW (1974) A physiological basis for assessing critical coronary stenosis: instanta-

neous flow response and regional distribution during coronary hyperemia as measures of coronary flow reserve. Am J Cardiol 33:84
29. Kirkeeide R, Gould KL, Parsel L, et al (1986) Assessment of coronary stenoses by myocardial imaging during coronary vasodilation: VII: Validation of coronary flow reserve as a single integrated measure of stenosis severity accounting for all its geometry dimensions. J Am Coll Cardiol 7: 103 – 113
30. Wilson RF (1996) Assessing the severity of coronary artery stenosis. N Engl J Med 334:1735 – 1737
31. Pohost GM, Alpert NM, Ingwall JS, et al (1980) Thallium redistribution mechanisms and clinical utility. Semin Nucl Med 10:70 – 93
32. Dilsizian V, Bonow RO (1992) Differential uptake and apparent Tl-201 washout after thallium reinjection: options regarding early redistribution imaging before reinjection or late redistribution imaging after reinjection. Circulation 85:1032 – 1038
33. Dilsizian V, Bonow RO (1993) Current diagnostic techniques of assessing myocardial viability in patients with hibernating and stunned myocardium. Circulation 87: 1 – 20
34. Dilsizian V, Rocco TP, Freedman NMT, et al (1990) Enhanced detection of ischemic but viable myocardium by the reinjection of thallium after stress-redistribution imaging. N Engl J Med 323:141 – 146
35. Dilsizian V, Freedman NMT, Bacharach SL, et al (1992) Regional thallium uptake in irreversible defects: magnitude of change in thallium activity after reinjection distinguishes viable from nonviable myocardium. Circulation 85:627 – 634
36. Cuocolo A, Pace L, Ricciardelli B, et al (1992) Identification of viable myocardium in patients with chronic coronary artery disease: comparison of Thallium-201 scintigraphy with reinjection and Technetium-99m-methoxyisobutyl isonitrile. J Nucl Med 33:505 – 511
37. Gibson RS, Beller GA (1986) Role of thallium-201 scintigraphy in predicting future cardiac events. In: Ohost GM, Higgins CB, Morganroth J, Ritchie JL, Schelbert HR (eds) New concepts in cardiac imaging 1986. Year Book Medical Publishers, Chicago
38. Maddahi J, Rodrigues E, Kiat J, Van Train KF, Berman DS (1995) Detection and evaluation of coronary artery disease by thallium-201 myocardial perfusion scintigraphy. In: DePuey EG, Berman DS, Garcia E (eds) Cardiac SPECT imaging. Raven, New York
39. Travin MI, Wexler JP (1999) Pharmacological stress testing. Semin Nucl Med 29:298 – 318
40. Okada RD (1988) Myocardial kinetics of technetium-99m hexakis 2-methoxyl 2 methylopropyl isonitrile. Circulation 77:491
41. Wackers FJTh, Berman DS, Maddahi HJ, et al (1989) Technetium-99m hexakis 2-methoxyisobutyl isonitrile: human biodistribution, dosimetry, safety, and preliminary comparison to thallium-201 for myocardial perfusion imaging. J Nucl Med 30:301 – 311
42. Germano G, Kiat H, Moriel M, Kavanagh P, Chua T, Friedman J, Berman DS (1993) Quantitative automatic measurement of left ventricular ejection fraction by gated SPECT. Development and preliminary validation. Clin Nucl Med 18:924
43. Palmas W, Silber W, Friedman J, Kiat H, Klein J, Takemono K, Berman D (1991) Simultaneous Tc99m sestamibi myocardial function/perfusion scintigraphy: information added by wall motion analysis of treadmill exercise first-pass studies. Circulation 84:II–303
44. Abbott BG, Wackers FJT (1998) Emergency department chest pain units and the role of radionuclide imaging. J Nucl Cardiol 5:73 – 79
45. Jain D (1999) Technetium-99m-labeled myocardial perfusion imaging agents. Semin Nucl Med 29:221 – 236
46. Iskandrian A, Heo J, Kong B, et al (1989) Use of technetium-99m isonitrile (RP-30A) in assessing left ventricular perfusion and function at rest and during exercise in coronary artery disease, and comparison with coronary arteriography and exercise thallium-201 SPECT imaging. Am J Cardiol 64:270
47. Maisey M, Lowry A, Bischof-Delaloye A, et al (1990) European multi-center comparison on thallium-201 and technetium-99m methoxisobutylisonitrile in ischemic heart disease. Eur J Nucl Med 16:869
48. Sinusas AJ, Shi QX, Saltzberg MT, et al (1994) Technetium-99m tetrofosmin to assess myocardial blood flow: experimental validation in an intact canine model of ischemia. J Nucl Med 35:664
49. Glover DK, Okada RD (1990) Myocardial kinetics of Tc-MIBI in canine myocardium after dipyridamole. Circulation 81:628 – 637
50. Glover DK, Ruiz M, Edwards NC, et al (1995) Comparison between Tl-201 and Tc-99m sestamibi uptake during adenosine induced vasodilation as a function of coronary artery severity. Circulation 91:813 – 820
51. Berman DS, Kiat H, Friedman JD, Wang FP, Van Train K, Metzer L, Maddahi J, Germano G (1993) Separate acquisition rest thallium-201/stress technetium 99m sestamibi dual-isotope myocardial perfusion single-photon emission computed tomography: a clinical validation study. J Am Coll Cardiol 22:1455 – 1464
52. Seldin DW, Johnson LL, Blood DK (1989) Myocardial perfusion imaging with technetium-99m SQ30217: comparison with thallium-201 and coronary anatomy. J Nucl Med 30:312 – 319
53. Henzlova MJ, Machac J (1994) Clinical utility of technetium-99m-teboroxime myocardial washout imaging. J Nucl Med 35:575 – 579
54. Diwakar J (1999) Technetium-99m-labeled myocardial perfusion imaging agents. Semin Nucl Med 29:221 – 236
55. Taillefer R, Gagnon A, Dufour K, et al (2003) Tc-99m NOET myocardial perfusion imaging (MPI): Is there a relationship between increased lung uptake and smoking history? J Nucl Med 44:155P (Abstract)
56. Detrano R (1989) Exercise-induced ST segment depression in the diagnosis of multivessel coronary disease: a meta analysis. J Am Coll Cardiol 14:1501 – 1508
57. Maddahi J, Rodrigues E, Kiat J, Van Train KF, Berman DS (1995) Detection and evaluation of coronary artery disease by thallium-201 myocardial perfusion scintigraphy. In: DePuey EG, Berman DS, Garcia E (eds) Cardiac SPECT imaging. Raven, New York
58. Detrano R, Gianrossi R, Froelicher VF (1989) The diagnostic accuracy of the exercise electrocardiogram: a meta-analysis of 22 years of research. Prog Cardiovasc Dis 33:173 – 205
59. Roger VL, Jacobsen SI, Pelikka PA, et al (1998) Prognostic value of treadmill exercise testing. a population based study in Olmsted County, Minnesota. Circulation 98: 2836 – 2841
60. Young M, Pan W, Wiesner J, et al (1994) Characterization of arbutamine: a novel catecholamine stress agent for diagnosis of coronary artery disease. Drug Dev Res 32:19 – 28
61. Iskandrian AS, Verani MS, Heo J (1994) Pharmacologic stress testing: mechanism of action, hemodynamic responses, and results in detection of coronary artery disease. J Nucl Cardiol 1:94 – 111
62. Taillefer R, Amyot R, Turpin S, Lambert R, Pilon C, Jarry M (1996) Comparison between dipyridamole and adenosine

as pharmacologic coronary vasodilators in detection of coronary artery disease with thallium 201 imaging. J Nucl Med 3:204 – 211
63. Ranhosky A, Kempthorne-Rawson J, and the Intravenous Dipyridamole Thallium Imaging Study Group (1990) The safety of intravenous dipyridamole thallium myocardial perfusion imaging. Circulation 81:1205 – 1209
64. Travin MI, Wexler JP (1999) Pharmacological stress testing. Semin Nucl Med 29:298 – 318
65. Thomas GS, Prill NV, Majmundar H, et al (2000) Treadmill exercise during adenosine infusion is safe, results in fewer adverse reactions, and improves myocardial perfusion images quality. J Nucl Cardiol 7:439 – 446
66. Vitola JV, Brambatti JC, Caligaris F, et al (2001) Exercise supplementation to dipyridamole prevents hypotension, improves electrocardiogram sensitivity, and increases heart-to-liver activity ratio on Tc-99m sestamibi imaging. J Nucl Cardiol 8:652 – 659
67. Pennell DJ, Mavrogeni SI, Forbat SM, et al (1995) Adenosine combined with dynamic exercise for myocardial perfusion imaging. J Am Coll Cardiol 25:1300 – 1309
68. Hendel RC, Jamil T, Glover DK (2003) Pharmacologic stress testing: new methods and new agents. J Nucl Cardiol 10:197 – 204
69. Kiat H, VanTrain KF, Friedman JD, et al (1992) Quantitative stress-redistribution thallium-201 SPECT using prone imaging: Methodologic development and validation. J Nucl Med 33:1509 – 1512
70. Hayes SW, DeLorenzo A, Hachamovich R, et al (2003) Prognostic implications of combined prone and supine myocardial perfusion SPECT. J Nucl Med 44:1633 – 1640
71. DePuey EG (1994) How to detect and avoid myocardial perfusion SPECT artifacts. J Nucl Med 35:699 – 702
72. Garcia E (1994) Quantitative myocardial perfusion single-photon emission computed tomographic imaging: Quo vadis? J Nucl Cardiol 1:83 – 93
73. Hansen CL, Woodhouse S, Kramer M (2000) Effect of patient obesity on the accuracy of thallium-201 myocardial perfusion imaging. Am J Cardiol 85:749 – 752
74. Bailey DL (1998) Transmission scanning in emission tomography. Eur J Nucl Med 25:774 – 787
75. Zaidi H, Hasegawa B (2003) Determination of the attenuation map in emission tomography. J Nucl Med 44:291 – 315
76. Lang TF, Hasegawa BH, Liew SC, et al (1992) Description of a prototype emission-transmission computed tomography imaging system. J Nucl Med 33:1881 – 1887
77. Bocher M, Balan A, Krausz Y, et al (2000) Gamma camera mounted anatomical X-ray tomography: Technology, system characteristics and first images. Eur J Nucl Med 27:619 – 627
78. Tan P, Bailey DL, Meikle SR, et al (1993) Scanning line source for simultaneous emission and transmission measurements in SPECT. J Nucl Med 34:1753 – 1760
79. Beekman FJ, Kamphuis C, Hutton BF, et al (1998) Hal-fan-beam collimators combined with scanning point sources for simultaneous emission-transmission imaging. J Nucl Med 39:1996 – 2003
80. Bockisch A, Beyer T, Antoch G, et al (2004) Positron mission tomography/computed tomography-imaging protocols, artifacts, and pitfalls. Imaging Biol 6:188 – 199
81. Heller EN, DeMan P, Yi-Hwa I, et al (1997) Extracardiac activity complicates quantitative cardiac SPECT imaging using a simultaneous transmission-emission approach. J Nucl Med 38:1882 – 1890
82. Hendel RC, Berman DS, Cullom SJ, et al (1999) Multicenter clinical trial to evaluate the efficacy of correction for photon attenuation and scatter in SPECT myocardial perfusion imaging. Circulation 99:2742 – 2749
83. Links JM, Becker LC, Rigo P, et al (2000) Combined corrections for attenuation, depth-dependent blur, and motion in cardiac SPECT: A multicenter trial. J Nucl Cardiol 7:414 – 425
84. Links JM, DePuey EG, Taillefer R, et al (2002) Attenuation correction and gating synergistically improve the diagnostic accuracy of myocardial perfusion SPECT. J Nucl Cardiol 9:183 – 187
85. Bateman TM, Heller GV, Johnson LL, et al (2003) Does attenuation correction add value to non-attenuation corrected ECG-gated technetium-99m sestamibi SPECT? J Nucl Cardiol 10:S91 (abstract)
86. Bateman TM, Heller GV, Johnson LL, et al (2003) Relative performance of attenuation-corrected and uncorrected ECG-gated SPECT myocardial perfusion imaging in relation to body mass index. Circulation 108:IV -455 (abstract)
87. Grossman GB, Garcia EV, Bateman TM, et al (2004) Quantitative technetium-99m sestamibi attenuation corrected SPECT: Development and multicenter trial validation of myocardial perfusion stress gender-independent normal database in an obese population. J Nucl Cardiol 11:263 – 272
88. Heller GH, Bateman TM, and the Multicenter Investigators (2004) Clinical value of attenuation correction in stress-only Tc-99m sestamibi SPECT imaging. J Nucl Cardiol 11:273 – 281
89. Bateman TM, O'Keefe JH Jr, Dong VM, et al (1995) Coronary angiographic rates after stress single photon emission computed tomographic scintigraphy. J Nucl Cardiol 2:217 – 223
90. Hachamovich R, Berman DS, Shaw IJ, et al (1998) Incremental prognostic value of myocardial perfusion single photon emission computed tomography for the prediction of cardiac death: differential stratification for risk of cardiac death and myocardial infarction. Circulation 97:535 – 543
91. Diamond GA, Forrester JS (1979) Analysis of probability as an aid in the clinical diagnosis of coronary artery disease. N Engl J Med 300:1350
92. Bateman TM (1997) Clinical relevance of a normal myocardial perfusion scintigraphic study. J Nucl Cardiol 4:172 – 173
93. Iskander S, Iskandrian AE (1998) Risk assessment using single-photon emission computed tomographic technetium-99m sestamibi imaging. J Am Coll Cardiol 32:57 – 62
94. Hachamovitch R, Berman DS, Kiat H, et al (1996) Exercise myocardial perfusion SPECT in patients without known CAD. Incremental prognostic value and use in risk stratification. Circulation 93:905 – 914
95. Mazzanti M, Germano G, Kiat H (1997) Identification of severe and extensive coronary artery disease by automatic measurement of transient ischemic dilatation of the left ventricle in dual isotope myocardial perfusion SPECT. J Am Coll Cardiol 27:1612 – 1620
96. Germano G, Erel J, Lewin H, et al (1997) Automatic quantification of regional myocardial wall motion and thickening from gated technetium-99m sestamibi myocardial perfusion single photon emission computed tomography. J Am Coll Cardiol 30:1360 – 1367
97. Gerson MC, Gerson MC (1997) Test accuracy, test selection, and test result interpretation in chronic coronary artery disease, chap 20. In: Gerson MC (ed) Cardiac nuclear medicine, 3rd edn. McGraw-Hill, New York
98. Farkouh ME, Smars RA, Reeder GS, Zinsmeiter AR, Evans RW, Meloy TD, Kopecky SL, Allen M, Allison TG, Gibons RJ, Gabriel SE (1998) A clinical trial of a chest-pain observation unit for patients with unstable angina. N Engl J Med 339:1882 – 1888

99. Tatum JL, Jesse RI, Kontros MC, et al (1997) Comprehensive strategy for the evaluation and triage of the chest pain patient. Ann Emerg Med 29:116 – 125
100. Heller GV, Stowers SA, Hendel RC, Herman SD, Daher E, Ahlberg AW, Baron JM, Deleon CM, Rizzo JA, Wackers FJ (1998) Clinical value of acute rest technetium-99m tetrofosmin tomographic myocardial perfusion imaging in patients with acute chest pain and nondiagnostic electrocardiograms. J Am Coll Cardiol 31:1011 – 10017
101. Gomez MA, Anderson JL, Karayounes LA, et al (1996) An emergency department-based protocol for rapidly ruling out myocardial ischemia reduces hospital time and expense: results of a randomized study (ROMIO). J Am Coll Cardiol 28:25 – 33
102. Weissman IA, Dickinson CZ, Dworkin HJ, et al (1996) Cost-effectiveness of myocardial perfusion imaging with SPECT in the emergency department evaluation of patients with unexplained chest pain. Radiology 199:353 – 357
103. Stowers SA, Heller GV, Henel RC, et al (1997) Potential cost-effectiveness of tetrofosmine SPECT for initial assessment of emergency department patients with chest pain and nondiagnostic ECG. Circulation 96:I-443 (abstract)
104. Gibson RS, Watson DD, Craddock GB, et al (1983) Prediction of cardiac events after uncomplicated myocardial infarction: a prospective study comparing predischarge exercise thallium-201 scintigraphy and coronary angiography. Circulation 68:321 – 336
105. Younis LT, Byers S, Shaw L, et al (1989) Prognostic importance of silent myocardial ischemia detected by intravenous thallium myocardial imaging in asymptomatic patients with coronary artery disease. J Am Coll Cardiol 14:1635 – 1641
106. Dakik HA, Kleiman NS, Farmer JA, He ZX, Wendt JA, Pratt CM, Verani MS, Mahmarian JJ (1998) Intensive medical therapy versus coronary angioplasty for suppression of myocardial ischemia in survivors of acute myocardial infarction. A prospective, randomized pilot study. Circulation 98:2017 – 2023
107. Boden WE, O'Rourke RA, Crawford MH, et al (1998) Outcomes in patients with acute non-Q-wave myocardial infarction randomly assigned to an invasive as compared with a conservative management strategy. Veterans Affairs Non-Q-Wave Infarction Strategies in Hospital (VANQUISH) Trial Investigation. N Engl J Med 338: 1785 – 1792
108. Mahmarian JJ, Mahmarian AC, Marks GF, et al (1995) Role of adenosine thallium-201 tomography for defining long-term risk in patients after acute myocardial infarction. J Am Coll Cardiol 25:1333 – 1340
109. Maddahi J, Weiss A, Garcia E, et al (1985) Split-dose thallium-201 quantitative imaging for immediate post-reperfusion assessment of intravenous coronary thrombolysis. Eur Heart 6 [Suppl E]:127 – 134
110. O'Keefe JH Jr, Grines CL, DeWood MA, et al (1995) Factors influencing myocardial salvage with primary angioplasty. J Nucl Cardiol 2:35 – 41
111. Gibbons RJ, Verani MS, Behrenbeck T, et al (1989) Feasibility of tomographic 99mTc-hexakis-2-methoxy-2-methylpropyl-isonitrile imaging for the assessment of myocardial area at risk and the effect of treatment in acute myocardial infarction. Circulation 80:1277 – 1286
112. Gibbons RJ, Balady GJ, Bricker TJ, et al (2002) ACC/AHA guideline update for exercise testing: summary article – A report of the American College of Cardiology/American Heart Association Task Force on Practice Guidelines (Committee to Update the 1997 Exercise Testing Guidelines). J Am Coll Cardiol 40:1531 – 1540
113. Young JD (1998) Cardiac transplantation: three decades of experience defines our challenge. Transplant Proc 30:1885 – 1888
114. Oyer PE, Stinson EB, Jamieson SW, et al (1983) Cyclosporin in cardiac transplantation: 2 and 1/2 year follow-up. Transplant Proc 15:2546 – 2552
115. Mairesse GH, Marwick TH, Hanet C, et al (1995) Use of exercise electrocardiography, technetium-99m MIBI perfusion tomography for coronary disease surveillance in a low-prevalence population of heart transplant recipients. J Heart Lung Transplant 14:222 – 229
116. Fang JC, Roco T, Jarcho J, et al (1998) Noninvasive assessment of transplant-associated arteriosclerosis. Am Heart J 125:980 – 987
117. Rigo P, VanBaxen P, Safi JF, et al (1998) Quantitative evaluation of a comprehensive motion, resolution, and attenuation correction program: initial experience. J Nucl Cardiol 5:458 – 468
118. Weich HF, Strauss HW, Pitt B (1977) The extraction of thallium-201 by the myocardium. Circulation 56:188 – 191
119. Cho ZH, Chan JK, Ericksson L, et al (1975) Positron ranges obtained from biomedically important positron-emitting radionuclides. J Nucl Med 16:1174 – 1176
120. Phelps ME, Hoffman EJ, Huang SC, et al (1975) Effect of positron range on spatial resolution. J Nucl Med 16: 649 – 652
121. Derenzo SE, Budinger TF (1977) Resolution limit for positron imaging devices. J Nucl Med 18:491
122. DeBenedetti S, Cowan CE, Konneker WR, et al (1950) On the angular distribution of two-photon annihilation radiation. Phys Rev 77:205 – 212
123. Phelps ME, Hoffman EJ, Huang SC, et al (1978) A new computerized tomographic imaging system for positron-emitting radiopharmaceuticals. J Nucl Med 19:635 – 647
124. Bergstrom M, Eriksson L, Bohm C, et al (1983) Correction for scattered radiation in a ring detector positron camera by integral transformation. J Comput Assist Tomogr 7:42 – 50
125. Phelps ME, Cherry SR (1998) The changing design of positron imaging systems. Clin Pos Imag 1:31 – 45
126. Schelbert HR (1987) Evolution and quantification of regional and myocardial blood flow with positron emission tomography. In: Pohost GM, Higging CB, Morgenroth J, Richie JK, Schelbert HR (eds) New concepts in cardiac imaging. Year Book Medical Publisher, Chicago
127. Tamaki N, Yonekura Y, Senda M, et al (1988) Valve and limitation of stress thallium-201 single photon emission computed tomography: comparison with nitrogen-13 ammonia positron tomography. J Nucl Med 29:1181 – 1188
128. Allan RM, Jones T, Rhodes CCC, et al (1981) Quantification of myocardial perfusion in man using oxygen-15 and positron tomography (abstract). Am J Cardiol 47:481
129. Schelbert HR, Wisenberg G, Phelps ME, et al (1982) Noninvasive assessment of coronary stenoses by myocardial imaging during pharmacologic coronary vasodilation, VI: detection of coronary artery disease in human beings with intravenous N-13 ammonia and positron computed tomography. Am J Cardiol 49:1197 – 1207
130. Gould Kl, Goldstein RA, Mullani NA, et al (1986) Noninvasive assessment of coronary stenoses by myocardial perfusion imaging during pharmacologic coronary vasodilation. VIII. Clinical feasibility of positron cardiac imaging without a cyclotron using generator produced rubidium-82. J Am Coll Cardiol 7:775 – 789
131. Deanfield JE, Shea M, Ribiero P, et al (1984) Transient ST segment depression as a marker of myocardial ischemia during daily life. Am J Cardiol 54:1195 – 1200

132. Deanfield J, Shea M, Wilson R, et al (1983) Mental stress and ischemia in patients with coronary artery disease. Circulation 68:III-258
133. Monahan WG, Tilbury RS, Laughlin JS (1972) Uptake of H-13 labeled ammonia. J Nucl Med 13:274
134. Bergmann SR, Hack S, Tewson T, et al (1980) The dependence of accumulation of N-13-NH_3 by myocardium on metabolic factors and its implications for quantitative assessment of perfusion. Circulation 61:34
135. Gould KL, Schelberth H, Phelps H, et al (1979) Noninvasive assessment of coronary stenosis with myocardial perfusion imaging during pharmacologic coronary vasodilation. V. Detection of 47 percent diameter coronary stenosis with intravenous N-14 ammonia and emission-computed tomography in intact dogs. Am J Cardiol 43: 200
136. Tamaki N, Yonekura Y, Senda M, et al (1985) Myocardial positron computed tomography with N-13 ammonia. Eur J Nucl Med 11:246 – 251
137. Mack RE, et al (1959) Myocardial extraction of Rb-86 in the rabbit. Am J Physiol 197:1175
138. Becker L, Ferreira R, Thomas M (1977) Comparison of Rb-86 and microsphere estimates of left ventricular blood flow distribution. J Nucl Med 15:969
139. Selwyn AP, Allan RM, L'Abbate A, et al (1982) Relation between regional myocardial uptake of rubidium-82 and perfusion: absolute reduction of cation uptake in ischemia. Am J Cardiol 50:112 – 121
140. Goldstein RA, Mullani NA, Marani SK, et al (1983) Myocardial perfusion with rubidium-82. II. Effects of metabolic and pharmacological interventions. J Nucl Med 24:907 – 915
141. Schelbert HR, Ashburn WL, Chauncey DM, et al (1977) Comparative myocardial uptake of intravenously administered radionuclides. J Nucl Med 15:1092
142. Gould KL (1978) Assessment of coronary stenoses by myocardial perfusion imaging during pharmacologic coronary vasodilatation. IV. Limits of stenosis direction by idealized experimental, cross-sectional myocardial imaging. Am J Cardiol 42:761 – 768
143. Blume ED, Altmann K, Mayer JE, et al (1999) Evolution of risk factors influencing early mortality of the arterial switch operation. J Am Coll Cardiol 33:1702 – 1709
144. Murthy KS, Cherian KM (1996) A new technique for ASO with in situ coronary reallocation for TGA. J Thorac Cardiovasc Surg 112:27 – 32
145. Go RT, Marwick TH, MacIntyre WJ, et al (1990) A prospective comparison of rubidium-82 PET and thallium-201 SPECT myocardial perfusion imaging utilizing a single dipyridamole stress in the diagnosis of coronary artery disease. J Nucl Med 31:1899 – 1905
146. Stewart RE, Schwaiger M, Molina E, et al (1991) Comparison of rubidium-82 positron emission tomography and thallium-201 SPECT imaging for detection of coronary artery disease. Am J Cardiol 67:1303 – 1310
147. Gould KL (1991) PET perfusion imaging and nuclear cardiology. J Nucl Med 32:579 – 606
148. Di Carli M, Czernin J, Hoh CK, et al (1995) Relation among stenosis severity, myocardial blood flow, and flow reserve in patients with coronary artery disease. Circulation 91:1944 – 1951
149. Schelbert HR, Wisenberg G, Phelps ME, et al (1982) Noninvasive assessment of coronary stenoses by myocardial imaging during pharmacologic coronary vasodilation. VI: Detection of coronary artery disease in human beings with intravenous N-13 ammonia and positron computed tomography. Am J Cardiol 49:1197 – 1207
150. Arrighi JA, Dione DP, Condos S, et al (1999) Adenosine Tc-99m sestamibi SPECT underestimates ischemia compared with N-13 ammonia PET in a chronic canine model of ischemia. J Nucl Med 40:6P (abstract)
151. Bateman TM, Heller GV, McGhie AI, et al (2005) Attenuation-corrected Tc-99m sestamibi SPECT compared with Rb-82 myocardial perfusion PET. J Nucl Cardiol 12: S118 (abstract)
152. Bateman TM, Heller GV, McGhie AI, et al (2006) Diagnostic accuracy of rest/stress ECG-gated tc99m sestamibi SPECT. J Nucl Cardiol 13:24 – 33
153. Patterson RE, Eisner RL, Horowitz SF (1995) Comparison of cost-effectiveness and utility of exercise ECG, single photon emission computed tomography, positron emission tomography, and coronary angiography for diagnosis of coronary artery disease. Circulation 91:54 – 65
154. Patterson RE, Eisner RI, Chu TS (1996) Cost-effectiveness comparisons: stress echocardiography (Echo) versus myocardial perfusion imaging (MPI) by single photon (SPECT) or positron emission (PET) tomography. J Nucl Med 37:P174 (abstract)
155. Merhige M, Houston T, Shelton V, et al (1998) PET myocardial disease management by eliminating unnecessary invasive diagnostic and therapeutic procedures. J Am Coll Cardiol 31:485 (abstract)
156. Summers RL, Tisdale B, Kolb JC, et al (1999) Role of technetium-99m sestamibi myocardial imaging in the emergency department evaluation of chest pain. J MSMA 39:176 – 179
157. Heller GV, Stowers SA, Hendel RC, et al (1998) Clinical value of rest technetium-99m tetrofosmin tomographic myocardial perfusion imaging in patients with acute chest pain and nondiagnostic electrocardiograms. J Am Coll Cardiol 31:1011 – 1017
158. Kontos MC, Jesse RL, Schmidt KL, et al (1997) Value of acute rest sestamibi perfusion imaging for evaluation of patients admitted to the emergency department with chest pain. J Am Coll Cardiol 30:976 – 982
159. Hilton TC, Thomson RC, Williams HJ, et al (1994) Technetium-99m sestamibi myocardial perfusion imaging in the emergency room evaluation of chest pain. J Am Coll Cardiol 23:1016 – 1022
160. Goldstein RA, Hicks CH, Kuhn JL, et al (1984) Myocardial infarct imaging with rubidium-82 and PET in man. Circulation 70 [Suppl II]:9
161. Parodi O, Schwaiger M, Krivokapich J, et al (1984) Regional myocardial blood flow and wall motion study in patients with designated acute "subendocardial infarction" (abstract). J Am Coll Cardiol 3:552
162. Marwick TH, Shan K, Patel S, et al (1997) Incremental value of rubidium-82 positron emission tomography for prognostic assessment of known or suspected coronary artery disease. Am J Cardiol 80:865 – 870
163. Yoshinaga K, Chow BJW, deKemp R, et al (2004) Prognostic value of rubidium-82 perfusion positron emission tomography: preliminary results from the consecutive 153 patients. J Am Coll Cardiol 43:338A (abstract)
164. Chow BJW, Wong JW, Yoshinaga K, et al (2005) Prognostic significance of dipyridamole-induced ST depression in patients with normal Rb-82 PET myocardial perfusion imaging. J Nucl Med 46:1095 – 1101
165. Nemirovsky D, Henzlova MJ, Machac J, et al (2005) Prognosis of normal rubidium-82 myocardial perfusion study. J Nucl Cardiol 12:S118 (abstract)
166. Schelbert HR, Phelps ME, Huang SC, et al (1981) N-13 ammonia as an indicator of myocardial blood flow. Circulation 63:1259 – 1272
167. Gewirtz H, Skopicki HA, Abraham SA, et al (1997) Quantitative PET measurements of regional myocardial blood

flow: observations in humans with ischemic heart disease. Cardiology 88:62 – 70
168. Bergmann S, Herrero P, Markham J, et al (1989) Noninvasive quantification of myocardial blood flow in human subjects with oxygen-15 labeled water and positron emission tomography. J Am Coll Cardiol 14:639 – 652
169. Huang SC, Schwaiger M, Carson RE, et al (1985) Quantitative measurement of myocardial blood flow with oxygen-15 water and positron computed tomography: an assessment of potential and problems. J Nucl Med 26:616 – 625
170. Mullani NA, Gould KL (1983) First-pass measurements of regional blood flow with external detectors. J Nucl Med 24:577 – 581
171. Mullani NA, Goldstein RA, Gould KL, et al (1983) Myocardial perfusion with rubidium-82. I. Measurement of extraction fraction and flow with external detectors. J Nucl Med 24:898 – 906
172. Goldstein RA, Mullani NA, Marani SK, et al (1983) Myocardial perfusion with rubidium-82. II. Effects of metabolic and pharmacological interventions. J Nucl Med 24:907 – 915
173. Yoshida K, Gould KL (1996) Coronary flow and flow reserve by PET simplified for clinical applications using rubidium-82 or nitrogen-13 ammonia. J Nucl Med 37: 1701 – 1712
174. Pethig K, Heublein B, Meliss RR, et al (1999) Volumetric remodeling of the proximal left coronary artery: early versus late after heart transplantation. J Am Coll Cardiol 34:197 – 203
175. Julius BK, Vassalli G, Mandonow L, et al (1999) Alpha-adrenergic blockade prevents exercise-induced vasoconstriction of stenotic coronary arteries. J Am Coll Cardiol 33:1499 – 1505
176. O'Driscoll G, Green D, Maiorana A, et al (1999) Improvement in endothelial function by angiotensin-converting enzyme inhibition in non-insulin-dependent diabetes mellitus. J Am Coll Cardiol 33:15 – 16
177. Kugiyama K, Motoyama T, Doi H, Kawano H, et al (1999) Improvement of endothelial vasomotor dysfunction by treatment with alpha-tocopherol in patients with high remnant lipoprotein levels. J Am Coll Cardiol 33: 1512 – 1518
178. Huggins GS, Pasternak RC, Alpert NM, et al (1998) Effects of short-term treatment of hyperlipidemia on coronary vasodilator function and myocardial perfusion in regions having substantial impairment of baseline dilator reverse. Circulation 98:1291 – 1296
179. Yokoyama J, Memomura S, Oktake T, Yonekura K, et al (1999) Improvement of impaired myocardial vasodilation due to diffuse coronary atherosclerosis in hypercholesterolemics after lipid-lowering therapy. Circulation 100:117 – 122
180. Gould KL, Martucci JP, Goldberg DL, et al (1994) Short-term cholesterol lowering decreases size and severity of perfusion abnormalities by positron emission tomography after dipyridamole in patients with coronary artery disease. Circulation 89:1530 – 1538
181. Schuler G, Hambrecht R, Schlierf G, et al (1992) Myocardial perfusion and regression of coronary artery disease in patients on a regimen of intensive physical exercise and low fat diet. J Am Coll Cardiol 19:34 – 42
182. Chan P, Machac J, Almeida O, et al (2003) The prevalence and impact of vertical heart movement during rest and stress rubidium-82 cardiac PET imaging. J Nucl Med 44:210 – 211P (abstract)
183. O'Connor MK, Kemp B, Anstett F, et al (2002) A multicenter evaluation of commercial attenuation compensation techniques in cardiac SPECT using phantom models. J Nucl Cardiol 9:361
184. Shaw LJ, Raggi P, Schisterman E, et al (2003) Prognostic value of cardiac risk factors and coronary calcium screening for all-cause mortality. Radiology 228:826 – 833
185. Berman DS, Wong ND, Gransar H, et al (2004) Relationship between stress-induced myocardial ischemia and atherosclerosis measured by coronary calcium tomography. J Am Coll Cardiol 44:923 – 930
186. Kim JH, Machac J, Travis A, et al (2006) Relationship between myocardial flow reserve and coronary calcium score measured by Rb-82 PET/CT in intermediate risk patients. Clin J Nucl Med (in press) (abstract)
187. Ropers D, Baum U, Phle K, et al (2003) Detection of coronary artery stenoses with thin-slice multidetector row spiral computed tomography and multiplanar reconstruction. Circulation 107:664 – 666
188. Paul JF, Ohanessian A, Caussin CH, et al (2004) Visualization of coronary tree and detection of coronary artery stenosis using a 6-slice, sub-millimeter computed tomography: Preliminary experience. Arch Mal Coeur Vaiss 97:31 – 36
189. Namdar M, Hany TF, Siegrist PT, et al (2004) Improved CAD assessment using a combined PET/CT scanner. J Nucl Med 45:117P
190. Namdar M, Hany TF, Koepfli P, et al (2005) Integrated PET/CT for the assessment of coronary artery disease: A feasibility study. J Nucl Med 46:930 – 935
191. DeWiner RJ, Koster RW, Stark A, et al (1995) Value of myoglobin, troponin T, CK-Mb mass in ruling out an acute myocardial infarction in the emergency room. Circulation 92:3401 – 3407
192. Tatum JL, Jesse RL, Kontos MC, et al (1997) Comprehensive strategy for the evaluation and triage of the chest pain patient. Ann Emerg Med 29:116 – 123
193. Fuster V, Chesebro JH (1986) Mechanisms of unstable angina. N Engl J Med 315:1023
194. Burke AP, Farb A, Malcolm GT, et al (1999) Plaque rupture and sudden death related to exertion in men with coronary artery disease. JAMA 281:921 – 926
195. Lam JYT, Chesebro JH, Steele PM, et al (1987) Is vasospasm related to platelet deposition? Relationship in a porcine preparation of arterial injury in vivo. Circulation 75:243
196. Piek JJ, Becker AE (1988) Collateral blood supply to the myocardium at risk in human myocardial infarction: a quantitative post-mortem assessment. J Am Coll Cardiol 1:1290 – 1296
197. Buja LM, Parkey RW, Dees JH, et al (1975) Morphologic correlates of technetium-99m stannous pyrophosphate imaging of acute myocardial infarcts in dogs. Circulation 52:596
198. Fuster V, Badimon L, Cohen M, et al (1988) Insights into the pathogenesis of acute ischemic syndromes. Circulation 77:1213 – 1220
199. Gibson RS (1987) Clinical, functional, and angiographic distinctions between Q wave and non-Q wave myocardial infarction: evidence of spontaneous reperfusion and implications for intervention trials. Circulation 75 [Suppl V]:V0128
200. Klimt CR, Knatterud GL, Stamler J, et al (1986) Persantine-aspirin reinfarction study. Part II. Secondary coronary prevention with persantine and aspirin. J Am Coll Cardiol 7:1192
201. Parkey RW, Bonte FJ, Meyer SL, et al (1974) A new method for radionuclide imaging of acute myocardial infarction in humans. Circulation 50:540 – 546

202. Willerson JT, Parkey RW, Bonte FJ, et al (1975) Technetium stannous pyrophosphate myocardial scintigrams in patients with chest pain of varying etiology. Circulation 51:1046 – 1052
203. Buja LM, Parkey RW, Bonte FJ, et al (1979) Pathophysiology of "cold spot" and "hot spot" myocardial imaging agent used to detect ischemia or infarction. Cardiovasc Clin 10:105
204. Beller GA, Chow BA, Haber E, et al (1977) Localization of radiolabeled cardiac myosin-specific antibody in myocardial infarction comparison with technetium-99m stannous pyrophosphate. Circulation 55:74 – 78
205. Wagner HW (1982) Radioisotopes in medical diagnosis. In: Spittel JA Jr (ed) Clinical medicine, vol 1. Lippincott, Philadelphia, chap 37, pp 1 – 92
206. Holman LB (1980) Radioisotopic examination of the cardiovascular system. In: Braunwald E (ed) Heart disease: a textbook of cardiovascular medicine. Saunders, Philadelphia, pp 363 – 409
207. Holman BL, Tanaka TT, Lesch M (1976) Evaluation of radiopharmaceuticals for the detection of acute myocardial infarction in man. Radiology 121:427
208. Huckell VF, Lyster DM, Morrison RT, et al (1985) Comparison of technetium-99m pyrophosphate and technetium-99m methylene diphosphonate with variable amounts of stannous chloride in the detection of acute myocardial infarction. Clin Nucl Med 10:455 – 462
209. Parkey RW, Bonte FJ, Buja LM, et al (1977) Myocardial infarct imaging with technetium-99m phosphates. Semin Nucl Med 7:15
210. Khaw BA, Fallon JT, Beller GA, et al (1979) Specificity of localization of myosin specific antibody fragments in experimental myocardial infarction: histologic, histochemical, autoradiographic and scintigraphic studies. Circulation 60:1527 – 1531
211. Khaw BA, Scott J, Fallon JT, et al (1982) Quantitation by cell sorting initiated with anti-myosin fluorescent spheres. Science 217:1050 – 1053
212. Khaw BA, Yasuda T, Gold HK, et al (1987) Acute myocardial infarct imaging with indium-111-labeled monoclonal antibody Fab. J Nucl Med 28:1671 – 1678
213. Khaw BA, Gold HK, Yasuda T, et al (1986) Scintigraphic quantification of myocardial necrosis in patients after intravenous injection of myosin-specific antibody. Circulation 74:501 – 508
214. Khaw BA, Strauss HW, Moore R, et al (1987) Myocardial damage delineated by indium-111 antimyosin Fab and technetium-99m pyrophosphate. J Nucl Med 28:76 – 82
215. Johnson LL, Seldin DW, Addonizio LJ (1988) Antimyosin imaging in acute myocardial infarction and cardiac transplant rejection. In: Pohost GM, Higgins CB, Morganroth J, Ritchie JL, Schelbert HR (eds) New concepts in cardiac imaging. Year Book Medical Publishers, Chicago
216. Johnson LL, Lerrick KS, Coromilas J, et al (1987) Measurement of infarct size and percentage myocardium infarcted in a dog preparation with single photon-emission computed tomography, thallium-2091, and indium-111-monoclonal antimyosin Fab. Circulation 76:181 – 190
217. Fornet B, Yasuda T, Wilkinson R, et al (1989) Detection of acute cardiac injury with techntetium-99m glucaric acid. J Nucl Med 30:1743
218. Narula J, Petrov A, Pak KY, et al (1997) Very early noninvasive detection of acute experimental non-reperfused myocardial infarction with technetium-99m-labeled glucarate. Circulation 95:1577 – 1584
219. Orlandi C, Crane PD, Edwards DS, et al (1991) Early scintigraphic detection of experimental myocardial infarction in dogs with technetium-99m-glucaric acid. J Nucl Med 2:263 – 268
220. Khaw BA (1999) The current role of infarct avid imaging. Semin Nucl Med 29:259 – 270
221. Ohtani H, Callahan RJ, Khaw BA, et al (1992) Comparison of technetium-99m glucarate and thallium-201 for the identification of acute myocardial infarction in rats. J Nucl Med 33:1988 – 1993
222. Mariani G, Villa G, Rossettin PF, et al (1997) Clinical phase I Tc-99m glucaric acid study for very early visualization of acute myocardial infarction. J Am Coll Cardiol 29:451A (abstract)
223. Cowie MR, Mosterd A, Wood DA, et al (1997) The epidemiology of heart failure. Eur Heart J 18:208 – 225
224. Ho KKI, Pinsky JL, Kannel WB, Levy D (1993) The epidemiology of heart failure: the Framingham Study. J Am Coll Cardiol 22 [Suppl A]:6A–13A
225. Kannel WB, Ho K, Thom T (1994) Changing epidemiological features of cardiac failure. Br Heart J 72:S3–S9
226. Teerlink JR, Goldhaber SZ, Pfeffer MA (1991) An overview of contemporary etiologies of congestive heart failure. Am Heart J 121:1852 – 1853
227. Levine TB, Francis GS, Goldsmith SR, et al (1982) Activity of the sympathetic nervous system and renin-angiotensin system assessed by plasma hormone levels and their relationship to hemodynamic abnormalities in congestive heart failure. Am J Cardiol 49:1659 – 1666
228. Goldsmith SR, Francis GS, Cowley AW Jr, et al (1983) Increased plasma arginine vasopressin levels in patients with congestive heart failure. J Am Coll Cardiol 1:1385 – 1390
229. Levine TB, Francis GS, Goldsmith SR, et al (1983) The neurohumoral and hemodynamic response to orthostatic tilt in patients with congestive heart failure. Circulation 67:1070 – 1075
230. Goldsmith SR, Francis GS, Levine TB, et al (1983) Regional blood flow response to orthostasis in patients with congestive heart failure. J Am Coll Cardiol 1:1391 – 1395
231. Cody RJ, Franklin KW, Kluger J, et al (1982) Mechanisms governing the postural response and baroreceptor abnormalities in chronic congestive heart failure: effects of acute and long-term converting-enzyme inhibition. Circulation 66:135 – 142
232. Francis GS, Goldsmith SR, Levine TB, et al (1984) The neurohumoral axis in congestive heart failure. Ann Intern Med 101:370 – 377
233. Kubo SH, Cody RJ (1983) Circulatory autoregulation in chronic congestive heart failure responses to head-up tilt in 41 patients. Am J Cardiol 52:512 – 518
234. Olivari MT, Levine TB, Cohn JN (1983) Abnormal neurohumoral response to nitroprusside infusion in congestive heart failure. J Am Coll Cardiol 2:411 – 417
235. Harlan WR, Obermann A, Grimm R, Rosati RA (1977) Chronic congestive heart failure in coronary artery disease: clinical criteria. Ann Intern Med 86:133 – 138
236. Wheeldon NM, MacDonald TM, Flucker CJ, et al (1993) Echocardiography in chronic heart failure in the community. QJM 86:17 – 23
237. Remes J, Reunanen A, Aromaa A, et al (1992) Incidence of heart failure in eastern Finland: a population-based surveillance study. Eur Heart J 13:588 – 593
238. Cleland JGF, Habib F (1996) Assessment and diagnosis of heart failure. J Intern Med 239:317 – 325
239. Tresch DD (1997) The clinical diagnosis of heart failure in older patients. J Am Geriatr Soc 45:1128 – 1133
240. Brater DC (1998) Diuretic therapy. N Engl J Med 339:387 – 395
241. Konstan MA, Remme WJ (1998) Treatment guidelines in heart failure. Prog Cardiovasc Dis 41:65 – 72

242. Dormans TPJ, Gerlag PGG, Russel FGM, et al (1998) Combination diuretic therapy in severe congestive heart failure. Drugs 55:165 – 172
243. Garg R, Yusuf S (1996) Overview of randomized trials of angiotensin-converting enzyme inhibitors on mortality and morbidity in patients with heart failure. JAMA 273:1450 – 1456
244. The Digitalis Investigation Group (1997) The effect of digoxin on mortality and morbidity in patients with heart failure. N Engl J Med 336:525 – 533
245. Zarembski DG, Nolan PE, Slack MK, et al (1996) Meta-analysis of the use of low-dose beta-adrenergic blocking therapy in idiopathic dilated cardiomyopathy. Am J Cardiol 77:1247 – 1250
246. Doughty RN, Rodgers A, Sharpe N, et al (1997) Effects of beta-blocker therapy on mortality in patients with heart failure. Eur Heart J 18:560 – 565
247. Heidenreich PA, Lee TT, Massie BM (1997) Effect of beta-blockade on mortality in patients with heart failure: a meta-analysis of randomized clinical trials. J Am Coll Cardiol 30:27 – 34
248. Avezum A, Tsuyuki RT, Pogue J, et al (1998) Beta-blocker therapy for congestive heart failure: a systematic overview and critical appraisal of the published trials. Can J Cardiol 14:1045 – 1053
249. Lechat P, Packer M, Cahlon S, et al (1998) Clinical effects of beta-adrenergic blockade in chronic heart failure: a meta-analysis of double-blind, placebo controlled, randomized trials. Circulation 98:1184 – 1191
250. Packer M, Bristow MR, Cohn JN, et al (1996) The effect of carvedilol on morbidity and mortality in patients with chronic heart failure. N Engl J Med 334:1349 – 1355
251. Kannel WB, Plehn JF, Cupples LA (1988) Cardiac failure and sudden death in the Framingham study. Am Heart J 115:869 – 875
252. Bigger JT Jr (1987) Why patients with congestive heart failure die: arrhythmias and sudden cardiac death. Circulation 75 [Suppl 5,2]:IV28–IV35
253. Amiodarone Trials Meta-Analysis Investigators (1997) Effect of prophylactic amiodarone on mortality after acute myocardial infarction and in congestive heart failure: meta-analysis of individual data from 6500 patients in randomized trials. Lancet 1997:1417 – 1424
254. Moss AJ, Hall WJ, Cannom DS, et al (1996) Improved survival with an implanted defibrillator in patients with coronary disease at high risk for ventricular arrhythmia. N Engl J Med 335:1933 – 1940
255. Levine MN, Raskob G, Landefeld S, et al (1995) Hemorrhagic complications of anticoagulant therapy. Chest 108:2765 – 2905
256. Ware JA, Simons M (1997) Angiogenesis in ischemic heart disease. Nat Med 3:158 – 164
257. Packer M, Yushak MN (1984) Hemodynamic and clinical limitations of long-term inotropic therapy with amrinone in patients with severe chronic heart failure. Circulation 70:1038 – 1047
258. Hinkle LE Jr, Thaler HT (1982) Clinical classification of cardiac death. Circulation 65:457 – 464
259. Feldman AM, Bristow MR, Parmley WW, et al (1993) Effects of vesnarinone on morbidity and mortality in patients with heart failure. N Engl J Med 329:149 – 155
260. Louie HW, Laks H, Milgalter E, et al (1991) Ischemic cardiomyopathy: criteria for coronary revascularization and cardiac transplantation. Circulation 84 [Suppl 111]:III-290–III-295
261. Kjekhus J (1990) Arrhythmias and mortality in congestive heart failure. Am J Cardiol 65:42I–48I
262. Packer M (1992) Lack of relation between ventricular arrhythmias and sudden death in patients with chronic heart failure. Circulation 85:I50–I56
263. Gradman A, Deedwania P, Cody R, et al (1989) Predictors of total mortality and sudden death in mild to moderate heart failure. J Am Coll Cardiol 14:564 – 570
264. Sugrue DD, Rodeheffer RJ, Codd MB, et al (1992) The clinical course of idiopathic dilated cardiomyopathy. Ann Intern Med 117:117 – 123
265. Ho KK, Anderson KM, Kannel WB, et al (1993) Survival after the onset of congestive heart failure in Framingham heart study subjects. Circulation 99:107 – 115
266. Kalon KJH, Keaven MA, Kannel WB, et al (1993) Survival after the onset of congestive heart failure in Framingham heart subjects. Circulation 88:107 – 115
267. Waldo AL, Camm AJ, deRuyter H, et al (1996) Effect of d-sotalol on mortality in patients with left ventricular dysfunction after recent and remote myocardial infarction. Lancet 348:7 – 12
268. Stevenson WG, Middlekauff HM, Stevenson LW, et al (1992) Significance of aborted cardiac arrest and sustained ventricular tachycardia in patients referred for treatment therapy of advanced heart failure. Am Heart J 124:123 – 130
269. Stevenson WG, Stevenson LW, Middlekauf HR, et al (1993) Sudden death prevention in patients with advanced ventricular dysfunction. Circulation 88:2953 – 2961
270. Lee KL, Pryor DB, Peiper KS, et al (1990) Prognostic value of radionuclide angiography in medically treated patients with coronary artery disease. A comparison with clinical and catheterization variables. Circulation 82:1705 – 1717
271. Francis GS, Goldsmith SR, Cohn JN (1982) The relationship of exercise capacity to resting left ventricular performance and basal plasma norepinephrine levels in patients with congestive heart failure. Am Heart J 104: 725 – 731
272. Franciosa JA, Park M, Levine TB (1981) Lack of correlation between exercise capacity and indexes of resting left ventricular performance in heart failure. Am J Cardiol 47:33 – 39
273. Consensus Recommendations for Heart Failure (1999) Evaluation of patients and treatment. Am J Cardiol 83:2A–8A
274. Polak JF, Holman BL, Wynne J, et al (1983) Right ventricular ejection fraction: an indicator of increased mortality in patients with congestive heart failure associated with coronary artery disease. J Am Coll Cardiol 2:217 – 224
275. CASS Principal Investigators and their Associates (1983) Coronary Artery Surgery Study (CASS): a randomized trial of coronary artery bypass surgery. Survival data. Circulation 68:939
276. Lansman SL, Cohen M, Galla JD, et al (1993) Coronary bypass with ejection fraction 0.20 or less using centigrade cardioplegia: long-term follow-up. Ann Thor Surg 56:480 – 486
277. Braunwald E, Kloner RA (1982) The stunned myocardium: prolonged, post-ischemic ventricular dysfunction. Circulation 66:1146 – 1149
278. Bolli R (1990) Mechanism of myocardial stunning. Circulation 82:723 – 772
279. Ferrari R, LaCanna G, Giubbini R, et al (1994) Left ventricular dysfunction due to stunning and hibernation in patients. Cardiovasc Drugs Ther 8 [Suppl 2]:371 – 380
280. Fuster V, Badimon L, Badimon JJ, et al (1992) The pathogenesis of coronary artery disease and the acute coronary syndromes. N Engl J Med 326:242 – 250, 310 – 318
281. Homans DC, Laxson DD, Sublett E, et al (1989) Cumulative deterioration of myocardial function after repeated

episodes of exercise-induced ischemia. Am J Physiol 256:H1462–H1471
282. Shivalkar B, Flameng W, Szilard M, et al (1999) Repeated stunning precedes myocardial hibernation in progressive multiple coronary artery stenosis. J Am Coll Cardiol 34:2126 – 2136
283. Rahimtoola SH (1989) The hibernating myocardium. Am Heart J 117:211 – 221
284. Haas F, Haehnel C, Augustin N, et al (1997) Prevalence and time course of functional improvement in stunned and hibernating myocardium in patients with CAD and CHF. J Am Coll Cardiol 29:788A (abstract)
285. Melon PG, DeLandsheere CM, Degueldre C, et al (1997) Relation between contractile reserve and positron emission tomographic patterns of perfusion and glucose utilization in chronic ischemic left ventricular dysfunction. J Am Coll Cardiol 30:1651 – 1659
286. Brunken R, Tillisch J, Schwaiger M, et al (1986) Regional perfusion, glucose metabolism, and wall motion in patients with chronic electrocardiographic Q-wave infarctions: evidence for persistence of viable tissue in some infarct regions by positron emission tomography. Circulation 73:951 – 963
287. Bax JJ, Wijns W, Cornel JH, et al (1997) Accuracy of currently available techniques for prediction of functional recovery after revascularization in patients with left ventricular dysfunction due to chronic coronary artery disease: comparison of pooled data. J Am Coll Cardiol 30:1451 – 1460
288. Smart S, Wynsen J, Sagar K (1997) Dobutamine-atropine stress echocardiography for reversible dysfunction during the first week after myocardial infarction: Limitations and determinations of accuracy. J Am Coll Cardiol 30:1669 – 1678
289. Dilsizian V, Bonow RO (1992) Differential uptake and apparent Tl-201 washout after thallium reinjection: options regarding early redistribution imaging before reinjection or late redistribution imaging after reinjection. Circulation 85:1032 – 1038
290. Dilsizian V, Bonow RO (1993) Current diagnostic techniques of assessing myocardial viability in patients with hibernating and stunned myocardium. Circulation 87: 1 – 20
291. Dilsizian V, Rocco TP, Freedman NMT, et al (1990) Enhanced detection of ischemic but viable myocardium by the reinjection of thallium after stress-redistribution imaging. N Engl J Med 323:141 – 146
292. Perrone-Filardi P, Bacharach SL, Dilsizian V, et al (1992) Regional left ventricular wall thickening: relation to regional uptake of F-18-fluorodeoxyglucose and Tl-201 in patients with chronic coronary artery disease and left ventricular dysfunction. Circulation 86:1125 – 1137
293. Dilsizian V, Freedman NMT, Bacharach SL, et al (1992) Regional thallium uptake in irreversible defects: magnitude of change in thallium activity after reinjection distinguishes viable from nonviable myocardium. Circulation 85:627 – 634
294. Gunning MG, Anagnostopoulos C, Knight CJ, et al (1998) Comparison of Tl-201, Tc-99m-tetrofosmin, and dobutamine magnetic resonance imaging for identifying hibernating myocardium. Circulation 98:1869 – 1874
295. Dilsizian V, Arrhighi JA, Diodati JG, et al (1994) Myocardial viability in patients with chronic coronary artery disease, comparison of Tc-99m sestamibi with thallium reinjection and F-18 fluorodeoxyglucose. Circulation 89:578 – 587
296. Kim YK, Lee DS, Cheon J, et al (1999) Myocardial viability assessment by nitroglycerine gated Tc-99m MIBI SPECT: comparison with rest-24-hour redistribution Tl-201 SPECT. J Nucl Med 40:1P(abstract)
297. Bax JJ, Maddahi J, Poldermans D, et al (1999) Enhanced diagnostic accuracy to predict improvement of LVEF post-revascularization by sequential thallium-201 imaging and dobutamine echocardiography. J Nucl Med 40:1P (abstract)
298. Gropler RJ, Geltman EM, Sampathkumaran K, et al (1993) Comparison of carbon-11 acetate with fluorine-18 fluorodeoxyglucose for delineating viable myocardium by positron emission tomography. J Am Coll Cardiol 22:1587 – 1597
299. Vanoverschelde J-L, Wijns W, Depre C, et al (1993) Mechanisms of chronic regional postischemic dysfunction in humans; new insights from the study of noninfarcted collateral-dependent myocardium. Circulation 87:1513 – 1523
300. Bolli R (1996) The early and late phases of preconditioning against myocardial stunning and the essential role of oxyradicals in the late phase: an overview. Basic Res Cardiol 91:57 – 63
301. Perrone-Filardy P, Bacharach S, Dilsizian V, et al (1994) Clinical significance of regional myocardial glucose uptake in regions with normal blood flow in patients with chronic coronary artery disease. J Am Coll Cardiol 23:608 – 616
302. Maes A, Flameng W, Nuyts J, et al (1994) Histological alterations in chronically hypoperfused myocardium: correlation with PET findings. Circulation 90:735 – 745
303. Fallavolita JA, Canty JM (1997) F-18 FDG utilization is regionally increased in fasting pigs with hibernating myocardium. J Am Coll Cardiol 29:130A (abstract)
304. Schelbert HR (1984) The emergence of positron-emission tomography as a clinical tool for studying local myocardial function. In: Freeman LM, Weissman HS (eds) Nuclear medicine annual. Raven, New York, p 141
305. Sandler MP, Videlefsky S, Delbeke D, et al (1995) Evaluation of myocardial ischemia using a rest metabolism/stress perfusion protocol with fluorine-18 deoxyglucose/technetium-99m MIBI and dual-isotope simultaneous acquisition single-photon emission computed tomography. J Am Coll Cardiol 26:870 – 888
306. Bax JJ, Cornel JH, Visser FC, et al (1997) F-18 fluorodeoxyglucose single-photon emission computed tomography predicts functional outcome of dyssynergic myocardium after surgical revascularization. J Nucl Cardiol 4:302 – 308
307. Burt RW, Perkins OW, Oppenheim BE, et al (1995) Direct comparison of fluorine-18-FDG SPECT, fluorine-18-FDG PET, and rest thallium-201 SPECT for detection of myocardial viability. J Nucl Med 36:176 – 179
308. Bax JJ, Cornel JH, Visser FC, et al (1998) Differentiating viability criteria on F-18 fluorodeoxyglucose imaging for the optimal prediction of functional recovery after revascularization. J Am Coll Cardiol 31:300A (abstract)
309. Hansen CL, Corbett JR, Pippin JJ, et al (1988) 123-I-phenylpentadecanoic acid and single photon emission computed tomography in identifying LV regional metabolic abnormalities in patients with coronary heart disease: comparison with thallium-201 myocardial tomography. J Am Coll Cardiol 12:78 – 87
310. Hansen CL, Rastogi A, Sangrigoli R, et al (1998) On myocardial perfusion, metabolism, and viability. J Nucl Cardiol 5:202 – 204
311. Fujiwara S, Takeishi Y, Atsumi H, et al (1998) Prediction of functional recovery in acute myocardial infarction: comparison between sestamibi reverse redistribution and sestamibi/BMIPP mismatch. J Nucl Cardiol 5:119 – 127

312. Knapp FT, Granken P, Kropp J (1995) Cardiac SPECT with iodine-123-labeled fatty acids: evaluation of myocardial viability with BMIPP. J Nucl Med 36:1022 – 1030
313. Shimonagata T, Nanto S, Kusuoka H, et al (1998) Metabolic changes in hibernating myocardium after percutaneous transluminal coronary angioplasty and the relation between recovery in left ventricular function and free fatty acid metabolism. Am J Cardiol 82:559 – 563
314. Bax JJ, Visser FC, Cornel JH, et al (1999) The extent of viable tissue determines the magnitude of improvement of LVEF post-revascularization. J Nucl Med 40:47P (abstract)
315. Tillisch J, Brunken R, Marshall R, et al (1986) Reversibility of cardiac wall motion abnormalities predicted by positron emission tomography. N Engl J Med 314:884 – 884
316. Pasquet A, Robert A, D'Hondt AM, et al (1999) Prognostic value of myocardial ischemia and viability in patients with chronic left ventricular ischemic dysfunction. Circulation 100:141 – 148
317. Layher J, Ziles D, Englestein E, et al (1997) PET mismatch identifies patients at risk for arrhythmic death. J Am Coll Cardiol 29:413A (abstract)
318. Huiting JM, Visser FC, Bax JJ, et al (1998) Predictive value of planar 18F-fluorodeoxyglucose imaging for cardiac events in patients after acute myocardial infarction. Am J Cardiol 81:1072 – 1077
319. Bax JJ, Poldermans D, Elhendy A, et al (1999) Improvement of left ventricular ejection fraction, heart failure symptoms and prognosis after revascularization in patients with chronic coronary artery disease and viable myocardium detected by dobutamine stress echocardiography. J Am Coll Cardiol 34:163 – 169
320. Langenburg SE, Cuchanan SA, Blackbourne LH, et al (1995) Predicting survival after coronary revascularization for ischemic cardiomyopathy. Ann Thorac Surg 60:1193 – 1196
321. Lansman SL, Cohen M, Galla JD, et al (1993) Coronary bypass with ejection fraction of 0.20 or less using centigrade cardioplegia: long-term follow-up. Ann Thorac Surg 56:480 – 485
322. Kaul TK, Agnihotri A, Fields BL, et al (1996) Coronary artery bypass grafting in patients with an ejection fraction of twenty percent or less. J Thorac Cardiovasc Surg 111:1001 – 1012
323. Eitzman D, Al-Aourar Z, Kanter HL, et al (1992) Clinical outcome of patients with advanced coronary artery disease after viability studies with positron emission tomography. J Am Coll Cardiol 20:559 – 565
324. DiCarli MF, Asgarzadie F, Schelbert HR, et al (1995) Quantitative relation between myocardial viability and improvement in heart failure symptoms after revascularization in patients with ischemic cardiomyopathy. Circulation 92:3436 – 3444
325. Chan RK, Raman J, Lee KJ, et al (1996) Prediction of outcome after revascularization in patients with poor left ventricular function. Ann Thorac Surg 61:1428 – 1434
326. Haas F, Haehnel CJ, Picker W, et al (1997) Preoperative positron emission tomographic viability assessment and perioperative and post-operative risk in patients with advanced ischemic heart disease. J Am Coll Cardiol 30:1693 – 700
327. Beanlands RSB, Hendry PJ, Masters RG, et al (1998) Delay in revascularization is associated with increased mortality rate in patients with severe left ventricular dysfunction and viable myocardium on fluorine 18-fluorodeoxyglucose positron emission tomography imaging. Circulation 98:II-51–II-56
328. Czernin J, Allen-Auerbach M, Shoder H, et al (1999) Impact of cardiac PET on management of patients with congestive heart failure. J Nucl Med 40:47P (abstract)
329. Mudge GH, Goldstein S, Addonizio LJ, et al (1993) Task force 3: recipient guidelines/prioritization. J Am Coll Cardiol 22:21 – 31
330. Evans RW, Manninen DL, Garrison LP, et al (1986) Donor availability as the primary determinant of the future of heart transplantation. JAMA 255:1982 – 1985
331. Schwartz F, Mall G, Zebe H, et al (1984) Determination of the survival in patients with congestive cardiomyopathy: quantitative morphologic findings and left ventricular hemodynamics. Circulation 70:923 – 928
332. Diaz RA, Obasohan A, Oakley CM (1987) Prediction of outcome in dilated cardiomyopathy. Br Heart J 58:393 – 399
333. Likoff MJ, Chandler SL, Kay HR (1987) Clinical determinants of mortality in chronic congestive heart failure secondary to idiopathic cardiomyopathy or to ischemic cardiomyopathy. Am J Cardiol 59:634 – 638
334. Keogh AM, Freund J, Baron DW, et al (1988) Timing of cardiac transplantation in idiopathic cardiomyopathy. Am J Cardiol 61:418 – 422
335. Mancini DM, Eisen H, Kussmaul W, et al (1991) Value of peak exercise oxygen consumption for optimal timing of cardiac transplantation in ambulatory patients with heart failure. Circulation 83:778 – 786
336. Cohn JN, Levine BT, Olivari MT, et al (1984) Plasma norepinephrine as a guide to prognosis in patients with chronic congestive heart failure. N Engl J Med 311:819 – 823
337. Creager MA, Faxon DP, Halperin JL, et al (1982) The determinants of clinical response and survival in patients with congestive heart failure treated with enalapril. Am Heart J 104:1147 – 1154
338. Rector TS, Olivari MT, Levine TB, et al (1987) Predicting survival for an individual with congestive heart failure using the plasma norepinephrine concentration. Am Heart J 114:148 – 152
339. Sisson JC (1993) The adrenergic nervous system of the heart and nuclear medicine. In: Freeman LM (ed) Nuclear medicine annual. Raven, New York, p 234
340. Sullebarger JT, Liang C (1991) Beta-adrenergic receptor stimulation and inhibition in chronic congestive heart failure. Heart Failure 7:154 – 160
341. Bristow MR, Anderson FL, Port JD, et al (1991) Differences in beta-adrenergic neuroeffector mechanisms in ischemic versus idiopathic dilated cardiomyopathy. Circulation 84:1024 – 1039
342. CIBIS Investigator and Committee (1994) A randomized trial of beta-blockade in heart failure; the cardiac insufficiency bisoprol study (CIBIS). Circulation 90:1765 – 1773
343. Sisson JC, Shapiro B, Meyers L, et al (1987) Meta-iodobenzylguanidine to map scintigraphically the adrenergic nervous system in man. J Nucl Med 28:1625 – 1636
344. Dae MW, O'Connell JW, Botvinick EH, et al (1989) Scintigraphic assessment of regional cardiac adrenergic innervation. Circulation 79:634 – 644
345. Schwaiger M, Kalff V, Rosenepire K, et al (1990) Noninvasive evaluation of sympathetic nervous system in human heart by positron emission tomography. Circulation 82:457 – 464
346. Deforge J, Syrota A, Lancon JP, et al (1991) Cardiac beta-adrenergic receptor density measured in vivo using PET, CGP 12177, and a new graphical method. J Nucl Med 32:739 – 748
347. Sisson JC, Wieland DM, Koeppe RA, et al (1991) Scintigraphic portrayal of beta receptors in the heart. J Nucl Med 32:1399 – 1407

348. Wieland DM, Brown LE, Rogers WL, et al (1981) Myocardial imaging with a radioiodinated norepinephrine storage analog. J Nucl Med 22:22 – 31
349. Nakajo M, Shimabukuro K, Yoshimura H, et al (1986) Iodine-131 metaiodobenzylguanidine intra- and extravesicular accumulation in the rat heart. J Nucl Med 27:84 – 89
350. Nakajo M, Shapiro B, Glowniak J, et al (1983) Inverse relationship between cardiac accumulation of meta-I-123-iodobenzylguanidine (I-131 MIBG) and circulating catecholamines in suspected pheochromocytoma. J Nucl Med 24:1127 – 1134
351. Kurata C, Shouda S, Mikami T, et al (1997) Comparison of I-123-metaiodobenzylguanidine kinetics with heart rate variability and plasma norepinephrine level. J Nucl Cardiol 4:515 – 523
352. Sisson JC, Shapiro B, Meyers L, et al (1987) Metaiodobenzylguanidine to map scintigraphically the adrenergic nervous system in man. J Nucl Med 28:1625 – 1636
353. Yamakado K, Takeda K, Kitano T, et al (1992) Serial change of iodine-123 metaiodobenzylguanidine (MIBG) myocardial concentration in patients with dilated cardiomyopathy. Eur J Nucl Med 19:265 – 270
354. Glowniak JV, Turner FE, Gray LL, et al (1989) Iodine-123 metaiodobenzylguanidine imaging of the heart in idiopathic congestive cardiomyopathy and cardiac transplants. J Nucl Med 30:1182 – 1191
355. Schofer J, Spielmass R, Schuchert A, et al (1988) Iodine-123 meta-iodobenzylguanidine scintigraphy: a noninvasive method to demonstrate myocardial adrenergic nervous system dysintegrity in patients with idiopathic dilated cardiomyopathy. J Am Coll Cardiol 12:1252 – 1258
356. Schofer J, Spielmann R, Schuchert A, et al (1988) Iodine-123 meta-iodobenzylguanidine scintigraphy: a noninvasive method to demonstrate myocardial adrenergic nervous system disintegrity in patients with idiopathic dilated cardiomyopathy. J Am Coll Cardiol 12:1252 – 1258
357. Merlet P, Duboi-Rande JL, Adnot S, et al (1992) Myocardial beta-adrenergic desensitization and neuronal norepinephrine uptake function in idiopathic dilated cardiomyopathy. J Cardiovasc Pharmacol 19:10 – 16
358. Toyama T, Aihara Y, Iwasaki T, et al (1999) Cardiac sympathetic activity estimated by I-123-MIBG myocardial imaging in patients with dilated cardiomyopathy after beta-blocker or angiotensin-converting enzyme inhibitor therapy. J Nucl Med 40:217 – 223
359. Choi JY, Lee KH, Lee SH, et al (1999) I-123 MIBG imaging before treatment to predict improvement of LV function after carvedilol medication in heart failure patients. J Nucl Med 40:162P (abstract)
360. Merlet P, Benvenuti C, Moyse D, et al (1999) Prognostic value of MIBG imaging in idiopathic dilated cardiomyopathy. J Nucl Med 40:917 – 923
361. Agostini D, Belin A, Filmont JE, et al (1999) Low cardiac MIBG uptake predicts for high risk of cardiac events in cardiomyopathy. J Nucl Med 40:P43–P44
362. Inoue H, Zipes DP (1988) Time course of denervation of efferent sympathetic and vagal nerves after occlusion of the coronary artery in the canine heart. Circ Res 62: 111 – 120
363. Kammerling JJ, Green FJ, Watanabe AM, et al (1987) Denervation supersensitivity of refractoriness in noninfarcted areas apical to transmural myocardial infarction. Circulation 76:383 – 393
364. Stanton MS, Tuli MM, Radtke NL, et al (1989) Regional sympathetic denervation after myocardial infarction in humans detected noninvasively using I-123-metaiodobenzylguanidine. J Am Coll Cardiol 14:1519 – 1526
365. Merlet P, Defolge J, Syrota A, et al (1993) Positron emission tomography with C-11 CGP-12177 to assess beta-adrenergic receptor concentration in idiopathic dilated cardiomyopathy. Circulation 87:1169 – 1178
366. Bristow MR, Ginsburg R, Monobe W, et al (1982) Decreased catecholamine sensitivity and beta-adrenergic-receptor density in failing human heart. N Engl J Med 307:205 – 211
367. Martinsson A, Larsson K, Hjemdahl P (1987) Studies in vivo and in vitro terbutaline – induced beta-adrenoreceptor desensitization in healthy subjects. Clin Sci 72: 47 – 54
368. Buja LM, Muntz KH, Rosenbaum T, et al (1985) Characterization of a potentially reversible increase in beta-adrenergic receptors in isolated, neonatal rat cardiac myocytes with impaired energy metabolism. Circ Res 57:640 – 645
369. Qing F, Rahman SU, Hayes MU, et al (1997) Effect of chronic B2-agonist dosing on human cardiac beta-adrenoceptor expression in vivo: comparison with changes in lung and mononuclear leukocyte beta-receptors. J Nucl Cardiol 4:532 – 538
370. Oyer PE, Stinson EB, Jamieson SW, et al (1983) Cyclosporine in cardiac transplantation: 2 1/2 year follow-up. Transplant Proc 15:2546 – 2552
371. Dawkins KD, Oldershaw PJ, Billingham ME, et al (1984) Changes in diastolic function as a noninvasive marker of cardiac allograft rejection. Heart Transplant 3:286 – 194
372. Clark MB, Spotnitz HM, Dubroff JM, et al (1983) Acute rejection after cardiac transplantation: detection by two-dimensional echocardiography. Surg Form 34:248 – 250
373. Keren A, Gillis AM, Freedman RA, et al (1983) Heart transplant rejection monitored by single-averaged electrocardiogram in patients receiving cyclosporin A (abstract). Circulation 68:II-151
374. Lerch RA, Bergmann SR, Carlson EM, et al (1982) Monitoring of cardiac antirejection therapy with In-111 lymphocytes. J Nucl Med 23:496 – 500
375. Farid NA, White SM, Heck LL, et al (1983) Tc-99m-labeled leukocytes. Preparation and use in identification of abscess and tissue rejection. Radiology 148:827 – 831
376. Want TST, Oluwole S, Fawwaz RA, et al (1982) Cellular basis for accumulation of In-111-labeled leukocytes and platelets in rejection cardiac allografts. Concise communication. J Nucl Med 23:993 – 997
377. Johnson LHJ, Seldin DW, Addonizio LJ (1988) Antimyosin imaging in acute myocardial infarction and cardiac transplant rejection. In: Pohost GM, Higgins CB, Morganroth J, Ritchie JL, Schelbert HR (eds) New concepts in cardiac imaging. Year Book Medical Publishers, Chicago, pp 117 – 140
378. Frist W, Yasuda T, McDougall R, et al (1986) Noninvasive detection of human cardiac transplant rejection with indium-111 antimyosin imaging. Circulation 74:II-219

Digestive System 1: Gastrointestinal Tract 16

Fuad Hassan, Eman Al-Enizi, Abdelhamid H. Elgazzar

The digestive system consists of the gastrointestinal tract, hepatobiliary system (Fig. 16.1), pancreas and salivary glands. Nuclear medicine is concerned with the evaluation of normal and abnormal functions of gastrointestinal tract and hepatobiliary system. To date the role of nuclear medicine in pancreatic disorders is limited to the evaluation of its tumors, which is dealt with elsewhere in the book. This chapter will deal with the gastrointestinal tract and salivary glands, while the next chapter is devoted to the hepatobiliary system.

16.1 The Esophagus

16.1.1 Anatomy and Physiology

The human esophagus is a hollow muscular tube that connects the pharynx to the stomach. The upper third consists of striated muscle, the lower third is composed of smooth muscle, and the middle third is a transitional mixture of the two. Functionally, the esophagus has three components: the upper esophageal sphincter (UES), the esophageal body, and the lower esophageal sphincter (LES). These components act to keep the esophagus empty, so that swallowed food or liquid is propelled from the pharynx to the stomach. Moreover, normal esophageal structure and function prevent retrograde movement of gastric or esophageal content.

Esophageal motility disorders result from sphincter dysfunction or abnormal peristalsis in the body of the esophagus or both. The diagnosis and treatment of motility disorders rest on an understanding of the functional anatomy of the upper esophageal sphincter, esophageal body, and lower esophageal sphincter.

16.1.1.1 Upper Esophageal Sphincter

The UES is defined as a high-pressure zone, 2–7 cm long, separating the pharynx from the body of the esophagus. It consists of opening and closing muscles. The opening muscles include the thyrohyoid and geniohyoid. The closing muscles include the cricopharyn-

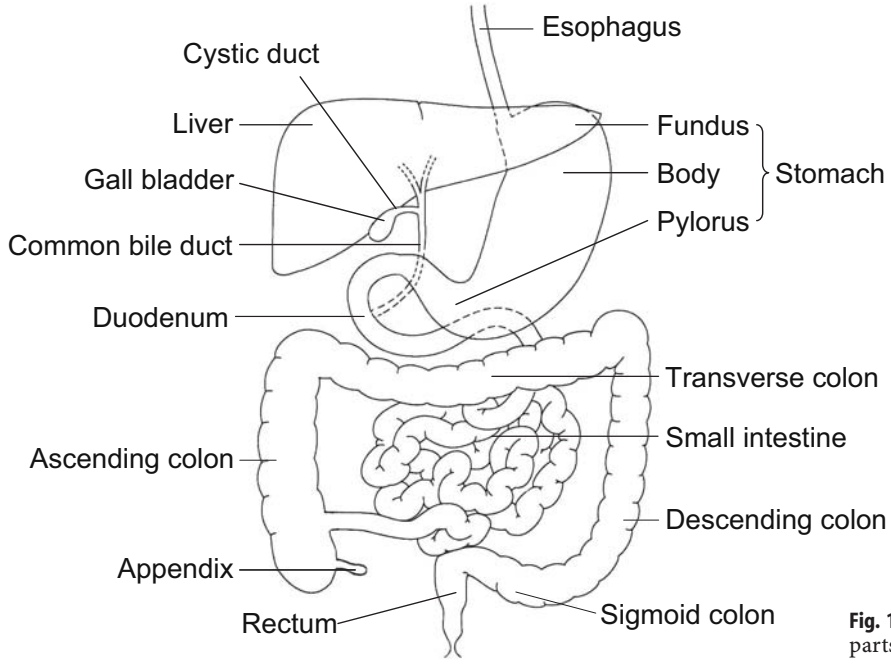

Fig. 16.1. Diagram of the relevant parts of the digestive system

geus and thyropharyngeus [1]. All UES muscles are striated and are innervated by vagal somatic nerves emanating from the nucleus ambiguus, located in the medulla oblongata of the brain stem. Between swallows the UES is tonically contracted to prevent reflux of esophageal contents and entry of air from the pharynx during inspiration. During swallowing, the cricopharyngeal and thyropharyngeal muscles relax momentarily. However, opening of the UES requires contraction of the opening muscles, namely the thyrohyoid and geniohyoid. After the passage of the food bolus, the UES returns to its tonically contracted state.

16.1.1.2 Esophageal Body

The esophageal body extends from the UES to the LES and measures 18 – 24 cm. The esophageal wall consists of mucosa, submucosa, and the tunicae muscularis and adventitia. The esophageal body is not surrounded by a tunica serosa. The esophageal mucosa is of the stratified squamous epithelium type, except for the distal 2 cm, where columnar epithelium of the gastric cardia type may be encountered. More proximal extension of gastric-type epithelium or the presence of intestinal-type columnar epithelium defines the pathological entity known as Barrett's esophagus. Outside the epithelial lining is a thin layer of longitudinally oriented smooth muscle fibers, the muscularis mucosa. Below the muscularis mucosa is the submucosa, which consists of connective tissue. The muscularis propria is made up of an inner, circular, muscle layer and an outer, longitudinal, muscle layer. In the proximal 5% of the esophageal body, the muscularis propria is made up of striated muscle fibers. The distal 50% – 60% consists entirely of smooth muscle. The middle 35% – 40% is composed of a mixture of smooth and striated muscle fibers.

Neuronal control of esophageal body motility is complex [2]. The esophageal wall receives extrinsic innervation via the vagus nerve. Striated muscle fibers are directly innervated by post-ganglionic neurons originating in the nucleus ambiguus and terminating on the motor end plate. Smooth muscle fibers are controlled by preganglionic nerve fibers originating in the dorsal motor nucleus. These cholinergic nerve fibers terminate on the intrinsic neurons of the myenteric plexus located between the circular and longitudinal muscle layers. Within the myenteric plexus two types of neurons have been identified. Excitatory neurons mediate contraction of both longitudinal and circular muscle layers via nicotinic cholinergic nerve receptors. Inhibitory neurons mediate the relaxation of mainly circular muscle fibers via noncholinergic, nonadrenergic neurotransmitters, most probably nitrous oxide and vasoactive intestinal peptide (VIP) [3]. Intrinsic sensory (afferent) neurons are within Meissner's plexus located in the submucosa. Sensory impulses are conveyed to the central nervous system via both vagal and thoracic sympathetic nerve fibers.

Swallowing initiates a progressive series of coordinated propulsive contractions throughout both the striated and the smooth muscle portions of the esophageal body. This form of esophageal motor activity is re-

ferred to as primary peristalsis. Intraluminal distention of the esophageal body results in a peristaltic wave at or proximal to the site of distention. This wave is termed secondary peristalsis and serves to clear the esophagus from contents that have not been cleared by primary peristalsis, or refluxed gastric contents. Primary and secondary peristaltic waves have similar amplitudes and travel at a velocity of 3 – 5 cm/s.

Deglutitory inhibition is a unique physiological phenomenon whereby repetitive swallowing inhibits all esophageal body activity while the LES is relaxed. A normal peristaltic contraction will follow the last swallow of such a series and clear the esophagus completely [4].

16.1.1.3 Lower Esophageal Sphincter

The LES refers to a high-pressure zone measuring 2 – 4 cm in length located between the esophageal body and the stomach. The high-pressure zone does not correlate with a distinct histological entity [5]. At rest the sphincter is tonically contracted with a normal pressure ranging from 10 to 45 mmHg. On swallowing the LES relaxes and its pressure approaches that of the stomach. The LES remains relaxed until the bolus reaches the end of the esophagus. Occasionally, especially after meals, the LES relaxes without swallowing or secondary peristalsis. This is referred to as transient LES relaxation and can occur in healthy individuals but is more frequent among patients with gastroesophageal reflux disease. In fact, transient LES relaxation is the most important mechanism of mild reflux. The trigger for transient LES relaxation is not known, but it could be due to postprandial receptive relaxation of the stomach or a response to pharyngeal stimulation.

LES relaxation is mediated by intramural (intrinsic) inhibitory nonadrenergic, noncholinergic neurons that most probably use nitrous oxide (NO) or VIP as their neurotransmitter. A number of endogenous compounds affect the LES tone when administered in pharmacological doses. For instance, large doses of gastrin increase the tone of LES. Exogenous substances such as beta-adrenergic receptor agonists and calcium channel blockers may induce relaxation of the LES.

16.1.2 Esophageal Motor Disorders

16.1.2.1 Disorders of the UES and Cervical Esophagus

Motor disorders affecting the skeletal (proximal) part of the esophagus result from either neurological abnormalities affecting the extrinsic innervation of the proximal esophagus, or skeletal muscle or neuromuscular disorders. More specifically these include:

- Neurological diseases
  - Cerebrovascular accident
  - Parkinsonism
  - Amyotrophic lateral sclerosis
  - Cranial nerve palsy
- Skeletal muscular disorders
  - Dermatomyositis
  - Polymyositis
  - Muscular dystrophy
- Cricopharyngeus dysfunction
- Others
  - Myasthenia gravis
  - Amyloidosis

Because of the difficulty of transferring food bolus from the hypopharynx into the esophageal body across the UES, most patients experience choking or regurgitation of liquids and/or solids. Videofluoroscopy is the best diagnostic modality for diagnosing oropharyngeal dysphagia. Scintigraphy is of limited value.

16.1.2.2 Disorders of Distal Esophagus and LES

Disorders of the distal esophageal body (smooth muscle) and LES can be broadly classified into hypermotility and hypomotility disorders, although overlap is not uncommon.

16.1.2.2.1 Hypermotility (Spastic) Disorders

The hypermotility disorders are characterized by high-amplitude, prolonged or repetitive contractions. They include achalasia and several other conditions, particularly the diffuse esophageal spasm (Table 16.1).

Table 16.1. Manometric features of distal esophageal disorders

Disorder	Features
Achalasia	Absent peristalsis in esophageal body Incomplete LES relaxation Increased LES pressure
Diffuse esophageal spasm	Simultaneous contractions (> 10% of wet swallows) Intermittent normal peristalsis Repetitive contracts Prolonged duration of contractions High amplitude of contractions Incomplete LES relaxation
Nutcracker esophagus	Normal progression of peristalsis Mean contractile amplitude ^{3}180 mmHg Prolonged duration Normal LES pressure
Hypertensive LES	Mean LES pressure ^{3}45 mmHg Normal LES relaxation Normal progression of peristalsis

Achalasia is the best-studied motor disorder of the esophagus. It occurs at a rate of 1:100,000 and affects both sexes equally. Age of onset is usually 25 – 65 years. It results from the degeneration of the inhibitory myenteric neurons in the body and the LES region. This leads to a hypertensive LES which relaxes poorly and also causes aperistalsis in the body of the esophagus. Patients usually present with dysphagia to liquids and solids. Barium esophagogram may show dilatation of the esophagus and "bird beaking" of the distal esophagus. Esophageal manometry confirms the diagnosis of achalasia. Typically, there is incomplete relaxation of the LES and aperistalsis. LES hypertension is detected in 20% – 40% of patients [6]. Although these changes are highly suggestive of achalasia, they are by no means pathognomonic. Other conditions that might mimic achalasia include adenocarcinoma of the cardia, esophageal squamous cell carcinoma, Chagas' disease, and lung cancer.

Several other spastic disorders have been characterized in patients with noncardiac chest pain (Table 16.1). They all share a similar clinical presentation. Diffuse esophageal spasm (DES) is the most severe form. It is less common than achalasia. The mean age at presentation is 40 years. Patients frequently complain of intermittent nonprogressive dysphagia for solids and liquids. Hot or cold liquids and stress may precipitate chest pain. Some patients with DES progress to achalasia.

16.1.2.2.2 Hypomotility Disorders

A number of systemic conditions are associated with esophageal hypomotility including scleroderma, diabetes mellitus, and amyloidosis. These disorders are characterized by low or absent contractions. The most clinically relevant condition is scleroderma.

Scleroderma (progressive systemic sclerosis) is a multisystem connective tissue disorder that affects the skin and internal organs, especially the vascular system, the gastrointestinal tract, the lungs, heart, and kidneys. It is more common in women than in men and appears at any age under 50 years. Scleroderma is associated with circulating autoantibodies including antinuclear, anti-centromere, and rheumatoid factor. Patients frequently present with Raynaud's phenomenon. Particularly when it presents as CREST syndrome (calcinosis, Raynaud's phenomenon, esophageal involvement, sclerodactyly and teleangiectasia), esophageal involvement occurs in 70% – 80% of patients. Histopathological findings include smooth muscle atrophy and fibrosis. The end result is impaired muscle contractions in the distal esophagus and incompetence of the LES. Hence, 50% of patients with scleroderma-associated dysmotility complain of heartburn and/or dysphagia. The other 50% may be asymptomatic. Gastroesophageal reflux disease may be severe enough to cause peptic stricture. Barium esophagogram may reveal a dilated esophagus with aperistalsis and patulous LES. Ulceration and stricture formation may also be evident. Manometry shows low or absent LES pressure/aperistalsis in the smooth muscle portion of the esophageal body and normal peristalsis in the proximal esophagus [7, 8].

16.1.2.3 Gastroesophageal Reflux Disease

Gastroesophageal reflux disease (GERD) involves the reflux of chyme from the stomach to the esophagus. The LES may relax spontaneously and transiently 1 – 2 h after the patient has eaten, allowing gastric contents to regurgitate into the esophagus. The acid is normally neutralized and cleared by peristalsis from the esophagus within 3 min and the tone of the sphincter is restored. When the reflux does not cause symptoms it is known as physiological but in some individuals it may cause a spectrum of inflammatory responses in the esophagus. GERD is the most prevalent condition originating from the gastrointestinal tract. It is estimated than 20% of the Western adult population suffer from heartburn more than three times a month [9]. It is particularly important in the pediatric age-group. Also, GERD is common among pregnant women, especially during the third trimester.

The typical symptom of GERD is heartburn. However, a number of atypical symptoms are also linked to GERD, such as noncardiac chest pain, hoarseness, asthma, water brash, teeth erosion, and halitosis.

Most children affected with gastroesophageal reflux (GER) are between 6 months and 2 years old; they suffer from poor weight gain, vomiting, aspiration, choking, asthmatic episodes, stridor, apnea, and failure to thrive. A small amount of physiological reflux occurs in infants and resolves spontaneously by 8 months of age. The Tuttle acid reflux test is generally considered the reference standard but is technically demanding. The radionuclide method has a number of potential advantages. It is physiological, easily performed, well tolerated by the patient, quantitative, and involves a low radiation dose to the child.

16.1.2.3.1 Pathophysiology

GERD is a multifactorial process. Causes of GERD can be categorized as follows: (a) decreased pressure of LES, (b) transient increase in intra-abdominal pressure, and (c) short intra-abdominal esophageal segment. Mechanisms involved are summarized in Table 16.2. As mentioned earlier, transient LES relaxation appears to be the most common mechanism of GERD,

Table 16.2. Mechanisms of gastroesophageal reflux disease

Mechanism	Causes
Anti-reflux barrier	Transient LES relaxation Incompetent LES Sliding hiatus hernia
Esophageal clearance	Impaired peristalsis Decreased salivary output
Refluxate composition	Acid Pepsin Bile salts Pancreatic enzymes
Gastric factors	Delayed gastric emptying Acid hypersecretion *Helicobacter pylori*
Defective esophageal mucosal protection	Lack of HCO_3 secretion Lack of mucus secretion

especially in patients without endoscopic evidence of esophagitis [10]. In patients with moderate to severe esophagitis LES incompetence plays a more important role in promoting reflux. The relation between a sliding hiatus hernia and GERD is controversial. Although most patients with severe GERD have hiatus hernia, most patients with hiatus hernia are asymptomatic. Recent data suggest that a large hiatus hernia may impair acid clearance [11, 12].

Esophageal body peristalsis plays an important role in clearing refluxed acid in both the upright and the supine position. Defective primary or secondary peristalsis leads to incomplete clearance of acid. Furthermore, salivary HCO_3 usually neutralizes acid that remains in contact with the esophageal mucosa. Thus, impaired salivation may contribute to mucosal injury [13].

There is consensus about the fact that the potency of the contents of the refluxate, particularly acid/pepsin, is important in the pathogenesis of reflux esophagitis. Bile and pancreatic enzymes may be additional contributing factors.

Delayed gastric emptying is documented in 6% – 30% of patients with GERD. Theoretically, gastric stasis can contribute to GERD. However, the relative importance of delayed gastric emptying is not well established [13]. *Helicobacter pylori* has recently been implicated as having a potential role in the pathogenesis of GERD [14]. *H. pylori* may secrete pro-inflammatory substances that can damage esophageal mucosa and sensitize vagal afferent nerves or lead to the reduction of LES tone. In contrast, there are data suggesting a protective role for *H. pylori* against GERD [15].

Finally, a significant proportion of patients with proven esophagitis do not have increased exposure to acid/pepsin. These patients probably have disruption of mucosal defense mechanisms such as the mucous layer, intercellular junctional complexes, intracellular mechanisms of handling acid, and blood flow to the esophagus [16].

16.2 The Stomach

16.2.1 Anatomic and Physiologic Considerations

16.2.1.1 Anatomic Features

The stomach is a storage sac located between the esophagus and duodenum (Fig. 16.1). The proximal stomach consists of the cardia, fundus and body. The antrum forms the distal stomach and is separated from the duodenum by the pyloric ring. The wall structure of the stomach is similar to that of the rest of the gastrointestinal tract, i.e., it consists of the mucosa, submucosa, muscularis propria and serosa. However, unlike other parts of the gastrointestinal tract, the muscularis consists of three layers, circular, longitudinal and oblique. This facilitates distension of the stomach and storage of food. The muscle layer in the antrum is modified to aid the mixing of food. The pyloric ring regulates the emptying of the stomach.

16.2.1.2 Overall Functions

Besides storage, the stomach has a number of exocrine, paracrine and endocrine functions. The exocrine secretions consist of HCl and pepsin produced by the mucosal parietal cells and chief cells respectively. These cells are located in the fundus and body of the stomach. Most cells within the lamina proprin and submuosa are responsible for the main paracrine function, namely the release of histamine which in turn stimulates the parietal cells to secrete acid. The antrum secretes the hormone gastrin, which enhances gastric emptying and acid secretion.

The intrinsic factor (IF) is a glycoprotein secreted by parietal cells. It binds to vitamin B_{12}. The IF-B_{12} complex in turn binds to specific receptors on the terminal ileal epithelium. Without IF, B_{12} cannot be absorbed and pernicious anemia develops. Usually failure to secrete IF results from gastric atrophy, which causes the destruction of parietal cells.

16.2.1.3 Gastric Motor Physiology

The motor activity of the stomach serves two main functions: (a) to act as a reservoir for ingested meals and ensure timed delivery of food particles to the duodenum at a rate compatible with optimal digestion; (b) to disperse solids into small particles and to mix them with gastric juice. The functions are accomplished by the coordinated activity of three functionally distinct parts of the stomach: (a) the proximal stomach, including the fundus and proximal body; (b) the distal stom-

ach, including distal body and antrum; (c) the pylorus, as part of the pyloroduodenal unit.

The proximal stomach has three muscle layers, longitudinal, circular, and oblique. No myoelectrical activity is recorded from the fundus during fasting except for the interdigestive migratory motor complexes (see below). In the fed state, the fundus exhibits two forms of motor activity: receptive relaxation and accommodation. Receptive relaxation refers to the reduction in proximal stomach tone initiated by swallowing or pharyngeal stimulation. Accommodation is reflex relaxation of the proximal stomach in response to gastric distention. It is not induced by swallowing or pharyngeal stimulation. Truncal vagotomy abolishes both receptive relaxation and accommodation, suggesting that they are mediated by the vagus nerve. Some gastrointestinal peptides such as cholecystokinin, secretin, VIP, and gastrin induce proximal stomach relaxation, whereas motilin increases fundic pressure [17, 18].

The distal stomach comprises two muscle layers: the longitudinal and circular. Slow waves or slow pacer potentials originate in the pacemaker region, located on the greater curvature of the stomach near the junction of the proximal and distal stomach. Slow waves pace the normal 3/min corpus-antral peristalsis, which mixes solid and liquid food with gastric juice and triturates larger particles. The distal gastric motor activity is regulated by cholinergic and noncholinergic vagal efferent nerve fibers. Cholinergic pathways stimulate antral contraction whereas noncholinergic vagal nerve stimulation inhibits antral activity through VIP and possibly nitrous oxide release from inhibitory neurons within the myenteric plexus.

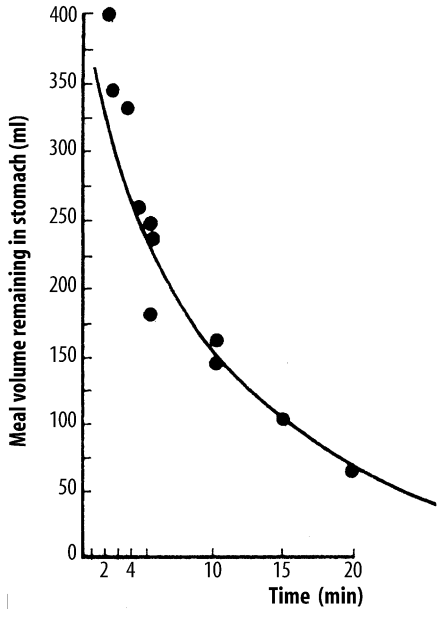

Fig. 16.2. Gastric emptying of 0.9% normal saline follows first-order kinetics. (From [20])

The pyloric sphincter functions, in coordination with the duodenum, as a sieve allowing particles l mm or smaller to pass into the duodenum in 2- to 4-ml aliquots with each gastric peristalsis [19]. Emptying of inert liquids such as 0.9% saline follows first-order kinetics; i.e., the volume of liquid emptied into the duodenum in a given time is a constant fraction of the volume that remains in the stomach (Fig. 16.2) [20]. Emptying of digestible solid particles is characterized by a lag phase and a linear phase (Fig. 16.3) [21]. However, the caloric density, viscosity, osmolarity, and volume of any specific meal will influence gastric emptying rates. Fibrous material in the stomach is emptied in the interdigestive state by migrating myoelectrical-contractile complexes comprising 3–10 min of strong lumen-obliterating antral contractions [17].

16.2.2 Disorders of Gastric Emptying

Conditions that cause abnormal gastric emptying can be divided into two groups: disorders associated with delayed emptying and disorders associated with dumping (Table 16.3). Diabetes is one of the most common causes of delayed gastric emptying in clinical practice. Most afflicted patients have had type I diabetes for more than 10 years, complicated by autonomic and peripheral neuropathy. Delayed emptying of both solids and liquids is attributed to the dysfunction of the proximal and distal stomach, as well as to increased pyloric resistance [22, 23].

Idiopathic gastroparesis is also encountered frequently in patients with bloating, early satiety, and nausea. The exact cause is unclear but it may be related to post-viral gastroenteritis [24]. Delayed gastric emptying is a known and frequent complication of gastric surgery. For instance, vagotomy delays emptying of

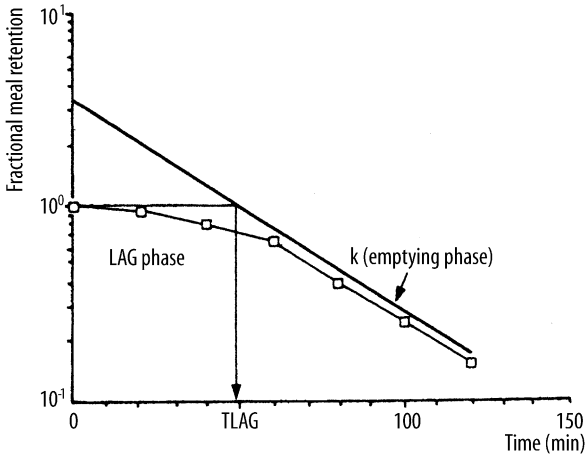

Fig. 16.3. Emptying of digestible solid particles has a lag phase and a linear phase. The curve represents modified power exponential function. (From [21])

Table 16.3. Causes of gastric dysmotility

Condition	Causes
Delayed gastric emptying	Mechanical obstruction Gastric outlet obstruction (e.g., tumor, peptic ulcer) Small intestinal obstruction Decreased gastric motility Post-surgical gastroparesis (vagotomy, Roux-en-Y, fundoplication, etc.) Endocrine disorders (DM, hypothyroidism, Addison's disease, hyper- or hypoparathyroidism) Drugs (narcotics, anticholinergics, calcium channel blockers) Connective tissue diseases (e.g., scleroderma, SLE) Muscular disorders (myotonic dystrophy, dermatomyositis) Paraneoplastic Post-viral Neurological disorders (migraine, CVA, Parkinson, dysautonomia) Intestinal pseudo-obstruction Idiopathic gastroparesis Others (anorexia nervosa, uremia, ischemic gastroparesis, pregnancy)
Rapid gastric emptying (dumping)	Duodenal ulcer disease (including ZE syndrome) Vagotomy Antrectomy Idiopathic

solids but promotes liquid emptying. Similarly antrectomy can cause rapid emptying of undigested solids and liquids due to the loss of mixing function and loss of pyloric resistance. Symptoms of delayed gastric emptying include early satiety, nausea, vomiting, postprandial abdominal bloating, distention, and pain. The symptoms of gastroparesis are nonspecific and cannot be easily differentiated from those of mechanical obstruction. Other diseases such as gastritis, irritable bowel syndrome, and nonulcer dyspepsia may cause similar complaints.

16.2.3 Duodenogastric Reflux

Duodenogastric reflux (DGR) has been suggested to occur in normal individuals in both fasting and postprandial periods [25, 26], although others have suggested that it does not occur physiologically [27]. The amount of refluxed bile in normal subjects is reported to be small and clears rapidly from the stomach [28]. This feature helps separate normal from abnormal subjects in the fasting state.

Pathologically, DGR has been associated with many conditions (Table 16.4), including postgastrectomy/vagotomy, gastric and duodenal ulcers, cholecystitis, and gastritis [29]. In some of these conditions, such as duodenal ulcer, duodenal hematoma, and cholecystitis, duodenal irritation is probably the underlying mechanism. Other causes may irritate the duodenal mucosa by the adjacent pancreatic inflammation. Slavin also proposed that deficiency of pancreatic secretions can explain DGR since volume, the alkaline pH, and the physiological components of the pancreatic secretions may be important for maintaining the outward flow of gastric contents [30].

Table 16.4. Causes of duodenogastric reflu

Causes	
Duodenal ulcer	Gastritis
Acute cholecystitis	Chronic cholecystitis
Enteritis	Pancreatitis
Gastric carcinoma	Surgery
Post-traumatic stress ulceration	Gastric surgery/vagotomy
Duodenal hematoma	Cholecystectomy
Erosive esophagitis	Gallstone dyspepsia
Physiological/unknown cause	

16.3 The Intestines

16.3.1 Small Intestine

16.3.1.1 Anatomy and Histology

The small intestine is a hollow muscular cylinder that measures 5–6 m in length. It consists of three regions: duodenum, jejunum and ileum. The intestinal wall is made up of four layers: the mucosa, the submucosa, the muscularis and the serosa. The small intestinal mucosa is fashioned into villi and crypts to increase the surface area, and enhance the absorptive function of the small bowel. The mucosa of the villi consists of absorptive columnar epithelial cells (enterocytes) and mucus secreting goblet cells. Within the crypts the most common cell type is the undifferentiated crypt cell, which secretes chloride and water into the lumen. The crypt also contains pleuripotent stem cells. Furthermore, the small bowel harbors the enteroendocrine cells which secrete a number of hormones including secretin, cholecystokinin, gastrin, gastric inhibitory peptide, motilin, glucagon, vasoactive intestinal peptide, somatostatin and others. These hormones play an important role in gastrointestinal motility. Finally, the intestinal mucosa and lamina propria contain the largest lymphoid organ in man: the gut associated lymphoid tissue (GALT) [31]. The latter consists of:

- M-cells
- Intraepithelical lymphocytes (IELs)
- Peyer's patches (lymphoid follicles)
- Lamina propria T and B lymphocytes
- Dendritic cells
- Macrophages

The M cells are specialized epithelial cells overlying lymphoid follicles. Because they are not covered by mucus, antigens can bind to M cells, which take in the antigens, process them and present them to lymphocytes and macrophages. However, the binding to antigens is highly selective. For instance, only pathogenic bacteria can attach to M cells, whereas commensals cannot. IELs are specialized T lymphocytes situated between the basolateral membranes of mucosal epithelial cells and the lamina propria. They appear to have an important immunologic function as they express CD45RO, a marker of memory cells. Dendritic cells are derived from the bone marrow and reside beneath M cells. They capture antigens, carry them across the mucosal barrier and present them to T lymphocytes.

The submucosa consists of connective tissue, lymphocytes, plasma cells, macrophages, mast cells, fibroblasts, eosinophils, nerve fibers, ganglion cells (Meissner's plexus), blood vessels and lymphatics.

The muscularis is made of inner circular and outer longitudinal muscle fibers. Between these two layers of smooth muscle lies the myenteric plexus, the network of intramural neurons that is essential for all coordinated and organized motor activity. The extrinsic (autonomic) nerves affect the gastrointestinal motility by means of these enteric nerves.

16.3.1.2 Function

Most of the digestion and absorption of nutrients takes place in the small bowel. Moreover, the motor function of the small bowel ensures the mixing of chyme with digestive enzymes and the propulsion of chyme towards the colon. Also, the small bowel plays an important role as a first line of defense against pathogenic microorganisms and harmful food antigens.

In most instances, nutrients cannot be absorbed by the cells that line the gastrointestinal tract in the forms in which they are ingested. *Digestion* is the breakdown of ingested molecules into small ones via reactions catalyzed by enzymes produced by the gastrointestinal organs.

The small intestinal epithelium participates in digestion by secreting oligosaccharidases such as lactase, enterokinase and peptidases.

Absorption refers to the process of transporting molecules through the epithelial lining of the gastrointestinal tract into the blood or lymph.

Water, electrolytes, monosaccharides, amino acids, small peptides, glycerol, fatty acid, vitamins and minerals are all absorbed via a number of mechanisms including passive diffusion, facilitated diffusion, active transport and endocytosis. Although absorption takes place along the entire length of the small intestine, the mucosa in certain regions selectively absorbs specific molecules. For instance, iron is primarily absorbed in the duodenum and proximal jejunum, whereas the terminal ileal mucosa has specific receptors for binding and absorbing vitamin B_{12} and bile salts [32].

Under physiologic conditions the small bowel exhibits two main motor patterns. During the fed state, and as a result of contact with nutrients a number of neuronal and hormonal signals are elicited including afferent vagal stimulation, and the release of cholecystokinin which mediate *segmentation* and *peristalsis*. *Segmentation* is the most frequent movement in the small bowel and is characterized by closely spaced contractions of the circular muscle layer. These contractions divide the small intestine into short neighboring segments. Segmentation helps mix chyme with digestive enzymes. *Peristalsis*, on the other hand, is the progressive contraction of successive sections of circular smooth muscle resulting in the propulsion of chyme towards the colon. Furthermore, during the fed state the small intestine especially the duodenum exerts negative feedback control on gastric emptying via neural and hormonal mechanisms (secretin, cholecystokinin and gastric inhibitory peptide).

During the fasting phase, the small intestine exhibits a different pattern of motility characterized by bursts of intense electrical and contractile activity separated by periods of lack of activity. This pattern is called *migrating myoelectric complex* (MMC). In humans MMC occurs every 90 – 120 min, originates from the stomach and sweeps through the small bowel until the terminal ileum. The function of MMC is to clear undigested particles and propagate them to the colon [33].

16.3.1.3 Small Intestinal Dysmotility

Motor disorders of the small bowel can lead to symptoms and signs of "functional" as opposed to mechanical small bowel obstruction. Patients frequently complain of abdominal distension, bloating, abdominal pain, and when small intestinal dysmotility is associated with gastroparesis, nausea and vomiting may be prominent. On physical examination, the abdomen is usually distended and bowel sounds are diminished. Features of bacterial overgrowth may be observed.

Small intestinal dysmotility may be acute or chronic. Acute dysmotility is termed adynamic ilens and is commonly seen following abdominal surgery, severe septicemia or electrolyte disturbances such as hypokalemia. Chronic dysmotility is termed pseudo-obstruction (Table 16.5).

Most cases of pseudo-obstruction are secondary to endocrine and metabolic causes, such as diabetes mellitus and hypothyroidism, to neurologic disorders such as Chagas' disease and parkinsonism, or are drug in-

Table 16.5. Motor disorders of the small intestine

Cause	Mechanism	Outcome
Acute illness	Impaired smooth muscle contraction Altered neurotransmission	Adynamic ileus
Pregnancy	Decreased smooth muscle contraction (progesterone)	Slow transit
Diabetes mellitus	Autonomic dysfunction	Slow or rapid transit
Scleroderma	Smooth muscle fibrosis Neuronal loss in gut wall	Weak contractions Slow transit
Primary pseudo-obstruction	Neuronal loss, plexus degeneration	Weak contractions Abnormal MMC Slow transit
Myopathies	Myocyte and mitochondrial abnormalities	Weak segmentation and peristalsis

duced (e.g., phenothiazines, narcotics). Primary pseudo-obstruction is rare. Few cases are due to familial visceral neuropathies and myopathies. However, the majority of cases of primary pseudo-obstruction are sporadic.

16.3.1.4 Malabsorption

Malabsorption syndrome is an alteration in the ability of the GI tract, usually the small intestine, to absorb one or more nutrients adequately from diet into the bloodstream. These may include fats, proteins, carbohydrates, vitamins or others. This may result from acquired or congenital defects. The syndrome may present with anemia (most commonly vitamin B_{12}, folate and iron deficiency), diarrhea, steatorrhea (excessive amount of fat in the stool), abdominal distention edema, malnutrition and weight loss, muscle cramping due to decreased vitamin D, calcium, and potassium levels, muscle wasting and atrophy due to decreased protein absorption and metabolism and perianal skin burning, itching, or soreness due to frequent loose stools. Protein depletion can lead to impaired bone formation and osteoporosis, and calcium deficiency leads to weakening and demineralization of the bone, causing osteomalacia.

Common causes of malabsorption syndrome include inflammatory bowel disease, tropical sprue, Whipple's disease, lactase deficiency, and parasitic diseases; other causes are past intestinal surgery, bacterial overgrowth, gluten entropathy (nontropical sprue), AIDS, radiation to the abdomen, diabetes, lymphoma or motility disorders. In addition to small bowel disease, malabsorption can occur in those who have had portions of their stomachs removed surgically. The pancreas produces enzymes that help to digest food, so if a condition exists where enzymes are not being produced it can result in maldigestion or malabsorption. This could include chronic alcoholic pancreatitis, trauma, cystic fibrosis, tumors or post surgical states. The diagnosis of malabsorption syndrome and identification of the underlying cause can require extensive diagnostic testing. Generally, an endoscopy is performed under mild sedation, at which time a biopsy can be obtained to be analyzed under the microscope. In addition, various blood tests are helpful to determine if a malnourished condition exists. These tests may include serum cholesterol, serum sodium, potassium, and chloride, serum calcium, serum protein and albumin, serum vitamin A and carotene, d-xylose test, Schilling test and others. Stool collections and cultures are useful as well as certain breath and hormone tests. Scintigraphic imaging and quantitation is also used in some forms.

16.3.1.4.1 Protein Losing Enteropathy

Protein losing enteropathy (PLE) is a condition in which excess protein loss into the gastrointestinal lumen is severe enough to produce hypoproteinemia. It occurs with many of the previously listed conditions causing malabsorption. Furthermore, diseases such as constrictive pericarditis, congestive heart failure, intestinal lymphangiectasia, nephrotic syndrome, and systemic lupus erythematosus may also cause protein loss from the gastrointestinal tract without any observable mucosal lesions in the bowel. The mechanism of the loss of plasma protein into the gastrointestinal tract in these diseases is not yet fully understood [34].

The previously reported materials used for the detection of protein loss have many limitations, such as rapid reabsorption of the radiolabel, unstable protein binding both in vivo and in vitro, and limited availability. The need for measurement of fecal radioactivity over 3–4 days has also been a drawback with some of the methods in which these materials are used. Imaging with other radioisotope-labeled materials such as ^{111}In-chloride and ^{111}In-transferrin has been reported [35].

^{99m}Tc-labeled HSA has been used to image protein losing entropathy since its introduction in 1986 [36]. Serial imaging for up to 24 h is useful in detecting protein loss from the gut, possibly because of the intermittent nature of this protein loss. ^{99m}Tc-HSA is also useful in viewing the entire gastrointestinal tract at one time to permit detection of multiple potential sites of protein loss. A new scintigraphic method using ^{99m}Tc-labeled dextran was first described in 1995 by Bhatnagar et al. [37–38]. This method demonstrates significant intestinal radiotracer accumulation at 3–4 h postinjection in 22 patients, giving information about localization and extension of the disease.

16.3.1.4.2
Vitamin B_{12} Malabsorption (see Chapter 5)

16.3.2
The Colon

16.3.2.1
Anatomy and Function

The colon is a tubular structure that extends from the ileocecal valve to the anal verge (Fig. 16.1). It measures approximately 1–5 m and consists of the cecum, ascending transverse, descending, sigmoid colon and rectum. Like the small intestine, the colonic wall consists of the mucosal submucosa, muscularis and serosa. However, the colonic mucosa lacks villi. Also, unlike the small intestine, the external longitudinal muscular layer is gathered into three flat longitudinal ribbons of smooth muscle called teniae coli. The continuous contractions of the teniae coli cause sacculations of the wall termed haustrations.

The primary function of the colon is to absorb water and electrolytes from its contents and to pack feces until defecation. The motility of the colon is geared towards this function. As stated above, throughout the colon localized segmental contractions take place and result in mixing chyme. In the cecum and ascending colon, retrograde (antipropulsive) contractions also occur. The net effect of these motility patterns is to slow transit and facilitate the absorption of water and electrolytes. Periodically, massive contractions start in the proximal colon to propel fecal material towards the sigmoid colon, where it is stored. One to three times a day mass contractions sweep the stool towards the rectum. Distension of the rectum by feces initiates the defecation reflex, which is mediated by the pelvic nerves and is integrated at the level of the sacral spinal cord.

16.3.2.2
Inflammatory Bowel Disease

Inflammatory bowel disease (IBD) refers to two disorders: Crohn's disease (CD) and ulcerative colitis (UC). Both conditions are characterized by chronic relapsing intestinal inflammation. UC affects the colon only, and the inflammation is limited to the mucosa + submucosa in most cases. CD can affect the entire gastrointestinal tract from mouth to anus. The inflammation in CD is granulomatous and transmural. Besides inflammation of the gut, IBD is associated with a number of systemic manifestations including anterior uveitis, axial and peripheral arthropathy, primary sclerosing cholangitis, erythema nodosum and pyoderma gangrenosum.

The etiology of IBD is unknown. However, many of the immunologic and molecular mechanisms that mediate inflammation have been elucidated in recent years [39]. Three groups of factors seem to play a role: genetic predisposition, mucosal immune dysregulation, and environmental agents (Table 16.6). The importance of genetic factors in the pathogenesis of IBD is evidenced by familial aggregation of CD and UC cases. Approximately 10%–20% of patients with IBD have an affected relative. Concordance among monozygotic twins especially in CD also supports the notion of genetic predisposition. Recently a gene on chromosome 16 has been linked to CD and has been designated the *NOD2* gene. This gene mediates the innate immune response to microbial pathogens. Similarly a number of other susceptibility genes have been identified in relation to CD and UC [40–41].

The mucosal immune system plays a central role in the pathogenesis of IBD. A defective mucosal barrier may allow the uptake of microbial and ingested antigens. Under physiologic conditions, GALT selectively removes harmful antigens. This process is mediated by the dentritic cells, which are the main antigen presenting cells in GALT. Interaction of dendritic cells with T lymphocytes results in immunosuppression (tolerance) towards commensals and beneficial antigens. In IBD patients, tolerance is lost due to a number of immunoregulatory abnormalities including an imbalance between proinflammatory and anti-inflammatory mediators in favor of the former. For instance, the levels of IL-1, IL-6, IL-18, tumor necrosis factor alpha (TNF-α) and interferon gamma are raised in patients with CD (TH1 response), whereas the levels of IL-1ra, TGF-β,

Table 16.6. Pathogenesis of inflammatory bowel disease[a]

Genetic predisposition	Environmental factors	Immunologic dysregulation
Family clustering *NOD2* gene variants Gene loci on chromosomes 2, 3, 12	Infectious agents Dietary antigens Intestinal commensals	Proinflammatory mediators Anti-inflammatory mediators

[a] In genetically predisposed individuals, environmental factors can participate in the disease by inducing a broad immunologic response characterized by an imbalance between an antiinflammatory mediators

4-Y, IL-10 (TH2 response), and prostaglandin E_2 are reduced. The role of TNF-α is of particular therapeutic significance. Monoclonal antibodies to TNF-α have been shown to be effective in treating CD [42].

The rising incidence of IBD especially CD in recent years is highly suggestive of the role of environmental factors in modulating the immune response. Furthermore, a number of studies have shown a positive correlation between smoking and CD and a negative association with UC. Other factors that have been implicated as environmental precipitants of IBD include the use of NSAIDS, antibiotics, infective diarrheal illnesses, and increased intake of refined sugar. In the genetically susceptible rodent model of IBD, colitis does not develop when the gut is sterile, and IBD is precipitated by the introduction of bacteria into the diet [39–42].

The primary pathophysiologic change in UC is inflammation of the colonic mucosa and submucosa with the formation of crypt abscesses and mucosal ulceration. The lining of the rectum is almost always involved with proximal spread to rest of the large bowl. No "skip areas" are present. The small intestine is essentially not involved. UC primarily involves the mucosa and the submucosa, with formation of crypt abscesses and mucosal ulceration.

Crohn's disease consists of segmental involvement by a nonspecific granulomatous inflammatory process involving all layers of bowl with skip areas. The disease involves the small bowl in addition to the colon, and rectal sparing is typical. Less commonly it involves mouth, tongue, esophagus, stomach and duodenum. For more details see Chapter 4.

16.3.2.3 Acute Appendicitis

The appendix is a diverticulum of an average length of 10 cm in adults arising from the posteromedial wall of the cecum and fixed to the cecum, while the remainder of the appendix is free. This fact accounts for its variable positions (retrocecal, subcecal, retroileal, pre-ileal, or pelvic) and is behind much of the diversity of clinical presentations among patients with acute appendicitis [43].

The pathophysiology of appendicitis begins with the obstruction of the narrow appendiceal lumen by causes such as fecaliths, lymphoid hyperplasia (related to viral illnesses such as upper respiratory infections, mononucleosis, or gastroenteritis), gastrointestinal parasites, foreign bodies, and Crohn's disease. Continued secretion of mucus results in elevated intraluminal pressure, leading to tissue ischemia, overgrowth of bacteria, transmural inflammation, appendiceal infarction, and possible perforation. Inflammation may subsequently extend into the parietal peritoneum and adjacent structures, causing abdominal abscesses.

Acute appendicitis is the most common reason for emergency abdominal surgery and must be differentiated from other causes of abdominal pain. The overall diagnostic accuracy achieved by medical history, physical examination, and laboratory tests has been approximately 80% as the presentation may be atypical. In atypical cases, ultrasonography and computed tomography (CT) may help lower the rate of unnecessary surgeries. The accuracy rates for ultrasonography range from 71% to 97% and the modality is highly operator dependent and difficult in patients with a large body habitus. The accuracy rate of CT scanning is between 93% and 98%. However, there is controversy regarding the use of contrast media and which CT technique is best. Additionally, radiation exposure, cost, and possible complications from contrast media are disadvantages [43].

16.3.2.4 Colorectal Cancer

The incidence of colorectal cancer is highest in developed countries such as the United States and Japan, and lowest in the developing countries in Africa and Asia. It is the third most common type of cancer in both men and women in the United States. Pathologically most (over 95%) of colorectal cancers are adenocarcinomas. Surgery, chemotherapy, radiation therapy and immunotherapy are the lines of treatment. Nuclear medicine has an important role in the follow-up to detect recurrence. FDG PET has an important role as it is more sensitive than computed tomography for the detection of metastatic (Fig. 16.12, see p. 415) or recurrent colorectal cancer and may improve clinical management in more than 25% of cases [44]. It is of particular importance to differentiate post-therapy fibrosis and inflammation from viable tumor in the presacral region.

16.4 Gastrointestinal Bleeding

The localization of the specific bleeding site in patients presenting with acute GI bleeding remains a serious clinical problem. Scintigraphy has emerged as the imaging modality of first choice for localizing bleeding sites in the lower gastrointestinal tract.

Acute gastrointestinal bleeding (GIB) can be divided into bleeding in the upper (proximal to the ligament of Treitz) or lower tract. If acute upper GIB is a possibility, lavage with a nasogastric tube should identify acute or subacute bleeding. Endoscopy will localize 80%–97% of cases of acute upper bleeding; of these 75% will resolve spontaneously or with conservative medical therapy and 10% will require surgery. Because of the length and tortuosity of the colon and contamination of fecal

matter and blood, endoscopy is not that successful in lower GIB cases. Peptic ulcers are the most common cause of upper GIB; other causes include gastritis, esophageal varices, Mallory-Weiss tear, esophagitis with or without hiatal hernia, and carcinoma [45]. The three leading causes of lower GIB are diverticular disease, angiodysplasia, and colorectal cancer. Other causes include inflammatory bowel disease, ischemic colitis, infectious colitis, and anorectal disease. This bleeding usually resolves spontaneously in 80% of cases and rebleeds in 25%. Angiodysplasias account for 20% of significant lower GIB and tend to rebleed.

Meckel's diverticulum is a vestige of the omphalomesenteric duct that is present in about 2% of the population, with two-thirds younger than 2 years. It is an outpouch usually found on the antimesenteric border of the ileum, 50 – 80 cm proximal to the ileocecal valve. Ectopic gastric mucosa is present in about 30% of cases. Nearly all diverticula responsible for rectal bleeding contain ectopic gastric mucosa. Bleeding, which is usually massive and painless, may result from ileal mucosal ulceration due to acid secretion.

Patients with lower GIB should be stabilized and supported while diagnostic studies are performed. More commonly, a nuclear medicine study is performed first to localize the bleeding because it is more sensitive for slow or intermittent bleeding, which is a common occurrence. If the scan is positive, arteriography can be employed to deliver vasopressin or embolic agents selectively into the bleeding artery.

16.5 Salivary Gland

16.5.1 Anatomy

The major salivary glands include the parotid and the submandibular gland. The parotid gland is located behind the mandible and consists of a superficial and a deep part. The main parotid duct (Stensen's duct) runs anteriorly to pierce the buccinator muscle, opening on a papilla on the buccal mucosa opposite the second upper molar tooth. The submandibular gland is smaller than the parotid and lies in the submaxillary triangle just below the mandible. The main duct (Wharton's duct) passes forward and medially to open on a papilla lateral to the frenulum at the base of the tongue. The sublingual glands are situated anteriorly in the floor of the mouth above the myelohyoid muscle, and each gland opens into the oral cavity through several small ducts.

16.5.2 Pathophysiology

Salivary glands secret saliva, which is a clear, viscous and watery fluid that contains two major types of protein secretions, a serous secretion containing the digestive enzyme ptyalin and a mucous secretion containing the lubricating aid mucin. Saliva also contains large amounts of potassium and bicarbonate ions, and to a lesser extent sodium and chloride ions as well as several antimicrobial constituents, including thiocyanate, lysozyme, immunoglobulins, lactoferrin and transferrin. Accordingly, saliva provides many functions including antimicrobial activity, mechanical cleansing action, control of pH, removal of food debris from the oral cavity, lubrication of the oral cavity, remineralization and maintaining the integrity of the oral mucosa. Nuclear medicine relevant conditions affecting salivary glands are numerous. These include inflammatory, neoplastic and mechanical disorders affecting the parenchyma and duct system. Xerostomia is defined as dry mouth resulting from reduced or absent saliva flow. It is not a disease, but is a symptom of various medical conditions. Xerostomia may result from such conditions as mumps, Sjögren's syndrome, sarcoidosis, radiation-induced atrophy, and drug sensitivity.

Inflammation of salivary glands usually presents as diffuse enlargement of the glands, unilateral or bilateral. Bilateral enlargement is caused by inflammation (mumps, Sjögren's syndrome), granulomatous disease (sarcoidosis), or diffuse neoplastic involvement (leukemia and lymphoma). The vast majority of salivary neoplasms occur in the parotid gland. Over two-thirds represent benign mixed or pleomorphic adenomas. Warthin's tumor is another benign tumor that can be bilateral. The more common malignant tumors include mucoepidermoid carcinoma, adenocarcinoma, and squamous cell carcinoma. Plain films are of limited use for evaluating these tumors. Sialography in conjunction with CT is the preferred technique [46, 47]. The CT sialogram demonstrates the location of the tumor within the gland and also defines any involvement of the deep structures of the neck.

The duct system of the parotid and the submandibular glands can be demonstrated by sialography, and the technique is particularly valuable in the diagnosis of diseases which affect the duct system such as calculus, stricture, and sialectasia.

16.6 Ascites

Ascites is the accumulation of excess fluid within the peritoneal cavity. It is most frequently encountered in patients with cirrhosis and other forms of severe liver

disease, but a number of other disorders may lead to either transudative or exudative ascites. Serous effusion into the peritoneum occurs in cases of general edema of both the cardiac and renal type, and is sometimes abundant; some fluid may accumulate also in severe anemias and wasting disease. The most severe ascites, however, results from portal obstruction, the most common cause being cirrhosis of the liver. Hepatic vein occlusion (Budd-Chiari syndrome) is also accompanied by gross ascites.

The pathogenesis of ascites is complex, and multiple factors have been postulated to be involved. In cirrhosis the major vascular obstruction is postsinusoidal, and the flow of lymph is considerably augmented. The lymphatic vessels, including the thoracic duct, are dilated but nevertheless appear inadequate to deal with the increased volume of lymph. Fluid oozes from the liver surface; this is called the weeping liver.

Another factor in the pathogenesis of ascites is hypoalbuminemia, since if this is combined experimentally with portal vein obstruction, ascites develops. It has been postulated that the major factor in the formation of ascites is retention of salt and water by the kidney, followed by an outflow of fluid into the peritoneal cavity. Another factor to consider in the pathogenesis of ascites is the increased capillary pressure in the splanchnic area secondary to portal hypertension. This leads to the formation of transudate.

Surgical management of ascites includes various shunt operations. Most are performed as therapy for esophageal bleeding. Which shunt operation is most effective in relieving ascites has not been established; in fact, ascites is reduced after any type of portosystemic shunt as a consequence of decreased portal flow and decreased intrahepatic congestion. Among the most commonly performed shunts, splenorenal and splenocaval shunts and their variants have proven effective in relieving ascites. Transjugular intrahepatic portosystemic shunt (TIPS) has been used to reduce portal hypertension in patients with bleeding esophageal varices. TIPS has been shown to relieve intractable ascites as well.

The peritoneovenous shunt is a pressure-activated shunt devised by LeVeen. One line of this shunt lies free in the peritoneal cavity, and the venous opening of the efferent inserts into the SVC near its entrance into the right atrium. Flow into the shunt is maintained if there is 3 – 5 cm H_2O pressure gradient between the valve and its venous end. Radionuclide studies using ^{99m}Tc-macroaggregated albumin (MAA) injected intraperitoneally are used to evaluate the patency of the shunts [48 – 51].

16.7 Scintigraphic Imaging Procedures

16.7.1 Radionuclide Esophageal Transit Time Study

This study has proven useful and sensitive in detecting esophageal disorders and their involvement in certain systemic disorders.

The patient should fast for 4 – 6 h. A dose of 250 – 500 μCi ^{99m}Tc-SC in 10 ml of water is taken through a straw. The multiple-swallow technique is preferred over the single-swallow test because of the considerable intraindividual variations in esophageal emptying among normal subjects and patients. It is preferable to do the imaging with the subject in the supine position to eliminate the effect of gravity; images of 1 s each are acquired to characterize the esophageal transit. Delayed images at 10 min may be helpful in patients with significant stasis of radioactivity in the esophagus. A time-activity curve can be generated; the esophageal transit time is the time interval between the peak activity of the proximal esophageal curve and the peak activity of the distal esophageal curve.

The normal transit time is 15 s, with a distinct peak in each third of the esophagus. A slowing of bolus progression can be noted at the mid-esophagus because of compression by the tracheal bifurcation and aortic arch. Prolonged transit time might be found in several esophageal and systemic disorders such as achalasia, progressive systemic sclerosis, diffuse esophageal spasm, nonspecific motor disorders, nutcracker esophagus, Zenker's diverticulum (an outpouch above the UES that is acquired), esophageal tumors and esophageal stricture.

16.7.2 Gastroesophageal Reflux Study

The patient should fast for 4 h. The dose is 0.5 – 1 mCi ^{99m}Tc-SC in 300 ml of acidic orange juice. Imaging is performed with the subject in a supine position at a rate of 1 frame/10 s for 60 min. All frames should be reviewed with contrast enhancement. GER is seen as distinct spikes of activity into the esophagus (Fig. 16.4). The episodes of reflux are graded as high or low level, by duration (less or more than 10 s), and by their temporal relationship to meal ingestion. The salivagram can often reveal aspiration when a GER study is negative.

This scintigraphic study has 89% correlation with the acid reflux test. Evidence of pulmonary aspiration is valuable in the pediatric age-group, though it is seen in up to 25% of cases of aspiration with reflux.

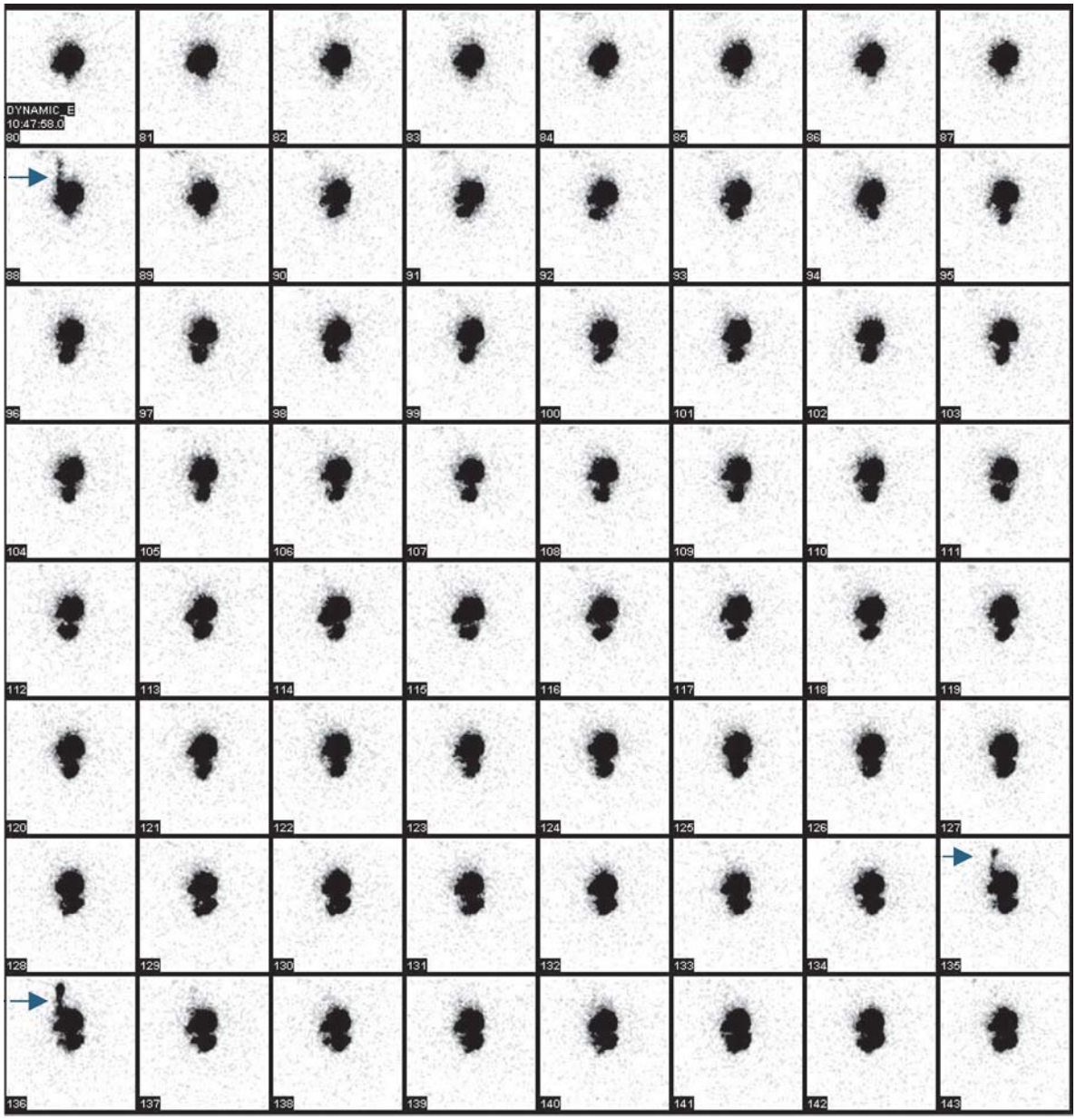

Fig. 16.4. A gastroesophageal reflux study obtained using ^{99m}Tc-sulfur colloid for a 2-year-old boy demonstrates reflux in three frames (*arrows*)

16.7.3 Gastric Emptying Study

The patient should avoid smoking, since it affects emptying, and should fast overnight. The dose is 0.5 – 1.0 mCi ^{99m}Tc-SC mixed with egg white or liver pâté as a solid meal. Dynamic images can be taken for 60 min (Figs. 16.5, 16.6), and if necessary static delayed images are taken every 15 min until at least 50% of the stomach activity (content) has gone into the bowel. Normally, the stomach should empty 50% of the activity measured at time zero, by 90 min. The lag phase corresponds to maximal filling of the distal stomach when trituration has been completed and the suspended solid particles begin to empty. Lag-phase abnormality may be the earliest finding in diabetic gastroparesis and can be corrected by the drugs used to treat this condition [17, 23]. Solids leave the stomach in a linear fashion. Acutely delayed emptying is seen in stress (as in cold or pain), due to drugs (morphine, anticholinergics, levodopa, nicotine, beta blockers), and due to hyperglycemia and hypokalemia.

Chronically delayed gastric emptying is encountered most frequently in gastric outlet obstruction, postvagotomy, gastric ulcer, scleroderma, dermatomy-

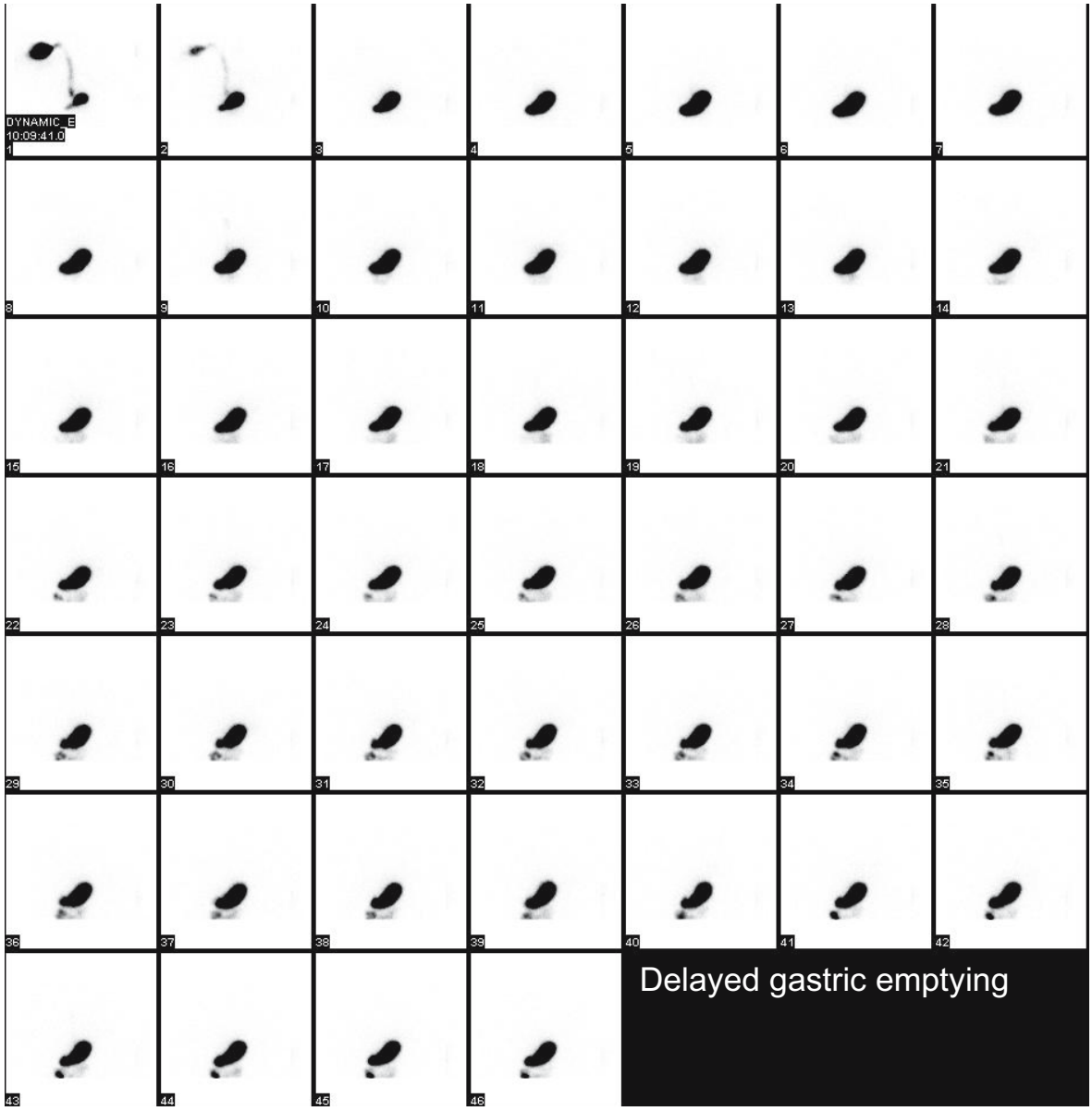

Fig. 16.5. Abnormal gastric emptying study. ^{99m}Tc-sulfur colloid gastric emptying study is shown. Gastric emptying half-clearance time was more than 160 min. Note activity in the stomach is not decreasing with time indicating delayed clearance. Compare with the normal pattern in Fig. 16.6

ositis, hypothyroidism, diabetes mellitus, amyloidosis, and uremia. Abnormally rapid gastric emptying is found in gastric surgery, Zollinger-Ellison syndrome, duodenal ulcer, hyperthyroidism, and diabetes. Figures 16.5 and 16.6 show images of patients with delayed and normal gastric emptying respectively.

16.7.4 Duodenogastric Reflux Study

The method of detecting duodenogastric reflux is to administer a radiopharmaceutical that can go to the duodenum without passing through the stomach. This can be achieved by using hepatobiliary radiopharmaceuticals in conjunction with stimulation of the gallbladder to empty by a fatty meal. This helps to increase the activity in the duodenum and thus to detect the reflux. The usual protocol is to acquire dynamically for 60 min following i.v. administration of ^{99m}Tc-IDA derivative (Fig. 16.7). The fatty meal is then ingested by the patient and another dynamic study is obtained for 30 min.

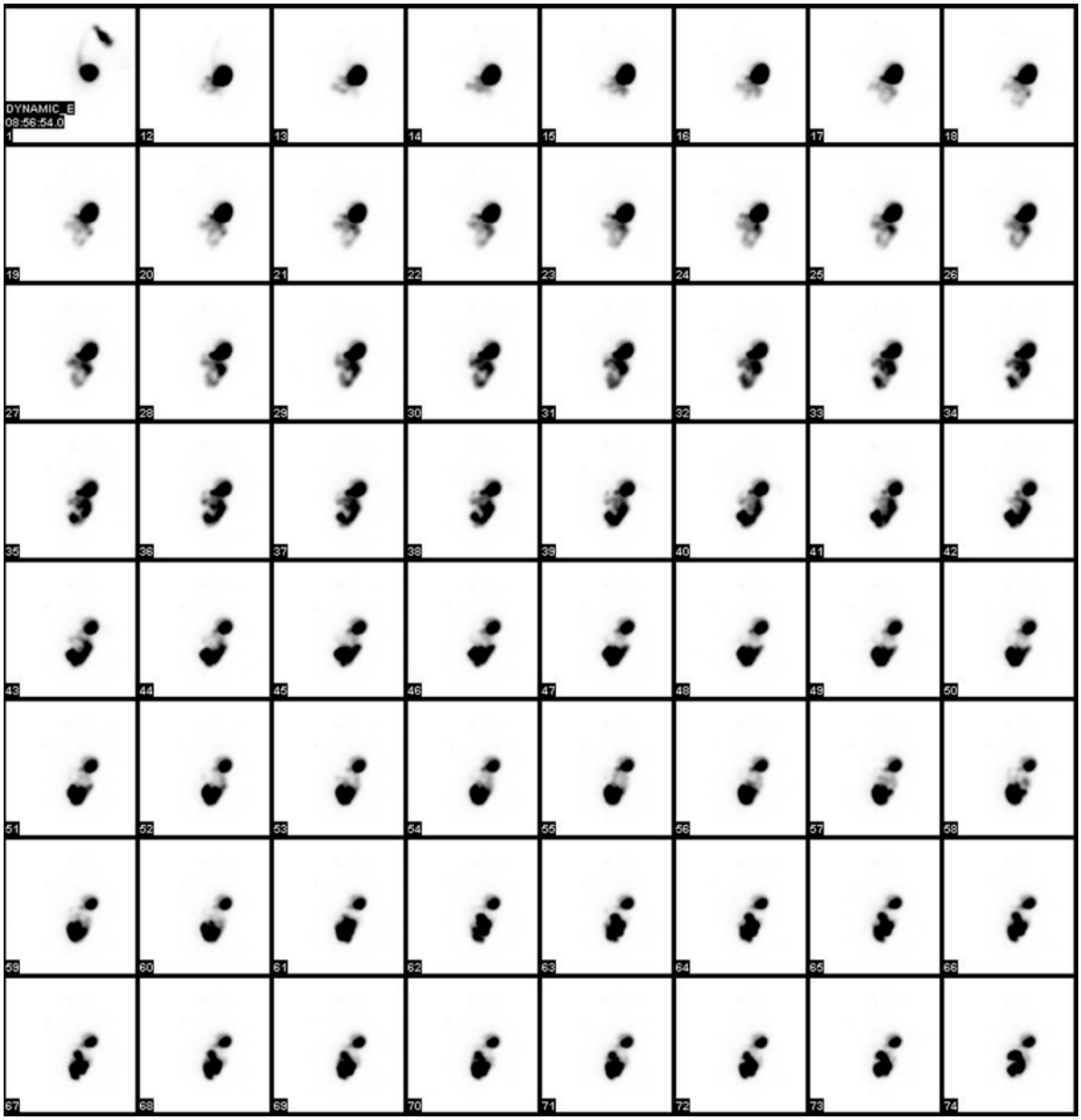

Fig. 16.6. Normal gastric emptying study. The study revealed normal gastric emptying quantitatively. Note the decreasing activity of gastric activity with time during the study, indicating prompt clearance

16.7.5 Gastrointestinal Bleeding Localization Study

This radionuclide study can detect a bleeding rate as low as 0.1 ml/min. The two common indications for a radionuclide bleeding scan are:

1. Suspected acute ongoing or intermittent lower GIB of unknown localization with nondiagnostic endoscopy
2. Follow-up of known bleeding to assess treatment effectiveness

A radionuclide bleeding scan plays only a very small role in the evaluation of upper GIB because of the high accuracy of endoscopy and because of potential interference from radiotracer activity normally excreted by the gastric mucosa. All patients with prior aortic graft surgery and GIB should be considered to have an aortoenteric fistula until proven otherwise.

Two radiopharmaceuticals are available for the study of lower GIB: ^{99m}Tc-labeled RBCs and ^{99m}Tc-sulfur colloid.

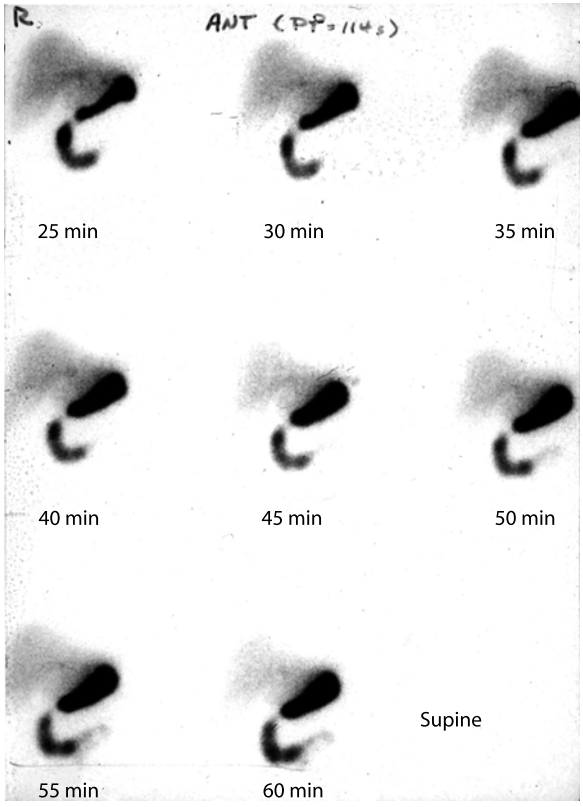

Fig. 16.7. Representative images of a hepatobiliary study of a 32-year-old male patient suspected of having acute cholecystitis. In addition to the nonvisualized gallbladder by 60 min shown in the images presented, significant duodenogastric reflux is seen (*arrow*)

1. ^{99m}Tc-labeled RBCs is the most commonly used method. The patient's RBCs should be labeled in vitro to get the highest labeling efficiency. Imaging is begun with injection of the radiolabeled RBCs, where dynamic images are taken at a rate of 1 frame/10 – 60 s. Rapid bleeding can be detected with first-minute flow images taken at a rate of 1 s/frame. The extravasation manifests as focal activity that appears during the blood pool phase, initially intensifies, and moves anterograde and retrograde in a bowel-like trajectory on subsequent images (Fig. 16.8). It is extremely important to view the study in cine mode, which can clarify difficult cases. If transit time is rapid, 1 mg glucagon can be given i.v. to reduce bowel motility. The sensitivity of this cinematic method is more than 90% [52].

To localize the bleeding site 5 cc or more of extravasation may be needed. The patients can be monitored for up to 24 h; however, the site of extravasation may be easily misinterpreted [53]. A negative radionuclide study is good evidence that angiography will not detect the site of hemorrhage.

2. ^{99m}Tc-sulfur colloid: This study can be performed, in approximately 30 min, in cases of active lower GIB (if no time is available for labeling the RBCs) where time is vital for the management of the patient. This tracer is cleared from the circulation with a half-time of 2.5 – 3.5 min. By 12 – 15 min most of the activity is cleared from the vascular system (background), resulting in a high target-to-

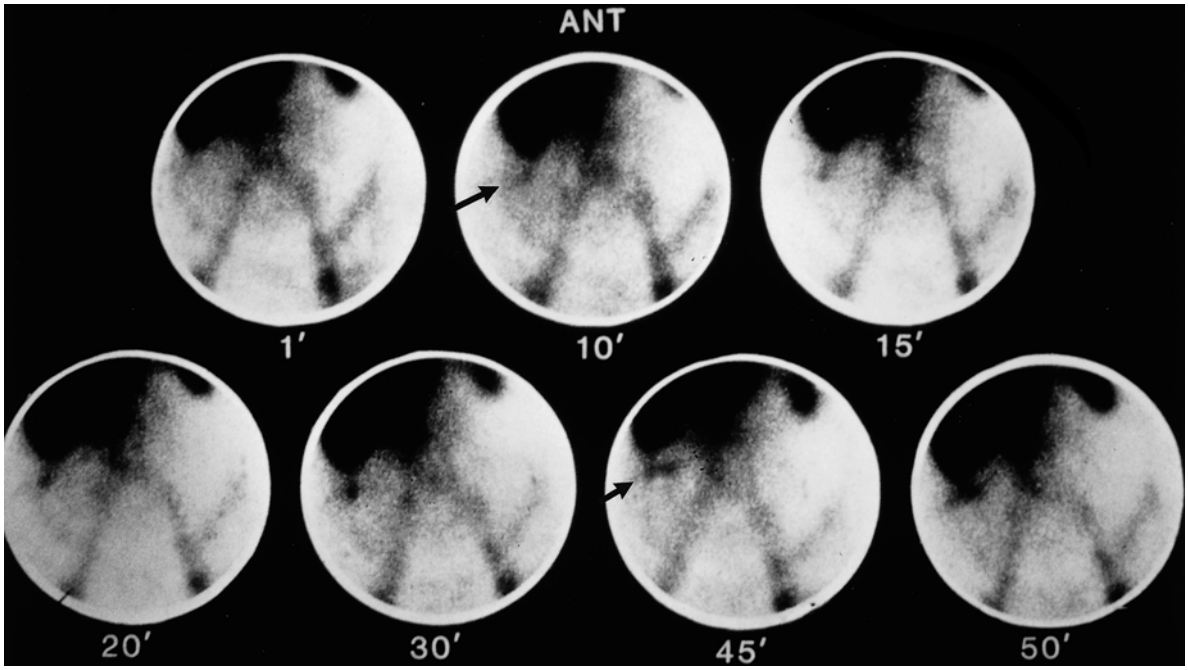

Fig. 16.8. ^{99m}Tc-labeled RBC study for localization of gastrointestinal bleeding showing a focus of extravasated activity in the right hepatic flexure, which progressed later during the study (*arrows*)

background ratio. The clearance is delayed in patients with diffuse liver disease. The study is fast and sensitive with quick results, but intermittent bleeding sites may be missed. Small bowel bleeding can be differentiated from colonic bleeding by the appearance of blood filling multiple loops of small bowel.

The technique of ^{99m}Tc-labeled RBCs is preferred. However, for acute or continuous bleeding, a ^{99m}Tc-SC study may be used, and in this case images are taken for 30 min, which can detect a blood loss of 0.1 ml/min. If this is negative or blood loss is known to be intermittent, a labeled RBC study is used.

16.7.6 Meckel's Diverticulum Study

Scintigraphy is performed using ^{99m}Tc-pertechnetate, since it is taken up by the gastric mucosa contained in Meckel's diverticulum. The radiotracer accumulates in and is excreted from the mucus-secreting cells in the ectopic gastric mucosa regardless of the presence of parietal cells.

The patient should be fasting for 4–6 h to reduce gastric secretion passing through the bowel. With ^{99m}Tc-pertechnetate, Meckel's diverticulum appears at the same time as the stomach and the activity increases in intensity with the stomach; it may change in position during the study and may empty its contents into the bowel. Pharmacological intervention improves the sensitivity of the study. Cimetidine enhances gastric uptake and blocks pertechnetate release from the mucosa. Glucagon is given i.v. 10 min after pertechnetate to inhibit peristalsis and delay emptying of gastric contents into the small bowel.

Any blood leaking into the bowel would be apparent, although it would not show the rounded appearance of Meckel's diverticulum. Among the false-positive cases are renal transplant, renal pelvis, ureter, bladder diverticulum, iliac vessels and uterus, ectopic gastric mucosa in small bowel other than Meckel's diverticulum, infection (as in acute appendicitis), and intussusception. Among the false-negative cases are absence of ectopic gastric mucosa in the diverticulum, and diverticulum hidden by bladder or stomach. The sensitivity of ^{99m}Tc-pertechnetate is more than 85%, but it drops after adolescence because patients asymptomatic throughout childhood are less likely to have ectopic gastric mucosa.

16.7.7 Imaging of Inflammatory Bowel Disease

The diagnosis of inflammatory bowl disease (IBD) needs a complex work-up. Beside varifying the disease itself, it is fundamental to assess disease extent and activity and to detect associated complications, to help

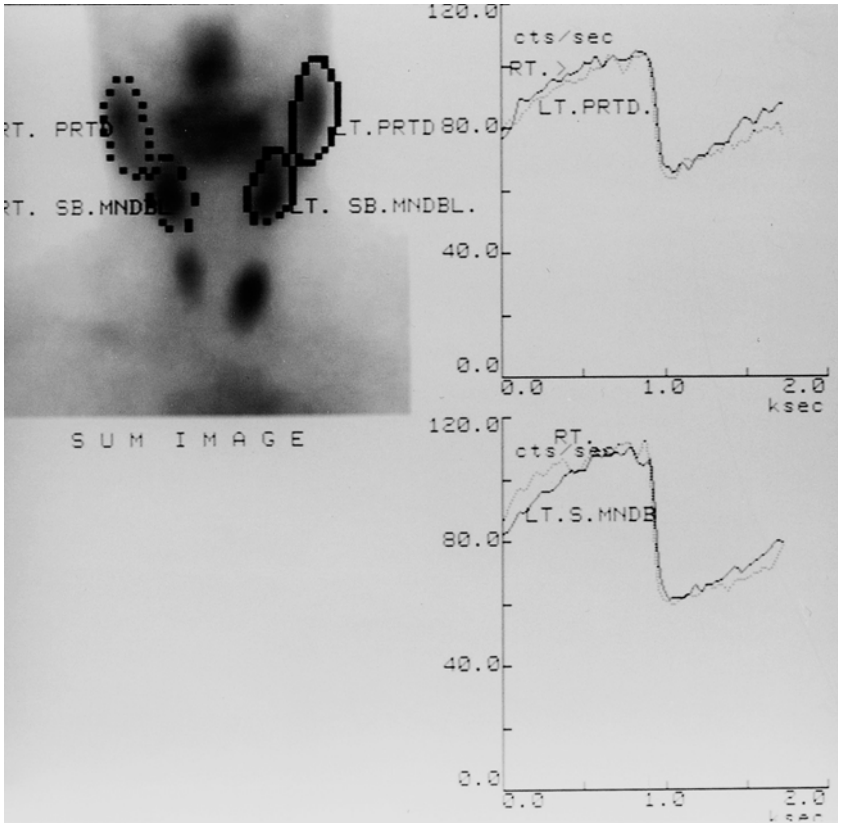

Fig. 16.9. Normal pattern on a salivary radionuclide study. Note the adequate accumulation of the radiotracer with good clearance

select the most effective treatment and for follow-up. Scintigraphy with radiolabeled leukocytes is able to provide a complete survey of the whole intestinal tract, both the small and large bowel, and detects septic complications successfully with negligible risk. Radionuclide procedures are useful in establishing or ruling out IBD in patients with intestinal complaints, in assessing disease severity, and in the evaluation of extraintestinal septic complications [54]. Radiolabeled leukocyte studies offer an accepted radionuclide method for imaging inflammation. Because of the many advantages of tecnetium-99m (^{99m}Tc) over indium-111 (^{111}In), ^{99m}Tc-HMPAO-leukocyte scintigraphy is preferred for the investigation of IBD. The ^{99m}Tc-HMPAO-leukocyte scintigraphy technique is highly accurate within the first few hours postinjection. It can reliably assess disease activity, but a normal scintigraphy does not exclude mild inflammation [55]. Recently, immunoscintigraphy with ^{99m}Tc-antigranulocyte antibodies has been carried out; however, ^{99m}Tc-HMPAO is the first choice agent. For more details please refer to Chapter 4.

16.7.8 Salivary Gland Imaging

Several modalities can be used for the diagnosis of salivary gland disorders. Standard radiographs are of limited value. Sialography is particularly useful for duct system conditions. Parenchyma diseases like tumors are better shown by CT and US. CT can be combined with sialography, and this combination is currently the most sensitive technique for localizing small tumors [46, 47]. Scintigraphy is needed in some conditions that cannot be evaluated by morphologic modalities particularly the functional conditions such as xerostomia.

Salivary gland scintigraphy is carried out after 5 – 15 mCi (185 – 550 MBq) of ^{99m}Tc-pertechnetate injected in the patient intravenously. Dynamic images are obtained as 1-min frames for 15 – 20 min. The patient is asked to drink two glasses of water before the study, and a sialagogue (20 ml lemon juice) is given at 10 min to stimulate salivation. The images are obtained for the anterior face and neck in the sitting position, using a low-energy, high-resolution collimator. Extra images for right and left laterals are obtained for 2 min each to localize the activity. Regions of interest (ROI) are drawn and a graph is plotted to assess the function of the salivary glands.

Findings on a normal scan are a stepwise rising curve of activity with an abrupt drop after the sialagogue and a subsequent rise again (Fig. 16.9). In Sjögren's syndrome there will be decreased accumulation of radiotracer compared with the thyroid gland and delayed clearance (Fig. 16.10). In Warthin's tumor (ade-

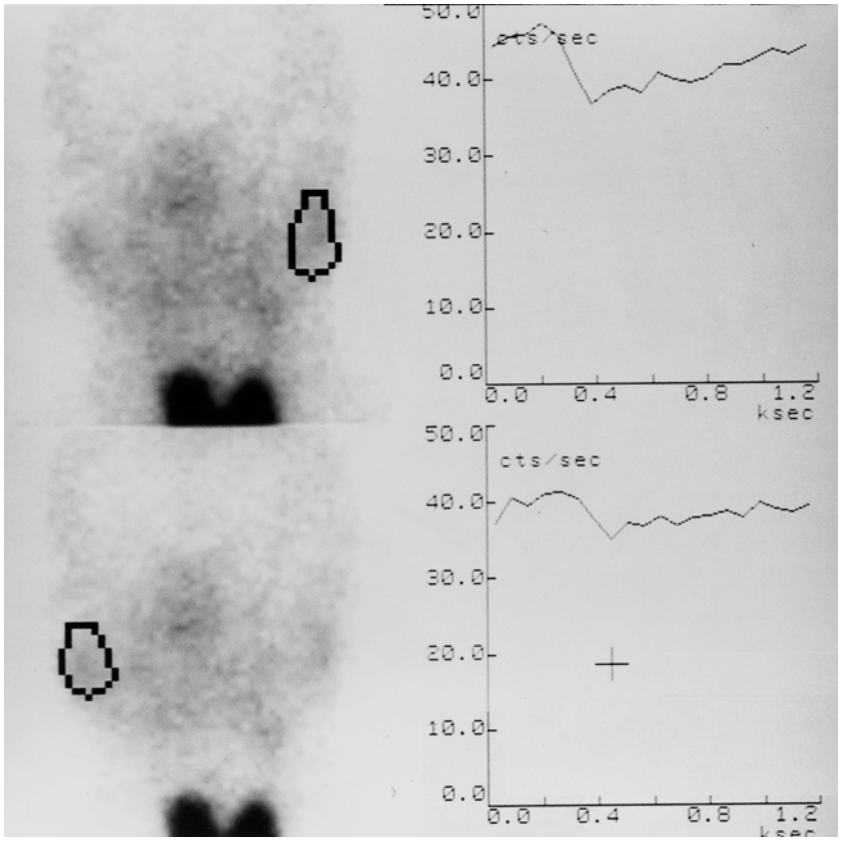

Fig. 16.10. A ^{99m}Tc-pertechnetate salivary gland study showing poor uptake and clearance of the radiotracer in a patient with Sjögren's syndrome

nolymphoma) there is an intense increase in the focal area of activity because it mimics thyroid tissue in pertechnetate uptake [56–59].

16.7.9 Imaging of Appendicitis

Radioisotope imaging using labeled white blood cells, and more recently antigranulocyte antibody technetium (^{99m}Tc) fanolesomab (NeutroSpec), has been used for appendicitis imaging patients with equivocal signs and symptoms of appendicitis. Localized uptake of tracer in the RLQ suggests appendiceal inflammation. ^{99m}Tc-HMPAO labeled leukocyte showed a sensitivity of 90%–98% and a specificity of 92%–96% [60, 61].

16.8 Scintigraphic Non-imaging Procedures

16.8.1 Carbon-14 Breath Tests

This simple carbon-14 breath test has been utilized increasingly in recent years in gastrointestinal practice. The test is based on detection and quantitation of radioactive carbon dioxide originating in the stomach or small intestines and exhaled through the respiratory system after being absorbed into the blood stream. The test is useful in the diagnosis of several disease processes, particularly *Helicobacter pylori* infections, lactose intolerance, and malabsorption due to bacterial deconjugation of bile acids.

16.8.1.1 Helicobacter pylori Infections

Helicobacter pylori has been known for many years and was previously called *Campylobacter pylori* or *Campylobacter pyloridis*. It is a small, curved, gram-negative rod found in the stomach and duodenum of many individuals. The prevalence correlates best with socioeconomic status. In the United States, the overall probability of infection is 20%–30%. Among African-Americans the probability is about 50%, and approximately 60% of immigrants such as Latinos are affected. The infection approaches 90% in the Third World countries, where it occurs in 10% of children between the age of 2 and 8 years per year and most teenagers become infected [62–69].

H. pylori infection is known to be associated with several pathological disorders. The organism causes the most common type of nonerosive gastritis, which characteristically involves the antrum and body of the stomach. It is found in almost all patients with duodenal ulcers and approximately 80% of those with gastric ulcer. Other conditions such as gastric adenocarcinoma and lymphoma, chronic fatigue syndrome, and acne rosacea are also linked to the organism [69, 70]. Recently it has also been suggested to be involved in the pathogenesis of coronary artery disease.

The diagnosis of *H. pylori* may be obtained by endoscopy specimen, by a blood test identifying anti-*Helicobacter* infection antibody, or by a carbon-13 or carbon-14 urea breath test. Endoscopy is needed in many cases to detect ulcers and other gross pathological changes. During endoscopy, biopsy material is obtained and examined microscopically, in addition to culturing for *H. pylori*. However, endoscopy cannot be used just to find whether *Helicobacter* infection is present and is not justified as a follow-up technique to evaluate the response to therapy. Antibody testing, on the other hand, has the shortcoming of not being suitable for patient follow-up since antibodies decline slowly after treatment and may remain elevated long after *Helicobacter* has been killed.

H. pylori is able to fight stomach acid containing a large amount of the enzyme urease. Urease converts urea, present in the saliva and gastric juices, into bicarbonate and ammonia, which are strong bases and act as acid-neutralizing agents around the *H. pylori*, protecting it from the stomach acidity. This action of urea hydrolysis is the basis of carbon-14 and carbon-13 urea breath tests (Fig. 16.11).

The test can be performed using a capsule or a liquid containing a minimal amount (2 μCi) of carbon-14

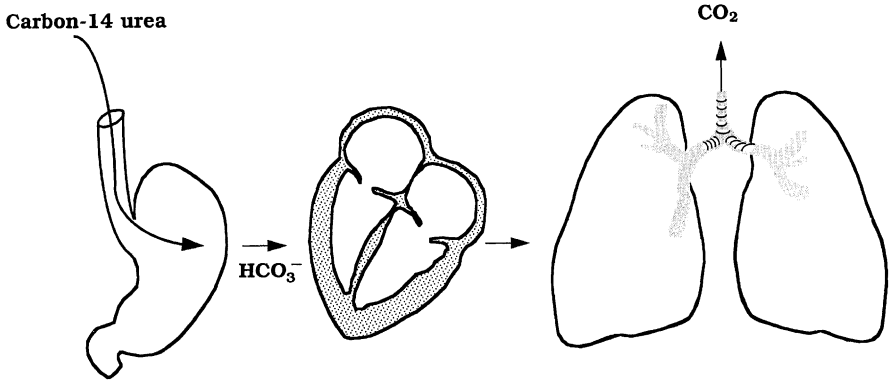

Fig. 16.11. The principle of carbon-14 breath tests

urea. The patient swallows a drink or capsule, and 10–20 min later samples of breath are taken with the patient blowing into a small bottle of liquid. The amount of radioactive carbon dioxide in blood and expired in breath is detected and quantitated by scintillation counter. In the presence of *H. pylori* infections, the count will be higher than normal. Carbon-14 urea contains a tiny amount of radioactive material, which passes out of the body in a day or so in the urine or breath [71–74]. The amount of radioactive exposure to the patient from the test is less than the individual normally receives in half a day from nature [64]. It is also equivalent to the radiation dose that an individual absorbs when flying in an airplane for 1 h. Since urea is present in saliva, patients must brush and rinse their teeth before taking the test.

16.8.1.2 Lactase Deficiency

Acquired lactase deficiency is a common disorder of carbohydrate absorption. The deficiency of intestinal lactase leads to decreased hydrolysis of ingested lactase in the small intestinal cells as occurs normally. Lactase is one of the most common disaccharides in diet and is a main constituent of milk and other dairy products. The intact lactose is not absorbed and increases the osmotic effect of the small intestinal contents, with subsequent outpouring of liquid into the intestinal lumen. This will result in increased intestinal motility with abdominal cramps, distention and diarrhea when a patient ingests milk [75, 76].

For lactose intolerance, ^{14}C-lactose-1 together with carrier lactose (50 g) dissolved in 400 ml of water is used. In patients with lactose intolerance, lactase deficiency leads to the inability to split lactose into glucose and galactose and subsequently to CO_2. When carbon-14-labeled lactose-1 is administered to patients with lactase deficiency, there will be decreased exhalation of labeled carbon dioxide.

16.8.1.3 Malabsorption Secondary to Bacterial Overgrowth

Bacterial overgrowth is one of the major reasons for luminal phase malabsorption. Bacterial overgrowth causes deconjugation of bile salts which are absorbed and cycled normally through the enterohepatic circulation but are ineffective in micelle formation. Since micelle formation is essential for the normal absorption of free fatty acids and monoglycerides, malabsorption results. Carbon-14-glycine cholate and more recently the carbon-14-xylose breath test are useful in the diagnosis of malabsorption secondary to bacterial overgrowth [76, 77]. Since carbon-14-glycine cholate is a conjugated bile salt it is absorbed by the ileum and metabolized in the liver. Only a small portion is attached normally by bacteria and causes deconjugation leading to the formation of carbon dioxide that is exhaled. The deconjugation increases with increased bacterial colonization in the intestines, and consequently the amount of labeled carbon dioxide present in the exhaled breath increases [78]. This test is useful in the diagnosis of blind or stagnant loop syndrome and of ileal absorptive function.

16.8.2 Schilling Test (see Chapter 5)

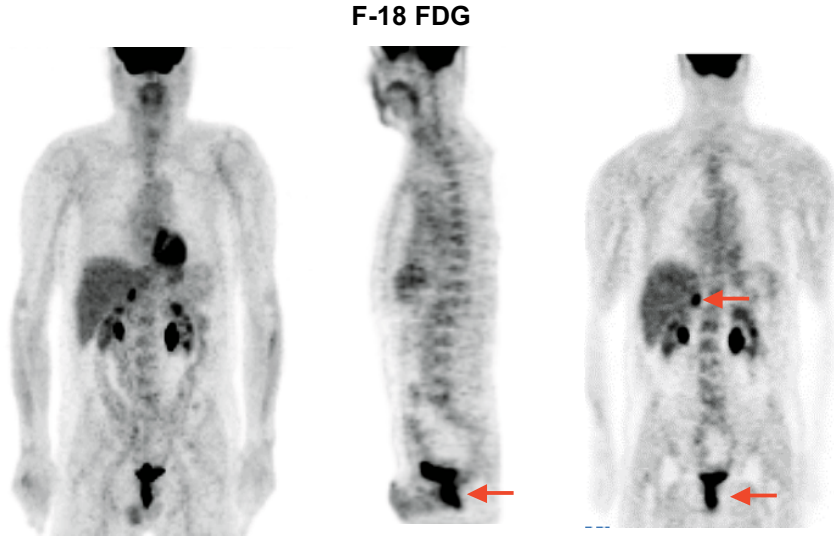

Fig. 16.12. F-18 FDG study of a patient who had rising CEA 5 years after resection of rectal adenocarcinoma. MRI and CT were inconclusive. Five biopsies were obtained from the rectum and were negative. The FDG study shows clearly viable local tumor recurrence and metastases in the right adrenal gland (*arrows*)

References

1. Sivarao DV, Goyal RK (2000) Functional anatomy and physiology of the upper esophageal sphincter. Am J Med 108 [Suppl]:27S–37S
2. Sarna SK, Daniel EE, Waterfall WE (1977) Myogenic and neural control systems for esophageal motility. Gastroenterology 73:1345 – 1352
3. Richards WG, Stamler JS, Kobzik L, et al (1995) Role of nitric oxide in human esophageal circular smooth muscle in vitro. J Thorax Cardiovasc Surg 110:157 – 164
4. Meyer GW, Gerhardt DC, Castell DO (1981) Human esophageal response to rapid swallowing: muscle refractory period or neural inhibition? Am J Physiol 241:G129–G136
5. Biancani P, Zabinski M, Kerstein M, Behar J (1982) Lower esophageal sphincter mechanics: anatomic and physiologic relationships of the esophageogastric junction of the cat. Gastroenterology 82:468 – 475
6. Wong RKH, Waysonovitch CL (1995) Achalasia. In: Castell DO (ed) The esophagus, 3rd edn. Little Brown, Boston, pp 219 – 245
7. Achem S, Benjamin S (1995) Esophageal dysmotility. In: Castell DO (ed) The esophagus, 3rd edn. Little Brown, Boston, pp 247 – 268
8. Fulp SR, Castell DO (1990) Scleroderma esophagus. Dysphagia 5:204 – 210
9. Howard PJ, Heading RC (1992) Epidemiology of gastroesophageal reflux disease. World J Surg 16:288 – 293
10. Penaginie R, Schoeman MN, Dent J, Tipnett MD, Holloway RH (1996) Motor events underlying gastroesophageal reflux in ambulant patient with reflux esophagitis. Eurogastroenterol Motil 8:131 – 141
11. Kahrilas PJ (1999) The role of hiatus hernia in GERD. Yale J Biol Med 72:101 – 111
12. Kahrilas PJ, Manka M, Shi G, Joehl RJ (2000) Increased frequency of transient lower esophageal sphincter relaxation induced by gastric distention in reflux patients with hiatal hernia. Gastroenterology 118:688 – 695
13. Galmiche JP, Janssens J (1995) The pathophysiology of gastroesophageal reflux disease: an overview. Scand J Gastroenterol [Suppl] 211:7 – 18
14. Labenz J, Malfertheiner P (1997) *Helicobacter pylori* in gastroesophageal reflux disease: causal agent, independent or protective factor? Gut 41:277 – 280
15. Fallone CA, Barkun AN, Friedman G, Mayrand S, Loo V, Beech R, Best L, Joseph L (2000) Is *Helicobacter pylori* eradication associated with GERD? Am J Gastroenterol 95:914 – 920
16. Goldstein JL, Waykins JL, Greger JA, Layden TL (1994) The esophageal mucosal resistance. J Lab Clin Med 123:653 – 659
17. Minami H, McCallum RW (1984) The physiology and pathophysiology of gastric emptying in humans. Gastroenterology 86:1592 – 1600
18. Hinder RA, Kelly KA (1977) Human gastric pacesetter potential: Site of origin, spread and response to gastric transection and proximal gastric vagotomy. Am J Surg 133:29 – 33
19. Meyer JH, Ohashi H, Jehn D, et al (1981) Size of liver particles emptied from the human stomach. Gastroenterology 80:1489 – 1496
20. Brener W, Hendrix TR, McHugh PR (1983) Regulation of the gastric emptying of glucose. Gastroenterology 85:76 – 82
21. Siegel JA, Urbain JL, Adler LP, Charkes ND, Maurer AH, Krevsky B, Knight LC, Fisher RS, Malmud LS (1988) Biphasic nature of gastric emptying. Gut 29:85 – 89
22. Loo FD, Palmer DW, Soergel KH, Kalbfleisch JH, Wood CM (1984) Gastric emptying in patients with diabetes mellitus. Gastroenterology 86:485 – 494
23. Horowitz M, Harding PE, Chatterton BE, et al (1985) Acute and chronic effects of domperidone on gastric emptying in diabetic autonomic neuropathy. Dig Dis Sci 30:1 – 9
24. Parkman HP, Hasler WL, Fisher RS; American Gastroenterological Association (2004) American Gastroenterological Association technical review on the diagnosis and treatment of gastroparesis. Gastroenterology 127:1592 – 622
25. Muller-Lissner SA, Fimmel CJ, Sonnenberg A, et al (1983) Novel approach to quantify duodenogastric reflux in healthy volunteers and in patients with type I gastric ulcer. Gut 24:510 – 518
26. Tolin RD, Malmud LS, Stelzer F, et al (1979) Enterogastric reflux in normal subjects and patients with Billroth II gastroenterostomy. Gastroenterology 77:1027 – 1033
27. Shaffer EA, McOrmond P, Duggant T (1980) Assessment of gall bladder filling and emptying and duodenogastric reflux. Gastroenterology 79:899 – 906
28. Markowitz JF (1990) Duodenogastric reflux: state of the art. J Pediatr Gastroenterol 10:287 – 289
29. Elgazzar AH, Fernandez-Ulloa M, Ryan JR, et al (1992) Scintigraphic evaluation of duodenogastric reflux: significance in the diagnosis of acute cholecystitis. Am J Physiol Imaging 3/4:239 – 241
30. Slavin JD, Sharzynski JJ, Spencer RP (1985) High incidence of gastric reflux during hepatobiliary imaging in pancreatitis. Clin Nucl Med 10:5 – 6
31. Chandran P, Satthaporn S, Robins A, Eremin O (2003) Inflammatory bowel disease; dysfunction of GALT and gut bacterial flora (I) (2003). Surg J R Coll Surg Edin Irel 2:63 – 75
32. Halsted CH (2003) Absorption of water-soluble vitamins. Curr Opin Gastroenterol 19:113 – 117
33. Kutchai HC (2000). Gastrointestinal system. In: Berne RM, Levy MN (eds) Principles of physiology, 3rd edn. Mosby, St. Louis, pp 366 – 371
34. Greenberger NJ, Isselbacher KJ (1998) Disorders of absorption. In: Fauci AS, Braunwald E, Isselbacher KJ, Martin JB (eds) Harrison's principles of internal medicine, 14th edn. McGraw-Hill, New York, NY, pp 1616 – 1633
35. Chiu NT, Lee BF (2001) Protein-losing enteropathy: diagnosis with ^{99m}Tc-labeled human serum albumin scintigraphy. Radiology 219:86 – 90
36. Divgi CR, Lisann NM, Yeh SD, Benua RS (1995) Technetium-99m albumin scintigraphy in the diagnosis of protein-losing enteropathy. J Nucl Med 27:1710 – 1712
37. Bhatnagar A, Lahoti D, Singh AK, et al (1995) Scintigraphic diagnosis of protein losing enteropathy using Tc-99m dextran. Clin Nucl Med 20:1070 – 1073
38. Bhatnagar A, Singh K (1996) Technetium-99m dextran: a promising new protein-losing enteropathy imaging agent. Eur J Nucl Med 23:572 – 578
39. Ardizzone S, Bianchi Porro G (2002) Inflammatory bowel disease: new insights into pathogenesis and treatment. J Intern Med 252:475 – 496
40. Guthbert AP, Fisher SA, Mirza MM, et al (2002) The contribution of *NOD2* gene mutations to the risk and site of disease in inflammatory bowel disease. Gastroenterology 122:867 – 874
41. Ahmad T, Tamboli CP, Jewell D, Colombel JF (2004) Clinical relevance of advances in genetics and pharmacogenetics of IBD. Gastroenterology 126:1533 – 1549
42. Wen Z, Fiocchi C (2004) Inflammatory bowel disease; autoimmune or immune-mediated pathogenesis? Clin Dev Immunol 11:195 – 204

43. Old JL, Dusing RW, Yap W, Dirks J (2005) Imaging for suspected appendicitis. Am Fam Physician 71:71 – 78
44. Whiteford MH, Whiteford HM, Yee LF, Ogunbiyi OA, Dehdashti F, Siegel BA, Birnbaum EH, Fleshman JW, Kodner IJ, Read TE (2000) Usefulness of FDG-PET scan in the assessment of suspected metastatic or recurrent adenocarcinoma of the colon and rectum. Dis Colon Rectum 43:759 – 767; discussion 767 – 770
45. Aabakken L (2005) Non variceal upper gastrointestinal bleeding. Endoscopy 37:195 – 200
46. Som PM, Biller HF (1980) The combined CT sialography. Radiology 135:387 – 390
47. Stone DN, Mancuso AA, Rice D, Hanafee WN (1981) Parotid CT sialography. Radiology 138:393 – 397
48. Arroyo V, Bernadi M, Epstein M (1998) Pathophysiology of ascites and functional renal failure in cirrhosis. J Hepatol 6:239
49. Bories P (1986) The treatment of refractory ascites by the Leveen shunts; a multicenter controlled trial of 57 patients. J Hepatol 3:212 – 218
50. Conn HO (1993) Transjugular intrahepatic porto-systemic shunts: the state of the art. Hepatology 17:148 – 158
51. Singh A (1996) Peritoneovenous shunts: patency studies. In: Henkin RE, Bles MA, Dillehay GL, Halama JR, Karesh SM, Wagner PH, Zimmer AM (eds) Textbook of nuclear medicine. Mosby, New York, pp 1041 – 1052
52. Kostamo KL (1996) Evaluation of gastrointestinal bleeding by nuclear medicine techniques. In: Henkin RE, Bles MA, Dillehay GL, Halama JR, Karesh SM, Wagner PH, Zimmer AM (eds) Textbook of nuclear medicine. Mosby, New York, pp 1016 – 1022
53. Nicholson ML, Neoptlemos JP, Sharp JF, et al (1989) Localization of lower gastrointestinal bleeding using in vivo technetium 99m-labeled red blood cell scintigraphy. Br J Surg 76:358 – 361
54. Gyorke T, Duffek L, Bratfai K, et al (2000) The role of nuclear medicine in inflammatory bowl disease. A review with experiences of aspecific bowl activity using immnoscintigraphy with ^{99m}Tc antigranulocyte antibodies. Eur J Radiol 3:183 – 192
55. Lantto E (1994) Investigation of suspected intra-abdominal sepsis: the contribution of nuclear medicine. Scand J Gastroenterol Suppl 203:11 – 14
56. Saha GB (1998) Fundamentals of nuclear pharmacy, 4th edn. Springer, New York
57. Mettler FA, Guiberteau MJ (1998) Essentials of nuclear medicine imaging, 4th edn. WB Saunders, Philadelphia, pp 361 – 363
58. Sarkady E, Sapi Z, Toth V, Kiss S (1999) Warthin-like tumor of the thyroid: a case report. Pathol Oncol Res 5:315 – 317
59. Loutfi I, Nair MK, Ebrahim AK (2003) Salivary gland scintigraphy: the use of semiquantitative analysis for uptake and clearance. J Nucl Med Technol 31:81 – 85
60. Rypins EB, Evans DG, Hinrichs W, et al (1997) Tc-99m-HMPAO white blood cell scan for diagnosis of acute appendicitis in patients with equivocal clinical presentation. Ann Surg 226:58 – 65
61. Kipper SL (1999) The role of radiolabeled leukocyte imaging in the management of patients with acute appendicitis. Q J Nucl Med 43:83 – 92
62. Graham DY, Malaty HM, Evans DG, et al (1991) Epidemiology of *Helicobacter pylori* in asymptomatic population in the United States. Gastroenterology 100:1495 – 1501
63. Peterson WL (1991) *Helicobacter pylori* and peptic ulcer disease. N Engl J Med 324:1043 – 1048
64. Parsonnet J, Friedman GD, Vandersteen DP, et al (1991) *Helicobacter pylori* infection and the risk of gastric carcinoma. N Engl J Med 325:1127 – 1131
65. Logan RP, Dill S, Baner FE, et al (1991) The European C13 urea breath test for the detection of *Helicobacter pylori*. Eur J Gastroenterol Hepatol 3:915 – 921
66. Marshall BL, Surveyor I (1988) Carbon-14 urea breath test for the diagnosis of *Campylobacter pylori*-associated gastritis. J Nucl Med 29:11 – 16
67. Philips M (1992) Breath tests in medicine. Sci Am 74 – 79
68. Ormand JE, Talley NJ, Carpenter HA, et al (1990) C-14 urea breath test for diagnosis of *Helicobacter pylori*. Dig Dis Sci 35:879 – 884
69. Caspary WF (1978) Breath tests. Clin Gastroenterol 7: 351 – 374
70. Debongnie JC, Pauwels S, Raat A, et al (1991) Quantification of *Helicobacter pylori* infection in gastritis and peptic ulcer disease using a simple and rapid carbon-14-urea breath test. J Nucl Med 32:1192 – 1198
71. NIH Consensus Statement (1994) Medical treatment of peptic ulcer disease. JAMA 272:65 – 69
72. Soll AH (1996) Consensus statement. Medical treatment of peptic ulcer disease – practice guidelines. JAMA 275:622 – 629
73. Marshall BJ, Plankey MW, Hoffman SR, et al (1991) A 20-minute breath test for *Helicobacter pylori*. Am J Gastroenterol 86:438 – 445
74. Strubbs JB, Marshall BJ (1993) Radiation dose estimates for the C-14 labeled urea breath test. J Nucl Med 34: 821 – 825
75. Sasaki Y, Lio M, Kameda H, et al (1970) Measurement of C-14 lactose absorption in the diagnosis of lactase deficiency. J Lab Clin Med 76:824 – 835
76. Sasaki Y (1991) Breath test by CO_2 analysis: I. Progress of breath test using isotopes of carbon in Japan. Radioisotopes 40:475 – 484
77. Sherr HP, Sasaki Y, Newman A, et al (1971) Detection of bacterial deconjugation of bile salts by a convenient breath analysis technique. N Engl J Med 285:656 – 661
78. Sasaki Y (1995) Carbon-14 and carbon-13 breath tests. In: Wagner HN (ed) Principles of nuclear medicine, 2nd edn. Saunders, Philadelphia, pp 958 – 965

Digestive System 2: Liver and Biliary Tract 17

Chun K. Kim, Borys R. Krynyckyi, Josef Machac

17.1 Introduction

Over the past two decades, the primary purpose of scintigraphic liver imaging has changed from the detection of focal hepatic lesions to tissue-specific characterization of such lesions, evaluation of functional liver mass, and evaluation of hepatobiliary function. Advances in instrumentation, use of pharmacological interventions in conjunction with cholescintigraphy, and development of new radiopharmaceuticals have significantly improved the efficacy of scintigraphic imaging with expanded clinical applications.

The current status of nuclear medicine evaluation of the primary liver and biliary tract diseases and the pathophysiology relevant to scintigraphic findings are reviewed in this chapter. The roles of positron emission tomography (PET), monoclonal antibody imaging, and somatostatin receptor scintigraphy in the evaluation of metastatic disease are not discussed.

17.2 Anatomical and Physiological Considerations

The liver is the largest organ in the body, weighing between 1200 and 1800 g. The liver lies in the abdominal cavity, where it is split into a large right and a small left lobe by the falciform ligament extending from the anterior abdominal wall. The Couinaud classification divides the liver into eight independent segments numbered 1 to 8, each of which has its own vascular inflow, outflow, and biliary drainage. The Couinaud segments and their corresponding traditional nomenclature are shown in Fig. 17.1.

Within the lobes and segments are multiple, smaller anatomical units called liver lobules. These lobules are formed of plates of hepatocytes, which are the functional cells of the liver. In addition, the parenchyma of the liver is composed of another type of cells: the reticuloendothelial cells or Kupffer's cells. Almost 90% of the reticuloendothelial cells in the body are found in the liver. The sinusoids are capillaries located between the plates of hepatocytes; they receive a mixture of venous and arterial blood from branches of the portal vein and the hepatic artery, respectively. Blood from the sinusoids drains to central veins that continue to empty into the hepatic vein, which enters the inferior vena cava. Kupffer's cells line the sinusoids and destroy micro-organisms.

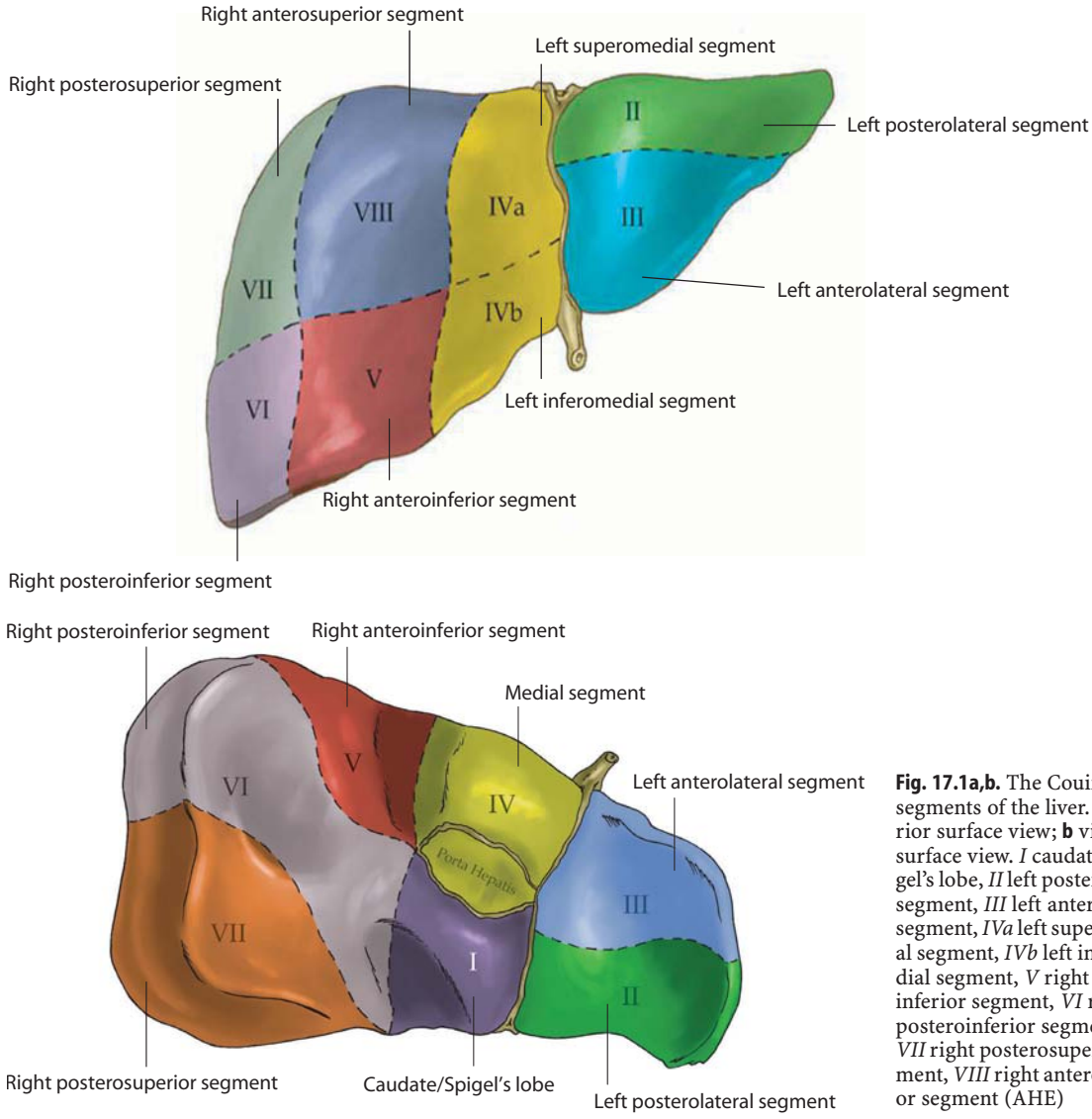

Fig. 17.1a,b. The Couinaud segments of the liver. **a** Anterior surface view; **b** visceral surface view. *I* caudate/Spigel's lobe, *II* left posterolateral segment, *III* left anterolateral segment, *IVa* left superomedial segment, *IVb* left inferomedial segment, *V* right anteroinferior segment, *VI* right posteroinferior segment, *VII* right posterosuperior segment, *VIII* right anterosuperior segment (AHE)

The liver has digestive, metabolic, hematological, and immunological functions. The hepatocytes synthesize approximately 1 l of bile per day and secrete it into the bile canaliculi, which are small channels between the hepatocytes. The bile canaliculi empty into bile ducts that unite and finally form the right and left hepatic ducts, which join to form the common hepatic duct. Past the point where the cystic duct begins, the hepatic duct is called the common bile duct, which drains into the duodenum through the major duodenal papilla. Bile is necessary for fat digestion and absorption. Unconjugated bilirubin is converted to water-soluble, conjugated bilirubin by hepatocytes and is secreted with bile. The gall bladder stores bile and ejects it when chyme enters the duodenum and stimulates the secretion of cholecystokinin. The hepatocytes are capable of regeneration. Most regeneration takes place in the left lobe in disease states such as alcoholic damage or chronic hepatitis.

17.3 Hepatobiliary Radiopharmaceuticals

Technetium-99m (Tc-99m)-sulfur colloid (SC) is a radiopharmaceutical for liver/spleen imaging. This compound is cleared by cells of the reticuloendothelial system: approximately 85% by Kupffer's cells in the liver, 10% by the spleen, and 5% by the bone marrow. Tc-99m-phytate is also used for liver/spleen imaging in some countries. However, due to smaller particle size, its splenic uptake is significantly less than that of SC.

Tc-99m-disofenin (2,6-diisopropyl iminodiacetic acid [DISIDA]) and Tc-99m-mebrofenin (2,4,6-trim-

ethyl, 5-bromoiminodiacetic acid [BrIDA]) are exclusively used for cholescintigraphy by most laboratories in the United States. Various other iminodiacetic acid (IDA) compounds are available in other countries. These compounds, after being injected intravenously, are bound to plasma albumin, transported to the liver, and actively taken up by the hepatocytes via carrier-mediated, non-sodium-dependent, organic anionic pathways similar to those responsible for bilirubin uptake [1]. The IDA compounds are not conjugated. They are excreted into the bile canaliculi by both active and passive transport mechanisms [2]. Compared with Tc-99m-disofenin, mebrofenin demonstrates higher hepatic excretion and lower urinary excretion, especially in patients with a high bilirubin level. Depending on the agents used, 2% – 15% of the injected dose is excreted in urine. The more severe the hepatic dysfunction, the greater the renal excretion [3, 4].

Tc-99m-galactosyl-neoglycoalbumin (Tc-99m-NGA) and Tc-99m-galactosyl human serum albumin (Tc-99m-GSA) are liver imaging agents that bind to the hepatocyte-specific asialoglycoprotein membrane receptors [5, 6]. These agents have been used primarily to evaluate the functional liver mass/reserve in various clinical settings.

17.4 Evaluation of Liver Diseases

17.4.1 Functional Hepatic Mass/Reserve

It is important to assess the functional hepatic reserve prior to major hepatic resection because postoperative liver failure can significantly affect the clinical course. Several parameters such as the indocyanine green retention/clearance rate, prothrombin time, hepaplastin test, and serum albumin level are useful for the assessment of total hepatic function. However, the regional distribution of hepatic function cannot be evaluated by these methods.

Prediction of the regional hepatic reserve has been attempted by morphologically measuring the remnant liver volume by CT scan [7, 8]. However, the liver morphology assessed with CT scan may not reflect the functional status [9, 10].

Functional hepatic reserve has been assessed scintigraphically using various radiopharmaceuticals, including Tc-99m-colloids, Tc-99m-DTPA-human serum albumin (blood pool imaging agent), and a hepatobiliary agent such as Tc-99m-IDA and Tc-99m-*N*-pyridoxyl-5-methyltryptophan (PMT). Bennink et al. found a strong positive association between hepatic function reserve determined with hepatobiliary scintigraphy (HBS) and indocyanine clearance, little or no association between CT volumetric analysis and indocyanine clearance, and a strong positive association between the remnant liver function determined preoperatively on hepatobiliary scintigraphy and the actually measured value postoperatively. These authors also reported that liver function determination using HBS was highly reproducible [10]. Erdogan et al. reported similar results [11].

Nowadays, Tc-99m-GSA appears to be the most widely used radiopharmaceutical for assessing functional hepatic reserve in a variety of clinical settings [12 – 18]. This tracer is taken up only by functional hepatocytes, independent of hepatic blood flow [19, 20]. A strong correlation has been found between parameters based on Tc-99m-GSA studies and previously known parameters of hepatic function [9, 21]. Tc-99m-GSA does not compete with bilirubin, which is an additional advantage in the evaluation of hepatic reserve in patients with hyperbilirubinemia [22]. Overall, Tc-99m-GSA imaging performed prior to surgery and/or other procedures such as a TIPS (transjugular intrahepatic portosystemic shunt) and percutaneous transhepatic portal embolization appears to be a reliable method of predicting functional hepatic reserve after the procedure.

17.4.2 Primary Hepatic Neoplasms and Tumor-Like Conditions

17.4.2.1 Hepatocellular Carcinoma

While hepatocellular carcinoma (HCC) usually displays marked arterial vascularity on dynamic perfusion imaging, its appearance on static colloid imaging (focally decreased activity) is nonspecific. Sulfur colloid imaging can be used to differentiate regenerating nodules from HCC in a cirrhotic liver. The presence of colloid uptake typically represents regenerating nodules, while decreased uptake is nonspecific but may include HCC [23].

Approximately 40% – 50% of HCCs concentrate hepatobiliary tracers (Fig. 17.2), i.e., Tc-99m-IDA or Tc-99m-PMT. The degree of uptake seems to correlate with tumor differentiation, as well as with survival [24, 25]. Tc-99m-IDA uptake was seen in 70% of well-differentiated tumors, in 30% of moderately differentiated tumors, and in no poorly differentiated tumors [24]. In another series of 162 patients, the median survival of 82 patients with increased tumor uptake on delayed Tc-99m-PMT imaging was 1013 days, compared with 398.5 days in 80 patients with no tumor uptake [25].

Uptake of hepatobiliary tracers on delayed imaging can be present in other liver lesions that contain hepatocytes, such as focal nodular hyperplasia (FNH) [26]. Kotzerke et al. claimed that the distinction be-

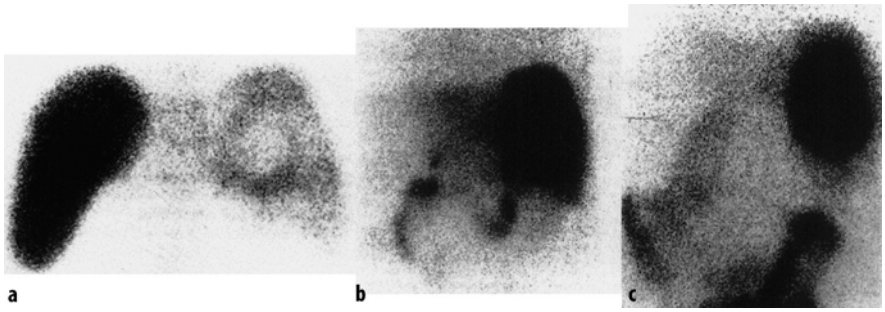

Fig. 17.2. a Hepatic scintigraphy with Tc-99m-SC in a patient with hepatoma complicating liver cirrhosis. A defect is observed in the posterior view. **b** Hepatic scintigraphy with Tc-99m-DISIDA 15 min after tracer administration (posterior view). Marked tracer uptake fills the cold area previously observed, as well as the rest of the liver parenchyma. **c** Hepatic scintigraphy with Tc-99m-DISIDA 3 h after tracer administration (posterior view). Tracer is clearly retained in the HCC area while it has been excreted from the nontumoral liver. (Reprinted from [24] with permission)

tween FNH and HCC is possible with 3-phase imaging (perfusion, 5–10 min, and 2–3 h) [27]. In their series, most FNH exhibited normal or increased uptake at 5–10 min, whereas most HCC displayed decreased or no uptake during this phase.

Gallium-67, thallium-201, and fluorine-18-fluorodeoxyglucose have been used in patients with HCC in various clinical settings which will not be discussed in detail here.

17.4.2.2 Hepatic Cavernous Hemangioma

Hemangioma is the most common benign tumor of the liver. Most hemangiomas are of the cavernous type, constituted by dilated nonanastomotic vascular spaces lined by flat endothelial cells and supported by fibrous tissue. Thrombi in different stages of organization are often encountered. Long-standing lesions can show extensive hyalinization or calcification [28].

Tc-99m-labeled RBC scintigraphy provides the most specific, noninvasive method for making the diagnosis of hepatic cavernous hemangiomas (HH), although the sensitivity varies depending on the imaging protocol, lesion size, and location.

The classic finding of HH on Tc-99m-RBC imaging is a perfusion/blood pool mismatch, i.e., decreased perfusion on early dynamic images and a gradual increase in activity on blood pool images over time [29, 30]. However, decreased flow is not always observed in small and/or deeply situated lesions due to the limited resolution of dynamic imaging. The sensitivity of planar Tc-99m-RBC imaging in reports published since 1989 ranges from 30% to 53% [30–36], although the specificity and positive predictive value approach 100%. Therefore, planar imaging should no longer be a routine part of the study.

SPECT has improved the sensitivity of RBC imaging. Reports published in the 1990s have shown 70%–80% sensitivity using single-head SPECT [33–35, 37]. Using triple-head cameras [30, 36], the sensitivity was

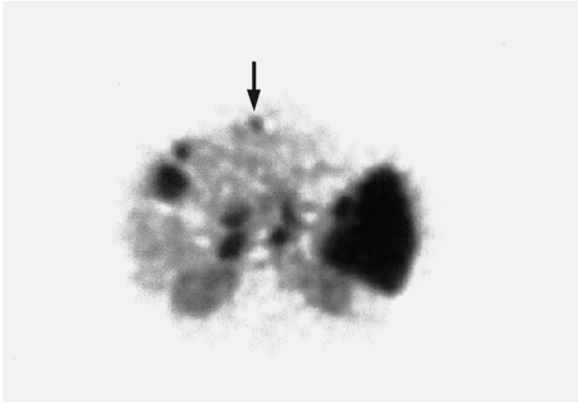

Fig. 17.3. Tc-99m-RBC SPECT images of the liver (triple-head) reveal multiple hemangiomas. The smallest one (*arrow*) was 0.7 cm

17%–20% for the detection of lesions smaller than 1 cm, 65%–80% for lesions between 1 cm and 2 cm, and virtually 100% for lesions equal to or larger than 1.4 cm (Fig. 17.3). It is notable that the specificity of RBC imaging with SPECT remains at 100% [33–35]. Multi-head SPECT systems add another advantage, namely the capability of obtaining several sequential dynamic SPECT scans at short intervals following injection of Tc-99m-RBC (Fig. 17.4) [38, 39]. This makes it possible to distinguish HH from vascular structures more easily, since HHs exhibit a gradual increase in blood pool activity over time, while blood vessels and vascular hepatic tumors do not.

False-negative results have been reported in cases of HH with extensive thrombosis and/or fibrosis [29, 40]. Several false-positive cases related to various malignancies, including HCC, angiosarcomas, metastases and hepatic lymphoma, have been reported in the literature [40–43]. However, the occurrence of such false-positive results seems extremely rare in view of the 100% specificity in virtually all studies other than case reports. Exceptionally, Rabinowitz et al. [40] reported four cases of HCC which showed increased activity on delayed images. They suggested that distinction be-

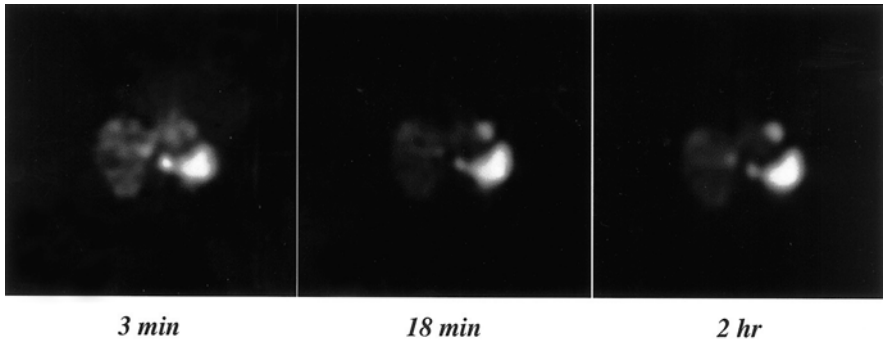

Fig. 17.4. Selected transverse views (*3 min* and *18 min*) from a dynamic Tc-99m-RBC SPECT of the liver and an image from a delayed SPECT (*right*) show a lesion in the tip of the left lobe of the liver that becomes progressively more intense. The findings are consistent with a hemangioma. (Courtesy of Alan Siegel, MD, Dartmouth Hitchcock Medical Center, Lebanon, NH, USA)

tween HH and HCC can be made on early dynamic imaging because HCCs show increased flow as well as increased activity on delayed images, whereas HHs do not show increased activity on flow images. However, other studies, including a large series from Japan, found no cases in which HCC demonstrated increased activity on either planar or SPECT delayed images [31, 44].

It is important to distinguish HH from other vascular structures and from the right kidney to avoid either false-negative or false-positive results [38]. In these circumstances, SPECT/CT fusion imaging can lower the false results [45, 46]. If a SPECT/CT hybrid system is not available, review of all three orthogonal SPECT slices can be helpful when the lesion is adjacent to these structures [38]. It is also essential that labeled RBC scans be correlated with anatomical images obtained seperately.

17.4.2.3 Focal Nodular Hyperplasia

Focal nodular hyperplasia contains variable quantities of normal hepatic cellular elements, including Kupffer's cells, hepatocytes, and bile ducts arranged in a characteristic pattern. The characteristic triad suggesting FNH has been described as arterial blood flow (Fig. 17.5), normal colloid uptake, and accumulation of Tc-99m-IDA tracer [47].

Thirty to 70% of FNHs have either normal or increased Tc-99m-colloid uptake (Fig. 17.5a) [26, 48, 49], reflecting the variable quantity of Kupffer's cells. Decreased Tc-99m-colloid uptake may be seen in approximately one-third of cases (Fig. 17.5b) [48, 49]. Because of the presence of hepatocytes in FNH, Tc-99m-IDA scintigraphy has also been evaluated for the diagnosis of FNH. Of 25 FNHs in a recent study, 19 (76%) showed hyperperfusion during the flow phase and 23 (92%) appeared as focal regions of increased uptake during the clearance phase of hepatobiliary imaging. Normal sulfur colloid uptake was seen in 16 (64%) [26]. The detectability of FNH by Tc-99m-IDA scintigraphy was 92%, greater than that of CT (84%) or MRI (84%).

17.4.2.4 Hepatocellular Adenoma

Hepatocellular adenomas typically appear as photopenic defects on Tc-99m-colloid scintigraphy. In the past, this was attributed to the absence of Kupffer's cells [50]. However, a recent pathological study demonstrated that all hepatic adenomas studied contained Kupffer's cells [51]. Yet most of these lesions (77%) did not demonstrate Tc-99m-colloid uptake for unknown reasons. The authors found no significant histological difference between those lesions that accumulate colloids and those that do not. They also suggested that adenoma should be added to the differential diagnosis of a hepatic lesion with Tc-99m-colloid uptake because of the presence of uptake in 23% of their cases.

17.5 Evaluation of Biliary Tract Diseases

Bile flowing through the common hepatic duct may flow either into the gall bladder or through the common bile duct (CBD) into the duodenum. The quantity of bile flowing in either direction is determined to a major degree by the pressure developed by the sphincter of Oddi. In normal individuals, bile flows into the gall bladder when the sphincter of Oddi is contracted. Foods containing lipids and amino acids enter the duodenum and cause release of endogenous cholecystokinin (CCK) from the duodenum and upper jejunum, which in turn contracts the gall bladder, dilates the sphincter of Oddi, and increases bile secretion from the hepatocytes. All of these enhance the flow of bile into the duodenum.

On a typical normal cholescintigram performed with Tc-99m-IDA agents, the CBD and gall bladder are visualized 10–30 min following the intravenous administration of Tc-99m-IDA (Fig. 17.6). Visualization of the small bowel varies depending on the sphincter tone and the degree of gall bladder filling.

Several drugs, including cholecystokinin (CCK), morphine, and phenobarbital, have been used to alter biliary kinetics at different levels (i.e., hepatocytes, gall

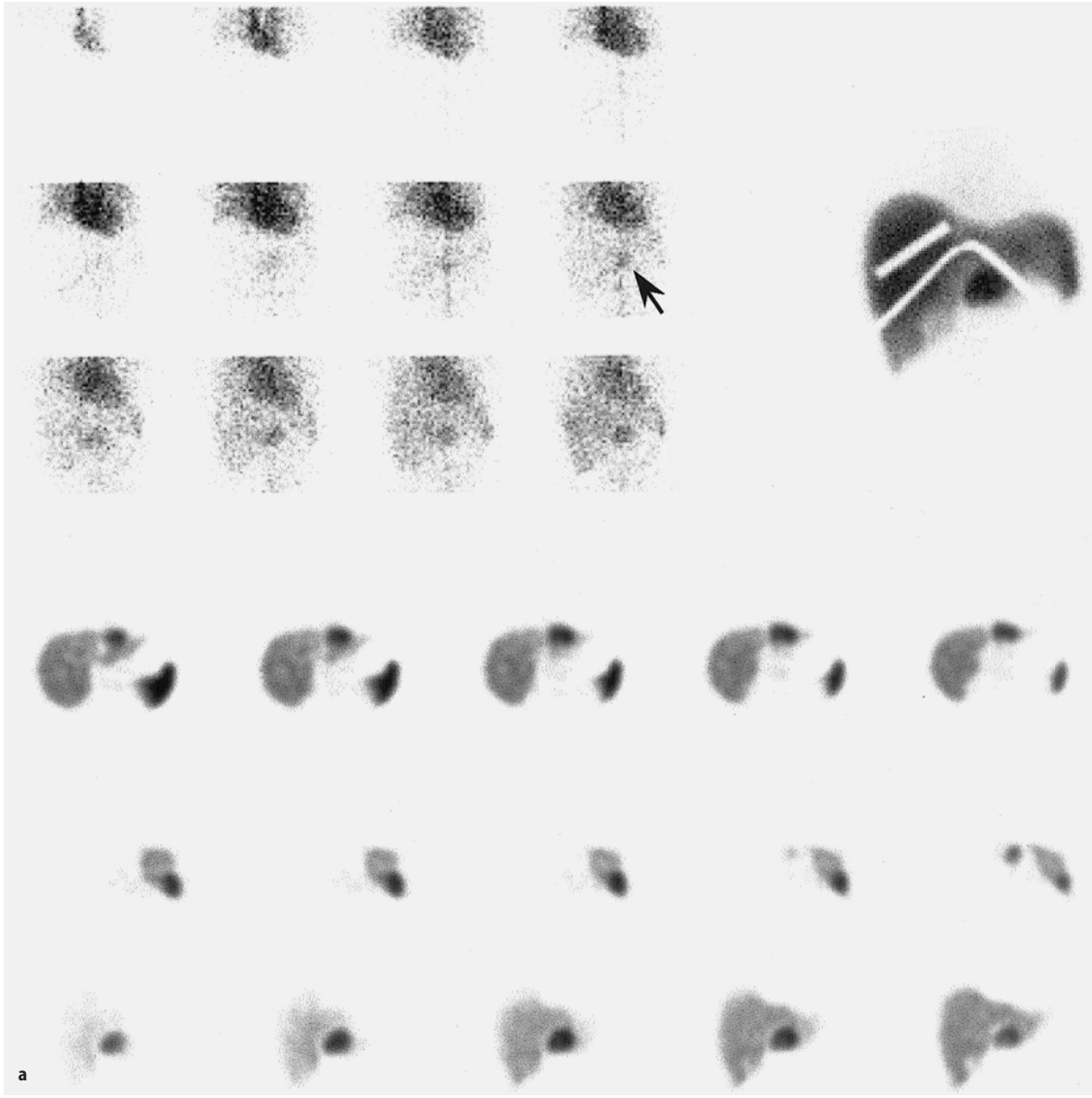

Fig. 17.5a,b. Tc-99m sulfur colloid studies in two cases of focal nodular hyperplasia. While both case **a** and case **b** show increased early arterial flow (*arrow, arrowhead*), colloid uptake is increased in case **a** and decreased in case **b** on delayed views. (Reprinted from [254] with permission)

bladder, and/or sphincter of Oddi) in an effort to increase the efficacy of hepatobiliary imaging. Sincalide (Kinevac, Squibb Diagnostics, Princeton, NJ), a synthetic C-terminal octapeptide of CCK, has been used in the diagnosis of acute cholecystitis in order to empty the gall bladder before cholescintigraphy, so that gallbladder filling can be enhanced during the study if the cystic duct is patent. These agents are also used to evaluate gall bladder ejection fraction (GBEF) and/or sphincter of Oddi response in patients with suspected chronic, acalculous biliary tract diseases to determine who might benefit from cholecystectomy or sphincterotomy.

17.5.1 Acute Cholecystitis

Although it is generally known that acute cholecystitis in 90%–95% of cases begins with obstruction of the neck of the gall bladder or the cystic duct by a gallstone, some authors feel that obstruction does not necessarily lead to acute cholecystitis [52]. Nevertheless, obstruction is present in almost all cases of acute cholecystitis. There are other important factors in the pathogenesis of acute cholecystitis, including chemical factors such as prostaglandins [53] and bacterial growth [54]. Inju-

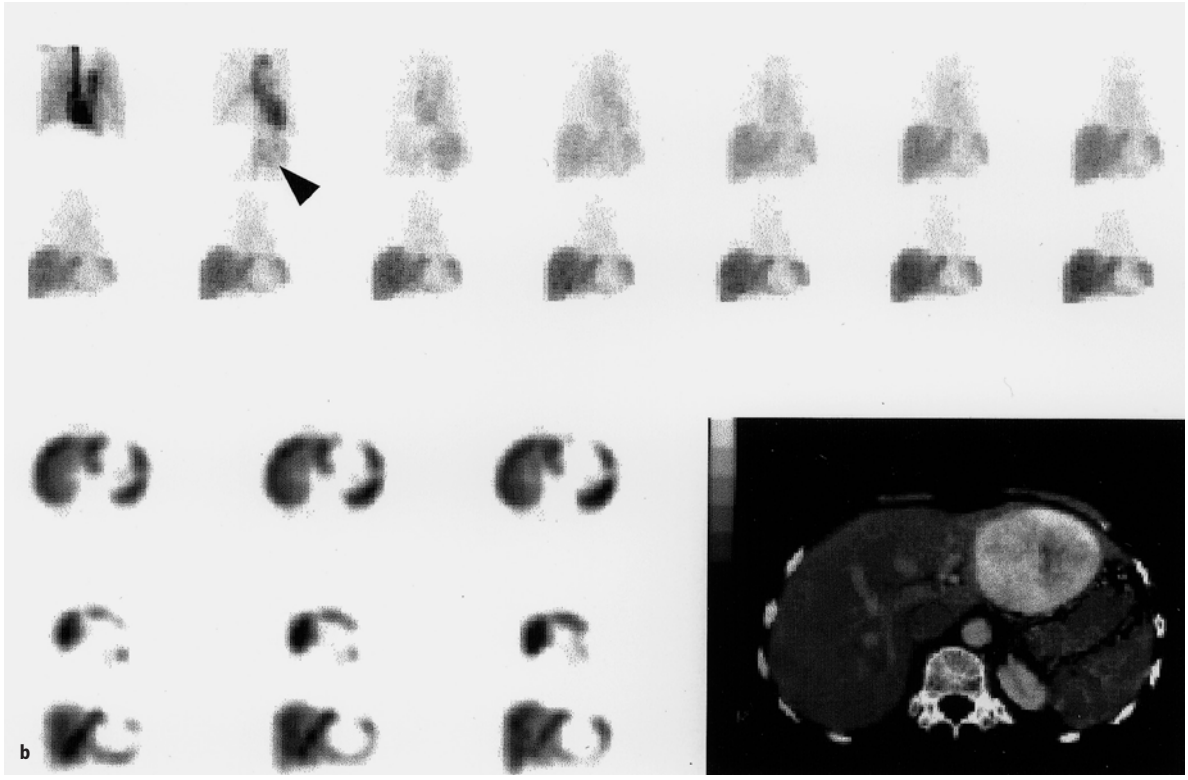

Fig. 17.5. (*Cont.*)

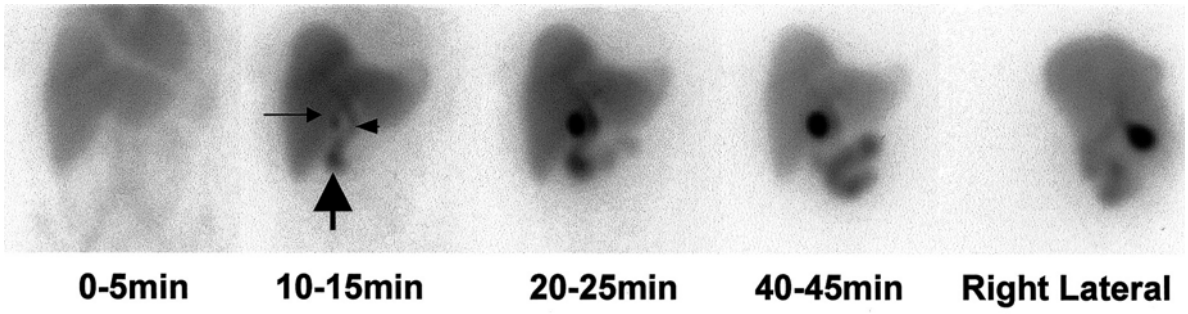

Fig. 17.6. Normal hepatobiliary scan. Hepatic uptake is prompt. The CBD (*short arrow*), gall bladder (*long arrow*), and duodenum (*thick arrow*) are visualized within 15 min following intravenous administration of Tc-99m-IDA

ry to the gall bladder mucosa by a mechanical or chemical factor stimulates the epithelial cells to secrete fluid. Active fluid secretion in the obstructed gall bladder lumen increases the intraluminal pressure, which may cause impairment of circulation and ischemia of the gall bladder mucosa and wall. Distention of the gallbladder further enhances formation of prostaglandin, establishing a vicious cycle [55]. Active fluid secretion in the gall bladder wall is markedly reduced by morphine. The acceleration of the process can be reduced by morphine [56].

Approximately 60% – 70% of patients report prior attacks that resolved spontaneously. The factors regulating the intraluminal pressure may determine the course of an attack of acute cholecystitis. Of the 75% of patients with acute cholecystitis who experience remission of symptoms, approximately one-quarter will experience a recurrence of cholecystitis within 1 year, and 60% will have at least one recurrent attack within 6 years [57]. Therefore, the histological pattern of acute cholecystitis is superimposed upon chronic inflammatory changes in at least 90% of cholecystectomy specimens [58].

Acalculous acute cholecystitis is less common (5% – 10%). Despite the absence of gallstones, the cystic duct is frequently obstructed, though the mechanism remains unclear. Precipitating factors include severe trauma or burns, the postpartum period following pro-

longed labor, a major operation, prolonged parenteral hyperalimentation, vasculitis, obstructing tumor of the gall bladder, and parasitic infestation of the gall bladder. It also may be seen with a variety of other systemic diseases (sarcoidosis, cardiovascular disease, tuberculosis, syphilis, actinomycosis, etc.) [57]. Save for the absence of stones, the pathology of acalculous and calculous cholecystitis is essentially identical [59].

Acute cholecystitis has been and still is the single most common indication for cholescintigraphy, which is considered the procedure of choice for its diagnosis [60]. Generally, nonvisualization of the gall bladder up to 4 h after radiotracer administration or within 30 min after the administration of morphine sulfate is interpreted as consistent with cystic duct obstruction, provided that there is normal hepatic uptake and excretion. Gall bladder visualization anytime during imaging virtually excludes the presence of acute cholecystitis.

Meta-analysis of 2466 patients showed a sensitivity of 97% and specificity of 90% [60]. Conventional imaging protocols frequently require delayed imaging for up to 4 h post injection [61], or even up to 24 h in patients with severe intercurrent disease [62] to achieve a sufficiently high level of accuracy. Delayed imaging is logistically inconvenient. It can be potentially disadvantageous to the patient, and it may not be feasible in some clinical settings. Efforts to increase the specificity of the test and/or to shorten the total imaging time have been made using pharmacological interventions, which include morphine augmentation [63] and CCK pretreatment [64].

Despite the superiority of cholescintigraphy over ultrasonography for evaluation of acute cholecystitis that has been known since more than two decades ago [65], the latter is still the first diagnostic test being ordered in many institutions. Recent reports published after the turn of this century confirm the previous results, i.e., superior efficacy of cholescintigraphy, which should be the initial imaging study of choice [66, 67].

17.5.1.1 Morphine Augmentation Versus Delayed Imaging

Bile is secreted continuously from the liver into the biliary system. The proportion of bile flowing into the gallbladder or the duodenum depends on the relative resistance to flow determined mainly by the contractile state of the gall bladder and the sphincter of Oddi. The resistance of the sphincter of Oddi is considered the principal factor in the regulation of the intracholedochal pressure and of the common bile duct-gall bladder pressure gradient [68]. The administration of morphine sulfate (morphine) results in contraction of the sphincter of Oddi. This, in turn, causes an increase in the intraductal pressure and forces the bile to flow into the gall bladder if the cystic duct is patent [69, 70]. A widely used protocol involves the administration of 0.04 mg/kg morphine intravenously over 3 min at 1 h after the injection of radiotracer, provided that activity is seen in the bowel. Generally, morphine is not administered during the first hour because the gall bladder is visualized within 1 h in the majority of patients undergoing cholescintigraphy. Another reason is that delayed filling of the gall bladder or delayed excretion into the bowel, suggesting the presence of chronic cholecystitis or other biliary tract disease, could be missed by administering morphine early. After morphine administration, imaging is continued for an additional 30 min. Typically, the gall bladder is visualized within 30 min if the cystic duct is patent (Fig. 17.7). If visualization does not occur within 30 min, the findings are interpreted as consistent with acute cholecystitis. Therefore, the entire study can be terminated at 90 min in contrast to 4 h or more with conventional delayed imaging without morphine augmentation.

Since the introduction in 1984 of morphine-augmented cholescintigraphy by Choy et al. [63], as an alternative to delayed imaging, a number of reports have been published on this subject [71–81]. The general conclusion in most early reports, in terms of efficacy, is that the two tests are diagnostically equivalent [71–75]. Morphine augmentation has been recommended primarily because of its logistic advantage (a short imaging time). However, the reported efficacy of morphine-augmentation has been based primarily on data excluding cases of early GB visualization without morphine. In contrast, patients with early GB visualization (<1 h) have been included in previous reports evaluating the efficacy of conventional cholescintigraphy with which the efficacy of morphine-augmentation has been compared. A reanalysis of published data (after excluding the cases with early gall bladder visualization from previous reports) indicated that delayed imaging has a significantly lower specificity (53% average: 33%–94%) for acute cholecystitis than morphine augmentation (85% average: 69%–100%) [80]. The sensitivity is still excellent at 98% (98%–100%). Another meta-analysis using a different statistical approach yielded nearly identical results and confirmed the higher specificity of the morphine-augmented technique than that of delayed imaging (84% vs. 68%) [81].

A number of potential shortcomings associated with morphine augmentation have been reported [74], including false-positive studies occurring in patients with chronic cholecystitis or hepatocellular disease, or in other severely ill patients [71, 80, 82]. However, this problem is not unique to morphine augmentation. It also occurs with delayed imaging [62, 83, 84] and can be even more serious. Whereas some investigators [74] have suggested more delayed imaging in addition to the

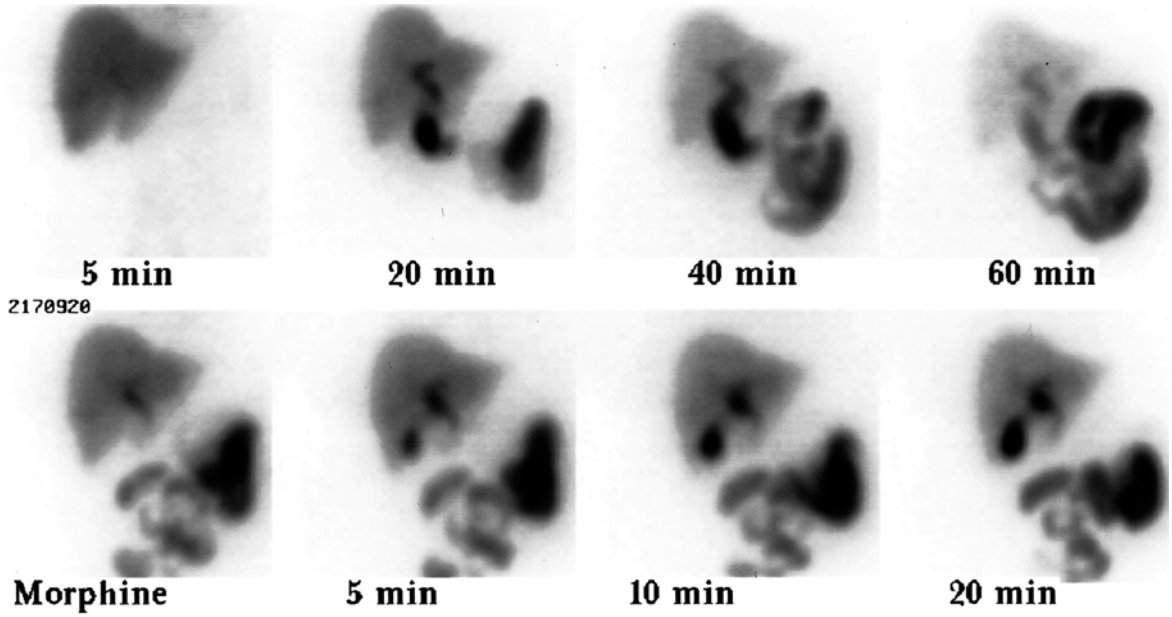

Fig. 17.7. The CBD and small bowel are promptly visualized in this study with Tc-99m-IDA, but the gall bladder is not visualized up to 60 min. Following morphine administration, the gall bladder filled promptly, excluding cystic duct obstruction

30 min after morphine administration to reduce false-positive examinations, others [71] found no additional benefit in imaging up to 1 h instead of 30 min. Secondly, in patients with acute acalculous cholecystitis or with the "dilated cystic duct sign", increased intraluminal pressure following morphine administration may potentially result in more false-negative studies than delayed imaging [72]. However, there is no significant difference in the sensitivity or the negative-predictive value between delayed imaging and morphine augmentation [80, 81]. This indicates that the occurrence of false-negative studies associated with acute acalculous cholecystitis or the dilated cystic duct sign is not frequent enough.

17.5.1.2 Sincalide Preadministration for the Diagnosis of Acute Cholecystitis

Administration of CCK prior to injection of Tc-99m-IDA will induce gall bladder emptying with a reduction of intraluminal pressure. It was introduced as a means of reducing potential false-positive results for acute cholecystitis and of shortening the total imaging time [64, 85]. Eikman et al. [86] attributed the improved efficacy of cholescintigraphy in their series to CCK pretreatment. The rationale of this approach is that gallbladder emptying before initiating the study is generally followed by more reliable gall bladder filling during the cholescintigraphy. In a series reported by Kim et al., approximately 50% of volunteers who had paired studies showed greater gall bladder filling after sincalide pretreatment [87]. Although sincalide pretreatment of all patients may not be necessary, it is often used in conditions such as alcoholism and total parenteral nutrition, and during a prolonged fasting state [88, 89], because functional resistance to tracer inflow may result from distention of the gall bladder with viscous contents. Fasting for 24 h or longer appears to have become a routine indication for the preadministration of sincalide in many laboratories.

It should be noted that a meticulous sincalide infusion technique is important to ensure good gall bladder emptying, not only for the gall bladder ejection fraction measurement (which will be discussed later) but also for the pretreatment. For the latter, it appears that less attention has been paid to the administration technique, perhaps because imaging is not performed during gall bladder emptying. A 30- to 45-min infusion is logistically inconvenient for pretreatment, unlike that for the measurement of gall bladder ejection fraction. A 3-min infusion at the physiological rate of 3.3 ng/kg/min [3], or an infusion for up to 10 min at the same or slightly lower rate approximately 30 min before injection of Tc-99m-IDA, is probably adequate for this application.

Some investigators believe that CCK preadministration decreases specificity and suggest that CCK not be given or, if given, that a minimum of 4 h should pass before a Tc-99m-IDA study is begun [90]. Further studies seem to be warranted to resolve this issue.

17.5.1.3 Sincalide Pretreatment Versus Morphine Augmentation

Reports by Chen et al. and Kim et al. [91, 92] show that morphine administration helps to visualize the gallbladder in 32% – 42% of patients with gall bladder nonvisualization at up to 60 – 90 min despite sincalide pretreatment. These results suggest that sincalide pretreatment alone is not sufficient to detect all patent cystic ducts.

17.5.1.4 Potential Causes of False-Positive Results

Insufficient fasting will result in gall bladder contraction induced by circulating endogenous CCK, thereby inhibiting bile flow into the gall bladder. Therefore, the gall bladder may not visualize even in normal subjects (up to 64%) in the nonfasting state [93]. A minimum of 2 – 4 h fasting is required before cholescintigraphy is performed for the evaluation of acute cholecystitis.

As discussed earlier, false-positive results can occur in conditions such as a prolonged fasting state, alcoholism, and total parenteral nutrition [88, 89].

Activity retained in the duodenum or dilated right renal pelvis may cause confusion. Conversely, activity in the gall bladder may not be clearly separated from that in the duodenum. In either situation, a right lateral view can be helpful: The gall bladder appears as an anteriorly positioned structure. If the right lateral view does not resolve the situation, a left anterior oblique view can clarify the question. Alternatively, water ingestion often clears duodenal activity [94, 95].

In the presence of perfectly normal hepatic function, the clearance of Tc-99m-IDA compounds is rapid, and thus there may be little residual parenchymal activity available for gall bladder visualization at the time of morphine-augmented or delayed filling. This may potentially cause a false-positive result. If only minimal residual hepatic activity is noted just before morphine-augmented or delayed imaging, an additional 2 – 3 mCi of radiotracer should be injected [64].

Radioactivity may be seen in a dilated cystic duct proximal to the site of obstruction in patients with acute cholecystitis [96]. This should not be mistaken for a small gall bladder.

If the study shows findings compatible with CBD obstruction or severe hepatocellular dysfunction, the presence or absence of acute cholecystitis cannot be determined.

Holbrook et al. [97] and Chandramouli et al. [98] reported that the gall bladder was not visualized in 18 of 62 patients (30%) and nine of 12 patients (75%), respectively, after sphincterotomy. These results indicate a significant alteration of bile flow due to sphincterotomy, which can affect the specificity of hepatobiliary scintigraphy for the diagnosis of acute cholecystitis.

Jacobson et al. reported that a considerable proportion of patients who had normal IDA scans developed abnormalities such as impaired liver uptake, gallbladder nonvisualization, etc., following bone marrow transplantation [99]. Nevertheless, no patient developed clinical or laboratory evidence of acute cholecystitis. These cholescintigraphic abnormalities may be due to the combined effects of hepatotoxic chemoradiation therapy, graft-versus-host disease, and prolonged parenteral alimentation.

17.5.1.5 Variants Associated with CCK Preadministration and Morphine

Significantly delayed tracer excretion into the bowel associated with prompt and progressive gall bladder filling can be a normal variant seen in the fasting state [100]. Morphine administered to the patient prior to the study can have the same result. This finding is well known and is now actually used in a positive way to enhance gall bladder visualization during cholescintigraphy.

In a series by Kim et al., approximately 40% – 50% of subjects with prompt gall bladder filling showed a markedly delayed biliary-to-bowel transit after sincalide pretreatment (Fig. 17.8) compared with only 4% of patients who did not receive sincalide [87]. Delayed biliary-to-bowel transit, when present, should not necessarily be read as abnormal, i.e., as hyperacute or partial CBD obstruction. However, a hyperacute or partial CBD obstruction may not be totally excluded in certain clinical settings, although this pattern, with intact gallbladder visualization, is not typical of CBD obstruction. In such a situation, CCK administration can help to exclude CBD obstruction by inducing gall bladder contraction and demonstrating bowel activity [87, 101]. Our group [102] assessed the frequency of the need for sincalide administration in this situation to exclude CBD obstruction. Delayed or no excretion into the bowel after sincalide administration was seen only in patients with delayed clearance of liver parenchymal activity but never in patients with prompt clearance. It appears that if both gall bladder filling and clearance of liver parenchymal activity are prompt, then the study can be terminated without giving CCK, despite the absence of bowel activity.

Oates et al. [103] and Shih et al. [104] reported that morphine administration increases the frequency and the degree of duodenogastric reflux.

Kim et al. [105] recently reported variable bile retention on cholescintigraphy following morphine administration for the evaluation of acute cholecystitis. No significant effect of 2 mg of intravenous morphine on biliary kinetics was detected scintigraphically in a con-

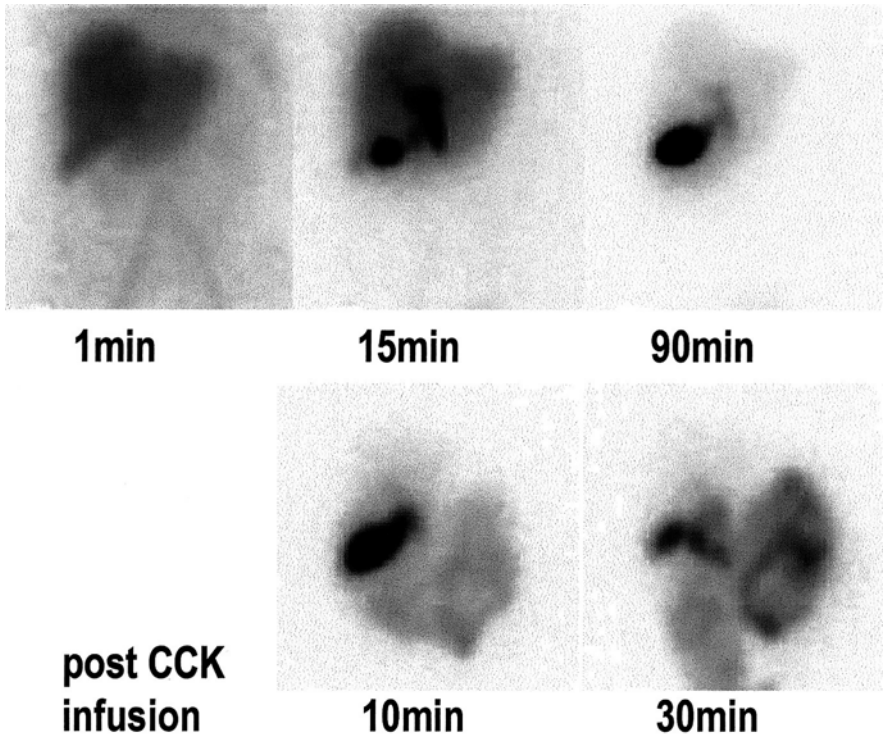

Fig. 17.8. The patient was pretreated with sincalide before receiving an injection of Tc-99m-IDA. The gallbladder filling is prompt but bowel activity is not identified until 90 min post injection. Following administration of a second dose of sincalide, there is prompt tracer excretion into the bowel, which excludes common duct obstruction

siderable proportion of patients. Also, there was considerable variation in the duration of the effect of morphine, when present. Preliminary data indicate that GB nonvisualization after morphine administration with the pattern of continually decreasing CBD activity is not as reliable for the diagnosis of acute cholecystitis as is nonvisualization of the GB with a pattern of increasing CBD activity [106].

17.5.1.6 Ancillary Findings

Increased IDA activity in the liver parenchyma around the gall bladder fossa is called a "rim sign" (Fig. 17.9). The presence of this sign is frequently associated with acute cholecystitis, which is often complicated, i.e., gangrenous gall bladder [107–112]. This pericholecystic activity appears to be caused by increased blood flow to [107] and/or delayed bile excretion from inflamed liver parenchyma adjacent to an inflamed gallbladder [112]. At times, a rim sign with marked tracer retention may mimic the gall bladder appearance (patient 3 in Fig. 17.9), in which case the presence of such activity on the early images before the appearance of bile duct activity can help to exclude the possibility of gall bladder filling. The rim sign, though suggestive of acute cholecystitis, is not sufficiently specific to obviate morphine augmentation or delayed imaging [58, 113].

In summary, recent data and reanalysis of the literature suggest that, in addition to its logistical advantage (shortening the imaging time), morphine augmentation provides more specific diagnosis for acute cholecystitis than does delayed imaging. Sincalide pretreatment, when administered at the physiological rate, will be helpful in conditions in which functional resistance to tracer flow into the gall bladder may be present. However, morphine augmentation will further improve the efficacy of the test even after sincalide pretreatment. The technique is therefore recommended for routine clinical use when the gall bladder is not visualized at 1 h. Further studies with larger samples will be necessary to assess the impact of variable or no visible effect of low-dose morphine on the efficacy of morphine-augmented cholescintigraphy.

17.5.2 Chronic Acalculous Biliary Diseases

Approximately 98% of patients with symptomatic gallbladder disease have gallstones. Occasionally, patients have signs and symptoms of gall bladder disease, but no stone can be demonstrated by repeated ultrasound or oral cholecystography [114]. Chronic biliary-type pain in patients with no stones may be due to chronic acalculous biliary disorders, including chronic acalculous cholecystitis, cystic duct syndrome, a functional disorder such as gall bladder dyskinesia, and sphincter of Oddi dysfunction. Nonbiliary disease such as the irritable bowel syndrome may cause the same symptoms. Sincalide has been used for the evaluation of gall blad-

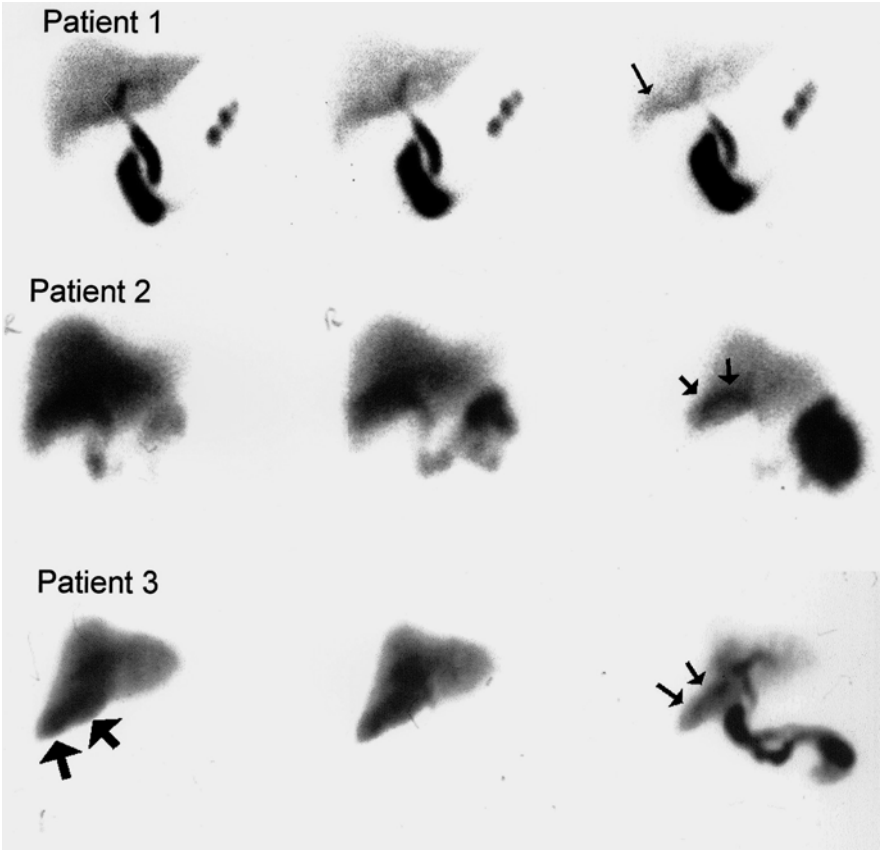

Fig. 17.9. A spectrum of rim signs. A mild rim sign is seen in the Tc-99m-IDA study of patient 1. The rim sign in patient 2 is quite prominent and clearly seen as a rim. The rim sign in patient 3 is more diffuse and may be confused with the gall bladder. However, this activity is present on the early image (*large arrows*) even before the tracer activity appears in the bile ducts. (Reprinted from [38] with permission)

der ejection fraction (GBEF) or sphincter of Oddi response in this patient group to determine who might benefit from cholecystectomy, sphincterotomy, or smooth muscle relaxants.

The technique for administration of sincalide is of the utmost importance. The degree of gall bladder emptying is dependent on the CCK dose and rate of administration, as well as on the total number of receptors in the gall bladder wall smooth muscle. Spasm of the neck of the gall bladder and decreased GBEF may occur due to unphysiologically high serum levels of sincalide following a bolus injection [115]. This paradoxical response is attributable to the different threshold level of the CCK receptors in the body and fundus of the GB and cystic duct [116]. The cystic duct does not contract when the dose of CCK is physiological. Therefore, this agent should not be given as a bolus. Although infusion of 20 ng/kg sincalide over 2–4 min (an average dose rate of 6.6 ng/kg/min) was once a popular technique [117–121], this dosage protocol has also been demonstrated to be unphysiological [3, 122]. Aside from frequent incomplete gall bladder emptying, infusion of 20 ng/kg over 3 min or less is often associated with such side effects as abdominal discomfort, pain, and nausea.

Comparison of various sincalide doses for a 3-min infusion technique demonstrated that 10 ng/kg (the rate of 3.3 ng/kg/min) produces maximal gall bladder emptying [3]. With further increase of the dose rate, i.e., 20 ng/kg/3 min, the GBEF actually decreases. The normal GBEF value using 10 ng/kg/3 min has been established as greater than 35%. Falsely reduced GB emptying associated with a 3-min infusion of 20 ng/kg of sincalide is illustrated well in Fig. 17.10 [123]. However, Ziessman et al. has shown that even the infusion at a so-called physiologic rate (10 ng/kg infused over 3 min) produces too an excessively variable GBEF response to establish a clinically useful normal range compared with the same dose infused over a longer period, i.e., 10 ng/kg infused for 60 min [124]. Normal and low GBEF values are reported to be reproducible in long-term studies [125]. Various dose rates, durations, and normal GBEF values have been employed by other investigators [126–128]. Although the optimal dose and duration of infusion is the subject of some controversy, a long infusion seems to produce more complete gall-bladder emptying and less severe side effects than a short infusion, probably due to the 2.5-min plasma half-life of sincalide. When performing and interpreting sincalide-augmented hepatobiliary imaging, it is important to adhere to a specific sincalide infusion technique and to use normal GBEF values that have been validated for that particular method. For an alter-

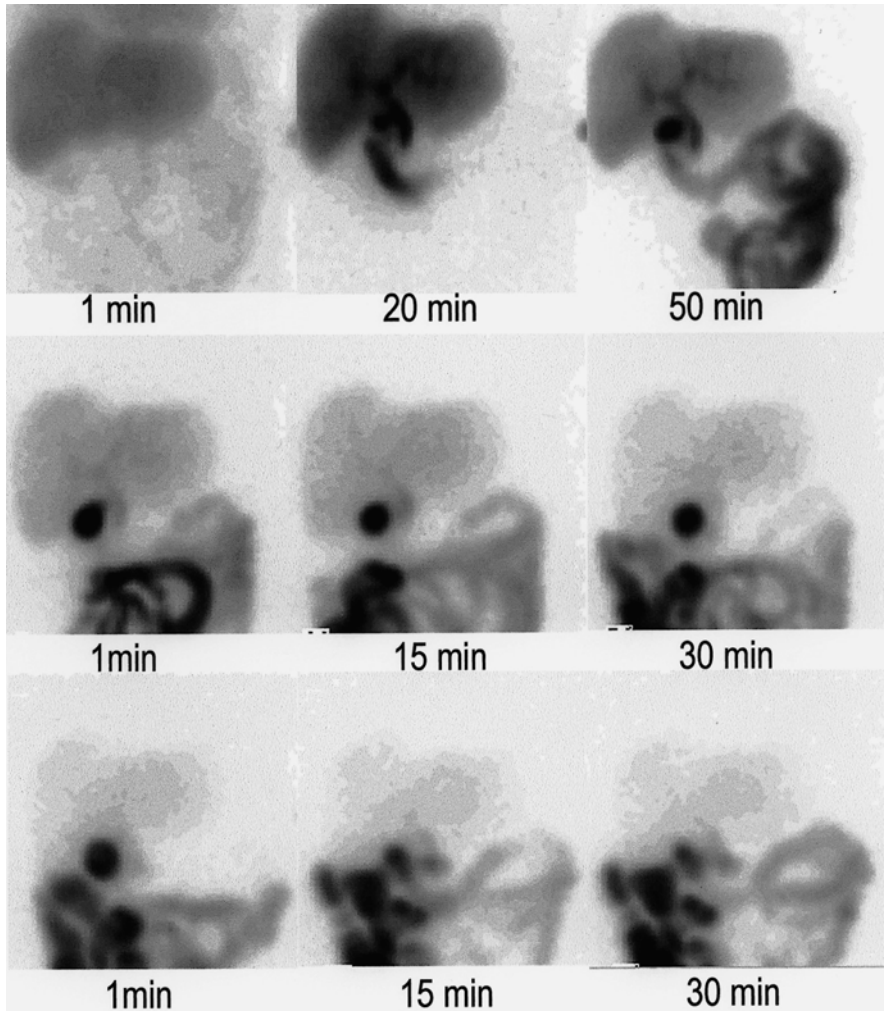

Fig. 17.10. A hepatobiliary scan using Tc-99m-IDA performed in a patient with suspected chronic acalculous biliary disease. The scan shows prompt visualization of the GB and small bowel (*top row*). Following a 3-min infusion of 20 ng/kg sincalide, the GB is poorly contracted, with an EF of approximately 10% (*middle row*). Immediately after this, a 10-min infusion of the same dose produced a GBEF of 80%

native infusion technique normal values need to be established.

Various fatty meals have been evaluated as an alternative to sincalide [129–132]. However, controversy exists over the use of fatty meals versus sincalide. The major disadvantage of meal stimulation is that an abnormal GB response may result from factors other than the GB, such as poor gastric emptying, pancreatic insufficiency, celiac disease, or abnormal bowel transit [133–136]. The onset of meal-induced GB emptying can also vary during different phases of the migrating motor complex at the time of ingestion [137]. The choice between fatty meal and sincalide can probably be made on the basis of the population being studied. Meal stimulation would be preferable when GB function in relation to the rest of the GI tract needs to be evaluated. However, evaluation of GB function independent of the digestive process may be better achieved with sincalide when different patient populations are studied [138]. Nonetheless, a fatty meal can serve as an alternative in the case that sincalide is not available for clinical use. However, when used, careful attention should be paid to the fat content, texture, taste, manner of administration, and measurement time sequence, all of which need to be standardized [139]. Normal values for each center must be established when choosing a meal.

17.5.2.1 Chronic Acalculous Gall Bladder and Cystic Duct Diseases

The pathological findings of chronic acalculous cholecystitis are nearly identical to those of chronic calculous cholecystitis, except for the absence of stones [140]. Intermittent acalculous cystic duct obstruction and chronic ischemia with active inflammatory changes have both been postulated as possible pathogenic mechanisms. The cystic duct syndrome results from a partial acalculous obstruction or narrowing of the cystic duct [141], which may be due to fibrosis, kinking, or adhesion [64]. A sphincter-like mechanism in the cystic duct may explain the possibility of cystic duct occlusion in the absence of

mechanical obstruction [65]. The cystic duct syndrome and chronic acalculous cholecystitis often coexist [117, 126, 142], but they may also occur independently.

In functional disorders, or gall bladder dyskinesia, the gall bladder is histologically normal. The mechanisms have not been fully elucidated. Abnormal and/or inhomogeneous CCK receptors within the gall bladder, which cause a paradoxical or inhomogeneous response to cholecystokinetic agents, have been suggested as a possible mechanism [117, 143]. In this condition, right upper quadrant pain occurs following meals as a result of increased intraluminal gall bladder pressure. Other possible mechanisms of impaired gall bladder motility include a primary smooth muscle disorder and altered release of endogenous CCK [68].

In cholesterosis, the mucosa of the gall bladder is studded with minute yellow lipid flecks, producing the strawberry appearance [144]. In some patients suspected of having chronic acalculous biliary disease, cholesterosis has occasionally been the only histological finding, without evidence of other diseases [118, 145, 146]. Although cholesterosis is not often of clinical significance [144], cholecystectomy is indicated when the condition is symptomatic [57].

There is controversy regarding the value of GBEF for the diagnosis of these diseases and its correlation with histopathology. While some investigators found abnormal pathology in most patients with a low EF [117, 121, 126], others did not [127, 147, 148]. However, some investigators have found no correlation even between histopathological findings and symptomatic relief following surgery [120, 146, 147, 149]. Whether or not the GBEF is a good predictor of symptomatic relief after surgery should be more clinically relevant than the correlation between GBEF and histopathology. Although there has been a report of a poor correlation in this regard [147], the vast majority of other reports have demonstrated a good symptomatic response after surgery in most patients with a low GBEF [117–120, 126, 128, 146, 149–152]. Among these reports, there was a randomized trial by Yap et al. [113], which is reassuring. A recent report suggests that children with chronic abdominal pain and delayed gall bladder emptying on CCK-stimulated cholescintigraphy are also likely to benefit from cholecystectomy [153].

On the other hand, the effectiveness of a normal GBEF as a predictor of clinical outcome is more difficult to assess, because only highly selected patients (those with higher clinical suspicion) with a normal EF were sent for surgery. The majority of patients with a normal EF who are placed on medical treatment for nonbiliary gastrointestinal diseases do well [117, 121, 126, 147, 150]. However, at the same time, the majority of patients who had surgery despite a normal EF also had symptomatic relief [117, 120, 126, 128]. These results are not surprising, as a 70%–75% cure rate is associated with cholecystectomy even when based on symptoms alone [154]. We have been reporting a GBEF of 40%–60% as indicating an intermediate probability of symptomatic relief following cholecystectomy. Similarly, Majeski suggested that cholecystectomy may be considered for patients with a GBEF between 35% and 60% if the patient's symptoms were classical for biliary disease and have been present for 1 year [152].

Several earlier reports suggested that pain reproduction induced by sincalide infusion is another useful positive sign of pathology [120, 155]. A brief infusion (i.e., 20–40 ng/kg over 3 min) was employed by these investigators. However, Kloiber et al. [138] and Yap et al. [126] did not detect pain reproduction in patients who benefited from surgery when a slow infusion (over 45–60 min) technique was used.

Conditions that may affect gall bladder contractility should be borne in mind when using CCK. Atropine significantly reduces the gall bladder ejection period and EF [156]. Gall bladder contractility can be decreased after or during octreotide therapy [157, 158]. An association between gastroesophageal reflux disease and gall bladder function has been reported [159]. These authors found abnormal GB function in 58% of patients with gastroesophageal reflux disease, with improved GB function in most of those patients after fundoplication. A markedly lower GBEF has been found in seven of ten patients with achalasia compared with controls [160]. The mechanism and clinical significance of this finding are uncertain. Other reported causes of reduced gall bladder ejection fraction are antiulcer gastric surgery particularly when truncal vagotomy is performed [161], and opioid intake immediately before the study [125].

It has been reported that normal and low GBEF values are reproducible in long-term studies [125].

In summary, the overall data favor the use of this test for the diagnosis of chronic acalculous gall bladder and cystic duct disease. A low GBEF can probably be interpreted as indicating a high probability for symptomatic relief after surgery, and vice versa. Bayes' theorem should then be applied, especially for the group with a normal EF, to make a clinical decision according to the post-test probability from a clinical suspicion (pretest probability) and the GBEF (test probability).

17.5.2.2 Sphincter of Oddi Dysfunction

Sphincter of Oddi dysfunction (SOD) can be responsible for approximately 14% of all postcholecystectomy pain [162, 163]. It is much more common in female patients. SOD can be classified into two broad categories: stenosis (a fixed structural narrowing) and dyskinesia (functional disorder: a primary disorder of tonic/phasic motor activity) [164, 165].

Measurement of sphincter of Oddi pressure using sphincter manometry is considered the gold standard for the diagnosis of SOD. In patients with sphincter of Oddi dyskinesia, manometry may reveal tachyoddia, retrograde contractions, or a paradoxical response (sphincter of Oddi spasm) to sphincter relaxants such as CCK [166]. When the basal sphincter pressure is elevated, a distinction between stenosis and dyskinesia can be made based upon the response to smooth muscle relaxants [167]. Relaxation after smooth muscle relaxant suggests dyskinesia rather than stenosis. To date, an elevated basal pressure (>40 mmHg) is considered the only consistent manometric criterion which is correlated with patients' symptoms and also with relief of symptoms with therapy [168].

The treatment of choice for patients with sphincter of Oddi stenosis is endoscopic sphincterotomy. Surgical sphincteroplasty or balloon dilatation of the sphincter of Oddi is less favorable in terms of both complication rate and success in long-term relief of symptoms [168]. In patients with sphincter of Oddi dyskinesia, a pharmacological treatment with calcium channel

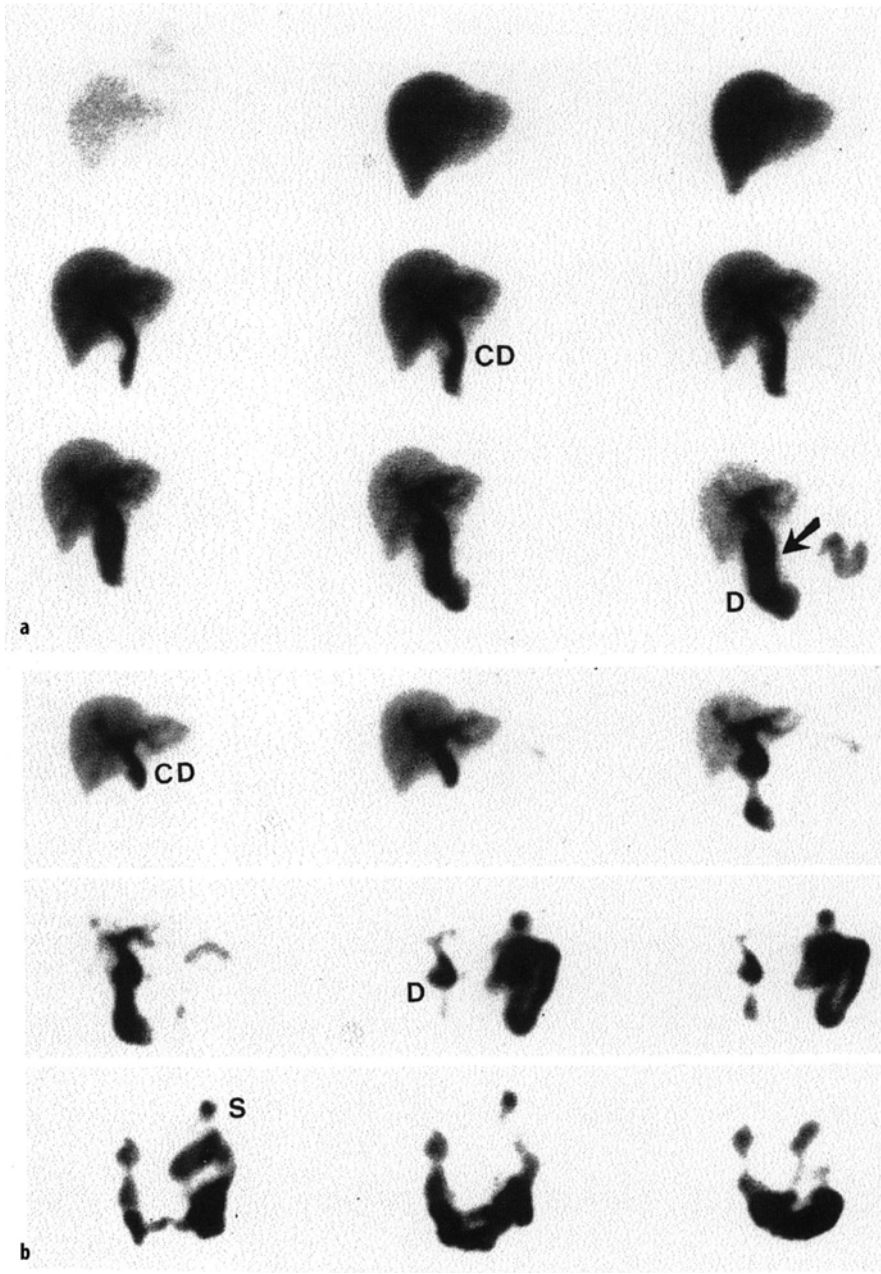

Fig. 17.11a,b. SOD: stenosis. This 50-year old woman was seen at 3 years post cholecystectomy with chronic recurrent pain. ERCP showed no mechanical obstruction, but the basal sphincter of Oddi pressure was elevated (45 mmHg). **a** Preoperative cholescintigraphy shows delayed hepatobiliary clearance with retention of activity in the common bile duct (CD) at 60 min (*arrow*). Increasing activity within the duodenum (D) is noted. A second preoperative study (not shown here) with constant CCK infusion (40 ng/kg/60 min) was not significantly different (i.e., there was a fixed papillary stenosis). **b** Postsphincterotomy study in the same patient shows significant improvement with rapid hepatobiliary and common duct clearance compared with the preoperative study. *S* stomach. (Reprinted from [185] with permission)

blocker or long-acting nitrate could be used. Endoscopic sphincterotomy is indicated for patients with elevated basal pressure who do not respond to pharmacological treatment [169].

Depending on the results of laboratory tests and endoscopic retrograde cholangiopancreatography (ERCP), SODs have been classified as biliary type I, II, and III [165]. Patients with biliary type I SOD have typical biliary pain, elevated liver enzymes on two or more occasions during episodes of pain, and an abnormal ERCP demonstrating a dilated CBD and delayed emptying of contrast into the small intestines (>45 min). Patients with type II SOD have biliary-type pain and one or two of the other abnormalities mentioned for type I. Patients with type III SOD have only biliary-type pain and none of the other criteria. Manometry is optional in patients with type I, necessary in type II patients, and mandatory in type III patients [165]. Generally, the greater the number of abnormalities (type I), the more likely it is that a structural disorder is present, e.g., stenosis, and vice versa.

Although the accurate diagnosis of SOD is important, ERCP may not detect many patients with functional SOD. Also, a concern has been raised about the validity of the 45-min delayed drainage criterion for sphincter of Oddi dysfunction [170]. Sphincter manometry, while being the gold standard, is invasive, difficult to perform, difficult to interpret, and associated with potential complications such as pancreatitis [171].

Hepatobiliary imaging with or without pharmacological intervention has also been shown to be useful in patients with SOD, and investigations have focused primarily on patients after cholecystectomy. A number of parameters have been derived from the time-activity curves of the liver parenchyma, hilum, CBD, entire hepatobiliary tract (liver and bile ducts), and bowel. These include the time of peak activity (T_{max}), excretion half-time ($T_{1/2}$), percentage of excretion at a certain time (i.e., 45 min, 60 min), excretion rate, and mean transit time. Visual parameters such as the time of first appearance of the intrahepatic biliary tree, and the bowel, CBD emptying, and CBD-to-liver ratio (comparison of CBD activity at 60 min with liver activity at 15 min and 60 min) have been added to the above semiquantitative parameters [172].

The experience of most authors has been satisfactory [172–180]. It has been recently reported that choledochoscintigraphy is useful for diagnosing SOD as well as predicting sphincterotomy outcome in biliary type I and II patients, irrespective of clinical classification and manometric findings [181]. Although some investigators did not find cholescintigraphy useful [182, 183], others believe that the discrepancy in the reported efficacies is due to differences in the technique [184]. An especially excellent separation between patients with and without SOD has been achieved in three reports, using a single parameter: the T_{max} of the entire liver and extrahepatic bile ducts, the $T_{½}$ of the right hepatic lobe [178, 179], and a combination of the scores from six parameters [172]. Although these authors did not agree on which parameters were the best, in essence, all more or less reflect hepatic parenchymal and biliary-to-bowel transit of bile. These parameters have also been found useful in assessing the benefit of endoscopic sphincterotomy (Figs. 17.11, 17.12) [173, 179, 182, 185].

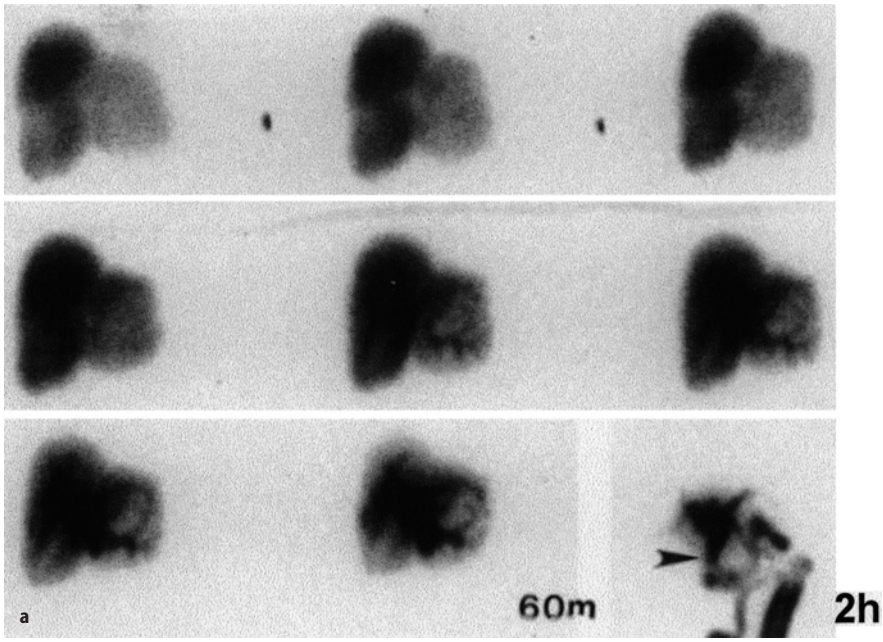

Fig. 17.12a. SOD: dyskinesia. Postcholecystectomy pain syndrome. An ERCP showed no mechanical obstruction. The sphincter of Oddi pressure was 48 mmHg. A sphincterotomy was performed. **a** Preoperative study. Sequential analog images over 60 min show a prominent intrahepatic collection system with dilatation in the region of the common hepatic duct at 60 min. A delayed image at 2 h shows that the obstruction is really at the level of the sphincter of Oddi (*arrowhead*).

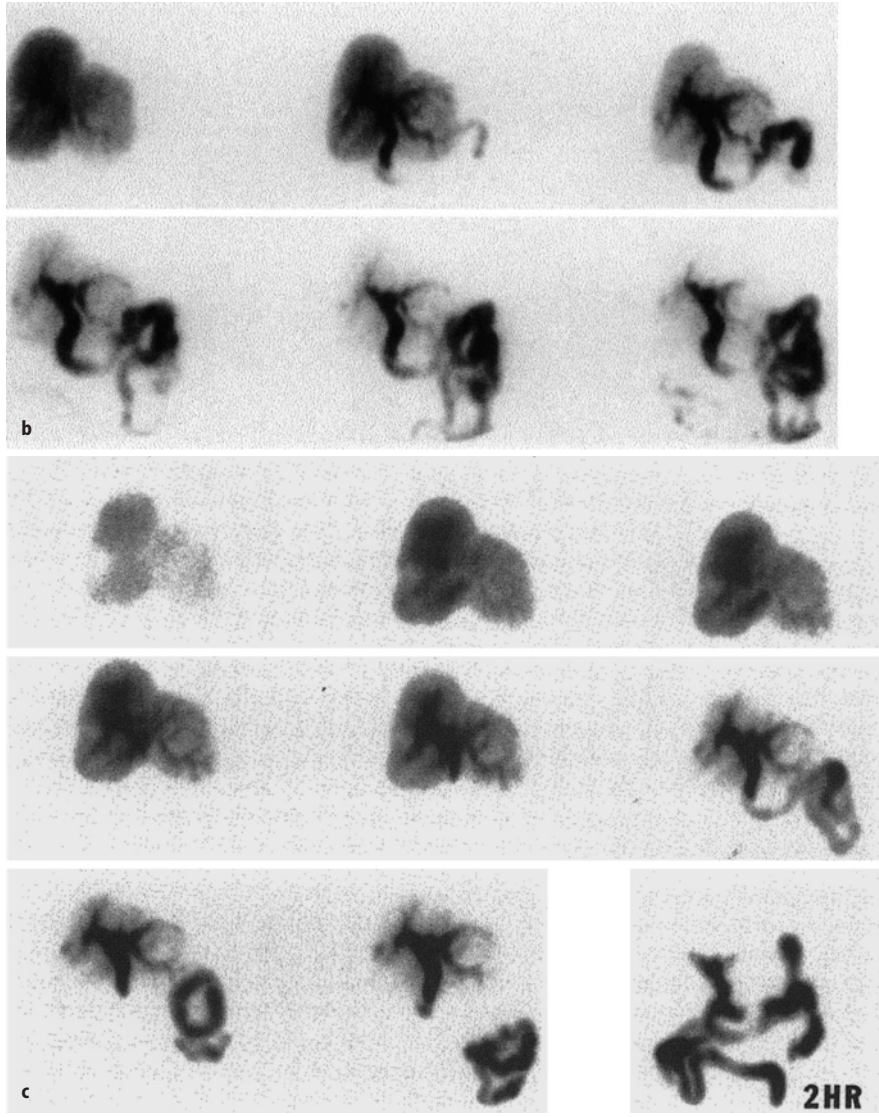

Fig. 17.12b–c. b Preoperative study with a continuous infusion of sincalide, 40 ng/kg/60 min. Hepatobiliary clearance is more rapid than the study without CCK. However, at the end of 60 min there is retained activity in a prominent common duct. This is an obstructed dyskinetic sphincter of Oddi. **c** Postsphincterotomy study. There is still prominent retention in the common duct, but hepatobiliary clearance has significantly improved since the baseline study (**a**) and, interestingly, looks similar to the preoperative CCK study (**b**). (Reprinted from [185] with permission)

Whereas most of the investigations with scintigraphic studies on this subject have focused primarily on the differentiation between the presence and absence of SOD, Madacsy et al. [186] reported excellent results in discriminating between stenosis and functional dyskinesia. Patients in their series inhaled amyl nitrite, a potent sphincter relaxant, during the washout phase of CBD activity. The rate of CBD washout was slow in both the stenosis and dyskinesia groups before amyl nitrite inhalation and normal in controls. Amyl nitrite inhalation resulted in prompt washout of CBD activity in patients with functional dyskinesia, whereas no change occurred in controls or in patients with organic stenosis (Fig. 17.13). Since the augmentation is started in the middle of CBD washout, this approach clearly cannot be used in conjunction with such parameters as T_{max} of liver parenchymal or CBD activity. If such parameters were to be used, then the augmented study would have to be performed on a separate day.

It should be noted that the criteria based on delayed transit through the bile ducts are not reliable for the diagnosis of SOD in patients with an intact gall bladder [187]. The gall bladder serves as a pressure reservoir [188], which can absorb a large amount of bile, thereby causing delayed bowel visualization. Indeed, delayed biliary-to-bowel transit, associated with preferential gall bladder filling, was demonstrated frequently even in normal volunteers after CCK pretreatment (Fig. 17.8). Kalloo et al. [189] and Ruffolo et al. [190] evaluated GBEF in patients with intact gall bladder function. They found that it cannot be used reliably to discriminate patients with SOD. Therefore, diagnosis of SOD seems difficult before cholecystectomy is performed, regardless of the criteria used.

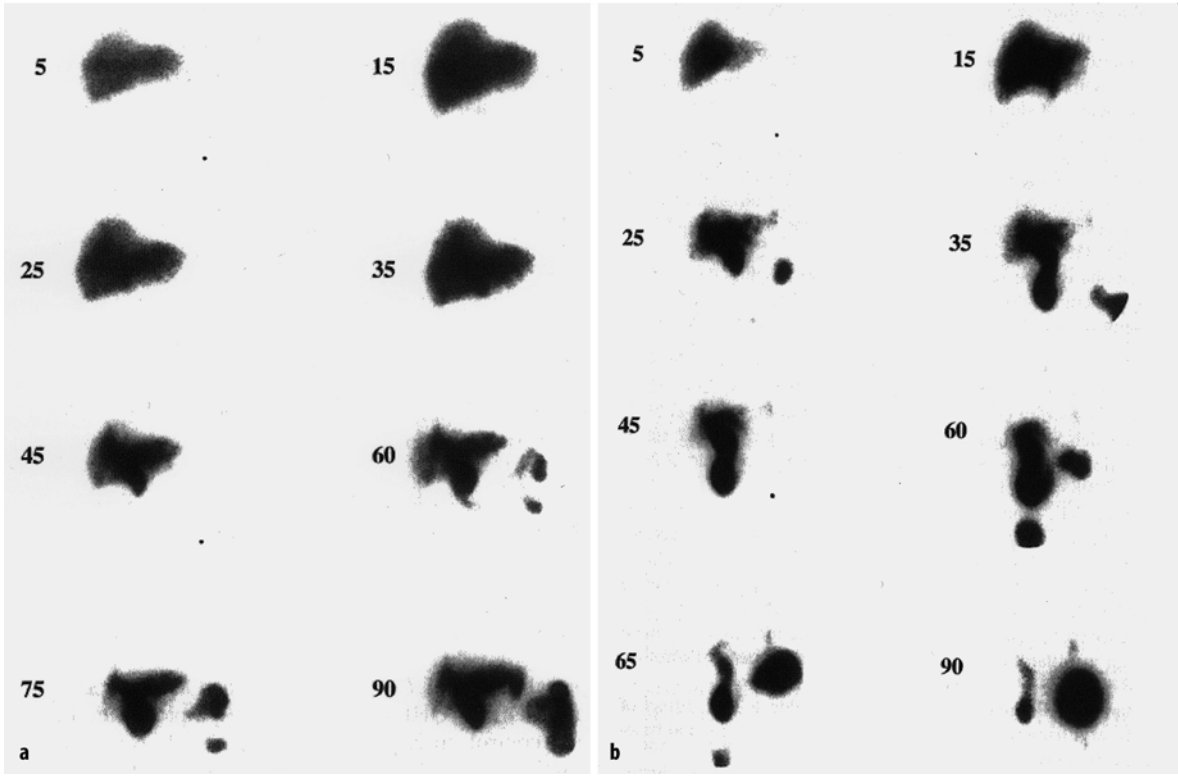

Fig. 17.13. a Stenosis of the sphincter of Oddi (structural SOD). Biliary tree activity is initially visualized at 25 min after injection of Tc-99m-IDA. The CBD and intrahepatic biliary tree appear prominently at 45 min and do not change significantly during amyl nitrate inhalation from 60 min to 90 min. **b** Sphincter of Oddi dyskinesia (functional SOD). Biliary tree activity is first visualized at 15 min. The CBD and intrahepatic biliary tree appear prominently from 25 min up to 60 min. The small bowel is first visualized at 25 min. Note a marked decline in CBD activity during amyl nitrate inhalation from 60 min to 90 min. (Reprinted from [186] with permission)

17.5.3 Hyperbilirubinemia

Cholescintigraphy is often performed to differentiate surgical jaundice (CBD obstruction and biliary atresia) from medical jaundice (intrahepatic cholestasis and/or hepatocellular disease) in both adults and neonates. Alternatively, CBD obstruction or intrahepatic cholestasis is occasionally detected incidentally on cholescintigraphy performed in patients who present with abdominal pain. Neonatal hyperbilirubinemia will be discussed separately in the following section.

17.5.3.1 Common Bile Duct Obstruction and Medical Jaundice

Cholescintigraphy has been shown to be more accurate than ultrasonography [191–193] for the diagnosis of CBD obstruction. Prompt hepatic uptake of IDA that persists 2–4 h (sometimes even up to 24 h) without evidence of biliary excretion is the obstructive pattern that has been commonly described (Fig. 17.14) [165, 191, 193]. The presence of an obvious photopenic defect in the area of the porta hepatis corresponding to dilated bile ducts or slow tracer filling of dilated bile ducts makes CBD obstruction more likely. The presence of intestinal activity without visualization of the CBD makes intrahepatic cholestasis more likely. However, without ancillary findings, the distinction between a high-grade CBD obstruction and a high-grade intrahepatic cholestasis (with relatively preserved hepatocyte function) may be difficult [194]. Ultrasonography may play a complementary role in this situation.

In patients with partial CBD obstruction, cholescintigraphy may demonstrate absence of intestinal activity, delayed biliary-to-bowel transit, and/or a prominent ductal pattern persistent for 2 h [191]. When CBD obstruction is suspected, the patient should not be pretreated with sincalide, which may cause prompt gallbladder filling with delayed biliary-to-bowel transit, as discussed earlier [86]. If this occurs after sincalide pretreatment, repeat sincalide administration can help to exclude CBD obstruction by contracting the gallbladder and demonstrating bowel activity [86, 100]. Krishnamurthy et al. [195] and Itoh et al. [196, 197] reported bile reflux from the gall bladder into the common hepatic and intrahepatic bile ducts instead of excretion into the bowel following sincalide administration. This

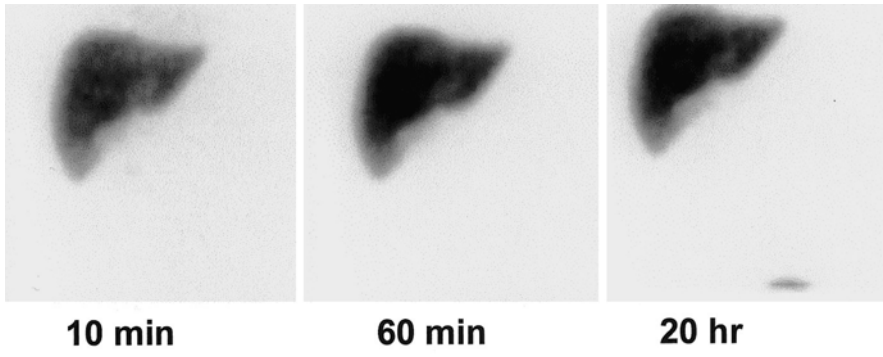

Fig. 17.14. The pattern of acute CBD obstruction imaged with Tc-99m-IDA. The initial hepatic uptake is prompt, with prolonged retention and no evidence of intestinal excretion throughout the study

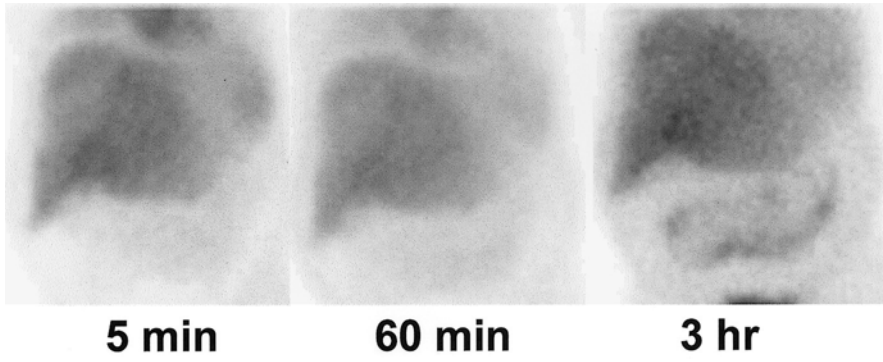

Fig. 17.15. A hepatobiliary scan performed in a jaundiced patient demonstrates poor hepatic uptake of Tc-99m-IDA with persistent blood pool activity. Bowel activity is noted in the image obtained at 3 h. The findings are suggestive of a hepatocellular disease rather than a CBD obstruction. The patient was found at follow-up to have severe hepatitis

finding indicates the presence of CBD obstruction/stricture or sphincter of Oddi spasm. Poor hepatic uptake with persistent blood pool activity of IDA in jaundiced patients generally indicates hepatocellular disease, regardless of the presence or absence of bowel activity (Fig. 17.15).

Quantification of hepatocyte function by measuring the hepatocyte extraction fraction (HEF) of IDA agents with deconvolutional analysis has been reported to be useful for the distinction between CBD obstruction and hepatocellular dysfunction [198–200]. Despite profound hyperbilirubinemia, patients with CBD obstruction typically have only slightly reduced HEF values compared with normal controls, whereas patients with hepatocellular dysfunction have markedly reduced HEF values.

17.5.3.2 Neonatal Hyperbilirubinemia

Persistent jaundice is considered to be pathologic beyond 3 weeks of age in full term babies and 4 weeks in preterm babies. Cholestasis with conjugated hyperbilirubinemia can be due to a wide variety of abnormalities including extrahepatic biliary tree abnormalities (i.e., extrahepatic biliary atresia [EHBA] and choledochal cyst) or intrahepatic diseases (i.e., interlobular bile duct paucity or neonatal hepatitis syndrome).

The cause and pathogenesis of biliary atresia remain largely unknown [201–203]. Both chronic and acute inflammatory changes have been shown histopathologically. Biliary atresia is typically a progressive panductular obliterative process. Without correction of bile flow obstruction within 2–3 months of life, irreversible hepatic damage and complete obliteration of the extrahepatic biliary tree will result. This process could be progressive even after surgical correction of the obstruction [204, 205]. The neonatal hepatitis syndrome includes various kinds of diseases such as idiopathic neonatal hepatitis, infectious hepatitis and hepatitis from metabolic or genetic causes.

The urgency in correctly diagnosing EHBA is reflected in the surgical results following portoenterostomy (Kasai procedure). Sustained bile flow is significantly greater in infants operated on before 60 days of age (91%), compared with those operated on after 3 months (17%) [206], The preoperative distinction of EHBA from the other disorders causing severe cholestasis is essential if the correct patients are to be selected for surgery.

Cholescintigraphy has been known to have 100% sensitivity for the diagnosis of extrahepatic biliary atresia, but low specificity [207–210]. In neonates, normal cholescintigraphy should show prompt and uniform uptake of tracer in the liver with a maximum tracer accumulation within 5 min [211, 212]. The gall bladder may be visualized as early as 10 min, but nonvisualization of the gall bladder can be a normal variant in the neonatal period. The hepatic, cystic, and common bile ducts are generally not visualized in the neonatal

period even when there is normal excretion and gall bladder visualization. Bowel activity is seen usually by 30 – 40 min.

In general, cholescintigraphy performed in patients with biliary atresia within the first 2 months of life usually shows reasonably good hepatic uptake, nonvisualization of the gall bladder, and prolonged retention of the tracer in the liver with no biliary excretion. In contrast, patients older than 3 months usually show evidence of decreased hepatic function with reduced hepatic extraction fraction and no biliary excretion [212].

If there is no excretion in an infant less than 2 months of age and the initial uptake suggests liver dysfunction, then the neonatal hepatitis syndrome should be suspected. A repeat study will show the improved function and transit as the condition resolves (Fig. 17.6). In infants under 2 months who do not excrete, those with biliary atresia tend to have better liver-to-heart ratios of radioactivity at 5 min than those with the neonatal hepatitis syndrome. However, no excretion with normal or near normal hepatic uptake may be seen in some cases of severe neonatal hepatitis syndrome [213]. Cholescintigraphy is most useful in excluding the diagnosis of biliary atresia with a sensitivity and negative predictive value of virtually 100% when intestinal and/or extrahepatic biliary activity is seen. Urine activity in the diaper or contamination of the skin of the abdomen should not be confused with intestinal activity. Acquiring delayed images after cleaning the skin and changing the diaper can prevent this from occurring. The reported specificity ranges from 43% to 90% [208 – 210, 213 – 217]. In a series by Spivac et al. [208], the specificity of absent bowel activity on the first DISIDA study was only 43% in all infants, but 92% in those with birth weight greater than 2200 g. All infants with either neonatal hepatitis ($n=6$) or inspissated bile syndrome ($n=3$) had demonstrable gastrointestinal excretion either on the first or second DISIDA study. Therefore, the study should be repeated if the diagnosis is unclear.

Patients are typically pre-medicated with phenobarbital, 5 mg/kg daily in two divided doses given for 5 days. Ursodeoxycholic acid, an additional choleretic agent, may also be given at a dose of 20 mg/kg daily in two divided doses in order to optimize bile flow prior to the study.

Phenobarbital stimulates the hepatic transport system for organic anions. This is primarily achieved by induction of hepatic microsomal enzymes, thereby increasing bilirubin conjugation and excretion. Thaler et al. [218] and Majd et al. [213] used preadministration of phenobarbital for several days before an I-131 rose bengal study and a Tc-99m IDA study, respectively, and found significantly improved specificity. More recently, Ben-Haim et al. [209] suggested that phenobarbital induction may not be needed when Tc-99m-mebrofenin, which has higher hepatic extraction and excretion than Tc-99m-DISIDA and HIDA, is used. This group found that, of 26 patients with bowel visualization, the time to visualize the bowel did not differ between patient groups with and without phenobarbital induction. Further prospective studies will be necessary before any strong conclusion can be drawn. However, false positives may occur even after phenobarbital pretreatment, especially when liver function is impaired [183]. Therefore, the study is diagnostic (excludes biliary atresia) only if radioactivity is seen in the bowel. Otherwise, the study is inconclusive. Administration of phenobarbital for several days can cause a delay in performing the test, which may be unacceptable in some clinical situations.

In an attempt to further improve the discrimination between biliary atresia from other causes of non-excretion, a hepatic extraction fraction (a measure of hepatocyte function) obtained from a deconvolutional analysis has been evaluated. While earlier investigations seemed to be encouraging [211, 219], more recent reports have found the use of hepatic extraction fraction not very useful [220, 221].

17.5.4 Postoperative Evaluation

17.5.4.1 Complications after Hepatobiliary Surgery

As laparoscopic cholecystectomy has gained popularity as an alternative to standard cholecystectomy, the rate of postoperative complications has increased. The increase in the number of liver transplantations, though performed as yet in only a limited number of institutions, has also increased the use of cholescintigraphy for the evaluation of postoperative complications [222]. Bile duct complications include bile leaks, common bile/hepatic duct injuries or strictures, retained biliary calculi, and obstruction. Most investigators agree that bile leaks are best detected by cholescintigraphy rather than by other anatomical imaging modalities [223 – 226]. When acquiring scintigraphic images, it is often helpful to enhance image intensity for accurate assessment of the extent of extravasation (Fig. 17.16). The extent of leak is often better identified on delayed images (Fig. 17.16b) [227]. Endoscopic retrograde cholangiopancreatography and/or percutaneous transhepatic cholangiography can be a supplement as needed for more definitive diagnosis and treatment [228, 229]. When ultrasonography or CT shows a fluid collection, cholescintigraphy can be helpful not only in confirming but also in excluding biloma [38].

Clinically insignificant leaks usually heal spontaneously. However, if a major leak is present, reoperation, percutaneous transhepatic biliary drainage, or endoscopic sphincterotomy with placement of a stent or nasobiliary drainage catheter is required. The effective-

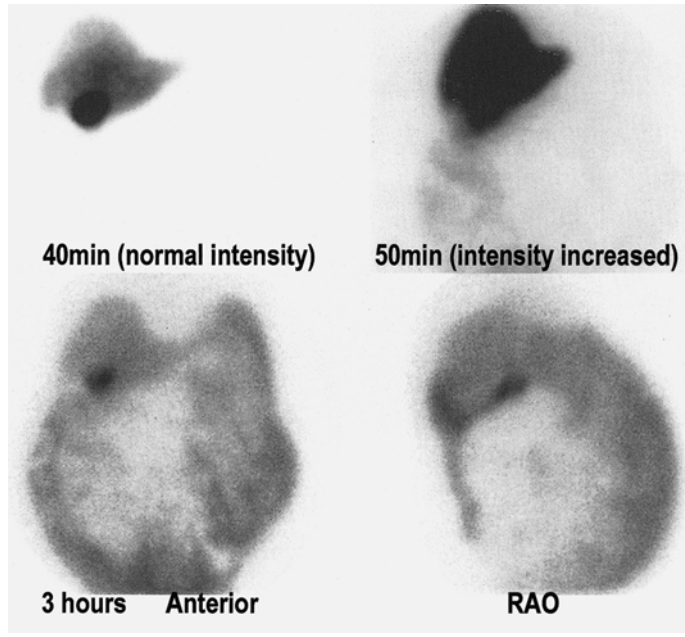

Fig. 17.16. The image obtained at 40 min after injection of Tc-99m-IDA reveals intense tracer accumulation, localized only in the gall bladder fossa. However, a subsequently obtained image at an increased intensity (*50 min*) shows that the leak is more extensive. Delayed images best delineate the extent of the leak. (Reprinted from [38] with permission)

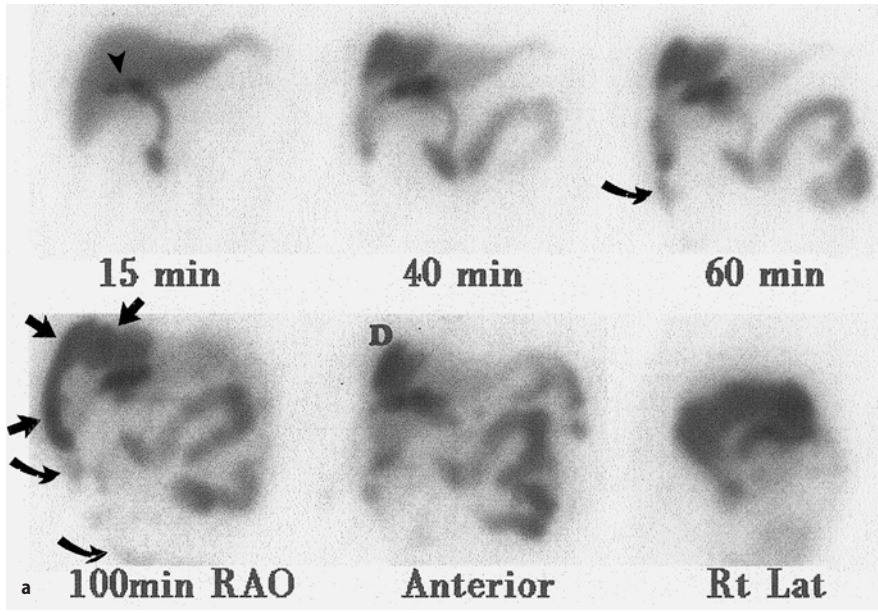

Fig. 17.17a,b. Post liver transplantation Tc-99m-IDA scan. **a** After removal of the t-tube, a bile leak is first noted at 15 min (*arrowhead*). The anterior images show localization of extravasated activity predominantly at the dome (*D*) of the liver. The right anterior oblique (*RAO*) image better delineates extravasated activity over the superior and posterolateral surface of the liver (*straight arrows*), in addition to the right paracolic gutter (*curved arrows*).

ness of such interventional procedures may be assessed with cholescintigraphy if clinically indicated (Fig. 17.17) [58, 230].

Investigators have found cholescintigraphy useful for assessing the patency of a biliary-enteric bypass or an afferent loop [231–235]. A case has been reported in which biliary stasis seen in the region of the biliary enteric anastomosis in the supine images disappeared almost completely when the images were repeated after 30 min with the patient in an upright position [236]. We have observed a similar finding in a patient postoperatively. These cases illustrate the importance of imaging in the upright position when biliary or afferent loop stasis is seen in postoperative patients.

17.5.4.2 Effect of Sphincter Dilation Procedures on Sphincter Function

Although endoscopic papillary balloon dilation (EPBD) for the treatment of bile duct stones may be a safe and effective procedure, and less hazardous to the sphincter of Oddi than endoscopic sphincterotomy, little is known about the function of sphincter muscle af-

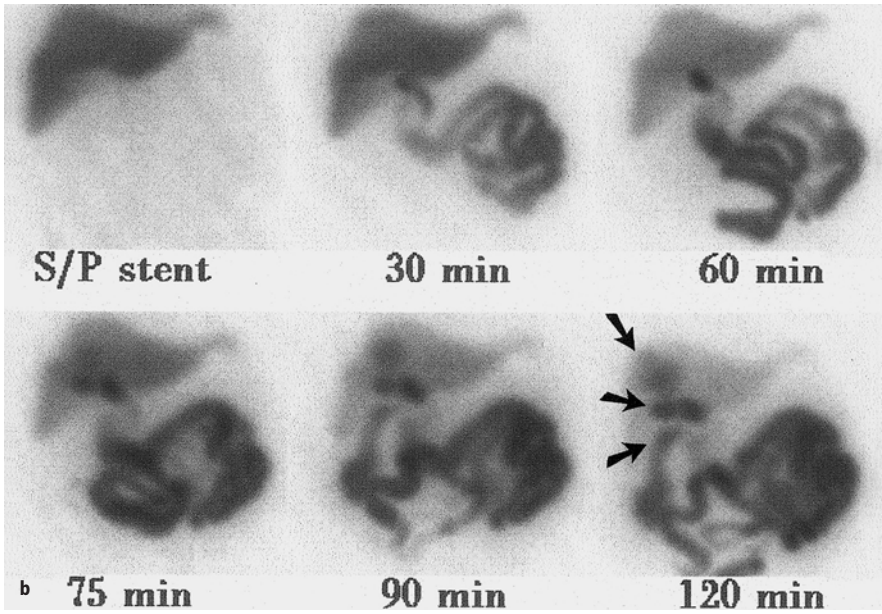

Fig. 17.17. b A repeat study after CBD stent placement shows markedly improved drainage of bile into the intestine. However, a milder degree of leak is still evident on the images acquired during the second hour (*arrows*). (Reprinted from [38] with permission)

ter the procedure. Isayama et al. demonstrated that the hepatic hilum-duodenum transit time on quantitative cholescintigraphy in patients after EPBD was not different from that in control patients, whereas that in endoscopic sphincterotomy patients was markedly shorter than both the control and EPBD groups. The authors concluded that the function of the sphincter of Oddi may be preserved after endoscopic papillary balloon dilation [237]. Further studies seem warranted.

17.5.4.3 Effectiveness of Gastrointestinal Reconstruction Surgery

The effectiveness of anti-enterogastric reflux procedures (e.g., Roux-en-Y diversion, Henley jejunal interposition, Braun enteroenterostomy) in diverting bile away from the stomach, or the effects of various reconstruction methods following gastrectomy on esophageal bile reflux, have been assessed with cholescintigraphy [238–241]. Cholescintigraphy has also been used to compare the degree of bile stasis in the proximal jejunal loop after different types of gastrointestinal reconstruction surgical procedures [242, 243].

17.5.5 Miscellaneous

Patients with sclerosing cholangitis have been evaluated with planar and SPECT imaging using Tc-99m-IDA [244]. Planar imaging showed beading or bandlike constrictions of the biliary tract corresponding to lesions seen on cholangiography. The SPECT images demonstrated multiple focal areas of tracer retention, representing bile stasis in intrahepatic bile ducts.

In patients with cystic fibrosis, ERCP often shows changes consistent with sclerosing cholangitis, with beading and stricturing of the intrahepatic ducts [245]. While various scintigraphic findings in these patients have been described, the most common finding by several groups of investigators appears to be retention of tracer in the intrahepatic ducts [245–248]. It has been suggested that cholescintigraphy is valuable for monitoring the therapeutic responses of cystic fibrosis patients with liver disease to ursodeoxycholic acid therapy [246] and in the early detection of liver involvement [248].

Cholescintigraphy has been found to be a useful noninvasive screening test in HIV-positive patients with right upper quadrant pain who are suspected of having AIDS-related sclerosing cholangitis, for the purpose of determining who should be referred for ERCP [249, 250]. The response to specific antimicrobial or surgical intervention can be monitored with cholescintigraphy [250].

Cholescintigraphy is a useful noninvasive test which complements an anatomical finding on ultrasonography in the diagnosis of choledochal cyst [217, 251, 252].

17.6 Summary

Cholescintigraphy plays a pivotal role in the evaluation of various biliary tract diseases, particularly when coupled with pharmacological intervention. The physician monitoring the study should be familiar with the most optimal technique for the pharmacological intervention and with conditions and medications that affect gall bladder contraction. It is also important to be aware of the various

physiological and pharmacological effects on imaging findings, i.e., not only those findings that are normal but also the undesirable variants [253]. Failure to recognize such effects can lead to incorrect interpretations.

Radionuclide imaging of the liver using the various tracers provides unique functional information, i.e., the functional reserve, presence or absence of hepatocytes/Kupffer's cells, and RBC pooling. This has been augmented further by the improved resolution with multi-head SPECT systems. Advances in instrumentation such as PET and development of new radiopharmaceuticals, including PET tracers specifically for the evaluation of the liver, will likely expand clinical applications further.

References

1. Harvey E, Loberg M, Ryan J (1979) Hepatic clearance mechanism of Tc-99m-HIDA and its effect on quantitation of hepatobiliary function: concise communication. J Nucl Med 20:310 – 313
2. Loberg MD, Cooper M, Harvey E, et al (1976) Development of new radiopharmaceuticals based on N-substitution of iminodiacetic acid. J Nucl Med 17:633 – 638
3. Krishnamurthy S, Krishnamurthy GT (1988) Quantitative assessment of hepatobiliary disease with Tc-99m-IDA scintigraphy. In: Freeman LM, Weissman HS (eds) Nuclear medicine annual. Raven, New York, pp 309 – 330
4. Doo E, Krishnamurthy GT, Eklem MJ, Gilbert S, Brown PH (1991) Quantification of hepatobiliary function as an integral part of imaging with technetium-99m-mebrofenin in health and disease. J Nucl Med 32:48 – 57
5. Stadalnik RC, Vera DR, Woodle ES, Trudeau WL, Porter BA, Ward RE, Krohn KA, O'Grady LF (1985) Technetium-99m NGA functional hepatic imaging: preliminary clinical experience. J Nucl Med 26:1233 – 1242
6. Woodle ES, Vera DR, Stadalnik RC, Ward RE (1987) Tc-NGA imaging in liver transplantation: preclinical studies. Surgery 102:55 – 62
7. Nagasue N, Yukaya H, Ogawa Y, Kohno H, Nakamura T (1987) Human liver regeneration after major hepatic resection. A study of normal liver and livers with chronic hepatitis and cirrhosis. Ann Surg 206:30 – 39
8. Henderson JM, Heymsfield SB, Horowitz J, Kutner MH (1981) Measurement of liver and spleen volume by computed tomography. Assessment of reproducibility and changes found following a selective distal splenorenal shunt. Radiology 141:525 – 527
9. Imaeda T, Kanematsu M, Asada S, Seki M, Doi H, Saji S (1995) Utility of Tc-99m GSA SPECT imaging in estimation of functional volume of liver segments in health and liver diseases. Clin Nucl Med 20:322 – 328
10. Bennink RJ, Dinant S, Erdogan D, Heijnen BH, Straatsburg IH, van Vliet AK, van Gulik TM (2004) Preoperative assessment of postoperative remnant liver function using hepatobiliary scintigraphy. J Nucl Med 45:965 – 971
11. Erdogan D, Heijnen BH, Bennink RJ, Kok M, Dinant S, Straatsburg IH, Gouma DJ, van Gulik TM (2004) Preoperative assessment of liver function: a comparison of 99mTc-Mebrofenin scintigraphy with indocyanine green clearance test. Liver Int 24:117 – 123
12. Stadalnik RC, Kudo M, Eckelman WC, Vera DR (1993) In vivo functional imaging using receptor-binding radiopharmaceuticals. Technetium 99m-galactosyl-neoglycoalbumin as a model. Invest Radiol 28:64 – 70
13. Kudo M, Todo A, Ikekubo K, Yamamoto K, Vera DR, Stadalnik RC (1993) Quantitative assessment of hepatocellular function through in vivo radioreceptor imaging with technetium 99m galactosyl human serum albumin. Hepatology 17:814 – 819
14. Hwang EH, Taki J, Shuke N, Nakajima K, Kinuya S, Konishi S, Michigishi T, Aburano T, Tonami N (1999) Preoperative assessment of residual hepatic functional reserve using 99mTc-DTPA-galactosyl-human serum albumin dynamic SPECT. J Nucl Med 40:1644 – 1651
15. Sasaki N, Hobo S, Yoshihara T (1999) Clinical usefulness of scintigraphy with 99mTc-galactosyl-human serum albumin for prognosis of cirrhosis of the liver. J Nucl Med 40:1652 – 1656
16. Nishiyama Y, Yamamoto Y, Hino I, Satoh K, Wakabayashi H, Ohkawa M (2003) 99mTc galactosyl human serum albumin liver dynamic SPET for pre-operative assessment of hepatectomy in relation to percutaneous transhepatic portal embolization. Nucl Med Commun 24:809 – 817
17. Kwon AH, Matsui Y, Kaibori M, Kamiyama Y (2004) Functional hepatic regeneration following hepatectomy using galactosyl-human serum albumin liver scintigraphy. Transplant Proc 36:2257 – 2260
18. Hirai I, Kimura W, Fuse A, Suto K, Urayama M (2003) Evaluation of preoperative portal embolization for safe hepatectomy, with special reference to assessment of nonembolized lobe function with 99mTc-GSA SPECT scintigraphy. Surgery 133:495 – 506
19. Kira T, Tomiguchi S, Kira M, Ohyama Y, Takahashi M (1997) Quantitative evaluation of the hepatic functional reserve using technetium-99m DTPA-galactosyl human serum albumin before and after transjugular intrahepatic portosystemic shunt. Eur J Nucl Med 24:1268 – 1272
20. Miki K, Kubota K, Kokudo N, Inoue Y, Bandai Y, Makuuchi M (1997) Asialoglycoprotein receptor and hepatic blood flow using technetium-99m-DTPA-galactosyl human serum albumin. J Nucl Med 38:1798 – 1807
21. Koizumi K, Uchiyama G, Arai T, Ainoda T, Yoda Y (1992) A new liver functional study using Tc-99m DTPA-galactosyl human serum albumin: evaluation of the validity of several functional parameters. Ann Nucl Med 6:83 – 87
22. Mitsumori A, Nagaya I, Kimoto S, Akaki S, Togami I, Takeda Y, Joja I, Hiraki Y (1998) Preoperative evaluation of hepatic functional reserve following hepatectomy by technetium-99m galactosyl human serum albumin liver scintigraphy and computed tomography. Eur J Nucl Med 25:1377 – 1382
23. Fujimoto H, Uchiyama G, Araki T, et al (1991) Exophytic regenerating nodule of the liver: misleading appearance on iodized-oil CT. J Comput Assist Tomogr 15:495 – 497
24. Calvet X, Pons F, Bruix J, et al (1988) Technetium-99m DISIDA hepatobiliary agent in diagnosis of hepatocellular carcinoma: relationship between detectability and tumor differentiation. J Nucl Med 29:1916 – 1920
25. Hasegawa Y, Nakano S, Hiyama T, et al (1991) Relationship of uptake of technetium-99m(Sn)-N-pyridoxyl-5-methyltryptophan by hepatocellular carcinoma to prognosis. J Nucl Med 32:228 – 235
26. Boulahdour H, Cherqui D, Charlotte F, et al (1993) The hot spot hepatobiliary scan in focal nodular hyperplasia. J Nucl Med 34:2105 – 2110
27. Kotzerke J, Schwarzrock R, Krischek O, et al (1989) Technetium-99m DISIDA hepatobiliary agent in diagnosis of hepatocellular carcinoma, adenoma, and focal nodular hyperplasia (letter). J Nucl Med 30:1278 – 1280

28. Barwick KW, Rosai J (1996) Liver (non-neoplastic disease). In: Rosai J (ed) Ackerman's surgical pathology. Mosby-Year Book, St Louis, pp 857 – 942
29. Brant WE, Floyd JL, Jackson DE, et al (1987) The radiological evaluation of hepatic cavernous hemangioma. JAMA 257:2471 – 2474
30. Ziessman HA, Silverman PM, Patterson J, et al (1991) Improved detection of small cavernous hemangiomas of the liver with high-resolution three-headed SPECT. J Nucl Med 32:2086 – 2091
31. Kudo M, Ikekubo K, Yamamoto K, et al (1989) Distinction between hemangioma of the liver and hepatocellular carcinoma: value of labeled RBC-SPECT scanning. AJR 152: 977 – 983
32. Langsteger W, Lind P, Eber B, et al (1989) Diagnosis of hepatic hemangioma with ^{99m}Tc-labeled red cells: single photon emission computed tomography (SPECT) versus planar imaging. Liver 9:288 – 293
33. Farlow DC, Chapman PR, Gruenewald SM, et al (1990) Investigation of focal hepatic lesions: is tomographic red blood cell imaging useful? World J Surg 14:463 – 467
34. Krause T, Hauenstein K, Studier-Fischer B, et al (1993) Improved evaluation of technetium-99m-red blood cell SPECT in hemangioma of the liver. J Nucl Med 34:375 – 380
35. Bonanno N, Baldari S, Cerrito A, et al (1991) Diagnosis of hepatic hemangiomas with ^{99m}Tc-labeled red blood cell scanning: value of SPECT. J Nucl Biol Med 35:135 – 140
36. Moon DH, Lee MH, Yang SK, et al (1992) Diagnosis of hepatic hemangioma (HH) with triple-head (3H) high-resolution SPECT. J Nucl Med 33:918 (abstract)
37. Birnbaum BA, Weinreb JC, Megibow AJ, et al (1990) Definitive diagnosis of hepatic hemangiomas: MR imaging versus Tc-99m-labeled red blood cell SPECT. Radiology 176:95 – 101
38. Kim CK (1998) Scintigraphic evaluation of the liver and biliary tract. In: Gazelle SG, Saini S, Mueller PR (eds) Hepatobiliary and pancreatic radiology: imaging and interventions. Thieme, New York, pp 108 – 153
39. Siegel A, Mazurek R (1997) Early dynamic SPECT acquisition for the imaging of hepatic hemangiomas utilizing Tc-99m-labeled red blood cells. Clin Nucl Med 22:745 – 748
40. Rabinowitz SA, McKusick KA, Strauss HW (1984) Technetium-99m red blood cell scintigraphy in evaluating focal liver lesions. AJR 143:63 – 68
41. Ginsberg F, Stavin JD, Spencer RP (1986) Hepatic angiosarcoma: mimicking of hemangioma on three-phase technetium-99m red blood cell scintigraphy. J Nucl Med 27:1861 – 1863
42. Swayne LC, Diehl WL, Brown TD, et al (1991) False-positive hepatic blood pool scintigraphy in metastatic colon carcinoma. Clin Nucl Med 16:630 – 632
43. Hod N, Pour MC, Juven Y, Horne T (2004) "Positive" Tc-99m red blood cell scintigraphy in a patient with hepatic lymphoma. Clin Nucl Med 29:272 – 274
44. Solomon RW, Palestro C, Kim CK, et al. (1989) Tc-99m-labeled red blood cell scintigraphy for hepatic hemangioma: are flow and early blood pool phases necessary? Clin Nucl Med 14:232 (abstract)
45. Zheng JG, Yao ZM, Shu CY, Zhang Y, Zhang X (2005) Role of SPECT/CT in diagnosis of hepatic hemangiomas. World J Gastroenterol 11:5336 – 5341
46. Schillaci O, Danieli R, Manni C, Capoccetti F, Simonetti G (2004) Technetium-99m-labelled red blood cell imaging in the diagnosis of hepatic haemangiomas: the role of SPECT/CT with a hybrid camera. Eur J Nucl Med Mol Imaging 31:1011 – 1015
47. Tanasescu D, Brachman M, Rigby J, et al (1984) Scintigraphic triad in focal nodular hyperplasia. Am J Gastroenterol 79:61 – 64
48. Rogers JV, Mack LA, Freeny PC, et al (1981) Hepatic focal nodular hyperplasia: angiography, CT, sonography, and scintigraphy. AJR 137:983 – 990
49. Welch TJ, Sheedy PF Jr, Johnson CM, et al (1985) Focal nodular hyperplasia and hepatic adenoma: comparison of angiography, CT, US, and scintigraphy. Radiology 156: 593 – 595
50. Salvo AF, Schiller A, Athanasoulis C, et al (1977) Hepatoadenoma and focal nodular hyperplasia; pitfalls in radiocolloid imaging. Radiology 125:451 – 455
51. Lubbers PR, Ros PR, Goodman ZD, et al (1987) Accumulation of technetium-99m sulfur colloid by hepatocellular adenoma: scintigraphic-pathologic correlation. AJR 148: 1105 – 1108
52. Schein CJ (1972) Acute cholecystitis. Harper and Row, New York, p 40
53. Sjodahl R, Wetterfors J (1974) Lysolecithin and lecithin in the gall bladder wall and bile; their possible roles in the pathogenesis of acute cholecystitis. Scand J Gastroenterol 9:519 – 525
54. Truedson H, Elmros T, Holm S (1983) The incidence of bacteria in gall bladder bile at acute and elective cholecystectomy. Acta Chir Scand 149:307 – 313
55. Jivegard L, Thornell E, Svanvik J (1987) Pathophysiology of acute obstructive cholecystitis: implications for non-operative management. Br J Surg 74:1084 – 1086
56. Jivegard L, Thornell E, Bjorck S, Svanvik J (1985) The effects of morphine and enkephaline on gall bladder function in experimental cholecystitis. Inhibition of inflammatory gall bladder secretion. Scand J Gastroenterol 20: 1049 – 1056
57. Greenberger NJ, Isselbacher KJ (1991) Diseases of the gallbladder and bile ducts. In: Wilson JD, Braunwald E, Isselbacher KJ, et al (eds) Harrison's principles of internal medicine, 12th edn. McGraw-Hill, New York, pp 1358 – 1368
58. Freitas JE (1994) Cholescintigraphy. In: Murray IPC, Ell PJ (eds) Nuclear medicine in clinical diagnosis and treatment. Churchill Livingstone, London, pp 77 – 86
59. Cotran RS, Kumar V, Robbins SL (1989) Pathologic basis of disease. Saunders, Philadelphia, p 971
60. Shea JA, Berlin JA, Escarce JJ, et al (1994) Revised estimates of diagnostic test sensitivity and specificity in suspected biliary tract disease. Arch Intern Med 154:2573 – 2581
61. Weissmann HS, Badia J, Sugarman LA, et al (1981) Spectrum of 99m-Tc-IDA cholescintigraphic patterns in acute cholecystitis. Radiology 138:167 – 175
62. Drane WE, Nelp WB, Rudd TG (1984) The need for routine delayed radionuclide hepatobiliary imaging in patients with intercurrent disease. Radiology 151:763 – 769
63. Choy D, Shi EC, McLean RG, et al (1984) Cholescintigraphy in acute cholecystitis: use of intravenous morphine. Radiology 151:203 – 207
64. Fink-Bennett D (1991) Augmented cholescintigraphy: its role in detecting acute and chronic disorders of the hepatobiliary tree. Semin Nucl Med 21:128 – 139
65. Weissmann HS, Freeman LM (1984) The biliary tract. In: Freeman LM (ed): Freeman and Johnson's clinical radionuclide imaging. Grune and Stratton, Orlando, pp 879 – 1049
66. Kalimi R, Gecelter GR, Caplin D, Brickman M, Tronco GT, Love C, Yao J, Simms HH, Marini CP (2001) Diagnosis of acute cholecystitis: sensitivity of sonography, cholescintigraphy, and combined sonography-cholescintigraphy. J Am Coll Surg 193:609 – 613
67. Alobaidi M, Gupta R, Jafri SZ, Fink-Bennet DM (2004) Current trends in imaging evaluation of acute cholecystitis. Emerg Radiol 10:256 – 258

68. Torsoli A, Corazziari E, Habib FI, Cicala M (1990) Pressure relationships within the human bile tract. Normal and abnormal physiology. Scand J Gastroenterol [Suppl] 175: 52 – 57
69. Murphy P, Solomon J, Roseman DL (1980) Narcotic anesthetic drugs: their effect on biliary dynamics. Arch Surg 115:710 – 711
70. Dedrick DF, Tanner WW, Bushkin FL (1980) Common bile duct pressure during enflurane anesthesia: effects of morphine and subsequent naloxone. Arch Surg 115:820 – 821
71. Kistler AM, Ziessman HA, Gooch D, et al (1991) Morphine-augmented cholescintigraphy in acute cholecystitis: a satisfactory alternative to delayed imaging. Clin Nucl Med 16:404 – 406
72. Fink-Benett D, Balon H, Robins T, et al (1991) Morphine-augmented cholescintigraphy: its efficacy in detecting acute cholecystitis. J Nucl Med 32:1231 – 1233
73. Vasquez TE, Greenspan G, Evans DG, et al (1988) Clinical efficacy of intravenous morphine administration in hepatobiliary imaging for acute cholecystitis. Clin Nucl Med 13:4 – 6
74. Fink-Bennett D, Balon HR (1993) The role of morphine-augmented cholescintigraphy in the detection of acute cholecystitis. Clin Nucl Med. 18:891 – 897
75. Ziessman HA (1992) Scintigraphy in the gastrointestinal tract. Curr Opin Radiol 4:105 – 116
76. Kim EE, Pjura G, Lowery P, et al (1986) Morphine-augmented cholescintigraphy in the diagnosis of acute cholecystitis. AJR 147:1177 – 1179
77. Keslar PJ, Turbiner E (1987) Hepatobiliary imaging and the use of intravenous morphine. Clin Nucl Med 12: 592 – 596
78. Flancbaum L, Choban PS, Sinha R, Jonasson O (1994) Morphine cholescintigraphy in the evaluation of hospitalized patients with suspected acute cholecystitis. Ann Surg 220:25 – 31
79. Kim CK, Juweid M, Woda A, et al (1993) Hepatobiliary scintigraphy: morphine-augmented versus delayed imaging in patients with suspected acute cholecystitis. J Nucl Med 34:506 – 509
80. Kim CK, Tse KM, Juweid M, et al (1993) Cholescintigraphy in the diagnosis of acute cholecystitis: morphine-augmentation is superior to delayed imaging. J Nucl Med 34:1866 – 1870
81. Cabana MD, Alavi A, Berlin JA, et al (1995) Morphine-augmented hepatobiliary scintigraphy: a meta-analysis. Nucl Med Commun 16:1068 – 1071
82. Fig LM, Wahl RL, Stewart RE, et al (1990) Morphine-augmented hepatobiliary scintigraphy in the severely ill: caution is in order. Radiology 175:467 – 473
83. Klingensmith WC III, Turner WM (1990) Cholescintigraphy for acute cholecystitis: false-positive results caused by chronic cholecystitis. Gastrointest Radiol 15:129 – 132
84. Carballo R, Worsch L, Bushnell D, et al (1992) Results of cholescintigraphy in a VA hospital. J Surg Res 53:4 – 6
85. Freeman LM, Sugarman LA, Weissmann HS (1981) Role of cholecystokinetic agents in ^{99m}Tc-IDA cholescintigraphy. Semin Nucl Med 11:186 – 193
86. Eikman EA, Cameron JL, Colman M, et al (1975) A test for patency of the cystic duct in acute cholecystitis. Ann Intern Med 82:318 – 322
87. Kim CK, Palestro CJ, Solomon RW, et al (1990) Delayed biliary-to-bowel transit in cholescintigraphy after cholecystokinin treatment. Radiology 176:553 – 556
88. Larsen MJ, Klingensmith WC, Kuni CC (1982) Radionuclide hepatobiliary imaging: nonvisualization of the gallbladder secondary to prolonged fasting. J Nucl Med 23: 1003 – 1005
89. Shuman WP, Gibbs P, Rudd TG, et al (1982) PIPIDA scintigraphy for cholecystitis: false positives in alcoholism and total parenteral nutrition. AJR 138:1 – 5
90. Krishnamurthy S, Krishnamurthy GT (1996) Cholecystokinin and morphine pharmacological intervention during ^{99m}Tc-HIDA cholescintigraphy: a rational approach. Semin Nucl Med 26:16 – 24
91. Chen CC, Holder LE, Maunoury C, et al (1997) Morphine augmentation increases gall bladder visualization in patients pretreated with cholecystokinin. J Nucl Med 38: 644 – 647
92. Kim CK, Goyal M, San Pedro E, et al (1995) The effect of CCK pretreatment on gall bladder visualization on delayed or morphine-augmented imaging (abstract). J Nucl Med 36:74
93. Klingensmith WC, Spitzer VM, Fritzberg AR (1981) The normal fasting and postprandial Tc-99m-diisopropyl-IDA hepatobiliary study. J Nucl Med 22:7
94. Freitas JE (9182) Cholescintigraphy in acute and chronic cholecystitis. Semin Nucl Med 12:18 – 26
95. Keller IA, Weissmann HS, Kaplun LL, et al (1984) The use of water ingestion to distinguish the gall bladder and duodenum on cholescintigrams. Radiology 152:811 – 813
96. Coleman RE, Freitas JE, Fink-Bennett D, Bree RL (1984) The dilated cystic duct sign – a potential cause of false-negative cholescintigraphy. Clin Nucl Med 9:134 – 136
97. Holbrook RF, Jacobson FL, Pezzuti RT, et al (1991) Biliary patency imaging after endoscopic retrograde sphincterotomy with gall bladder in situ. Clinical impact of nonvisualization. Arch Surg 126:738 – 741
98. Chandramouli B, Gupta SM, Cohen GE (1994) Scintigraphic evaluation of bile dynamics before and after endoscopic sphincterotomy. Clin Nucl Med 19:800 – 802
99. Jacobson AF, Teefey SA, Lee SP, et al (1993) Frequent occurrence of new hepatobiliary abnormalities after bone marrow transplantation: results of a prospective study using scintigraphy and sonography. Am J Gastroenterol 88:1044 – 1049
100. Klingensmith WC (1988) Hepatobiliary imaging: normal appearance and normal variations. In: Gottschalk A, Hoffer PB, Potchen J (eds) Diagnostic nuclear medicine. Williams and Wilkins, Baltimore, pp 575 – 581
101. Blue PW (1985) Biliary scanning interpretations using technetium-99m DISIDA. Clin Nucl Med 10:742 – 751
102. Lee SO, Kim CK, Palestro CJ, et al (1991) Is CCK necessary to separate normal from CBD obstruction when prompt gall bladder filling but no bowel activity is seen during cholescintigraphy (abstract)? J Nucl Med 32:976
103. Oates E, Achong DM (1992) Incidence and significance of enterogastric reflux during morphine-augmented cholescintigraphy. Clin Nucl Med 17:926 – 928
104. Shih WJ, Lee JK, Magoun S, et al (1995) Morphine-augmented cholescintigraphy enhances duodenogastric reflux. Ann Nucl Med 9:225 – 228
105. Kim CK, Lim JK, Machac J (1996) Variable bile retention on cholescintigraphy after morphine administration. Eur J Nucl Med 23:1464 – 1467
106. Kim CK, Yun M, Lim JK, Lin X, Krynyckyi BR, Machac J (2000) Refinement of the positive-predictive value of gallbladder non-visualization after morphine administration for acute cholecystitis based on the temporal pattern of common bile duct activity. Clin Nucl Med 25:603 – 607
107. Colletti PM, Cirimelli KM, Radin DR, et al (1989) Radionuclide angiography in suspected acute cholecystitis: further observations. Clin Nucl Med 14:867 – 873
108. Swayne LC, Ginsberg HN (1989) Diagnosis of acute cholecystitis by cholescintigraphy: significance of pericholecystic hepatic uptake. AJR 152:1211 – 1213

109. Meekin GK, Ziessman HA, Klappenbach RS (1987) Prognostic value and pathophysiologic significance of the rim sign in cholescintigraphy. J Nucl Med 28:1679 – 1682
110. Aburano T, Yokoyama K, Taniguchi M, et al (1990) Diagnostic values of gall bladder hyperperfusion and the rim sign in radionuclide angiography and hepatobiliary imaging. Gastrointest Radiol 15:229 – 232
111. Bohdiewicz PJ (1993) The diagnostic value of grading hyperperfusion and the rim sign in cholescintigraphy. Clin Nucl Med 18:867 – 871
112. Brachman MB, Goodman MD, Waxman AD (1993) The rim sign in acute cholecystitis. Comparison of radionuclide, surgical, and pathologic findings. Clin Nucl Med 18:863 – 866
113. Oates E, Selland DL, Chin CT, Achong DM (1996) Gallbladder nonvisualization with pericholecystic rim sign: morphine-augmentation optimizes diagnosis of acute cholecystitis. J Nucl Med 37:267 – 269
114. Nahrwold DL (1991) Chronic cholecystitis and cholelithiasis. In: Sabiston DC (ed) Textbook of surgery, 14th edn. Saunders, Philadelphia, pp 1057 – 1063
115. Hopman WP, Jansen JB, Rosenbusch G, Lamers CB (1986) Gall bladder contraction induced by cholecystokinin: bolus injection or infusion? Br Med J 292:375 – 376
116. Courtney DF, Clanachan AS, Scott GW (1983) Cholecystokinin constricts the canine cystic duct. Gastroenterology 85:1154 – 1159
117. Fink-Bennett D, DeRidder P, Kolozsi WZ, et al (1991) Cholecystokinin cholescintigraphy: detection of abnormal gall bladder motor function in patients with chronic acalculous gall bladder disease. J Nucl Med 32:1695 – 1699
118. Halverson JD, Garner BA, Siegel BA, et al (1992) The use of hepatobiliary scintigraphy in patients with acalculous biliary colic. Arch Intern Med 152:1305 – 1307
119. Reed DN Jr, Fernandez M, Hicks RD (1993) Kinevac-assisted cholescintigraphy as an accurate predictor of chronic acalculous gall bladder disease and the likelihood of symptom relief with cholecystectomy. Am Surg 5: 273 – 277
120. Pickleman J, Peiss RL, Henkin R, et al (1985) The role of sincalide cholescintigraphy in the evaluation of patients with acalculus gall bladder disease. Arch Surg 120:693 – 697
121. Zech ER, Simmons LB, Kendrick RR, et al (1991) Cholecystokinin enhanced hepatobiliary scanning with ejection fraction calculation as an indicator of disease of the gall bladder. Surg Gynecol Obstet 17:21 – 24
122. Ziessman HA, Fahey FH, Hixson DJ (1992) Calculation of a gall bladder ejection fraction: advantage of continuous sincalide infusion over the three-minute infusion method. J Nucl Med 33:537 – 541
123. Kim CK, Worsley DF, Machac J (1996) Interventions in gastrointerventional nuclear medicine. In: Freeman LM (ed) Nuclear medicine annual. Raven, New York, pp 213 – 257
124. Ziessman HA, Muenz LR, Agarwal AK, ZaZa AA (2001) Normal values for sincalide cholescintigraphy: comparison of two methods. Radiology 221:404 – 410
125. Krishnamurthy GT, Krishnamurthy S, Brown PH (2004) Constancy and variability of gall bladder ejection fraction: impact on diagnosis and therapy. J Nucl Med 45:1872 – 1877
126. Yap L, Wycherley AG, Morphett AD, et al (1991) Acalculous biliary pain: cholecystectomy alleviates symptoms in patients with abnormal cholescintigraphy. Gastroenterology 101:786 – 793
127. Raymond F, Lepanto L, Rosenthall L, et al (1988) Tc-99m-IDA gall bladder kinetics and response to CCK in chronic cholecystitis. Eur J Nucl Med 14:378 – 381
128. Watson A, Better N, Kalff V, et al (1994) Cholecystokinin (CCK)-HIDA scintigraphy in patients with suspected gall-bladder dysfunction. Austr Radiol 38:30 – 33
129. Ryu JS, Moon DH, Lee MH, Lee SK, Kim MH, Min YI (1993) Gallbladder emptying in normal healthy volunteers (abstract). J Nucl Med 34:76P
130. Ziessman HA, Jones DA, Muenz LR, Agarval AK (2003) Cholecystokinin cholescintigraphy: methodology and normal values using a lactose-free fatty-meal food supplement. J Nucl Med 44:1263 – 1266
131. Hadigan C, Fishman SJ, Connolly LP, Treves ST, Nurko S (2003) Stimulation with fatty meal (Lipomul) to assess gall bladder emptying in children with chronic acalculous cholecystitis. J Pediatr Gastroenterol Nutr 37:178 – 182
132. Krishnamurthy GT, Brown PH (2002) Comparison of fatty meal and intravenous cholecystokinin infusion for gall bladder ejection fraction. J Nucl Med 43:1603 – 1610
133. Fisher RS, Rock E, Malmud LS (1987) Effects of meal composition on gallbladder and gastric emptying in man. Dig Dis Sci 32:337 – 344
134. Maton PN, Selden AC, Fitzpatrick ML, Chadwick VS (1985) Defective gallbladder emptying and cholecystokinin release in celiac disease: reversal by gluten-free diet Gastroenterology 88:391 – 396
135. Masclee AA, Jansen JB, Corstens FHM, Lamers CBHW (1989) Reversible gallbladder dysfunction in severe pancreatic insufficiency. Gut 30:866 – 872
136. Masclee AA, Jansen JB, Driessen WM, Geuskens LM, Lamers CB (1991) Gallbladder sensitivity to cholecystokinin in coeliac disease. Coirelation of gallbladder contraction with plasma cholecystokinin-like immunoreactivity during infusion of cerulein. Scand J Gastroenterol 26:1279 – 1284
137. Oster-Jorgensen E, Qvist N, Pedersen SA, Rasmussen L, Hovendal CP (1992) Postprandial gallbladder emptying is related to intestinal motility at the time of meal ingestion. Scand J Gastroenterol 27:699 – 702
138. Kloiber R, Molnar CP, Shaffer EA (1992) Chronic biliary-type pain in the absence of gallstones: the value of cholecystokinin cholescintigraphy. AJR 159:509 – 513
139. Brugge WR (1991) Motor function of the gallbladder: measurement and clinical significance. Semin Roentgenol 16:226-231
140. Weedon D (1984) Pathology of the gall bladder. Masson, New York
141. Cozzolino HJ, Goldstein F, Greening RR, et al (1963) The cystic duct syndrome. JAMA 185:100 – 104
142. Baxter JN, Grime JS, Critchley M, et al (1984) Gall bladder emptying. Nucl Med Commun 5:477 – 478
143. Bolen G, Javitt NB (1982) Biliary dyskinesia: mechanisms and management. Hosp Pract 17:115 – 130
144. Robbins SL, Cotran RS, Kumar V (1984) Pathologic basis of disease, 3rd edn. Saunders, Philadelphia
145. Misra DC Jr, Blossom GB, Fink-Bennett D, et al (1991) Results of surgical therapy for biliary dyskinesia. Arch Surg 126:957 – 960
146. Smith A, Chapman C, Cunningham P (1995) The utility of the CCK DISIDA scan in the treatment of occult biliary tract disease. Am Surg 6:220 – 225
147. Westlake PJ, Hershfield NB, Kelly JK, et al (1990) Chronic right upper quadrant pain without gallstones: does HIDA scan predict outcome after cholecystectomy? Am J Gastroenterol 85:986 – 990
148. DeCamp JR, Tabatowski K, Schauwecker DS, et al (1992) Comparison of gall bladder ejection fraction with histopathologic changes in acalculous biliary disease. Clin Nucl Med 17:784 – 786
149. Patel NA, Lamb JJ, Hogle NJ, Fowler DL (2004) Therapeu-

tic efficacy of laparoscopic cholecystectomy in the treatment of biliary dyskinesia. Am J Surg 187:209 – 212
150. Sorenson MK, Fancher S, Lang NP, et al (1993) Abnormal gall bladder nuclear ejection fraction predicts success of cholecystectomy in patients with biliary dyskinesia. Am J Surg 166:672 – 674
151. Middleton GW, Williams JH (1993) Is gall bladder ejection fraction a reliable predictor of acalculous gall bladder disease? Nucl Med Commun 14:509 – 510
152. Majeski J (2003) Gall bladder ejection fraction: an accurate evaluation of symptomatic acalculous gall bladder disease. Int Surg 88:95 – 99
153. Campbell BT, Narasimhan NP, Golladay ES, Hirschl RB (2004) Biliary dyskinesia: a potentially unrecognized cause of abdominal pain in children. Pediatr Surg Int 20:579 – 581
154. Nora PF, Davis RP, Fernandez MJ (1984) Chronic calculous gall bladder disease: a clinical enigma. World J Surg 8:106 – 112
155. Davis GB, Berk RN, Scheible FW, et al (1982) Cholecystokinin cholecystography, sonography, and scintigraphy: detection of chronic acalculous cholecystitis. AJR 139:1117 – 1121
156. Garrigues V, Ponce J, Cano C, et al (1992) Effect of selective and nonselective muscarinic blockade on cholecystokinin-induced gall bladder emptying in man. Dig Dis Sci 37:101 – 104
157. Zhu XF, Harris AG, Yang MF, et al (1994) Effect of octreotide on dynamic excretion of bile in Chinese acromegalic patients assessed by [^{99m}Tc]EHIDA hepatobiliary scan. Dig Dis Sci 39:284 – 288
158. Grimaldi C, Darcourt J, Harris AG, et al (1993) Cholescintigraphic study of effect of somatostatin analog, octreotide, on bile secretion and gall bladder emptying in normal subjects. Dig Dis Sci 38:1718 – 1721
159. Morton JM, Bowers SP, Lucktong TA, Mattar S, Bradshaw WA, Behrns KE, Koruda MJ, Herbst CA, McCartney W, Halkar RK, Smith CD, Farrell TM (2002) Gall bladder function before and after fundoplication. J Gastrointest Surg 6:806 – 810
160. Annese V, Caruso N, Accadia L, et al (1991) Gall bladder function and gastric liquid emptying in achalasia. Dig Dis Sci 36:1116 – 1120
161. Pechlivanides G, Xynos E, Chrysos E, et al (1994) Gallbladder emptying after antiulcer gastric surgery. Am J Surg 168:335 – 339
162. Steinberg WM (1988) Sphincter of Oddi dysfunction: a clinical controversy. Gastroenterology 95:1409 – 1415
163. Bar Meir S, Halpern Z, Barden E, et al (1984) Frequency of papillary dysfunction among cholecystectomized patients. Hepatology 4:328 – 330
164. Guelrud M (1988) Papillary stenosis. Endoscopy 20:193 – 202
165. Hogan WJ, Geenen JE (1988) Biliary dyskinesia. Endoscopy 20:179 – 183
166. Toouli J, Baker RA (1991) Innervation of the sphincter of Oddi: physiology and considerations of pharmacological intervention in biliary dyskinesia. Pharmacol Ther 49: 269 – 281
167. Lans JL, Parikh NP, Geenen JE (1991) Application of sphincter of Oddi manometry in routine clinical investigations. Endoscopy 23:139 – 143
168. Coelho JC, Wiederkehr JC (1996) Motility of Oddi's sphincter: recent developments and clinical applications. Am J Surg 172:48 – 51
169. Khuroo MS, Zargar SA, Yattoo GN (1992) Efficacy of nifedipine therapy in patients with sphincter of Oddi dysfunction: a prospective, double-blind, randomized, placebo-controlled, crossover trial. Br J Clin Pharmacol 33:477 – 485
170. Elta GH, Barnett JL, Ellis JH, et al (1992) Delayed biliary drainage is common in asymptomatic post-cholecystectomy volunteers. Gastrointest Endosc 38:435 – 439
171. King CE, Kalvaria I, Sininsky CA (1988) Pancreatitis due to endoscopic biliary manometry. Proceed with caution (abstract). Gastroenterology 94:A227
172. Sostre S, Kalloo AN, Spiegler EJ, et al (1992) A noninvasive test of sphincter of Oddi dysfunction in postcholecystectomy patients: the scintigraphic score. J Nucl Med 33:1216 – 1222
173. Shaffer EA, Hershfield NB, Logan K, et al (1986) Cholescintigraphic detection of functional obstruction of the sphincter of Oddi. Effect of papillotomy. Gastroenterology 90:728 – 733
174. Grimon G, Buffet C, Andre L, et al (1991) Biliary pain in postcholecystectomy patients without biliary obstruction. A prospective radionuclide study. Dig Dis Sci 36:317 – 320
175. Darweesh RMA, Dodds WJ, Hogan WJ, et al (1988) Efficacy of quantitative hepatobiliary scintigraphy and fatty meal sonography for evaluating patients with partial common bile duct obstruction. Gastroenterology 94: 779 – 785
176. Persson B, Axelsson B, Jacobsson H (1993) Cholescintigraphy in the diagnosis and assessment of benign papillary stenosis. Eur J Nucl Med 20:770 – 775
177. Kloiber R, AuCoin R, Hershfield NB, et al (1988) Biliary obstruction after cholecystectomy: diagnosis with quantitative cholescintigraphy. Radiology 169:643 – 647
178. Fullarton GM, Allan A, Hilditch T, et al (1988) Quantitative ^{99m}Tc-DISIDA scanning and endoscopic biliary manometry in sphincter of Oddi dysfunction. Gut 29:1397 – 1401
179. Farup PG, Tjora S (1989) Sphincter of Oddi dysfunction: dynamic cholescintigraphy and endoscopic retrograde cholangiopancreatography with papillotomy in diagnosis, treatment and follow up study. Scand J Gastroenterol 24:956 – 960
180. Corazziari E, Cicala M, Habib FI, et al (1994) Hepatoduodenal bile transit in cholecystectomized subjects. Relationship with sphincter of Oddi function and diagnostic value. Dig Dis Sci 39:1985 – 1993
181. Cicala M, Habib FI, Vavassori P, Pallotta N, Schillaci O, Costamagna G, Guarino MP, Scopinaro F, Fiocca F, Torsoli A, Corazziari E (2002) Outcome of endoscopic sphincterotomy in post cholecystectomy patients with sphincter of Oddi dysfunction as predicted by manometry and quantitative choledochoscintigraphy. Gut 50:665 – 668
182. Roberts-Thomson IC, Toouli J, Blanchett W, Lichtenstein M, Andrews JT (1986) Assessment of bile flow by radioscintigraphy in patients with biliary-type pain after cholecystectomy. Aust NZ J Med 16:788 – 793
183. Craig AG, Peter D, Saccone GT, Ziesing P, Wycherley A, Toouli J (2003) Scintigraphy versus manometry in patients with suspected biliary sphincter of Oddi dysfunction. Gut 52:352 – 357
184. Madácsy L, Szepes A, Bertalan V, Funch-Jensen P (2003) Is hepatobiliary scintigraphy insensitive for the diagnosis of sphincter of Oddi dysfunction? Gut 52:1385 – 1386
185. Ziessman HA (1992) Atlas of cholescintigraphy: selective update. In: Ziessman HA, Van Nostrand D (eds) Selected atlas of gastrointestinal scintigraphy. Springer, Berlin Heidelberg New York, pp 1 – 34
186. Madacsy L, Velosy B, Lonovics J, et al (1994) Differentiation between organic stenosis and functional dyskinesia of the sphincter of Oddi with amyl nitrite-augmented

quantitative hepatobiliary scintigraphy. Eur J Nucl Med 21:203 – 208
187. Sostre S, Spiegler E, Kallo A, Camargo E (1990) Cholecystokinin-stimulated biliary scintigraphy in patients with sphincter of Oddi dysfunction (abstract). Radiology 177:322
188. Tanaka M, Ikeda S, Nakayama F (1984) Change in bile duct pressure responses after cholecystectomy: loss of gall bladder as a pressure reservoir. Gasteroenterology 87:1154 – 1159
189. Kalloo AN, Sostre S, Meyerrose GE, et al (1994) Gallbladder ejection fraction. Nondiagnostic for sphincter of Oddi dysfunction in patients with intact gall bladders. Clin Nucl Med 19:713 – 719
190. Ruffolo TA, Sherman S, Lehman GA, et al (1994) Gallbladder ejection fraction and its relationship to sphincter of Oddi dysfunction. Dig Dis Sci 39:289 – 292
191. Zeman RK, Lee C, Jaffe MH, et al (1984) Hepatobiliary scintigraphy and sonography in early biliary obstruction. Radiology 153:793 – 798
192. Miller DR, Egbert RM, Braunstein P (1984) Comparison of ultrasound and hepatobiliary imaging in the early detection of acute total common bile duct obstruction. Arch Surg 119:1233 – 1237
193. Kaplun L, Weissmann HS, Rosenblatt RR, et al (1985) The early diagnosis of common bile duct obstruction using cholescintigraphy. JAMA 254:2431 – 2434
194. Klingensmith WC III, Ashdown B (1991) Cholescintigraphy in the diagnosis of intrahepatic cholestasis. How specific is it? Clin Nucl Med 16:621 – 626
195. Krishnamurthy GT, Lieberman DA, Brar HS (1985) Detection, localization, and quantitation of degree of common bile duct obstruction by scintigraphy. J Nucl Med 26:726 – 735
196. Itoh H, Murase K, Hamamoto K (1989) Reflux sign in cholescintigraphy after administration of a gall bladder contracting agent. J Nucl Med 30:1192 – 1197
197. Itoh H, Shimono R, Hamamoto K (1988) Evaluation of common bile duct stenosis in chronic pancreatitis using cholescintigraphy. Eur J Nucl Med 14:137 – 140
198. Brown PH, Juni JE, Lieberman DA, et al (1988) Hepatocyte versus biliary disease: a distinction by deconvolutional analysis of technetium-99m IDA time-activity curves. J Nucl Med 29:623 – 630
199. Juni JE, Reichle R (1990) Measurement of hepatocellular function with deconvolutional analysis: application in the differential diagnosis of acute jaundice. Radiology 177:171 – 175
200. Lieberman DA, Brown PH, Krishnamurthy GT (1990) Improved scintigraphic assessment of severe cholestasis with the hepatic extraction fraction. Dig Dis Sci 35:1385 – 1390
201. Balistreri WF, Grand R, Hoomagle JH, et al (1996) Biliary atresia: current concepts and research directions. Summary of a Symposium. Hepatology 23:1682 – 1692
202. Bezerra JA, Tiao G, Ryckman FC, et al (2002) Genetic induction of proinflammatory immunity in children with biliary atresia. Lancet 360:1653 – 1659
203. Perlmutter DH, Shepherd RW (2002) Extrahepatic biliary atresia: a disease or a phenotype? Hepatology 35: 1297 – 1304
204. Miyano T, Fujimoto T, Ohya T, Shimomura H (1993) Current concept of the treatment of biliary atresia. World J Surg 17:332 – 336
205. McEvoy CF, Suchy FJ (1996) Biliary tract disease in children. Pediatr Clin North Am 43:75 – 98
206. Kasai M, Suzuki K, Ohashi E, et al (1978) Technique and results of operative management of biliary atresia. World J Surg 2:571 – 580
207. Gerhold JP, Klingensmith WC III, Kuni CC, et al (1983) Diagnosis of biliary atresia with radionuclide hepatobiliary imaging. Radiology 146:499 – 504
208. Spivak W, Sarkar S, Winter D, et al (1987) Diagnostic utility of hepatobiliary scintigraphy with ^{99m}Tc-DISIDA in neonatal cholestasis. J Pediatr 110:855 – 861
209. Ben-Haim S, Seabold JE, Kao SC, et al (1995) Utility of Tc-99m mebrofenin scintigraphy in the assessment of infantile jaundice. Clin Nucl Med 20:153 – 163
210. Cox KL, Stadalnik RC, McGahan JP, et al (1987) Hepatobiliary scintigraphy with technetium-99m disofenin in the evaluation of neonatal cholestasis. J Pediatr Gastroenterol Nutr 6:885 – 891
211. Howman-Giles R, Moase A, Gaskin K, Uren R (1993) Hepatobiliary scintigraphy in a pediatric population: determination of hepatic extraction fraction by deconvolution analysis. J Nucl Med 34:214 – 221
212. Howman-Giles R, Uren R, Bernard E, Dorney S (1998) Hepatobiliary scintigraphy in infancy. J Nucl Med 39:311 – 319
213. Majd M, Reba RC, Altman RP (1981) Effect of phenobarbital on ^{99m}Tc-IDA scintigraphy in the evaluation of neonatal jaundice. Semin Nucl Med 11:194 – 204
214. Balistreri WF (1985) Neonatal cholestasis. J Pediatr 106:171 – 184
215. Larrosa-Haro A, Caro-Lopez AM, Coello-Ramirez P, et al (2001) Duodenal tube test in the diagnosis of biliary atresia. J Pediatr Gastroenterol Nutr 32:311 – 315
216. Lin WY, Liu CG, Changlai SP, et al (1997) Comparison technetium of Tc-99m disofenin cholescintigraphy with ultrasonography in the differentiation of biliary atresia from other forms of neonatal jaundice. Pediatr Surg Int 12(l):30 – 33
217. Johnson K, Alton HM, Chapman S (1998) Evaluation of mebrofenin hepatoscintigraphy in neonatal-onset jaundice. Pediatr Radiol 28:937 – 941
218. Thaler MM (1972) Effect of phenobarbital on hepatic transport and excretion of ^{131}I-rose bengal in children with cholestasis. Pediatr Res 6:100 – 110
219. Heyman S, Chapman PR (1990) The extraction ratio, initial uptake and visual grading (using 99mic DISIDA) in the differential diagnosis of neonatal hyperbilirubinemia. J Nucl Med 31:742 (abstr)
220. Gilmour SM, Hershkop M, Reifen R, Gilday D, Roberts EA (1997) Outcome of hepatobiliary scanning in neonatal hepatitis syndrome. J Nucl Med 38:1279 – 1282
221. Tolia V, Kottamasu SR, Tabassum D et al (1999) The use of hepatocyte extraction fraction to evaluate neonatal cholestasis. Clin Nucl Med 24:655 – 659
222. Kim CK, Heyman S (1994) Scintigraphic evaluation of liver transplants. In: Murray IPC, Ell PJ (eds) Nuclear medicine in clinical diagnosis and treatment. Churchill Livingstone, London, pp 69 – 75
223. Rayter Z, Tonge C, Bennett C, et al (1991) Ultrasound and HIDA: scanning in evaluating bile leaks after cholecystectomy. Nucl Med Commun 12:197 – 202
224. Brugge WR, Rosenberg DJ, Alavi A (1994) Diagnosis of postoperative bile leaks. Am J Gastroenterol 89:2178 – 2183
225. Walker AT, Shapiro AW, Brooks DC, et al (1992) Bile duct disruption and biloma after laparoscopic cholecystectomy: imaging evaluation. AJR 158:785 – 789
226. Banzo I, Blanco I, Gutierrez-Mendiguchia C, Gomez-Barquin R, Quirce R, Carril JM (1998) Hepatobiliary scintigraphy for the diagnosis of bile leaks produced after T-tube removal in orthotopic liver transplantation. Nucl Med Commun 19:229 – 236
227. Worsley DF, Kim CK (1994) Hepatic and splenic trauma. In: Murray IPC, Ell PJ (eds) Nuclear medicine in clinical

diagnosis and treatment. Churchill Livingstone, London, pp 63 – 67
228. Trerotola SO, Savader SJ, Lund GB, et al (1992) Biliary tract complications following laparoscopic cholecystectomy: imaging and intervention. Radiology 184:195 – 200
229. Peters JH, Ollila D, Nichols KE, et al (1994) Diagnosis and management of bile leaks following laparoscopic cholecystectomy. Surg Laparosc Endosc 4:163 – 170
230. Brugge WR, Alavi A (1993) Cholescintigraphy in the diagnosis of the complications of laparoscopic cholecystectomy. Semin Ultrasound CT MR 14:368 – 374
231. Rosenthall L, Fonseca C, Arzoumanian A, et al (1979) ^{99m}Tc-IDA hepatobiliary imaging following upper abdominal surgery. Radiology 130:735 – 739
232. Zeman RK, Lee C, Stahl RS, et al (1982) Ultrasonography and hepatobiliary scintigraphy in the assessment of biliary-enteric anastomoses. Radiology 145:109 – 115
233. Weissmann HS, Gliedman ML, Wilk PJ, et al (1982) Evaluation of the postoperative patient with ^{99m}Tc-IDA cholescintigraphy. Semin Nucl Med 12:27 – 52
234. Belli G, Romano G, Monaco A, et al (1988) HIDA scan in the follow-up of biliary-enteric anastomoses. HPB Surg 1:29 – 32
235. Aigner RM, Fueger GF, Schimpl G, Sauer H, Nicoletti R (1997) Cholescintigraphy in the evaluation of bile flow after Roux-en-Y hepatico-jejunostomy and hepatico-antrostomy in infants with choledochal cysts. Pediatr Radiol 27:850 – 854
236. Lucas MH, Elgazzar AH, Cummings DD (1995) Positional biliary stasis: scintigraphic findings following biliary-enteric bypass surgery. J Nucl Med 36:104 – 106
237. Isayama H, Komatsu Y, Inoue Y, Toda N, Shiratori Y, Tsujino T, Yamada H, Saitou K, Kawabe T, Omata M (2003) Preserved function of the Oddi sphincter after endoscopic papillary balloon dilation. Hepatogastroenterology 50:1787 – 1791
238. Wickremesinghe PC, Dayrit PQ, Manfredi OL, et al (1983) Quantitative evaluation of bile diversion surgery utilizing ^{99m}Tc HIDA scintigraphy. Gastroenterology 84: 354 – 363
239. Sousa JE, Troncon LE, Andrade JI, et al (1988) Comparison between Henley jejunal interposition and Roux-en-Y anastomosis as concerns enterogastric biliary reflux levels. Ann Surg 208:597 – 600
240. Vogel SB, Drane WE, Woodward ER (1994) Clinical and radionuclide evaluation of bile diversion by Braun enteroenterostomy: prevention and treatment of alkaline reflux gastritis. An alternative to Roux-en-Y diversion. Ann Surg 219:458 – 465
241. Adachi S, Takeda T, Fukao K (1999) Evaluation of esophageal bile reflux after total gastrectomy by gastrointestinal and hepatobiliary dual scintigraphy. Surg Today 29: 301 – 306
242. Hashimoto N (2005) Hepatobiliary imaging after pancreaticoduodenectomy – a comparative study on Billroth I and Billroth II reconstruction. Hepatogastroenterology 52:1023 – 1025
243. Hashimoto N, Kotoura Y, Ohyanag H (2005) Hepatobiliary scintigraphy after biliary reconstruction-Roux Y and RY-DJ. Hepatogastroenterology 52:200 – 202
244. Rodman CA, Keeffe EB, Lieberman DA, et al (1987) Diagnosis of sclerosing cholangitis with technetium 99m-labeled iminodiacetic acid planar and single photon emission computed tomographic scintigraphy. Gastroenterology 92:777 – 785
245. O'Brien S, Keogan M, Casey M, et al (1992) Biliary complications of cystic fibrosis. Gut 33:387 – 391
246. Colombo C, Castellani MR, Balistreri WF, et al (1992) Scintigraphic documentation of an improvement in hepatobiliary excretory function after treatment with ursodeoxycholic acid in patients with cystic fibrosis and associated liver disease. Hepatology 15:677 – 684
247. Dogan AS, Conway JJ, Lloyd-Till JD (1994) Hepatobiliary scintigraphy in children with cystic fibrosis and liver disease. J Nucl Med 35:432 – 435
248. O'Connor PJ, Southern KW, Bowler IM, et al (1996) The role of hepatobiliary scintigraphy in cystic fibrosis. Hepatology 23:281 – 287
249. Buscombe JR, Miller RF, Ell PJ (1992) Hepatobiliary scintigraphy in the diagnosis of AIDS-related sclerosing cholangitis. Nucl Med Commun 13:154 – 160
250. Quinn D, Pocock N, Freund J, et al (1993) Radionuclide hepatobiliary scanning in patients with AIDS-related sclerosing cholangitis. Clin Nucl Med 18:417 – 422
251. Kim OH, Chung HJ, Choi BG (1995) Imaging of the choledochal cyst. Radiographics 15:69 – 88
252. Camponovo E, Buck JL, Drane WE (1989) Scintigraphic features of choledochal cyst. J Nucl Med 30:622 – 628
253. Kim CK (1997) Pharmacologic intervention for the diagnosis of acute cholecystitis: cholecystokinin pretreatment or morphine, or both? (Editorial) J Nucl Med 38:647 – 649
254. Kim CK, Worsley WF, Lentle B (1998) Scintigraphic evaluation of tumors of the liver. In: Murray IPC, Ell PJ (eds) Nuclear medicine in clinical diagnosis and treatment, 2nd edn. Churchill Livingstone, London, pp 775 – 782

18 Basis and Clinical Application of Brain Imaging

James M. Mountz, Elmer C. San Pedro

18.1 Anatomy and Physiology

The central nervous system consists of the brain and the spinal cord. The major anatomical divisions of the brain are the cerebrum and the cerebellum, together weighing about 1400 g in the adult. The cells in the brain are classified as glia or neurons. About 10,000 different types of neurons totaling approximately 100 billion neurons comprise the human brain. The cerebral cortex consists of two hemispheres connected by a large mass of white matter called the corpus callosum. The surface layer of each hemisphere is folded into gyri comprising the gray matter. The brain is divided into functional areas called the frontal lobe (anterior to the central sulcus) and the parietal lobe (posterior to this sulcus). The occipital lobe lies below the parieto-occipital sulcus, and the temporal lobe is situated below the lateral sulcus (Figs. 18.1, 18.2). Knowledge of cross sectional anatomy of the brain (Figs. 18.3 – 18.5) is a prerequisite for proper interpretation of brain imaging since tomographic imaging is the rule in current functional neuroimaging.

Neuronal blood flow utilization is related primarily to synaptic activity at the neuron cell body; thus gray matter requires about four times as much blood flow as white matter. In the normal brain the overall determinant of regional cerebral blood flow (rCBF) is dependent on vascular integrity, cerebral anatomy, and cerebral function. Since diseases of the brain can disrupt

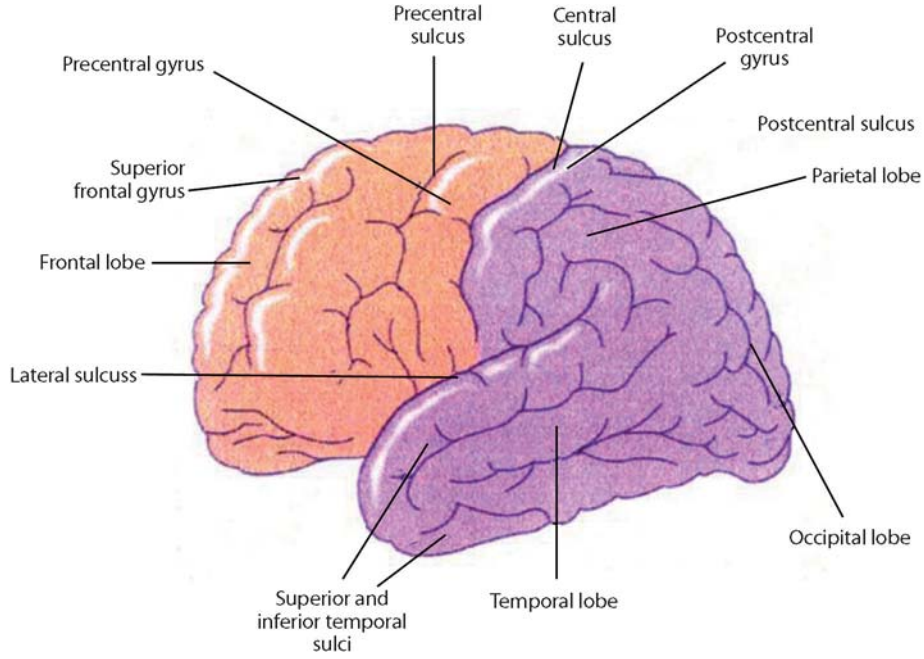

Fig. 18.1. Diagram of the lateral surface of the brain illustrating its main anatomic features (AHE)

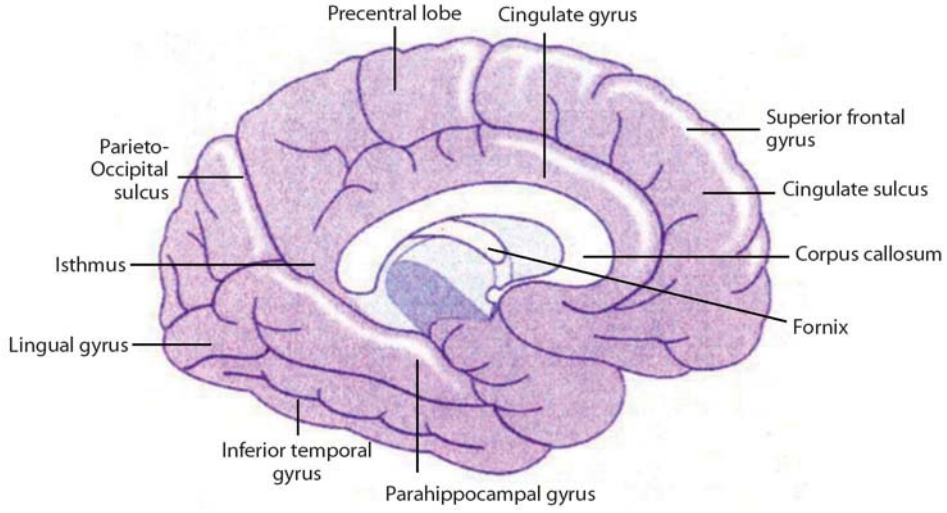

Fig. 18.2. Diagram of the brain illustrating the main internal structures (AHE)

one or more of these functions, for accurate diagnosis it is important to integrate these three physiological functions with the pattern of rCBF change from normalcy to arrive at an accurate diagnosis of disease. In this chapter a review of radiopharmaceuticals commonly used to diagnose brain diseases is presented. This is followed by classes of disease which result in relatively specific patterns of abnormal tracer distribution, thus allowing for a specific diagnosis from the nuclear medicine scan.

Interpretation of brain SPECT studies depends on a background of neuroanatomy which with current techniques allow co-registration of MRI and CT with the functional images of SPECT and PET (Figs. 18.3 – 18.5). Perfusional changes noted with SPECT radiotracers are appreciated due to the differences in the cortical gray to white matter perfusion related to the large amount of neurons in the cortex. Coupling of perfusion and metabolism provides functional information regarding the state of the patient during tracer injection with Tc-99m-HMPAO and Tc-99m-ECD. Outside the US other perfusional tracers in use include I-123-IMP. Magnetic resonance imaging evaluating the degree of myelination, I-123-IMP SPECT, and O-15-PET studies have re-

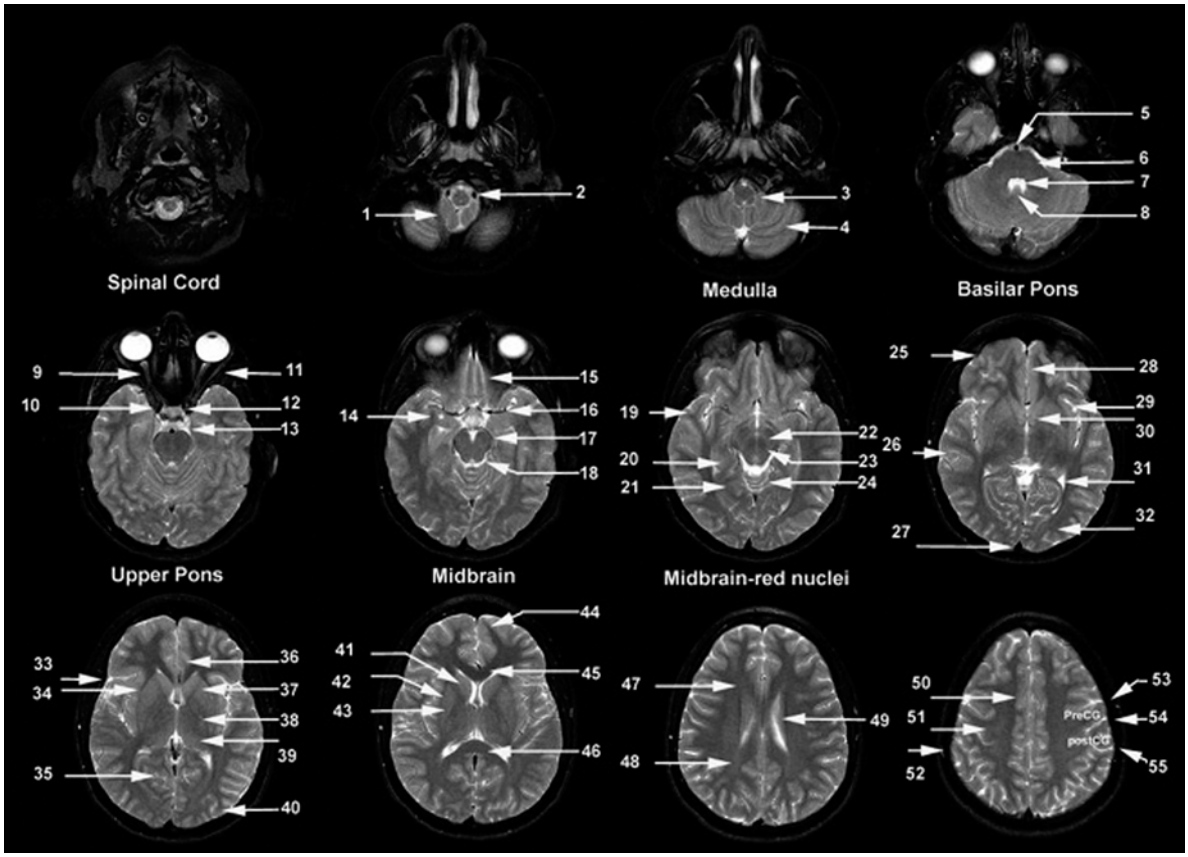

Fig. 18.3. Axial T2 weighted MR images: *1* cerebellar tonsil, *2* vertebral artery, *3* medulla, *4* cerebellar hemisphere, *5* basilar artery, *6* pons, *7* 4th ventricle, *8* uvula, *9* optic nerve, *10* internal carotid artery siphon, *11* lateral rectus muscle, *12* pituitary gland, *13* ambient cistern, *14* amygdala, *15* gyrus rectus, *16* middle cerebral artery, *17* posterior cerebral artery, *18* mesencephalic cistern, *19* temporal pole, *20* hippocampus, *21* parahippocampal gyrus, *22* substantia nigra, *23* red nucleus, *24* cerebellar vermis, *25* frontal lobe, *26* temporal lobe, *27* superior sagittal sinus, *28* gyrus rectus *29* insular cortex, *30* anterior commissure, *31* posterior horn lateral ventricle, *32* occipital lobe, *33* sylvian fissure, *34* external capsule, *35* calcarine sulcus, *36* cingulate gyrus, *37* anterior limb of the internal capsule, *38* posterior limb of the internal capsule, *39* thalamus, *40* occipital lobe, *41* head of the caudate nucleus, *42* putamen, *43* globus pallidus, *44* frontal pole, *45* genu of the corpus callosum, *46* splenium of the corpus callosum, *47* forceps minor, *48* forceps major, *49* caudate nucleus, *50* cingulate gyrus, *51* centrum semiovale, *52* calvarial marrow, *53* precentral sulcus, *54* central sulcus, *55* postcentral sulcus, *PreCG* precentral gyrus, *PostCG* postcentral gyrus

vealed a parallel course of cortical gray and white matter maturation and cerebral perfusion during child development. From these studies, an adult regional cerebral blood flow pattern is reached at 2 years of age [1, 2, 2a, 2b]. Figure 18.6 illustrates the correlative anatomy to help understand the normal distribution of the commonly used Tc-99m-HMPAO in relation to morphologic details of the brain.

▷

Fig. 18.4. Coronal FLAIR MR images: *1* superior frontal gyrus, *2* orbit, *3* interhemispheric fissure, *4* frontal pole, *5* orbital gyrus, *6* superior sagittal sinus, *7* cingulate gyrus, *8, 9* gyrus rectus, *10* superior sagittal sinus, *11* genu of the corpus callosum, *12* temporal pole, *13* anterior horn lateral ventricle, *14* mesial temporal lobe, *15* cingulate gyrus, *16* corpus callosum, *17* optic nerve, *18* cavernous sinus, *19* head of the caudate nucleus, *20* lenticular nucleus, *21* sylvian fissure, *22* insular cortex, *23* amygdala, *24* corpus callosum, *25* hippocampus, *26* basilar artery, *27* sylvian fissure, *28* superior temporal gyrus, *29* middle temporal gyrus, *30* inferior temporal gyrus, *31* cingulate gyrus, *32* thalamus, *33* parahippocampal gyrus, *34* vestibulocochlear nerve, *35* central sulcus, *36* sylvian fissure, *37* mesencephalon, *38* medulla, *39* paracentral lobule, *40* cingulate gyrus, *41* 4th ventricle, *42* transverse sinus, *43*, tentorium, *44* cerebellar vermis, *45* cerebellar hemisphere, *46* cuneus

▷

Fig. 18.5. Sagittal T1 weighted MR images: *1* central sulcus, *2* temporal pole, *3* parahippocampal gyrus, *4* frontal pole, *5* ascending branch of cingulate sulcus, *6* paracentral sulcus, *7* cingulate sulcus, *8* ascending branch of cingulate sulcus, *9* scalp, *10* calvarium, *11* superior sagittal sinus, *12* cerebellar tonsil, *13* genu of the corpus callosum, *14* pituitary gland, *15* clivus, *16* splenium of the corpus callosum, *17* tectal plate, *18* aqueduct of the 3rd ventricle, *19* 4th ventricle, *20* mammillary body, *21* head of the caudate nucleus, *22* thalamus, *23* parieto-occipital sulcus, *24* calcarine sulcus, *25* central sulcus, *26* post-central sulcus, *27* insular cortex, *28* sylvian fissure, *OL* occipital lobe, *P* pons, *TH* thalamus

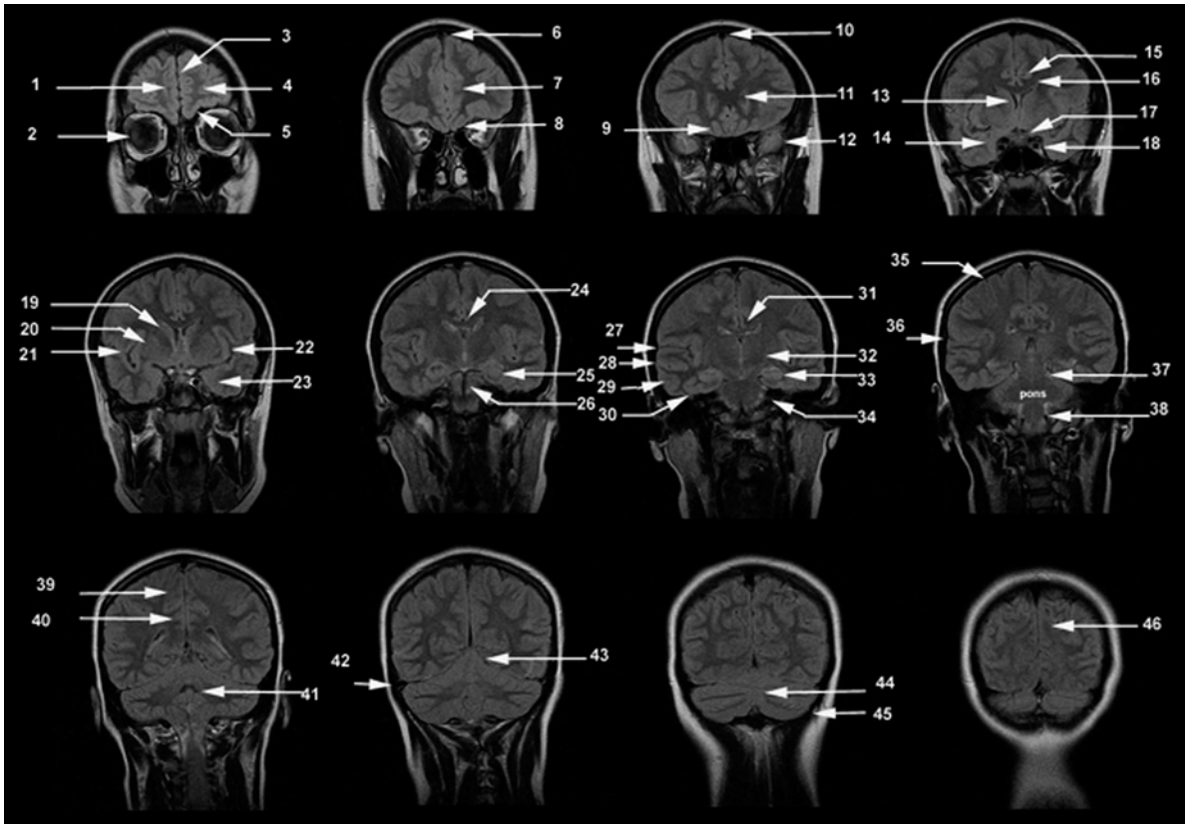

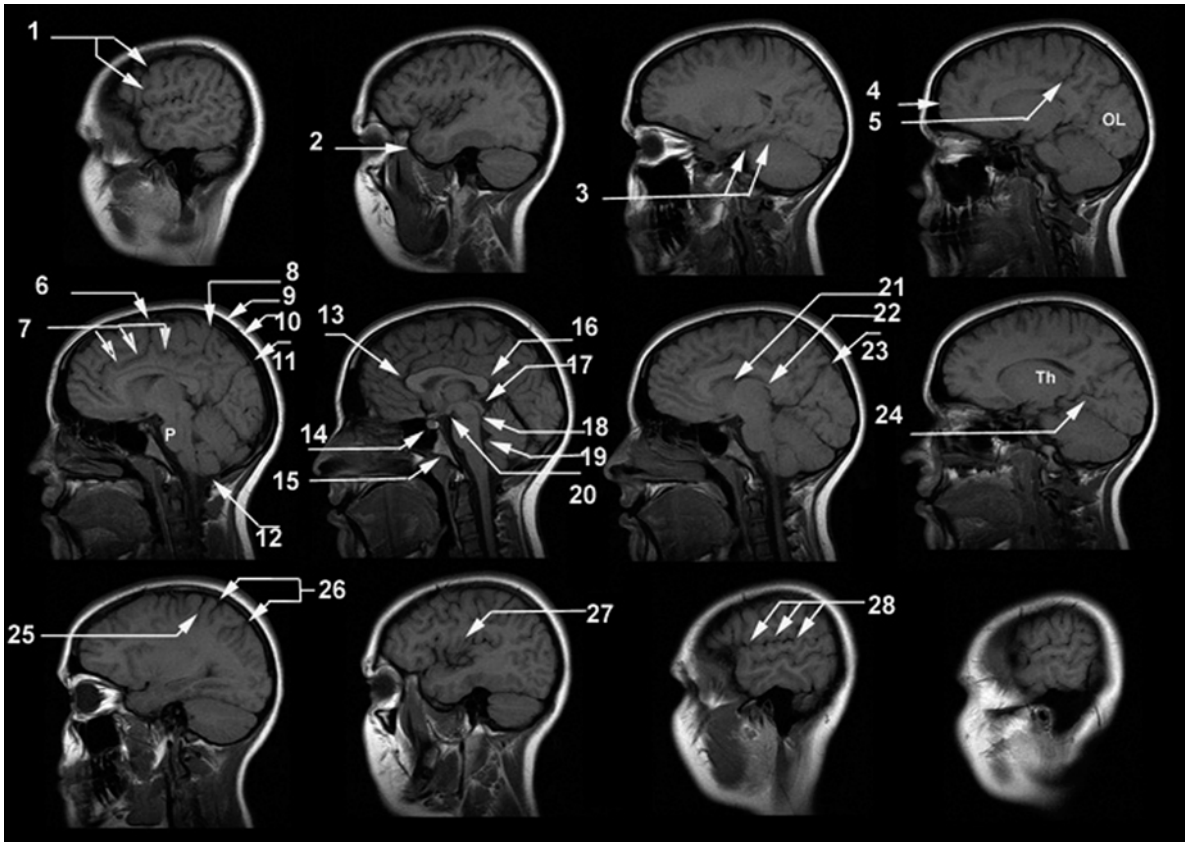

Fig. legends 18.4 (top) and 18.5 (bottom) see p. 450

18.2 Radiopharmaceuticals

There are three main classes of radiopharmaceuticals now available for functional brain imaging in nuclear medicine: (1) regional cerebral blood flow, (2) regional cerebral metabolism and (3) central nervous system receptor binding agents. After intravenous injection the regional uptake and distribution of radiotracers are measured by single photon emission computed tomography (SPECT) or positron emission tomography (PET) imaging systems. The following review describes the most important tracers routinely employed in clinical nuclear medicine practice. More comprehensive descriptions of radiopharmaceuticals for brain imaging have been provided in numerous previous reports [1].

SPECT radiopharmaceuticals used for measuring regional cerebral blood flow (rCBF) are lipophilic agents which are transported from the arterial vascular compartment to the normal brain tissue compartment by diffusion, and are distributed proportional to regional tissue blood flow. After this first phase of transport the tracers are essentially irreversibly trapped in the tissue compartment. The two major blood flow agents used in brain SPECT imaging are technetium-99m-hexamethylpropylene amine oxime (Tc-99m-HMPAO) and Tc-99m-ethyl cysteinate dimer (Tc-99m-ECD) [2, 3]. Xenon-133 is unique since it is freely diffusable, and not trapped in the tissues. Inhaled or I.V. injection of Xe-133 dissolved in saline can more accurately and quantitatively provide measurements of blood flow by determination of the clearance rate of this tracer from the cerebral compartment, after a brief uptake period (Lassen) [4]. The major PET radiopharmaceutical used to measure cerebral perfusion is O-15 H2O [5].

The second major class of radiopharmaceuticals is those that measure brain metabolism. These radiopharmaceuticals are transported to the brain tissues by regional cerebral blood flow, but subsequent regional cerebral distribution reflects the utilization rate of the tracer in a cerebral metabolic pathway. Currently, there are no SPECT tracers that specifically measure normal cerebral metabolism. However, in brain tumor imaging, where the blood brain barrier is broken, ionic tracers such as thallium-201 [6], or other SPECT tracers such as Tc-99m-methoxylisobutylnitrile (Tc-99m-MIBI) [7], can be used to detect new, recurrent or residual viable tumor. The PET radiopharmaceutical predominantly used is F-18 2-fluoro-2-deoxy-d-glucose (F-18-FDG) [8]. [F-18]-fluoro-3'-deoxy-3'-l-fluorothymidine (FLT) is a new tracer used to indicate tumor proliferation to more specifically identify new, recurrent or residual viable brain tumor.

The third class of radiotracers important in brain imaging is central nervous system receptor binding agents, which measure neuronal receptor density and binding affinity [9]. In SPECT, a tracer which has been well characterized is I-123 β-CIT. This benzamide compound has been used to image the dopaminergic (D_2) transporter system in the corpus striatum [10].

Numerous reviews have been published describing the hundreds of PET tracers that have been developed for application in brain PET imaging, primarily for brain receptor studies or metabolic incorporation into essential biochemical pathways [11, 12]. After I.V. injection, these tracers initially follow first order kinetics compartmental distribution since their delivery depends on cerebral blood flow. Over time there is clearance of nonspecific uptake, and the delayed scan reflects specific receptor binding.

18.2.1 Tc-99m-Hexamethylpropylene Amine Oxime

To understand the uptake mechanism of Tc-99m hexamethylpropylene amine oxime (Tc-99m-HMPAO), a three compartmental analysis model can be used for analysis [13]. In this model the first compartment is the lipophilic tracer in the blood pool of the brain, but outside of the blood brain barrier. The second compartment comprises the lipophilic tracer inside of the blood brain barrier. The third compartment is the hydrophilic form of the tracer that is retained in the brain. Transport from the first compartment to the second compartment represents efflux of lipophilic tracer from the blood compartment to the brain compartment. Back-exchange from the third compartment to the second compartment represents back-diffusion of the lipophilic form of the tracer, and is essentially equal to zero since the tracer is irreversibly trapped (by intracellular reaction with glutathione) in the brain. Figure 18.6 shows a normal Tc-99m-HMPAO brain SPECT scan after injection of 20 mCi (740 MBq) I.V. acquired on the Picker Prism triple head camera (Picker International, Cleveland, OH). Excellent uptake of this tracer in the gray matter of the brain is noted, and there is clear distinction of small brain structures.

18.2.2 Tc-99m-Ethyl Cysteinate Dimer

The second tracer commonly used in brain SPECT to measure regional cerebral perfusion is Tc-99m-ethyl cysteinate dimer (Tc-99m-ECD) [14]. This radiopharmaceutical is lipophilic, similar toTc-99m-HMPAO and rapidly traverses the endothelium and capillary membranes into the brain cells [15]. However, in the third compartment irreversible trapping mechanism of this tracer differs from Tc-99m-HMPAO, since Tc-99m-ECD is enzymatically metabolized to a polar complex,

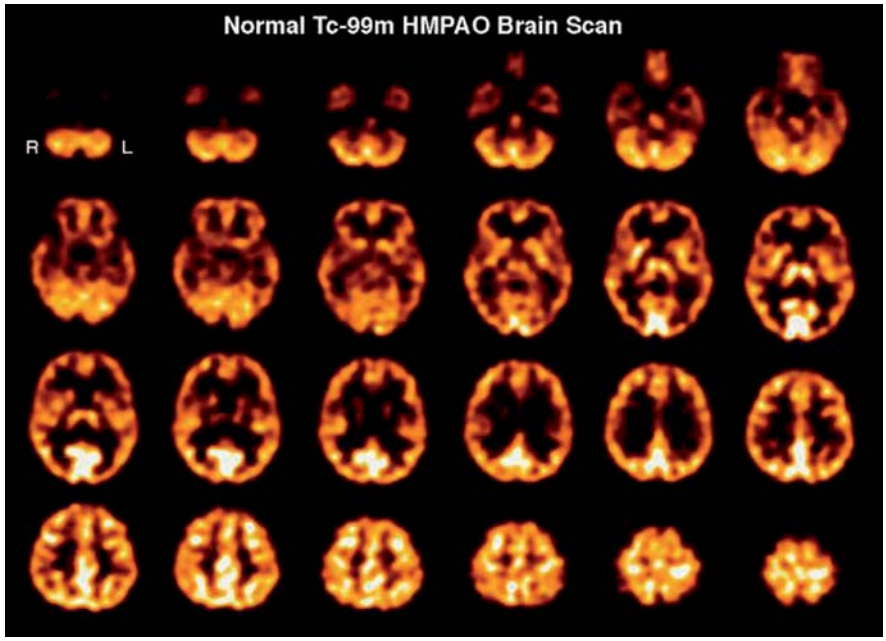

Fig. 18.6. Transverse tomographic images from a normal 42-year-old female subject after injection of 20 mCi Tc-99m-HMPAO. The transverse images are arranged parallel to and sequentially above the canthomeatal line, with the cerebellum at the *top left* and the vertex of the brain at the *bottom right*. The scan slice thickness is 4 mm. The scan resolution is approximately 7 mm full width at half maximum. There is seen to be high uptake of tracer in the cerebellum (*top row*), the thalamus and basal ganglia (*2nd row from top*), and the primary visual cortex (*2nd and 3nd row from top*). There is high uptake in all cortical structures compared to white matter. This is expected since the white matter physiologically has approximately 25% lower blood flow than gray matter. The ventricles in this patient are extremely small and the central reduction in tracer uptake is almost completely due to lower uptake in the white matter. These differences in uptake bestow the functional scan with anatomic definition

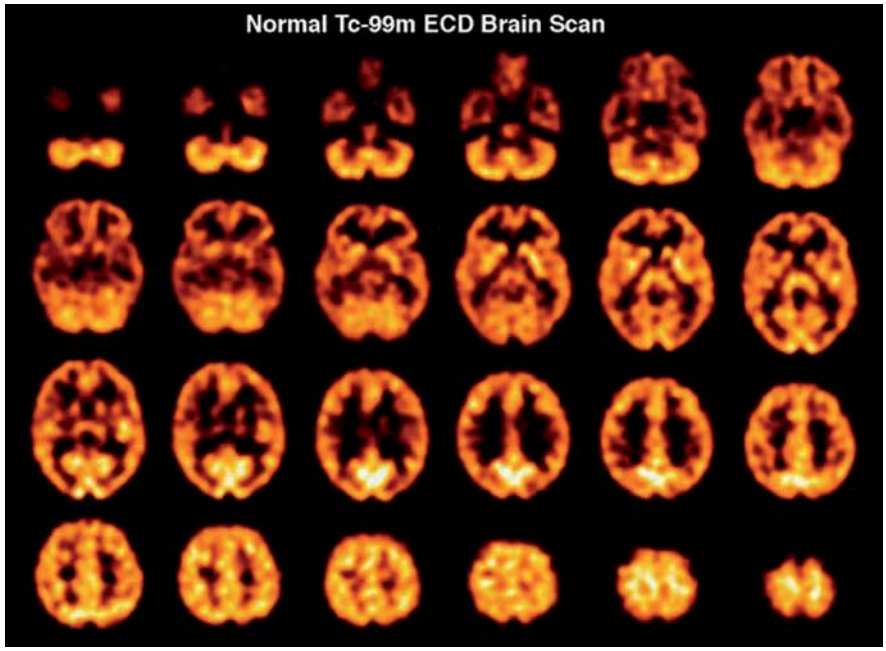

Fig. 18.7. Transverse tomographic images from a normal 41-year-old female subject after injection of 20 mCi Tc-99m-ECD. The transverse images are arranged parallel to and sequentially above the canthomeatal line, with the cerebellum at the *top left* and the vertex of the brain at the *bottom right*. The scan slice thickness is 4 mm. The scan resolution is approximately 7 mm full width at half maximum. While the distribution of Tc-99m-ECD is similar to Tc-99m-HMPAO, it is not identical, as described in the text

which is trapped in the brain. This tracer has been reported to demonstrate less non-specific scalp and facial tissue background activity compared with Tc-99m-HMPAO. Figure 18.7 shows a normal Tc-99m-ECD scan brain SPECT scan after injection of 20 mCi (740 MBq) I.V. However, it has been reported that there are differences in regional uptake of these tracers, predominantly in the thalamus and the cerebellum.

This difference in distribution is illustrated by scans from a 42-year-old female normal subject who received both tracers separated by a 48-h time period (Fig. 18.8).

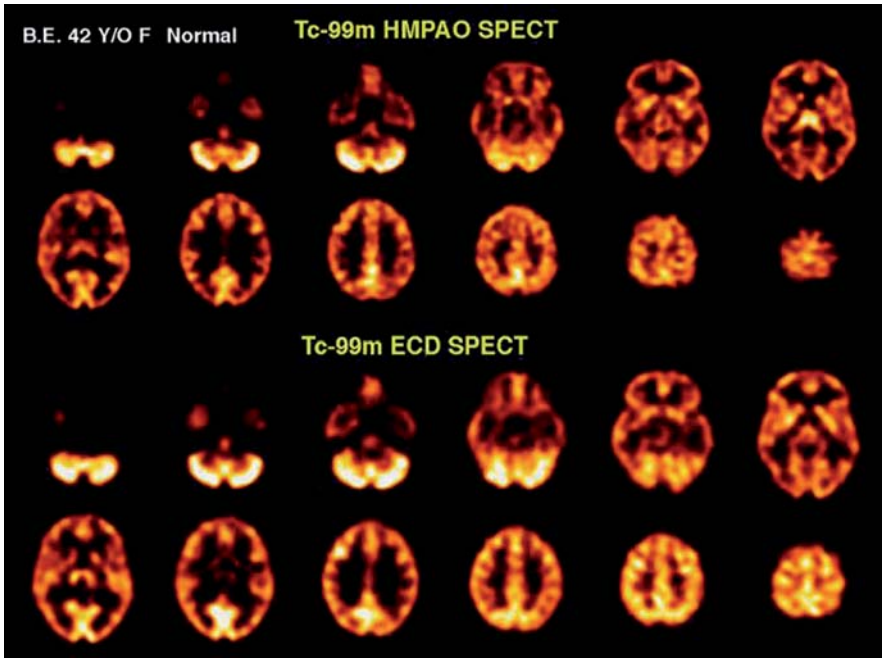

Fig. 18.8. Images of a Tc-99m-HMPAO brain SPECT scan (*top*) compared with a Tc-99m-ECD brain SPECT scan (*bottom*) from a 42-year-old normal female. The Tc-99m-HMPAO SPECT scan was oriented parallel to and sequentially above the canthomeatal line (*rows 1 and 2*). The Tc-99m-ECD brain SPECT scan from the same patient was count normalized and spatially co-registered with the Tc-99m-HMPAO SPECT scan and corresponding sections are displayed in *rows 3 and 4* to facilitate comparison. Each scan section is 8 mm thick. The Tc-99m-HMPAO brain SPECT scan shows increases in tracer uptake in the thalami but less uptake in the parietal and occipital regions, as compared to the Tc-99m-ECD brain SPECT scan

18.2.3 Xe-133 for Quantitative Regional Cerebral Blood Flow

Another recent advancement in brain SPECT imaging has been the development of special software primarily used on the Picker Prism triple head camera system which allows dynamic scan acquisition (10 s per scan for 7 min). This acquisition results in a total of 42 scans of temporally separated individual tomographic image data sets. This allows calculation of tomographically displayed absolute quantification of regional cerebral perfusion (rCBF) in milliliters per 100 g of tissue per minute [16]. This is possible since the clearance of xenon-133 is linearly proportional to the rCBF, and unlike tracers such as Tc-99m-HMPAO or Tc-99m-ECD, Xe-133 does not underestimate rCBF due to the limitations on extraction fractions at high cerebral blood flow rates. In our experience we have found that the xenon-133 clearance technique is more sensitive to changes in blood flow during Diamox augmentation of rCBF in the evaluation of hemodynamically significant vascular stenosis, and in cases of cortical blood flow changes in brain activation studies. One of the major limitations of xenon-133 SPECT is the relatively low energy of the emission photon, resulting in a significant attenuation and loss of spatial resolution of the central structures of the brain. In addition, due to the rapid SPECT acquisition necessary to obtain accurate clearance on a pixel by pixel basis, the count rate is low, requiring use of a 64× 64 matrix, resulting in reduction in spatial resolution throughout the scan.

Dynamic Xe-133 SPECT is excellent in assessing large territorial vascular abnormalities due to its ease of quantitation and its ability to detect large major vessel territorial reductions in regional cerebral perfusion. Its utility is exemplified in a study designed to measure cerebrovascular perfusion reserve with rest/stress SPECT brain scans in patients with cerebrovascular disease (CVD) and suffering from TIA undergoing evaluation for extracranial/intracranial (EC/IC) arterial anastomosis or superficial temporal artery (STA)/middle cerebral artery (STA-MCA) bypass to assess and to specifically identify the presence or the absence of a vascular reserve constraint, which has been previously documented to be of value using increased oxygen extraction fraction PET [17].

Figure 18.9 illustrates the imaging results of a 62-year-old female with TIA. The angiogram showed the presence of a 99% left ICA stenosis. The Xe-133 SPECT study confirms the presence of hemodynamic vascular reserve constraint due to a high-grade stenosis of the left internal carotid artery.

In a study on nine CVD patients, Tc-99m-HMPAO SPECT was found to be a more specific indicator of hemodynamic constraint since it was asymmetric only in cases of severe ischemia [18]. Xe-133 SPECT detected asymmetries, even in the mild ischemic group, and therefore is a more sensitive detector of vascular disease. Because xenon-133 SPECT measures absolute rCBF (ml/100 g/min), it has one major advantage (i.e., to measure absolute perfusion) and thus can establish parameters of significant ischemia independently from semiquantitative asymmetry values.

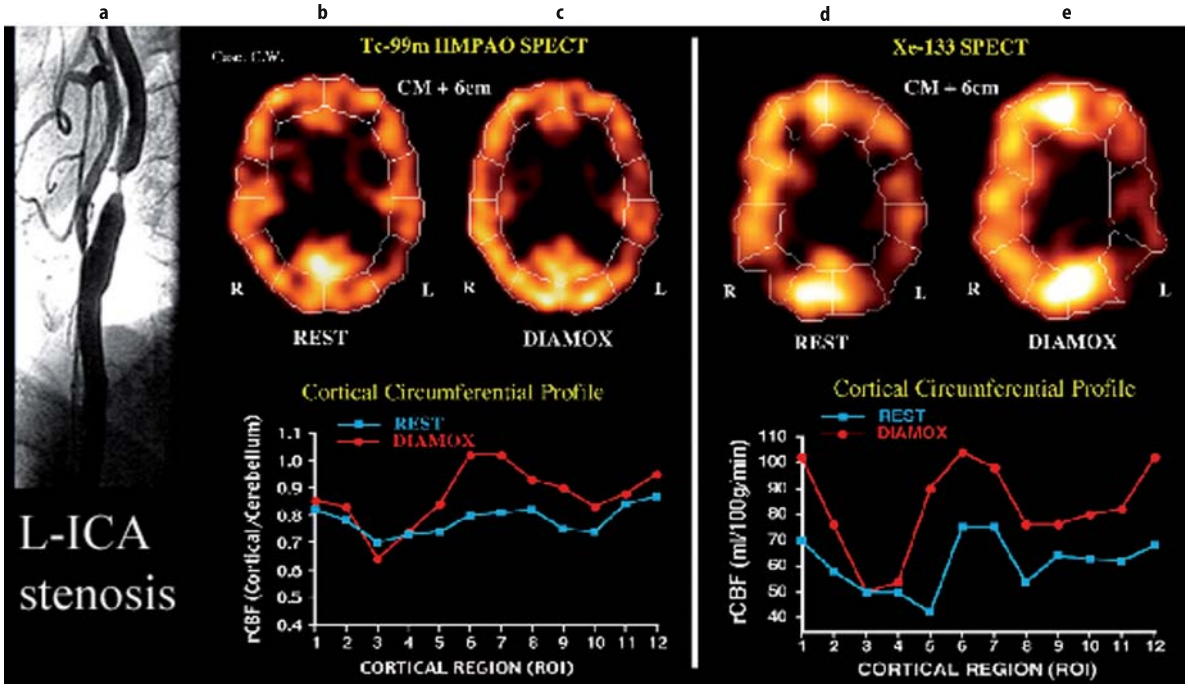

Fig. 18.9. Case of severe ischemia in a 62-year-old female with 99% stenosis of the left ICA (**a**). The resting state Tc-99m-HMPAO SPECT scan (**b**) was normal. The post-Diamox Tc-99m-HMPAO SPECT scan (**c**) showed mild perfusion reduction in the left ICA territory. This can be seen on the circumferential graphs (*regions 3 and 4 shown on the red graph below figures*). The Xe-133 SPECT at rest showed mild vascular compromise (**d**). The post-Diamox Xe-133 SPECT showed severe vascular constraint in the left ICA territory (**e**). This can be seen as a more clear reduction compared with the Tc-99m-HMPAO SPECT scan (*regions 3 and 4 shown on the circumferential red graph below figures*)

18.2.4 O-15 H_2O for Quantitative Regional Cerebral Perfusion Measured by PET

Dynamic O-15 H_2O PET scans with arterial sampling provide the ability for quantitative assessment of regional cerebral perfusion. Each emission scan is short, approximately 3 min in duration. Data are typically analyzed using a one-tissue compartment model to obtain K1 (ml/min/ml) and quantification is expressed in standard units of ml/100 g/min [19].

The PET scans shown in Fig. 18.10a were acquired on a Siemens/CTI ECAT HR+ scanner in 3D imaging mode (63 parallel planes); axial field-of-view: 15.2 cm; in-plane resolution: 4.1 mm full-width at half-maximum; slice width: 2.0 mm. The scanner gantry was equipped with a Neuro-insert (CTI PET Systems, Knoxville, TN) to reduce the contribution of scattered photon events. PET data was reconstructed using filtered back-projection (Fourier rebinning and 2D back-projection with a Hann filter: kernel FWHM = 3 mm). Data was corrected for photon attenuation, scatter, and radioactive decay. A windowed transmission scan (10 – 15 min) was obtained for attenuation correction using rotating 68Ge/68Ga rods and a model-based correction was applied to account for the 3D scatter fraction. The final reconstructed PET image resolution was about 6 mm (transverse and axial planes). PET-MRI fusion images shown in Fig. 18.10b are obtained from the MRI data that were transferred to the PET facility and co-registered to the dynamic O-15 H_2O PET scans by automated image registration (AIR) software [20].

18.2.5 Thallium-201

Thallium-201 in the form of thallous chloride is a cyclotron produced radiopharmaceutical shown to have affinity for brain tumors as early as the 1970s [21]. Although more commonly used as a myocardial perfusion imaging agent, thallium has high sensitivity for detection of new, recurrent or residual viable tumors, which are difficult to differentiate from post-radiation necrosis and edema on CT or MRI.

Thallium decays by electron capture with a half-life of 73 h and emits photons with a range of 0.78 – 167.4 keV [22]. The useful energy for imaging is at 80 keV, corresponding to mercury X-rays when thallium decays to stable Hg-201. In its intravenous form, thallium-201 is supplied in isotonic solution at pH 4.5 – 7.0 and contains NaCl for isotonicity and 0.9% benzyl alcohol as a bactericidal agent [23]. The uptake of thallium in normal tissues has been hypothesized to act as a potassium analogue.

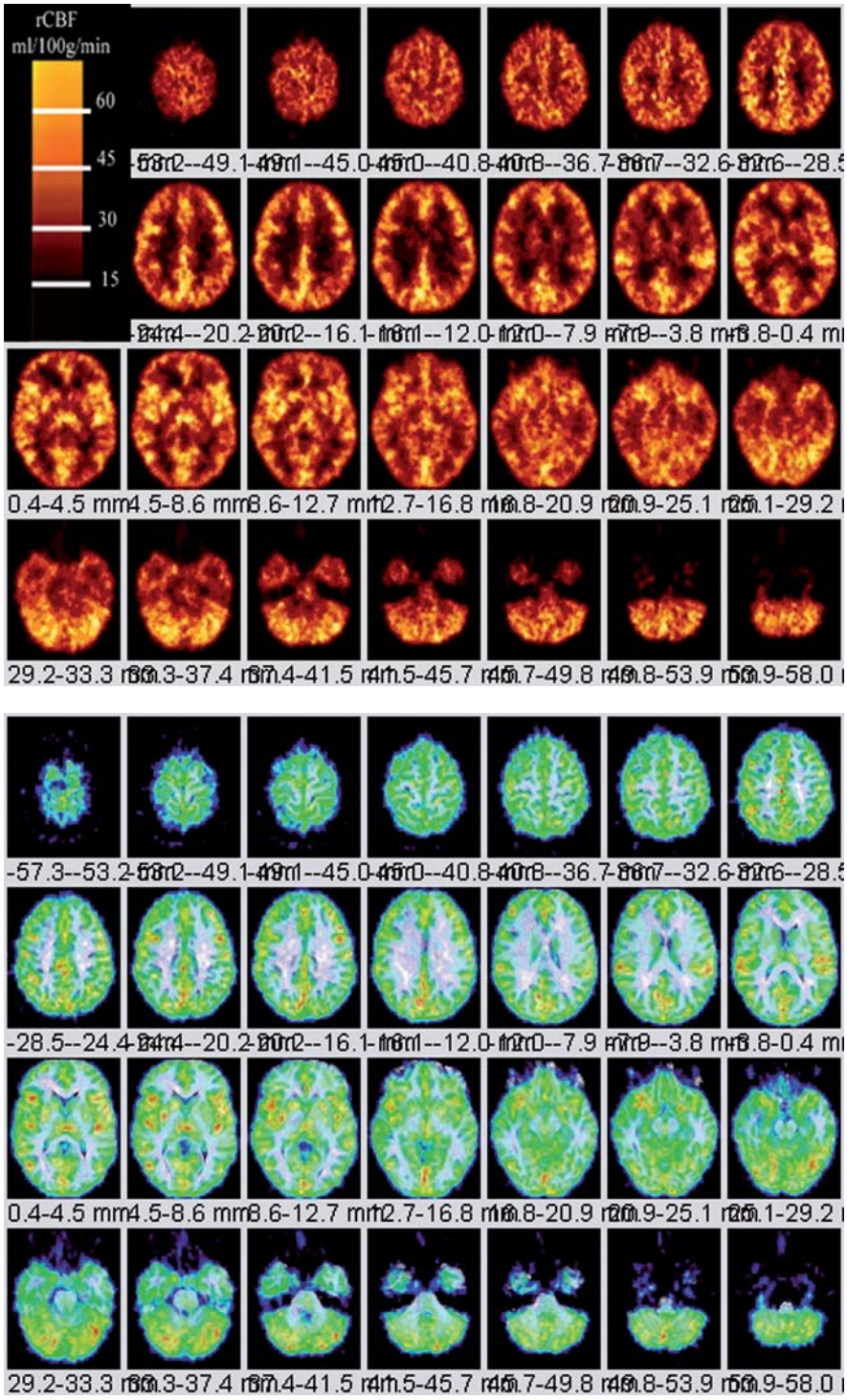

Fig. 18.10. a Dynamic O-15 H_2O water PET scans from the top of the brain (*top left*) through the cerebellum (*bottom right*) from a 36-year-old normal female volunteer for measurement of quantitative regional cerebral perfusion. PET scans are obtained from a Siemens CTI ECAT HR+ operating in 3D mode. Regional cerebral blood flow (*rCBF*) quantified in units of ml/100 g/min (*color bar*). **b** PET scan was co-registered using the Automated Image Registration Software onto a spoiled gradient echo (SPGR) MRI data volume (1-mm-thick MRI sections) resectioned and co-registered using the AIR routine to the O-15 H_2O PET scans. Careful examination reveals increased blood flow localized to the gray matter regions of brain

Both elements belong to group IIIA of the periodic table. The distribution and retention of thallium-201 in the normal brain and tumors is an active process related to blood flow, loss of integrity of the blood-brain-barrier, tumor cell viability, tumor type, tumor cell membrane function and the Na^+K^+ ATP^{ase} pump activity.

Normal brain tissues show minimal to no uptake of thallium-201. The normal physiologic distribution in the head and neck region includes the scalp, lachrymal gland, nasopharyngeal area, salivary gland and the pituitary gland. There is also minimal thallium uptake in the choroid plexus. Thallium is normally taken up by

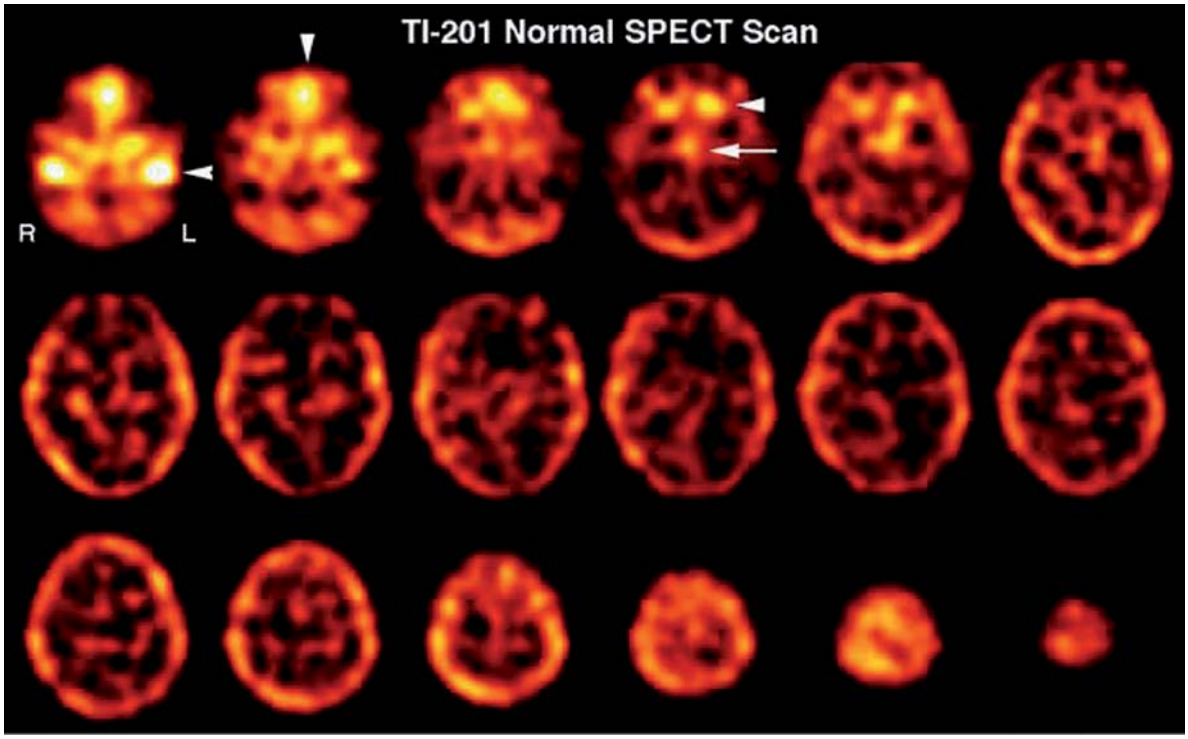

Fig. 18.11. SPECT scan of thallium-201 in normal brain. Uptake of thallium-201 in normal brain is very low. It is important to note that there is significant uptake by some of the structures just inferior to the cranium, which can interfere with the positive detection of tumor in the inferior frontal and inferior mid-portions of the brain. There is significant uptake in the jugular veins (*row one, image one, arrow*), the nasopharynx (*row one, image two, arrow*), the salivary glands and pituitary glands (*row one, image four, arrowhead and arrow, respectively*)

regions of the brain which do not have a blood brain barrier (BBB) such as the pituitary gland, pineal gland, and are minimally taken up by the choroid plexus (Fig. 18.11). The evaluation of viable tumor can be performed with great accuracy using brain SPECT or brain PET imaging. Brain SPECT imaging employs the tracer thallium-201 to detect new, residual, or recurrent viable tumor due to the fact that there is transport of thallium-201 across the breakdown in the blood brain barrier, and uptake of thallium-201 into regions of hypermetabolism. Thallium-201 is postulated to represent a "potassium analogue" with affinity for the sodium potassium ATPase enzyme [24]. Thallium accumulates in the residual or recurrent viable tumor cells in proportion to malignant grade and total viable tumor bulk.

18.2.6 Tc-99m-Hexakis-2-methoxy-2-isobutyl Isonitrile

Tc-99m-Hexakis-2-methoxy-2-isobutyl isonitrile (Tc-99m-sestamibi) (Tc-99m-MIBI) is a monovalent cation complex formed by a central technetium atom surrounded by six 2-methoxy-2-isobutyl isonitrile groups. This compound is also used extensively in myocardial perfusion imaging. Normal brain tissue shows minimal uptake of Tc-99m-sestamibi. The normal physiologic distribution in the head and neck region is similar to that of thallium and includes the scalp, nasopharyngeal area, salivary gland, and the pituitary gland. There is notable significant choroid plexus uptake, much greater when compared to thallium-201. The choroid plexus uptake may be due in part from the pertechnetate in the solution that is known to be actively taken up and secreted by the cells. This may account for secretion into the CSF and the presence of activity in the fourth ventricle which is visible on careful scrutiny of MIBI brain SPECT images (Fig. 18.12). It is postulated that after crossing the cell membrane MIBI is taken by the mitochondria in relation to negative electric potential. Normal myocardial uptake of MIBI depends on blood flow and the uptake of the mitochondria in metabolically active tissue. In brain tumors the mechanism of tumor uptake is also thought to be dependent on mitochondrial activity and the presence of P-glycoprotein [25].

18.2.7 2-[F-18]Fluoro-2-deoxy-d-glucose

A 36-year-old normal female volunteer underwent a fully dynamic 2-[F-18]fluoro-2-deoxy-d-glucose (F-18-

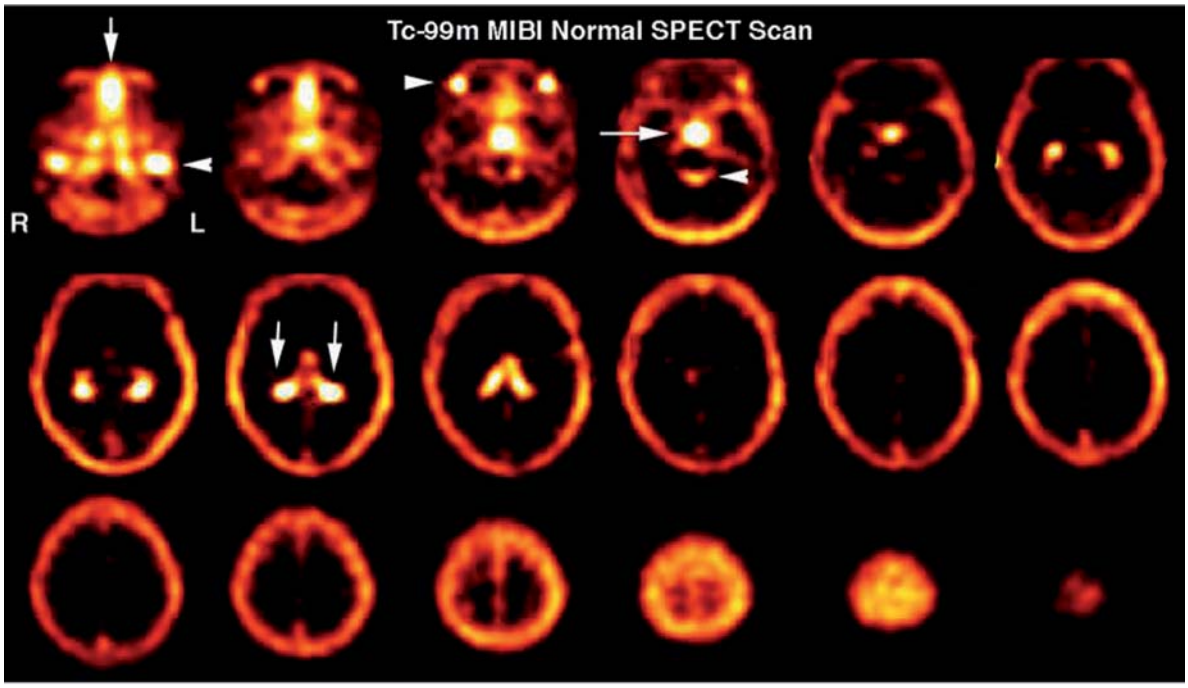

Fig. 18.12. Normal Tc-99m-MIBI brain SPECT scan. The figure shows very low uptake of MIBI in normal brain. However, similar to the thallium brain SPECT scan there are several structures just inferior to the cranium which can interfere with accuracy of tumor recurrence identification. As seen in the normal thallium-201 brain SPECT scan there is intense uptake in the jugular veins (*row one, image one, arrow*), the nasopharynx (*row one, image one, arrow*). There is also intense uptake in the salivary glands (*row one, image three, arrow*) and the pituitary gland (*row one, image three, arrow*). In addition, there is increased uptake in the ambient cistern (*row one, image four, arrow*) due to secretion of significant Tc-99m-MIBI through the choroid plexus (*row two, image two, arrows*). This secretion by the choroid plexus often significantly limits the utility of this tracer in the detection of recurrent tumor since many tumors tend to recur in the region of the basal ganglia

FDG) PET with arterial sampling at rest as shown in Fig. 18.13. F-18-FDG PET scan image slice thickness = 2.0 mm and reconstructed in plane image resolution = 4 mm FWHM. The F-18-FDG PET data is acquired over 90 min (34 frames) with arterial blood sampling throughout the scan period. The method of quantitative assessment of F-18-FDG PET has been well established [26–30].

F-18-FDG PET has led to a more widespread capability in allowing evaluation of cerebral neoplasms as well as other diseases of the brain which were previously imaged using SPECT radiopharmaceuticals [31, 32]. In addition, due to the relatively long half-life of F-18 (109 min), it can be transported regionally (within approximately 2–4 h travel time from a cyclotron production facility), enabling a centrally located production facility to supply several camera sites.

18.2.8 Dopamine Transporter Receptor Binding Agents

A relatively new tracer which will have a significant impact on nuclear medicine is the I-123-labeled I-123-*N*-methyl-2-beta-carbomethoxy-3-beta-(4-iodophenyl)-tropane (I-123-β-CIT), which is used for imaging of the dopamine and serotonin transporters by SPECT [33, 34]. It has currently been used for evaluations of patients with Parkinson's disease [34]. Imaging is performed after the injection of 185 MBq (5 mCi) of I-123-β-CIT 90–120 min post-injection. In most patients with Parkinson's disease there is a marked asymmetric uptake in the putamen and caudate head nuclei. The degree of diminution can estimate the extent of niagrostriatal degeneration in Parkinson's disease patients.

The evaluation of movement disorders, principally Parkinson's disease, has been greatly advanced using dopamine tracers. Several studies have now established that the posterior-inferior aspect of the globus pallidus shows diminution of tracer uptake using I-123-β-CIT, as illustrated in Fig. 18.14. Use of this tracer in conjunction with anatomic-functional fusion imaging can be used for precision stereotactic ablation or dopamine supplementary implants. Preliminary results of these studies show excellent utility in patients with Parkinson's disease who otherwise are refractory to l-dopa therapy.

The cocaine derivative I-123-β-CIT binds with high affinity to dopamine uptake sites in the striatum and

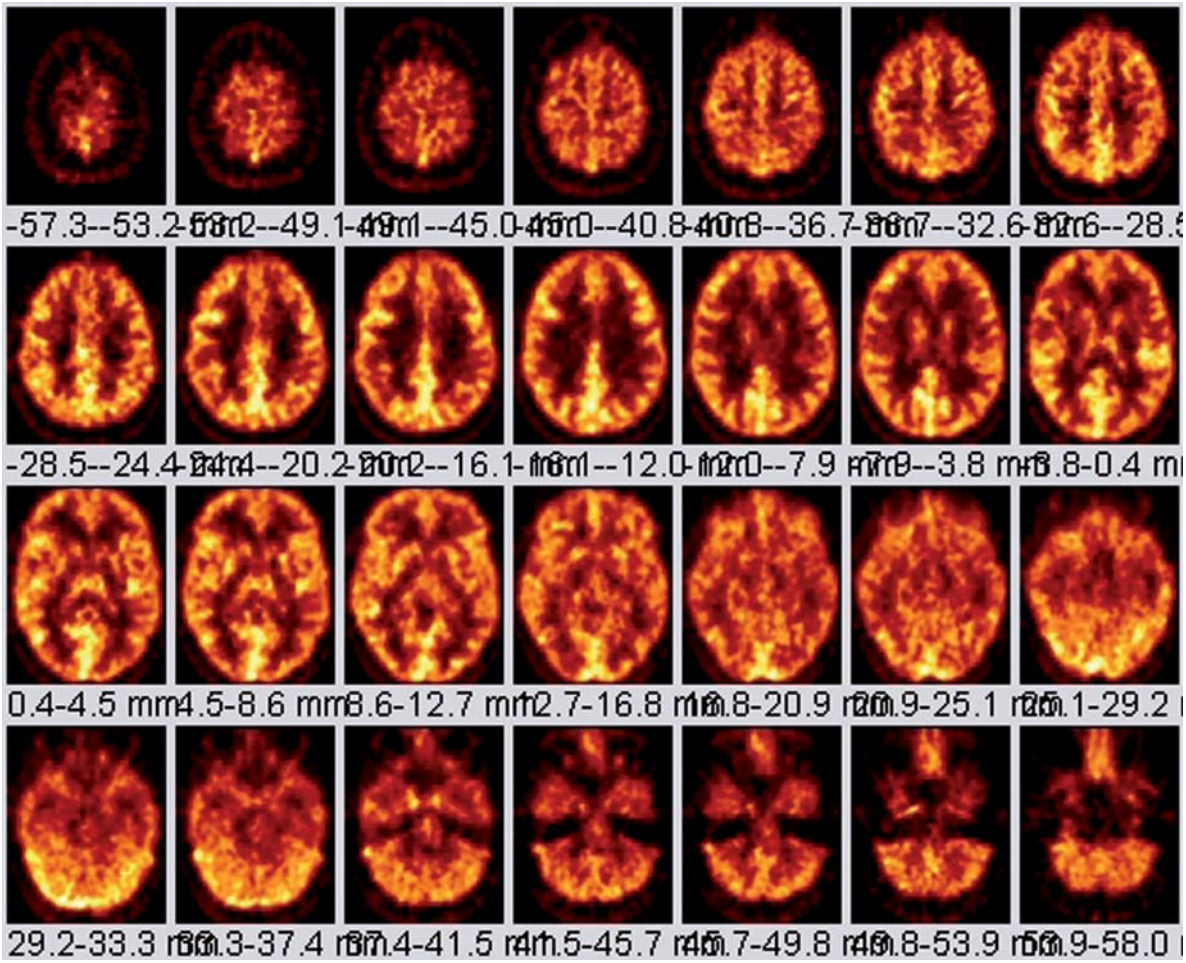

Fig. 18.13. Normal F-18 FDG PET brain scan in a 36-year-old normal female volunteer who underwent fully dynamic F-18-FDG PET with arterial sampling at rest

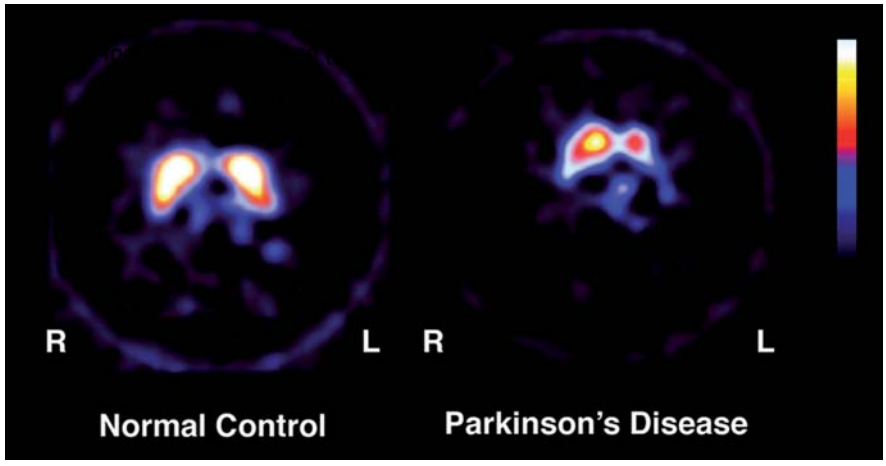

Fig. 18.14. Delayed images of I-123-β-CIT. Images were obtained 4 h after the intravenous injection of 5 mCi of I-123-β-CIT in a 57-year-old normal control (*left*), compared with a 62-year-old male with Parkinson's disease (*right*). The normal control shows almost complete clearance of the tracer from all cortical and white matter regions of the brain except for the corpus striatum, which appears as "bright" comma shaped objects in the center of the brain. There is symmetry comparing the left corpus striatum to the right corpus striatum. The specificity of binding is due to the specific prevalence of dopamine uptake sights in these brain structures. The *image on the left* shows significant reduction of uptake, which is asymmetric and lower in the left corpus striatum. Semiquantitative analysis comparing the uptake in the corpus striatum to cerebellum shows that there is a 41% reduction in striatal binding on the left and a 30% reduction in striatal binding on the right in this patient with Parkinson's disease. This is indicative of the loss of the dopaminergic input from the substantia nigra, which is the etiology of Parkinson's disease

can be used to visualize dopaminergic nerve terminals in vivo in the human brain with SPECT. It has been validated that the calculation of a simple ratio of specific/nonspecific binding during a period of binding equilibrium in the striatum about 2 – 4 h after bolus injection of the tracer gives a strong and reliable index of the binding potential of dopamine uptake sites. Previous studies have shown that the dopaminergic deficit in patients with Parkinson's disease (PD) can clearly be visualized and quantified using this method. Investigation of a group of 113 patients with PD demonstrated a 45% loss of striatal I-123-β-CIT binding in comparison to age corrected control values [35]. Highly significant correlations of SPECT findings with clinical data such as akinesia, rigidity, axial symptoms and activities of daily living are demonstrated.

The radiotracer I-123-β-CIT is a sensitive marker of dopamine uptake sites that can be used to visualize dopaminergic nerve endings in vivo in the human brain. In a study reporting on I-123-β-CIT SPECT findings in a patient with DOPA-responsive dystonia [36], I-123-β-CIT SPECT showed a striatal radiotracer uptake in the upper range of normal, indicating intact dopamine transporters and structural integrity of nigrostriatal neurons. This differentiates DOPA-responsive dystonia from clinically similar cases with juvenile-onset parkinsonism with dystonia that have a poorer prognosis.

18.2.9
Cell Proliferation Imaging Using [F-18]-Fluoro-3′-deoxy-3′-l-fluorothymidine PET

[F-18]-Fluoro-3'-deoxy-3'-l-fluorothymidine (F-18-FLT) has been used to indicate tumor proliferation in both pre-clinical and clinical studies [37, 38]. Imaging of brain tumor proliferative activity has been performed using semi-quantitative measures of standard uptake values. F-18-FLT imaging can be correlated with stereotactic biopsies representing the Ki-67 proliferation index. Recurrent or residual viable tumor demonstrate increased quantitative F-18-FLT utilization and can provide a useful index to separate residual or recurrent viable tumor from radiation or chemotherapy necrosis. F-18-FLT is more specific for detection of viable tumor proliferation since the background activity in normal brain is low (Fig. 18.15), unlike F-18-FDG, which has a high normal brain background.

18.3 Technical Considerations

18.3.1 Image Acquisition

18.3.1.1 SPECT Image Acquisition

In SPECT of the brain, triple head Anger gamma cameras are now in common use and can provide very high resolution images [approximately 7 mm full width half maximum (FWHM) extrinsic resolution] [39]. The resolution has improved, primarily due to the increased count detection capability of these cameras. In addition, these cameras allow faster throughput of patients since the scan time can be decreased. Scanning can be performed in temporal segments, with summation of the projection images at the end of acquisition. This enables salvaging of studies in which patient motion might occur. For example, a 30-min scan can be divided

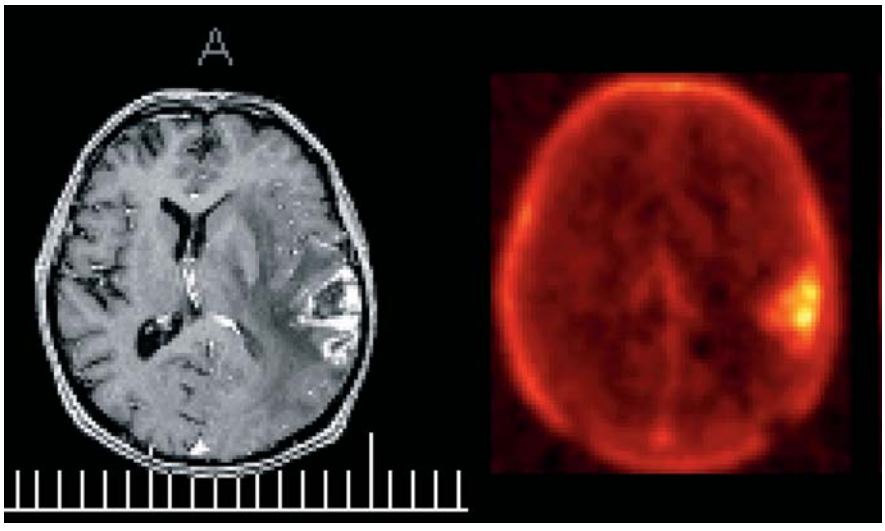

Fig. 18.15. *Left* MRI scan from a 48-year-old male with contrast enhancement in the left posterior temporal lobe consistent with question of recurrence of high grade glioma. *Right* F-18-FLT PET scan section. There is increased F-18-fluorothymidine uptake in the left temporal lobe, in the area of contrast enhancement on the MRI scan consistent with high grade tumor recurrence. It is noted that the background uptake in normal brain is very low, and therefore F-18-FLT provides a more useful and specific measure of cell proliferation since the cell proliferation in normal brain is very low compared to recurrent or residual viable tumor. This therefore is a more specific tracer for recurrent tumor compared to F-18-FDG, which has high background uptake in normal brain. (Courtesy of Dr. Badreddine Bencherif, University of Pittsburgh Medical Center)

into two 15-min segments, each obtaining a 360° set of projection images. If the patient moves during the last 15-min imaging segment, the first 15-min imaging segment can be used for reconstruction of the complete set of tomographic images. If the patient does not move, both sets of projection images can be summed together to obtain a higher count rate examination. Patient motion occasionally occurs in the evaluation of severe dementia or epilepsy. Fortunately, in many of these cases, the cortical regions under investigation are relatively large, and a scan with only moderate counts or mild motion is still adequate for clinical diagnosis.

In conjunction with the advancements in radiopharmaceuticals and cameras, there have also been advances in computer software. Algorithms for SPECT reconstruction and post-processing are now simplified and more routine, which reduces pre-acquisition and post-processing errors by the technologist. In addition, images are DICOM compatible [40], allowing the SPECT imaging computer to be used to store anatomic images from CT or MRI, which permits image registration methods to be routinely employed to compare anatomy and function.

18.3.1.2 PET Image Acquisition

Subject environmental conditions during the performance of F-18-FDG PET scans should be standardized whenever possible. F-18-FDG PET studies should be performed during "a resting state" (e.g., eyes open, ears unoccluded in a dark room with minimal ambient noise). Procedures to minimize head movement during scan acquisition should be implemented using well tolerated head immobilization procedures). The use of medications and the behavioral state of patients at the time of the scan also should be carefully taken into account since they may produce changes in cerebral metabolism that could alter F-18-FDG tracer distribution.

The normal brain has high F-18-FDG uptake and therefore administration of approximately 10 mCi F-18-FDG I.V. is sufficient. The PET scanner should be of the latest generation, full ring and multislice to cover the entire brain. The 3D acquisition mode should be used to accommodate lower dosimetry and to improve the count statistics of the data. Measured attenuation correction should be employed. The image should be reconstructed with the standard clinical reconstruction including all necessary corrections (such as for randoms, scatter, and attenuation). Quality control with calibration phantoms should be performed in order to assure qualitative accuracy (e.g., using the Hoffman brain phantom), and quantitative accuracy (e.g., using a uniform cylinder phantom) should be run periodically to assess scanner stability [41].

18.3.2 Registration and Analysis Methods

18.3.2.1 Image Registration

The main techniques for registration of images are use of atlases (e.g. the Talairach atlas [42]) or the use of a computer based automated routine for aligning and reslicing tomographic image data using automated image registration algorithms (AIR) [20].

The Talairach [42] atlas method relies on identification of the anterior (AC) and posterior (PC) commissures of the brain to define the AC-PC line. After the AC-PC line is identified, an origin (O) is defined along this line. A perpendicular line is then drawn from O to the top of the brain. This gives longitudinal and vertical dimensions. The width of the brain is defined from the scan itself. Thus, in this coordinate system, three Cartesian axes are defined, with the edges of the brain identified to yield measurable dimensions. When comparing separate patients on SPECT or PET scans, these dimensions are stretched proportionally such that the dimensions of the brain along this axis are the same lengths in all patients.

Automated image registration (AIR) algorithms include computer routines for aligning and reslicing tomographic image data. The typical strategy for AIR is as follows: The brain SPECT or PET scans are converted to analyze format. These analyze format image sets are resized (spatially co-registered) for conversion of image pixel size and x, y, and z to common units. The registration algorithms are used from a family of automated image registration programs to align image data set to the same position [20]. The images can then be registered into standardized image spaces, such as the patient's functional image space or standardized space, such as the Montreal Neurological Institute (MNI) space [43].

An example of the precision to which these techniques can provide image registration between F-18-FDG PET and MRI is illustrated by a 36-year-old normal female volunteer who underwent a resting state fully dynamic F-18-FDG PET scan with arterial sampling at the University of Pittsburgh PET Center, as shown in Fig. 18.16. A two-tissue compartment model was used to analyze the data, and spoiled gradient echo (SPGR) MRI volume data (1 mm thick MR sections) were transferred to the PET facility over the electronic network from the MRI Center and registered with the PET data. MR data were spatially normalized and sectioned in the patient's PET space to preserve the maximum resolution of the original PET data. F-18-FDG PET scan image slice thickness = 2.0 mm with reconstructed in plane image resolution = 4 mm FWHM. The F-18-FDG PET data is acquired over 90 min (34 frames) with arterial blood sampling for each scan time period.

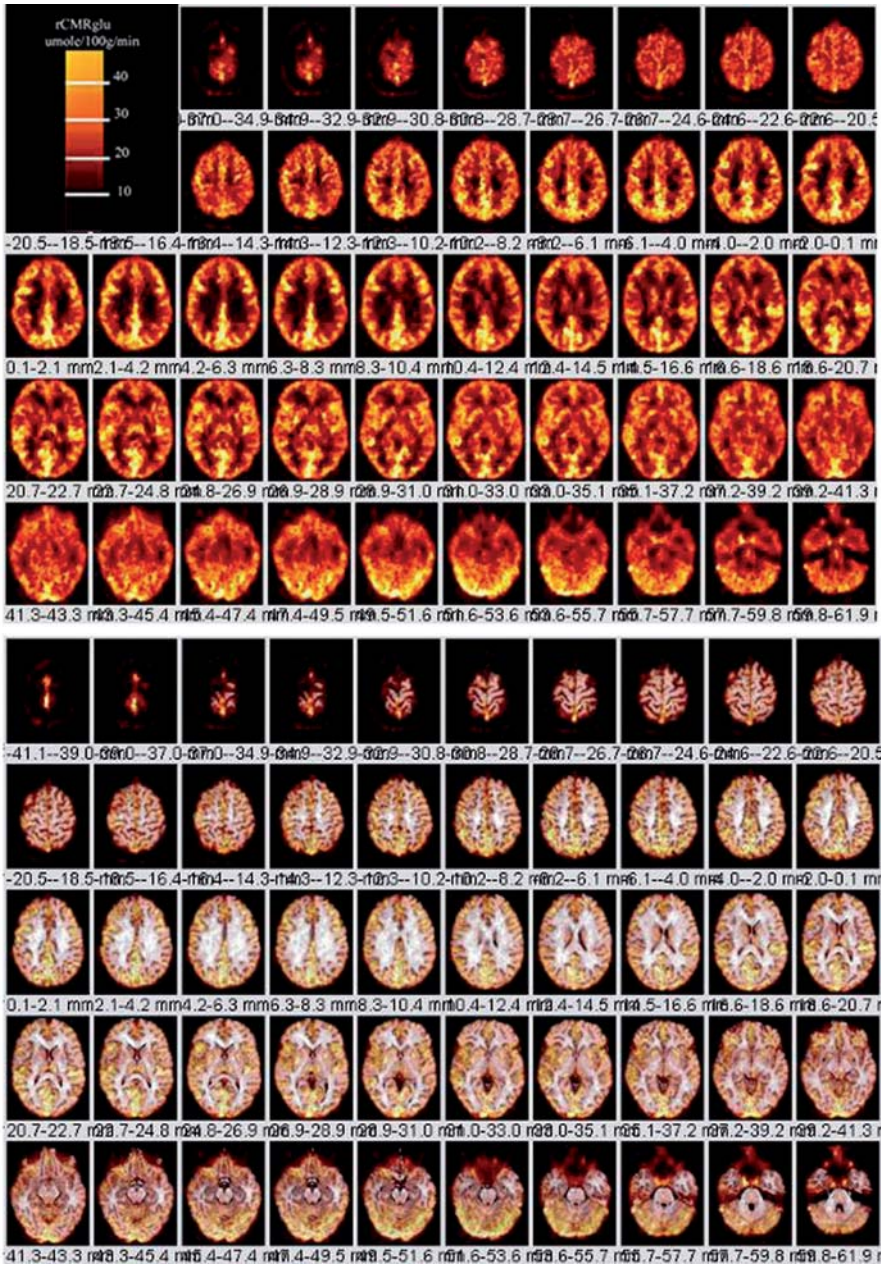

Fig. 18.16. F-18-FDG PET scan sections through the brain (**a**) and corresponding PET-MRI co-registered fusion images (**b**). Images are from a 36-year-old normal female volunteer who underwent fully dynamic F-18-FDG PET with arterial sampling at rest. Regional cerebral metabolic rates of glucose utilization expressed as rCMRglu in units of µmol/100 g/min (*color bar*). PET images are registered to a spoiled gradient echo (SPGR) MRI volume data (1-mm-thick MR sections) that were transferred to the PET facility over the electronic network and registered with the PET data. The F-18-FDG PET scan image slice thickness = 2.0 mm with reconstructed in plane image resolution = 4 mm FWHM. **b** MRI-PET fusion image. In general the fusion technique is clinically helpful to assess structural versus functional changes on F-18-FDG brain PET scans or regional cerebral blood flow brain SPECT scans

18.3.2.2 SPECT and PET Image Analysis

Statistical parametric mapping (SPM) refers to the construction and assessment of spatially extended statistical processes used to test hypotheses about functional imaging data. In rCBF SPECT or F-18-FDG PET image data analysis this translates to methods to test hypotheses about regionally specific effects (e.g., the probability of finding a region of increased regional cerebral perfusion or metabolism by chance). It was originally developed in the early 1980s by Friston et al. [44] for the routine statistical analysis of functional neuroimaging data from PET. When two image data sets are evaluated by SPM, all voxels contained within the scans are compared in the same space on a voxel-by-voxel basis using linear constraints to test hypotheses for specific focal effects using a univariate statistical test. The resulting statistical parameters are then assembled onto an image (i.e. the statistical parametric map). Statistical differences are interpreted as regionally specific effects, attributable to some alteration in brain function from one scan to the other. The significance of these differences is assessed using statistical tests (usually the *t* or *F* statistic). Criteria for accepting voxels (those intend-

ed to represent true changes in regional cerebral perfusion can be set for voxel height (p) and extent of contiguous cluster of voxels (k). For visualization of the results, a pseudo-color scale can be applied to accepted significant voxels, which are then overlaid in a semi-transparent fashion onto the MRI of either the normative atlas or the patient's own MRI anatomy. The most recent version of SPM (SPM2) combines the general linear model to create the statistical map and the random field theory to make statistical inference about regional effects. Software for SPM analysis is available as Freeware from the Welcome Department of Imaging Neuroscience [45]. Although the SPM package includes most of the programs required for image processing and analysis, visualization of images and some processing or image editing and reformatting may require more dedicated biomedical image processing software.

Statistical parametric mapping was performed to compare the regional distribution of Tc-99m-HMPAO brain SPECT scans with Tc-99m-ECD brain SPECT scans in normal patients [46]. All patients were screened for drug use, head injury, medication status, and other psychiatric or mental illnesses. The two groups were matched for age, sex and race, and analysis was performed on a group of 35 normal patients undergoing Tc-99m-HMPAO brain SPECT scans and 55 patients undergoing Tc-99m-ECD brain SPECT scans. Statistical parametric mapping was performed after the patients' data were spatially normalized to a standardized stereotactic atlas (Talairach Atlas). The results showed that these tracers had differences in their regional perfusion patterns, presumably due to the differences in the pharmacokinetics of tracer extraction and trapping. Specifically, large areas of parietal, occipital, and superior temporal cortices demonstrated lower uptake in the Tc-99m-HMPAO brain SPECT scan group as compared to the Tc-99m-ECD brain SPECT scan group. There were increases in tracer uptake seen in the subcortical nuclei, thalami, and parts of the brain stem and hippocampus as well as small areas of the cerebellum in the Tc-99m-HMPAO group as compared to the Tc-99m-ECD group. The importance of this study is to point out that, when performing rCBF SPECT, one should be aware of the differences in the perfusion pattern. In cases of repeat studies, these data suggest that one tracer cannot be substituted for the other.

18.4 Clinical Applications

18.4.1 Cerebrovascular Disease

It is ironic that tracers which directly measure regional cerebral perfusion have not assumed greater clinical application in the evaluation of cerebrovascular disease. This is partly due to the fact that, in many cases, identification of a post-stroke blood flow defect has not provided unequivocal useful clinical information beyond that offered by neurological exam combined with CT or MRI. Furthermore, the use of rCBF tracers in patients with TIA has had (until recently) unclear clinical usefulness since a rest perfusion scan may not provide significant additional clinical information beyond the neurological examination. However, in a recent study of 64 patients in which cerebral perfusion and vascular reactivity was assessed before and after carotid endarterectomy using Diamox enhanced SPECT, the authors concluded that Diamox SPECT assessment of vascular reserve was of value in identification of patients at risk for stroke [47]. After carotid endarterectomy these patients underwent repeat SPECT which confirmed improvement in vascular reactivity. Therefore, Diamox SPECT scans may provide objective evidence for the selection of patients with a high-grade asymptomatic carotid stenosis who will benefit from carotid endarterectomy [47].

The standard vasoreactive stress protocol is to first perform a resting state Tc-99m-HMPAO brain SPECT scan to assess the blood flow to the vascular territories of the brain. In many cases in patients with TIA, the blood flow is often symmetric or may show small regions of cortical hypoperfusion due to small embolic infarctions. The vasoreactive challenge SPECT is either performed using the same dose of Tc-99m-HMPAO after a 24- to 48-h wait, or by using a much higher dose than the initial dose (the so-called low-dose/high-dose method). The main problem with this method is that, in order to comply with regulatory requirements pertaining to the total amount of injected Tc-99m-HMPAO, the low dose scan usually has relatively poor count statistics. Therefore, it is best to perform the rest-vasoreactive comparative test on two separate days using the same dose. After the intravenous administration of 1 g of Diamox and waiting 15 min, there is an increase in CO_2 in the brain, which causes dilatation of the vasculature. There is an increase in the blood flow to normal brain of about 30%, and areas of hemodynamic constraint can be identified since CVD patients may be at the limit of their vasoreactive reserve before Diamox and, therefore, will illustrate no increase in perfusion as compared to normal vascular territories of the brain, which can accommodate a 30% increase in blood flow.

Figure 18.17 illustrates the clinical utility of vasoreactive challenge rCBF SPECT in a 58-year-old man who presented with transient ischemic attack characterized by transient neurological deficits in motor function of the right upper and right lower extremities. On angiography there was 100% narrowing of the left internal carotid artery. The MRI scan was normal. The resting state Tc-99m-HMPAO (pre-Diamox) brain SPECT scan showed only mild decrease in perfusion. The post-Diamox vasoreactive stress scan showed a large region of

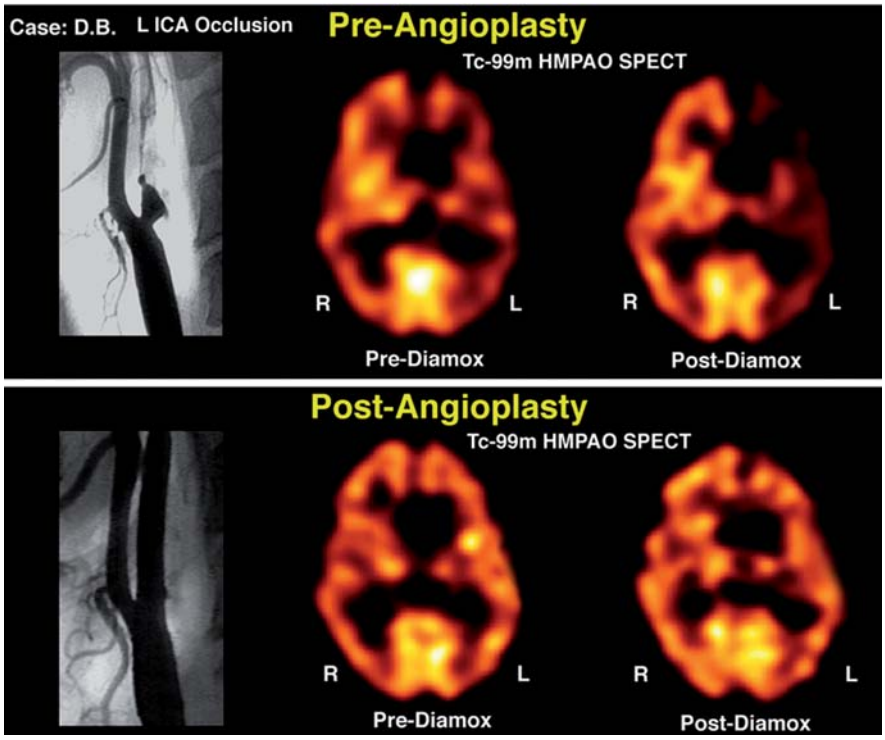

Fig. 18.17. Angiogram showing complete left ICA occlusion in a patient with transient ischemic symptoms (*top, left*). The resting scan (*top, middle*) shows slight reduction of blood flow to the left ICA distribution. The post-Diamox scan (*top, right*) shows significant relative reduction of rCBF to the left ICA territory as compared to the remainder of the brain. The *bottom row of images* show the results after angioplasty. The angiogram (*bottom, left*) now shows a patent left internal carotid artery. The resting Tc-99m-HMPAO brain SPECT scan (*bottom, middle*) shows a more symmetric perfusion of tracer distribution at rest. More importantly, after Diamox, there is no relative reduction in the left hemisphere as compared to the right hemisphere (*bottom, right*)

decreased regional cerebral perfusion in the left frontal, temporal, and parietal lobes representing severe rCBF compromise in the distribution of the left internal carotid artery. This patient subsequently underwent left ICA balloon angioplasty. A follow-up rest and vasoreactive challenge rCBF SPECT indicated that all regions of the brain increased in blood flow as a result of Diamox flow augmentation, and the left internal carotid artery vascular territory was no longer constrained. It is important to diagnose areas of hemodynamic vascular constraint since patients with this degree of vascular compromise have significant risk for sudden infarction in addition to a chronic risk for selective neuronal loss and vascular dementia.

18.4.2 Dementia

Approximately 3% – 4% of the adult population in the United States demonstrates significant cognitive impairment. In general, the causes of dementia include primary neurodegenerative disorders, with the most prevalent being Alzheimer's disease, followed by frontal-temporal dementia, Lewy body dementias, parkinsonian dementia, progressive supernuclear palsy, Pick's disease, cortical basilar degeneration, Huntington's disease, and Wilson's disease [48]. Vascular dementias are categorized as multi-infarct, Binswanger's, cerebral autosomal dominant arteriopathy with subcortical infarctions and leukoencephalopathy. Inflammatory etiologies include multiple sclerosis and vasculitis. Infectious etiologies include syphilis, human immunodeficiency virus, Lyme disease, and other viral disease, and fungal diseases. Cancers are a rare cause of dementia which can be attributed to the primary result of the disease, metastatic disease to the brain, and perineoplastic syndromes. Other causes and physical abnormalities include trauma and hydrocephalus.

The prevalence of dementia in the population increases significantly with age, with approximately 13% of the population having dementia in the 77- to 84-year-old range, and almost 50% in the population 95 years and older. With the increasing age of the population of the United States, dementia is expected to be a significant health care problem. It has been documented [49] that approximately 80% of all dementias are attributable to Alzheimer's disease or Lewy body dementia. Vascular dementia comprises approximately 18% of the dementias, with the other dementias comprising approximately 5.5%.

18.4.2.1 Alzheimer's Disease

Alzheimer's disease was first described by Alois Alzheimer in 1906 and was described as an unusual disease of the cerebral cortex with primary clinical symptomatology as a pre-senile dementia which affected a woman in

her 50's, causing memory loss, disorientation, hallucinations, and ultimately death by the age of 55. The classic neuropathological changes were identified as senile plaques and neurofibrillary tangles. He also described a granulovascular degeneration and amyloid angiopathy. The diagnosis of Alzheimer's disease has traditionally been through the NINCDS/ADRDA criteria [50]. Using these clinical criteria, dementia is established by clinical examination and documented by the Mini-Mental Test or Blessed Dementia Scale and confirmed by a neuropsychological examination. Alzheimer's dementia requires cognitive deficits in two or more areas, with progressive worsening of memory and other cognitive function. There should be no disturbances in consciousness. The age of onset is typically between the ages of 40 and 90 years, most often after 65 years. In addition, the absence of systemic disorders or other brain diseases is required as these can confound the diagnosis of Alzheimer's disease.

The two basic types of Alzheimer's disease are familial and sporadic. Familial AD (FAD) is a rare form of AD, affecting less than 10% of AD patients. All FAD is early-onset, meaning the disease develops before age 65. Apolipoprotein E (APOE) epsilon4 gene dose (i.e., the number of epsilon4 alleles in a person's APOE genotype) is associated with a higher risk of AD and a younger age at dementia onset [51], and correlates with reduced regional hypometabolism in brains of patients with AD. In addition, advanced age, prior head trauma, low educational levels and gender, with female greater than male predominance, have been associated with an increased risk for Alzheimer's disease.

The rationale for imaging as a diagnostic tool for Alzheimer's disease is based on the disease associated reduction in metabolic brain activity, which can be visualized on both F-18-FDG brain PET and Tc-99m-HMPAO or Tc-99m-ECD brain SPECT. There is a reduction of brain glucose metabolism identified on PET due to reduced neuronal metabolism and synaptic activity. A reduction in brain perfusion on regional cerebral perfusion SPECT is identified as a decrease in blood flow and a reduction in neuronal and synaptic activity (proportional to the blood flow) in areas of reduced metabolism caused by amyloid deposition, a finding characteristic of Alzheimer's disease. The characteristic findings on F-18-FDG brain PET and regional cerebral perfusion SPECT are as follows: (1) frequent bilateral involvement with asymmetry of reduction in the posterior temporo-parietal cortical areas; (2) reduction of metabolism and blood flow to the posterior cingulate gyrus; (3) relatively early onset (less than 65 years) with more marked abnormalities on reduction of F-18-FDG uptake and blood flow; (4) less common primary visual cortex involvement (which is more common in Lewy body dementia); and (5) coexisting micro- or macrovascular disease involvement resulting in neuronal injury and death.

18.4.2.2 Imaging of Alzheimer's Disease with rCBF SPECT Tracers

Alzheimer's disease (the most common progressive degenerative dementia) is characterized by low global blood flow with accentuation of the diminution in the

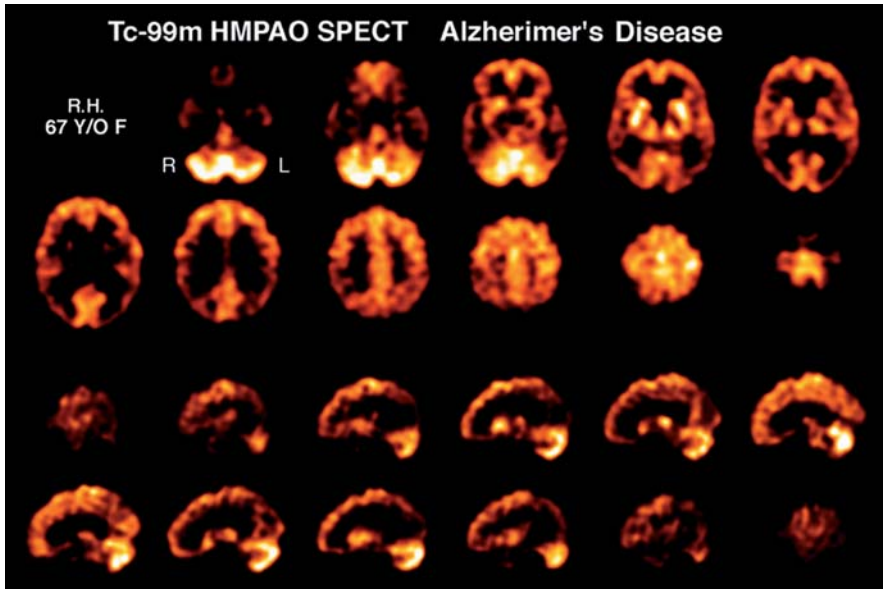

Fig. 18.18. Transverse sections (*top*) and sagittal sections (*bottom*) from a Tc-99m-HMPAO brain SPECT scan of a 67-year-old female with Alzheimer's disease. The scans show global decrease in blood flow to essentially all cortical structures (relative to the cerebellum) with accentuation of the decrease in the posterior temporal parietal region. There is relatively spared uptake in the cerebellum, caudate head, lentiform, and thalamus. Alzheimer's disease is characterized by globally diminished blood flow throughout the cortex, accentuation of that diminution in the posterior temporal parietal regions, and relative sparing of the basal ganglia structure and sensorimotor cortex, as well as the cerebellum. All of these major features characteristic of the cerebral blood flow pattern defects seen in Alzheimer's disease are seen in this patient

posterior temporoparietal lobes, relative sparing of the thalamus and corpus striatum as well as the sensorimotor cortex, and late involvement of the frontal lobes. Figure 18.18 shows a 67-year-old woman with a progressive cognitive decline. Her Tc-99m-HMPAO brain SPECT scan shows significant diminution in global perfusion with accentuation of the rCBF decrease in the posterior temporoparietal regions. In the differential diagnosis of both Alzheimer's disease and vascular dementia, the cerebellum is often useful as a structure for semiquantitative normalization of blood flow since it is relatively uninvolved in most cases of progressive cerebral cognitive decline.

It is important to distinguish, on a rCBF brain SPECT scan, the differences between a progressive degenerative dementia such as Alzheimer's disease from a vascular dementia, usually from hemodynamic compromise or embolic vascular disease at the internal carotid artery level, or higher. The importance of this differentiation now extends beyond the theoretical issue of clinical diagnosis and prognosis, since therapeutic protocols have now been established for these two causes of memory impairment [52]. Recent therapeutic advances are emerging from clinical trials of cholinomimetic drugs, indicating that these drugs may improve the abnormal behavioral symptoms of Alzheimer's disease [53]. Inhibition of acetylcholinesterase (AChE) by acetylcholinesterase inhibitors reduces the enzymatic breakdown of endogenously released acetylcholine (ACh), resulting in greater synaptic concentrations of ACh at the postsynaptic ACh receptors. Inhibitors (such as donepezil) have been reported to significantly improve many manifestations of behavioral disturbance including agitation, apathy, hallucinations, and aberrant motor behavior. Cholinesterase inhibitors can be effective in slowing the memory loss in Alzheimer's disease. Figure 18.19 shows a Tc-99m-HMPAO brain SPECT scan of a 66-year-old patient with early Alzheimer's disease before and after 1 year of therapy with the acetylcholinesterase inhibitor donepezil.

18.4.2.3 Imaging of Alzheimer's Disease with F-18-FDG PET

Accurate and early diagnosis of Alzheimer's disease (AD) is vital to ensure patients receive the proper treatment, research is targeted correctly, and prevention and cures are found. However, it can be difficult to distinguish between AD and other forms of dementia, or even from other reversible disorders. The standard tools for assessing AD include neuropsychological or cognitive evaluation, physical exam, neurological exam, laboratory testing, neuroimaging, behavioral assessment, and patient history. F-18-FDG PET imaging has been reported to have a sensitivity of 93% and a specificity of 63% [54]. Figures 18.20 and 18.21 show examples of F-18-FDG PET scanning in the diagnosis of AD. In the analysis of F-18-FDG uptake in these patients the three-dimensional stereotactic surface projection (3D SSP) algorithm was employed. The 3D SSP

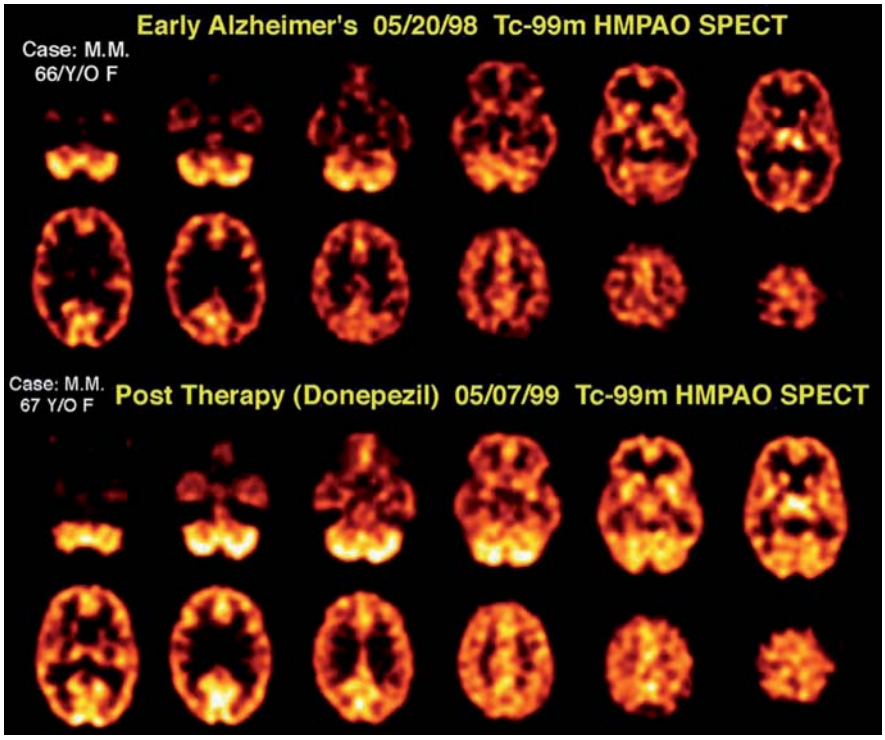

Fig. 18.19. Tc-99m-HMPAO brain SPECT scan of a 66-year-old patient with early Alzheimer's disease who was treated with donepezil. The *top two rows of images* show sequential transverse sections from this patient's Tc-99m-HMPAO scan before beginning therapy. There is diminution of rCBF to the posterior temporal parietal regions. The 1-year post-donepezil therapy (*bottom*) transverse sections show markedly increased blood flow to the frontal lobes and slightly increased blood flow to the posterior temporal parietal regions

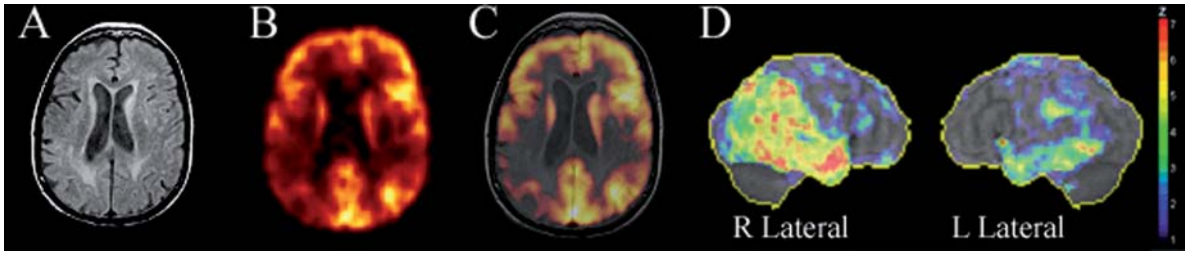

Fig. 18.20A–D. Brain images from a 72-year-old female who was seen with concerns of cognitive decline for 6 months, but on questioning there was memory loss beginning about 4 years prior to the FDG PET scan. Her Folstein Mini-Mental score was 9/30, and the ADRDA criteria for probable Alzheimer's disease were satisfied. **A** MRI scan reveals chronic small vessel ischemic changes and mild diffuse atrophy without a specific pattern which would be diagnostic for Alzheimer's disease. **B** F-18-FDG brain PET scan section obtained from the Siemens HR+ shows F-18-FDG reduction involving the posterior temporal and parietal lobes bilaterally, right more severely affected as compared to the left. **C** F-18-FDG brain PET scan fused with the T1 weighted MRI scan. In the areas of decreased F-18-FDG uptake there is no cerebral atrophy out of proportion with other areas of the brain to indicate that the reduction of F-18-FDG uptake is an atrophy effect, and therefore decreased F-18-FDG uptake can be attributed to reduced neuronal metabolic activity as a result of neuronal impairment attributable to the amyloidopathy of Alzheimer's disease. **D** Three-dimensional stereotactic surface projection (3D SSP) results (lateral projections) of the patient's brain PET scan fused on a MRI standard brain. There is significant reduction of metabolism in the right temporoparietal region as indicated by the color overlay map, which ranges from a *z* score difference between the patient and normal control database of 2 for blue areas of the brain and 6 for red areas of the brain. There is also reduction in the left temporal lobe with *z* scores ranging between 2 and 5. The overall constellation of findings is typical for Alzheimer's disease, slightly asymmetric, with greater impairment of the right hemisphere

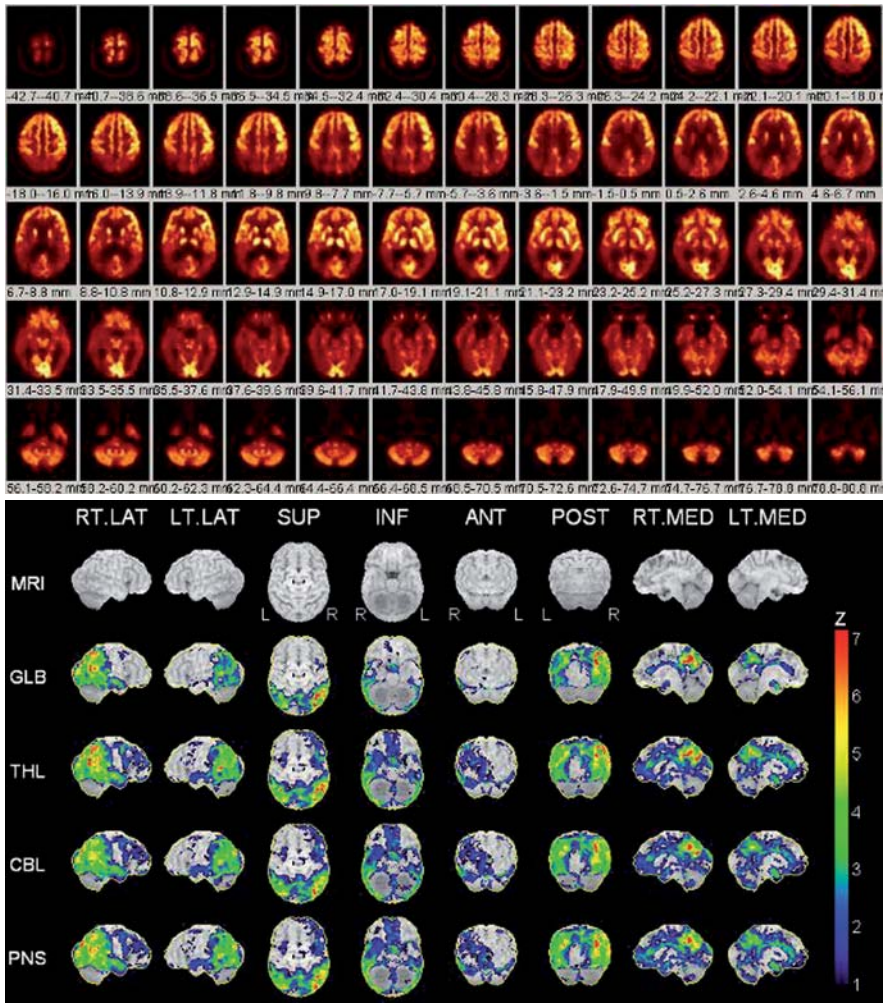

Fig. 18.21. *Top* F-18-FDG brain PET scan in transverse section illustrating significant reduction in regional glucose metabolism in the posterior temporoparietal lobes bilaterally. The patient is a 52-year-old male with symptoms of cognitive impairment and memory loss for 2 years. The patient satisfied the ADRDA criteria for probable Alzheimer's disease with a Folstein Mini Mental Status measuring 16 out of 30. In addition to significant reduction of F-18-FDG uptake involving the temporoparietal lobes bilaterally, there is also significant reduction in the posterior cingulate gyrus region. There is relative sparing in the sensorimotor cortical area and basal ganglia region. *Bottom* The 3D SSP map of statistically significant differences between the patient and age matched normal controls shows significantly reduced glucose metabolism in the posterior temporoparietal lobes bilaterally, right slightly greater than left (lateral views) and posterior cingulate (medial views)

statistical map shows the difference between a single subject and normal age-matched controls [55].

Figure 18.21 shows F-18-FDG PET images of a 53-year-old male with symptoms of cognitive impairment and memory loss for 2 years. The patient satisfied the ADRDA criteria for probable Alzheimer's disease and had a Folstein mini-mental status score 16 out of 30. The MRI scan revealed mild diffuse atrophy. Figure 18.16, left, shows standard PET images in transverse section illustrating reduction of F-18-FDG uptake in the posterior temporo-parietal regions. The patient's MRI scan showed non-specific atrophy for age. Figure 18.16, right, illustrates the value of analysis of F-18-FDG PET statistical parametric mapping using 3D SSP. The 3D SSP statistical map shows the difference between this patient and normal age-matched controls. The 3D SSP map shows a significant reduction of metabolism in the temporoparietal regions bilaterally, on this image with *Z* scores showing a significant reduction in F-18-FDG uptake of between 4 and 6 in the posterior temporal parietal regions.

18.4.2.4
Center for Medicare and Medicaid Services Decision Memorandum for PET Imaging in Suspected Dementia

The Center for Medicare and Medicaid Services (CMS) issued a decision memorandum for positron emission tomography and other neuroimaging devices for suspected dementia on September 15, 2004 [56]. CMS decided that an F-18-FDG brain PET scan is reasonable and necessary in patients with a recently established diagnosis of dementia with documented cognitive decline for at least 6 months who have met the criteria for both Alzheimer's disease and frontal temporal dementia, and who have been evaluated for specific alternate neurodegenerative diseases or causative factors for which the cause of clinical symptoms remains uncertain. The coverage criteria for Alzheimer's disease requires the following additional criteria to be met:

1. The onset, clinical presentation, or course of cognitive impairment is atypical for Alzheimer's disease, and frontal temporal dementia is suspected as an alternative neurodegenerative cause of cognitive decline. Specifically, symptoms such as social dysinhibition, awkwardness, difficulties with language, or loss of executive function are more prominent early in the course of frontal temporal dementia than the memory loss typical of Alzheimer's disease.
2. The patient must have had a comprehensive clinical evaluation encompassing a medical history including formal documentation of cognitive decline by two time points with intervals at least of 6 months apart. This should be aided by cognitive scales of neuropsychological testing, laboratory tests, and structural imaging such as MRI or computer tomography.
3. The patient must be evaluated by a physician experienced in the diagnosis and assessment of dementia, and in that evaluation a likely or specific neurodegenerative disease or cause of clinical symptoms has not been identified and information available through F-18-FDG PET is reasonably expected to clarify the differential diagnosis between frontal temporal dementia and Alzheimer's disease.
4. A brain SPECT or a prior F-18-FDG PET scan should not have been performed for this same indication.
5. The referring or billing provider will collect and maintain and furnish upon the request of CMS the following documentation to verify that the conditions for coverage described have been met [Date of onset of symptoms; Mini mental status examination or similar test score; Report from any neuropsychological testing performed; Diagnosis of clinical syndrome (e.g., mild cognitive impairment, dementia, etc.); Presumptive cause (e.g., possible, probable or uncertain AD; Results of structural imaging such as MRI and CT; Relevant laboratory tests) B_{12} or thyroid hormone levels; Any prescribed medications including the quantity and name].

18.4.2.5
Imaging of Vascular Dementia with rCBF SPECT Tracers

Patients with vascular dementia may show relatively normal perfusions in areas not involved with vascular disease. These patients may benefit from a revascularization procedure before any further dementia or frank infarction occur. A common form of vascular dementia is produced by small embolic events and, therefore, small punctate cortical ribbon breaks may be observed in these patients. In addition, there tends to be more involvement of the frontal lobes as compared to the posterior regions of the brain. Finally, the subcortical structures or internal capsule region may demonstrate asymmetry in blood flow due to the presence of small embolic events in these locations. Figure 18.22 illustrates a case of vascular dementia in a 62-year-old male with bilateral MCA chronic ischemia and transient ischemic attacks. The image shows a CT scan of the patient and a corresponding section from the Tc-99m-HMPAO brain SPECT scan and the CT-SPECT fusion image. The CT scan shows atrophy with areas of tissue loss characteristic of small embolic infarctions. The Tc-99m-HMPAO brain SPECT shows diminution at the 2 o'clock and 4 o'clock as well as the 8 o'clock and 11 o'clock positions, which is characteristic of embolic disease. There is no specific reduction of rCBF to the

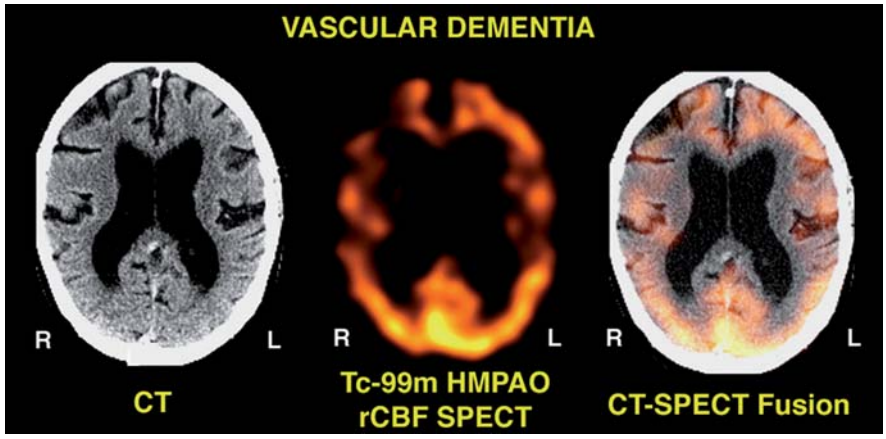

Fig. 18.22. Sixty-two-year-old male described in the text with bilateral MCA chronic ischemia and transient ischemic attacks. The image shows a CT scan of the patient (*left*), a corresponding section from the Tc-99m HMPAO brain SPECT scan (*middle*), and the CT SPECT fusion image (*right*). The CT scan shows atrophy with areas of tissue loss characteristic of small embolic infarctions. The Tc-99m-HMPAO brain SPECT scan through the same level shows the regular uptake in the cortical structures with diminutions at the 2 o'clock and 4 o'clock as well as the 8 o'clock and 11 o'clock positions, which is characteristic of embolic disease. There is no reduction of rCBF to the posterior portion of the brain as noted in the case of Alzheimer's disease (Figs. 18.18 – 18.20)

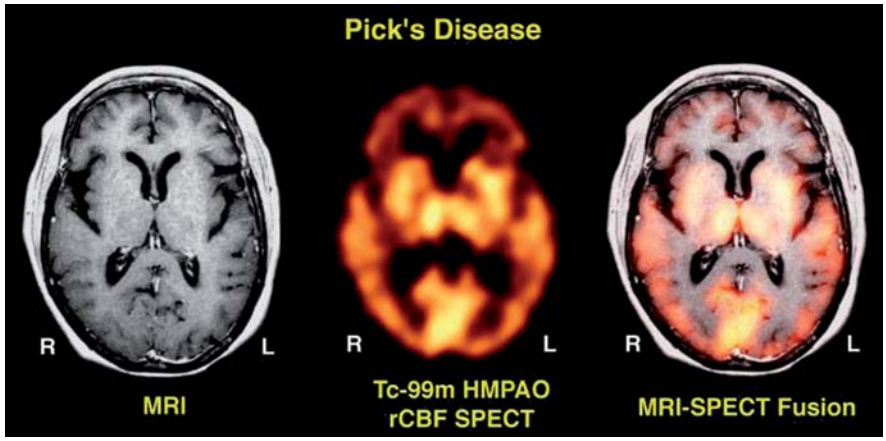

Fig. 18.23. Tc-99m HMPAO brain SPECT scan of a patient with early Pick's disease. The scan is of a 67-year-old female with a rapidly progressing frontal lobe type dementia. The CT scan (*left*) shows mild atrophy in the sylvian regions but no frontal lobe atrophy. The Tc-99m-HMPAO brain SPECT scan shows marked diminution of tracer uptake in the frontal lobes (*middle*). The fusion image (*right*) shows that the diminution is due to loss of cortical synaptic activity (which is proportional to regional cerebral perfusion) since there is no substantial cortical gray matter loss in the region of frontal lobe hypoperfusion seen on the Tc-99m-HMPAO brain SPECT scan

posterior regions of the brain as would be characteristic of Alzheimer's disease.

18.4.2.6 Other Causes of Dementia

Pick's disease is a rapidly progressing frontal lobe type dementia. A Tc-99m-HMPAO brain SPECT scan of a patient with early Pick's disease is shown in Fig. 18.23. The scan is of a 67-year-old female with rapidly progressing frontal lobe type dementia. The CT scan shows mild atrophy in the peri-sylvian regions but no significant frontal lobe atrophy. The Tc-99m-HMPAO brain SPECT scan shows marked diminution of tracer uptake in the frontal lobes. The fusion image shows that the diminution is due to loss of regional cerebral activity, since there is no substantial cortical gray matter loss.

Primary progressive aphasia (PPA) is an uncommon type of degenerative dementia characterized by gradual impairment of language function that remains neuropsychologically focal for several years with sparing of the memory domain [57]. Compared with other neurodegenerative disorders that initially affect cognition followed by language impairment, many patients with PPA retain their cognitive functions, allowing them to continue with their activities of daily living [57]. "Word-finding" or "naming" difficulty (dysnomia) is the most common and earliest clinical presentation of PPA [58]. Figure 18.24 shows an MRI and Tc-99m-HMPAO SPECT scan of a 65-year-old woman with a mild degree of dysnomia. The subject presented with a 7 year history of "tripping" over words. Initially she had trouble with multisyllable words, but progressed to have difficulty even with single syllable words. She complained of problems with her decreasing fluency. She claims to know what she wanted to say but is "not able to get the words out". She used to play the piano and sing with accompaniment but lately complains of

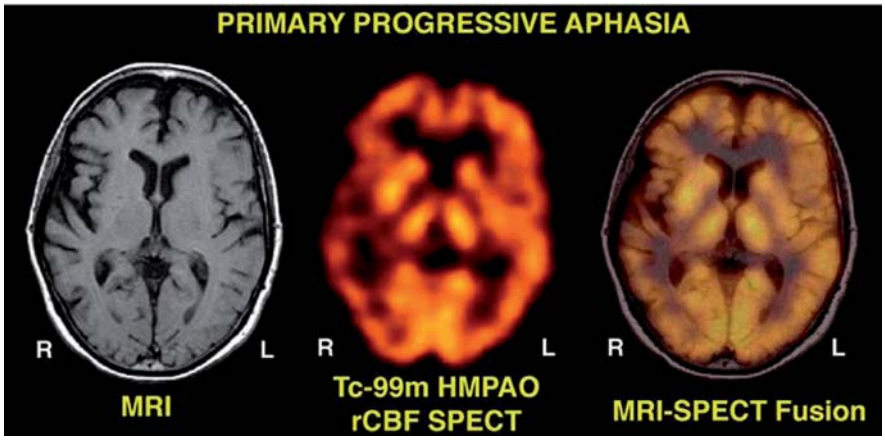

Fig. 18.24. MRI scan (*left*), Tc-99m-HMPAO brain SPECT scan (*middle*), and a MRI-SPECT fusion image (*right*) of a 65-year-old female with a mild degree of dysnomia. The subject presented with a 7-year history of "tripping" over words. She initially had trouble with multisyllable words but currently has difficulty even with single syllable words. The images show right frontotemporal atrophy on MRI. The SPECT scan, however, shows a much larger region of decreased perfusion involving the frontotemporal region as well as the posterior temporal region. This case is an unusual presentation of primary progressive aphasia since it involves the right side of the brain in a right handed woman. The images demonstrate that there is a functional deficit extending beyond the mild degree of anatomic atrophy

loss of her interest due to her inability to get the right tune. She scored 30/30 on the mini mental status examination (MMSE). Her right frontotemporal region shows atrophy on MRI and reduced rCBF on SPECT. There is a larger area of right frontotemporal hypoperfusion on rCBF SPECT in relation to the degree of atrophy identified on MRI.

18.4.3 Epilepsy

Regional cerebral perfusion evaluation in patients with epilepsy has proven to be of significant clinical value for identification of the epileptogenic focus location. The underlying pathophysiology concerning the advantages of using regional cerebral perfusion tracers in epilepsy is based on the clinical observation that was first reported by Sir Victor Horsley more than 100 years ago. He described (by direct observation of the brain during surgery) an increase in cortical blood flow in the area of seizure discharge. Therefore, the most valuable use of Tc-99m-HMPAO evaluation of the epilepsy patient is to localize the epileptogenic focus during the ictal state.

18.4.3.1 Epileptogenic Focus Localization Using Ictal Tc-99m-HMPAO or Tc-99m-ECD SPECT

In order to perform these studies, Tc-99m-HMPAO must be readily available at the patient's bedside, allowing for rapid injection by a trained technologist or other personnel immediately available at the time of seizure onset. The ictal injection should be performed in a rapid bolus fashion such that the entire tracer is injected before the seizure abates. The patient is then stabilized and transferred to the SPECT scanner within several hours to receive a brain SPECT scan, which will indicate the regional cerebral perfusion at the time of ictus. This method is feasible since Tc-99m-HMPAO is irreversibly trapped in the epileptogenic hyperemic region at the time of seizure, and during the period between injection and scan there is essentially no redistribution. The subsequent scan (albeit several hours after the injection) still shows hyperemia in the region of the epileptogenic focus. Several articles [59–63] characterize the brain propagation patterns of the epileptogenic electrocortical discharge and resultant rCBF hyperemia to allow for more accurate localization of the epileptogenic focus in cases where two or more cortical areas are seen to be hyperemic on the brain SPECT scan. A very common pattern of propagation of activity observed in frontal lobe seizures is ipsilateral basal ganglia activation and contralateral cerebellar activation.

Figure 18.25 illustrates the value of ictal SPECT in a 9-year-old right-handed boy who had a 7-year history of intractable seizures. The figure shows a Tc-99m-HMPAO brain SPECT scan which was performed 2 h after tracer injection. The tracer was injected at the bedside 3 s after seizure onset (the seizure lasted ~25 s).

The ictal SPECT scan shows a focal area of intense uptake in the right frontal lobe. The patient's developmental history and neurological findings on examination were normal. Computed tomographic (CT) and magnetic resonance imaging (MRI) studies carried out at our and other institutions were normal. Multiple EEG investigations were inconclusive. On referral to our institution the patient averaged 20–30 seizures a day characterized by an aura of tingling in the mouth, followed by simultaneous extension of the

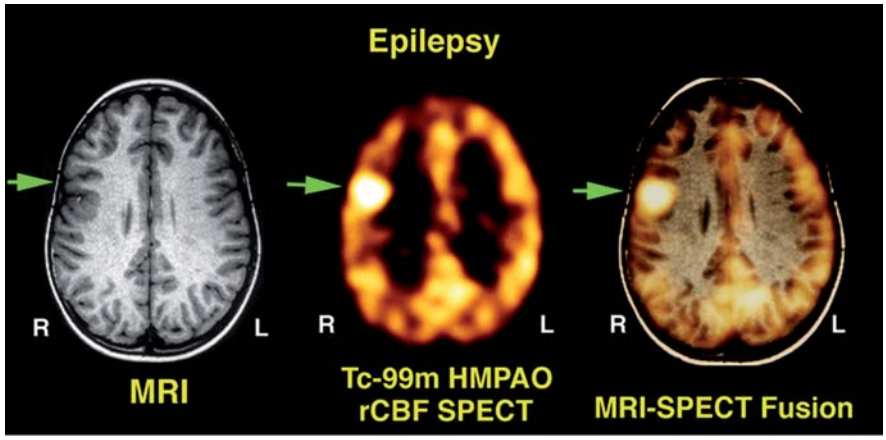

Fig. 18.25. Frontal lobe epilepsy in a 9-year-old right-handed boy. The MRI scan (*left*) is normal. The Tc-99m-HMPAO brain SPECT scan (*middle*) reflects the regional cerebral perfusion at the time the tracer was injected during the epileptogenic seizure. The intense region of hyperemia is seen at the 10 o'clock position. A SPECT MRI fusion image (*right*) clearly identifies the location of the focus on the MRI scan

legs and flexion of the right upper extremities with non-purposeful movements of both legs lasting 20 s. Previous EEGs revealed infrequent slowing over the right hemisphere. Multiple video EEG monitoring studies performed at our and other institutions showed stereotypical seizures with no ictal scalp localization. Interictal activity revealed occasional sharp discharges involving the right frontal central parietal regions.

The Tc-99m-HMPAO ictal brain SPECT scan showed a focal area of hyperperfusion in the right premotor area. The right to left asymmetry in blood flow for this region was 1.32, and the intensity of uptake in the right frontal lobe measured 1.13 (cortical to cerebellar ratio) with a range of normals = mean $\pm$ 1 SD of 0.90 ± 0.07. The result of the ictal brain SPECT scan was subsequently co-registered with the MRI scan and placement of subdural grid electrodes confirmed the epileptogenic focus location. Based on the fusion image, the anatomic location was determined, the epileptogenic focus was surgically excised, and the patient was rendered seizure free.

It has been shown that ictal SPECT in patients with extratemporal lobe epilepsy have superior localization capability as compared to interictal F-18-FDG PET. On the other hand, if ictal SPECT is not available, identification of the epileptogenic focus during the interictal state using Tc-99m-HMPAO is less sensitive compared to interictal F-18-FDG PET. In cases of suspected temporal lobe epilepsy, the preferred diagnostic method is to perform interictal F-18-FDG PET in addition to ictal and interictal SPECT.

18.4.3.2 F-18-FDG Brain PET Assessment in the Interictal State

Figure 18.26 illustrates concordance between abnormalities on MRI and F-18-FDG PET in a 16-year-old boy with temporal lobe epilepsy and hippocampal sclerosis of the right mesial temporal lobe on MRI. The MRI shows abnormal high signal intensity in the right hippocampal region. The FDG PET shows a corresponding area of focal reduction of F-18-FDG uptake in the right hippocampal region. After right temporal lobectomy the patient was rendered seizure free.

Figure 18.27 demonstrates the significant advantage of ictal SPECT as compared to interictal F-18-FDG PET. The patient, a 42-year-old female with seizure activity felt to arise from the frontal lobe regions, underwent a F-18-FDG brain PET scan which was non-localizing. An interictal technetium-99m-HMPAO brain SPECT scan also showed minimal reduction in the frontal lobe, as well as other areas of the brain. An ictal brain SPECT scan showed significant hyperemia in the right frontal lobe. The figure shows correlative images of the significant hyperemia on ictal SPECT as compared with nonspecific reduction on F-18-FDG PET.

18.4.3.3 Ictal and Interictal SPECT Analysis

A subgroup of "frontal" focal cortical epilepsy involves the pericallosal gyrus. This type of epilepsy, termed "cingulate epilepsy", demonstrates variable clinical semiology, and poorly localizing scalp electroencephalography patterns [64]. Seizures in most patients consist of "pseudoabsences" often mistaken for inattention and can be confused with "absence" attacks, resulting in misdiagnosis and unsuccessful seizure control. Dropping or nodding of the head is commonly observed. Head turning to the side contralateral to the involved cingulum and autonomic phenomena are observed in some patients. There is also a strong association between psychotic behavior and cingulate epilepsy. A complete clinical, neuropsychological and neuroimaging investigation is therefore usually performed in an attempt to localize the epileptogenic focus in this subgroup of patients. Due to the difficulty in identification of these seizure foci, we illustrate the value of com-

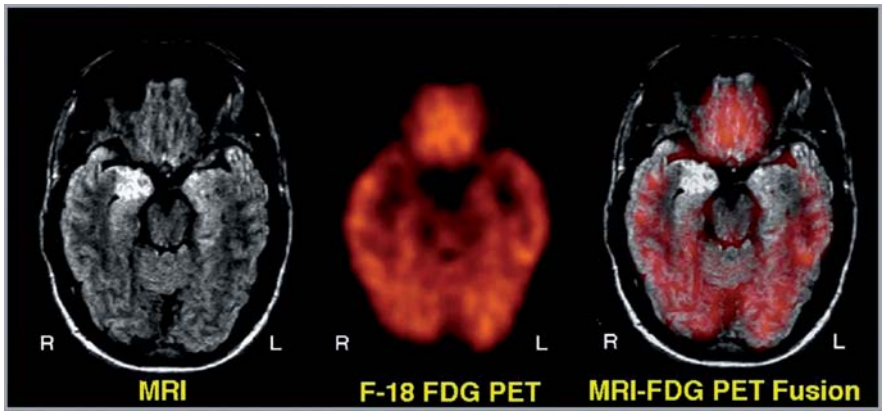

Fig. 18.26. Right mesial temporal lobe sclerosis in a 16-year-old boy. *Left* MRI shows abnormal high signal intensity in the right mesial temporal lobe (hippocampal region). *Middle* FDG PET scan shows a focal reduction of FDG uptake in the right mesial temporal lobe (hippocampal region). *Right* MRI-PET fusion image illustrating that the reduction in FDG corresponds to the region of MRI increase in signal intensity

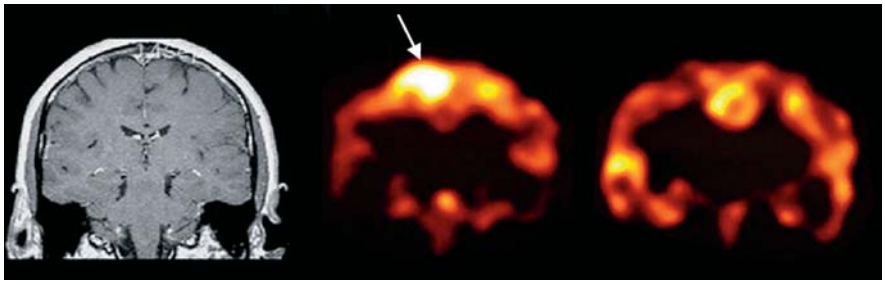

Fig. 18.27. Coronal images from MRI (*left*), ictal Tc-99m-HMPAO SPECT (*middle*), and interictal F-18-FDG PET scan (*right*) of a 42-year-old female with intractable seizures. *Left* The MRI scan is normal. *Middle* The ictal Tc-99m-HMPAO brain SPECT scan showed a focal area of significant hyperemia in the right mesial frontal lobe (*arrow*). *Right* There was minimal reduction of F-18-FDG uptake in this location, but this was not specific for identification of the epileptogenic focus. This scan illustrates the relative nonspecificity of mild areas of reduction on F-18-FDG brain PET scan in cases of frontal lobe epilepsy, and in these cases an ictal Tc-99m-HMPAO brain SPECT scan can provide greater accuracy in diagnosis

paring ictal SPECT with normal controls using statistical parametric mapping (SPM). Figure 18.28 shows a high resolution MRI and ictal Tc-99m-HMPAO brain SPECT scan of a 39-year-old man with cingulate gyrus epilepsy. Evaluation of the frontal lobes and cingulate region on MRI failed to reveal any structural abnormalities to suggest a possible seizure focus.

The ictal SPECT scan showed a focal region of hyperperfusion in the right anterior cingulate region. Count data were obtained by drawing regions of interest (ROI) around the right and left cingulate gyrus and showed that the right to left blood flow ratio was 1.3 and the right cingulate gyrus blood flow relative to cerebellar counts is 1.54, which is >4 SD above our normal control population (cingulate gyrus/cerebellum = 1.05 ± 0.12). Figure 18.29 shows the transverse, coronal, and sagittal projection of the fusion image between statistically significant increases in blood flow values and the Talairach standard anatomic brain atlas using the MEDx SPM software package (Sensor Systems, Sterling, Virginia).

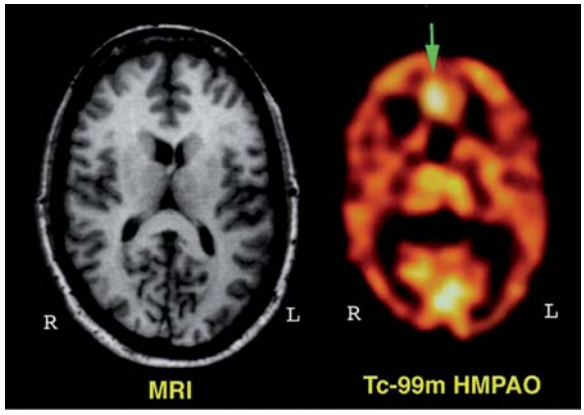

Fig. 18.28. High resolution MRI (*left*) and ictal Tc-99m-HMPAO brain SPECT scan (*right*) of a patient with cingulate gyrus epilepsy. Evaluation of the frontal lobes and cingulate region on MRI failed to reveal any structural abnormalities to suggest a possible seizure focus. The ictal SPECT scan (*right*) showed a focal region of hyperperfusion in the right anterior cingulate region (*arrow*)

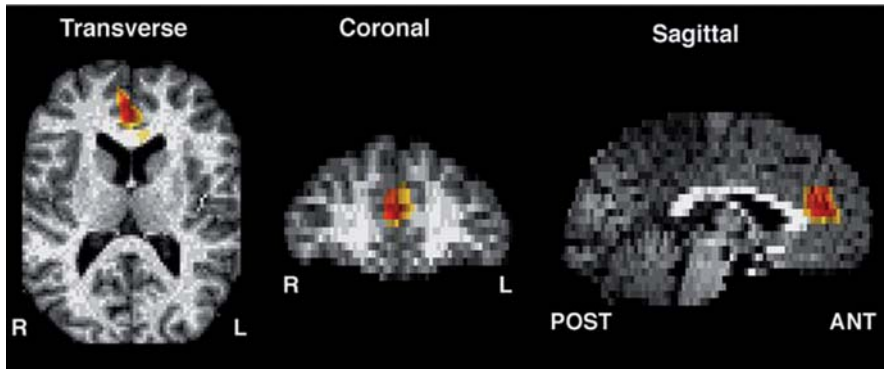

Fig. 18.29. Transverse (*left*), coronal (*middle*), and sagittal (*right*) projection of the fusion image between statistically significant increases in blood flow values (identified using statistical parametric mapping) and Talairach standard anatomic brain atlas from MEDx SPM. The highest values of statistically significant pixel values are shown in *red*. The region demonstrating maximum statistical significance was located in the right anterior cingulate gyrus; SPM coordinates (*x, y, z*) (millimeters) = (–6, +42, +24) in the transverse, coronal, and sagittal sections respectively

18.4.3.4 Method and Illustration of SPM Image Analysis in Epilepsy

The use of SPM image analysis is now increasingly being applied in the clinical diagnosis of neuroimaging of numerous disorders including epilepsy. An ictal SPECT scan can be compared with the interictal SPECT scan and correlated with a normal brain SPECT atlas using SPM to identify regions of significant alterations in regional cerebral blood flow related to seizure activity, and to localize these regions in Montreal Neurological Atlas space. Recent studies support SPM analysis of ictal SPECT scans [65]. Blinded analysis demonstrated correct lateralization in 18 of 21 mesial temporal lobe epilepsy cases with no false lateralization compared with subtraction analysis that showed correct lateralization in 16 and false lateralization in one patient.

Figures 18.30 and 18.31 illustrate the application of subtraction ictal SPECT co-registered to MRI (SISCOM) [66] with epilepsy analysis in an 11-year-old male suffering from seizure disorder since age 7. The patient has tonic clonic seizures, and the patient's MRI scan shows an arterial venous malformation in the right parietal lobe. But, prior to surgery the epileptogenic focus required unequivocal localization. An interictal SPECT scan shows reduced perfusion in the re-

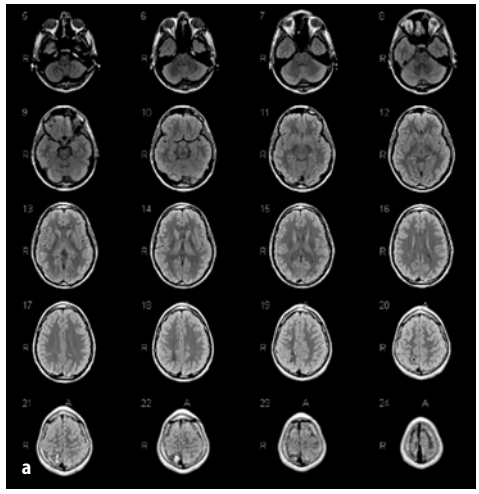

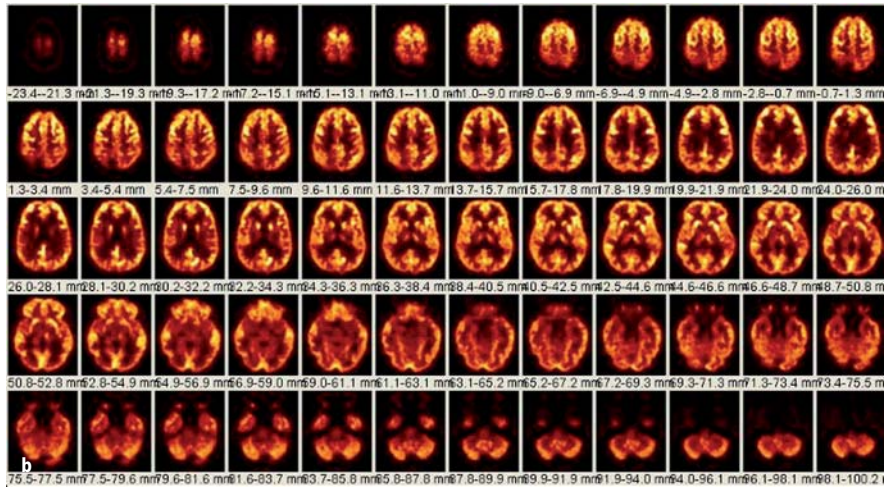

Fig. 18.30. a MRI scan sections of a 11-year-old boy suffering from seizure disorder since age 7. The patient has tonic clonic seizures. The MRI scan shows an arterial venous malformation in the right parietal lobe. **b** The interictal brain F-18-FDG PET scan shows an area of reduced metabolic activity in the right parietal lobe consistent with the location of the arterial venous malformation

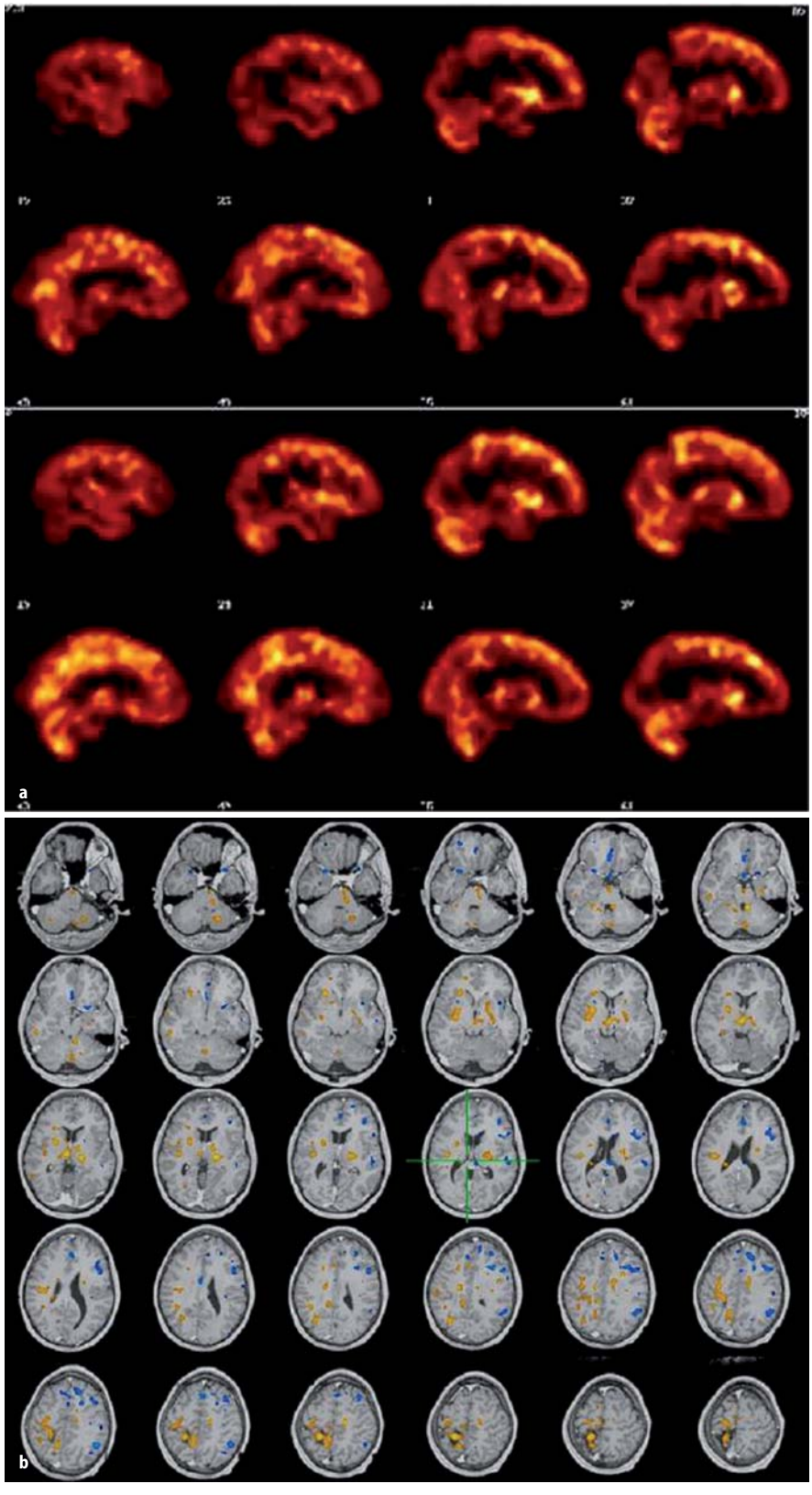

Fig. 18.31. a Images from an interictal Tc-99m-ECD brain SPECT (*top*) as compared to an ictal Tc-99m-ECD brain SPECT scan (*bottom*). One can see significant hyperemia anterior and inferior to the region of the arterial venous malformation on the ictal Tc-99m-ECD brain SPECT scan as compared to the interictal Tc-99m-ECD brain SPECT scan. **b** SISCOM analysis where the ictal and interictal SPECT are compared and statistically significant differences between the two are mapped onto the patient's MRI scan. One can see significantly increased differences in the ictal SPECT study as compared to the interictal SPECT study in the region anterior and in the location of the arterial venous malformation (*highlighted yellow areas*). The *highlighted blue area* shows areas of decreased uptake on the ictal scan as compared to the interictal scan, which can be seen to be positioned randomly throughout the cortex and has no clinical or localizing significance

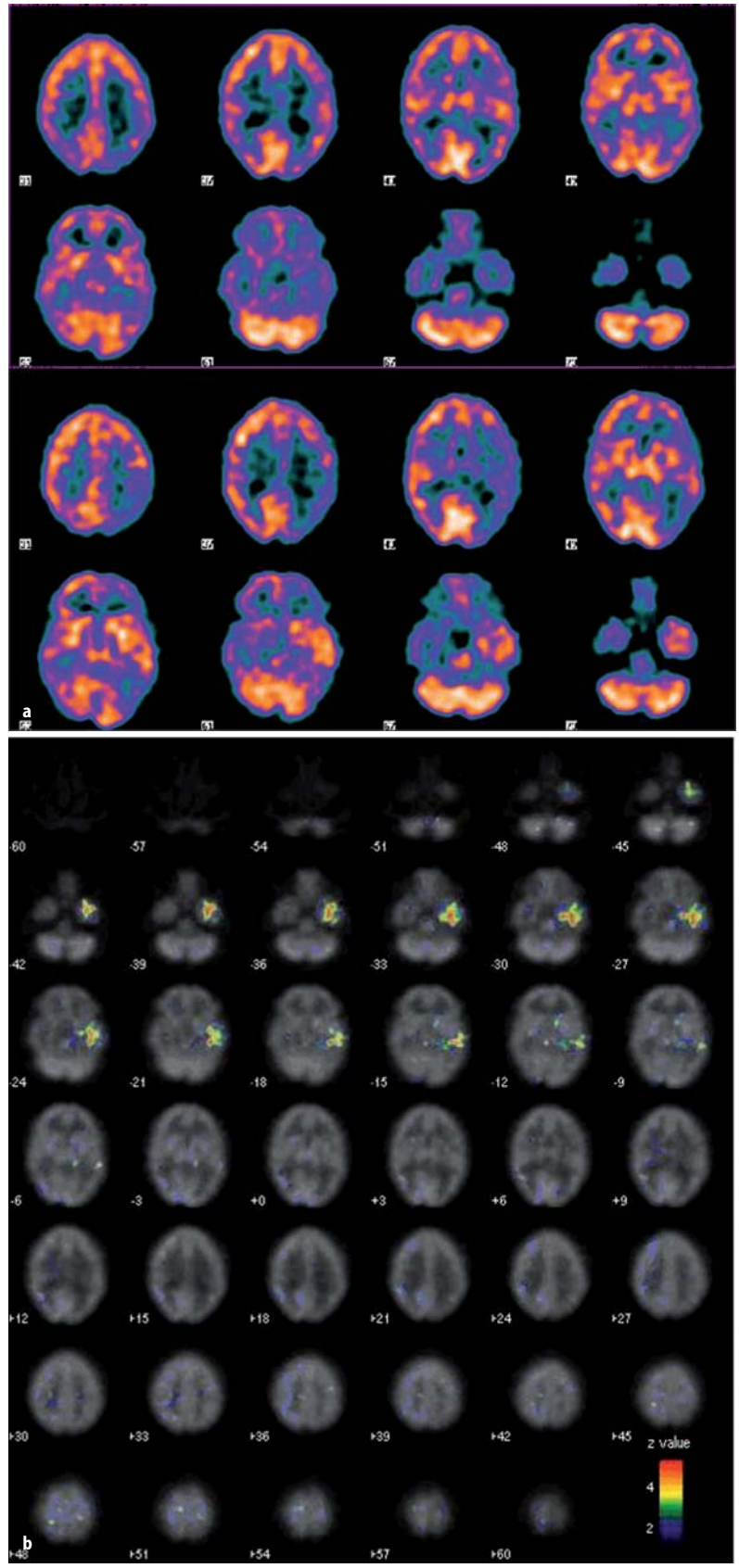

Fig. 18.32. a An interictal Tc-99m-ECD brain SPECT scan (*top*) as compared with an ictal Tc-99m-ECD brain SPECT scan (*bottom*). On the ictal brain SPECT scan one can see increased hyperemia involving the left temporal lobe. **b** Using SPM statistical comparison one can see statistically significant differences between the ictal and interictal scan involving the left temporal lobe. The test for statistical significance has *z* values between 3 and 4 (*coded color bar on the image*)

gion of the arterial venous malformation, in addition to a large area around the lesion. A F-18-FDG PET scan also shows reduction around the large AVM area. Ictal SPECT showed hyperperfusion in a region anterior and inferior to the AVM, confirming the location of epileptogenesis. This is shown on an SPM analysis fusion scan correlating regional cerebral perfusion with a T1 weighted MRI scan.

Figure 18.32 shows ictal SPECT as compared to interictal F-18-FDG PET in a 39-year-old right-handed male who has a 25-year history of refractory complex partial epilepsy of possible multifocal origin versus an indeterminate focal origin.

18.4.4 Psychiatry and Learning Disabilities

The diagnostic application of rCBF SPECT brain scanning in psychiatry is limited (on an individual patient basis), since most prior studies which showed statistical significance were performed on large patient groups. For example, in one study comparing regional cerebral blood flow in patients with major depressive disorder with that of healthy subjects, there was found to be a relationship between rCBF and negative depressive symptoms [67]. The study found decreased frontal lobe rCBF (hypofrontality) in a group of patients, with lower blood flow to the dorsolateral prefrontal cortex bilaterally, the right orbitofrontal cortex and the cingulate gyrus. This study suggests that decreased perfusion is associated specifically with negative symptom severity. These results support the hypothesis that, in major depressive disorder, negative symptoms and symptoms of depression are distinct phenomena and underscore the importance of negative symptom evaluation in neuroimaging studies of major depressive disorder and other disorders. Figure 18.33 shows a Tc-99m-HMPAO brain SPECT scan from a 42-year-old female presenting with a 6-year history of depression characterized with significant negative symptomatology. However, on an individual basis, patients with depression may have normal frontal lobe rCBF.

We have performed a study to evaluate changes in rCBF in children with autistic disorder [68]. In this study the autistic children underwent Tc-99m-HMPAO brain SPECT scans, which showed significant decreases in rCBF to the temporal lobes and frontal lobes. The corresponding CT and MRI scans failed to show any abnormality. This confirmed the sensitivity of rCBF brain SPECT to assist in the diagnosis of this severe brain disorder. Figure 18.34 shows images from a 14-year-old boy with autistic disorder who had a performance IQ of 70 and an Autistic Behavior Checklist score of 80 [69]. The subject was severely autistic, with severe language deficits. The reduction of perfusion to the temporal lobes is in accord with the neuropsychological location of the abnormalities identified in this disorder.

18.4.5 Evaluation of Brain Tumor

18.4.5.1 Brain Tumor Evaluation With Thallium-201

Identification of viable tumor after brain tumor therapy is a significant clinical problem since distinction between necrosis and residual or recurrent viable tumor cannot be accurately evaluated by either computed tomography or magnetic resonance imaging [70–72]. Functional imaging can distinguish cerebral necrosis from viable brain tumor and determine viability grade [73–75]. Figure 18.35 illustrates an example of the clinical utility of Tl-201 SPECT in a 14-year-old female with recurrent high grade astrocytoma involving the right

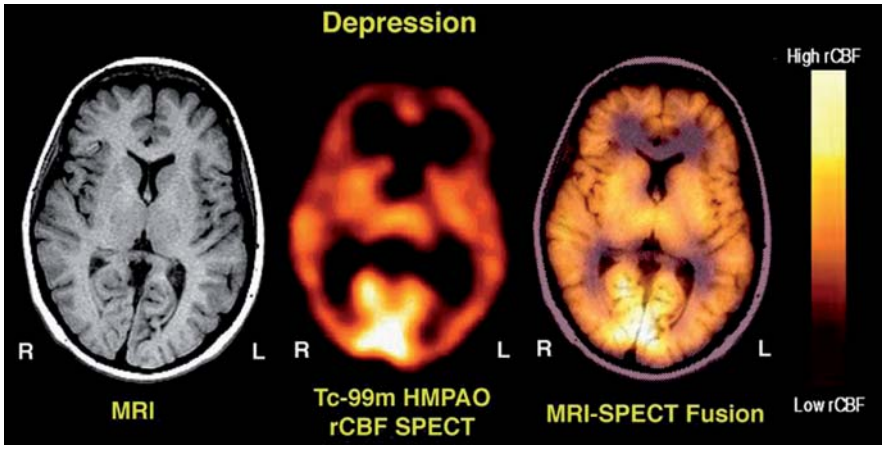

Fig. 18.33. A 42-year-old female presented with a 6-year history of depression. The patient had a normal MRI scan (*left*). The Tc-99m-HMPAO brain SPECT scan shows significant decrease in perfusion to the frontal lobe (*middle*). The MRI-SPECT fusion images (*right*) show that the diminution of rCBF is functional since there is no corresponding anatomic atrophy to account for the low reduction in frontal lobe perfusion. In addition, there was no evidence for cerebral vascular disease. This image illustrates that patients with severe depression can show reduction in frontal blood flow due to a relative reduction in synaptic activity with resultant loss of frontal lobe function and the concomitant associated mood of depression

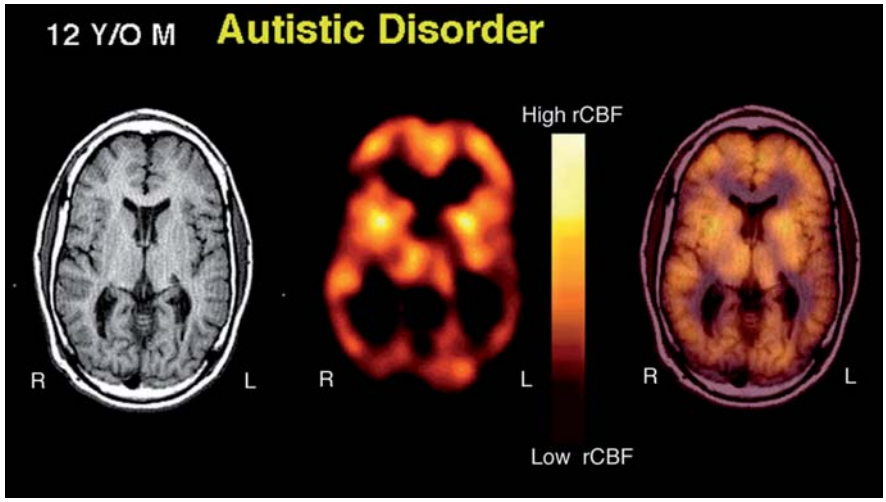

Fig. 18.34. Images from a 12-year-old boy with autistic disorder demonstrating low temporal lobe activity. The MRI scan (*left*) is normal. The co-registered Tc-99m-HMPAO brain SPECT scan (*middle*) shows bilateral posterior temporal (*left, lower than right*) and bilateral occipital diminution of tracer uptake with no corresponding anatomic abnormality, as demonstrated by the MRI-SPECT fusion image (*right*)

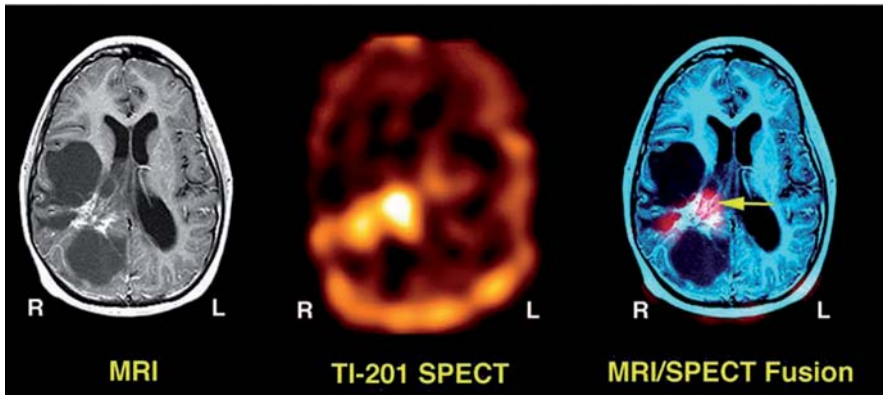

Fig. 18.35. Tl-201 brain SPECT scan and MRI images from a 14-year-old female with recurrent high grade astrocytoma involving the right hemisphere of the brain. The patient was diagnosed 2 years prior to the scans shown in this figure and underwent two courses of chemotherapy and radiation therapy. The MRI scan (*left*) shows radiation necrosis and cystic lesions but residual tumor viability cannot be assessed. The thallium-201 brain SPECT scan (*middle*) shows a focal region of intense uptake; however, the exact location cannot be determined with certainty. Because this patient was a candidate for gamma knife surgery, it was important to correlate the functional and anatomic image to locate the region of high grade viable tumor. The MRI-SPECT fusion image (*right*) clearly showed a localized region of intense uptake (*green arrow*)

hemisphere of the brain. The patient was initially diagnosed 2 years prior to the scans shown in this figure and underwent two courses of chemotherapy and radiation therapy. The thallium-201 brain SPECT scan was performed in order to determine if there was residual or recurrent viable tumor in this patient, who now presented with recurrent symptoms. It is not uncommon for patients to present with recurrent symptoms; however, the etiology of the symptoms can be due to either radiation necrosis and brain edema or recurrent viable tumor growth, and often these cannot be differentiated by an anatomic scan such as MRI. The MRI scan, in this case, shows radiation necrosis and cystic lesions, but viability cannot be determined.

The thallium-201 brain SPECT scan shows a focal region of intense uptake; however, the exact location cannot be determined with certainty. Because this patient was a candidate for gamma knife surgery, it was important to correlate the functional and anatomic images to obtain specific coordinates of the region of high grade viable tumor. Using the fiduciary reference system and fusion software described earlier, the MRI/SPECT fusion image clearly showed an area of intense uptake which was localized to the MRI scan, and subsequent gamma knife surgery allowed the patient to have extremely high doses of radiation directed only to the area of viable tumor, and the patient remains free of additional symptoms 1 year after gamma knife surgery.

The main utility of thallium in brain SPECT imaging is in the visualization of primary and metastatic CNS tumor. Blood brain barrier (BBB) breakdown in any lesion of the brain allows the passage and localization of thallium-201. After intravenous administration, the first 5 min of Tl-201 uptake depend on rCBF, rCBV and BBB breakdown. Subsequently the uptake depends on active transport by the tumor cell [76], tumor grade

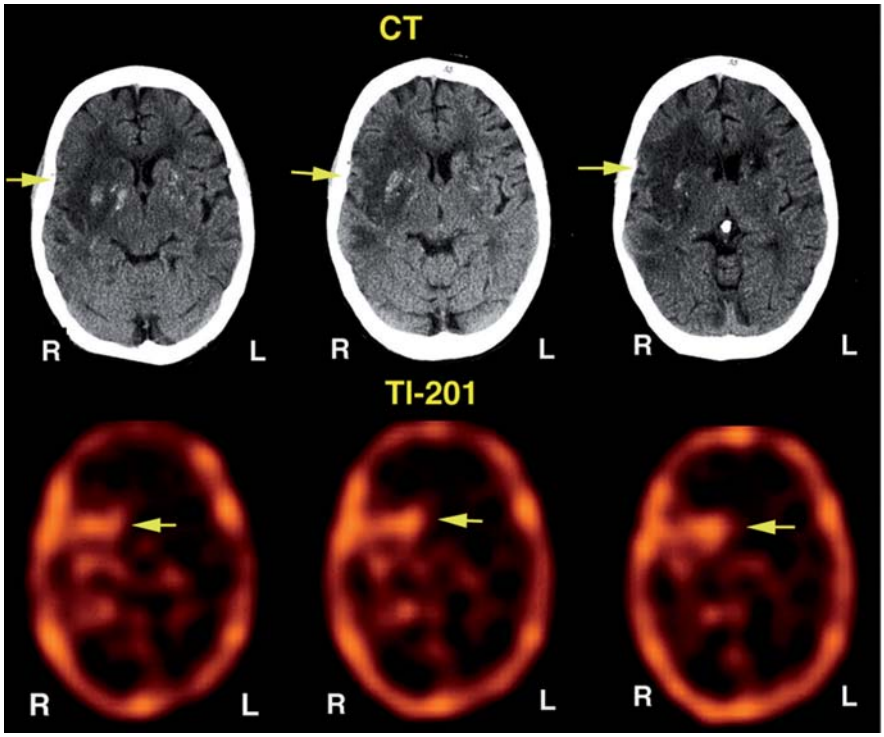

Fig. 18.36. An example of this nonspecific uptake in a patient with stroke. The patient is a 65-year-old man who was originally referred to our institution to evaluate for infarction versus tumor. The thallium-201 scan shows slight nonspecific uptake in the right basal ganglia region. The MRI scan shows an enhancing lesion in that location. The question of tumor versus stroke remained and an F-18-FDG PET scan was performed which was entirely negative in the location of the enhancing lesion on CT and the uptake on thallium-201, ruling out tumor

[77] and activity of the Na^+K^+ ATP^{ase} pump. Thallium-201 is therefore an extremely sensitive, but sometimes non-specific indicator of residual recurrent viable tumor since there is nonspecific uptake in regions of blood brain barrier breakdown not due to tumor. Figure 18.36 shows an example of this nonspecific uptake in a patient with stroke. The patient is a 65-year-old man who was originally referred to our institution to evaluate for infarction versus tumor. The Thallium-201 scan shows slight non-specific uptake in the right basal ganglia region. The MRI scan shows an enhancing lesion in that location. The question of tumor versus stroke remained, and an F-18-FDG PET scan was performed which was entirely negative in the location of the enhancing lesion on CT and the uptake of thallium-201, ruling out tumor. This case also shows that F-18-FDG has greater specificity in detection of recurrent or residual viable tumor but may have decreased sensitivity since F-18-FDG is also taken up by normal brain. Therefore, early and delayed Tl-201 SPECT imaging with semi-quantification may aid in the differentiation of specific thallium versus nonspecific BBB breakdown uptake when BBB breakdown is present in lesions which are low grade, inflammatory, or stroke.

18.4.5.2 Tc-99m-Sestamibi (Tc-99m-Hexakis-2-methoxy-2-isobutyl isonitrile) and Brain Tumor

A comparison of the differences in uptake of Tl-201 and Tc-99m-MIBI is illustrated in a 47-year-old female with glioblastoma multiforme who previously underwent radiation therapy and chemotherapy (Fig. 18.37). The MRI scan shows high signal intensity in the right cerebral hemisphere. From the MRI image one cannot distinguish between residual viable tumor versus radiation necrosis and edema. The thallium-201 brain SPECT scan section through the same level shows intense uptake, indicating tumor recurrence. The Tc-99m-sestamibi scan shows intense uptake with better anatomic delineation of the tumor boundary as noted by extension of the tumor through the anterior commissure, whereas in the same location the thallium scan has less clear definition.

18.4.5.3 Effect of Chemotherapy on Metabolism

It has been observed that there is greater uptake of Tc-99m-MIBI in malignant gliomas compared to Tl-201 in patients who did not receive chemotherapy or have been remotely treated [78]. Conversely, those patients who had recent chemotherapy have low Tc-99m-MIBI uptake in the tumor. Tissue fractionation studies have

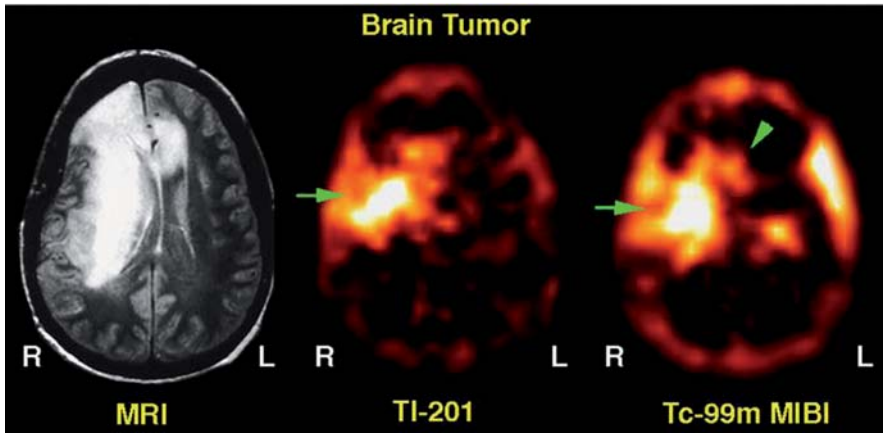

Fig. 18.37. This figure shows images from a 47-year-old female with glioblastoma multiforme who previously underwent radiation therapy and chemotherapy. The MRI scan (*left*) shows high signal intensity in the right cerebral hemisphere. From the MRI image one cannot distinguish between residual viable tumor versus radiation necrosis and edema. The thallium-201 brain SPECT scan section through the same level (*middle*) shows intense uptake indicating tumor recurrence. A Tc-99m sestamibi scan (*right*) shows intense uptake with better anatomic delineation of the tumor boundary as noted by extension of the tumor through the anterior commissure (*green arrowhead*), whereas in the same location the thallium scan has less clear definition. Also note Tc-99m-MIBI in the mid portion of the left hemisphere, which is unrelated to tumor uptake but due to choroid plexus secretion of Tc-99m-MIBI

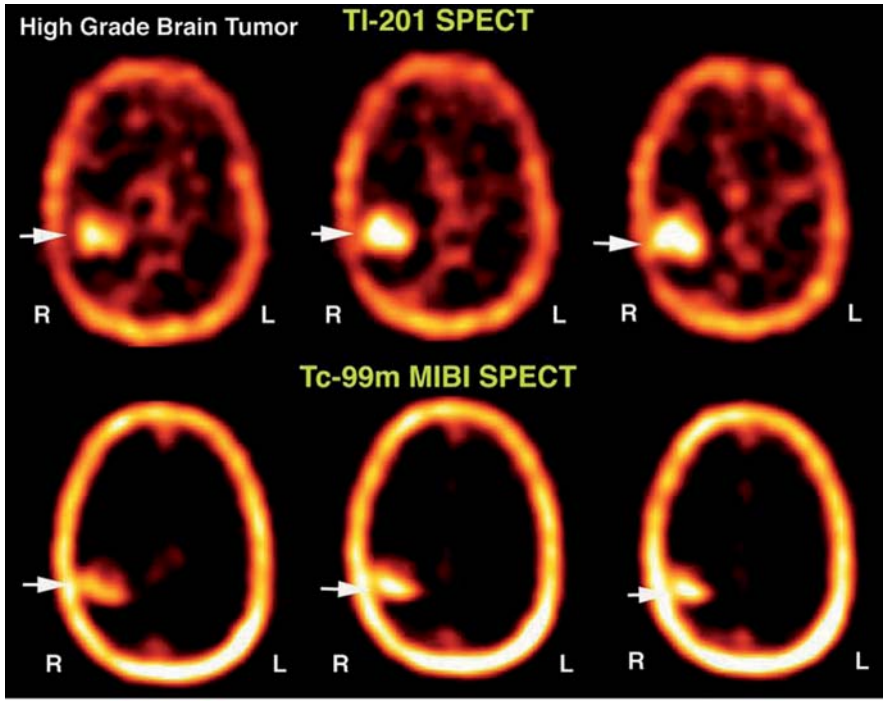

Fig. 18.38. Tl-201 and Tc-99m-MIBI SPECT scans of a 45-year-old female with high grade brain tumor in the right temporal lobe who had recent chemotherapy and who had low Tc-99m-MIBI uptake in the tumor, compared with Tl-201. This case compares the diagnostic capability of thallium-201 SPECT (*top row*) as compared with Tc-99m-HMPAO MIBI SPECT (*bottom row*). Each of the tracers shows increased uptake in recurrent viable tumor. The reduction of MIBI immediately after chemotherapy indicates that there is DNA damage and the tumor is less able to recover from chemotherapy damage and, therefore, the patient has a better prognosis

demonstrated the release of Tc-99m-MIBI from the mitochondria and a decline in Tc-99m-MIBI uptake in the presence of Ca^{2+} [79]. It is conceivable that irreversible tissue injury leads to sequestration of extracellular Ca^{2+} into the cell and the mitochondria, leading to cell death. Injury to brain tumor cells from radiation or chemotherapy will theoretically increase the Ca^{2+} level and alter the mitochondrial membrane potential, leading to a decline in Tc-99m-MIBI uptake. Early response to treatment can therefore theoretically be determined by comparing Tc-99m-MIBI uptake before and after a course of radiation or chemotherapy. Decline in the Tc-99m-MIBI or Tl-201 uptake ratio may indicate lethal injury or decreased viability of neoplastic cells and effective response to treatment.

The cellular uptake mechanisms of Tc-99m-MIBI in brain tumor are postulated to represent mitochondrial energetics. Figure 18.38 shows an example of the increased uptake of Tc-99m-MIBI in a 45-year-old female with right parietal astrocytoma. Several studies [72, 78]

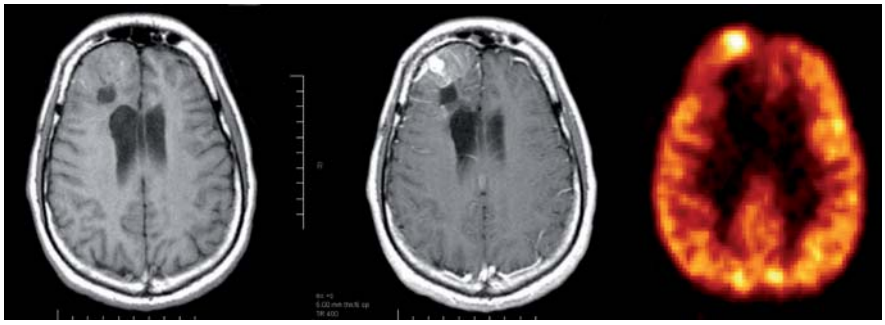

Fig. 18.39. *Left* Non-contrast MRI scan with abnormality involving the right frontal lobe. *Middle* Contrast MRI scan shows enhancement in the right frontal lobe. *Right* Focal area of increased F-18-FDG uptake involving the right frontal lobe consistent with high grade transformation and recurrence of tumor in the right frontal lobe eight years after initial diagnosis, therapy and complete remission

have established that in the evaluation of brain tumor a semiquantitative method using counts from the tumor region to counts in normal brain can be useful in the assessment of viability, tumor bulk, and chemotherapeutic efficacy.

The differential effect of tumor therapy on Tl-201 and Tc-99m-MIBI uptake is illustrated in a 45-year-old female with high grade brain tumor in the right temporal lobe. This case compares the diagnostic capability of thallium-201 SPECT with Tc-99m-MIBI SPECT (Fig. 18.33). Each of the tracers shows increased uptake in recurrent viable tumor. It has been postulated that thallium-201 is taken up by the sodium potassium ATPase activity and reflects global cellular energetics. On the other hand, the uptake of Tc-99m-MIBI is related to mitochondrial energetics, and high uptake of Tc-99m MIBI possibly indicates a poor prognosis since the tumor continues to have a high glycolytic rate, glucose utilization, and good repair mechanisms. The reduction of MIBI immediately after chemotherapy indicates that there is DNA damage (both to the nucleus and the mitochondrial DNA) with impairment of the TCA cycle and involved glycolytic enzymes. This compromises the production of ATP and cripples the cellular reparative mechanisms such that the tumor is less able to recover from chemotherapy damage and, therefore, the patient has a better prognosis. It is suggested that the use of MIBI before and after chemotherapy treatment may be used as an indicator for the efficacy of a specific type of chemotherapy, possibly after one dose. This would permit several trials to be performed to determine the most efficacious chemotherapy before complete treatment is instituted allowing the patient to remain relatively refractory from the hematologic and other side effects of the chemotherapy.

18.4.5.4 2-[F-18]Fluoro-2-deoxy-d-glucose (F-18-FDG) for Detection of Recurrent or Residual Viable Brain Tumor

Figure 18.39 shows a PET scan with abnormal uptake of F-18-FDG in a patient with recurrent brain tumor involving the anterior frontal lobe after 8 years of remission. The MRI shows contrast enhancement. F-18-FDG is a less sensitive but more specific tracer for the detection of recurrent or residual viable tumor as compared to thallium-201, which is a more sensitive but less specific tracer due to non-specific BBB breakdown accumulation. The lack of sensitivity of F-18-FDG is due to the fact that it is taken up by the normal brain. The lack of specificity of thallium-201 is due to the fact that it accumulates at the site of blood brain barrier breakdown prior to its uptake through the Na^+K^+ ATP^{ase} pump.

References

1. Saha GB, MacIntyre WJ, Go RT (1994) Radiopharmaceuticals for brain imaging. Semin Nucl Med 24:324 – 349
2. Lassen NA, Blasberg RG (1988) Technetium-99m-d,l-HM-PAO, the development of a new class of 99mTc-labeled tracers: an overview. J Cereb Blood Flow Metabol 8:S1 – 51

2a. Tokumaru AM, Barkovich AJ, O'uchi T, Matsuo T, Kusano S (1999) The evolution of cerebral blood flow in the developing brain: evaluation with iodine-123 iodoamphetamine SPECT and correlation with MR imaging. Am J Neuroradiol 20:845 – 852

2b. Takahashi T, Shirane R, Sato S, Yoshimoto T (1999) Developmental changes of cerebral blood flow and oxygen metabolism in children. Am J Neuroradiol 20:917 – 922

3. Walovitch RC, Hill TC, Garrity ST, Cheesman EH, Burgess BA, O'Leary DH, Watson AD, Ganey MV, Morgan RA, Williams SJ (1989) Characterization of technetium-99m-l,l-ECD for brain perfusion imaging, part 1: Pharmacology of technetium-99m ECD in nonhuman primates. J Nucl Med 30:1892 – 1901
4. Lassen NA (1985) Cerebral blood flow tomography with xenon-133. Semin Nucl Med 15:347 – 356
5. Mintun MA, Raichle ME, Martin WR, Herscovitch P (1984) Brain oxygen utilization measured with O-15 radiotracers and positron emission tomography. J Nucl Med 25:177 – 187
6. Mountz JM, Raymond PA, McKeever PE, Modell JG, Hood TW, Barthel LK, Stafford-Schuck KA (1989) Specific localization of thallium-201 in recurrent high grade astrocytoma by microautoradiography. Cancer Res 49:4053 – 4056
7. O'Tuama LA, Treves ST, Larar JN, et al (1993) Thallium-201 versus technetium-99m-MIBI SPECT in evaluation of childhood brain tumors: A within-subject comparison. J Nucl Med 34:1045 – 1051
8. Conti PS (1995) Introduction to imaging brain tumor metabolism with positron emission tomography (PET). Cancer Invest 13:244 – 259

9. Meegalla S, Plossl K, Kung MP, Chumpradit S, Stevenson DA, Frederick D, Kung HF (1996) Tc-99m-labeled tropanes as dopamine transporter imaging agents. Bioconjugate Chem 7:421 – 429
10. Emond P, Chalon S, Garreau L, Dognon AM, Bodard S, Frangin Y, Baulieu JL, Besnard JC, Guilloteau D (1997) A new iodinated tropane derivative (beta-CDIT) for in vivo dopamine transporter exploration: comparison with beta-CIT. Synapse 26:72 – 80
11. Maisey MN (2002) Overview of clinical PET. Br J Radiol 75:S1–S5
12. Ell PJ, Gambhir S (2004) Nuclear medicine in clinical diagnosis and treatment, 3rd edn. 2 volumes. Elsevier/Churchill Livingstone, Edinburgh
13. Andersen AR, Friberg H, Knudsen KB, Barry DI, Paulson OB, Schmidt JF, Lassen NA, Neirinckx RD (1988) Extraction of [99mTc]-d,l-HM-PAO across the blood-brain barrier. J Cereb Blood Flow Metabol 8:S44 – 51
14. Leveille J, Demonceau G, De Roo M, Rigo P, Taillefer R, Morgan RA, Kupranick D, Walovitch RC (1989) Characterization of technetium-99m-l,l-ECD for brain perfusion imaging, part 2: Biodistribution and brain imaging in humans. J Nucl Med 30:1902 – 1910
15. Jacquier-Sarlin MR, Polla BS, Slosman DO (1996) Cellular basis of ECD brain retention. J Nucl Med 37:1694 – 1697
16. Slosman DO, Chicherio C, Ludwig C, Genton L, de Ribaupierre S, Hans D, Pichard C, Mayer E, Annoni J-M, de Ribaupierre A (2001) Xe-133 SPECT cerebral blood flow study in a healthy population: determination of T-scores. J Nucl Med 42:864 – 870
17. Yamauchi H, Fukuyama H, Nagahama Y, Nabatame H, Ueno M, Nishizawa S, Konishi J, Shio H (1999) Significance of increased oxygen extraction fraction in five-year prognosis of major cerebral arterial occlusive diseases. J Nucl Med 40:1992 – 1998
18. Deutsch G, Mountz JM, Liu HG, San Pedro EC, Sutor RJ (1997) Xenon-133 brain SPECT provides improved sensitivity to cerebrovascular stress studies. J Nucl Med 38:37P
19. Price JC (2003) Principles of tracer kinetic analysis. Neuroimaging Clin North Am 13:689 – 701
20. Woods RP, Cherry SR, Mazziotta JC (1992) Rapid automated algorithm for aligning and reslicing PET images. J Comput Assist Tomogr 16:620 – 633
21. Ancri D, Basset JY, Longchampt MF, Etavard CH (1978) Diagnosis of cerebral lesions by Tl-201. Radiology 128:417
22. Nass HW (1977) New Tl-201 nuclear decay data. J Nucl Med 18:1047 – 1048
23. Saha GB (1992) Miscellaneous radiopharmaceuticals of medical interest. In: Fundamentals of nuclear pharmacy, 3rd edn. Springer, New York, p 130
24. Sehweil AM, McKillop JH, Milroy R, et al (1989) Mechanism of 201 Tl uptake in tumours. Eur J Nucl Med 15:376
25. Piwnica-Worms DP, Kronauge JF, LeFurgey A, et al (1994) Mitochondrial localization and characterization of 99-Tc-sestamibi in heart cells by electron probe x-ray microanalysis and 99Tc-NMR spectroscopy. Magn Reson Imaging 4:641 – 652
26. Sokoloff L, Reivich M, Kennedy C, Rosiers MD, Patlak C, Pettigrew K, et al (1977) The [^{14}C]deoxyglucose method for the measurement of local cerebral glucose utilization: theory, procedure, and normal values in the conscious and anesthetized albino rat. J Neurochem 28:897 – 916
27. Huang SC, Phelps ME, Hoffman EJ, Sideris K, Selin CJ, Kuhl DE (1980) Noninvasive determination of local cerebral metabolic rate of glucose in man. Am J Physiol 238:E69 – 82
28. Lucignani G, Schmidt KC, Moresco RM, Striano G, Colombo F, Sokoloff L, Fazio F (1993) Measurement of regional cerebral glucose utilization with fluorine-18-FDG and PET in heterogeneous tissues: theoretical considerations and practical procedure. J Nucl Med 34:360 – 369
29. Patlak CS, Blasberg RG (1985) Graphical evaluation of blood-to-brain transfer constants from multiple-time uptake data. Generalizations. J Cereb Blood Flow Metab 5: 584 – 590
30. Sokoloff L (1997) Relation between physiological function and energy metabolism in the central nervous system. J Neurochem 29:13 – 26
31. Liu HG, Mountz JM (2003) PET FDG method F-18-FDG brain positron emission tomography and Tl-201 early and delayed SPECT in distinguishing atypical cerebral tumor from cerebral infarction. Clin Nucl Med 28:241 – 242
32. Chao ST, Suh JH, Raja S, Lee SY, Barnett G (2001) The sensitivity and specificity of FDG PET in distinguishing recurrent brain tumor from radionecrosis in patients treated with stereotactic radiosurgery. Int J Cancer 20;96:191 – 197
33. Emond P, Chalon S, Garreau L, Dognon AM, Bodard S, Frangin Y, Baulieu JL, Besnard JC, Guilloteau D (1997) A new iodinated tropane derivative (beta-CDIT) for in vivo dopamine transporter exploration: comparison with beta-CIT. Synapse 26:72 – 80
34. Tatsch K, Schwarz J, Mozley P, Linke R, Pogarell O, Oertel WH, Fieber RS, Hahn K, Kung HF (1997) Relationship between clinical features of Parkinson's disease and presynaptic dopamine transporter binding assessed with [^{123}I]IPT and single-photon emission tomography. Eur J Nucl Med 24:415 – 421
35. Brucke T, Asenbaum S, Pirker W, Djamshidian S, Wenger S, Wober C, Muller C, Podreka I (1997) Measurement of the dopaminergic degeneration in Parkinson's disease with [^{123}I] beta-CIT and SPECT. Correlation with clinical findings and comparison with multiple system atrophy and progressive supranuclear palsy. J Neural Transm 50:9 – 24
36. Naumann M, Pirker W, Reiners K, Lange K, Becker G, Brucke (1997) [^{123}I]beta-CIT single-photon emission tomography in DOPA-responsive dystonia. Mov Dis 12:448 – 451
37. Barthel H, Cleij MC, Collingridge DR, Hutchinson OC, Osman S, He Q, Luthra SK, Brady F, Price PM, Aboagye EO (2003) 3'-Deoxy-3'-[^{18}F]fluorothymidine as a new marker for monitoring tumor response to antiproliferative therapy in vivo with positron emission tomography. Cancer Res 63:3791 – 3798
38. Chen W, Cloughesy T, Kamdar N, Satyamurthy N, Bergsneider M, Liau L, Mischel P, Czernin J, Phelps ME, Silverman DHS (2005) Imaging proliferation in brain tumors with 18F-FLT PET: comparison with 18F-FDG. J Nucl Med 46:945 – 952
39. d'Asseler YM, Koole M, Lemahieu I, Achten E, Boon P, De Deyn PP, Dierckx RA (1997) Recent and future evolutions in NeuroSPECT with particular emphasis on the synergistic use and fusion of imaging modalities. Acta Neurol Belg 97:154 – 162
40. Blume H, Hemminger BM (1997) Image presentation in digital radiology: perspectives on the emerging DICOM display function standard and its application. Radiographics 17:769 – 777
41. Bartenstein P, Asenbaum S, Catafau A, Halldin C, Pilowski L, Pupi A, Tatsch K (2002) European Association of Nuclear Medicine (2002) European Association of Nuclear Medicine procedure guidelines for brain imaging using F-18 FDG. Eur J Nucl Med Mol Imaging 29:43 – 48
42. Talairach J, Szikla G, Tournoux P, Prossalentis M, Bordasferrer L, Covello L, Jacob M, Mempel E (1967) Atlas of stereotaxis anatomy of the telencephalon. Masson, Saint-Germain, Paris
43. Evans AC, Collins DL, Mills SR, Brown ED, Kelly RL, Peters TM (1993) 3D statistical neuroanatomical models from

305 MRI volumes. Proc. IEEE Nucl Sci Symp Med Imaging Conf, pp 1813 – 1817
44. Friston KJ, Holmes AP, Worsley KJ, Poline JP, Frith CD, Frackowiak RSJ (1995) Statistical parametric maps in functional imaging: A general approach. Hum Brain Mapp 2:189 – 210
45. Wellcome Department of Imaging Neuroscience, Functional Imaging Laboratory, 12 Queen Square, London, WC1N 3BG; http://www.fil.ion.ucl.ac.uk/
46. Asenbaum S, Brucke T, Pirker W, Pietrzyk U, Podreka I (1998) Imaging of cerebral blood flow with technetium-99m-HMPAO and technetium-99m-ECD: a comparison. J Nucl Med 39:613 – 618
47. Cikrit DF, Dalsing MC, Harting PS, Burt RW, Lalka SG, Sawchuk AP, Solooki B (1997) Cerebral vascular reactivity assessed with acetazolamide single photon emission computer tomography scans before and after carotid endarterectomy. Am J Surg 174:193 – 197
48. Ropper AH, Brown RJ (2005) Adams and Victor's principles of neurology. McGraw-Hill, New York
49. von Strauss E, Viitanen M, De Ronchi D, Winblad B, Fratiglioni L (1999) Aging and the occurrence of dementia: findings from a population-based cohort with a large sample of nonagenarians. Archiv Neurol 56:587 – 592
50. McKhann G, Drachman D, Folstein M, Katzman R, Price D, Stadlan EM (1984) Clinical diagnosis of Alzheimer's disease: report of the NINCDS-ADRDA Work Group under the auspices of Department of Health and Human Services Task Force on Alzheimer's Disease. Neurology 34:939 – 944
51. Reiman EM, Chen K, Alexander GE, Caselli RJ, Bandy D, Osborne D, Saunders AM, Hardy J (2005) Correlations between apolipoprotein E å4 gene dose and brain-imaging measurements of regional hypometabolism. Proc Natl Acad Sci U S A 102:8299 – 8302
52. Cummings JL (2004) Alzheimer's disease. N Engl J Med 351:56 – 67
53. Petersen RC, Thomas RG, Grundman M, Bennett D, Doody R, Ferris S, Galasko D, Jin S, Kaye J, Levey A, Pfeiffer E, Sano M, van Dyck CH, Thal LJ (2005) Alzheimer's Disease Cooperative Study Group. Vitamin E and donepezil for the treatment of mild cognitive impairment. N Engl J Med 352:2379 – 2388
54. Silverman DHS (2004) Brain 18F-FDG PET in the diagnosis of neurodegenerative dementias: comparison with perfusion SPECT and with clinical evaluations lacking nuclear imaging. J Nucl Med 45:594 – 607
55. Burdette JH, Minoshima S, Vander Borght T, Tran DD, Kuhl DE (1996) Alzheimer's disease: improved visual interpretation of PET images by using three-dimensional stereotaxic surface projections. Radiology 198:837 – 843
56. Decision Memo for Positron Emission Tomography (FDG) and Other Neuroimaging Devices for Suspected Dementia (CAG-00088R). Centers for Medicare & Medicaid Services 7500 Security Boulevard Baltimore, MD 21244; http://www.cms.hhs.gov/mcd/viewdecisionmemo.asp?id=104
57. Mesulam MM, Johnson N, Grujic Z, Weintraub S (1997) Apolipoprotein genotypes in primary progressive aphasia. Neurology 49:51 – 55
58. Westbury C, Dan B (1997) Primary progressive aphasia: a review of 112 cases. Brain Lang 60:381 – 406
59. Kuzniecky R, Mountz JM, Thomas F (1993) Ictal ^{99m}Tc-HM-PAO brain single photon emission computed tomography in electroencephalographic non-localizable partial seizures. J Neuroimag 3:100 – 102
60. Kuzniecky R, Mountz JM, Wheatley G, Morawetz R (1993) Ictal single photon emission computed tomography demonstrates localized epileptogenesis in cortical dysplasia. Ann Neurol 34:627 – 631
61. Laich E, Kuzniecky R, Mountz JM, Liu HG, Gilliam F, Bebin M, Faught E, Morawetz R (1997) Supplementary sensorimotor area epilepsy: identification of the epileptogenic zone and propagation pathways using ictal SPECT. Brain 120:855 – 864
62. Knowlton RC, Lawn ND, Mountz JM, Buddhiwardhan O, Miller S, Burneo JG, Kuzniecky RI (2004) Ictal single-photon emission computed tomography imaging in extra temporal lobe epilepsy using statistical parametric mapping. J Neuroimaging 14:324 – 330
63. Knowlton RC, Lawn ND, Mountz JM, Kuzniecky RI (2004) Ictal SPECT analysis in epilepsy: subtraction and statistical parametric mapping techniques. Neurology 63:10 – 15
64. Mazars G (1970) Criteria for identifying cingulate epilepsies. Epilepsia 11:41 – 47
65. Zubal IG, Spencer SS, Imam K, et al (1995) Difference images calculated from ictal and interictal technetium-99m-HMPAO SPECT scans of epilepsy. J Nucl Med 36:684 – 689
66. O'Brien TJ, So EL, Mullan BP, Hauser MF, Brinkmann BH, Bohnen NI, Hanson D, Cascino GD, Jack CR Jr, Sharbrough FW (1998) Subtraction ictal SPECT co-registered to MRI improves clinical usefulness of SPECT in localizing the surgical seizure focus. Neurology 50:445 – 454
67. Galynker II, Cai J, Ongseng F, Finestone H, Dutta E, Serseni D (1998) Hypofrontality and negative symptoms in major depressive disorder. J Nucl Med 39:608 – 612
68. Mountz JM, Tolbert LC, Lill DW, Katholi CR, Liu HG (1995) Functional deficits in autistic disorder: characterization by technetium-99m HMPAO and SPECT. J Nucl Med 36:1156 – 1162
69. Krug DA, Arick JR, Almond PG (1980) Behavior checklist for identifying severely handicapped individuals with high levels of autistic behavior. J Child Psychol Psyc 21:221 – 229
70. Wilms G, Marchall G, Demaerel PH, et al (1991) Gadolinium enhanced MRI of intracranial lesions. A review of indications and results. Clin Imaging 15:153
71. Valk PE, Dillon WP (1991) Diagnostic imaging of central nervous system radiation injury. In: Gutin PH, Leibel SA, Sheline GE (eds) Radiation injury to the central nervous system. Raven Press, New York, pp 211 – 237
72. Mountz JM, Deutsch G, Kuzniecky R, Rosenfeld SS (1994) Brain SPECT: 1994 update. In: Freeman LM (ed) Nuclear medicine annual 1994. Raven Press, New York, pp 1 – 54
73. Schwartz RB, Holman BL, Polk JF, et al (1998) Dual-isotope single photon emission computerized tomography scanning in patients with glioblastoma multiforme: association with patient survival and histopathological characteristics of tumor after high-dose radiotherapy. J Neurosurg 89:60
74. Kaplan WD, Takvorian T, Morris JH, et al (1987) Thallium-201 brain imaging: a comparative study with pathologic correlation. J Nucl Med 28:47
75. Black KL, Hawkins RA, Kim KT, et al (1989) Use of thallium-201 SPECT to quantitate malignancy grade of gliomas. J Neurosurg 71:342
76. Lastoria S, Castelli L, Vergara E, et al (1990) Human gliomas radioimmunoimaging with I-131 BC-2 murine IgG: preliminary report. J Nucl Med Allied Sci 34:173
77. Ueda T, Kaji Y, Wakisaka S, et al (1993) Time sequential single photon emission computed tomography studies in brain tumour using 201 Tl. Eur J Nucl Med 20:138
78. San Pedro EC, Yilmaz M, Liu HG, Rosenfeld SS, Mountz JM (1999) A new semiquantitative method for comparing brain tumor uptake of Tc-99m sestamibi and thallium-201. Clin Nucl Med 24:868 – 873
79. Crane P, Laliberte R, Heminway S, et al (1993) Effect of mitochondrial viability and metabolism on technetium-99m-sestamibi myocardial retention. Eur J Nucl Med 20:20

18.5 Cerebrospinal Fluid (CSF) Imaging

Abdelhamid H. Elgazzar

18.5.1 CSF Anatomy and Physiology

CSF is a clear fluid similar to blood plasma. The intracranial and spinal cord structures float in CSF and are protected from jolts and blows. Principally, the choroid plexus in the lateral, third, and fourth ventricles produces the major portion of CSF. Normally, between 125 and 150 ml of CSF is circulating within the ventricles and subarachnoid space at any given time. Approximately 600 ml of CSF is produced daily. The CSF normally drains from the lateral ventricles sequentially through the interventricular foramen of Monro, the third ventricle, and the cerebral aqueduct of Sylvius into the fourth ventricle and then leaves the ventricular system through the median foramen of Magendie and two lateral foramina of Luschka. Here the CSF enters the subarachnoid space. Along the base of the brain, this space extends into a number of lakes called cisterns. The CSF is absorbed through the pacchionian granulations of the pia-arachnoid villi into the superior sagittal sinus.

18.5.2 Pathophysiology

18.5.2.1 Hydrocephalus

The term hydrocephalus generally refers to those conditions that produce an imbalance between the rate of production and absorption of the cerebrospinal fluid, leading to dilatation of the ventricular system. Hydrocephalus normally occurs as a result of obstruction to the flow and absorption of CSF, although there are rare cases of choroid plexus papillomas causing hydrocephalus by overproduction of CSF.

Hydrocephalus is traditionally classified as communicating and noncommunicating, based on whether ventricular obstruction is present. In the former, the ventricular system continues to communicate with the subarachnoid spaces outside the brain through the fourth ventricular foramina of Luschka and Magendie. Noncommunicating hydrocephalus correspondingly refers to the presence of occlusion within the ventricular system. Hydrocephalus may be either congenital or acquired. Arnold-Chiari malformation, Dandy-Walker malformations, and aqueductal stenosis/atresia are common causes of the congenital variety. In the acquired type many pathological conditions, including inflammatory, infectious, traumatic and neoplastic disorders, can cause hydrocephalus [1, 2].

Noncommunicating hydrocephalus can be the result of intraventricular mass, aqueductal obstruction, or fourth ventricular obstruction. Communicating hydrocephalus, on the other hand, results from meningitis, meningeal carcinomatosis, or cerebral dural sinus thrombosis, or it is idiopathic in elderly patients. Normal-pressure hydrocephalus (NPH) is a communicating hydrocephalus of particular interest to nuclear medicine professionals since radionuclide cisternography is useful in its diagnosis and management.

In NPH, the usual flow of CSF is impaired somewhere in the intracranial subarachnoid space, resulting in a reversal of CSF flow and dilatation of the lateral ventricles. There is free communication between the ventricular system and the subarachnoid pathways and no elevation of CSF pressure. Clinically, the entity occurs in patients 50 – 70 years of age and is characterized by dementia, gait disturbances, and fecal and urinary incontinence. Most commonly, this condition results from subarachnoid hemorrhage or meningoencephalitis.

18.5.2.2 Cerebrospinal Fluid Leakage

Leaking of CSF may be etiologically classified into:

1. Traumatic: occurring in about 30% of basilar skull fractures. Two percent of all head injuries develop a CSF fistula. This leak is usually unilateral, scanty, seen within 48 h after trauma, and resolves in 1 week.
2. Nontraumatic: taking place in tumors (pituitary, brain, skull), skull infections, and congenital defects (encephalocele). This leak is profuse and may persist for years. Infection complicates the untreated leak in 25% – 50% of cases.
   CSF rhinorrhea may occur anywhere from the frontal sinus to the temporal bone. The cribriform plate is the most susceptible to fracture and rhinorrhea. Otorrhea is much less common [3, 4].
3. Spontaneous intracranial hypotension (SIH). This is an increasingly recognized condition due to CSF leak without apparent prior cause. This condition is recognized now among causes of postural headache, which in this case is secondary to low CSF pressure [5 – 7].

18.5.3 Radionuclide Cisternography

When hydrocephalus is suspected, the goal of imaging evaluation in general is to identify any abnormality of the ventricular or the subarachnoid space morphology and, if other unexplained ventriculomegaly is present, to demonstrate the site and nature of any impediment to the flow of CSF. MRI is generally the best imaging

method for achieving this goal. It also visualizes CSF movement and evaluates ventricles and sulci. On T_2-weighted images, the low signal intensity of CSF flowing in the cerebral aqueduct stands out in contrast to the high signal intensity of the adjacent tectum of the mesencephalon, a useful sign of aqueductal patency [1]. In children with patent anterior fontanels, the ventricular size can be assessed by ultrasound. When NPH is suspected and to assess patient's qualification for a shunting surgery, several diagnostic modalities have been utilized. These include the infusion test for measurement of intracranial pressure of the ventricular system or the subarachnoid space on the spinal cord level, the neuropsychological evaluation as well as the brain imaging using Tc-99m-HMPAO SPECT or FDG PET and radionuclide cisternography. Radionuclide cisternography has been repeatedly proven to be the most physiological method. The results of this procedure have been the most reliable criterion in the diagnosis of NPH [8, 9].

The procedure has proven to be the most specific in differentiating patients with normal-pressure hydrocephalus (NPH) from those with other forms of degenerative brain disorder who would clearly not benefit from surgical treatment (Fig. 18.40) by ventricular shunting [10].

A radionuclide (usually In-111-DTPA) is injected into the CSF system, usually via the lumbar subarachnoid space. For NPH, skull imaging is performed up to 72 h following injection of the radiopharmaceutical in the anterior, posterior, lateral, and vertical projections. SPECT studies are now commonly being used. For CSF leaks, images are also obtained for the same duration and projections, depending on the suspected site of leakage [2, 3]. SPECT and quantitation are also used to detect leaks and diagnose the spontaneous intracranial hypotension due to cerebrospinal fluid (CSF) leaks and other causes of leak including postoperative. The quantitation of pledgets and blood samples are used [5–7, 11].

There are characteristic findings in NPH. Imaging performed as early as 2–4 h post-injection shows radioactivity in the lateral ventricles which persists for 24–48 h (Fig. 18.41), indicating ventricular reflux [2]. There is delayed clearance of the tracer as evidenced by minimal visualization of the convexities as late as 24–48 h.

Radionuclide studies have proven to be a sensitive and accurate method of detecting CSF leaks [3, 4]. The site is most likely to be identified during heavy leakage. Imaging in the appropriate projections is important; posterior imaging is used for otorrhea whereas lateral and anterior imaging is used for rhinorrhea. Alternatively, radioactive counts may be obtained from an absorbent material placed in the orifice in question to determine whether CSF is indeed leaking. Counting blood samples have also more recently been used along with pledget counting [6].

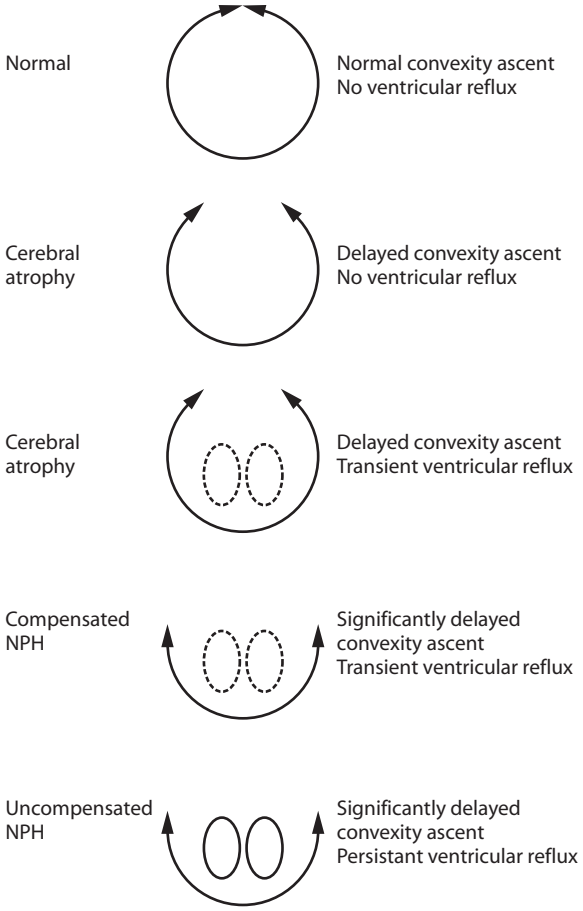

Fig. 18.40. Diagram illustrating different patterns seen on ^{111}In-DTPA cisternography. The pattern of uncompensated normal pressure hydrocephalus is the pattern that indicates benefit from shunting surgery

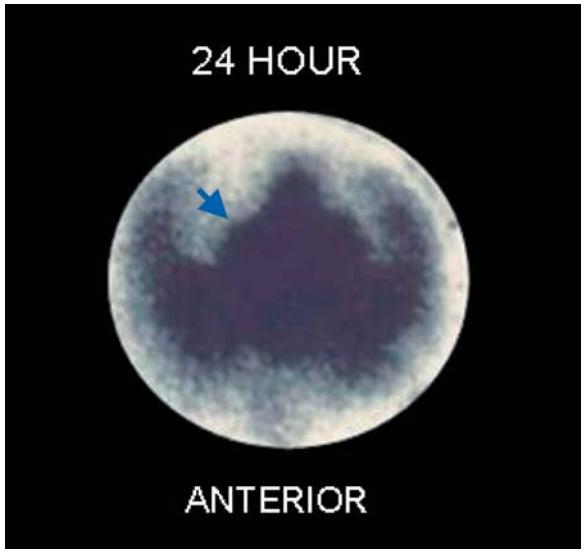

Fig. 18.41. ^{111}In-DTPA cisternography study shows markedly delayed flow over the convexities by 48 h and persistent activity in the lateral ventricles (*arrow*). This is the typical pattern of uncompensated normal pressure hydrocephalus

References

1. Brodley WG, Kortman KE, Burgoyne B (1986) Flowing cerebrospinal fluid in normal and hydrocephalic states. Appearance on MRI imaging. Radiology 159:611
2. Shih WJ, Ryo UY (1988) Radionuclide brain imaging. In: Yeh SD, Chen DC (eds) Nuclear medicine update. Chinese American Society of Nuclear Medicine. The Society of Nuclear Medicine, ROC, Taipei, pp 246 – 271
3. Kawaguchi S, Lio M, Murata H, et al (1986) Comparative study of NPH by RN cisternography and CT scan in aged. J Nucl Med 27:84
4. Silbersteib EB (1983) Brain scintigraphy in the diagnosis of the sequela of head trauma. Semin Nucl Med 13:153
5. Mitjavila M, Balsa MA, Penin J, Pey C (2004) Radionuclide cisternography in spontaneous intracranial hypotension syndrome. Rev Esp Med Nucl 23:338 – 342
6. Takahashi M, Momose T, Kameyama M, Mizuno S, Kumakura Y, Ohtomo K (2005) Detection of cerebrospinal fluid leakage in intracranial hypotension with radionuclide cisternography and blood activity monitoring. Ann Nucl Med 19:339 – 343
7. Ozaki Y, Sumi Y, Kyogoku S, Shindoh N, Katayama H (1999) Spontaneous intracranial hypotension: characteristic findings of radionuclide cisternography using In-111 DTPA. Clin Nucl Med 24:823 – 825
8. Chmielowski K, Podgorski JK, Twarkowski P, Pietrzykowski J, Szalus N (2004) Radionuclide cisternography in the diagnosis of normal pressure hydrocephalus. Pol Merkuriusz Lek 16:576 – 580
9. Cernochova I, Lipina R (2004) Radionuclide cisternography in diagnostics of obstruction hydrocephalus in introduced ventriculoperitoneal shunt. Nucl Med Rev Cent East Eur 7:85 – 86
10. Borbely K (2004) Functional imaging of cerebrospinal fluid pathology. Ideggyogy Sz 20:301 – 312
11. Okizaki A, Shuke N, Aburano T, Hashizume K, Nakai H, Tanaka T (2001) Detection of cerebrospinal fluid leak by dual-isotope SPECT with In-111 DTPA and Tc-99m HMDP. Clin Nucl Med 26:628 – 629

19 Basis of Antibody Imaging and Therapy

Lionel Zuckier

19.1 Introduction

The true physiologic function of antibodies is in effecting humoral immunity. As vehicles for targeting of radionuclides, we are less interested in this native role, but are instead concerned with attributes that predict the behavior and ability of radiolabeled antibodies and their derivatives to target antigen when injected into patients. This chapter will consequently focus on the properties of antibodies, fragments, and recombinant immunologic constructs that have a bearing on nuclear medicine imaging and therapy.

Many comprehensive reviews relating to technical aspects of antibody production [1], radiolabeling [2–4], radiobiology [5], and the diagnostic [6–8] and therapeutic [9, 10] applications of radiolabeled antibodies have been published. In the clinic, the role of radiolabeled antibodies as successful diagnostic agents must be viewed in the context of competing modalities, such as ^{18}F-FDG PET-CT, contrast MRI, and other emerging technologies. Questions such as the optimal role and position of radiolabeled antibodies in the therapeutic armamentarium, and the use of antibodies in adjuvant or combination therapy, are important issues that must be addressed when considering use of radiolabeled antibodies in the therapeutic realm.

The present chapter will focus on *physiologic* aspects of radioimmunotargeting, especially with respect to the biology and pharmacology of the immunoglobulin-derived proteins that are employed. This information will provide a theoretical basis to understanding present and future trends and issues in the rapidly evolving fields of radioimmunodiagnosis and radioimmunotherapy.

19.2 Structure and Function of the Immunoglobulin Molecule

Composition of the antibody molecule, and the structure-function relationships that govern its behavior, are basic to understanding radioimmunologic imaging and therapy [11–13]. An *antibody* is a member of a family of structurally related glycoproteins, secreted by B cells or their progeny, that have the potential to bind to antigen. An *antigen* is a foreign or endogenous macromolecule to which an antibody binds; the specific region of the antigen where the antibody binds is termed an *epitope*.

The term *immunoglobulin* can be used synonymously with antibody, and derives historically from the migration pattern of these proteins on electrophoresis. In mice, as in man, there are five different *classes* of immunoglobulins (IgM, IgD, IgG, IgE and IgA), with IgG subdivided into four and IgA into two *subclasses*. Each class or subclass of immunoglobulin shares a similarity of functional and structural properties and is encoded by a specific heavy-chain immunoglobulin gene.

To date, the majority of immunoglobulins employed in clinical studies have been murine IgG molecules. The typical IgG antibody is a heterodimer composed of two identical *heavy* and two identical *light* polypeptide chains, covalently linked by disulfide bonds, thereby forming a "Y"-shaped molecule with paired antigen-binding arms (Fig. 19.1). Heavy and light chains of the immunoglobulin are divided into several relatively compact globular regions of approximately 110 amino acids long, termed *domains*. Domains of both the heavy and light chains which are located at the antigen-binding ends of the molecule are relatively variable in composition, and have been termed the *variable-heavy* (V_H) and *variable-light* (V_L) domains. It has been noted

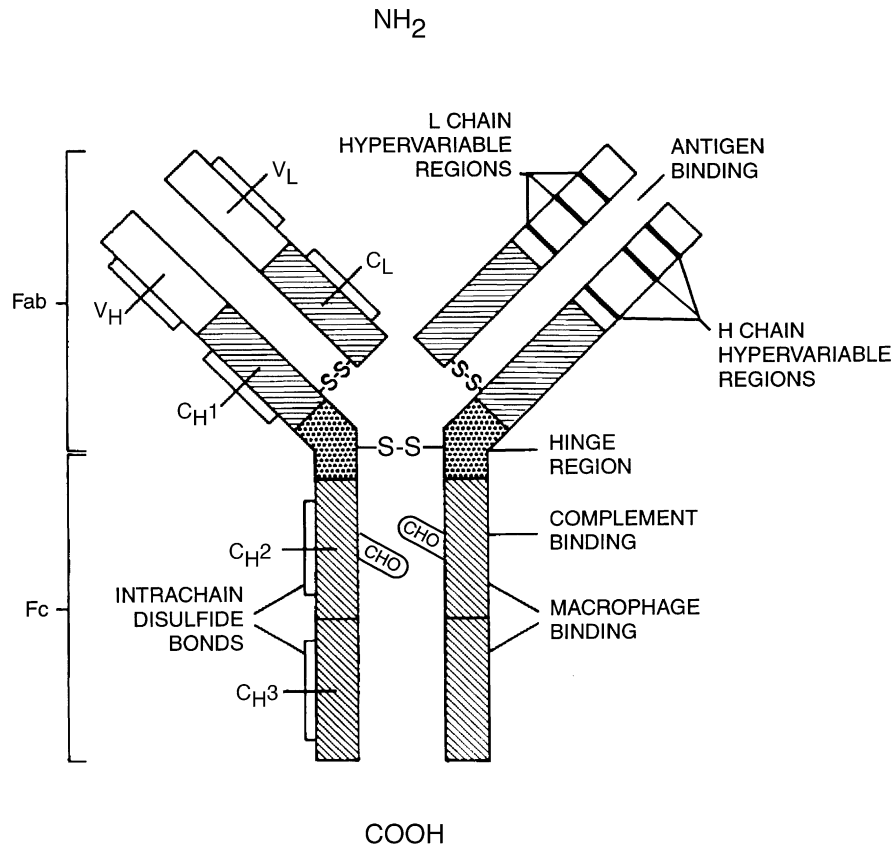

Fig. 19.1. Schematic structure of an IgG molecule. Inter- and intra-chain disulfide bonds (-*S*-*S*-) and the C_H2 region carbohydrates (*CHO*) are indicated schematically on the molecule. (Reprinted from [132] with permission)

that three specific sites within each V_H and V_L are especially varied, or *hypervariable*, interspersed between more-constant *framework* residues. These six hypervariable regions of the V_H and V_L pair form a contiguous antigen-binding groove while the intervening framework residues provide a structural scaffold. The properties of the hypervariable regions therefore dictate the epitope to which the antibody will bind, and consequently they have also been called *complementarity-defining regions* (CDRs). Composition of the third heavy-chain CDR appears especially dominant in determining antigen-binding specificity of the antibody.

Excluding the V_H and V_L domains, the remainder of the antibody molecule is relatively invariable within each class or subclass of immunoglobulin and is therefore called the *constant region*. The constant region of the IgG heavy chain comprises three domains (C_H1, C_H2 and C_H3) and a hinge which provides segmental flexibility between C_H1 and C_H2 (Fig. 19.1). A carbohydrate moiety is present in the C_H2 region which has been used for radiolabeling. The light chain is composed of only a single constant-region domain (C_L) in addition to V_L. Of the other classes of immunoglobulins, IgD and IgA also have three constant and one variable domains within the heavy chain; however, IgE and IgM have an additional fourth constant domain (C_H4) which contributes to a higher molecular weight. A unique *joining* (J) chain is present in IgM, leading to formation of pentamers, and in IgA, which leads to polymerization into bi- or trimeric forms.

Composition of the heavy-chain constant domain determines the class and subclass of an immunoglobulin, and confers specific effector functions on the molecule, such as binding to Fc receptors or phagocytic cells, activation of the complement cascade, and regulation of catabolic rate (Fig. 19.1) [11–13]. These functions have generally not been relevant to antigen-directed targeting, with the exception of intravascular half-life, which is an important parameter that predicts an antibody's bioavailability and persistence in background [14]. For example, by selection of novel heavy-chain domain sequences, it has been possible to create immunoglobulins with a prolonged [15] or shortened [16] serum half-life. An interesting observation regarding the various subclasses of human IgG is that, in spite of a great degree of homology, there is a threefold variation in serum half-life, ranging from approximately 3 weeks for IgG_1, IgG_2, and IgG_4 to 1 week for IgG_3 [17]. The half-lives of the non-IgG antibody classes are considerably shorter [17]. Until recently, the mechanisms

responsible for regulation of immunoglobulin catabolism were largely unknown. It was noted that increasing IgG levels, such as in hypergammaglobulinemia, resulted in an accelerated rate of catabolism, a unique finding known as the *concentration-catabolism phenomenon* [18, 19]. Brambell [20] hypothesized a specific receptor for IgG, which conferred protection from degradation, but which was saturable with increasing IgG levels. While eluding detection for some 3 decades, its identity has recently been shown by several groups to be the MHC class I-related receptor FcRn [21–24], which binds sequences in the C_H2 and C_H3 regions of the IgG molecule which have been implicated in regulation of murine immunoglobulin metabolism [25, 26]. Additional regions of the IgG molecule also appear to influence immunoglobulin half-life, possibly by exerting conformational changes on C_H2 and C_H3 [15, 16]. It is anticipated that further understanding of the specific interaction of regions on the immunoglobulin with receptors that control catabolism of the molecule will lead to a revolution in design of constructs with made-to-order half-lives.

19.3 Derivative Immunologic Molecules and the Effect of Size and Valence

One of the major limitations of immunoglobulin delivery to tumor tissues is the "tumor physiology", which restricts delivery of molecules to tumor tissue [27]. Normal tissues have organized capillary networks and low interstitial pressures such that diffusion of molecules from the bloodstream into the tissue readily occurs. Tumor, in contrast, is characterized by disordered structures and unorganized growth. This often leads to a relative paucity of blood flow and nutrient delivery to the tumors, as well as to an elevated intracellular pressure, caused by absence of lymphatic drainage. It has been shown by mathematic modeling [28], as well as experimentally [29], that decreasing the size of molecules improves their penetration from the blood into tissue. In radioimmunotargeting, this has been achieved by design of novel constructs that delete portions of the constant and framework regions of the molecule and preserve the six hypervariable regions (Table 19.1). These alterations also affect intravascular half-life, immunogenicity, and valence, the implications of which will be discussed in greater detail below.

Amongst the first generation of modified molecules produced were enzymatically derived fragments of the IgG molecule [30–32]. When digested by papain, the heavy chains are cleaved above the inter-heavy chain disulfide bonds and the resultant *Fab* fragments consist of the V_H, V_L, C_L and C_H1 domains (Fig. 19.2). The residual duplicated C_H2 and C_H3 domains are termed the

Table 19.1. Characteristics of immunologically derived molecules for potential use in radioimmunotargeting. $T_{1/2}$ representative terminal, *b* intravascular half-lives, *CDR/BS* number of CDRs per binding site. (After Adams [50])

Molecule	Size (kDa)	CDR/BS	Valence	$T_{1/2}$ (h)
CDR3	<1	1	1	0.9
V_H	12	3	1	–
scFv	25	6	1	1.5–3.9
Diabody	50	6	2	6.4
Fab	50	6	1	1.5
$(scFv')_2$	55	6	2	2.4
Minibody	80	6	2	4.8–5.3
$F(ab')_2$	100	6	2	6–12
IgG	150	6	2	50–113
$F(ab')_3$	152	6	3	–
$(IgG)_2$	300	6	4	26
IgM	970	6	10	18–32

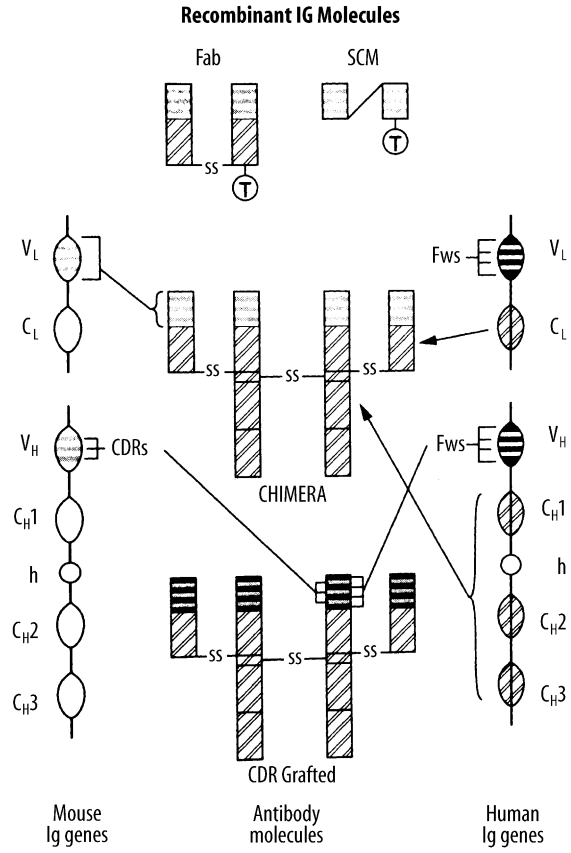

Fig. 19.2. Recombinant immunoglobulin (*Ig*) molecules. *Upper panel* Small engineered fragments are illustrated with a targeted group (designated *T*), representing a chelated diagnostic or therapeutic radionuclide, conjugated to *Fab* and single-chain Fv molecule (*SCM*) constructs. *Middle* and *lower panels* depict construction of chimeric and CDR-grafted antibodies. Mouse and human Ig genes are represented on the *left* and *right* of the figure, respectively. Genes coding for the antibodies consist of exons, depicted as *ovals*, with intervening introns, shown as *lines*. Heavy and light chain complementary-determining regions (*CDRs*) and surrounding framework regions (*Fws*) are schematically illustrated. (Reprinted from [43] with permission)

Fc (crystallizable) fragment and do not bind antigen. The enzyme pepsin cleaves the heavy chains below their inter-chain disulfide bonds, producing a bivalent *F(ab')*$_2$ fragment and small polypeptide fragments derived from the Fc region. F(ab')$_2$ may be chemically reduced, resulting in 2 *Fab'* fragments, each slightly larger than the Fab fragment described above. Of the five monoclonal antibodies which have been recently FDA-approved for radioimmunoimaging, one is an IgM [33], two are intact whole IgG antibodies, and one each are Fab and Fab' fragments of IgG [6]. F(ab')$_2$, Fab' and Fab fragments retain antigen binding but, by virtue of their smaller size, have accelerated intravascular half-life [14], decreased immunogenicity, and superior penetration into the tumor interstitium [34]. Both Fab and F(ab')$_2$ tend to accumulate in the kidneys [32, 35, 36], which can impair visualization of adjacent uptake elsewhere in the abdomen. Reduced valence of Fab and Fab' fragments can impact upon antigen binding, and will be discussed below. IgM has a short half-life; however, its size is 5 times larger than the intact IgG molecule. A favorable aspect of IgM is the presence of ten binding sites, which leads to enhanced avidity of bindings, as will be discussed below. The two radiolabeled antibodies approved for radioimmunotherapy are both whole murine immunoglobulins.

Recombinant DNA techniques may also be used to produce Fab fragments [37, 38], or even smaller immunologically active reagents (Table 19.1), most notably *single chain Fv* (scFv) molecules [39], also known as *single chain variable regions* [40, 41], *single chain antigen binding proteins* (SCAs) [42], or *single chained molecules* (SCMs) [43]. These are composed of only the heavy and light chain variable regions (V_H and V_L), attached by linker peptides (Fig. 19.2). Small peptides such as scFvs have been shown to exhibit more rapid and homogeneous penetration of tumor compared with larger immunoglobulin forms, with tumor-to-normal tissue ratios equal or superior to larger fragments [41, 44]. Even smaller molecules such as the heavy chain variable region alone [45], known as a *single* or *variable domain antibod*y (dAb), and even solitary hypervariable regions [46, 47], called *molecular recognition units* (MRUs), have been described. In these last two constructs, reducing the number of hypervariable regions to less than the original complement of six can lead to compromised affinity and specificity of binding. In certain cases, this low affinity has been overcome by tandem repeats of the CDR's binding sequence [48, 49]. One of the major advantages of very small peptides, such as MRUs, is that they can be chemically synthesized de novo without the complexity and regulatory requirements relevant to cell-line produced reagents.

Another advantage of small peptides, in certain contexts, is a greatly increased rate of clearance from the blood pool as compared to whole antibodies (Table 19.1) (reviewed in [50]). In general, uncharged proteins of less than 20 Å in size can pass through the glomerulus without restriction while those greater than 40 Å are effectively restricted. For antibodies, this is translated as meaning that constructs with a molecular weight of less than approximately 65 kDa undergo very rapid renal excretion while those with weight over 65 kDa, such as minibodies and larger (Table 19.1), have a more prolonged retention. Addition of negative charge tends to decrease the rate of renal excretion and accumulation because of repulsion between the negatively charged protein and the electronegative cells of the endothelium and glomerular basement membrane. Another technique which has been used to reduce renal uptake of radiolabeled antibody fragments is the systemic co-administration of cationic amino acids and their derivatives with the radiolabeled targeting moieties [51]. These reagents inhibit tubular resorption of peptides and proteins, thereby successfully lowering their renal uptake in patients and animal models.

Crucial to understanding the effect of changes in antibody valence is an understanding of the concepts *affinity* and *avidity*. With respect to antibody binding, *affinity* refers to the strength of interaction between an individual Fab binding site and the epitope to which it binds. In contrast, *avidity* refers to strength of the sum total of interactions between an antibody and antigen [52], taking into account the effect of multivalency. Avidity also depends on density of antigen [53–56]. If overly low, multivalent interaction between antibody and target cannot occur and binding will not be enhanced. Decrease in binding caused by reduced valence has been shown experimentally in an in vivo model [57].

This concept of avidity explains the natural ability of IgM, which typically has a relatively low affinity, to effectively bind antigen. Even though any particular binding site on the antibody may be dissociated from antigen at a given time, it is likely that at least one of the other nine binding sites will be attached to the target, thereby ensuring binding. Effectiveness of polymerization of IgG molecules in enhancing binding has been noted in a spontaneous constant-region mutation which resulted in formation of covalently linked IgG_1 oligomers [58]. Following these examples of nature, and using techniques of antibody engineering or chemical manipulation, trimers and tetramers of Fab fragments [59–61] as well as polymers of IgG [62–64] have been constructed with the goal of increasing the valence and hence the avidity of these molecules (Table 19.1).

The importance of avidity and valence in antibody targeting has also been reflected in a concomitant trend in design of small immunologic molecules. Originally, efforts were expended towards developing very small

molecules with high affinity, such as monovalent scFvs [39, 40], with the overall goal of increasing tissue penetration and accelerating background clearance. Because reduced valence leads to decreased avidity, a subsequent generation of molecules were designed with restored valence, including diabodies [65], $(scFv)_2$ [66] and minibodies [67]. In carefully controlled animal studies, improved binding of divalent constructs has been shown to be independent of size and rate of vascular clearance [66, 68].

Another means of increasing avidity when targeting with multivalent molecules is to increase the density of the antigen target, especially important when antibody affinity and baseline antigen density are low. Experimental strategies designed to improve antibody targeting by increasing antigen density, such as administering biological response modifiers (reviewed in [69] and [70]), can therefore be understood not only as a means of quantitatively increasing the total number of antigen binding sites [71 – 73], but also qualitatively as a means of increasing the avidity of binding.

Other modifications of the antibody molecule have been performed to improve targeting, including mutating critical amino acid residues in the binding site to improve affinity [74]. Targeting molecules have also been produced that combine two variable regions with differing specificities (bispecific antibodies) [75 – 81]. Use of antibodies that bind two distinct antigens which coexist only in a given tumor tissue may be a means of potentially increasing specificity of tumor targeting. Another promising use of bispecific antibodies is "pretargeting" [82]. In this technique, a non-radioactive bispecific immunologic molecule is constructed with specificity both to the antigen target and to a small radiolabeled carrier peptide. The bispecific construct is then "pretargeted" to the antigen site, and allowed to clear from the blood, followed hours to days later by injection of the radiolabeled small moiety, which in turn binds with high specificity to the bispecific construct.

Other molecules have been constructed that add functionality of another biological agent, such as a cytokine [83], hormone [84] or ligand [85], to the immunoglobulin. For example, ligands that are actively transported through the blood-brain barrier, such as transferrin, may be attached to the immunoglobulin molecule, thereby acting to ferry the antibody across this normally impervious barrier [85]. Avidin or biotin has been attached to the constant region [86 – 89] in another method of pretargeting of tumors. In this technique, a non-radioactive immunoglobulin molecule, bearing streptavidin, is "pretargeted" to the antigen site, followed subsequently by a small radiolabeled moiety incorporating biotin that rapidly binds with high specificity to the initially targeted agent, while the remainder is promptly excreted. More complicated schemes with three "layers" of reagents have also been described [90].

19.4 Immune Responses to Administered Immunoglobulins and Humanization

A limitation of many of the antibodies presently in clinical trials is that they are murine in origin, and in a small percentage of cases can stimulate an immune response in the human recipient. This so-called *HAMA* (human anti-mouse antibody) response does not result in acute injury, but limits future use of antigenically related reagents, where presence of HAMA will result in rapid clearance of the infused antibody from the blood and non-specific accumulation in the reticuloendothelial system [91]. Smaller molecules, such as fragments or scFvs, generally have reduced but not absent immunogenicity.

The obvious solution of replacing murine immunoglobulins with human antibodies has been limited by ethical problems in obtaining immunized human lymphocytes. The human hybridoma process is also more technically challenging [92, 93], though progress has led to greater ease in generating human monoclonal antibodies by Epstein-Barr virus transformation [94 – 96] or by human-mouse or human-human fusions [97, 98].

As an alternative, researchers have developed methods for combining murine-derived binding specificity with the constant-region structure of human immunoglobulins. Initially, murine DNA coding for the variable region was spliced onto human DNA coding for the constant region and expressed in previously non-secreting lymphocytes to produce *chimeric* antibodies [99, 100] (Fig. 19.2). While functionally similar to human antibodies [101], the murine-derived variable regions may still elicit an immune response [102]. To minimize this problem, *humanized* or *CDR-grafted* antibodies have been constructed where both the constant regions and framework portion of the variable regions are derived from human immunoglobulins, with only the hypervariable regions cloned from the immunized mouse [103 – 106]. These antibodies often have diminished antigen binding, due to altered interactions between the native framework regions and the grafted murine hypervariable regions [107, 108]. To compensate, modeling [108, 109] and labor-intensive substitution of flanking amino-acids [108, 109] has been used to restore affinity. Transgenic mice carrying human immunoglobulin genes have also been developed as a means of generating human antibodies from an animal species [111 – 113]. These animals, endowed genetically with a functional human humoral immune system, may be immunized with a given antigen and

their B cells used for subsequent hybridoma production.

An additional method of producing small antigen-binding proteins utilizes immunoglobulin genes expressed in bacteria, circumventing the need for immunization of live subjects. In this method, termed the *phage display library* technique [37, 45, 114, 115], hundreds of thousands of human variable-region derived amino-acid sequences or scFvs are expressed or "displayed" on the surface of filamentous phage, and are then selected for binding to the antigen of interest. By using multiple rounds of *panning* with the phage-display library, sequences that bind are retained and enriched, making it ultimately possible to isolate peptides with desired specificity.

19.5 The Importance of Affinity

Over the course of the last 10 – 15 years, there has been a gradual change in how we view the importance of affinity in antibody imaging and therapy. At one time, it was thought that higher affinity was synonymous with improved targeting, as has in fact been shown to be true in many situations [116]. In a carefully controlled animal model, Adams has shown that increased affinity initially resulted in improved tumor targeting [117]; however, above a given threshold no additional benefit was realized [118]. Current understanding of the interrelationship between affinity, valence, antigen density and avidity suggests that not only are there situations where increased affinity is superfluous, but increased affinity can increase binding to circulating and background antigen and therefore be detrimental [119, 120]. In fact, it may one day be routine to tailor the antibody to the specific clinical usage at hand. Taking into account the relative density of antigen on target and non-target tissues, one could select antibodies of specific affinity and valence so as to better differentiate tissues bearing high and low density antigen.

It should be stressed that optimal affinity also depends on the targeting application. Weinstein, Fujimori and coworkers [121, 122] have presented persuasive modeling work suggesting that antibodies with overly-high affinity may be harmful in therapy applications because they would tend to accumulate at the periphery of tumor deposits and not be homogeneously distributed throughout the tumor. This phenomenon, which they termed the "binding site barrier", would thereby deprive the innermost tumor of a therapeutic effect. In fact, this concept has been supported by experimental data [123].

19.6 Other Factors

This review has concentrated on several interesting and current topics relating to the immunoglobulin. Many other factors enter into the "physiology" of radioimmunotargeting and merit a brief discussion. Because of non-specific uptake of antibody by various sites within the recipient's body, increasing the mass of antibody or other immunologically derived targeting agents is a means of optimizing tumor to non-tumor uptake [14]. This variable is generally studied in the initial trials of new agents, where antibody dose is escalated to study safety and targeting efficacy. Another question which has been investigated is the optimal route of administration for given antibodies and diseases. Earlier studies of radioimmunotargeting included administration of the antibody by the intracavitary route, especially in the case of localized peritoneal disease [124, 125], or by lymphoscintigraphy, where the antibody is administered subcutaneously in a manner where it is taken up by the lymphatic system [126]. As a general rule, these methods were not shown to be advantageous, and have fallen out of favor, with intravenous administration being the overwhelmingly selected route of administration. Nonetheless, these techniques are still being investigated in specific applications, such as administration of radiolabeled antibody into the cavity formed following resection of malignant glioma [127].

Strategies that increase accretion of antibody include biologic response modifiers administered systemically as adjuvants to radioimmunotargeting [128], or directly attached to the antibody by chemical [129] or genetic [83] means. External radiation or local heat has also been used to enhance antibody delivery in radioimmunotherapy, while hypoxic cell sensitizers have been used to enhance the efficacy of treatment [130]. Methods of pretargeting of antibodies, discussed above, maximize delivery of radionuclide to the tumor, while minimizing background activity. Means of minimizing marrow depression and toxicity after aggressive therapy include immunoadsorption of unbound antibody from the patient's plasma or marrow harvesting and transplantation after therapy [130, 131]. As therapeutic applications of radioimmunotargeting become more common, these methods of maximizing therapy while minimizing toxicity will increase in importance.

While outside of the scope of this review, the choice of antigen targeted is a crucial variable in radioimmunotargeting as is selection of an optimal radionuclide with which to label the antibody. In all cases, the physical half-life of the radionuclide should roughly approximate its biologic half-life. For therapeutic radionuclides, the nature of the particulate emission and path length should optimally be matched with the anticipated size and architecture of the malignant tumor depos-

its being treated. Whether the radioconjugate is internalized, or even retained within the cells, is another factor of great importance in predicting therapeutic response, and again influences the choice of optimal antigen to target.

19.7 Summary

Immunologically derived molecules for use in radioimmunotargeting are rapidly evolving from whole murine-derived antibodies to novel recombinant molecules. In the age of antibody engineering, it is important to understand the various physiologic factors which dictate behavior of these constructs. When evaluating a molecule for immunological targeting, issues of importance include affinity of binding, density and distribution of the antigen, and valence of the molecule, which together affect avidity. Size of the targeting molecule is important in that smaller molecules have potentially increased tissue penetration, reduced immunogenicity, and accelerated clearance from blood and background, but also exhibit decreased bioavailability, and potentially altered excretion pathways which may obscure areas of interest. Incorporation of foreign protein sequences, derived from other species, into the targeting molecule may lead to immunization of the host and altered biodistribution but can potentially be circumvented by recombinant DNA techniques. Identifying extremely high-affinity antibodies, which was once the holy grail of radioimmunotargeting, is now believed to be of more selected benefit, depending on valence, presence and density of antigen on target and background tissues, and the need for homogeneous targeting of the tumor, as in therapy applications.

The field of radioimmunotargeting is evolving from the use of whole or fragmented murine antibodies for antibody imaging to development of novel engineered molecules for therapy and imaging applications. Understanding the physiologic behavior of immunologically derived molecules is therefore of ever-growing importance to the nuclear medicine practitioner.

References

1. Bogard WC Jr, Dean RT, Deo Y, Fuchs R, Mattis JA, McLean AA, et al (1989) Practical consideration in the production, purification, and formulation of monoclonal antibodies for immunoscintigraphy and immunotherapy. Semin Nucl Med 19:202 – 220
2. Hnatowich DJ (1990) Recent developments in the radiolabeling of antibodies with iodine, indium, and technetium. Semin Nucl Med 20:80 – 91
3. Hiltunen JV (1993) Search for new and improved radiolabeling methods for monoclonal antibodies. Acta Oncol 32:831 – 839
4. Zimmer AM, Spies SM (1993) New approaches to radiolabeling monoclonal antibodies. Cancer Treat Res 68:99 – 109
5. Kassis AI, Adelstein SJ (2005) Radiobiologic principles in radionuclide therapy. J Nucl Med 46 Suppl 1:4S–12S
6. Zuckier LS, DeNardo GL (1997) Trials and tribulations: oncological antibody imaging comes to the fore. Semin Nucl Med 27:10 – 29
7. Pinkas L, Robins PD, Forstrom LA, Mahoney DW, Mullan BP (1999) Clinical experience with radiolabelled monoclonal antibodies in the detection of colorectal and ovarian carcinoma recurrence and review of the literature. Nucl Med Commun 20:689 – 696
8. Goldenberg DM, Nabi HA (1999) Breast cancer imaging with radiolabeled antibodies. Semin Nucl Med 29:41 – 48
9. Jhanwar YS, Divgi C (2005) Current status of therapy of solid tumors. J Nucl Med 46 Suppl 1:141S–150S
10. Sharkey RM, Goldenberg DM (2005) Perspectives on cancer therapy with radiolabeled monoclonal antibodies. J Nucl Med 46 Suppl 1:115S–127S
11. Winkelhake JL (1978) Immunoglobulin structure and effector functions. Immunochemistry 15:695 – 714
12. Burton DR (1985) Immunoglobulin G: functional sites. Mol Immunol 22:161 – 206
13. Ward ES, Ghetie V (1995) The effector functions of immunoglobulins: implications for therapy. Ther Immunol 2:77 – 94
14. Zuckier LS, Rodriguez LD, Scharff MD (1989) Immunologic and pharmacologic concepts of monoclonal antibodies. Semin Nucl Med 19:166 – 186
15. Zuckier LS, Chang CJ, Scharff MD, Morrison SL (1998) Chimeric human-mouse IgG antibodies with shuffled constant region exons demonstrate that multiple domains contribute to in vivo half-life. Cancer Res 58:3905 – 3908
16. Pollock RR, French DL, Metlay JP, Birshtein BK, Scharff MD (1990) Intravascular metabolism of normal and mutant mouse immunoglobulin molecules. Eur J Immunol 20:2021 – 2027
17. Waldmann TA, Strober W (1969) Metabolism of immunoglobulins. Progr Allergy 13:1 – 110
18. Lippincott SW, Korman S, Fong C, et al (1960) Turnover of labeled normal gamma globulin in multiple myeloma. J Clin Invest 39:565 – 572
19. Birke G, Liljedahl S-O, Olhagen B, Plantin L-O, Ahlinder S (1963) Catabolism and distribution of gammaglobulin. A preliminary study with ^{131}I-labelled gammaglobulin. Acta Med Scand 173:589 – 603
20. Brambell FWR, Hemmings WA, Morris IG (1964) A theoretical model of t-globulin catabolism. Nature 203: 1352 – 1355
21. Junghans RP, Anderson CL (1996) The protection receptor for IgG catabolism is the b2-microglobulin-containing neonatal intestinal transport receptor. Proc Natl Acad Sci USA 93:5512 – 5516
22. Ghetie V, Hubbard JG, Kim TK, Tsen MF, Lee Y, Ward ES (1996) Abnormally short serum half-lives of IgG in beta-2-microglobulin-deficient mice. Eur J Immunol 26:690 – 696
23. Israel EJ, Wilsker DF, Hayes KC, Schoenfeld D, Simister NE (1996) Increased clearance of IgG in mice that lack b2-microglobulin: possible protective role of FcRn. Immunology 89:573 – 578
24. Junghans RP (1997) Finally: The Brambell receptor (FcRB). Mediator of transmission of immunity and protection from catabolism for IgG. Immunol Res 16:29 – 57
25. Kim JK, Tsen MF, Ghetie V, Ward ES (1994) Catabolism of the murine IgG1 molecule: evidence that both CH2-CH3 domain interfaces are required for persistence of IgG1 in the circulation of mice. Scand J Immunol 40:457 – 465

26. Kim J-K, Tsen M-F, Ghetie V, Ward ES (1994) Identifying amino acid residues that influence plasma clearance of murine IgG1 fragments by site-directed mutagenesis. Eur J Immunol 24:542 – 548
27. Jain RK (1990) Physiological barriers to delivery of monoclonal antibodies and other macromolecules in tumors. Cancer Res (Suppl) 50:814s–819s
28. Fujimori K, Covell DG, Fletcher JE, Weinstein JN (1990) A modeling analysis of monoclonal antibody percolation through tumors: a binding-site barrier. J Nucl Med 31: 1191 – 1198
29. Buchegger F, Halpern SE, Sutherland RM, Schreyer M, Mach J-P (1986) In vitro and in vivo tumor models for studies of distribution of radiolabelled monoclonal antibodies and fragments. Nuklearmedizin 25:207 – 209
30. Larson SM, Carrasquillo JA, Krohn KA, et al. (1983) Localization of ^{131}I-labeled p97-specific Fab fragments in human melanoma as a basis for radiotherapy. J Clin Invest 72:2101 – 2114
31. Parham P (1983) On the fragmentation of monoclonal IgG1, IgG2a, and IgG2b from BALB/c mice. J Immunol 131:2895 – 2902
32. Wahl RL, Parker CW, Philpott GW (1983) Improved radioimaging and tumor localization with monoclonal F(ab')$_2$. J Nucl Med 24:316 – 325
33. Thakur ML, Marcus CS, Kipper SL, Ahdoot R, Diggles L, Pham HL, et al (2001) Imaging infection with LeuTech. Nucl Med Commun 22:513 – 519
34. Sutherland R, Buchegger F, Schreyer M, Vacca A, Mach J-P (1987) Penetration and binding of radiolabeled anti-carcinoembryonic antigen monoclonal antibodies and their antigen binding fragments in human colon multicellular tumor spheroids. Cancer Res 47:1627 – 1633
35. Holton ODI, Black CDV, Parker RJ, et al (1987) Biodistribution of monoclonal IgG1, F(ab')$_2$, and Fab' in mice after intravenous injection. Comparison between anti-B cell (anti-LyB8.2) and irrelevant (MOPC-21) antibodies. J Immunol 139:3041 – 3049
36. Covell DG, Barbet J, Holton OD, Black CDV, Parker RJ, Weinstein JN (1986) Pharmacokinetics of monoclonal immunoglobulin G_1, F(ab')$_2$, and Fab' in mice. Cancer Res 46:3969 – 3978
37. Huse WD, Sastry L, Iverson SA, Kang AS, Alting-Mees M, Burton DR, et al (1989) Generation of a large combinatorial library of the immunoglobulin repertoire in phage lambda. Science 246:1275 – 1281
38. Kang AS, Barbas CF, Janda KD, Benkovic SJ, Lerner RA (1991) Linkage of recognition and replication functions by assembling combinatorial antibody Fab libraries along phage surfaces. Proc Natl Acad Sci USA 88:4363 – 4366
39. Huston JS, Levinson D, Mudgett-Hunter M, Tai M-S, Novotny J, Margolies MN, et al (1988) Protein engineering of antibody binding sites: recovery of specific activity in an anti-digoxin single-chain Fv analogue produced in *Escherichia coli*. Proc Natl Acad Sci USA 85:5879 – 5883
40. Bird RE, Hardman KD, Jacobson JW, Johnson S, Kaufman BM, Lee S-M, et al (1988) Single-chain antigen-binding proteins. Science 242:423 – 426
41. Milenic DE, Yokota T, Filpula DR, Finkelman MAJ, Dodd SW, Wood JF, et al (1991) Construction, binding properties, metabolism, and tumor targeting of a single-chain Fv derived from the pancarcinoma monoclonal antibody CC49. Cancer Res 51:6363 – 6371
42. Schlom J (1991) New approaches to improved antibody targeting. Antibody Immunoconjug Radiopharm 4:819 – 828
43. Pirofski L-A, Casadevall A, Scharff MD (1992) Current state of hybridoma technology. ASM News 58:613 – 617
44. Yokota T, Milenic DE, Whitlow M, Schlom J (1992) Rapid tumor penetration of a single-chain Fv and comparison with other immunoglobulin forms. Cancer Res 52:3402 – 3408
45. Ward ES, Gussow D, Griffiths AD, Jones PT, Winter G (1989) Binding activities of a repertoire of single immunoglobulin variable domains secreted from *Escherichia coli*. Nature 341:544 – 546
46. Williams WV, Moss DA, Kieber-Emmons T, Cohen JA, Myers JN, Weiner DB, et al (1989) Development of biologically active peptides based on antibody structure. Proc Natl Acad Sci USA 5537 – 5541
47. Taub R, Gould RJ, Garsky VM, Cicarone TM, Hoxie J, Friedman PA, et al (1989) A monoclonal antibody against the platelet fibrinogen receptor contains a sequence that mimics a receptor recognition domain in fibrinogen. J Biol Chem 264:259 – 265
48. Williams WV, Kieber-Emmons T, VonFeldt J, Greene MI, Weiner DB (1991) Design of bioactive peptides based on antibody hypervariable region structures: Development of conformationally constrained and dimeric peptides with enhanced affinity. J Biol Chem 266:5182 – 5190
49. Knight LC, Radcliffe R, Maurer AH, Rodwell JD, Alvarez VL (1994) Thrombus imaging with technetium-99m synthetic peptides based upon the binding domain of a monoclonal antibody to activated platelets. J Nucl Med 35:282 – 288
50. Adams GP (1998) Improving the tumor specificity and retention of antibody-based molecules. In Vivo 12:11 – 22
51. Behr TM, Goldenberg DM, Becker W (2005) Reducing the renal uptake of radiolabeled antibody fragments and peptides for diagnosis and therapy: present status, future prospects and limitations. Eur J Nucl Med 25:201 – 212
52. Macmillan Dictionary of Immunology (1989) Macmillan Press, New York
53. Hornick CL, Karush F (1972) Antibody affinity – III. The role of multivalence. Immunochemistry 9:325 – 340
54. Crothers DM, Metzger H (1972) The influence of polyvalency on the binding properties of antibodies. Immunochemistry 9:341 – 357
55. Kaufman EN, Jain RK (1992) Effect of bivalent interaction upon apparent antibody affinity: experimental confirmation of theory using fluorescence photobleaching and implications for antibody binding assays. Cancer Res 52:4157 – 4167
56. Zuckier LS, Berkowitz EZ, Sattenberg RJ, Zhao QH, Deng HF, Scharff MD (2000) Influence of affinity and antigen density on antibody localization in a modifiable tumor targeting model. Cancer Res 60:7008 – 7013
57. Chapman PB, Lonberg M, Houghton AN (1990) Light chain variants of an IgG3 anti-GD3 monoclonal antibody and the relationship among avidity, effector functions, tumor targeting, and antitumor activity. Cancer Res 50: 1503 – 1509
58. Pollock RR, French DL, Gefter ML, Scharff MD (1988) Identification of mutant monoclonal antibodies with increased antigen binding. Proc Natl Acad Sci USA 85: 2298 – 2302
59. Schott ME, Frazier KA, Pollack DK, Verbanac KM (1993) Preparation, characterization, and in vivo biodistribution properties of synthetically cross-linked multivalent antitumor antibody fragments. Bioconjugate Chem 4:153 – 165
60. King DJ, Turner A, Farnsworth APH, Adair JR, Owens RJ, Pedley RB, et al (1994) Improved tumor targeting with chemically cross-linked recombinant antibody fragments. Cancer Res 54:6176 – 6185
61. Werlen RC, Lankinen M, Offord RE, Schubiger PA, Smith A, Rose K (1996) Preparation of a trivalent antigen-bind-

ing construct using polyoxime chemistry: improved biodistribution and potential for therapeutic application. Cancer Res 56:809 – 815
62. Wolff EA, Schreiber GJ, Cosand WL, Raff HV (1993) Monoclonal antibody homodimers: enhanced antitumor activity in nude mice. Cancer Res 53:2560 – 2565
63. Smith RIF, Morrison SL (1994) Recombinant polymeric IgG: an approach to engineering more potent antibodies. Bio/Technology 12:683 – 688
64. Poon PH, Morrison SL, Schumaker VN (1995) Structure and function of several anti-dansyl chimeric antibodies formed by domain interchanges between human IgM and mouse IgG2b. J Biol Chem 270:8571 – 8577
65. Holliger P, Prospero T, Winter G (1993) "Diabodies": small bivalent and bispecific antibody fragments. Proc Natl Acad Sci USA 90:6444 – 6448
66. Adams GP, McCartney JE, Tai M-S, Oppermann H, Huston JS, Stafford WF III, et al (1993) Highly specific *in vivo* tumor targeting by monovalent and divalent forms of 741F8 Anti-c-*erb*B-2 single-chain Fv. Cancer Res 53:4026 – 4034
67. Hu S, Shively L, Raubitschek A, Sherman M, Williams LE, Wong JYC, et al (1996) Minibody: a novel engineered anti-carcinoembryonic antigen antibody fragment (single-chain Fv-C_H3) which exhibits rapid, high-level targeting of xenografts. Cancer Res 56:3055 – 3061
68. Adams GP, Schier R, McCall AM, Wolf EJ, Marks JD, Weiner LM (1996) Tumor targeting properties of anti-C-ERB-2 single-chain Fv molecules over a wide range of affinities for the same epitope. Tumor Targeting 2:154
69. Buchsbaum DJ (1997) Experimental tumor targeting with radiolabeled ligands. Cancer (Suppl) 80:2371 – 2377
70. Roselli M, Buonomo O, Piazza A, Guadagni F, Vecchione A, Brunetti E, et al (1998) Novel clinical approaches in monoclonal antibody-based management in colorectal cancer patients: radioimmunoguided surgery and antigen augmentation. Semin Surg Oncol 15:254 – 262
71. Fischman AJ, Khaw BA, Strauss HW (1989) Quo vadis radioimmune imaging (editorial). J Nucl Med 30:1911 – 1915
72. Sung C, Shockley TR, Morrison PF, Dvorak HF, Yarmush ML, Dedrick RL (1992) Predicted and observed effects of antibody affinity and antigen density on monoclonal antibody uptake in solid tumors. Cancer Res 52:377 – 384
73. Blumenthal RD, Sharkey RM, Kashi R, Natale AM, Goldenberg DM (1989) Influence of animal host and tumor implantation site on radio-antibody uptake in the GW-39 human colonic cancer xenograft. Int J Cancer 44:1041 – 1047
74. Riechmann L, Weill M, Cavanagh J (1992) Improving the antigen affinity of an antibody Fv-fragment by protein design. J Mol Biol 224:913 – 918
75. Suresh MR, Cuello AC, Milstein C (1986) Bispecific monoclonal antibodies from hybrid hybridomas. Methods Enzymol 121:210 – 228
76. Clark M, Gilliland L, Waldmann H (1988) Hybrid antibodies for therapy. Progr Allergy 45:31 – 49
77. Phelps JL, Beidler DE, Jue RA, Unger BW, Johnson MJ (1990) Expression and characterization of a chimeric bifunctional antibody with therapeutic applications. J Immunol 145:1200 – 1204
78. Moran TM, Usuba O, Shapiro E, Rubinstein LJ, Ito M, Bona CA (1990) A novel technique for the production of hybrid antibodies. J Immunol Methods 129:199 – 205
79. Stickney DR, Anderson LD, Slater JB, Ahlem CN, Kirk GA, Schweighardt SA, et al (1991) Bifunctional antibody: a binary radiopharmaceutical delivery system for imaging colorectal carcinoma. Cancer Res 51:6650 – 6655
80. Le Doussal J-M, Chetanneau A, Gruaz-Guyon A, Martin M, Gautherot E, Lehur P-A, et al (1993) Bispecific monoclonal antibody-mediated targeting of an indium-111-labeled DTPA dimer to primary colorectal tumors: pharmacokinetics, biodistribution, scintigraphy and immune response. J Nucl Med 34:1662 – 1671
81. Peltier P, Curtet C, Chatal J-F, LeDoussal J-M, Daniel G, Aillet G, et al (1993) Radioimmunodetection of medullary thyroid cancer using a bispecific anti-CEA/anti-indium-DTPA antibody and an indium-111-labeled DTPA dimer. J Nucl Med 34:1267 – 1273
82. Sharkey RM, Cardillo TM, Rossi EA, Chang CH, Karacay H, McBride WJ, et al (2005) Signal amplification in molecular imaging by pretargeting a multivalent, bispecific antibody. Nat Med 11:1250 – 1255
83. Fell HP, Gayle MA, Grosmaire L, Ledbetter JA (1991) Genetic construction and characterization of a fusion protein consisting of a chimeric F(ab') with specificity for carcinomas and human IL-2. J Immun 146:2446 – 2452
84. Shin S-U, Morrison SL (1990) Expression and characterization of an antibody binding specificity joined to insulin-like growth factor 1: potential applications for cellular targeting. Proc Natl Acad Sci USA 87:5322 – 5326
85. Shin S-U, Friden P, Moran M, Olson T, Kang Y-S, Pardridge WM, et al (1995) Transferrin-antibody fusion proteins are effective in brain targeting. Proc Natl Acad Sci USA 92:2820 – 2824
86. Paganelli G, Magnani P, Siccardi AG, Fazio F (1995) Clinical application of the avidin-biotin system for tumor targeting. In: Goldenberg DM (ed) Cancer therapy with radiolabeled antibodies. CRC Press, Boca Raton, pp 239 – 254
87. Paganelli G, Malcovati M, Fazio F (1991) Monoclonal antibody pretargetting techniques for tumour localization: the avidin-biotin system. Nucl Med Commun 12:211 – 234
88. Kalofonos HP, Rusckowski M, Siebecker DA, Sivolapenko GB, Snook D, Lavender JP, et al (1990) Imaging of tumor in patients with indium-111-labeled biotin and streptavidin-conjugated antibodies: preliminary communication. J Nucl Med 31:1791 – 1796
89. Hnatowich DJ, Virzi F, Rusckowski M (1987) Investigations of avidin and biotin for imaging applications. J Nucl Med 28:1294 – 1302
90. Boerman OC, van Schaijk FG, Oyen WJG, Corstens FH (2003) Pretargeted radioimmunotherapy of cancer: progress step by step. J Nucl Med 44:400 – 411
91. Hand PH, Kashmiri SVS, Schlom J (1994) Potential for recombinant immunoglobulin constructs in the management of carcinoma. Cancer (Suppl) 73:1105 – 1113
92. James K, Bell GT (1987) Human monoclonal antibody production: Current status and future prospects. J Immunol Methods 100:5 – 40
93. James K (1990) Human monoclonal antibodies and engineered antibodies in the management of cancer. Semin Cancer Biol 1:243 – 253
94. Steinitz M, Klein G, Koskimies S, Markel O (1977) EB virus-induced B lymphocytic cell lines producing specific antibody. Nature 269:420 – 422
95. Nakamura M, Burastero SE, Ueki Y, Larrick JW, Notkins AL, Casali P (1988) Probing the normal and autoimmune B cell repertoire with Epstein-Barr virus. Frequency of B cells producing monoreactive high affinity autoantibodies in patients with Hashimoto's disease and systemic lupus erythematosus. J Immun 141:4165 – 4172
96. Kozbor D, Lagarde AE, Roder JC (1982) Human hybridomas constructed with antigen-specific Epstein-Barr virus-transformed cell lines. Proc Natl Acad Sci USA 79:6651 – 6655
97. Ostberg L, Pursch E (1983) Human X (mouse X human) hybridomas stably producing human antibodies. Hybridoma 2:361 – 367
98. Cote RJ, Morrissey DM, Houghton AN, Thomson TM, Daly

ME, Oettgen HF, et al (1986) Specificity analysis of human monoclonal antibodies reactive with cell surface and intracellular antigens. Proc Natl Acad Sci USA 83:2959–2963
99. Morrison SL, Johnson MJ, Herzenberg LA, Oi VT (1984) Chimeric human antibody molecules: mouse antigen-binding domains with human constant region domains. Proc Natl Acad Sci USA 81:6851–6855
100. Morrison SL (1985) Generations of human monoclonal antibodies reactive with cellular antigens. Science 229: 1202–1207
101. Bruggemann M, Williams GT, Bindon CI, Clark MR, Walker MR, Jefferis R, et al (1987) Comparison of the effector functions of human immunoglobulins using a matched set of chimeric antibodies. J Exp Med 166:1351–1361
102. Bruggemann M, Winter G, Waldmann H, Neuberger MS (1989) The immunogenicity of chimeric antibodies. J Exp Med 170:2153–2157
103. Jones PT, Dear PH, Foote J, Neuberger MS, Winter G (1986) Replacing the complementarity-determining regions in a human antibody with those from a mouse. Nature 321:522–525
104. Reichmann L, Clark M, Waldmann H, Winter G (1988) Reshaping human antibodies for therapy. Nature 332: 323–327
105. Winter G, Milstein C (1991) Man-made antibodies. Nature 349:293–299
106. Wright A, Shin S-U, Morrison SL (1992) Genetically engineered antibodies: progress and prospects. Crit Rev Immunol 12:125–168
107. Verhoeyen M, Milstein C, Winter G (1988) Reshaping human antibodies: grafting an antilysozyme activity. Science 239:1534–1536
108. Queen C, Schneider WP, Selick HE, Payne PW, Landolfi NF, Duncan JF, et al (1989) A humanized antibody that binds to the interleukin 2 receptor. Proc Natl Acad Sci USA 86:10029–10033
109. Roberts S, Cheetham JC, Rees AR (1987) Generation of an antibody with enhanced affinity and specificity for its antigen by protein engineering. Nature 328:731–734
110. Co MS, Queen C (1991) Humanized antibodies for therapy. Nature 351:501–502
111. Mosier DE, Gulizia RJ, Baird SM, Wilson DB (1988) Transfer of a functional human immune system to mice with severe combined immunodeficiency. Nature 335:256–259
112. McCune JM, Namikawa R, Kaneshima H, et al (1988) The SCID-hu mouse: murine model for the analysis of human hematolymphoid differentiation and function. Science 241:1632–1639
113. Bruggemann M, Neuberger MS (1996) Strategies for expressing human antibody repertoires in transgenic mice. Immunol Today 17:391–397
114. Sastry L, Alting-Mees M, Huse WD, Short JM, Sorge JA, Hay BN, et al (1989) Cloning of the immunological repertoire in *Escherichia coli* for generation of monoclonal catalytic antibodies: Construction of a heavy chain variable region-specific cDNA library. Proc Natl Acad Sci USA 86:5728–5732
115. Wells JA, Lowman HB (1992) Rapid evolution of peptide and protein binding properties in vitro. Curr Opin Biotechnol 3:355–362
116. Schlom J, Eggensperger D, Colcher D, Molinolo A, Houchens D, Miller LS, et al (1992) Therapeutic advantage of high-affinity anticarcinoma radioimmunoconjugates. Cancer Res 52:1067–1072
117. Adams GP, Schier R, Marshall K, Wolf EJ, McCall AM, Marks JD, et al (1998) Increased affinity leads to improved selective tumor delivery of single-chain Fv antibodies. Cancer Res 58:485–490
118. Adams GP, Schier R, McCall AM, Simmons H, Horak E, Marks JD, et al (1998) What are the determinants of antibody-based targeting? Proc Am Assoc Cancer Res 39:436
119. Sharkey RM, Goldenberg DM, Goldenberg H, Lee RE, Ballance C, Pawlyk D, et al (1990) Murine monoclonal antibodies against carcinoembryonic antigen: immunological, pharmacokinetic, and targeting properties in humans. Cancer Res 50:2823–2831
120. Goldenberg DM, Larson SM (1992) Radioimmunodetection in cancer identification. J Nucl Med 33:803–814
121. Weinstein JN, Eger RR, Covell DG, Black CDV, Mulshine J, Carrasquillo JA, et al (1987) The pharmacology of monoclonal antibodies. Ann NY Acad Sci 507:199–210
122. Fujimori K, Covell DG, Fletcher JE, Weinstein JN (1989) Modeling analysis of the global and microscopic distribution of immunoglobulin G, $F(ab')_2$, and Fab in tumors. Cancer Res 49:5656–5663
123. Juweid M, Neumann R, Paik C, Perez-Bacete MJ, Sato J, van Osdol W, et al (1992) Micropharmacology of monoclonal antibodies in solid tumors: direct experimental evidence for a binding site barrier. Cancer Res 52:5144–5153
124. Wahl RL, Barrett J, Geatti O, Liebert M, Wilson BS, Fisher S, et al (1988) The intraperitoneal delivery of radiolabeled monoclonal antibodies: studies on the regional delivery advantage. Cancer Immunol Immunother 26:187–201
125. Epentos AA, Munro AJ, Stewart S, et al (1987) Antibody-guided irradiation of advanced ovarian cancer with intraperitoneally administered radiolabeled monoclonal antibodies. J Clin Oncol 5:1890–1899
126. Keenan AM, Weinstein JN, Carrasquillo JA, et al (1987) Immunolymphoscintigraphy and the dose dependence of ^{111} In-labeled T101 monoclonal antibody in patients with cutaneous T-cell lymphoma. Cancer Res 47:6093–6099
127. Reardon DA, Akabani G, Coleman RE, Friedman AH, Friedman HS, Herndon II JE, et al (2005) Phase II trial of murine 131I-labeled antitenascin monoclonal antibody 81C6 administered into surgically created resection cavities of patients with newly diagnosed malignant gliomas. J Clin Oncol 20:1389–1397
128. Guadagni F, Roselli M, Nieroda C, Dansky-Ullmann G, Schlom J, Greiner JW (1993) Biological response modifiers as adjuvants in monoclonal antibody-based treatment. In Vivo 7:591–599
129. LeBerthon B, Khawli LA, Alauddin M, Miller GK, Charak BS, Mazumder A, et al (1991) Enhanced tumor uptake of macromolecules induced by a novel vasoactive interleukin 2 immunoconjugate. Cancer Res 51:2694–2698
130. Sautter-Bihl ML (1994) Radioimmunotherapy with monoclonal antibodies: A new horizon in nuclear medicine therapy. Nucklearmedizin 33:167–173
131. Corcoran MC, Eary J, Bernstein I, Press OW (1997) Radioimmunotherapy strategies for non-Hodgkin's lymphomas. Ann Oncol (Suppl) 8:S133–S138
132. Zuckier LS (1999) Monoclonal antibodies in oncology. In: Aktolun C, Tauxe WN (eds) Nuclear oncology. Springer, Berlin, pp 359–369

20 Lymphoscintigraphy

Arthur Z. Krasnow, Abdelhamid H. Elgazzar, Nafisah Kazem

20.1 Introduction

Lymphoscintigraphy has recently acquired an expanding role in clinical medicine. Over the past three decades, in addition to its increasing utilization in the evaluation of lymphedema, it has been used to determine metastatic drainage sites in breast cancer, melanoma and other cancer patients. Most evaluations of lymphedema have assessed the lower extremities, but the upper extremities have also been studied, especially in patients with breast cancer who develop lymphedema following axillary dissection. In breast cancer patients, lymphoscintigraphy was originally used to detect tumor metastases to the axillary and internal mammary lymph node chains. Later, it was applied to the localization of lymph nodes for radiation therapy planning and for determining the completeness of surgical adenectomies. Currently, it is used mainly to determine the location of sentinel lymph node(s) (SLNs).

20.2 Anatomy and Physiology of the Lymphatic System

The physiology of the lymphatic system is not completely understood but appears to be highly dependent on increased regional pressure for fluid transport. It is a complex microtubular system consisting of lymphatic vessels and lymph nodes that transport the ultrafiltrate of extracellular fluid back to the intravascular space. Normally, some fluid is forced out of the vascular space at the arterial end of the capillary bed but is reabsorbed at the venous end. Capillary egress, however, exceeds venous reabsorption by approximately 3 l/day (approximately 10% of capillary contents), leaving behind fluid in the interstitial tissue [1]. This fluid can contain protein and often fat, especially after meals. The peripheral lymphatic capillary collection site has a single layer of overlapping endothelial cells with a poorly developed basement membrane [2]. When the volume of fluid in the interstitial space increases, the intercellular gaps between the endothelial cells widen to allow the surplus of fluid to enter [2]. Lymphatic vessels coalesce into increasingly larger vessels that eventually contain smooth muscle and one-way valves to promote forward flow back toward the vascular space via the thoracic duct or the right lymphatic duct. Fluid travels through the lymphatic system at an average rate of 120 ml/h or 2 – 3 l/day, encountering numerous lymph nodes which serve as filters to remove foreign elements such as tumor cells and bacteria. Lymph enters the nodes through the afferent lymphatic vessel, filtering through the sinusoids of the node, and subsequently leaving through the efferent lymphatic vessel. The lymphatic system plays an important role in the dynamic control of fluid volume, protein concentration, and, consequently, the pressure in the interstitial space.

All organs and tissues of the body are supplied with a lymphatic drainage system except the brain, bone marrow, and endomysium of muscle [2]. All human beings have similar lymphatic system anatomy; however, there can be considerable variation in the exact route of drainage from different locations of the body. The lym-

phatic vessels are usually located in close proximity to the venous system. Approximately 800 lymph nodes are present in the human body, with a short axis diameter that ranges from a few millimeters to 1 cm [3, 4]. Lymph nodes contain reticuloendothelial cells, primarily tissue phagocytes, that remove abnormal substances.

Lymphatic vessels have the capability of regeneration and can establish their own anastomoses within a short period (weeks) after organ transplantation [5, 6]. Additionally, new lymph tracts can develop and may subsequently reconnect to the main system. This occurs when small lymphatics are surgically transected or there is an attempt to circumvent flow obstruction.

20.3 Pathophysiology

20.3.1 Lymphedema

Lymphedema is the excess accumulation of protein-rich fluid in the interstitial space. It may develop due to excess production of lymph, obstruction of lymphatic drainage, or disruption of the integrity of the lymphatic system. Excess production occurs when there is: (a) obstruction of the capillary or venous system with resultant increased pressure, (b) excessive fluid migration from the vascular space due to low oncotic pressure, or (c) a leak in the system. Obstruction of lymphatic drainage occurs secondary to scarring following trauma, radiation, surgery, and infection, or when there is abnormal development of the lymphatic system or compression of a main lymphatic by a mass [7]. These conditions force fluid to travel back to the vascular space via the nearest accessible lymphatic route.

Lymphedema may be primary or secondary (Table 20.1). The primary type is uncommon, may be congenital or developmental, and usually causes only minimal disturbances in lymphatic flow [8]. The more common secondary type can be due to several factors including infection, trauma, and other venous disorders. Since lymph is rich in protein, it promotes a cycle of inflammation that may be followed by fibrosis, leading to progressive scar formation which can worsen lymphatic obstruction [7].

Table 20.1. Causes of lymphedema

Class	Causes
Primary	Congenital lymphedema Praecox (before age 35) Tarda (after age 35)
Secondary	Inflammation Malignancy Radiation therapy Filiariasis Surgical dissection Trauma Recurrent dermatitis

20.3.2 Lymph Nodes with Metastases

In general, tumors can metastasize by several routes including venous, arterial, lymphatic, and local invasion. It is believed that while most tumors initially spread through the lymphatic system, temporarily being retained at successive levels of lymph nodes by the body's defense system, some tumors may spread through both the vascular and lymphatic systems nearly simultaneously. Since lymph nodes are common sites of metastasis, knowledge of their involvement is crucial for patient management and prognosis. When small numbers of tumor cells (micrometastases) are found in lymph nodes, the architecture and physiological characteristics of the lymph node are not altered. Even with larger tumor loads lymph nodes may remain normal in size, making them difficult to detect with anatomical imaging studies. Determination of focal defects within lymph nodes secondary to tumor infiltration is usually unreliable with all current imaging modalities [9].

20.3.3 Sentinel Node

20.3.1.1 Concept

The lymph node(s) that receives initial lymphatic drainage from a location harboring tumor has been termed the "sentinel node". There can be single or multiple sentinel nodes which may be located in one or different lymphatic beds [10]. Since determination of lymph node involvement is an integral part of tumor staging and management, lymph node excision with pathological evaluation is commonly performed. A complete nodal dissection (often involving large areas of tissue), however, can cause considerable morbidity, including lymphedema, and still fail to remove small diseased nodes [11]. If the sentinel node(s) can be identified, extensive pathological examination can forecast whether tumor dissemination has occurred, since it is the first filter that metastatic cells encounter. Identification of the sentinel node can be done by injections of blue dye around the tumor just before surgery or by using a radiopharmaceutical injected in a similar fashion [12, 13, 14].

There are two important parameters to measure the utility of the SLN, namely identification rate and the false-negative rate. The SLN identification rate is the proportion of successful procedures in which an SLN is located and removed. Failure to identify the SLN is

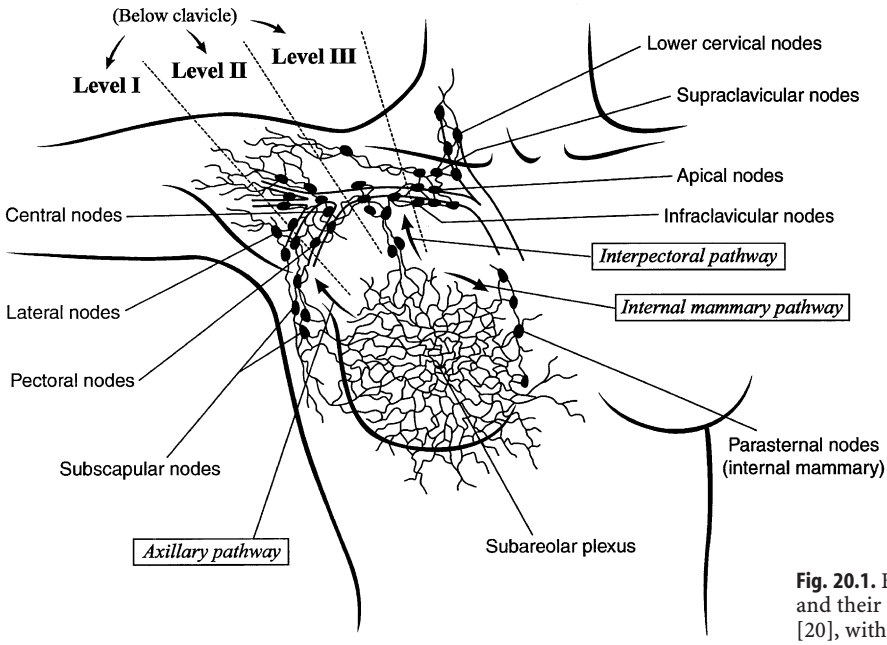

Fig. 20.1. Breast lymphatic tracts, nodes, and their surgical classification. (From [20], with permission)

though unfortunate, but leads to exploration of lymph nodes, so the consequence is that the patient will not be spared extensive surgery. In order to correctly determine the false negative rate, SLN biopsy should be carried out in a validation study where all patients receive standard lymphadenectomy and so in this context the false negative SLN biopsy is defined as presence of metastasis in a non-SLN. The consequence of false negative SLN is devastating since the patient is improperly downstaged, does not receive definitive therapy and possibly has relapse and higher mortality [15]. Therefore, the most important factor in SLN biopsy is the false negative rate [16].

20.3.1.2 Tumors

20.3.1.2.1 Breast Cancer

The breast has three main lymphatic pathways: internal mammary, axillary, and supraclavicular/infraclavicular [17]. Drainage into the associated groups of nodes occurs from cutaneous, subcutaneous, or parenchymal collection sites. Most individuals have drainage into the axillary lymph nodes from all locations in the breast, with only about 9% having regions that drain exclusively into the internal mammary chain [18, 19]. There are approximately 25 lymph nodes in the axilla, ten in the internal mammary chain, and 15 other nodes scattered about the breast region [18]. Most of the breast sites that drain into the internal mammary chain are on the medial aspect of the breast, but they can be located elsewhere. Direct drainage to other nonaxillary sites occurs but is even less frequently encountered. No drainage to the opposite axilla or contralateral internal mammary chain occurs, although drainage from one internal mammary chain to the other is common. Axillary nodes are divided surgically into three groups or levels: I, II, III, in relation to the pectoral muscle (Fig. 20.1). In the past this was presumed to represent the sequence in which lymph nodes become involved with metastatic cells from primary breast tumors. Nodes can also be present within the breast itself. Each individual has variable drainage routes to different sentinel nodes.

Strategies for the diagnosis and management of breast cancer are constantly changing [21]. Radical resections have mostly been replaced by more limited operations such as lumpectomies and level I and II axillary node dissections. Knowledge about the histological features of the tumor and the extent of local and distal disease determines the treatment strategy. When metastatic disease to any lymph node is discovered, chemotherapy is usually administered, since there is a decrease in 5-year survival by approximately 40% [22]. The presence of dissemination to both the internal mammary and axillary nodes indicates an even poorer prognosis than when disease is located in only one of these groups [18]. Clinical evaluation of the axilla for abnormal nodes is unreliable, with 39% false-positive and 27% false-negative rates for determining metastases [18]. Therefore, axillary nodal dissection is primarily a staging procedure to determine if systemic spread has already occurred, whether there is microscopic or macroscopic disease, and how many nodes are involved. A typical dissection consists of removal of both

level I and level II lymph nodes for pathological evaluation. Level III nodes are not routinely excised because of the increased incidence of postoperative lymphedema in the adjacent upper extremity [23]. Because axillary nodes are numerous, vary greatly in both number and location, and can be buried deep in fatty tissue, a complete resection is difficult. Lymph nodes harboring disease may therefore be missed because of sampling error. This may partially explain why 25% of patients with initially negative axillary nodes subsequently develop recurrent disease [19]. Alternatively, removal of uninvolved nodes potentially eliminates a filter that may be able to slow further tumor migration. Finally, morbidity from a complete axillary dissection can be significant and includes the postoperative development of lymphedema, seromas, neuromas, paresthesia, problems with wound healing, and a decrease in adjacent arm motion. These problems can potentially be avoided by removal of only the sentinel node(s).

20.3.1.2.2 Melanoma

Malignant melanoma originates from melanocytes (melanin-producing cells) and currently has the fastest increase in incidence among all types of cancer [24]. Primary neoplasms are usually found in the skin but can also develop in melanocytes of the eye. Factors implicated in the pathogenesis of the tumor are:

- Genetic predisposition
- Exposure to ultraviolet light
- Fair hair
- Light skin
- Steroid hormone activity
- Freckles

Elevated steroid hormone levels have been linked to the development of melanoma since it can initiate the pigmentation process in unpigmented nevi. The tumor arises from malignant degeneration of melanocytes in the basal layer of the epidermis or in a melanocytic nevus consisting of an aggregation of melanocytes. The biology of this tumor is complex, with the lymphatic system playing a key role in its metastatic dissemination. It has been suggested that some unknown immunological function of the lymphatic system controls and/or regulates metastatic melanoma, making identification of the pattern of lymphatic drainage important in the management of this neoplasm.

Determination of metastatic spread is the most important prognostic factor for survival in patients with melanoma [24, 25]. There is sequential dissemination of malignant cells from the primary tumor first to the lymphatic system prior to systemic spread. Propagation of tumor cells to the initial lymph node (sentinel node) for a prolonged interval can occur before higher-station nodes become involved. Lymph node dissection studies have shown a low incidence of skip metastases to second-echelon nodes (less than 1%) [26, 27, 28]. A metastasis can also localize in the lymphatic vessel itself (in-transit metastasis) [24]. Ninety percent of regional nodal metastases will develop within the first 3 years after initial examination [29], but they can recur even 10 years later. Patients without lymph node involvement have a 10-year survival rate of 70% – 80%, but it is only 20% – 30% for those with nodal metastasis [30, 31]. Patients with palpable adenopathy (clinically positive disease) have an unfavorable prognosis that decreases further as the number of involved nodes increases [32] and as the thickness of the lesion at initial examination increases [24]. The depth of the primary lesion is the most powerful indicator of metastatic disease. Lesions less than 0.76 mm deep almost never disseminate, whereas those deeper than 4.0 mm have invariably spread (Breslow scale) [33]. Tumors between 0.76 and 4.0 mm deep are designated as intermediate thickness lesions and have an increasing frequency of metastasis the deeper they are situated. The level of invasion through the different skin zones is also important (Clark level). Histological features that denote an improved prognosis include the presence of radial (not vertical) growth, a decreased cell mitotic rate, and an increased number of infiltrating lymphocytes [34]. Melanoma of the extremities has the best prognosis while those of the head, neck, and trunk have the worst.

Routine pathological evaluation of lymph nodes involves microscopic review of serial 2- to 3-mm sections stained with hematoxylin and eosin. Reverse transcriptase polymerase chain reaction (RT-PCR) methods evaluating for tyrosinase messenger RNA (a substance used to produce melanin) have recently been used for detecting small numbers of melanoma cells missed on routine procedures and have proven useful in determining prognosis (Table 20.2) [35, 36].

Treatment of cutaneous melanoma is surgical, with excision of the tumor along with the surrounding zone of skin and subcutaneous fat as well as the regional lymph nodes. The extent of surgery, however, is determined by the stage of the tumor. In high-risk patients, especially those with nodal metastasis, the long-term (1 year) therapeutic use of high-dose recombinant interferon alpha-2b has recently been shown to improve the relapse-free and overall survival [37].

Table 20.2. Microscopic evaluation of sentinel node(s) by combined H&E and RT-PCR (from [36])

H&E	RT-PCR	2-Year relapse rate (%)
Negative	Negative	2.3
Negative	Positive	13
Positive	Positive	62

20.4 Nuclear Medicine Applications

20.4.1 Basic Principles of Nuclear Medicine Imaging

Tracer is injected into a specific location, and imaging is then performed while the material crosses into the lymphatic system and migrates toward the vascular space. Agent movement will depend on the specific radiopharmaceutical used and the location of the injection. Particulate agents such as colloids are not transported into the peripheral collection sites as well because of their larger size. However, they are better retained in the lymph nodes because of their localization within RES cells. Nonparticulate agents travel much faster and efficiently but are not retained within a lymph node because they do not localize to any of the tissue components but are simply passing through. Because of the very rich supply of lymphatics in the skin, injections into this location will show very efficient uptake and movement of tracer, while breast injections move much slower due to a much sparser lymphatic system.

20.4.2 Detection and Follow-up of Lymphedema

Lymphoscintigraphy can demonstrate: (a) clearance of radiolabeled colloid from an interstitial injection and (b) flow to regional lymph node(s), along with some lymph node anatomical features. Several acquisition protocols can be used. Most investigators have found this test to be sensitive but not specific for determining the etiology of a patient's edema. The procedure usually consists of a 45-min dynamic acquisition followed by delayed imaging, usually at 90 min post-injection. For lower-extremity disease, if movement of the tracer through the lymphatic system is not seen on early images, patients may be instructed to exercise their calf muscles by walking. Interpretation of images includes visual assessment of the injection sites, lymphatic tracts, lymph nodes, and time-activity curves, along with review of the early dynamic acquisition via a computer-generated cine display. Several quantitative procedures have been advocated for use in detecting lymphatic flow disturbances, with some attempting to define the cause of the disease [38–41]. These include determination of the timing as well as the amount of tracer uptake in the draining lymph nodes. However, care is advised when using such measures because there is a normal decrease in lymphatic flow parameters with age, and the use of different radiopharmaceuticals, different injection techniques, and additional procedures such as exercise can alter expected values.

20.4.2.1 Normal Scintigraphic Pattern

Normally, there is rapid and fairly symmetrical transport of the radiotracer from foot injections through one or two lymphatic vessels in the calf and one lymphatic vessel in the thigh. Multiple pelvic lymph nodes should be clearly visualized within 1 h, but may be seen within 6 min when a nonparticulate agent such as Tc-99m-HSA is used [42]. Time-activity curves generated with a region of interest over the inguinal lymph nodes in lower-extremity studies and over axillary nodes in upper-extremity studies normally show a steady rise of activity, especially if a particulate agent is used. Considerable activity usually remains at the injection site throughout the study, with approximately only 40% having migrated by 90 min.

20.4.2.2 Scintigraphic Patterns of Lymphedema

Scan findings in patients with lymphedema will depend on the cause of the swelling, the length of time that the process has been present, and compensatory mechanisms that have developed to circumvent the flow disturbance [43]. Figure 20.2 shows the pathological mechanisms that lead to lymphedema and the corresponding scan patterns. Nawaz et al. described three abnormal patterns for lower-extremity lymphedema: a pattern of stasis, an obstructed pattern, and an enhanced pattern [44]. Lymphatic obstruction will initially cause proximal vessel dilatation and delayed flow, followed by dermal back-diffusion with dispersion of activity into the soft tissues where the tracer originated, along with the development of collateral lymphatic channels. Rapid flow from the injection site is the hallmark of the enhanced pattern, with fast visualization of draining lymph nodes [39].

20.4.3 Detection of Lymph Node Metastases

Since lymph nodes have reticuloendothelial cells (RES) that phagocytose foreign material, radiocolloids are used to visualize them. Direct determination of the presence of tumor is extremely difficult, since the desired space-occupying defects caused by tumor infiltration require a significant portion of the node to be involved. When lymphatic tissue is largely replaced by tumor, lymph nodes may not be visualized because the tracer is blocked from entering. Tumor-involved nodes can even show more tracer uptake than normal nodes [10]. This may be explained by reactive changes in the lymph node, with increased numbers of RES cells being present, possibly in reaction to the presence of tumor antigens.

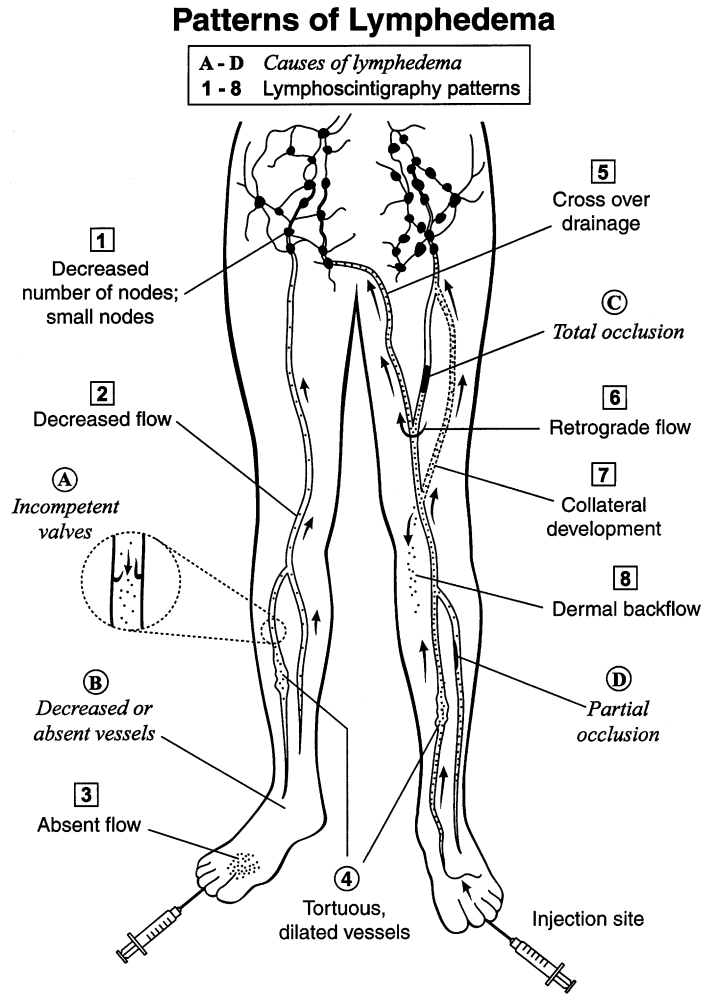

Fig. 20.2. Pictorial representation of the causes of lymphedema and the scan patterns that are created. (From [20], with permission)

Lymphoscintigraphy with radiolabeled anti-tumor antibodies such as anti-CEA have been used to detect occult tumor in lymph nodes. Contrary to radiocolloid lymphoscintigraphy, which depends on phagocytosis, radiolabeled antibody localization requires attachment of the antibody directly to tumor cells. Interstitial injection of these agents has the advantage of producing a higher concentration of tracer at the tumor site in the lymph node than when the antibody is injected intravenously. However, the presence of a definitive number of metastatic cells is required for detection, depending on the agent and the imaging technique used. More recently PET-FDG is being used to detect more effectively lymph node metastasis of many tumors. It has been shown to be particularly useful in detecting lymph node metastasis of lung cancer, changing the mode of therapy in a significant number of cases [45].

20.4.4 Sentinel Node Detection

Radioactive sentinel nodes can be detected using imaging with a gamma camera and/or a gamma probe at surgery. Lymphoscintigraphy using dynamic and static imaging better defines the sequence of lymphatic flow from the tumor site to draining lymph nodes, especially the sentinel node.

20.4.4.1 In Breast Cancer

The typical procedure includes injecting Tc-99m-nanocolloid or Tc-99m-sulfur colloid (filtered or unfiltered) interstitially around the tumor at one to four locations. Ultrasonography can be used to help localize the tumor when needed. The radiotracer is injected along with saline intradermally around the tumor. Some investigators use injections around the areola. The volume used varies from 0.2 to 0.8 ml per injection

site. Dynamic imaging is obtained in the morning of surgery for up to 2 h and is followed by intraoperative probe localization. Alternatively, imaging can be obtained at the end of the day, with surgery and probe localization the following morning. Images are obtained usually in the anterior oblique projections. Static images with transmission and markers are also obtained in the anterior oblique and optionally anterior and lateral projections according to the location of the visualized node(s). Although the accuracy of sentinel node detection is high, the procedure has not currently replaced axillary dissection in patients with breast cancer. This is because there are treatments that can be effective when used early in the course of disease, and, therefore, missing the diagnosis of lymph node metastasis because of a limited nodal evaluation (sentinel node only) could prevent the use of such therapy [22]. Sentinel node biopsy alone can be accepted only when the surgical risk of a full axillary dissection outweighs the chance of understaging metastatic disease.

20.4.4.2 In Cutaneous Melanoma

Lymphoscintigraphy has been used extensively to determine the location and number of lymph node drainage basins in melanoma patients with primary lesions that have a high potential for variable flow. Lymphoscintigraphy often demonstrates lymphatic drainage discordant from clinically predicted patterns and alters surgical management for about one-third of patients [46]. These discrepant results occur more frequently in melanomas of the head and neck than in those of the trunk (64% – 73% vs 35%) [47]. Drainage to more than one lymph node basin and to the contralateral side occurs [48]. Berger et al. documented that 49% of their 297 patients had multiple drainage sites (median 30 months) and that lymphoscintigraphy accurately predicted (98.6%) the basins in which lymph node metastases subsequently occurred (Fig. 20.3) [49]. Some investigators believe that lymphoscintigraphy overestimates the number of draining lymphatic beds, which could ultimately lead to unnecessary surgery. Lymphoscintigraphy for sentinel node localization is most likely to benefit patients with primary melanoma of intermediate thickness (1 – 4 mm) and no clinical evidence of lymph node involvement, because they have up to a 45% chance of metastasis [50]. No benefit would be expected for patients with thin primary lesions (less than 0.76 mm), as these patients have less than a 5% incidence of undetected disease, or for patients with primary lesions more than 4 mm thick, because these patients are likely to have distant disease.

The technique involves multiple injections around the primary lesion into the dermis [51, 52]. If the injection is deeper, if it is distant from the primary lesion, or if a large volume is injected, tracer may travel through undesirable lymphatic vessels, possibly leading to the wrong sentinel node [53]. Imaging should be performed shortly after injection in patients with melanomas of the skin because radiopharmaceuticals can travel rapidly through these lymphatics. Mudun et al. and others have shown good reproducibility of sentinel node detection using lymphoscintigraphy [54 – 56]. All studies have reported a greater than 88% success rate for sentinel node detection, with up to five nodes per patient being labeled as sentinel.

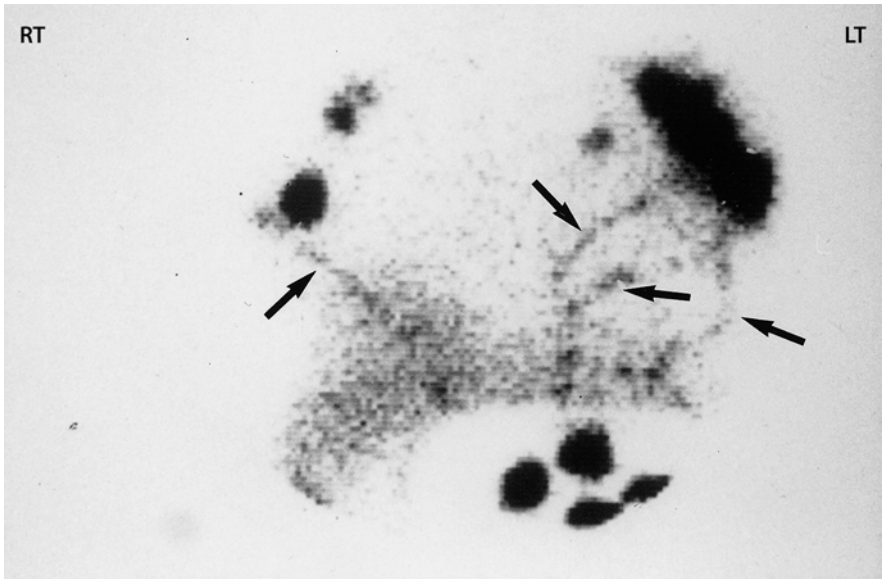

Fig. 20.3. Melanoma: multiple lymphatic tracts (*arrows*) are seen emerging from the injection site and traveling to both axillae from a melanoma on the mid-chest (3 h image). (From [20], with permission)

20.4.4.3 In Urological Malignancies

20.4.4.3.1 Penile Squamous Cell Carcinoma

Penile squamous cell carcinomas metastatic to local lymph nodes are the most amenable to detection by clinical examination among all urological malignancies. A considerable percentage of patients have clinically negative inguinal lymph nodes at presentation; however, up to 20% have occult micrometastasis [57]. The presence of positive nodes is a very important prognostic factor. Since extended clinical and imaging modalities are still not accurate for detection of micrometastasis, prophylactic groin dissection is carried out in the majority of patients. This procedure shows a high cure rate. Nevertheless, as many as 80% of patients have negative lymph nodes, and the procedure for these patients carries morbidity and mortality without clinical benefit when metastases are not present. Sentinel node lymphoscintigraphy aims to select a subpopulation of patients that will benefit from this surgery of node dissection. Kroon and his coworkers [57] have validated the procedure in 140 patients studied over 10 years. The combination of preoperative ultrasound-guided FNA of the node and intraoperative probe-guided sentinel lymph node biopsy (and careful histopathological examination) has yielded a high detection rate. To decrease false negative examinations, prophylactic groin dissection is undertaken in cases where no sentinel nodes could be detected [58–60].

Tanis et al. [61] studied 90 patients with clinically node negative penile cancer. In 88 patients, lymphoscintigraphy visualized 217 sentinel nodes, and a total of 208 sentinel nodes were intraoperatively identified. Sentinel node metastasis was found in 19 inguinal regions of 18 patients. Regional recurrence after excision of a tumor negative sentinel node or after nonvisualization on lymphoscintigraphy was seen in 5 patients, resulting in a false-negative rate of 22% (5 of 23), yet a high negative predictive value of 93%. The 3-year disease specific survival was 98% and 71% for patients with a tumor negative or tumor positive sentinel node, respectively.

20.4.4.3.2 Prostate Cancer

The presence of nodal metastasis is a poor prognostic factor in prostate cancer. The risk of micrometastasis in patients with low-risk prostate cancer (initial PSA <10 ng/ml, a Gleason score[1] of biopsies <7 (3+4 or $<50\%$ of grade 4) is existent though low. The traditional approach of extended pelvic lymphadenectomy (removal of all external and internal iliac nodes up to a point above the common iliac artery bifurcation, the obturator nodes and the presacral nodes) is not only associated with considerable morbidity (lymphocele, lower extremity edema, deep venous thrombosis, ureteral injury and pelvic abscess) but also considerably prolongs the time of surgery. In patients with limited disease (T1-T2), lymphadenectomy provides important prognostic information. Limited lymphadenectomy (removal of nodes along the external iliac vein and obturator nerve) has decreased sensitivity for detection of micrometastasis. Heidenreich et al. found in a series of 103 patients that among all metastatic lymph nodes metastasis was detected in 42% of nodes outside the extent of limited lymphadenectomy [62].

Use of radionuclides for demonstration of prostatic lymphatic drainage was described several decades ago [63–66], although it was only following the successful implementation of the sentinel lymph node concept in breast cancer and melanoma when this was further expanded to evaluate prostate cancer in the late 1990s. The preliminary reports on this procedure from several investigators were encouraging and lead the way for application in larger groups of patients [67–69].

Wawroschek et al. reported a large group of 350 patients with prostate cancer in whom SLN biopsy was carried out. The tracer was adiminstered transrectally. SLN were identified by gamma probe detection and lymphoscintigraphy and removed intraoperatively. Later, most of the cases had different types of pelvic lymphadenectomy; 24.7% of the 335 patients who showed at least one SLN in lymphoscintigraphy had lymph node metastases. There were two false-negative patients [70].

In 235 patients with low risk prostate cancer (PSA =10 ng, Gleason score =6 and positive biopsies in only one lobe), positive lymph nodes were identified by radio-guided surgery in 6.8% (positive biopsies in one lobe) and 10.7% (positive biopsies in both lobes). Up to four positive SLNs were found [71].

Another group in France validated the procedure in 34 patients with clinically localized prostate cancer. Preoperative lymphoscintigraphy allowed identification of sentinel nodes in 85.3% of patients. Four of the five failures had a history of pelvic surgery. Sentinel node mapping and biopsy were possible in 23 patients (67.7%). Microscopic lymph node metastasis was identified in four patients (11.7%), located in a sentinel node in three cases. In two cases, the micrometastasis was situated in a sentinel node outside of the pelvic chain. All four patients had a high clinical risk for nodal metastasis [72].

SLN biopsy in prostate cancer is a very promising procedure with appealing implications; however, a con-

1 Gleason grade refers to architectural prostate patterns, numbered 1 (well differentiated) to 5 (poorly differentiated). The Gleason score is arrived at by adding the Gleason grade of the most abundant pattern to the Gleason grade of the second most abundant pattern.

sensus is awaited to allow widespread application in patients with localized disease. Large well controlled studies are needed to assure involved professionals.

20.4.4.4 In Squamous Cell Carcinoma of Head and Neck

The incidence of occult metastases in squamous cell carcinoma of the head and neck depends on the primary site. If elective neck dissection is to be carried out in all stage N0 patients, then probably more than 50% are exposed to lymphadenectomy that may not be necessary. Following successful output of SLN concept in surgical management of melanoma in the head and neck, many investigators expanded the procedure to squamous cell carcinoma of the head and neck. The initial experience with a few patients using either blue dye or radioactive tracer was hampered by the low success rate of SLN identification of sentinel lymph nodes [73–76]. Several hypotheses were proposed, including rapid transit through the mucosal lymphatics into the systemic circulation, extravasion due to tissue tension, and qualitative differences from dermal drainage sites. Multiple technical difficulties were encountered, and the future utility of SLN biopsy in squamous cell carcinoma of the head and neck was doubted.

The notion that the highest detection rate and clinical benefit was seen in N0 squamous cell carcinoma of the head and neck patients drew the attention to this subclass of disease [77]. To this end, in a retrospective review of 33 patients with squamous cell carcinoma of the head and neck, sentinel lymph node was accurately identified in 19 of 20 (95%) N0 patients. Additionally, in the five patients with previous neck dissection, the lymphatics delineated by lymphoscintigraphy were outside the levels that had been dissected [78]. Ross et al. [79] reported an identification rate of 90% in 48 clinically N0 squamous cell carcinoma of the head and neck patients using a triple approach of preoperative lymphoscintigraphy, intraoperative gamma probe and blue dye. In a large multicenter study [80] on 227 patients with clinically N0 squamous cell carcinoma of the head and neck, sentinel lymph node biopsies were carried out (including 134 combined intraoperative and blue dye/gamma probe). In 125/134 cases (93%), a sentinel node was identified. Of 59 positive nodes, 57 were identified with the intraoperative gamma probe and 44 with blue dye. Upstaging of disease occurred in 42/125 cases (34%). With a follow-up of at least 12 months (mean 24 months), the sensitivity of the combined blue dye and gamma probe technique was 42/45 (93%). However, floor of the mouth tumors showed a lower identification of SLN (86%) and sensitivity (80%), as compared with other squamous cell carcinomas of the head and neck (97% and 100%, respectively). These studies showed that multiple sentinel lymph nodes are common and that the histological appearance of the SLN correctly predicts the nodal (N) stage of the disease. These studies suggest that SLN biopsy is feasible in squamous cell carcinoma of the head and neck and is a promising technique to accurately stage the regional lymphatics.

Several modifications of the technique were also introduced to allow improved detection by dynamic and SPECT acquisitions. In order to achieve better anatomical localization of lymph node, a multimodality imaging approach (using ultrasound or computed tomography) has been utilized to guide the injection of radiotracer into the tumor or to define the exact location of a sentinel lymph node seen in lymphoscintigraphy [81, 82]. Even-Sapir et al. [83] assessed the clinical benefit of fused SPECT/CT images to planar images for SN mapping. Thirty-four patients were studied, including six with squamous cell carcinoma of the head and neck. In 9 of 21 patients (43%) with a primary tumor located in the head and neck or trunk region, SPECT/CT-fused images identified sentinel lymph nodes that were missed on planar images (three were hidden by the scattered radiation from injection site, two in transit nodes, four located in an additional basin to those identified on planar images). Muhle et al. [84] performed CT-guided lymphoscintigraphy in 13 patients with inaccessible squamous cell carcinoma of the hypopharynx and larynx. Lymphatic drainage was identified in 9 out of 13 patients. The procedure was feasible and well tolerated. In another series of 30 patients with squamous cell carcinoma of the head and neck planar, SPECT and SPECT-CT lymphoscintigraphy were compared. Forty-nine sentinel nodes were identified by SPECT-CT. Thirty-eight out of these 49 could be located in lymphoscintigraphic planar imaging, as compared to 24/49 detected in SPECT alone [85].

In conclusion, combined functional and anatomical imaging using SPECT-CT is feasible for sentinel lymph node detection and seems to enhance diagnostic sensitivity [86].

20.4.4.5 In Colorectal Cancer

Colorectal cancer is the commonest form of gastrointestinal cancer and is one of the top leading causes of death from cancer in many developed countries. Surgical treatment involves extensive resection together with all regional lymph nodes. Patients with colorectal cancer stage III benefit from adjuvant therapy. The role of such therapy in stage II patients is still controversial. About 20–25% of stage II patients despite good surgical excision develop either local or distant metastasis. Among the multifactorial causes of recurrence, a very probable and valid explanation is micrometastases in small lymph nodes that were missed during the initial

surgery. Detailed histopathological examination (including multilevel sectioning, immunohistochemistry staining, monoclonal antibody staining, and reverse transcriptasepolymerase chain reaction assay) can reveal micrometastases and leads to ultrastaging, but application of the technique to all lymph nodes in a resected specimen is not practically feasible. The sentinel lymph node concept is therefore a method capable of pointing out the first node to receive drainage from the tumor and to represent the first to harbor micrometastasis if any. The utilization of the concept in the context of colorectal cancer is different than that in breast cancer as an example. In the latter, SLN identification aims to avoid unnecessary surgical exploration and resection of axillary nodes in the basin if the SLN is negative for tumor. In colorectal cancer, however, the regional lymph nodes are already removed en block and there is no change in surgical extent out of the information derived from SLN status. Alternatively, the aim is to identify (either intraoperatively or during pathological examination) a smaller group of nodes in the specimen and to focus all histopathological efforts on such nodes in order to dramatically increase the yield. In addition, an appealing feature is that colorectal cancer exhibits a very predictable pattern for lymphatic drainage channels. Despite all of these observations and expectations, the application of the sentinel lymph node concept in colorectal cancer (as in all gastrointestinal cancers) has not gained wide acceptance and has not been validated, and unified practical guidelines as in melanoma or breast cancer have not been issued.

Earlier reports showed a high failure rate for detection of sentinel lymph node (up to 30%) and failure of detected sentinel nodes to represent the status of the rest of regional lymph nodes (up to 60%) [87, 89].

Reports in the new millennium revisited the issue, and attention to technique and pathological examination have attained a high rate of SLN detection approaching 100% in some series [90, 91]. In 30 patients with invasive adenocarcinomas of the colon, the tumor status in identified sentinel node(s) was compared with the status in all other harvested regional nodes for each of the patients who were clinically followed for more than 30 months. SLNs were identified in all patients and were diagnostic for the entire lymphatic field in 28 patients. In four cases, the sentinel nodes were the only metastatic nodes. After a minimum of 30 months, three patients had died of colon cancer metastases, two of whom had metastatic SLN [92]. Paramo et al. [93] performed intraoperative SLN mapping in 55 patients with colon cancer. In this series SLNs adequately predicted regional status in 44 of 45 (98%) cases and in 9 of 45 cases (20%) were the only sites of metastases. In 55 patients with primary cancer colon studied using SLN mapping, the procedure had a high negative predictive value of 95%, where in only one case was metastasis found in a non-SLN [94].

All the efforts in SLN identification so far discussed were based on injection of a dye into the subserosal layer (intraoperatively) or in the submucosal layer (preoperatively using a colonoscope or proctoscope). The use of a radiotracer to delineate the lymphatic channels was highlighted in a very small number of publications. A group of 56 colorectal cancer patients had sentinel lymph node mapping intraoperatively using gamma probe guidance as the only method for SLN identification. SLNs were detected in 91% of patients. Metastasis was seen in 22% of SLNs as opposed to 3% of non-SLNs. In four cases SLNs were falsely negatively in the presence of metastasis in other non-SLNs, and an advanced case of colorectal cancer was a common finding (a T3 primary tumor) [95]. Whether tumor burden causes blocking or diversion of lymphatic channels remains to be investigated.

Trocha et al. [96] studied 48 colorectal patients using a combination of radiotracer and blue dye.

In all identified nodes there were significantly fewer nodes positive by both methods “blue and hot” than “blue only”. In addition, nodal metastasis was more common in those blue and hot than blue only nodes. This signifies that dual-agent examination more accurately identifies SLN and accordingly further decreases the number of nodes to be examined by the pathologist. The advantages and cost effectiveness of the addition of radioguidance for SLN detection have not been addressed otherwise in literature.

Sentinel lymph node mapping is feasible and easy to perform in colorectal cancer. The most important issue remains how to utilize information from this technique, and whether those patients with micrometastasis will benefit from more aggressive management. The answer is awaited from randomized clinical trials.

20.5 Summary

Lymphoscintigraphy plays an important role in the evaluation of lymphedema and several types of tumors, primarily melanoma and breast cancer. Confirmation of a lymphatic etiology for extremity swelling, along with localization of sites of lymphatic obstruction and leakage, can be achieved with lymphoscintigraphy. Its utilization to detect the sentinel node in melanoma patients is well established, while controversy still exists regarding its similar use in patients with breast cancer. In general, isolated removal of the sentinel node is a simpler, more limited surgical procedure that can be performed on an outpatient basis with the patient under local anesthesia and with far fewer complications than more extensive lymph node dissections.

References

1. McCance KL (1998) Pathophysiology, biological basis of disease in adults and children, Mosby, St. Louis, pp 968 – 1023
2. Guyton AC, Hall JE (1966) Textbook of medical physiology, 9th edn. Saunders, Philadelphia, pp 193 – 197
3. Weissleder R, Thrall JH (1989) The lymphatic system: diagnostic imaging studies. Radiology 172:315 – 317
4. Weiss L (1988) Cell and tissue biology, 6th edn. Urban and Schwarzenberg, Baltimore, pp 499 – 514
5. Ruggiero R, Muz J, Fietsam R Jr (1993) Reestablishment of lymphatic drainage after canine lung transplantation. J Thorac Cardiovasc Surg 106:167 – 171
6. Ruggiero R, Fietsam R Jr, Thomas GA (1994) Detection of canine allograft lung rejection by pulmonary lymphoscintigraphy. J Thorac Cardiovasc Surg 108:253
7. Clodius L (1990) Lymphedema. In: McCarthy JG (ed) Plastic surgery. Saunders, Philadelphia, pp 4093 – 4120
8. Larcos G, Foster DR (1995) Interpretation of lymphoscintigrams in suspected lymphoedema: contribution of delayed images. Nucl Med Commun 16:683 – 686
9. Peyton JW, Crosbie J, Bell TK (1981) High colloidal uptake in axillary nodes with metastatic disease. Br J Surg 68:507 – 509
10. Bergqvist L, Strand SE, Hafstrom L (1984) Lymphoscintigraphy in patients with malignant melanoma: a quantitative and qualitative evaluation of its usefulness. Eur J Nucl Med 9:129 – 135
11. Baas PC, Schraffordt KH, Hoekstra HJ, Van Bruggen JJ, Van der Weele LT, Oldhoff J (1992) Groin dissection in the treatment of lower-extremity melanoma. Short term and long term morbidity. Arch Surg 127:281 – 286
12. Morton DL, Wen DR, Wong JH (1992) Technical details of intraoperative lymphatic mapping for early stage melanoma. Arch Surg 127:392 – 399
13. Alex JC, Weaver DL, Fairbank JT (1993) Gamma-probe-guided lymph node localization in malignant melanoma. Surg Oncol 2:303 – 308
14. Thompson JF, Uren RF, Scolyer RA, Stretch JR (2005) Selective sentinel lymphadenectomy: Progress to date and prospects for the future. Cancer Res 126:269 – 287
15. Guenther JM, Krishnamoorthy M, Tan LR (1997) Sentinel lymphadenectomy for breast cancer in a community managed care setting. Cancer J Sci Am 3:336 – 340
16. McMasters KM, Giuliano AE, Ross MI, Reintgen DS, Hunt KK, Byrd DR, et al (1998) Sentinel-lymph-node biopsy for breast cancer – not yet the standard of care. N Engl J Med 339:990 – 995
17. Vendrell-Torne E, Setoain-Quinquer J, Domenech-Torne FM (1972) Study of normal mammary lymphatic drainage using radioactive isotopes. J Nucl Med 13:801 – 805
18. Donegan WL, Spratt JS (1995) Cancer of the breast, 4th edn. Saunders, Philadelphia
19. Glass EC, Essner R, Giuliana AE (1999) Sentinel node localization in breast cancer. Semin Nucl Med 24:57 – 68
20. Krasnow AZ, Hellman RS (1999) Lymphoscintigraphy revisited: 1999. In: Freeman LM (ed) Nuclear medicine annual. Mosby, St. Louis, pp 17 – 97
21. Hortobagy GN (1998) Treatment of breast cancer. N Engl J Med 339:974 – 984
22. McMasters KM, Giuliano AE, Ross MI, Reintgen DS, Hunt KK, Byrd DR, Klimberg VS, Whitworth PW, Tafra LC, Edwards MJ (1998) Sentinel-lymph-node biopsy for breast cancer – not yet the standard of care. N Engl J Med 339:990 – 995
23. Albertini JJ, Lyman GH, Cox C, Yeatman T, Balducci L, Ku N, Shivers S, Berman C, Wells K, Rapaport D, Shons A, Horton J, Greenberg H, Nicosia S, Clark R, Cantor A, Reintgen DS (1966) Lymphatic mapping and sentinel node biopsy in the patient with breast cancer. JAMA 276: 1818 – 1822
24. Balch CM, Reintgen DS, Kirkwood JM, Houghton A, Peters L, Ang KK (1997) Cutaneous melanoma. In: Devita VT (ed) Cancer: principles and practice of oncology, 5th edn. Lippincott-Raven, Philadelphia, pp 1947 – 1994
25. Homsi J, Kashani-Sabet M, Messina JL, Daud A (2005) Cutaneous melanoma: Prognostic factors. Cancer Control 12:223 – 229
26. Godellas CV, Berman CG, Lyman G (1995) The identification and mapping of melanoma regional nodal metastases: minimally invasive surgery for the diagnosis of nodal metastases. Am Surg 61:97 – 101
27. Morton DL, Wen DR, Cochran AJ (1992) Management of early-stage melanoma by intraoperative lymphatic mapping and selective lymphadenectomy: an alternative to routine lymphadenectomy or "watch and wait". Surg Oncol Clin North Am 1:247 – 259
28. Johnson TM, Bradford CR, Gruber SB, Sondak VK, Schwartz JL (2004) Staging workup, sentinel node biopsy, and follow-up tests for melanoma: Update of current concepts. Arch Dermatol 140:107 – 113
29. Alex JC, Krag DN, Harlow SP (1998) Localization of regional lymph nodes in melanomas of the head and neck. Arch Otolaryngol Head Neck Surg 124:135 – 140
30. Queirolo P, Taveggia P, Gipponi M, Sertoli MR (2004) Sentinel lymph node biopsy in melanoma patients: The medical oncologist's perspective. J Surg Oncol 85:162 – 165
31. Coit DG, Rogatko A, Brennan MF (1991) Prognostic factors in patients with melanoma metastatic to axillary or inguinal lymph nodes. Ann Surg 215:627 – 636
32. Alazraki NP, Eshima D, Eshima LA (1997) Lymphoscintigraphy, the sentinel node concept, and the intraoperative gamma probe in melanoma, breast cancer, and other potential cancers. Semin Nucl Med 27:55 – 67
33. American Joint Committee on Cancer (1997) AJCC Cancer Staging Manual, 5th edn, Lippincott-Raven, Philadelphia
34. Halpern AC, Shuchter LM (1997) Prognostic models in melanoma. Semin Oncol 24[Suppl 4]:S2 – 7
35. Reintgen DS, Conrad AJ (1997) Detection of occult melanoma cells in sentinel lymph nodes and blood. Semin Oncol 24[Suppl 4]:S11 – 15
36. Shivers SC, Wang X, Li W, Joseph E, Messina J, Glass LF, DeConti R, Cruse CW, Berman C, Fenske NA, Lyman GH, Reintgen DS (1998) Molecular staging of malignant melanoma. JAMA 280:1410 – 1415
37. Kirkwood JM, Resnick GD, Cole BF (1997) Efficacy, safety, and risk-benefit analysis of adjuvant interferon alfa-2b in melanoma. Semin Oncol 24[Suppl 4]:S16 – 23
38. Carena M, Campini R, Zelaschi G (1988) Quantitative lymphoscintigraphy. Eur J Nucl Med 14:88 – 92
39. Weissleder H, Weissleder R (1988) Lymphedema: evaluation of qualitative and quantitative lymphoscintigraphy in 238 patients. Radiology 167:729 – 735
40. Rijke AM, Croft BY, Johnson RA (1990) Lymphoscintigraphy and lymphedema of the lower extremities. J Nucl Med 31:990 – 998
41. Baulieu F, Baulieu JL, Secchi V (1989) Factorial analysis of dynamic lymphoscintigraphy in lower limb lymphoedema. Nucl Med Commun 10:109 – 119
42. Szuba A, Shin WS, Strauss HW, Rockson S (2003) The third circulation: Radionuclide lymphoscintigraphy in the evaluation of lymphedema. J Nucl Med 44:43 – 57
43. Ohtake E, Matsui K (1986) Lymphoscintigraphy in patients with lymphedema. A new approach using intradermal injections of technetium-99m human serum albumin. Clin Nucl Med 11:474 – 478

44. Nawaz MK, Hamad MM, Abdel-Dayem HM (1990) Tc-99m human serum albumin lymphoscintigraphy in lymphedema of the lower extremities. Clin Nucl Med 15:794 – 799
45. Mavi A, Lakhani P, Zhuang H, Gupta NC, Alavi A (2005) Fluorodeoxyglucose-PET in characterizing solitary pulmonary nodules, assessing pleural diseases and the initial staging, restaging, therapy planning, and monitoring response of lung cancer. Radiol Clin North Am 43:1 – 24
46. Wells KE, Cruse CW, Daniels S (1994) The use of lymphoscintigraphy in melanoma of the head and neck. Plastic Reconstr Surg 93:757 – 761
47. Berman CG, Norman J, Cruse CW (1992) Lymphoscintigraphy in malignant melanoma. Ann Plastic Surg 28:29 – 32
48. Jonk A, Kroon BB, Mooi WJ (1989) Contralateral inguinal lymph node metastasis in patients with melanoma of the lower extremities. Br J Surg 76:1161 – 1162
49. Berger DH, Feig BW, Podoloff D (1997) Lymphoscintigraphy as a predictor of lymphatic drainage from cutaneous melanoma. Ann Surg Oncol 4:247 – 251
50. Cole DJ, Baron PL (1996) Surgical management of patients with intermediate thickness melanoma: current role of elective lymph node dissection. Semin Oncol 23:719 – 724
51. Yeung H, Yeh S, Colt D, El-Shirbiny A, Brady M, Lewis J, Larson SM (1996) Lymphoscintigraphy with sulphur colloid for identification of sentinel node in malignant melanoma. J Nucl Med 37:138P (abstract)
52. Wong JH, Terada K, Ko P (1988) Lack of effect of particle size on the identification of the sentinel node in cutaneous malignancies. Ann Surg Oncol 5:77 – 80
53. Zinsmeister MS (1977) Lymphoscintigraph: current techniques and indications. Appl Radiol 26:32 – 39
54. Mudun A, Murray DR, Herda SC (1996) Early-stage melanoma: lymphoscintigraphy, reproducibility of sentinel node detection, and effectiveness of the intraoperative gamma probe. Radiology 199:171 – 175
55. Kapteijn BA, Nieweg OE, Valdes Olmos RA (1996) Reproducibility of lymphoscintigraphy for lymphatic mapping in cutaneous melanoma. J Nucl Med 37:972 – 975
56. Tonakie A, Yahanda A, Sondak V, Wahl RL (1998) Reproducibility of lymphoscintigraphy drainage patterns in sequential Tc-99m HSA and Tc-99m sulfur colloid studies: implications for sentinel node identification in melanoma. J Nucl Med 39:25P (abstract)
57. Kroon BK, Horenblas S, Estourgie SH, et al (2004) How to avoid false-negative dynamic sentinel node procedures in penile carcinoma. J Urol 171:2191 – 2194
58. Kroon BK, Horenblas S, Meinhardt W, van der Poel HG, Bex A, van Tinteren H, Valdes Olmos RA, Nieweg OE (2005) Dynamic sentinel node biopsy in penile carcinoma: evaluation of 10 years experience. Eur Urol 47:601 – 651
59. Kroon BK, Horenblas S, Estourgie SH, Lont AP, Valdes Olmos RA, Nieweg OE (2004) How to avoid false-negative dynamic sentinel node procedures in penile carcinoma. J Urol 171:2191 – 2194
60. Kroon BK, Horenblas S, Deurloo EE, Nieweg OE, Teertstra HJ (2005) Ultrasonography-guided fine-needle aspiration cytology before sentinel node biopsy in patients with penile carcinoma. BJU Int 95:517 – 521
61. Tanis PJ, Lont AP, Meinhardt W, Olmos RA, Nieweg OE, Horenblas S (2002) Dynamic sentinel node biopsy for penile cancer: reliability of a staging technique. J Urol 168:76 – 80
62. Heidenreich A, Varga Z, Von Knobloch R (2002) Extended pelvic lymphadenectomy in patients undergoing radical prostatectomy: high incidence of lymph node metastasis. J Urol 167:1681 – 1686
63. Gardiner RA, Fitzpatrick JM, Constable AR, Cranage RW, O'Donoghue EP, Wickham JE (1979) Human prostatic lymphoscintigraphy. A preliminary report. Br J Urol 51: 300 – 303
64. Stone AR, Merrick MV, Chisholm GD (1979) Prostatic lymphoscintigraphy. Br J Urol 51:556 – 560
65. Gardiner RA, Fitzpatrick JM, Constable AR, Cranage RW, O'Donoghue EP, Wickham JE (1979) Improved techniques in radionuclide imaging of prostatic lymph nodes. Br J Urol 51:561 – 564
66. Whitmore WF 3rd, Blute RD Jr, Kaplan WD, Gittes RF (1980) Radiocolloid scintigraphic mapping of the lymphatic drainage of the prostate. J Urol 124:62 – 67
67. Wawroschek F, Vogt H, Weckermann D, Wagner T, Harzmann R (1999) The sentinel lymph node concept in prostate cancer – first results of gamma probe-guided sentinel lymph node identification. Eur Urol 36:595 – 600
68. Wawroschek F, Vogt H, Weckermann D, Wagner T, Hamm M, Harzmann R (2001) Radioisotope guided pelvic lymph node dissection for prostate cancer. J Urol 166:1715 – 1719
69. Takashima H, Egawa M, Imao T, Fukuda M, Yokoyama K, Namiki M (2004) Validity of sentinel lymph node concept for patients with prostate cancer. J Urol 171:2268 – 2271
70. Wawroschek F, Vogt H, Wengenmair H, Weckermann D, Hamm M, Keil M, Graf G, Heidenreich P, Harzmann R (2003) Prostate lymphoscintigraphy and radio-guided surgery for sentinel lymph node identification in prostate cancer. Technique and results of the first 350 cases. Urol Int 70:303 – 310
71. Weckermann D, Wawroschek F, Harzmann R (2005) Is there a need for pelvic lymph node dissection in low risk prostate cancer patients prior to definitive local therapy? Eur Urol 47:45 – 50
72. Bastide C, Brenot-Rossi I, Garcia S, Dumas S, Anfossi E, Ragni E, Rossi D (2004) Feasibility and value of the isotope sentinel node mapping technique in prostate cancer. Prog Urol 14:501 – 506
73. Terui S, Terauchi T, Ebihara S, et al (1992) Lymphoscintigraphy of head and neck cancer. Angiology 43:925 – 932
74. Koch WM, Choti MA, Civelek AC, et al (1998) Gamma probe-directed biopsy of the sentinel node in oral squamous cell carcinoma. Arch Otolaryngol Head Neck Surg 124:455 – 459
75. Pitman KT, Johnson JT, Edington H, et al (1998) Lymphatic mapping with isosulfan blue dye in squamous cell carcinoma of the head and neck. Arch Otolaryngol Head Neck Surg 124:790 – 793
76. Shoaib T, Soutar DS, Prosser JE, et al (1999) A suggested method for sentinel node biopsy in squamous cell carcinoma of the head and neck. Head Neck 728 – 733
77. Kosuda S, Kusano S, Kohno N, Ohno Y, Tanabe T, Kitahara S, Tamai S (2003) Feasibility and cost-effectiveness of sentinel lymph node radiolocalization in stage N0 head and neck cancer. Arch Otolaryngol Head Neck Surg 129:1105 – 1109
78. Pitman KT, Johnson JT, Brown ML, Myers EN (2002) Sentinel lymph node biopsy in head and neck squamous cell carcinoma. Laryngoscope 112:2101 – 2113
79. Ross GL, Soutar DS, Shoaib T, Camilleri IG, MacDonald DG, Robertson AG, Bessent RG, Gray HW (2002) The ability of lymphoscintigraphy to direct sentinel node biopsy in the clinically N0 neck for patients with head and neck squamous cell carcinoma. Br J Radiol 75:950 – 958
80. Ross GL, Soutar DS, Gordon MacDonald D, Shoaib T, Camilleri I, Roberton AG, Sorensen JA, Thomsen J, Grupe P, Alvarez J, Barbier L, Santamaria J, Poli T, Massarelli O, Sesenna E, Kovacs AF, Grunwald F, Barzan L, Sulfaro S, Alberti F (2004) Sentinel node biopsy in head and neck cancer: preliminary results of a multicenter trial. Ann Surg Oncol 11:690 – 696

81. Nieuwenhuis EJ, Colnot DR, Pijpers HJ, Castelijns JA, van Diest PJ, Brakenhoff RH, Snow GB, van den Brekel MW (2000) Lymphoscintigraphy and ultrasound-guided fine needle aspiration cytology of sentinel lymph nodes in head and neck cancer patients. Recent Results Cancer Res 157:206 – 217
82. Freire AR, Lima EN, Almeida OP, Kowalski LP (2003) Computed tomography and lymphoscintigraphy to identify lymph node metastases and lymphatic drainage pathways in oral and oropharyngeal squamous cell carcinomas. Eur Arch Otorhinolaryngol 260:148 – 152
83. Even-Sapir E, Lerman H, Lievshitz G, Khafif A, Fliss DM, Schwartz A, Gur E, Skornick Y, Schneebaum S (2003) Lymphoscintigraphy for sentinel node mapping using a hybrid SPECT/CT system. J Nucl Med 44:1413 – 1420
84. Muhle C, Brenner W, Sudmeyer M, Hoft S, Galalae R, Czech N, Biederer J, Ahn JM, Maune S, Henze E (2004) CT-guided lymphoscintigraphy in patients with squamous cell carcinoma of the head and neck: a feasibility study. Eur J Nucl Med Mol Imaging 31:940 – 944
85. Wagner A, Schicho K, Glaser C, Zettinig G, Yerit K, Lang S, Klug C, Leitha T (2004) SPECT-CT for topographic mapping of sentinel lymph nodes prior to gamma probe-guided biopsy in head and neck squamous cell carcinoma. J Craniomaxillofac Surg 32:343 – 349
86. Lopez R, Payoux P, Gantet P, Esquerre JP, Boutault F, Paoli JR (2004) Multimodal image registration for localization of sentinel nodes in head and neck squamous cell carcinoma. J Oral Maxillofac Surg 62:1497 – 1504
87. Joosten JJ, Strobbe LJ, Wauters CA, Pruszczynski M, Wobbes T, Ruers TJ (1999) Intraoperative lymphatic mapping and the sentinel node concept in colorectal carcinoma. Br J Surg 86:482 – 486
88. Cserni G, Vajda K, Tarjan M, Bori R, Svebis M, Baltas B (1999) Nodal staging of colorectal carcinomas from quantitative and qualitative aspects. Can lymphatic mapping help staging? Pathol Oncol Res 5:291 – 296
89. Bertagnoll MI, Miedema B, Redston M, Dowell J, Niedzwiecki D, Fleshman J, Bem J, Mayer R, Zinner M, Compton C (2004) Sentinel node staging of resectable colon cancer results of a multicenter study. Ann Surg 240: 624 – 630
90. Wiese DA, Saha S, Badin J (1999) Sentinel lymph node mapping in staging of colorectal carcinoma. Am J Clin Pathol 112:542
91. Saha S, Wiese D, Badin J, Beutler T, Nora D, Ganatra BK, et al (2000) Technical details of sentinel lymph node mapping in colorectal cancer and its impact on staging. Ann Surg Oncol 7:120 – 124
92. Dahl K, Westlin J, Kraaz W, Winqvist O, Bergkvist L, Thorn M (2005) Identification of sentinel nodes in patients with colon cancer. Eur J Surg Oncol 31:381 – 385
93. Paramo JC, Summerall J, Poopiti R, Mesko TW (2002) Validation of sentinel node mapping with colon cancer. Ann Surg Oncol 9:550 – 554
94. Bembenek A, Schneider U, Gretschel S, Fischer J, Schlag PM (2005) Detection of lymph node micrometastases and isolated tumor cells in sentinel and nonsentinel lymph nodes of colon cancer patients. World J Surg 29:1172 – 1175
95. Kitagawa Y, Watanabe M, Hasegawa H, Yamamoto S, Fujii H, Yamamoto K, Matsuda J, Mukai M, Kubo A, Kitajima M (2002) Sentinel node mapping for colorectal cancer with radioactive tracer. Dis Colon Rectum 45:1476 – 1480
96. Trocha SD, Nora DT, Saha SS, Morton DL, Wiese D, Bilchik AJ (2003) Combination probe and dye-directed lymphatic mapping detects micromerastasis in early colorectal cancer. J Gastrointest Surg 7:340 – 346

Basis of Pediatric Genitourinary Imaging 21

Abdelhamid H. Elgazzar

21.1 Introduction

This chapter includes certain procedures of pediatric nuclear medicine, namely radionuclide imaging studies for the evaluation of important renal diseases in the pediatric age-group, as well as vesicoureteral reflux and testicular torsion. Other pediatric procedures are covered in the other chapters. Radionuclide imaging of the genitourinary tract in children is extensively requested by pediatricians and pediatric surgeons in order to assess renal function by the aid of quantitative analysis as well as by the morphological data gained in these studies. These informative data, along with those provided by ultrasonography and excretory urography, provide physicians with valuable objective criteria for diagnosing and following patients. In neonates, radionuclide studies are much used to evaluate flank masses such as cystic kidneys, hydronephrosis, tumors, and congenital abnormalities, e.g., horseshoe kidney, renal ectopia, absence of a kidney, which are often encountered on antenatal ultrasonographic examinations. Older children are frequently examined with radionuclide studies for evaluation of genitourinary tract disorders such as infection, hydronephrosis, hydroureteronephrosis, vesicoureteral reflux, hypertension, trauma, tumors, and problems resulting from kidney transplantation.

21.2 Anatomic Considerations

Scintigraphic studies concerned with the genitourinary system in children show certain findings that require a knowledge of the anatomy of the kidney and testicle since studies on the evaluation of bladder disorders, namely reflux, provide essentially functional information. Therefore, the main features of the kidney and testicle are shown in Figs. 21.1 and 21.2.

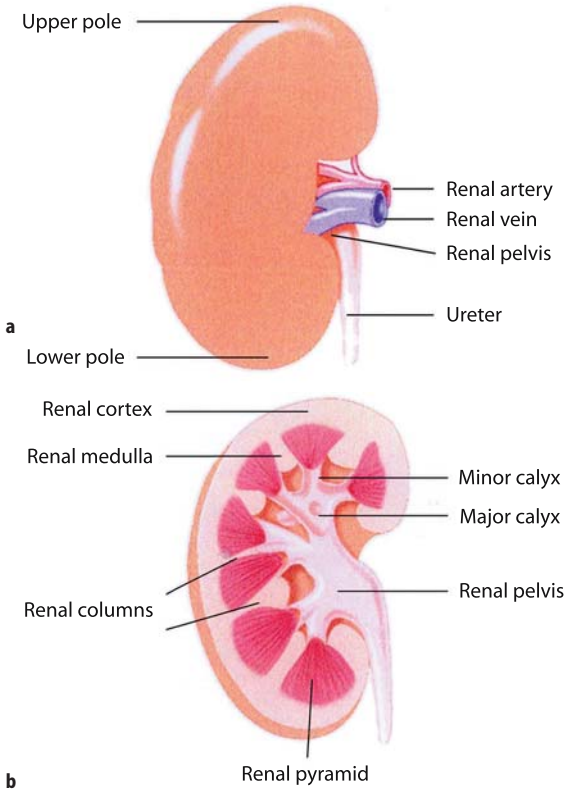

Fig. 21.1a,b. Diagram illustrating the main anatomic features of the kidney. a illustrates the external surface while **b** illustrates the cut surface

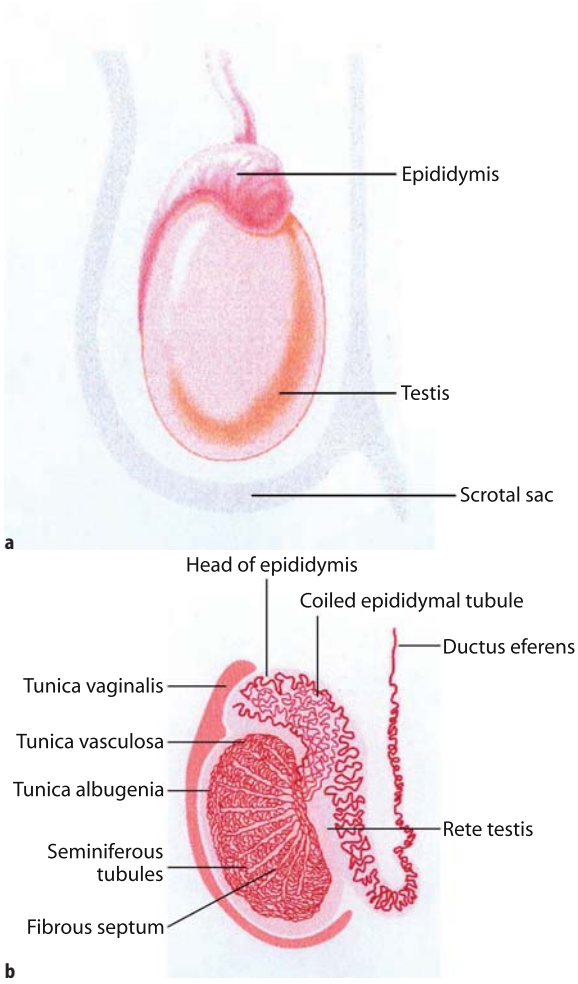

Fig. 21.2a,b. Diagrams showing the main anatomic parts of the testis

21.3 Urinary Tract Infections

21.3.1 Pathophysiology

Urinary tract infections (UTIs) are particularly important in the pediatric age-group as it is one of the most common diseases in children. The overall incidence of UTIs in children ranges between 1.5% and 2% [1, 2]. In the neonatal period UTIs are relatively rare and are usually caused by bacteria from the blood stream. The incidence in newborns is higher for boys, while girls are affected (1%) more than boys (0.3%) between the ages of 1 and 5 years [1 – 3]. The incidence increases up to 5% among girls of school age, and infections result most commonly from bacteria – usually a pathogenic strain of *Escherichia coli* – ascending the urethra.

Table 21.1. Factors predisposing to and affecting the severity of UTI in children

Individual susceptibility
Bacterial virulence
Host's anatomical abnormalities
Presence of reflux
Obstruction and stasis
Hydronephrosis with or without pelviureteral junction obstruction
Horseshoe kidney
Crossed renal ectopia
Renal duplication with ectopic ureters
Urethral polyps or diverticula
Posterior urethral valves or ureterocele

Many predisposing factors affect the incidence and the severity of the disease in different age-groups. These factors include individual susceptibility, bacterial virulence, and the host's anatomical abnormalities such as presence of vesicoureteral reflux (VUR), obstruction, stasis, or stones (Table 21.1). However, UTIs may occur also in healthy children with an anatomically normal urinary tract. Individual susceptibility may be variable and can be related to familial or hereditary factors. These include congenital abnormalities such as VUR or ureteral duplication, blood group secretor status, or familial preference for circumcision or breastfeeding

The recent application of molecular techniques has changed clinical practice in clarifying how bacteria establish urinary infection by exploiting host cell features for their own benefit. One of the most important examples of clinical intervention to diminish the risk of urinary infection is circumcision, which decreases the risk of periurethral bacterial adherence [4].

Acute pyelonephritis involves acute inflammation of the pyelocaliceal lining and renal parenchyma centrifugally along medullary rays. This can occur by more than one route. Most often it occurs because of ascending infection from the lower urinary tract. The initial colonization of the walls of the ureter is in areas of turbulent flow, which leads to loss of peristalsis. Dilation and functional obstruction result, with subsequent pyelonephritis. Another way is by direct reflux of bacteria. Hematogenous spread to the kidney by organisms is another route that can occur (Fig. 21.3). This has become less prevalent since the advent of rapid use of antibiotics. Little or no evidence supports lymphatic spread. Chronic pyelonephritis results from recurrent or persistent renal infection. It occurs almost exclusively in patients with major anatomic anomalies, including urinary tract obstruction, renal dysplasia, or, most commonly, vesicoureteral reflux (VUR) in young children.

Severe long term sequelae, such as hypertension, and renal failure may develop if urinary infection leads

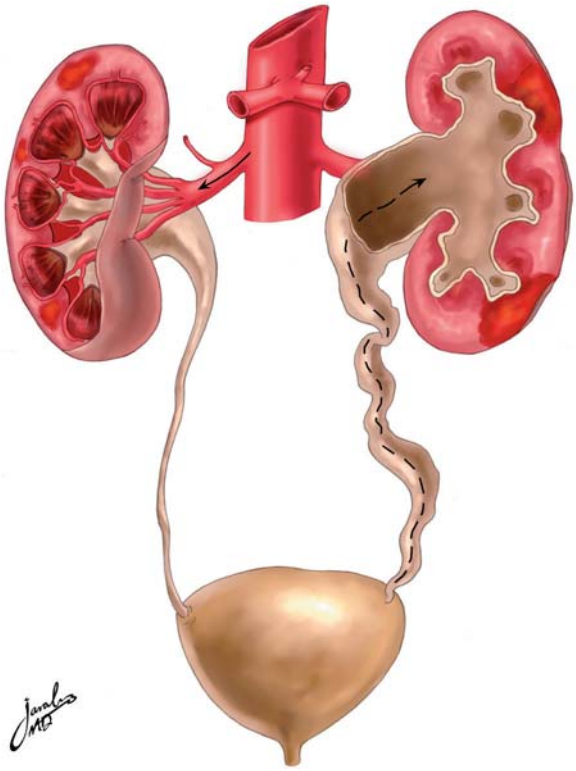

Fig. 21.3. Diagram illustrating the routes of inducing urinary tract infection. The *left-hand side* represents the hematogenous route while the *right-hand side* represents the retrograde route such as with vesicoureteral reflux

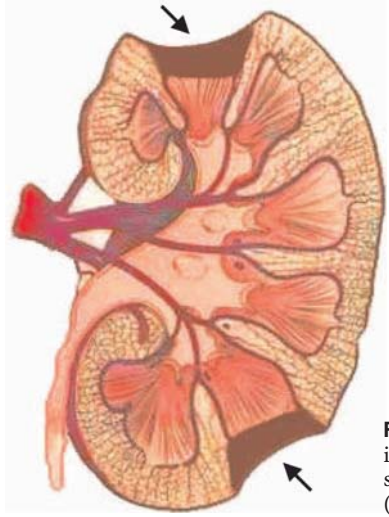

Fig. 21.4. Diagram illustrating cortical scars in renal cortex (*arrows*)

to acute pyelonephritis and subsequently to renal scarring (Fig. 21.4). The pathophysiology of renal scarring is still obscure. Numerous factors may contribute to tissue damage following acute infection. Inflammatory responses are activated by host defense mechanisms as well as by specific bacterial virulence factors [5]. It was found that patients with increased transforming growth factor-beta1 (TGF-β1), which is a potent proinflammatory and fibrogenetic cytokine known to have a key role in the regulation of renal tissue fibrosis, may be at higher risk for renal damage following reflux [6]. Non-secretor status of blood type antigen has been associated with higher risk of urinary tract infection (UTI) in women. Recently, a study has shown that the nonsecretor status significantly correlated with the presence of focal renal scarring (41% vs 22% for children with and without scarring, respectively) as determined by ^{99m}Tc-DMSA renal scan. These results demonstrate that secretor status represents unrecognized host disposition that affects the clinical course of primary VUR [7].

Although *Pseudomonas* was found to be common in UTIs following reflux, particularly severe ones [8], the usual pathogenesis of UTIs is proliferation of *E. coli* in the colon. This bacterial proliferation allows movement of the bacteria into the periurethral mucosa. In order to be able to multiply, bacteria that reach the urinary tract must overcome the tendency to be washed away by urine flow and bladder voiding. Accordingly, prolonged intervals between voiding, increased storage pressure, or significant residual urine volume favor the growth of bacteria and allow even relatively nonpathogenic bacteria to cause significant infections [9]. Vaginal filling secondary to high voiding velocity and turbulent urine flow related to a dysfunctional voiding pattern is an important factor leading to bacterial contamination and urinary infections in girls [10].

Urinary tract infections are divided into lower and upper infections. Lower UTI or infection of the bladder (cystitis) results in mucosal inflammation and congestion, which causes hyperactivity of the detrusor muscle and results in a decrease of the bladder capacity [1, 11]. This can also lead to urine reflux up the ureter. This reflux can send bacteria all the way to the kidney, leading to acute or chronic pyelonephritis which may cause renal abscesses or scarring.

21.3.2 Diagnosis

The upper UTIs, or infections of the kidneys, cannot be easily differentiated clinically from cystitis based only on symptoms. However, differentiation between upper and lower UTI is important, since the former is often associated with renal parenchymal damage. It is particularly difficult in infants, who usually develop nausea, vomiting, diarrhea, or jaundice. In children, fever, frequency, urgency, enuresis or incontinence in a previously dry child, abdominal pain, foul-smelling urine, and sometimes hematuria are the most common clinical presentations. It is estimated that about 20% of children with UTI are asymptomatic [2, 11, 12].

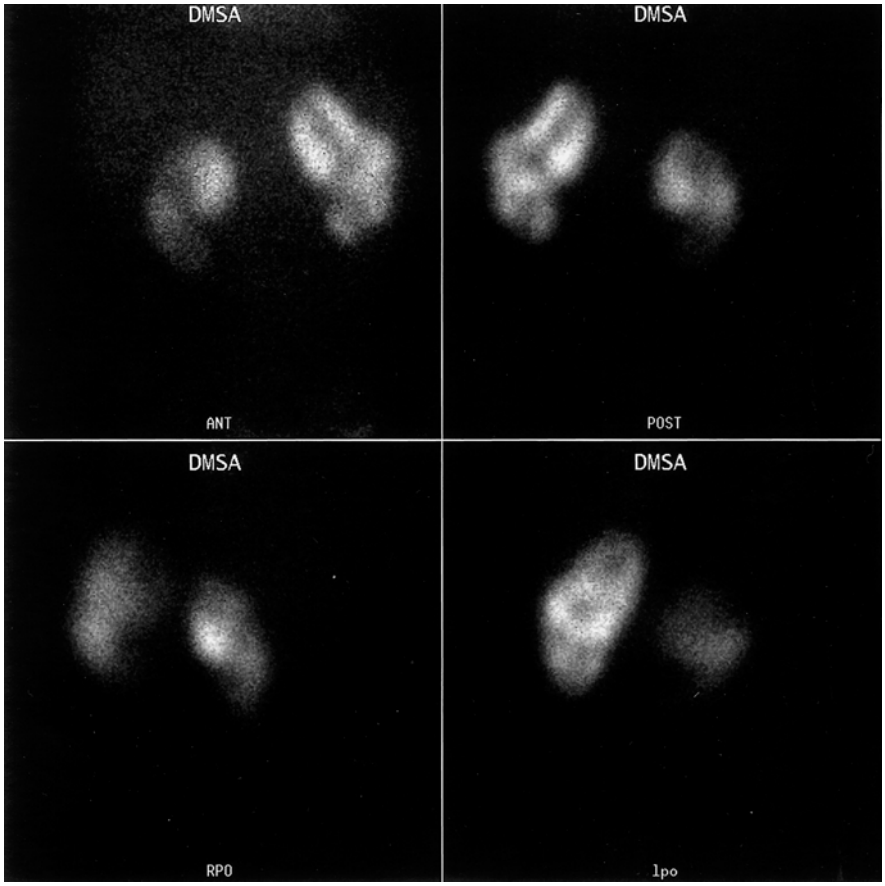

Fig. 21.5. ^{99m}Tc-DMSA scan of a 9-year-old girl with a long history of recurrent urinary tract infections. The right kidney is smaller than the left, with nonuniform and decreased uptake, particularly in the lower pole. Multiple photon-deficient areas are also seen in both kidneys. These findings are due to multiple cortical scars

Various tests can be utilized to diagnose and localize the site of UTI. For diagnosis, urine culture along with routine urine analysis is the test of choice. Urine analysis may show microscopic hematuria and pyorrhea. In addition, the presence of casts in the urine can be an indication of pyelonephritis. Other laboratory tests are of limited value and have proven more useful in adults than in children. These include determination of serum level of C-reactive protein, urine lactate dehydrogenase, and urine lactic acid [13].

21.3.3 Imaging

Imaging strategies in pediatric urinary tract infection are controversial. The recent literature illustrates the complementary roles of ultrasound, diagnostic radiology and nuclear medicine [14]. Ultrasonography, computed tomography (CT), intravenous urography (IVU), diuretic renography, and ^{99m}Tc-DMSA renal scan may be necessary to rule out abscesses, obstruction, or cortical scars. In a child with recurrent UTI, however, the first imaging study to be performed is a micturating cystourethrogram (MCUG) in a boy or a radionuclide cystogram in a girl to rule out vesicoureteral reflux as a common associated condition. Cyclic radionuclide voiding cystograms are also useful in certain groups of children with symptoms and signs suggesting severe UTI [15].

21.3.4 Scintigraphic Evaluation

Radionuclide static renal scan [16–18] with or without SPECT acquisition plays an important role in the evaluation of renal tumors and congenital abnormalities (horseshoe kidney or renal ectopia), and detection of the effects of kidney infection that appear as focal cortical defects (Figs. 21.5, 21.6) [19–21]. Urinary tract infection is known to be associated with an increased risk of permanent renal cell damage and scarring which may lead to generation of pathological conditions such as hypertension, preeclampsia during pregnancy, renal insufficiency, and end-stage kidney disease. The radionuclide renal scan is more sensitive than IVU or ultrasonography in detecting cortical lesions, since it may take up to 2 years after the initial insult to show demarcation in such morphological studies [2, 21]. Although the debate regarding this fact is continuing, recent studies confirmed the value of ^{99m}Tc-DMSA in the diag-

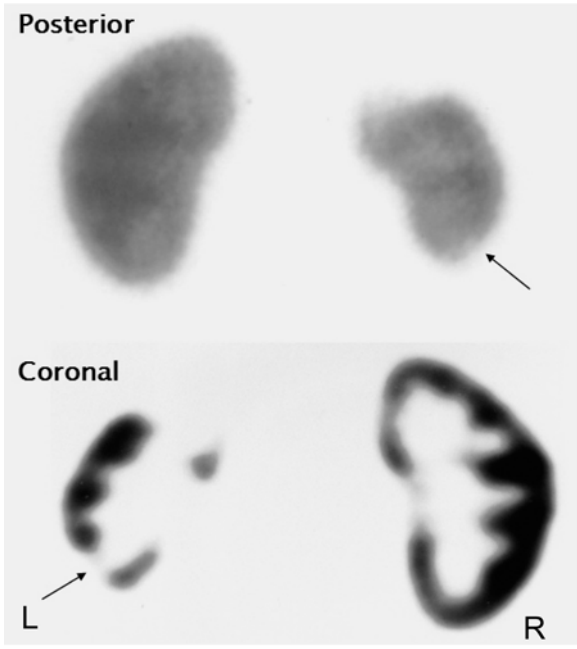

Fig. 21.6. ^{99m}Tc-DMSA study of a child with urinary tract infection. Planar images show a large defect in the left kidney upper pole and questionably in the lower pole. Representative coronal cuts of the SPECT study show clearly the defect in the lower pole

nosis and follow-up of kidneys with UTI [22]. Screening of children with acute UTI by ultrasonography and IVU is inadequate and renal scanning with ^{99m}Tc-DMSA or ^{99m}Tc-GH is more sensitive for detecting the acute effects of renal infection. ^{99m}Tc-DMSA studies have a high yield even among patients with first-time UTIs [22, 23]. The acute kidney infectious lesion is often seen on the radionuclide cortical scan as a flare-shaped pattern of decreased uptake radiating from the pelvicalyceal region to the periphery, or it appears as a focal defect (see also Chapters 4 and 10). These lesions, usually located in the polar regions, may resolve completely with adequate treatment, but permanent scarring occurs if the lesions persist for 6 – 8 weeks [16, 20, 21].

In acute infection the visualization of the foci of decreased uptake is most likely due to ischemia, since vasoconstriction has been observed in rabbits with acute renal infection. Another possibility could be the alteration of the transport mechanism for the radiopharmaceutical across tubular cell membrane [20, 21]. Gallium-67 citrate may also be quite helpful in confirming the diagnosis of pyelonephritis. It is shown as increased tracer uptake at the site of infection. However, delayed images are necessary, because Ga-67 citrate is normally excreted by the kidneys up to 48 h post-injection [19, 24].

Sometimes it is difficult to distinguish between intrarenal and perirenal infections, and the renal uptake of Ga-67 citrate could also have other causes such as interstitial nephritis, vasculitis, nephrotic syndrome, and some tumors. ^{111}In-labeling of WBCs is another scintigraphic modality for the diagnosis of acute inflammatory renal disease in pediatric patients. Although it is not appropriate as an initial screening examination for renal infection because of its associated radiation dose and the difficulty of preparation, particularly in young children, it is highly sensitive for detecting acute pyelonephritis and renal abscesses [25].

The importance of ^{99m}Tc-DMSA for patients with urinary tract infections was reemphasized by recent studies. One study found that ^{99m}Tc-DMSA should be used for evaluation of the children over 5 years with acute pyelonephritis as well as below this age. The study shows a high frequency of scintigraphic changes, did not confirm the conventional opinion that the risk of renal scarring after pyelonephritis is low in children over the age of 5 years and found that a strategy based exclusively on ultrasound findings would miss about 61% of the abnormal renal lesions. These investigators recommend that all children, irrespective of age, will benefit from further investigations that might prevent or limit the development of scarring process and renal complications [22]. Another three recent studies again confirmed the high yield of ^{99m}Tc-DMSA [26 – 28]. One study also suggested that prophylactic antibiotics can be safely discontinued when children with UTI and persistent vesicoureteral reflux meet certain conditions. This applies to children who are free of UTI for 2 years while on prophylactic antibiotics, have no hydronephrosis, have normal voiding patterns and no new kidney scars as determined by ^{99m}Tc-DMSA [26]. These emphasize the fact that DMSA is very useful for initial evaluation and follow-up of children with UTI.

21.4 Vesicoureteral Reflux

21.4.1 Pathophysiology

VUR is the retrograde flow of the urine from the bladder into the ureter. Normally, urine is propelled from the kidney to the urinary bladder through the ureter in only one direction. The valvular role of the ureterovesical junction depends on the anatomical relationship between the ureter and the bladder. The ureter follows a retroperitoneal course from the kidney to the bladder. After penetrating the bladder wall, the ureter is securely anchored to it throughout its entire transmural course. There is a specific arrangement that serves to maintain a competent one-way valve at the ureterovesical junction with a mechanism that is best described as a flap valve.

VUR allows the infected urine to be repeatedly returned to the kidneys from the bladder; and the reflux

drains back into the bladder at the end of each voiding. Pyelonephritis, especially in children younger than 3 years, is often a result of combined reflux and infection. VUR occurs more frequently in girls by a ratio of 10:1 and the incidence is approximately 1 in 1000 children. Reflux may be unilateral or bilateral and is commonly classified into five grades (Table 21.2, Figs. 21.7, 21.8) [1, 11, 29].

The flap mechanism of the ureterovesical junction depends on several anatomical relationships and physiological parameters. Any condition that alters these relationships can lead to reflux. Examples include abnormal obliquity of the ureter during its intramural course, conditions that weaken the muscular support the bladder provides to the ureter, and sphincter dysynergia. VUR may be primary or secondary [30–31]. Primary reflux results from congenitally abnormal or ectopic insertion of the ureter into the bladder. Occasionally, the condition is hereditary [32]. Siblings of patients with vesicoureteral reflux (VUR) are at greater risk of having reflux than the general population, and screening in this group is accordingly widely accepted.

In a recent study, at 48 months after diagnosis, 75% of the cases of mild reflux (I–III) and 37% of severe reflux (IV–V) of prenatally detected primary VUR had resolved, indicating a relatively benign clinical course [33]. Secondary reflux is more serious and may be transient or persistent [11, 34]. It develops in association with infection, malformations of the ureterovesical junction, increased intravesical pressure, and surgery to the ureterovesical junction.

Interstitial cells of Cajal (ICCs) are pacemaker cells that create and coordinate peristaltic motility. It was recently found that refluxing ureteral endings significantly lack these pacemaker cells, implying a malfunctioning valve mechanism permitting VUR. Connexin 43 (gap junction protein) immunoreactivity was significantly decreased in all refluxing ureteral specimens, whereas it was homogeneously distributed in normal controls A substantial decrease in gap junctions in this region adversely affects intercellular signaling, aggravating coordinated peristalsis, which is essential for a competent anti-reflux mechanism [35].

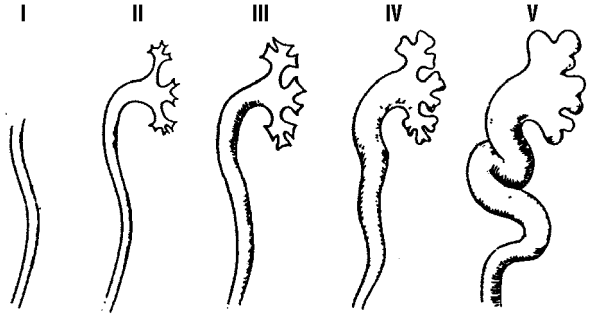

Fig. 21.7. Different grades of vesicoureteral reflux, according to the international classification. (From [30] with permission)

Table 21.2. Grading of vesicoureteral reflux

Grade	Features
I	Reflux into a nondilated ureter
II	Reflux into the upper collecting system without dilatation
III	Reflux into mildly dilated ureter and pelvicalyceal system
IV	Reflux into a grossly dilated ureter and pelvicalyceal system
V	Massive reflux with marked ureteral dilatation and tortuosity and marked dilatation of the pelvicalyceal system

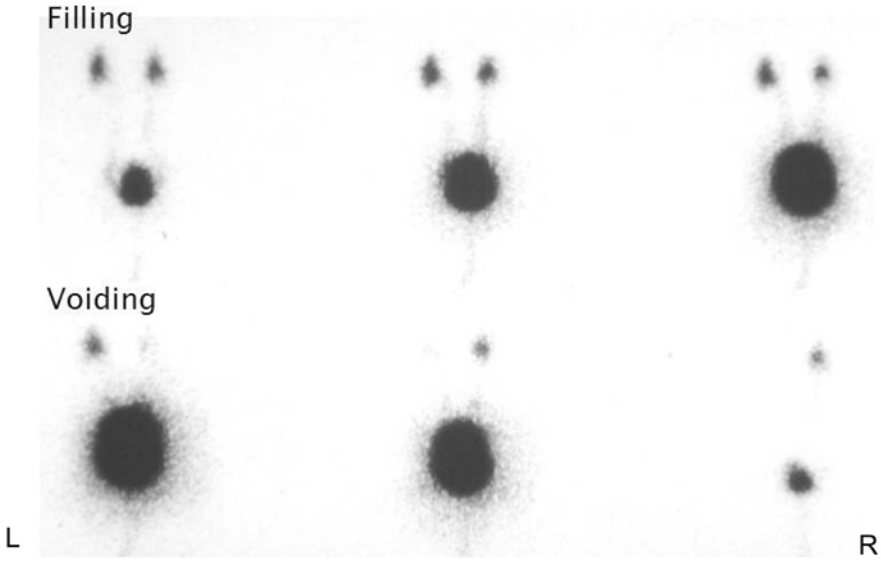

Fig. 21.8. Bilateral vesicoureteral reflux as seen on radionuclide voiding cystography corresponding to grade III

21.4.2 Scintigraphic Evaluation

Voiding radionuclide cystography is a sensitive procedure for early detection and monitoring of VUR. This modality is considered the gold standard for diagnosis of VUR. Early diagnosis of VUR with subsequent follow-up helps to prevent cortical scarring. Cystography is especially attractive because of its excellent sensitivity and low absorbed radiation dose compared with the radiographic conventional contrast enhanced micturating cystourethrogram (MCUG). It was estimated recently that its radiation exposure is less than 1/20 the radiation exposure of the MCUG [36]. The sensitivity of indirect voiding urosonography without the use of contrast-media and without filling of the bladder through a catheter for the detection of VUR in children is inadequate as its overall sensitivity is only 49% [37]. Other investigations may be needed after the definitive diagnosis of VUR to assess the function of the affected kidney. These include radionuclide renography, IVU and ultrasonography. IVU provides anatomical features in a well-functioning kidney but provides mainly qualitative information regarding function [38]. Ultrasonography may help in diagnosing obstructive uropathy, but it usually requires further evaluation by diuretic renography [11, 34].

Approximately 20% of patients with vesicoureteral reflux diagnosed before 6 months of age demonstrated dysfunctional voiding after the age of toilet training [39]. Accordingly follow-up of patients is important. The duration and methods of follow-up of VUR patients are controversial. Voiding cystography, however, may not be used in certain groups of patients for routine follow-up. For instance, follow-up of uncomplicated ureteral reimplantation in children is usually done by ultrasonography. Additionally, in this group of patients follow-up for more than 1 year postoperatively is not warranted and ultrasonography can be eliminated beyond the year [40]. Similarly ultrasonography is used for screening for siblings of patients with vesicoureteral reflux who are at higher risk than the general population. If ultrasonography is abnormal, the gold standard test of radionuclide voiding cystography is performed [41]. On the other hand, follow-up of newborns with prenatally detected VUR may require radionuclide voiding cystourethrogphy and DMSA scan. In a recent study, 58% of such infants had bilateral VUR. Severe reflux (grades IV and V) was more common and present in 54% of infants. Renal damage was detected in 34% of the kidneys on first renal scan with significant correlation between severe reflux and renal damage scars [33].

21.5 Testicular Torsion

21.5.1 Pathophysiology

Testicular torsion occurs when the spermatic cord is twisted, and it has been argued that the correct term should be spermatic cord torsion. Although a variety of factors may predispose to torsion [42], a narrow mesenteric attachment from the spermatic cord to the testis and epididymis is regarded as the dominant cause, i.e., a slender attachment occurring as a result of a narrowed testicular bare area. This bare area may reach nearly one-third of the testicular circumference, allowing the testis to fall forward within the cavity of the tunica vaginalis and to rotate like a bell-clapper, the intravaginal type of torsion [43].

Other forms of testicular torsion are recognized. In neonates, the gubernaculum is not attached to the scrotal wall and the testis is susceptible to torsion. This is termed extravaginal torsion, as the entire testis, epididymis, and tunica vaginalis twist in a vertical axis on the spermatic cord. A number of vestigial testicular appendages are susceptible to torsion. There are four testicular appendages: the paradidymis (organ of Giraldés), the appendix testis (hydatid of Morgagni), the appendix epididymis, and the vas aberrans of Haller (divided into superior and inferior components). Most consistently encountered is the appendix testis, present in 92% of autopsies and found to be multiple in 8% [43–46].

Two factors are of critical importance in testicular torsion: the extent of spermatic cord twist and the duration of the torsion. The degree of torsion can vary from 90° to three complete turns of the vascular pedicle. Not surprisingly, blood flow may be variably compromised. The initial disruption will be to the venous and lymphatic drainage, rather than to the arterial input of the testis, and venous infarction occurs earlier and at lesser levels of torsion [47].

Experimentally, complete cessation of blood flow to the testis occurs with the spermatic cord twisting 720° [48]. In other studies of the normal rabbit testis, a 450° twist consistently produced testicular infarction, whereas a 360° twist resulted in decreased flow [49].

In patients with torsion, a twist between 360° and 720° is found. Experimental studies have shown that testicular infarction begins to appear within 2 h of complete occlusion of the testicular artery [49]; irreversible ischemia occurs after 6 h [50–52], and complete infarction is established by 24 h.

With complete vascular occlusion, the testis appears grossly swollen and hemorrhagic. Microscopically, the picture is that of hemorrhagic infarction. The degree of necrosis depends upon the duration of occlusion. If this has been longer than 10 h, the necrosis of the seminifer-

ous epithelium is usually complete and irreversible. With incomplete occlusion, necrosis may be delayed. Torsion that lasts less than 6 h probably will not cause a testicular infarct. If torsion lasts longer than 24 h, the testis almost certainly will infarct [53, 54]. Although exceedingly rare, testicular torsion can be asynchrously bilateral [55].

Since epididymitis is the most common cause of acute testicular pain to be differentiated from torsion, its pathophysiology is discussed. The condition may be acute (symptoms last less than 6 weeks) or chronic (more than 3 months). Acute epididymitis is almost always unilateral. Acute epididymitis in children or following urinary tract instrumentation is commonly caused by gram-negative bacilli. The epididymis is sometimes the site of metastatic infection, such as tuberculosis.

21.5.2 Diagnosis

Testicular torsion results in acute pain and ischemia. The most common signs and symptoms include a red, swollen scrotum and acutely painful testicle, often in the absence of trauma. Nausea and vomiting are common. The most common conditions in the differential diagnosis include epididymitis, strangulated inguinal hernia, traumatic hematoma, testicular tumor, or testicular fracture. Physical examination techniques such as scrotal elevation can be helpful in differentiating between epididymitis and testicular torsion. However, clinical examination of the scrotum is difficult due to the small size of the testes and the epididymis in infants and young children, and eliciting patients' history is challenging. Epipidymitis has been considered uncommon in childhood but its frequency has been increasing among children admitted with the diagnosis of acute scrotum [56]. Long-term prognosis for a functional, nonatrophied testicle is improved the sooner the torsion is diagnosed and treated. Therefore confirming the diagnosis and quick management is crucial. Accordingly imaging of the scrotum in children suspected of having the condition bears great importance [57].

21.5.3 Scrotal Imaging

The classification of scrotal disorders in children into three typical clinical manifestations, namely acute scrotal disorders, scrotal masses, and cryptorchidism – is a helpful and practical basis for choosing the most suitable imaging modality among the commonly available and commonly used modalities. These include sonography, scintigraphy, and magnetic resonance imaging. Acute scrotal pediatric disorders include acute epididymitis, torsion of an appendix testis or appendix epididymis, and torsion of the spermatic cord. Either scintigraphy or sonography may be used as the first imaging study, and both can aid in distinguishing among the disorders to different degrees. Although sonography provides superior anatomic details to scintigraphy, it may not be as accurate as it is thought for the diagnosis of the most serious emergency reason for scrotal pain [58, 59]. Scrotal masses are also best depicted with sonography with MRI as an adjunctive modality. In cases of suspected cryptorchidism with equivocal clinical findings, both sonography and MRI are useful but sonography is usually the initial study [60].

This strategy for imaging for acute scrotal disorders most relevant to nuclear medicine is not uniform and varies between the institutions based on the experience. In most institutions, Doppler ultrasound is used most commonly as the standard imaging technique of choice to confirm the diagnosis in most cases. Scintigraphy is used when color Doppler is inadequate, raising doubts about the suspected torsion. Radionuclide testicular scintigraphy is used also more commonly after the acute phase of the first 12 h and vascular compromise has prolonged [57]. Recent studies, however, comparing both modalities indicate that scintigraphy is more accurate for the diagnosis of testicular torsion [58, 59, 61–63].

A recent study performed on 41 boys with suspected testicular torsion compared scintigraphy and Doppler ultrasound. There was no statistically significant difference in the sensitivity between modalities. Specificity was 77% for color Doppler US and 97% for scintigraphy ($P=0.05$). Due to the higher specificity, scintigraphy can help avoid unnecessary surgery when color Doppler US shows equivocal flow [62]. In another study, 20 patients with possible acute testicular torsion were studied by ultrasonography followed by scintigraphy within 3 h of ultrasound study. All patients with clinically suspected acute testicular torsion underwent surgery. The surgical findings, pathologic reports of these patients and clinical follow-up data were reviewed and definite diagnoses were established for all patients. Four patients with testicular torsion, 13 patients with inflammatory testicular disease, and three healthy persons had a final surgical and pathologic diagnosis or clinical follow-up, and all were accurately diagnosed by ^{99m}Tc-pertechnetate radionuclide imaging. In contrast, ultrasonography was less accurate in the diagnosis and differentiation of acute testicular torsion from inflammation. Only 1 of 4 patients with testicular torsion, 5 of 13 patients with inflammatory testicular disease, and 2 of 3 healthy persons were diagnosed by ultrasonography. The study indicates again that scintigraphy is a more accurate imaging method than Doppler ultrasonography [63]. Furthermore in conditions of testicular

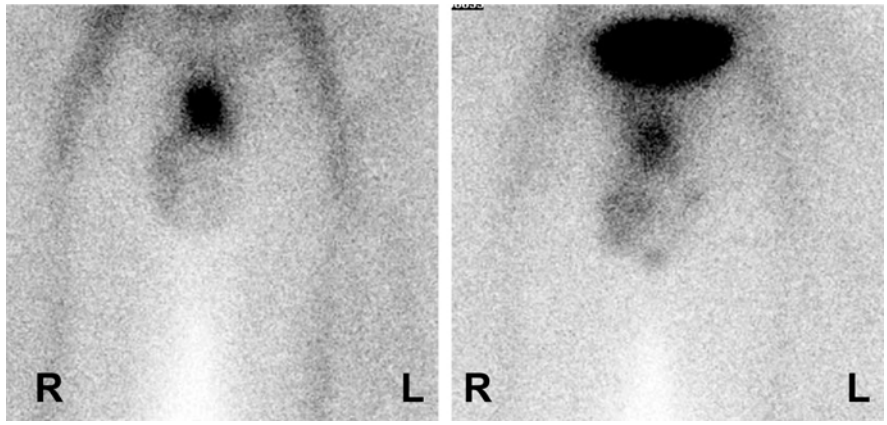

Fig. 21.9a,b. ^{99m}Tc-pertechnetate scrotal scan of a patient with acute scrotal pain in the left side. The study (**a**) shows essentially absent activity in the region of the left hemiscrotum corresponding to the left testicle by palpation markers (**b**). This case illustrates a pattern of acute testicular torsion

torsion and epididymo-orchitis, the most common differential diagnosis of testicular torsion, ultrasound findings can be inconclusive and further evaluation is required [58, 59]. A study of 49 patients with acute scrotal pain compared radionuclide scrotal scintigraphy and ultrasonography. Of 37 patients with decreased radioactivity in the abnormal side scrotum, 35 were diagnosed with testicular torsion surgically and the other 2 were diagnosed with indirect inguinal hernia. Only 17 of the 35 patients were diagnosed by ultrasonography as having testicular torsion. The remaining 12 patients with increased radioactivity in the abnormal side of the scrotum were all diagnosed with orchiepididymitis through conservative treatment and clinical follow-up, but only 8 of the 12 were correctly and exactly diagnosed by ultrasonography. In the process of diagnosing acute scrotal pain, radionuclide scrotum scintigraphy has the obvious advantage over ultrasonography. It also has the advantage of being simple, fast and accurate but without any detrimental effect on the human body [61].

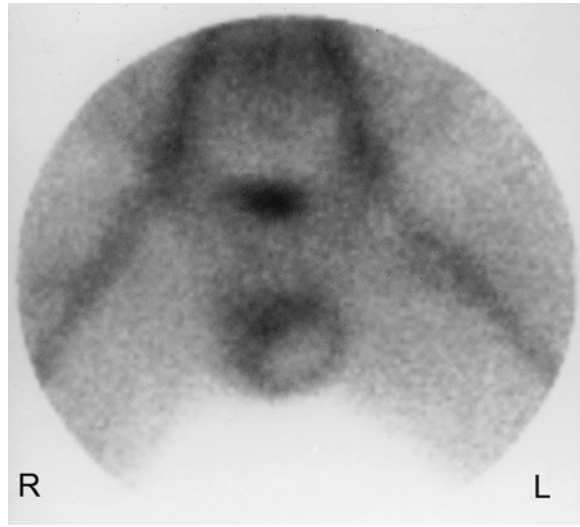

Fig. 21.10. ^{99m}Tc-pertechnetate testicular imaging study showing the rim of increased uptake around the area of decreased uptake, illustrating the classic pattern of missed torsion of the left testis

21.5.4 Scintigraphic Evaluation

The study is performed using 10–20 mCi (370–740 MBq) of ^{99m}Tc-pertechnetate injected intravenously as a bolus in adults. In children a dose of 300 μCi (11.1 MBq)/kg, with a minimal dose of 3 mCi (111 MBq), is recommended [64].

The study is acquired in two phases, the flow phase consisting of 1-s frames for 60 s and the blood pool phase acquired statically for 5 min/image at 5, 10, and 15 min. This may be followed by pinhole images in children, making a total of 30 min for the whole study [65]. Marker images for the testicles must be obtained as well in all studies. The patient's position is supine; the penis is strapped up to the abdomen, and the scrotal sac is elevated. The camera is placed over the anterior pelvis and a low-energy high-resolution collimator is used, with or without a pinhole collimator, as mentioned earlier.

Findings on a normal scan are symmetrical perfusion with little uptake in the blood pool images. In acute torsion (early) there will be decreased perfusion on flow images and the blood pool images will show no activity in the affected side (Fig. 21.9).

In missed torsion (late) there will be a halo of activity surrounding the torsion (a doughnut shape) due to increased perfusion to the surrounding tissue through the pudendal vessels (Fig. 21.10). Figure 21.11 demonstrates a different pattern caused by inguinal hernia. In acute epididymitis there will be increased perfusion and hyperemia in the affected side (Fig. 21.12) due to vascular changes associated with the inflammation [64].

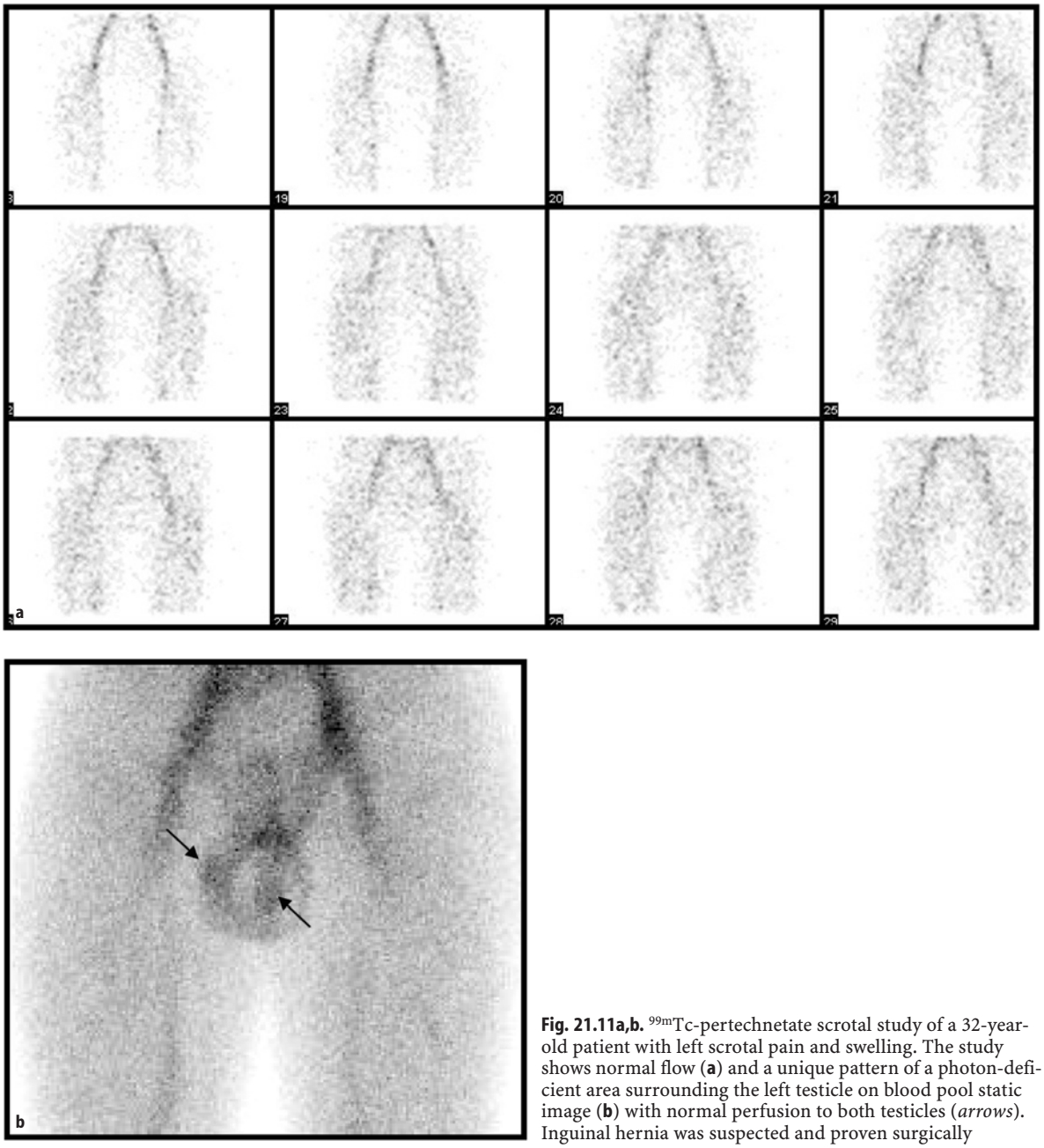

Fig. 21.11a,b. ^{99m}Tc-pertechnetate scrotal study of a 32-year-old patient with left scrotal pain and swelling. The study shows normal flow (**a**) and a unique pattern of a photon-deficient area surrounding the left testicle on blood pool static image (**b**) with normal perfusion to both testicles (*arrows*). Inguinal hernia was suspected and proven surgically

References

1. Gilman CM, Mooney KH (1998) Alteration of renal and urinary tract function in children. In: McCance KL, Huether SE (eds) Pathophysiology, 3rd edn. Mosby, Philadelphia, pp 1237 – 1287
2. Heyman S (1994) Radionuclide studies of the genitourinary tract. In: Miller J, Gelfand M (eds) Pediatric nuclear imaging. Saunders, Philadelphia, pp 195 – 211
3. Reich BS, Bender TM (1988) Radiographic evaluation of children with urinary tract infections. Radiol Clin North Am 26:303 – 407
4. Wiswell TE, Smith FR, Bass TW (1985) Decreased incidence of urinary tract infections in circumcised male infants. Pediatrics 75:901
5. Jahnukainen T, Chen M, Celsi G (2005) Mechanisms of renal damage owing to infection. Pediatr Nephrol 20:1043 – 1053
6. Solari V, Owen D, Puri P (2005) Association of transforming growth factor-beta1 gene polymorphism with reflux nephropathy. J Urol 174:1609 – 1611
7. Kanematsu A, Yamamoto S, Yoshino K, Ishitoya S, Terai A, Sugita Y, Ogawa O, Tanikaze S (2005) Renal scarring is associated with nonsecretion of blood type antigen in children with primary vesicoureteral reflux. J Urol 174:1594 – 1597

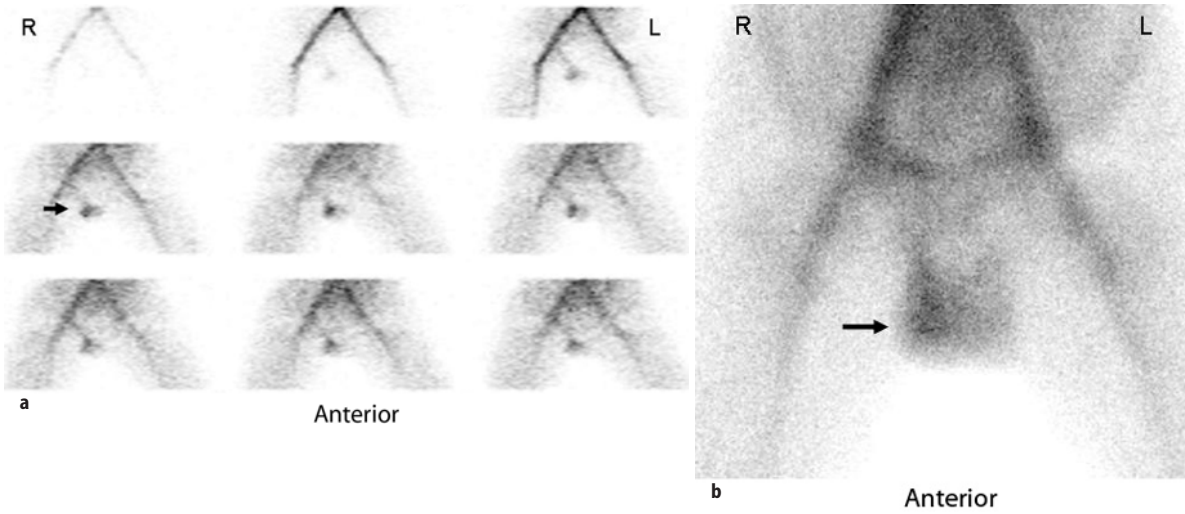

Fig. 21.12. A 14-year-old male referred for testicular scan to rule-out testicular torsion. The patient presented with 4 hour-history of right-sided acute testicular pain and swelling. The pain was dull in nature, with no radiation, and was associated with nausea and vomiting. There was no history of fever, or any urinary symptoms. The patient denied any history of trauma. On examination: Temperature was 37.4 °C. Left testis was grossly normal, and the right testis was tender and swollen. Lab investigations showed leucocytosis at 14,400. Testicular scan was performed, using 17-mCi Tc-99m Pertechnetate given as a bolus intravenous injection. The scan shows increased flow (**a**) and blood pool (**b**) activity in the right hemiscrotum (*arrows*) in comparison to the left testis indicating an inflammatory process in the right hemiscrotum consistent with right epididymitis

8. Rachmiel M, Aladjem M, Starinsky R, Strauss S, Villa Y, Goldman M (2005) Symptomatic urinary tract infections following voiding cystourethrography. Pediatr Nephrol 20:1449 – 1452
9. Johnson DE, Russel RG, Lockatell CV, et al (1993) Urethral obstruction of 6 hours or less causes bacteruria, bacteremia and pyelonephritis in mice challenged with "non-pathogenic" *Escherichia coli*. Infect Immunol 61:3422
10. Fowler JE Jr, Stamey TA (1977) Studies of introital colonization in women with recurrent urinary tract infection: the role of bacterial adherence. J Urol 117:472
11. Kaefer M, Diamond D (1987) Vesicoureteral reflux. In: Retik A, Cukier J (eds) Pediatric urology. Williams and Wilkins, Baltimore, pp 463 – 486
12. Behrman R, Kliegman R, Arvin AM (eds) (1996) Nelson textbook of pediatrics, 15th edn. Saunders, Philadelphia
13. Strok JE (1987) Urinary tract infection in children. Adv Pediatr Infect Dis 2:115 – 134
14. Dacher JN, Hitzel A, Avni FE, Vera P (2005) Imaging strategies in pediatric urinary tract infection. Eur Radiol 15:1283 – 1288
15. Gelfand MJ, Koch BL, Elgazzar AH, et al (1999) Cyclic cystography: diagnostic yield in selected pediatric populations. Radiology 213:118 – 120
16. Sty JR, Wells RG, Starshak RJ, Schroeder BA (1987) Imaging in acute renal infection in children. AJR 148:471 – 477
17. Traisman ES, ConwayJJ, Traisman HS, et al (1986) The localization of urinary tract infection with ^{99m}Tc-glucoheptonate scintigraphy. Pediatr Radiol 16:403 – 406
18. Stoller MI, Kogan BA (1986) Sensitivity of 99m-technetium dimercaptosuccinic acid for the diagnosis of chronic pyelonephritis: clinical and theoretical considerations. J Urol 135:977 – 980
19. Handmaker H (1982) Nuclear renal imaging in acute pyelonephritis. Semin Nucl Med 12:246 – 253
20. Thelle T, Biskjaar N (1985) Combined ^{99m}Tc-DMSA kidney scintigraphy and ^{131}I hippuran renography in children with urinary tract infections. Acta Pediatr Scand 74:720 – 725
21. Gordon I (1986) Indications for 99m-technetium dimercaptosuccinic acid scan in children. J Urol 137:464 – 467
22. Ataei N, Madani A, Habibi R, Khorasani M (2005) Evaluation of acute pyelonephritis with DMSA scans in children presenting after the age of 5 years. Pediatr Nephrol 20: 1439 – 1444
23. Loutfi I, Al-Zaabi, ElgazzarAH (1999) Tc-99m DMSA renal scan in first time versus recurrent urinary tract infection yield and patterns of abnormalities. Clin Mucl Med 24:931 – 935
24. Long SE, Sonnemaker RE, Burdine JA (1984) Renal accumulation of gallium-67 citrate. Semin Nucl Med 14:52 – 54
25. Fawcett HD, Goodwin DA, Lantieri RI (1981) In-111 leukocyte scanning in inflammatory renal disease. Clin Nucl Med 6:237 – 241
26. Georgaki-Angelaki H, Kostaridou S, Daikos GL, Kapoyiannis A, Veletzas Z, Michos AG, Syriopoulou VP (2005) Long-term follow-up of children with vesicoureteral reflux with and without antibiotic prophylaxis. Scand J Infect Dis 37:842 – 845
27. Ajdinovic B, Krstic Z, Dopuda M, Jaukovic L (2005) Renal scintigraphy in children with urinary tract. Vojnosanit Pregl 62:745 – 749
28. Zaki M, Badawi M, Al Mutari G, Ramadan D, Adul Rahman M (2005) Acute pyelonephritis and renal scarring in Kuwaiti children: a follow-up study using 99mTc DMSA renal scintigraphy. Pediatr Nephrol 2005 20:1116 – 1119
29. International Reflux Study Committee (1981) Medical versus surgical treatment of primary vesicoureteral reflux: A prospective international reflux study in children. J Urol 125:277 – 283
30. Silva JM, Santos Diniz JS, Marino VS, Lima EM, Cardoso LS, Vasconcelos MA, Oliveira EA. (2006) Clinical course of 735 children and adolescents with primary vesicoureteral reflux. Pediatr Nephrolo 21:981 – 988

31. Dacher JN, Hitzel A, Avni FE, Vera P (2005) Imaging strategies in pediatric urinary tract infection. Eur Radiol 15:1283 – 1288
32. Rodriguez MM (2004) Developmental renal pathology: its past, present, and future. Fetal Pediatr Pathol 23:211 – 229
33. Penido Silva JM, Oliveira EA, Diniz JS, Bouzada MC, Vergara RM, Souza BC (2005) Clinical course of prenatally detected primary vesicoureteral reflux. Pediatr Nephrol 86 – 91
34. Walker RD (1994) Vesicoureteral reflux update: effect of prospective studies on current management. Urology 32:279
35. Schwentner C, Oswald J, Lunacek A, Fritsch H, Deibl M, Bartsch G, Radmayr C (2005) Loss of interstitial cells of Cajal and gap junction protein connexin 43 at the vesicoureteral junction in children with vesicoureteral reflux. J Urol 174:1981 – 1986
36. Schlussel R (2005) Imaging studies after a first febrile urinary tract infection in young children. Curr Urol Rep 6:131 – 132
37. Kopac M, Kenig A, Kljucevsek D, Kenda RB (2005) Indirect voiding urosonography for detecting vesicoureteral reflux in children. Pediatr Nephrol 20:1285 – 1287
38. Verrier Jones K (2005) Time to review the value of imaging after urinary tract infection in infants. Arch Dis Child 90:663 – 664
39. Homayoon K, Chen JJ, Cummings JM, Steinhardt GF (2005) Voiding dysfunction: outcome in infants with congenital vesicoureteral reflux. Urology 66:1091 – 1094
40. Charbonneau SG, Tackett LD, Gray EH, Caesar RE, Caldamone AA (2005) Is long-term sonographic follow up necessary after uncomplicated ureteral reimplantation in children? J Urol 174:1429 – 1431
41. Giel DW, Noe HN, Williams MA (2005) Ultrasound screening of asymptomatic siblings of children with vesicoureteral reflux: a long-term followup study. J Urol 174:1602 – 1604
42. Scorer CG, Farrington GH (1971) Congenital deformities of testis and epididymis,1st edn. Butterworth, London
43. Corriere JN (1972) Horizontal lie of the testicle: a diagnostic sign and torsion of the testis. J Urol 107:616 – 617
44. Blackhouse KM (1982) Embryology of testicular descent and maldescent. Urol Clin North Am 9:315
45. Skoglund RW, McRoberts JW, Ragde H (1970) Torsion of testicular appendages: presentation of 43 new cases and collective review. J Urol 104:598 – 600
46. Rolinck D, Kawanove S, Szanto P (1968) Anatomical incidence of testicular appendages. J Urol 100:755 – 756
47. Rencken RK, Duplessis DJ, De Haas LS (1990) Venous infarction of the testes – a cause of non-response to conservative therapy in epididymo-orchitis: a case report. S Afr Med J 78:337 – 338
48. Kogan SJ (1991) Acute and chronic scrotal swellings. In: Gillenwalter JY (ed) Adult and pediatric urology, 2nd edn. Mosby Year Book, Chicago
49. Frush DP, Babcock DS, Lewis AG, et al (1995) Comparison of color Doppler sonography and radionuclide imaging in the evaluation of torsion of the testes in the rabbit. Acad Radiol 2:945 – 951
50. Luker GD, Siegel MJ (1994) Color Doppler sonography of the scrotum in children. Am J Roentgenol 163:649 – 655
51. Herbener TE (1996) Ultrasound in the assessment of the acute scrotum. J Clin Ultrasound 24:405 – 421
52. Patriquin HB, Yazbeck S, Trinh B, et al (1993) Testicular torsion in infants and children: diagnosis with Doppler sonography. Radiology 188:781 – 785
53. Muschat M (1932) The pathological anatomy of testicular torsion: explanation of its mechanism. Surg Gynaecol Obstet 54:758 – 763
54. Allan WR, Brown RB (1966) Torsion of the testes: a review of 58 cases. Br Med J 1:1396 – 1397
55. Olguner M, Akgur FM, Aktug T, Derebek E (2000) Bilateral asynchronous perinatal testicular torsion: a case report. J Pediatr Surg 35:1348 – 1349
56. Klin B, Zlotkevich L, Horne T, Efrati Y, Serour F, Lotan G (2002) Epididymitis in childhood: a clinical retrospective study over 5 years. Isr Med Assoc J 3:833 – 835
57. Lavallee ME, Cash J (2005) Testicular torsion: evaluation and management. Curr Sports Med Rep 4:102 – 104
58. Hormann M, Balassy C, Philipp MO, Pumberger W (2004) Imaging of the scrotum in children. Eur Radiol 14:974 – 983
59. Stav K, Zisman A, Leibovici D, Sandbank J, Lindner A (2003) Acute epididymitis. Harefuah 142:451 – 455
60. Frush DP, Sheldon CA (1998) Diagnostic imaging for pediatric scrotal disorders. Radiographics 18:969 – 985
61. Yuan Z, Luo Q, Chen L, Zhu J, Zhu R (2002) Clinical study of scrotum scintigraphy in 49 patients with acute scrotal pain: a comparison with ultrasonography. Ann Nucl Med 15:225 – 229
62. Paltiel HJ, Connolly LP, Atala A, Paltiel AD, Zurakowski D, Treves ST (1998) Acute scrotal symptoms in boys with an indeterminate clinical presentation: comparison of color Doppler sonography and scintigraphy. Radiology 207: 223 – 231
63. Wu HC, Sun SS, Kao A, Chuang FJ, Lin CC, Lee CC (2002) Comparison of radionuclide imaging and ultrasonography in the differentiation of acute testicular torsion and inflammatory testicular disease. Clin Nucl Med 27:490 – 493
64. Saha GB (2005) Fundamentals of nuclear pharmacy, 5th edn. Springer, Berlin
65. Mettler FA, Guiberteau MJ (2005) Essentials of nuclear medicine imaging, 5th edn. Saunders

Basis of Therapeutic Nuclear Medicine

22

Abdelhamid H. Elgazzar, Abdullatif Al-Bader

22.1 Introduction

Therapeutic applications of nuclear medicine are expanding (Table 22.1). Until recently, the use of radioisotopes in therapy was limited predominantly to treatment of hyperthyroidism, thyroid cancer, and polycythemia rubra vera. Strontium-89 (^{89}Sr), rhenium-186 (^{186}Re), samarium-153 (^{153}Sm), and tin-117m (^{117}Sn) are now increasingly used in treating bone pain secondary to metastases. Additionally, treatment of certain neuroendocrine tumors with ^{131}I-MIBG and labeled octreotide and pentreotide, the use of radiolabeled monoclonal antibodies for lymphomas, and radionuclide synovectomy have revolutionized the field of therapeutic nuclear medicine.

It is not the objective of this chapter to discuss different protocols and experiences in the treatment of various conditions using radioisotopes. Rather, the objective is to explore some of the pathological features of the disease processes being treated, and the underlying theory behind the action of the radioisotopes that induce therapeutic effects.

Table 22.1. Therapeutic applications of nuclear medicine

Oncologic
1. Lymphomas and leukemias 2. Polycythemia rubra vera 3. Solid tumors (thyroid carcinoma, neuroblastoma, ovarian, prostate, breast, osteogenic sarcoma, others) 4. Treatment of metastasis-induced bone pain
Non-oncologic
1. Benign thyroid disease particularly hyperthyroidism 2. Radionuclide synovectomy 3. Bone marrow ablation 4. Intravascular radionuclide therapy for prevention of restenosis

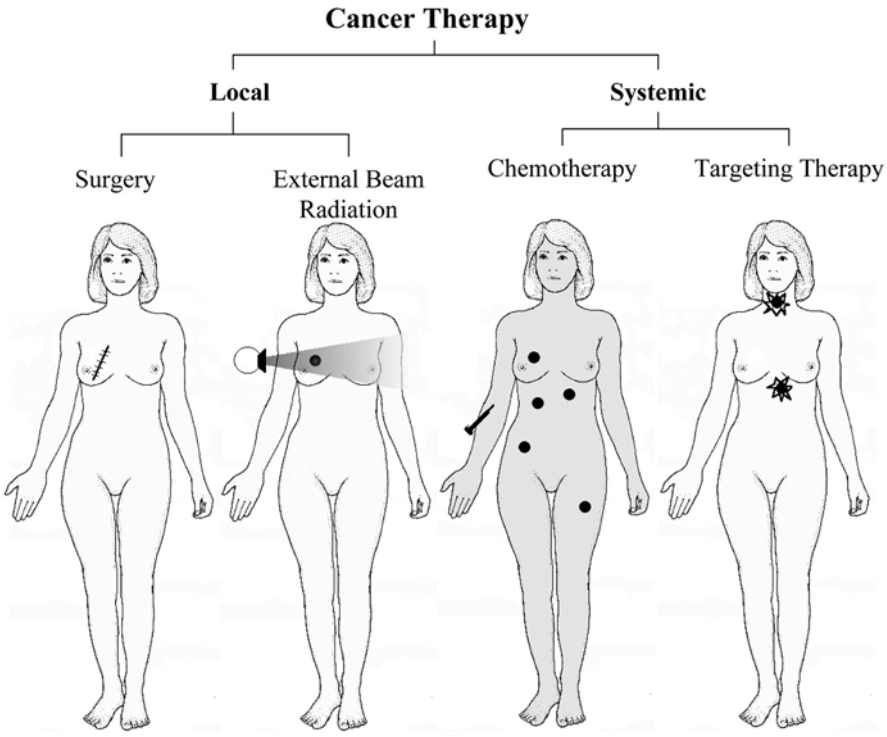

Fig. 22.1. The major types of cancer therapy. Nuclear medicine uses principally the targeting method in treating cancer and cancer metastases. (Modified from [66])

Regarding cancer therapy, treatment options may be local (surgery or external beam radiation) or systemic. The role of nuclear medicine focuses on a targeted systemic approach (Fig. 22.1), whether dealing with a primary tumor or with its metastatic foci.

22.2 Treatment of Hyperthyroidism

For more than 60 years, iodine-131 has been used to treat most cases of Graves' disease and hyperfunctioning nodules. It has become the modality of choice in treating Graves' disease, with the result that surgeons are becoming less and less experienced in thyroidectomy since the number of operations has decreased significantly. In a recent Canadian survey study, endocrinologists were found to be the specialists most commonly prescribing iodine-131 for malignant disease, while nuclear medicine physicians were most commonly prescribing it for benign disease [1].

The normal thyroid gland varies in shape between individuals, and its average weight is approximately 20 g. The gland utilizes iodine for the synthesis of thyroid hormones (see Chapter 7). The cells of the gland do not differentiate between stable iodine and radioactive iodine. Accordingly, if radioactive iodine is administered, it is trapped and then organified by the thyroid follicular cells exactly like the nonradioactive iodine.

22.2.1 Pathophysiology

After oral administration, ^{131}I-iodide is absorbed rapidly from the upper gastrointestinal tract, 90% within 60 min. After entering the blood stream, the iodide is distributed in the extrathyroid compartment similar to the stable iodide and leaves this compartment to be taken up by the thyroid and by renal excretion. Approximately 20% of the administered activity is taken up normally by the thyroid gland. A small amount of iodine-131 is also found in the salivary glands, gastric mucosa, choroid plexus, breast milk, and placenta. Up to 75% is excreted by the kidney and 10% by fecal excretion. Approximately 40% of the administered activity has an effective half-life of 0.43 days while 60% has an effective half-life of 7.6 days.

Graves' disease is the most common form of hyperthyroidism, comprising approximately 56% of all cases. It is also the major immunologically mediated form. It occurs most commonly in young women and is characterized by symptoms of hyperthyroidism with or without ophthalmopathy and dermopathy. Rarely, lymphadenopathy and splenomegaly may be present. The thyroid gland is usually diffusely enlarged but sometimes normal in size. The condition is an autoimmune process with autoantibodies directed against the TSH receptors on thyroid follicular cells which may be stimulatory and/or destructive [2]. Thyroid stimulatory an-

tibodies include long-acting thyroid stimulator (LATS). This antibody is detected in most patients with Graves' disease and behaves like TSH, stimulating the production of thyroid hormones and consequently trapping and organifying radioiodine. The other stimulatory antibody is the LATS protector, the antibody that prevents degradation of LATS; accordingly, it helps to stimulate thyroid cells indirectly. The disease is associated with other autoimmune disorders such as pernicious anemia and myasthenia gravis.

Graves' disease is also known to be associated in Caucasians with HLA B8, DR2, and DR3 and with an inability to secrete certain glycoproteins coded for chromosomes 6 and 19. A 50% concordance rate is seen among monozygous twins while 5% concordance is noted in dizygous twins. These facts suggest a genetic susceptibility for the disease. The observation that *Yersinia enterocolitica* and *Escherichia coli* and other gram-negative organisms contain TSH binding sites raised the possibility that the initiating event in the pathogenesis of the disease may be infectious in genetically susceptible individuals.

Histologically, there is hyperplasia of the thyroid epithelium, sometimes with papillary unfolding. Lymphocytic infiltration is present, usually less than in other forms of autoimmune diseases as postpartum thyroiditis. Little colloid storage is also seen. With time, the untreated gland will show progressive fibrosis and the end stage will lead to hypothyroidism, which may be considered part of the natural history of the disease [3, 4].

Thyroid scintigraphy shows uniform uptake throughout the gland or, less commonly, varying degrees of nonuniform uptake. This nonuniformity is related predominantly to different stages of involution of the disease with variable amounts of fibrosis based on the duration of the disease or the presence of nodules (Fig. 22.2). The presence of a TSH dependent functioning nodule in a diffusely toxic gland has been referred to as Marine-Lenhart's syndrome (Fig. 22.2). Since the function of such nodules is much less than the sur-

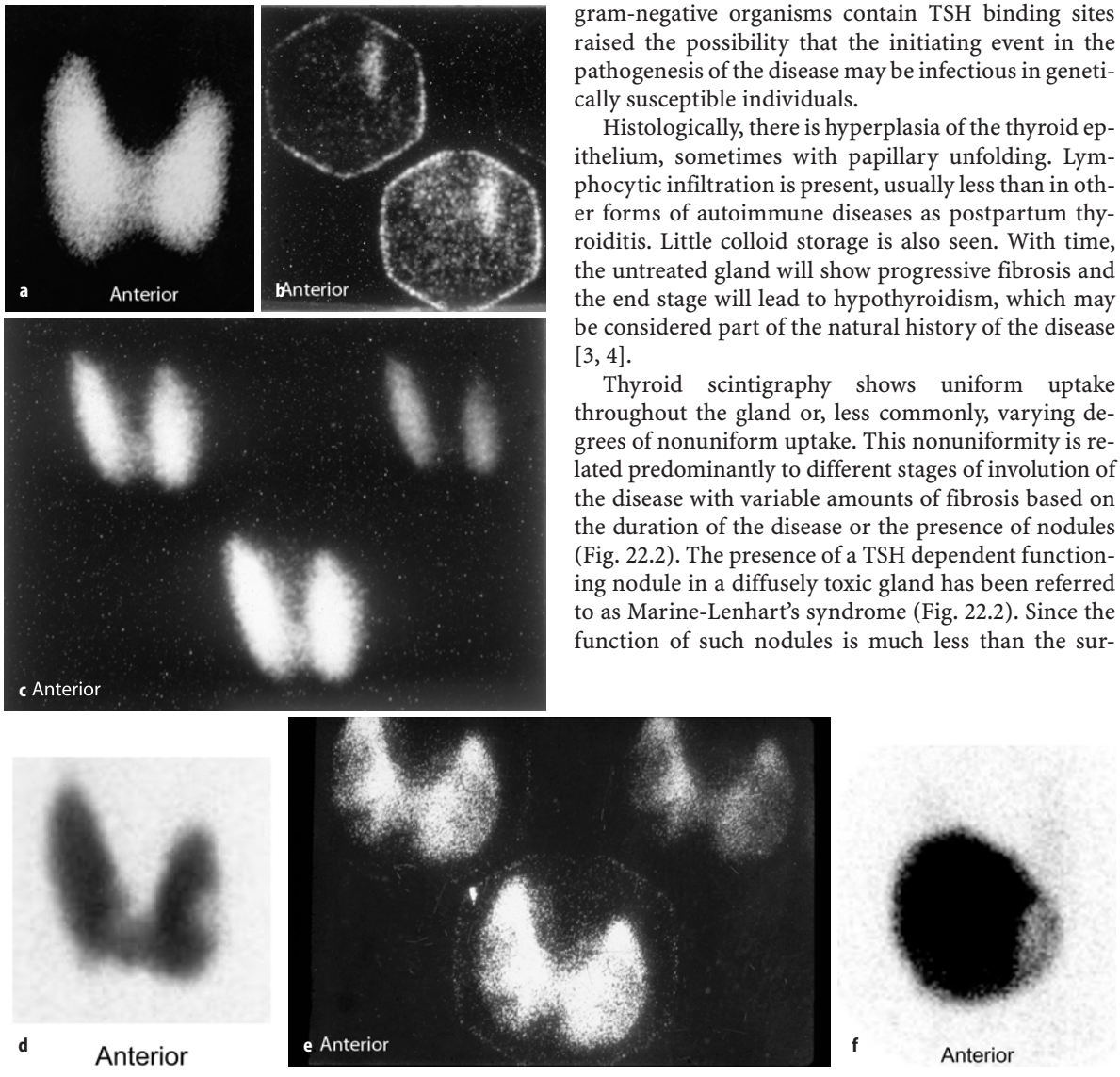

Fig. 22.2a–f. Examples of thyroid scans of patients with hyperthyroidism illustrating patterns that affect the treatment strategy using iodine-131. **a** illustrates pattern of uniform uptake in a patient with Graves' disease. Note that scans of patients during recovery phase of thyroiditis may simulate Graves' disease scintigraphically and show high uptake. Example **b** is of a patient with subacute thyroiditis. Scan shows decreased and non-uniform uptake with a 24-h uptake of 1%. Follow-up scan (**c**) shows uniform uptake throughout the gland with an uptake of 38%. This may be mistaken for Graves' disease if the patient is referred first during this phase. Example **d** shows diffusely toxic gland with significant non-uniformity and multiple cold nodules. Example **e** shows a scan of a patient with Graves' disease and a colloid nodule illustrating another pattern of "Marine-Lenhart" syndrome which is more resistant to iodine-131 therapy. Compare this pattern to that of multiple toxic nodules (Chapter 7, Fig. 7.2). This pattern also needs to increase activity per gram of tissue for successful treatment. Example **f** is for autonomous single toxic adenoma which is treated by relatively high activity

rounding hyperfunctioning tissue, it appears scintigraphically cold.

Ophthalmopathy occurs in approximately 50% of patients with Graves' disease [5]. Infiltration of extraocular muscles by an inflammatory reaction consisting predominantly of lymphocytes is the main pathological feature of ophthalmopathy. These lymphocytes are believed to be sensitized to antigens common to the orbital muscles and thyroid gland. Similar inflammatory infiltrates may also be present in the dermis, causing the dermopathy or pretibial myxedema which may be present in up to 10% of patients with unclear etiology.

Single thyroid nodules can, via an autonomous function, secrete sufficient thyroid hormone to cause hyperthyroidism. These nodules are usually greater than 3 cm in diameter in order to be capable of producing this level of function [6]. Hyperfunction may also arise in a gland containing multiple nodules [7]. In this case the secretion of thyroid hormones can be either from hyperfunctioning nodules that are assumed to be autonomous or from the internodule parenchyma, which may be an expression of Graves' disease in an otherwise nodular goiter. The nodules in the latter situation may be cold or a mixture of cold and hot, hypertrophic nodules. The term Plummer's disease, or toxic nodular goiter, has been used to designate hyperthyroidism in glands with both single and multiple toxic nodules. The term nodular toxic goiter may be reserved for a toxic gland that contains nodules that are not hyperactive. The presence of cancer in toxic nodular goiter is extremely rare and varies from 0.1% to 0.9%. The toxic nodular goiter may have a cold nodule representing a TSH-dependent adenoma. Scintigraphic imaging cannot exclude malignancy in the cold nodule that is not TSH dependent.

The therapeutic effects of ^{131}I-sodium iodide are due to the emission of ionizing radiation from the decaying radionuclide. In benign conditions such as Graves' disease, division of some metabolically active cells is prevented by the effect of this ionizing radiation. Cell death is another mechanism activated when the cells are exposed to high levels of radiation, particularly when high doses are given to patients with toxic adenoma, where the suppressed normal thyroid tissue is essentially spared with delivery of a very high concentration to the cells of the toxic nodule. Cell death is followed by replacement with connective tissue, which may lead to hypothyroidism, depending on the number of cells destroyed, and be replaced by fibrous nonfunctioning tissue. Since 90% of the radiation effects of iodine-131 are due to beta radiation, which has a short range in tissue of 0.5 mm, the extrathyroid radiation, and consequently the side effects, are minimal. It has been estimated that 15% of patients treated with iodine-131 may show worsening of ophthalmopathy [8, 9]. Since post-treatment hypothyroidism has been associated with exacerbation of ophthalmopathy, lower dose radioactive iodine or starting replacement hormones early (2 weeks) after therapy along with the use of prednisone 40 – 80 mg/day tapered over up to 3 months may prevent severe eye disease in up to two-thirds of patients [10 ,11]. It is interesting that cigarette smoking has been also implicated as a risk factor for progression of Graves' ophthalmopathy [12].

22.2.2 Factors Affecting the Dose of Iodine-131 Used for Therapy

Several factors affect the therapeutic dose to be administered to patients suffering from hyperthyroidism. These include some parameters related to the patient, such as age, sex, medical history, and duration of treatment with anti-thyroid medications, and factors related to the gland itself, particularly its size, the level of radioiodine uptake, scintigraphic findings of uniform or nonuniform uptake, and whether nodules are present. Additionally, the dose is dependent on how the therapist defines the goals of therapy. If the control of thyrotoxicosis is the most important consideration, the total dose or the dose per gram of estimated thyroid tissue weight will be higher than when the therapist is trying to avoid or delay hypothyroidism [13]. Using empirical low dose iodine therapy to avoid hypothyroidism has been shown to result in persisting hyperthyroidism in up to 54% of patients [14]. Additionally it has been found that the rate of hypothyroidism is not different among those treated with low dose and high dose radioiodine [15, 16].

22.3 Treatment of Differentiated Thyroid Cancer

Radioactive iodine is the mainstay of therapy for residual, recurrent, and metastatic thyroid cancer that takes up iodine and cannot be resected. The tissue of normal thyroid and its tumors expresses a variety of oncogenes, growth factors, and growth-factor receptors. There is increased expression of some oncogenes, namely c-*myc*/c-*fos* and c-*ras*, in some epithelial and medullary thyroid carcinomas.

C-*myc* mRNA and c-*fos* mRNA are found in high levels in papillary carcinomas compared with the surrounding normal thyroid tissue. Patients with an unfavorable prognosis were twice as likely to overexpress c-*myc* as patients with good prognosis [17].

Ras oncogenes were found in 80% of follicular and 20% of papillary carcinomas. This high prevalence of transforming *ras* oncogenes in follicular carcinomas may explain its aggressive behavior in comparison to papillary carcinoma and may suggest a role of this on-

cogene in the metastatic phenotype of this cancer [18]. Recently a tissue-specific oncogene associated with papillary carcinoma has been identified.

Excessive growth factor and increased expression of oncogenes encoding growth factors or growth factor expression, such as the oncogene of c-*ras B* were identified in papillary carcinoma, adenomas, and anaplastic carcinoma.

Besides the importance of growth factors in the development of thyroid carcinoma, links have also been found to certain risk factors. The most important of these is radiation exposure. Exposure to radiation following the explosion of the atomic bombs in Japan, as well as after head and neck radiation, resulted in a 30-fold increase in the incidence of thyroid cancer [19].

About 90% or more of thyroid carcinomas are well differentiated, of the papillary, papillofollicular, follicular, and Hürthle-cell types, which take up iodine and accordingly can be successfully treated with iodine-131. The therapeutic effects on differentiated thyroid cancer, where larger doses of radioactive iodide are administered, are based on destruction of cells of the residual thyroid tissue and the functioning carcinoma cells by the high dose of administered radionuclide. The mortality of patients treated with less than total thyroidectomy and limited iodine-131 therapy was found to be three to four times higher than that of patients treated with total thyroidectomy and iodine-131 therapy to ablate known foci of radioiodine uptake [20]. Because of the larger dose of radionuclide and the lower uptake by the tissue in the case of thyroid cancer, more side effects can be seen, particularly transient sialadenitis, than in treatment of hyperthyroidism. This, however, does not justify using limited therapy such as 30 mCi. A recent study confirmed the high rate of efficiency of the high ablative dose of 100 mCi of iodine-131 particularly in patients with less than 2% neck uptake values [21]. This study confirmed also that success rate is dependent on the pre-therapy neck uptake. The success rate was 94% when pre-ablation uptake was less

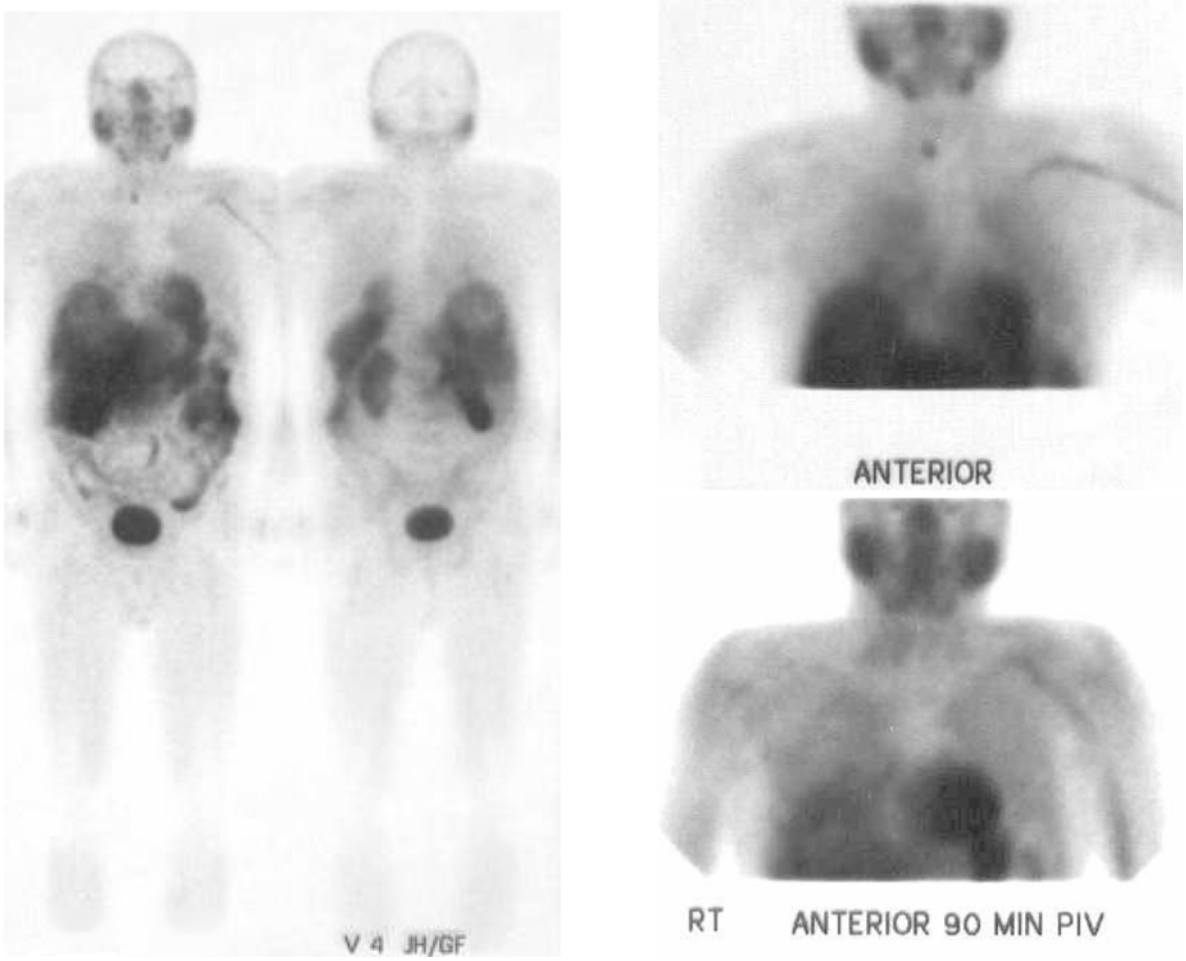

Fig. 22.3. Forty-two-year-old female with history of well differentiated thyroid carcinoma; total thyroidectomy 6 weeks earlier. A ^{99m}Tc-MIBI study was obtained

than 2%, 80% with uptake between 2% and 5% and 60% when uptake value was more than 5% [21].

Thyroglobulin and calcitonin are the major tumor markers for thyroid cancer of the follicular epithelium and parafollicular C cells, respectively. These markers are unique, in the sense that they are not only specific for tumor tissue but are also specific components of normal thyroid tissue. Thyroglobulin is an iodinated glycoprotein essential for synthesis and storage of thyroid hormones. Since thyroglobulin is produced exclusively by thyroid tissue, only very small amounts can be found in the blood after thyroidectomy and ablative radioiodine therapy. Accordingly, any post-therapeutic elevation of its levels indicates either remnant thyroid tissue, requiring further ablative treatment, or the presence of metastases or local recurrence. Other tumor markers used for many other tumors, such as carcinoembryonic antigen (CEA) and tissue polypeptide antigen (TPA), are not specific for thyroid cancer. TPA, which is a cytokeratin-related nonspecific proliferation marker, has a sensitivity of 40% – 60% for thyroid cancer. However, it has a good correlation with tumor progression or therapeutic response, with a high positive predictive value of 90%. Evaluation of ablative therapy and follow-up of patients post-ablation to monitor disease recurrence has been further improved and facilitated by the availability of recombinant human thyrotropin as well as the use of ^{18}F-FDG positron emission tomography. The value of recombinant human thyrotropin (rhTSH) rests on providing the opportunity to obtain diagnostic whole body iodine-131 scans under adequate TSH elevation as well as representative thyroglobulin levels while the patients receive their thyroid hormone [22]. FDG-PET is useful in evaluating patients in instances where radioiodine imaging fails to identify known or suspected recurrent or metastatic disease [23]. Additionally the use of ^{201}Tl- and ^{99m}Tc-MIBI (Fig. 22.3) particularly when FDG-PET is not available is of value for this purpose [24].

22.4 Treatment of Pain Secondary to Skeletal Metastases

Approximately 75% of patients with advanced cancer have pain, with a high percentage due to skeletal metastases. Bone metastases cause intractable pain, which affects the quality of life for the patient, especially if it is associated with immobility, anorexia, and anxiety, with the consequent long-term use of narcotic analgesics. The mechanism of bone pain may not be clear in many of these patients and could be due to cell-secreted pain modulators such as interleukin-1β, interleukin-8, and interferon [25]. Depending on the extent of bone metastases, radiation therapy or radiopharmaceuticals can be used instead of narcotics to alleviate the pain with the objective of improving the quality of life.

Radiotherapy for focal painful metastases with delivery of 2000 – 3000 rads induces pain relief in 60% – 90% of cases [26, 27]. Controlling pain of multiple metastases using external beam radiotherapy is difficult. Hemibody irradiation using 800 rads to the lower half of the body and 600 rads to the upper half has resulted in complete response in 30%, partial response in 50%, and no response in 20% of patients. Radiotherapy used for painful skeletal metastases often produces significant side effects such as nausea, vomiting, and diarrhea, as well as bone marrow toxicity in one-third of patients. Vomiting and diarrhea can be severe in 10% of cases and hematological side effects can be life threatening in approximately 9% of patients [28].

Bone-seeking radiopharmaceuticals emitting beta particles have been used to deliver local radiotherapy to metastases to decrease pain at their sites. Radiopharmaceuticals which are taken up at the sites of bone metastases will cause less toxicity than external radiation therapy. These radiopharmaceuticals control pain while cause only transient bone marrow depression, which is usually mild. The uptake of these radiopharmaceuticals by metastases is severalfold (up to 15 – 20 times) that of normal bone. These agents are absorbed to hydroxyapatite crystals at the site of active new bone, similar to ^{99m}Tc-MDP. They include phosphorus-32, strontium-89, rhenium-186-diphosphonate, and samarium-153-EDTMP. The list of radiopharmaceuticals for bone palliation has been increasing and includes rhenium-188, lutetium-177 and others [29].

22.4.1 Radiopharmaceuticals

22.4.1.1 Strontium-89-Chloride

Systemic radionuclide therapy with ^{89}Sr-chloride was first used to relieve pain from bone metastases in 1937 and regained popularity in the 1980s. It is a pure beta-emitter with a relatively long half-life of 50.5 days. It is a chemical analogue of calcium, and accordingly it concentrates avidly in areas of high osteoblastic activity. After intravenous injection, strontium quickly accumulates in the mineral bone matrix, where active bone formation takes place. Therefore, there is preferential uptake in and around metastatic tumor deposits, which has been confirmed by external measurements using the gamma emitting radionuclide strontium-85 and by autoradiography. It was found that strontium-89 concentration is 2 – 20 times greater in bone metastases

than normal bone [30]. The biological half-life of strontium-89 in bone lesions is about 90 days, compared to about 2 weeks in normal bone, which can be explained by the immature nature of reactive bone compared to normal lamellar bone. This selective uptake and prolonged retention at sites of increased bone mineral turnover provide precise targeting of bone lesions. The radionuclide is typically administered as a single 150 MBq (4 mCi) intravenous dose. Overall, pain relief occurs in up to 80% of patients, of whom 10% – 40% became effectively pain free. The mean duration of palliation is 3 – 4 months [31, 32]. Furthermore, ^{Sr}89-chloride may cause slowing of metastatic progression due to inhibition of expression of cell adhesion molecules (E-selectins) that participate in the metastatic process. The significant transient decrease in serum E-selectin concentration as observed after systemic radionuclide therapy in a study on 25 men with metastatic prostate carcinoma is an indication of such an observation [33] and may provide opportunities for clinical trials.

22.4.1.2 Phosphorus-32-Orthophosphate

This radionuclide is used uncommonly for the treatment of bone metastases. Dosimetric studies have demonstrated a relatively high dose to the bone marrow from the highly energetic beta particles of the radionuclide, causing myelosuppression with pancytopenia. Increased incidence of acute leukemia has been reported although this was associated with ^{32}P therapy in patients with polycythemia vera.

22.4.1.3 Samarium-153-Ethylene Diamine Tetramethylene Phosphonate

Samarium-153 is produced in the nuclear reactor by neutron activation of both natural samarium-203 and 98% enriched samarium-152 targets. It has a relatively short half-life of about 48 h. Coupling of the radionuclide to ethylene diamine tetramethylene phosphonate (EDTMP) leads to the high uptake of the radionuclide by bone. Gamma camera imaging is possible due to the 103-KeV gamma ray emitted during decay of samarium-153. The resulting images are similar to those obtained with ^{99m}Tc-MDP or other diphosphonates, showing increased uptake at the site of metastases. The calculated lesion to normal-bone ratio was reported to be 4.0 and the soft tissue ratio to be 6.0 [34].

Administration of ^{153}Sm-EDTMP according to the supplier's recommendations at 37 MBq (1 mCi)/kg would deliver a bone marrow dose of 3.27 – 5.90 gray (Gy), which would induce myelotoxicity as a side effect. Dosimetric calculation by urine collection and whole body scintigraphy has been used to limit the bone marrow dose to 2 Gy by Cameron and associates [35]. This was achieved by anterior and posterior whole-body images obtained 10 min and 5 h after the intravenous injection of 740 MBq (20 mCi) of ^{153}Sm-EDTMP with determination of bone activity by imaging and by counting urine collected for 5 h. The total administered activity of ^{153}Sm-EDTMP predicted on a 2-Gy bone marrow dose was found to be 35% – 63% of the standard recommended dose of 37 MBq/kg. The authors reported pain relief in eight of the ten patients treated using this dosimetric method [35].

22.4.1.4 Rhenium-186-Ethylene Hydroxy Diphosphonate

Similarly to samarium-153, rhenium-186 has been coupled to a bone-seeking phosphonate, ethylene hydroxy diphosphonate (EHDP). This radionuclide emits beta particles with a maximum energy of 1.07 MeV and gamma photons with an energy of 137 KeV, which allows bone scanning. ^{186}Re-EHDP undergoes renal excretion within 6 h after intravenous injection, as is the case with the common bone scanning agents. At 4 days, 14% of the radioactivity remains in bone [36].

Several studies have shown encouraging clinical results of palliative therapy using ^{186}Re-HEDP with an overall response rate of approximately 70% for painful osseous metastasis from prostate and breast cancer. Myelosuppression has been limited and reversible, which makes repetitive treatment safe [37, 38]; 31 patients with various cancers (10 prostate, 10 breast, 4 rectum, 5 lung, 2 nasopharynx) and bone metastases were studied. Therapy was delivered using a fixed dose of 1295 MBq (35 mCi) of ^{186}Re-HEDP. When necessary, the same dose was repeated two to three times after an interval of 10 – 12 weeks. The mean response rate was 87.5% in patients with breast and prostate cancer, 75% in patients with rectal cancer and 20% in patients with lung cancer. The overall response rate was 67.5% and the palliation period varied between 6 and 10 weeks. The maximal palliation effect was observed between the 3rd and 7th weeks [38].

22.4.1.5 Tin-117m-Diethylenetriaminepentaacetic Acid

Tin-117m is a reactor produced radionuclide, with a half-life of 13.6 days. Contrary to the other radionuclides mentioned above, this radionuclide emits internal conversion electrons. Tin-117m is linked to diethylenetriaminepentaacetic acid (DTPA). More than 50% of the administered activity is absorbed by bone in patients with metastatic carcinoma with a bone to red marrow ratio of up to 9:1. Its 159 KeV photon energy al-

lows correlative imaging with a similar uptake pattern to ^{99m}Tc-MDP [39].

In a preliminary study in ten patients by Atkins et al. [40], none of the patients who received ^{117m}Sn-DTPA for palliation developed marrow toxicity. Another recent study on 47 patients treated with ^{117}Sn-DTPA showed that the experimental mean absorbed dose to the femoral marrow was 0.043 cGy/KBq. In comparison to ^{32}P-orthophosphate, ^{117m}Sn-DTPA yielded up to an eightfold therapeutic advantage over the energetic beta emitter ^{32}P. Accordingly, it was suggested that the internal conversion electron emitter ^{117m}Sn offers a large dosimetric advantage over the energetic beta-particle emitters, allowing higher administered activity for alleviating bone pain, while minimizing marrow toxicity [41].

22.4.1.6 Rhenium-188-Dimercaptosuccinic Acid Complex

Rhenium-188-dimercaptosuccinic acid complex (^{188}Re-(V)DMSA), a potential therapeutic analogue of the tumor imaging agent ^{99m}Tc-(V)DMSA, is selectively taken up in bone metastases. In a study by Blower et al. [42] on ten patients with metastastatic prostate cancer studied by ^{99m}Tc-(V)DMSA and ^{188}Re-(V)DMSA to compare their biodistribution, only minor differences between both radiopharmaceuticals were found. Accordingly ^{99m}Tc-(V)DMSA scans are predictive of ^{188}Re-(V)DMSA biodistribution and could be used to estimate tumor and renal dosimetry and assess suitability of patients for ^{186}Re-(V)DMSA treatment [42]. This advantage makes this tracer a candidate for more trials as a potentially successful agent for bone metastases palliation.

22.4.2 Mechanism of Action

Metastatic bone pain is believed to be due to mechanical factors due to local bony destruction and to humoral factors resulting from secretion of certain mediators by tumor and peri-tumoral cells (Table 22.2). Although the mechanism of action of these radiopharmaceuticals in relieving bone pain is not completely known, the therapeutic effect is thought to be achieved by delivering sufficient energy from the sites of reactive bone directly to the cells of metastases and/or to peritumor cytokine-secreting cells that may be responsible for the patient's pain. Pain relief by radiation was found to be independent of the radiosensitivity of the tumor and therefore the mechanism of action does not involve actual killing of the tumor cell. It is more likely that radiation interrupts processes that are maintained by humoral pain mediators in the microenvironment of the tumor [43]. This view is also supported by absence of a dose-response relationship [44].

Table 22.2. Possible mechanisms of metastases-induced bone pain

1.	Stretching periosteum
2.	Pressure on nerves
3.	Direct bone invasion and local destruction
4.	Cell secreted pain modulators such as interleukin-1 beta, interleukin-8 and interferon

22.4.3 Choice of Radiopharmaceutical

It has been demonstrated that myelosupression is less severe using radionuclides with relatively shorter half-lives favoring the use of ^{153}Sm, ^{186}Re, ^{117}Sn and ^{89}Sr. Other physical properties including radiolabeled conjugate biological uptake and clearance, product-specific activity, range and type of emissions, and resultant effects on tumor and normal tissue cellular survival should be all considered along with the clinical outcome to choose a radiophamaceutical.The response rate of different radiopharmaceuticals currently in use appears not to differ significantly [45]. The side effects which are mainly hematologic vary among the agents used, being more pronounced with ^{32}P than with the newer agents. ^{117m}Sn-DTPA differs from the other radiopharmaceuticals in that its emission is internal conversion electrons rather than beta particles. Since internal conversion electrons have low energy and a shorter path in tissue, they may result in less marrow toxicity.

22.4.4 Clinical Use

Radiopharmaceutical therapy is indicated for the treatment of patients with painful widespread bone metastases. However, the patient with pain secondary to either spinal cord or peripheral nerve invasion by adjacent metastases will not benefit from such treatment. The contraindication in pregnancy is absolute, and relative contraindications include preexisting severe myelosuppression, urinary incontinence, severe insufficiency, and spinal cord compression or pathological fracture. A pretherapy bone scan, neurological examination, and blood counts should be available before the patient is treated. Follow-up blood counts should be performed at least biweekly to evaluate myelotoxicity.

The response to these radiopharmaceuticals is more or less similar, with an average success rate of 70% – 80% [46 – 52].

The difference in half-life of the radiopharmaceuticals and the extent of bone metastases have consequences both for the onset and the duration of pain relief. Relief rates using the newer agents are not signifi-

cantly different and are comparable with those of external beam radiotherapy, but side-effects are minimal and compare favorably with those of the older agent ^{32}P.

Using radionuclide along with chemotherapy for palliation is being investigated and may prove useful. Palmedo et al. reported a case of a patient with disseminated bone metastases due to breast cancer and multifocal pain. Because of persisting pain after a first cycle of chemotherapy, 1295 MBq ^{186}Re-HEDP was administered and pain relief was significant. Subsequently, the patient received combined chemotherapy along with ^{186}Re-HEDP therapy and remained pain free. Follow-up ^{99m}Tc-MDP bone scan showed significant regression of osseous metastases. The authors speculated that the combination of ^{186}Re-HEDP and chemotherapy resulted in significantly increased palliation of metastatic bone disease [53].

The side effects, which are mainly hematological, vary among the agents used, being more pronounced with ^{32}P than with the newer agents. Some agents have the advantage of emitting gamma energy suitable for scintigraphy such as ^{153}Sm-EDTMD (ethylene diamine tetramethylene phosphonate). ^{117m}Sn-DTPA differs from the other radiopharmaceuticals in that it emits conversion electrons rather than beta particles. These conversion electrons have low energy and a shorter path in tissue and may then result in less marrow toxicity.

22.5 Treatment of Neuroendocrine Tumors

The goal of radionuclide therapy for neuroendocrine tumors is to control symptoms and pain to improve the quality of life, reduce medical requirements and stabilize the disease. Additionally, in limited disease to reduce tumor volume, reduce hormone secretion and complete remission.

Several neuroendocrine tumors are candidates for radionuclide therapy. ^{131}I labeled radiopharmaceuticals have been used to treat neuroblastoma, pheochromocytoma and paraganglioma. More recently, octreotide labeled with ^{111}In, ^{90}Y and ^{177}Lu has been used.

^{131}I-meta-iodobenzylguanidine (MIBG) is being used in increasing trials and applications for therapy. It is used for the treatment of pheochromocytoma, malignant paraganglioma, neuroblastoma, medullary thyroid carcinoma, and symptomatic carcinoid tumors. The radiopharmaceutical resembles guanithidine and is concentrated by normal and abnormal sympathetic adrenergic tissue.

When ^{131}I-MIBG is administered intravenously, it is transported by blood to be taken up by normal adrenergic tissue such as the adrenal medulla and sympathetic nervous system and by tumors of neuroectoderm-derived tissue. The uptake by these tumors is secondary to active uptake-1 mechanism and passive diffusion through the cell membrane, followed by active intracellular transport to the neurosecretory granules in the cytoplasm, where it is retained.

In normal adrenergic tissue such as the adrenal medulla, heart, and salivary glands, as well as in pheochromocytoma, 90% of MIBG is stored in the neurosecretory granules, while in neuroblastoma it was found that up to 60% is stored within the extragranular cells. The major part of the radiopharmaceutical is excreted unchanged in urine. Other than in the adrenergic tissues, uptake is normally noted in the liver, spleen, urinary bladder, bowel, lungs, nose, near the trapezium muscle in children, and in the uterus in some women [54, 55]. The radiation effect is due to emission of beta particles from the decaying ^{131}I with a mechanism similar to that in treating thyroid disorders. A long list of medications are known to block the uptake and/or retention of MIBG by the target tissues, while some reports have suggested that others such as calcium channel blockers may increase its uptake. The mechanism of interference of these drugs varies. Beta blockers, for example, interfere with the uptake by inhibiting the uptake mechanism-1 and by depleting the neurosecretory granules, while reserpine exerts this action by depleting the granules and inhibiting the intracellular transport. More recently peptide therapy has been increasingly used to treat these tumors (shown later in the chapter).

22.5.1 Neuroblastoma

Therapeutic amounts of ^{131}I-MIBG can be delivered to neuroblastoma with acceptable bone marrow toxicity [56–58]. Among patients with stage 3 and 4 neuroblastoma who had failed treatment with chemotherapy, ^{131}I-MIBG induced partial remission in many children and complete remission in a small number of patients. The agent has also been used for early therapy at the time of diagnosis, with a success rate comparable to that of chemotherapy with fewer side effects [57].

22.5.2 Pheochromocytoma

Malignant pheochromocytoma and its metastases are known to be resistant to chemotherapy and external beam radiation therapy. ^{131}I-MIBG has a limited role in the treatment of malignant pheochromocytoma, functioning paraganglioma, and medullary carcinoma of the thyroid. Palliative effects have been achieved in patients with pheochromocytoma [59]. Several reports from the USA and Europe have collectively shown a response of 62.5% among patients with pheochromocy-

toma [45]. Soft tissue metastases responded better than skeletal metastases.

22.5.3 Carcinoid Tumor

Carcinoid liver metastases are common and rarely can be resected. Treatment for symptomatic patients with unresectable disease includes chemotherapy, interferon-alpha, and the somatostatin analog, octreotide. The response to these medical therapies is usually poor. Hepatic artery ligation and embolization are alternatives and have a better response rate. Preliminary experience also suggests that external beam radiotherapy can be useful. ^{131}I-MIBG and radiolabeled octreotide have recently been tried. ^{131}I-MIBG is highly concentrated by more than 60% of carcinoid metastases. Carcinoid tumor cells stain positive for chromogranin A [60]. ^{131}I-MIBG targets the metabolically active lesions, reduces the hormonal secretion, and improves symptoms [61, 62]. Data indicate a partial response in 20% of patients and a palliative effect in more than 50% of those with end-stage disease. ^{131}I-MIBG causes temporary myelosuppression, which makes its use favorable compared with chemotherapy. It is also preferred to interferon-alpha and octreotide, which require frequent subcutaneous injections.

Pathologically, ^{131}I-MIBG produces gross cystic changes in liver metastases which probably are due to ischemic necrosis. Surgical deroofing and aspiration of cysts can lead to regeneration of normal liver tissue [62].

22.6 Radioimmunotherapy

Monoclonal antibodies are now contributing increasingly to cancer treatment, following early disappointments. ^{131}I-anti-CD-20 and ^{131}I-anti-CD-22 are good examples which are used for non-Hodgkin's lymphomas. These antibodies can be used alone to kill tumor cells or conjugated with drugs, cytotoxic agents, and radionuclides to improve their effects.

Radioimmunotherapy using monoclonal antibodies conjugated with isotopes allows the delivery of radiation to tumor tissue while sparing normal tissue. This radiation can be administered as a single large dose of radiolabeled monoclonal antibodies or, more commonly, in multiple fractions [63–65].

Although the way they work is not entirely clear, generally monoclonal antibodies can kill tumor cells through the following mechanisms [66]:

1. Activation of host immune system to lyse tumor cells, e.g., complement, antibody-dependent cellular cytotoxicity (ADCC)
2. Directing biologically active agents to tumor cells (e.g., drugs, toxins, cytokines, isotopes)
3. Triggering or interfering with the function of physiologically important cell receptors
4. Inducing indirect antitumor response by triggering the formation of autoantibodies or activation of cellular responses to tumor antigens to destroy tumor cells
5. Killing tumor cells by apoptosis, which is simply an intrinsic "programmed" cell death characterized by chromatin condensation and DNA degeneration

The use of radioimmunotherapy for treating lymphoma has been expanding in the last decade. It is currently being used for recurrent and relapsed disease of low grade B-cell (Fig. 22.4), follicular and transformed lymphomas. Clinical trials are being conducted for aggressive B cell, mantle cell and non-follicular indolent B

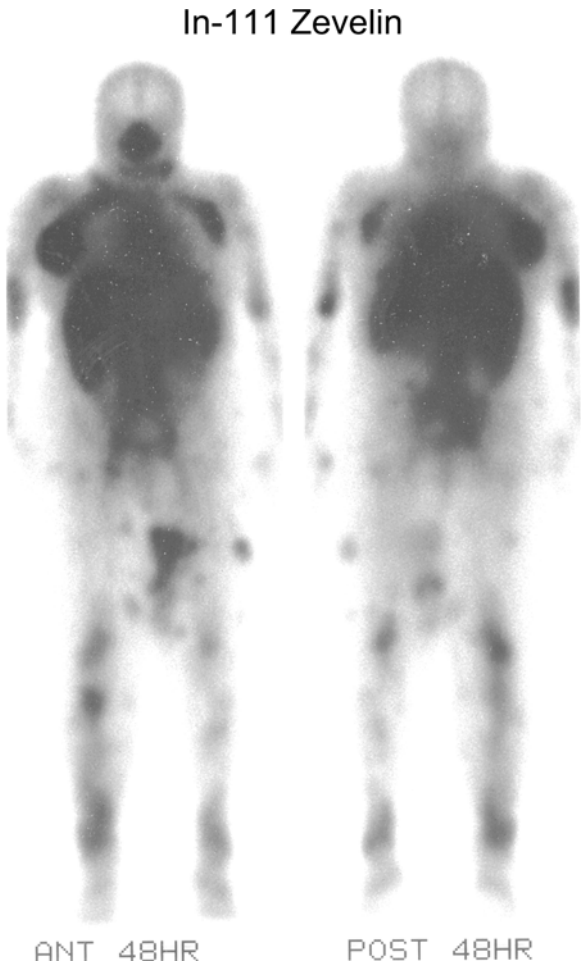

Fig. 22.4. Fifty-one-year-old female with low grade refractory non-Hodgkin's lymphoma. ^{111}In-Zevalin images were obtained 48 h after injection. The patient was treated subsequently with 32 mCi of ^{90}Y-Zevalin given slowly intravenously. Note the significant degree of uptake in lymph nodes involved with the disease including some in the extremities

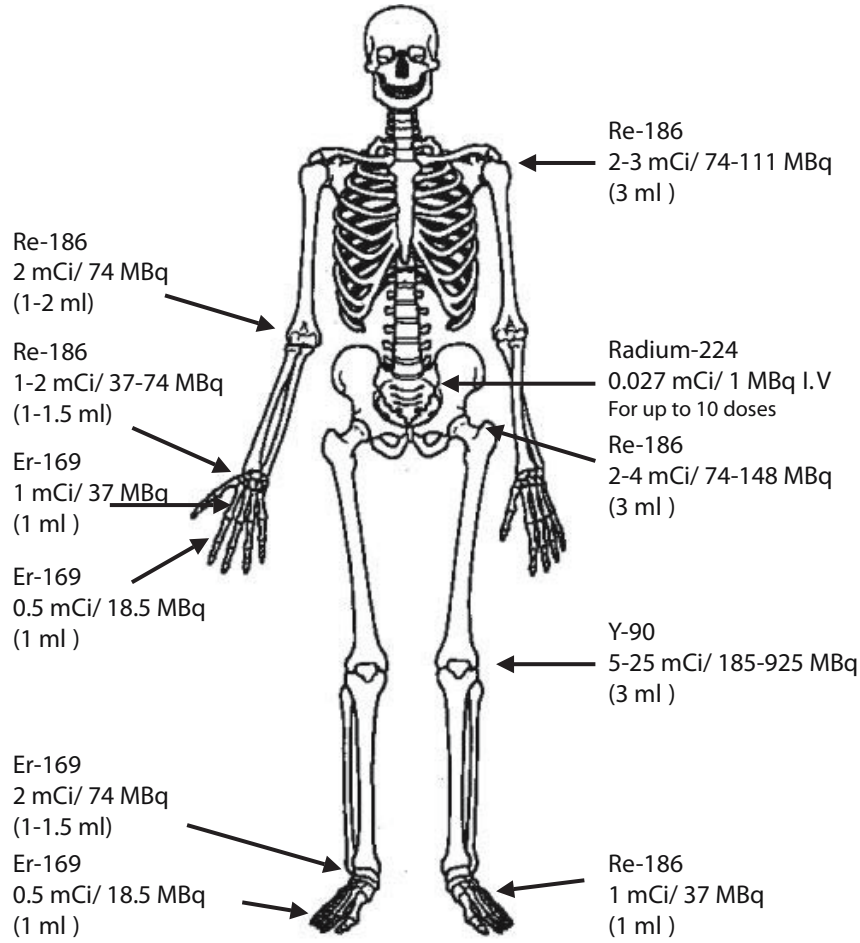

Fig. 22.5. Diagram illustrating the choice of radiopharmaceuticals for radiosynovectomy of different joints

ell types as well as chronic lymphocytic leukemia. See Chapter 19 for details.

22.7 Radionuclide Synovectomy

There may be a need for a definitive solution to the joint pain of many arthropathies, particularly rheumatoid arthritis, after failure of conventional medications. Therapeutic nuclear medicine offers an alternative to surgical synovectomy. Several radiopharmaceuticals can destroy the synovial membrane when injected intra-articularly (radionuclide synovectomy or radiosynoviorthesis) and the patients become pain free.

Yttrium-90 colloid, erbium-169 citrate colloid, rhenium-186 colloid, phosphorus-32 colloid and others are all used to treat synovial disease [67, 68]. Since these colloids vary in their physical characteristics and thus in their range of penetrability, they are used differently to achieve the therapeutic effects and avoid injuring the surrounding tissue. Accordingly, some radiopharmaceuticals are used for the knee while others are used for small joints (Table 22.3). Yttrium-90-citrate or silicate is generally used for big joints such as the knee, rhenium-186-colloid is used for the shoulder, elbow, hip, and ankle, and erbium-169-citrate for the small joints in the hands and feet (Fig. 22.5).

22.7.1 Radiopharmaceuticals for Synovectomy

22.7.1.1 Yttrium-90-Colloid

This radionuclide is used predominantly for radionuclide synoviorthesis of the knee joint. It is also for malignant pleural and peritoneal effusions. The pharmacological characteristics of the silicate and citrate forms are the same. The average range in tissue is 3.6 mm and the maximum is 11 mm. After direct intra-articular administration the colloid penetrates into the surface cells of the synovia. Small amounts of particles are transported through the lymphatics, mainly after active or passive movement of the joint, from the knee to the regional lymph nodes. The safety of this modality of management has been reported and hence the pa-

Table 22.3. Physical properties and main uses of major radiopharmaceuticals for synovectomy

Isotope	Mode of decay	Physical half-life	Main energy	Penetration range	Main use/adult dose
^{90}Y-silicate- or -citrate colloid with an average particle size of 10 nm	Emission of beta particles	2.7 days	2.24 MeV	3 – 5 mm in soft tissue, 2.8 mm in cartilage, max. 11 mm in soft tissues	Knee joint; 185 MBq
^{169}Er-citrate colloid with an average particle size of 10 nm	Emission of beta particles	9.4 days	0.4 MeV	Max 1 mm in soft tissue and 0.7 mm in cartilage	Small joints of hand and feet; 37 MBq
^{186}Re-sulfide colloid with an average particle size of 5 – 10 nm	Emission of beta particles and gamma rays (92.2%); electron capture (7.8%)	3.7 days	Gamma 137 KeV, beta 1.07 MeV	1.2 mm in soft tissues and 0.9 mm in cartilage	Shoulder, elbow and wrist joints; 74 MBq
^{32}P-colloid with an average particle size of 5 – 20 nm	Emission of beta particles	14 days	1.7 MeV	Max 7.9 mm in soft tissue	Knee, elbows and ankles; 37 MBq

tient's age should not be regarded as a limiting factor [69]. It is recommended that yttrium-90 synoviorthesis should be performed also in very young patients, when the amount of synovium is still moderate. Once the degree of synovitis has become severe, the expected results of radioactive synoviorthesis are worse [70].

22.7.1.2 Rhenium-186-Sulfide (^{186}Re-Colloid)

This radiopharmaceutical is used particularly for radionuclide synoviorthesis of the hip, shoulder, elbow, wrist, or ankle joint. After intra-articular injection, it is absorbed by the superficial cells of the synovia. Beta radiation leads to coagulation necrosis and sloughing of these cells.

22.7.1.3 Erbium-169-Citrate (^{169}Er-Colloid)

This is more suitable for the radionuclide synoviorthesis of metacarpophalangeal, metatarsophalangeal, and proximal interphalangeal joints. Beta radiation of the absorbed radiopharmaceutical in the synovia causes coagulation necrosis and sloughing of cells, as with other colloids used for other joints. ^{169}Er-colloid has an affinity to chelates; therefore, the simultaneous administration of iodine contrast medium containing EDTA should be avoided.

22.7.1.4 Phosphorus-32-Chromic Sulfate

^{32}P-chromic phosphate has a 14-day half-life, is several times larger than ^{90}Y-silicate, ^{186}Re, ^{169}Er, or ^{198}Au colloids, and emits only beta radiation. Its beta radiation has a soft tissue penetration midway between them at 2 – 3 mm. These physical advantages have led some investigators to use it for the treatment of rheumatoid arthritis and hemophilic arthritis [71, 72].

22.7.1.5 Radioactive Gold (^{198}Au)

Radioactive gold (^{198}Au) has a mean soft tissue penetration of only 1 – 2 mm. It has also been used for radiosynovectomy. It has a physical half-life of 197 days and a colloid particle size ranging from 20 to 70 ìm.

22.7.1.6 Rhenium-188-Colloid

Rhenium-188 is a generator-produced beta-emitting radionuclide, and the importance of ^{188}Re for radionuclide therapy is increasing rapidly. Jeong [73] prepared ^{188}Re-colloid and compared its properties with ^{188}Re-colloid. They found that ^{188}Re-tin-colloid is more advantageous over ^{188}Re-sulfur-colloid since it showed higher labeling efficiency, allowed better control of the particle size, and lower residual activity in the injection syringes [73].

22.7.1.7 Dysprosium-165

This radionuclide has a short half-life of 2.3 h, energetic beta emission with a tissue penetration of 5.7 mm and a very large particle size. Furthermore, it has a 3.6 abundance of gamma emission that can be used by the gamma camera to detect any possible leak. It showed a response rate of 65% – 70% with the best results in patients with early stage joint disease [74].

22.7.1.8 Holmium-166-Ferric Hydroxide

The first experience with ^{166}Ho was recently reported [75]. Knee joints of 22 patients were treated with a mean activity of 1.11 GBq (mCi). Holmium-166 has a maximum beta energy of 1.85 MeV with a mean penetration in inflamed synovial layer of 2.2 mm and a maximum of 8.7 mm. Its particle size is 1.2 – 12 nm

22.7.2 Mechanism of Action

Although the mechanism of action cannot be totally explained, the current belief is that after intra-articular administration the radioactive particles are absorbed by superficial cells of the synovium. Beta radiation leads to coagulation necrosis and sloughing of these cells.

22.7.3 Choice of Radiopharmaceutical

The choice of radiopharmaceutical depends on the physical characteristics and the size of the joint to be treated as well as the disease status. The therapeutic agents are particulate in nature and labeled with beta emitting radionuclides. Radiation tissue penetration is proportional to the energy of the beta particles. For example, yttrium-90, with its highly energetic beta, has a mean soft tissue penetration of 3 – 4 mm, while rhenium-186 has a mean penetration of 1 – 2 mm, the beta of phosphorus-32 has a soft tissue penetration midway between them at 2 – 3 mm and both radioactive gold and rhenium-186 have a mean soft tissue penetration of only 1 – 2 mm. Radiopharmaceuticals with shallow depth of penetration are not optimal for large joints such as the knee or for patients with extensively thickened synovium such as cases with rheumatoid arthritis and pigmented villonodular synovitis. Since the rate of exposure to the radiation is proportional to the severity of the post-therapy inflammatory reaction, a radionuclide with a moderately long half-life of days may be preferred to that with a half-life of a few hours. It appears that there is an inverse relationship between the size of radioactive particle used and the tendency for the radiocolloid to leak from the joint space which, in general, makes the choice of a relatively large radiocolloid more appropriate. A radionuclide that emits only beta radiation would have more advantages than those which emit both beta and gamma radiation in order to minimize whole-body radiation.

22.7.4 Clinical Use

Hemophiliac patients with chronic synovitis and hemarthropathy, rheumatoid arthritis, pigmented villonodular synovitis, psoriatic arthritis, ankylosing spondylitis, and collagenosis are candidates for this treatment modality. Furthermore, persistent effusion after joint prosthesis is a relative indication [76].

The absolute contraindications for the use of the therapeutic radiopharmaceutical colloids for synovectomy are pregnancy and continued breast feeding. Fresh fracture, serious liver disease, myelosuppression and acute infections are other contraindications. In children or young adults therapy should only be administered if the estimated benefit outweighs the potential risks [77]. The presence of a Baker cyst in the knee joint is considered by some workers in the field as a contraindication. Ultrasonography is particularly important for the knee joint to exclude the presence of a Baker cyst, which is an evagination of the medial dorsal part of the joint capsule in communication with the main joint. If there is inflammation in the knee joint, the effusion can be pumped into the Baker cyst by enhanced motion. If a valve mechanism exists in the connection duct, this could have a deleterious effect after radiosynovectomy. The increased pressure in the cyst might lead to its rupture and the radioactive fluid getting into the surrounding tissue of the joint. The consequence could be possible necrosis of the muscles, nerves and blood vessels. Radiosynovectomy should be delayed for 4 – 6 weeks after arthroscopy [77].

Two or three phase bone scan should be obtained before planning therapy to assess the degree of inflammation of the joint and soft tissue and in order to be able to decide if radiosynovectomy is possible and if the patient would benefit from this therapy. Scintigraphy is particularly important to evaluate the extent of abnormalities in the joint being treated and quantitation methods could be used before and after therapy. History of arthroscopy must be checked. Ultrasound or MRI is also helpful to assess the amount of effusion, joint space and the status of the synovium to ensure homogeneous distribution of the radiopharmaceutical. A complete blood cell count must be obtained before therapy as well as a pregnancy test for women of child bearing age. Injection should be done using aseptic technique. Radiosynovectomy can generally be repeated in 6 months.

The largest number of treated patients are those with rheumatoid arthritis and hemophilia. Good results are generally obtained from among those patients as well as those with psoriatic arthropathy. On the other hand, in osteoarthritis with recurrent joint effusion radiosynovectomy has not been as successful in relieving the symptoms. Good response is reported in 40% – 70% of patients [78]. In patients with advanced cartilage destruction or bone-on-bone interaction, the synovial membrane is likely to be practically non-existent. Accordingly, patients with less radiological damage generally show better results than those with more severe

damage. If there is initially a poor response or a relapse, more than half the patients may benefit from a reinjection [79, 80]. In a report of more than 2000 joints treated, the success rate for rheumatoid arthritis was 67% whereas it was 56% for osteoarthritis, 91% for hemophilia and Willebrand's disease and 77% for pigmented villonodular synovitis [80].

22.8 Treatment of Malignant Effusions

Radiopharmaceuticals can also be used in the treatment of malignant effusions. After intrapleural or intraperitoneal administration, ^{90}Y-colloid is distributed in the effusion and penetrates the surface cells of tumors. The radionuclide destroys free tumor cells in malignant effusions and may have an additional radiation effect on metastases and mesothelioma by tumor penetrational intratumoral distribution.

22.9 Other Therapeutic Procedures

22.9.1 Peptide Receptor Radionuclide Therapy

Since cells express on their plasma membranes, receptor proteins with high affinity for regulatory peptides such as somatostatin, peptide analogs are used to image and treat receptor positive tumors. The amount of these receptors changes with diseases. Overexpression of such receptors is the pathophysiologic basis of visualization and treatment of receptor positive tumors [81].

There is a high level of expression of somatostatin receptors on several tumor cells in the molecular basis of the utilization of radiolabeled somatostatin analogues in diagnostic and therapeutic nuclear oncology. Since peptides can be produced easily, and have rapid clearance, rapid tissue penetration and low antigenicity, several labeled peptides have been developed over the last few years. These include somatostatin, cholecystokinin (CCK), gastrin, vasoactive intestinal peptide (VIP), bombesin, substance P and neuropeptide (NPY (Y) analogues [81, 82]. A recent study [82] has shown that ^{111}In-DTPA octreotide effect is dependent on tumor size in animal models bearing somatostatin pancreatic tumor expressing somatostatin receptor type2 (sst_2). Complete response was seen in 50% of tumors of 1 cm or less in diameter while the response was less pronounced with increasing tumor size. This study indicates that this therapy may be preferred to start as early as possible when tumors are small.

Yttrium-90-DOTA octreotide and lanreotide can be of benefit in the following:

1. Iodine-negative metastases of differentiated thyroid cancer may express somatostatin receptors and could benefit from ^{90}Y-DOTA octreotide or lanreotide [83]. Detection of somatostatin-positive metastases before considering this treatment should be done using diagnostic ^{111}In-octreotide or lanreotide. Some metastases respond to octreotide while others respond to lanreotide, and there is no apparent explanation. A combination of ^{131}I- and ^{90}Y-DOTA octreotide or lanreotide is being considered.
2. Treatment of endocrine gastropancreatic (GEP) tumors which express somatostatin receptors.

22.9.2 Treatment of Bone Tumors

22.9.2.1 Osteogenic Sarcoma

Targeted radionuclide therapy using ^{153}Sm-EDTMP has been reported to give a substantial palliative effect in a case of relapsed primary osteogenic sarcoma in the first lumbar vertebra with progressive back pain after conventional treatment modalities had failed. The patient was bed-ridden, and developed paraparesis and impaired bladder function. On a diagnostic bone-scan intense radioactivity was localized in the tumor. The patient was treated twice, at an interval of 8 weeks, using 35 and 32 MBq/kg body weight respectively. After a few days the pain was significantly relieved and by the second radionuclide treatment the paresis subsided. For 6 months he was able to be up and about without any neurological signs or detectable metastases. Eventually, however, the patient redeveloped local pain and paraparesis, was reoperated on and died 4 months later. The investigators recommended further exploration using ^{153}Sm-EDTMP as a boost technique, supplementary to conventional external radiotherapy, given the dramatic transient improvement observed in this case [84].

Another case was also reported which illustrated high-activity ^{153}Sm-EDTMP therapy within a multimodal therapy concept to improve local control of an unresectable osteosarcoma with poor response to initial polychemotherapy. A 21-year-old woman with an extended, unresectable pelvic osteosarcoma and multiple pulmonary metastases was treated with a high activity of ^{153}Sm-EDTMP. Subsequently, external radiotherapy of the primary tumor site was performed and polychemotherapy continued, followed by autologous peripheral blood stem cell reinfusion. Within 48 h after ^{153}Sm-EDTMP treatment the patient had complete pain relief. Three weeks later the response was documented by 3-phase ^{99m}Tc-MDP bone scan, which showed a decrease in tracer uptake in the primary tumor and metastases. Whole-body ^{18}F-FDG-PET also demonstrated an interval decrease of uptake. Further evaluation of feasibility and efficacy of this multimodal therapy com-

bination of high-activity ^{153}Sm-EDTMP therapy, external radiation, polychemotherapy and stem cell support for unresectable osteosarcomas is warranted [85].

An animal study was conducted on 15 dogs with spontaneous osteogenic sarcoma, and local pain. They were treated with ^{153}Sm-EDTMP. The tumors were located in the extremities, scapula, maxilla, and the frontal bone. The dogs were injected intravenously one to four times with ^{153}Sm-EDTMP, 36 – 57 MBq/kg body weight. Three dogs had surgery in addition to the radionuclide treatment. Platelet and WBC counts showed a moderate and transient decrease with no other toxicity observed. The average tumor doses after a single injection were approximately 20 Gy. Seven dogs had metastases on autopsies. Even though none of the dogs was cured, nine of the dogs had obvious pain relief, and five of them seemed pain free: one for 20 months and one for 48 months [86].

22.9.2.2 Multiple Myeloma

Recent use of high-dose ^{166}Ho-DOTMP (^{166}Ho-1,4,7,10-tetraazcyclododecane-1,4,7,10-tetramethylene-phosphonic acid) in patients with multiple myeloma has been reported [87]. Thirty-two patients were treated with 581 – 3987 mCi with an average of 2007 mCi (74.3 GBq). Holmium-166 has a half-life of 26.8 h and a beta emission of 1.85 MeV (51%) and 177 MeV (48%) as well as an 80.6 KeV (6.6%) gamma emission suitable for gamma camera imaging. The beta particles have a mean range of 4 mm in soft tissue and can deliver high levels of radiation to the marrow and trabecular bone [88]. This radiopharmaceutical has selective bone uptake and rapid urinary excretion of the remaining activity. However, due to the high doses used, catheterization and continuous irrigation of the urinary bladder after therapy has to be used to reduce radiation dose to bladder mucosa. This agent has a potential to treat patients with resistant multiple myeloma. However, clinical studies with emphasis on the outcome in comparison with the currently used high dose of chemoradiotherapy with or without stem cell rescue are warranted to evaluate the impact on the poor survival of patients affected by the tumor. Also more studies are needed to compare the adverse effects of this agent with the high incidence of systemic toxicities of the currently available radiopharmaceuticals [89 – 92].

22.9.2.3 Metastatic Prostate Carcinoma

A study was conducted to explore the effects of ^{186}Re-HEDP treatment on the progression of lumbar skeletal metastasis in an animal model using the Copenhagen rat model and to correlate the eventual treatment efficacy with the radionuclide tissue distribution. The ^{186}Re-HEDP administration, given either 1 day or 8 days after surgical induction of lumbar metastasis, was found to significantly increase the symptom-free survival of the animals. These results were confirmed by a significant decrease in the presence of histologically detectable tumor tissue. Biodistribution studies demonstrated the uptake of the major part of the radionuclide within bone tissue. The uptake of radioactivity within the lumbar vertebrae on a microscopic scale, as shown by phosphor screen autoradiography, was concentrated in areas of bone formation and turnover. These results show that radionuclide treatment with ^{186}Re-HEDP is a potentially efficacious treatment option in prostate cancer disseminated to the skeleton [93].

22.9.3 Treatment of Hepatocellular Carcinoma

Blood supply to the normal liver depends on portal vein and to a much lesser extent on hepatic artery. Tumors on the other hand depend for their blood supply on arterial supply and are additionally hypervascular. This forms the basis of intra-arterial therapy for hepatocellular carcinomas. Radionuclides have been used in several national and multinational trials of different phases in treating liver cancer. ^{166}Ho-chitosan, ^{166}Ho-microspheres, ^{188}Re-microspheres, ^{188}Re-Lipiodol and ^{90}Y-microspheres are all being used. This therapy is used as an adjunct therapy before and after surgery and it may be curative. Combined ^{131}I-Lipiodol and chemotherapy is also being studied [94 – 100].

22.10 Combined Therapeutic Approach

Recently several trials have used a combined approach combining radionuclide with other treatment modalities [101, 102]. Strontium-89 in combination with doxorubicin has been used for bone metastases. This combination was found to be associated with a longer time interval to disease progression and a longer overall survival when compared with those who only received doxorubicin [103, 104]. Combining low dose cisplatin with the standard dose of ^{89}Sr-chloride was found to improve pain palliation significantly [105].

CHOP was also used in combination with ^{131}I-tostumomab and ^{90}Y-ibritumomab and rituxetan-CHOP combinations for untreated non-Hodgkin's lymphoma [106, 107].

Combining ^{131}I-MIBG and chemotherapy or myeloablative chemotherapy has also been used in a limited number of patients [108, 109]. In a pilot study ^{90}Y-biotin was used as an adjunct to surgery and radiation

therapy for malignant glioma [110]. The disease free interval and overall survival was significantly longer among patients with this adjunct therapy than in the control group. External beam radiotherapy has been used in combination with ^{131}I-MIBG for neuroblastoma and paraganglioma, and with ^{131}I for a large thyroid metastasis. This combined method takes into consideration the non-uniform dose distribution on the basis of tumor function and the radionuclide therapy dose delivered [111]. Combined chemotherapy and ^{131}I-Lipiodol for the treatment of hepatocellular carcinoma is being studied as mentioned above.

22.11 Summary

Radionuclide therapy is effective, safe and cost effective, and deserves consideration earlier in the management of cancer patients rather than being left as a terminal choice. Several radiopharmaceuticals are being used with varying degrees of success in treating several benign and malignant disease processes. The mechanisms of action are not entirely clear for all of them. Table 22.4 summarizes the probable mechanisms of action of the major radiopharmaceutical tracers currently used. More choices in radionuclide therapy are now available to physicians for local and systemic uses and for palliation and definitive therapy. Clinical acceptance is expected to increase as oncologists accept more the limitations of the curative and palliative role of chemotherapy and external radiation. The areas of research in the field of therapeutic nuclear medicine are wide open for developing new therapeutic radiopharmaceuticals and clinical applications

Table 22.4. Effects and mechanisms of action of therapeutic radiopharmaceuticals

Therapeutic procedure/ target	Probable mechanism
Hyperthyroid	Cell injury/death to reduce or ablate the thyroid gland
Thyroid cancer	Cell death to ablate residual thyroid tissue, tumor, and metastases
Synovectomy	Phagocytosis of radiolabeled colloid by synoviocytes which are distributed uniformly on the surface of the synovium, with subsequent destruction of the synovium by the beta particles
Radioimmunotherapy	Destruction of tumor cells through multiple mechanisms including cell lysis, formation of autoantibodies, and/or apoptosis
Painful bone metastases	Uptake of the radiopharmaceutical by metastases and/or surrounding bone, with radiation injury or death to the tumor cells or the surrounding cytokine-secreting cells
Peptide therapy	High expression of peptide receptor such as somatostatin and cholecystokinin by cells of specific tumors

References

1. Demeter S, Leslie WD, Levin DP (2005) Radioactive iodine therapy for malignant and benign thyroid disease: a Canadian national survey of physician practice. Nucl Med Commun 26:613 – 621
2. McKenzie JM, Zakrija M, Sato A (1978) Humoral immunity in Graves' disease. Clin Endocrinol Metab 7:31
3. Maxon HR, Thomas SR, Saenger EL, et al (1977) Ionizing irradiation and induction of clinically significant disease in human thyroid. Am J Med 63:967
4. Sofa AM, Skillern PG (1975) Treatment of hyperthyroidism with a large initial dose of sodium iodide I-131. Arch Intern Med 135:673
5. Woeber KA (2000) Update on the management of hyperthyroidism and hypothyroidism. Arch Intern Med 160:1067 – 1071
6. Hamburger JI (1980) Evaluation of toxicity in solitary nontoxic autonomously functioning thyroid nodules. J Clin Endocrinol Metab 50:1089 – 1093
7. Peter HJ, Studer H, Forster T, Herber H (1982) The pathogenesis of "hot" and "cold" follicle in multinodular goiters. J Clin Endocrinol Metab 55:941 – 946
8. Ginsberg J (2003) Diagnosis and management of Graves' disease. CMAJ 168:575 – 585
9. Bartalena L, Marcocci C, Bogazzi F, Manetti L, Tanda ML, Dell'Unto E, et al (1998) Relation between therapy for hyperthyroidism and the course of Graves' ophthalmopathy. N Eng J Med 338:73 – 78
10. Reid JR, Wheeler SF (2005) Hyperthyroidism: diagnosis and treatment. Am Famil Physician 72:623 – 630
11. Perros P, Kendall-Taylor P, Neoh C, Frewin S, Dickinson J (2005) A prospective study of the effects of radioiodine therapy for hyperthyroidism in patients with minimally active Graves' ophthalmopathy. J Clin Endocrinol Metab 90:5321 – 5323
12. Bartalena L, Marcocci C, Bogazzi F, Manetti L, Tanda ML, Dell'Unto E, et al (1998) Relation between therapy for hyperthyroidism and the course of Graves' ophthalmopathy. N Eng J Med 338:73 – 78
13. Maxon HR, Thomas SR, Chen IW (1981) The role of nuclear medicine in the treatment of hyperthyroidism and well differentiated thyroid adenocarcinoma. Clin Nucl Med 6:87 – 98
14. Sankar R, Sekhri T, Sripathy G, Walia RP, Jain SK (2005) Radioactive iodine therapy in Graves' hyperthyroidism: a prospective study from a tertiary referral center in North India. J Assoc Physicians India 53:603 – 606
15. Allahabadia A, Daykin J, Sheppard MC, Gough SC, Franklyn JA (2001) Radioiodine treatment of hyperthyroidism. Prognostic factors for outcome. J Clin Endocrinol Metab 86:3611 – 3617
16. Weetman AP (2000) Graves' disease. N Engl J Med 343:1236 – 1248
17. Terrier P, Sheng ZM, Schlumberger M, et al (1988) Structure and expression of c-*myc* and c-*fos* proto-oncogenes in thyroid carcinomas. Oncogene 2:403
18. Lemoine NR, Mayall ES, Wyllie FS, et al (1988) Activated *ras* oncogenes in human the thyroid cancers. Cancer Res 48:44 – 59
19. Atay-Rosenthal S (1999) Controversies on treatment of well-differentiated thyroid carcinoma and factors influ-

encing prognosis. In: Freeman L (ed) Nuclear medicine annual. Lippincott, Williams and Wilkins, Philadelphia, pp 303 – 334
20. Beierwaltes WH (1978) The treatment of thyroid carcinoma with radioiodine. Semin Nucl Med 8:79
21. Rosario PW, Barroso AL, Rezende LI, Padrao EL, Fagundes TA, Reis JS, Purisch S (2005) Outcome of ablation of thyroid remnants with 100 mCi (3.7 GBq) iodine-131 in patients with thyroid cancer. Ann Nucl Med 19:247 – 250
22. Kolfuerest S, Igerc I, Lind P (2005) Recombinant human thyrotropin is helpful in the follow up and I-131 therapy of patients with thyroid cancer: A report of the results and benefits using recombinant thryrotropin in clinical routine. Thyroid 15: 371 – 376
23. Intenzo CM, Jabbour S, Dam HQ, Capuzzi DM (2005) Changing concepts in the management of differentiated thyroid cancer. Semin Nucl Med 35:257 – 265
24. Fujie S, Okumura Y, Sato S, Akaki S, Katsui K, Himei K, Takemoto M, Kanazawa S (2005) Diagnostic capabilities of I-131, Tl-201, and Tc99m MIBI scintigraphy for metastatic differentiated thyroid carcinoma after total thyroidectomy. Acta Medica Okayama 59:99 – 107
25. Ferreira SH, Lorenzethi BB, Bristow AF, et al (1988) Interleukin-1 beta as a potent hyperalgesic agent antagonized by a tripeptide analogue. Nature 334:698 – 700
26. Poulson HS, Nielsen OS, Klee M, et al (1989) Palliative irradiation of bone metastases. Cancer Treatment Rev 16:41 – 48
27. Tong D, Gillick L, Hendrickson FR (1982) Palliation of symptomatic osseous metastases. Cancer 50:893 – 899
28. Salazar OM, Rubin P, Hendrickson FR, et al (1986) Single-dose half-body irradiation for palliation of multiple bone metastases from solid tumors. Final Radiation Therapy Oncology Group report. Cancer 58:29 – 36
29. Bauman G, Charette M, Reid R, Sathya J (2005) Radiopharmaceuticals for the palliation of painful bone metastasis – a systemic review. Radiother Oncol 75:258 – 270
30. Pauwels EKJ, Stokkel MPM (2001) Radiopharmaceuticals for bone lesions imaging and therapy in clinical practice. Q J Nucl Med 45:18 – 26
31. Giammarile F, Mognetti T, Resche I (2001) Bone pain palliation with strontium-89 in cancer patients with bone metastases. Q J Nucl Med 45:78 – 83
32. Patel BR, Flowers WM Jr (1997) Systemic radionuclide therapy with strontium chloride Sr-89 for painful skeletal metastases in prostate and breast cancer. Southern Med J 90:506 – 508
33. Papatheofanis FJ (2000) Decreased serum E-selectin concentration after 89Sr-chloride therapy for metastatic prostate cancer bone pain. J Nucl Med 41:1021 – 1024
34. Ramamoorthy N, Saraswathy P, Das MK, Mehra KS, Ananthakrishnan M (2002) Production logistics and radionuclidic purity aspects of 153Sm for radionuclide therapy. Nucl Med Commun 23:83 – 89
35. Cameron PJ, Klemp PF, Martindale AA, Turner JH (1999) Prospective 153Sm-EDTMP therapy dosimetry by whole-body scintigraphy. Nucl Med Commun 20:609 – 615
36. Maxon HR, Thomas S, Hertzberg VS, Schroder LE, Englaro EE, Samaratunga R, et al (1992) Rhenium-186 hydroxyethylidene diphosphonate for the treatment of painful osseous metastases. Semin Nucl Med 22:33 – 40
37. Han SH, De Klerk JM, Zonnenberg BA, Tan S, Van Rijk PP (2001) 186Re-etidronate. Efficacy of palliative radionuclide therapy for painful bone metastases. Q J Nucl Med 45:84 – 90
38. Kucuk NO, Ibis E, Aras G, Baltaci S, Ozalp G, Beduk Y, Canakci N, Soylu A (2000) Palliative analgesic effect of Re-186 HEDP in various cancer patients with bone metastases. Ann Nucl Med 14:239 – 245
39. Atkins HL, Mausner LF, Srivastava SC, Meinken GE, Cabahug CJ, D'Alessandro T (1995) Tin-117m (4+)-DTPA for palliation of pain from osseous metastases: a pilot study. J Nucl Med 36:725 – 929
40. Atkins HL, Mausner LF, Srivastava SC, Meinken GE, Straub RF, Cabahug CJ, et al (1993) Biodistribution of Sn-117m DTPA for palliative therapy of painful osseous metastases. Radiology 186:279 – 283
41. Bishayee A, Rao DV, Srivastava SC, Bouchet LG, Bolch WE, Howell RW (2000) Marrow-sparing effects of ^{117m}Sn-diethylenetriaminepentaacetic acid for radionuclide therapy of bone cancer. J Nucl Med 41:2043 – 2050
42. Blower PJ, Kettle AG, O'Doherty MJ, Coakley AJ, Knapp FF Jr (2000) 99mTc(V)DMSA quantitatively predicts 188Re(V)DMSA distribution in patients with prostate cancer metastatic to bone. Eur J Nucl Med 27:1405 – 1409
43. Krishnamurthy GT, Krishnamurthy S (2000) Radionuclides for metastatic bone pain palliation: a need for rational re-evaluation in the new millennium [comment]. J Nucl Med 41:688 – 691
44. Hoskin PJ, Ford HT, Harmer CL (1989) Hemibody irradiation (HBI) for metastatic bone pain in two histologically distinct groups of patients. Clin Oncol R Coll Radiol 1: 67 – 69
45. Fischer M (1998) I-131 therapy of neural crest tumors. Nucl Med Newslett (King Saud Univ) 5:9 – 10
46. Quilty PM, Kirk D, Bolger JJ, et al (1994) A comparison of the palliative effects of strontium-89 and external beam radiotherapy in metastatic prostate cancer. Radiother Oncol 31:33 – 40
47. Silberstein EB, Elgazzar AH, Kapilivsky A (1992) Phosphorus-32 radiopharmaceuticals for the treatment of painful osseous metastases. Semin Nucl Med 17:17 – 27
48. Maxon HR, Thomas SR, Hertzberg VS, et al (1982) Rhenium-186 hydroxyethylidene diphosphorate for the treatment of painful osseous metastases. Semin Nucl Med 22:30 – 40
49. Elgazzar AH, Maxon HR (1993) Radioisotope therapy for cancer related bone pain. Imaging Insights 2:1 – 6
50. Windsor PM (2001) Predictors of response to strontium-89 (Metastron) in skeletal metastases from prostate cancer: report of a single centre's 10-year experience. Clin Oncol (R Coll Radiol) 13:219 – 227
51. Dickie GJ, Macfarlane D (1999) Strontium and samarium therapy for bone metastases from prostate carcinoma. Australas Radiol 43:476 – 479
52. Sciuto R, Festa A, Pasqualoni R, Semprebene A, Rea S, Bergomi S, Maini CL (2001) Metastatic bone pain palliation with 89-Sr and 186-Re-HEDP in breast cancer patients. Breast Cancer Res Treat 66:101 – 109
53. Kvinnsland Y, Skretting A, Bruland OS (2001) Radionuclide therapy with bone-seeking compounds: Monte Carlo calculations of dose-volume histograms for bone marrow in trabecular bone. Phys Med Biol 46:1149 – 1161
54. Gelfand MJ, Elgazzar AH, Kriss VM, et al (1994) Iodine-123 MIBG SPECT versus planar imaging in children with neural crest tumors. J Nucl Med 35:1753 – 1757
55. Paltiel HJ, Gelfand MJ, Elgazzar AH, Washburn LC, et al (1994) Neural crest tumors: I-123 MIBG imaging. Radiology 190:117 – 121
56. Hoefnagel CA, deKraner J, Voute PA, Valdes Olmos RA (1991) Preoperative I-131 MIBG therapy in the management of neuroblastoma (abstract). J Nucl Med 32:921
57. Hoefnagel CA, deKraner J, Valdes Olmos RA, Voute PA (1994) I-131 MIBG as a first time treatment in high risk neuroblastoma patients. J Nucl Med 15:712 – 717
58. Mastrangelo R, Lasorell A, Troncone L, et al (1991) I-131 metaiodobenzylguanidine in neuroblastoma patients. J Nucl Med 35:248 – 251

59. Sisson JC, Shapiro B, Beirwaltes WH, et al (1984) Radiopharmaceutical treatment of malignant pheochromocytoma. J Nucl Med 25:197 – 206
60. Hoefnagel CA (1991) Radionuclide therapy revisited. Eur J Nucl Med 18:408 – 431
61. Taal BG, Hoefnagel CA, Vables Olmos RA, Boot H, Beijen JK (1996) Palliative effect of metaiodobenzylguanidine in metastatic carcinoid tumors. J Clin Oncol 14:1829 – 1839
62. Prvulovich EM, Stein RC, Bomanji JB, et al (1998) Iodine-131 MIBG therapy of a patient with carcinoid liver metastases. J Nucl Med 39:1743 – 1745
63. Press OW, Eary JF, Applelbaum FR, Martin PJ, Badger CC, Nelp WB, Glenn S, Buchko GM, Fisher LD, Porter B, et al (1993) Radiolabeled-antibody therapy of B-cell lymphoma with autologous bone marrow support. N Engl J Med 329:1219 – 1224
64. Press OW, Eary JF, Applbaum FR, Martin PJ, Nelp WB, Glenn S, Fisher DR, et al (1995) Phase II trial of I-131-B1 (anti-CD20) antibody therapy with autologous stem cell transplantation for relapsed B cell lymphomas. Lancet 346:336 – 340
65. De Nardo GL, De Nardo SJ, O'Grady LF, Levy NB, Adams GP, Mills SL (1990) Fractionated radioimmunotherapy of B-cell malignancies with I-131-Lym-1. Cancer Res 50:1014 – 1016
66. DeNardo GL, O'Donnell RT, Oldham RK, DeNardo SJ (1998) A revolution in the treatment of non-Hodgkin's lymphoma. Cancer Biother Radiopharm 13:213 – 223
67. Deutsch E, Brodack JW, Deutsch KF (1993) Radiation synovectomy revisited. Eur J Nucl Med 20:1113 – 1127
68. Gschwend N (1989) Synovectomy. In: Kelly WN, Harris ED, Ruddy S, et al (eds) Textbook of rheumatology. WB Saunders, Philadelphia, pp 1934 – 1961
69. Heim M, Goshen E, Amit Y, Martinowitz U (2001) Synoviorthesis with radioactive yttrium in haemophilia: Israel experience. Haemophilia 7 (Suppl 2):36 – 39
70. Rodriguez-Merchan EC, Jimenez-Yuste V, Villar A, Quintana M, Lopez-Cabarcos C, Hernandez-Navarro F (2001) Yttrium-90 synoviorthesis for chronic haemophilic synovitis: Madrid experience. Haemophilia 7 Suppl 2: 34 – 35
71. Onetti CM, Guyierrez F, Hiba E, et al (1982) Synoviorthesis with P-32 colloid chromic phosphate in rheumatoid arthritis and hemophilia, clinical, histopathological and arthographic changes. J Rheumatol 9:229 – 238
72. Rivard GE, Givard M, Belanger R, et al (1994) Synoviortheses with colloidal P-32 chromic phosphate for the treatment of hemophilic arthropathy. J Bone Joint Surg Am 76:482 – 487
73. Jeong JM, Lee YJ, Kim YJ, Chang YS, Lee DS, Chung JK, Song YW, Lee MC (2000) Preparation of rhenium-188-tin colloid as a radiation synovectomy agent and comparison with rhenium-188-sulfur colloid. Appl Radiat Isotopes 52:851 – 855
74. Siegel ME, Siegel HJ, Luck JV Jr (1997) Radiosynovectomy's clinical applications and cost effectiveness: A review. Semin Nucl Med 28:364 – 371
75. Ofluoglu S, Schwameis E, Zehetagruber I, Havlic E, Wanivenhaus A, Schweeger I, Weiss K, et al (2002) Radiation synovectomy with Ho-166-ferric hydroxide: A first experience. J Nucl Med 43:1489 – 1494
76. Fischer M, Modder G (2002) Radionuclide therapy of inflammatory joint disease. Nucl Med Commun 23:829 – 831
77. Hauss F (1992) Radiosynoviorthese in der Orthopadie. Akt Rheumatol 17:64 – 66
78. Paijit Asavatanabodee, et al (1997) Yttrium-90 radiochemical synovectomy in chronic knee synovitis: a one year retrospective review of 133 treatment interventions. J Rheumatol 24:639 – 642
79. Deutsch E, et al (1993) Radiation synovectomy revisited. Eur J Nucl Med 20:1113 – 1127
80. Kresnik E, Mikososch P, Gallowitsch HJ, Jesenko R, Just H, Kogler D, Gasser J, Heinisch M, Unterweger O, Kumnig G, Gomez I, Lind P (2002) Clinical outcome of radiosynoviorthesis: a meta-analysis including 2190 treated joints. Nucl Med Commun 23:683 – 688
81. Jong M, Kwekkeboom D, Volkema R, Krenning ER (2003) Radiolabelled peptides for tumor therapy: current status and future directions. Eur J Nucl Med 30:463 – 469
82. Capello A, Krenning E, Bernard B, Reubi J, Beerman W, de Jong M (2005) In-111-labelled somatostatin analogues in a rat tumour model: somatostatin receptor status and effects of peptide receptor radionuclide therapy. Eur J Nucl Med Mol Biol 32:1288 – 1295
83. Mazzaferi E (1997) Thyroid remnant I-131 ablation for papillary and follicular thyroid carcinoma. Thyroid 7: 265 – 271
84. Bruland OS, Skretting A, Solheim OP, Aas M (1996) Targeted radiotherapy of osteosarcoma using 153Sm-EDTMP. A new promising approach. Acta Oncologica 35:381 – 384
85. Franzius C, Bielack S, Sciuk J, Vollet B, Jurgens H, Schober O (1999) High-activity samarium-153-EDTMP therapy in unresectable osteosarcoma. Nucl Medizin 38:337 – 340
86. Aas M, Moe L, Gamlem H, Skretting A, Ottesen N, Bruland OS (1999) Internal radionuclide therapy of primary osteosarcoma in dogs, using 153Sm-ethylene-diamino-tetramethylene-phosphonate (EDTMP). Clin Cancer Res 5(10 Suppl):3148s–3152s
87. Boyouth JE, Macey DJ, Kasi LP, et al (1995) Pharmacokinetics, dosimetry and toxicity of holmium-166 DOTMP for bone marrow ablation multiple myeloma. J Nucl Med 36:730 – 737
88. Rajendran JG, Eary JF, Bensinger W, Durack LD, Vernon C, Fritzberg A (2002) High-dose 166Ho-DOTMP in myeloablative treatment of multiple myeloma: pharmacokinetics, biodistribution, and absorbed dose estimation. J Nucl Med 43:1383 – 1390
89. Alexanan R, Dimopoulos M (1994) The treatment of multiple myeloma. N Engl J Med 330:484 – 489
90. Barlogie B, Alexanian R, Dick KA, et al (1987) High dose chemotherapy and autologous bone marrow transplantation for resistant myeloma. Blood 70:869 – 872
91. Hoefnagel CA(1988) Radionuclide cancer therapy. Ann Nucl Med 12:61 – 70
92. Srivastava S, Dadachova E (2001) Recent advances in radionuclide therapy. Semin Nucl Med 31:330 – 341
93. Geldof AA, van den Tillaar PL, Newling DW, Teule GJ (1997) Radionuclide therapy for prostate cancer lumbar metastasis prolongs symptom-free survival in a rat model. Urology 49:795 – 801
94. Sundram FX, Yu SWK, Jeong JM, Somanesan S, Premaraj J, Saw MM, et al (2001) 188 Rhenium-TDD-lipiodol treatment of inoperable primary hepatocellular carcinoma – a case report. Ann Acad Med Singapore 30:542 – 545
95. Keng G, Sundram FX, Yu S, Somanesan S, Premaraj, Oon CJ et al. (2002) Preliminary experience in radionuclide therapy of hepatocellular carcinoma using hepatic intra-arterial radioconjugates. Ann Acad Med Singapore 31:3
96. Jong JM, Kim YJ, Lee YS, KO Jl, Son M, Lee DS, et al (2001) Lipiodol solution of a lipophilic agent, Re-188 TDD for the treatment of liver cancer. Nucl Med Biol 28:197 – 204
97. Buscombe JR, Padhy AK (2001) Treatment of hepatocellular carcinoma: a pivotal role for nuclear medicine? Nucl Med Commun 22:119 – 120
98. Sundram FX, Jiomg JM, Zanzonico P, Bernal P, Chau T, Onkhuudai P, Divgi C, Knapp FF Jr, Padhy AK (2002)

Trans-arterial rhenium-188 Lipiodol in the treatment of inoperable hepatocellular carcinoma – results of a multicentre phase-1 study. World J Nucl Med 1:5 – 11
99. Padhy AK, Bernal P (2001) A CD Rom on the preparation of Re-188 Lipiodol (Perth, Australia, April, 2001)
100. Sundram F, Chau TC, Onkhuudai P, Bernal P, Padhy AK (2004) Preliminary results of transarterial rhenium-188 HDD lipiodol in the treatment of inoperable primary hepatocellular carcinoma. Eur J Nucl Mol Imaging 31:250 – 257
101. Valdes Olmos RA, Hoefnagel CA (2004) Radionuclide therapy in oncology: the drawing of its concomitant use with other modalities? Eur J Nucl Med Mol Imaging 31:929 – 931
102. Bodey RK, Flux GD, Evans PM (2003) Combining dosimetry for targeted radionuclide and external beam therapies using the biologically effective dose. Cancer Biother Radiopharm 18:89 – 97
103. Logothetis C, Tu S, Navone N (2003) Targeting prostate cancer bone metastases. Cancer 07:758 – 788
104. Tu SM, Millikan RE, Menigistu B, et al (2001) Bone-targeted therapy for advanced androgen-independent carcinoma of the prostate: a randomized phase II trial. Lancet 357:336 – 341
105. Sciuto R, Festa A, Rea S, et al (2002) Effects of low dose cisplatin on Sr-89 therapy for painful bone metastases from prostate cancer: a randomized clinical trial. J Nucl Med 43:79 – 86
106. Horning SJ (2003) Future directions in radioimmunotherapy for B-cell lymphoma. Semin Oncol 30 (Suppl 17):29 – 34
107. Press OW, Unger JM, Braziel RM, et al (2003) A phase 2 trial of CHOP chemotherapy followed by tositumomab/iodine I-131 tositumomab for previously untreated non Hodgkin's lymphoma: Southwest Oncology Group Protocol S9911. Blood 102:1606 – 1612
108. Mastrangelo S, Tornesello A, Diociaiuti L, et al (2001) Treatment of advanced neuroblastoma; feasibility and therapeutic potential chemotherapeutic potential of a novel approach combining I-131-MIBG and multiple drug chemotherapy. Br J Cancer 84:460 – 464
109. Yanik GA, Levine JE, Matthay KK, et al (2002) Pilot study of iodine-131-metaiodobenzylguanidine in combination with myeloablative chemotherapy and autologous stem-cell support for the treatment of neuroblastoma. J Clin Oncol 20:2142 – 2149
110. Grana C, Chinol M, Robertson C, et al (2002) Pretargeted adjunct radioimmunotherapy with yttrium-90-biotin in malignant glioma patients: a pilot study. Br J Cancer 86:207 – 212
111. Bodey RK, Evans PM, Flux GD (2005) Targeted radionuclide therapy. Spatial aspects of combined modality radiotherapy. Radiother Oncol 77:301 – 309

23 Biological Effects of Ionizing Radiation

Abdelhamid H. Elgazzar, Nafisah Kazem

23.1 Introduction

The main tool in nuclear medicine is ionizing radiation; therefore it is important for its users to be familiar with its biological effects and pathophysiological basis. Ionization is the process of ion production by ejection of electrons from atoms and molecules after exposure to high temperature, electrical discharges or electromagnetic and nuclear radiation. Ionizing radiation is subdivided into electromagnetic radiation (X-rays and gamma rays) and particulate radiation including neutrons and charged particles (alpha and beta particles).

Exposure to ionizing radiation comes from several natural and man-made sources (Table 23.1). The nuclear medicine professional should be able to provide information to the patient and the public about the radiation risks from these sources and to provide a comparison of exposure from medical procedures to natural sources. Biological effects of ionizing radiation depend on several factors that make them variable and inconsistent. The effects are classified based on their nature and timing after exposure into early or delayed, somatic or hereditary, stochastic or deterministic (Fig. 23.1). Stochastic effects refer to random and unpredictable

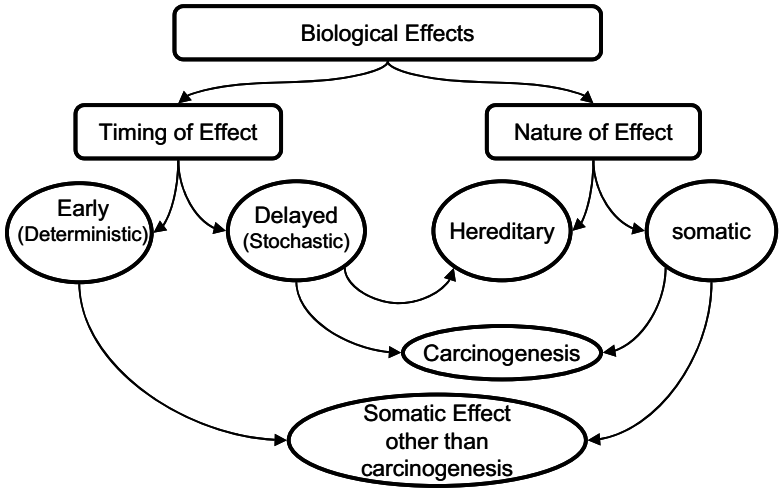

Fig. 23.1. The various biological effects of ionizing radiation. The effects can be classified into early or deterministic, which have a threshold, and delayed or stochastic, with no threshold. Effects are also classified into somatic and hereditary. The somatic include early and delayed effects (cancer)

Table 23.1. Sources of ionizing radiation

Natural sources	Man-made sources
External radiation – Cosmic rays – Terrestrial radiation (radioactive material in rocks, such as potassium-40) Internal radiation – Inhalation (Radon gas) – Ingestion	Medical Occupational Nuclear power Nuclear explosions Nuclear accidents

effects usually following chronic exposure to low dose radiation. Hereditary effects and carcinogenesis following diagnostic imaging is of a stochastic nature.

Deterministic (non-stochastic) effects are non-random and have a highly predictable response to radiation. There is a threshold of radiation dose after which the response is dose-related. Some of the known deterministic effects are radiation-induced lung fibrosis and cataract.

23.2 Mechanisms of Radiation Effects

Ionizing radiation exerts its effects on biological targets through two major mechanisms [1, 2], direct and indirect (Fig. 23.2).

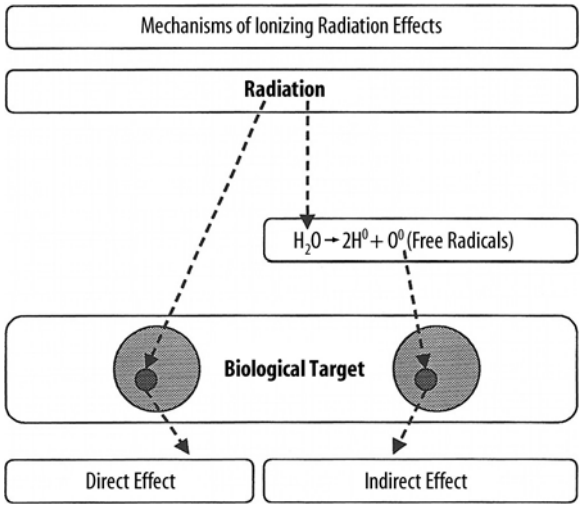

Fig. 23.2. The two mechanisms of ionizing radiation effects on biological tissue, the direct, or target, mechanism and the indirect, through production of free radicals that consequently cause damage

23.2.1 Direct Effect

The direct effect theory or target theory proposes that ionizing radiation acts by direct hits on target atoms. All atoms or molecules within the cells, such as enzymatic and structural proteins and RNA, are vulnerable to radiation injury. DNA, however, is the principal target, in which ionizing radiation produces single- or double-stranded chromosomal breaks.

23.2.2 Indirect Effect

The direct mechanism theory was found to be inadequate in explaining cellular radiation injuries. The indirect theory proposes that ionizing radiation exerts its effect via radiolysis of cellular water, forming free radicals. These free radicals interact with atoms and molecules within the cells, particularly DNA, to produce chemical modifications and consequently harmful effects. When X-rays interact with water two types of free radicals are formed:

$$H^o \rightarrow H^o \text{ (hydrogen)} + OH^o \text{ (hydroxy)}$$

The presence of an excess of oxygen during irradiation of cells allows the formation of additional free radicals:

$$H^o + O_2 \rightarrow HO_2^o \text{ (hydroxyperoxy free radicals)}$$
$$HO_2^o + HO_2^o \rightarrow H_2O_2^o + O_2$$

It is worth noting that antioxidants block hydroxyperoxy free radical combination into the highly unstable hydrogen peroxide.

It has been estimated that about two-thirds of biological damage caused by low linear energy transfer (LET) radiation is due to indirect action [3]. Biological damage by high LET is primarily by direct ionization action. Figure 23.3 illustrates how radiation leads to tissue damage.

Radiation effects have been observed in extents beyond that explained by effects exerted on directly irradiated cells. Cells in temporal or spatial distance from the initial radiation insult have been shown to have delayed effects of radiation. Two phenomena are described: the bystander effect and genomic instability.

Bystander Effect. The cells in the vicinity of irradiated cells show effects that cannot be attributed to targeting by ionizing radiation tracks. Additionally, when cells are irradiated and later transferred to another medium, the cells in proximity in the new medium exhibit DNA damage, mutation and carcinogenesis. Through cell-to-cell interaction, the directly irradiated cells communicate with adjacent cells and spread the effect of radiation to a larger number of cells. The mechanism

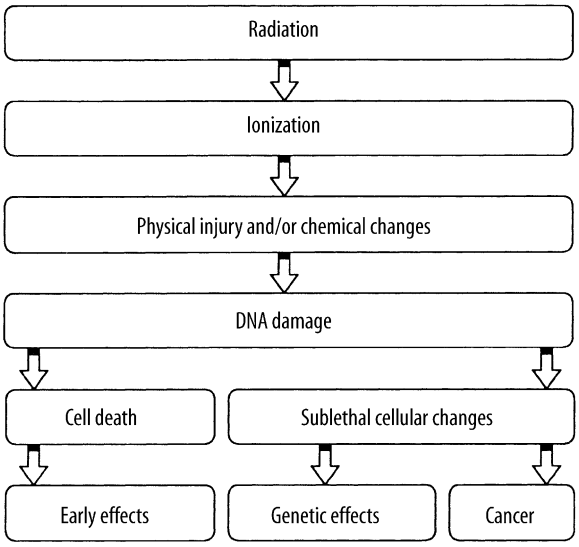

Fig. 23.3. Intracellular changes induced by ionizing radiation that lead to cell damage

is not clearly understood; however, gap junctional intercellular communication [4] or release of soluble factors (such as cytokines) [5] from irradiated cells has been proposed. The bystander effect has been mainly described for densely ionizing radiation (such as alpha particles) [6], but also is seen in low LET radiation (such as gamma or X-rays).

Genomic Instability. Maximal radiation-induced genetic damage is formed shortly (minutes to hours) after radiation exposure. Nevertheless, it has been observed that not only the irradiated cells but also descendents may show delayed effects. Cells that sustain non-lethal DNA damage show increased mutation rate in descendent cells several generations after the initial exposure [7]. Delayed effects include delayed reproductive death up to six generations following the primary insult [8].

23.3 Factors Affecting Radiation Hazards

Radiation injury can be modified by factors related to the ionizing radiation and the target tissue.

23.3.1 Factors Related to Ionizing Radiation

Certain factors related to radiation itself determine the various effects for the same radiation dose to biological organs.

Type of Radiation. Various types of radiation differ in penetrability based on LET, which expresses energy loss per unit distance travelled (kiloelectron volts per micrometer). This value is high for alpha particles, lower for beta particles, and even less for gamma rays and X-rays. Thus alpha particles penetrate a short distance but induce heavy damage, whereas beta particles travel a longer distance but much shorter than gamma rays.

Mode of Administration. The radiation dose is obviously an important factor. In addition, a single dose of radiation causes more damage than the same dose being divided (fractionated). Collectively these two factors are expressed as dose per fraction.

Dose Rate. Dose rate expresses the time for which dose is administered. The longer the duration for the same total dose, the better the chance of cellular repair and the smaller the damage.

23.3.2 Factors Related to Biological Target

Certain properties of tissues and cells can significantly modify the biological effects of ionizing radiation.

Radiosensitivity. Although all cells can be affected by ionizing radiation, normal cells and their tumors vary in their sensitivity to radiation. Slowly and rapidly growing cells have different radiosensitivity in relation to their movement through the cell cycle. Radiosensitivity varies with the rate of mitosis and cellular maturity. Blood-forming cells are very sensitive to radiation, while neurons, muscle and parathyroid cells are highly radioresistant. Within a given cell, the nucleus in general is relatively more radiosensitive than the cytoplasm. When cells in G_0/G_1 phase of the cell cycle are exposed to radiation they tend to halt their progression into G_2/M phase. G_2 synchronization produces a cluster of radiosensitive cells. A second hit within a time frame of 5–12 h leads to a higher proportion of deleterious effects. This is expected for radioisotopes with sequential alpha or beta decay as in $^{90}Sr/^{90}Y$ [9].

Repair Capacity of Cells. Some cells are known to have a higher capacity than others to repair the damage caused by ionizing radiation; consequently, the biological effects of the same radiation dose are different. Significant repair is known to occur quickly, within 3 h.

Cell-Cycle Phase. The life cycle of the cell includes several phases: the pre-DNA synthetic phase (G_1), the DNA synthetic phase (S), the post-DNA synthetic phase (G_2), mitosis (M), and the more recently identified phase of no growth (0), which represents the time after mitosis to the start of the G_1 phase. All phases of the cell cycle can be affected by ionizing radiation. The radiosensitivity of a given cell varies from one cell-cycle phase to another. Overall, sensitivity appears to be

greatest in G_2 phase; irradiation during this phase retards the onset of cell division. Irradiation during mitosis induces chromosomal aberrations, i.e., breaks, deletions, translocations, and others. The sensitivity of a given cell-cycle phase also differs from one cell type to another and by alteration of radiation injury [3]. For example, the reproductive cells are most sensitive during the M phase, while damage to DNA synthesis and chromosomes occurs mostly when the cell is in the G_2 phase. Recovery from sublethal damage occurs in all phases of the cell cycle. However, this is most pronounced in the S phase, which is also the most radioresistant phase [10].

Degree of Tissue Oxygenation. Molecular oxygen is known to have the ability to potentiate the response to radiation; this is known as the oxygen effect. The amount of molecular oxygen rather than the rate of oxygen utilization by the cells is the most important factor for increasing the sensitivity of cells to radiation. The probable mechanism is the allowance of additional free radicals, which enhance the damage of cells [10].

23.4 Radiation-Induced Cell Injury

In general, an injury which has a high chance of repair is sublethal, that which can be repaired with treatment is potentially lethal, and that which is permanent is lethal. The nucleus is relatively more radiosensitive than the cytoplasmic structures. Nuclear changes after radiation include swelling of the nuclear membrane and disruption of chromatin materials. Cytoplasmic changes include swelling, vacuolization, disintegration of mitochondria and endoplasmic reticulum, and reduction in the number of polysomes [2, 10]. Depending on the dose of radiation and the subcellular changes, along with the previously described factors, the potential effects on the cell vary (Table 23.2). After ionizing radiation exposure, cellular injury occurs in one of the following forms [11]:

1. Division delay: after exposure to radiation in the range of 0.5 – 3 Gy delayed mitosis is observed; however, near normal restoration of mitotic activity is achieved following several generations.
2. Reproductive failure: the failed mitotic activity is permanent and eventually cell death ensues. This is observed in a linear fashion after exposure to more than 1.5 Gy. Below this level the reproductive failure is random in nature and nonlinear.
3. Interphase death: apoptosis, or programmed cell death, is defined as a particular set of microscopic changes associated with cell death. Radiation-induced apoptosis is highly related to the type of involved cell. Lymphocytes, for example, are highly susceptible to radiation by this mechanism.

23.5 Various Effects of Radiation

The biological effect of low-level radiation is extremely difficult to study in a controlled environment. The effects of high radiation exposure to populations during accidents or nuclear war have been the main source of information.

At low doses, radiation can trigger only partially understood effects that can lead to cancer or genetic damage. These effects take years or generations to appear. At high doses, the effect may become evident within minutes, hours, or days. It is important for physicians to be familiar with the early effects of high radiation doses (1 Gy or more to the whole body), since the possibility that people may be exposed to such doses is increasing.

23.5.1 Dose-Response Models

There are many models predicting relationships between the radiation dose and the effect of such an exposure to a biological target. The differences between these models arise from different underlying assump-

Table 23.2. Types of cellular damage in relation to approximate radiation dose. (Modified from [3] with permission)

Dose [Grays (rads)]	Type of damage	Comments
0.01 – 0.05 (1 – 5)	Mutation (chromosomal aberration, gene damage)	Irreversible chromosome breaks, may repair
1 (100)	Mitotic delay, impaired cell function	Reversible
3 (300)	Permanent mitotic inhibition, impaired cell function, activation and deactivation of cellular genes and oncogenes	Certain functions may repair; one or more divisions may occur
>4 – 10 (>400 – 1000)	Interphase death	No division
500 (50,000)	Instant death	No division Proteins coagulate

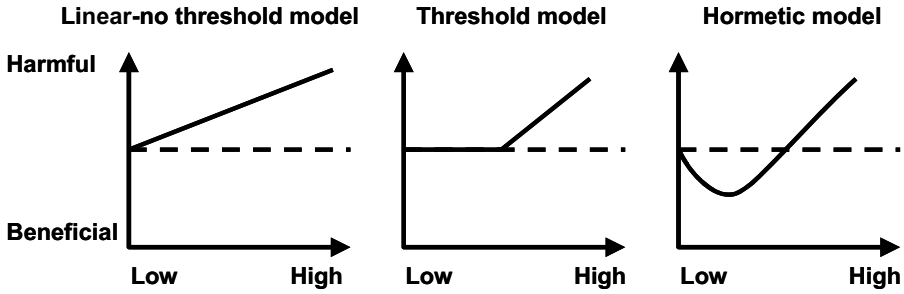

Fig. 23.4. Comparison between three different dose-response models. The *dashed line* represents health effects in the absence of radiation. *y*- and *x*-axes represent health effects and radiation dose, respectively. (Reproduced from [12] with permission)

tions. Figure 23.4 illustrates three models describing the response of a biological system to various radiation doses.

1. Linear-No Threshold Model. This model assumes that any level of radiation is harmful and that the risk increases linearly with increments of dose. This model is applied for radiation protection purposes and is meant to limit the risk to workers in radiation fields.
2. Threshold Model. This model assumes that the risk of radiation is linearly related to the dose; however, this occurs only after a certain threshold level is exceeded. Below the threshold level no risk is to be expected. The theory behind the threshold level is that some degree of cellular damage should accumulate and produce cell damage.
3. Hormesis Model. In this model there is a bimodal effect of radiation, where below a certain threshold level radiation is protective, and harmful effects are seen only when this threshold is exceeded. The rationale is that radiation at low levels induces protective cellular mechanisms which prevent DNA damage occurring spontaneously or due to other stresses [13, 14] (Fig. 23.5).

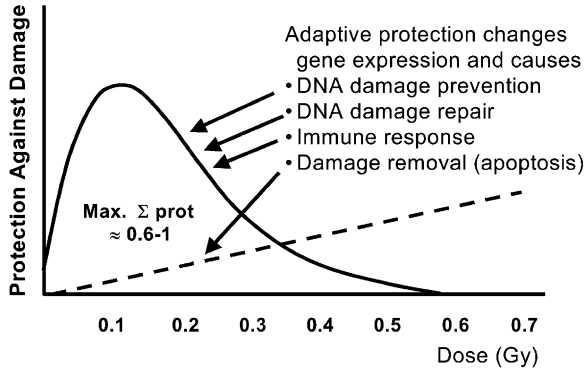

Fig. 23.5. Low-dose (low-LET) induced adaptive protection. Scheme of dose response function. (Reproduced with permission from [15])

23.5.2 Early Radiation Effects

23.5.2.1 Acute Whole-Body Exposure Syndromes

Following exposure to a large, single, short-term whole-body dose of ionizing radiation, the resulting injury is expressed as a series of clinical symptoms. The sequence of events can be generally divided into four clinical periods:

1. The prodromal period, up to 48 h, when the symptoms include anorexia, nausea, vomiting, and diarrhea
2. The latent period, from 48 h to 2 – 3 weeks after exposure, when the patient becomes asymptomatic
3. The manifest phase, from week 6 to week 8 after exposure, when variable symptoms appear based on the radiation dose
4. The recovery period: if the patient survives, recovery occurs from 6 weeks to several months after exposure.

The presentation of these periods and their duration depends on the amount of radiation exposure [2, 3]. In general, about half of those who receive doses of 2 Gy suffer vomiting within 3 h, and symptoms are rare after doses below 1 Gy. With a sufficiently high radiation dose, acute radiation sickness may result. Additional symptoms related to specific organ injury may occur, based on the dose, and can be divided according to the known acute radiation syndromes:

Radiation Sickness. The symptoms can be mild, such as loss of appetite and mild fatigue, or evident only on laboratory tests with mild lymphopenia (subclinical), or may be severe, appearing as early as 5 min after exposure to very high doses of 10 Gy or more and also include fatigue, sweating, fever, apathy, and low blood pressure. Lower doses delay the onset of symptoms and produce less severe symptoms or a subclinical syndrome that can occur with doses of less than 2 Gy to the whole body, and recovery is complete with 100% survival.

Hematopoietic (Bone Marrow) Syndrome. This occurs at higher doses of more than 1.5 – 2 Gy to the whole

body. With doses up to 4 Gy, a radiation prodrome is seen, followed by a latent period of up to 3 weeks. The clinical effects are not seen for several weeks after the radiation dose, when anemia, petechiae, increased blood pressure, fatigue, ulceration in the mouth, epilation, purpura, and/or infection appear. At doses in the order of 4 – 8 Gy, a modified bone marrow syndrome occurs. The initial problem is more severe, the latest period is shortened, and the manifest illness is more severe. Death is possible due to bleeding with exposure in this dose range.

Gastrointestinal Syndrome. This syndrome occurs with still higher doses of 6 – 10 Gy which cause manifestations related to the gastrointestinal tract in addition to those of the bone marrow syndrome. Initially, loss of appetite, apathy, nausea, and vomiting occur for 2 – 8 h. These effects may subside rapidly. Several days later, malaise, anorexia, nausea, vomiting, high fever, persistent diarrhea, abdominal distention, and infections appear. During the second week of irradiation, severe dehydration, hemoconcentration, and circulatory collapse may be seen, eventually leading to death.

Central Nervous System Syndrome. The central nervous system is generally resistant to radiation effects. A dose higher than 10 Gy is required to cause substantial effects on the brain and the nervous system. Symptoms include intractable nausea and vomiting, confusion, convulsions, coma, and absent lymphocytes. The prognosis is poor, with death in a few days.

23.5.2.2 Acute Regional Effects

When enough radiation is delivered locally to a certain part of the body, as in the case of radiation therapy, which focuses on a certain field, acute effects can appear in the exposed area. Examples include skin erythema and gastrointestinal edema and ulceration.

23.5.3 Delayed Radiation Effects

There is considerable debate over the effects of low level radiation. On the one hand, there are several theories and reports describing the harmful effects of low level radiation and how underestimated the risks are. At the other extreme, there are theories and reports of harmless and even potentially useful effects of exposure to such levels of radiation.

The theories describing the effects of low level radiation and the projected risk estimates of cancer development or genetic effects in humans are purely mathematical and not actual observations. The data from populations exposed to high level radiation were extrapolated to determine the likelihood of these events at low level radiation exposure. Such events in any given population occur at extremely low rates and to further complicate the issue after long latency periods; therefore solid epidemiological data are difficult to obtain.

23.5.3.1 Cancer

Cancer is the most important concern of radiation. It has been recognized for more than 90 years that ionizing radiation causes cancers. Tissues with a high rate of cell proliferation are more prone to radiation tumor induction. Cancer becomes evident only long after the first damage is done, following a period of latency. Leukemia first appears at least 2 – 5 years after exposure while solid tumors appear after at least 10 years, often several decades later. The tumors reported to be associated with radiation include leukemia, multiple myeloma, and cancers of the breast, colon, thyroid, ovary, lung, urinary bladder, stomach, CNS (other than brain), and esophagus.

There is no clear evidence that low-level radiation causes cancer. Holm et al. [16] studied 6000 patients given a diagnostic dose of iodine-131. There was no increase in the incidence of thyroid cancer in this population, including a subset of 2000 children. Saenger et al. [17] also studied 2000 patients treated with iodine-131 in doses of up to several hundreds of MBq with 20 years follow-up. The incidences of thyroid cancer and leukemia were identical to those among patients treated surgically for the same conditions.

To complicate the issue further, recently acquired data minimize the effects of low-level radiation in the induction of cancer and even suggest that such levels of radiation exposure may be useful [18, 19]. DNA mutations unrelated to radiation are produced continuously. It is estimated that each day the intrinsic human metabolism produces 240,000 DNA mutations in each cell of the body [20]. During youth, these are repaired and, in general, cancer occurs infrequently. With old age, the capability to repair may decrease and cancer appears more frequently. A high dose of 2 Gy adds 4000 (20 mutations/cGy) to the daily 240,000 mutations. Ward [10, 21] determined that a low radiation dose of 0.2 Gy stimulates repair by 50% – 100% and adds only 400 mutations to the intrinsic 240,000 mutations. It is the reduced ability of our repair mechanism to correct the very high background of intrinsic mutations that increases the risk of developing cancer. Genetic impairment of DNA repair capacity results in death from cancer at an early age. Loss of DNA repair capacity with age increases the risk of cancer. Exposure to high doses of radiation similarly reduces the repair capacity of cellular DNA and increases the risk of cancer [22, 23] (see chapter on oncology).

23.5.3.2 Genetic Effects

Genetic effects may include changes in the number and structure of chromosomes and gene mutations, dominant or recessive. They depend on the following factors:

1. The stage of germ cell development: Immature germ cells appear to be capable of repair, while in mature germ cells there is little or no repair (Table 23.3).
2. Dose rate: The repair process starts simultaneously with radiation damage. The damage with a high dose rate is greater; lower dose rates produce fewer mutations. At a low-intermediate dose rate the time period is an important factor as far as the final outcome of the radiation injuries is concerned. However, this does not hold true in the case of a high radiation rate, where the repair process is minimal due to the direct action of injury.
3. Dose fractionation: The time interval between fractions is very important for the frequency of mutations. The number of translocations will be reduced by dose fractionation; however, the incidence of mutations will not be affected by increasing the time interval between fractions.
4. Interval between exposure and conception: The frequency of mutation is very low if conception occurs after 7 weeks, but it is high when the interval between radiation exposure and conception is 7 weeks or less.

23.5.3.3 Effects on the Unborn Child

The embryonic stage is one of the most radiosensitive stages in the life of any organism. The classical triad of effects of radiation on the embryo is growth retardation, embryonic, fetal, or neonatal death, and congenital malformation. The probability of finding one or more of these effects is dependent upon radiation dose, the dose rate, and the stage of gestation at exposure. Stage of development is particularly important, since the organ which is differentiated at that time will be most vulnerable; this determines the type of abnormality or malformation that will be observed. During the first 2 weeks of conception the effect of radiation is an all or none effect, where the embryo is aborted. Following this period and up to 8 weeks the embryo is very vulnerable to congenital malformations. Organogenesis starting then might lead to mental retardation, congenital malformation as well as organ-specific effects. For example, radioactive iodine administered to a pregnant mother who passed 10 – 13 weeks of gestation will cross the placenta and accumulate in the already formed fetal thyroid. A summary of the possible effects from irradiation at various stages of gestation is shown in Table 23.3.

Table 23.3. Effects of radiation on the unborn child

Stage of gestation (days)	Possible effects
1 – 9	Death of embryo is most likely, with little chance of malformation
10 – 12	Reduced lethal effect with still little chance of malformation
13 – 56	Production of congenital malformation and retarded growth
57 – 112	Extreme mental retardation (time of most severe effect on CNS)
113 – 175	Less frequent effect on CNS
After 175	Very low frequency of CNS effects (no reported case of severe retardation)

Development of cancer at an early age is controversial. Studies have suggested an increased risk of hematopoietic and solid tumors at an early age [24, 25]. However, a comparison between individuals whose parents were exposed to radiation during the atomic bombing of Hiroshima and Nagasaki and those whose parents were not showed no significant differences in a large number of variables including congenital effects, still births, and cancer at an early age.

23.5.3.4 Other Delayed Somatic Effects

Cataract. Chronic and acute exposure of the eyes can lead to cataracts secondary to inducing lens fiber disorganization. Not all radiation is equally effective in producing cataracts; neutrons are much more efficient than other types of radiation. In man the cataractogenic threshold is estimated at 2 – 5 Gy as a single dose or 10 Gy as a fractionated dose. The period between exposure and the appearance of the lens opacities averages 2 – 3 years, ranging from 10 months to more than 30 years [26, 27].

Hypothyroidism. The thyroid gland is exposed to irradiation during radiation therapy of malignant head and neck tumors or the treatment of hyperthyroidism with iodine-131. Patients who received doses of 10 – 40 Gy to the thyroid for the treatment of other malignant diseases developed hypothyroidism a few months to many years after exposure. A lower moderate dose of 10 – 20 Gy can result in hypothyroidism, while 500 Gy or more is required to destroy the thyroid completely.

Aplastic Anemia. Human exposure to radiation can cause aplastic anemia, depending upon the dose and fractionation. Death may be the end result of aplastic anemia. It has been suggested that permanent anemia

is caused by a reduced capability of cellular proliferation due to accumulation of residual injury in stem cells. It is important to realize that when part of the body is irradiated, bone marrow that survives unimpaired will replace what is damaged. If only 10% of active bone marrow escapes irradiation, mortality can be decreased from 50% to zero, based on animal studies.

23.6 Exposure from Medical Procedures

For medical radiation, the chest X-ray delivers 0.1 – 0.2 mSv to the chest wall and the gallbladder series approximately 0.25 rem (Table 23.4). The average nuclear medicine procedure delivers 3 mSv to the whole body. The absorbed dose from the C-14 urea breath test is equivalent to that received during a 1-h flight. When these values are compared with those of natural sources of radiation, particularly cosmic rays, which deliver an average of 3.6 mSv/year in the United States and are higher in certain areas, the real magnitude of the low level of radiation can be appreciated. These levels of exposure from diagnostic medical procedures have no detectable biological effects. It is estimated that less than 0.006% of those undergoing nuclear medicine procedures in the United States might be affected annually. PET studies deliver higher doses to the patient to compensate for the short half-life of positron-emitting radioisotopes. Because these radioisotopes are of high energy and prepared in high initial dosing to account for the rapid decay, PET technologists, radiopharmacists and workers at cyclotrons are usually exposed to higher doses than other workers in the nuclear medicine field.

Therapeutic applications of radioisotopes involve not only malignant but also benign conditions, such as hyperthyroidism and arthroplasty, and are widely expanding. In the treatment of thyroid cancer, large doses of iodine-131 may cause depression of bone marrow. For example, 3.7 GBq of iodine-131 delivers 0.5 – 1 Gy to the hematopoietic system, simulating an effect of external whole body radiation.

Table 23.4. Absorbed radiation dose from common natural and medical sources

Source	Radiation dose [mSv (mrem)]
Diagnostic X-ray procedures	
Chest X-ray	0.1 – 0.2 (10 – 20)
Intravenous pyelogram	2.5 (250)
Mammography (one film)	4 (400)
Gallbladder series	5.3 (530)
Panoramic dental X-ray	9 (900)
X-ray CT of the head	58 (5800)
Barium enema series	80 (8000)
Diagnostic nuclear medicine procedures	
^{99m}Tc-DTPA lung ventilation study	0.15 – 0.25 (15 – 25)
^{99m}Tc-MAA lung perfusion study	1.1 (110)
^{99m}Tc-MDP bone scan (20 mCi)	3.6 (360)
^{201}Tl study (2 mCi)	5 (500)
Natural sources	
Two-hour flight	0.05 (5)
Drinking water	0.05 (5)
Natural gas at home (mainly radon)	0.09 (9)
Radionuclide in human body	0.39 (39)
Cosmic radiation	
at sea level)	0.36 (36)
at 2000 m)	5 (500)

23.7 Possible Positive Health Effects

Recently, positive health effects have been noted, i.e., decreased mortality and decreased cancer rates, in human populations exposed to low-level radiation and reported in large studies [28, 29]. Several studies were carried out to compare areas of high background to those with low radiation. Lower cancer incidence and/or mortality rates in the former were the finding in many such studies in China [30], India [31], Iran [32] and the USA [33]. It has to be noted, however, that this form of epidemiological study does not compare the individual's radiation exposure to cancer rate; therefore strong conclusions cannot be based solely on such studies. On the other hand, none of these studies has found a higher cancer incidence in high background radiation zones. An epidemiological study [34] comparing cancer mortality in Canada's nuclear industry workers to that in non-radiation workers has found similar favorable effects for low-radiation exposure. The former group of workers had a cancer mortality of 58% of the national average as compared to 97% of that in the latter. Cohen [11] studied the relationship between lung cancer death rates and residential radon gas in the USA. He found that lung cancer decreased for increments in radon levels. These findings were consistent even after reanalysis and correction for confounding factors such as smoking. To date, there is considerable debate regarding this study.

23.8 Summary

Several biological effects can result from ionizing radiation. These can be due to direct or indirect mechanisms, and they can be acute or delayed. Acute effects occur with exposure to high-level radiation. Delayed effects may appear after a long time and include cancer, genetic effects, effects on the unborn child, and other effects such as cataracts and hypothyroidism. Based on

our current knowledge, no level of exposure to radiation can be described as absolutely safe and no level is uniformly dangerous. Radiation doses have to reach a certain level to produce acute injury but not to cause cancer or genetic damage. No biological effects in individuals have ever been documented as being due to levels of ionizing radiation employed for medical diagnosis. Absorbed doses from nuclear medicine procedures are very low. Fear of radiation must not be permitted to undermine the great value of radiation in clinical practice. However, safe handling of all levels of radiation is important to prevent or minimize possible biological effects.

References

1. United Nations Environment Program (1988) Radiation: doses, effects, risks. Blackwell, Oxford, pp 65 – 84
2. Cotran RS, Kumar V, Collins T (eds) (1999) In: Robbins pathologic basis of disease, 5th edn. Saunders, Philadelphia, pp 50 – 88
3. Prasad KN (1995) Handbook of radiobiology, 2nd edn. CRC Press, Boca Raton
4. Azzam EI, de Toledo SM, Little JB (2001) Direct evidence for the participation of gap junction-mediated intercellular communication in the transmission of damage signals from alpha-particle irradiated to nonirradiated cells. Proc Natl Acad Sci U S A 98:473 – 478
5. Ramesh R, Marrogi AJ, Munshi A, Abboud CN, Freeman SM (1996) In vivo analysis of the 'bystander effect': a cytokine cascade. Exp Hematol 24:829 – 838
6. Iyer R, Lehnert BE (2000) Factors underlying the cell growth-related bystander responses to α-particles. Cancer Res 60:1290 – 1298
7. Morgan WF (2003) Non-targeted and delayed effects of exposure to ionizing radiation: II. Radiation-induced genomic instability and bystander effects in vivo, clastogenic factors and transgenerational effects. Radiat Res 59:581 – 596
8. Suzuki K, Ojima M, Kodama S, Watanabe M (2003) Radiation-induced DNA damage and delayed induced genomic instability. Oncogene 13;22:6988 – 6993
9. Kendall GM (2000) Second-event theory reviewed. J Radiol Prot 20:79 – 80
10. Ward JF (1988) DNA damage produced by ionizing radiation in mammalian cells: identities, mechanisms of formation, and reparability. Prog Nucl Acid Res Mol Biol 35:95
11. Bolus NE (2001) Basic review of radiation biology and terminology. J Nucl Med Technol 29:67 – 73
12. Ernest M, Freed ME, Zametkin AJ (1996) Health hazards of radiation exposure in the context of brain imaging research: special consideration for children. J Nucl Med 39:689 – 698
13. Johansson L (2003) Hormesis, an update of the present position. Eur J Nucl Med Mol Imaging 30:921 – 933
14. Feinendegen LE (2005) Low doses of ionizing radiation: relationship between biological benefit and damage induction. A Synopsis. World J Nucl Med 4:21 – 34
15. Feinenegen LE (2005) Evidence for beneficial low level radiation effects and radiation hormesis. Br J Radiol 78:3 – 7
16. Holm I, Hall P, Wiklund K, et al (1991) Cancer risk after iodine-131 therapy for hyperthyroidism. J Natl Cancer Inst 83:1072
17. Saenger EL, Thomas GE, Tompkins EA (1968) Incidence of leukemia following treatment of hyperthyroidism. Preliminary report of the cooperative thyrotoxicosis therapy follow-up study. JAMA 205:855
18. Matanoski GM (1991) Health effects of low-level radiation in shipyard workers: final report. DOE DE-AC0279 EV10095
19. Cameron J (1992) The good news about low-level radiation exposure: health effects of low-level radiation in shipyard workers. Health Phys Soc Newslett 20:9
20. Billen D (1990) Spontaneous DNA damage and its significance for the "negligible dose" controversy in radiation protection. Radiat Res 124:242
21. Ward JF (1987) Radiation chemical methods of cell death. In: Fielden EM, Fowler JF, Hendry JH, Scott D (eds) Proceedings of the 8th international congress of radiation research, vol II. Taylor and Francis, London, pp 162 – 168
22. Quingyi W (1993) DNA repair and aging in basal cell carcinoma: a molecular epidemiology study. Proc Natl Acad Sci USA 90:1614
23. Koshland DE, Sancar A, Hanawalt PC, Modrich P (1994) DNA repair enzymes and mechanisms. Science 266:1925 – 1927
24. Kneala GW, Sterwart AM (1976) Mantil-Haenzel analysis of Oxford data. II. Independent effects of fetal irradiation subfactors. J Natl Cancer Inst 57:1009
25. Committee on the Biological Effects of Ionizing Radiations (1980) The effects on population of exposure to low levels of ionizing radiation. National Academic Press, Washington DC
26. International Commission on Radiological Protection, Radiosensitivity and Spatial Distribution of Dose (1969) Publication no 14. Pergamon, Oxford
27. Dodo T (1975) Cataract. J Radiat Res Suppl 16:132
28. Cohen BL (1995) Test of the linear-no threshold theory of radiation carcinogenesis in the low dose rate region. Health Phys 68:157
29. UNSCEAR (United Nations Scientific Committee on the Effects of Atomic Radiation) (1994) Annex B: adaptive responses to radiation in cells and organisms. Document A/Ac. 82/R.542, approved 11 March 1994
30. High Background Radiation Research Group (1980) Health survey in high background radiation areas in China. Science 209:877 – 880
31. Nambi KS, Soman SD (1987) Environmental radiation and cancer in India. Health Phys 52:653 – 657
32. Ghiassi-Nejad M, Mortazavi SMJ, Cameron JR, Niroomand-Rad A, Karam PA (2002) Very high background radiation areas of Ramsar, Iran: preliminary biological studies. Health Phys 82:87 – 93
33. Jagger J (1998) Natural background radiation and cancer death in Rocky Mountain states and Gulf Coast states. Health Phys 75:428 – 430
34. Cohen BJ (1995) Test of the linear-no threshold theory of radiation carcinogenesis for inhaled radon products. Health Phys 68:157 – 174

Glossary

Abscess: A collection of pus in tissues, organs, or confined spaces, usually caused by bacterial infection.

Absorbed dose: Amount of energy absorbed per unit mass of target material.

ALARA: „As low as reasonably achievable". A concept recommended by the US national regulatory commission for safe radiation practice.

Amplitude image: A computer generated image representing analysis of a process whereby each pixel in the heart is evaluated with respect to movement changes over time. The amplitude image shows the magnitude of blood ejected from each pixel within the ventricular chamber.

Anion: Negatively charged ion.

Ankylosing spondylitis: The most common type of spondyloarthropathy with chronic inflammatory changes leading to stiffening and fusion (ankylosis) of the spine and sacroiliac joints with a strong genetic predisposition associated with HLA B27. Other joints such as hips, knees and shoulders are involved in approximately 30% of patients.

Antibody: A protein formed by the body to defend it against infection and other diseases.

Antisense oligonucleotides: Synthetic single-strand DNA (or RNA) molecules designed to bind with high affinity to the complementary sequences of mRNA. Several antisense oligodeoxynucleotide pharmaceuticals have been developed as therapeutic agents that act to block protein synthesis by inactivating mRNA. This is the basis of antisense imaging.

Apophysis: An accessory secondary ossification center that develops late and forms a protrusion from the growing bone where tendons and ligaments insert or originate.

Apoptosis: A type (programmed) of cell death implicated in both normal and pathological tissue, designed to eliminate unwanted host cells in an active process of cellular self-destruction effected by a dedicated set of gene products.

Atrophy: A decrease in size and function of the cell.

Attenuation: The reduction of radiation intensity during its passage through matter due to absorption, scatter or both.

Avulsion: Complete separation of tendons or ligaments, with or without a portion of bone and/or cartilage.

Behçet's syndrome: An uncommon disorder characterized by recurrent oral and genital ulceration, uveitis, or retinal vasculitis, cutaneous pustules or erythema nodosum or cutaneous pathergy and synovitis. The disease is more common in Mediterranean countries and Japan than in the United States.

Biologic half-life: Time required for half of the radioactivity to be eliminated from the body or an organ.

Brodie's abscess: An intraosseous abscess in the cortex that becomes walled off by reactive bone.

Bronchial circulation: Part of the high pressure systemic circulation that supplies oxygenated blood to the lung tissue itself.

Budd-Chiari syndrome: An uncommon condition usually caused by thrombosis of the hepatic veins such as associated with polycythemia vera, following oral contraceptive use or renal cell carcinoma with tumor involving veins. Sulfur colloid liver scan typically shows decreased uptake in the right lobe with increased uptake in the caudate lobe representing hypertrophy of that lobe.

Bystander effect: The directly irradiated cells communicate with adjacent cells and spread the effect of radiation to a larger number of cells.

Calcinosis cutis: A term used to describe a group of disorders in which calcium deposits form in the skin, subcutaneous tissue and connective tissue sheaths around the muscles but not within the muscles.

Calciphylaxis: A condition of soft tissue calcification affecting mainly patients with chronic renal failure. The calcification involves the media of small and medium sized cutaneous arterioles with extensive intimal hyperplasia and fibrosis. There is also subcutaneous calcification and necrosis which may lead to sepsis, the main cause of morbidity which may be significant.

Cation: Positively charged ion.

Chemotaxis: Directional migration of leukocytes at varying rates of speed in interstitial tissue towards a chemotactic stimulus in the inflammatory focus. Through chemoreceptors at multiple locations on their plasma membranes, the cells are able to detect where the highest concentrations are of chemotactic factors and to migrate in their direction.

Costochondritis (Tietze's syndrome): This is a common painful condition affecting the costochondral junction usually in young patients and is self limited. The etiology remains unknown although trauma and infection are proposed. It can affect any rib but the first and second ribs are most commonly involved.

Chronic obstructive airway disease: Chronic bronchitis, emphysema, and bronchial asthma are collectively known as obstructive airway disease.

Colloid: A substance that will not easily diffuse through membranes when dissolved in a liquid.

Complex regional pain syndrome type I (reflex sympathetic dystrophy): A pain syndrome that usually develops after an initiating noxious event with no identifiable major nerve injury, is not limited to the distribution of a single peripheral nerve, and is disproportional to the inciting event or expected healing response.

Connective tissue: Body tissue that provides and maintain form in the body. It serves to connect and bind the cells and organs and gives support to the body. Unlike the other tissue types of the body that are formed mainly by cells, the major constituent of connective tissue is its extracellular matrix, composed of protein fibers, an amorphous ground substance, and tissue fluid in addition to cells such as fibroblasts, fat cells and bone cells.

Conn's syndrome: Primary aldosteronism with increased production of aldosterone by abnormal zona glomerulosa (adenoma or hyperplasia) leading to hypertension through the increased reabsorption of sodium and water from the distal tubules. A benign adenoma accounts for 75% of cases of this syndrome.

CPPD: Calcium pyrophosphate dihydrate deposition disease, also called pseudogout and chondrocalcinosis, a type of crystal deposition arthropathy with such crystals deposited in cartilage, synovium, tendons, and ligaments.

Cushing's syndrome: A disease caused by abnormal stimulation of zona fasciculata of adrenal gland leading to excessive secretion of cortisol. The stimulation of the zona fasciculata may be stimulated by excess ACTH from the pituitary gland, or less commonly the ectopic production of ACTH (as in small cell lung cancer and neural crest tumors) or corticotropin-releasing factor (CRF) (as in bronchial carcinoid and prostate cancer). The disease may also be due to autonomous adrenal cortisol production due to adrenal adenoma, or hyperfunctioning adrenal carcinoma.

Detector sensitivity: The ratio between the output and the input variable being measured.

Dose rate: Dose rate expresses the time for which dose is administered.

Dosimetry: A process of calculating the level of radiation exposure from a radioactive source.

Dystrophic calcification: A type of soft tissue calcification that occurs in the setting of normal serum calcium and phosphate levels and occurs in damaged, inflamed, neoplastic, or necrotic tissue.

Ectopic hyperparathyroidism: Parathyroid disease due to abnormalities in ectopically located glands.

Effective half-life: Time required to reduce radioactivity by half by a combination of physical and biologic elimination processes.

Endochondral ossification: Most of the skeleton forms by this type of ossification where a preexisting cartilage forms first and then undergoes ossification.

Enteropathic arthropathies: Arthropathies associated with inflammatory bowel diseases including ulcerative colitis, Crohn's disease, Whipple's disease, intestinal bypass surgery and celiac disease.

Entheses: The sites of insertion of tendons, ligaments and articular capsule to bone.

Enthesopathies: A pathologic process affecting entheses particularly trauma and or inflammation resulting in regional periosteal reaction with osteoblastic bone activity.

Epididymis: A comma shaped structure lying on the testicle on its posterolateral surface.

Epididymitis: An inflammatory condition affecting the epididymis usually in adults secondary to infection or following trauma. Bacteria usually reach the epididymis from the prostate, seminal vesicles, urethra or uncommonly hematogenously.

Erythropoiesis: The formation of mature red blood cells in the bone marrow starting with the first stem cell progeny committed to erythroid differentiation and ending with the release of red cells into the circulation.

Eutopic hyperparathyroidism: Parathyroid disease with typical location of glands.

Exudate: An inflammatory extravascular fluid with a high protein content, much cellular debris, and a specific gravity above 1.020. This is the hallmark of acute inflammation, which may also be called exudative inflammation. It indicates significant alteration in the normal permeability of small blood vessels in the region of injury.

Fibrous dysplasia: A benign bone disorder characterized by the presence of the fibrous tissue in lesions of trabeculae of nonlamellar bone (woven bone), which remains essentially unchanged.

First-pass radionuclide angiography: Examination of the initial transit of a radionuclide bolus through the different major vascular compartments can provide information about the function of each chamber.

Flare pattern on bone scan: An initial apparent deterioration of primary or some or all metastatic lesions on the bone scan, followed by improvement usually accompanying successful treatment.

Fracture delayed union: Fracture union is delayed beyond the expected time (usually 9 months).

Fracture non-union: Complete cessation of repair process of a fracture.

Fracture: A break in the continuity of a bone.

Ganglioneuroma: A benign tumor found in older children and young adults that is most commonly present in the adrenal medulla and the posterior mediastinum. The tumor consists of mature ganglion cells and is well encapsulated; it is frequently calcified and rarely hormone active.

Gas exchange airways: Consists of the more distal bronchioles (respiratory) and the alveoli that are lined by nonciliated mucus membrane.

Gene therapy: A method designed to manipulate the expression of genes in order to inhibit tumor growth.

Gout: A metabolic disorder that results in hyperuricemia and leads to deposition of monosodium urate monohydrate crystals in various sites in the body, especially joint cartilage.

Heterotopic ossification: A specific type of soft tissue calcification that may or may not follow trauma and is due to a complex pathogenetic mechanism believed to be due to transformation of certain primitive cells of mesenchymal origin in the connective tissue septa within muscles, into bone forming cells.

Hibernated myocardium: Hibernation occurs in myocardium that has undergone a downregulation of contractile function, thus reducing cellular demand for energy, in response to chronic ischemia. It requires the restoration of blood flow in order to improve function.

Homeostasis: The term describing maintenance of static, or constant, conditions in the internal environment by means of positive and negative feedback of information.

Hydrocephalus: Conditions that produce imbalance between the rate of production and absorption of the cerebrospinal fluid, leading to dilatation of the ventricular system. They may result from obstruction to the flow and absorption of CSF or rarely from overproduction of CSF.

Hyperplasia: An increase in cell number.

Hypertrophic cardiomyopathy: An idiopathic process that affects mainly the LV myocardium, but the right ventricle may also be involved. Other causes of myocardial hypertrophy such as systemic hypertension and aortic valve stenosis must first be excluded.

Hypertrophic osteoarthropathy: A form of periostitis that may be painful and may be associated with clubbing of fingers and toes, sweating and thickening of skin. It may be primary or follows a variety of pathologic conditions predominantly intrathoracic and is characterized by periosteal new bone formation.

Hypertrophy: An increase in cell size which can lead to enlargement of an organ or part of it.

Immigrant cells: The cells that travel transiently through blood or lymph and enter connective tissue as needed. These cells include erythrocytes (red blood cells), granulocytes , monocytes, lymphocytes, plasma cells and platelets.

Impingement syndromes: A group of painful conditions caused by friction of joint tissue which include bone impingement, soft tissue impingement and entrapment neuropathy depending on the type of tissue involved.

Inflammation: A complex nonspecific tissue reaction to injury by living agents such as bacteria and viruses leading to infection, or nonliving agents including chemical, physical, immunologic or radiation injurious agents.

Inflammatory bowel disease (IBD): An idiopathic disease, probably involving an immune reaction of the body to its own intestinal tract. The two major types of IBD are ulcerative colitis and Crohn's disease.

Information density: The count number per square centimeter within an image.

Intensity: A term describing the energy or number of particles passing through an area unit per unit of time.

Intramembranous ossification: Occurs through the transformation of mesenchymal cells into osteoblasts seen in flat bones of the skull, part of the mandible and part of the clavicle.

Involucrum: A layer of new bone formation around the site of skeletal infection formed secondary to the body response to infection.

Ionizing radiation: A radiation that causes ionization (production of ion pair) when passing through a material.

Isotope dilution: Diluting a radiotracer (or tracer) of known activity (or mass) in an unknown volume. By measuring the degree to which the radiotracer was diluted by the unknown volume, one can determine the total volume (or mass) of the unknown volume.

Jodbasedow: The condition of iodine-induced hyperthyroidism, which characteristically occurs in persons with nodular thyroid glands after iodine supplementation in endemic goiter areas. Iodine-containing medical products, including amiodarone, radiographic dyes, and kelp, may also cause jodbasedow.

Juxtaglomerular apparatus: The afferent arteriole has specialized smooth muscle cells called juxtaglomerular (JG) cells that form this system and store renin and stretch receptors which respond to changes in arteriolar pressure. The system releases renin when stimulated.

Lactase deficiency: A common cause of malabsorption that is found in 15% of Caucasian, 50% of blacks and about 90% of Asians. Often, patients may have partial lactase deficiency that causes symptoms but not full-blown malabsorption syndrome. Treatment is to avoid lactose-containing dairy products (milk, ice cream, and cheese), and use lactose enzymes to aid in digestion.

Lisfranc injury: Fracture or fracture dislocation of tarsometatarsal joints.

List mode: An acquisition method for cardiac blood pool studies in patients with arrhythmias. Following acquisition of cardiac gated blood pool study, each individual beat can be reviewed to eliminate atrial or ventricular premature beats that exceed a determined R-R interval duration (arrhythmia rejection). The acceptable beats can then be framed in the most appropriate timing interval for the type of analysis needed.

Lower respiratory airways: Trachea, bronchi, bronchioles, and alveolar ducts connected by the larynx.

Maffucci syndrome: A nonhereditary disorder characterized by multiple enchondromas and multiple bony hemangiomas.

Malunion: Healing of a bone in a nonanatomic orientation.

Marine-Lenhart syndrome: Grave's disease with incidentally functioning nodule(s) which are responsive to thyroid stimulating hormone. It is not responsive to thyroid stimulating immunoglobulins. It appears as cold but after successful treatment with radioiodine, it will show uptake on follow-up thyroid scan since TSH level starts to rise.

Mast cells: The secretory cells that mediate immediate hypersensitivity reactions. These cells are distributed along blood vessels in connective tissue. Stimulation of these cells by a variety of stimuli such as mechanical trauma, heat, X-rays and toxins induces secretion of their granule contents, mainly histamine.

Megaloblastosis: A morphological abnormality that occurs predominantly in the erythroid precursor cells in the bone marrow and in other replicating cells in human subjects due to deficiency of vitamin B_{12} and folate or metabolic abnormalities involving these vitamins.

MEN (multiple endocrine neoplasia): An autosomal dominant syndrome that involves hyperfunctioning of two or more endocrine organs. Primary hyperparathyroidism, pancreatic endocrine tumors, and anterior pituitary gland neoplasms characterize type 1 MEN. Medullary thyroid carcinoma, pheochromocytoma, and hyperparathyroidism caused by parathyroid gland hyperplasia characterize type MEN 2A. MEN 2B is defined by medullary thyroid tumor and pheochromocytoma.

Metachondromatosis: A hereditary (autosomal dominant) disorder characterized by the presence of multiple enchondromas and osteochondromas.

Metaplasia: An alteration of cell differentiation.
Metastatic calcification: The type of soft tissue calcification that involves viable undamaged normal tissue as a result of hypercalcemia and/or hyperphosphatemia associated with increased calcium phosphate product locally or systematically.

Monoclonal antibody: An antibody derived from a single clone of cells and hence binds only to one unique epitope.

Moyamoya disease: A noninflammatory, nonatherosclerotic, nonamyloid vasculopathy characterized by chronic progressive stenosis or occlusion of the terminal internal carotid arteries. It occurs mainly under the age of 10 with a smaller peak during the 4th decade. It presents with transient ischemic attacks and occasionally headache and seizures. Intracranial hemorrhage is the serious complication.

Murine antibody: An antibody produced by mouse.

Mutation: Any inherited change in the genetic material involving irreversible alterations in the sequence of DNA nucleotides.

Myositis ossificans progressive: The congenital and rare form of heterotopic ossification.

Necrosis: Cellular death resulting from the progressive degradative action of enzymes on the lethally injured cells, ultimately leading to the processes of cellular swelling, dissolution, and rupture. The morphological appearance of necrosis is the result of denaturation of proteins and enzymatic digestion (autolysis or heterolysis) of the cell.

Nephron: The functional unit of the kidney. It consists of a glomerulus and a tubule. Urine is formed as a result of glomerular filtration, tubular reabsorption, and tubular secretion.

Neuroblastoma: A malignant tumor of the sympathetic nervous system of childhood. It accounts for up to 10% of childhood cancers and 15% of cancer deaths among children. Seventy-five percent of neuroblastoma patients are younger than 4 years. The tumor has the potential to mature into pheochromocytoma or ganglioneuroma.

Nonuniformity: A term describing variations of intensity of an image.

Ollier disease: A nonhereditary disorder characterized by multiple enchondromas with a predilection for unilateral distribution.

Osteochondritis dissecans: Transchondral fracture with fragmentation and separation of portions of cartilage or cartilage and bone which is most prevalent in adolescents.

Osteomalacia: Abnormal mineralization of bone with a decrease in bone density secondary to lack of both calcium and phosphorus with no decrease in the amount of osteoid (bone formation).

Osteomyelitis: A term applied to skeletal infection when it involves the bone marrow.

Osteopetrosis: A rare inherited metabolic bone disease characterized by a generalized increase in skeletal mass due to a congenital defect in the development or function of the osteoclasts leading to defective bone resorption.

Osteoporosis: Reduction of bone tissue amount increasing the likelihood of fractures.

Oxalosis: Deposition of calcium oxalate crystals that leads to arthropathy.

Pair production: When a photon with energy greater than 1.02 MeV is converted into an electron and a positron the process is called pair production. It occurs when the high energetic photon passes through a strong electric field.

Paraganglioma: Pheochromocytoma arising at sites other than adrenal medulla (extra-adrenal).

Parkinson's disease: A neurologic disorder characterized by tremor, rigidity, akinesia, bradykinesia and postural instability.

Pathologic fracture: A fracture at a site of preexisting abnormalities that weakens bone.

Phase image: A computer generated image representing evaluation of each pixel in the heart with respect to count changes over time. This helps identify abnormal timing of ventricular contraction.

Pheochromocytoma: A rare tumor arising from chromaffin cells of the adrenal medulla. It commonly produces excessive amounts of norepinephrine, attributable to autonomous functioning of the tumor, although large tumors secrete both norepinephrine and epinephrine and in some cases also dopamine. Releasing the catecholamine into the circulation causes hypertension and other signs.

Physical half-life: Time required for half of a radioactivity to decay.

Plantar fasciitis (calcaneal periosteitis): An inflammatory condition that can occur as an isolated entity such as secondary to occupation, degenerative or it may accompany spondyloarthropathies.

***Pneumocystis carinii (jiroveci)*:** An opportunistic pathogen currently classified as a fungus. It causes an infection leading to significant morbidity and mortality in human immunodeficiency virus and nonhuman immunodeficiency virus-associated immunosuppressed patients although it also occurs in nonimmunocompromised patients.

Podagra: A term describing affection of the metatarsophalangeal joint of the great toe in gout and the most typical finding of gouty arthritis.

Primary hyperparathyroidism: Hyperparathyroidism caused by neoplastic or hyperplastic parathyroid glands or when nonparathyroid tumors such as bronchogenic or renal cell carcinomas secrete ectopically parathyroid hormone or a biologically similar product.

Pseudoarthrosis: A gap between the fracture bone ends containing a space filled with fluid. Also termed false joint.

Pulmonary circulation: A low-pressure, low-resistance system through which oxygen enters and carbon dioxide is removed.

Radiolabeling: The process of attaching radioactive isotope.

Reactive arthritis (Reiter's disease): A syndrome characterized by a combination of nongonococcal urethritis, arthritis and conjunctivitis.

Renal osteodystrophy: A metabolic condition of bone associated with chronic renal failure.

Resolution: Ability to separate or discriminate very close quantities by a detector.

Rheumatoid arthritis: An autoimmune disease causing inflammation of connective tissue mainly in the joints with synovial inflammatory response triggered by immune complexes in the blood and synovial tissue through activation of plasma protein complement. This inflammation spreads from the synovial membrane to the articular cartilage, joint capsule and the surrounding tendons and ligaments leading to pain, loss of function and joint deformity.

SAPHO syndrome: A syndrome characterized by synovitis, acne, palmoplantar pustulosis, hyperostosis, and osteitis. The small and large joints of the feet, ankles, knees, hips, sacroiliac joints, and shoulders are affected by the synovitis.

Sarcoidosis: A multisystem granulomatous disorder, occurring most commonly in young adults, more commonly in blacks and in temperate areas with an unknown etiology, but it is believed to be due to exaggerated cellular immune response on the part of helper/inducer T lymphocytes to exogenous or autoantigens.

Scattered radiation: This term describes radiation that during its passage through a substance deviates in direction with possible loss of energy.

Secondary hyperparathyroidism: Hyperparathyroidism due to compensatory hyperplasia of parathyroids in response to hypocalcemia.

Septic tenosynovitis: An inflammatory condition affecting generally the flexor tendons of the hands and feet of diabetic patients and resulting from penetrating injuries or spread of infection from a contiguous focus of infection.

Sequestrum: Segmental bone necrosis that develops when normal blood supply to the bone is interrupted by the edema and ischemia produced by the inflammation.

Shin splints: Periosteal elevation with reactive bone formation secondary to extreme tension on muscles or muscle groups inserting on bones.

Slipped capital femoral epiphysis: Displacement of the proximal femoral epiphysis or simply femoral head from the femoral neck at the site of the growth plate during the growth condition.

Spondyloarthropathies: A group of seronegative arthropathies formerly called rheumatoid variants that

share common clinical and radiographic features with characteristic involvement of the sacroiliac joints, spine, and to various degrees the peripheral joints, which are linked to HLA B27 histocompatibility antigen and include ankylosing spondylitis, psoriatic arthritis , reactive arthritis (Reiter's disease), and enteropathic spondylitis.

Spondylolysis: A loss of continuity of bone of the neuroarch of the vertebra due to stress or trauma.

Spondylolisthesis: Forward movement of one vertebra on another usually as a result of fracture of the neuroarch.

Spontaneous intracranial hypotension (SIH): An increasingly recognized condition due to CSF leak without apparent prior cause. It can cause postural headache, which in this case is secondary to low CSF pressure.

Sprains: Tears to tendons.

Stem cells: Undifferentiated cells in adults known also as pluripotent cells, precursor cells that are not totally committed to a specific function.

Strains: Tears to ligaments.

Stress fracture: A pathologic condition of bone due to repeated episodes of stress; each is less forceful than that needed to cause acute fracture of the bony cortex.

Stunned myocardium: Continued dysfunction due to ischemia-induced oxidative stress.

Synovial joints: Specialized joints found mainly in the appendicular skeleton and which allow free motion.

Tertiary hyperparathyroidism: The condition of patients who develop hypercalcemia following long-standing secondary hyperparathyroidism due to the development of autonomous parathyroid hyperplasia, which may not regress after correction of the underlying condition, as with renal transplantation.

Thyrotropin-releasing hormone (TRH): A tripeptide originating from the hypothalamic median eminence, which stimulates the secretion and synthesis of thyroid stimulating hormone from anterior pituitary.

Toddler's fracture: Fracture in preschool children which is typically a nondisplaced spiral fracture of the mid tibia but also involves other fractures including the fibula, calcaneus, talus, metatarsal and cuboid bones in this age group.

Transient synovitis: A joint inflammation of unknown origin and self-limited course affecting most frequently boys between 5 and 10 years of age. It was known as toxic synovitis and affects preferentially the hip or knee and subsides without antibiotics.

T-score: A parameter used to express bone mineral density by relating an individual's bone density to the mean BMD of healthy young adults, matched for gender and ethnic group.

Tumor grading: Grading is a scheme that attempts to determine the degree of malignancy and is based on the evaluation of certain parameters such as degree of tumor cellularity, resemblance of tumor cells to their normal forebears morphologically and functionally, cellular pleomorphism or anaplasia, mitotic activity (number and abnormality), and necrosis.

Tumoral calcinosis: A type of soft tissue calcification characterized by large, calcified, periarticular soft-tissue masses of calcium phosphate near the large joints such as the hip, the shoulder, and the elbow, in addition to the wrist, feet, and hands.

Uniformity correction: Addition or subtraction of counts to the image in order to correct for flood field irregularities.

Upper respiratory airways: Nasopharynx and oropharynx.

Ventilation: The process by which air flows in and out of the gas exchange airways.

Ventricular ejection fraction: The stroke volume divided by the end-diastolic volume.

Whipple's disease: A systemic bacterial illness usually affecting middle age men causing malabsorption and presenting diarrhea, arthritis, fever, weight loss, swollen lymph nodes and skin pigmentation. It is diagnosed mainly by a small bowel biopsy through an endoscope, and the treatment is antibiotics for 1 year or longer.

Wolff-Chaikoff effect: An intrathyroid autoregulatory mechanism other than the hypothalamus-pituitary-thyroid axis mechanism. When intrathyroid iodine concentrations are significantly increased, the rate of thyroid hormone synthesis is decreased, with a reduction in iodothyronine synthesis and a decrease in the DIT/MIT ratio.

Woven bone: Immature nonlamellar bone that is later normally converted to lamellar bone.

Z-score: A parameter used to express bone mineral density by comparing the bone density value of an individual to the mean value expected for his/her age matched peer.

Subject Index

Printing and Binding: Stürtz GmbH, Würzburg